Nanophase and Nanocomposite Materials III

DISTRIBUTION STATEMENT A
Approved for Public Release
Distribution Unlimited

20000825 039

DTIC QUALITY INSPECTED 4

MATERIALS RESEARCH SOCIETY
SYMPOSIUM PROCEEDINGS VOLUME 581

Nanophase and Nanocomposite Materials III

Symposium held November 29–December 2, 1999, Boston, Massachusetts, U.S.A.

EDITORS:

Sridhar Komarneni
The Pennsylvania State University
University Park, Pennsylvania, U.S.A.

John C. Parker
CirQon Technologies Corporation
Gurnee, Illinois, U.S.A.

Horst Hahn
Darmstadt University of Technology
Darmstadt, Germany



Materials Research Society
Warrendale, Pennsylvania

This work was supported in part by the Office of Naval Research under Grant Number ONR: N00014-00-1-0029. The United States Government has a royalty-free license throughout the world in all copyrightable material contained herein.

Single article reprints from this publication are available through
University Microfilms Inc., 300 North Zeeb Road, Ann Arbor, Michigan 48106

CODEN: MRSPDH

Copyright 2000 by Materials Research Society.
All rights reserved.

This book has been registered with Copyright Clearance Center, Inc. For further information, please contact the Copyright Clearance Center, Salem, Massachusetts.

Published by:

Materials Research Society
506 Keystone Drive
Warrendale, PA 15086
Telephone (724) 779-3003
Fax (724) 779-8313
Web site: http://www.mrs.org/

Library of Congress Cataloging-in-Publication Data

Nanophase and nanocomposite materials III : symposium held November 29–December 2, 1999, Boston, Massachusetts, U.S.A. / editors, Sridhar Komarneni, John C. Parker, Horst Hahn
p.cm.—(Materials Research Society symposium proceedings, ISSN 0272-9172 ; v. 581)
Includes bibliographical references and indexes.
ISBN 1-55899-489-0
1. Nanostructure materials—Congresses. 2. Composite materials—Congresses. 3. Nanotechnology—Congresses. I. Title: Nanophase and nanocomposite materials 3. II. Title: Nanophase and nanocomposite materials three. III. Komarneni, Sridhar IV. Parker, John C. V. Hahn, Horst VI. Materials Research Society symposium proceedings ; v. 581
TA418.9.N35 N336 2000
620.1'1—dc21 00-028750

Manufactured in the United States of America

CONTENTS

Preface xvii

Materials Research Society Symposium Proceedings xviii

NANOPHASE CERAMICS, METALS AND ALLOYS

Solution-Based Synthesis of Magnesium Oxide Nanorods 3
Q. Wei and C.M. Lieber

Stoichiometry Control in Molecular Beam Deposited Nanocrystalline SnO_2 and TiO_2 Thin Films 9
H. Hoche, H. Hahn, F. Edelman, R. Nagel, and P. Werner

Electrical Properties of Nanocrystalline Tungsten Trioxide 15
A. Hoel, L.B. Kish, R. Vajtai, G.A. Niklasson, C.G. Granqvist, and E. Olsson

Preparation and Properties of Colloidal Particles: Silica on Yttrium Iron Garnet 21
R.H.M. Godoi, M. Jafelicci, Jr., and Joaquim Portillo

Synthesis of Cubic and Rhombohedral Phased Nanocrystalline SnO_2 Doped In_2O_3 [ITO] Powders With Coprecipitation Method 27
Bong-Chull Kim, Jeong-Joo Kim, and Se-Hong Chang

Effect of Vapor Pressure of H_2O on the Formation of Nanocrystalline TiO_2 Ultrafine Powders 33
K.R. Lee, S.J. Kim, J.S. Song, and S. Park

Superparamagnetic Ferrites Realization and Physical Obstacles 41
D. Vollath, E. Pellegrin, and D.V. Szabó

Synthesis of Passivated Metal Nanoparticles 47
Mark Green and Paul O'Brien

Preparation of Nanocrystalline Bismuth-Containing Powders Through Solution-Phase Reductions 53
Edward E. Foos, Alan D. Berry, Arthur W. Snow, and J. Paul Armistead

Synthesis and Characterization of Resorcinarene-Encapsulated Nanoparticles 59
Alexander Wei, Kevin B. Stavens, Stephen V. Pusztay, and Ronald P. Andres

Protein Supported Metallic Nanostructures as Catalysts 65
S. Behrens, W. Habicht, N. Boukis, E. Dinjus, M. Baum, and E. Unger

The Formation of High-Coercivity, Oriented, Nanophase Cobalt Precipitates in Al_2O_3 Single Crystals by Ion Implantation 71
S. Honda, F.A. Modine, T.E. Haynes, A. Meldrum, J.D. Budaik, K.J. Song, J.R. Thompson, and L.A. Boatner

Can We Determine the Barrier Resistance for Electron Transport in Ligand Stabilized Nanoparticles from Integral Conductance Measurements? 77
U. Simon

Synthesis, Characterization, and Utilization of Single Crystalline Nanoparticles of Silver 83
Yadong Yin, Ziyi Zhong, Byron Gates, and Younan Xia

Structure and Stability of Nanoscale Melt Spun Mg-Ca-Zn Alloys 89
P.M. Jardim, I.G. Solórzano, J.B. Vander Sande, B.S. You, and W.W. Park

Structure and Magnetic Property Correlation in Nanocrystalline $SmFe_9$ 95
C. Djega-Mariadassou and L. Bessais

Glass Formation and Nanostructure Development in Al-Based Alloys 101
R.I. Wu, G. Wilde, and J.H. Perepezko

Transmission Electron Microscopy Study of Gold-Coated Iron Core-Shell and Au/Fe/Au Onion-Like Nanoparticles Synthesized Using Reverse Micelles 107
W.L. Zhou, E.E. Carpenter, J. Sims, A. Kumbhar, and C.J. O'Connor

NANOPHASE SEMICONDUCTORS AND NON-OXIDE CERAMICS

Solution-Processed Inorganic Transistors and Sub-Micron Non-Lithographic Patterning Using Nanoparticle Inks 115
Brent A. Ridley, Babak Nivi, Brian N. Hubert, Colin A. Bulthaup, Eric J. Wilhelm, and Joseph M. Jacobson

***Nano-Sized Semiconducting Oxide Powders for Thick Film Gas Sensors: From Powder Processing to Environmental Monitoring Devices** 121
Enrico Traversa, Maria Cristina Carotta, and Giuliano Martinelli

Synthesis and Characterization of Mn Doped CdS Quantum Dots From a Single Source Precursor 133
M. Azad Malik, Paul O'Brien, and N. Revaprasadu

Synthesis and Characterization of Strongly Fluorescent CdTe Nanocrystal Colloids 139
Frederic V. Mikulec and Moungi G. Bawendi

Electrochemical Atomic-Layer Epitaxy: Electrodeposition of III-V and II-VI Compound Semiconductors 145
Travis L. Wade, Billy H. Flowers, Jr., Raman Vaidyanathan, Kenneth Mathe, Clinton B. Maddox, Uwe Happek, and John L. Stickney

Nanocrystalline Alloys of II-VI Semiconductors From Molecular Multilayer Templates 151
L. Cristofolini, P. Facci, and M.P. Fontana

Solar Cell Contacts Using Nanosized Dispersions 157
Doug Schulz, R. Ribelin, X. Wu, K.M. Jones, R.J. Matson, C.J. Curtis, T. Gessert, and D.S. Ginley

Size Effect in Germanium Nanostructures Fabricated by Pulsed Laser Deposition 163
K.M. Hassan, A.K. Sharma, J. Narayan, J.F. Muth, C.W. Teng, and R.M. Kolbas

Functionalization of CdSe and GaAs Quantum Dots 169
Sebastian J. Nørager, Michael Lazell, and Paul O'Brien

*Invited Paper

Synthesis of Self-Capped Metal Sulfide Nanoparticles 175
Mike Lazell and Paul O'Brien

Sputtering Effects and Two Dimensional Arrangement of Nanoparticles in Insulators Under High Flux Cu^- Implantation 181
N. Kishimoto, C.G. Lee, N. Umeda, Y. Takeda, and V.T. Gritsyna

Crystallization Behavior of Amorphous $Si_{0.5}Ge_{0.5}$ Films Observed by Positron Annihilation 187
F. Edelman, F. Börner, R. Krause-Rehrberg, P. Werner, R. Weil, W. Beyer, and R. Butz

Synthesis of Nanostructured WC Films by Supersonic Impaction of Nanoparticle Aerosols 193
W.T. Nichols, G. Malyavanatham, M.P. Beam, D.E. Henneke, J.R. Brock, M.F. Becker, and J.W. Keto

Structure of Polycrystalline Silicon Films by Glow-Discharge Decomposition Using $SiH_4/H_2/SiF_4$ at Low Temperature 199
R. Tsuchida, M. Syed, T. Inokuma, Y. Kurata, and S. Hasegawa

Formation of Nanocrystalline SiC Powder from Chlorine-Containing Polycarbosilane Precursors 205
Brian S. Mitchell, Haoyue Zhang, Martin Ade, Dirk Kurtenbach, and Eberhard Müller

NANOWIRES

Structure and Composition of Bismuth Nanowire Arrays 213
M.S. Sander, Y-M. Lin, M.S. Dresselhaus, and R. Gronsky

Synthesis of Single Crystal Bismuth-Telluride and Lead-Telluride Nanowires for New Thermoelectric Materials 219
Q. Wei and C.M. Lieber

Controlled Growth of Amorphous Silicon Nanowires Via a Solid-Liquid-Solid (SLS) Mechanism 225
H.F. Yan, Y.J. Xing, Q.L. Hang, D.P. Yu, J. Xu, H.Z. Zhang, Z.H. Xi, and S.Q. Feng

Oriented Si Nanowires Grown Via an SLS Mechanism 231
Y.J. Xing, Z.H. Xi, Q.L. Hang, H.F. Yan, S.Q. Feng, J. Xu, H.Z. Zhang, and D.P. Yu

Composite Nanowires From Ion Beam Modification of Si Nanowires 235
X.T. Zhou, H.Y. Peng, N.G. Shang, N. Wang, I. Bello, C.S. Lee, and S.T. Lee

Arc Discharge for the Synthesis of Monoclinic Ga_2O_3 Nanowires 239
Young Chul Choi, Dong Jae Bae, Seung Mi Lee, Young Soo Park, Young Hee Lee, Gyeong-Su Park, Won Bong Choi, Nae Sung Lee, and Jong Min Kim

Structural Magnetic Properties of the Electrochemically Deposited Arrays of Nickel Nanowires 245
H.R. Khan and K. Petrikowski

MECHANICAL MILLING AND OTHER TECHNIQUES FOR ALLOYS

Nanocomposites in the Systems $Fe_{1-x}O$-Fe_3O_4 and MgO-$MgFe_2O_4$ Produced by Mechanical Alloying 253
A. Huerta, H.A. Calderon, H. Yee-Madeira, M. Umemoto, and K. Tsuchiya

Magnetic Hardening of Mechanically Alloyed $SmFe_{11-x}Co_xTi$ 259
L. Bessais and C. Djega-Mariadassou

The Role of Boron in the Mechanical Milling of Titanium-6%Aluminum-4%Vanadium Powders 265
A.P. Brown, R. Brydson, C. Hammond, T.M.T. Godfrey, and A. Wisbey

Steady State Phase Diagram of Cu-Ag Under Ball Milling: An XRD and APFIM Study 271
F. Wu, P. Bellon, A.J. Melmed, and T.A. Lusby

Formation of Bulk Magnetic Nanostructured $Fe_{40}Ni_{40}P_{14}B_6$ Alloys by Metastable Liquid State Phase Separation 277
Q. Li and H.W. Kui

Supersonic Cluster Beam Synthesis of Nanophase Materials 283
P. Milani, S. Iannotta, F. Biasioli, P. Piseri, and E. Barborini

NANOCOMPOSITES

Synthesis and Characterization of CdSe/CdS Core-Shell and CdSe/CdS Composites 291
M. Azad Malik, Paul O'Brien, and N. Revaprasadu

Magnetic Entropy Change of Nanocomposites Composed of a Silver Matrix and Grains of Iron-Oxide or -Nitride 297
T.A. Yamamoto, M. Tanaka, K. Shiomi, T. Nakayama, K. Nishimaki, T. Nakagawa, T. Numazawa, M. Katsura, and K. Niihara

Residual Stress Determination and Subsurface Microstructure in Ground and Polished Alumina/Silicon Carbide Nanocomposites and Monolithic Alumina Ceramics 303
H.Z. Wu, S.G. Roberts, A.J. Winn, and B. Derby

Nanocomposite Material, Liquid Crystal-Aerosil Particles: Dielectric and Photon Correlation Spectroscopy Investigations 309
F.M. Aliev and G.P. Sinha

The Microstructure and Properties of Framework Zirconium Phosphates Based Nanocomposites-Catalysts of Alkane Isomerization 315
Vladislav A. Sadykov, S.N. Pavlova, G.V. Zabolotnaya, R.I. Maximovskaya, D.I. Kochubei, V.V. Kriventsov, G.V. Odegova, N.M. Ostrovskii, O.B. Bel'skaya, V.K. Duplyakin, V.I. Zaikovskii, E.A. Paukshtis, E.B. Burgina, S.V. Tsybulya, M.V. Chaikina, N.N. Kuznetsova, V.V. Lunin, R. Roy, and D.K. Agrawal

Nanocomposites nc-TiN/a-Si_3N_4/a- and nc-$TiSi_2$ With Hardness Exceeding 100 GPa and High Fracture Toughness 321
S. Veprek, A. Niederhofer, K. Moto, P. Nesládek, H. Männling, and T. Bolom

Crack Healing in an Alumina/Silicon Carbide Nanocomposite After Grinding and Annealing 327
H.Z. Wu, J.M. Titchmarsh, S.G. Roberts, and B. Derby

Fe-Al_2O_3 Nanocomposite: Synthesis and Magnetic Properties 333
A. Santos, W.A.A. Macedo, J.D. Ardisson, A.D.C. Viegas, and J.E. Schmidt

CVD of Carbide Multi-Phased Coatings 339
K.E. Versprille, Hua Xia Ji, C.C. Amato-Wierda, P.J. Ramsey, and D.A. Wierda

XPS Study of Pt/$Ce_xZr_{1-x}O_2$/Si Composite Systems 345
A. Norman, R. Sporken, A. Galtayries, F. Mirabella, K. Keveney, M. Pijolat, R. Baker, and S. Bernal

SOL-GEL AND ORGANIC-INORGANIC NANOCOMPOSITES

***Transparent Monolithic Metal Ion Containing Nanophase Aerogels** 353
William M. Risen, Jr., Xiangjun Hu, Shuang Ji, and Kenneth Littrell

Preparation of Aerogel and Xerogel Nanocomposite Materials 363
M.F. Casula, A. Corrias, and G. Paschina

Fiber Reinforced Epoxy Resin Composite Materials Using Carboxylate-Alumoxanes as Cross-Linking Agents 369
Cullen T. Vogelson, Yoshihiro Koide, and Andrew R. Barron

Thin Polytetrafluoroethylene Organosilane Nanocomposite Films Used as Ultra Low Dielectric Constant Materials in Microelectronics 375
Shichun Qu, Tom Rosenmayer, Ping Xu, and Perry Spevack

Proton Conducting Organic/Inorganic Nanocomposite Polymer Electrolytic Membrane Synthesized by Sol-Gel Process 381
I. Honma, S. Nomura, and H. Nakajima

Modified Sol-Gel Synthesis of Vanadium Oxide Nanocomposites Containing Surfactant Ions 387
Arthur Dobley, Peter Y. Zavalij, and M. Stanley Whittingham

Vanadium Oxide Nanotubes With Diamine Templates 393
F. Krumeich, H-J. Muhr, M. Niederberger, F. Bieri, M. Reinoso, and R. Nesper

*Invited Paper

A Nanocomposite Poly(methyl-methacrylate) Bone Cement 399
Andreas H. Gomoll, Anuj Bellare, Wolfgang Fitz,
Thomas S. Thornhill, Richard D. Scott, Peter R. Jemian,
and Gabrielle G. Long

Electroluminescence Devices With CdS and CdS:Mn Nanoparticles and Polymer Blends 405
Ch. Brugger, S. Tasch, M. Lal, P.N. Prasad, and G. Leising

Preparation of Submicron and Micron Size Cr (IV) Optical Composites 411
L.L. Isaacs, V. Petricevic, BaoPing Wang, Jinpin Ying,
and R.R. Alfano

NANOCOMPOSITES USING MESOPOROUS AND LAYERED HOSTS

Quantum Confined Gallium Nitride in a Mesoporous Matrix of MCM-41 417
H. Winkler, R.A. Fischer, R. Schmechel, and H. von Seggern

Preparation of Highly Ordered Mesoporous Thin Film With Alkyltrimethylammonium ($CnTMA^+$) 423
Y. Goto, N. Sugimoto, Y. Fukushima, Y. Imada, Y. Kubota,
and Y. Sugi

Phase Transition and Control of Self-Assembled Mesostructured Vanadia/Surfactant Composites 429
I. Honma, Y. Yagi, H.S. Zhou, A. Endo, M. Miyayama, and
T. Kudo

Nanocomposites Based Upon Alumina and Zirconia Pillared Clays Loaded With Transition Metal Cations and Clusters of Precious Metals: Synthesis, Properties and Catalysis of NOx Selective Reduction by Hydrocarbons 435
Vladislav A. Sadykov, R.V. Bunina, G.M. Alikina, V.P. Doronin,
T.P. Sorokina, D.I. Kochubei, B.N. Novgorodov, E.A. Paukshtis,
V.B. Fenelonov, A.Yu. Derevyankin, A.S. Ivanova, V.I. Zaikovskii,
T.G. Kuznetsova, B.A. Beloshapkin, V.N. Kolomiichuk, L.M. Plasova,
V.A. Matyshak, G.A. Konin, A.Ya. Rozovskii, V.F. Tretyakov,
T.N. Burdeynaya, M.N. Davydova, J.R.H. Ross, J.P. Breen, and
F.C. Meunier

Soft Chemical Design of Transition-Metal-Oxide/Clay Layered Nanocomposites 441
Kiyoshi Fuda, Shuji Narita, Shuji Kudo, Kenji Murakami, and Toshiaki Matsunaga

CHARACTERIZATION, PROPERTIES AND APPLICATIONS OF NANOPHASES AND NANOCOMPOSITES

***Catalytic Activity and Surface Characterization Study of Pd Supported on Nanocrystalline and Polycrystalline CeO_2** 449
Gar B. Hoflund, Zhenhua Li, Timothy J. Campbell, William S. Epling, and Horst W. Hahn

Electrical Resistivity as a Characterization Tool for Nanocrystalline Metals 461
J.L. McCrea, K.T. Aust, G. Palumbo, and U. Erb

Characterization of Voids in Rutile Nanoparticles by Transmission Electron Microscopy 467
S. Turner

Ultrasonic Force Microscopic Characterization of Nanosized Copper Particles 473
E.J. Schumaker, L. Shen, M.J. Ruddell, S. Sathish, and P.T. Murray

Power of Mass Spectrometry for Analyzing Organometallic Molecules as Precursor of Nanomaterials 479
G.F. Strouse and J.J. Gaumet

Optical Characterization of a Spheroidal Nanoparticle on a Substrate 485
Carlos E. Román-Velázquez, Cecilia Noguez, and Rubén G. Barrera

Dielectric Characterization of Thin Films Consisting of Tin Doped Indium Oxide Nanoparticles 491
A. Hultåker and G.A. Niklasson

Synthesis and Characterization of Manganese Vanadium Oxides as Cathodes in Lithium Batteries 497
Fan Zhang, Peter Zavalij, and M. Stanley Whittingham

*Invited Paper

Z-Contrast STEM Imaging and EELS of CdSe Nanocrystals: Towards the Analysis of Individual Nanocrystal Surfaces 503
A.V. Kadavanich, T. Kippeny, M. Erwin, S.J. Rosenthal, and S.J. Pennycook

Hysteresis Loop Shifts in Magnetic Field Cooled FeOOH Nanoparticles 511
M.S. Seehra, Paromita Roy, and A. Manivannan

Atomic Scale Characterization of Electrodeposited Nanocrystalline Ni-P Alloys 517
Matthias Abraham, Mattias Thuvander, Helen M. Lane, Alfred Cerezo, and George D.W. Smith

Nanoporous Alumina Coatings for Medical Implants and Stents—Radiotherapy, Drug Delivery, Biological Compatibility 523
T. Sawitowski, W. Brandau, A. Fischer, A. Heilmann, and G. Schmid

Micro-Raman Study of Self-Assembled Nanostructures: (1-x)PZN:xPT Solid Solution 529
S. Gupta, R.S. Katiyar, R. Guo, and A.S. Bhalla

Microstructural and Magnetic Properties on Graphitic Encapsulated Ni Nanocrystals and Pure Ni Nanoparticles with NiO Layer 535
Xiangcheng Sun, M. Jose Yacaman, and F. Morales

Temperature Dependence of the Electrical Resistivity in Nanocrystalline Gold Films Made by Advanced Gas Deposition 541
J. Ederth, L.B. Kiss, G.A. Niklasson, C.G. Granqvist, and E. Olsson

Sintering Behavior of Nano-Ceramic Coatings 547
J.Th.M. De Hosson, R. Popma, and J. Hooijmans

Nanoporous Alumina Films Prepared From Colloidal Solution 553
Vladimir Petrovsky, Harlan U. Anderson, and Tatiana Petrovsky

Chemical Reactions on the Surface of SnO_2 Nanosized Powders at the Origin of the Gas Sensing Properties: FTIR Investigation 559
M-I. Baraton and L. Merhari

Optical Properties of Nanocrystalline Silicon Films With Different Deposition Temperatures 565
A.M. Ali, T. Inokuma, Y. Kurata, and S. Hasegawa

Insulator-Metal Transition in Nanostructured Ni-Al Thin Films 571
H.P. Ng and A.H.W. Ngan

Microstructure and Mechanical Properties of Oxide Eutectic Fibers 577
S.D. Durbin, A. Yoshikawa, K. Hasegawa, J-H. Lee, B.M. Epelbaum, T. Fukuda, and Y. Waku

***Features of Fracture Surface and Grain Boundary Structure of Boride/Nitride Materials** 583
R.A. Andrievski, G.V. Kalinnikov, and D.V. Shtansky

Thermoelectric Properties of Bi_2Te_3-Sb_2Te_3 Compounds Prepared by MA-Pulse Discharge Sintering Process 591
R.E. Park, Y.H. Park, and T. Abe

Raman Shift and Broadening in Stress-Minimized Ge Nanocrystals in Silicon Oxide Matrix 597
Y.X. Jie, C.H.A. Huan, A.T.S. Wee, and Z.X. Shen

Morphological Stability of Ni(Al)/Ni_3Al Nanolaminate Composites 603
Jason P. Fain, Rajarshi Banerjee, Daniel Josell, Peter M. Anderson, Hamish Fraser, Natalia Tymiak, and William Gerberich

Relationship Between Thermally Activated Atomic Diffusion Processes in Co-Cu Nanoscale Granular Films and Electric/Magnetic Properties 609
F. Spizzo, F. Ronconi, P. Vavassori, G. Bordin, D. Bisero, L. Pareti, and G. Turilli

Understanding the Second Harmonic Generation of Light From Nanometal Composites 615
M.L. Sandrock and Colby A. Foss, Jr.

Measuring the Dielectric Properties of Nanostructures Using Optical Reflection and Transmission: Bismuth Nanowires in Porous Alumina 623
M.R. Black, Y.M. Lin, M.S. Dresselhaus, M. Tachibama, S. Fang, O. Rabin, F. Ragot, P.C. Eklund, and Bruce Dunn

*Invited Paper

Colossal Hopping Magnetoresistance of GaAs/ErAs Nanocomposites 629
A.G. Petukhov, M. Foygel, and A. Chantis

Thermally Driven Shape Instability of Multilayer Structures 635
P. Troche, J. Hoffmann, C. Herweg, Ch. Lang, H.C. Freyhardt, and D. Rudolph

Magnetic Hardening Induced by Exchange Coupling in Mechanically Milled Antiferromagnetic-Ferromagnetic Composites 641
J. Sort, J. Nogués, X. Amils, S. Suriñach, J.S. Muñoz, and M.D. Baró

Study of the Luminescence of Eu-Doped Nanocrystalline Si/SiO_2 Systems Prepared by RF Co-Sputtering 647
G.A. Nery, A. Mahfoud, L.F. Fonseca, H. Liu, O. Resto, and S.Z. Weisz

Screen-Printed Dye-Sensitized Large Area Nanocrystalline Solar Cell 653
T.K. Gupta, L.J. Cirignano, K.S. Shah, L.P. Moy, D.J. Kelly, M.R. Squillante, G. Entine, and G.P. Smestad

Carboxylate-Alumoxanes: Precursors for Heterogeneous Catalysts 659
Christopher D. Jones, David S. Brown, Larry L. Marshall, and Andrew R. Barron

MOLECULAR-DYNAMICS SIMULATIONS

Intercluster Interaction of TiO_2 Nanoclusters Using Variable-Charge Interatomic Potentials 667
Shuji Ogata, Hiroshi Iyetomi, Kenji Tsuruta, Fuyuki Shimojo, Rajiv K. Kalia, Aiichiro Nakano, and Priya Vashishta

Tight-Binding Molecular Dynamics of Ceramic Nanocrystals Using PC-Based Parallel Machines 673
Kenji Tsuruta, Hiroo Totsuji, and Chieko Totsuji

Author Index 679

Subject Index 685

PREFACE

This volume contains the proceedings of Symposium F, "Nanophase and Nanocomposite Materials III," held November 29–December 2, at the 1999 MRS Fall Meeting in Boston, Massachusetts. This symposium is the third one of this series which began at the 1992 MRS Fall Meeting. The objective of this third symposium was to provide a forum to review the recent advances in nanophase and nanocomposite materials and to address the future prospects for these materials. Scientists from many parts of the world participated to present and discuss synthesis, processing, properties and applications of nanophase and nanocomposite materials. A total of about 240 papers from 23 countries were presented from academic institutions, government research organizations, and private industries. The 107 papers published in this proceedings have been refereed and presented as nine chapters.

Sridhar Komarneni
John C. Parker
Horst Hahn

January 2000

MATERIALS RESEARCH SOCIETY SYMPOSIUM PROCEEDINGS

Volume 557— Amorphous and Heterogeneous Silicon Thin Films: Fundamentals to Devices—1999, H.M. Branz, R.W. Collins, H. Okamoto, S. Guha, R. Schropp, 1999, ISBN: 1-55899-464-5

Volume 558— Flat-Panel Displays and Sensors—Principles, Materials and Processes, F.R. Libsch, B. Chalamala, R. Friend, T. Jackson, H. Ohshima, 2000, ISBN: 1-55899-465-3

Volume 559— Liquid Crystal Materials and Devices, T.J. Bunning, S.H. Chen, L.C. Chien, T. Kajiyama, N. Koide, S-C.A. Lien, 1999, ISBN: 1-55899-466-1

Volume 560— Luminescent Materials, J. McKittrick, B. DiBartolo, K. Mishra, 1999, ISBN: 1-55899-467-X

Volume 561— Organic Nonlinear Optical Materials and Devices, B. Kippelen, H.S. Lackritz, R.O. Claus, 1999, ISBN: 1-55899-468-8

Volume 562— Polycrystalline Metal and Magnetic Thin Films, D.E. Laughlin, K.P. Rodbell, O. Thomas, B. Zhang, 1999, ISBN: 1-55899-469-6

Volume 563— Materials Reliability in Microelectronics IX, C.A. Volkert, A.H. Verbruggen, D.D. Brown, 1999, ISBN: 1-55899-470-X

Volume 564— Advanced Interconnects and Contacts, D.C. Edelstein, T. Kikkawa, M.C. Öztürk, K-N. Tu, E.J. Weitzman, 1999, ISBN: 1-55899-471-8

Volume 565— Low-Dielectric Constant Materials V, J. Hummel, K. Endo, W.W. Lee, M. Mills, S-Q. Wang, 1999, ISBN: 1-55899-472-6

Volume 566— Chemical-Mechanical Polishing—Fundamentals and Challenges, S.V. Babu, S. Danyluk, M. Krishnan, M. Tsujimura, 2000, ISBN: 1-55899-473-4

Volume 567— Ultrathin SiO_2 and High-K Materials for ULSI Gate Dielectrics, H.R. Huff, C.A. Richter, M.L. Green, G. Lucovsky, T. Hattori, 1999, ISBN: 1-55899-474-2

Volume 568— Si Front-End Processing—Physics and Technology of Dopant-Defect Interactions, H-J.L. Gossmann, T.E. Haynes, M.E. Law, A.N. Larsen, S. Odanaka, 1999, ISBN: 1-55899-475-0

Volume 569— *In Situ* Process Diagnostics and Modelling, O. Auciello, A.R. Krauss, E.A. Irene, J.A. Schultz, 1999, ISBN: 1-55899-476-9

Volume 570— Epitaxial Growth, A-L. Barabási, M. Krishnamurthy, F. Liu, T.P. Pearsall, 1999, ISBN: 1-55899-477-7

Volume 571— Semiconductor Quantum Dots, S.C. Moss, D. Ila, H.W.H. Lee, D.J. Norris, 2000, ISBN: 1-55899-478-5

Volume 572— Wide-Bandgap Semiconductors for High-Power, High-Frequency and High-Temperature Applications—1999, S.C. Binari, A.A. Burk, M.R. Melloch, C. Nguyen, 1999, ISBN: 1-55899-479-3

Volume 573— Compound Semiconductor Surface Passivation and Novel Device Processing, H. Hasegawa, M. Hong, Z.H. Lu, S.J. Pearton, 1999, ISBN: 1-55899-480-7

Volume 574— Multicomponent Oxide Films for Electronics, M.E. Hawley, D.H.A. Blank, C-B. Eom, D.G. Schlom, S.K. Streiffer, 1999, ISBN: 1-55899-481-5

Volume 575— New Materials for Batteries and Fuel Cells, D.H. Doughty, L.F. Nazar, M. Arakawa, H-P. Brack, K. Naoi, 2000, ISBN: 1-55899-482-3

Volume 576— Organic/Inorganic Hybrid Materials II, L.C. Klein, L.F. Francis, M.R. DeGuire, J.E. Mark, 1999, ISBN: 1-55899-483-1

Volume 577— Advanced Hard and Soft Magnetic Materials, M. Coey, L.H. Lewis, B-M. Ma, T. Schrefl, L. Schultz, J. Fidler, V.G. Harris, R. Hasegawa, A. Inoue, M.E. McHenry, 1999, ISBN: 1-55899-485-8

Volume 578— Multiscale Phenomena in Materials—Experiments and Modeling, D.H. Lassila, I.M. Robertson, R. Phillips, B. Devincre, 2000, ISBN: 1-55899-486-6

Volume 579— The Optical Properties of Materials, J.R. Chelikowsky, S.G. Louie, G. Martinez, E.L. Shirley, 2000, ISBN: 1-55899-487-4

Volume 580— Nucleation and Growth Processes in Materials, A. Gonis, P.E.A. Turchi, A.J. Ardell, 2000, ISBN: 1-55899-488-2

Volume 581— Nanophase and Nanocomposite Materials III, S. Komarneni, J.C. Parker, H. Hahn, 2000, ISBN: 1-55899-489-0

Volume 582— Molecular Electronics, S.T. Pantelides, M.A. Reed, J. Murday, A. Aviram, 2000, ISBN: 1-55899-490-4

MATERIALS RESEARCH SOCIETY SYMPOSIUM PROCEEDINGS

Volume 583— Self-Organized Processes in Semiconductor Alloys, A. Mascarenhas, B. Joyce, T. Suzuki, D. Follstaedt, 2000, ISBN: 1-55899-491-2
Volume 584— Materials Issues and Modeling for Device Nanofabrication, L. Merhari, L.T. Wille, K. Gonsalves, M.F. Gyure, S. Matsui, L.J. Whitman, 2000, ISBN: 1-55899-492-0
Volume 585— Fundamental Mechanisms of Low-Energy-Beam-Modified Surface Growth and Processing, S. Moss, E.H. Chason, B.H. Cooper, T. Diaz de la Rubia, J.M.E. Harper, R. Murti, 2000, ISBN: 1-55899-493-9
Volume 586— Interfacial Engineering for Optimized Properties II, C.B. Carter, E.L. Hall, C.L. Briant, S. Nutt, 2000, ISBN: 1-55899-494-7
Volume 587— Substrate Engineering—Paving the Way to Epitaxy, D.P. Norton, D.G. Schlom, N. Newman, D.H. Matthiesen, 2000, ISBN: 1-55899-495-5
Volume 588— Optical Microstructural Characterization of Semiconductors, J. Piqueras, T. Sekiguchi, M.S. Unlu, N.M. Kalkhoran, 2000, ISBN: 1-55899-496-3
Volume 589— Advances in Materials Problem Solving with the Electron Microscope, J. Bentley, U. Dahmen, C. Allen, I. Petrov, 2000, ISBN: 1-55899-497-1
Volume 590— Applications of Synchrotron Radiation Techniques to Materials Science V, S.R. Stock, D.L. Perry, S.M. Mini, 2000, ISBN: 1-55899-498-X
Volume 591— Nondestructive Methods for Materials Characterization, T. Matikas, N. Meyendorf, G. Baaklini, R. Gilmore, 2000, ISBN: 1-55899-499-8
Volume 592— Structure and Electronic Properties of Ultrathin Dielectric Films on Silicon and Related Structures, H.J. von Bardeleben, D.A. Buchanan, A.H. Edwards, T. Hattori, 2000, ISBN: 1-55899-500-5
Volume 593— Amorphous and Nanostructured Carbon, J. Robertson, J.P. Sullivan, O. Zhou, T.B. Allen, B.F. Coll, 2000, ISBN: 1-55899-501-3
Volume 594— Thin Films—Stresses and Mechanical Properties VIII, R. Vinci, O. Kraft, N. Moody, P. Besser, E. Shaffer II, 2000, ISBN: 1-55899-502-1
Volume 595— GaN and Related Alloys—1999, R. Feenstra, T. Myers, M.S. Shur, H. Amano, 2000, ISBN: 1-55899-503-X
Volume 596— Ferroelectric Thin Films VIII, R.W. Schwartz, S.R. Summerfelt, P.C. McIntyre, Y. Miyasaka, D. Wouters, 2000, ISBN: 1-55899-504-8
Volume 597— Thin Films for Optical Waveguide Devices and Materials for Optical Limiting, K. Nashimoto, B.W. Wessels, J. Shmulovich, A.K-Y. Jen, K. Lewis, R. Pachter, R. Sutherland, J. Perry, 2000, ISBN: 1-55899-505-6
Volume 598— Electrical, Optical, and Magnetic Properties of Organic Solid-State Materials V, S.P. Ermer, J.R. Reynolds, J.W. Perry, A.K-Y. Jen, Z. Bao, 2000, ISBN: 1-55899-506-4
Volume 599— Mineralization in Natural and Synthetic Biomaterials, P. Li, P. Calvert, R.J. Levy, T. Kokubo, C.R. Scheid, 2000, ISBN: 1-55899-507-2
Volume 600— Electroactive Polymers, Q.M. Zhang, T. Furukawa, Y. Bar-Cohen, J. Scheinbeim, 2000, ISBN: 1-55899-508-0
Volume 601— Superplasticity—Current Status and Future Potential, P.B. Berbon, M.Z. Berbon, T. Sakuma, T.G. Langdon, 2000, ISBN: 1-55899-509-9
Volume 602— Magnetoresistive Oxides and Related Materials, M. Rzchowski, M. Kawasaki, A.J. Millis, M. Rajeswari, S. von Molnár, 2000, ISBN: 1-55899-510-2
Volume 603— Materials Issues for Tunable RF and Microwave Devices, Q. Jia, F.A. Miranda, D.E. Oates, X. Xi, 2000, ISBN: 1-55899-511-0
Volume 604— Materials for Smart Systems III, M. Wun-Fogle, K. Uchino, Y. Ito, R. Gotthardt, 2000, ISBN: 1-55899-512-9
Volume 605— Materials Science of Microelectromechanical Systems (MEMS) Devices II, M.P. deBoer, A.H. Heuer, S.J. Jacobs, E. Peeters, 2000, ISBN: 1-55899-513-7
Volume 606— Chemical Processing of Dielectrics, Insulators and Electronic Ceramics, A.C. Jones, J. Veteran, S. Kaushal, D. Mullin, R. Cooper, 2000, ISBN: 1-55899-514-5
Volume 607— Infrared Applications of Semiconductors III, B.J.H. Stadler, M.O. Manasreh, I. Ferguson, Y-H. Zhang, 2000, ISBN: 1-55899-515-3
Volume 608— Scientific Basis for Nuclear Waste Management XXIII, R.W. Smith, D.W. Shoesmith, 2000, ISBN: 1-55899-516-1

Prior Materials Research Society Symposium Proceedings available by contacting Materials Research Society

Nanophase Ceramics, Metals
and Alloys

SOLUTION-BASED SYNTHESIS OF MAGNESIUM OXIDE NANORODS

Q. WEI, C.M. LIEBER
Department of Chemistry and Chemical Biology, Harvard University, Cambridge, MA 02138

ABSTRACT

A solution-based synthesis route was developed to produce large quantities of MgO nanorods. Hydrated basic magnesium chloride, which has needle-like crystal structure, was used as a precursor. A subsequent two-step transformation process with magnesium hydroxide as an intermediate product was used to preserve the morphology of the precursor to yield magnesium oxide nanorods. Scanning electron microscopy, powder X-ray diffraction and energy dispersive X-ray spectroscopy show that the products are very pure (>95%) crystalline MgO nanorods with diameters from 40 nm to 200 nm and lengths 10 microns or longer. High-resolution transmission electron microscopy and electron diffraction further reveal that these MgO nanorods are single crystals and that the rod axis is along the <110> crystal direction. A model for the structural transformation from hydrated basic magnesium chloride to magnesium oxide has been developed and compared to our experimental results. This solution-based process can be easily scaled-up, and is a low-cost source of pure magnesium oxide nanorods needed in many industrial applications, for example, as reinforcing agents in matrix composites and as flux-pinning centers in high-T_C superconductors.

INTRODUCTION

Magnesium oxide is an inorganic compound having very good heat resistance, thermal conductivity and alkali resistance [1]. Magnesium oxide whiskers have been produced and utilized as filling agents in composite materials to achieve better mechanical strength, thermal shock resistance and thermal conductivity [2]. For example, MgO whiskers were shown to be effective reinforcing agents for improved thermomechanical properties of BSCCO high-T_C superconductors [3,4]. More interestingly, MgO whiskers with diameters in the nanometer range, that is, MgO nanorods, can act as effective flux-pinning centers when incorporated into high-T_C superconductors and lead to enhanced critical current densities [5-7], which are crucial to most large-scale applications of the high-T_C superconductors. It is also expected that MgO nanorods are better reinforcing agents compared to their micron-sized cousins because the toughness and strength of single-crystalline whiskers increase with decreasing whisker diameters [8].

Currently most magnesium oxide nanorods are synthesized via vapor phase process. For example, carbothermal reduction of MgO at at least 1200 °C and subsequent re-oxidization of Mg vapor and condensation of MgO nanorods has been reported [5-7]. However, it is difficult to scale up this process without the formation of thick whiskers and round particles. In addition, this method is not cost-effective because of the high processing temperatures. In this paper, we report a simple solution-based procedure capable of producing large quantities of very pure (>95%) magnesium oxide nanorods.

EXPERIMENTAL METHODS

Basic magnesium chloride was chosen as a precursor because of its needle-like crystal morphology [9,10]. Precursor nanorods were prepared by the reaction between magnesium chloride solution and magnesium oxide supersaturated in the solution. After 48 hours of reaction

Mat. Res. Soc. Symp. Proc. Vol. 581 © 2000 Materials Research Society

at room temperature the precipitate was collected and washed with isopropanol. Basic magnesium chloride nanorods were then transformed into magnesium hydroxide nanorods by base (NaOH) treatment at 60 °C in a mixed solvent of ethanol and water (3:1). Lastly the dried magnesium hydroxide nanorods were heated in flowing oxygen slowly to 900 °C and calcined at 900 °C for one hour to finish the conversion to crystalline magnesium oxide nanorods.

The morphology and structure of the products were examined by field-emission scanning electron microscopy (SEM) (LEO 982) and transmisson electron microscopy (TEM) (Philips EM420 and JEOL 2010) equipped with energy dispersive X-ray (EDX) spectroscopy to evaluate the chemical composition. The phase analysis was performed using powder X-ray diffraction (XRD) (Scintag XDS2000).

RESULTS AND DISCUSSION

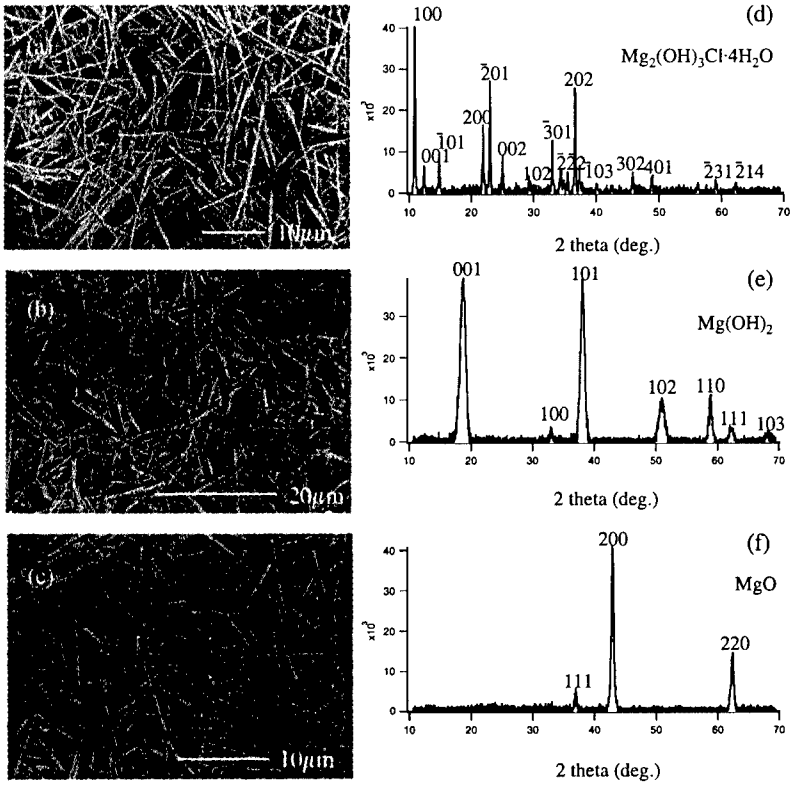


Figure 1. (a) - (c) SEM images of the precursor, the intermediate product after base treatment, and the final product after calcination, respectively. (d) - (f) Corresponding powder XRD patterns of products from each of the step in (a) - (c).

Figure 1 shows typical SEM images of the products from each step and their corresponding powder XRD patterns. The SEM data show clearly that they all have similar rod-like morphology with aspect ratios of at least 50 and relatively good uniformity. XRD patterns show that they are $Mg_2(OH)_3Cl{\cdot}4H_2O$, $Mg(OH)_2$ and MgO, respectively, and that no second phase is present. This demonstrates a successful transformation from hydrated basic magnesium chloride nanorods to magnesium oxide nanorods via intermediate magnesium hydroxide nanorods. In general, the diameters of MgO nanorods range from 40 nm to 200 nm with an average of 120 nm and the lengths usually are 10 μm or longer. The nanorods have rectangular cross section and are straight and uniform in diameter along the axis. EDX spectroscopy measurements of these rods show no other heavy elements, such as Cl, other than Mg. Powder XRD pattern (figure 1(f)) can be indexed as cubic MgO structure. Together with the EDX measurement, it shows very high phase purity of these nanorods. In addition, from the SEM images it can be seen that particulate impurities are rarely found. Therefore the products are very pure (>95%) crystalline MgO nanorods.

Figure 2 shows a TEM image of a single MgO nanorod. The rod surface looks rough at this magnification. To determine whether the rods are single-crystalline or polycrystalline, electron diffraction patterns were recorded on a number of nanorods. Figure 3 shows three most commonly seen electron diffraction patterns. The arrows in the patterns indicate the direction of the rod axes. Clearly they are single crystalline patterns and can be indexed to the FCC MgO lattice with electron beam directions along [$\bar{1}$11], [001] and [$\bar{1}$ 12] zone axes, respectively. It can be seen that in all three cases the rod axis goes along the <110> crystal direction. The fact that diffraction patterns of different zone axes can be found in the nanorods is a supplemental evidence of their rod-like morphology. When a rod is rotated around its axis which is the <110> direction of an FCC lattice, it is expected that electron beam will be coincident with [$\bar{1}$ 11], [001]

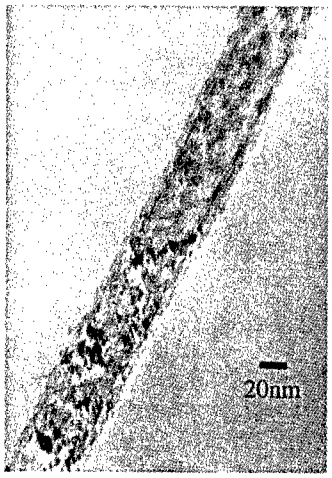


Figure 2. TEM micrograph of a MgO nanorod.

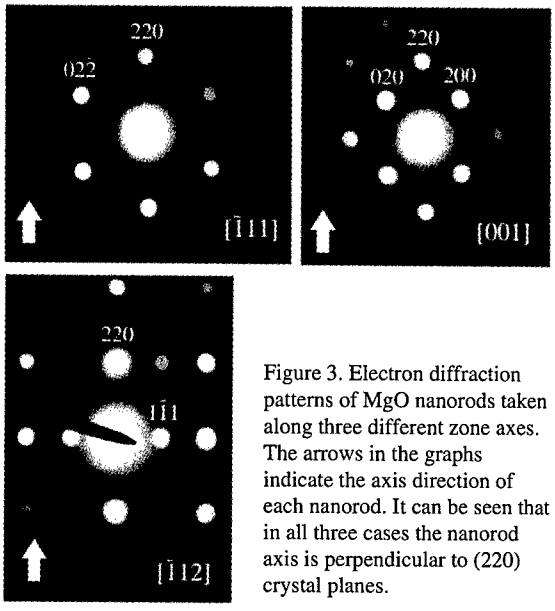


Figure 3. Electron diffraction patterns of MgO nanorods taken along three different zone axes. The arrows in the graphs indicate the axis direction of each nanorod. It can be seen that in all three cases the nanorod axis is perpendicular to (220) crystal planes.

and [$\bar{1}$12] zone axes. The single crystal nature of these nanorods was further confirmed by high-resolution TEM (HRTEM) studies. Figure 4 shows a HRTEM micrograph of the nanorod. The HRTEM image agrees well with the electron diffraction patterns. The lattice fringe shown is from (220) planes with an inter-plane distance of 1.50Å. These data confirm that the rod axis is along the <110> direction, and that the lattice is nearly perfect across the rod.

The <110> axis direction is also expected in the structural transformation from $Mg_2(OH)_3Cl{\cdot}4H_2O$ to MgO. $Mg_2(OH)_3Cl{\cdot}4H_2O$ has a triclinic structure [11]. The backbone of the structure is formed by puckered layers parallel to (100), consisting of infinite double chains of MgO_6 octahedra extending in the b direction. Figure 5(a) is the schematic plan and elevation view of the backbone structure. The Cl anions, alternating with an equal number of water molecules so as to form rows parallel to b, are situated between the layers. The forces between double chains within one layer or from neighboring layers are relatively weak hydrogen bonds formed by adjacent water molecules, hydroxyl and chloride anions. This explains the needle-like crystal habit of $Mg_2(OH)_3Cl{\cdot}4H_2O$. In the transformation to hexagonal $Mg(OH)_2$, which has a layered CdI_2 structure, double chains within one layer move to each other to form a continuous layer by removing one half of the oxygen atoms (in the form of water) situated at the MgO_6

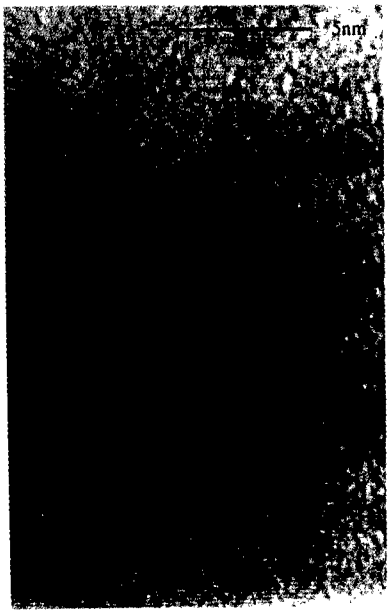


Figure 4. High-resolution TEM micrograph of the MgO nanorod. The edge of the nanorod is along the right edge of the micrograph. The lattice fringes shown are (220) planes with an inter-plane distance of 1.50Å.

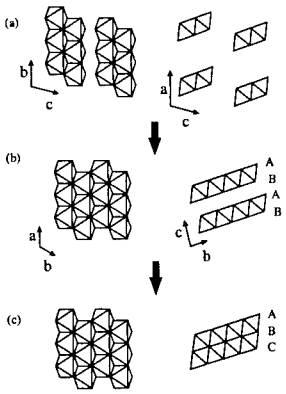


Figure 5. Schematic view of the backbone structures of
(a) $Mg_2(OH)_3Cl{\cdot}4H_2O$ from a direction in the (001) plane perpendicular to the b axis (left), and from parallel to the b axis (right),
(b) $Mg(OH)_2$ from parallel to the c axis (left), and perpendicular to the c axis (right),
(c) MgO from parallel to the <111> direction (left), and perpendicular to the <111> direction (right).
$Mg_2(OH)_3Cl{\cdot}4H_2O$ has a triclinic needle-like structure. $Mg(OH)_2$ has a hexagonal layered structure. MgO has a face-center cubic (FCC) structure.
Octahedra in the graph stand for MgO_6 octahedra.

octahedron corners between two neighboring double chains. Upon release of the chloride anions and water molecules sitting between the layers, hexagonal $Mg(OH)_2$ is formed (figure 5(b)). The axis of $Mg(OH)_2$ nanorods formed in this way will be the a (or b) direction of the hexagonal lattice. Lastly, in the transformation from $Mg(OH)_2$ to MgO, layers of MgO_6 octahedra in $Mg(OH)_2$ move to each other to form the continuous three dimensional FCC structure by removing one half of the oxygen atoms (in the form of water) between neighboring layers and changing the stacking sequence from ABABAB... to ABCABC...(figure 5(c)). Therefore the axis of the MgO nanorods should be the <110> direction of the FCC structure, as we find in our experiments.

The analysis of the structural transformation also helps us understand the importance of using $Mg(OH)_2$ as an intermediate product in the conversion from $Mg_2(OH)_3Cl{\cdot}4H_2O$ nanorods to MgO nanorods. Experiments show that direct conversion of $Mg_2(OH)_3Cl{\cdot}4H_2O$ to MgO by heat invariably breaks the nanorods into nanoparticles. In removing all the oxygen atoms required in one step, double chains are cut into from at least two faces. This likely promotes the collapse of the double chains and thus the nanorods. Pressure built up at elevated temperature by large amount of side products (three H_2O/HCl molecules per one MgO unit) not released promptly is likely to break the nanorods too. However, in the two-step transformation two thirds of the side products are easily released through the channels between the layers in $Mg(OH)_2$ by anion exchange reaction operated at close to room temperature. Moreover the structural change is less drastic in the two-step transformation, which also helps to maintain the crystal morphology.

CONCLUSIONS

In summary, a three-step solution-based process using hydrated basic magnesium chloride as a precursor and magnesium hydroxide as an intermediate product has been employed to make very pure single crystalline magnesium oxide nanorods with diameters from 40 nm to 200 nm and an average aspect ratio of 80. This process can be easily scaled-up, and should provide a low-cost source of pure magnesium oxide nanorods needed in many industrial applications.

ACKNOWLEDGMENTS

We thank M. Frangillo and Y. Lu for help with TEM. C.M.L. acknowledges support of this work by the Office of Naval Research.

REFERENCES

1. J.D. Lee, *Concise Inorganic Chemistry, 5th ed.*, Chapman and Hall, New York, 1996, pp. 339.
2. N.S. Gaenko, et al, Ogneupory, (**6**), p. 13 (1984).
3. Y.S. Yuan, M.S. Wong and S.S. Wang, J. Mater. Res. **11**(1), p. 8 (1996).
4. Y.S. Yuan, M.S. Wong and S.S. Wang, J. Mater. Res. **11**(7), p. 1,645 (1996).
5. P. Yang and C.M. Lieber, Science **273**, p. 1,836 (1996).
6. P.Yang and C.M. Lieber, Appl. Phys. Lett. **70**(23), p. 3,158 (1997).
7. P.Yang and C.M. Lieber, J. Mater. Res. **12**(11), p. 2,981 (1997).
8. E.G. Wolff, J. Am. Ceram. Soc. **48**, p. 279 (1965).
9. H. Heritsch, Miner. Petrogr. Mitt. (**3**), p.150 (1948).
10. P.M. De Wolff, Acta Cryst. **5**, p. 286 (1952).
11. P.M. De Wolff and Mme L. Walter-Levy, Acta Cryst. **6**, p. 40 (1953).

STOICHIOMETRY CONTROL IN MOLECULAR BEAM DEPOSITED NANOCRYSTALLINE SnO_2 AND TiO_2 THIN FILMS

H.HOCHE*, H.HAHN*, F.EDELMAN*, R.NAGEL* and P.WERNER**
*Materials Science Dept., Darmstadt Technical University, Petersenstrasse 23, 64287 Darmstadt, GERMANY
**Max Planck Institute of Microstructure Physics, Halle/Saale D-06120, GERMANY

ABSTRACT

Molecular beam deposition (MB) of thin film metal oxide is prospective for application in gas sensor technology due to the well-controlled oxide molecular fluxes during creation of multi-oxide structures with improved characteristics. However, the MB process leads to some oxygen deficiency in the oxide. Further application of the MB technology (and, in general, the e-beam oxide deposition in vacuum) for processing of sensor structures needs the control and correction of the oxygen stoichiometry by adding in-situ atomic oxygen to the growing material or via the thin film oxidation after deposition.

Thin films (50 to 500 nm) of SnO_x and TiO_x were deposited on SiO_2/(001)Si substrates at 100°C by MB from SnO_2 and TiO_2 sources. The film stoichiometry in the as-deposited state and after annealing in vacuum and in oxygen is characterized by XRD, TEM and RBS. Oxygen annealing transformed the strongly non-stoichiometric SnO (Romarchite) in the as-deposited state to Cassiterite, SnO_2. Structure transformations in the TiO_2 films during annealing are also discussed.

INTRODUCTION

Tin and titanium dioxides, SnO_2 and TiO_2, are prospective materials for gas sensors[1-3]. Both oxides are polycrystalline materials, with similar crystallography (both are tetragonal), inherently non-stoichiometric (with O-deficit). Electrical conductivity of SnO_2 and TiO_2 strongly depends on the environmental gases.

SnO_2 sensors are sensitive to reducing gases (H_2, CO, CH_4 etc.) due to the low-temperature chemisorption of the environmental gases on the grain surface that changes the surface electron state level, governing the grain surface conductivity. The TiO_2 sensors are sensitive to gases-oxydants (O_2 , NO_x etc.). The bulk diffusion of oxygen from outside into the TiO_2, compensating an original deficiency of oxygen in the TiO_2-lattice, increases the TiO_2 resistivity by oxygen atoms occupation of O-vacancies (the donor centers). TiO_2 sensors are stable at high temperatures and used in combustion systems to control CO/O_2 ratio. Both oxides have good resistance to corrosive gases, low cost and are easy to handle. Main disadvantage of SnO_2 sensors as compared to TiO_2 are their poor selectivity and structure instability at temperatures above 400°C.

Similarly to other metal-oxide sensors, SnO_2 and TiO_2 sensors are produced by sintering and sol-gel processes (in the case of thick films) or by reactive ion sputtering (metal targets) and e-gun deposition (oxide targets) in the case of thin films. Recently, molecular beam deposition (alternative version of the e-gun deposition) demonstrated some advantages for thin film processing: clean substrate surface and simple controlled oxide flux in a high-vacuum molecular beam chamber is useful in preparation the oxides that are uniform on a large-area scale, and oxide mixtures with stable composition. However, in the case of oxides with low oxygen pressure (as SnO_2), the film deposition complicates due to oxygen and oxides evaporation in high vacuum from the high-temperature melt. Fig.1a shows the calculated oxygen pressure temperature dependence for the SnO_2 or TiO_2 melts[5]. In this study we have studied the behaviour of SnO_2 and TiO_2 films molecular beam deposited and annealed in vacuum or in oxygen to correct an initially oxygen non-stoichiometry.

EXPERIMENTAL

The SnO_2 and TiO_2 films were deposited by means of electron gun molecular beam (MB) deposition from the appropriate commercial targets. During deposition the substrates, SiO_2/(001)Si and amorphous carbon covered Ni grids (for in-situ TEM experiments), were kept at a temperature of 100°C. The film thickness ranged from 50 to 500nm. Rutherford

Mat. Res. Soc. Symp. Proc. Vol. 581 © 2000 Materials Research Society

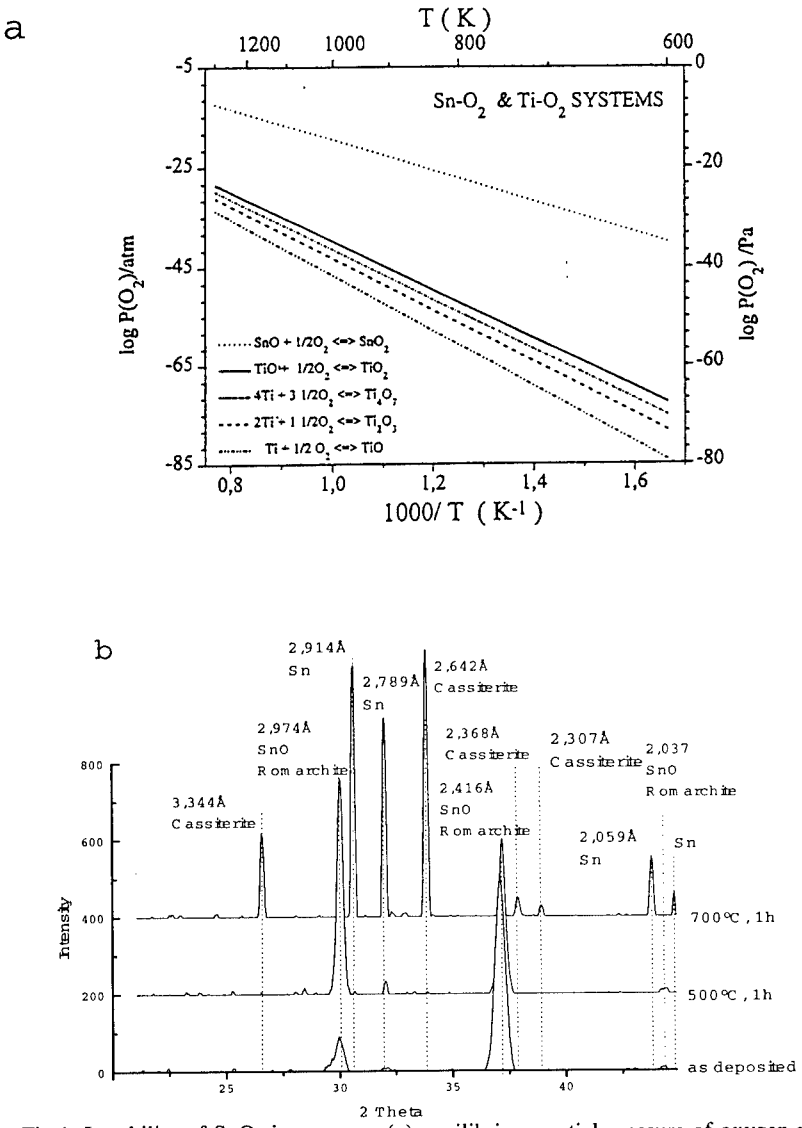


Fig.1. Instability of SnO_2 in vacuum: (**a**) equilibrium partial pressure of oxygen $p(O_2)$ vs. the temperature[5] and (**b**) XRD phase analysis of the SnO_2 molecular beam deposited film, 200 nm thick, in the as-deposited state and after annealing in vacuum 10^{-4} Pa for 1h.

backscattering (RBS) and electron probe microanalysis (EPMA) were used for compositional analysis. The RBS spectra were obtained with the 7MeV accelerator (3,05 MeV He^+ ions were used) at the Institute of Nuclear Physics, University Frankfurt. The SnO_2 films were polycrystalline in the as-deposited state. The TiO_2 films were amorphous in the as-deposited state and transformed to their nano/microcrystalline structure during annealing in a hot-wall furnace in dry oxygen between 400 and 800°C (the SnO_2 films were also annealed in oxygen environment

for stoichiometry regulation). The kinetics of the film phase transformation was investigated in-situ in a JEM-1000 microscope (1 MeV acceleration voltage) at a vacuum of 10^{-3} Pa in the above mentioned temperature range. The film morphology was studied by high-resolution SEM. Phase analysis of the SnO_2 and TiO_2 films after different treatments was done also by XRD using the grazing beam geometry.

RESULTS AND DISCUSSION

a. TiO_2 films annealing in dry oxygen

Earlier[4,6], we demonstrated the structural transformation in TiO_2 reactive sputtered films, initially amorphous, during annealing in vacuum and in air up to 900°C. In both cases the final TiO_2 structure modification was rutile. However, the same heat treatment of the e-gun deposited TiO_2 films produced the anatase phase[6]. Fig.2 illustrates the MB-TiO_2 film stability: after amorphous-to-crystalline (anatase) transformation, only anatase dominated in the film structure during annealing in dry oxygen at the temperature up to 800°C. Nevertheless, RBS data shows that MB-TiO_2 in the as deposited state and after oxidation annealing is non-stoichiometric having a large deficit of oxygen (~20%).

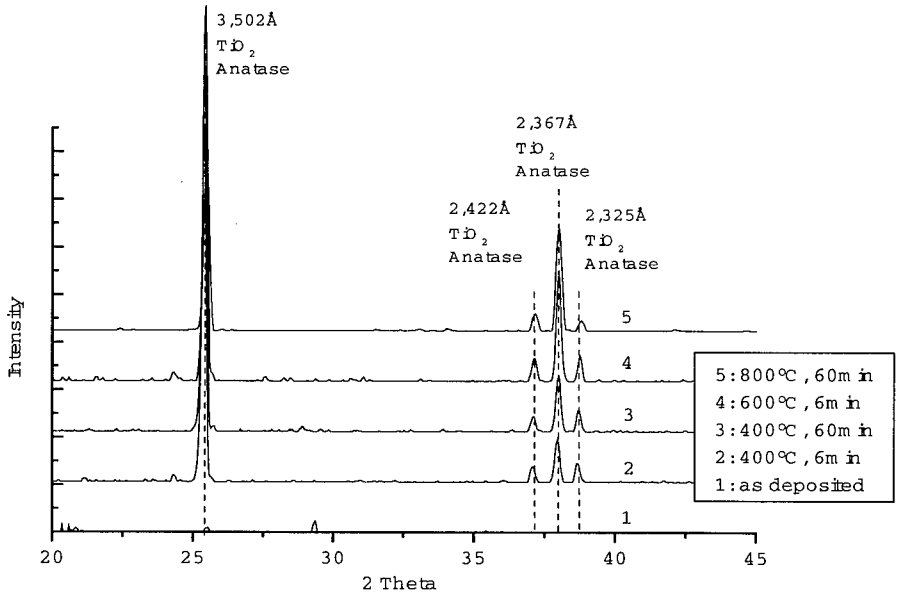


Fig.2. XRD spectra of MB-TiO_2 film, 500nm thick, annealed in dry oxygen.

b. SnO_2 films annealing in dry oxygen

The SnO_2 film changed the composition depending on the annealing conditions. The SnO_2 film in the as-deposited state (MB deposition in a high vacuum from a SnO_2 target) was compositionally closer to SnO than to SnO_2 (Fig.3). Large romarchite grains (up to tens micrometers in size) were preferently oriented by <001> tetragonal 4-fold symmetry basal axis perpendicular to amorphous carbon substrate. Annealing in oxygen returns the SnO_x film to the SnO_2 stoichiometry after 800°C, 1h treatment. Fig.4 illustrates the SnO_x recovery process upon oxidation annealing by RBS spectroscopy.

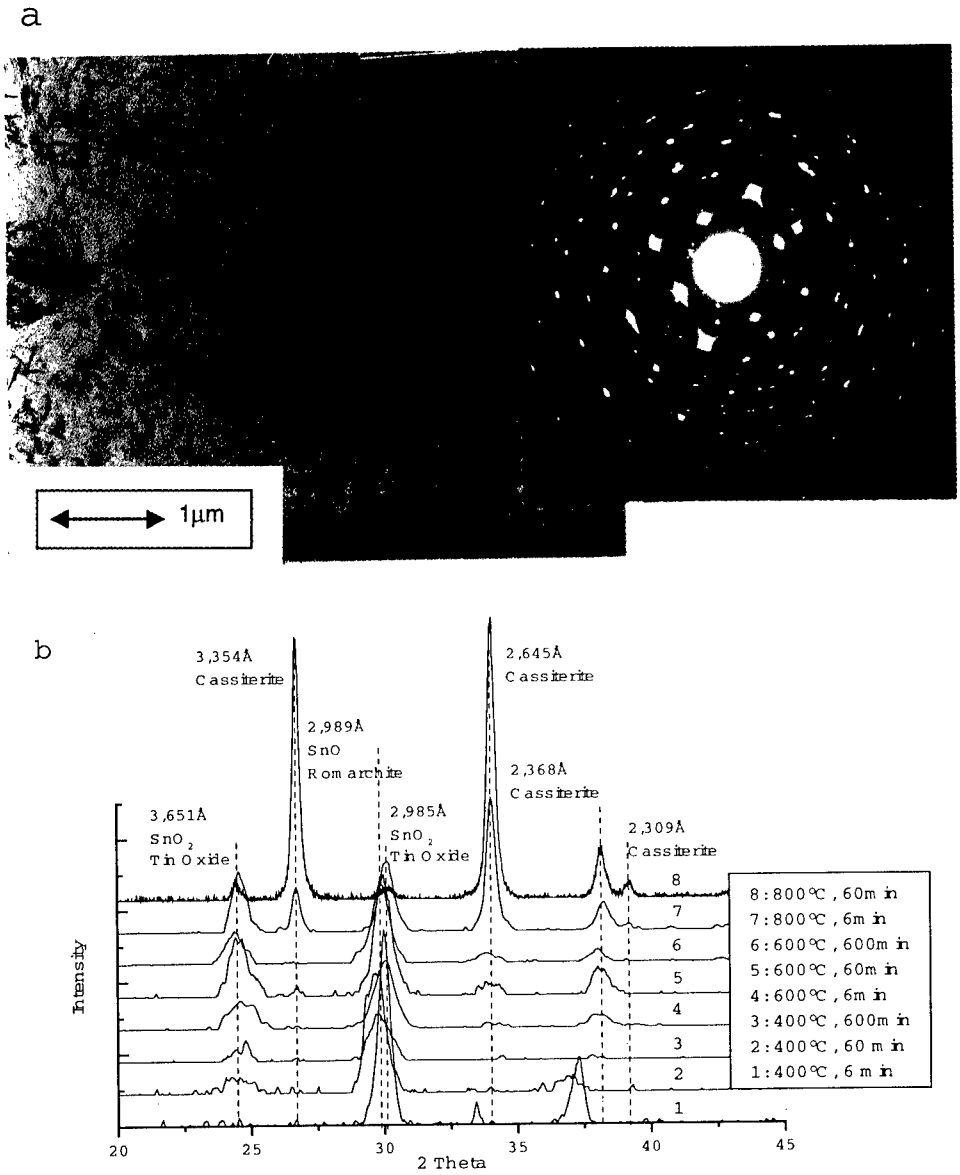


Fig.3. The MB-SnO_x film (**a**) in the as-deposited state (layered romarchite, TEM) and in course of annealing in dry air (**b**) transforming to cassiterite phase (XRD).

c. Crystallization of the MB TiO_2 film observed via in-situ TEM

As it can be seen in Fig.2, the TiO_2 MB-films crystallized during annealing in dry oxygen very fast just at 400°C forming polycrystalline anatase. This result correlates with our in-situ

TEM data (Fig.5) obtained in vacuum annealing (vacuum in microscope heating stage was 10^{-6} Torr). The grain growth rate in the amorphous TiO_2 film at 300°C was estimated as 0.3-0.5 nm/s and the nucleation rate as 2.10^5 $cm^{-2}s^{-1}$. The incubation time to detect the first nuclei in TEM at 300°C was about 10 min.

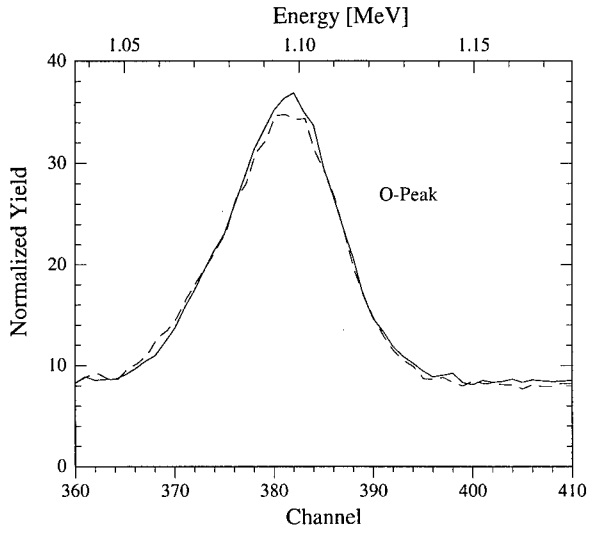


Fig.4. RBS oxygen signal of the tin oxide in the MB as-deposited state (————) and after 800°C annealing for 1h in dry oxygen (– – – – – –).

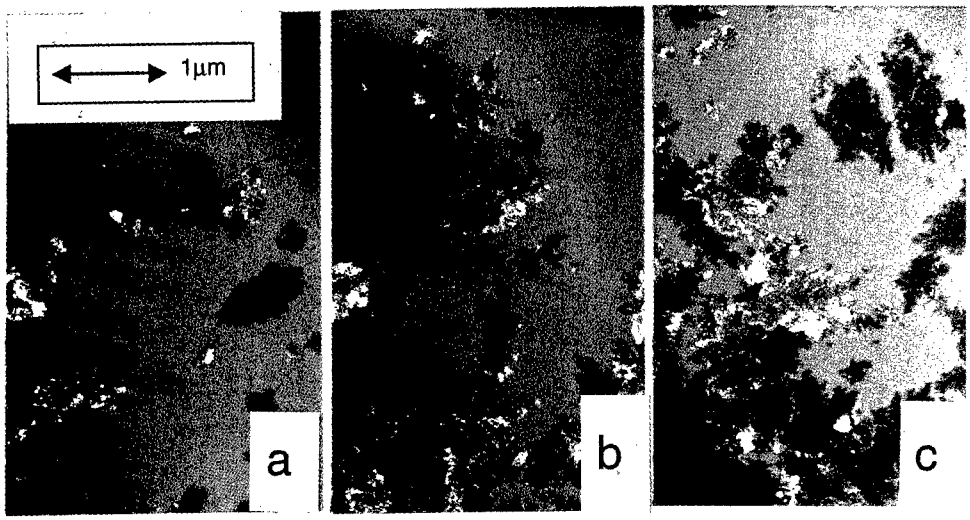


Fig.5. Plane-view TEM micrograph of MB amorphous TiO_2 film during in-situ annealing at 300°C for a) 15, b) 25 and c)45 min.

CONCLUSIONS

1. The composition and structure of SnO_2 and TiO_2 films for gas sensors deposited by molecular beam in a high vacuum and annealed in dry oxygen have been investigated by means of x-ray diffraction, Rutherford backscattering and electron microscopy.

2. The TiO_2 films, deposited on SiO_2/Si substrate using molten TiO_2 precursor and amorphous in the as-deposited state, crystallized at 300°C during oxidation in dry oxygen forming stable up to 800°C anatase structure.

3. The SnO_2 films, deposited under the same conditions as TiO_2, presented polycrystalline tin suboxides in the as-deposited state (SnO romarchite pase dominated). Vacuum annealing transformed SnO up to metallic tin. However, annealing in dry oxygen was found capable to return tin oxide stoichiometry reaching (after 800°C annealing) a highly oxidation stoichiometric form, cassiterite, SnO_2. Therefore, the reversibility of oxidation/reduction in SnO_2 film is demonstrated. Further application of post deposition oxidation treatment apparently allows to obtain a compositionally controlled MB deposited oxides-mixtures for gas sensor application.

REFERENCES

1. S.R.Morrison, in *Semiconductor Sensors*, edited by S.M.Sze (J.Wiley & Sons, N.Y., 1994).

2. K.Ihokura and J.Watson, *Stannic Oxide Gas Sensor: Principles and Applications*, CRC Press, Florida, 1994.

3. P.T.Mosely and B.C.Tofield (Eds.), *Solid State Gas Sensors*, Adam Hilger, Bristol, 1987.

4. F.Edelman, H.Hahn, S.Seifried, C.Alof, H.Hoche, A.Balogh, P.Werner, K.Zakrzewska, M.Radecka, P.Pasierb, A.Chack, V.Mikhelashvili, and G.Eisenstein, EMRS'99 Meeting Proceeds. Strasbourg, 1999, to be published.

5. M.Radecka, K.Zakrzewska, and M.Rekas, Sensors and Actuators, **B47**, p.194 (1998).

6. F.Edelman, A.Rothshild, Y.Komem, V.Mikhelashvili, A.Chack and F.Cosandey, Solid State Phenomena, **67/68**, p.269 (1999).

ELECTRICAL PROPERTIES OF NANOCRYSTALLINE TUNGSTEN TRIOXIDE

A. HOEL, L.B. KISH, R. VAJTAI, G.A. NIKLASSON, C.G. GRANQVIST, E. OLSSON
Department of Materials Science, The Ångström Laboratory
Uppsala University, P.O. Box 534, S-751 21 Uppsala, Sweden

ABSTRACT

Tungsten oxide is a material of significant interest for applications in several areas. It can, for example, be used as the electrochromic film in smart windows. Tungsten trioxide nanoparticles were produced using an advanced gas evaporation unit in which the tungsten was oxidized in low pressure ambient air. The tungsten trioxide particles were formed via vapor condensation and were deposited by gas deposition technique to avoid coagulation effects. The average size of the primary particles was around 5 nm, depending on the heating power and the pressure. The particles exhibited a body centred cubic structure. The impedance spectrum of particle deposits showed resonance and negative capacitance effects. The correlation between fabrication conditions, structure and impedance spectrum is discussed.

INTRODUCTION

Tungsten trioxide (WO_3) is a very versatile material. It is widely used in different thin film technologies, for example as the absorber in solar collectors, as the electrochromic film in smart windows [1] and as the active layer in chemical sensors[2]. A large variety of processes have been used for the fabrication of WO_3 films. A technique that has attracted increased interest during the last decades for deposition of all types of materials is advanced gas deposition (AGD). Nanocrystalline films can be deposited with AGD, and the formed particles have a narrow size distribution[3]. Such AGD deposited films exhibit several different extreme properties such as outstanding hardness, thermal stability, chemical resistance and interesting electrical properties. This paper, reports on dielectric properties, in particular the phenomenon of negative capacitance (NC). NC was first reported by Jonscher in 1977 [4]. The mechanism behind the NC is yet poorly understood.

EXPERIMENTS

WO_3 samples were fabricated using an AGD unit (ULVAC/VMC, Japan). The technique of gas evaporation was introduced in 1976 [5] and has become a leading method for the production of high-quality nanoparticles [6-8]. In the classical case, the evaporation of the material takes place in the presence of an inert gas. The vapor is then cooled so that nucleation and growth of ultrafine particles take place in the gas. The primary particles can have a narrow size distribution [9]. The gas evaporated particles are normally single crystals.

Figure 1 illustrates the experimental equipment for particle fabrication. In this particular case, a pellet of 99.99% pure tungsten is placed on a pedestal in the lower chamber and is surrounded by synthetic air that works as reactive gas and as cooling gas. The pellet is inductively heated by a surrounding copper coil. The synthetic air is introduced below the pedestal. The surface of the pellet is oxidized and the tungsten oxide is sublimated. The transfer pipe is positioned centrally in the vapor zone where particles are formed. Particles in the outer part of the zone are removed by an exhaust pipe connected to a pump. The particles are thereby collected from a small part of the super

Mat. Res. Soc. Symp. Proc. Vol. 581 © 2000 Materials Research Society

saturated vapor zone and the size distribution is kept narrow. A stream of gas transports the particles through the transfer pipe into the evacuated upper chamber where the particles are collected. Strong precautions were taken to avoid turbulence and eddy formation.

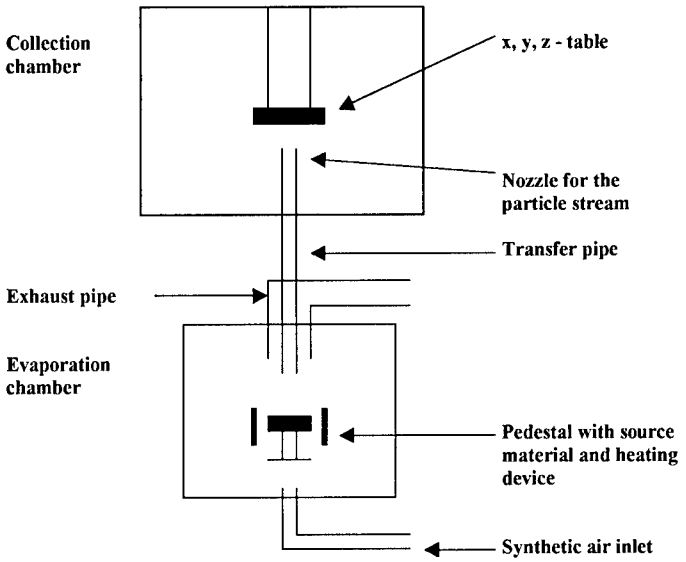


Fig. 1: Schematic picture of the gas-evaporation equipment

Particles were deposited onto an indium tin oxide (ITO) coated glass substrate in the deposition chamber. The substrate was mounted on a computer controlled x,y,z- table which allowed various patterns to be made. Two samples, referred to as I and II below, were fabricated at a heating power of 1.1 kW. The substrate was kept at room temperature during deposition. The difference in the production between the two samples was the linear speed of the x,y,z- table. Sample I was deposited with a speed of 0.38 mm/s and sample II with a speed of 0.19 mm/s. This resulted in a factor of two more particles per unit length in the latter case.

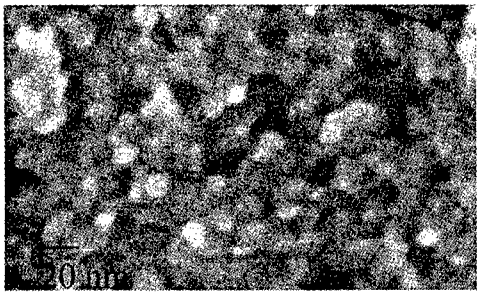
Particle size distributions were determined by transmission electron microscopy (TEM), using a Jeol 2000 FX II instrument, and by scanning electron microscopy (SEM), using a LEO 1550 Field Emission Gun with a Gemini column. The film thickness was determined using a FEI XL 30 Environmental SEM with a field emission gun.

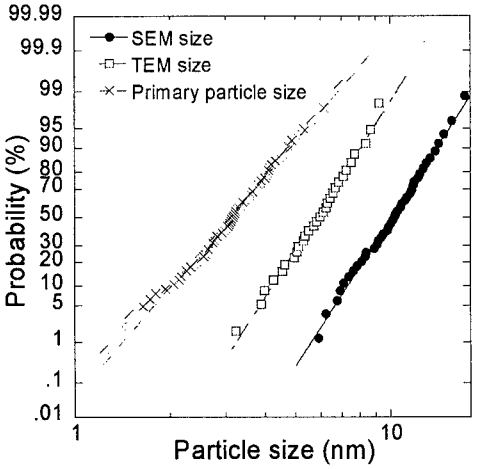
Dielectric measurements were carried out with a Solartron Instruments SI-1260 impedance/gain-phase analyzer, a Novocontrol broadband converter and an additional probe station. In order to characterize the dielectric properties of the samples, contacts of aluminium were evaporated onto the surface of the WO_3. The diameter of the evaporated contacts were 1mm. One probe was contacted to the ITO layer and the second to the Al contact.

RESULTS

Structural characterization of the samples

Figure 2a shows a SEM image of the surface of sample I and Fig 2b depicts a representative TEM micrograph of a cross section. The corresponding size distributions are shown in Fig 2c, together with a size distribution of the primary particles [9]. The data are presented in a log-probability plot adequate for samples expected to have a size distribution resembling the log normal distribution.





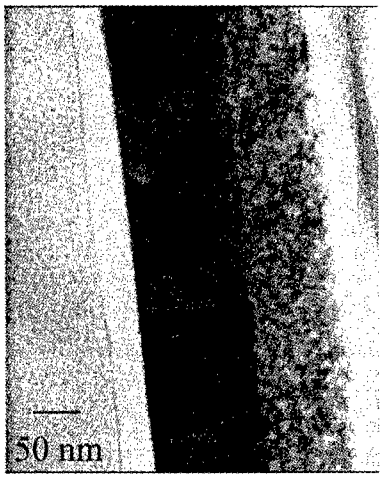


Fig 2: a) A SEM micrograph showing the particles on the surface of sample I. b) A TEM image of the corresponding cross section. The darker band corresponds to the ITO layer. c) The size distribution from each set of images together with the size distribution of the primary particles. In the plot every fifth data point is shown.

The difference in size distribution of the sets of particles determined from images taken by SEM and TEM is only partly due to uncertainties in the measurements. One reason for the difference can be that the sintering of the particles is different within the film and at its surface. The TEM data indicate smaller particles than the SEM data. In fact the sizes determined by TEM are intermediate between those of the primary particles (mean diameter of 3.1 nm according to Fig 2c) and the sizes determined by SEM (being ~10nm). The thickness of sample I is found to be 110nm, whilst the thickness of sample II is 140 nm, so that the thickness ratio is 1.3. Since sample II contains twice as many particles as sample I it follows that sample II has a higher density by a factor of 1.6. Sample II thus is more sintered.

Dielectric characterization of the samples

An AC voltage of 50 mV was applied to the sample under study and the frequency was varied from 10^7 Hz down to a frequency corresponding to the limit of accurate measurement of the capacitance ($1*10^{-3}$ F). When we applied a DC voltage of $\pm U_{DC}$, with $20<U_{DC}<40$ mV, the dielectric data displayed negative values of the real part of the capacitance, C'. This is clearly seen in Figs. 3a and b, pertaining to samples I and II, respectively. There is no significant difference between the responses at +40 mV and at – 40mV, which indicates that there are no contact effects. At a specific frequency, a resonance appeared and C' went to zero. When the frequency decreased the capacitance became negative. At even lower frequency, the real part of the capacitance decreased further and large negative values of C' were obtained. The graphs show the absolute values of the negative capacitances. The pronounced difference in resonance frequency should be noted; it appeared at 100 Hz for sample I and at 3 Hz for sample II.

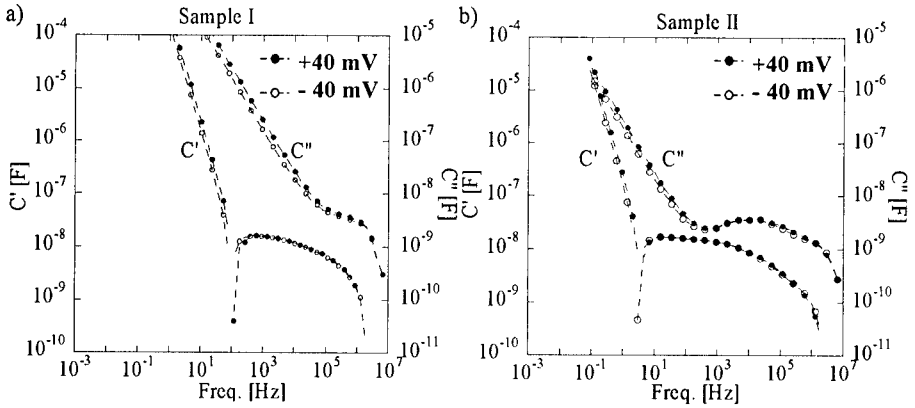


Fig 3: The dielectric response of sample I (a) and sample II (b) at a DC - voltage of ±40 mV. C' and C'' denote real and imaginary parts of the capacitance respectively.Note the difference in resonance frequency. The negative capacitance, plotted as an absolute value, is found to the left of the resonance frequency.

A RC-model

The phenomenon of negative capacitance was discovered by Jonscher [4]. There are several approaches to interpret it; for example there are speculations whether hopping or trapping-detrapping effects are responsible. A multiple-trapping model described by Rybicki and Chybicki [10] is a possible explanation. It embraces a time-dependent relation for multiple-trapping transient currents within thin insulating layers with a non-homogenous trap distribution. This may be a possible approach for our present nano crystalline films.

In 1960 Miller and Abrahams [11] studied a random-resistor network which was subsequently modified by Böttger and Bryksin in order to explain AC hopping in disordered materials[12]. The network consisted of random resistances connected at points corresponding to sites in the material. Each of these points is connected to earth via a capacitor and an AC -

voltage supply. If the frequency approaches zero, the network turns in to the network of Miller and Abrahams.

In fig 4a we present a simplified model of the network of Böttger and Bryskin. This new RC circuit, is the simplest possible model for NC [13]. The model consists of two capacitors and two resistors. The impedance is represented by the transfer admittance of the circuit. The NC is the result of two parallel current channels, with positive and negative phase shifts, respectively. At a certain frequency the phases are equal and a resonance appears. Calculated responses for three different parameter settings are shown in Fig 4b. Magnitudes of C' are presented as the absolute values below the resonance frequency. The resonance frequency can be changed by an adjustment of the values of the components. In order to obtain a negative capacitance, the value of C_2 must be less than the value of C_1. A basic similarity between the computed and the experimental data gives credence to our theoretical model.

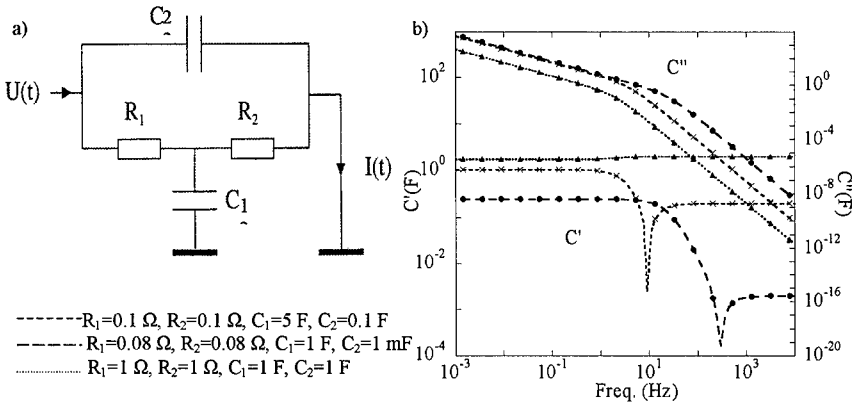


Fig. 4 a) A phenomenological network for the dielectric response of our samples. b) The corresponding dielectric response of the network. The negative capacitance, plotted as an absolute value, is found to the left of the resonance frequency.

CONCLUSION

We have produced nanocrystalline films of WO_3 in a new way using an advanced gas evaporation unit. The film thickness and size distribution of the particles of two typical samples were characterized by electron microscopy. The film thicknesses were 110 nm and 140 nm. The average particle size lay between 3 and 10 nm. The dielectric responses of the two films were measured, and the films were found to exhibit a negative capacitance. We present a phenomenological model describing the negative capacitance. It is possible to tune a resonance frequency by changing the values of the components in the RC network to match the response of the WO_3 films.

REFERENCE

[1] C.G. Granqvist, Handbook of Inorganic Electrochromic Materials, Elsevier, Amsterdam 1995

[2] J. Tamaki, Z. Zhang, K. Fujimori, M. Akiyama, T. Harada, N. Miura, N.Yamazoe, J. Electrochem. Soc. 141 (1994) 2207

[3] J. Söderlund, L.B. Kiss, G.A. Niklasson, C.G. Granqvist, Phys. Rev. Lett.80 (1998) 2386

[4] A.K. Jonscher, Nature 267, 673 (1977)

[5] C.G. Granqvist, R.A. Buhrman, J. Appl. Phys. 47 (1976) 2200

[6] C. Hayashi, R. Uyeda, A. Tasaki, Ultra-Fine Particles, Noyes, Westwood, U.S.A, 1997

[7] R.W. Siegel, Ann. Rev. Mater. Sci. 21 (1991) 559

[8] H. Gleiter, Nanostruct. Mater. 1 (1992) 1

[9] A. Hoel, L.B. Kish, R. Vajtai, E. Olsson, Proc. 51st Ann Meeting Scandinavian Soc. Electron Microscopy, Bergen, Norway (1999), page 51

[10] J. Rybicki, M. Chybicki, J. Phys.: Cond. Matter 1 (1989) 4623

[11] A. Miller, B. Abrahams, Phys. Rev. 120 (1960) 745

[12] H. Böttger and V.V. Bryksin, Phys.Stat.Sol. (b) 78, (1976) 9

[13] R. Vajtai, L.B. Kish, A. Hoel, G.A. Niklasson, C.G. Granqvist, E. Olsson, to be published

For further information:
A. Hoel : anders.hoel@angstrom.uu.se
Telephone: +46 18 471 71 26;Fax: +46 18 50 01 31

PREPARATION AND PROPERTIES OF COLLOIDAL PARTICLES. SILICA ON YTTRIUM IRON GARNET

R.H.M.GODOI, M.JAFELICCI JR, JOAQUIM PORTILLO*.
São Paulo State University- Chemistry Institute, Campus of Araraquara, Brazil and
*Seveis Cientifico Tecnics, University of Barcelona, Barcelona, Spain
E-mail: ricgodoi@iq.unesp.br

ABSTRACT

Various properties of particles can be altered by coating them with a layer of different chemical composition. Yttrium iron garnet (YIG) particles has been coated with silica for control of their sintering, corrosion resistance, and stabilization of magnetic properties. This silica cover was obtained by hydrolysis of tetraethylorthosilicate (TEOS) in 2-propanol. This material was characterized by transmission (TEM) electron microscopy, (XEDS) X-ray energy-dispersive spectrometry, (XPS) X-ray photoemission spectroscopy and (VSM) vibrating sample magnetometry. YIG was heterocoagulated by silica as indicated by TEM micrographies. XPS measurements indicated that only binding energy for silicon and oxygen was found on the silica shell, which confirms that the YIG was covered. The values of the saturation magnetization differ from the heterocoagulated system to well-crystallized YIG.

INTRODUCTION

There are several reasons to make it useful to cover core materials with shells of different chemical composition by heterocoagulation process [1-4]. One is to change physical (optical, magnetic, conductive, etc.) or chemical properties of dispersions by choising coating material. Furthermore, when a required particle shape is impossible to achieve by direct synthesis, desired core can be coated with another compound necessary for the given application. Thus, the coating process can be influenced by several properties of the particle. After the covering process, the external surface of the particle can show special properties, such as a catalytic property becoming a more efficient catalytic material, being the internal material protected against environmental aggressiveness[5]. The heterocoagulation process is similar to those used for obtaining the uniform particles, as described by Matijevic [6,7] and others [8,9]. However, the heterocoagulation process requires rigorous controls of the nucleation conditions and growth of the involved phases. It is known that magnetic properties depend strongly on the size, as well as on the dispersion medium where the particles are formed. Specifically, the preparation of magnetic powders with defined properties and a protecting layer by heterocoagulation is, therefore, of great interest for the increase of magnetic material performance which is drastically affected by environment[1,10]. An alternative way to eliminate or to minimize these problems is the heterocoagulation of these particles with protecting layer, for instance, with silica. In this study, a procedure is described for building up of silica layers on yttrium iron garnet (YIG) particles. YIG, especially that of interest as magnetic pigment, microwave absorption and magnetic fluids have been coated with silica in order to protect its magnetic property from environment enlarging its technological applications.

Mat. Res. Soc. Symp. Proc. Vol. 581 © 2000 Materials Research Society

EXPERIMENTAL

YIG Cores

Yttrium chloride, iron chloride, yttrium nitrate, iron nitrate, urea, ammonium hydroxide, and poly (vinylpyrrolidone) were all reagents used without further purification. YIG amorphous particles were obtained by hydrolysis of metal chloride or nitrate solutions[11,12]. The starting solution was a mixture of iron chloride (1.10^{-3} mol L^{-1}) and yttrium chloride in chloridic acid 1.10^{-2} mol L^{-1} or iron nitrate (1.10^{-3} mol L^{-1}) and yttrium nitrate in nitric acid 1.10^{-2} mol L^{-1}. These solutions were mixed, keeping the ratio of Fe to Y at 5:3. Urea was added in different concentrations in order to increase the pH and improve the hydrolysis process. In some cases, poly(vinylpyrrolidone) and ammonium iron (III) sulfate [$NH_4Fe(SO_4)_2$ 12 H_2O in (w/w %) were added to avoid aggregation[13]. After keeping the solution at the temperature of 90°C for 3 hours, the powder was then dried in a desiccator under vacuum. Precipitates were calcinated at 1100°C for one hour, yielding cubic YIG particles. Table 1 describes the precipitation conditions of yttrium iron garnet.

Table I: Identification and precipitation conditions of the yttrium iron garnet obtained from different anions by using urea as the precipitation agent in presence of PVP and/or iron ammonium sulfate. Different concentrations of urea was used as precipitation agent.

Samples	Urea agent ($mol.L^{-1}$)	Concentration of iron chloride or nitrate ($mol.L^{-1}$)	Addition of PVP (% w/w)	Addition of $NH_4Fe(SO_4)_2$ (% w/w)
P16	0.5	1.10^{-3}	-	-
P24	0.5	1.10^{-3}	1	50%
N3	0.5	1.10^{-3}	-	50%
N4	0.5	1.10^{-3}	1	50%
N5	0.5	1.10^{-3}	-	-
N6	1.0	1.10^{-3}	-	-

Coated Particles

Yttrium iron garnet was coated with silica by using the tetraethylorthosilicate (TEOS) hydrolysis process[14] adapted from Stober[15]. YIG particles dispersed in 2-propanol were heterocoagulated with silica through the nucleation of TEOS solution forming the silica layer on YIG. The dispersion of the particles was then heated up to 50°C for 30 minutes under ultrasonic agitation. Solution of TEOS and NH_4OH in appropriated concentration was added to the suspension of YIG and then placed into a constant-temperature water bath at 50°C and kept in it for different periods of time (from 0.5 to 3 h) in order to produce different coating layer thickness. The resulting solids were dried in a vacuum. The identification of the heterocoagulated samples and the conditions of precipitation in system are described in table 2.

Dried products were investigated by transmission electron microscopy (Hitachi H-800-MT), X-ray energy-dispersive spectra (Kevex 8000 analytical system, model Quantum), X-ray photoemission spectra (Physical Electronics 5500) and vibrating sample magnetometry (VSM4500 Princeton Applied Research).

Table 2. Conditions of heterocoagulation systems YIG-SiO_2. The system was kept in water bath at 50^0C. The concentration of yttrium iron garnet is 1.10^{-3} mol.L^{-1}, TEOS 1.10^{-3} mol.L^{-1}, NH_3 0.45 mol.L^{-1} in 2-propanol medium in a reactor with volume of 10 ml.

Samples YIG core / SiO_2 cover	Heterocoagulation time	Samples YIG core / SiO_2 cover	Heterocoagulation time
H1 - P24 / SiO_2	0.5 hours	**H7 - P24 / SiO_2**	1 hour
H2 - P24 / SiO_2	0.75 hour	**H8 - P16 / SiO_2**	1 hour
H3 - P24 / SiO_2	3 hours	**H9 - N3 / SiO_2**	1 hour
H4 - P16 / SiO_2	0.5 hour	**H10 - N4 / SiO_2**	1 hour
H5 - P16 / SiO_2	0.75 hour	**H11 - N5 / SiO_2**	1 hour
H6 - P16 / SiO_2	3 hours	**H12 - N6 / SiO_2**	1 hour

RESULTS

All experiments were designed to investigate the heterocoagulation of the YIG particles and to find out the effect of this layer in the magnetic properties in the samples. The transmission electron microscopy in figure 1 shows that the samples were covered and also shows the thickness of the coated layer. There should also be pointed out that the heterocoagulated samples are related to *in situ* the growth layer on YIG. A black arrow indicates the identification of the nucleus of YIG and an empty black shows the shell.

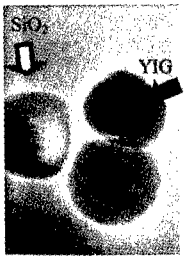


Figure 1. TEM micrograph of SiO_2-cover YIG, sample H7.

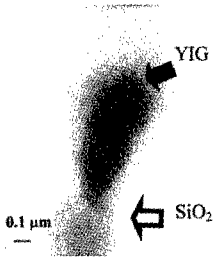


Figure 2. TEM micrograph of SiO_2-cover YIG, sample H9.

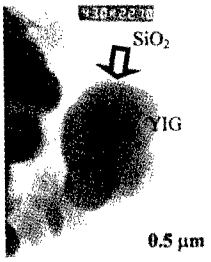


Figure 3. TEM micrograph of SiO_2-cover YIG, sample H8.

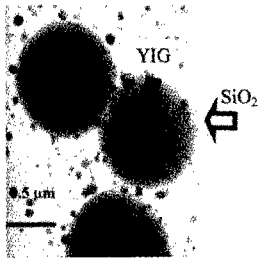


Figure 4. TEM micrograph of SiO_2-cover YIG, sample H11.

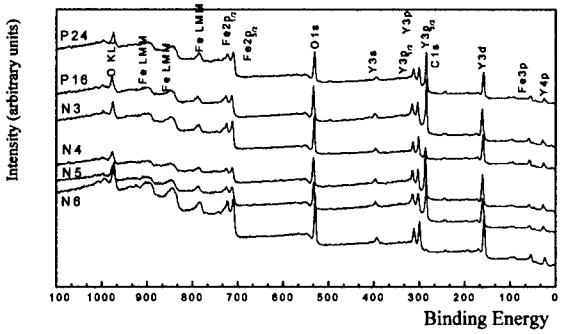


Figure 5. XPS spectra of samples P24, P16, N3, N4, N5 and N6. The samples were bombardment with Ar^+ by 0.3 minutes.

The spectra presented in figure 5 show that all the surfaces of the samples have the characteristic energy of the yttrium iron garnet and this confirms the values of the connection energy described in literature [21,22]. Analyzed samples presented an atomic percentage of Fe 2p3/2 = 23.6 %, Y3d = 14.6 % and O1s = 61.8 %, in agreement with the stoichiometry relationships of the YIG. What can be observed in these samples is the presence of intense peaks of carbon of 284.5 eV that were ascribed to the urea decomposition product.

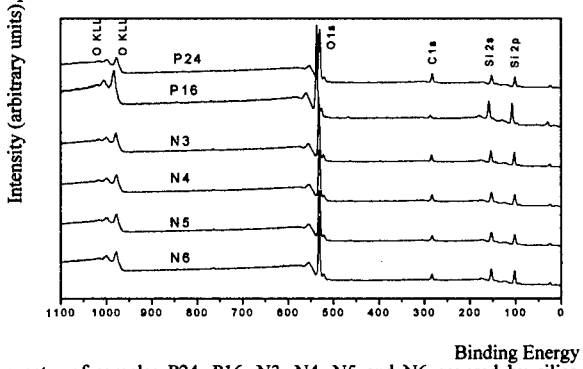


Figure 6. XPS spectra of samples P24, P16, N3, N4, N5 and N6 covered by silica. The samples were bombardment with Ar^+ by 0.3 minutes.

Although all measured binding energy was detected, the emphasis of the discussion will be on the binding energy of silica, since the aim of the investigation is to identify the elements on the surface of the particle. The binding energy value 284.8 eV to Si 2p and 531.0 eV to O 1s measured for silica coincides fairly well with most values reported in the literature [21,22]. Through XPS spectra, figure 6, it is seen that the silica cover of the samples does not present the elements iron and yttrium on the surface such as in figure 5. Thus, as the binding energies were only detected for oxygen and silicon, we can conclude that the ferrite surface was totally covered by silica. Theoretical and experimental energies

comparison obtained from these samples confirms that the analyzed surface is constituted of silica, with its stoichiometric proportions.

Figure 7 shows the hysteresis loops for pure YIG sample and covered YIG sample. It must be emphasized that the crystalline samples show their magnetization, *M*s next to the bulk[23,24] value, 26 emu.g^{-1} while the magnetization of heterocoagulated samples show lower values.

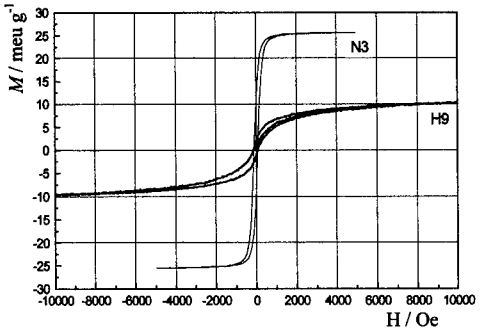


Figure 7. Hysteresis loops of samples N3 (Crystalline YIG) and H9 (silica cover on N3) recorded at room temperature.

Table 3 shows the values of coercive field Hc and magnetization of crystalline and heterocoagulated samples.

Table 3. Magnetic measurements for YIG samples

Samples	Ms (emu/g)	Hc (Oe)	Samples	Ms (emu/g)	Hc (Oe)
P16	27.01	72.05	**H7 - P24 / SiO_2**	14.6	86.7
P24	25.12	72.05	**H8 - P16 / SiO_2**	14.6	120.0
N3	25.48	98.25	**H9 - N3 / SiO_2**	11.0	136.2
N5	17.13	98.25	**H10 - N4 / SiO_2**	9.2	119.7
N6	24.24	98.25	**H11 - N5 / SiO_2**	17.9	177.5
N4	25.22	98.25	**H12 - N6 / SiO_2**	17.3	152.7

Table 3 lists the initial magnetic properties (coercive force, *H*c, and the specific magnetization, *M*s) of cover samples measured by VSM. The value of *M*s decreased with silica on the YIG surface due to the presence of the nonmagnetic silica coating and it was lower than that of pure yttrium iron garnet in all cases. Another property that can be evaluated by figure 7 is the variation in the hysteresis curve where the field applied to saturate the heterocoagulated sample is five times larger than that for crystalline yttrium iron garnet. The variation of coercive field and saturation magnetization was observed by Matijevic *et al* in their work on silica covered hematite [25] which shows the variation of magnetic properties regarding the silica shell thickness. This behavior can be explained through surface and or shape anisotropy.

CONCLUSION

The method of covering YIG with silica shell by growing *in situ* showed satisfactory results. All samples showed silica cover; however, some surfaces were not totally covered. Particle shape seems not to be the decisive factor in the cover because there

were agglomerate covered particles. By XPS it can be compared the surface of pure YIG and silica on YIG. Analyzing the surfaces of covered samples it could be observed that the relative peaks of Fe and Y were absent, which confirms the heterocoagulation. Comparing the magnetic measures of the YIG and silica on YIG samples was observed that the magnetic properties *Ms* and *Hc* were reduced; however, these samples present good characteristics to be used as magnetic inks.

REFERENCES

01 - A. P. Philipse, P. B. Van Bruggen, C. Pathmamanoharan, *Langmuir*, 10, 92, 1994.
02 - H. Kihira, N.Ryde, E. Matijevic, *Colloids and Surfaces*, 64, 317, 1992.
03 - H. Kihira, N.Ryde, E. Matijevic., *J. Chem. Soc. Faraday Trans*, 88, 2379, 1992.
04 - N.Ryde, E. Matijevic, *J. Chem. Soc. Faraday Trans*, 90, 167 , 1994.
05 - H. Giesche, *J.Disp. Sci and Technology*, 19(2&3), 249, 1998
06 - E. Matijevic, *Langmuir*., 10, 8, 1994.
07 - E. Matijevic, *Formation of monodispersed inorganic particulates*; p39-59 in Controlled Particle, dropled and bubble formation, ed D.J. Wedlock, Butterworth-Heinemann Ltd, Oxford 1994.
08 - J. A Maroto, F. J. Nieves, *Colloids and Surfaces*, 145, 271, 1998.
09 - P. R. Roy, K. S. Roy, C. Ganguly, Advanced Ceramics; Proceeding of an Internascional Symposium on Advanced Ceramics ISAC'90,Bombay India. Ramini, G, V., Agrawal, D, C., Majumder, S, B., Key Eng. Mater, 56-57, 165, 1991.
10 – E. Matijevic, M. Ohmori, *J. Colloid Interface Sci.* 150, 594, 1992.
11 - R.H.M.Godoi, M.Jafelicci Jr, R.F.C.Marques and L.C.Varanda. *Materials Research Society*, Symposium Proceedings 517, 583, 1998.
12 – R. H. M. Godoi, M. Jafelicci Jr, R. F. C. Marques, L. C. Varanda, R. C. Lima. *Química Nova*, in press, 1999.
13 - E. Matijevic, W. P. Hsu and G. Wang, *Colloids and Surfaces*, 61, 255, 1991.
14 - R. H. M. Godoi, L. Fernandes, M. Jafelicci Junior, R. C. Marques, L C. Varanda, M. R. Davolos. *Journal of Non-Crystalline Solids* 247, 141, 1999.
15 - W. Stober, A. Fink and E. Bohn, *J.Colloid Interface Sci* 26, 62, 1968.
16 - S. Kratohvil, E. Matijevic, *Adv. Ceramic Mater* 2, 798, 1987.
17 - B. Aiken, E. Matijevic, *J. Colloid Interface Sci*, 126, 645, 1988.
18 - A .Garg, E. Matijevic, *Langmuir* 4, 38, 1988.
19 - A Garg, E. Matijevic, *J. Colloid Interface Sci* 126, 243, 1988.
20 - M. Ohmori, E. Matijevic, *J. Colloid Interface Sci* 150, 594, 1992.
21 - A .Chernakova, K. Kostov, V. Shapovalov, *Nucl. Inst. and Meth.* BB62, 228, 1991.
22 - G. N. Wyk, S. Priggemeyer, W. D. Roos, W. Heiland, *Applied Surface Sci*, 52, 351, 1991
23 - P. Vaqueiro, et all, *J. Mater. Chem.* 7(3), 501, 1997.
24 - S. Taketomi, K. Kawasaki, Y. Osaki, S. Yuasa, *J. Am. Ceram Soc.* 77, 1787, 1994.
25 - M. Ohmori and E. Matijevic, *J. Colloid Interface Sci* 160, 288, 1993.

ACKNOWLEDGEMENTS

We acknowledge financial support from *FAPESP*.

SYNTHESIS OF CUBIC AND RHOMBOHEDRAL PHASED NANOCRYSTALLINE SnO_2 DOPED In_2O_3 [ITO] POWDERS WITH COPRECIPITATION METHOD

Bong-Chull Kim, Jeong-Joo Kim, Se-Hong Chang*
Dept. of Inorganic Materials Engineering, Kyungpook Nat'l Univ., Taegu 702-701 KOREA
*KETI, PyungTeak 451-860, KOREA

ABSTRACT

Nanocrystalline ITO powders have been prepared by a hydroxide coprecipitation method. Through the variation of aging time after precipitation, we have characterized the size, morphology and the structure of the precipitates. It was found that the precipitates are in the state of InOOH at first. Further aging up to 48 h changed it to $In(OH)_3$ structure. After calcinations of the precipitates, rhombohedral nanocrystalline ITO powder with spherical shape was produced from InOOH structured precipitates, while cubic nanocrystalline ITO powder was produced from $In(OH)_3$. Fraction of the rhombohedral ITO powder decreased as the aging time increased. The particle size of the cubic ITO increased with aging time but that of rhombohedral ITO (~15 nm) was almost invariant.

INTRODUCTION

Tin doped indium oxide (ITO) film, which is used for transparent electrodes for display devices, transparent coating for solar energy heat mirrors and windows films in n-p heterojunction solar cells, is manufactured by evaporation, sputtering, chemical vapor deposition and painting process[1~3]. For the good quality ITO films, processing with good controlled ITO powders is necessary[4].

Several chemical processing techniques, such as hydrothermal, so-gel, and coprecipitation have been investigated to prepare active nanocrystalline ITO powders for dense target and precursors[5~7]. Among these powder processing techniques, coprecipitation has been suggested as a simple and economic way to obtain nanocrystalline ITO powders with good controlled particle size and morphology. In the coprecipitation method, the morphology, particle size, and composition of precipitates depend on several parameters such as aging, concentration, temperature, pH, and the kinds of anions present[8-10]. In the present work, the morphology and the structure of the precipitate were controlled by varying aging time. As a result, cubic and rhombohedral nanocrystalline ITO powders were produced, and the fraction of the phases was dependent on the aging time. Therefore, selective production of nanocrystalline ITO powders with cubic or rhombohedral structure was available.

EXPERIMENT

Indium nitrate hydrate [$In(NO_3)_3 \cdot xH_2O$] and tin chloride hydrate($SnCl_4 \cdot xH_2O$) were used as starting materials. Mixed solutions of indium and tin were prepared by dissolving indium nitrate hydrate and tin chloride hydrate in doubly deionized water, respectively. Concentration and In/Sn atomic ratio in mixed solution were fixed to 1 N and 92/8, respectively. NH_4OH was added directly to a continuously stirred mixed solution until the pH reaches to 8.5. Then precipitate in Pyrex glass was sealed with silicon cover and aged for 0, 12, 24, and 48h. After the aging process, precipitates were washed several times with deionized water using ultrasonic equipment and dried at 85°C. The dried precipitates were calcined at 600°C for 1 h in air and nanocrystalline ITO powders were produced. In/Sn atomic ratios in the nanocrytalline ITO

Mat. Res. Soc. Symp. Proc. Vol. 581 © 2000 Materials Research Society

powders were confirmed as 92/8 by a X-ray fluorescence spectrometer (XRF; Model PW 2400, Philips).

Phase identification and particle size measurement were performed by a X-ray diffractometer of the powders (XRD; Mac Science) using CuK_{α} radiation. Fractions of cubic and rhombohedral phases in calcined nanocrystalline ITO powders were obtained by calculating integrated intensities of the (110) peak of rhombohedral ITO (JCPDS No. 21-0406) and the (222) peak of cubic ITO (JCPDS No. 44-1087) after being subtracted $K_{\alpha 2}$ and split multi-peak by using a software. The particle size of the powder was calculated from X-ray peak broadening using the Scherrer equation[11]. Si standard powders were used as a reference. The morphology and size of precipitates and ITO powders were examined by a transmission electron microscopy (TEM; Model H-7100, Hitachi). In addition, the dried precipitates were characterized by Fourier transform infrared (FT-IR) spectroscopy (Model IFS120HR, Bruker).

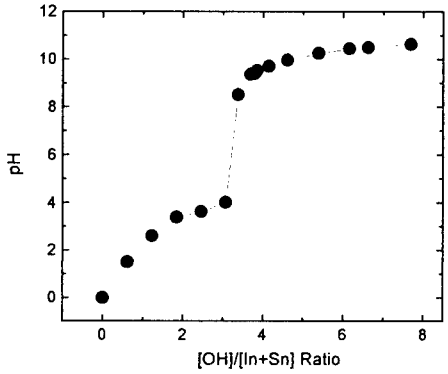


Fig. 1. NH_4OH titration of [Sn+In] solution at 15°C and concentration of 1 N.

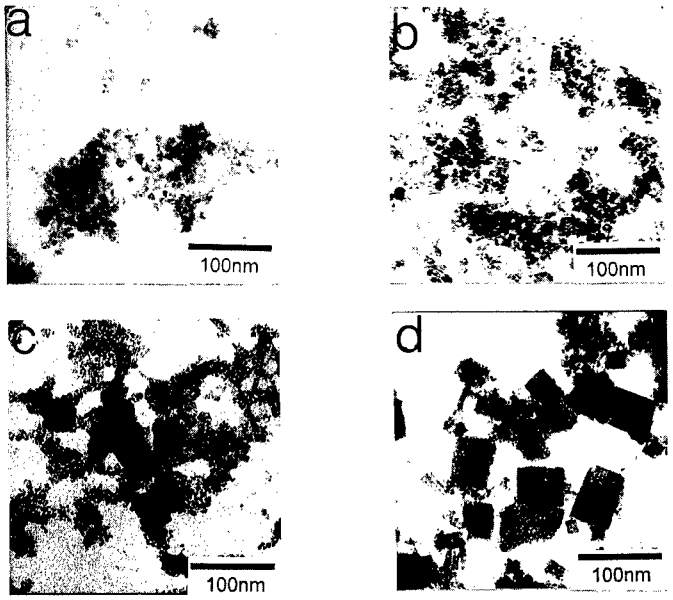


Fig.2. TEM images of the precipitates with aging time of (a) 0, (b) 12, (c) 24, and (d) 48 h.

RESULTS and DISCUSSION

Figure 1 shows the change of pH value of the mixed solution with the addition of NH_4OH. The pH value rose steeply from 4 to 8.5 at 3.1 of [OH]/[In+Sn] ratio, which implies that the formation of hydroxide is almost completed at this point. The optimum coprecipitation condition of pH was estimated based on the solubility diagrams of individual hydroxides[12] and pH 8.5 was selected as the optimum condition of pH where the In and Sn hydroxides can precipitate simultaneously.

TEM micrographs of the precipitates with various aging times are shown in Figure 2. When the precipitate was not aged (Figure 2 (a)), it has spherical morphology with ~5 nm particle size in diameter. However, the precipitate aged for 48 h showed rectangular morphology with 80 nm · 60 nm, as shown in Figure 2(d). As the aging time increased, the volume fraction of precipitate with rectangular morphology increased.

Figure 3 shows the XRD patterns of precipitate aged for (a) 0, (b) 12, (c) 24, and (d) 48 h. The XRD pattern of precipitate shown in Figure 3(a), which has spherical morphology well matched with InOOH structure[JCPDS No. 17-0549]. However the XRD pattern of precipitate aged for 48 h in Figure 3 (d), which showed the rectangular morphology corresponded to $In(OH)_3$ structure[JCPDS No. 16-0161]. This result shows that the precipitate transforms from spherical morphology with InOOH structure to rectangular morphology with $In(OH)_3$ structure as the aging time increases, which signifies that InOOH is meta-stable developed at first then transforms to $In(OH)_3$ phase during the aging process.

Figure 4 shows the FT-IR spectra of the dried precipitates aged for (a) 0 h and (b) 48 h. The absorption peaks in Figure 4 (b) well matched with $In(OH)_3$ reported[13]. But in Figure 4 (a), the stretching peaks at 780, 852, and 1067 cm^{-1} originated from $In(OH)_3$ are not observed. Several types of phase transformations in many gels and precipitates of hydrous oxides can occur during aging because the aging of the solution allows reorganization of the structure by dissolution and reprecipitation[14]. Therefore, it is believed that the structural change of the

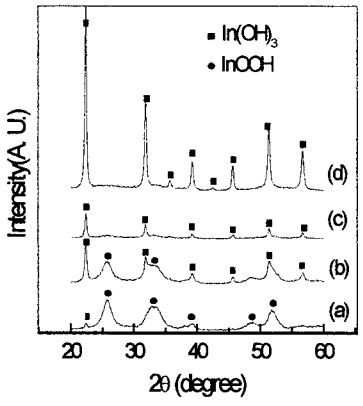


Fig.3.X-ray diffraction of the dried precipitates with aging time of (a) 0, (b) 12, (c) 24, and (d) 48 h.

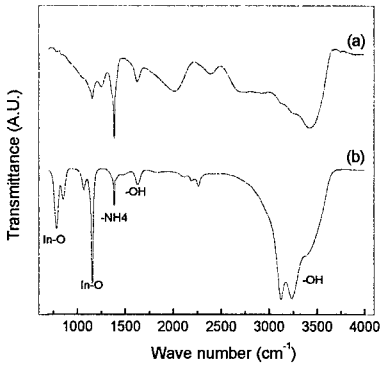


Fig. 4. FT-IR spectra of the dried precipitates with aging time of (a) 0 and (b) 48 h.

precipitates as a function of aging time seems to be caused by the reorganization of the structure during the aging process. The absorption peak near 1380 cm^{-1}, which corresponds to NH_3 was observed in both Figure 4 (a) and 4 (b) indicating NH_3 species still exist after washing. Meanwhile the NH_3 stretching is higher in Figure 4 (a) than 4 (b). Since small particles have large surface area, more NH_3 might be adsorbed in the InOOH structured precipitate, which has smaller than with small particle size than $In(OH)_3$.

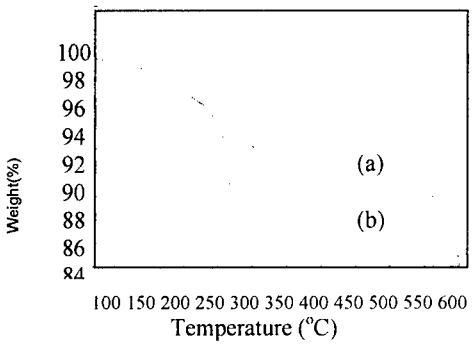


Fig. 5. TG curves for the dried precipitates with aging time of (a) 0 and (b) 48h.

Figure 5 shows the TG curve of the dried precipitates aged for (a) 0 h and (b) 48 h (b). The weight loss of InOOH structured precipitate containing small amount of -(OH) ligand was 12% and that $In(OH)_3$ structured precipitate was 18%. Further weight loss was not observed above 450°C.

TEM photographs of ITO powders produced by a calcination of precipitates aged for various times are presented in Figure 6. The ITO powders in Figure 6 (a) produced from InOOH structure showed spherical morphology with ~15nm in diameter, while the ITO powders in Figure 6 (d) showed mostly rectangular morphology with a particle size of ~(80 60) nm . This result signifies that the morphology of the precipitate was still maintained after calcination.

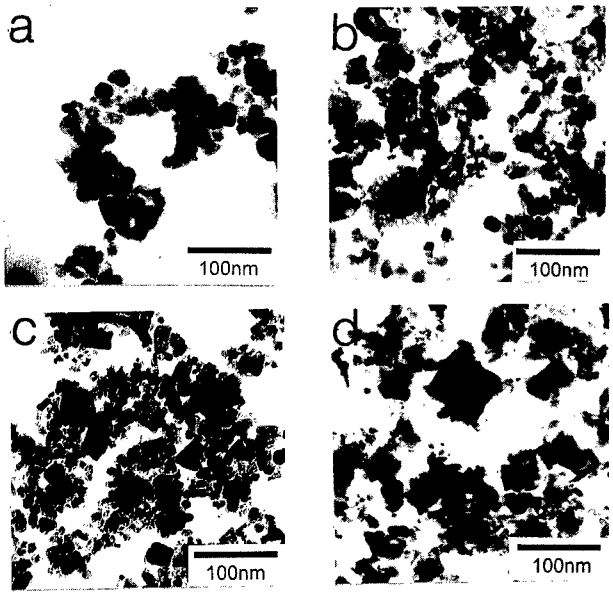


Fig.6. TEM photographs of the nanocrystalline ITO powders calcined at 600°C with precipitates aged for (a) 0, (b) 12, (c) 24, and (d) 48 h.

Figure 7 shows the XRD patterns of the ITO powders calcined with precipitates aged for various times. The XRD result indicates that cubic and rhombohedral ITO coexist in all of the powders. However the volume fraction of each phase was changed as the aging time of the precipitates varied. Consequently, the longer aging time produced the more cubic phase, and InOOH and $In(OH)_3$ structured precipitates finally produce rhombohedral and cubic ITO powders, respectively. We also confirmed that the rhombohedral phase disappears and only cubic single phase exists above 800°C.

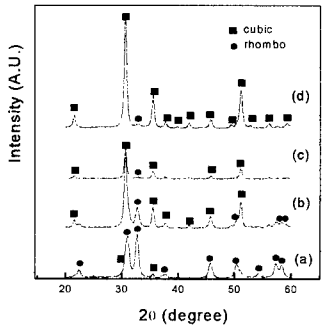


Fig. 7. XRD patterns of the nanocrystalline ITO powders calcined at 600°C with precipitates with aging time of (a) 0, (b) 12, (c) 24, and (d) 48 h.

The volume fraction of cubic and rhombohedral phase of ITO powders was calculated from the integrated intensities of its main diffraction peak and the results are shown in Figure 8. The volume fraction of rhombohedral phase of the nanocrystalline ITO powders decreased greatly from 75% to 6% as the aging time increased.

The particle sizes of powders calculated from X-ray peak broadening are summarized and presented in Figure 9. The particle size of cubic ITO powder increased greatly from 20 to 95nm with aging time but the size of rhombohedral powder was invariant. Over 12 h of aging time, we could not measure the particle size of rhombohedral ITO powder due to its weak diffraction of XRD.

There is a pressure difference given by between large and small particle due to its particle size, which is $\Delta P = 2\gamma / r$, where ΔP is pressure difference, γ is surface energy and r is the radius of particle. In the case of 15 nm particle size, for example, ΔP is approximately 1300 atm

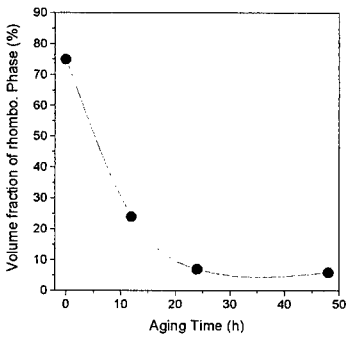


Fig.8. Variation of fraction of rhombohedral phase in the nanocrystalline ITO powders as a function of aging time.

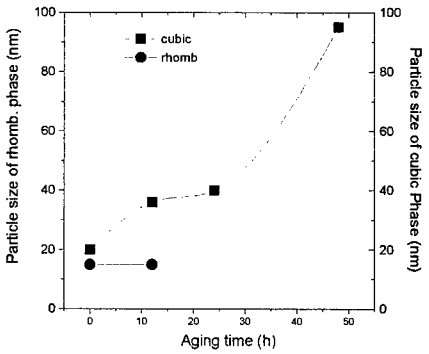


Fig.9. Cubic and rhombohedral particle sizes in the ITO powders as a function of aging time.

(γ=~1000 erg in conventional ceramic). Concerning the crystallographic structure of ITO, rhombohedral structure is more stable at high pressure than cubic structure[15~16]. The particle size dependence on crystallographic structure is well known in $BaTiO_3$ ceramics that the tetragonality of $BaTiO_3$ powder starts to decrease near 0.3 μm and more cubic structure developed as the particle size decreased[17]. From this respect of view, small particle with high ΔP may form its structure stable at high pressure. Also, the crystallographic similarity between precipitate and calcined powder seem to have close correlation. However, further detail studies are required to clarify the results.

SUMMARY

Nanocrystalline ITO powders were prepared by the coprecipitation method. After precipitation aging was followed up to 48 h, and it greatly influenced on the morphology and size of the precipitates. It was found that the aging process brought phase transformation of the precipitate from InOOH to $In(OH)_3$ structure. After calcinations at 600°C for 1 h, InOOH and $In(OH)_3$ structured precipitates produced rhombohedral and cubic structured ITO powders, respectively. Therefore, the crystallographic structure of ITO powder and its volume fraction could be controlled by aging time. The structural change of the precipitates was explained by the reorganization of the structure during aging process. The stability and similarity of structure between precipitates and final product of ITO powders seem to have close correlations, however, further studies are needed for more evidence.

ACKNOWLEDGMENTS

The authors are thankful to Korea Basic Science Institute Taegu Branch for providing measurement and analysis facilities.

REFERENCES

1. H.Hoffmann, J. Pickl, M. Schmidt, and D. Krause, Appl. Phys., **16**, p.239 (1978).
2. J. C. C. Fan, F. J. Bachner, and G. H. Foley, Appl. Phys. Letters, **31**, p773 (1977).
3. M. Buchanan, J. B. Webb, and D. F. Williams, Appl. Phys. Letters, **37**, p213 (1980).
4. T. Iwamoto, Functional materials (kino Zairyo, in Japanese), **11**, p35 (1991).
5. S. Nagashima, T. Yoshida, A. Kato, Materials Letters, **19**, p171 (1994).
6. D. W. Kim, S. G. Oh, and J. D. Lee, Langmuir, **15**, p1599 (1999).
7.T. Kayukawa, H. Shigetani, and M. Sennia, J. Mat. Science Letter, **14**, p252 (1995).
8. S. Kratohvil and E. Matijevic, J. Mater. Res., **6**, p766 (1991).
9. D. Sordelet, and Mufit Akinc, J. Colloid and Interface Science, **122**, p47 (1998).
10. R. Roy and M. W. Shafer, J. Phys. Chem., **58**, p372 (1954).
11.B. D. Cullity, Elements of X-ray Diffraction 2nd, Addison-Wesley Publishing Co., Massachusetts, 1978, pp284~285.
12. F. B. Charles and E. M. Robert, Hydrolysis of Cation, Krieger Pub. Co., 1986, pp293~300.
13. C.J. Brinker, et al., Sol-Gel Science, Academic Press, 1990, pp370~371
14. D. F. Mullica, G. W. Beall, and W. O. Milligan, J. Inorg. Nucl. Chem., **41**, p277 (1979).
15. A. N. Christensen, R. Gronbek, and S. E. Rasmussen, ACTA Chemica Scandinavica, **18**, p1261 (1964).
16. A. N. Christensen and N. C. Broch, ACTA Chemica Scandinavica, **21**, 1046 (1967).
17. K. Uchino, E. Sadanaga, and T. Hirose, J. Am. Ceram. Soc., **72**, p1555 (1989).

EFFECT OF VAPOR PRESSURE OF H_2O ON THE FORMATION OF NANO-CRYSTALLINE TiO_2 ULTRAFINE POWDERS

K. R. Lee*, S. J. Kim**, ,J. S. Song***, and S. Park*
*Dept. of Ceramic Eng., Myong-Ji University, Yongin, 449-728, spark@wh.myongji.ac.kr,
**KAERI, Yusong, Taejon, 305-600
***KERI, Changwon, 641-120, ROK

ABSTRACT

Mono-dispersed TiO_2 ultrafine particles with diameters 40-400nm were obtained from aqueous $TiOCl_2$ solution with 0.67M Ti^{4+} concentration prepared diluting $TiCl_4$ by homogeneous precipitation process in the ranges of 17-230℃. With the spontaneous hydrolysis of $TiOCl_2$, which means the natural decrease of pH value in the aqueous solution, all mono-dispersed precipitates were crystallized with the anatase or rutile TiO_2 phase. TiO_2 precipitate with the pure rutile phase was fully formed at the temperatures below 65℃, not involving the evaporation of H_2O, and above 155℃, which were available by suppressing it. TiO_2 precipitate with rutile phase including a small amount of the anatase phase started to be formed in the intermediate temperatures above 70℃ showing the full formation of the anatase above 95℃ under the free evaporation of H_2O. However, in the case of completely suppressing H_2O evaporation at the temperatures above 70℃, TiO_2 precipitate with anatase phase was fully transformed into the precipitate with the rutile phase by the vapor pressure of H_2O. Therefore, the formation of TiO_2 precipitates with the rutile phase around room temperature would be caused due to the existence of the capillary pressure between the agglomerated needle-shaped particles or the ultrafine clusters, together with the slow reaction rate.

INTRODUCTION

TiO_2 with rutile phase has been widely used as a white pigment material due to an excellent light scattering effect as well as a coating material for optical or electronic devices due to its high dielectric constant, high refractive index and chemical stability even in strongly acidic or basic environments[1-4]. TiO_2 with rutile phase for applications in optical or electronic devices has been generally adopted in the form of a thin film using various fabrication methods such as RF-sputtering, E-beam evaporation, chemical vapor deposition, sol-gel and so on. However, these methods resulted in a thin film of TiO_2 with the substoichiometry or amorphous phase. Thus, it is necessary to dope other elements during the deposition of the film for the stability of the anatase phase or to anneal it for the conversion of anatase to rutile phase at temperatures above 400℃ for a long times. On the other hand, the screen printing or casting method with the nano-sized rutile TiO_2 powders has recently received the attention to the direct application for the dielectric layer of an AC powder electroluminescent device in place of the heat-treatment of the thin film prepared using various vacuum techniques[5].

Up to now, the various processes such as the sulfate, the chloride, the hydrothermal, and the sol-gel processes for the fabrication of TiO_2 powder with the rutile phase have been developed[6-10]. To prepared the rutile TiO_2 ultrafine powder using one of above processes, however, many disadvantages, such as high costs for high temperatures of synthesis and heat treatment, difficulties in continuous processing, low efficiencies in production, and contamination of impurities during the crushing or pulverizing should be overcome. Park et al. have recently developed a very economical process for ultrafine TiO_2 homogeneous powder with the rutile phase by just heating an aqueous $TiOCl_2$ solution from $TiCl_4$, which enhances the spontaneous precipitation of TiO_2 [11, 12]. Therefore, there is an ample interest in closely examining the homogeneous precipitation mechanism of crystalline TiO_2 ultrafine powder in aqueous $TiOCl_2$ solution. The object of this paper, for the extension of the development for a new synthesis method of the ultrafine TiO_2 powder, is to investigate in detail the reaction of $TiOCl_2$ with H_2O for the homogeneous precipitation. Thus, the shapes and changes in the crystalline state of the TiO_2 precipitates under various precipitation conditions were observed to find the precipitation mechanism of ultrafine TiO_2 powder from aqueous $TiOCl_2$ solution.

Mat. Res. Soc. Symp. Proc. Vol. 581 © 2000 Materials Research Society

EXPERIMENT

Transparent titanium tetrachloride ($TiCl_4$, 3N, Aldrich. Co.) was used as a starting material to fabricate the ultrafine TiO_2 powder using the homogeneous precipitation method. First, in order to prepare aqueous $TiOCl_2$ solution with a high viscosity to use as a stock solution, $TiCl_4$, which had been cooled below 0℃, was put into a constant temperature(0℃) reaction container, and then distilled water ice pieces were slowly added to the container for a hydrolysis reaction. During the reaction, yellow cakes, such as an unstable $TiO(OH)_2$ intermediate product, were formed at first together with the slow melting of ice pieces, and then dissolved with the continuously added ice pieces to form a yellow aqueous $TiOCl_2$ solution with a Ti^{4+} ion concentration of 4.7M. Finally, distilled water was added to this stock solution to obtain a transparent aqueous $TiOCl_2$ solution with a Ti^{4+} concentration of 0.67M for the homogeneous precipitation. For the precipitation of TiO_2 from aqueous $TiOCl_2$ solution, a cylindrical reservoir (inner diameter 80mm× length 100mm× thickness 6mm) obtained by machining the Teflon rod was utilized to completely seal itself using a cover with a Vitron O-ring in the water bath or oven during the reaction at 17-230℃. Also, for the safety of experiments, the mini autoclave of the SS 316 with Teflon lining was used because the precipitation reactions above 160℃ were performed under the pressures above 5bar of water vapor.

After completing the precipitation and keeping it untouched for 24hrs, the precipitates were filtered using distilled water or ethyl alcohol and a PTFE membrane filter(Micro-Filtration, System Co.) with a porosity of 0.1 ㎛ to completely remove Cl^- ions from the precipitates. The filtered precipitates were dried at 150℃ for 12hrs to obtain the final powder. All of the chemical agents used in this study have analytical reagent grades. The pH values of aqueous $TiOCl_2$ solution during the precipitation were measured using a 355-ion analyzer (Mettler Toledo Co.). The crystallinities of the dried precipitates were analyzed using XRD (Rigaku D/Max-111c : 3kW/40kV, 45mA) with CuK_α radiation and TEM diffraction and the shape of the precipitates was examined by SEM (JEOL ABT DX-BOS : 3kV). Also, the specific surface area of the precipitates was measured by the BET method after drying at 200℃ for 24hrs. The efficiencies of the precipitates in production were calculated by weighing the precipitates after the heat-treatment at 1000℃ for 60min or by analyzing the concentration of Ti^{4+} ion remaining in the aqueous $TiOCl_2$ solution using ICP-AES after the filtration.

RESULTS

First of all, to compare the precipitation behavior in aqueous $TiOCl_2$ solutions with various concentrations of Ti^{4+}, the precipitates were prepared using the simple heating method in the closed reaction reservoir made of Teflon. Fig. 1 shows SEM photographs for the powders obtained from the precipitation in aqueous $TiOCl_2$ solutions with 4.7M and 0.67M Ti^{4+} concentrations by simple heating method at 140℃ for 60min. All the precipitates were the rutile phase of TiO_2. Largely elongated particles with sizes ranging from 60 to 100 ㎛ due to the severe agglomerations of the small precipitates are formed in the case of a higher concentration of Ti^{4+}. However, in the case of a lower concentration of Ti^{4+} by the large addition of H_2O to aqueous $TiOCl_2$ solution with a Ti^{4+} concentration of 4.7M, the obtained precipitates are very fine and mono-dispersed with sizes of 0.2-0.4 ㎛ (specific surface area of about 179m^2/g). On the other hand, no precipitates were observed when the original $TiCl_4$ solution was heated without the addition of H_2O under the same conditions. Therefore, these indicate that the addition of H_2O alone to make $TiOCl_2$ dilute for the reaction can control the shapes and amounts of the precipitates even if none of the special additives containing important elements such as O^{2-} or OH^- are furnished to form the crystalline precipitates of TiO_2.

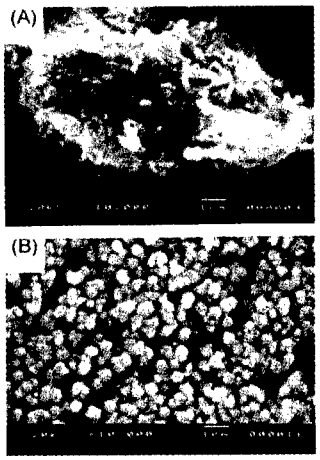


Fig. 1 SEM photographs for the crystalline TiO_2 powders prepared from (A) 4.7M and (B) 0.67M Ti^{4+} aqueous solution at 140℃ for 60 min

Fig. 2 shows the productive efficiencies for the powders that were precipitated for 4hrs with the extra additions of various amounts of ethyl alcohol to the $TiOCl_2$ solution including the same amount of H_2O during the same reaction time. After the precipitation, the precipitates were filtered using the paper with a porosity of 0.1 ㎛, and then were dried at 150℃ for 12hrs in open air. As the amount of the added ethyl alcohol increases the productive efficiency of the precipitated powders decreases dramatically. It was, however, confirmed that, at the reaction times more than 24hrs, the concentration of Ti^{4+} remaining in the aqueous $TiOCl_2$ solution after filtration was almost the same, as low as 10wt%, regardless of the amount of added ethyl alcohol according to the result of ICP-AES analysis.

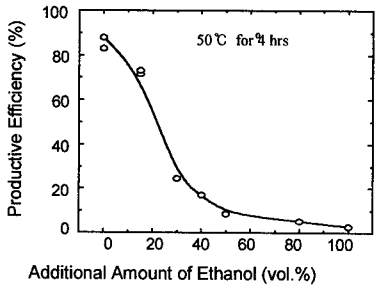


Fig. 2 The productive efficiency for the crystalline TiO_2 powders prepared from 0.67M Ti^{4+} aqueous solution with the various additional amounts of ethanol

It was also confirmed that because the precipitates formed together with the addition of ethyl alcohol were very ultrafine or not formed, compared to the case of no addition of ethyl alcohol, they were mostly passed through the filtering paper in the case of the short time reaction condition. On the other hand, it was found from many preliminary experiments that the ethyl alcohol did not take part in the reaction and did not provide OH^- ions for the hydrolysis of $TiOCl_2$. Thus, it can be assumed that the site number for the nucleation of TiO_2 in the solution is the same as the amount of H_2O supplied, regardless of the various amounts of ethyl alcohol. Therefore, it can be said that the decrease of the efficiency in production would be due to the slow growth rate of the precipitates by the screening effect of ethyl alcohol based on the real decrease in the volume fraction of the amount of H_2O surrounding the $TiOCl_2$ molecules. Conclusively, it is suggested that the precipitation of TiO_2 ultrafine particle in aqueous $TiOCl_2$ solution occurs easily and rapidly when the sufficient amounts of H_2O are supplied.

The precipitation of TiO_2 was carried out in aqueous $TiOCl_2$ solution with 0.67M Ti^{4+} concentration under the reaction conditions with the same efficiency in production and then the shape of the precipitate was observed, as shown in the SEM photographs of Fig. 3. It was confirmed that longer times were necessary to obtain the same productive efficiency at lower temperatures due to thermal diffusion in the solution.

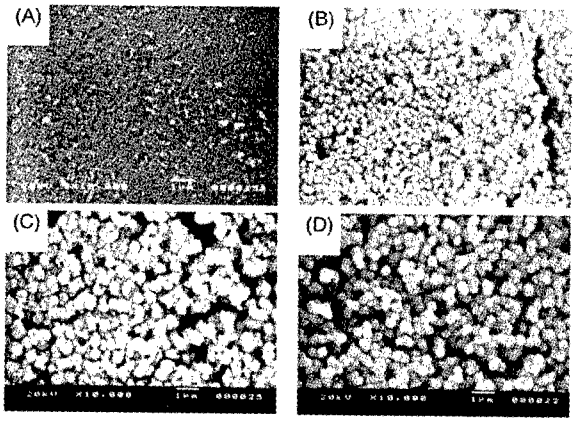


Fig. 3 SEM photographs for the crystalline TiO_2 powders precipitated from 0.67M Ti^{4+} aqueous solution under the reaction conditions of (A) 17℃ for 7 days, (B) 60℃ for 4hrs, (C) 100℃ for 2hrs and (D) 150℃ for 1hr

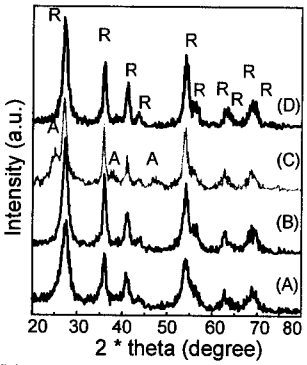


Fig. 4 XRD patterns for the TiO_2 powders shown in Fig. 3 under the reaction conditions of (A) 17℃ for 7 days, (B) 60℃ for 4hrs, (C) 100℃ for 2hrs and (D) 50℃ for 1hr (R : rutile, A : anatase)

The mono-dispersed precipitates are formed having increasing spherical sizes in the range of 40nm~400nm with the reaction temperatures. As shown in Fig. 4, with respect to the XRD results, the precipitates consist of the completely rutile phase of TiO_2 at 17℃, 60℃ and 150℃, and consist of the rutile phase including a small amount of the anatase phase of TiO_2 at 100℃ alone. On the other hand, it was observed that the crystalline structure of the dried precipitates was not changed with the annealing temperatures below 400℃, regardless of long annealing time in air. Generally the anatase phase of TiO_2, formed thermodynamically at low temperature, is obtained around 400℃ by the transformation from the amorphous phase formed at lower temperatures. Therefore, it can be known that all our precipitates were crystallized with the stable structures at temperatures lower than 150℃, even at room temperature.

In the dilute $TiOCl_2$ solution obtained from $TiCl_4$, crystalline TiO_2 particles were directly precipitated and at that time their structure was also purely rutile at the lower as well as the higher reaction temperatures, except for the intermediate temperatures at round 100℃. Various experiments were made to investigate these reasons. At first, to confirm how the direct precipitation of TiO_2 from aqueous $TiOCl_2$ solution occurred, pH value changes of aqueous $TiOCl_2$ solution with the reaction time were measured below 80℃, as shown in Fig. 5.

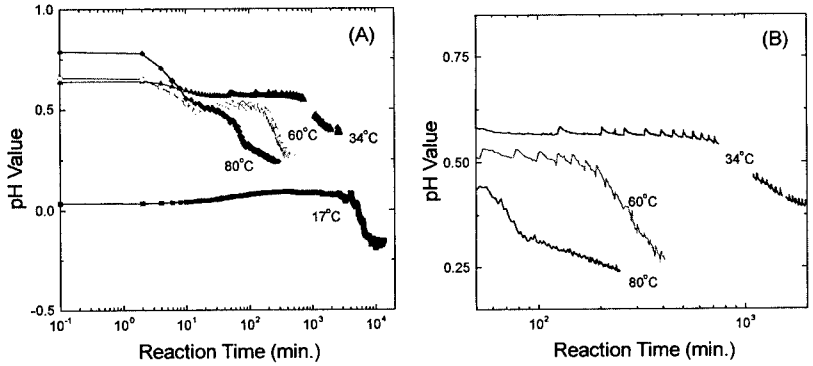


Fig. 5 The pH value changes of 0.67M Ti^{4+} aqueous solution with the reaction time at various temperatures, where Fig. 5(B) is an enlarged part of Fig. 5(A)

Here, the pH value was not measured above 80℃ due to boiling of the solution. At the same concentration of Ti^{4+}, as the reaction temperature increases, despite the pH value becoming relatively higher by the temperature effect, the pH values are almost constant or show a little decrease at the early stage and then greatly decrease after some time. This abrupt decrease in the pH value with the time agreed with the starting of the large precipitation in the aqueous $TiOCl_2$ solution, This also occurs at a faster time with a greater increase in the reaction temperature. In other words, a higher reaction temperature enhances the large precipitation in shorter time. Thus, it can be known that the precipitation of TiO_2 with the reaction time resulted in the decrease of OH^- ion concentration or the increase of H^+ ion concentration in aqueous $TiOCl_2$ solution from the measurement of the decrease in the pH value. Therefore, irrespective of the reaction temperatures, the entire precipitation reaction occurred accompanied by the hydrolysis of $TiOCl_2$ like the reaction Eq. (1) via the formation of intermediate hydroxide.

$$TiOCl_2 + 2H_2O \Leftrightarrow TiO(OH)_2 + 2HCl \qquad (1)$$

Also, as shown in Fig. 5(B) as an enlarged part of Fig. 5(A), it is observed that a repeatedly small increase and decrease in the pH value of a shape such as saw tooth is displayed continuously during the decrease in the pH value over the entire reaction time. Because this was repeatedly measured in all the conditions, the local variations in the pH value of the solution like this phenomenon may indicate the release of H_2O from $TiO(OH)_2$ during the crystallization or precipitation, as shown in the reaction Eq. (2).

$$TiO(OH)_2 + 2HCl \Leftrightarrow TiO_2\,xH_2O + 2HCl \qquad (2)$$

Therefore, it can be suggested that the synthesis of crystalline TiO_2 by the reaction of H_2O with $TiOCl_2$ is occurred by the precipitation with the hydrolysis, together with the crystallization.

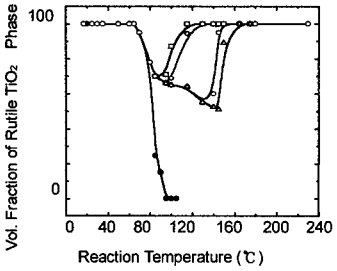


Fig. 6 The volume fraction of rutile TiO_2 phase formed with the various reaction times (closed data : ● 300min under free evaporation of H_2O, open data : 300min at the temperatures below 65℃ and △ 20min, ○ 30min, ▽ 40min, ◇ 60 min and □ 120min at the temperatures above 70℃ under no evaporation of H_2O)

In Fig. 3, all the TiO_2 precipitates from the reaction of H_2O with $TiOCl_2$ were crystalline, not amorphous. They were pure rutile phase at all the reaction temperature except for the mixture of rutile and anatase phases at 100℃ alone. During the precipitation reaction, to investigate how the crystalline status of TiO_2 was determined, all the TiO_2 powders formed at the range of 17-230℃ were characterized using XRD and SEM. Because the formed precipitates always consisted of rutile and/or anatase phases of TiO_2 in this experiment, the volume fraction of the rutile phase of TiO_2 prepared under various conditions was calculated using K. N. P. Kumar's equation[13] after the measurement of XRD, and the results are shown in Fig. 6. Here, the rutile phase of TiO_2 alone is always formed regardless of the various reaction times in the temperatures of 70-150℃, the anatase phase of TiO_2 is mainly formed under the free evaporation completely, the rutile phase of TiO_2 including a small amount of the anatase phase, is formed. In this range, the amount of the anatase phase increases with the increase in the reaction temperature for increasingly shorter reaction times and the amount of the rutile phase increases for increasingly longer reaction times. As reported previously[11, 12], the increase in the amount of the anatase phase above 70℃ may have occurred by the easy formation of the anatase phase due to the rapid rate of the precipitation reaction. However, it is not explained by the reaction rate that, at the same temperature, the anatase phase of TiO_2 was transformed into the rutile phase with an increasing reaction time. Fig. 7 shows the SEM photographs for the powders prepared with the reaction time. As the reaction time increases the size of the mono-dispersed particles increases somewhat, not showing changes of the shape. Here, because the precipitates at 850℃ for 120 min consisted of a rutile phase including an anatase phase and those at 115℃ for 60 min consisted of a pure rutile phase, for the precipitation reaction appropriately.

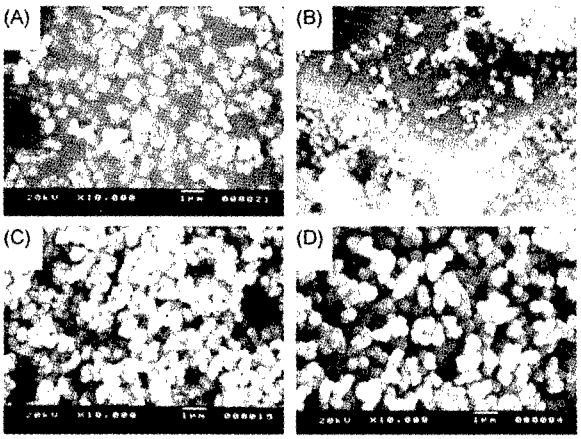


Fig. 7 SEM photographs for the crystalline TiO_2 powders precipitated from 0.67M Ti^{4+} solution under the reaction conditions of (A) 85℃ for 120min, (B) 115℃ for 20min, (C) 115℃ for 60min and (D) 115℃ for 180min, respectively

On the other hand, the formation of the rutile phase of about 65-volume fraction was observed in the reaction at 115℃ for 40 min under the condition to prevent the evaporation of H_2O completely. However, the formation of the rutile phase of 100-volume fraction is observed under the same conditions by the extra addition of ethyl alcohol to the reaction reservoir, as shown in the XRD results of Fig. 8. However, when the ethyl alcohol was added to the reaction solution,

the anatase phase still existed in times shorter than 40 min. It was also confirmed that the anatase phase was almost transformed into the rutile phase if the precipitates were filtered after applying a pressure of more than 4 bar for 24hrs. These mean that the crystalline structure of the TiO_2 precipitate during the reaction could be affected by applying a large internal pressure by the vapor pressures of H_2O and ethyl alcohol in the reservoir. Therefore, it is possible to make out that the rutile phase of TiO_2 precipitation above 70℃ was transformed from the anatase phase, which had been formed first, because the internal pressure in the reaction reservoir applied or increased at higher temperatures. In other words, it can be thought that the higher internal pressure by the vapor pressure of H_2O at the higher reaction temperature cause the already formed anatase phase to transform into the rutile phase.

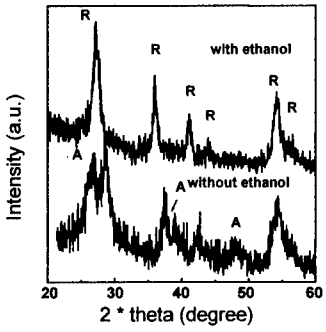


Fig. 8 XRD patterns for the crystalline TiO_2 powders prepared from 0.67M Ti^{4+} aqueous solution with and without the addition of ethanol under the reaction conditions of 115℃ for 40min

However, as shown in Fig. 6, all the TiO_2 precipitates consisted of the rutile phase alone, regardless of the various reaction temperatures below 65℃, and the precipitates obtained in short time were also the rutile phase showing a weak crystalline state, not the anatase, or amorphous phase. Therefore, it is not understood the fact that, although below 65℃ the reaction rate was not only very low but the internal pressure by the reaction reservoir were also not almost applied, the pure rutile phase was more easily formed compared to the conditions at the high reaction temperature. In accordance with H. Zhang and J.F. Banfield's simulated results[14], they showed that the anatase phase of TiO_2 is more stable thermodynamically with the decrease in size of a TiO_2 particle. They also insisted that to form the rutile phase of TiO_2, the size of the particle should be more than about 8nm not considering the surface stress, whereas more than about 14nm considering the surface stress. However with respect to our XRD and TEM measurements, the size of the primary particles for the rutile phase of TiO_2 was in the range of 3-10nm by the homogeneous spontaneous precipitation method.

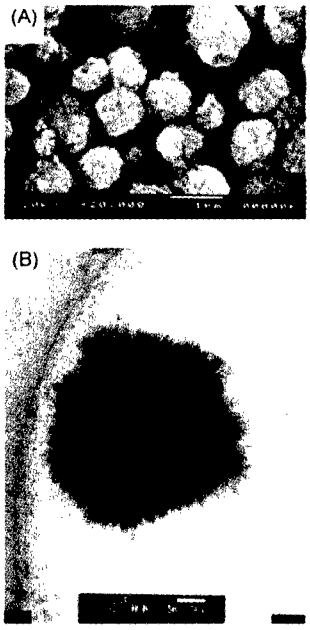


Fig. 9 SEM and TEM photographs for the representative rutile TiO_2 powder from 0.67M Ti^{4+} aqueous solution; (A) by ultrasonically stirring at 50℃ and (B) by normally stirring at 50℃

Thus, their results are not applied to our conditions because our value were smaller than those of the anatase phase for the primary particle. Fig. 9 shows the SEM and TEM photographs for the particles(~1 ㎛ and ~0.3 ㎛) of the rutile phase precipitated at 50℃ using ultrasonic stirring and magnetic stirring method, respectively. It is observed that a particle consists of many fine particles, not a primary particle(Fig. 9A), on the surface of the particle, and the particle also consist of many fine acicular or needle-shaped particles, as shown at the edge of the particle (Fig. 9B). Thus it can be carried out together with the agglomeration of fine clusters or fine acicular shaped particles. Also, the rutile phase of TiO_2 is of higher symmetry crystallographically than the anatase phase. It may be thought from these results, therefore, that at lower reaction temperatures the capillary pressure(negative pressure) formed between the clusters or the fine particles would easily enhance the formation of the rutile phase of higher symmetry than the anatase phase.

CONCLUSIONS

The mono-dispersed TiO_2 ultrafine particles with diameters of 40-400nm were obtained from aqueous $TiOCl_2$ solution with 0.67M Ti^{4+} concentration prepared diluting $TiCl_4$ by the homogeneous spontaneous precipitation process. The process was carried out under conditions to prevent H_2O evaporation completely in the range of 100-230℃ and to make it freely or to prevent it thoroughly in the range of 17-100℃. The results are as follows:

The precipitation of the TiO_2 ultrafine particle by the reaction of $TiOCl_2$ with H_2O occurred easily and rapidly when sufficient amounts of H_2O were supplied. With the spontaneous hydrolysis of $TiOCl_2$, which means the natural decrease in the pH value of the aqueous $TiOCl_2$ solution, all the mono-dispersed precipitates were crystallized with the anatase or rutile TiO_2 phase during the reaction regardless of various conditions. The TiO_2 precipitate with a pure rutile phase was fully formed at temperatures below 65℃, which did not involved the evaporations of H_2O, and above 155℃, which were available by suppressing it. The TiO_2 precipitate with the rutile phase including small amounts of the anatase phase, started to be formed in the intermediate temperatures above 70℃, and showed the full formation of anatase above 95℃ under the free evaporation of H_2O. However, in the case of completely suppressing H_2O evaporation at temperatures above 70℃, the TiO_2 precipitate with the anatase phase that had already been formed by rapid reaction was fully transformed with the reaction time into the precipitate with the rutile phase by the vapor pressure of H_2O. Therefore, it can be thought that these crystallization behaviors of TiO_2 precipitates such as the formation of the rutile phase around room temperature would be caused due to the existence of capillary pressure between the agglomerated needle-shaped particles or the ultrafine clusters, together with the slow reaction rate.

REFERENCES

1. K.L. Siefering and Griffin, J. Electrochem. Soc. **137**, p. 814 (1990).
2. T. Fuyuki and H. Matsunami, Jpn. J. Appl. Phys. **25**, p. 1,288 (1986).
3. A. Bally, K. Prasad, R. Sanjines, P.E. Schmid, F.Levy, J. Benoit, C. Barthou, and P. Benalloul, Mat. Res. Soc. Symp. **424**, p. 471 (1997).
4. K. Prasad, A.R. Bally, P.E. Schmid, F.Levy, J. Benoit, C. Barthou and P. Benalloul, Jpn. J. Appl. Phys. **36**, p. 5,696 (1997).
5. Y. A.Ono in *Electorluminescent Displays,* edited by Chief Hiap L. Ong (World Scientific Pub. Co. Ltd, Singapore 1995), p.10-13.
6. E. Santacesaria, M. Tonello, G. storti, R.C.Pace and S. Carra, J. Colloid and interface Science **111**, p. 44 (1986).
7. Matijevic, M. Budnik, and L. Meites, J. Colloid and interface Science **61**, p. 302 (1977).
8. Xing-Zhao Ding, Zhen-Zhong Qi and Yi-Zhen He, J. Mat, Sci. Lett. **14,** p. 21 (1995).
9. M.K. Akhtar, Y. Xiong and S.E. Pratsinis, AIChE Journal, **37**, p. 1,561 (1991).
10. E.A. Barringer, and H.K. Bowen, Langmuir **1,** p. 414 (1985).
11. S. Park, S. J. Kim, S. D. Park and Y. H. Jeong, J. Am. Ceram. Soc. **82**, p. 927 (1999).
12. S. Park, H. D. Nam, B. H. Lee, S. J. Kim, C. H. Jung and J. H. Lee, Jpn. J. Appl. Phys. **37**, p. 4,603 (1998).
13. Krishnankutty-Nair P. Kumar, Scripta Metallurgica et Materialia **32**, p. 873 (1995).
14. H. Zhang and J. F. Banfield, J. Mater. Chem. **8,** p. 2073 (1998).

SUPERPARAMAGNETIC FERRITES REALIZATION AND PHYSICAL OBSTACLES

D. VOLLATH, E. PELLEGRIN, D. V. SZABÓ
Forschungszentrum Karlsruhe, P.O.Box 3640, D-76021 Karlsruhe, Germany

ABSTRACT

In superparamagnetic materials, the change of the direction of the magnetization is not associated with the movement of Bloch walls, but with thermal fluctuation of the magnetization vector. Therefore, the resonance frequency of the Bloch walls is no longer limiting the maximum frequency for applications. The limit found in superparamagnetic materials is given by the frequency of electron spin resonance. This behavior was verified for spinelle type ferrites made of ceramic or polymer coated oxide nanoparticles produced by the microwave plasma process. By selecting the composition of the spinelle type ferrites the energy of magnetic anisotropy controlling the susceptibility and the maximum frequency for applications can be adjusted. Superparamagnetic materials have their frequency limit beyond 2 GHz. Coating of the particles reduces dipole – dipole interaction destroying superparamagnetism. Even when the susceptibility is in the order of magnitude of today's commercial ferrites, the saturation magnetization is found to be smaller than the theoretically expected value. This phenomenon is partly clarified by soft X-ray magnetic circular dichroism (SXMCD) measurements, showing a significant orbital magnetic moment antiparallel to the direction of the spin moment. Additionally, it was found that the amount of Fe^{2+} ions is possibly larger than expected by thermodynamic data of bulk materials.

INTRODUCTION

Maghemite (γ-Fe_2O_3) with grain sizes in the range of micrometers is ferrimagnetic. Provided that the particle size is sufficiently small, nanocrystalline iron oxides are known to be superparamagnetic. A thermally fluctuating vector of magnetization characterizes superparamagnetic materials. Provided the particles fulfil the condition

$$Kv < kT \qquad (1)$$

(K ... constant of magnetic anisotropy, v ... volume of the particle, Kv ... energy of magnetic anisotropy, kT ... thermal energy) the material is superparamagnetic [1,2]. This leads to zero coercivity. This condition may be fulfilled in two different ways [3, 4]: Either the particles are embedded in a liquid and free to rotate or the particles are bond together in a solid. In the first case, Brownian superparamagnetism with relatively large relaxation times is observed. The second case leads to the Néel superparamagnetism. In this case the orientation of the electron spins is fluctuating relative to the particle. In this case the relaxation time may be significantly less than one nanosecond. The proof for this type of superparamagnetism is the Mößbauer effect. The Mössbauer spectra of superparamagnetic materials show a pure quadrupole splitting above and a magnetic sextet structure below the blocking temperature.

The transition temperature between the ferrimagnetic and the superparamagnetic state as given in Eq. 1 is called the "blocking temperature". Superparamagnetic materials exhibit a magnetisation curve free of hysteresis in the range between the blocking temperature and the Curie temperature. Below the blocking temperature a non-zero remanence is observed.

Mat. Res. Soc. Symp. Proc. Vol. 581 © 2000 Materials Research Society

Superparamagnetic nanocrystalline ferrites with relaxation times below one nanosecond have a high potential for applications in high frequency systems such as cellular phones. As the change of the direction of magnetization is not associated with movements of Bloch walls [1], but with thermal fluctuations of the magnetization vector [3,4], the resonance frequency of the Bloch walls, found at frequencies below 200 MHz, is no longer limiting the maximum frequency for applied purposes. This limit found in superparamagnetic materials is given by the frequency of electron spin resonance, which is in the gigahertz range [5]. This postulated behavior was found in spinelle type ferrites, based on γ-Fe_2O_3 [6,7] embedded in nanocomposites.

Manufacturing of macroscopic superparamagnetic parts faces a severe problem. Superparamagnetism as described above is a property of a single isolated particle. Producing a technical component by pressing and sintering a superparamagnetic powder does not lead to a superparamagnetic solid. There are obstacles: sintering a superparamagnetic powder leads to grain growth, thus destroying superparamagnetism. Additionally, two superparamagnetic particles touching each other behave like a single large one. This is due to spin – spin and dipole – dipole interactions between the particles. This can be avoided by keeping the particles at a certain distance. Theoretical considerations conclude that the only way to keep the particles at a distance and to make sure that there is no pair of particles touching each other, is to coat the particles with a second phase. This coating may be a ceramic or polymer material. This leads to nanocomposites of the ceramic – ceramic or ceramic - polymer type. For most applications in communication technology, polymer coated nanoparticles are sufficient. Nanocomposites – as introduced in this contribution – are composite materials with at least one phase exhibiting the specific properties of a nanomaterial. A random arrangement of these magnetic cores in the composite is assumed. As the core and coating materials are homogeneously distributed on a nanometer scale, the magnetic properties of a densified solid can be changed continuously by varying the thickness of the coating.

Gas phase synthesis of coated nanoparticles is possible only by means of the microwave plasma process. This is because the particles leave the reaction zone with high electrical charges of the same sign thus avoiding agglomeration. Other gas phase processes like the inert gas condensation [8] or the conventional chemical vapor synthesis process [9] are not capable to coat nanoparticles individually. Compared with chemical precipitation processes, the amount of ferrite in the polymer matrix obtained by the microwave plasma process is significantly higher. Therefore, both types of nanocomposites used to obtain superparamagnetism have been produced by the microwave plasma process [10, 11, 12].

SYNTHESIS AND MORPHOLOGY OF THE NANOCOMPOSITES

A microwave plasma enhances the kinetics of chemical reactions by the interaction of charged particles such as electrons, ions or radicals in the plasma with the uncharged species. Therefore, chemical reactions that are thwarted kinetically under normal conditions can be performed at significantly lower temperatures. Additionally, the as-synthesised particles leave the reaction zone with electrical charges of the same sign. Both phenomena are essential, because together they reduce the probability for the formation of hard agglomerates.

This low temperature level has its origin in the energy distribution within a microwave plasma. This energy distribution is caused by the mechanism of energy transfer to charged particles in an oscillating electric field, which is proportional to the electric field strength and inversely proportional to the mass of the charged particle and the frequency squared [13]. This results in an energy distribution for which the energy of the ions is substantially lower than the energy of the electrons. The energy of uncharged particles is even lower. The total energy

transferred is limited by the collision of electrons with neutral particles. The gas pressure and temperature determine the collision frequency. Therefore, the gas pressure is a handle to control the temperature in the system. This method has already been applied for synthesis of many oxides and nitrides. Depending on the process conditions, the reaction product is a powder with mean particle sizes in the range from 4 to 10 nm. This process can be used to synthesise pure γ-Fe_2O_3 or other ferrites with spinelle structure.

Coating of the particles is performed in a second reaction step. For ceramic coating, the particles formed in a first reaction step pass through a second microwave plasma zone, where the coating occurs. Polymer coating is performed downstream the plasma zone by introducing a monomer. This monomer condenses on the particle surface and polymerises under the influence of the UV radiation stemming from the plasma. Fig. 1 shows a typical morphology of polymer-coated ferrite particles.

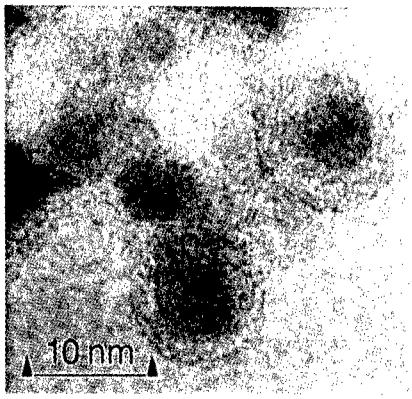


Fig. 1: Electron micrograph of a PMMA coated particle of γ-Fe_2O_3.

MAGNETIC PROPERTIES

Two types of magnetic properties were determined. Static ones with relaxation times in the range of 100 s and dynamic measurements of the susceptibility from 20 kHz to 2 GHz. Changing the composition of the spinelle changes the energy of the magnetic anisotropy controlling the susceptibility and the maximum frequency for applications. As the superparamagnetic properties depend strongly on the energy of anisotropy, it is important to change the composition in order to adjust the product Kv to the value needed. A reduction of K is obtained by adding Mn or Mg, whereas Co increases K. By this doping, one has handles to optimize the material either for maximum susceptibility or frequency. Fig. 2 depicts the magnetization curves for a nano-ferrite consisting of polymer coated $MnFe_2O_4$ particles. Two features typical for superparamagnetic materials are visible in this figure: The magnetization curve is not linear in the range of low fields and free of any hysteresis.

The final proof for superparamagnetism is the quadrupole split doublet in the Mößbauer spectrum. This is shown in Fig. 3. As the Mößbauer spectrum does not show any sign of the magnetic sextet, it is proven that this material is superparamagnetic with a relaxation time in the range of nanoseconds. Starting with these results, it makes sense to analyze the frequency response of the susceptibility. A typical plot of this dependency is presented in Figure 4.

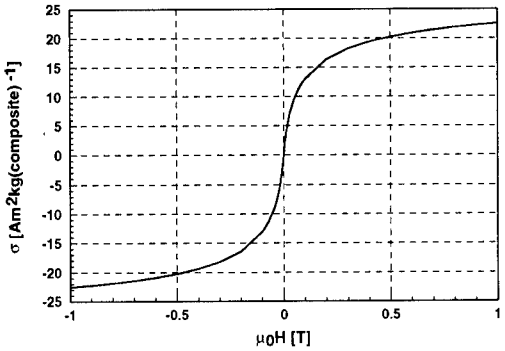


Fig. 2: Magnetization curve of a $MnFe_2O_4$ – PMMA nanocomposite.

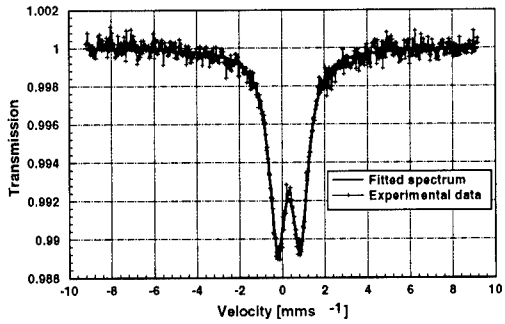


Fig. 3: Mößbauer spectrum of a $MnFe_2O_4$ – PMMA nanocomposite.

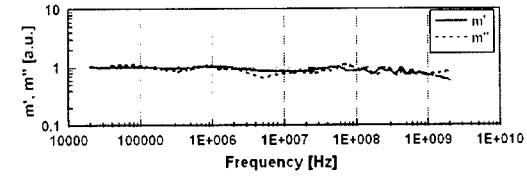


Fig. 4: Real and imaginary part of the suszeptibility of a $MnFe_2O_4$ – SiO_2 nanocomposite sintered at 300 °C.

Based on the Figures 2, 3, and 4 it is obvious that the material in question is superparamagnetic. Additionally, one can see that there are no resonances in the range from 20 kHz to 2 GHz. Therefore, the ultimate frequency of application for this type of material is beyond 2 GHz.

VALENCY OF IRON IONS IN NANOCRYSTALLINE FERRITES

It is well known that nanocrystalline ferrites have a smaller magnetisation than coarse-grained ones. There exists a well-proven dependence of the magnetisation on the particle size [14]. This decrease of the magnetisation is explained with the canting of surface spins [14, 15]. The actual site distribution of the iron ions and their valency was never shown in detail. Using X-ray absorption spectroscopy (XAS) as well as soft X-ray magnetic circular dichroism (SXMCD), it is possible to answer these open questions [16, 17, 18]. A detailed evaluation of

the Fe*L*-edge XAS and SXMCD spectra gives additional information on the ratio of the orbital moment over the spin magnetic moment [19]. Experimental results obtained on bulk-like epitaxially grown Fe_3O_4 thick films and nanocrystalline γ-Fe_2O_3 are given in Figs. 5 and 6 for comparison.

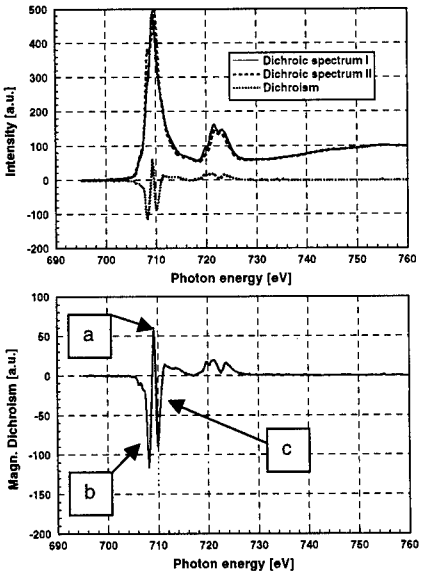


Fig. 5: X-ray circular dichroism spectra for Fe_3O_4. These results are used as reference for the analysis of the spectra from nano-γ-Fe_2O_3 .

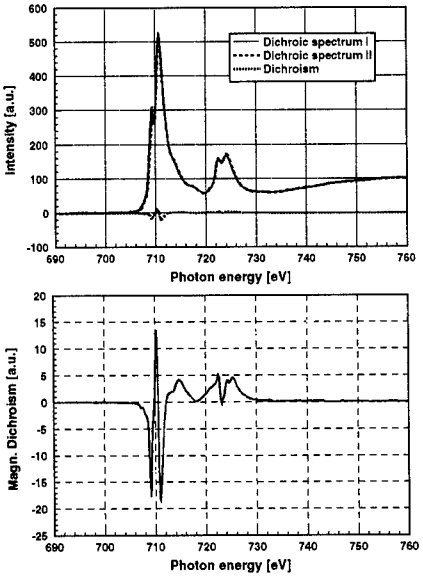


Fig. 6: X-ray circular dichroism spectra for nano-γ-Fe_2O_3.

The dichroic spectra have been measured by the absorption of circular polarised soft X-rays using the total electron yield detection mode at the soft X-ray beamline (ID12B) of the European Synchrotron Radiation Facility (ESRF). These measurements have been performed in a magnetic field parallel and antiparallel to the photon spin of the incoming monochromatic synchrotron radiation yielding the dichroic spectra I and II. The difference between these two spectra - the dichroic difference spectrum - contains information about the valency and the distribution of the iron ions on the different lattice sites. In figure 5 the labels next to the dichroic difference spectrum denote the different iron ions and lattice sites: (a) Fe^{3+} ions on tetrahedral A-sites, (b) Fe^{2+} ions on octahedral B-sites and (c) Fe^{3+} ions on B-sites. These results clearly reflect the well-known fact that Fe_3O_4 crystallises in the inverse spinelle structure. Looking at the results obtained from nano-γ-Fe_2O_3 in Fig. 6 one realises from the dichroic difference spectrum that a distinct percentage of the Fe ions in nano-γ-Fe_2O_3 is present as Fe^{2+}. This is astonishing as the oxygen partial pressure during synthesis was in range that makes the existence of Fe^{2+} not probable. Additionally, an iron oxide with such a high content of Fe^{2+} ions should be black. However, this nano-Fe_2O_3 exhibits the reddish brown colour, typical for Fe_2O_3. A detailed analysis of the SXMCD data yields a considerably enhanced orbital magnetic moment on the iron sites for the γ-Fe_2O_3 nanomaterial as compared to that of bulk γ-Fe_2O_3 [19].

CONCLUSIONS

It has been shown that it is possible to produce technical ferrite parts exhibiting superparamagnetism. This is possible since the ferrite starting material consists of nanoscaled ferrite particles coated with a second ceramic or polymer phase. The thickness of this coating is selected in order to minimise the magnetic interaction between the particles. Superparamagnetism of this material was proven by static magnetisation curves without hysteresis, by Mößbauer spectra exhibiting the quadrupole split doublet instead of the magnetically split sextette. Additionally, it was shown that the ac-susceptibility shows no resonance up to 2 GHz.

A detailed analysis of the cation distribution in the ferrite lattice indicates that possibly a larger amount of Fe^{2+} ions than expected by thermodynamics is present in the lattice of the nanocrystalline γ-Fe_2O_3. The magnetisation is reduced significantly due to the small size of the nanocrystals. In spite of this reduction, the susceptibility of the superparamagnetic nanocomposites is sufficiently large for technical applications. So far it has not been possible to decide if the phenomena described in this paper are bulk phenomena or if they are caused by the large surface of the nanoscaled material.

REFERENCES

1. I. S. Jacobs and C. P. Bean, *Magnetism*, edited by G. T. Rado and H. Suhl (Academic Press, New York, 1963), pp. 271 ff.
2. D. Vollath, D. V. Szabó, R. D. Taylor, J. O. Willis, J. Mater. Res. **12**, 2175 (1997).
3. S. Morup, J. Magn. Magn. Materials **37**, 39 (1983).
4. J. C. Bacri, R. Perzinski, D. Salin, V. Cabuil, R. Massart, J. Magn. Magn. Materials **62**, 36 (1986).
5. J. Smit, H. P. J. Win, *Ferrite*, (Philips Technical Library 1962), pp. 305 ff..
6. D. Vollath, D. V. Szabó, J. Fuchs, Nanostructured Materials **12**, 433 (1999).
7. D. Vollath, D. V. Szabó, J. Fuchs in *Amorphous and Nanocrystalline Materials for Hard and Soft Magnetic Applications* (Mater. Res. Soc. Symp. Spring Meeting 1999) in the print.
8. H. Hahn, J. A. Eastman, R. W. Siegel, Ceram. Trans. **B1**, 1115 (1988).
9. W. Chang, G. Skandan, H. Hahn, S. C. Danforth, B. H. Kear, Nanostructured Materials **4**, 345 (1994).
10. D. Vollath, D. V. Szabó, Nanostructured Materials **4**, 927 (1994).
11. D. Vollath, German Patent G 94 03 581.4 (1994).
12. D. Vollath, D. V. Szabó, B. Seith, German Patent DE 19 638 601.2-43 (1996).
13. A. D. MacDonald, *Microwave Breakdown in Gases*, John Wiley & Sons, 1966.
14. D. H. Han, J. P. Wang, H. L. Luo, J. Magn. Magn. Materials **136**, 176 (1994).
15. F. T. Parker, M. W. Foster, D. T. Margulies, A. E. Berkowitz, Phys. Rev. B **47** 7885 (1993).
16. F. M. F. de Groot, J. Electron Spectrosc. Relat. Phenom. **67**, 529 (1994).
17. B. T. Thole, P. Carra, F. Sette, G. van der Laan, Phys. Rev. Letters **68** 1943 (1992).
18. C. T. Chen, Y. U. Idzerda, H.-J. Lin, N. V. Smith, G. Meigs, E. Chaban, G. H. Ho, E. Pellegrin, F. Sette, Phys. Rev. Letters **75** 152 (1995).
19. E. Pellegrin, M. Hagelstein, S. Doyle, H. O. Moser, J. Fuchs, D. Vollath, S. Schuppler, M. A. James, S. S. Saxena, L. Niesen, O. Rogojanu, G. A. Sawatzky, C. Ferrero, M. Borowski, O. Tjernberg, N. B. Brookes (unpublished).

SYNTHESIS OF PASSIVATED METAL NANOPARTICLES

MARK GREEN[†], PAUL O'BRIEN*
Department of Chemistry, Imperial College of Science, Technology and Medicine, South Kensington, London, SW7 2AY, UK.

Present addresses:
[†] Department of Inorganic Chemistry, University of Oxford, South Parks Rd, Oxford, OX1 3QR.
*Manchester Materials Science Centre and the Department of Chemistry, University of Manchester, Oxford Road, Manchester, M13 9PL.

ABSTRACT

Here we report the synthesis of organically passivated nanoparticles of gold, chromium and nickel. The routes involve the reduction of a metal precursor in various Lewis base solvents, which appear to affect the final nanoparticle morphology. The preparation of highly monodispersed samples can lead to the potential for further manipulation of dots into ordered 2D and 3D arrays. These colloidal thin films and crystals have potential application in magnetic data storage devices.

INTRODUCTION

Nanoparticles of metals have been known since 1857 when Faraday prepared colloidal gold sols [1]. There have been many reported routes to colloidal inert metals, most of which have centred on the reduction of the metals salt in aqueous solution [2-4]. Brust *et al.* recently described the synthesis of high quality gold nanoparticles passivated with thiol compounds [5]. These nanoparticles could be manipulated into ordered arrays and potential device structures [6]. This was one of the first routes leading to organically soluble nanoparticles of metals.

Similar quality nanoparticles of semiconductors with an organic capping agent have also been prepared. Murray *et al.* first reported the preparation of TOPO (tri-*n*-octylphosphine oxide) capped CdE (E = S, Se and Te) in 1993, which has become a popular method of preparing robust, monodispersed high quality semiconductor quantum dots [7]. The nanoparticles, capped with a monolayer of the ligand could be incorporated into simple devices and films, and manipulated into ordered colloidal crystals [8,9]. This method has been extended to cover the preparation of III-V, IV-VI and II_3-V_2 materials, and the use of single molecule precursors [10-13].

Murray also described the preparation of cobalt nanoparticles using an alteration of the original TOPO route [14]. Various Lewis base ligands were utilised as passivating agents and reaction solvents for the reduction of $CoCl_3$ by superhydride. Altering the ligand could control the size of the nanoparticle. The size distribution was small (*ca.* 5 % - comparable to TOPO capped II-VI materials); manipulation into ordered structures was possible. Bawendi also prepared nanoparticulate cobalt by the thermolysis of $Co_2(CO)_8$ in TOPO, leading to a new phase of cobalt designated ε Co [15].

The preparation of high quality, single domain particles can lead to high-density storage devices, an area of intense current research. Nanoparticles of metal have other potential applications, such as catalysts. Recently, Heath *et al.* demonstrated a metal – insulator transition in films of silver nanoparticles, which has obvious industrial applications [16]. Here we report the preparation of passivated nanoparticulate Cr, Ni and Au. The nanoparticles were prepared in

Mat. Res. Soc. Symp. Proc. Vol. 581 © 2000 Materials Research Society

a TOPO or modified TOPO system and investigations have been undertaken into the effects of basicity and ligand chain length on the particle morphology. In certain cases, we have been able to manipulate the particles into ordered 2D and 3D arrays.

EXPERIMENTAL

UV/Vis Absorption and IR Spectroscopy

The optical measurements of the nanoparticles were carried out on a Philips PU 8710 spectrophotometer. The sample solutions were placed in silica cuvettes (path length = 1 cm). The samples dispersed in toluene. Infra-red spectra were carried out using a Matteson Polaris FT-IR spectrometer as CsI pressed discs (1% sample).

Nuclear Magnetic Resonance spectroscopy (NMR)

The ^{1}H and ^{31}P solution NMR spectra were recorded on a Bruker AM 500 or a DRX 400 in deuterated chloroform. H_3PO_4 was used as a phosphorus standard.

X-ray Powder Diffraction (XRD)

X-ray powder diffraction patterns were measured using a Siemens D500 series automated powder diffractometer using Cu-K_α radiation at 40kV/40mA with a secondary graphite crystal monochromator. Samples were supported on glass slides (5cm^2).

Transmission Electron Microscopy and Scanning electron microscopy (TEM, SEM)

A JOEL 2000 FX MK1 electron microscope operating at 200 kV with an Oxford Instrument AN 10000 EDS analyser was used for the conventional TEM micrographs. The samples for TEM were prepared by placing a drop of a dilute solution of sample in toluene on a copper grid (400 mesh, Agar). The excess solvent was wicked away with a paper tip and the sample allowed to dry completely at room temperature.

SYNTHESIS

Preparation of TOPO capped Au

In a typical synthesis, 0.07 g (23 mmol) $AuCl_4$ was dissolved in 7 mls 4-*t*- butylpyridine. This was then injected into a reaction flask containing 15 g TOPO and 0.0325 g $NaBH_4$ stabilised at 190 °C. The reaction mixture turned an immediate yellow, then changed through orange, red and eventually blue. The temperature dropped to *ca.* 155 °C and the reaction vessel left for 30 minutes, then removed from the heat source. The nanoparticles were isolated by solvent-non solvent interactions; whilst the reaction vessel was at 60 °C, 30 mls of dry methanol was added causing a precipitate which was isolated by centrifugation. The precipitate was stable in toluene for *ca.* 10 hours.

Preparation of TOPO/amine capped Au

As above, injecting gold chloride dissolved in 4-*t*-butylpyridine into a mix of 10 g octadecylamine, 25 g TOPO and 0.0325 g $NaBH_4$ at 190 °C, with a growth time of 30 minutes.

Upon injection, the reactants turned deep red. The nanoparticles were isolated using methanol as described above, and were found to be indefinitely stable in toluene. Once isolated as a powder, the nanoparticles were washed several times with methanol to remove excess capping agent before analysis.

Preparation of TOPO capped Cr

In a typical synthesis, 2.5 ml 2 M LiBH4/THF solution was added to 20 g pure TOPO, then the solvent removed *in vacuo*. The TOPO was then heated to 270 °C and stabilised. $CrCl_2$ (0.1 g, 0.8 mmol) was dissolved in 5 mls tri-*n*-octylphosphine, then injected into the TOPO. The reaction mixture turned an immediate black. The temperature was raised to *ca.* 290 °C over half an hour, left for a further 30 minutes then removed from the heat source. The nanoparticles were isolated by addition of petroleum spirits, acetone or ether. The nanoparticles were then soluble in toluene for a limited time. Dispersing the nanoparticles directly in toluene after the reaction resulted in an apparently indefinitely stable colloid. It is assumed the addition of a non-solvent removes some of the capping ligand. Samples isolated by methanol were usually unstable, unless redispersed in pyridine, which probably co-ordinated to the surface.

Preparation of TBPO (tributylphosphine oxide) capped Ni

In a typical synthesis, 0.046 g $NaBH_4$ was added to 10 g TBPO (tributylphosphine oxide). This was heated to 160 °C and stabilised. $[Ni(acac)_2]$ (0.2 g, 0.7 mmol)was then dissolved in 5 ml tributylphosphine then injected into the phosphine oxide. The temperature was stabilised at 160 °C and stabilised for 30 mins, then removed from the heat source and left to cool to room temperature. The black solid was then re-dispersed directly in pyridine as no effective non-solvent was found. The solid however, could be readily dispersed in a variety of organic solvent but appeared stable in only pyridine.

RESULTS

The nanoparticles were analysed by TEM, HRTEM, NMR, XRD and IR and UV spectroscopy. Nanoparticles of gold gave clear broad X-ray diffraction patterns associated with FCC gold particles with a small crystalline domain (Figure 1). Chromium and nickel nanoparticles, however, gave broad weak reflections, which could not be properly indexed. SAED (selected area electron diffraction) gave broad diffuse ring patterns associated with nanodispersed materials with no defractive crystalline phase.

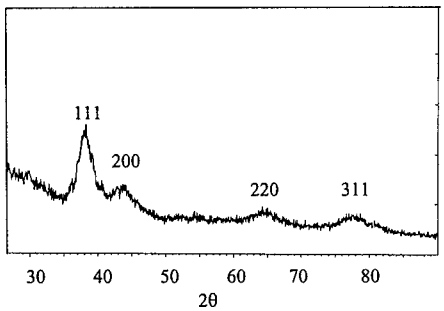


Figure 1 - XRD pattern of TOPO/octadecylamine capped Q-Au (190 °C, 30 mins.)

Electron microscopy revealed a broad and interesting set of sizes and morphologies for the different metals. Gold nanoparticles capped with TOPO alone were of various size and shapes, ranging from small spherical, square and triangular particles (5-10 nm diameter) to large faceted particles of *ca.* 100 nm (Figure 2). Gold nanoparticles capped with a mix of TOPO and the long chain amine (octadecylamine) were highly monodispersed spherical particles of *ca.* 7 nm diameter (Figure 2).

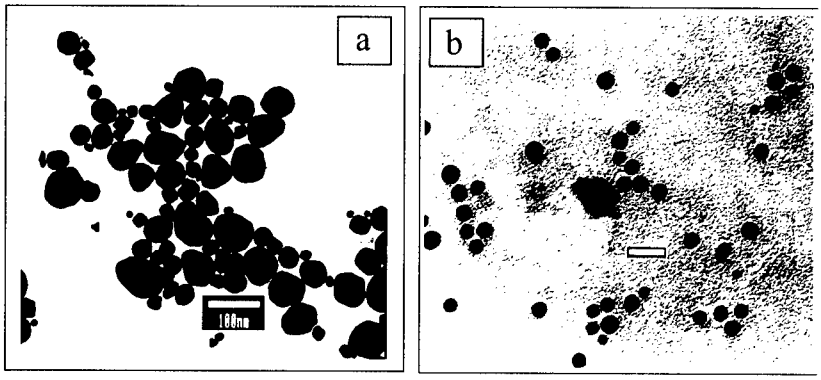


Figure 2 - a) TEM of TOPO capped Q-Au (190 °C, 30 mins.), bar = 100 nm; b) TEM of TOPO/octadecylamine capped Q-Au (190 °C, 30 mins.), bar = 20 nm.

The monodispersed gold particles could self-organise on a copper grid to form 2-D arrays. Slow evaporation of the solvent from a solution resulted in bright red, cubic colloidal crystals (Figure 3). The TOPO passivated chromium quantum dots were small spherical particles, slightly prolate, approximately 4 nm in diameter. HRTEM images of the TBPO capped nickel particles revealed the presence of both small metal particles between 2 and 4 nm in diameter and nanowires of up to 20 nm long (Figure 4).

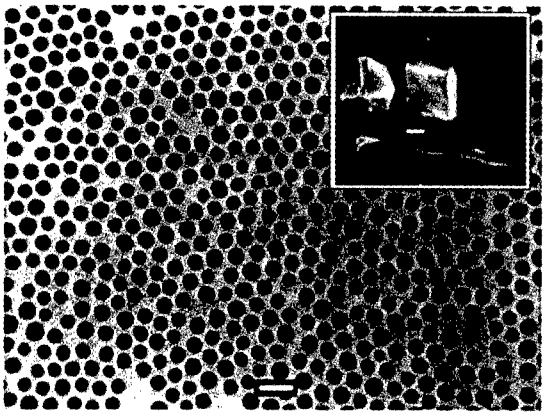


Figure 3 - 2D lattice of octadecylamine/TOPO capped gold, bar = 20 nm. Inset; SEM of cubic colloidal crystal prepared from octadecylamine/TOPO capped gold nanoparticles (190 °C), bar = 80 micrometers.

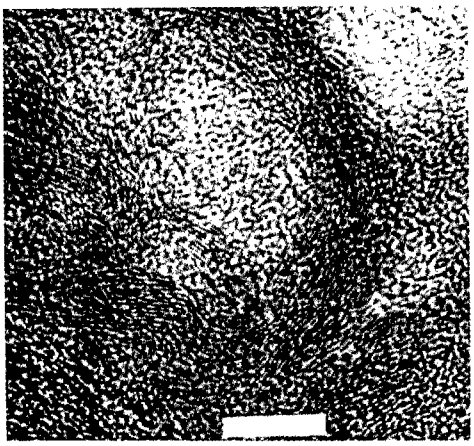


Figure 4 - HRTEM image of TBPO/TBP capped nanowire Ni, bar = 10 nm.

The effect of the Lewis basicity and the length of the capping ligand upon nanoparticle morphology are well documented. UV spectroscopy of the nanoparticles displayed a range of plasmon resonances. The absorption spectrum of colloidal gold is well documented and a single plasmon peak was observed at *ca.* 540 nm (Figure 5). Colloidal chromium displayed no resonances when prepared as described above, whilst nickel displays three. Altering the preparation of chromium nanoparticles by including an amine into the reaction mixture resulted in nanoparticles which displayed two plasmon resonances. The origin of such effects is still under investigation. The presence of multiple plasmon resonances in metals has also been observed by Lutz *et al.*[17].

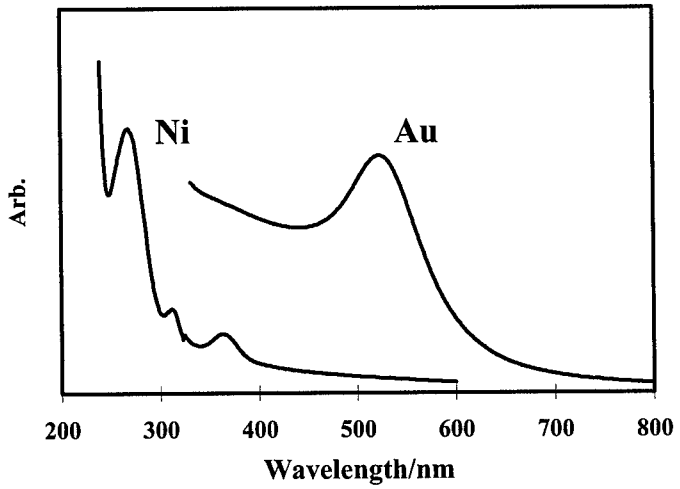


Figure 5- Electronic spectra for colloidal Ni and Au.

Nuclear magnetic resonance (solution ^{1}H and ^{31}P NMR) reveals the ligands are bound to the surface. The broadening of proton spectra is typical for an inhomogeneous magnetic environment and is observed in all nanoparticles reported here. The ^{31}P NMR spectra show a shift in the resonance from the free ligand, consistent with de-shielding effects. TOPO capped Au and Cr have resonances at *ca.* 45 ppm, a shift from the bulk ligand (*ca.* 50 ppm). TBPO capped Ni has a distinct resonances at *ca.* 46 ppm, and others at -18 and -31 ppm.

Infra red spectroscopy of TOPO capped gold displayed a shift in the υ(P=O) stretch from *ca.* 1145 cm^{-1} to 1130 cm^{-1} again suggesting the ligand is tightly bound to the surface of the quantum dot. TOPO capped Cr displayed the stretch at the same energy but broadened. TBPO capped Ni displayed the υ(P=O) stretch at 1128 cm^{-1}.

CONCLUSION

Colloidal routes to organically passivated metal nanoparticles have been developed. The quantum dots are passivated by various Lewis base ligands, which dictate the morphology of the nanoparticles. Highly monodispered nanoparticles can self assemble under the correct condition into 2D and 3D arrays.

REFERENCES

[1] For an interesting summary see *Michael Faraday and the Royal Institution*, by J. M. Thomas and A. H. Bristol, Philadelphia and New York 1991, pp. 78.
[2] A. Henglein and M. Giersig, J. Phys. Chem. B. **103**, p. 9533 (1999).
[3] B. V. Enustun and J. Turkevich, J. Am. Chem. Soc. **85**, p. 3317 (1963).
[4] J. Turkevich and G. Kim, Science **169**, p. 873 (1970).
[5] M. Brust, M. Walker, D. Bethell, D. J. Schiffrin and R. Whyman, J. Chem. Soc., Chem. Comm. p. 801 (1994).
[6] D. Gittens, D. J. Schiffrin, R. Nichols and D. Bethell, Adv. Mater. **11**, p.737 (1999).
[7] C. B. Murray, D. J. Norris and M. G. Bawendi, J. Am. Chem. Soc. **115**, p. 8706 (1993).
[8] V. L. Colvin, M. C. Schlamp and A. P. Alivisatos, Nature **370**, p. 354 (1994).
[9] C. B. Murray, C. R. Kagan and M. G. Bawendi, Science **270**, p. 1335 (1995).
[10] A. A. Guzelian, J. E. B. Katari, U. Banin, A. V. Kadavanich, X. Peng, A. P. Alivisatos, K. Hamed, E. Juban, R. H. Wolters, C. C. Arnold and J. R. Heath, J. Phys. Chem. **100**, p. 7212 (1996).
[11] T. Trindade and P. O'Brien, Adv. Mater **8**, p. 161 (1996).
[12] M. Green and P. O'Brien, Adv. Mater **10**, p. 527 (1998).
[13] M. Green and P. O'Brien, J. Chem. Soc., Chem. Comm. p. 2235 (1999).
[14] S. Sun and C. B. Murray, J. Appl. Phys. **85**, p. 4325 (1999).
[15] D. P. Dinega and M. G. Bawendi, Angew. Chem. Int. Ed. **38**, p. 1788 (1999).
[16] C. P. Collier, R. J. Saykally, J. J. Shiang, S. E. Henrichs and J. R. Heath, Science **277**, p. 1978 (1997).
[17] T. Lutz, C. Estournes, J. C. Merle and J. L. Guille, J. Alloys. Comp. **262**, p. 438 (1997).

PREPARATION OF NANOCRYSTALLINE BISMUTH-CONTAINING POWDERS THROUGH SOLUTION-PHASE REDUCTIONS

Edward E. Foos, Alan D. Berry, Arthur W. Snow*, and J. Paul Armistead**
Chemistry Division, Code 6174, Naval Research Laboratory, Washington, DC 20375
*Code 6123; **Code 6126

ABSTRACT

In an attempt to both prepare nanocrystalline bismuth and understand the fundamental chemistry behind the formation of this potentially interesting material, we have examined the reduction of $BiCl_3$ in the presence of strongly coordinating solvents and ligands. These studies have resulted in the formation of bismuth powders with approximate average particle sizes of between 20 and 40 nm which exhibit large size distributions. The simultaneous reduction of both gold and bismuth precursors, done in an attempt to better control the final particle size, instead produces Au_2Bi of comparable dimensions. There is no evidence that the ligands utilized in either of these systems remain bound to the final product. These nanocrystalline powders have been characterized through XRD and TEM, and full details of the synthesis are presented.

INTRODUCTION

The current interest in nanocrystalline materials has been motivated primarily by the immense potential such materials hold for future applications. This potential stems from the unusual properties such compounds exhibit in comparison to their bulk counterparts as a result of quantum confinement and extremely large surface-to-volume ratios. The majority of the research that has developed in this area has been focused on the study of transition metal[1] and semiconductor particles[1,2], while the study of nanocrystalline main group metals has been all but ignored. This is surprising since these materials have many potential applications which have not been explored, and several recent publications have suggested[3,4] that quantum confined bismuth may exhibit enhanced thermoelectric properties. In spite of these results, we are aware of only one report in the literature of nanocrystalline bismuth being prepared through wet chemical methods[5], and the product was prepared only at very low reaction concentrations. Recently, in an attempt to synthesize such materials and understand the fundamental chemistry behind their formation, we have begun to examine the preparation of nanocrystalline bismuth through straightforward solution reductions. By reducing $BiCl_3$ in the presence of strongly coordinating ligands and solvents, we have obtained nanocrystalline bismuth powders. In addition, carrying out these reductions in the presence of $HAuCl_4$ has led to the isolation of Au_2Bi of similar dimensions. Herein we report the details of the synthesis and characterization of these materials using XRD and TEM.

EXPERIMENTAL

General Considerations: The reductions were carried out using commercially available reagents and standard Schlenk techniques, when necessary. The compounds $BiCl_3$, $NaBH_4$, $LiBEt_3H$ (1 M in THF), $HAuCl_4$, $(C_8H_{17})_4NBr$, and $C_8H_{17}SH$ were purchased from Aldrich and used as received. In general, rigorous drying of solvents was found not to be necessary, and was not performed unless otherwise indicated. XRD measurements were obtained on a Phillips XRG

Mat. Res. Soc. Symp. Proc. Vol. 581 © 2000 Materials Research Society

2500 X-ray instrument using Cu $K\alpha$ radiation, from powder samples attached to a glass slide using hydrocarbon grease. TEM measurements were performed on a Zeiss EM-10C instrument, operating at 60 kV. The samples were prepared by sonicating the appropriate powder for 1 to 2 minutes in MeOH and placing a drop on a carbon coated copper grid, which was wicked off after 10 seconds. ^{1}H NMR measurements were obtained on a Bruker AC-300 spectrometer, using 5-mm tubes which were septum sealed under argon. Peaks were referenced to the residual protons of deuterated-benzene at δ 7.15. IR measurements were obtained on a Nicolet Magna 750 FTIR using KBr pellets.

Preparation of Nanocrystalline Bi: A typical reaction was carried out as follows: $BiCl_3$ (0.027 g; 0.09 mmol) was added to a flask in a He filled dry-box, the flask was removed, and approximately 25 mL of ethylenediamine added under an Ar purge. The resulting hazy white mixture was stirred for several minutes at room temperature while the reducing agent, $NaBH_4$ (0.0102 g; 0.27 mmol) was dissolved in 10 mL of warm ethylenediamine. Once the $NaBH_4$ solution had cooled to room temperature, it was added to the $BiCl_3$ mixture *via* pipet, once again under Ar. This resulted in a gradual darkening in color to black while the mixture was stirred overnight at room temperature. The black solid was isolated by centrifuge, washed twice with EtOH, and dried yielding a black powder (0.272 g; 145% yield). The extra weight present in the final product can be attributed to reaction byproducts not removed by the EtOH. This black powder was examined by XRD and found to predominately contain elemental bismuth (JCPDS card 5-519) with an approximate average particle size of 20 nm calculated using the Scherrer equation.

Variations to this synthesis included using other solvents, changing the reaction temperature, the addition of a coordinating ligand prior to the reduction, or the use of other reducing agents, however the basic procedure described above remained unchanged. For the reduced temperature reductions, the reaction temperature was lowered using a solvent bath (toluene/liquid N_2 for -95 °C; dry ice/ethanol for -78 °C; CCl_4/liquid N_2 for -23 °C), and was maintained for 1 h following the addition of the reducing agent. At this point the mixture was allowed to warm to room temperature and stirred for the amount of time listed in Table I before workup. Coordinating ligands were added neat under a purge of Ar, and the contents of the flask stirred for several minutes before addition of the reducing agent. Finally, a number of the reactions were reduced with 1 M $LiBEt_3H$ in THF, which was handled using Schlenk techniques and added to the reaction dropwise *via* syringe.

Preparation of Nanocrystalline Bi from Alkyl- and Aryl-Bismuth Halides: The sodium salt of 1-octanesulfonic acid (0.108 g; 0.50 mmol) was added to a Schlenk flask, which was evacuated and transferred to the dry-box. Next, $BiCl_3$ (0.158 g; 0.50 mmol) was added, the flask was removed, and approximately 25 mL of THF stored over Na/benzophenone was vacuum distilled into the flask. It was then allowed to warm to room temperature and the mixture stirred for approximately 1 h. A 1 M THF solution of $LiBEt_3H$ (1 mL; 1 mmol) was added under Ar dropwise *via* syringe with vigorous stirring, and a black color quickly developed. After 2 h, black solid was evident in the flask. The solid was isolated by centrifuge, washed with Et_2O and petroleum ether, and dried. The powder was examined by XRD, and contained elemental bismuth (JCPDS card 5-519) and several unidentified peaks attributed to salts produced from the reduction. These extra peaks were removed by washing with H_2O, resulting in 0.0786 g (75% yield) of bismuth. The particle size was estimated at 20 nm using the Scherrer equation. IR of the isolated powder showed no evidence of coordinated alkyl groups. An identical reaction was performed using the sodium salt of stearic acid as the ligand, and similar results were obtained.

A reduction reaction of phenylbismuth dichloride was also carried out, however the procedure was analogous to that described above for reduction of $BiCl_3$ in ethylenediamine. The resulting powder contained elemental bismuth, and no residual phenyl groups were detected by FTIR.

Preparation of Nanocrystalline Au_2Bi: A bismuth precursor was first prepared by dissolving $BiCl_3$ (1.014 g; 3.20 mmol) in 0.20 mL of concentrated HCl, forming a saturated solution with an approximate composition equal to $HBiCl_4 \cdot 3H_2O$[6]. This stock solution was then used as needed. In a typical reaction, $(C_8H_{17})_4NBr$ (0.109 g; 0.2 mmol) was dissolved in 50 mL of toluene, and the "$HBiCl_4$" stock solution added (2.0 μL; 0.03 mmol), forming a clear yellow solution. The $HAuCl_4$ (0.02 g; 0.05 mmol) was dissolved in approximately 10 mL of H_2O and added to the bismuth solution; a dark orange color quickly developed in the toluene phase, along with a small amount of white precipitate. The $C_8H_{17}SH$ (0.012 g; 0.083 mmol) dissolved in 2 mL of toluene was added next, and the biphasic mixture purged with Ar for 10 minutes, at which point the flask was sealed. A solution of $NaBH_4$ (0.1 g; 2.6 mmol) dissolved in 10 mL of H_2O was added dropwise *via* pipet under Ar purge, and a dark brown color developed which turned to black on continued addition. The mixture was stirred at room temperature for 1 h, at which point both the layers were clear and colorless, and a black solid was present. The solid was isolated by centrifuge and dried, leaving a black powder (0.0958 g) which was identified as Au_2Bi by XRD (JCPDS card 12-734). Once again, this additional weight can be attributed to unidentified byproducts not washed out of the powder. An approximate average particle size of 20 nm was calculated using the Scherrer equation.

Alternatively, the reductions were carried out using $(C_8H_{17})_4NBiBr_4$ (**1**) as the starting material. In these reactions, $HAuCl_4$ dissolved in H_2O was added to a toluene solution of $(C_8H_{17})_4NBr$, and when the gold had completely transferred to the toluene phase (indicated by migration of the orange color) it was removed and added to a solution of **1** in toluene. At this point the ligand was added and the reduction carried out as described above for preparation of Au_2Bi from "$HBiCl_4$".

Preparation of $(C_8H_{17})_4NBiBr_4$ (1): Solid $(C_8H_{17})_4NBr$ (0.547 g; 1.00 mmol) was added to a flask which was evacuated and transferred into a He-filled dry-box, where $BiBr_3$ (0.449 g; 1.00 mmol) was added. Approximately 25 mL of THF stored over Na/benzophenone was vacuum-distilled into the flask, and the contents allowed to warm to room temperature. The clear yellow solution which resulted was stirred for 18 h at room temperature. The THF was removed *in vacuo*, and **1** was isolated as a sticky yellow solid in near quantitative yield. ^1H NMR: δ 1.05 (s, 12H, $CH_3(CH_2)_6CH_2$-), δ 1.46 (s, 48H, $CH_3(CH_2)_6CH_2$-), δ 3.07 (bs, 8H, $CH_3(CH_2)_6CH_2$-). IR (cm^{-1}): 2926 (s), 2857 (s), 1481 (s), 1379 (m), 730 (w).

RESULTS AND DISCUSSION

The results of the reduction reactions of $BiCl_3$ under various conditions are shown in Table I, while Table II shows the results of the reduction of bismuth dichlorides with covalently bound ligands.

In carrying out these reactions, it was hoped that the addition of a Lewis basic ligand or solvent would help to restrict the growth of the particles through an interaction with the $BiCl_3$, which is known to function as a Lewis acid. The ligand ideally would remain bound to the $BiCl_3$ throughout the reduction, restricting growth of the particles, and perhaps allow the final product to be dispersed in organic solvent. Examining the data presented in Table I, it is clear that the majority of the attempted reactions have resulted in the production of nanocrystalline material,

Table I: Reduction of $BiCl_3$

Reaction	Temp (°C)	Stirring Time	Reducing Agent	Solvent/ Ligand	Bi:Ligand Ratio	Avg. Particle Size (nm)
1	RT	18 h	$NaBH_4$	ED/ED	n/a	20
2	RT	1h	$LiBEt_3H$	ED/octanethiol	1:1	20
3	RT	18 h	$NaBH_4$	ED/dodecylamine	1:1	30
4	RT	18 h	$LiBEt_3H$	ED/TOPO	1:10	20
5	RT	18 h	$LiBEt_3H$	ED/TETA	1:10	20
6	-95	18 h	$LiBEt_3H$	THF/octanethiol	1:1	NR
7	-95	1 h	$LiBEt_3H$	THF/octanethiol	1:1	30
8	-95	1 h	$LiBEt_3H$	THF/THF	n/a	30
9	-95	18 h	$LiBEt_3H$	THF/THF	n/a	40
10	-78	1 h	$LiBEt_3H$	toluene/octane-thiol	1:1	15
11	-78	1 h	$LiBEt_3H$	toluene/TETA	1:10	20
12	-23	1 h	$LiBEt_3H$	pyridine/octane-thiol	1:1	30
13	RT	1 h	$NaBH_4$	EtOH/TETA	1:10	NR
14	RT	18 h	$LiBEt_3H$	TOP/TOPO	1:1	20
15	200	15 min	$LiBEt_3H$	TOP/TOPO	1:1	NR
16	RT	18 h	$LiBEt_3H$	THF/HMPT	1:2	20

ED = ethylenediamine; TOPO = trioctylphosphine oxide; TETA = triethylenetetramine; TOP = trioctylphosphine; HMPT = hexamethylphosphorus triamide; NR = no reduction in particle size.

Table II: Reduction of alkyl- and aryl-bismuth dichlorides

Reaction	Stirring Time	Compound Reduced	Reducing Agent	Solvent	Avg. Particle Size (nm)
17	2 h	$C_8H_{17}SO_3Na + BiCl_3$	$LiBEt_3H$	THF	20
18	2 h	$C_{17}H_{35}CO_2Na + BiCl_3$	$LiBEt_3H$	THF	20
19	18 h	$PhBiCl_2$	KBH_4	ED	20

however there is no evidence that any of the ligands remain bound to the surface of the bismuth to any appreciable degree following the reaction. Of particular interest is the fact that all of the room temperature reductions using ethylenediamine as the solvent (even when no other coordinating ligand was used) produced nanocrystalline material with an average size of 20 nm, which is among the smallest observed in these systems. Clearly, the anticipated bidentate coordination of this compound with the Lewis acidic $BiCl_3$ effectively hinders the agglomeration of the bismuth particles, resulting in smaller particle sizes. Figure 1 shows a TEM image of the bismuth powder obtained from Reaction 4. While the broadening of the XRD peaks leads to calculation of an average particle size of 20 nm, it is clear from the TEM that the sample exhibits a wide size distribution, with particles as large as 80 nm and as small as 10 nm found in different areas of the sample.

Attempts to bind an organic group covalently to the bismuth were also moderately successful. Average particle sizes were again calculated, and all three reactions produced approximately 20 nm bismuth. It appears that the Bi-O and Bi-C bonds in the starting materials



Figure 1: TEM images of the material obtained from Reaction 4.

were broken during the reduction, however, and IR analysis of the final products shows no evidence of coordinated organic groups.

In an attempt to produce material with a narrower size distribution, a gold precursor, $HAuCl_4$, was added to the reaction. This was done in the hopes that it would have one of two possible affects: first, that the gold might provide a large number of nucleation sites for the rapid growth of the bismuth particles, and second, that the gold would form a shell on the bismuth particles as they were growing, restricting the size and providing a site for the added thiol to bind. The occurrence of either condition would ideally reduce the overall size of the particles produced as well as the size distribution. The preparation of gold nanoclusters from $HAuCl_4$ in a two-phase system[7] has been intensely studied, and was chosen as the model for this experiment. For consistency with this reaction, a bismuth precursor of the form "$HBiCl_4$" was needed. A species roughly corresponding to this formula was obtained from a saturated solution of $BiCl_3$ in HCl[6], and was used as the initial bismuth source. The reduction reaction resulted in the isolation of Au_2Bi with an approximate particle size of 20 nm and noticeable contamination from gold. The ill-defined character of the starting material, and thus the uncertainty in the amount of bismuth added to the reaction, was a possible reason for this excess gold in the final product, thus an alternative bismuth source was sought. The 1:1 reaction of $(C_8H_{17})_4NBr$ with $BiBr_3$ resulted in the formation of $(C_8H_{17})_4NBiBr_4$ (**1**), a toluene-soluble compound which was used in an analogous reaction. The final product obtained from the reduction of **1** and $HAuCl_4$ was still contaminated with gold, however, and displayed approximately the same average size of 20 nm. A TEM image of the material obtained from this reaction is shown in Figure 2, and a wide size distribution is again seen. Several other ligands were also evaluated in this reaction (pyridine, dodecylamine, stearic acid, and TOPO) with similar results. In addition, none of the Au_2Bi samples produced were dispersible in organic solvents, a strong indication that the ligands do not remain bound to the particle surface after the reduction.

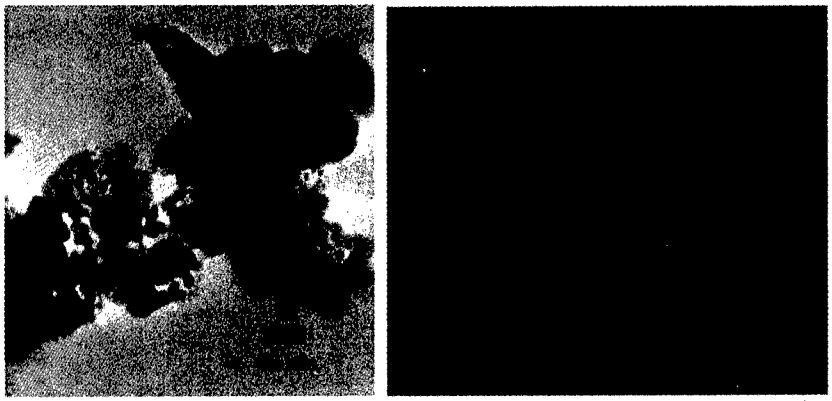


Figure 2: TEM images of the material obtained from the reduction of **1** and $HAuCl_4$.

CONCLUSIONS

The above results demonstrate that it is possible to prepare nanocrystalline bismuth from the described procedure, which consists of reduction of $BiCl_3$ in the presence of strongly coordinating species. There appeared to be little control over the size of the final product obtained, however, and the reduced bismuth surface did not appear to bind readily to any of the any of the species examined. The addition of a gold precursor to the reaction resulted in the formation of nanocrystalline Au_2Bi but failed to yield any increased control over the size of the particles produced. Studies to address these issues by further modification of the reaction conditions are currently underway.

ACKNOWLEDGEMENTS

We wish to thank the Office of Naval Research for their financial support of this work, which was performed while E.E.F. held a National Research Council-Naval Research Laboratory Research Associateship.

REFERENCES

1. See the following and the references contained therein: (a) J. Z. Zhang, Acc. Chem. Res. **30,** 423 (1997). (b) M. J. Hostetler, *et al.*, Langmuir **14**, 17 (1998).
2. See the following and the references contained therein: A. P. Alivisatos, J. Phys. Chem. **100,** 13226 (1996).
3. L. D. Hicks, T. C. Harman, X. Sun, and M. S. Dresselhaus, Phys. Rev. B **53**, 10493 (1996).
4. M. S. Dresselhaus, G. Dresselhaus, X. Sun, Z. Zhang, S. B. Cronin, and T. Koga, Phys. Solid State **41**, 679 (1999).
5. M. Gutierrez and A. Henglein, J. Phys. Chem. **100**, 7656 (1996).
6. S. Ulvenlund and L. A. Bengtsson, Acta. Chem. Scand. **48**, 635 (1994).
7. M. Brust, M. Walker, D. Bethell, D. J. Schiffrin, and R. Whyman, J. Chem. Soc., Chem. Commun. *1994*, 801.

Synthesis and Characterization of Resorcinarene-Encapsulated Nanoparticles

Alexander Wei,* Kevin B. Stavens,§ Stephen V. Pusztay,* Ronald P. Andres§
*Department of Chemistry, Purdue University, West Lafayette, IN 47907 (alexwei@purdue.edu)
§Department of Chemical Engineering, Purdue University, West Lafayette, IN 47907

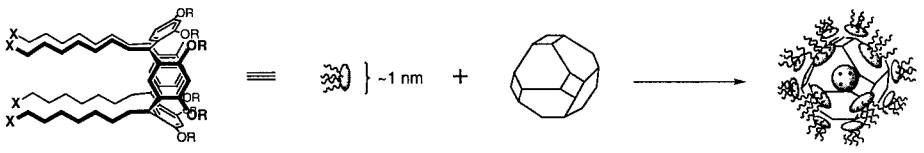
ABSTRACT

A new strategy for stabilizing inorganic nanoparticles in nonpolar solutions is described. Resorcinarenes **1-3** were synthesized and evaluated as surfactants because of their large concave headgroups with multiple contact sites. Au nanoparticles ranging from 3-20 nm in diameter were generated in the vapor phase and dispersed into dilute hydrocarbon solutions of **1-3**, where they were stabilized for up to several months. Chemisorption is most likely mediated by multiple Au-O interactions, as indicated by several control experiments and by surface-enhanced Raman spectroscopy. The resorcinarenes were readily displaced by dodecanethiol, which resulted in the precipitation of particles >5 nm as determined by absorption spectroscopy and transmission electron microscopy. This suggests that the mobility of the resorcinarene tailgroups are important for maintaining the larger nanoparticles in a dispersed state. Resorcinarene surfactants with stronger chemisorptive properties are currently being explored.

INTRODUCTION

Nanoparticle-based devices are being envisioned as the next generation in electronics miniaturization because of their quantized electromagnetic and photonic properties.[1] However, quantum devices can be expected to be highly sensitive to charge defects, so an important consideration during fabrication is the ability to stabilize and manipulate charge-neutral nanoparticles in a low-dielectric medium. Chemisorptive surfactants such as the alkanethiols have been successful in stabilizing small (<10 nm) gold nanoparticles against agglomeration in hydrocarbon solutions, but alkanethiol-passivated clusters >10 nm do not exhibit long-term stability and precipitate at ambient temperatures.[2] This behavior is due largely to the rapid increase in the attractive van der Waals force between particles as a function of their size,[3] but entropic effects can also play an important role. In the case of the alkanethiols the small headgroups encourage a dense packing of the hydrocarbon chains, which promotes flocculation.

Here we address the issue of size-dependent agglomeration by using resorcinol-derived calixarenes (resorcinarenes[4]) as nanoparticle surfactants (see Figure 1). These macrocycles are appended by several hydrocarbon tails and are well suited for nanoparticle encapsulation. First, the resorcinarene headgroup is rimmed with multiple oxygen atoms for polydentate binding to the nanoparticle surface. Second, the relatively high surface area of the concave headgroup (ca. 1 nm diameter) decreases the surfactant/particle ratio and consequently the entropic cost of self-assembly.[5] Finally, the tailgroups are spaced such that they are highly mobile and do not form tightly packed domains, thereby increasing the solubility of the encapsulated materials. These surfactant properties are demonstrated by stabilizing neutral gold nanoparticles of up to 20 nm in hydrocarbon solutions.



1: R=H, X=CH_2CH_3
2: R=CH_3, X=CH_2CH_3
3: R=CH_3, X=CH=CH_2

Figure 1. Encapsulation of Au nanoparticles by resorcinarenes **1-3**.

Mat. Res. Soc. Symp. Proc. Vol. 581 © 2000 Materials Research Society

EXPERIMENT AND RESULTS[6]

Neutral gold nanoparticles were prepared in the gas phase by condensation of pure metal vapor and were captured by passage through surfactant solutions in mesitylene.[7] Resorcinarenes **1-4** were synthesized according to literature procedures[8] and were diluted to 0.1-1.2 mM. Aerosols of gold nanoparticles of controlled size ranges were generated using a distributed arc cluster source (DACS)[9] and bubbled directly into the resorcinarene solutions, which turned deeply purple upon capture. This procedure was noteworthy in at least two respects. First, we noted that the resorcinarenes were several times more efficient at capturing nanoparticles than dodecanethiol (C12SH) at equimolar surfactant concentrations; at 520 nm, the characteristic Mie resonance for isolated gold particles, solutions of 3.7±1.5 nm Au particles captured in 1.2 mM of **1** or **2** absorbed 5-6 times more strongly than solutions of particles captured in 1.2 mM C12SH. Second, both large (>10 nm) and small (<10 nm) nanoparticles remained well dispersed in millimolar solutions of **1** and **2** at ambient temperature over a period of several months, with minimal loss of absorption intensity or precipitation. Transmission electron microscopy (TEM) of nanoparticles captured by **1** revealed a significant proportion of fused particles, suggesting that the kinetics of aggregation were competitive with surfactant passivation (see Figure 2a). It is likely that hydrogen-bonded aggregation of **1** interferes with adsorption of the headgroups to the nanoparticle surface. In contrast, minimal aggregation was observed among the nanoparticles captured by octamethyl derivative **2** (see Figure 2b). The nanoparticle size distributions did not change over time in either case, indicating that the encapsulated materials were quite stable under these conditions.

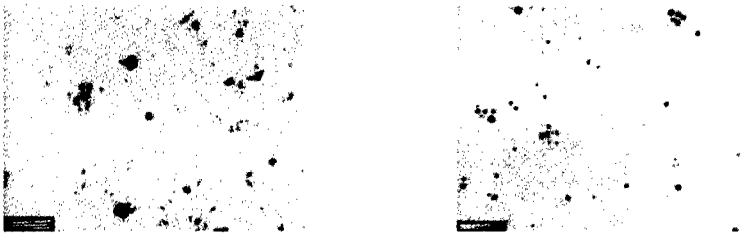
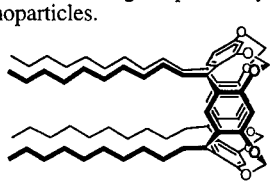


Figure 2. Transmission electron micrographs (Jeol 2000 FX, 200 KeV) of Au nanoparticles generated in the gas phase and dispersed into 1.2 mM solutions of resorcinarenes **1** (*a, left*) and **2** (*b, right*). Bar = 50 nm.

Stabilization of the Au nanoparticles by the resorcinarene headgroup is most likely mediated by chemisorption via multiple Au-O interactions. The eight oxygen atoms along the rim of the resorcinarene headgroup can adsorb to the Au surface in a cooperative fashion, similar to the ion-binding properties of the macrocyclic polyethers, the prototypical supramolecular receptor.[10] The enthalpy of Au-O chemisorption is remarkably low,[11] but its role in nanoparticle stabilization is supported by the observation that tetra-*O,O*-methylene resorcinarene derivative **4**,[8b] whose oxygen lone pairs are prevented from chemisorbing cooperatively due to steric hindrance, completely failed to capture or stabilize Au nanoparticles.



4

Surface adsorption was characterized by surface-enhanced Raman spectroscopy (SERS), a powerful and highly sensitive method for characterizing monolayer adsorbates on noble metal particles.[12] Large Au clusters encapsulated by **2** were gently precipitated by addition of one volume of CH_3CN to remove excess surfactant, then redissolved in mesitylene and drop-coated onto a glass surface. This substrate was observed to produce strong Raman signals (see Figure 3a), which we presume to be generated only by molecules adsorbed onto the nanoparticle surfaces. In

the absence of nanoparticles, thin films of **2** did not generate detectable amounts of Raman backscattering. Although we are presently unable to make an unambiguous assignment of all the group frequencies, there are two pieces of evidence which are strongly suggestive of a specific mode of chemisorption. First, many of the signals in Figure 3a are substantially different in frequency and/or intensity from those produced by polycrystalline samples of pure **2** (see Figure 3b). Second, several of the peaks in Figure 3a are significantly broadened, most notably those at 720 and 856 cm^{-1} ($\Delta\nu_{1/2}$~30 cm^{-1}). This broadening is commonly attributed to inhomogeneities due to chemisorption on different surface lattices or a decrease in vibrational excited-state lifetimes, both of which can strongly affect the bandwidths of the vibrational modes of surfactants which are directly adsorbed onto the metal surface.[13]

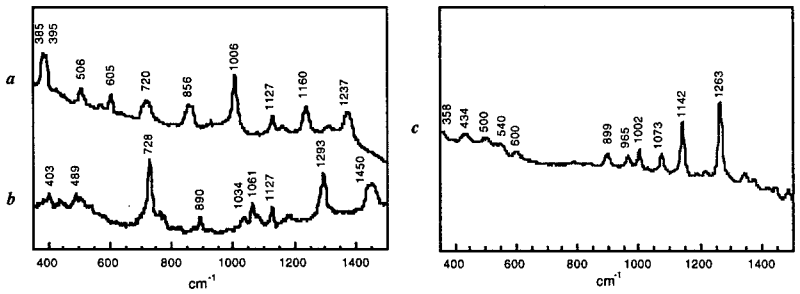


Figure 3. Raman spectra (500 mW diode laser, λ=785 nm, integration time=30 sec) of substrates containing resorcinarene **2**. *a*, large Au nanoparticles encapsulated by **2**. *b*, **2** in bulk polycrystalline phase. *c*, charge-stabilized Au nanoparticles with an overlayer of **2**.

A sample in which **2** was physisorbed to the surface of charge-stabilized Au colloid was prepared and examined by SERS for comparison (see Figure 3c). 15-20 nm Au particles generated by citrate reduction[14] were precipitated onto a glass slide and coated with a thin film of **2**. This sample produced completely different Raman scattering frequencies and intensity patterns than those generated by the encapsulated nanoparticles. We have recently ascertained that these Raman signals originate from adsorbates other than **2**, but interestingly, none of these were observed prior to addition of **2**, suggesting a surface dielectric effect.[15] Nevertheless, this result also indicates that the signals in Figure 3a are the result of direct chemisorption of **2** to the nanoparticle surface.

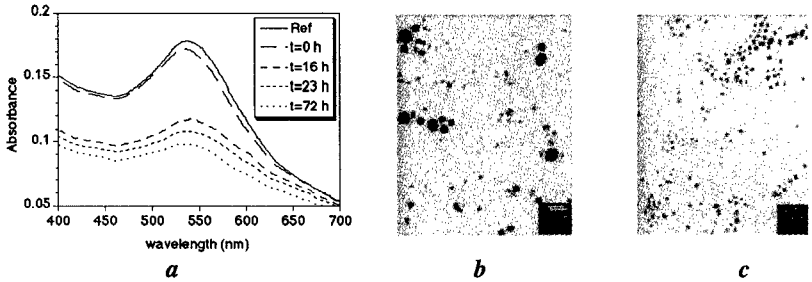


Figure 4. *a*: UV-vis absorption spectra of 3-15 nm Au particles dispersed into a 0.1 mM solution of resorcinarene **3** (Ref). Treatment with one equivalent of dodecanethiol resulted in a loss of absorbance over time (*t*=0-72 h). *b,c*: Transmission electron micrographs of Au nanoparticle dispersion before (*b*) and after (*c*) addition of dodecanethiol.

Displacement of the resorcinarenes by the more strongly adsorbing dodecanethiol (C12SH) resulted in the precipitation of the larger nanoparticles. A solution containing 3-15 nm Au particles

stabilized in a 0.1 mM solution of **3** was treated with one molar equivalent of C12SH and was observed to lighten over time, as quantified by UV-vis absorption spectroscopy (see Figure 4a). TEM analysis of the dispersions before and one week after C12SH addition indicate that particles >5 nm in diameter were no longer present, correlating the loss of color to the agglomeration and precipitation of the larger particles (see Figures 4b,c). This demonstrates the resorcinarenes' exceptional ability to prevent the larger nanoparticles from aggregating in solution.

Although resorcinarenes **1-3** have shown potential for maintaining large Au nanoparticles in a dispersed state, attempts to isolate the encapsulated nanoparticles from solution were unsuccessful. Purification by repeated precipitation or by chromatography resulted in extensive degradation. Excessive dilution of the surfactant also led to the gradual precipitation of the resorcinarene-encapsulated particles, suggesting facile chemical exchange. Appropriate modification of the resorcinarene headgroup can increase the robustness of the encapsulation shell, so that charge-neutral nanoparticles can be isolated and characterized as discrete chemical entities.

To this end, we have recently synthesized tetrakis(phenylphosphinyl)resorcinarene **5**[16] and have found it to be an excellent surfactant for large Au nanoparticles. The four phosphorus(III) atoms on the headgroup of **5** bond more strongly to the Au surface than the ether oxygens, and are also able to act synergetically for exceptionally strong chemisorption. A polydisperse mixture of Au nanoparticles was generated as described above and captured in a 0.1 mM mesitylene solution of **5**. These encapsulated particles could be separated from excess surfactant by preparative gel-permeation chromatography (GPC) and concentrated to dryness without degradation. Analytical GPC analysis using a Waters Styragel HR 4E column ($CHCl_3$) identified a high molecular-weight species with strong absorptivities at both 254 and 540 nm; TEM analysis of this fraction revealed large Au nanoparticles (see Figure 5).

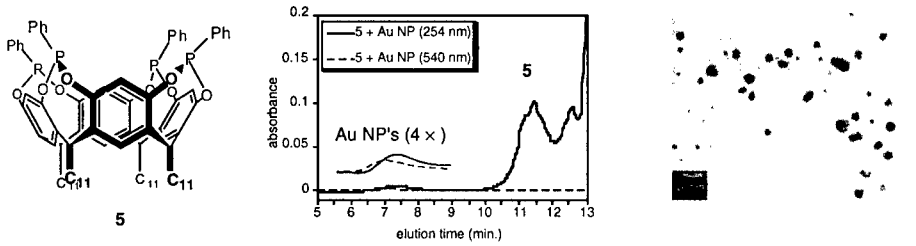


Figure 5. Large Au nanoparticles encapsulated by resorcinarene **5** (*left*) were isolated by gel permeation chromatography (*middle*) and visualized by transmission electron microscopy (*right*).

CONCLUSIONS

We have shown that gold nanoparticles up to 20 nm in diameter can be successfully stabilized by resorcinarene-based surfactants. The chemisorption of resorcinarenes **1-3** to the Au surface is most likely mediated by multidentate Au-O interactions, which were of sufficient strength to prevent agglomeration as demonstrated by TEM and UV-vis absorption spectroscopy. This specific mode of chemisorption is supported by the inability of methylene-bridged resorcinarene **4** to stabilize Au nanoparticles, as well as by surface-enhanced Raman spectroscopy. The displacement of resorcinarenes by dodecanethiol resulted in a marked precipitation of the larger Au nanoparticles, indicating that tailgroup mobility is an important factor for maintaining the encapsulated nanoparticles in a dispersed state. The surface bonding of resorcinarenes **1-3** is not strong enough to enable isolation of the encapsulated particles, but functionalizing the surfactant with highly chemisorptive phosphorus groups addresses this limitation. With this modification, we anticipate that encapsulation of Au nanoparticles by resorcinarene-based surfactants will provide a significant advance in the controlled fabrication of nanoparticle-based devices.

ACKNOWLEDGEMENTS

The authors gratefully acknowledge financial support from DARPA (DAAH04-96-1-0437: K.B.S., R.P.A.), the Purdue Research Foundation (fellowship to S.V.P.) and the Research Corporation Innovation Award program (RI-0333: A.W.), and to Prof. Michael Weaver for helpful discussions and the use of his laser system.

REFERENCES

[1] (a) Andres, R. P.; Bein, T.; Dorogi, M.; Feng, S.; Henderson, J. I.; Kubiak, C. P.; Mahoney, W.; Osifchin, R. G.; Reifenberger, R. *Science* **1996**, *272*, 1323-25. (b) Andres, R. P.; Bielefeld, J. D.; Henderson, J. I.; Janes, D. B.; Kolagunta, V. R.; Kubiak, C. P.; Mahoney, W. J.; Osifchin, R. G. *Science* **1996**, *273*, 1690-93. (c) Service, R. F. *Science* **1996**, *271*, 920-22. (d) Alivisatos, A. P. *Science* **1996**, *271*, 933-37. (e) Klein, D. L.; Roth, R.; Lim, A. K. L.; Alivisatos, A. P.; McEuen, P. L. *Nature* **1997**, *389*, 699-701. (f) Feldheim, D. L.; Keating, C. D. *Chem. Soc. Rev.* **1998**, *27*, 1-12. (g) Smith, C. G. *Science* **1999**, *284*, 274.

[2] Osifchin found that alkanethiol-passivated gold clusters with diameters larger than ~7 nm do not form stable colloidal solutions in hydrocarbon solvents: Osifchin, R. G. PhD Thesis, Purdue University, **1994**. The flocculation of alkanethiol-coated Au nanoclusters with diameters larger than 10 nm has also been studied in some detail as a function of surfactant: Weisbecker, C. S.; Merritt, M. V.; Whitesides, G. M. *Langmuir* **1996**, *12*, 3763-72.

[3] Israelachvili, J. *Intermolecular and Surface Forces*; 2nd ed.; Academic Press: New York, **1992**. Chapter 10.

[4] Timmerman, P.; Verboom, W.; Reinhoudt, D. N. *Tetrahedron* **1996**, *52*, 2663-704.

[5] Whitesides, G. M.; Simanek, E. E.; P., M. J.; Seto, C. T.; Chin, D. N.; Mammen, M.; Gordon, D. M. *Acc. Chem. Res.* **1995**, *28*, 37-44.

[6] Parts of this section have been described in a recently submitted publication: Stavens, K. B.; Pusztay, S. V.; Zou, S.; Andres, R. P.; Wei, A. *Langmuir*, in press.

[7] Chao, L. C., Andres, R. P. *J. Colloid Interface Sci.* **1994**, *165*, 290-95.

[8] (a) Aoyama, Y.; Tanaka, Y.; Sugahara, S. *J. Am. Chem. Soc.* **1989**, *111*, 5397-404. (b) van Velzen, E. U. T.; Engbersen, J. F. J.; Reinhoudt, D. N. *Synthesis* **1995**, 989-97.

[9] Mahoney, W. J. and Andres, R. P. *Materials Sci. Eng.* **1995**, *A204*, 160.

[10] (a) Cram, D. J. *Angew. Chem. Int. Ed. Engl.* **1986**, *25*, 1039-1134. (b) Lehn, J.-M. *Supramolecular Chemistry: Concepts and Perspectives*; VCH Publishers: New York, NY, **1995**.

[11] Masel, R. I. *Principles of Adsorption and Reaction on Solid Surfaces*, John Wiley and Sons, New York, **1996**, Chapter 3.

[12] (a) Freeman, R. G.; Grabar, K. C.; Allison, K. J.; Bright, R. M.; Davis, J. A.; Guthrie, A. P.; Hommer, M. B.; Jackson, M. A.; Smith, P. C.; Walter, D. G.; Natan, M. J. *Science* **1995**, *267*, 1629-32. (b) Freeman, R. G.; Hommer, M. B.; Grabar, K. C.; Jackson, M. A.; Natan, M. J. *J. Phys. Chem.* **1996**, *100*, 718-24. (c) Vo-Dinh, T. *Trends Anal. Chem.* **1998**, *17*, 557-82.

[13] Weaver, M. J., Zou, S. in *Advances in Spectroscopy 26*, John Wiley and Sons, Chichester, **1998**, Chapter 5, and references therein.

[14] (a) Turkevich, J.; Stevenson, P. C.; Hillier, J. *Disc. Farad. Soc.* **1951**, *11*, 55-75. (b) Frens, G. *Nature Phys. Sci.* **1973**, *241*, 20-22. (c) Handley, D. A. *Colloidal Gold: Principles, Methods, and Applications*; Hayat, M. A., Ed.; Academic Press: San Diego, **1989**; Vol. 1, pp 14-32.

[15] These signals presumably arise from citrate ions and/or their degradation byproducts adsorbed to the gold surface, although their frequencies do not overlap with those from crystalline sodium citrate or from citrate adsorbed onto Ag colloid: Blatchford, C.G.; Siiman, O.; Kerker, M. *J. Phys. Chem.* **1983**, *87*, 2503-08. These authors have suggested that the absorbate spectra and peak intensities may be strongly affected by the surface potential and by variable aggregation states.

[16] Xu, W.; Rourke, J. P.; Vittal, J. J.; Puddephatt, R. J. *Inorg. Chem.* **1995**, *34*, 323-29.

PROTEIN SUPPORTED METALLIC NANOSTRUCTURES AS CATALYSTS

S. Behrens*, W. Habicht*, N. Boukis*, E. Dinjus*, M. Baum**, E. Unger**
*Institut für Technische Chemie, Forschungszentrum Karlsruhe, Germany
**Institut für Molekulare Biotechnologie, Jena, Germany

ABSTRACT

Highly oriented proteins with characteristic nanometer dimensions are used as a template for the synthesis and support of metallic nanoparticles. Following a bottom-up approach, noble metal particles in the nanometer size range were obtained by the reduction of the corresponding metal salts in the presence of the protein assemblies. The catalytic activity of the protein-supported particles was determined by hydrogenation reactions.

INTRODUCTION

There is an increasing interest in nano-sized metal particles due to their new catalytic and electronic properties. With decreasing particle size the ratio of surface to volume increases continuously, so that the particle properties are more influenced by the surface atoms instead of the lattice atoms [1]. Particles in the nanometer size range reveal a great potential for heterogeneous catalysis [2]. The smaller and the more monodisperse the particles are, the better should be their catalytic activity. One disadvantage of such particles, however, is a tendency to aggregate. Aggregation can be avoided by subsequent particle nucleation and growth on a supporting template.
Highly oriented protein assemblies with characteristic nanometer-sized patterns are used as a template for the nucleation, growth and support of metallic nanoparticles (figures 1 and 2). These microtubules (MT) are built by protofilaments consisting of longitudinally connected αβ tubulin heterodimers of about 8 nm length. Thirteen protofilaments are arranged in parallel and form the hollow microtubule cylinders with outer diameters of 25 nm and lengths of several micrometers [3].

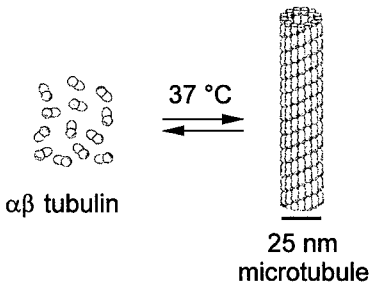


Figure 1: Microtubules are formed by a self assembly process at physiological pH and temperature.

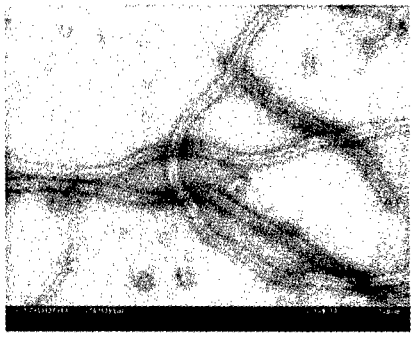


Figure 2: Scanning electron micrograph of microtubules, negatively stained with 1% uranyl acetate solution, 20 kV, m=100000 x

Mat. Res. Soc. Symp. Proc. Vol. 581 © 2000 Materials Research Society

EXPERIMENTS

Microtubule assembly

The microtubule (MT) samples were prepared by an in vitro self-assembly process of pure tubulin heterodimer isolated from porcine brain. The final protein concentration was about 1 mg/ml. The MTs were assembled in a buffer solution of 20 mM PIPES (1,4-piperazine diethane sulfonic acid, pK_a 6.8), 80 mM NaCl, 0.5 mM $MgCl_2$, 1 mM EGTA (ethylene glykole-bis-(2-aminoethyle)-tetraacetic acid) by adding of 0.25 M GTP (guanosin-5'-triphosphate) and 10 mM taxol (from taxus brevifolia) and warming the sample up to 37 °C. The MT formation was accompanied by turbidity measurements at 340 nm wavelength. The steady state level, at which the tubublin mass in the polymerized state shows no further increase, was usually observed after 20 min. The assembled microtubules were chemically fixed by vigorous stirring in 0.05% and then after 5 min in 3% glutaric aldehyde. The samples were dialyzed against buffer/H_2O to eliminate excess glutaric aldehyde.

Synthesis of nanoparticles

200 µl of an aqueous Na_2PdCl_4 (0,0125 M, pH 6.8) solution were added to 100 µl of the assembled microtubules and 280 µl of H_2O. The Pd^{2+} ions were reduced with trisodium citrate (0.25 M in H_2O) at 90°C in 1 h. The sample was dialyzed against buffer/H_2O to eliminate excess Pd^{2+}.

15 ml of a commercial gold colloid (5 nm, 10 nm, 20 nm and 60 nm in diameter) were concentrated, each added to 100 µl of the assembled microtubules and immobilized on the microtubules within 30 min at room temperature. 2 nm gold particles were synthesized on microtubules by reduction of a $HAuCl_4$ solution (1 g/ml in H_2O) with $NaBH_4$ (0.5 eq in H_2O) at 0° C. These gold particles served as nucleation seeds for the following reduction of 400 µl Na_2PdCl_4 (0.0125 M in buffer/H_2O 1:10, pH 6.8) with 40 µl trisodium citrate (0.25 M in H_2O) at 70°C within 30 min. The sample was dialyzed against buffer/H_2O to eliminate excess Pd^{2+}.

Catalytic Activity

The catalytic activity for the hydrogenation of crotonic acid was determined by measuring the hydrogen consumption per mass of noble metal and time in a standard test reactor at 25 °C and atmospheric pressure. The total metal content was analyzed by ICP measurements.

RESULTS

Following a bottom-up approach noble metal particles in the nanometer size range are obtained by the reduction of the corresponding metal salts in the presence of the protein assemblies. By reduction of an aqueous Na_2PdCl_4 solution, palladium particles (1 - 5 nm) could be nucleated and immobilized on the tubulin lattice of microtubules (figure 3).

The catalytic activity of these microtubule-immobilized palladium nanoparticles in the hydrogenation reaction of crotonic acid was examined. In H_2O a high catalytic activity was measured for the palladium protein material (figure 4). Under these reaction conditions the catalytic activity is even higher than for commercial Pd-charcoal catalysts. One problem is, however, the low stability of the protein assemblies as support. Additional stabilization of the Pd protein material can be performed by its adsorption on Al_2O_3. Under reaction conditions the life-time of the catalyst is improved by the Al_2O_3 support.

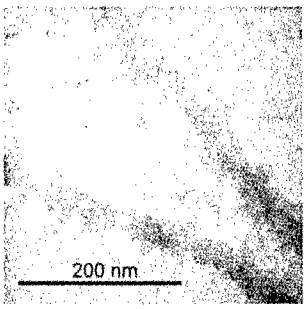


Figure 3: Transmission electron micrograph of small palladium particles immobilized on microtubules.

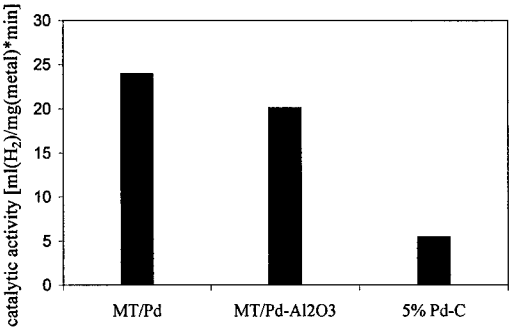


Figure 4: Catalytic activity (hydrogenation of crotonic acid in H_2O) for different Pd catalysts.

Layered bimetallic Au/Pd particles in the size range of 3 to 60 nm have been synthesized on microtubules by a seed-growth mechanism: Au seeds of different sizes linked to the proteins by thiol groups were covered with a Pd layer by reduction of Na_2PdCl_4 with sodium citrate at 70°C in 30 min (figures 5 and 6). Figures 7 and 8 show particle size distributions for pure gold particles and for the corresponding bimetallic Au/Pd particles determined from TEM images.

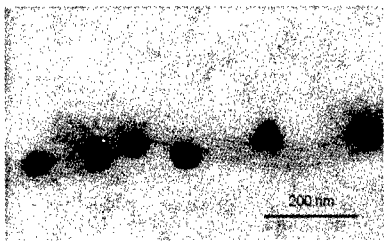


Figure 5: Transmission electron micrograph of bimetallic Pd/Au particles (mean particle diameter 61.6 nm) immobilized on a microtubule.

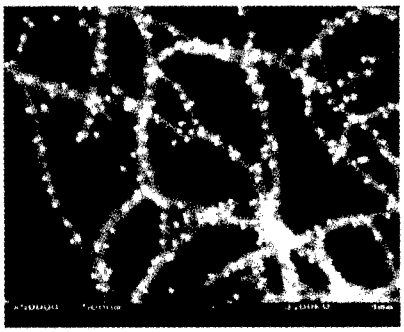


Figure 6: Scanning electron micrograph of bimetallic Pd/Au particles (20 nm), 3 kV, m=50000 x.

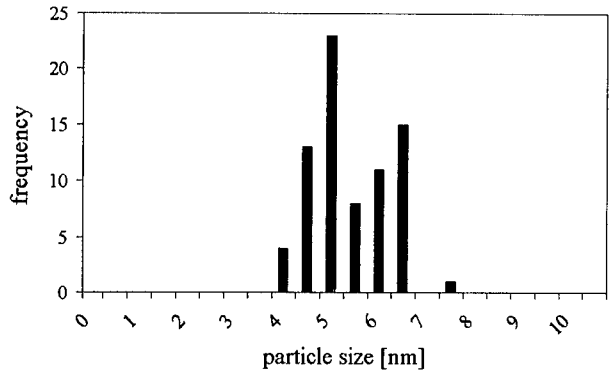


Figure 7: Particle size distribution of Au particles (mean particle diameter 5.7 ± 0.7(σ)nm).

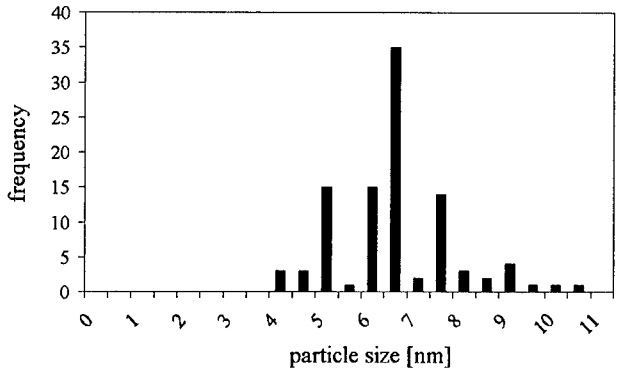


Figure 8: Particle size distribution of bimetallic Au/Pd particles (mean particle diameter 6.7 ± 1.2(σ)nm).

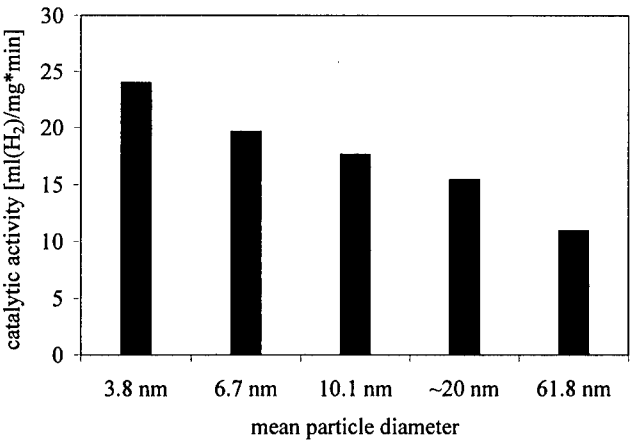


Figure 9: Catalytic activity for different bimetallic Au/Pd particles on microtubules

The catalytic activity of the microtubule supported bimetallic Pd/Au particles was investigated using the crotonic acid test. The resulting activity values of the bimetallic systems plotted versus the mean particle diameter are shown in figure 9. The highest values

were observed for bimetallic particles of 3.8 nm mean particle diameter. Within the range of the investigation an increase in catalytic activity is observed with decreasing particle diameter. The synthesis of smaller particles is still under investigation.

SUMMARY

Pure Pd as well as bimetallic Pd/Au particles in the nanometer size range have been nucleated and immobilized on the protein matrix of microtubules. These Pd and Pd/Au protein materials show a high catalytic activity for the hydrogenation reaction of crotonic acid in H_2O.

REFERENCES

1. H. Weller, Angew. Chem. 108, 1996, p. 1159.
2. a) H. Bönnemann, W. Brijoux, R. Brinkmann, R. Fretzen, T. Joußen, R. Köppeler, B. Korall, P. Neiteler, J. Richter, J. Mol. Catal. 86, 1994, p. 129; b) H. Bönnemann, W. Brijoux, R. Brinkmann, E. Dinjus, T. Joußen, B. Korall, Angew. Chem. 103, 1991, p. 1344.
3. R. Kirsch, M. Mertig, W. Pompe, R. Wahl, G. Sadowski, K. J. Böhm, E. Unger, Thin Solid Films 305, 1997, p. 248.

THE FORMATION OF HIGH-COERCIVITY, ORIENTED, NANOPHASE COBALT PRECIPITATES IN Al_2O_3 SINGLE CRYSTALS BY ION IMPLANTATION

S. HONDA, F. A. MODINE, T. E. HAYNES, A. MELDRUM, J. D. BUDAI, K. J. SONG*, J. R. THOMPSON*, L. A. BOATNER, Solid State Division, Oak Ridge National Laboratory, Oak Ridge, TN 37831, lb4@ornl.gov, *Also at the University of Tennessee, Knoxville, TN

ABSTRACT

Ion-implantation and thermal-processing methods have been used to form nanophase magnetic precipitates of metallic cobalt that are embedded in the near-surface region of single crystals of Al_2O_3. The Co precipitates are isolated, single-crystal particles that are crystallographically oriented with respect to the host Al_2O_3 lattice. Embedded nanophase Co precipitates were formed by the implantation of Co^+ at an energy of 140 keV and a dose of 8×10^{16} ions/cm^2 followed by annealing in a reducing atmosphere. The implanted/annealed Co depth profile, particle size distributions and shapes, and the orientational relationship between the nanophase precipitates and the host crystal lattice were determined using RBS/channeling, transmission electron microscopy, and x-ray diffraction. Magneto-optical effects arising from Co precipitates formed in the near-surface region of Al_2O_3 were observed and characterized using magnetic circular dichroism. Magnetic properties of the Co-particle/host nanocomposites were investigated in the temperature range of 77 to 295 K in applied fields of up to 10 kG using a superconducting quantum interference device (SQUID) magnetometer. Implantation of the Co particles by Pt or Xe ions produced a large anisotropic increase in their coercivity. Accordingly, these magnetic nanoparticle systems may be of interest for magnetic data storage applications. Details of the magnetic properties of the Co/Al_2O_3 nanocomposites including their retentivity, coercivity, saturation field, and magnetic anisotropy are presented.

INTRODUCTION

Recent work has shown that "smart" surfaces can be created on inactive host materials by using ion implantation and thermal processing to form embedded active nanophase precipitates [1,2]. "Smart" surfaces have intrinsic properties that combine both sensing and actuating functions, and the implantation/thermal-processing concept for the creation of smart surfaces was first established in the case of VO_2 precipitates that were formed in single-crystal Al_2O_3 [1]. Recently, the ion-implantation/annealing approach to the formation of active nanocomposite surfaces has been extended to include nanophase magnetic precipitates, and magnetic nanocomposite surfaces have been formed in yttrium stabilized (cubic) zirconia (ZrO_2) by using implantation and thermal processing to create embedded metallic α-Fe, magnetite (Fe_3O_4) and Ni nanophase particles [3,4]. These precipitates exhibit a unique combination of properties: e.g., each particle is a single crystal that is crystallograhically aligned with respect to the host crystal, the precipitates are isolated from each other by the host so there are effectively no interparticle grain-boundary effects, the particles are often faceted, and they are protected from the environment by the surrounding host matrix. These surface nanocomposites represent a new class of materials with potential data storage and optical communications applications.

The present work extends our prior investigations of magnetic nanocomposite surfaces to the formation and characterization of Co precipitates in a single-crystal Al_2O_3 host. In this case, the magnetic properties of the crystallographically oriented Co particles can be altered by Pt-ion

Mat. Res. Soc. Symp. Proc. Vol. 581 © 2000 Materials Research Society

implantation to induce highly anisotropic magnetic properties and to increase the Co-particle coercivity up to a value of ~1.3 kG.

EXPERIMENT

The implantation of Co^+ ions into (0001)-oriented α-Al_2O_3 single crystals was carried out at a temperature of ~302 K, an implant energy of 140 keV, and a dose of 8.0×10^{16} ions/cm^2. An average implanted-Co-ion depth of ~50 nm below the Al_2O_3 surface was calculated using the TRIM code. In order to form precipitates of the implanted species, subsequent thermal treatments were carried out for 2 h in a slightly reducing atmosphere of Ar + 4%H_2 using a tube furnace at T = 1100 °C. After 2 h at this temperature, the samples were quenched to room temperature. The implantation of Pt^+ ions subsequent to the formation of metallic Co precipitates in Al_2O_3 was carried out at a sample temperature of ~302 K and an implant energy of 230 keV. Pt^+ implant doses ranging from 10^{15} to 10^{16} ions/cm^2 were used in order to investigate the effect of Pt doping on the magnetic properties of Co particles in Al_2O_3. The Pt-ion implantation depth was calculated using the TRIM code in order to superimpose the Pt-implant depth with that of the metallic Co precipitates.

The metallic Co precipitates in single-crystal Al_2O_3 were characterized prior to and after Pt-ion implantation by using Rutherford backscattering (RBS)/channeling spectroscopy, x-ray diffraction, transmission electron microscopy (TEM), and magnetic circular dichroism (MCD). MCD is a magneto-optical technique that measures the difference in absorption between right- and left-circularly polarized light. MCD measurements were made using a 10 kG electromagnet and utilized photoelastic-polarization modulation to investigate the magneto-optical effects as a function of wavelength and applied magnetic field with both the polarization of the light and the applied field oriented perpendicular to the specimen surface [5]. The anisotropic magnetic properties of the precipitate system were determined using a superconducting quantum interference device (SQUID) magnetometer. The magnetization and magnetic anisotropy of the Co precipitates both prior to and after Pt implantation were investigated, and magnetization curves were measured at ~297 K and 77 K with the applied magnetic field oriented parallel or perpendicular to the plane containing the implanted particles. Complementary chemical analysis in the precipitate region was carried out during the TEM examination by using energy-dispersive spectroscopy (EDS), and x-ray diffraction measurements were performed using a rotating-anode Cu $K_{\alpha 1}$ x-ray source, a vertically focusing LiF monochromator, and a Huber four-circle diffractometer.

RESULTS AND DISCUSSION

TEM and X-ray Analysis of Co Particles in Al_2O_3

TEM micrographs illustrating both plan-view (a) and cross-sectional (b) images of metallic Co particles formed by ion implantation and thermal processing are shown in Fig. 1. Moiré fringes can be seen in the cross-sectional view and provide an indication of the degree of crystallographic alignment of the Co particles. The relatively strong faceting observed previously in the case of metallic α-Fe particles in cubic zirconia [4] is not evident in the Co particles, and the Co-particle shape, as indicated by the two perpendicular TEM images, is essentially spheroidal.

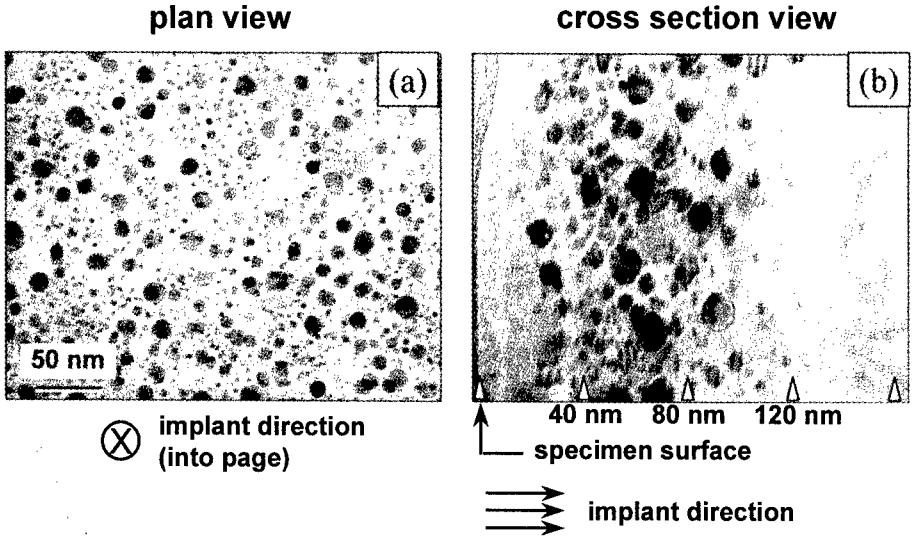


Fig. 1 (a) plan view and (b) cross-section TEM micrographs for metallic Co particles in Al_2O_3 illustrating the spheroidal precipitate shape.

The details of the crystallographic properties of the Co/Al_2O_3 nanocomposite system are presented in Fig. 2. Part (a) of Fig. 2 is a θ-2θ scan along the surface normal that shows the Al_2O_3 substrate peak along with a Co nanocrystal peak which can be indexed either as a close-packed hexagonal (hcp) Co (002) or as a face-centered cubic (fcc) Co (111) reflection. Figure 2(b) shows an X-ray scan along a direction that was specifically chosen to distinguish between the hcp and fcc Co structures. Labeled in hcp units, this scan is along the [001] direction through the (10L) reciprocal-lattice positions [6]. Peaks at integral L values correspond to the hcp

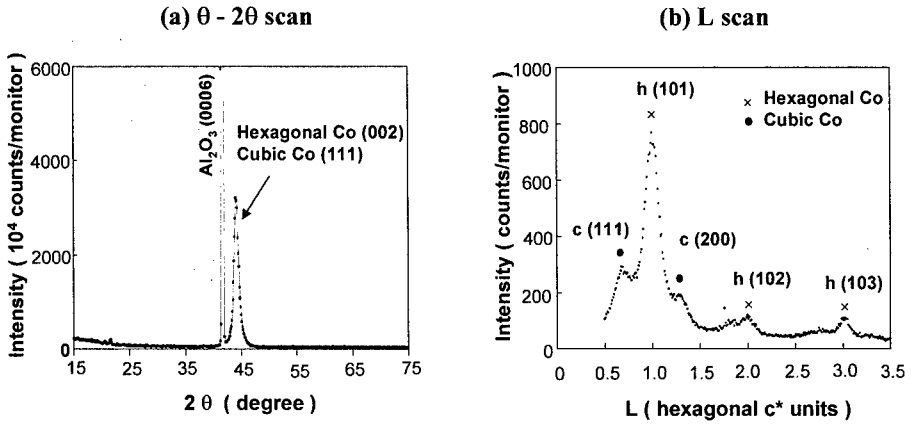
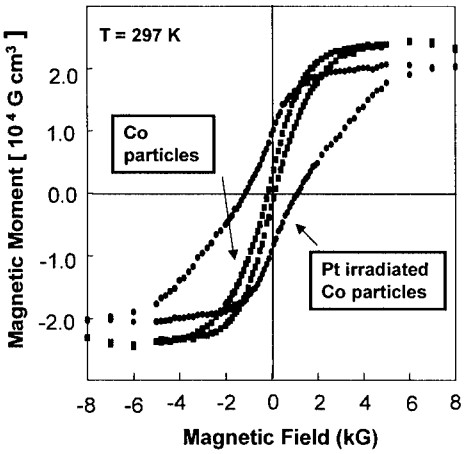


Fig. 2 X-ray diffraction patterns for Co particles in Al_2O_3, (a) θ–2θ scan and (b) L-scan.

structure, while peaks at n/3 positions correspond to the fcc structure. Both types of peaks are present in this scan, indicating that the Co precipitates have mixed crystal structures. A mixed structural character is, in fact, common in bulk Co crystals when a high density of stacking faults is present. An x-ray phi scan established that the Co precipitates are three-dimensionally aligned with the Al_2O_3 substrate. The orientational relationships are given by: hcp Co (001) || Al_2O_3 (001) out of plane, Co [100] || Al_2O_3 [110] in plane, and fcc Co (111) || Al_2O_3 (001) out of plane, Co [$2\bar{1}\bar{1}$] || Al_2O_3 [110] in plane.

Magnetic Properties of Co particles in Al_2O_3 Before and After Pt Implantation

Figure 3 shows the magnetization curve of Co nanoparticles in Al_2O_3 as determined by SQUID-magnetometer measurements at T = ~297 K. As indicated in the table accompanying Fig. 3, the Co-particle coercivity and remanence are 150 G and 4% respectively. It is well established that the addition of Pt to bulk Co alloys can significantly increase the coercive field, and alloys of this type are routinely used in, for example, hard disk drives for magnetic data storage. Accordingly, Pt implants into the region occupied by the Co particles in the Al_2O_3 host were undertaken in order to determine whether increases in the coercivity could be induced in the Co nanoparticle case. The magnetization curve observed after Pt implantation into the region occupied by the Co particles is also shown in Fig. 3. The accompanying Table shows that, as a result of the Pt-ion implantation, the Co-particle coercivity has increased from 150 to 1140 G while the remanence increased from 4 to 46%.



	Before Pt implant	After Pt implant
Coercive Force (G)	150	1140
Remanence (%)	4	46

Fig. 3 Magnetization curve for metallic Co particles in Al_2O_3 and Pt-implanted Co particles in Al_2O_3.

Figure 4 shows the anisotropy of the magnetization curves at 297 K for unimplanted Co and Pt-implanted Co nanoparticles in Al_2O_3 as determined by SQUID magnetometer measurements made with the applied magnetic field perpendicular or parallel to the plane occupied by the precipitates [see the insets in Figs. 4(a) and (b).] Prior to Pt-ion implantation, the magnetization curves in Fig. 4(a) are similar for the parallel and perpendicular orientations of the applied magnetic field. After Pt implantation, however, the magnetization curve of the Co-particle/Al_2O_3 nanocomposite [see Fig. 4(b)] shows a significant difference between the parallel and perpendicular applied-field cases. Accordingly, the Pt-implanted material is characterized

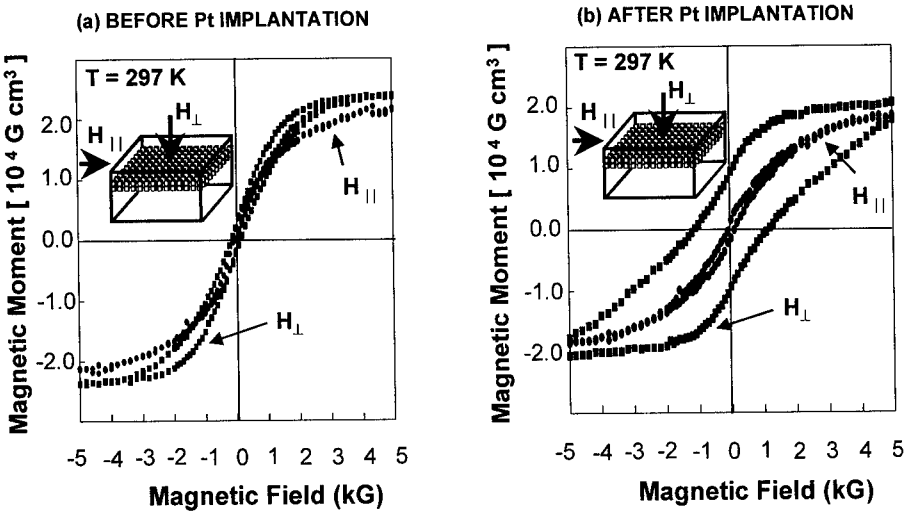


Fig. 4 Magnetization curves of metallic Co particles in Al_2O_3 (a) prior to and (b) after implantation with Pt, measured at T = 297 K. The magnetic field is applied parallel or perpendicular to the Al_2O_3 surface (i.e., parallel or perpendicular to the plane containing the precipitates as shown in the inset.)

by highly anisotropic magnetic properties at room temperature that are not observed for the unimplanted Co precipitates. One interesting feature of the magnetic anisotropy of the Pt-implanted Co nanocomposite is that the larger coercive field occurs when the external magnetic field is applied perpendicular to the Al_2O_3 surface.

During the ion-implantation process, the introduction of the implanted species into a given region of a host is also accompanied by the creation of a significant amount of displacive radiation damage. Accordingly, experiments were undertaken in which chemically inactive Xe ions were implanted into the Co-precipitate region in order to ascertain whether the coercivity increase found for the case of Pt ion implantation was due to doping or radiation effects. The MCD-detected hysteresis loops shown in Fig. 5(a) provide a comparison of the effect of Pt or Xe ion implantation on the magnetic properties of Co nanoparticles in Al_2O_3. A Xe implantation dose of 9.0×10^{15} ions/cm^2 was calculated using the TRIM code in order to produce approximately the same damage in dpa as Pt implantation at a dose of 6.4×10^{15} ions/cm^2. A significantly larger effect on the Co-particle magnetic properties was observed in the case of the Pt ion implantation, however. Moreover, the coercivities obtained from the MCD-detected hysteresis loops are plotted in Fig. 7(b) as a function of dose for Pt^+ and Xe^+ ion implantation. The Co-particle coercivities for both Pt and Xe implantation initially increase with increasing ion dose and eventually reach a saturation value. As shown in Fig. 5(b), the saturation value of the Co-particle coercivity for the Pt-implantation case is significantly larger than for the case of Xe-ion implantation. This result suggests that, in addition to a radiation-induced increase of the Co-precipitate coercivity, a Pt-doping effect may be operative in the case of the Pt-implantation-induced increase in the Co-particle coercivity.

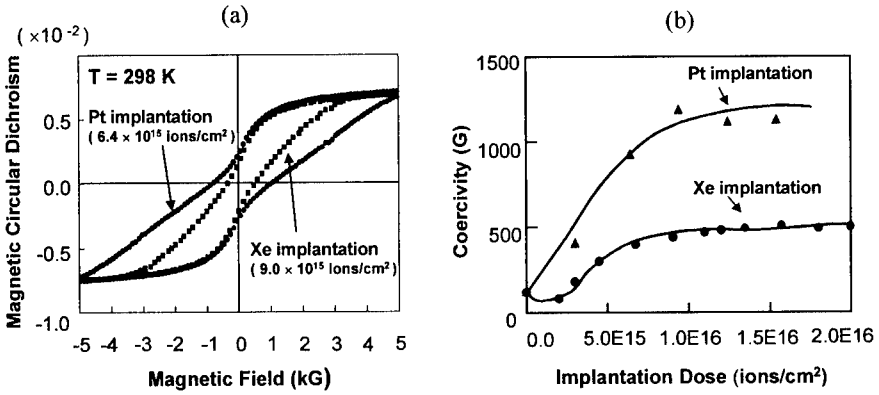


Fig. 5 The effect of Pt- and Xe-ion implantation on the magnetic properties of Co nanoparticles in Al_2O_3 as determined from MCD measurements. (a) Magnetization curves at 298 K for a Pt dose of 6.4×10^{15} ions/cm^2 and a Xe ion dose of 9.0×10^{15} ions/cm^2. The Pt ion implantation is more effective in increasing the Co-particle coercivity. (b) a plot of the coercivity increase versus implant dose for Pt and Xe implantation.

SUMMARY

Crystallographically oriented, single-crystal Co nanoparticles have been formed in near-surface region of Al_2O_3 single-crystal hosts by ion implantation and thermal treatment. Subsequent implantation of the Co particles by Pt or Xe produced a significant increase in the Co-particle coercivity at room temperature with the applied magnetic field oriented perpendicular to the plane occupied by the Co particles. The coercivity after Pt or Xe implantation was significantly lower when the applied magnetic field was oriented in the plane containing the precipitates.

ACKNOWLEDGEMENT

This research was sponsored by the Division of Materials Sciences, U.S. Department of Energy under Contract No. DE-AC05-96OR22464 with Lockheed Martin Energy Research Corp.

REFERENCES

1. L. A. Gea and L. A. Boatner, Appl. Phys. Lett. **68**, 3081 (1996).
2. L. A. Gea, J. D. Budai, and L. A. Boatner, J. Mater. Res. **14**, 2602–2610 (1999).
3. L. A. Gea, S. Honda, L. A. Boatner, T. E. Haynes, B. C. Sales, F. A. Modine, A. Meldrum, J. D. Budai, and L. Beckers, Mat. Res. Symp. Proc. **501**, 137 (1998).
4. S. Honda, F. A. Modine, A. Meldrum, J. D. Budai, T. E. Haynes, L. A. Boatner, and L. A. Gea, Mat. Res. Symp. Proc. **540**, 225 (1999).
5. R. Laiho, Phys. Stat. Sol. (b) **69**, 579 (1975).
6. T. Lei, K. F. Ludwig, Jr., and T. D. Moustakas, J. Appl. Phys. **74**, 4430 (1993).

CAN WE DETERMINE THE BARRIER RESISTANCE FOR ELECTRON TRANSPORT IN LIGAND STABILIZED NANOPARTICLES FROM INTEGRAL CONDUCTANCE MEASUREMENTS?

U. SIMON
University of Essen, Institute of Inorganic Chemistry, 45127 Essen, GERMANY

ABSTRACT

By means of integral temperature dependent conductance measurements, the effective capacitance of ligand stabilized nanoparticles, arranged in dense packings or networks, can be deduced from the activation energy of the charge transport, for which the use of the Landauer formula is proposed. According to this, the barrier resistance in ligand stabilized nanoparticle arrangements depends predominantly on the inter particle spacing rather than on the chemical composition of the molecules. Comparison with data of the single molecule resistance determined by local probe techniques or by theoretical methods shows remarkable aggreement.

INTRODUCTION

During the nineties chemical synthesis of nanoparticles or nanostructured solids has evolved to an important field in science and technology. The topic of many developments is the designed formation of specific structures of matter, for example the generation of single quantum dots [1] or solids with quantum dot [2] or quantum anti-dot superstructures [3]. Inspired by the unique properties of these materials a lot of efforts have been made to tailor one, two and three dimensional nanoparticle arrangements utilizing the principles of supermolecular chemistry. When such small conducting objects of a few nanometers like metal or semiconductor nanoparticles are arranged in a small spatial distance of approx. 1 nm in one, two or three dimensions, tunnel junctions with electrical capacitances of less than 10^{-18} F are generated [1]. This allows the handling of individual charges by means of single electron tunneling (SET), which has been recognized to be the fundamental concept for ultimate miniaturization in electronics [4]. In order to realize SET the following two conditions must be fulfilled: (i) The insulating barriers must be high and thick enough, to provide an essential decay of the electron wave function outside the nanoparticle. In spite of relatively complex and rigorous quantum mechanical consideration, this condition can be formulated quantitatively using the tunneling resistance R_T as a characteristic of the tunneling junction, which must exceed the resistance quantum $R_q = h/2e^2 \approx 12.9\ k\Omega$, i.e. $R_T >> R_q$. Then, the electrons can be considered being localized and their number already behaves classically, although they are subjected to thermodynamic fluctuations as well as every statistical variable. (ii) In order to suppress thermal fluctuations the energy E_C required to add an extra electron to the nanoparticle should be significantly higher than k_BT, i.e. $E_C = e^2/2C >> k_BT$ where C is the effective capacitance of the nanoparticle.

The family of ligand stabilized metal clusters like $Au_{55}(PPh_3)_{12}Cl_6$, $Pt_{309}phen^*_{36}O_{30}$ or $Pd_{561}phen_{36}O_{200}$ (phen* = *batho*-phenanthroline, phen = 1,10-phenantroline) are uniform chemically tailored metallic nanoparticles in the size range from 1.4 - 2.4 nm [5], and they fulfill these requirements for SET. They consist of a metal core with a well defined atom number, which

Mat. Res. Soc. Symp. Proc. Vol. 581 © 2000 Materials Research Society

is surrounded or "dressed" by a protecting ligand shell. If these particles are attached to each other the ligand shell acts like an insulating spacer between the metal cores (see Fig. 1). While the incremental charging energy E_C follows the scaling law $E_C \sim 1/r$ (r = radius), in those nanoparticles SET can be observed up to the range of room temperature [6]. This experimental evidence indicates that, however, R_T of the surrounding stabilizing ligand molecules is large enough to overcome R_q.

Although organic molecules display a rich variety in their electrical properties when they are in the condensed state, about the insulation or conduction properties of individual organic molecules, which determine the charge transport through nanoparticle arrangements or molecular devices, just a little is known.

In this work an attempt has been made to deduce the resistance of organic ligand and spacer molecules from integral conductance measurements according to the approach, which is described in the following.

EXPERIMENTAL BACKGROUND

Most recently the chemical tailoring of the activation energy by insertion of bifunctional dielectric spacer molecules into a three dimensional arrangement of $Au_{55}(PPh_3)_{12}Cl_6$ and $Pd_{561}phen_{36}O_{200}$ clusters has been reported [7].

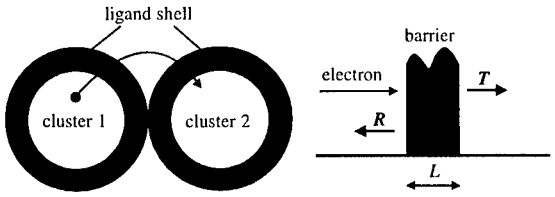


Figure 1: Two attached ligand stabilized metallic particles forming a tunnel junction via the ligand shell of length L. An electron entering the barrier from the left-hand space (cluster 1) has the transmission probability T and the reflection probability R, where $T = 1 - R$.

The initial idea was to strech the cluster package in comparison to a densiest sphere packing and by this to increase the inter-particle spacing, which denotes the spatial distance L between the surface of neighboring clusters (see Fig. 1). This should lead to an increase of the activation energy, i. e. a decrease of the electrical capacitance between the clusters. The activation energy E_A, i.e. the energy barrier that has to be overcome to transfer a single electron from an initially neutral cluster to a neutral nearest neighboring cluster, is dependent on the capacitance C, as follows from $E_C = e^2/2C$. It can be determined directly from the temperature dependence of the dc conductance $G(T)$ of the cluster arrangements, which have been investigated on pressed pellets or on thick films deposited on microelectrode structures. Earlier investigations on the electrical properties of this ligand stabilized metal clusters have already shown that particularly at high temperatures thermally activated electron hops between nearest neighbors instead of hops of variable range dominate the charge transport. This is reflected by a temperature dependence according to the Arrhenius relation $log\ G(T) \sim E_A/k_BT$. As an example Fig. 2 shows the Arrhenius plot of the Pd_{561}-cluster in dense packing ($E_A = 0.02\ eV$) and with inserted spacer molecules (cluster network, $E_A = 0.05\ eV$).

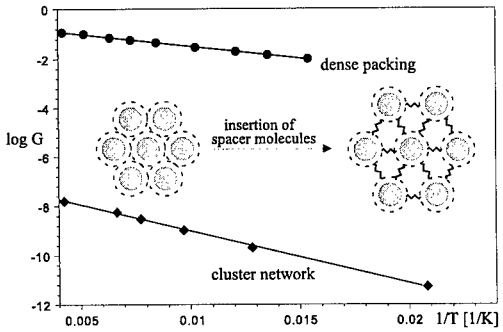


Figure 2: Plot of the conductance G (T) in a.u. versus 1/T (80K-300K) of a dense packing of Pd_{561}-clusters as well as of a Pd_{561}-cluster network (as shown in the simplifying model)

While the cluster size is kept constant when the cluster spacing in increased by the spacer molecules, it could be shown that that the E_A increases linearly with the length of the spacer molecules according to the classical description of a junction capacitance $C = \varepsilon_0 \varepsilon A/d$, where A/d is the geometric parameter and ε is the dielectric constant of the dielectric in a parallel plate capacitor. These results are summarized in Tab. 1.

THEORETICAL APPROACH

Since the activation energy reflects the barrier an electron has to overcome to hop from an uncharged nanoparticle to an uncharged neighboring nanoparticle, the value of E_A is assumed to be equivalent to the absolute barrier hight in the concept of the Landauer formalism [8]. This model decribes conduction as transmission and allows to estimate the electrical resistance of arbitray barriers in mesoscopic systems. The Landauer formula

$$G = \frac{2e^2}{h} M T \qquad (1)$$

connects the conductance G (or resistance G^{-1}, resp.) of a barrier with the transmission probability T of an electron, passing from one electrode through a barrier (insulator or conductor) into another electrode. M is the number of transverse modes, i.e. the number of energy channels through the barrier. As long as the voltage between the two electrodes is small enough (with much less than ~1V being droped across the molecule), the conduction through the barrier will involve tunneling rather than propagation [8]. The transmission probability is approximated by

$$T \approx \exp^{(-\,2\sqrt{m\,(V-E)}\,L\,/\,\hbar)}\,, \qquad (2)$$

where V is the absolute height of the barrier and V-E is the barrier height an electron with energy E and mass m "feels", when it enters the barrier. Thus, the resistance of the barrier is

$$G^{-1} \approx 12.9\ k\Omega\ e^{0.7245\sqrt{(V-E)}\,L}\ M^{-1}\,. \qquad (3)$$

Regarding the transport of electrons between nanoparticles, $M = 1$ is assumed, since the charging of the particle by one excess electron will change the electrical potential essentially to prevent further charging. Assuming that the effective height of the barrier is represented by the activation energy, the resistance of the barrier can be calculated via (3).

RESULTS AND DISCUSSION

Since this is a very simplicistic approximation, the results need to be compared with results determined by different methods for consistency. Actually, there are three different methods, which are predominatly discussed in the current literature to determine the resistance of individual molecules. These are:

- measuring the conductance through individual ligand stabilized metal nanoparticles via scanning tunneling spectroscopy (STS) [9] or in a SET transistor arrangement with ligand stabilized nanoparticles as central electrode [10]
- measuring G(T) through highly ordered two dimensional or three dimensional nanoparticle arrays (superlattices). This method assumes that at infinitely high temperature ($T \to \infty$), which can be approximated via the Arrhenius relation, all linking spacer or ligand molecules contribute to the overall conductance. Then the resistance of the individual molecules can be deduced via Kirchhoff's laws from an idealized resistor network [11,12]. This approach can just be applied to highly ordered systems, it is not applicable to the cluster samples examined in this work, which exhibit a certain degree of disorder
- computation of the transmission function and calculation of the midgap resistance of individual molecules, taking into account the electronic and geometric structure of the molecules obtained from the extended Hückel method [12,13].

The results of the conductance measurements on the ligand stabilized clusters and those of the three methods described above are plotted in Fig. 3, where each measuring point is labeled according to Tab. 1.

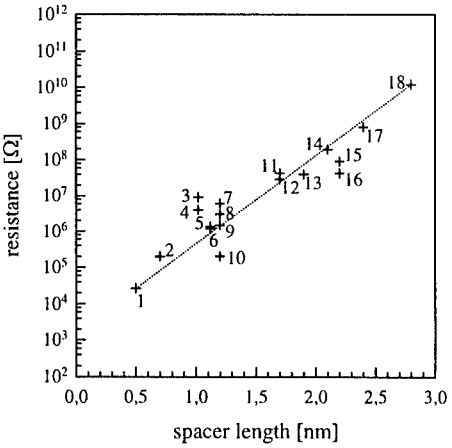


Figure 3: Plot of the resistance of individual molecules with length L, forming a tunneling barrier between metallic electrodes. The dotted line represents the linearized trend of the whole set of data.

The plot reflects remarkable aggreement between the values, which have been deduced from our experiments according to the approach described here, and those values, which have been obtained from the three diffent methods described above. In spite of its simplicity the approach introduced allows an estimation of the ligand/spacer resistance. According to this the resistance is, however, predominantly determined by the length of the molecules rather than by their chemical composition. This was somehow surprising, since from aliphatic molecules, like hexanedithiol or dodecanethiol, an insulating behavior was expected, while conjugated molecules, like BATA or ADI, should behave like molecular wires with significant conductance. Thus, the ligands/spacers act like dielectrics which are suffciantly insulating to fulfill $R_T >> R_q$.

Table 1: Summary of the experimental results and refence data determined by different methods

No.	Electrode/Spacer	Method	Length [nm]	E_A [eV]	Resistance [Ω]	Reference
1	Pd_{561}/phenantroline	E_A, R(Landauer)	0.5	0.02	2.66E4	this work
2	$Au_{55}(Ph_2C_6H_4SO_3H)_{12}Cl_6$	E_A, R(Landauer)	0.7	0.16	2.ooE5	this work
3	1.2nm Au/α,α'-xylenedithiol	STS on a single cluster	1.02	-	8.8±1.2E6	[9]
4	bulk Au/α,α'-xylendithiol	Ext. Hückel	1.02	-	4.5±0.5E6	[13]
5	$Cu_{72}Se_{36}(PPh_3)_{20}$/single cryst.	E_A, R(Landauer)	1.12	0.16	1.2E6	this work,[14]
6	$Cu_{146}Se_{73}(PPh_3)_{20}$/single cryst.	E_A, R(Landauer)	1.12	0.17	1.36E6	this work,[14]
7	10nm Au/hexanedithiol	SET transistor	1.2	-	6E6	[10]
8	10nm Au/hexanedithiol	SET transistor	1.2	-	3E6	[10]
9	Au_{55}/hexanedithiol	E_A, R(Landauer)	1.2	0.15	1.51E6	this work
10	Pd_{561}/DDE	E_A, R(Landauer)	1.2	0.05	2.01E5	this work
11	bulk Au/ADT	Ext. Hückel	1.7	-	4.3E7	[13]
12	3.7 nm Au/ADT	2D superlattice G(T→∞)	1.7	-	2.9E7	[11]
13	Au_{55}/DDE	E_A, R(Landauer)	1.9	0.17	4.00E7	this work
14	Au_{55}/BATA	E_A, R(Landauer)	2.1	0.23	1.95E8	this work
15	3.7 nm Au/ADI	2D superlattice G(T→∞)	2.2	-	4.30E10	[12]
16	3.7 nm Au/BPdT	2D superlattice G(T→∞)	2.2	-	9.00E10	[12]
17	3.7 nm Au/dodecanethiol	3D superlattice G(T→∞)	2.4	-	8.00E11	[12]
18	Au_{55}/POB	E_A, R(Landauer)	2.8	0.20	1.22E10	this work

DDE = 4,4'-diamino-1,2-diphenylethane, ADI = 1,4-di(4-isocyano-phenylethynyl)-2-bencene, ADT = dithiol derivative of ADI, BATA = bis{5-[(4-aminophenyl)-ethinyl]-3-methyl-thiene-2-yl}acetylene, BPDT = 4,4'-diphenyledithiol, POB = 1,4-bis{3-propeneacid[1-(8-N-pyridiniumbromide)octyleester)]bencene

CONCLUSIONS

A simple approach is introduced to derive the resistance of ligand and spacer molecules in nanoparticle arrangements from the activation energy of charge transport, obtained from integral temperature dependent conductance measurements. This approach makes use of the Landauer formula and it allows a first-order estimate of the resistance of single molecule, which is found to be in remarkable aggreement with the reference data, obtained by different methods. This leads to the conclusion that the charge transport through the organic molecules in volves tunneling rather than propagation. A more precise determination of the conducting properties of individual molecules requires more sophisticated experimental techniques, like local probe measuring techniques, but the likewise simple experimental and theoretical procedure described here might be useful for future work on structure/property-relations in nanoparticle arrangements, or in general, in nanocomposite materials.

ACKNOWLEDGEMENTS

The author would like to thank G. Schmid and D. Fenske for providing the cluster material for numerous measurements and V. Gasparian for many helpful discussions. Financial support by the DFG under contract SI 609/3-1 is gratefully acknowledged.

REFERENCES

1. G. Schön, and U. Simon, Colloid Polym. Sci. **273**, p. 101 (1995); idid. **273**, p. 202 (1995).

2. D. Fenske, and H. Krautscheid, Angew. Chem. Int. Ed. Engl. **29**, p. 1425 (1990)

3. U. Simon, F. Schüth, S. Schunk, X. Wang, and F. Liebau, Angew. Chem. Int. Ed. Engl. **36**, p. 1117 (1997)

4. K.K. Likharev, IBM J. Res. Develop. **32**, p.144 (1988)

5. G. Schmid (Ed.), *Clusters and Colloids*, VCH -Wiley, Germany, 1994

6. see e.g. U. Simon in P. Braunstein, L.A. Oro, and P.R. Raithby, (Eds.), *Metal Clusters in Chemistry*, Wiley-VCH, Germany, 1999, Vol. 3, pp. 1342-1363 and references therein

7. U. Simon, R. Flesch, H. Wiggers, G. Schön, and G. Schmid, J. Mater. Chem. **8**, p. 517 (1998); G. Schmid, L.F. Chi, Adv. Mater. **10**, p. 515 (1998)

8. S. Datta, *Electronic Transport in Mesoscopic Systems*, Cambridge University Press, Cambridge, 1995

9. M. Dorogi, J. Gomez, R. Osifchin, R. P. Andres, and R. Reifenberger, Phys. Rev. B **52**, p. 9071 (1995)

10. T. Sato, H. Ahmed, D. Brown, and B. F. H. Johnson, J. Appl. Phys. **82**, p. 969 (1997)

11. R.P. Andres, J.D. Bielefeld, J.I. Henderson, D.B. Janes, V.R. Kolagunta, C.P. Kubiak, W.J. Mahoney, and R.G. Osifchin, Science, **272**, p. 1323 (1996)

12. R.P. Andres, S. Datta, D.B. Janes, C.P. Kubiak, and R. Reifenberger, in N.S. Nalwa (Ed.), *Handbook of Nanotechnology and Nanostructured Materials*, Vol. 3, pp. 180-226, Academic Press, San Diego, 1999

13. M.P. Samanta, W. Tian, and S. Datta, Phys. Rev. B **53**, R7626 (1996)

14. U. Simon, and D. Fenske, unpublished results

SYNTHESIS, CHARACTERIZATION, AND UTILIZATION OF SINGLE CRYSTALLINE NANOPARTICLES OF SILVER

YADONG YIN, ZIYI ZHONG, BYRON GATES and YOUNAN XIA*
Department of Chemistry, University of Washington, Seattle, WA 98195-1700
xia@chem.washington.edu

ABSTRACT

This paper describes a procedure based on the Tollens' process for preparing crystalline nanoparticles of silver with well-controlled, uniform sizes. The starting reagents are similar to those commonly used for electroless deposition of silver and are commercially available from the Peacock Laboratories (Philadelphia, PA). Only under appropriate conditions, mixing of these reagents was able to generate stable dispersions of silver colloids, rather than thin films of silver coated on surfaces of objects immersed in the solution (including the inner surface of the container). We have demonstrated the capability and feasibility of this method by forming stable dispersions of highly monodispersed, single crystalline colloids of silver with dimensions in the range of 20-50 nm.

INTRODUCTION

Nanoparticles have been intensively investigated because of their unique electronic and optical properties that are substantially different from those of the bulk materials [1]. A lot of efforts have been, in particular, devoted to the synthesis and characterization of stable colloidal dispersions of silver, gold, and other noble metals [2]. A rich variety of methods have been developed in the past two decades for preparing these colloidal particles; notable examples include condensation from the vapor phase, chemical reduction or photoreduction in solutions or reverse micelles, chemical vapor deposition on solid substrates, and thermal decomposition in solvents or polymer matrixes [3]. The solutions of these colloidal particles usually display a very intense color, which can be attributed to the collective oscillation of conduction electrons induced by an electromagnetic field. It has been shown that the size, morphology, stability, and properties (chemical or physical) of these colloidal particles have a strong dependence on the specificity of the preparation method and the experimental conditions [4].

Here we would like to describe a simple and convenient method for preparing crystalline nanoparticles of silver with uniform sizes and well-defined morphologies. The fundamental reaction step of this approach is the Tollens' reaction:

$$Ag(NH_3)_2^+ (aq) + RCHO\ (aq) \longrightarrow Ag\ (s) + RCOO^-\ (aq)$$

Mat. Res. Soc. Symp. Proc. Vol. 581 © 2000 Materials Research Society

The final colloidal dispersions were stable in air, for at least 4-5 months. To demonstrate the versatility of this method, silver nanoparticles were also prepared (using a similar procedure) as coatings on mesoscale silica beads. Previous studies have indicated that such hybrid materials may find a broad range of uses in developing nonlinear optical devices, static electronic shielding coatings, and catalysts [5].

EXPERIMENTAL

A commercial kit (HE-300, Peacock Laboratories) that is commonly used for electroless deposition of silver films was employed to produce silver nanoparticles in the form of a stable aqueous dispersion. This kit consists of three separated solutions: (A) silver solution (silver nitrate), (B) activator solution (sodium hydroxide), and (C) reducer solution (sugar). Solution *A* contains silver ions that have been stabilized by coordinating to ammonia. The silver ions in solution *A* will become reducible by solution *C* only after they have been activated by reacting with solution *B*. Silver colloids usually appeared in the solution after several minutes to half an hour. The length of this period depends on the reaction conditions such as the environment (air versus nitrogen), the concentrations of the reagents, the ratio between different components, and the temperature. The reaction rate increased greatly when the concentrations of the reagents increased.

In our experiment, the reaction was performed under sonication (Branson 1210). Extreme high temperature and pressure are generated at the center of the collapsed bubbles that result from the acoustic cavitation process. These conditions often lead to enhanced chemical reactivities. The reaction performed under magnetic stirring was much slower than that carried out under sonication. Also, the yield of the product under magnetic stirring was much lower.

RESULTS

For a wide range of reaction conditions, the solution went from clear and colorless at the time of mixing, through light brown, brown, yellow-green, and finally to bright yellow. As an advantage of the present method, the appearance of the first color change did not occur until all the reagents had been mixed and sonicated for a certain period of time (usually, several minutes to half an hour). All reactants can, therefore, be mixed well before reacting to each other. As a result, the reaction will begin and proceed in a homogeneous and well-characterized environment, and the final product of silver nanoparticles will have a narrow size-distribution. We believe the yellow-green stage involves a mixture of both brown and bright yellow solutions. The transition from brown to bright yellow was relatively fast: usually within two minutes. Hyning and co-workers have also reported a similar color transition for their studies on the

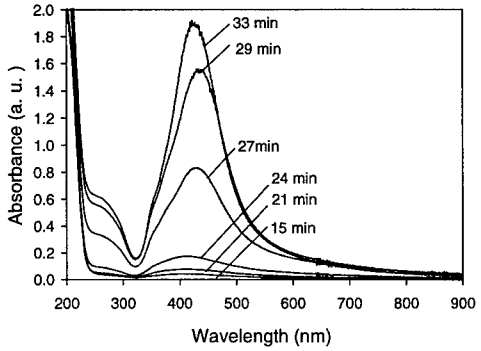


Fig. 1. UV-vis absorption spectra of a solution after the reactants have been mixed and sonicated at 27 °C for different periods of time.

formation mechanism and aggregation behavior of silver colloids prepared by reducing silver perchlorate with borohydride [6]. Unfortunately, the initial reaction of their system was so fast (less than 0. 5 s) that they were unable to completely resolve the transition from colorless to brown. Because the reactants were not evenly mixed, they also had difficulty in obtaining reproducible measurements.

The homogeneity in the initial mixture of the reactants also makes it possible to follow the formation and evolution of silver nanoparticles *in situ* using UV-vis absorption spectroscopy and transmission electron microscopy (TEM). Fig. 1 shows some typical UV-vis spectra of the solution after the reactants have been mixed and sonicated for different periods of time at 27 °C. In this case, the color of the solution started to change from colorless to light brown after the reaction has proceeded for ~15 min. Fig. 2A gives a TEM image of the sample taken from this solution. This TEM image indicates that only a very small amount of silver nanoparticles had formed up to this point, and the system was relatively unstable because the quasi-spherical particles exhibited a heterogeneous distribution in size. As the reaction proceeded (15-27 min), the brown color increased greatly in intensity, and the absorption also increased slightly at all wavelengths. The appearance of a brown color is largely due to the absorption in the long

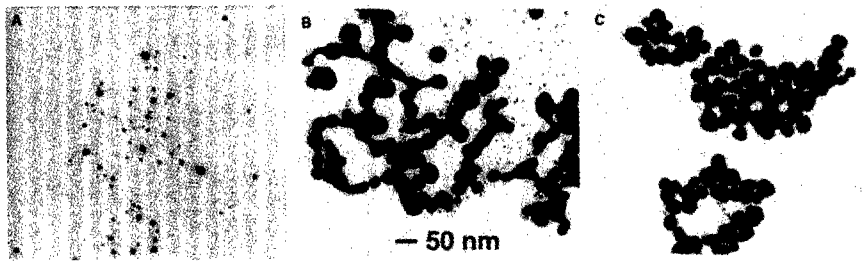


Fig. 2. TEM images of silver nanoparticles that were sampled from the solution after the reaction has proceeded at 27 °C for (A) 15 min, (B) 27 min, and (C) 33 min.

wavelength range (500 - 800 nm). A typical TEM image of the silver particles during this period is shown in Fig. 2B. Compared with Fig. 2A, it is clear that most of the silver particles had significantly increased in size and the morphology had changed from quasi-spherical to highly irregular shapes. At this stage, the silver nanoparticles largely existed as aggregates. After the reaction had proceeded for approximately 29 min, the intensity of the brown color reached a maximum. Although a few of the particles still remained aggregated, most of them were discrete particles with distinctive crystalline facets. As the reaction proceeded further, the intensity of the surface plasmon peak at ~410 nm increased significantly and the absorption at wavelengths longer than 400 nm also increased slightly. As a result, a green color started to appear in the solution, changing the solution to a yellow-green appearance. At ~33 min, the whole solution showed a clear, bright yellow color, with no further color changes. The intensity of the surface plasmon peak increased to its maximum value, and this value remained almost constant over time. The sharp plasmon peak indicates a very narrow distribution in the particle size. We also noted that the absorbance at wavelengths longer than 450 nm decreased slightly between 29-33 min, indicating a change of large particles into smaller ones in the solution. Again, our TEM observation is consistent with the UV-vis spectroscopic measurements. As shown in Fig. 2C, the sample consisted mainly of individual crystalline nanoparticles of silver. No aggregation was observed. Based on Figs.1 and 2, we can conclude that the optical properties of the solution was dominated by the presence of silver aggregates that shrank by more than one order of magnitude in size during the course of the reaction. A similar observation for the formation of silver, or gold colloids has also been reported by Zukoski et al. [6,7]. According to their proposed mechanism, the nanoparticles were formed first in the solution and subsequently aggregated into

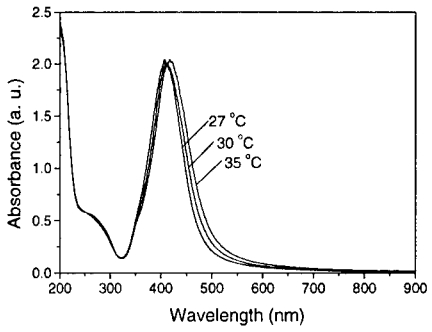


Fig. 3. UV-vis absorption spectra of colloidal solutions of silver nanoparticles that were obtained as the final products when the reaction was carried out at different temperatures.

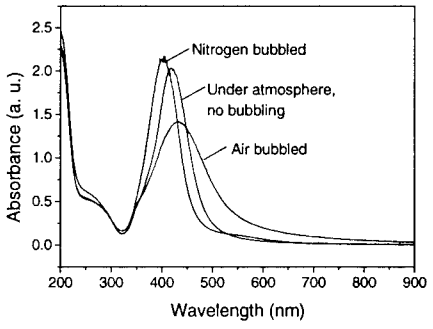


Fig.4. UV-vis absorption spectra of colloidal solutions of silver nanoparticles that were prepared under different reaction environments.

large particles due to the electrostatic interactions. At the end of the reaction, a change in the electrostatic condition led to a breakdown (similar to Ostawald rupture of a liquid jet) and redispersion of the nanoparticles.

We also found that the formation and evolution of silver nanoparticles was very sensitive to the temperature and the reaction atmosphere. Fig. 3 shows UV-vis absorption spectra of colloidal solution of silver nanoparticles prepared at three different temperatures. As temperature increased, the surface plasmon peak red shifted gradually. TEM observations show that all of the products are crystalline, discrete particles of silver with a similar morphology. The particle size increased from ~20, to ~30 to ~40 nm when the temperature was changed from 27 to 30 to 35 ^{o}C, respectively. We believe that the frequency of collision between small particles increases as the temperature increases, and thus leads to the formation of larger particles. Fig. 4 shows that the surface plasmon peaks shifted to longer wavelengths when the reaction environment became more oxidative. This result indicates the formation of larger silver particles under a more oxidative environment.

When silica beads were added into the mixture of the silver solutions, the silver nanoparticles were formed as decorative coatings on the surfaces of silica beads, rather than as a dispersion in water. The silica beads coated with silver particles were centrifuged and washed three times with deionized water. Fig. 5 is a typical TEM image of 100 nm silica beads that have been coated with silver nanoparticles. It is clearly seen that many silver nanoparticles were homogeneously immobilized on the surface of each silica bead. The size of silver nanoparticles and their dispersion density on the surface of a silica bead could be easily controlled by changing the concentration of the silver solutions.

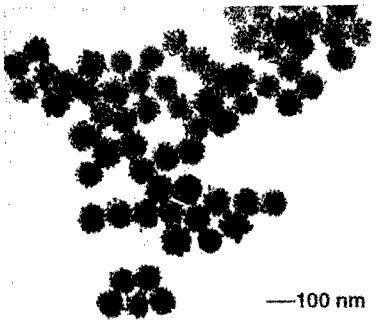


Fig.5 The TEM image of 100 nm silica beads that have been decorated with silver nanoparticles of ~20 nm in diameter.

CONCLUSIONS

In summary, we have demonstrated a simple, effective, and reproducible method for preparing crystalline silver nanoparticles with well-controlled sizes in the range of 20-50 nm.

These silver particles could be easily prepared either as stable aqueous dispersions or as decorative coatings on mesoscale silica beads. Our UV-vis and TEM measurements indicate that the formation of these silver nanoparticles involves at least three distinctive stages: (1) nucleation, (2) growth and aggregation, and (3) Ostawald rupture of aggregates into discrete particles with a tight size-distribution. We believe this method can be easily scaled up for the production of large volumes of silver nanoparticle since the reactants can be thoroughly mixed before precipitation takes place.

ACKNOWLEDGEMENTS

This work was supported in part by a New Faculty Award from the Dreyfus Foundation, a subcontract from the AFOSR MURI Center at the University of Southern California, and start-up funds from the UW. We thank Dr. Sagar Vankateswaren of Peacock Laboratories for providing the silvering solutions as a free gift.

REFERENCES

1. G. A. Ozin, Adv. Mater. **4**, 612 (1992).
2. See, for example, (a) U. Kreibig, M. Vollmer, Optical Properties of Metal Clusters, Springer, Berlin, 1995. (b) S. Link and M. A. El-Sayed, J. Phys. Chem. B **103**, 4212 (1999). (c) A. Henglein, J. Phys. Chem. **97**, 5457 (1993).
3. Recent studies: (a) C. Petit, P. Lixon, M. P. Pileni, J. Phys. Chem. **97,** 12974 (1993). (b) A. Henglein, Chem. Mater. **10**, 444 (1998). (c) M. Ji, X. Chen, C. M. Wai and J. L. Fulton, J. Am. Chem. Soc., **121**, 2631 (1999). (d) N. Yanagihara, K. Uchida, M. Wakabayashi, Y. Uetake, and T. Hara, Langmuir, **15**, 3038 (1999). (e) S. Kapoor, Langmuir, **14**, 1021 (1998).
4. See, for example, (a) C. D. Sanguesa, R. H. Urbina, and M. Figlar, J. Solid State Chemistry, **100**, 272 (1992). (b) I. Pastoriza-Santos and L. M. Liz-Marzan, Langmuir, **15**, 948 (1999). (c) D. Burshtain, L. Zeiri, and S. Efrima, Langmuir, **15**, 3050 (1999).
5. See, for example, (a) Z. Qi and P. G. Pickup, Chem. Comm. 1008, (1997). (b) C. W. Chen, M. Q. Chen, T. Serizawa, and M. Akashi, Adv. Mater. **10**, 1122 (1998).
6. D. L. V. Hyning and C. F. Zukoski, Langmuir, **14**, 7034 (1998).
7. M. K. Chow and C. F. Zukoski, J. Colloid Interface Sci. **165**, 97 (1994).

STRUCTURE AND STABILITY OF NANO-SCALE MELT SPUN Mg-Ca-Zn ALLOYS

P.M.JARDIM*, I.G. SOLÓRZANO*,J.B. VANDER SANDE**, B.S.YOU***,W.W.PARK***
*Department of Material Science and Metallurgy, PUC-Rio, C.P.38008 – Gávea, 22452, Brasil
**Department of Material Science and Engineering – MIT, Cambridge, MA 02139, USA
***Korea Institute of Machinery & Materials, 66, Sangnam-dong, Changwon, Kyungnam, Korea

ABSTRACT

Alloys, with six different compositions in the system Mg-Ca-Zn were produced by melt spinning. The aging behavior of alloys was investigated by measuring the changes in microhardness after isochronal aging and the microstructure was analyzed by means of Transmission Electron Microscopy(TEM), Energy Dispersive X-ray Spectrometry (EDS), Scanning Transmission Electron Microscopy (STEM) and Scanning Electron Microscopy (SEM). All six compositions in the as-solidified condition show a difference in microstructure between the wheel contact side (zone A) and the free surface side (zone B) as a result of the differences in the solidification rate across the ribbons. One of the alloys was chosen to be more deeply investigated in this work as it exhibited grain boundary films and presented the highest peak hardness among the low Ca alloys. The comparison between the two microstructural zones in this alloy can aid in understanding of the phase transformation steps during cooling with a model which is proposed here.

INTRODUCTION

For over 50 years considerable attention has been given to magnesium-based alloys, primarily from the physical metallurgy point of view. The driving force for this effort has been the potential applications of Mg alloys in light weight structural components, namely in the automotive and aircraft industries. However, the processing of these alloys through conventional casting technologies have not succeeded in reaching a high level of formability and ductility while preserving high specific strength. The combination of ultra-rapid solidification and consolidation techniques has become a promising approach to overcome these limitations[1,2]. Ultra-rapid solidification technologies are opening a wide field for fundamental studies, since different sets of thermodynamic (stability), kinetic and structural conditions are established to control a variety of solid-state phase transformations and resulting properties[3].

EXPERIMENTAL PROCEDURE

Alloys with six different compositions in the system Mg-Ca-Zn (Table1) in the form of ribbons approximately 70μm thick and 3mm wide were produced by melt spinning under argon using a Cu-Be wheel with a speed of 30-50m/s. The alloys thermal behavior was investigated by measuring the changes in microhardness after isochronal aging for 1 hour at temperatures ranging from 50 to 400 °C. The alloys as solidified and MCZ-2 heat treated at 200°C for 1 hour (corresponding to its hardness peak) were analyzed by means of Transmission Electron Microscopy(TEM), Energy Dispersive X-ray Spectrometry (EDS) and Scanning Transmission Electron Microscopy (STEM). Cross-section SEM samples were also prepared in order to compare the microstructure variation through the thickness of the ribbons. These samples were polished and etched with a solution of 2 vol. % nitric acid + water. For TEM studies, thin foils

Mat. Res. Soc. Symp. Proc. Vol. 581 © 2000 Materials Research Society

were produced by dimpling and ion-milling techniques and the microscope was operated under diffraction contrast mode.

Table 1: Sample compositions in wt%

	MCZ-1	MCZ-2	MCZ-3	MCZ-4	MCZ-5	MCZ-6
Mg	95.5	92.5	88.5	92	89	85
Ca	1.5	1.5	1.5	5.0	5.0	5.0
Zn	3	6	10	3	6	10

RESULTS

All six compositions in the as-solidified condition have shown a difference in microstructure between the wheel contact side to the free surface side as a result of the differences in the solidification rate across the ribbons. This variation can be appreciated in the cross-section SEM micrographs in figure 1, where the presence of two microstructural zones, zone A (near the wheel contact side) and zone B (near the free surface) can be seen. This can also be seen comparing the microstructures in the TEM micrographs of MCZ-2 zone A and zone B in figures 2 and 3, respectively.

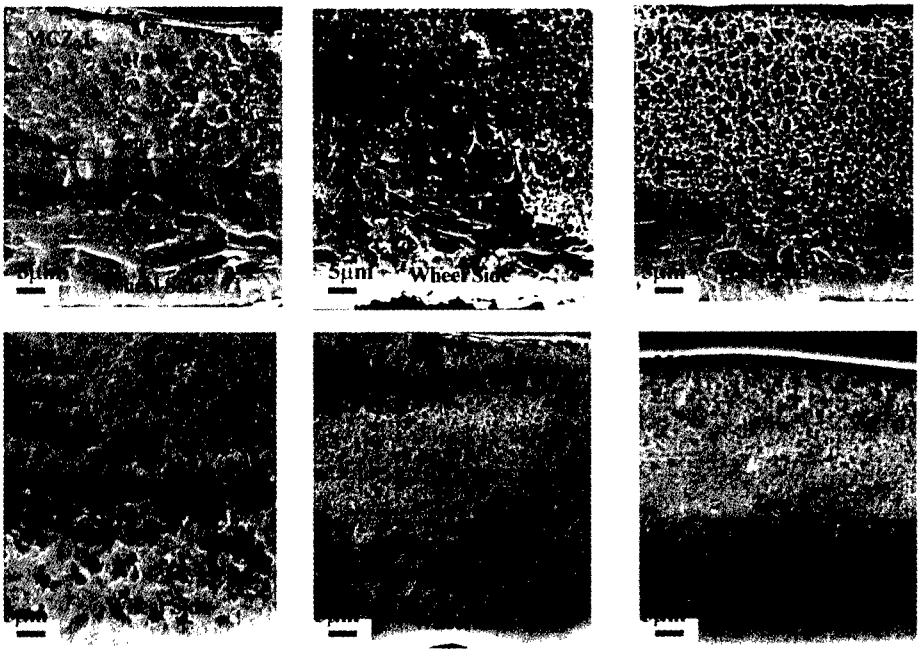


Figure 1: Cross-section SEM micrographs

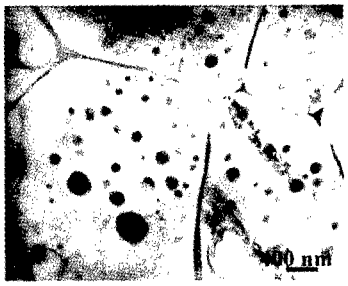


Figure 2: TEM micrograph of MCZ-2 zone B



Figure 3: TEM micrograph of MCZ-2 zone B



Figure 4: TEM micrograph of MCZ-4 zone B as solidified

An important feature observed in zone B of the as solidified alloys was that the three alloys containing 1.5wt% Ca consistently exhibited spherical matrix precipitates as well as elongated precipitates at the grain boundaries (grain boundary films) while the other three alloys (5wt% Ca) did not display the grain boundary films. This can be seen in TEM micrographs of zone B of samples MCZ-2 and MCZ-4, from figures 2 and 4,respectively.

Sample MCZ-5 showed the highest peak hardness of 180Hv (Vickers Hardness) when aged at 200°C for 1 hour as can be seen in figure 5a and, among the low Ca alloys, MCZ-2 showed the highest peak hardness of 120Hv when aged at 200°C for 1 hour (figure 5b).

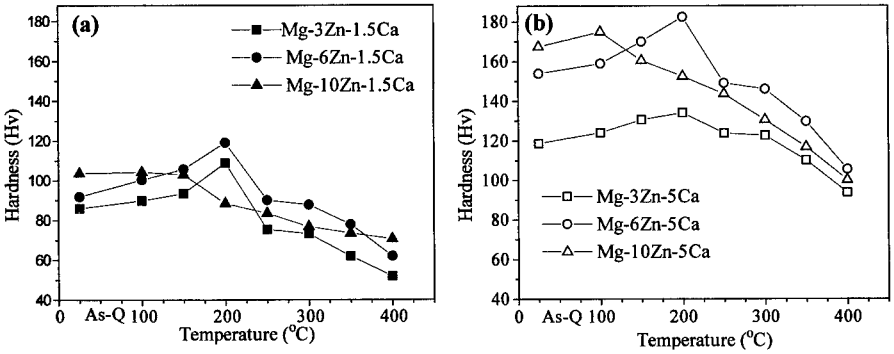


Figure 5a and 5b:Hardness change of Mg-xZn-1.5Ca alloys(a) and Mg-xZn-5Ca alloys (b) after heat treatment for 1 hour at various temperatures

As MCZ-2 exhibited grain boundary films and presented the highest peak hardness among the low Ca alloys it was chosen to be more thoroughly investigated in this work. Zone B of this alloy as solidified was analyzed by STEM and EDS in order to identify the precipitate compositions. In the X-ray maps shown in figure 6 it can be seen that both the grain boundary and matrix precipitates are ternary compounds and appear to have the same composition. After quantitative analysis of the EDS spectrum of the grain boundary precipitate shown in figure 7, including absorption corrections, the composition of this precipitate was found to be 56 at.% Mg, 14at.% Ca and 30 at.% Zn ($CaMg_4Zn_2$). The closest compound found in the literature was $Ca_2Mg_6Zn_3$ [4], although, no crystallographic data is available for this compound.

Zone B of this alloy was also investigated by TEM after heat treatment at 200°C for 1 hour, which corresponds to its hardness peak. These samples exhibited cuboidal precipitates as well as spherical precipitates but was devoid of grain boundary films. This can be seen in the TEM micrographs in figures 8 and 9.

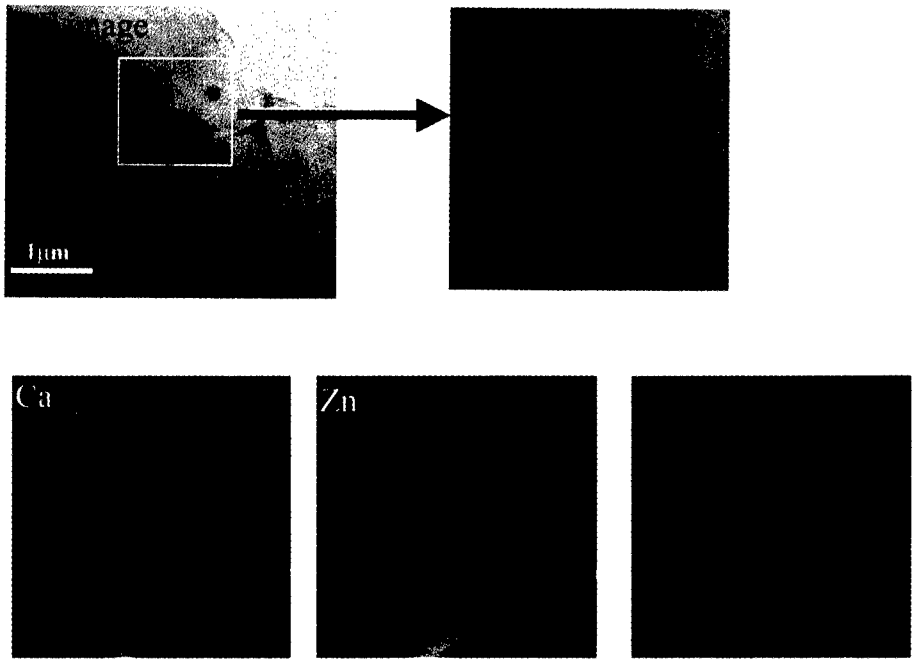


Figure 6: STEM images and X-Ray maps of MCZ-2 zone B as solidified

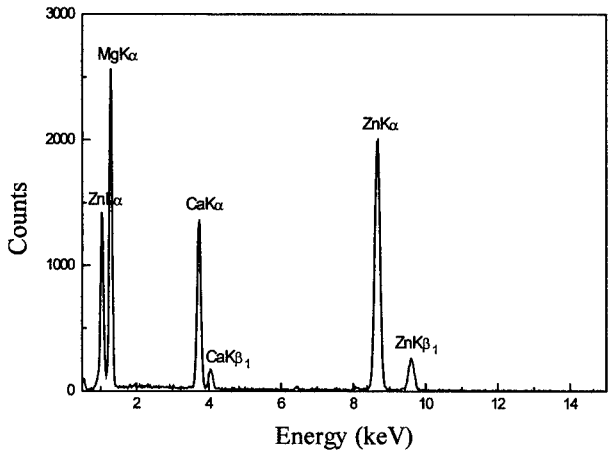
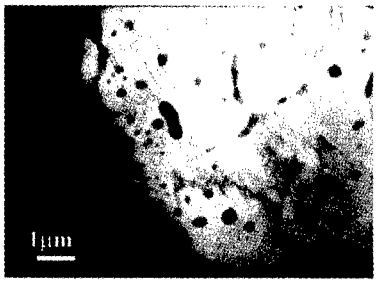


Figure 7: EDS spectrum of the grain boundary precipitate in MCZ-2 zone B as solidified



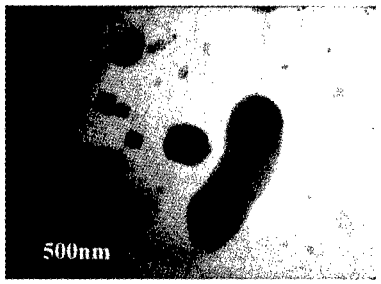


Figure 8 and 9: TEM micrograph of MCZ-2 zone B heat treated at 200°C for 1 hour

DISCUSSION

The cooling rate across the ribbons, during melt spinning, is not homogeneous resulting in two microstructural zones. The zone near the wheel contact side (zone A) is cooled more rapidly than the zone near the free surface (zone B) which is usually the thicker zone. The comparison between these two microstructures can aid in understanding of the phase transformations during cooling. In MCZ-2 zone A we can see precipitates in the grain boundaries only at the triple points (no grain boundary films), suggesting that these precipitates first appear at the higher energy sites (triple points and grain boundaries) and then, if there is sufficient time and temperature (slower cooling rate as in zone B), the film can be formed through precipitate coarsening. All the steps proposed for phase transformations during cooling can be seen in figure 10.

The heat treated MCZ-2 samples showed "cuboidal" precipitates as well as spherical precipitates. Although the actual composition was not obtained, according to EDS analysis the cuboidal precipitates were also ternary compounds. As the cuboidal precipitates were always the smallest ones and their faceted interfaces suggests they are coherent or semi-coherent with the matrix, it is likely that these precipitates are the same composition as the spherical precipitates but at an early stage of growth. During growth the particles become incoherent and spherical to minimize strain and interfacial energy.

Further investigation is currently in progress in order to determine the precipitates' crystal structure as no crystallographic data was found for the precipitate composition obtained.

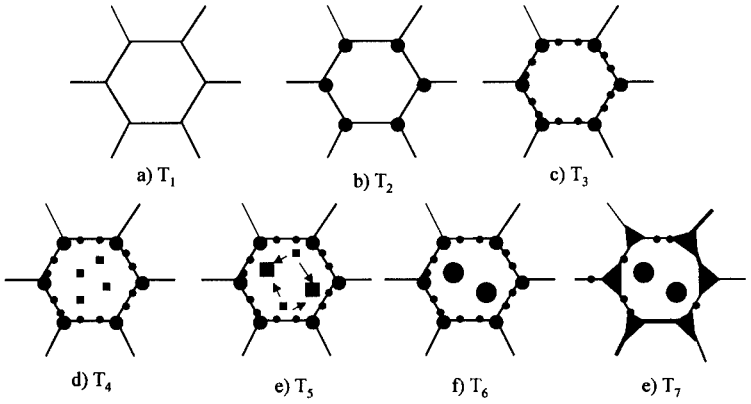


Figure 10: Steps in phase transformation during cooling, where $T_1>T_2>T_3>T_4>T_5>T_6$.
a)supersaturated Mg solid solution; b)precipitation at the higher energy sites (triple points); c)precipitation at the second higher energy sites (grain boundaries); d)precipitation of cuboidal coherent precipitates in the matrix; e)coarsening of the matrix precipitates; f) cuboidal precipitates become spherical and incoherent; e)coarsening of the grain boundary precipitates through grain boundary diffusion.

ACKNOWLEDGMENTS

The authors acknowledge the support of the Korea Institute of Machinery & Materials, access to the experimental facilities within the CMSE at MIT and CAPES (Brazil).

REFERENCES

1. P.Vostrý, I.Stulíková, B.Smola, W.Riehemann and B.L. Mordike, Mater. Sci. Eng., A137,87 (1991)
2. S. H. Kim, D.H. Kim, N. J. Kim, Mater. Sci. Eng., A226-228, 1030 (1997)
3. A.P.Tsai, T. Kamiyama, Y.Kawamura, AInoue and T.Masumoto, Acta Mater.Vol. 45, No.4, 1477 (1997)
4. JCPDS card number 12-0266

STRUCTURE AND MAGNETIC PROPERTY CORRELATION IN NANOCRYSTALLINE $SmFe_9$

C. DJEGA-MARIADASSOU and L. BESSAIS
CNRS, LCMTR UPR 209, 94320 Thiais, France. bessais@glvt-cnrs.fr

ABSTRACT

Sm_xFe_{100-x} samples with $x = 7.6$, 10.5 and 12.5 were prepared by high energy ball-milling and subsequent annealing at various temperature T_a, $600 < T_a < 1200$ °C. Rietveld analysis coupled to Curie temperature measurements and Mössbauer spectroscopy revealed for $600 < T_a < 900$ °C an hexagonal phase *P6/mmm* derived from $TbCu_7$ with stoichiometry $SmFe_9$. At $T_a > 900$ °C, the ordered $R\bar{3}m$ Sm_2Fe_{17} structure is obtained so that $SmFe_9$ appears as the out-of-equilibrium precursor of Sm_2Fe_{17}. The Curie temperature and hyperfine field augmentation found for $SmFe_9$ results from an increase of the interatomic distance in the Fe-Fe dumbbell, responsible for a reduction of the negative exchange interaction.

INTRODUCTION

Since its discovery by Coey [1], the interstitial $R\bar{3}m$ $Sm_2Fe_{17}N_x$ compound has been extensively studied owing to its high performance permanent magnetic properties which compete nowadays with $Nd_2Fe_{14}B$. However, its precursor Sm_2Fe_{17} appears to be, still, the subject of discrepancies. Out-of-equilibrium elaboration techniques like melt-spinning, thin layer sputtering, and high energy ball-milling lead after annealing, to a nanocrystalline hexagonal phase of $TbCu_7$ type *P6/mmm*. This is derived from the RT_5 structure (R = rare earth, T = Transition metal) by a random substitution of R atoms by T-T dumbbells. When annealing is performed at high temperature, close to 1000 °C, the binary ordered Sm_2Fe_{17} phase is observed. Wei et al [2] have found for mechanically alloyed $TbCu_7$ type Sm_xFe_{1-x} compounds (x=0.11 to 0. 14) Curie temperature in the range 138 °C to 150 °C, but these values were assigned to Sm_2Fe_{17} [3-7].

The aim of this work is to correlate the Curie temperature to the structure change related respectively to the *P6/mmm* and $R\bar{3}m$ phases. This paper will be first devoted to the structure analysis of both phases by means of the Rietveld method. Curie temperature measurements coupled to Mössbauer spectroscopy experiments will be used, afterwards, to clarify the structure evolution .

EXPERIMENT

Three samples of Sm_xFe_{100-x} of nominal atomic composition 7.6 (A), 10.5 (B) and 12.5 (C) were obtained by ball-milling 40 mesh Sm and Fe powders (99.9 % pure), under Ar atmosphere for 5 hours. The samples were annealed under 10^{-6} torr vacuum at temperature between 600 and 1200 °C for 30mn. Analysis by atomic emission spectroscopy was used to check the overall sample composition. X-ray diffraction was carried out with CuKα radiation on Brucker diffractometer. The data was fitted with the Rietveld method by using the FULLPROF computer code with the 'goodness-of-fit' indicator Rb [8] expressed as :

$$Rb = \sum_k | I_k(o) - I_k(c) | / \sum_k I_k(o)$$

Mat. Res. Soc. Symp. Proc. Vol. 581 © 2000 Materials Research Society

where I_k (o) is the observed Bragg intensity and I_k(c) is the calculated one.

The Curie temperature T_C were measured on a differential sample magnetometer Manics, in a field of 1000 Oe. Mössbauer spectra at room temperature were collected with a conventional constant acceleration 512 channel spectrometer with α Fe line-width of 25mm/s and Fe sample concentration of 12mg/cm^2 .The spectra were least-square-fitted in the assumption of Lorentzian lines.

RESULTS

Structure studies

The x-ray diagrams of the as-milled samples show a diffuse maximum at low angle assigned to an amorphous Sm based phase and nanocrystalline Fe with diffraction domain size around 7 nm. The diagrams of the three samples A, B, C annealed at temperature between 600 and 1200 °C, can be classified into three types (Fig.1). In the range 600 °C < Ta < 820 °C , the

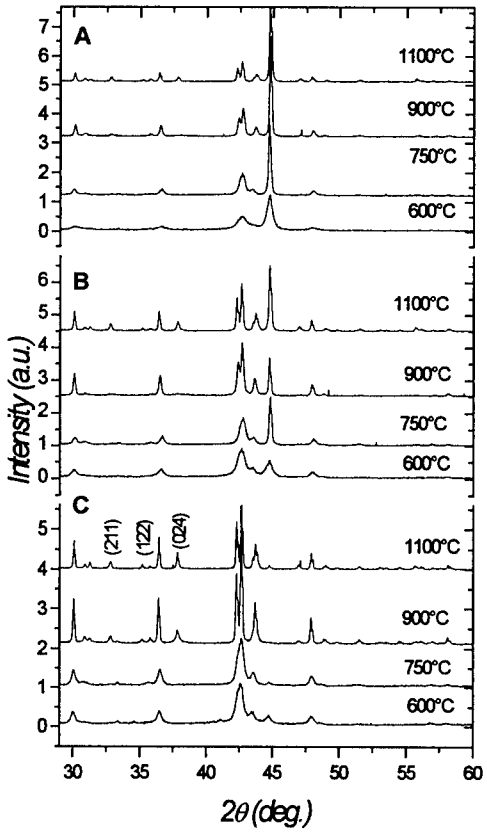


Fig. 1. X-ray diagrams for samples A, B, C annealed at various temperatures. (hkl) indices are related to the ordered Sm_2Fe_{17} phase

hexagonal phase P6/mmm derived from $TbCu_7$ is observed as the main phase. Above 820°C up to 1000 °C, the emergence of extra-lines (104), (211), (122), (024) attributed to the superlattice $R\bar{3}m$ can be observed. Their intensity is governed by the Sm content. From 1000°C up to 1200 °C, the $R\bar{3}m$ phase is unambiguously obtained. It must be pointed out that the broadening of the diffraction lines attests for the nanocrystalline state preserved up to 1200°C (100nm).The amount of Fe decreases from A to C as the nominal Sm content increases but, it always coexists with small quantities of Sm_2O_3 or SmO-N and the hexagonal phase composition cannot be deduced from the nature of the coexisting phases, like in binary system equilibrium diagrams.

The problem concerning the $TbCu_7$ hexagonal phase is effectively its stoichiometry domain $R_xT_{(1-x)}$. The structure is derived from RT_5, it might lay theoretically from x=0.16 (RT_5) down to x=0.07 prelude to the 1:12 structure. Due to the nanoscale of the hexagonal phases preventing from a pertinent x-ray dispersive analysis, the phase composition had to be deduced from a Rietveld refinement.

We have explained the disordered $TbCu_7$ type structure according to the general model developed previously by Givord [9]. Let be (1-s) the occupation rate of Sm (site 1a in 0,0,0 position), with decreasing Sm content, 2s Fe in 2e site (site of Fe dumbbells in 0,0,Z position) will be distributed on both sides of the empty Sm position. It results that only 2(1-3s) atoms remain located in the 2c special position 1/3,2/3,0, and due to the presence of the 2e Fe dumbbells, 6s Fe are shifted towards the c axis in the more general 6l position X,2X,0, (X<1/3). The 3g site 1/2,0,1/2, is totally occupied by the Fe atoms. One must underline that the $TbCu_7$ model structure (x=0.125) proposes only three Fe positions 2e, 2c and 3g ignoring the steric effect of the Fe dumbbells [10].

The Rietveld refinement of the hexagonal phase was consequently carried out with the usual parameters, a and c cell parameters, X and Z position parameters, Debye-Waller factor, strain rate U, diffraction domain size D and the s occupancy parameter. Figure 2 shows such a Rietveld fit for sample C annealed at 750 °C.

The characteristics of the hexagonal phase are reported as an example in table I for sample B annealed at 600°C ,750°C and 900°C. They reflect the parameter values obtained for other samples and all the fits converge to a Samarium content x equal to 0.1011 ±0.0017 in agreement with the stoichiometry of $SmFe_9$.

The refined parameter of the $R\bar{3}m$ phase obtained at Ta > 1000°C are a=0.4941√3=0.8559nm and c=3x0.4147=1.2443nm in agreement with [4] (Fig. 3.).These values

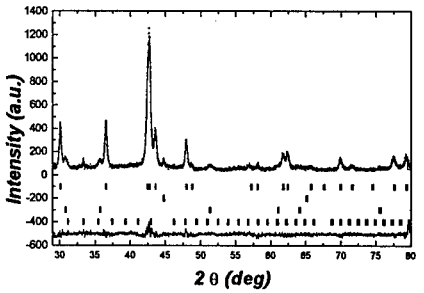


Fig. 2. Rietveld analysis for sample C annealed at 750 °C. The set of ticks refers respectively to $SmFe_9$, α-Fe, SmO-N, Sm_2O_3.

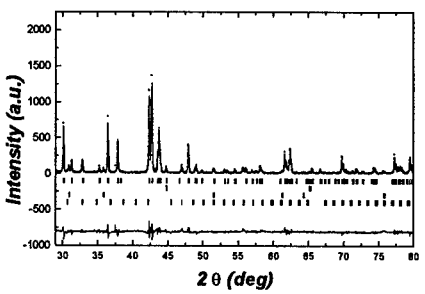


Fig. 3. Sample C annealed at 1100 °C

corroborate the variation observed for the hexagonal phase and attest for the replacement of Fe dumbbell by Sm up to the stoichiometry 0.105 (2:17).

Table I. Structure parameters deduced from Rietveld fit for sample B.

Ta (°C)	*a* (nm)	*c (nm)*	*c/a*	X	Z	*X*	% strain	D (nm)
600	0.4919 (3)	0.4162 (3)	0.8461	0.285	0.294	10.2 (2)	0.73	14
750	0.4925 (3)	0.4160 (3)	0.8446	0.286	0.285	10.0 (2)	0.48	37
900	0.4932 (3)	0.4152 (3)	0.8418	0.287	0.284	10.1 (1)	0.34	45

Magnetic properties

In table II are reported the Curie temperatures T_C of samples B and C annealed at 600 °C, 820 °C and 1000 °C. The 1:9 phase shows a higher Curie temperature than the 2:17 one. It varies from 205°C down to 144°C with decreasing axial *c/a* ratio and increasing annealing temperature (table II). The T_C variation reflects the evolution of the Sm content from 1:9 to 2:17 but, for the same Ta, the samples A , B ,C exhibit the same T_C within the measurement accuracy. This points out that for a given temperature, the 1/9 phase stoichiometry remains constant. However, for sample C annealed at 900°C, the T_C value is the same as those measured at 1000°C. In this particular case, the $R\bar{3}m$ superstructure lines are already observed (see figure1).

Table II. Curie temperatures relative to samples A, B, C, annealed at different temperature Ta.

Sample	Ta (°C)				
	600	750	820	900	1000
A	206	174	173	162	143
B	205	173	174	160	143
C	207	171	174	143	144

Mössbauer spectroscopy was performed according to the various measured T_C. The spectra relative to sample C annealed at 600°C, 750°C, and 100°C are presented on figure 4 ,their respective T_C being 207°C ,171°C and 144°C.The spectrum profiles are similar but the mean hyperfine fields <H> decrease with decreasing T_C from 232 to 222 and 219 kOe. The Sm_2Fe_{17} Mössbauer spectra were fitted with seven sextets according to the model yet presented for the $R\bar{3}m$ structure[11-14]. For the 1:9 samples, five broadened sextets gave a good agreement with the experimental spectra, consistent with the relative Fe population 2*e*, 3*g* , 6*l*. In the last step of the refinement , the closer isomer shift values were averaged and fixed, the other parameters were liberated. The highest field sextet is unambiguously assigned to the dumbbell 2*e* family in perfect agreement with the expected population value. The remaining sextets are assigned to the 3*g* and 6*l* sites but the accuracy of their respective contribution is spoiled due to the vicinity of the hyperfine parameters.

Table III Hyperfine parameters of sample C annealed at 600 °C and 750 °C. H_{hf} hyperfine field, δ isomer shift and S relative area.

Sample C annealed at	Hyperfine parameters	2*e*	3*g*	6*l*
600 °C	δ (mm/s)	0.045	-0.079	-0.172
	H_{hf} (kOe)	281	225	231
	S (%)	11.8	58.2	30.0
750 °C	δ (mm/s)	0.057	-0.078	-0.167
	H_{hf} (kOe)	272	210	221
	S (%)	11.8	50.1	38.1

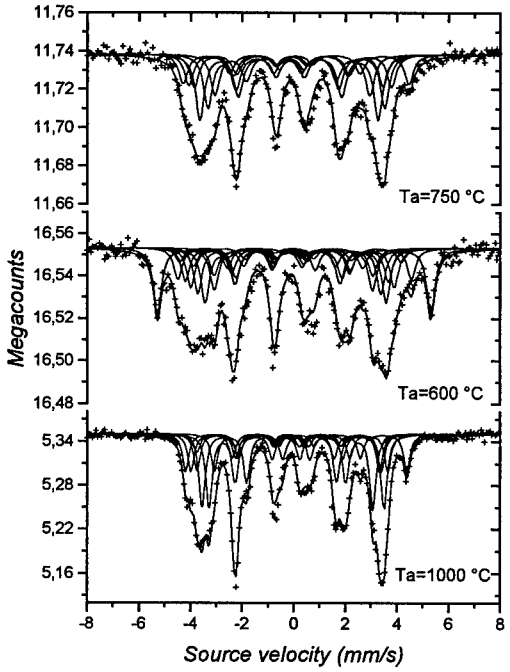


Fig. 4. Mössbauer spectra for sample C annealed at different temperature.

It was shown in Sm_2Fe_{17} $R\bar{3}m$ compound that the exchange integral between Fe atoms in the Fe-Fe dumbbells is negative [14]. The explanation for the T_C and hyperfine field dumbbell increases in the disordered 1:9 phase is brought by the increase of the dumbbell pair intra-distances which reduces the negative interaction between Fe atoms with regard to the $R\bar{3}m$ ordered Sm_2Fe_{17} phase.

Table IV Hyperfine parameters of sample C annealed at 1150 °C.

	6c	9d	9d	18f	18f	18h	18h
δ (mm/s)	0.103	-0.179	-0.179	-0.098	-0.098	-0.065	-0.065
H_{hf} (kOe)	266	219	221	235	211	206	200
S (%)	11.7	5.9	11.6	11.8	23.9	23.4	11.7

Conclusion

Mechanical milling and subsequent annealing at 600 °C <T<900 °C lead to the disordered *P6/mmm* hexagonal nanocrystalline phase of 1:9 stoichiometry as deduced from the Rietveld fits. This phase is the precursor of the ordered $R\bar{3}m$ Sm_2Fe_{17} compound.

The unit cell parameters, a and c of the hexagonal phase vary as a function of the annealing temperature, implying an increase of the Fe-Fe atom distance into the dumbbell pairs with regard to the ordered $R\bar{3}m$ phase.

The increase of the hexagonal disordered phase Curie temperature is associated to an increase of the dumbbell hyperfine field.

The T_C and hyperfine field dumbbell increase in the disordered 1:9 phase results from a reduction of the negative interaction between Fe atoms in the Fe-Fe dumbbell sites.

REFERENCES

1. J.M.D. Coey, H. Sun, Y. Otani and D.P.F. Hurley, J. Magn. Magn. Mater. **98,** 76 (1991).

2. L. Wei, W. Qun, X.K. Sun, Z. Xing-guo, Z. Tong, Z. Zhi-dong and Y.C. Chuang J. Magn. Magn. Mater. **131**, 413 (1994).

3. S.A. Sinan, D.S. Edgley and I.R. Harris, J. Alloy Compounds **226,** 170 (1995).

4. J. Hu, B. Hofmann, T. Dragon, R. Reisser, L. Sun, B. Hu, L. Cao, B. Shen and H. Kronmmüller, Phys. Stat. Sol. (a) **148,** 275 (1995).

5. X.C. Kou, R. Grössinger, T.H. Jacobs and K.H.J. Buschow, J. Magn. Magn. Mater **88,** 1 (1990).

6. K. Machida, E.Y. Yamamoto and G.Y. Adachi, J. Alloy Compounds **193,** 271 (1993).

7. K. Schnitzke, L. Schultz, J. Wecker and M. Katter, App. Phys. lett. **57,** 2853 (1990).

8. J. Rodriguez-Carvajal, Physica B **192**, 55 (1993).

9. D. Givord, J. Laforest, J. Schweizer and F. Tasset, J. Appl. Phys. **50**, 2008 (1979).

10. P. Villars and L.D. Calvert, *Pearson's Handbook of Crystallographic data for Intermetallic Phases* 2nd ed. (ASM international, 1991) p. 3012.

11. B.P. Hu, H. S. Li, H. Sun and J.M.D. Coey, J. Phys.: Condens. Matt. **3**, 3983 (1991).

12. R.J. Zhou, M. Rosenberg, M. Katter and L. Schultz, J. Magn. Magn. Mater. **118**, 110 (1993).

13. G.J. Long, S. Mishra, O.A. Pringle, F. Grandjean and K. H. J. Buschow, J. Appl. Phys. **75**, 5994 (1994).

14. Z.W. Li and A.H. Morrish, Phys. Rev. B **55**, 3670 (1997).

GLASS FORMATION AND NANOSTRUCTURE DEVELOPMENT IN AL-BASED ALLOYS

R. I. WU*, G. WILDE**, J. H. PEREPEZKO*
*Department of Materials Science and Engineering,
University of Wisconsin-Madison, WI 53706, USA, wur@cae.wisc.edu
**Forschungszentrum Karlsruhe INT, 76021 Kalsruhe, Germany

ABSTRACT

Al-Sm and Al-Y-Fe alloys with a high number density of nanocrystalline fcc-Al homogeneously dispersed within the amorphous matrix have been synthesized by devitrifying the precursor metallic glasses produced by rapid solidification. The kinetics of metallic glass formation and the development of the nanostructure during devitrification are discussed in terms of the rate limiting mechanism. The glass transition temperature of the two metallic glasses has been successfully assessed with the application of the modulated-temperature differential scanning calorimetry (DDSC). In addition, the formation of quenched-in nuclei was investigated by a comparison study on the cold-rolled and melt-spun $Al_{92}Sm_8$ amorphous samples. Furthermore, the enhancement of the particle density of the fcc-Al nanocrystals in the amorphous matrix after devitrification has been demonstrated by the incorporation of nanosize Pb particles.

INTRODUCTION

Al-based amorphous alloys with microstructures containing finely dispersed nanocrystalline Al embedded within an amorphous matrix have been reported to display attractive mechanical properties such as ultrahigh tensile strength and improved corrosion resistance [1,2]. Amorphous materials can be synthesized by rapid solidification processing [1-4], or by mechanical intermixing [5, 6]. The appearance of the characteristic endothermic response signal in the differential scanning calorimetry (DSC) during heating is generally considered as the evidence of the existence of a glassy phase [7, 8]. The assessment of the glass transition temperature is important in providing a fundamental basis for kinetic analysis in metallic glasses. However, the characteristic glass transition signal in some Al-based melt-spun ribbons is often masked by the exothermic signal from the primary crystallization reaction during continuous heating in DSC. In the present work it is demonstrated that modulated-temperature calorimetry (DDSC) has the capability to separate the signal of reversible reaction from that of irreversible reaction and enable the assessment of the glass transition temperature of these amorphous alloys.

Nanostructured materials can be produced from alloy melts either directly by choosing a cooling path that intersects the tip of the transformation curve during rapid solidification or by devitrifying the precursor amorphous phase prepared by rapid solidification processing. Devitrification of amorphous alloys allows for the formation of a high number density of nanocrystals ($> 10^{21}$ m^{-3}) and offers better control in synthesizing nanostructured materials [1-4, 9,10]. The capability to control the nucleation density is the key issue in the controlled synthesis of nanocrystalline Al microstructures [11]. An approach to enhance the nucleation density for the nanocrystals in the Al-based amorphous alloys has been developed by incorporating insoluble elements.

Mat. Res. Soc. Symp. Proc. Vol. 581 © 2000 Materials Research Society

EXPERIMENTAL DETAILS

Bulk alloy ingots with nominal compositions of Al-7at%Y-5at%Fe and Al-8at%Sm were prepared by repeated arc-melting high purity elements (Al: 99.999%; Y: 99.9%; Fe: 99.995%; Sm: 99.9%) at proper mixtures in an argon-protected environment. Amorphous ribbons were produced by rapid solidification processing using a single roller melt-spinning facility with a tangential wheel speed of 33m/s. The production of Al-Y-Fe-Pb melt-spun ribbons follows the procedures described above except that Pb is not included in the ingot during arc-melting due to its much lower melting point compared with the other three constituent elements. High purity Pb (99.99%) of desired weight was incorporated into the liquid alloy during melt-spinning. The amorphous melt-spun ribbon (MSR) samples were devitrified by continuous heating or by isothermal annealing in a differential scanning calorimetry (DSC, Perkin-Elmer DSC7). Mechanical intermixing was applied to fabricate amorphous $Al_{92}Sm_8$ sample at ambient temperatures by manually cold rolling stacked arrays of elemental foils of high purity Al (99.999%) and Sm (99.9%) at suitable composition mixture [6]. Phase identification was carried out with standard X-ray diffraction method (XRD, Philips XRD) in the reflection mode using Cu-Kα radiation. Microstructural characterization of the samples was performed by transmission electron microscopy with selected area electron diffraction (TEM/SAED, Philips CM200). The TEM samples were prepared by standard thinning procedures using a Gatan ion mill with liquid nitrogen cooling. The size and volume fraction of the nanocrystalline Al dispersions in different samples were determined from the TEM bright-field micrographs with image analysis software (ImagePro). Calorimetric signals from phase transformations during heating and isothermal annealing were monitored by DSC. Moreover, modulated-temperature DSC (DDSC) was applied to assess the glass transition temperature of the amorphous alloys.

RESULTS AND DISCUSSION

The TEM bright-field image of the as-spun ribbon sample of $Al_{88}Y_7Fe_5$ in Figure 1-a shows a homogeneous and fully amorphous structure with no evidence of a crystalline fraction. The diffuse ring in the corresponding selected area electron diffraction (SAED) pattern and the diffuse scattering maximum in the XRD trace in separate experiments indicate that the ribbon samples are amorphous. However, the DSC trace in Figure 1-b of an $Al_{88}Y_7Fe_5$ as-spun sample during continuous heating at 40°C/min displays two exothermic peaks but no indication of an endothermic reaction that corresponds to the glass transition. XRD study indicated the first exothermic peak is the primary crystallization reaction of α-Al [12]. Moreover, TEM investigation on the samples that were isothermally annealed at 245°C revealed a high density

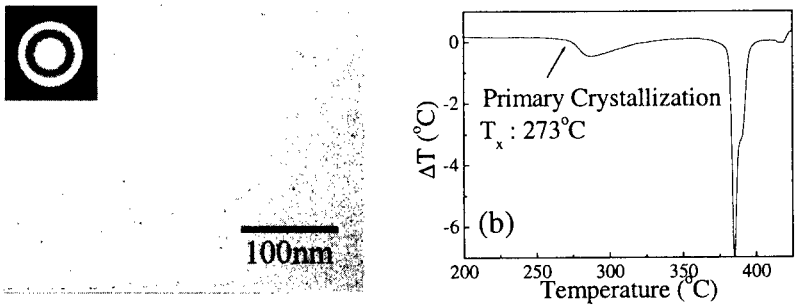


Figure 1: TEM bright-field image of an as-spun $Al_{88}Y_7Fe_5$ sample (a). The inset shows the corresponding SAED pattern that indicates the absence of a detectable crystalline fraction. The DSC trace (b) exhibits a primary crystallization peak but no glass transition is observed.

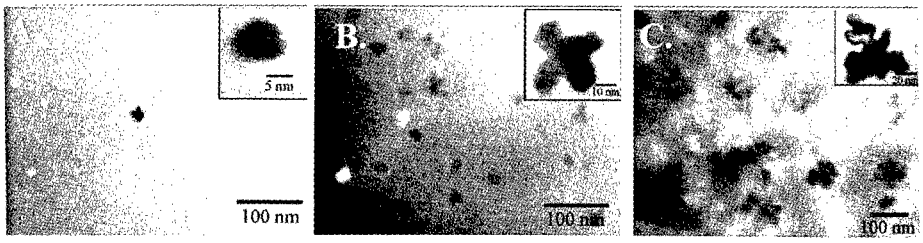


Figure 2: TEM bright-field images on $Al_{88}Y_7Fe_5$ as-spun ribbon samples that were isothermally annealed at 245°C for 10min (a); 30min (b); and 100min (c). The Al nanocrystals developed into a dendritic morphology after extended annealing [12].

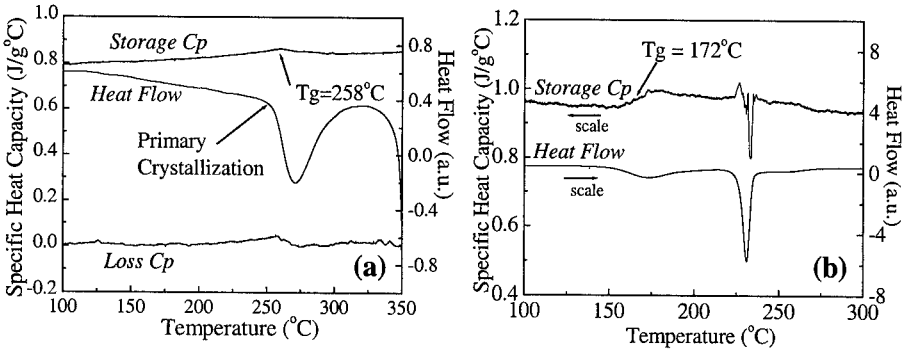


Figure 3: Results of the modulated-temperature DSC results on the as-spun sample of (a) $Al_{88}Y_7Fe_5$ and (b) $Al_{92}Sm_8$. The glass transition temperatures (T_g) were obtained as 258°C in (a) [15] and 172°C in (b), respectively.

($10^{21}m^{-3}$) of pure Al nanocrystals within the amorphous matrix [3]. The kinetics analysis on the development of the nanocrystals revealed that diffusion field impingement occurs quickly at temperatures near the crystallization onset and provides for a kinetic stabilization. Figure 2 shows the evolution of the Al nanocrystals from a spherical shape to a dendritic morphology at different annealing times. The formation of a dendritic morphology indicates that the kinetics of diffusion changes as the composition of the remaining amorphous matrix alters along with the growth of the Al nanocrystals. An analysis for the development of the dendritic morphology will be treated in more detail elsewhere [13]. The microstructural characterization and DSC analysis of $Al_{92}Sm_8$ as-spun samples yielded the same results. The results of modulation calorimetry experiments on the as-spun ribbon samples are shown in Figure 3 in comparison to the DSC trace obtained from the underlying static heat flow. The time series analysis of the modulated heat flow signal has excluded the exothermic signal that corresponds to the irreversible primary crystallization. In the Fourier analysis of the response signal in DDSC, the storage specific heat capacity and the loss specific heat capacity represent the real part and imaginary part of the contributions to the dynamic specific heat signal respectively [14]. The storage specific heat capacity is associated with dissipative processes such as a relaxation of the glassy state and the loss specific heat capacity is related to atomic motions such as molecular rearrangement that occurs during a glass transition. Therefore, both storage and loss specific heat capacity exhibit a change during the occurrence of a glass transition in the sample. The endothermic signal due to the glass transition is observed in the storage and loss specific heat curves at 258°C for $Al_{88}Y_7Fe_5$

and 172°C for $Al_{92}Sm_8$ [15]. The DDSC results confirm that a glass state has actually been achieved during the melt-spinning process on the alloys.

The schematic illustration in Figure 4 highlights two controlling mechanisms in metallic glass formation. Under nucleation control, the cooling path bypasses the nucleation reaction and the cluster distribution that may be retained during the quenching process does not overlap with the critical nucleus size at the crystallization temperature (T_x). Consequently, a clear separation in temperature between the glass transition temperature (T_g) and T_x can be observed during reheating. This is observed in the amorphous Al-Y-Fe alloys with similar compositions produced at a higher tangential wheel speed (50m/s) [16]. Under growth control, some small fraction of crystallites may form initially during rapid quenching, but the rapid increasing viscosity with decreasing temperature near T_g hinders their growth. Most importantly, the cluster distribution that is retained overlaps with the critical nucleation size at T_g. In either case, upon heating rapid crystallization occurs at T_g which will coincide with T_x. This is observed in the amorphous alloys under study that form a high number density of nanocrystals during primary crystallization. Therefore, it is possible to fabricate a uniform and fully glassy state without "quenched-in" nuclei by applying higher cooling rates during rapid solidification. However, this might not be practical in all systems.

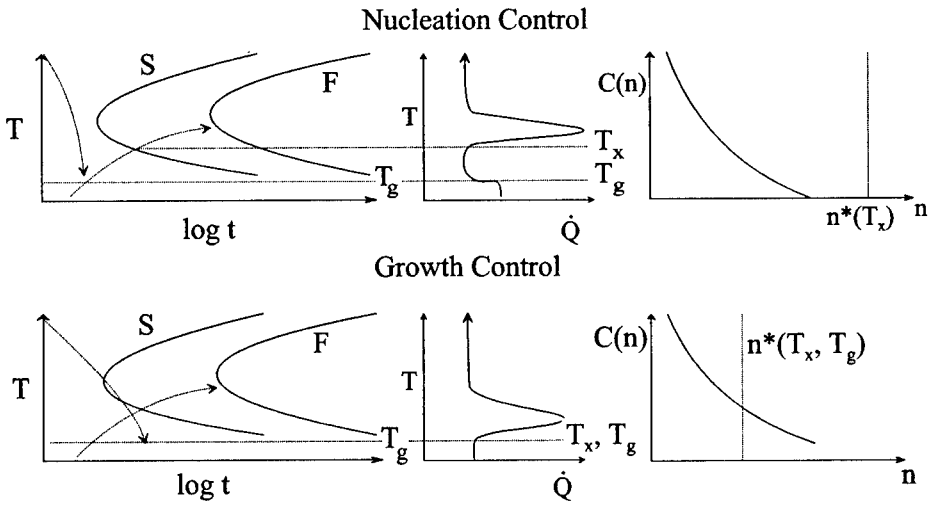


Figure 4: Schematics showing kinetics of metallic glass formation: nucleation control vs. growth control. Quenching and reheating paths are shown on the TTT diagrams (S-start; F-finish) and thermograms (dQ/dt: heat evolution rate).

In addition to the rapid solidification process, amorphous $Al_{92}Sm_8$ samples have been successfully produced by cold-rolling [6]. Figure 5-a shows the TEM bright-field image with the corresponding SAED pattern of a cold-rolled $Al_{92}Sm_8$ sample in comparison with that on a melt-spun ribbon sample (Figure 5-b). The thermal responses upon heating the amorphous samples prepared by different processes are completely different. A clear glass transition at 170°C is displayed in the DSC heating curve on the cold-rolled sample and no primary crystallization is present (Figure 5-c). Moreover, the high particle density of Al nanocrystals formed in the melt-spun sample after isothermal annealing (Figure 5-f) was not observed in the cold-rolled sample

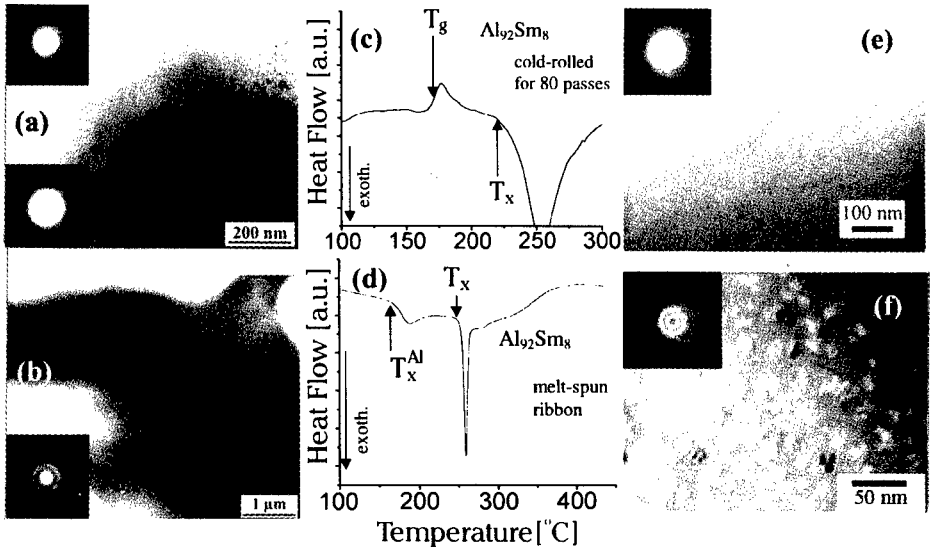


Figure 5: Glass formation and nanocrystallization of $Al_{92}Sm_8$. TEM and SAED of the amorphous and crystalline regions in a cold-rolled sample (a) and a melt-spun sample (b); DSC obtained from continuous heating (20°C/min) on a cold-rolled sample (c) and a melt-spun sample (d); TEM and SAED of a cold-rolled sample after annealed at 150°C for 60min (e) and a melt-spun sample after annealed at 150°C for 10min (f) [6].

after isothermal annealing at the same temperature with a longer time (Figure 5-e), The apparent differences in the thermal responses and the microstructural development in the samples produced by the two approaches suggest that the quenched-in nuclei result from the rapid melt cooling process. By choosing an appropriate reaction pathway to avoid these quenched-in nuclei, the crystallization of Al nanocrystals can be prevented and fabrication of bulk amorphous alloys could be possible.

On the other hand, the nanoscale Al particles that are smaller than the thickness of the shear deformation bands in the amorphous alloy can act as effective barrier against subsequent deformation of the matrix and a high particle density is favorable to enhance the mechanical

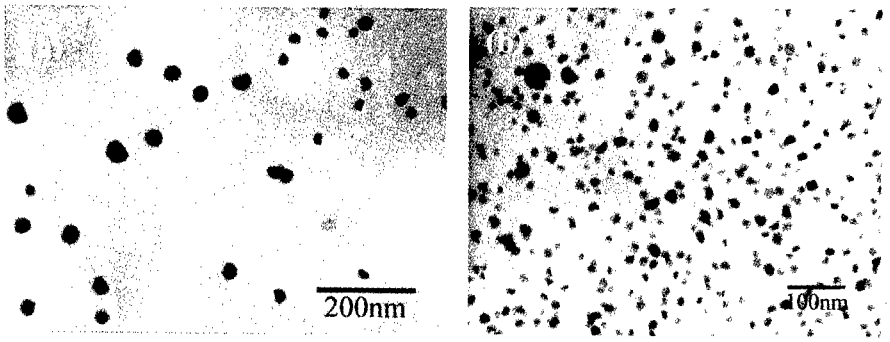


Figure 6: TEM of an $Al_{87}Y_7Fe_5Pb_1$ as-spun sample showing nanosize Pb particles within the amorphous matrix (a). TEM of an annealed sample showing Pb particles and high density Al nanocrystals in an amorphous matrix (b).

properties in the amorphous alloys. An approach to increase the particle density of the Al nanocrystals has been developed. The underlying strategy is to provide nucleation catalysts for Al nanocrystals by adding insoluble elements that form ultra-fine second phase dispersions in the amorphous matrix. The selection of Pb is based on its immiscibility in the liquid Al which will result in a liquid phase separation and a microstructure with discrete Pb nano-particles within the amorphous matrix that can be formed during melt-spinning. Moreover, the element is not reported to form intermetallic phases with other constituent elements at the Al-rich part in the ternary phase diagram. The TEM in Figure 6-a shows that the as-spun ribbons is predominantly amorphous with discrete spherical regions of crystalline Pb and the particle density is about $10^{20}m^{-3}$. Upon isothermal annealing at 245°C for 10min, Al nanocrystals were formed and the particle density is increased by more than a factor of 2 to 2.9×10^{22} m^{-3} (Figure 6-b), compared to that without Pb addition (1.4×10^{22} m^{-3}). The result suggests that the insoluble Pb particles are effective in catalyzing Al nanocrystals during devitrification.

CONCLUSIONS

It has been demonstrated that amorphous Al-based alloys can be synthesized by rapid solidification process and cold-rolling. The glass transition temperature that was not assessed previously has been measured by the modulated-temperature DSC. The crystallization experiments on the cold-rolled and melt-spun samples suggest that the quenched-in nuclei originate from the rapid quenching process and they are effective in developing high density of Al nanocrystals. The incorporation of nanosized Pb particles in the amorphous matrix has successfully increased the nano-particle density.

ACKNOWLEDGEMENT

The support of the ARO (DAAG55-97-1-0261) and the Humboldt Foundation (GW, V-3-FLF-1052606) is gratefully acknowledged by the authors.

REFERENCE

1. A. Inoue, K. Ohtera, A. Tsai, and T. Masumoto, Jpn. J. Appl Phys., **27** (4), p. L479 (1988).
2. Y. He, G. H. Dougherty, G. J. Shiflet, and S. J. Poon, Acta metall., **41** (2), p. 337 (1993).
3. D. R. Allen, J. C. Foley, and J. H. Perepezko, Acta mater., **46** (2), p. 431 (1998).
4. B. Cantor, Mat. Sci. Forum, **307**, p. 143 (1999).
5. A. Sagel, H. Sieber, H. J. Fecht, and J. H. Perepezko, Acta mater., **46**, 4233 (1998).
6. G. Wilde, H. Sieber, and J. H. Perepezko, J. Non-Cryst. Solids, **252**, p. 621 (1999).
7. G. P. Johari, S. Ram, G. Astl, and E. Mayer, J. Non-Cryst. Solids, **116**, 2282 (1990).
8. L. C. Chen and Spaepen, Mat. Sci. Eng., **A133**, p. 342 (1991).
9. L. Battezzati, M. Baricco, P. Schumacher, W. C. Shih, and A. L. Greer, Mat. Sci. Eng., **A179-190**, p. 600 (1994).
10. H. Chen, Y. He, G. J. Shiflet, and S. J. Poon, Scripta Met. **25**, p. 1421 (1991).
11. S. Das, J. H. Perepezko, R. I. Wu, and G. Wilde, Mat. Sci. Eng., in press.
12. R. I. Wu, G. Wilde, J. H. Perepezko, in press.
13. R. I. Wu, J. H. Perepezko, in preparation.
14. J. E. K. Schawe, Thermochimica Acta, **260**, p. 1 (1995).
15. G. Wilde, R. I. Wu, J. H. Perepezko, in preparation.
16. Q. Li, E. Johnson, A. Johansen, L. Yu, and L. Sarholt-Kristensen, Mat. Sci. Eng., **A151**, p. 107 (1992).

TRANSMISSION ELECTRON MICROSCOPY STUDY OF GOLD-COATED IRON CORE-SHELL AND AU/FE/AU ONION-LIKE NANOPARTICLES SYNTHESIZED USING REVERSE MICELLES

W.L. Zhou, E.E. Carpenter, J. Sims, A. Kumbhar, and C.J. O'Connor
Advanced Materials Research Institute, University of New Orleans, New Orleans, LA 70148

ABSTRACT

Gold-coated iron core-shell structure and Au/Fe/Au onion-like nanoparticles synthesized using reverse micelles were characterized by transmission electron microscopy (TEM). The average nanoparticle size of the core-shell structure is about 8 nm, with about 6 nm diameter core and 2 nm shell. The gold shell structure can be resolved from both high resolution electron microscopy (HREM) image and energy dispersive X-ray spectrum (EDS). Even though the gold and iron electron diffraction rings overlap a little bit, they can still be identified due to the slight mismatch of the diffraction rings. The Au/Fe/Au onion-like nanoparticles were also observed. The nanoparticles were formed with about 6 nm diameter gold core , 1 nm iron interlayer and 2 nm gold shell. The shell structure coated on the core appeared unhomogeneous, however, in both cases the iron core and interlayer iron shell stay air-stable.

INTRODUCTION

Recently the most successful way to improve the quality of the particles is to achieve chemical passivation of the surface of the crystallites, which has been applied on inorganic coating of semiconductor nanoparticles [1-7]. The idea is to cover the particle with another semiconductor which allows the confinement of the electron and holes inside the inner core particles, known as core-shell structure. Generally two similar crystal structure compounds were selected to make such kind of core-shell nanostructure, where epitaxial growth of the shell structure may occur.

Currently, one of most versatile methods to synthesize core-shell structure is wet chemical method such as microemulsion techniques which rely on the self-assembly nature of surfactants to push aqueous reactants into micelle [8]. Due to the dynamic nature of micelles, aqueous components can come together and react to form particles that are constrained to the size of the micelle. By changing the reaction conditions the methods can be even applied sequentially to form core-shell structure. By careful controlling of the synthesis using reserve micelles the nanoparticles can be obtained in a very narrow size distribution and quite uniform.

Pure metal iron nanoparticles are unstable in the air. By a coating an iron nanoparticles with a stable noble metal like gold, these air-stable nanoparticles are protected from the oxidation and retain most of the favorable magnetic properties, which possess the potential application in high density memory device by forming self-organization nanoarrays. In this paper, we present transmission electron microscopy study of these kinds of gold coated iron core-shell and Au/Fe/Au onion-like nanostructures.

Mat. Res. Soc. Symp. Proc. Vol. 581 © 2000 Materials Research Society

EXPERIMENT

The reserve micelle reaction is carried out using cetyltrimethylammonium bromide (CTAB) as the surfactant, octane as the oil phase, and aqueous reactant as the water phase. By varying the water to surfactant ratio (ω=[H_2O]/[CTAB]), we are able to carefully control the particle size ranging from 5 to 30 nmometers. A co-surfactant of n-butanol is used to help decrease the fraction of the micellar head group that is neutralized and thereby increase the stability of the micelle. Without the addition of the co-surfactant the amount of free water that is available to carry on reactions is greatly reduced as most of the water is locked in the head group of the CTAB. The metal particles are formed inside the reverse micelle by reduction of a metal salt using sodium borohydride. In our experiment we are utilizing the sequential synthesis offered by the reduction of ferrous sulfate by sodium borohydride. After the reaction has been allowed to go completion, the micelles within the reaction mixture are expanded to accommodate the shell using a large micelle containing additional sodium borohydride. The shell is formed using an aqueous hydrogen tetracholoroaurate solution. The particles are then washed, collected in a magnetic field and dried under vacuum.

The Au/Fe/Au onion-like structure was basically synthesized using same method, but in three steps: In step one, two micelle solutions were prepared using 0.1M $HAuCl_4$ (aq) and the other with 0.6M $NaBH_4$ (aq). These solutions (ω=6) were mixed together using a magnetic stirrer and allowed to react for two hours to ensure that all the gold was reduced. The reaction was carried out in the presence of long wave ultra-violet (UV) light and the solution turns out clear red as expected for a gold colloid after two hours. The reaction was carried out under flowing argon gas; The interlayer iron shell was synthesized in step two. Two additional micelle solutions were prepared using 0.1M $FeSO_4$ and 0.6M $NaBH_4$ respectively. These solutions were degassed and added to the reaction mixture. In this case, the $NaBH_4$ solution was prepared slightly larger to expand the micelles to allow for the growth of about one nanometer thick shell. The solution turned black upon the addition of the iron. The reaction was stirred under flowing argon for 2 hours as well; The second shell was prepared in a similar method to the first step that is two additional micelles were prepared using 0.1M $HAuCl_4$ and 0.6M $NaBH_4$. Once again the $NaBH_4$ was made slightly larger (ω=12) to accommodate about a two nanometer thick gold shell. After two hours reaction under UV light and flowing argon, the micelles in the reaction mixture were disrupted using aceton causing nanoparticles to precipitate. Repeated washing using a 1:1 mixture of chloroform/methanol removed the surfactant. The iron containing nanoparticles were separated using a permanent magnet (5000 Oe). The nanoparticles were then dried under vacuum, resulting in a black powder. After passivation with the second coating of gold, the particles became air stable with no oxidation detectable in the magnetic data after six weeks.

TEM samples were prepared by ultrasonically dispersing the nanoparticles in acetone for 10 minutes and then dropping them to the carbon grids with filter paper underside to absorb the acetone. TEM observation were performed on JEOL 2010 transmission electron microscopy equipped with EDAX DPrime energy dispersive X-ray analysis.

RESULTS

Gold-coated Iron Nanoparticles

Fig.1(a) and (b) are selected-area diffraction patterns from pure gold nanoparticles and gold-coated iron nanoparticles, respectively. As gold crystal structure is fcc with lattice parameter a=0.408 nm and α-Fe is bcc structure with lattice parameter a=0.287 nm, the diffraction rings appear very close to each other as shown in Fig.1(b). Due to slight mismatch they can be resolved from the broaden diffraction rings of gold 111, 200, 220, 311, and 222 which is caused by overlapping with iron 110, 200, 112, 220, 310, respectively. The separation of two kinds of diffraction rings become much clear at high index diffraction rings such as 220, 311, and 222. By focusing the electron beam to 2 nm

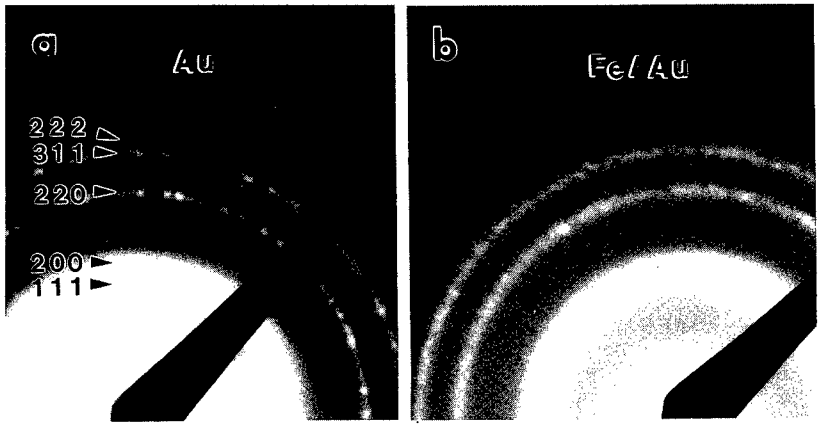


Fig.1 (a) and (b) are diffraction patterns from pure Au and Fe/Au core-shell nanoparticles

probe and putting on the nanoparticles to do EDS microanalysis both gold and iron peaks appeared in most nanoparticles as shown in Fig.2. If we moved the electron probe to the edge of the nanoparticles, it showed high concentration of gold, which implied gold shell structure formed. The mean size of nanoparticles is about 8 nm. Fig.3 is the HREM micrograph of gold-coated iron nanoparticles. In most cases, gold shell lattice can be easily identified and the core of iron appears as dark black in the center of the nanoparticles. The morié patterns were often found in the black iron cores as shown in particles A, B and C in Fig.3. The images of the nanoparticles appear different even at the same defocus because of unhomogeneous shape and different orientations of the nanoparticles.

Generally speaking, the iron core and gold shell should get smaller lattice mismatch as gold shell grows in terms of the orientation relationship of $[100]_{Fe}//[100]_{Au}$ and $[010]_{Fe}//[110]_{Au}$. Since the iron core grew as sphere-like shape inside reverse micelles, the gold epitaxial growth couldn't perfectly extend to three dimension. Thus another orientation growth or mismatch could occur during gold shell coating. This is also the

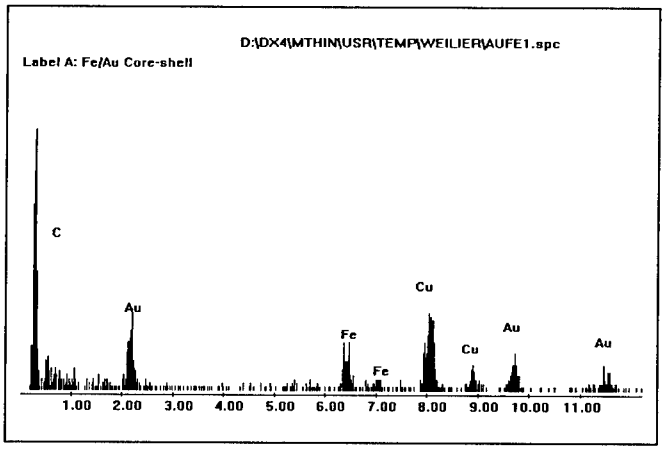


Fig.2 Gold-coated iron EDS spectrum by focusing electron probe to 2 nm.

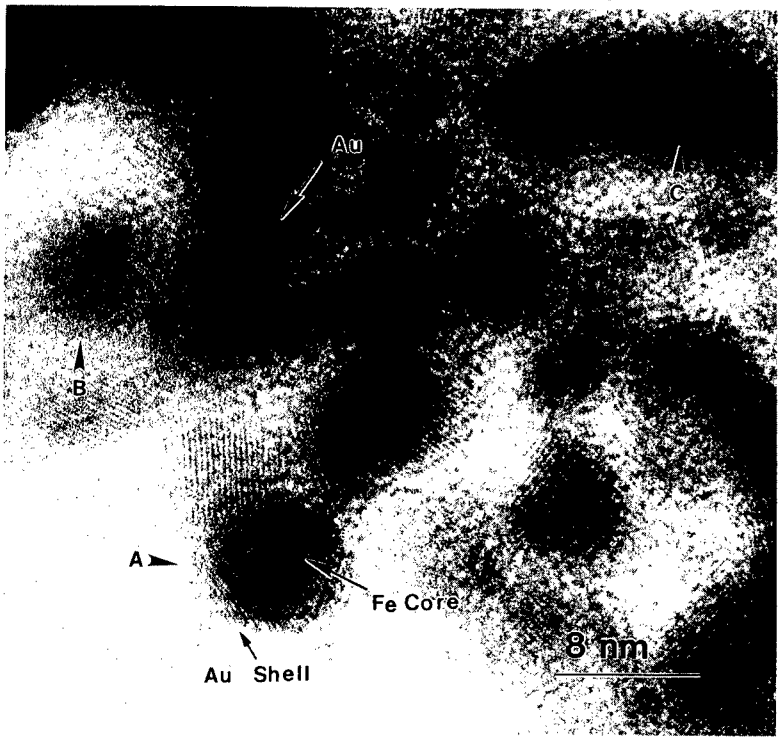


Fig.3 A HREM micrograph showing Fe/Au core-shell structure. Au shell lattice can be clearly seen. Iron cores (darker contrast) overlap with gold shells forming morié patterns.

reason sometimes we can see morié patterns in the center iron cores in Fig.3. Until now only those materials with similar structure and close lattice constant presented perfect epitaxial growth in inverted micelle synthesis [9]. Even though the permanent magnet was employed to separate gold-coated iron nanoparticles from gold or incompletely coated iron particles, some gold nanoparticles sticking on Fe/Au core-shell nanoparticles can still be observed (denoted by arrow) in Fig.3.

Au/Fe/Au Onion-like Nanoparticles

The selected-area diffraction pattern of Au/Fe/Au nanoparticles are almost same as gold coated iron nanoparticles, where Au and Fe diffraction rings can be seen separated at high index diffraction rings. EDS analysis shows that the cores are in higher concentration of gold, compared to gold-coated iron nanoparticles. Fig.4 is the micrograph of Au/Fe/Au onion-like nanoparticles. The size of Au cores is quite close to each other about 6 nm, appearing as dark black contrast. Then about 1 nm iron core can be seen formed as interlayer and the outside gold shell is more about 2 nm as denoted by arrows in Fig.4. Due to step by step reactions some core-shell nanoparticles (denoted by arrows) were also formed instead of onion-like structure.

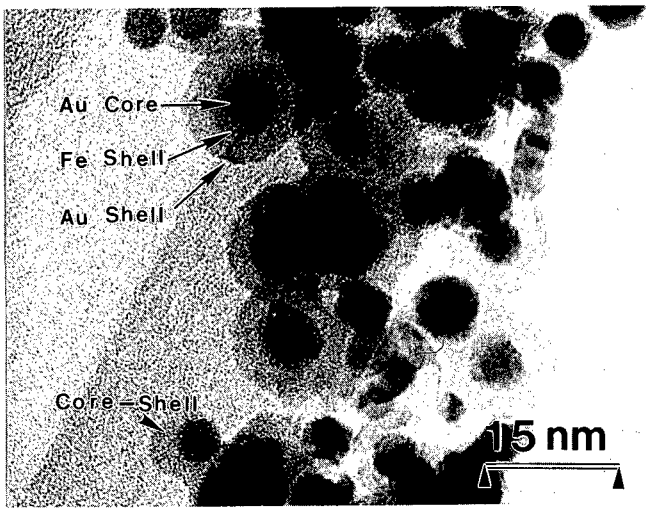


Fig.4 High magnification of TEM image of Au/Fe/Au onion-like structure. Au core, iron interlayer, and outside shell are denoted by arrows, respectively.

CONCLUSIONS

Gold-coated iron core-shell structure and Au/Fe/Au onion-like nanoparticles synthesized using reverse micelles were studied by transmission electron microscopy. Both kinds of nanoparticles were successfully synthesized. The average particle size of

the core-shell structure is about 8 nm, with about 6 nm diameter core and 2 nm shell. The gold shell structure can be identified from both high resolution electron microscopy and energy dispersive X-ray analysis. Even though the gold and iron electron diffraction rings overlapped a bit, the mismatch of diffraction rings still can be resolved. The Au/Fe/Au onion-like nanoparticles were formed with about 6 nm diameter gold core , 1 nm iron interlayer and 2 nm gold shell. Though the shell structure coated on the core appeared unhomogeneous, both kinds of nanoparticles stay air stable.

ACKNOWLEDGEMENTS

This work was supported by DARPA grant no. MDA972-97-1-0003.

REFERENCES

1. L. Spahnel, M. Haas, H. Weller, and A. Henglein, J. Am. Chem. Soc., **109**, 5649 (1987).

2. C.F. Hoener, K.A. Allan, A.J. Campion, M.A. Fox, T.E. Mallouk, S.E. Weber, and J.M. White, J. Phys. Chem., **96**, 3812 (1992).

3. M. Danek, K.F. Jensen, C.B. Murray, M.G. Bawendi, Chme. Mater., **8**, 173 (1996)

4. A.R. Kortan, R. Hull, R.L. Opila, M.G. Bawendi, M.L. Steigerwald, P.J. Karrol, and L.E. Brus, J. Am. Chem. Soc., **112**, 1327 (1990).

5. A. Mews, A. Eychmuller, M. Giersig, D. Schooss, and H. Weller, J. Phys. Chem., **98**, 934 (1994).

6. Y. Tian, T. Newton, N.A. Kotov, D.M. Guldi, and J.H. Fendler, J. Phys. Chem., **100**, 8927 (1996).

7. X. Peng, M.C. Schlamp, A.V. Kadavanich, and A.P. Alivistos, J. Am. Chem. Soc. **119**, 7019 (1997).

8. H. Wennerstrom, O. Soderman, U. Olsson, B. Lindman, Colloids and surface A: Physicochemical and engineering aspects **123-124,** 13 (1997).

9. L. Audinet, C. Ricolleau, M. Ganadais, T.Gacoin, J.P. Boilot, and P.A. Buffat, Phil. Mag. A **79**, 2379 (1999).

Nanophase Semiconductors and Non-Oxide Ceramics

SOLUTION-PROCESSED INORGANIC TRANSISTORS AND SUB-MICRON NON-LITHOGRAPHIC PATTERNING USING NANOPARTICLE INKS

Brent A. Ridley, Babak Nivi, Brian N. Hubert, Colin A. Bulthaup, Eric J. Wilhelm, and Joseph M. Jacobson
MIT Media Laboratory, 20 Ames Street, Cambridge, MA 02139

ABSTRACT

Pyridine solutions of CdSe nanocrystals were solution-deposited in the fabrication of thin film transistors (TFTs). A peak mobility of 1 $cm^2V^{-1}s^{-1}$ and an ON/OFF ratio of 3×10^4 were observed for TFTs processed at 350 °C. The nanocrystals acted as a precursor to the bulk material, coalescing to form a semiconductor thin film when heated at plastic-compatible temperatures. Single crystalline regions several hundred times the size of the original semiconductor nanocrystals were observed for films processed at 350 °C. We also report a process for direct liquid phase deposition and patterning of nanoparticle inks at sub-micron resolutions by elastomeric embossing and AFM nanospotting. These results suggest that microelectronic devices produced from nanoparticle-based inks can enjoy the processing advantages usually associated with organic materials while retaining the performance advantages typically associated with inorganic materials.

INTRODUCTION

We have recently published what we believe to be the first demonstration of a printable inorganic semiconductor processed at plastic-compatible temperatures [1]. Despite excellent performance characteristics, until recently [1,2] inorganic materials have not been considered for low-cost microelectronics fabrication due to high-temperature processing and complex patterning. In contrast, organic semiconductors have been widely studied because low-temperature and non-lithographic patterning makes them attractive candidates for a number of low-cost and large-area applications [3]. Unfortunately, experiment [4] and theory [5] indicate that the range of applications for these materials is limited by their mobility, which peaks at ~1 $cm^2V^{-1}s^{-1}$. This mobility is comparable to amorphous silicon and is useful for a number of applications. However, there are also a number of compelling applications for low-cost, large-area microelectronics at clock rates that organic materials cannot support. In an effort to combine the processing advantages of organic materials with the performance advantages of inorganic materials, we have developed a means of printing inorganic electronic materials.

The high-temperature processing requirements and insolubility of common inorganic semiconductors are problematic. Fortunately, both of these problems disappear in the nanometer size regime. Nanoparticles are readily soluble in appropriate solvents, and their size-dependent melting point depression is remarkable. Semiconductor nanoparticles have been reported to melt at greater than 1000 °C below their bulk melting points [6-8]. These size-dependent properties are the result of the nanoparticles having properties somewhere between those of an atomic species and a bulk crystal [9]. These size-dependent properties enabled the use of nanocrystal solutions as precursors to bulk thin films in the fabrication of thin film transistors (TFTs).

Nanoparticle-based inks can be deposited by conventional laboratory techniques such as solution casting or spin coating, or deposited and patterned by printing methods such as ink jet printing [10]. Patterning of these inks can also be carried out through techniques such as elastomeric embossing and direct writing by atomic force microscope (AFM) nanospotting,

Mat. Res. Soc. Symp. Proc. Vol. 581 © 2000 Materials Research Society

which we describe here. These techniques allow the precision patterning of nanoparticulate materials without the use of masking steps.

EXPERIMENTAL DETAILS

CdSe semiconductor nanocrystals were synthesized by both a pyrolytic route [11] and by a metathetic route [12] which was modified to yield smaller particles [1]. The CdSe nanocrystal solutions were deposited with a micropipet onto the source-drain electrodes of a TFT test structure. The test structure was a coplanar inverted TFT with n+ Si gate, 100 nm dry thermal SiO_2 oxide, and Cr/Au (10 nm/100 nm) source and drain electrodes. The channel length and width were 8 μm and 293 μm, respectively. After deposition, the solvent was allowed to evaporate, and the TFT was heated for an hour at 350 °C on a hot plate. After cooling, the devices were encapsulated with Norland Optical Adhesive 73, a photo-curable adhesive. Electrical characterization of the completed TFT was carried out in air in a dark box.

An elastomeric stamp used for embossing was prepared by pouring Sylgard 184 over a patterned silicon wafer, thermally curing the polymer, and then peeling off the elastomeric stamp. The stamp had 1 μm raised features. A thin film (50-1000 nm) of a silver or gold nanoparticle ink was deposited onto a glass, Si, or polyimide substrate by spin coating, dip coating, or with a draw-down bar. While this film was still in a liquid state, the stamp was brought into contact with the film. The raised features of the stamp pushed through the film and made contact with the underlying substrate, displacing the liquid in those areas. The stamp was removed, leaving a patterned film on the surface. This process is illustrated in figure 1. The film was then heated on a hot plate or with a laser to sinter the nanocrystals.

Silver and gold nanoparticle inks were directly written onto a glass slide using an AFM nanospotting method. A 100 micron ink droplet was applied to the glass slide with a needle. The tip of an AFM cantilever was used to transfer the ink from the pool to the glass slide. Typical writing speed was 5 to 10 microns per second. All ink lines were laid down in a single pass. The completed ink-on-glass patterns were cured for 10 minutes at 250 °C on a hot plate.

DISCUSSION

Nanocrystals synthesized by pyrolysis showed an ultraviolet-visible (UV-Vis) absorption peak at 470 nm, indicating that the average particle size was ~25 Å [11]. Nanocrystals formed by metathesis in methanol/pyridine [1] showed a sharp UV-Vis spectra absorption feature at 400 nm, indicating that the nanoparticles were ~17 Å in diameter. These crystallites are believed to be similar in structure to previously reported CdS [13] and CdSe [14] tetrahedral clusters.

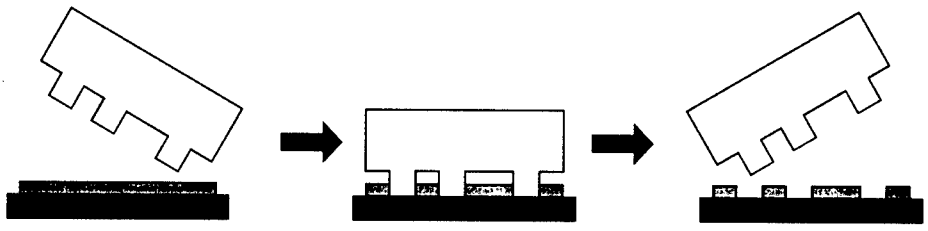


Figure 1. A schematic of the liquid nanoembossing process.

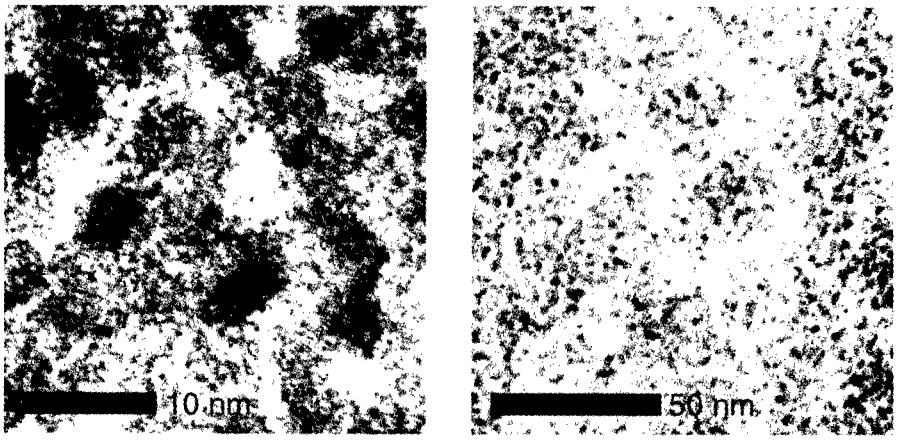


Figure 2. TEM images showing limited grain growth and granular morphology of fused ~25 Å CdSe nanoparticles produced by pyrolysis. The grains are the size of two or three individual nanocrystals.

Despite their small size, the nanocrystals formed by pyrolysis were found to be inappropriate for field-effect devices. Due to incomplete cap exchange [15,16], some of the alkylphosphine capping groups remained on the nanocrystal surfaces. In the reported literature, these heavy capping groups have contaminated sintered nanocrystal films by more than 50 at% [17]. In our films x-ray photoelectron spectroscopy (XPS) confirmed significant P contamination.

Additional problems arise with the thin films derived from the sintering of these nanoparticles at 350 °C. As seen in figure 2, transmission electron microscopy (TEM) indicates that a granular morphology consisting of small, oblate grains is produced. In contrast, fused films of metathetic CdSe nanocrystals exhibited smoother morphology and larger crystal grains (figure 3), even though the nanocrystals themselves were initially smaller than the pyrolytic ones.

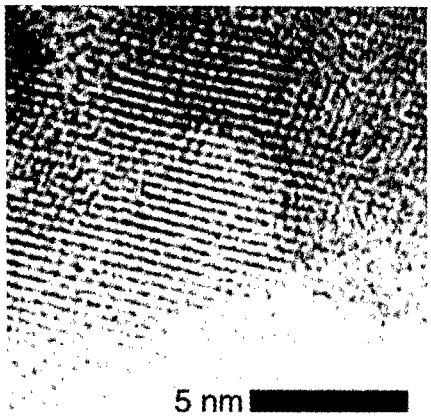
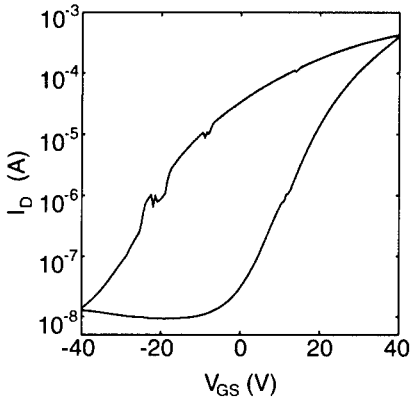


Figure 3. TEM image demonstrating the grain growth that resulted from heating CdSe nanocrystals produced by a metathesis reaction in methanol/pyridine. We have observed grain sizes that correspond to the coalescence of hundreds of nanocrystals and are 10-15 nm across. This is comparable to grain sizes observed in vapor deposited CdSe films [18].

Figure 4. Drain current versus gate source voltage (I_D-V_{GS}) characteristics of a TFT processed at 350 °C. An ON/OFF ratio of 3.1×10^4 for a gate sweep of V_{GS} = +/- 40 V at V_{DS} = 2.5 V is indicated by the I_D-V_{DS} plot. The subthreshold slope was 7 to 10 V per decade. A linear regime mobility (μ) of 1 $cm^2V^{-1}s^{-1}$ was extracted by equating the slope of an I_D-V_{GS} plot to $(W/L)\mu C_{ox}$ V_{DS} at V_{DS} = 2.5 V, where C_{ox} is the capacitance of the gate oxide. A threshold voltage of 6.7 V was extracted from the V_{GS} intercept of the I_D-V_{GS} plot.



No field effect was observed for TFTs fabricated from nanocrystal solutions of particles produced by pyrolysis. For metathesis-produced particles, TFTs processed at 350 °C had a maximum field effect mobility of 1 $cm^2V^{-1}s^{-1}$ and an ON/OFF ratio of 3×10^4, as shown in figure 4. A number of devices with similar characteristics were fabricated. Although this is the highest mobility of any solution processed semiconductor reported in the literature, it should be noted that vapor deposited CdSe TFTs have been observed with mobilities up to 450 $cm^2V^{-1}s^{-1}$and ON/OFF ratios of 10^{11} [19]. Thus, further improvements in nanoparticle synthesis, purity, and processing conditions are expected to improve device characteristics.

We have developed several deposition and patterning techniques for low-temperature microelectronics fabrication with nanoparticle inks. Nanoembossed patterns in Ag and Au films can be seen in figures 5-8.

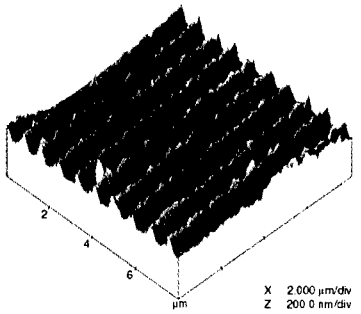


Figure 5. AFM image of nanoembossed conductive Ag lines with a 833 nm period.

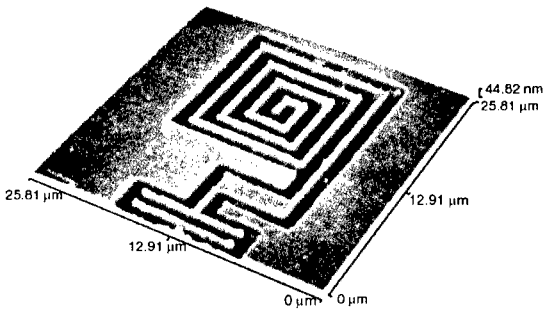


Figure 6. AFM image of a spiral with 500 nm features nanoembossed in Au.

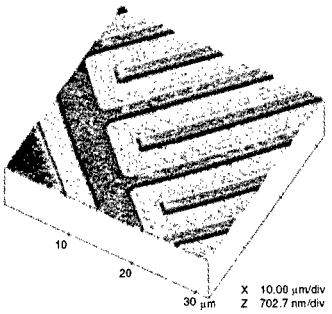


Figure 7. AFM image of interleaved 3 µm lines patterned in Au by nanoembossing.

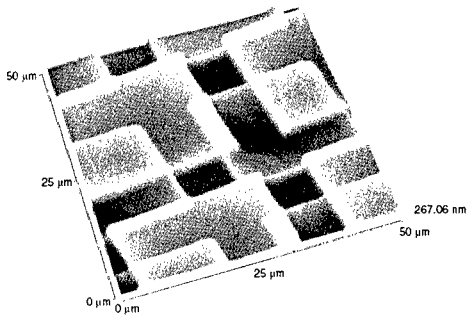


Figure 8. AFM image of multiple layers of Au nanoembossed on top of each other.

Sub-500 nm features were reliably patterned over areas greater than 25 cm^2 in less than 10 seconds. The recessed features of the stamp made contact with the surface of the liquid film but had no adverse effect upon the quality of the patterning, and the stamp came away clean without removing any material from the substrate. Additional layers of liquid material were patterned on top of previously patterned layers by simply repeating the process, as seen in figure 8. Because the patterning of these subsequent layers of material is conformal to the underlying layers, the nanoembossing process should be suitable for the formation of vias or other complex geometries for multi-layered devices. Finally, conductivity measurements of test structures indicated that the nanoembossed material had resistance values within a factor of four of the bulk material.

As shown in the AFM images presented in figures 9 and 10, AFM nanospotting was used to directly deposit liquid phase nanoparticle gold and silver inks with line widths as small as 55 to 75 nm at 5 to 10 microns per second. As shown in figure 9, thicker lines were created by increasing the force applied by the AFM tip to the substrate. A single dip of the AFM tip in the ink pool was sufficient to create unbroken lines that exceeded 30 microns in length. We expect the nanospotting technique to be useful for ultra-high precision deposition of solution-based electronic and structural materials such as conductors, semiconductors, insulators, and encapsulants.

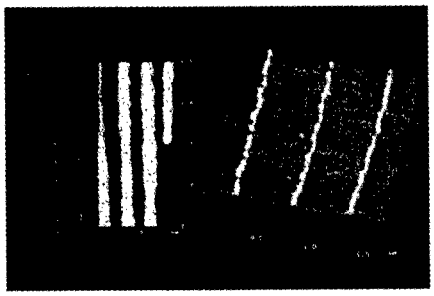


Figure 9. AFM image of 65-400 nm Au lines created by varying the force applied by the tip during AFM nanospotting.

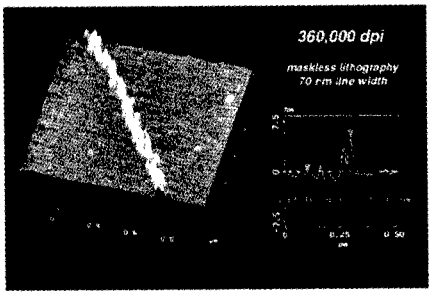


Figure 10. AFM image of a 70 nm wide line of a conductive Ag nanoparticle ink patterned by AFM nanospotting.

CONCLUSIONS

We have demonstrated an all-inorganic printable semiconductor. The observed mobilities are, to date, the highest reported for a solution-processed semiconductor and are at a level comparable to the maximum for room-temperature organic semiconductors. The inorganic semiconductor was printed at plastic-compatible temperatures by exploiting both the solubility of the semiconductor nanocrystals and the size-dependent melting point, which is heavily depressed for the <2 nm CdSe nanocrystals used here. Because melting point depression at small sizes is a generalized effect not only in semiconductors, but also in conductors and insulators, this approach can be extended to a variety of electronic materials. AFM nanospotting and elastomeric nanoembossing, as demonstrated here, may be useful means for patterning such electronic materials on the nanometer scale at low temperatures over large areas onto flexible plastics.

ACKNOWLEDGMENTS

We thank M. Frongillo for assistance with TEM, and L. Shaw for assistance with XPS. TFT test structures were fabricated at the MTL at MIT. This work made use of MRSEC Shared Facilities supported by NSF under award number DMR-9400334. This work was also supported by Defense Advanced Research Project Agency contract DABT63-99-C-0033 and by the Things That Think (TTT) consortium at the MIT Media Lab.

REFERENCES

1. B.A. Ridley, B. Nivi, J.M. Jacobson, Science **286**, 746 (1999).
2. C. R. Kagan, D. B. Mitzi, C. D. Dimitrakopoulos, Science **286**, 945 (1999).
3. R.F. Service, Science **278**, 383 (1997).
4. Y.-Y. Lin, D.J. Gundlach, S.F. Nelson, T.N Jackson, IEEE Electron Device Lett. **18**, 606 (1997).
5. F. Garnier, Phil. Trans. R. Soc. Lond. A **355**, 815 (1997).
6. Mat. Res. Soc. Symp. Proc. **206**, 271 (1991).
7. A.N Goldstein, C.M. Echer, A.P. Alivisatos, Science **256**, 1425 (1992).
8. A.N. Goldstein, Appl. Phys. A **62**, 33 (1996).
9. A.P. Alivisatos, MRS Bull **23**, 18 (February 1998).
10. S.B. Fuller, J.M. Jacobson, conference presentation to be given at IEEE MEMS-2000, Miyazaki, Japan (January 2000).
11. C.B. Murray, D..J. Norris, M.G. Bawendi, J. Am. Chem. Soc. **115**, 8706 (1993).
12. Mat. Res. Soc. Symp. Proc. **272**, 229 (1992).
13. N. Herron, J.C. Calabrese, W.E. Farneth, Y. Wang, Science **259**, 1426 (1993).
14. S. Behrens *et al.*, Angew. Chem. Int. Ed. Engl. **35**, 2215 (1996).
15. J.E. Bowen Katari, V.L. Colvin, A.P. Alivisatos, J. Phys. Chem. **98**, 4109 (1994).
16. M. Kuno, J.K. Lee, B.O. Dabbousi, F.V. Mikulec, M.G. Bawendi, J. Chem. Phys. **106**, 9869 (1997).
17. Mat. Res. Soc. Symp. Proc. **382**, 461 (1995).
18. A. Van Calster, A. Vervaet, I. De Rycke, J. De Baets, J. Cryst. Growth **86**, 924 (1988).
19. T.P. Brody, Information Display **2**, 5 (1992).

NANO-SIZED SEMICONDUCTING OXIDE POWDERS FOR THICK FILM GAS SENSORS: FROM POWDER PROCESSING TO ENVIRONMENTAL MONITORING DEVICES

Enrico TRAVERSA *, Maria Cristina CAROTTA **, Giuliano MARTINELLI **
*Department of Chemical Science and Technology, University of Rome Tor Vergata, 00133 Rome, Italy, traversa@uniroma2.it
**INFM, Department of Physics, University of Ferrara, 44100 Ferrara, Italy

ABSTRACT

This paper reports the study of semiconducting oxides to develop gas sensors in thick-film form for use in atmospheric pollutant monitoring devices. The investigation was achieved with the following steps: selection of the suitable oxides and of their most appropriate processing method to obtain nano-sized powders, fabrication using screen-printing technology of thick-film sensors from these powders, and electrical measurements in laboratory and in the field. Chemical routes such as sol-gel techniques and thermal decomposition of heteronuclear complexes have been used to prepare nano-sized powders of *n*-type (TiO_2) and *p*-type ($LaFeO_3$ and $SmFeO_3$) semiconducting oxides. Thick-film gas sensors have been produced by screen-printing technology. Pastes have been prepared and printed on laser precut 96% alumina substrates, each 2x2 mm element being provided with a heater, comb-type Au contacts and a Pt-100 resistor for controlling the operating temperature. The firing of the films has been performed in conditions able to keep grain size at nanometer level. Electrical responses to some major polluting gases (CO, NO, NO_2 and O_3) have been tested in laboratory and in the field, and compared with results of the analytical techniques approved by the international standards.

INTRODUCTION

Recently, one of the topic in materials science which has being given great emphasis is the control of materials structure at the nanometer size to study the unique physical properties deriving from the size reduction at this scale [1]. The discovery that nano-sized materials may show improved or unexpected properties has been first presented in 1989 [2]. Their use in a range of innovative technological applications is expected. The surface-to-bulk ratio is much larger for nano-sized than for coarse materials, so that surface properties become predominant. This makes the use of nano-sized materials principally attractive for applications where surface properties are exploited, as in gas sensors [3]. Grain size reduction is one of the main factors exalting gas-sensing properties of semiconducting oxides [4]: given their currently-accepted gas-sensing mechanism, sharp increases in gas sensitivity are expected when the grain size becomes smaller than the space-charge depth (or Debye length) [5]. The use of nanostructured materials, either in powder or thin-film form, is rapidly arousing interest in gas sensor studies [6,7]

Both physical and chemical methods are being widely studied for the synthesis of nano-sized ceramic powders [8-11]. Controlled, homogeneously-sized, and ultrafine ceramic powders can be prepared using chemical routes [12]. The first step to keep full control of the microstructure of a ceramic product is to control the preparation method of the starting powders. Chemical processing is mainly important for heterometallic oxides, because standard production methods (solid-state reaction at high temperatures) have several problems such as crystal growth, changes in stoichiometry, and ease of second phase formation [13].

This paper reports our work on using semiconducting oxide powders for the fabrication of thick-film gas sensors by screen-printing technology [14-16], with special attention to TiO_2, and perovskite-type $LaFeO_3$ and $SmFeO_3$. Screen-printing technology is a simple and automated manufacturing technique that allows the production of low-cost and robust chemical

Mat. Res. Soc. Symp. Proc. Vol. 581 © 2000 Materials Research Society

sensors [17,18] with a good reproducibility, if the starting materials are well controlled. A comparison of the results of using commercial and chemically-processed nano-sized powders has demonstrated that the performance of subsequent sensors is improved by employing the latter. In the literature, several groups have reported studies on thick-film gas sensors [19], but only a few used nano-sized powders for the thick-film processing [20-23]. Our main goal is to study cheap gas sensors in environmental-monitoring applications, and therefore outdoor field tests were performed using the prepared thick-film prototype sensors [24,25]. Previous work reported in the relevant literature investigated the use of gas sensors based on semiconducting oxides only for the control of air quality indoors [26] and inside passenger cars [27,28].

EXPERIMENTAL PROCEDURE

Powder Preparation

The thermal decomposition at low temperatures of heteronuclear complexes is a very interesting method for the preparation of homogeneous heterometallic perovskite-type oxides [29-32], as recently found even for YBCO [33]. A simple technique for preparing $LnTO_3$ perovskite-type oxides (with Ln = rare earth, and T = Fe, Co) is the thermal decomposition of hexacyanocomplexes, easily precipitated in aqueous solutions [34], as proposed by Gallagher in 1968 [35]. The complexes are single source precursors with the same stoichiometry as the desired oxides. This versatile method [36] also allows the synthesis of single-phase, trimetallic complexes, the decomposition of which may produce single-phase, trimetallic perovskite-type oxides [37-40]. This method was found to be the best for the production of high-quality powders of nano-sized perovskite-type oxides. The formation of $LaFeO_3$ was achieved at a temperature as low as 350°C, much lower than the temperature needed for its formation using the conventional solid-state reaction method [41]. The nano-sized $LaFeO_3$ and $SmFeO_3$ powders obtained by the thermal decomposition of the corresponding complexes at 700°C for 1 h were used for the preparation of the thick-film sensors [16,42].

Nano-sized powders of TiO_2 were prepared using a sol-gel route, particularly suitable for the homogeneous doping of TiO_2 with Nb or Ta. The pure titania powders were synthesized according to a procedure described in the literature [10], slightly modified to prepare Ta- or Nb-doped (5 or 10 at %) powders, and using alkoxides as precursors [43,44]. The nano-sized TiO_2 -based powders obtained by calcination at 400°C for 2 h were used for the preparation of the thick-film sensors [43,44].

Fabrication of Thick Films by Screen-Printing Technology

The preparation of all the thick films was performed for all the oxide powders using the screen-printing. This technology implies a processing sequence with the following major steps: (1) careful selection of the oxide powders to be deposited; (2) preparation of pastes (or inks) using an organic vehicle, normally consisting of a rheological agent mixed in a light solvent to ensure the correct rheology necessary for printing [17]; (3) printing of the pastes on suitable substrates; (4) drying at low temperatures (150-200°C) for the removal of the light part of the organic vehicle; and (5) firing at higher temperatures (600-900°C) to obtain the formation of a consolidated layer with the desired microstructure.

This technology has been adapted for the fabrication of layers composed of nano-sized particles. The powder selection is crucial and many factors have to be considered, such as grain shape and size, size distribution, intragranular porosity, surface conditions, etc. The pastes were prepared by adding to each oxide powder an organic vehicle, containing mainly ethyl-cellulose and α-terpineol, and 0.5 wt% of a glass frit to improve the adhesion to the substrates.

For the preparation of the prototype sensors, the pastes were printed on 96% alumina substrates, laser precut into 2 mm x 2 mm squares, 0.25 mm thick. Each substrate was provided with a heater element on the backside, a Pt-100 resistor for controlling the sensor operating

temperature, and comb-type gold electrical contacts on the front. This structure allows the device to work at relatively high operating temperatures (250°C-450°C) with relatively low power consumption (approximately 0.5 W). The dimensions of the deposited layers were about 1.5 mm long, 1.5 mm wide, with thickness in the 20-50 μm range. The films were fired for 1 h at temperatures able to keep the grain size at the nanometer level, *i.e.*, 750°C for the perovskite-type oxides and 850°C for the TiO_2-based sensors. Figure 1 shows a SEM (scanning electron microscopy) micrograph of a thick film deposited on an alumina substrate, while Figure 2 shows the assembly of a prototype sensor.



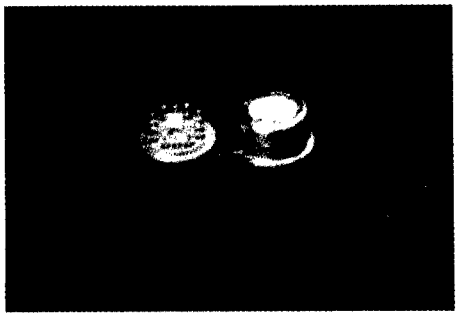


Figure 1 - A thick film deposited on an alumina substrate.
Figure 2 - A prototype sensor assembly.

Electrical Measurements in Laboratory and in the Field

Electrical tests on thick film sensors were performed in the laboratory. The conductance measurements were carried out in a sealed test chamber (850 cm^3) with different gases (various concentrations of CO or NO_2) in dry or wet (at about 40% of relative humidity, RH) air, at a flow rate of 0.5 l/min and at different operating temperatures.

For field tests, an array of these sensors based on the various oxides was exposed to real atmosphere in locations near conventional monitoring stations, which are managed by the ARPA (Regional Agency for Environment Protection), sections of Ferrara and Padova. The gas-sensitive electrical properties of the sensors were studied by measuring their conductance changes when exposed to real atmosphere. The electrical response was measured at 270°C for both the perovskite-type sensors and at 450°C for the TiO_2-based sensors. The temperature and RH in the chamber containing the sensors were simultaneously monitored, with signal acquisition performed by computer. The sensors' response was compared with the concentrations of the major pollutants (CO, CO_2, NO, NO_2, ozone, etc.) in the atmosphere, as measured with the methods approved by the international standards.

RESULTS AND DISCUSSION

$LaFeO_3$ and $SmFeO_3$ Perovskite-Type Oxide Thick Films

As shown by TG-DTA, the thermal decomposition of the hexacyanocomplexes begins with the loss of crystallization water, followed by cyanide groups' decomposition starting at 300°C [42]. The decomposition ends at 600°C. Above this temperature the weight loss remains constant. X-ray diffraction (XRD) analysis of the LaFe-complex decomposed between 350°C and 600°C, showed some peaks attributed to $LaFeO_3$, together with a broad band centered at about 30° in 2θ. When the complex was decomposed at 600°C and higher temperatures for 1 hour, only the pattern corresponding to perovskite-type $LaFeO_3$ (JCPDS file No. 37-1493, orthorhombic) was observed, without peaks attributable to La_2O_3 and/or Fe_2O_3 [42].

The $LaFeO_3$ formation temperature was thus as low as 600°C, much lower than the temperature needed for its formation using the conventional solid-state reaction method. However, the $LaFeO_3$ perovskite-type oxide was obtained even at 350°C, *i.e.*, the temperature at which the cyanide groups decompose, when the holding time was increased up to 100 hours [41]. The holding time did not affect the crystal growth of the nano-sized particles, as shown by the measurement of the crystallite size from XRD analysis and TEM observation.

SEM and TEM observations confirmed the direct formation of $LaFeO_3$ from the thermal decomposition of the LaFe-complex [42,45]. SEM findings showed that the typical morphology of the complex powders consisted of large grains (2 to 10 μm) with sharp edges. The morphology of the complex heated up to 600°C did not significantly change with respect to the morphology of the precursor, with micron sized grains. At higher temperatures, the same morphology was maintained, but nano-sized particles started to be evident within the grains. The powders were made of agglomerates of about the same size and shape of the precursor grains, each one consisting of nano-sized particles, which diffract in the orthorhombic system ($LaFeO_3$). The size of these particles increased with increasing the calcination temperature [42].

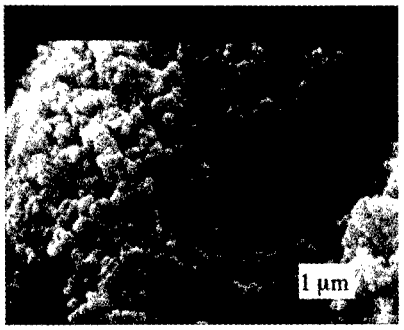
TEM observations of the complex decomposed at 400°C showed that pores of about 10 nm, not observed by SEM, were clearly formed [45]. The relative SADP showed the formation of polycrystalline, orthorhombic $LaFeO_3$ phase, with no traces of the broad band observed in the XRD pattern. TEM analysis of the complex heated to 500°C showed that each single, micron sized grain was made of particles of about 20 nm. SADP measurements on each grain showed the presence of $LaFeO_3$ with a single orientation. This surprising result means that the nano-sized particles of $LaFeO_3$ are formed from the evolution of cyanide groups, which caused the diffuse porosity of about 10 nm in the large grains, but keeping the same orientation. In this stage, $LaFeO_3$ is present as a porous single crystal [45]. The explanation of these results can be found in the crystalline structures of the complex and the oxide, which are very similar. The higher the temperature, the larger the size of pores and particles. At 600°C, the primary particle size was 40 nm. At 700°C, SADP on the micron sized grains showed a ring pattern typical of polycrystalline materials, demonstrating that the primary particles started to have different orientations [45]. A similar microstructural evolution with the temperature was observed also for $SmFeO_3$ formed by the thermal decomposition of the SmFe-complex.

Nano-sized $LaFeO_3$ and $SmFeO_3$ powders prepared by the thermal decomposition of the hexacyanocomplexes at 700°C were used for the preparation of the thick-film sensors. Ball milling in ethanol was effective in destroying the agglomerates, with formation of powders made of uniform particles in the 20-60 nm size range. As shown by TEM, these powders were free of intragranular pores [45], which makes them suitable for the preparation of thick films by screen-printing technology.

The $LaFeO_3$ and $SmFeO_3$ thick films were fired at various temperatures in the range 750-1000°C [15,16]. SEM observations showed that the morphology of the thick films heated to 750°C was very similar to the morphology of the powders. Figure 3 shows a typical SEM micrograph of a $LaFeO_3$ thick-film sensor fired at 750°C. The films were highly porous, sintering of the grains was very limited, and the presence of necks was rarely observed. However, the inner layer of the oxide was adhered to the substrate, as checked by scotch tape tests. With increasing the firing temperature, a growth of the oxide grains was observed. The higher the temperature, the larger the grains and the larger the number of necks between particles. For both oxides, the average size of the grains was 200 nm at 900°C, and 400 nm at 1000°C. Therefore, it was decided to measure the gas response of the films sintered at 750°C.

The gas-sensitive electrical response of both the perovskite-type thick-films were tested in laboratory, in environments with different gases (CO and NO_2) in dry and wet air [15,16]. Both oxides responded to CO and NO_2, with *p*-type semiconducting behavior. Figure 4 shows the electrical response of a $LaFeO_3$ film fired at 750°C to various NO_2 concentrations in wet (30% RH) air, measured at 250°C. The alarm limits set in Italy (in agreement with European Union

regulations) for environmental monitoring are about 0.1 ppm of NO_2 and 10 ppm CO in air. Keeping in mind these values, the response of the $LaFeO_3$ and $SmFeO_3$ films to 1 ppm of NO_2 is greater than their response to 100 ppm of CO, a concentration two orders of magnitude larger. However, the perovskite-type oxide films in these tests did not detect the alarm values.



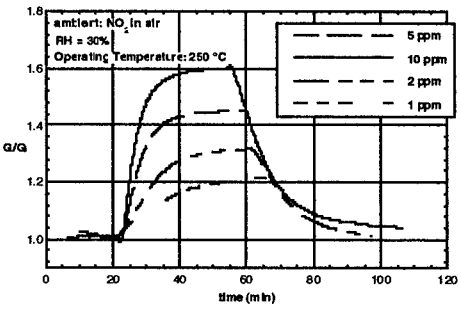


Figure 3 - SEM micrograph of a $LaFeO_3$ thick-film sensor fired at 750°C.
Figure 4 - Electrical response a $LaFeO_3$ thick-film sensor fired at 750°C, measured at 250°C at various NO_2 concentrations in wet (30% RH) air.

TiO_2-Based Thick Films

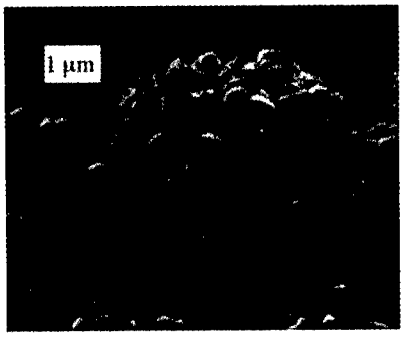
XRD analysis showed that the precipitates dried at 100°C were amorphous. All the samples were calcined at 400°C to obtain homogeneous and nano-sized (30-50 nm) anatase TiO_2 powders. XRD analysis was also performed on pure and doped samples heated to selected temperatures (650, 850, and 1050°C) to check the crystalline structure and the phases present. The pure TiO_2 powder heated to 650°C showed still the presence of anatase. Heating up to 850°C induced the phase transition from anatase to rutile.

The presence of Ta and Nb dramatically affected the phase transition between anatase and rutile observed for the pure titania. The 10 at% Ta-doped powder showed the presence of almost only anatase (accompanied by small amounts of rutile) up to the heating temperature of 850°C. At 1050°C, anatase transformed into rutile accompanied by traces of Ta_2O_5. This means that the solubility of Ta is almost complete in the titania crystalline structures even at a concentration of 10 at%. The 10 at% Nb-doped powder showed the presence of only the anatase phase up to 650°C, while the sample heated to 850°C contained mainly anatase, but also rutile and Nb_2TiO_7. At 1050°C, anatase transformed into rutile accompanied by Nb_2TiO_7. The 5 at% Nb-doped powder heated to 850°C showed the presence of anatase and a small amount of rutile, and at 1050°C the presence of rutile structure with traces of an unidentified phase. The Nb solubility in the titania crystalline structures is thus lower than that of Ta.

SEM observations of the thick films showed that the phase transformation from anatase to rutile occurred with a significant grain growth. The pure TiO_2 film fired at 650°C was very porous and made of homogeneous spherical particles with grain size in the range 40-60 nm. The doped samples fired at 650°C showed the same morphology with similar grain size. Figure 5 shows the SEM micrograph of the pure TiO_2 film fired at 850°C. The grain size was in the 200-600 nm range, showing a grain growth of about one order of magnitude, and a reduction in total porosity. Figure 6 shows the SEM micrograph of the 10 at% Ta-doped TiO_2 film fired at 850°C, having morphology similar to that of the pure titania films fired at 650°C. Grain size was in the 40-70 nm range. All the doped samples fired at 850°C showed the same features.

The doping at both concentrations was effective in hindering the grain growth and the anatase-to-rutile phase transformation at 850°C. This might be due to the substitution of Ta^{5+}

(or Nb^{5+}) in the Ti^{4+} sites that reduces the oxygen vacancy concentration and inhibits the transformation from anatase to rutile [46]. Similar results were obtained with pure and doped (V or Nb) TiO_2 powders prepared using laser-induced pyrolysis, which also led to the preparation of nanocrystalline powders with the anatase structure [47].



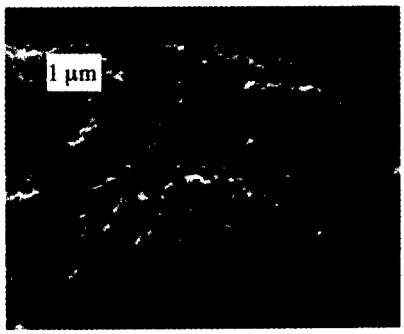


Figure 5 - SEM micrograph of pure titania sample fired at 850°C.
Figure 6 - SEM micrograph of Ta (10 at%) doped titania sample fired at 850°C

Electrical measurements of the thick films performed at 400°C in wet (40% air showed that conductance increased with Ta and Nb addition. The pure TiO_2 films showed conductance values in the range 1-3 nS, while 7-10 nS were measured for the Ta-doped films, and 20-50 nS for those doped with Nb. The Nb doping was more effective than the Ta doping in decreasing the film resistance. The valence band occupancy of the fifth electron of Ta is smaller than for Nb. Hence, Ta-doped films were expected to show a better CO response than Nb-doped films.

Figure 7 shows the electrical response (the ratio between the conductance in the tested gas, G_{gas}, and the conductance in air, G_{air}) to CO (100 ppm) in wet air (40% RH) of all the TiO_2-based films tested. The microstructure of the films dramatically affected the response of the sensors: in fact, the pure TiO_2 film fired at 850°C was almost insensitive to CO while all the other films that showed nanosized grains were sensitive to CO. As far as the doped samples are concerned, the films fired at 850°C and doped with Ta showed better responses. Moreover, the 10 at% doped samples responded better than the corresponding 5 at% doped samples. The best response, about 2.5, was thus observed for the 10 at% Ta-doped film heated to 850°C. Considering the films fired at 650°C, in agreement with the conductance measurements, the CO response followed the order: pure TiO_2 > 10 at% Ta-doped TiO_2 > 10 at% Nb-doped TiO_2.

The influence of RH on the CO response of the titania-based thick films was negligible. Figure 8 shows the electrical response of the doped films fired at 850°C, measured in wet (40% RH) and dry air at 400°C. This feature is very important for air quality monitoring [25], which is the target application of these sensors, given that the sensors have to be exposed to environmental atmosphere.

The maximum response to 10 ppm of NO_2 (expressed in this case as G_{air}/G_{gas}, being NO_2 an oxidizing gas) in wet air (40% RH) was about 2.3, measured at 400°C for the 10 at% Nb-doped film fired at 850°C. The films which showed the larger CO responses were only slightly sensitive to NO_2. As an example, the NO_2 response of the 10 at% Ta-doped film fired at 850°C was 1.6. Again, only the nanostructured films showed some sensitivity to NO_2.

Thus, these results demonstrate that titania sensors can be used in the environmental pollutant control only if nanostructured. Titania-based sensors needs to work at relatively high operating temperatures larger than 400°C. The sensors based on TiO_2 films doped with Ta and fired at 850°C offer the best combination of characteristics for CO control in air quality

monitoring. They show enhanced thermal stability keeping the grain size at the nano-sized level, and thus a large CO response almost unaffected by relative humidity.

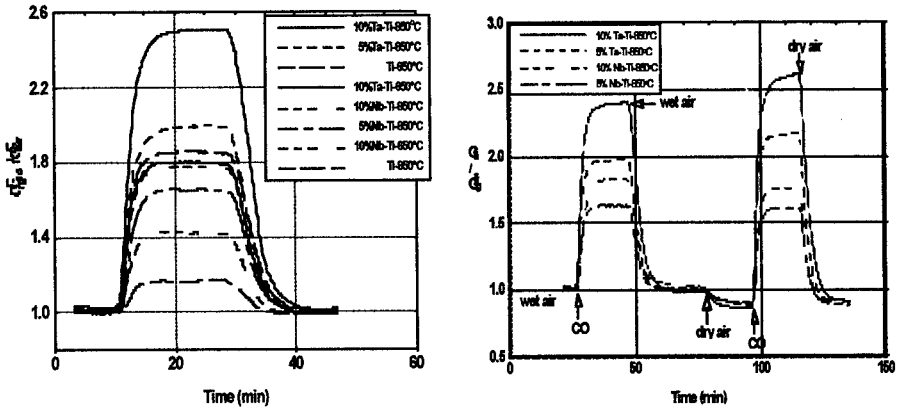


Figure 7 – Electrical response to CO (100 ppm) in wet air (40% RH) of the various TiO_2-based thick films (the legend list the samples from top to bottom), measured at 400°C.

Figure 8 – Electrical response to CO (100 ppm) in wet (40% RH) and dry air of the various doped TiO_2 thick films fired at 850°C (from top to bottom, 10 at% Ta-doped, 5 at% Ta-doped, 10 at% Nb-doped, and 5 at% Nb-doped), measured at 400°C.

Environmental Monitoring Field Tests

The control and monitoring of pollutants for ambient air quality is at present limited by the high costs of the analytical equipment needed by the techniques currently approved by the existing standards [48]. Therefore, environmental monitoring is one of the most desired among the industrial and civil applications for which the development of reliable and selective solid-state gas sensors is needed [49]. Devices based on solid-state gas sensors would be dramatically cheaper than analytical equipment, and their use would lead to the possibility of wider distribution of environmental monitoring locations than exist at present, resulting in an improved picture of air quality [50].

These are the reasons that have driven us to study the gas-sensitive electrical properties of the thick films during field tests, performed by measuring the change in conductivity of the various films, placed in an array and exposed to real atmosphere. Several sensors' arrays have been installed. The first test started on February 12, 1997, using SnO_2 and $LaFeO_3$ sensors, while other sensors ($SmFeO_3$, TiO_2, and In_2O_3) were added later. The first array is up to date still running without major problems of stability for the sensors.

During the field tests, very good agreement was observed between the sensors' output and the gas concentrations measured by the ARPA analytical equipment [51,52]. Figure 9 shows the output of the sensor array during field tests between April 3rd and 5th, 1999. This output consisted of the electrical response of the $LaFeO_3$ sensor fired at 750°C, of the 10 at% Ta-doped TiO_2 sensor fired at 850°C, and in the monitoring of RH and temperature (T). For reading the RH and T values, one needs to consider that 10 mV = 1% RH, and 10 mV = 1°C. During the three days examined, the temperature and RH were extremely variable. However, the responses of the sensors were not affected by these parameters, as demonstrated from the correct zero line of the signals that was not changed during tests. Pollutant emissions are inevitably concentrated during rush hours. In fact, as shown in Fig. 9, also the activity of the semiconducting sensors was observed during rush hours.

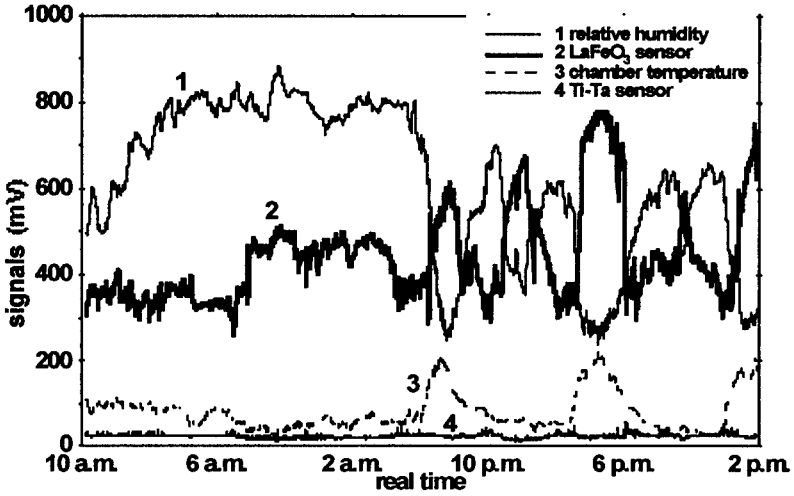


Figure 9 – Output of the array of thick-film sensors during field tests on April 3-5, 1999 (10 mV = 1% RH, 10 mV = 1°C).

The $LaFeO_3$ and $SmFeO_3$ sensors were mainly sensitive to nitrogen oxides, as shown in Figure 10, where the $LaFeO_3$ sensor response is compared with the NO_x concentration measured by the analytical equipment, during the same period of time of the sensor array response of Fig. 9. According to the Italian regulations, the concentrations of CO, NO, NO_2, and O_3 measured with the analytical equipment are provided as average concentrations in a hour. Therefore, also for the sensor response the values are reported as average values in a hour. The Ta-TiO_2 sensors were mainly sensitive to CO reducing gas. Figure 11 shows that the response of this sensor is in good agreement with the CO output of the analytical equipment.

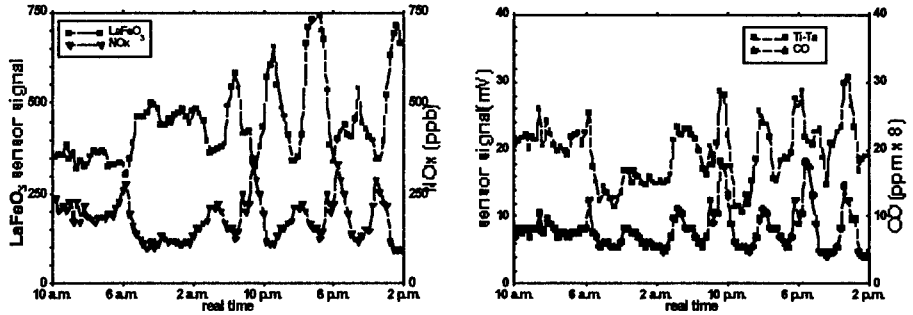


Figure 10 – Response (mV, average in a hour) of the $LaFeO_3$ sensor compared to the NO_x concentration measured by the analytical equipment.

Figure 11 – Response (mV, average in a hour) of the Ta-TiO_2 sensor compared to the CO concentration measured by the analytical equipment.

The emissions of a car with a diesel engine and one with an Otto-cycle engine have been unambiguously correlated to the response of $LaFeO_3$ and SnO_2 sensors [24]. The test was performed during night (around 11 p.m.) to avoid interference with polluting emissions of other cars. When a car with a diesel engine was turned on near the monitoring station, the $LaFeO_3$ sensor detected 394 ppb of NO_2, when the average level was 70 ppb. The diesel engine was shut off, and after the $LaFeO_3$ sensor had recovered to the average potential value, the gasoline-powered car was turned on. A positive peak was observed for the SnO_2 sensor, while a small negative signal was observed for the $LaFeO_3$ sensor, corresponding to a measured CO level of 5.6 ppm (an average value of about 1 ppm). Surprisingly, these absolute values and changes are much smaller than those that the sensors appeared able of measuring during laboratory tests.

These results obviously showed only qualitative gases and not quantitative polluting-gas-monitoring capabilities. Nevertheless, an attempt was made to find a quantitative correlation between the concentrations measured by the conventional analytical equipment and the sensors' output, using calibration curves [24]. These calibration curves were used to evaluate quantitatively the CO and NO concentrations from the electrical response of $Ta\text{-}TiO_2$ and $LaFeO_3$ sensors, and they showed good agreement with the values measured with the standard analytical equipment, although there were large errors involved in this procedure (which neglected the influence of interference gases on sensor response) [24]. However, phenomena like inversion temperature make also difficult a correct evaluation, due to NO_2 and O_3 interference. This problem might be overcome by increasing the number of the sensors in the array, particularly with materials able to selectively detect these gases.

CONCLUDING REMARKS

It has been demonstrated that the properties of gas sensing materials can be improved by the use of nano-sized semiconducting oxide powders. Our approach is trying to design the performance of a given oxide to obtain the suitable conductance and improved selectivity. This can be obtained by controlling the microstructure of the oxide (through chemical processing of the powders), and the composition of the oxides (additives can be used to control the conductance in air, and to control the microstructure). All the thick-film processing parameters are also of primary concern in tailoring structural and electrical properties. The combined use of theory and experimental analysis provides the instruments for achieving such aims.

Another very important result is that the feasibility of using semiconducting-oxide thick-film sensors in cheap, innovative, environmental-monitoring stations has been demonstrated. In field tests, the sensors were able to detect atmospheric pollutants at very low concentrations and exhibited the same trend as those recorded by conventional analytical instruments.

Although it is still not possible to claim that semiconducting sensors are selective, their performances have been undoubtedly enhanced in this respect. Therefore, the use of an array of sensors based on different semiconducting oxides can be very helpful in overcoming interference problems, and the use of simpler signal-processing methods than in many current systems can be foreseen. It may be concluded that there is still considerable room for improvement in the field of gas sensors via the relevant sensing materials.

ACKNOWLEDGMENTS

The authors wish to thank the friends who actively collaborated to the development of this research: Prof. Y. Sadaoka and Dr. H. Aono (Ehime University, Matsuyama, Japan), Prof. M. Sakamoto (Yamagata University, Japan), Dr. M. Merli, Dr. M.A. Butturi, Dr. L. Crema, and Dr. M. Gallana (University of Ferrara), Prof. G. Gusmano, Prof. S. Licoccia, Dr. M.L. Di Vona, and Dr. P. Nunziante (University of Roma "Tor Vergata"), Prof. G. Ghiotti and Prof. A. Chiorino (University of Torino), and Dr. M.C. Casale (ENEL Ricerca, Segrate, Milano).

Thanks to ARPA (sezioni di Ferrara e di Padova) and ORION s.r.l. for useful collaboration and discussion on the innovative monitoring station. The National Research Council of Italy (CNR) is acknowledged for financial support under the auspices of the Targeted Projects "MADESS 2" and "MSTA 2".

REFERENCES

1. Y.M. Chiang, J. Electroceram. **1**, 205 (1997).

2. H. Gleiter, Prog. Mater. Sci. **33**, 223 (1989).

3. N.L. Wu, S.Y. Wang, and I.A. Rusakova, Science **285**, 1375 (1999).

4. Y. Shimizu and M. Egashira, MRS Bull. **24** (6), 18-24 (1999).

5. C. Xu, J. Tamaki, N. Miura, and N. Yamazoe, Sensors and Actuators B **3**, 147 (1991); D.E. Williams, ibid., **57**, 1 (1999).

6. M. Schweizer-Berberich, J.G. Zheng, U. Weimar, W. Göpel, N. Barsan, E. Pentia, and A. Tomescu, Sensors and Actuators B **31**, 71 (1996); G. Sberveglieri, P. Nelli, L. Sangaletti, M. Ferroni, V. Guidi, G. Martinelli, G. Marca, and L.E. Depero, ibid., **36**, 381 (1996); Z. Jin, H.J. Zhou, Z.L. Jin, R.F. Savinell, and C.C. Liu, ibid., **52**, 188 (1998); M.J. Willett, V.N. Burganos, C.D. Tsakiroglou, and A.C. Payatakes, ibid., **53**, 76 (1998).

7. L.F. Dong, Z.L. Cui, and Z.K. Zhang, Nanostructured Mater. **8**, 815 (1997); D.G. Rickerby, M.C. Horrillo, J.P. Santos, and P. Serrini, ibid., **9**, 43 (1997); H. Lin, C. Keng, and C. Tung, ibid., **9**, 747 (1997); D.G. Rickerby and M.C. Horrillo, ibid., **10**, 357 (1998).

8. C.D. Terwilliger and Y.M. Chiang, Nanostructured Mater. **2**, 37 (1993).

9. H. Hahn, Nanostructured Mater. **2**, 251 (1993).

10. D.C. Hague and M.J. Mayo, J. Am. Ceram. Soc. **77**, 1957 (1994).

11. J.Y. Ying and T. Sun, J. Electroceram. **1**, 219 (1997).

12. C.N.R. Rao, J. Mater. Chem. **9**, 1 (1999).

13. M. Kakihana, J. Sol-Gel Sci. Technol. **6**, 7 (1996).

14. G. Martinelli and M.C. Carotta, Sensors and Actuators B **15-16**, 363 (1993); **23**, 157 (1995).

15. M.C. Carotta, M.A. Butturi, G. Martinelli, Y. Sadaoka, P. Nunziante, and E. Traversa, Sensors and Actuators B **44**, 590 (1997); A. Chiorino, G. Ghiotti, M.C. Carotta, and G. Martinelli, ibid., **47**, 205 (1998); M.C. Carotta, G. Martinelli, Y. Sadaoka, P. Nunziante, and E. Traversa, ibid., **48**, 270 (1998); M.C. Carotta, M. Ferroni, D. Gnani, V. Guidi, M. Merli, G. Martinelli, M.C. Casale, and M. Notaro, ibid., **58**, 310 (1999).

16. E. Traversa, S. Villanti, G. Gusmano, H. Aono, and Y. Sadaoka, J. Am. Ceram. Soc. **82**, 2442 (1999).

17. M. Prudenziati and B. Morten, Sensors and Actuators **10**, 65 (1986).

18. N.M. White and J.D. Turner, Meas. Sci. Technol., **8**, 1 (1997).

19. M. Honoré, S. Lenaerts, J. Desmet, G. Huyberechts, and J. Roggen, Sensors and Actuators B **19**, 621 (1994); J. Mizsei, ibid., **23**, 173 (1995); A. Heilig, N. Barsan, U. Weimar, M. Schweizer-Berberich, and W. Göpel, ibid., **43**, 45 (1997); Y. Shimizu, T. Maekawa, Y. Nakamura, and M. Egashira, ibid., **46**, 163 (1998); J.L. Solis and V. Lantto, ibid., **48**, 322 (1998).

20. S.G. Ansari, P. Boroojerdian, S.R. Sainkar, R.N. Karekar, R.C. Aiyer, and S.K. Kulkarni, Thin Solid Films **295**, 271 (1997).

21. G. Williams and G.S.V. Coles, J. Mater. Chem. **8**, 1657 (1998); MRS Bull. **24** (6), 25-29 (1999).

22. A. Diéguez, A. Romano-Rodríguez, J.L. Alay, J.R. Morante, N. Barsan, J. Kappler, U. Weimar, and W. Göpel, in *Techn. Digest of The 7th Int. Meet. on Chemical Sensors* (Int. Academic Publishers, Beijing, 1998) p. 389.

23. D.S. Lee, S.D. Han, J.S. Huh, and D.D. Lee, Sensors and Actuators B **60**, 57 (1999).

24. G. Martinelli, M.C. Carotta, M. Ferroni, Y. Sadaoka, and E. Traversa, Sensors and Actuators B **55**, 99 (1999); E. Traversa, Y. Sadaoka, M.C. Carotta, and G. Martinelli, ibid., in press; M.C. Carotta, G. Martinelli, L. Crema, M. Gallana, M. Merli, G. Ghiotti, and E. Traversa, ibid., submitted.

25. G. Martinelli, M.C. Carotta, E. Traversa, and G. Ghiotti, MRS Bull. **24** (6), 30-36 (1999).

26. T. Oyabu, Y. Matsuura, and H. Kimura, Sensors and Actuators B **36**, 308 (1996).

27. G. Wiegleb and J. Heitbaum, Sensors and Actuators B **17**, 93 (1994).

28. H. Nakagawa, S. Okazaki, S. Asakura, K. Fukuda, H. Akimoto, S. Takahashi, and T. Shigemori, in *Techn. Digest of The 7th Int. Meet. on Chemical Sensors* (Int. Academic Publishers, Beijing, 1998) p. 187.

29. M. Sakamoto, Y. Komoto, H. Hojo, and T. Ishimori, Nippon Kagaku Kaishi *1990*, 887.

30. S. Nakayama and M. Sakamoto, J. Ceram. Soc. Jpn. **100**, 342 (1992); M. Sakamoto, K. Matsuki, R. Ohsumi, Y. Nakayama, Y. Sadaoka, S. Nakayama, N. Matsumoto, and H. Okawa, ibid., **100**, 1211 (1992).

31. M. Sakamoto, T. Igoshi, M. Sato, S. Matsushima, M. Miwa, H. Aono, and Y. Sadaoka, J. Alloys and Compounds **260**, 59 (1997).

32. H. Aono, M. Tsuzaki, A. Kawaura, M. Sakamoto, E. Traversa, and Y. Sadaoka, Chem. Lett. *1999*, 1175.

33. E. Hasegawa, H. Aono, T. Igoshi, M. Sakamoto, E. Traversa, and Y. Sadaoka, J. Alloys and Compounds **287**, 150 (1999).

34. Y. Sadaoka, K. Watanabe, Y. Sakai, and M. Sakamoto, J. Ceram. Soc. Jpn. **103**, 519 (1995); J. Alloys and Compounds **224**, 194 (1995).

35. P.K. Gallagher, Mater. Res. Bull. **3**, 225 (1968).

36. E. Traversa, M. Sakamoto, and Y. Sadaoka, Particulate Sci. Technol. **16**, 185 (1998).

37. Y. Sadaoka, E. Traversa, and M. Sakamoto, J. Mater. Chem. **6**, 1355 (1996).

38. Y. Sadaoka, E. Traversa, P. Nunziante, and M. Sakamoto, J. Alloys and Compounds **261**, 182 (1997).

39. M. Sakamoto, P. Nunziante, E. Traversa, S. Matsushima, M. Miwa, H. Aono, and Y. Sadaoka, J. Ceram. Soc. Jpn. **105**, 963 (1997).

40. E. Traversa, P. Nunziante, M. Sakamoto, Y. Sadaoka, and R. Montanari, Mater. Res. Bull. **33**, 673 (1998).

41. Y. Sadaoka, H. Aono, E. Traversa, and M. Sakamoto, J. Alloys and Compounds **278**, 135 (1998).

42. E. Traversa, M. Sakamoto, and Y. Sadaoka, J. Am. Ceram. Soc. **79**, 1401 (1996).

43. M.C. Carotta, M.A. Butturi, G. Martinelli, M.L. Di Vona, S. Licoccia, and E. Traversa, Electron Technol. **33**, in press (2000).

44. E. Traversa, M.L. Di Vona, S. Licoccia, M. Sacerdoti, M.C. Carotta, M. Gallana, and G. Martinelli, J. Sol-Gel Sci. Technol., in press.

45. E. Traversa, P. Nunziante, M. Sakamoto, Y. Sadaoka, M.C. Carotta, and G. Martinelli, J. Mater. Res. **13**, 1335 (1998).

46. M.K. Akhtar, S.E. Pratsinis, and S.V.R. Mastrangelo, J. Am. Ceram. Soc. **75**, 3408 (1992).

47. M. Musci, M. Notaro, F. Curcio, C. Casale, and G. De Michele, J. Mater. Res. **7**, 2846 (1992).

48. N. Yamazoe and N. Miura, IEEE Trans. Compon., Packag., Manuf. Technol., Part A **18**, 252 (1995).

49. E. Traversa, J. Am. Ceram. Soc. **78**, 2625 (1995).

50. E. Traversa, in *Progress in Ceramic Basic Science: Challenge Toward the 21st Century*, edited by T. Hirai, S.i. Hirano, and Y. Takeda (The Ceram. Soc. of Japan, Tokyo, 1996) p. 145.

51. E. Traversa, P. Nunziante, Y. Sadaoka, M.C. Carotta, and G. Martinelli, in *Proc. of the 11th Europ. Microelectronics Conf.* (Venice, 1997) p. 52.

52. M.C. Carotta, M.C. Casale, L. Crema, M. Ferroni, M. Merli, G. Martinelli, and E. Traversa, in *Proc. 3rd Conf. on Sensors and Microsystems*, edited by A. D'Amico and C. Di Natale (World Scientific, Singapore, 1999) p. 143.

SYNTHESIS AND CHARACTERIZATION OF Mn DOPED CdS QUANTUM DOTS FROM A SINGLE SOURCE PRECURSOR

M. Azad Malik[a] Paul O'Brien,[b*] and N. Revaprasadu[ac]
a.Department of Chemistry, Imperial College of Science, Technology and Medicine, Exhibition Road, London, SW7 2AZ, UK. b. Manchester Materials Science Centre and Department of Chemistry, University of Manchester , Oxford Rd, Manchester M13 9PL. c. Department of Chemistry, University of Zululand, Private Bag X1001, Kwadlangezwa, 3886. South Africa. E-mail: p.obrien@ic.ac.uk

ABSTRACT

CdS and Mn-doped CdS capped with TOPO (tri-*n*-octylphosphineoxide) have been prepared by a single source route using bis(methylhexyldithiocarbamato)cadmium(II) and manganese dichloride as precursors. The nanoparticles obtained show quantum size effects in their optical spectra with the CdS nanoparticles exhibiting near band-edge luminescence. The PL spectrum of the doped CdS nanoparticles have an emission maximum at 585 nm attributed to the $^4T_1$-$^6A_1$ electronic transition of Mn in a tetrahedral site. However the PL spectrum changes over time (weeks) and gave a deep trap emission. The Selected Area Electron Diffraction (SAED) and X-ray diffraction (XRD) pattern show both CdS and the Mn doped CdS particles to be of the hexagonal phase. Transmission Electron Microscopy (TEM) and High Resolution TEM show well-defined images of nanosize particles with clear lattice fringes. ESR spectra and ICP results confirm the presence of Mn in the CdS nanoparticles.

INTRODUCTION

Semiconductor particles with diameters on the order of nanometers have generated considerable interest in these materials in recent years because of their unique size dependent properties. The incorporation of Mn into the crystal lattice of II/VI semiconductor nanoparticles have yielded another new class of materials.[1] Mn doped ZnS and CdS quantum dots have demonstrated an orange luminescence attributed to the spin forbidden $^4T_1$-$^6A_1$ electronic transition of Mn.[1-7] These properties are due to the strong exchange coupling between the localized moments of the paramagnetic dopant and the band electrons of the semiconductor. Most reports on Mn doped ZnS and CdS nanoparticles involve a colloidal route based on the simultaneous precipitation of both CdS (or ZnS) and MnS.[1-6] $Cd_{1-x}Mn_xS$ have also been synthesized by coprecipitation in reverse micelle solutions.[7] All studies have concluded that only a small fraction of the initial Mn added is incorporated into the crystal lattice with a large proportion of the Mn remaining on the surface or forming MnS precipitates. The location of the Mn in the dots is important as it effects the optical properties. Murphy *et al.*[4] reported that manganese doped ZnS displays orange emission (585 nm) whereas the ZnS dots with Mn on the surface emit in the ultraviolet (435 nm). The local structure of these particles has been studied by transmission electron microscopy (TEM), x-ray diffraction (XRD), energy dispersion spectroscopy (EDS) and electron paramagnetic resonance (EPR).

We report the synthesis and complete characterization of TOPO capped Mn doped CdS nanoparticles using an air stable single source precursor, bis(methylhexyldithiocarbamato) cadmium(II)[$Cd(S_2CNMe(^nHex))_2$] and manganese dichloride.

Mat. Res. Soc. Symp. Proc. Vol. 581 © 2000 Materials Research Society

EXPERIMENTAL

Chemicals

Tri -*n*- octylphosphine oxide (TOPO), tri-*n*-octylphosphine (TOP), *n*-methylhexylamine, carbon disulfide and manganese(II) chloride were purchased from Aldrich Chemical Company Ltd and methanol, toluene from BDH..
TOPO was purified by vacuum distillation at ca. 250 °C (0.1 torr). The solvents used for air sensitive chemistry were distilled , deoxygenated under a nitrogen flow and stored over molecular sieves (type 4 Å, BDH) before use.

Instrumentation

UV/VIS Absorption Spectroscopy: A Philips PU 8710 spectrophotometer was used to carry out the optical measurements of the semiconductor nanoparticles. The samples were placed in silica cuvettes (1 cm path length).

Photoluminescence Spectroscopy: A Spex FluoroMax instrument with a xenon lamp (150W) and a 152 P photomultiplier tube as a detector was used to measure the photoluminescence of the particles. Good spectral data was recorded with the slits set at 2nm and an integration time of 1 second. The samples were quantitatively prepared by dissolving 25 mg in 10 ml toluene.

The samples were placed in quartz cuvettes (1 cm path length) used as blank for all measurements. The wavelength of excitation was set at a lower value than onset of absorption of a particular sample.

X-Ray Diffraction (XRD): X- Ray diffraction patterns were measured using a Philips PW 1700 series automated powder diffractometer using Cu- K(radiation at 40kV/40mA with a secondary graphite crystal monochromator. Samples were prepared on glass slides (5 cm). A concentrated toluene solution was slowly evaporated at room temperature on a glass slide to obtain a sample for analysis.

Electron microscopy: A Joel 2000 FX MK 1 operated at 200KV electron microscope with an Oxford Instrument AN 10000 EDS Analyser was used for the conventional TEM (transmission electron microscopy) images. Selected area electron diffraction (SAED) patterns were obtained using a Jeol 2000FX MK 2 electron microscope operated at 200kV. The samples for TEM and SAED were prepared by placing a drop of a dilute solution of sample in toluene on a copper grid (400 mesh, agar). The excess solvent was wicked away with a paper tip and completely dried at room temperature.

Electron spin resonance (ESR): Measurements were made on a Bruker 200D X-band spectrometer employing 100 kHz modulation, magnetic field markers from an NMR gaussmeter and an external microwave frequency counter.

Synthesis

All experiments were carried out by using dry solvents and standard Schlenck techniques. Glassware was dried in the oven before use and TOPO (tri-*n*-octylphosphineoxide) was used after purification by vacuum distillation

Preparation of $Cd(S_2CNMe(^nHex))_2$

$Cd(S_2CNMe(^nHex))_2$ was synthesised according to the literature method.[8] A mixture of $Cd(OH)_2 2H_2O$ (8.43g, 46.2 mmol), CS_2 (4.6 cm^3, 77.2 mmol) and *N*-methyl-hexylamine (11.6 cm^3, 76.3 mmol) in ethanol (50 cm^3) was refluxed for 1 h. The mixture was filtered to remove the solid impurities and the clear filtrate was evaporated under vacuum. The yellow solid product

was recrystallized from chloroform at room temperature to give $Cd(S_2CNMe(^nHex))_2$. (m.p. 74 °C, yield: 14.11 g, 28.6 mmol, 75 %).

Preparation of CdS quantum dots

The method used was essentially as described by Trindade and O' Brien.[9,10] $Cd(S_2CNMe(^nHex))_2$ (1.0 g) was dissolved in TOP (15 ml) and injected into hot TOPO (20 g). A decrease in temperature of 20 - 30 °C was observed. The solution was then allowed to stabilize at 250 °C and heated for 40 min. at this temperature. The pale white solution was cooled to approximately 70°C and an excess of methanol added, a flocculant precipitate formed. The precipitate was separated by centrifugation and redispersed in toluene.

Preparation of Mn doped CdS quantum dots

In a typical experiment $Cd(S_2CNMe(^nHex))_2$ (1.0 g) and $MnCl_2$ (2.56 mg, 1%) are dissolved in TOP (15 ml). The resulting deep red solution was then injected into hot TOPO (20 g) at 250 °C. After an initial drop in temperature to 210 °C the temperature was stabilised at 240 °C and the reaction was allowed to proceed for 40 minutes. The mixture was cooled to 70 °C and methanol was then added to it to flocculate the nanoparticles. After centrifugation, the supernatant solution was discarded and the pale white precipitate of nanoparticles was washed further with methanol to remove the excess TOPO, followed by dissolution in toluene.

RESULTS AND DISCUSSION

The shift of the band edge to high energy with decreasing particle size in semiconductor nanoparticles as a result of quantum size effects is widely reported. The incorporation of Mn^{2+} into the crystal lattice of the nanometric semiconductor should have an effect on the optical properties. The TOPO capped CdS nanoparticles synthesized from $Cd(S_2CNMe(^nHex))_2$, exhibits a band edge at 4.75nm (2.61 eV) with a distinct excitonic shoulder at 440 nm (Figure 1). The optical absorption spectrum of Mn doped CdS is slightly broader than that of CdS with the band edge red shifted at 506 nm (2.45 eV). The shoulder visible at 440 nm in CdS is smoothened out in the doped sample. This effect could be due to a broader size distribution in the doped sample. The band edges of both CdS and Mn doped CdS show blue shifts with respect to bulk CdS (512 nm, 2.42 eV) (Figure 1). The photoluminescence spectrum of the CdS nanoparticles shows a very narrow emission curve with an emission maximum at 514 nm. This is consistent with previously observed photoluminescence behavior for CdS synthesized by a similar method with the emission attributed to band to band electron-hole recombination.[11] The TOPO electronically passivates the surface traps, normally responsible for the luminescence in CdS nanoparticles, through surface trap recombinations. The photoluminescence spectrum of Mn doped CdS nanoparticles differs from that of CdS. A narrow, slightly more intense spectrum is observed, with an emission maximum red shifted at 585 nm. This emission is characteristic of the Mn^{2+} internal $^4T_1$-$^6A_1$ transition. The absence of any deep trap emission in both the samples suggests that the nanoparticles that surface coverage by TOPO is very efficient. However, a photoluminescence spectrum carried out on the Mn doped sample after three weeks shows remarkably different features. The emission maximum is further red shifted to 705 nm, with a "hump" at 544 nm and the Mn^{2+} emission peak at 585 nm no longer present. This means that the dominant emission at 705 nm is due to recombination from the trap states. The appearance of surface traps could be due to the uncapping of the nanoparticles with time as a result of their instability in solution. This suggestion is confirmed by the appearance of a fine yellow precipitate of CdS nanoparticles in the toluene solution.

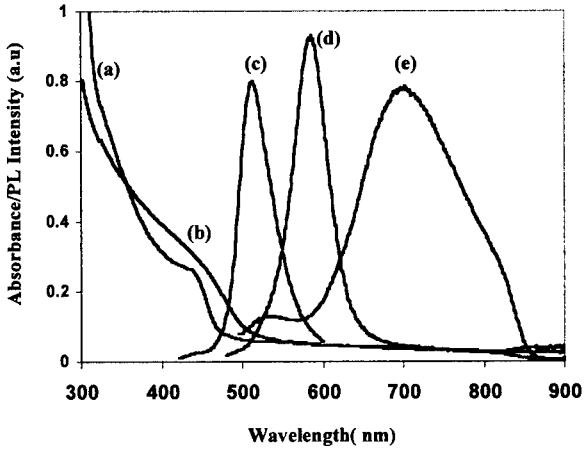


Figure 1. Optical spectra (a) absorption spectrum of CdS, (b) absorption spectrum for Mn doped CdS ,(c) PL spectrum of CdS, (d) PL spectrum of Mn doped CdS (fresh) and (e) after 3 weeks.

The diffraction pattern of Mn doped CdS shows broad peaks typical of particles in the nanosize regime (Figure 2). The (110), (103) and (112) planes of wurtzite CdS are clearly distinguished in the pattern. The SAED pattern consists of broad diffuse rings again typical of small particles. The diffraction rings are indexed , with the (100), (102), (103) and (112) planes confirming the wurtzite phase. The diffraction pattern is similar to CdS without any change in phase, however the (110), (103) and (112) planes are slightly broader in the doped sample.

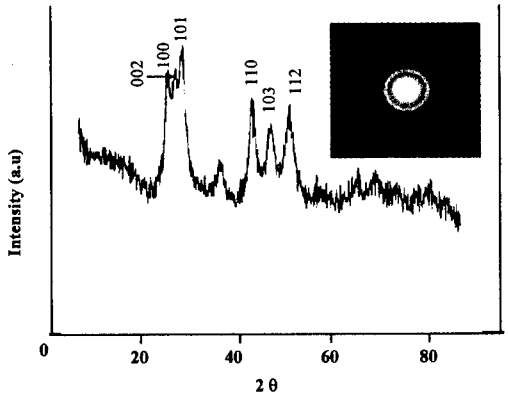


Figure 2. The XRD and SAED patterns of Mn doped CdS sample

This effect could be as a result of the smaller size of the Mn doped CdS particles or because of the substitution of Mn in the sulfur sites of CdS crystal lattice. The latter is more likely since the TEM micrographs and the absorption spectrum indicates that the Mn doped CdS particles are larger than those of CdS (Figure 3a). The TEM micrograph of the Mn doped sample shows particles with a diameter of. 5.44 nm (± 8%) the CdS nanoparticles had an average diameter of 5.12 nm (± 7%). The particles appear clustered forming "islands" of particles. The HRTEM micrograph shows well-defined particles. The lattice fringes visible in the HRTEM micrograph of a single quantum dot is indicative of the crystalline nature of the particles (Figure 3c).

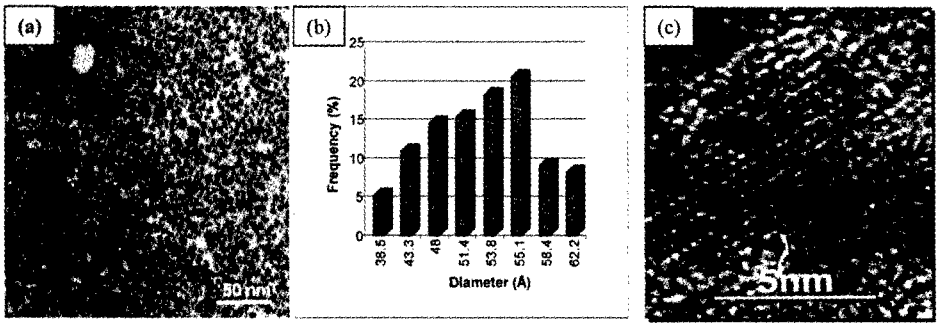


Figure 3. (a) TEM image of Mn doped CdS, (b) corresponding particle size distribution and (c) HRTEM image of a single quantum dot.

The ESR spectrum of a fresh powdered sample shows an intense broad signal, which could be attributed to Mn-Mn interactions (Figure 4a).[1,2,6] The ESR spectrum of a toluene solution of the same sample shows weak partially resolved hyperfine structure superimposed on a broad background signal (Figure 4b). This spectrum is characteristic of Mn^{2+} ions in a tetrahedral site which could be attributed to manganese incorporated into the CdS lattice. The spectrum of the sample taken 5 days later shows the resolution of the fine structure to have decreased (Figure 4c). The weak 6-line spectrum shows that manganese is present in the CdS lattice, the PL emission at 585 nm confirms the incorporation of Mn into the lattice. The ESR behaviour of the solid sample is probably due to poor resolution of the measurement by the instrument, beacause the subsequent measurements in solution and after a few days show the presence of the 6-line structure of Mn. The amount of Mn present in the sample as measured by ICP-AES analysis is 0.65 %, which is reasonably high compared to previous measurements.[6,7]

CONCLUSIONS

Nanoparticles of CdS and Mn-doped CdS close to mono-dispersed, capped with TOPO have been prepared by a single source route using bis(methylhexyldithiocarbamato)cadmium(II). The optical properties of the Mn doped CdS nanoparticles differ from those of CdS due to the presence of Mn in the crystal lattice. X-ray diffraction and electron microscopy show the particles to be nanometric in size with the hexagonal phase dominant. The ESR spectra confirm the presence of Mn in CdS lattice.

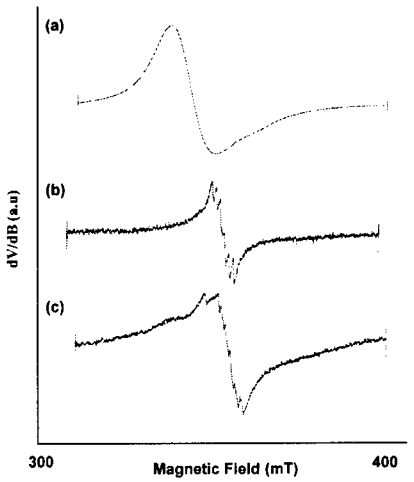


Figure 4. ESR spectra (a) solid Mn doped CdS, (b) in toluene solution (fresh) and (c) after weeks.

ACKNOWLEDGEMENTS

We thank the Royal Society and the National Research Foundation (NRF) for support to NR and a program of collaboration between UZULU and ICSTM. P.O.B thanks the EPSRC for grant. P.O.B was the Sumitomo/STS Professor of Materials Chemistry at IC and is Professor of Inorganic Materials at The Manchester Materials Science Centre and The Chemistry Department. We also thank M. Wei (IC) for Electron microscopy and Dr.A.D.Oduwole (QMW) for ESR spectroscopy.

REFERENCES

1. R.N. Bhargava, D. Gallagher, X. Hong and A. Nurmikko , Phys. Rev. Lett. **72**, 416 (1994).
2. D. Gallagher, W.E. Heady, J.M. Racz and R.N. Bhargava , J. Crystal Growth **138**, 970 (1994).
3. Y.L. Soo, Z.H. Ming, S.W. Huang, Y.H. Kao, R.N. Bhargava and D. Gallagher, Phys. Rev. **B50**, 7602(1994).
4. K. Sooklal, B.S. Cullum, S.M.Angel, and C.J.Murphy, J. Phys. Chem. **100**, 4551 (1994).
5. Y. Wang, N. Herron , K. Moller and T. Bein , Solid State Commun. **77**, 33 (1991).
6. L.Levy, N. Feltin, D. Ingert, and M.P. Pileni, J.Phys. Chem. B, **101**, 9153 (1997).
7. G. Counio, T. Gacoin and J.P. Boilot, J.Phys. Chem. B, **102**, 5237, (1998).
8. P O' Brien, D.J. Otway and J.R. Walsh, Adv. Mater. CVD, **3**, 227 (1997).
9. T. Trindade and P O' Brien, Adv. Mater., **8**, 161 (1996).
10. T. Trindade and P. O' Brien, Chem. Mater.,**9**, 523 (1997).
11. B. Ludolph, M.A. Malik, P. O' Brien and N. Revaprasadu, J.Chem. Soc. Chem. Commun., 1849 (1998).

Synthesis and Characterization of Strongly Fluorescent CdTe Nanocrystal Colloids

Frederic V. Mikulec and Moungi G. Bawendi
Department of Chemistry, Massachusetts Institute of Technology,
Cambridge, MA 02139

ABSTRACT

We present a synthesis of colloidal CdTe nanocrystals whose absolute room temperature quantum yields are routinely above 60%. The preparation is based on the trioctylphosphine oxide (TOPO) method reported by Murray, with a more stalbe tellurium precursor now used as the chalcogenide source. The photoluminescence is continuously tunable over the range 590-760 nm and is as narrow as 135 meV (45 nm) FWHM. No deep trap luminescence is detected for the diameter range 4-11 nm. CdTe nanocrystals are characterized by UV/vis absorption, photoluminescence emission, transmission electron microscopy, and powder X-ray diffraction.

INTRODUCTION

There exists a need for semiconductor nanocrystals which display narrow, intense band edge photoluminescence (PL), especially if such materials are to be routinely used in biological labeling experiments [1] or electroluminescent devices [2]. Recently reported (core)shell materials (CdSe)ZnS [3] and (CdSe)CdS [4] can achieve quantum yields as high as 50 and 85%, but these optimal values have only been seen for samples emitting in the green through orange (~ 490-590 nm) region of the spectrum. Far red emitters (> 620 nm) would cover a portion of the spectrum for which there is presently no nanocrystalline semiconductor material – and very few molecular dyes – with very narrow, intense band edge PL. Fluorophores which posses these qualities would be extremely useful for multicolor detection schemes and in whole blood assays. In this letter we present a synthesis of colloidal CdTe nanocrystals whose PL is much brighter, narrower, and cleaner than that of previously reported samples [5]. The PL can be tuned continuously from 590 to 760 nm, thus complementing the (core)shell work described above. The absolute quantum yield of the CdTe nanocrystals reported here is as high as 70% and – attesting to the reproducibility of the method – the average quantum yield of 15 of the best samples is 60 ± 8%. Like commercial laser dyes, solutions of these nanocrystals glow brightly in room lighting. These nanocrystals are as bright as the best (core)shell composites mentioned above, even though the CdTe samples do not yet have a protective inorganic overcoating.

EXPERIMENTAL

Synthesis of CdTe nanocrystals. Unless otherwise noted, all procedures are carried out under nitrogen. A stock solution of hexapropylphosphorustriamide telluride (HPPTTe) is prepared by adding 6.38 g tellurium shot (99.999%, low oxide, Alfa/Aesar) to 45.00 g hexa-n-propyl phosphorous triamide (97% Lancaster; distilled and collected from 83-103 °C @ 0.55 Torr {uncorrected}) and stirring until dissolved (1-2 days). Dimethyl cadmium (99+% Strem) (CAUTION: pyrophoric, toxic, readily absorbed

Mat. Res. Soc. Symp. Proc. Vol. 581 © 2000 Materials Research Society

through skin) is vacuum transferred to remove impurities. 20g TOPO (90% Strem) is dried under vacuum (~ 0.5 Torr) at 180 °C for 1 hour, then filled with N_2 and heated to 350 °C. In a N_2 atmosphere glovebox a solution containing 50 μL dimethyl cadmium (0.69 mmol), 0.35 mL HPPTTe stock (0.35 mmol), and 12 mL trioctylphosphine (95% Fluka) is mixed very well and loaded into a syringe. This solution is smoothly injected (~ 0.5 sec) into the vigorously stirring TOPO, which immediately turns red and cools to 270 °C. The initial UV/vis spectrum of an aliquot in hexane displays a first absorption feature at 570-580 nm. The temperature is raised to 290 °C and the sample is grown to the desired wavelength. The flask is then cooled to ~ 60 °C and mixed with 10 mL butanol.

Nanocrystals are isolated in air by a modified size selective precipitation with acetonitrile. Size selective precipitation using methanol was found to be unreliable. The reaction solution prepared above is mixed with an additional 10 mL butanol. Acetonitrile is added until the mixture becomes turbid. Upon sitting for a few minutes the solution separates into two layers. The colorless hydrophilic phase is removed and discarded. The clear red hydrophobic phase is mixed with approximately one third its original volume of butanol. The process of adding acetonitrile until turbidity and separating layers is repeated until a powder or very thick oil is obtained. Freshly prepared CdTe nanocrystals isolated in this fashion are moderately soluble in hexane and extremely soluble in tetrahydrofuran (THF). Addition of a small amount of TOP (~ 1% vol) and storage under N_2 helps preserve the luminescence intensity of the size selected material. Yields of crude CdTe range from 50 mg (small sizes) to 75 mg (large sizes) of dry powder.

RESULTS AND DISCUSSION

Our synthesis is based on the trioctylphosphine oxide (TOPO) method reported by Murray [6]. CdTe nanocrystals synthesized by this method possessed poor optical properties, owing to the low reaction temperatures necessitated by the relatively unstable chalcogenide precursor trioctylphosphine telluride. Even the first reported synthesis of trialkylphosphine tellurides mentions their facile room temperature decomposition [7]. In order to maintain controlled nucleation and growth of nanocrystals, lower injection temperatures had to be used (240 °C for CdTe vs. 300 °C for CdSe). Nanocrystals grown at lower temperatures generally display smaller quantum yield values. An improvement in precursor stability enables higher synthesis temperatures to be used; higher reaction temperatures improve both crystal quality and PL intensity. In searching for more stable compounds we were led to investigate tris(dialkylamino)phosphines by the report describing their improved "tellurium basicity," attibuted to lone pair donation by the phosphorus-bonded nitrogen atoms [8]. Dissolving elemental tellurium in tris(dialkylamino)phosphine produces a phosphine telluride precursor solution which is stable for months and easily incorporated into the TOPO based nanocrystal synthesis, allowing us to take advantage of this highly refined method.

CdTe nanocrystals were synthesized using a 1M tris(di-n-propylamino)phosphine telluride solution as the chalcogenide source. This precursor enables 350 °C injection temperatures to be used. Figure 1 displays representative absorption spectra for a series of CdTe nanocrystals ranging from ~ 4.4 to 13 nm in diameter. The position of the first absorption feature can be tuned continuously from 570 to 740 nm, clearly illustrating the effects of quantum confinement. The inset shows the variation of the first absorption

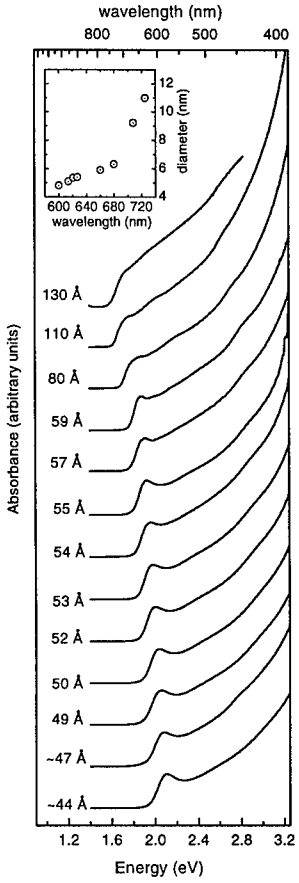


Figure 1. UV/vis absorption spectra of size-selected CdTe nanocrystals in hexane (RT). Inset: Relationship between lowest energy absorption feature and nanocrystal diameter, determined by TEM.

feature with diameter. Particle size was determined by high resolution transmission electron microscopy (HRTEM), with each data point representing the average of at least 250 (in most cases 500) measurements. The polydispersities of the samples in Figure 1 are in the range 10-20%.

Although there is nothing outstanding about the absorption spectra, the PL emission spectra display two quite remarkable features. Figure 2 shows room temperature emission spectra of aliquots of CdTe nanocrystals removed at different times during a single reaction. Emission spectra in hexane have been standardized relative to rhodamine 640 (quantum yield = 100%) so as to accurately reflect the quantum yield during synthesis. The inset in Figure 3 plots quantum yield as a function of time. The first noteworthy feature is simply the magnitude of the emission intensity. The highest quantum yields of correspondingly sized TOPO passivated CdSe are only 15%, so these CdTe nanocrystals have significantly improved emission properties.

The second improvement in luminescence properties is the lack of any low energy "deep trap" emission, even for the smallest CdTe sizes. Each spectrum in Figure 2 consists exclusively of band edge luminescence. This lack of deep trap emission in CdTe is a surprising result, since at room temperature nearly all colloidal semiconductor nanocrystal systems show some amount of non band edge luminescence. For example, although the smallest CdTe samples synthesized here (35-40 nm diameter) display no deep trap luminescence, the PL of correspondingly sized CdSe samples usually contains 10-30% deep trap emission. There is a significant difference between the positions of the valence and conduction bands of these materials relative to the vacuum level. For bulk CdTe the valence and conduction bands are 1.0 and 0.7 eV higher in energy than in CdSe [9]. These are very large offsets, and even though the corresponding values for nanocrystals are not accurately known, differences of similar magnitude are likely present. If the deep trap emission – which is known to be surface related – is caused by a surface chemical reaction involving one of the carriers, then the band offsets could be the explanation for the observed differences between CdTe and CdSe. In CdTe the hole is a weaker oxidizing agent (by ~ 1eV). A surface reaction involving a hole that occurs spontaneously in CdSe may not occur in CdTe. Such band offset considerations also affect the choice of materials for protective

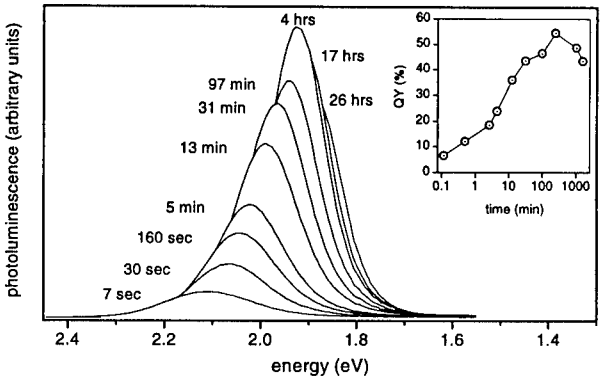


Figure 2. Evolution of the photoluminescence (PL) emission of CdTe nanocrystals during a typical synthesis (290 °C growth temperature). Inset shows the evolution of the quantum yield.

shell overcoatings (see below) and charge injection/extraction applications.

Figure 3 is a bright field high resolution transmission electron microscopy (HRTEM) image of a close packed monolayer of CdTe nanocrystals. During this study we observed that many particles display continuous lattice fringes (left nanocrystal, Figure 3 inset), although a small number clearly posses a stacking fault or crystal imperfection of some kind (right nanocrystal, Figure 3 inset). Most nanocrystals appear nearly spherical. Some of the largest sizes examined display evidence of faceting and contain a small population of distinctly prolate species. These are qualitatively the same observations recorded for CdSe nanocrystals [6,10].

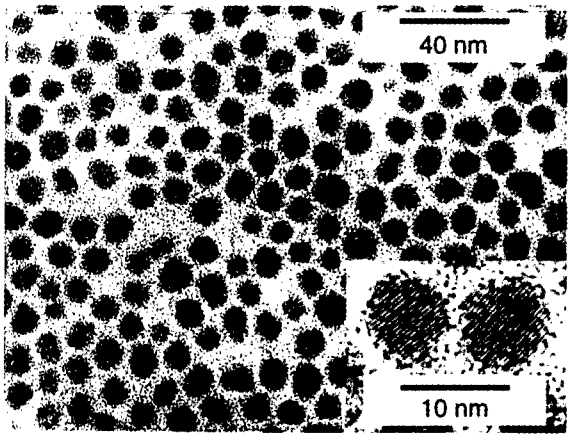


Figure 3. Bright field TEM image of a close-packed monolayer of CdTe nanocrystals. The inset shows two nanocrystals which display lattice fringes (3.7 Å spacing) due to the (111) plane.

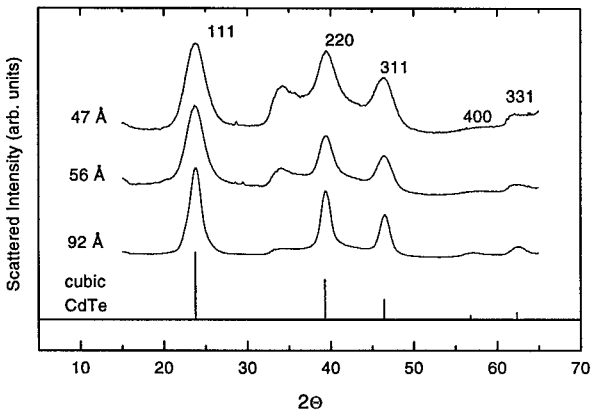


Figure 4. Powder X-ray diffraction (XRD) patterns (Cu anode) for three sizes of CdTe nanocrystals. The peak near 34 ° is likely due to a crystal imperfection.

Figure 4 displays powder X-ray diffraction (XRD) patterns from three different size CdTe samples. Peak positions match those of cubic CdTe, the thermodynamically stable bulk phase. The data clearly illustrate the well known line broadening seen with decreasing particle size. Particle diameter estimations using the Scherrer equation [11] and the full width at half maximum of the (111) reflection are only slightly smaller than those obtained by HRTEM (45, 54, 81, vs. 47, 56, 92 Å). Since the Scherrer method actually measures the coherence length of the X-rays, the fact that XRD sizes are close to HRTEM sizes implies that the samples are very crystalline in the direction perpendicular to the (111) plane. The identity of the peak at 34° is unknown, but the likely cause is a crystal imperfection. Theoretical modeling of the X-ray patterns is in progress to determine the true identity of this peak.

While high quantum yield from unovercoated or "bare" CdTe nanocrystals is very important in and of itself, it also affects the outcome of subsequent protective shell growth attempts. Empirical observations from (CdSe)ZnS and (CdSe)CdS studies [3,4] show that this overcoating process generally has a multiplicative effect on the quantum yield of the starting material: the brightest (core)shell samples generally come from the brightest nanocrystal cores. Bulk energy band offset considerations predict that a ZnS or a ZnSe shell provides potential energy barriers for both the CdTe electron and hole (a type I interface). Preliminary experiments confirm this assertion. Growth of ZnS or ZnSe shells onto a CdTe core produces a composite material which is much more robust during processing and manipulation, and also has a slightly higher quantum yield than the bare sample. Experiments are in progress to optimize this process and further characterize the (core)shell products.

REFERENCES

1. (a) Bruchez, M. J.; Moronne, M.; Gin, P.; Weiss, S.; Alivisatos, A. P. *Science* **1998**, *281*, 2013-2016. (b) Chan, W. C. W.; Nie, S. *Science* **1998**, *281*, 2016-2018.
2. (a) Colvin, V. L.; Schlamp, M. C.; Alivisatos, A. P. *Nature* **1994**, *370*, 354-357. (b) Dabbousi, B. O.; Bawendi, M. G.; Onitsuka, O.; Rubner, M. F. *App. Phys. Lett.* **1995**, *66*, 1316-1318. (c) Schlamp, M. C.; Peng, X. G.; Alivisatos, A. P. *J. Appl. Phys.* **1997**, *82*, 5837-5842. (d) Mattoussi, H.; Radzilowski, L. H.; Dabbousi, B. O.; Thomas, E. L.; Bawendi, M. G.; Rubner, M. F. *J. Appl. Phys.* **1998**, *83*, 7965-7974.
3. (a) Hines, M. A.; Guyot-Sionnest, P. *J. Phys. Chem.* **1996**, *100*, 468-471. (b) Dabbousi, B. O.; RodriguezViejo, J.; Mikulec, F. V.; Heine, J. R.; Mattoussi, H.; Ober, R.; Jensen, K. F.; Bawendi, M. G. *J. Phys. Chem. B* **1997**, *101*, 9463-9475.
4. Peng, X.; Schlamp, M. C.; Kadavanich, A. V.; Alivisatos, A. P. *J. Am. Chem. Soc.* **1997**, *119*, 7019-7029.
5. (a) Jarvis, R. F. J.; Müllenborn, M.; Yacobi, B. G.; Haegel, N. M.; Kaner, R. B. *Mat. Res. Soc. Symp. Proc.* **1992**, *272*, 229-234. (b) Rajh, T.; Micic, O. I.; Nozik, A. J. *J. Phys. Chem.* **1993**, *97*, 11999-12003. (c) Pehnt, M.; Schulz, D. L.; Curtis, C. J.; Jones, K. M.; Ginley, D. S. *App. Phys. Lett.* **1995**, *67*, 2176-2178. (d) Gao, M.; Kirstein, S.; Möhwald, H.; Rogach, A. L.; Kornowski, A.; Eychmüller, A.; Weller, H. *J. Phys. Chem. B* **1998**, *102*, 8360-8363.
6. Murray, C. B.; Norris, D. J.; Bawendi, M. G. *J. Am. Chem. Soc.* **1993**, *115*, 8706-8715.
7. (a) Zingaro, R. A. *J. Organomet. Chem.* **1963**, *1*, 200. (b) Zingaro, R. A.; Steeves, B. H.; Irgolic, K. *J. Organomet. Chem.* **1965**, *4*, 320-323.
8. Rømming, C.; Iversen, A. J.; Songstad, J. *Acta Chem. Scand. A* **1980**, *34*, 333-342.
9. Capasso, F.; Margaritondo, G. *Heterojunction Band Discontinuities: Physics and Device Applications*; Elsevier Science: New York, 1987.
10. Shiang, J. J.; Kadavanich, A. V.; Grubbs, R. K.; Alivisatos, A. P. *J. Phys. Chem.* **1995**, *99*, 17417-17422.
11. Guinier, A. *X-ray Diffraction in Crystals, Imperfect Crystals, and Amorphous Bodies*; W. H. Freeman and Company: San Francisco, 1963.

ELECTROCHEMICAL ATOMIC-LAYER EPITAXY: ELECTRODEPOSITION OF III-V AND II-VI COMPOUND SEMICONDUCTORS

Travis L. Wade*, Billy H. Flowers Jr.*, Raman Vaidyanathan*, Kenneth Mathe*, Clinton B. Maddox**, Uwe Happek** and John L. Stickney*,
*Department of Chemistry, **Department of Physics, University of Georgia, Athens, Georgia 30602

ABSTRACT

Electrochemical atomic-layer epitaxy (EC-ALE) is an approach to electrodepositing thin-films of compound semiconductors. It takes advantage of underpotential deposition (UPD), deposition of a surface limited amount (a monolayer or less) of an element at a potential less negative than bulk deposition, to form a thin-film of a compound--one atomic layer at a time. Ideally, the 2-D growth mode should promote epitaxial deposition.

Many II-VI and a few III-V compounds have been formed by EC-ALE. II-VI films such as CdSe, CdS, and CdTe have been successfully formed. In addition, deposition of III-V compounds of InAs and InSb are being explored, along with initial studies of GaAs deposition. Depositions of the II-VI systems are better understood so this report will focus on the III-V's, particularly InAs and InSb.

Building compounds an atomic layer at a time lends electrochemical-ALE to nanoscale technology. Deposited thickness ranged from a few nanometers to a few hundred. The films are typically characterized by atomic-force microscopy (AFM), X-ray diffraction (XRD), electron microprobe analysis (EPMA) and ellipsometry. InAs deposits are also characterized by infrared reflection absorption.

INTRODUCTION

The electronic and opto-electronics industries provide some of the largest markets and challenges for thin-film formation. Electrodeposition of metal films, such as Cu and Cr, are well studied and understood. Cu electrodeposition is becoming an important step in some ultra-large scale integration (ULSI) programs. Technology for the electrodeposition of semiconductors has lagged far behind that for metals, even though electrodeposition is generally performed near room temperature and is thus appealing as a low-temperature, low-interdiffusion technology. Electrodeposition also has the potential to form films on three-dimensional surfaces since line of sight deposition is not required.

Electrodeposition of II-VI compounds such as CdTe has been studied for many years,[1-4] and high efficiency photovoltaics, for instance, have been produced commercially. The standard compound electrodeposition methodology, codeposition, involves the use of a single solution, containing oxidized precursors for all the elements involved in the compound. The deposit is formed by reduction at a set potential or current density.[5-7] Some researchers have attempted to deposit III-V compounds in this way. However, reports of the electrodeposition of III-V compounds have been few, and have generally involved molten salts or post-electrodeposition annealing to produce the compound. GaAs,[8-11] InSb,[12] InP[13-15] and InAs [16-18] have been electrochemically formed using codeposition from either aqueous or nonaqueous solutions. As electrodeposited InAs showed XRD peaks due to elemental In, even though the

Mat. Res. Soc. Symp. Proc. Vol. 581 © 2000 Materials Research Society

composition was stoichiometric.[18] This highlights a major problem with compound electrodeposition: the need to maintain stoichiometry and form a phase pure material.

Recently, the electrochemical analog of atomic-layer epitaxy (ALE) has been developed to form compound thin films.[19-25] ALE refers to a methodology developed in the mid 70s for the formation of compounds an atomic layer at a time, using surface limited reactions.[26-28] Surface limited reactions encourage layer-by-layer growth, and thus epitaxial deposition. Surface limited reactions are well known in electrochemistry and are referred to as underpotential deposits.[29-31] By selecting a potential prior to (under) that needed to deposit an element on itself, an atomic layer of the element can frequently be formed on a second element. Electrochemical ALE then involves using these underpotentials to form individual atomic layer of the elements making up a compound, using a cycle. Different solutions and potentials are used for each element then they are alternated in a cycle. The cycle is repeated to achieve the desired deposit thickness.

The main benefit of electrochemical ALE is that it breaks the deposition process into a series of controllable steps, each of which can be optimized individually. The degrees of freedom available in compound electrodeposition are thus expanded, allowing the growth of materials that may not have been possible using conventional codeposition methodologies.

EXPERIMENTAL

Most of the hardware used in the present study has been described in previous articles.[20,21] The instrument consists of a series of solution reservoirs, pumps, a selection valve, a potentiostat and a thin-layer flow cell. A diagram of the flow cell is shown in Figure 1. The cell is designed for a flat substrate, laid on top of a gasket that defines a deposit area of about 1.0 cm by 2.8 cm. The silicone gasket (McMaster-Carr Supply; Atlanta, GA) was 0.4 mm thick, producing a cell volume of 0.11 ml. Laminar flow over the substrate was intended. The transparent indium tin oxide (ITO) (Delta Technologies, Limited; Stillwater, MN) auxiliary electrode was the opposite wall of the flow cell from the substrate. This allowed observation of the deposit during the deposition process, and provided an optimal current distribution.

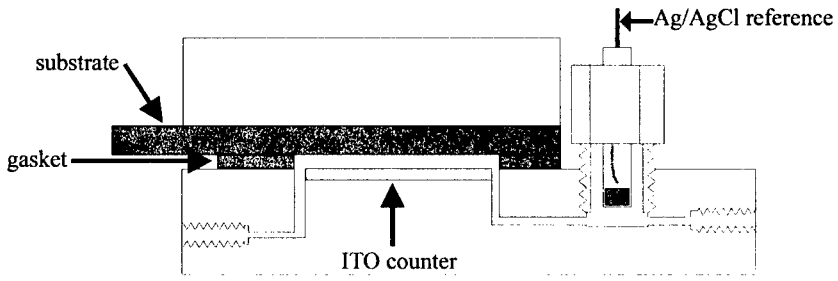


Figure 1. Deposition cell for EC-ALE.

The As_2O_3 concentration was 2.5 mM with a pH of 4.5, buffered with 50.0 mM $CH_3COONa{\cdot}3H_2O$. The $In_2(SO_4)_3$ concentration was 0.3 mM, pH of 3.0. A pH 3.0 blank solution was used as well. The Sb_2O_3 solution was pH 5.0, buffered with 50 mM $CH_3COONa{\cdot}3H_2O$. The concentration was less than 0.05 mM due to the insolubility of Sb_2O_3.[32] Solution pHs were adjusted with H_2SO_4. The supporting electrolyte was 0.1 M $NaClO_4$. Solutions were made with water from a Nanopure water filtration system (Barnstead; Dubuque, IA), fed by a house-distilled water line. All chemicals were reagent grade or better. The potentials were measured relative to a Ag/AgCl reference electrode (Bioanalytitical Systems, Inc.; West Lafayette, IN).

Substrates were glass microscope slides onto which a thin, 10 nm, film of Ti was first vapor deposited, followed by 400 nm of Au. The substrates were annealed in a tube furnace at 550 C for twelve hours under a stream of N_2 followed by H_2 flame anneal. They were cleaned before use by dipping in hot nitric acid (Fisher) and rinsing with Nanopure water. The surface appeared optically rough, but was composed of crystallites with atomically flat terraces as large as 150 nm, observed with an atomic force microscope (AFM) (NanoScope III; Digitial Instruments; Santa Barbara, CA).

Annealed Cu foil was also tried as a substrate for InSb deposition. The foil was cleaned in glacial CH_3COOH, rinsed with Nanopure water, and then annealed in the tube furnace for twelve hours at 700 C under flowing N_2. This procedure resulted in a highly terraced surface as seen by an optical microscope. The AFM revealed that it was very heterogeneous with micron-scale flat areas and stepped regions several atomic layers high.

Films were deposited on the substrates as follows: The cell was filled by a pump from a reservoir containing an electrolyte solution of the element of interest. A surface limited amount (~0.4 monolayers) of the element was deposited at a set potential. The cell was then rinsed with a blank electrolyte solution and filled with another electrolyte solution of the next element. A stoichiometric amount of this element was then deposited on the previous element and the cycle repeated.

RESULTS

From voltammetry, a program using –0.25 V for As UPD and –0.3 V for In UPD was suggested for the InAs cycle. In practice, the program worked for the first few cycles, but then the currents died out. This is understandable, considering that the potentials were chosen for deposition on a Au surface (Figure 2), not for deposition of the elements on the compound. The cycle was sequentially stepped more negative during the deposition by 10-25 mV per cycle. After about 25 cycles final deposition potentials of –0.775 V for In and –0.675 V for As were used for the rest of the deposit. Ellipsometric measurements (Sentech SE 400; Micro Photonics Inc.; Allentown, PA) were used to determine the thickness of the deposits.

Figure 2 is a glancing angle X-ray diffraction pattern (Scintag 2000) for a 500 cycle InAs film. The deposit was 160 nm thick. Diffraction maxima for InAs are evident, as are maxima for Au.[33] The breadths of the diffraction maxima suggest InAs crystallites of a few nanometers. The factors controlling deposit grain size are the subject of ongoing studies, but the lattice mismatch is probably a contributing factor. Earlier films showed larger crystallites, but also included maxima for elemental In.[34] Electron microprobe analysis (EPMA) reveals that the InAs films are As rich (As/In ~1.2). AFM analysis shows cauliflower morphology with round 50 nm features.

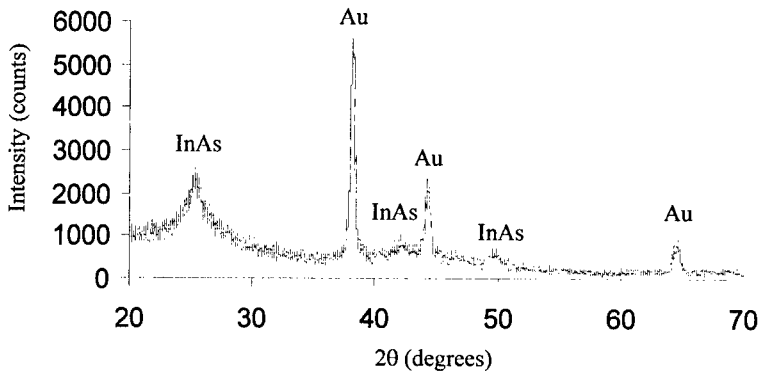


Figure 2. Glancing angle XRD pattern of electrodeposited InAs on Au.

Infrared absorption measurements were performed on the InAs films to determine the bandgap of the obtained material. Since the films are grown on a gold substrate, transmission measurements were not possible. Reflection measurements using a variable angle reflection rig in conjunction with a Bruker 66v FTIR spectrometer equipped with a cooled InSb detector were made. The incident angle of the p-polarized radiation was set to match the angle where the reflectance of parallel-polarized light is zero (Brewester's angle) for InAs.

The bandgap was estimated from the absorption measurements by plotting $(\alpha\ h\nu)^2$ versus $h\nu$, with α being the experimentally determined absorption coefficient and $h\nu$ the energy of the infrared radiation.[35] The analysis gave film bandgaps from 0.36 to 0.50 eV, the measurement for an InAs single crystal was 0.36 eV. We attribute this blue shift to the $1/D^2$ dependence of the bandgap on the diameter, D, of crystallites within the deposited film.[36-38]

InSb films were made in a manner very similar to the InAs films. However, the final potentials used for the In deposition were –0.670 V and –0.785 V for the Sb. Deposits made on Au had an Sb/In ratio of 1.1. They also had isolated areas that were rougher than the substrate. The rough areas were islands with an Sb/In ratio of 0.3. AFM revealed that the smother areas had morphology similar to the InAs deposits. The less stable element, In, is apparently depositing three-dimensionally in these areas.

Annealed Cu foil was also tried as a substrate for InSb deposition. Optical images, taken at 1000 magnification, of the foil and an InSb deposit on it are shown in figure 3. The deposit was run for 200 cycles. As can be seen deposit is very conformal with the Cu foil. Ellipsommetry of this gave a thickness of 68 nm.

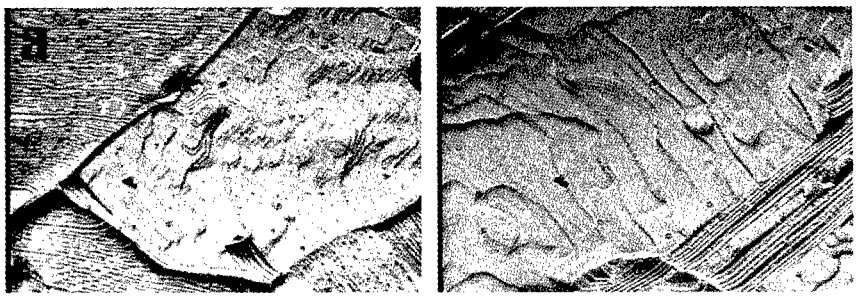


Figure 3. (a) 1000 x optical image of annealed Cu foil; (b) 1000 x optical image of InSb electrodeposited on annealed foil by EC-ALE.

ACKNOWLEDGEMENTS

Support of the NSF-DMR is gratefully acknowledged, as is support of Dr. Travis Wade by a grant from the University of Georgia's research foundation (UGARF).

REFERENCES

1. G. F. Fulop and R. M.Taylor, Ann. Rev. Mater. *Sci.*, **15**, p. 197 (1985).
2. K. Rajeshwar, Adv. Mater., **4**, p. 23 (1992).
3. G. Hodes, Sol. Energy Mater., **32**, p. 323 (1994).
4. R. K. Pandey, S. N. Sahu and S. Chandra, *Handbook of Semiconductor Electrodeposition*, Vol. 5, Marcel Dekker, Inc., New York, (1996).
5. H. Gobrecht, H. D. Liess, and A. Tausend, Ber. Bunsenges. Phys. Chem., **67**, p. 930 (1963).
6. G. Hodes, J. Manassen, and D. Cahen, D. Nature, **261**, p. 403 (1976).
7. M. P. R. Panicker, M. Knaster, and F. A. Kroger, J. Electrochem. Soc., **125**, p. 566 (1978).
8. S. Chandra and N. Khare, Semicond. Sci. Technol., **2**, p. 220 (1987).
9. Y. K. Gao, A. Z. Han, Y. Q. Lin, Y. C. Zhao and J. D. Zhang, Thin Solid Films, **232**, p. 278 (1993).
10. Y. Gao, A. Han, Y. Lin, Y. Zhao and J. Zhang, J. Appl. Phys., **75**, p. 549 (1994).
11. K. S. Murali, V. Subramanian, N. Rangarajan, A. S. Lakshmanan and S. K. Rangarajan, Journal of Materials Science-Materials in Electronics, **2**, p. 149 (1991).
12. J. Ortega and J. Herrero, J. Electrochem. Soc., **136**, p. 3388 (1989).
13. S. N. Sahu, J. Mater. Sci. Lett., **8**, p. 533 (1989).
14. S. N. Sahu, *J. Mater. Sci.*, **3**, p. 102 (1992).
15. S. N. Sahu, Journal of Materials Science-Materials in Electronics, **3**, p. 102 (1992).
16. G. Mengoli, M. M. Musiani and F. Paolucci, J. Electroanal. Chem., **332**, p. 199 (1992).
17. S. Cattarin, M. Musiani, U. Casellato, G. Rossetto, G. Razzini, F. Decker and B. Scrosati, J. Electrochem. Soc., **142**, p. 1267 (1995).
18. E. Dalchiel, S. Cattarin, M. Musiani, U. Casellato, P. Guerriero, G. Rossetto, *J.* Electroanal. Chem., **418**, p. 83 (1996)

19. B. W. Gregory, D. W. Suggs and J. L. Stickney, J. Electrochem. Soc., *138*, p. 1279 (1991).
20. B. M. Huang, L. P. Colletti, B. W. Gregory, J. L. Anderson and J. L. Stickney, J. Electrochem. Soc., **142**, p. 3007 (1995).
21. L. P. Colletti, B. H. Flowers Jr. and J. L. Stickney, J. Electrochem. Soc., **145**, p. 1442 (1998).
22. L. P. Colletti and J. L. Stickney, J. Electrochem. Soc., **145**, p. 3594 (1998).
23. U. Demir and C. Shannon, Langmuir, **10**, p. 2794 (1994).
24. G. D. Aloisi, M. Cavallini, M. Innocenti, M. L. Foresti, G. Pezzatini and R. Guidelli, J. Phys. Chem., **101**, p. 4774 (1997).
25. I. Nandhakumar and B. Hayden, J. Phys. Chem., **102**, p. 4897 (1998).
26. C. H. L. Goodman and M. V. Pessa, J. Appl. Phys., **60**, R65 (1986).
27. *Atomic Layer Growth and Processing*; T. F. Kuech, P. D. Dapkus and Y. Aoyagi, Editors, Vol. 222, p. 360, Materials Research Society, Pittsburgh, (1991).
28. S. Bedair, in *Atomic Layer Epitaxy*; S. Bedair, Editor, p.304, Elsevier, Amsterdam, (1993).
29. D. M. Kolb, in *Physical and Electrochemcial Properties of Metal Monolayers on Metallic Substrates*; D. M. Kolb, Editor, Vol.11, p.125, John Wiley, New York, (1978).
30. R. R Adzic, in *Advances in Electrochemistry and Electrochemical Engineering*; H. Gerishcher, and C. W. Tobias, Editors, Vol. 13, p. 159, Wiley-Interscience, New York, (1984).
31. A. A. Gewirth and B. K. Niece, Chem. Rev., **97**, p. 1129 (1997).
32. G. Jung, and C. K. Rhee, J. Electroanal. Chem. **438**, p. 277 (1977).
33. *Powder Diffraction File Alphabetical Index, Inorganic Phases*; W. F. McClune, Editor, Card Numbers: InAs, (15-869); In, (5-642); Au, (4-784), JCPDS International Center for Diffraction Data, Swarthmore, PA, (1992).
34. T. L. Wade, L. C. Ward, C. B. Maddox, U. Happek, and J. L. Stickney, Electrochemical and Solid-State Letters, **2**, p. 616 (1999).
35. K. Seeger, in *Semiconductor Physics* p. 40, Springer Series in Solid State Science, Springer Verlag, New York, (1982).
36. O. Alvarez-Fregoso, J. G. Mendoza-Alvarez, and O. Zelaya-Angle, J. Appl. Phys., **82**, p. 708 (1997).
37. L. Levy, D. Ingert, N. Feltin and M. P. Pileni, Journal of Crystal Growth, **184/185**, p. 377 (1998).
38. T. van Buuren, L. N. Dinh, L. L. Chase, W. J. Siekhaus, and L. J. Terminello, Phys. Rev. Lett., **80**, p. 3803 (1998).

NANOCRYSTALLINE ALLOYS OF II-VI SEMICONDUCTORS FROM MOLECULAR MULTI-LAYER TEMPLATES

L. CRISTOFOLINI*, P. FACCI**, M.P. FONTANA*
*Dipartimento di Fisica and INFM, Università di Parma, Parco Area delle Scienze 7/A, I-43100 Parma, Italy. Cristofolini@fis.unipr.it
** INFM and Università della Tuscia, Viterbo, Italy.

ABSTRACT

We present the synthesis and characterization of nanocrystalline II-VI semiconductors of mixed composition (CdSe/ZnSe, CdS) grown in fatty acid Langmuir-Schaefer multi-layer templates. The controlled production of *i)* homogeneous nanocrystalline $Cd_xZn_{1-x}Se$ alloys and *ii)* heterogeneous mixtures of different pure composition II-VI semiconductors such as CdSe and ZnSe provides, in addition to the size control, the parameter of the chemical composition for the fine tuning of the electronic properties. The samples are characterized by optical and quasi-resonance micro-Raman spectroscopy.

INTRODUCTION

Among semiconductor nanostructures particularly interesting are nanocrystals or nanoclusters, given the relative ease and inexpensiveness of their production. Nanocrystals exhibit a wide range of properties which can be altered just by size control. The case of II-VI family semiconductors is paradigmatic. For instance, in CdS nanocrystals the value of the band gap can be varied from 2.5 (bulk value) to 4 eV; the melting point ranges from 1600 to 400°C; the pressure required to induce solid-solid phase transitions (e.g. zinc blend to rock salt structure) increases from 2 to 9 GPa [1].

The possibility of size-tailoring the properties of semiconductor nanocrystals along with that of their synthesis in different environments has also led to interesting studies aimed to exploit their properties in fields such as e.g. nanoelectronics [2] and non-linear optics [3]. Indeed, semiconductor nanocrystals have been synthesized so far in various environments and using several different chemical-physical techniques (see f.i. [4])

Among the several approaches developed for the nanocrystal synthesis, that which takes advantage of the lamellar structure of fatty acid salt Langmuir-Schaefer films used as templates [5] has been shown to provide an easy route for achieving clusters of about 3 nm in size, embedded in an organic matrix which prevents them from degradation. This special synthesis moreover, allows to exploit the "plasticity" of the Langmuir-Schaefer architecture for coating electrodes, screens, etc. with a thin film of semiconductor nanoclusters [6]. Nanocrystals produced by this technique can be partially tailored in size by processing with chemical (washing in non polar solvent [7]) or physical (thermal annealing [8]) means and display structural anisotropy and consequent different electronic properties in the non-degenerate spatial orientations (in-plane vs out-of-plane). However, since the synthetic route is mainly ruled by the template structure, the available range of sizes is not very large. Therefore, it would be very interesting to have techniques which can finely tune the electronic structure and properties of these nanocrystals not only by size, but also by chemical composition.

We report the synthesis, optical and Raman characterization of mixed CdSe-ZnSe

Mat. Res. Soc. Symp. Proc. Vol. 581 © 2000 Materials Research Society

nanocrystals obtained by the LS template approach. The composition of the mixed crystals has been obtained by varying the concentration of the relative salts in aqueous sub-phase of the Langmuir trough, demonstrating the possibility of a fine tuning of the band gap in semiconductor nanocrystals not only by size-tailoring but also by varying chemical composition. The mixed nanocrystals stoichiometry was verified by means of the observed two mode behavior of the LO fundamental Resonance Raman peak. Furthermore, through variations in Raman LO peak position and shape- and in Linear Dichroism spectra - we were able to determine the effects on the nanoparticles shape and size of the sample preparation and of the following treatments (for a preliminary report, see [8]).

EXPERIMENTAL

Nanoparticle $Cd_xZn_{1-x}Se$ multi-layers were prepared according to the following protocol: in the high purity water sub-phase of a commercial trough (KSV-5000) we dissolved a mixture of metal chlorides $(CdCl_2)_x/(ZnCl_2)_{(1-x)}$ - with varying composition parameter x - for a total concentration of 1mM; a chloroform solution of arachidic acid (1mg/ml) was then spread onto the liquid surface and slowly compressed up to the surface pressure of 28mN/m. After a suitable incubation time, typically 100 layers of metal (Cd, Zn) arachidate were transferred onto clean Si or quartz substrates (for Raman and UV-Vis spectrometry respectively) by the horizontal dipping (Langmuir Schaefer, LS) technique. As we demonstrate in the following, the composition x of the salt dissolved in the sub-phase determines the final composition of the nanocrystals.

The multi-layers were then exposed to a hydrogen selenide or sulfide (H_2Se, H_2S) atmosphere for a minimum of 12 hrs and a maximum of 5 days. The acid was produced by reaction of FeSe or FeS with 1:1 water-diluted HCl in a glass reactor connected trough suitable glass/Teflon piping to the sample chamber. The formation of the semiconducting metal-selenide implies the reduction of the metal-arachidate into arachidic acid. We routinely followed the completion of the reaction by monitoring the FT-IR absorption due to the $-COO^-$ and -COOH subgroup vibrations, which occur at $1540cm^{-1}$ and $1701cm^{-1}$ respectively.

The micro-Raman spectra were collected at RT in back-scattering geometry with a long working distance/high numeric aperture 50x objective. The scattered light was appropriately filtered and detected with a LN_2 cooled CCD micro-Raman spectrometer. The excitation light was provided by an Ar^+ laser with wavelength λ=488.0 nm, power on the sample $\approx$1mW. We have also used the 632.8nm He-Ne laser line to investigate resonance effects. The sample was placed at an angle of $\approx 45°$ with the optical axis of the system, in order to maximize the amplitude of the Raman signal. The optical characteristics of the notch filter imposed a 150 cm^{-1} lower limit on the spectral range of the spectrometer, so that basically only the higher frequency LO phonons could be observed. Our spectral resolution was 3 cm^{-1} and typical integration time was 10-15 sec. Finally, optical absorption spectra were taken with a double beam spectrophotometer equipped with a Glan-Thompsom quartz linear polarizer mounted on a goniometer (accuracy 1°). In the case of polarized spectra, V and H polarized absorption was measured with the sample oriented at 45° to the direction of incident light in the wavelength range 250-500 nm. The LD parameter $LD=(A_V-A_H)/(A_V+A_H)$ was then calculated from the measured spectra.

RESULTS AND DISCUSSION

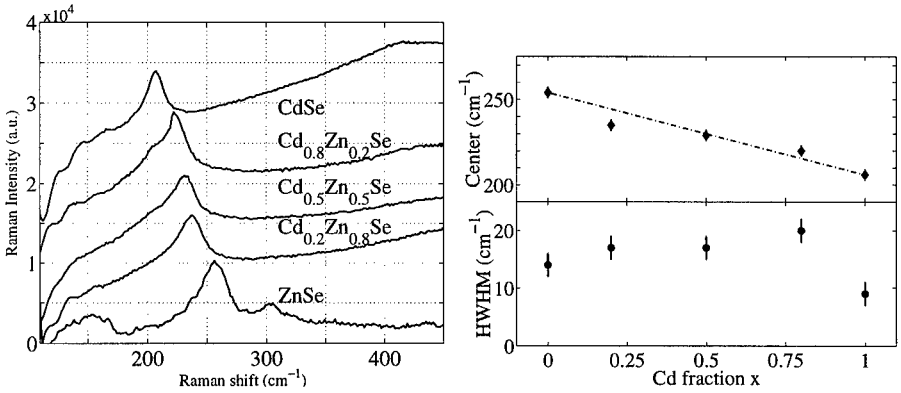


Figure 1: **Left:** *Raman spectra of nanocrystals of different $Cd_xZn_{1-x}Se$ compositions.* **Right:** *LO phonon peak position (top panel) and width (bottom panel) in $Cd_xZn_{1-x}Se$ as a function of the composition parameter x, the line is a guide to the eye.*

We first characterized the multi-layers by UV-Vis spectrometry. The onsets of the absorption bands in bulk CdSe and ZnSe (which occur at 720 nm and 480 nm respectively at RT) are known to blue shift when the particle size is reduced [1] due to quantum confinement effects. In spite of a broad distribution of the observed onset of the absorption, which is most probably due to the particle size distribution, and which results in a smearing of the feature, we measured a blue shift of the order of 100 nm, which is consistent with the previously found blue-shift from the bulk value of 520 nm to 400 nm in 1.5-2 nm size CdS nanoparticles [8]. The broad distribution of particle sizes probed by the UV-Vis spectrometry results in a relaxation of the sharpness of the conditions for resonance Raman scattering. Raman spectroscopy has been used to study the small size-induced folding of acoustic vibrations, the structural and morphological non-homogeneities via their effect on the position, width and shape of selected vibrations, particularly the LO phonons, the quantum size effects on electron-vibration coupling [9]. In the case of II-VI semiconductors Raman spectroscopy is particularly useful since their band gaps fall in the visible part of the spectrum, thus allowing the dramatic signal enhancement due to resonance effects and the further useful size dependent effects connected with the fundamental mechanism of resonant Raman scattering [10]. Furthermore in CdS nanocrystals of varying size (1 to 7 nm) the Resonance Raman LO phonon energy is found almost independent on the particle size, while its width increases with decreasing the particle size [9]. In CdSe nanoparticles (45±3Å in size) the Raman intensity of the LO phonon and of its overtones was used to determine the size of the nanocrystals and the strength of the coupling between the HOMO-LUMO transition and the LO phonon in the nanoparticles [11]. In our case we collected spectra with a given excitation wavelength, thus most effectively probing those nanoparticles whose band gap more closely matches the energy of the excitation light. In spite of the broad distribution of particles sizes, resonance Raman scattering selects a narrow distribution, whose peak however depends on the excitation wavelength. This can lead to the complication that

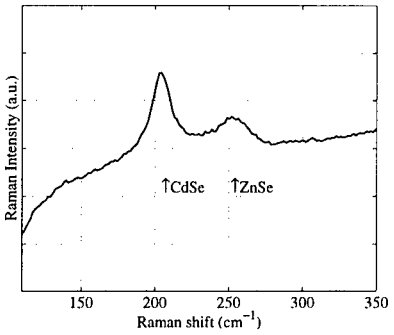


Figure 2: *Raman simultaneous observation of the LO phonon peaks of CdSe and ZnSe in a single multi-layer. The arrows mark the energy of the LO phonons in CdSe and ZnSe.*

upon changing the wavelength, as is customarily done in resonance Raman studies, two parameters are simultaneously changed: the resonance condition, and the effective particle size probed. Keeping this in mind, we selected the excitation wavelength λ=488nm because it effectively couples with $Cd_xZn_{1-x}Se$ nanoparticles of all compositions x in a quasi-resonance Raman condition, thus minimizing the effect of changing the effective resonance condition with particle size, and still yield spectra with good signal to noise ratio. The LO phonon is characterized by different energies in different compounds: 305 cm^{-1} in CdS, 205 cm^{-1} in CdSe, 253 cm^{-1} in ZnSe [1]. In the present work we use the shift in energy of the LO phonon and its broadening to infer information about the composition and the inhomogeneities of the $Cd_xZn_{1-x}Se$ nanoparticles.

In figure 1, left panel we compare the Raman spectra collected on multi-layers of different $Cd_xZn_{1-x}Se$ compositions x. In each spectrum the peak corresponds to the LO phonon in that particular compound. It is evident that the LO phonon energy shifts smoothly as the composition x is varied, from 205 cm^{-1} in CdSe to 253 cm^{-1} in ZnSe. The decrease in the Raman intensity on the low energy side of all the spectra is due to the effect of the Notch filter. In figure 1 (top right panel) we report the fitted Raman peak positions; its continuous shift as a function of the composition parameter x indicates the formation of an homogeneous solid solutions $Cd_xZn_{1-x}Se$ for each composition. The width of the LO peak (bottom right panel of Fig. 1) is invariably higher in the intermediate compositions than in pure CdSe or ZnSe. This may be attributed to the local structure which is more disordered in the alloys than in the pure compounds, due to composition fluctuations and/or to lattice mismatch.

We have also shown the possibility of producing heterogeneous mixtures of nanocrystals of different composition. We started by synthesizing a CdSe nanocrystal multilayer as described above. The sample was subsequently kept in $ZnCl_2$ 1mM water solution for 16 hours. This reverted almost completely the arachidic acid into Zn-arachidate, as checked by FT-IR absorption, while leaving the adherent CdSe nanocrystals unchanged, as checked by the observation of the corresponding Raman peak. The sample was then exposed to H_2Se for 24 hours, which allowed the production of ZnSe nanocrystals by reducing the Zn-arachidate

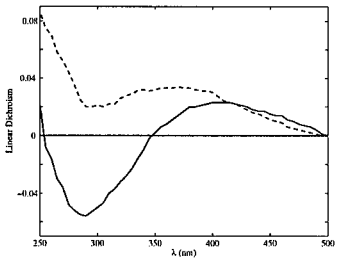


Figure 3: *Linear dichroism in CdS nanoparticles. The dashed line is the fatty acid-CdS nanocluster sample, while the solid line is the same sample after washing in chloroform.*

to arachidic acid, as checked by FT-IR. The resulting film, as characterized by Raman spectroscopy (figure 2), shows the simultaneous presence of the CdSe and ZnSe nanocrystals, as indicated by the two, distinct, LO phonon peaks. By this procedure we have exploited the arachidic acid matrix as a template for the repeated production of nanocrystals of different compositions.

Finally, we wish to report on the effects of washing the sample with non polar solvents, (typically $CHCl_3$ or benzene) and of thermal annealing on the pre-formed samples. Both these approaches influence the size of the nanocrystals as shown by variations of the onset of their optical absorbance and the ratio of the first overtone to fundamental LO peak in Raman spectra. In particular, the washing action, while removing up to 95% of the organic matrix, induces an increase of the effective nanocrystal size. This was shown (Fig. 3) in the case of CdS by the analysis of dichroic optical absorption spectra of the samples before and after washing: in particular, we measured a shift in the in-plane optical absorption onset from 400 to 450 nm; according to the Empirical Pseudopotential Method developed by Rama Krishna and Friesner [12], this would indicate a size increase from 3 to about 4.5 nm. We note that this increase does not seem to alter the shape, and in particular the anisotropy, of our nanocrystals, as evidenced by both dichroic absorption and polarized resonant Raman data. In fact the lower energy part of both the dichroic spectra show a decrease of the ratio which is connected to the increase of the absorption polarized in the direction perpendicular to that of the film plane. This fact implies a remarkable anisotropy in the nanocrystal shape (a nanocluster thickness of 1.5-2 nm can be inferred from the position of the onset of the absorption band using the out-of-plane polarization). Note that the washing treatment (dashed curve) has also led to the loss of dichroism at higher energies: this shows that such continuous background is due to the Rayleigh scattering from highly anisotropic fatty acid domains. On the other hand, thermal annealing performed for 1 h at 50°C (i.e. below the melting point of the organic matrix), shows a systematic increase of the integrated overtone to fundamental ratio in the LO peak, suggesting that the nanocrystal size has increased. In this case, however, the quantification of the effect is more problematic since varying the crystal size affects also the resonance conditions for Raman scattering. A possible explanation can be found in the result that if annealing is performed above the organic arachidate melting temperature (f.i. 100°C), the integrated overtone to fundamental

ratio tends to decrease and LD is destroyed. This fact is connected with the irreversible loss of the lamellar order of the original template (melting of the LS film) which results in an average of the anisotropic nanocrystal orientations and possibly in a loss of the anisotropy, which was due after all to the growth in the confined geometry of the fatty acid.

CONCLUSIONS.

By FT-IR and quasi-resonance Raman spectroscopy we have demonstrated the controlled production of *i)* homogeneous nanocrystalline $Cd_xZn_{1-x}Se$ alloys and *ii)* heterogeneous mixtures of different pure composition II-VI semiconductors such as CdSe and ZnSe. The annealing may have two effects: that of disordering the fatty acid matrix to a larger or smaller extent depending on temperature, and hence lead to an isotropization of the orientational distribution of the nanocrystals, and that of allowing growth in the "third" dimension, which would reduce the anisotropy of the single nanocrystal.

References

[1] A.P. Alivisatos J. Phys. Chem. 100, 13226 (1996); S.V. Gaponenko, Optical properties of semiconducting nano-crystals, Cambridge University Press (1998).

[2] D.L. Klein, R. Roth, A.K.L. Lim, A. P. Alivisatos, P.L. McEuen Nature 389, 699 (1997).

[3] S. Schmitt-Rink, D.A.B. Miller, D.S. Chemla Phys. Rev. B: Condens. Matter 35, 8113 (1987).

[4] L.E. Brus J. Phys. Chem. 91, 257 (1987); Y. Wang and W. Mahler Opt. Commun. 61, 233 (1987); A.J. Ekimov, A. Onushchenko JEPT Lett. 40, 1136 (1984); Y. Wang, N. Herron J. Phys. Chem. 91, 257 (1987); M.P. Pileni J. Phys. Chem. 97, 6961 (1993). K.K.W. Wong, S. Mann Adv. Mater 8, 928 (1996).

[5] E.S. Smotkhin, C. Lee, A.J. Bard, A. Champion, M.A. Fox, T.E. Mallouk, S.I. Webber, J.M. White Chem. Phys. Lett., 152, 265 (1988).

[6] P. Facci, V. Erokhin, S. Carrara, C. Nicolini Proc. Natl. Acad. Sci. 93, 10556 (1996); V. Erokhin, P. Facci, L. Gobbi, S. Dante, F. Rustichelli, C. Nicolini Thin Solid Films 327-329, 503 (1998).

[7] P. Facci, V. Erokhin, A. Tronin, C. Nicolini J. Phys. Chem. 98, 13323 (1994).

[8] P. Facci, M. P. Fontana, Solid State Comm. 108, 5 (1998).

[9] J.J. Shiang, S.H. Risbud, A.P. Alivisatos, J. Chem. Phys. 98, 8432 (1993).

[10] M. Cardona, and G. Gntherodt (Eds.), Light Scattering in Solids II, Topics in Applied Physics, Vol. 50. Springer, Berlin Heidelberg, New York, (1982).

[11] A.P. Alivisatos, T.D. Harris, P.J. Carrol, M.L.Steigerwald, L.E.Brus J. Chem. Phys. 90, 3463 (1989).

[12] M.V. Rama Krishna, R.A. Friesner, J. Chem. Phys. 95, 8309 (1991).

SOLAR CELL CONTACTS USING NANO-SIZED DISPERSIONS

Doug Schulz, R. Ribelin, X. Wu, K.M. Jones, R.J. Matson, C.J. Curtis, T. Gessert, D.S. Ginley
National Renewable Energy Laboratory, Golden, CO, USA 80401-3393

ABSTRACT

Nano-sized dispersions have been employed as precursor inks for the spray deposition of contacts to both Si and CdTe materials. In the case of Si, nano-sized Al particles (nano-Al) were dispersed and spray deposited onto p-type Si. Annealing above the eutectic temperature causes alloy formation yielding a p+ layer with $\rho \sim 10^{-4}$ Ω•cm. For CdTe, nano-sized Te particles (nano-Te) were dispersed and sprayed onto CdTe/CdS/SnO_2/glass heterostructures. Contact to the CdTe layer occurred during a 30 min anneal in He (T = 215 to 255 °C). These solar cells were finished by spin-coating the Te layer with Ag paint and subsequently annealing in air (100 °C / 1 h). This approach produces solar cells with open circuit voltages (V_{oc}) from 720 to 800 mV, short circuit current densities (J_{sc}) from 18 to 20 mA/cm^2 and efficiencies up to 10.3%. The performance of these cells was similar to those produced using the standard NREL contact.

INTRODUCTION

Solar cells are semiconductor devices that transform incident photons into usable electrical energy through the photovoltaic effect. As no C fuel is used in this process, it is considered a green energy source. With increasing concerns about the environmental effects of greenhouse gases, solar energy alternatives are being more closely examined for central power applications. Photovoltaics offer a viable alternative, but, the transition from the present markets to mainstream power generation may require some device/process improvements.

One metric often quoted as a break-even point for solar-derived electricity (i.e., becomes competitive with C-based fuel) is $1/Watt for new panels. Today, commercial solar panels cost ~ $4/Watt. Reducing the cost to $1/Watt, and thereby bringing solar energy into the electrical energy generation marketplace, can be realized by one of two ways:

1. Reduction of the costs to produce product;
2. Increase in the efficiency of the product.

We are evaluating the use of nano-sized dispersions for the spray deposition of contacts to solar cells. We anticipate that the technique should be useful for both cost reduction and efficiency maximization. Potentially, production costs can be markedly decreased as the capital investment of spray deposition (i.e., $10Ks) is orders of magnitude lower than for vacuum systems (i.e., $1Ms). In addition, the use of nano-sized dispersions may provide a number of advantages: (1) improved alloying owing to improved contact areas; (2) the ability to direct write hundred-micron features (e.g., ink jet); and, (3) the ability to easily change the stoichiometry of the sprayed film by modifying the dispersion composition.

Mat. Res. Soc. Symp. Proc. Vol. 581 © 2000 Materials Research Society

In this paper we present results on two efforts to improve the large area back contacts on solar cells by spray depositing nano-sized dispersions. In each example, the goal is to produce a highly-doped p+ layer on a p-type semiconductor which, in turn, can be easily contacted for current extraction. Towards increased efficiency via improved alloying, we use nano-Al as an alternative to micron-Al for p+ contact to Si. Towards cost reduction, we use spray deposition as an alternative to sputtering for the application of Te as a contact to CdTe solar cells. In each case, our initial results are very encouraging.

EXPERIMENTAL AND RESULTS

Solar cells are multilayer devices consisting typically of an opaque electrode, a junction region where the photons are absorbed and carriers generated, and a transparent electrode. For example, Figure 1a shows a typical Si solar cell and Figure 1b a CdTe solar cell. For Si, one side is p-doped and the other n-doped to form a homojunction. Contact is normally made to the p- and n-type sides by alloying Al and Ag metals to form p+ and n+ contacts, respectively. These Al and Ag contacts act as both contacts and electrodes, with sunlight passing between Ag grid lines. For CdTe, the incident sunlight passes through a glass superstrate that is coated with a transparent conductor, a heterojunction partner (i.e., n-type CdS) and then a photon absorbing p-type CdTe layer. Contact is made to the back-side of the CdTe layer with one of many p+ materials (e.g., Hg(Cu)Te [1,2], Sb-Te [2,3], or Te [4]). A metal electrode (e.g., Ag or Al) is placed on top of the p+ contact layer.

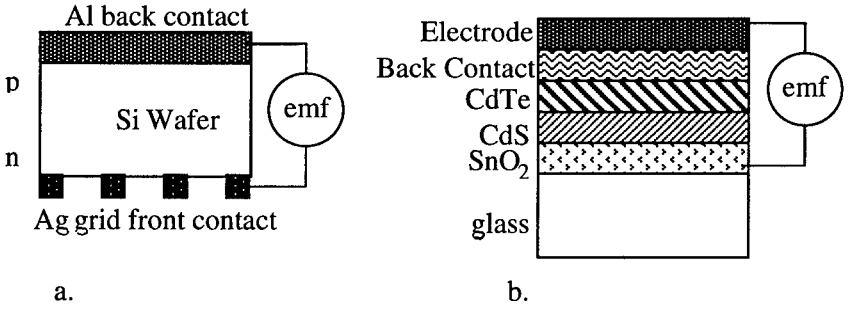


Figure 1. Pictorial representations of (a) a Si solar cell and (b) a CdTe solar cell.

Nano-Al Back Contacts To Silicon

Nano-Al was obtained from the Argonide Corporation (Sanford, FL) and was produced by an electroexplosion process. TEM characterization of this dry powder shows crystalline particles 10 to 500 nm in diameter. This nano-Al was dispersed in an organic solvent and directly spray deposited onto the p-doped side of a Si wafer giving a film approximately 1 μm in thickness (Fig. 2a). This nano-Al on Si film was loaded into a quartz tube and the tube was purged with N_2 (g). A 10 min anneal was performed at a temperature greater than the Al-Si

eutectic point. Figure 2b shows an SEM image of one such annealed nano-Al on Si film. Surface resistance (R_s) measurement was performed using 4 point probe. A value of 1.4 Ω/square was observed which, given a 1 μm thick film, corresponds to $\rho \sim 10^{-4}$ Ω•cm. This value is quite encouraging and plans are underway to fabricate solar cells using these contacts.

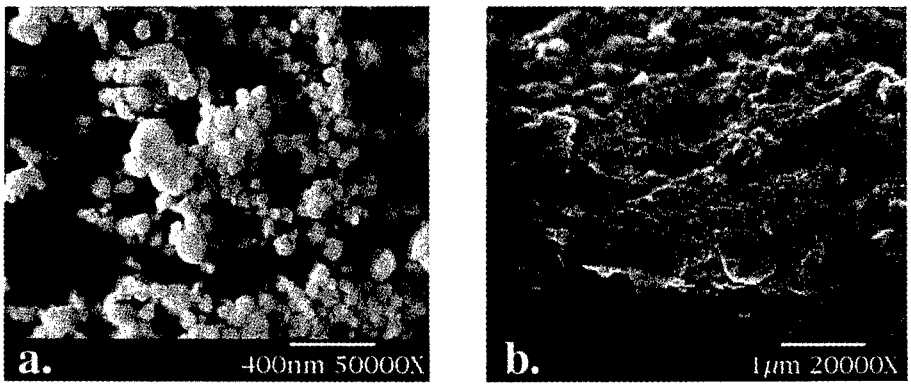


Figure 2. SEM images of nano-Al on Si films (a) as-sprayed; and (b) after an anneal under N_2.

Nano-Te Back Contacts to CdTe

Nano-Te was synthesized by oxidation of sodium telluride in methanol, e.g.,

$$Na_2Te + \text{oxidant} \xrightarrow{\text{methanol}, -78^{\circ}C} \text{Nano} - \text{Te} + \text{sodium salts} \qquad (1)$$

TEM characterization of the product nano-Te shows 50 to 200 nm primary particles with some agglomeration. TEM-EDS shows an oxygen impurity in the product with a peak height Te to O ratio ~ 8. These nanoparticles were dispersed in an organic solvent and spray deposited onto CdTe/CdS/SnO_2/glass heterostructures. The CdTe heterostructures were obtained from First Solar, Inc. (Toledo, OH). Figure 3 shows SEM images of the as-deposited Te layer on the CdTe heterostructure at low (Fig. 3a) and high (Fig. 3b) magnification. Apparent in Figure 3a is the 2-3 μm thick Te layer on top of the 4 μm thick CdTe layer. The Te on CdTe interface shown in Figure 3b illustrates the contact of the semiconductor with the Te layer and the agglomeration of the particles in the Te layer.

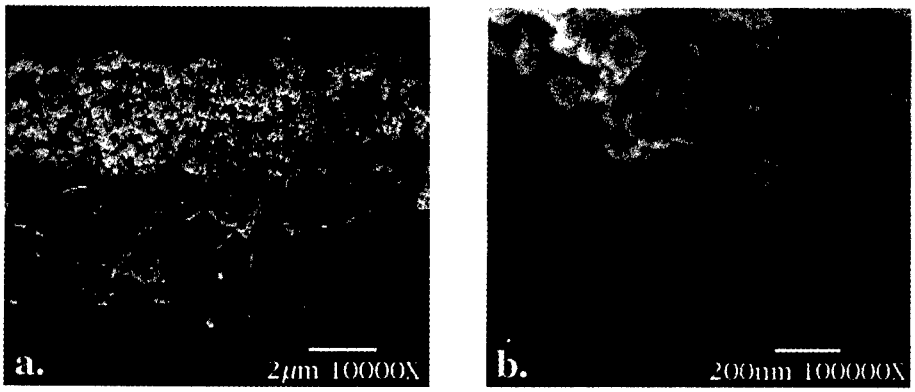


Figure 3. SEM images of nano-Te on CdTe films as-sprayed.

The Te on CdTe heterostructure films were annealed under He (g) for 30 min at temperatures from 215 to 255 °C. This annealing step, referred to as a contact anneal, functions to diffuse the p+ layer (i.e., Te) into the p-layer (i.e., CdTe) thereby forming a contact. Figure 4 show SEM images of a Te on CdTe film that was contact annealed at 215 °C. When compared to the as-sprayed sample (i.e., Fig. 3), very little morphological change is observed at either low (Fig. 4a) or high (Fig. 4b) magnification.

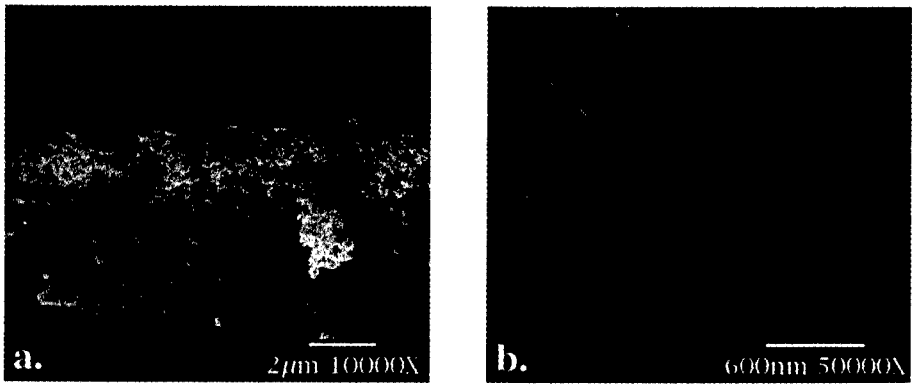


Figure 4. SEM images of Te on CdTe films after a contact anneal at 215°C for 30 min under He.

To evaluate the effectiveness of the Te nanoparticle contact, two control devices were fabricated according the standard NREL process [1] as follows:
(1) 20-25 s etch of the CdTe heterostructure in phosphoric/nitric acid and DI rinse;
(2) application of a Kapton tape mask;
(3) paint brush coating the CdTe film with a HgTe/Cu_xTe containing graphitic Electrodag; and,
(4) contact annealing under He for 30 min.

After the contact anneal step, all films were finished into devices by (1) masking an area with Kapton tape, (2) spin coating the finished contact with Ag paint and annealing in air (100 °C / 1 h), (3) removing the Kapton tape, (4) removing the extra CdTe with a razor, and (5) soldering In to the SnO_2 layer. The devices were characterized by standard light-dark IV. Table 1 shows the results of these electrical characterizations.

Table 1. Electrical Characteristics of Nano-Te on CdTe Solar Cells.

Anneal Temp (C)	Effic. (%)	V_{oc} (mV)	J_{sc} (mA/cm^2)	R_{se} (Ω)	R_{sh} (Ω)	FF (%)	Device Area (cm^2)	
205	1.3	708	4.5	24.4	236	42.0	0.815	
215	9.9	779	18.5	5.3	1482	68.9	0.192	
215	9.4	803	19.1	7.0	774	61.4	0.356	
220	7.2	771	18.1	9.7	501	51.8	0.466	
225	10.3	727	19.9	2.8	985	71.2	0.099	
230	9.1	764	17.3	4.8	646	69.2	0.100	
235	9.9	794	18.6	5.6	856	67.1	0.418	C
235	8.6	784	17.8	7.3	1499	61.7	0.342	
235	6.8	783	16.4	7.4	168	53.1	0.136	C
245	6.9	750	17.2	12.5	395	53.8	0.716	
255	8.6	766	20.2	8.2	896	55.4	0.112	
255	8.0	750	19.0	8.1	387	56.1	0.115	
255	5.6	748	17.1	12.9	287	43.9	0.084	

Note: C denotes control cells

Figure 5 shows plots of the contact annealing temperature versus the device metrics listed in Table 1. Interesting trends appear when this data is presented graphically. For example, the plot of temp vs. efficiency (Fig. 5a) is similar to that of temp vs. fill factor (Fig. 5d). Also, an inverse relationship is noted between short circuit current density (Fig. 5b) and series resistance (Fig. 5e). Especially noteworthy is the scatter in the shunt resistance (Fig. 5f); an observation that illustrates a possible factor limiting device performance. While the observation of shunt resistance exceeding 800 Ω in these nano-Te on CdTe devices is encouraging, the cause of irregularity is of special concern. With such marked non-linearities in R_{sh}, it is not surprising that a clear correlation between anneal temperature and electrical properties is not observed in our data analysis. After isolation of the shunting problem, an optimum contact annealing schedule will be determined. Finally, there is no marked difference in the device performance for the nano-Te on CdTe solar cells versus those finished by the standard NREL approach.

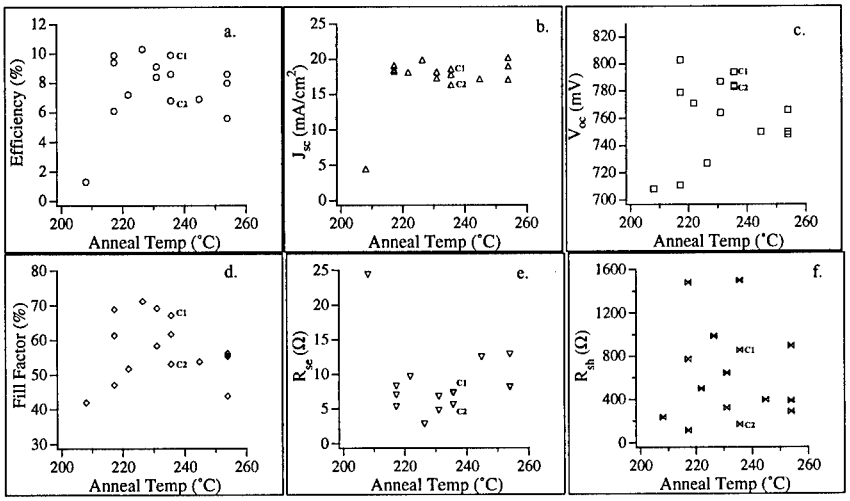


Figure 5. Electrical data for nano-Te on CdTe solar cells. C1 and C2 are control cells.

CONCLUSIONS

Nano-Al and nano-Te dispersions have been used as contacts to p-type Si and p-type CdTe, respectively. Annealed nano-Al on Si films exhibit good resistivities around 10^{-4} Ω•cm. CdTe solar cells that employ a nano-Te contact show efficiencies in excess of 10% with good open circuit voltages and short circuit current densities. These nano-Te contacts exhibit similar electrical characteristics to those obtained using the standard HgTe-based contact. Optimization of these nano-Te on CdTe solar cells is hindered by variable shunt resistance.

ACKNOWLEDGEMENTS

The authors wish to thank Drs. Doug Rose and Rick Powell from First Solar for the gift of CdTe heterostructures and helpful discussions. The gift of nano-Al from Dr. Fred Tepper is greatly appreciated. The gift of Si wafers from Mr. Ted Ciszek and Dr. Bhushan Sopori from NREL is acknowledged. This research was funded by the U.S. Department of Energy (Contract # DE-AC36-99-GO10337) through the National Photovoltaics Program and the Office of Science.

REFERENCES

1. D.H. Rose, F.S. Hasoon, R.G. Dhere, D.S. Albin, R.M. Ribelin, X.S. Li, Y. Mahathongdy, T.A. Gessert, P. Sheldon, Prog. Photovoltaics: Res. Appl, **7** (5), 331-340 (1999).
2. D.L. Schulz, R. Ribelin, C.J. Curtis, D.S. Ginley, AIP Conf. Proc., **462**, 206-211 (1999).
3. N. Romeo, A. Bosio, R. Tedeschi, V. Canevari, presented at the 1998 World Conference and Exhibition on Photovoltaic Solar Energy Conversion, Vienna, Austria, 1998.
4. D.W. Niles, X. Li, D. Albin, D. Rose, T. Gessert, P. Sheldon, Prog. Photovoltaics: Res. Appl, **4**, 225-229 (1996).

Size Effect In Germanium Nanostructures Fabricated By Pulsed Laser Deposition

K.M. Hassan, A.K. Sharma and J. Narayan
Department of Materials Science and Engineering and NSF Center for Advanced Materials and Smart Structures,
North Carolina State University, Raleigh, NC 27695-7916.
J.F. Muth, C.W. Teng and R.M. Kolbas
Department of Electrical and Computer Engineering, North Carolina State University, Raleigh, NC 27695-7911.

ABSTRACT

We have fabricated Ge nanostructures buried in AlN and Al_2O_3 matrices grown on Si(111) and sapphire substrates by pulsed laser deposition. Our approach involved three-dimensional island growth of low band-gap material followed by a layer of wide band-gap material. The nanodots were uniformly distributed in between alternating layers of AlN or Al_2O_3. It was observed that these nanodots exhibit crystalline structure when grown at 300-500 ^{0}C. The average size of Ge islands was determined to be ~5-15 nm, which could be varied by controlling laser deposition and substrate parameters. The Raman spectrum showed a peak of the Ge-Ge vibrational mode downward shifted upto 295 cm^{-1} which is caused by quantum confinement of phonons in the Ge-dots. The photoluminescence of the Ge dots (size ~15nm) was blue shifted by ~0.266 eV from the bulk Ge value of 0.73 eV at 77 K, resulting in a distinct peak at ~1.0 eV. The spectral positions of both E_1 and E_2 transitions in the absorption spectra at room temperature and 77K shift toward higher energy as the Ge dot size decreases. The interpretation of these behaviors in terms of quantum confinement is discussed in this work, and the importance of pulsed laser deposition in fabricating novel nanostructures is emphasized

INTRODUCTION

The quantum confinement effects in semiconductor systems with reduced dimensions have attracted considerable attention[1-3]. Their optical and electronic properties are of special interest as they can be modified by altering their structure. This makes quantum-confined semiconductors very promising for photoelectronic device applications. Indirect bandgap semiconductors such as Si and Ge have very poor luminescent efficiency since the band center transition is optically forbidden. By making the crystallite size of these semiconductors smaller than the exciton Bohr radius, the resulting quantum confinement produces[4]a sharp increase in the oscillator strength and shifts the luminescence to higher energies. The effective Bohr radius a_B for excitons in bulk Ge is calculated to be about 24 nm[5], which is much larger than that of bulk Si (4.9 nm)[6]. These electronic conditions lead to an expectation that it is much easier to change the electronic structure around the band gap of Ge.

Mat. Res. Soc. Symp. Proc. Vol. 581 © 2000 Materials Research Society

EXPERIMENT

In this work, we report a novel technique[7] to fabricate multilayers of Ge nanostructures buried in aluminum nitride (AlN) and aluminum oxide (Al_2O_3) matrices on Si(111) and sapphire substrates. Our approach involved three-dimensional growth of Ge islands on AlN or Al_2O_3 substrate, the size of Ge islands (dots) is controlled by the amount of Ge and substrate temperature. AlN is a wide bandgap material (E_G~ 6.2 eV) with dc dielectric constant ~9.14[8]. The pulsed laser deposition (PLD) technique[9], used in the present work, is known for growing high quality structures at lower substrate temperatures. Moreover, using pulsed laser deposited Ge/AlN heterostructures, we can minimize the possibility of defect induced photoluminescence from interfacial GeO_x layers. By comparing the optical and structural properties we can study the interfacial reactions, if any, in nanocrystalline Ge embedded in different matrices. The laser energy density used in this experiment was ~2.5 J/cm^2 and the substrate temperature ~400-500 ^{0}C. The p-type Si(111) wafers were cleaned in acetone and methanol ultrasonically prior to surface oxide removal by 10% HF solution. The thickness of AlN or Al_2O_3 layers was typically ~10 to 40 nm followed by 4-6 monolayers of Ge. The size of Ge nanocrystals was varied by changing the thickness of Ge layers and deposition temperature. Topcon 002B transmission electron microscope (resolution ~0.18 nm) was used to analyze these nanostructures. The size distribution of the Ge nanodots and crystallinity of the AlN/Al_2O_3 matrix and Ge nanostructures in these multilayers were investigated by cross-sectional HRTEM. Atomic force microscopy (AFM) was done to study the morphology and size uniformity of the dots. Raman spectroscopy was performed on the samples using Ar^+ ion laser (λ~514.5 nm) in the backscattering geometry. The photoluminescence was excited by an argon ion laser (λ~514.5 nm) at 77K. We also carried out absorption measurements at room temperature to study the shift in the E_1 and E_2 transitions.

RESULTS AND DISCUSSIONS

Germanium nanostructures were deposited at various deposition temperatures and laser energy density. It was found that the structural quality and size of these nanodots is critically dependent on the growth temperature. For samples deposited above 600 °C, we observed grain growth and coalescence in the germanium dots. Germanium formed an amorphous layer for samples grown below 300 °C. These nanodots exhibited crystalline structure when grown between 300-500 ^{0}C. The size of islands increased as a function of deposition temperature and decreased with the thickness of Ge layer. The selected area diffraction revealed that AlN is polycrystalline and Ge nanodots have diamond cubic structure. In the high resolution image we observe lattice fringes corresponding to {111} planes of Ge (spacing 0.326 nm) with the diamond cubic structure. The average size of the nanodots for the different Ge layers is ~7-15 nm depending on growth conditions. It was also observed that Ge dots had an atomically sharp interface with AlN matrix with no indication of any interfacial reaction. Figure 1 shows the cross-sectional TEM image of the Ge nanodot multilayers having darker contrast embedded in Al_2O_3 matrix. These nanodots are uniformly distributed in between alternating layers of Al_2O_3 with average thickness ~45nm. The selected area diffraction in the right inset reveals that Al_2O_3 is

amorphous and the Ge dots have a diamond cubic structure with an indication of some texturing along <113> and <133> directions. The HRTEM image shown in the left inset indicates that these islands are dislocation free and are pyramidal shaped. These nanodots exist as isolated islands in the Al_2O_3 matrix with no overlap between neighboring dots. The size distribution is fairly uniform (±4%). Raman spectroscopy studies of these samples did not reveal any peak other than Ge-Ge peak in the range 100-1200 cm^{-1}. The morphology of the germanium nanostructures was studied using an atomic force microscope. Figure 2 shows the AFM image from a $0.015um^2$ scan area. The distribution is fairly uniform with majority of islands of size 9nm. This result is found to be quite consistent with HRTEM analysis done on the same set of samples. The islands appear to be pyramidal shaped with a domed top, similar to what was observed in the HRTEM analysis. The nanodots appear randomly distributed with no clustering. So using pulsed laser deposition we can fabricate germanium nanostructures with a uniform size distribution at a lower deposition temperature compared to other techniques.

Raman spectrum from the sample containing a single layer of Ge dots displaying a peak at 296 cm^{-1} and a small peak arising from the silicon substrate at 521 cm^{-1}. The effect of strain is expected to shift this peak position to a higher wavenumber rather than towards a lower value, which can be explained based on the phonon confinement effect. The photoluminescence spectra of the Ge dots measured at 77K was blue shifted by ~0.266 eV from the bulk value of 0.73 eV at 77K, resulting in a distinct peak at ~1.0 eV. Absorption spectroscopy revealed a distinct blue shift of the E_1 transition for 7, 8 and 13 nm size nanodots.

CONCLUSIONS

In conclusion, we have successfully fabricated Ge nanostructures embedded in AlN and Al_2O_3 matrices with fairly uniform size distribution. Raman signatures suggest phonon confinement due to downward shift of the Ge-Ge peak. High resolution microscopy revealed dislocation free pyramidal shaped Ge nanocrystals with average size ~7-15 nm depending on growth condition. Quantum confinement effect was confirmed by absorption spectroscopy measurement and by the distinct blue shifted photoluminescence peak observed at ~1.0 eV at 77 K. Thus PLD is an attractive technique for fabricating nanostructures with a narrow size distribution at lower substrate temperatures.

This work was supported by National Science Foundation Center for Advanced Materials and Smart Structures.

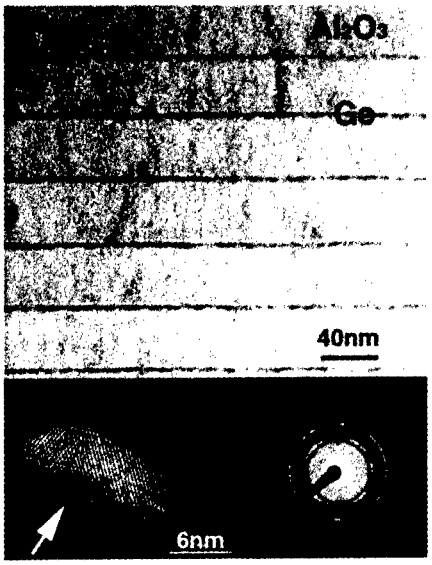


Figure 1. Cross-sectional TEM image of Ge nanodot multilayers embedded in Al_2O_3 matrix. Left inset shows the HRTEM image of a pyramidal shaped Ge nanodot. The arrow indicates the growth direction. SAD in the right inset shows that the Ge nanodots are crystalline and textured along <113> and <133> directions and the Al_2O_3 matrix is amorphous.

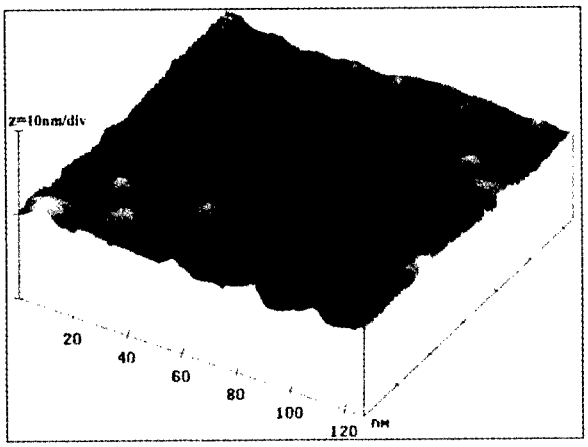


Figure 2. AFM image from scan size=125.5nm shows that the islands are pyramidal with a rounded top. (x=20nm/div, z=10nm/div). Note that these are isolated from their neighbors.

REFERENCES

1. Microcrystalline Semiconductors: Materials Science & Devices, ed. Philippe M. Fauchet, Chuang Chuang Tsai, Leigh T. Canham, Isamu Shimizu, and Yoshinobu Aoyagi, MRS Symp. Proc., **283** (1992).
2. Microcrystalline and Nanocrystalline Semiconductors, ed. Robert W. Collins, Chuang Chuang Tsai, Masataka Hirose, Frederick Koch, and Louis Brus, MRS Symp. Proc., **358**(1994).
3. Advances in Microcrystalline and Nanocrystalline Semiconductors, ed. Robert W. Collins, Philippe M. Fauchet, Isamu Shimizu, Jean-Claude Vial, Toshikazu Shimada, and A. Paul Alivisatos, MRS Symp. Proc., **452**(1996).
4. B. Delley and E.F. Steigmeier, Phys. Rev. B **47**, 1397 (1993).
5. Yoshihito Maeda, Nobuo Tsukamoto, Yoshiaki Yazawa, and Yoshihiko Kanemitsu, and Yasuaki Masumoto, Appl. Phys. Lett. **59**, 3168 (1991).
6. A.G. Cullis, L.T. Canham, and P.D.J. Calcott, J. Appl. Phys. **82**, 909 (1997).
7. K.M. Hassan, A.K. Sharma, J.Narayan, J. Muth, C.W. Teng, R.M. Kolbas, *Appl. Phys. Lett.* **75**, 1222 (1999).
8. A.T. Collins, E.C. Lightowlers and P.J. Dean, Phys. Rev. **158**, 833 (1967).
9. J. Narayan et. al., *Appl. Phys. Lett.*, **51**, 1845, (1987).

FUNCTIONALISATION OF CdSe AND GaAs QUANTUM DOTS

SEBASTIAN J. NØRAGER[†]*, MICHAEL LAZELL*, PAUL O'BRIEN*
[†]Department of Chemistry, Imperial College of Science, Technology and Medicine, South Kensington, London, SW7 2AY, UK.
*Manchester Materials Science Centre and the Department of Chemistry, University of Manchester, Oxford Road, Manchester, M13 9PL.

ABSTRACT

In this communication we report the preliminary results of *in-situ* functionalisation, of Q-CdSe and Q-GaAs using thiols, ($HSC_{12}H_{25}$), dithiols, ($HSC_9H_{18}SH$), pyridine derivatives (4-ethylpyridine, 4-butylpyridine) and carboxylic acids (mercaptopropionic acid).

The functionalisation of the capping group provides a potential route to the assembly of 2D arrays and supperlattices. Anchorage of the nanocrystals to surfaces for use in devices, such as solar cells and Grätzel type cells is also discussed.

INTRODUCTION

Semiconductor nanoparticles capped with trioctylphosphine oxide (TOPO) and trioctylphosphine (TOP) have generated a substantial amount of interest in recent years due to their interesting optoelectronic properties [1-5]. A direct consequence of these particles residing between the molecular and bulk states of matter, size quantisation effects unlock a potential for a wide range of applications in devices, such as: light-emitting diodes, [6,7], photocatalysts [8,9] and electrochemical cells [1,10,11] have been reported.

The TOPO route currently offers narrow size-distribution, high degrees of crystallinity, colloidal stability over time and robust surface passivation. These characteristics are very important as they directly influence the quality of photoluminescence exhibited by the nanoparticles, *e.g.* quantum yields and deep trap luminescence. However, there are problems, as TOPO causes complications when the nanoparticles are integrated into devices, as it is an insulating waxy solid. In order to use the interesting opto-electronic properties in applications the problem of how to handle the ready made particles arises. Due to their small size, chemically fixing the particles to surfaces is advantageous. This gives rise to a need for functionalising the nanoparticles surfaces with 'smart' ligands such as thiols and pyridines, which can then be reacted further to give nanocomposites. There are two approaches to synthesising these functionalised nanocrystals. One way is to synthesise the nanocrystals in TOPO and then to replace the capping group with the desired ligand. The other way is to prepare the nanoparticles in the functional ligand. We have previously reported work on Cd_3P_2 and InP quantum dots capped with 4-ethylpyridine prepared from the novel single source precursors, cadmium or indium di-*tert*-butylphosphide respectively [12,13].

In this work we report on CdSe and GaAs nanoparticles synthesised directly in capping agents such pyridines, thiols and dithiols, and mixtures of these and trioctylphosphine (TOP) or TOPO. Optical measurements such as UV and photoluminescence have been carried out. The particles have been characterised by X-Ray diffraction, (XRD), Energy Dispersive X-ray Analysis, (EDAX) and microscopy imaging. Emphasis has been put on surface functionalising the particles for specific uses during synthesis, so the particles can be reacted with surfaces or self assemble into arrays.

Mat. Res. Soc. Symp. Proc. Vol. 581 © 2000 Materials Research Society

EXPERIMENTAL

UV/Vis Absorption and IR Spectroscopy

The optical measurements of the nanoparticles were carried out on a Philips PU 8710 spectrophotometer. The sample solutions were placed in silica cuvettes (path length = 1 cm). The samples were pyridine solutions and pyridine was used as the reference. Infra-red spectra were carried out using a Matteson Polaris FT-IR spectrometer as nujol mulls.

Photoluminescence Spectroscopy (PL)

PL measurements were obtained using a Spex FluoroMax instrument with a xenon lamp (150W) and a 152 P photomultiplier tube as a detector. Silica cuvettes of 1 cm path length were used. Solutions were made using pyridine.

Scanning/Transmission Electron Microscopy (SEM, TEM)

A JOEL 2000 FX MK1 electron microscope operating at 200 kV with an Oxford Instrument AN 10000 EDS analyser was used for the conventional TEM micrographs. The samples for TEM were prepared by placing a drop of a dilute solution of sample in toluene on a copper grid (400 mesh, Agar). The excess solvent was wicked away with a paper tip and the sample allowed to dry completely at room temperature.

Syntheses

Preparation of CdSe nanocrystals in TOPO

The precursor $[Cd\{Se_2CN(CH_3)(C_6H_{13})\}_2]$ was prepared by the literature method [14]. The precursor (0.5 g, 0.73 mmol) was then dissolved in TOP (5 ml, 2.8 mmol) and then injected into TOPO (20 g, 51 mmol, degassed at 100 °C for 30 mins prior to use) at 200 °C. The colour of the mixture changed to red. This mixture was allowed to stir for *ca.* 30 mins where upon the heat was removed. At approximately 60 °C methanol (40 ml) was added to precipitate the nanoparticles. The nanoparticles were centrifuged and would readily redissolve in toluene.

Preparation of functionalised CdSe nanoparticles, method 1

The already prepared CdSe/TOPO nanoparticles were taken and washed with methanol to remove most of the capping TOPO. These were then added to the desired ligand and heated whilst stirring for several hours. The nanoparticles were then collected by centrifugation following the addition of a non-solvent. Nonanedithiol capped CdSe nanoparticles were prepared by the same method but using $CdSe/C_{12}H_{25}SH$ instead of CdSe/TOPO.

Preparation of functionalised CdSe nanoparticles, method 2

The precursor [Cd{$Se_2CN(CH_3)(C_6H_{13})$}$_2$] (0.22 g, 0.32 mmol) was dissolved in TOP (2.5 ml, 5.6 mmol) and injected into $C_{12}H_{25}SH$ (10 ml, 41.7 mmol) stabilised at 190 °C. The mixture was heated for 20 min and then left to cool. The particles were isolated by centrifugation after addition of a mixture of MeOH and $HCCl_3$. These were readily redispersed in $C_{12}H_{25}SH$ or toluene.

Preparation of GaAs nanocrystals

Gallium chloride, ($GaCl_3$, 0.8 g, 4.6 mmol), was dissolved in 4'ethylpyridine (25 ml, xmol) and to it was added *tris*(dimethylamino)arsenide, ([$As(NMe_2)_3$], 0.95 ml, 4.6 mol). This mixture was then slowly heated to 167 °C and allowed to reflux for 5 days at. The solution was allowed to cool and 40 - 60 petroleum spirit was added to flocculate the GaAs nanocrystals. The particles were then isolated by centrifugation and could be readily redispersed in pyridines.
6- Mercaptonicotinic acid (0.3 g, 1.9 mmol) was then added to a solution of these particles in pyridine and heated to 60 °C for 24h.

RESULTS

By exchanging the capping media of the nanocrystals, the functionalisation of the dots is achieved and they can be reacted with other surfaces to form composites. The CdSe quantum dots have been synthesised in dodecanthiol. Particles capped with nonanedithiol were prepared by exchanging the capping group after synthesis. Particles capped with 4-ethylpyridine were prepared by Methods 1 and 2. The thiols were chosen as they promote self-assembly into 2D arrays [15, 16]. Pyridines were chosen as they form a more labile surface ligand which allows for electronic transitions.

GaAs particles were synthesised in 4-ethylpyridine and then functionalised with 6-mercaptonicotinic acid. The carboxylic acid was chosen to bind the Q-GaAs to TiO_2 nanoparticles.

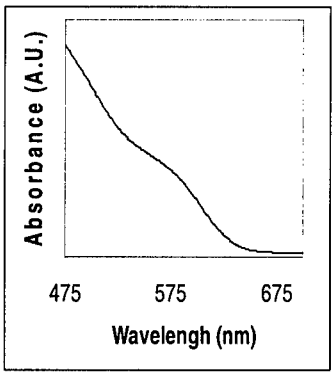
Q-CdSe

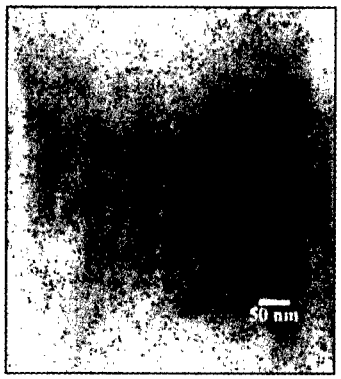
The preparation of the CdSe quantum dots in 1,9-nonanedithiol, dodecanthiol and 4-ethylpyridine, (4-Etpy), was successfully achieved by adapting the TOPO method. The single source precursor, [Cd{$Se_2CN(CH_3)(C_6H_{13})$}$_2$], was refluxed in the capping solvents and then the nanoparticles were collected by flocculation and centrifugation. These dots were readily redispersable in toluene.

For CdSe nanoparticles and generally II-VI materials, methods 1 and 2 present the following advantages and disadvantages. Due to the ionic nature of the lattice, the TOPO route offers high degrees of crystallinity, close size-distribution, good colloidal stability over time and effective surface passivation. These properties promote high quality luminescence, i.e. relatively high quantum yields and low proportions of surface traps. However, if these particles are to be chemically fixed to other bodies, some or all of the TOPO has to be replaced with a functional ligand, (Method 1). When this method is utilised the nanoparticles need to be isolated first, and then the TOPO capping group needs to be removed using methanol. This procedure effects the surface and introduces surface traps, which deteriorate the desired luminescence properties as

well as lowering the overall yield. Furthermore, if too much TOPO is removed the nanoparticles become irreversibly insoluble.

Conversely, Method 2 presents problems when the synthesis is performed in the presence of a high concentration of functional capping agent. Although the yield of ready to use particles is increased, the quantum yields is decreased. This effect is illustrated in the CdSe particles synthesised by Method 2, (capping group $C_{12}H_{25}SH$), which exhibit similar size-distribution and absorption spectra, Figure 1, although no photoluminescence could be observed. Figure 2 is a TEM image of the particles. This result is probably due to the poor surface passivation, which promotes non-radiative recombination of the excited states. Our current work focuses on optimising the balance between the concentrations of TOPO to functional ligand, for the one pot synthesis.





Figures 1 & 2. Absorption Spectrum and TEM image of Q-CdSe/$C_{12}H_{25}SH$.

The luminescence properties of TOPO capped CdSe particles are well documented. By changing the capping group we can investigate the change in luminescence. Figure 3 shows the UV and photoluminescence spectra obtained from CdSe samples capped with TOPO and 4-Etpy. By comparing the onset of absorption for TOPO and 4-Etpy capped particles, (545 nm, 2.274 eV), (417 nm, 2.972 eV) respectively, we can see that the 4-Etpy sample is smaller in size (diameter) as the onset of absorption occurs at a lower wavelength. This observation is expected as the preparation temperature for TOPO and 4-Etpy are 200 and 167 °C respectively. The sizes can be approximated to 3.1 nm (4-Etpy) and 4.5 nm (TOPO) by utilising the Brus equation (Direct Band Gap method). Another contrast between the two samples is the TOPO sample shows band edge luminescence from the CdSe quantum dots, this effect does not depend upon the excitation wavelength. However, the 4-Etpy samples there is a Stokes shift in the luminescence spectrum. The Stokes shift is 86 nm, (0.51 eV).

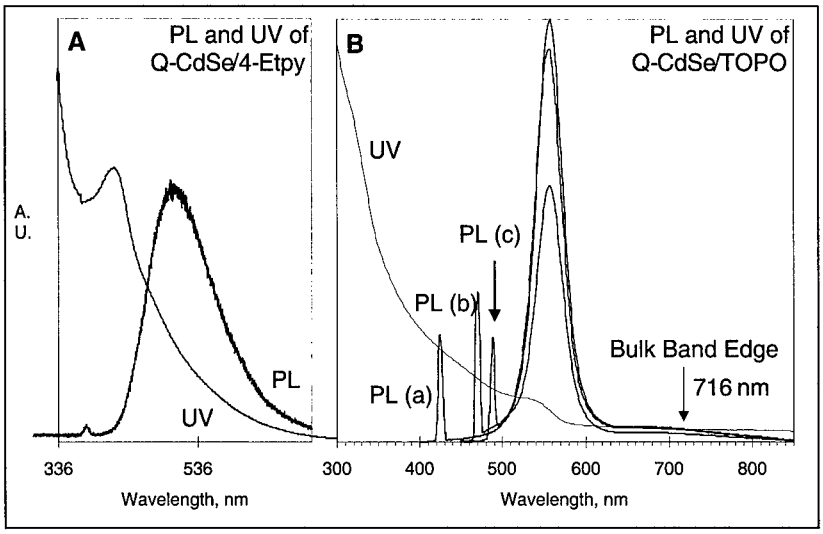
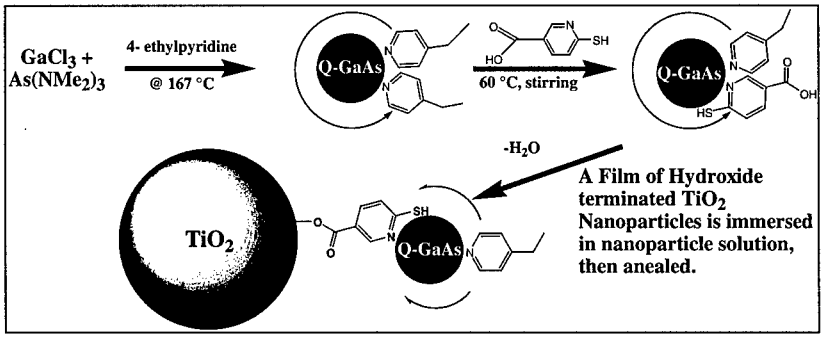


Figure 3. UV and PL spectra of CdSe quantum dots capped with A) 4-ethylpyridine and B) TOPO a) λ_{exc} = 425 nm b) λ_{exc} = 470 nm c) λ_{exc} = 488 nm

Q-GaAs

The preparation of crystalline GaAs nanoparticles is successful when using the arsenic precursor $As(NMe_2)_3$ and $GaCl_3$. The nanocrystals have to be left for 5 days in refluxing 4-Etpy to grow. The nanoparticles showed a wide size distribution.

The GaAs nanocrystals have been capped using 4-ethylpyridine, biprimidine and mercaptopropionic acid. The proposed reaction scheme to functionalise and bind Q-GaAs to TiO_2 is presented in Scheme 1.



Scheme 1. Proposed reaction scheme for synthesis, functionalisation and binding of Q-GaAs.

The GaAs nanoparticles functionalised with 6-mercaptonicotinic acid were repeatedly precipitated and redissolved to remove impurities and excess capping material prior to IR analysis. The spectra confirmed the presence of 6-mercaptonicotinic acid capping the surface. As III-V materials have a more inert lattice, the capping agent of choice to achieve controlled growth is of a more labile nature than TOPO. For this reason the replacement of such a ligand after synthesis presents fewer problems, and surface funtionalisation was carried out by Method 1. We are currently investigating the bonding between the GaAs and TiO_2 particles. Experiments to research the possibility of charge transfer between the particles are being planned.

CONCLUSIONS

Good quality crystalline nanoparticles of CdSe and GaAs have been synthesised with functional capping groups. Two approaches, where functionalisation has been carried out during and after synthesis, have been used. For CdSe nanoparticles, several ligands other than TOPO have been used, although the resulting luminescence properties were not ideal. Further work is needed to assess weather preparations carried out in mixtures of TOPO and functional ligands will yield the desired reactivity and luminescence properties. GaAs nanoparticles have been capped with 6-mercaptonicotinic acid, which can be reacted with hydroxides to form composites.

ACKNOWLEDGEMENTS

We would like to thank Mr. Keith Pell (QMW) for TEM and Dr. Gary Rumbles (IC) for discussion on photoluminescence. P.O.B is the visiting Sumitomo/STS Professor of Materials Chemistry at IC and Professor of Inorganic Materials in The Manchester Materials Science Centre and The Department of Chemistry at The University of Manchester.

REFERENCES

1. D. Dounghong, J. Ramsden, and M. Grätzel, J. Am. Chem. Soc. **104**, p. 2977 (1982).
2. R. Rossetti, J. L. Ellison, J. M. Gibson, and L. E. Brus, J. Chem. Phys. **80**, p. 4464 (1984).
3. A. Henglein, Chem. Rev. **89**, p. 1861 (1989).
4. M. L. Steigerwald and L. E. Brus, Acc. Chem. Res. **23**, p. 183 (1990).
5. Y. Wang and N. Herron, J. Phys. Chem. **95**, p. 525 (1991).
6. B. O. Dabbousi, M. G. Bawendi, O. Onitsuka, and M. F. Rubner, Appl. Phys. Lett. **66**, p. 1316 (1995).
7. V. L. Colvin, M. C. Schlamp, and A. P. Alivisatos, Nature **370**, p. 354 (1994).
8. F. Hakimi, M. G. Bawendi, R. Tumminelli, and J. R. Haavisto, U.S. Patent **5,260,957** (1993).
9. C. K. Grätzel and M. Grätzel, J. Am. Chem. Soc. **101**, p. 7741 (1979).
10. H. Weller, Adv. Mater. **5**, p. 88 (1993).
11. A. Hagfeldt and M. Grätzel, Chem. Rev. **95**, p. 49 (1995).
12. M. Green and P. O'Brien, J. Chem. Soc, Chem. Commun. p. 2459 (1998).
13. M. Green and P. O'Brien, J. Mat. Chem. **9**, p. 243 (1999).
14. B. Ludolph, M. A. Malik, P. O'Brien and N. Revaprasadu, J. Chem. Soc, Chem. Commun. p. 1849 (1998).
15. T. Sato, D. G. Hasko, H. Ahmed, J. Vac. Sci. Technol. B **15(1)**, p. 45 (1997).
16. T. Sato, D. Brown, B. F. G. Johnson, J. Chem. Soc., Chem. Commun. p. 1007 (1997).

SYNTHESIS OF SELF-CAPPED METAL SULFIDE NANOPARTICLES

MIKE LAZELL, PAUL O'BRIEN
Manchester Materials Science Centre and the Department of Chemistry, University of Manchester, Oxford Road, Manchester, M13 9PL.
Email: michael.r.lazell@man.ac.uk paul.obrien@man.ac.uk

ABSTRACT

In this paper we report the synthesis of metal sulfide nanocrystals, (CdS and ZnS), from the thermolysis, between 150 - 300 °C, in a dynamic vacuum, of the novel long chain asymmetric metal dithiocarbamates, *bis*(N-methyloctadecyldithiocarbamato) cadmium(II) or zinc(II), $[M\{S_2CN(C_{18}H_{37})(CH_3)\}_2]$.

These nanoparticles 'self-cap' during preparation. Different size nanocrystals were synthesised, at different temperatures and there was a change in phase from cubic to hexagonal CdS at a decomposition temperature greater than 300 °C.

INTRODUCTION

Nanocrystalline semiconductors have electronic properties intermediate between those of molecular entities and macrocrystalline solids and are at present the subject of intense research [1-6]. Nanometric semiconductor particles exhibit novel properties due to the large number of surface atoms (and resultant states) and/or the three dimensional confinement of electrons. Altering the size of the particle alters the degree of confinement of the electrons, and affects the electronic structure of the solid, in particular the position of 'band edges', are tunable with particle size. Nanoparticles of semiconductors have many potential applications and demonstration devices including: light-emitting diodes, [7,8], photocatalysts [9,10] and electrochemical cells [1,6,11] have been reported.

We are interested in developing novel routes to these materials and have previously reported the use of single source precursors to prepare several II/VI chalcogenides [12-14]. These nanocrystals are organically capped with tri-*n*-octylphosphine oxide (TOPO). Other capping groups such as 4-ethylpyridine have also been used to solubilise nanocrystals, for example, InP [15]. We have also recently reported the use of trioctylphosphine sulfide as an air/moisture stable sulfiding precursor [16] for cadmium or zinc sulfide.

However, to date there has only been one paper [17] describing the synthesis of nanocrystals in a process in which the particle is capped by a ligand transferred from the precursor; we term this process 'self-capping'. Finely divided silver has been prepared from the salts of fatty acids by a bulk pyrolysis. Here we report the first synthesis of self-capped CdS and ZnS nanocrystals from the thermolysis at 150 - 300 °C, in a dynamic vacuum, of the novel asymmetric metal dithiocarbamates, *bis*(N-methyloctadecyldithiocarbamato) cadmium(II) or zinc(II) $[M\{S_2CN(C_{18}H_{37})(CH_3)\}_2]$.

EXPERIMENTAL

UV/Vis Absorption and IR Spectroscopy

The optical measurements of the nanoparticles were carried out on a Philips PU 8710 spectrophotometer. The sample solutions were placed in silica cuvettes (path length = 1 cm).

Mat. Res. Soc. Symp. Proc. Vol. 581 © 2000 Materials Research Society

The samples were pyridine solutions and pyridine was used as the reference. Infra-red spectra were carried out using a Matteson Polaris FT-IR spectrometer as nujol mulls.

Nuclear Magnetic Resonance spectroscopy (NMR)

The ^{1}H and ^{13}C solution NMR spectra were recorded on a Bruker AM 500 or a DRX 400 in deuterated chloroform.

X-ray Powder Diffraction (XRD)

X-ray powder diffraction patterns were measured using a Siemens D500 series automated powder diffractometer using Cu-K_α radiation at 40kV/40mA with a secondary graphite crystal monochromator. Samples were supported on glass slides ($5cm^2$).

Photoluminescence Spectroscopy (PL)

PL measurements were obtained using a Spex FluoroMax instrument with a xenon lamp (150W) and a 152 P photomultiplier tube as a detector. Silica cuvettes of 1 cm path length were used. Solutions were made using pyridine.

Energy Dispersive Analysis by X-rays (EDAX)

EDAX was performed on samples deposited by evaporation on glass substrates by using a JEOL JSM35CF scanning electron microscope.

Scanning/Transmission Electron Microscopy (SEM, TEM)

A JOEL 2000 FX MK1 electron microscope operating at 200 kV with an Oxford Instrument AN 10000 EDS analyser was used for the conventional TEM micrographs. The samples for TEM were prepared by placing a drop of a dilute solution of sample in toluene on a copper grid (400 mesh, Agar). The excess solvent was wicked away with a paper tip and the sample allowed to dry completely at room temperature.

X-ray Photoelectron Spectroscopy (XPS)

The XPS measurements were performed in the ultra-high vacuum chamber (base pressure 10^{-8} Pa) of a VG ESCALAB-Mk II (VG Scientific) using Al Kα excitation (analyser pass energy of 50 eV). The energy scale was calibrated using C_{1s} (at 284.8 eV) as a reference.

Syntheses

Preparation of Bis(N-methyloctadecyldithiocarbamato) cadmium(II) $[Cd\{S_2CN(C_{18}H_{37})(CH_3)\}_2]$

Into a beaker was put methanol (40 ml) and NaOH (0.48 g, 0.012 mol), which was stirred until dissolved. To this stirred solution was added $[HN(C_{18}H_{37})(CH_3)]$ (3.42 g, 0.012 mol) and left for 30 mins. CS_2 (0.92 g, 0.012 mol) was then syringed into the solution. A slightly yellow tinged clear solution resulted and was left to stir for 30 mins. To this solution was added $CdCl_2$ (1.11 g, 6 mmol) in deionised water (100 ml). On addition a white precipitate was produced, the

mixture was allowed to stir for one hour. The mixture was filtered and recrystallised from hot dichloromethane to give a fine white powder. Yield = 4.32 g, 86.4 %; ^{1}H NMR ($CDCl_3$, 400 MHz, δ) 0.88 [3H, *t*, CH_3-R]; 1.25 [22H, *s*, -CH_2-], 1.31 [6H, *s*, -CH_2-], 1.55 [2H, *s*, -CH_2-], 1.75 [2H, *m*, -CH_2-], 3.47 [3H, *s*, CH_3-N], 3.88 [2H, *t*, N-CH_2-] ^{13}C NMR ($CDCl_3$, 100MHz, δ) 14.12 [CH_3-R], 22.69 [-CH_2-], 26.77 [-CH_2-], 26.90 [-CH_2-], 29.36 [-CH_2-], 29.55 [-CH_2-], 29.61 [-CH_2-], 29.66 [-CH_2-], 31.92 [-CH_2-], 44.28 [CH_3-N], 59.25 [-CH_2-N], 203.70 [C-NR'R''], Elemental analysis, Calc for $C_{40}H_{80}CdN_2S_4$: C, 57.9; H, 9.7; N, 3.4 %, Found: C, 57.5; H, 9.8; N, 3.4 %. Mass spec. m/z 830 = $C_{40}H_{80}CdN_2S_4$. Mp = 89 °C

Preparation of Bis(N-methyloctadecyldithiocarbamato) zinc(II) [$Zn\{S_2CN(C_{18}H_{37})(CH_3)\}_2$]

The method above was used to prepare the zinc precursor, using NaOH (0.51 g, 12.75 mmol), [$HN(C_{18}H_{37})(CH_3)$] (3.62 g, 12.75 mmol), CS_2 (0.97 g, 12.75 mmol) and $ZnCl_2$ (0.87g, 6.38 mmol). Yield = 4.23, 84.6%, Elemental analysis, Calc. for $C_{40}H_{80}N_2S_4Zn$: C, 61.3; H, 10.3; N, 3.6 %, Found: C, 60.2; H, 10.6; N, 3.5 %. Mass spec. m/z 783 = $C_{40}H_{80}N_2S_4Zn$. Mp = 85 °C

Preparation of CdS and ZnS nanocrystals

Into a vessel (Figure 1) was put *ca.* 0.5 g of [$M\{S_2CN(C_{18}H_{37})(CH_3)\}_2$] where M = Cd or Zn. The decomposition apparatus was then put into a carbolite furnace. The apparatus was opened to a dynamic vacuum, *ca.* 0.01 mmHg. There was also a liquid nitrogen trap to condense any volatiles from the thermolysis. The decomposition apparatus was heated at a range of temperatures, 150 - 300 °C, for 1 hour (timed from temperature stabilisation). The vessel was allowed to cool and the contents, varying from off-white yellow (150 °C) to dark orange (300 °C) in colour, for CdS and white (150 °C) to light grey (300 °C) in colour for ZnS, were removed.

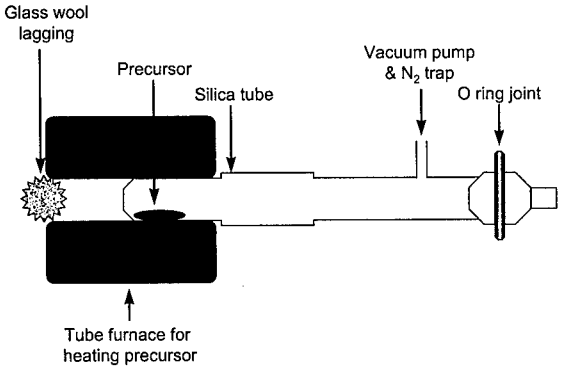


Figure 1. Decomposition apparatus used for synthesis of self-capping nanoparticles

RESULTS

The characterisation of the CdS dots is very complete with analysis using TEM, PL, UV-Vis, IR, XRD and XPS, however with the ZnS, only XRD has been used. The XRD patterns for the CdS samples can be seen in Figure 2. The sample synthesised from the decomposition of the precursor at 150 °C shows the CdS grown is cubic in phase [18]. There are no reflections

associated with the β-CdS phase [19]. The broadening of the peaks in the XRD, suggests that the particles are small, this broadening is a common feature in nanoparticles. Using the Scherrer equation, the diameter of the nanocrystals can be estimated as ~ 5 nm. As the decomposition temperature increases from 150 to 250 °C, an increase in size is observed in the XRD, from the narrowing of the peaks. However, when the precursor is heated to 300 °C, there is the appearance of some very broad new peaks above 2θ values of 40°. These new peaks are associated with a hexagonal phase of CdS [20,21]. This observation suggests a complete phase change from cubic to hexagonal has occurred.

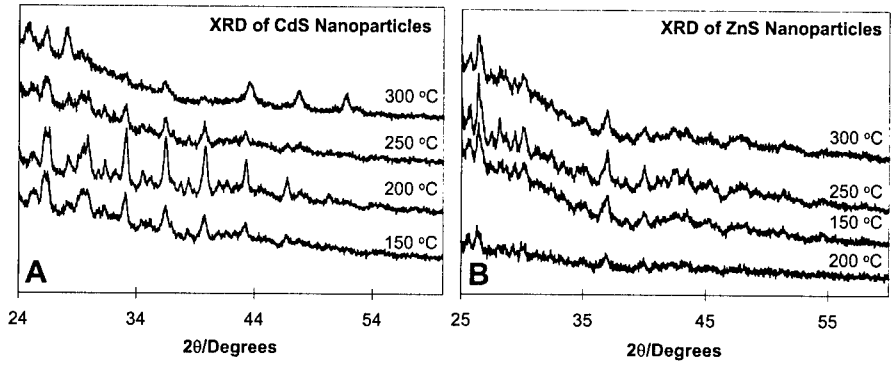


Figure 2. XRD patterns of a) CdS and b) ZnS nanocrystals obtained from different thermolysis temperatures

The XRD pattern for the ZnS nanoparticles suggest that only the hexagonal phase is prepared.

These observations from the CdS XRD patterns, suggest that the cubic phase synthesised from the precursor, heated at temperatures 150 - 250 °C, is the kinetically stable phase, whereas the phase synthesised from heating the precursor at 300 °C would suggest the thermodynamically stable hexagonal phase is produced.

Although there is evidence from the XRD that a phase change from cubic to hexagonal occurs when the temperature of preparation is raised from 250 to 300 °C, there is no evidence of phase mixing as seen by Bawendi, in CdSe [22]. The major peaks associated with the hexagonal and the cubic phases are at different 2θ values, so any phase mixing could easily be seen in the XRD.

The optical properties of the CdS nanoparticles has been explored both with photoluminescence and UV-Vis spectroscopy. The spectra can be seen in Figure 3. The absorption edge of the nanoparticles were calculated using the direct band gap method. The onset of absorption for all the samples showed a clear blue shift: 150 °C, ~ 430 nm (2.88 eV), 200 °C, 449 nm (2.76 eV), 250 °C, 465 nm, (2.66 eV) as compared to that of bulk CdS, 515 nm (2.41 eV). The CdS samples all showed Stokes shifts in their photoluminescence spectra. However, the observed Stokes shift decreases as the particles size increases: 150 °C, absorption maxima, A_{max}, at 454 nm (2.73 eV) (λ_{exc} = 370 nm) a Stokes shift, (S.S), of 0.15 eV; 200 °C, A_{max} at 472 nm (2.63 eV) (λ_{exc} = 400 nm), a S.S of 0.13 eV; 250 °C A_{max} at 482 nm (2.57 eV) (λ_{exc} = 390 nm), a S.S. of 0.09 eV. This observed trend is as expected.

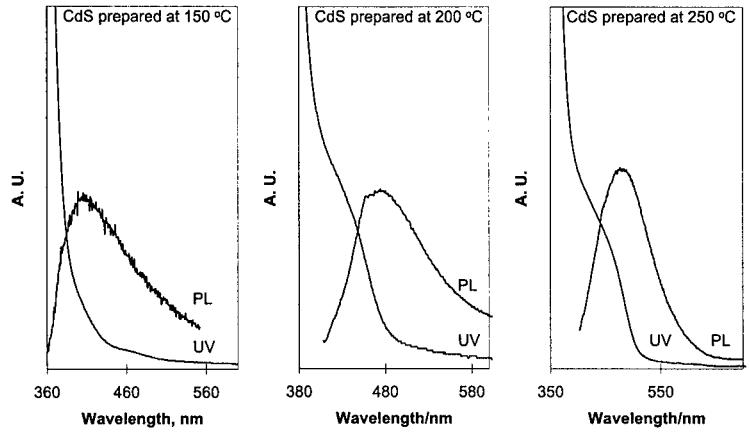


Figure 3. Photoluminescence and UV-Vis spectra of CdS nanoparticles

The nanoparticles were analysed by infra-red spectroscopy to establish the nature of the capping group. The capping agent of the nanocrystals could either be the amine HNR'R'' or the dithiocarbamate $S_2CNR'R''$. The IR spectra showed no stretches associated with the C-N bond from the CdS nanocrystal samples (a typical C-N bond stretch was seen in the precursor sample). This would infer that the CdS nanocrystals are organically capped by the amine, $[HN(C_{18}H_{37})(CH_3)]$. ^1H and ^{13}C NMR spectroscopy show resonances associated with the amine $[HN(C_{18}H_{37})(CH_3)]$. When the NMR and IR data is considered together there is good evidence that the capping group is $[HN(C_{18}H_{37})(CH_3)]$.

X-ray photoelectron spectroscopy was used to analyse the CdS samples prepared at 200 and 300 °C. The analysis of the binding energies shows the presence of Cd, S, N and C. The ratio of C to Cd in the 200 °C sample was significantly more than in the sample prepared at 300 °C. One suggestion for this is less capping amine on the 300 °C sample than the 200 °C another is surface area increases with increasing diameter. Hence, the CdS samples prepared at 150 - 250 °C are very soluble in pyridine and the sample prepared at 300 °C is only partially soluble.

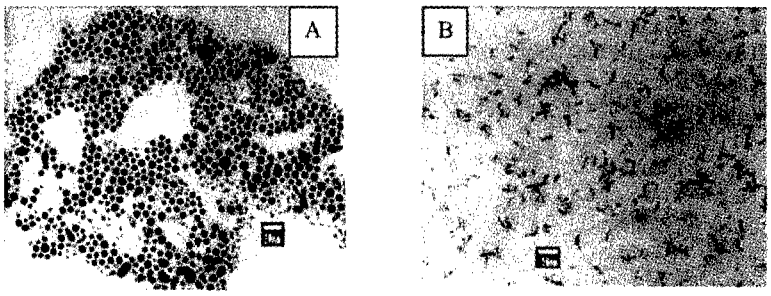


Figure 4. TEM of CdS nanoparticles prepared at a) 150 °C and b) 250 °C

TEM images show quantum dots of CdS synthesised at 150 °C (Figure 4a) which are not agglomerated. The dots are predominately of size 5.5 to 6 nm. The dots synthesised at 250 °C (Figure 4b) appear to have a halo like tail structure. This could be the capping group emanating

from the CdS nanoparticle. The estimated diameters of the dots are between 5 and 7 nm, these were calculated using the Scherrer equation and the direct band gap method from the onset of absorption in the UV spectra. These values compared well with those obtained from the TEM images.

CONCLUSIONS

Good quality, self-capped CdS nanoparticles have been synthesised, from the vapour phase thermolysis of the novel cadmium dithiocarbamate, $[Cd\{S_2CN(C_{18}H_{37})(CH_3)\}_2]$. The CdS nanoparticles are cubic in nature when prepared at 150 - 250 °C and hexagonal at 300 °C. The CdS samples were characterised by UV-Vis, IR, PL, XRD, XPS, NMR and TEM. The study of self-capped ZnS nanoparticles using this route is at present being further developed.

ACKNOWLEDGEMENTS

This work has been funded by an EPSRC grant to P.O.B. We would like to thank Mr. Keith Pell (QMW) for TEM, Mr. Jin-Ho Park (IC) for XRD and Dr. Karol Senkiw (IC) for XPS. P.O.B is the visiting Sumitomo/STS Professor of Materials Chemistry at IC and Professor of Inorganic Materials in The Manchester Materials Science Centre and The Department of Chemistry at The University of Manchester.

REFERENCES

1. D. Dounghong, J. Ramsden, and M. Grätzel, J. Am. Chem. Soc. **104**, p. 2977 (1982).
2. R. Rossetti, J. L. Ellison, J. M. Gibson, and L. E. Brus, J. Chem. Phys. **80**, p. 4464 (1984).
3. A. Henglein, Chem. Rev. **89**, p. 1861 (1989).
4. M. L. Steigerwald and L. E. Brus, Acc. Chem. Res. **23**, p. 183 (1990).
5. Y. Wang and N. Herron, J. Phys. Chem. **95**, p. 525 (1991).
6. H. Weller, Adv. Mater. **5**, p. 88 (1993).
7. B. O. Dabbousi, M. G. Bawendi, O. Onitsuka, and M. F. Rubner, Appl. Phys. Lett. **66**, p. 1316 (1995).
8. V. L. Colvin, M. C. Schlamp, and A. P. Alivisatos, Nature **370**, p. 354 (1994).
9. F. Hakimi, M. G. Bawendi, R. Tumminelli, and J. R. Haavisto, U.S. Patent **5,260,957** (1993).
10. C. K. Grätzel and M. Grätzel, J. Am. Chem. Soc. **101**, p. 7741 (1979).
11. A. Hagfeldt and M. Grätzel, Chem. Rev. **95**, p. 49 (1995).
12. T. Trindade, P. O'Brien, and Xiao-mei Zhang, Chem. Mater. **9**, p. 523 (1997).
13. M. Green and P. O'Brien, Adv. Mater. Optics Elect. **7**, p. 277 (1997).
14. B. Ludolph, M. A. Malik, P. O'Brien, and N. Revaprasadu, J. Chem. Soc., Chem. Comm. p. 1849 (1998) and references therein.
15. M. Green and P. O'Brien, J. Chem. Soc., Chem. Comm. p. 2459 (1998).
16. M. Lazell and P. O'Brien, J. Mat. Chem. **7**, p. 1381 (1999).
17. K. Abe, T. Hanada, Y. Yoshida, N. Tanigaki, H. Takiguchi, H. Nagasawa, M. Nakamoto, T. Yamaguchi, and K. Yase, Thin Solid Films **329**, p. 524 (1998).
18. JCPDS file 21-829.
19. JCPDS file 10-454.
20. C. B. Murray, B. G. Norris, and M. G. Bawendi, J. Am. Chem. Soc. **115**, p. 8706 (1993).
21. JCPDS file 41-1049.
22. M. G. Bawendi, A. R. Kortan, M. L. Steigerwald and L. E. Brus, J. Chem Phys. **11**, p. 7282 (1989).

SPUTTERING EFFECTS AND TWO DIMENSIONAL ARRANGEMENT OF NANOPARTICLES IN INSULATORS UNDER HIGH FLUX Cu^- IMPLANTATION

N. Kishimoto, C.G. Lee, N. Umeda*, Y. Takeda and V.T. Gritsyna**
National Research Institute for Metals, 1-2-1 Sengen, Tsukuba, Ibaraki 305-0047, Japan
kishin@nrim.go.jp
*Tsukuba University, 1-1 Ten-nodai, Tsukuba, Ibaraki 305-0006, Japan
**Kharkov State University, Kharkov 310077, Ukraine

ABSTRACT

Application of negative heavy ions, alleviating surface charging on insulators, enables us to conduct low-energy and high-flux implantation, and leads to a well-defined tool to fabricate near-surface nanostructures. Negative Cu ions of 60 keV, at high doses, have generated nanocrystals in amorphous(a-)SiO_2 with a size (~10 nm) suitable for nonlinear optical devices. The kinetic processes, inside the solid and at the surface, are studied by cross-sectional TEM and tapping AFM, respectively. In a-SiO_2, nanoparticles spontaneously grow with dose rate, being controlled by the surface tension and radiation-induced diffusion. Furthermore, the nanospheres give rise to a two-dimensional (2D) arrangement around a given dose rate. The 2D-distribution occurs in coincidence with enhanced sputtering where a considerable Cu fraction sublimates from the surface. The dose-rate dependence of nanoparticles indicates that the surface-sputtering process influences the intra-solid process and contributes to the 2D-distribution. A self-assembling mechanism for 2D-arrangement of nanospheres is discussed taking into account contribution of the surface sputtering.

INTRODUCTION

Metal nanoparticles embedded in insulators exhibit nonlinear optical susceptibility and the fast response of pico-seconds with the surface plasmon resonance [1,2], and are demanded for photonic applications. We have focused on a nanoparticle system distributed within a thin thickness, ideally a two-dimensional (2D) configuration, which may provide an electronic and/or optical element of the integrated devices in future. To seek such a special nanophase, we have employed negative-ion implantation of a relatively low energy, e.g., 60 keV[3-5]. Negative ions cause the same intra-solid processes as positive ions, but have a merit of accurate implantation by virtue of little surface charging on insulators[6]. In comparison with conventional methods, e.g., glass forming or molecular-beam epitaxy, advantages of the present method are the kinetic variety with ion energy deposition and the spatial controllability of implants. In a common insulating substrate of amorphous (a-)SiO_2, kinetic variations of nanoparticles have emerged in significant dose-rate dependence of optical absorption and depth-oriented migration of implants, e.g., bimodal distribution in depth [7,8]. Particularly, it has been occasionally found [9] that strong depth-oriented rearrangement of nanoparticles gives rise to a 2D-configuration of nanoparticles at a certain irradiation condition. As well as those ion-induced kinetics, a variety of the nanoparticle morphology may be contributed by the metastable natures of a-SiO_2, i.e., less densely packed structure, radiolysis, a variety of defects, ring structures[10] and radiation-induced viscous flow [11]. Since stochastic collision events of implants lead to a gaussian-like broad profile of implants, a normal precipitation process is unlikely to cause a 2D-distribution and there must be a centripetal force to a certain depth which causes self-assembly of nanoparticle distribution. A solute diffusion model due to ion-energy gradient [9] was presented to explain the narrowing and shallowing process of nanoparticle distribution. It has been also observed that surface sputtering concurrently occurs and suggests correlation with the nanoparticle profile[4,5]. In this paper, we focus on relationship between the sputtering process and the 2D-arrangement of nanoparticles in a-SiO_2. A self-assembling mechanism of nanoparticles is discussed with respect to the ion-induced sputtering process.

Mat. Res. Soc. Symp. Proc. Vol. 581 © 2000 Materials Research Society

EXPERIMENTAL PROCEDURES

Negative Cu ions of 60 keV were implanted into substrates at various dose rates (ion current density) up to 100 $\mu A/cm^2$, at a fixed total dose of 3×10^{16} ions/cm^2. The negative ion technique including the apparatus was described elsewhere [12]. Optical grade a-SiO_2 (KU-1: 820 ppm OH^-) of 15 mm in diameter and 0.5 mm in thickness was employed for the substrates. Depth profiles and sputtering yields for 60 keV Cu were estimated with the TRIM code[13], besides the succeeding atomic rearrangement. The projectile range and the straggling width calculated are 45 nm and ±15 nm, respectively. The total dose of 3×10^{16} ions/cm^2 corresponds to about 10 atomic% at the projected peak. An aperture mask(Cu), with a 12 mmϕ hole, was mounted on the specimen surface to fasten to the specimen temperature was monitored by a thermocouple and an infrared pyrometer.

After optical measurements of an implanted specimen [illegible] morphology was measured by atomic-force microscopy (AFM) in the tapping [illegible] surface sputtering was estimated with the roughness, as well as the step height at the mask. Cross-sectional electron microscopy (X-TEM) was next conducted to evaluate nanostructures along the Cu-implanted depth. A thin Cr film (5 nm thick) as a marker layer was pre-coated onto the implanted surface, and thickness of the cross-section was measured by tilting the Cr layer. Depth profiles of Cu atomic density were obtained from the nanoparticle volume; Cu spheres (or parts of a sphere) were statistically counted in the X-TEM photos.

RESULTS AND DISCUSSION

In-beam formation of metal nanoparticles is a highly dynamical process in the a-SiO_2 under high flux ions. With increasing dose rate, not only the particle size increases, but also the depth profile of nanoparticles significantly varies [4,5,9]. Concurrently, the surface texture varies with dose rate, as will be shown. Our major interest has been cast on a special in-plane structure of nanoparticles which is attained by chance at a certain dose rate, while usual depth profiles at high dose rates are bimodal distributions in depth[7,8]. Dose-rate dependence of nanoparticle morphology changes systematically with the mask-aperture size [9], and the mask size for the present data is fixed to be 12 mm diameter. After showing a typical image of the nanostructure, we will next discuss a mechanism in terms of correlation with the sputtering process.

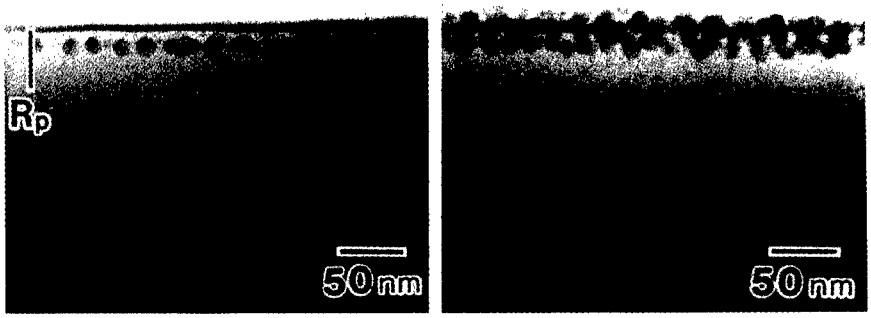


Fig. 1 Cross-sectional TEM images of a-SiO_2 implanted with 60 keV Cu^- at 45 $\mu A/cm^2$ to 3×10^{16} ions/cm^2. The upper and the lower are the edge-on cross-section (a) and the 15°-tilted image (b), respectively. A dark layer on the surface is a Cr coating as a marker.

Figures 1 (a) and (b) show cross-sectional TEM images, edge-on (a) and 15°-tilted (b), respectively, of an a-SiO_2 implanted with 60 keV Cu^- at 45 μA/cm^2 to 3×10^{16} ions/cm^2. As seen in these images, spherical nanoparticles are spontaneously aligned in a linear chain in the as-implanted specimen. Tilting the specimen from the edge-on direction (Fig. 1(b)) demonstrates fairly uniform dispersion of nanoparticles. The nanospheres, without applying post-irradiation annealing, were confirmed to be single Cu crystals by electron diffraction. Accordingly, the nanostructure can be regarded as a *self-assembled two-dimensional structure* of nanospheres. The depth position is much shallower than the projected range (R_P = 45 nm), which implies that significant atomic rearrangement has occurred.

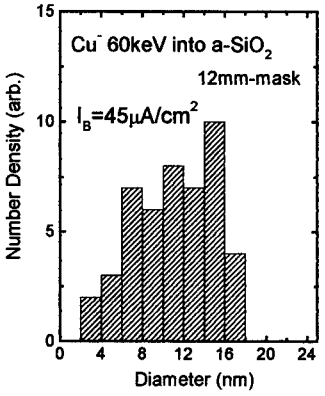


Fig. 2 Size distribution of nanocrystals in the specimen Cu^--implanted at 45μA/cm^2 to 3×10^{16} ions/cm^2.

Fig.2 shows size distribution of the nanospheres in the specimen implanted with Cu^- at 45 μA/cm^2 to 3×10^{16} ions/cm^2. Although the nanoparticle size distributes from 2 to 18 nm, the major part of the size ranges around the average diameter of 11 nm. The nanoparticle size is suitable for optical applications with respect to surface plasmon resonance [4,5,9,14], whereas a smaller size less than a few nm rather weakens the resonance mode. The average mutual distance among the in-plane particles is 26 nm. This structure consists of copious in-plane nanoparticles being transformed from a gaussian profile whose predicted peak was about 10 % with the TRIM code. The nanosphere formation is dominated by the Ostwald ripening, since roundness of nanoparticles indicates a mechanism of surface tension-controlled growth under radiation-induced diffusion[4]. Furthermore, the 2D-arrangement claims the presence of a depth-directional driving force in addition to the isotropic ripening.

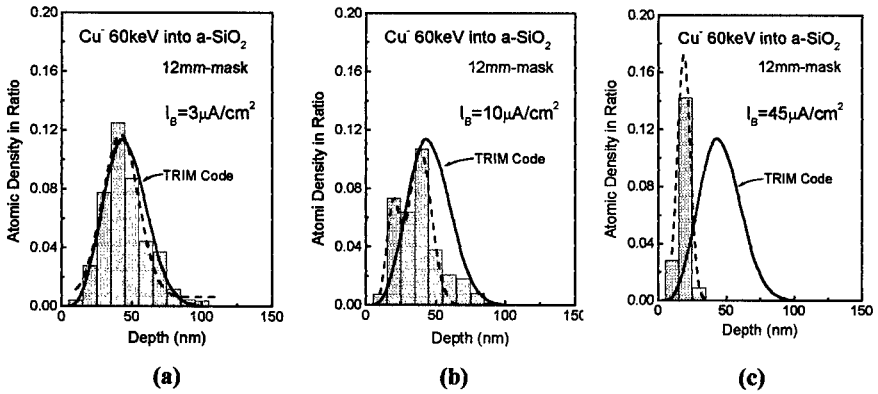


Fig. 3 Dose-rate dependence of depth profiles of Cu atomic density in the a-SiO_2 implanted with Cu^- at 3 μA/cm^2 (a), 10 μA/cm^2 (b) and 45 μA/cm^2 (c), to 3×10^{16} ions/cm.

Up to the present, we have proposed one of the possible mechanisms that dose-rate dependent narrowing and shallowing of atomic profiles results from ion-energy deposition and its depth gradient[9]. Figs. 3 (a)-(c) show depth profiles of the atomic density of

nanoparticles in a Cu^-- implanted a-SiO_2, at 3, 10 and 45 $\mu A/cm^2$, respectively. Below about 10 $\mu A/cm^2$, the Cu depth-profile agrees with that of the TRIM-code. It should be noted that the depth-oriented rearrangement, including the 2D-arrangement, never occurs at low dose rates. With increasing the dose rate, the Cu profile becomes shallower towards the surface and narrower, as compared to those at the lower dose rates. The narrowing effect implies enrichment of the Cu implants to the shallow position, instead of diffusive broadening. The atomic rearrangement in depth indicates that a depth-directional driving force operates, since the Ostwald mechanism simply gives isotropic ripening of nanoparticles. Fig. 4 shows comparison between depth profiles of Cu atomic density at 45 $\mu A/cm^2$ (Fig. 3(c)) and the one predicted, as well as electronic and damage energies, calculated by the TRIM code[13]. For Cu ions around 60 keV, the peaks of energy depositions and the implants do not agree with each other but the formers are located shallower than the latter. The basis of the energy-gradient-driven model is the atomic-profile shift with dose rate, towards the energy peak.. The atomic migration may be explained by a negative coupling between the energy flow and the atomic flow. In the present case, the electronic excitation effect is more likely to be responsible, since changing the aperture mask varied the Cu depth profiles[5, 9]. In details, the experimental profile of atomic density (the hatched area in Fig. 4) seems to be even shallower than those energy peaks and the total area of the histogram is smaller than that implanted. These tendencies suggest additional contribution of the surface sputtering, although the previous model is not inconsistent. Here, the main question is whether or not, and how, the surface process can affect the intra-solid process.

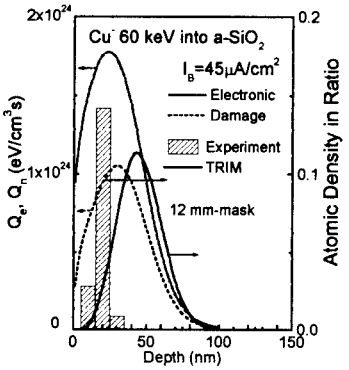


Fig. 4 Depth profiles of Cu atomic density in the a-SiO_2 implanted at 45 $\mu A/cm^2$, in comparison with the calculated one, electronic and damage energy depositions predicted by the TRIM code[13].



(a) (b) (c)

Fig. 5 Surface textures by AFM of a-SiO_2 implanted with Cu^- at 10 $\mu A/cm^2$ (a), 45 $\mu A/cm^2$ (b) and 100 $\mu A/cm^2$ (c), to 3×10^{16} ions/cm. The scanned area is 10 $\mu m \times 10$ μm.

It is naturally presumed for heavy ions in this energy range (>~1 keV) that surface sputtering becomes dominant. The sputtered thickness predicted by the TRIM code is about 10 nm with 3×10^{16} ions/cm^2, irrespective of dose rate[4]. Actual surface morphology varies with dose rate in the higher dose-rate range. Fig. 5 shows AFM images of the surface textures of a-SiO_2 at various dose rates, 10, 45 and 100 $\mu A/cm^2$. Up to 10 $\mu A/cm$, the implantation creates dense small bumps on the surface, whose height is about a few nm or less. Around 30-50 $\mu A/cm^2$, the fine bumps are rather smoothened away and there emerge long worm-like

textures. Around 100 μA/cm^2, the worm-like textures increase the number density but each height rather decreases. Fig. 6 shows dose-rate dependence of the surface roughness of a-SiO_2 implanted with Cu^- to 3×10^{16} ions/cm^2. Corresponding the surface morphology of Fig. 5, the roughness increases up to 10 μA/cm^2 and becomes rather smoother above 10 μA/cm^2. The smoothing in the higher dose-rate region indicates enhanced sputtering, where the step height becomes larger and optical absorption to rapidly decreases with dose rate, indicating a loss of Cu implants[4, 5]. Around 100 μA/cm^2, the sputtering process gives rise to a complete loss of implants, as well as disappearance of optical absorption. The loss of Cu implants was also verified in the RBS spectra[15].

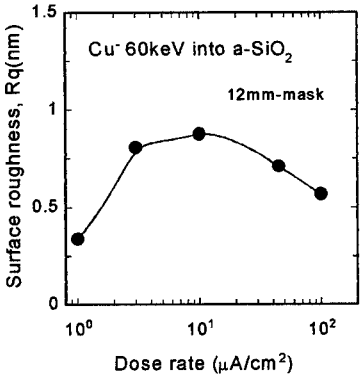


Fig. 6 Dose-rate dependence of surface roughness of a-SiO_2 implanted with Cu^- to 3×10^{16} ions/cm.

It is important that the two-dimensional arrangement of nanoparticles occurs in coincidence with the enhanced sputtering, somewhat before the complete loss of implants. A ratio of the Cu implants in nanoparticles to the incident amount is evaluated to be about 25 % from the X-TEM (Fig. 3(c)). The coincidence between the outer- and intra-solid processes indicates that the mass transport via the surface influences on the intra-solid nanoparticle arrangement, especially on the 2D-configuration. Fig. 7 shows a schematic diagram of a narrowing/shallowing mechanism of nanoparticles in a-SiO_2, where the energy deposition rates of electronic (Q_e) and damage (Q_n) processes are the ones calculated for a constant dose rate, 45 μA/cm^2. Figs. (a)-(c) correspond to the initial, intermediate and final stages (depending on time or dose). There are three important features in this diagram: The first is a driving force J towards the energy peak [9]. The second is the surface recession at a constant rate due to surface sputtering, whereas Q_e and Q_n do not move with respect to the surface. The third is presence of a precipitate-free zone beneath the surface, i.e., a depleted or low-concentration zone of implants, which has been justified by the X-TEM observation. The depleted zone implies escaping motion of solutes either outward to the surface or inward to the peak of C, but the latter is actually dominant because the total mass transport is outward (loss of implants). Accordingly, the model presumes solute concentration at the surface, $C(x=0)$, to be zero, which is caused by radiation-induced sublimation(or evaporation) of solutes, as suggested by the results of evaporation of Ag nanoparticles [16] and thermal annealing-induced loss of Cu nanoparticles in a-SiO_2 [17].

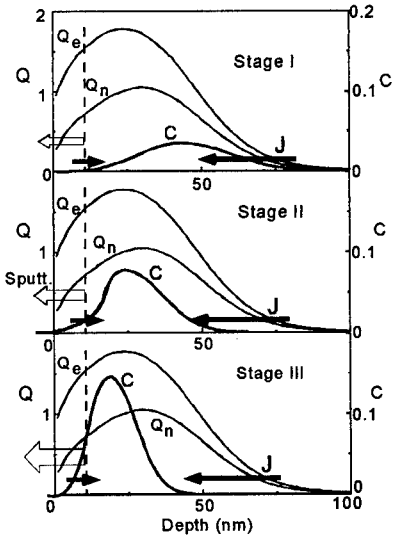


Fig. 7 Schematic diagram of a narrowing/shallowing mechanism of a concentration profile C in a-SiO_2. The energy deposition rates of electronic (Q_e) and damage (Q_n) are depicted in a unit of 10^{24} eV/cm·s.

At the first stage (Stage I), the driving force J operates but the concentration profile does not greatly differ from the original profile. With increasing dose (Stage II), the driving force J keeps operating and the shallowing of the C-

profile occurs to some extent. The surface recession concurrently proceeds with increasing dose, i.e., the *C*-profile relatively moves towards the surface, but the total loss in *C*. is not yet significant. In the Stage III, the formerly accumulated region further moves shallower, keeping the near-surface region being depleted. Although the loss in *C* becomes significant, a critical condition sharpens the *C*-peak. Once a fairly sharp peak in *C* is attained, the Ostwald ripening process may enhance the centripetal tendency. It is here noted that the sputtering process solely can not explain the phenomenon, because the narrowing effect begins even before the loss of implants becomes significant. The self-assembly of 2D-arrangement has been thus qualitatively explained by the model based on the sputtering process.

CONCLUSIONS

Negative-Cu ions of 60 keV have been implanted into a-SiO_2 at various dose rates up to 3×10^{16} ions/cm^2. Nanoparticles of single Cu crystal spontaneously grow with dose rate, being dominated by surface tension and radiation-induced diffusion. The nanospheres give rise to a 2D-arrangement in a critical dose-rate range where in-beam rearrangement and dominant sputtering of implants attain a certain balance. The dose-rate dependence of nanoparticles indicates that the surface-sputtering process influences the intra-solid atomic profile and significantly contributes to the 2D-distribution of nanoparticles by sharpening the depth profile. This self-assembly is caused by both the ion-induced processes at high fluxes and the metastable natures of a-SiO_2. It has been thus demonstrated in the present result that surface-sputtering process occasionally contributes to the in-plane arrangement, as a self-assembling driving force. By virtue of this mechanism, relatively high energy ions of more than 10 keV may fabricate thin layered- or 2D- nanostructures embedded in a solid. To apply this method to a nanoparticle system, understandings of the respective beam-solid kinetics are required.

REFERENCES

[1] R. Ruppin, J. Appl. Phys. **59**, 1355 (1986).
[2] T. Tokizaki, A. Nakamura, S. Kaneko, K. Uchida, S. Omi, H. Tanji and Y. Asahara, Appl. Phys. Lett. **65**, 941(1994).
[3] N. Kishimoto, V.T. Gritsyna, K. Kono, H. Amekura and T. Saito, Nucl. Instrum. and Methods in Phys. Res. **B127/128**, 579 (1997).
[4] N. Kishimoto, V.T. Gritsyna, K. Kono, H. Amekura and T. Saito, Mater. Res. Soc. Symp. Proc. Vol. 438, 435 (1997).
[5] N. Kishimoto, V.T. Gritsyna, Y. Takeda, C.G. Lee and T. Saito, Nucl. Instrum. Methods in Phys. Res. **B141**, 299 (1998).
[6] J. Ishikawa, H. Tsuji, Y. Toyota, Y. Gotoh, K. Matsuda, T. Tanjo and S. Sasaki, Nucl. Instrum and Methods in Phys. Res. **B96**, 7 (1995).
[7] R.H. Magruder III, R.F. Haglund, Jr, L.Yang, J.E. Wittig and R.A. Zuhr, J. Appl. Phys., **76**, 708 (1994).
[8] H. Hosono, H.Fukushima,Y.Abe, R.A.Weeks and R.A.Zuhr, J. Non-Cryst.Solids, **143**, 157 (1992).
[9] N. Kishimoto, N. Umeda, Y. Takeda, C.G. Lee, V.T. Gritsyna, Nucl. Instrum. and Methods in Phys.Res. **B148**, 1017 (1999).
[10] R.A.B. Devine, Nucl. Instrum. Methods in Phys. Res. **B91**, 378 (1994).
[11] M.L. Brongersma, E. Snoeks and A. Polman, Appl. Phys. Lett. **71**, 1628 (1997).
[12] N. Kishimoto, Y. Takeda, *V.T. Gritsyna and **E. Iwamoto and T. Saito, Proc. of 12th Int. Conf. on Ion Implantation Technology, IEEE (1999) in press.
[13] J.F. Ziegler, J.P. Biersack and U. Littmark, The Stopping and Range of Ions in Solids, (Pergamon Press, New York, 1985), Chap 8.
[14] Y. Takeda, V.T. Gritsyna, N. Umeda, C.G. Lee and N. Kishimoto, Nucl. Instrum. and Methods. in Phys. Res. **B148**, 1029 (1999).
[15] Thi Thi Lay, H. Amekura, Y. Takeda and N. Kishimoto Mater. Res. Soc. Symp. 1999 Spring Meeging (2000) in press.
[16] S.Y. Park, R.A. Weeks and R.A. Zhur, J. Non-Cryst. Solids, **191**, 281(1995).
[17] N. Umeda [a], N. Kishimoto [b], Y. Takeda [b], C.G. Lee [b] and V.T. Gritsyna, Nucl. Instrum. and Methods in Phys. Res. (1999) in press.

CRYSTALLIZATION BEHAVIOUR OF AMORPHOUS $Si_{0.5}Ge_{0.5}$ FILMS OBSERVED BY POSITRON ANNIHILATION

F. EDELMAN*, F. BÖRNER**, R. KRAUSE-REHRBERG**, P.WERNER***, R.WEIL****, W.BEYER*****, and R.BUTZ*****
*Materials Engng. Faculty, Technical University of Darmstadt, 64287 Darmstadt, GERMANY
Martin-Luther-Universität Halle-Wittenberg, Fachbereich Physik, D-06099 Halle(Saale), GERMANY, ***e-mail: krause@physik.uni-halle.de (corresponding author)*
***Max Planck Institute of Microstructure Physics, Halle/Saale D-06120, GERMANY
**** Technion-Israel Institute of Technology, Solid State Institute, 32000 Haifa, ISRAEL
*****Institut für Schicht- und Ionentechnik, Forschungszentrum Jülich, D-52425 Jülich, GERMANY

ABSTRACT

The crystallization behavior (ordering) of undoped and boron-doped $Si_{0.5}Ge_{0.5}$ films, deposited on SiO_2/Si(001) substrate by molecular beam epitaxy in high vacuum at room temperature, were studied by XRD, HRTEM and in situ by Doppler broadening spectroscopy using monoenergetic positrons. Some decomposition features of SiGe solid solutions were demonstrated via splitting the XRD peaks at high temperatures. The SiGe decomposition was detected in the precrystalline state of the SiGe undoped and doped films in the temperature range from 450 to 600 K by compaering S- and W-parameters of SiGe with that of amorphous silicon and germanium. In conclusion, we discuss model of internim ordering states before crystallization.

INTRODUCTION

Amorphous and polycrystalline $Si_{1-x}Ge_x$ films show prospective opto- and microelectronic applications in stacked solar cells and in liquid crystal display drivers[1,2]. According to the equilibrium phase diagram[3], the Si-Ge system presents a miscible solid solution in the whole range of composition, with random distributions of Si and Ge atoms. However, it is calculated theoretically[4] and demonstrated experimentally[5,6] that in a certain cases the crystalline SiGe ordered phase can be formed via the SiGe solid solution decomposition. Fig.1 demonstrates the decomposition featutres in the SiGe films deposited on amorphous SiO_2 substrates and annealed at high temperatures.

In this study, specially devoted to the amorphous SiGe films, stability, we prove, whether ordering in the Si-Ge system is also typical in the precrystalline state, below crystallization temperature, which was found close to 873 K for amorphous molecular-beam (MB) deposited $Si_{0.5}Ge_{0.5}$ films[7] (crystallization starts in a-Ge at 773 K and in a-Si (both MB) at 973 K[7-9]).

EXPERIMENT

Amorphous $Si_{0.5}Ge_{0.5}$ films (~ 0.5 μm), undoped and boron doped, were deposited at room temperature by molecular beam in ultrahigh vacuum (~ 10^{-10} Torr) on SiO_2(0,1 μm)/Si substrates. The amorphous films were crystallized during the experiments by vacuum annealing at temperatures between 573 and 1173 K for 10 min. High resolution TEM showed that crystallized $Si_{1-x}Ge_x$ films are partially ordered[3].

In addition, samples were analyzed by positron annihilation as references. Also for comparison, Si and Ge substrates were used which were implanted by ions of different species with doses which guarantee the amorphous state in the implanted layer. Four samples were prepared: Si:Si (200 keV with 5×10^{15} cm^{-2}), Ge:Si (400 keV with 5×10^{16} cm^{-2}), Ge:Ge (600 keV with 5×10^{15} cm^{-2}), and Si:Ge (300 keV with 5×10^{16} cm^{-2}).

The positron annihilation experiments were done with the slow positron beam system (POSSY) at Halle University. POSSY consists of a ^{22}NaCl positron source (0.5 GBq), a linear accelerator (up to 40 keV), and a Ge-γ-detector. The resolution (FWHM) of the detector is 1.6 keV measured with ^{85}Sr at 514 keV. Details about the setup can be found elsewhere[10].

During diffusion in a crystal a positron can be trapped by open-volume defects. In the case of our samples this results in a narrowing of the 511-keV annihilation line compared to defect-free material. Experimentally, the annihilation line is characterized by the line-shape

Mat. Res. Soc. Symp. Proc. Vol. 581 © 2000 Materials Research Society

parameters *S* and *W*. *S* relates to the relative fraction of counts in the center of the Doppler-broadened annihilation spectrum (511±0.8 keV), *W* is the relative fraction of counts in the wings of the spectrum (2.76 keV< $|E_\gamma$-511 keV|<3.96 keV). Positron trapping at vacancy-type defects results in an increase (decrease) of *S* (*W*) since annihilations at defects occur mainly with low momentum electrons. Every type of annihilation sites, e.g. bulk, surface, and different defects yields characteristic values of *W* and *S*.

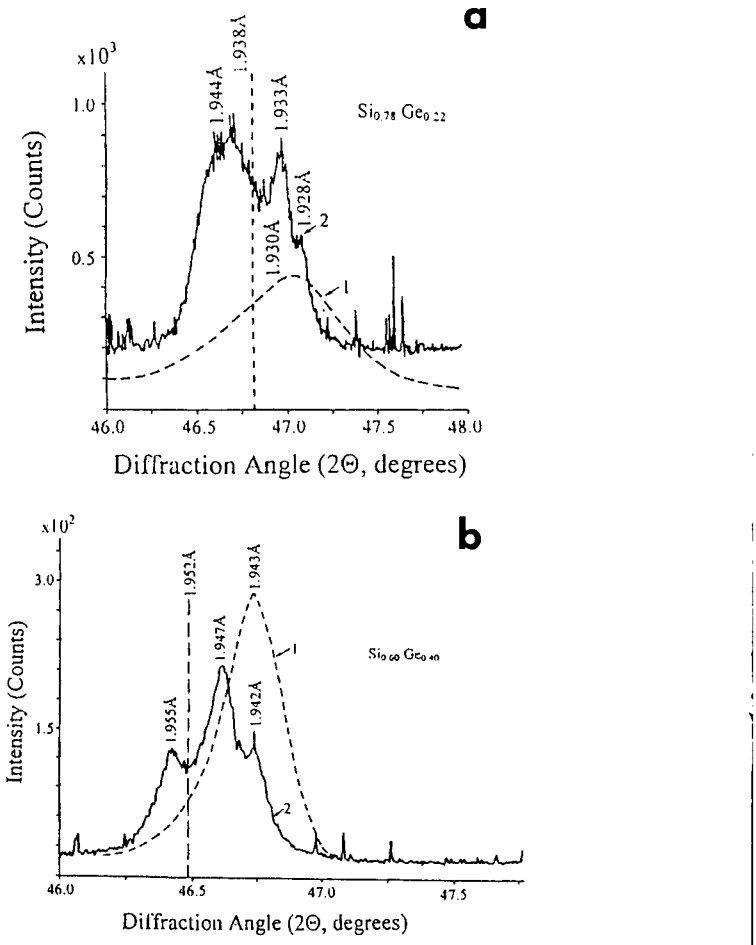


Fig.1. (220) x-ray diffraction spectra of an SiGe films.
a) $Si_{0.78}Ge_{0.22}$ film annealed at 873 K for 1 h (line 1) and at 1173 K for 1 h (line 2) revealing the change of the lattice constants during the progress from the crystallization beginning to the SiGe decomposition. The broken vertical line marks the expected peak position for a polycrystalline alloy without decomposition[3];
b) same as Fig.1a, but for $Si_{0.6}Ge_{0.4}$ film.

RESULTS

From XRD measurements it is shown that crystallization of amorphous $Si_{0.5}Ge_{0.5}$ films starts at 873 K. One may distinguish three stages of crystallization. In stage 1, up to 820 K there is no crystalline lattice structure detectable. Stage 2 (873 K–1073 K) shows broadened XRD spectra of crystalline SiGe. This broadening of the peaks can be explained by defects in the crystal structure. The films are fully crystallized in stage 3 after annealing higher than 1123 K. High resolution TEM showed that crystallized $Si_{1-x}Ge_x$ films are partially ordered[8].

The structure of the layer system of the as-grown samples (undoped and boron-doped): structure of the layer system is detectable by Doppler-broadening spectroscopy using slow monoenergetic positrons. As a result, the line-shape parameter *S* versus the implantation energy of the positrons is plotted (see Fig.2). The measured values for positron energies up to 8 keV can be assigned to the amorphous SiGe layer. For positron energies lower than 2 keV the influence of the surface of the sample can be seen. This part of the profile is of no relevance for this study. A minimum of the *S* parameter profile can be seen at about 15 keV. This part of the curve can be assigned to the SiO_2 buffer layer[11] . For positron energies higher than 20 keV, the *S* parameter belongs to the Si substrate of the sample. All measured values are normalized to the measured *S* parameter of crystalline Si(100) which can be used as a reference for defect-free material.

A short effective diffusion length of the positrons ($L_{+,eff}$ = 11.7 ± 1.5 nm) was found in the as-grown state of undoped SiGe layer. This value was obtained by a best fit on the *S(E)* curve (Fig.2) by the program VEPFIT[12]. It is a sign for the detection of saturated trapping of the positrons in open-volume defects in the as-grown SiGe layer. This behavior corresponds to a very high concentration of open-volume defects in the amorphous layer.

Isochronal annealings (10 min) of the undoped and B-doped SiGe layer were performed in steps of 50 K. The *S* parameter profile was measured at RT after every annealing step. The *S* parameter of the SiGe layer (S_{layer}) was plotted versus the annealing temperature (Fig. 3a). Three significant parts of the curve can be observed. Up to 450 K, the *S* parameter shows a strong decrease up to a value of 0.998, whereas the *S* parameter increases from 450 K to 600 K to about 1.036. After this behavior, there is another decrease up to the end of the annealing experiment.

The temperature of the detected changes of the *S* parameter is lower than at the begin of the crystallization at about 900 K observed by XRD[6]. So the observed changes should be related to structural modifications of the amorphous layer. There is no significant difference observable for the undoped and the B-doped sample.

The *S* parameter results from a superposition of the individual specific *S* parameters of the different annihilation sites weighted by the fraction of positrons trapped at these annihilation sites. Thus, nothing can be concluded about a change in the concentration or the kind of the detected defects by only observing the *S* parameter. For this reason the *S*-versus-*W* plot[13] has to be analyzed (Fig.3b). The *S* parameter of the SiGe layer S_{layer} (normalized to S_{Slicon}) measured after each annealing step was plotted versus the corresponding *W* parameter of the layer W_{layer}. Measured points, which form a straight line, correspond to two different positron annihilation sites with different fractions of trapped positrons in these two annihilation sites. Such a behavior is observable for the temperature region of the annealing experiment from 300K to 450K and the temperature range from 450K up to the end of the annealing experiment at 1000K.

Amorphous Si and Ge layers grown at low temperatures were also measured by Doppler broadening using slow positrons. The resulting (*W,S*) pairs of values are shown in the same *S*-versus-*W* plot (Fig. 3b). The same procedure was used to get the measurement values of the ion implanted Si and Ge samples.

At 300 K, the as-grown, amorphous SiGe layers are characterized by positron annihilation at a site which is characterized by a stronger silicon-rich surrounding. This can be concluded when comparing the observed *W,S* values with the amorphous silicon and germanium layers in the *S*-versus-*W* plot. After annealing at 450 K, the *W,S* values changes, and the annihilation site, is now closer to the value of amorphous germanium. In the following this will be called the interim state "a". We conclude that a structural change in the amorphous SiGe layer occurred during this low-temperature annealing step, and the positron is trapped in an open volume with Si surrounding (as-grown state) and at an open volume with Ge surrounding (state "a").

In the temperature interval from 450 to 600 K the measured line-shape parameters form another straight line which ends at a distinctive point. We assign this point with another interim

state on the way to the crystallization and call it state "b". The (*W*,*S*) pairs measured for higher annealing temperatures lay on the identical straight line. This behavior can be explained by the detection of the same open-volume defects with different annihilation fraction.

The study shows some interesting results. There is a noteworthy difference between amorphous Si produced by ion implantation and amorphous Si grown at low temperatures. There is an analog behavior of the Ge. Unfortunately, it can't be said, what's the difference in these structures.

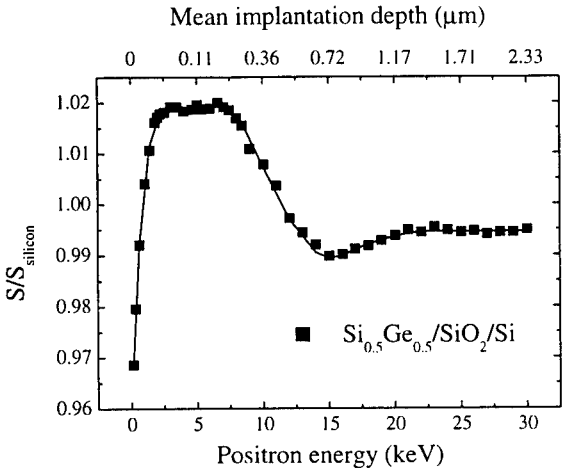


Fig.2. Results of Doppler-broadening spectroscopy measurements at an undoped amorphous $Si_{0,5}Ge_{0,5}$ film MB deposited at room temperature on a SiO_2(0,1 μm)/Si substrate. The *S* parameter is shown as a function of the positron incident energy. The measured values between 2 and 8 keV can be assigned to the amorphous SiGe layer. All values are normalized to the measured S parameter for defect-free crystalline Si(100).

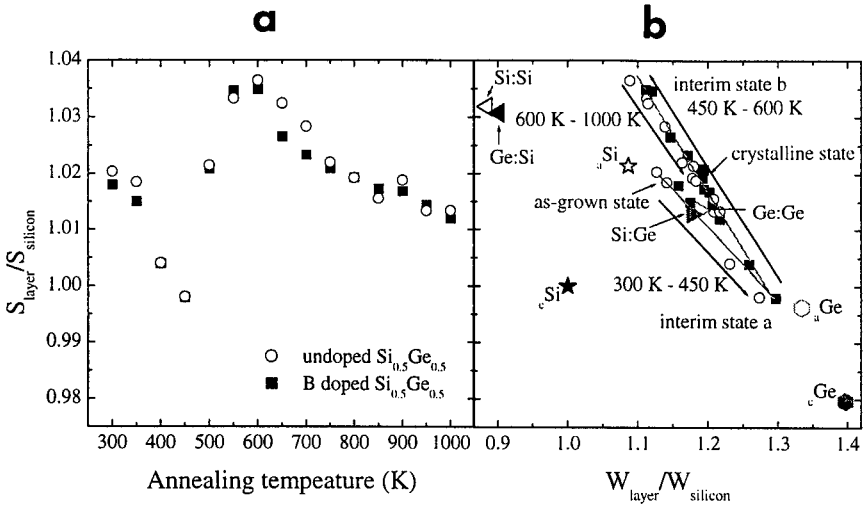


Fig. 3. a) Results of the annealing experiment of the undoped and B-doped $Si_{0,5}Ge_{0,5}$ films. The layer *S* parameter of the SiGe film is plotted versus the annealing temperature. It can be seen that there are three annealing steps detectable. b) *S*-versus-*W* plot of the annealing of the undoped and the B-doped $Si_{0,5}Ge_{0,5}$ films. It can be distinguish between three different positron annihilation sites: the as-grown state, the interim state a, and the interim state b. Some measured reference points are added for comparison, c-Si(100), a-Si, c-Ge(100), a-Ge, Si:Si(100), Ge:Si(100), Ge:Ge(100), Si:Ge(100). The implantation doses were sufficient to obtain amorphous layers in all samples.

CONCLUSIONS

Doppler broadening spectroscopy using slow positrons is able to detect the layer structure of the a-$Si_{0,5}Ge_{0,5}/SiO_2/Si$ samples. An increase of the temperature during the annealing experiment have the consequence that there are structural changes in the amorphous layer far below the crystallization temperature observed by different methods, e.g. XRD, TEM. It can be distinguished between two interim states before crystallization. The state "a" can be explained by a first structural ordering process after the growth of the amorphous layer which is characterized by a more germanium-surrounded open volume seen by the positron, than the layer in the as-grown state. The change to state "b" is reflected by the fact that the detected open volume is increased compared to the as-grown state and the interim state a. The changes can be interpreted as structural ordering processes of the amorphous SiGe-layer which separates the two species Si and Ge.

REFERENCES

1. Y.Hamakawa, W.Ma, and H.Okamoto, MRS Bulletin, **18**, p.38 (1992).

2. T.Sameshima and S.Usui, Mater. Res. Symp. Proc. **258**, p.117 (1992).

3. R.W.Olesinski and G.J.Abbaschian, Bull. Alloy Phase Diagrams, **5**, p.180, (1984).

4. A.Qteish and R.Resta, Phys. Rev. **B.37**, p.1,308; p.6,983 (1988).

5. A.Ourmazd and J.B.Bean, Phys. Rev. Lett., 55, p.765 ((1985).

6. F.Edelman, Y.Komem, P.Werner, J.Heydenreich, and S.S.Iyer, Solid State Phenomena, **37/38**, p.323 (1994).

7. F.Edelman, R.Weil, P.Werner, M.Reiche, and W.Beyer, phys. stat. sol.,**a150**, p.407 (1995).

8. F.Edelman, Y.Komem, S.S.Iyer, J.Heydenreich, and D.Baither, Thin Solid Films, 222, p.57 (1992).

9. (F.Edelman, J.Heydenreich, D.Hoehl, J.Matthäi, I.Melnik, A.Rzhanov, M.Voelskov, and P.Werner, phys. stat. sol., **a98**, p.383 (1986).

10. R. Krause-Rehberg and H.S. Leipner: *Positron annihilation in semiconductors,* (Springer-Verlag, Berlin 1999).

11. P. Asoka-Kumar, K.G. Lynn, and D.O. Welch: J. Appl. Phys. **76**, p.4,935 (1994)

12. A. van Veen, H.Schut, J.Haakvoort, R.A. de Vries, and M.R.Ijpma, AIP Conf. Proc. **218**, p.171 (1990).

13. L.Liszkay, C.Corbel, L.Baroux, P.Hautojärvi, M.Bayhan, A.W.Brinkmann, and S.Tatarenko, Appl. Phys. Lett. **64**, p.1,380 (1994).

SYNTHESIS OF NANOSTRUCTURED WC FILMS BY SUPERSONIC IMPACTION OF NANOPARTICLE AEROSOLS

W.T. Nichols[1], G. Malyavanatham[2], M.P. Beam[1], D.E. Henneke[3], J.R. Brock[3], M.F. Becker[2,4] and J.W. Keto[1,2]

[1] Department of Physics
[2] Texas Materials Institute-Materials Science and Engineering
[3] Department of Chemical Engineering
[4] Department of Electrical and Computer Engineering,
University of Texas at Austin, Austin, TX 78712

ABSTRACT

Tungsten carbide (WC) coatings were prepared using supersonic impaction of nanoparticles produced by pulsed laser ablation of microparticle aerosols. The influence of experimental parameters such as, carrier gas type and impaction velocity on the structure, composition and physical properties of the resultant particles and films were studied. It was found that stoichiometric, crystalline films could be grown. These films pass both the adhesive lift off and scratch tests. TEM investigations indicate that the laser ablation forms individual particles with mean size of 7 ± 3 nm. At the highest aersol pressures small aggregates were also observed, and adjustment of the gas pressure in the laser interaction cell was found to control the degree of aggregation. Upon impaction, the separate particles form dense, self sintering nanocrystalline films, with helium forming the most dense as determined from SEM images.

INTRODUCTION

Presently there is a great deal of interest in nanostructured films and coatings. Materials consolidated from nanoparticles have shown improved physical and mechanical properties such as, sinterability and hardness. A natural application of such materials would be in protective and wear resistant coatings to enhance performance and lifetime of moving parts. Important considerations are the creation of hard and adherent coatings that are chemically compatible with substrates while maintaining a low substrate temperature throughout the coating process. Tungsten carbide is well suited for these hard coatings due to its low coefficient of friction, high corrosion resistance in acidic media and its ability to maintain a high degree of hardness at elevated temperatures [1].

The process of supersonic impaction of aerosol particles has been studied in detail [2]. It was shown that particles down to molecular scale can be deposited onto plates with high efficiency. The minimum particle size impacted depends primarily on the extent to which the gas jet expands before encountering the substrate. This expansion can be controlled by the pressure ratio, gas type and nozzle-substrate distance. Aerosol particle impaction has been used to deposit a number of technologically useful films. Kashu et al. used a subsonic gas jet with 20-70 nm particles to produce nanostructured films of TiN and a number of metals [3]. More recently, Rao et al. has demonstrated the growth of SiC films at high rates by supersonically impacting nanoparticles produced in a DC arc source [4-6]. In that process precursors react chemically, in a

Mat. Res. Soc. Symp. Proc. Vol. 581 © 2000 Materials Research Society

hot plasma producing SiC of the proper stoichiometry. In this work we describe a complementary physical technique that has many of the same advantages as in the work of Rao and co-workers.

The Laser Ablation of Microparticles (LAM) process is well suited for producing tribological coatings for several reasons. First, laser ablation transfers the target material stoichiometrically to the substrate [7]. Second, low substrate temperature (< 300 C) can be maintained throughout the coating process. This is important because the structural integrity of the substrate can be compromised at elevated temperatures. For example, high speed steel loses its hardness at temperatures above 550 C [8]. In addition, a heated substrate will lead to grain growth within the nanostructured film, degrading its properties. A third advantage of the LAM process is its versatility in both the type of material that can be deposited and the control over such process parameters as mean nanoparticle size, impaction velocity, and film growth rate. The fourth attribute of the LAM process is its demonstrated ability for high volume production and deposition of coating materials which would allow the utilization of this process for manufacturing.

EXPERIMENTAL APPARATUS

A schematic of the laser ablation of microparticle aerosol apparatus is shown in Fig. 1. The system utilizes a small aerosol generator employing a fluidized bed which produced microparticle densities of 10^5-10^7 cm^{-3}. The feedstock is nominally 5 micron dia. , > 99% pure tungsten

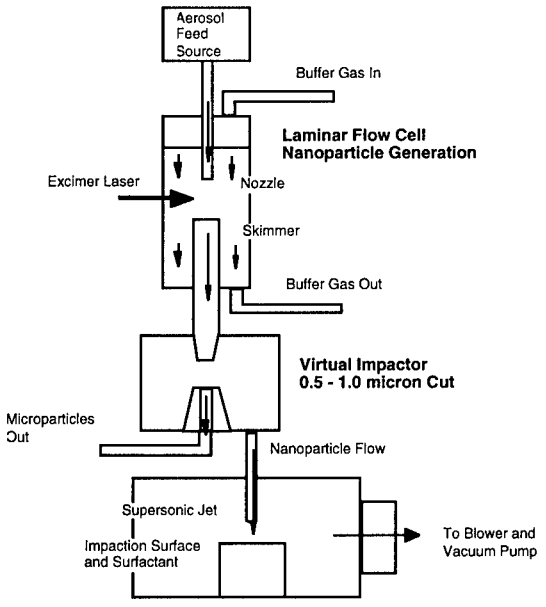


Fig. 1. Schematic view of the nanoparticle generator connected to the film growth chamber.

carbide microparticles and is delivered in either helium or argon carrier gas into the laser interaction cell at a well defined mass flow rate. Here the aerosol is ablated using a pulsed KrF excimer laser (λ = 248 nm, 200 Hz rep. rate) with 10 ns pulse width focused to fluences between 2-9 J/cm^2. The pressure within the system was adjusted by throttling an exhaust leak valve to maintain a steady-state.

After ablation the nanoparticle aerosol is skimmed and enters a virtual impactor to remove the few remaining particles larger than 500 nm. The nanoparticle output of the virtual impactor is then fed through a supersonic nozzle into the collection chamber. The jet is operated with either a 150 or 200 μm orifice and a pressure ratio of ~10^4. Supersonic impaction produces stream lines near the impaction surface that have a radial component with respect to the symmetry axis of the flow. This in turn produces a radial distribution of particles on the collection surface that is graded slightly from the largest particles in the center to smaller particles moving outward [2]. The smallest particles (< 1 nm) have insufficient normal momentum component to be collected. Thus, by controlling the initial particle size, coupled with low substrate temperatures, films of well-defined grain sizes can be grown.

For characterization of the nanoparticles and nanostructured films a number of techniques have been employed. Individual particles have been collected onto carbon coated TEM grids for studies of size, size distribution, crystal structure and morphology. Samples were collected either just below the laser breakdown region, before the skimmer, and on the collection substrate in the supersonic impaction chamber. To study the composition, nanostructure and mechanical properties of the grown films, high velocity impaction of the nanoparticles onto a variety of substrates such as glass, silicon wafers, stainless steel and aluminum were carried out as described below.

RESULTS AND DISCUSSION

Particle Size and Morphology

Figure 2 shows a representative transmission electron micrograph taken of nanoparticles collected near the ablation region using a helium aerosol at 1 atm. Tungsten Carbide nanoparticles show very similar attributes to other materials ablated in this system [9-11]. The formed particles are generally spheroidal and non-agglomerated with a mean size for the size distribution of 7 nm and a standard deviation of 2.7 nm. This dispersion is larger compared to most materials, and similar to earlier experiments on permaloy nanoparticles, it probably results from the larger spread in size for the feedstock microparticles.[12] Inherent in the LAM process, nanoparticles acquire a large positive charge during laser ablation. This charge is responsible for inhibiting nanoparticle coagulation and agglomeration prior to impaction. We observe in high resolution transmission electron micrographs that smaller (< 10 nm) particles were generally single crystals with well defined lattice planes, while larger particles typically displayed twinning behavior with a corresponding grain boundary. These larger particles are also observed in Fig. 2 to be non-spherical and likely result from coalescence late in the cooling of the expanding nanoparticle cloud which results from the exploded microparticle. These late nanoparticle collisions within the aerosol lead to coagulation, which is responsible for the twinning behavior. For longer residence times the charge on the nanoparticles is reduced by recombination. By decreasing the pressure within the ablation cell the recombination times are increased and mean free paths for collisions

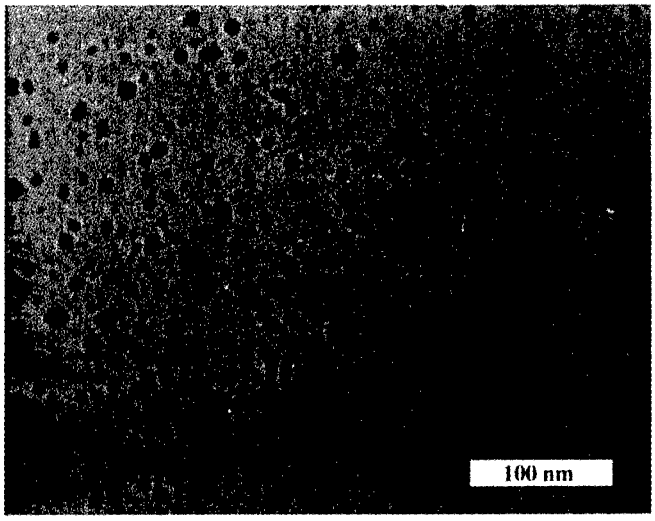


Fig. 2. Representative transmission electron micrograph of as produced tungsten carbide nanoparticles. Collection was from just below the laser ablation region shown in fig. 1. prior to the skimmer. Ablation was carried out at a laser fluence of 2 J/cm^2 in 1 atm of Helium.

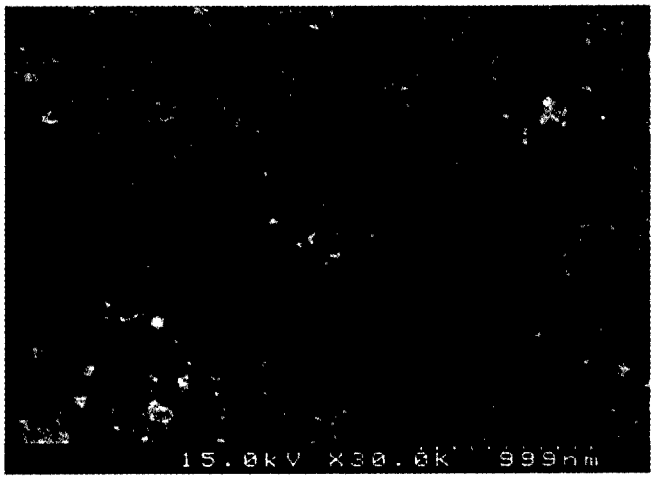


Fig. 3 Scanning electron micrograph of a nanostructured tungsten carbide film. The film was grown at room temperature from nanoparticles ablated at 2 J/cm^2 in helium.

increased; both effects lead to reduced coagulation [13]. Decreasing the pressure also has the negative effect of decreasing the expansion velocity of the supersonic jet which then prevents the impaction of smaller particles and lowering the kinetic energy of the nanoparticles which produces sintering at room temperatures. Consequently, it was determined that 1 atm was the best pressure for film growth. In addition, individual particle size was tested as a function of laser fluence and gas type. It was found that above the dielectric breakdown threshold of the microparticles that the laser fluence has little effect on the particle size and morphology. Similarly, argon, nitrogen and helium all produced quality nanoparticles, with helium yielding a higher percentage of smaller nanoparticles due to the reduced coagulation.

Film Structure and Composition

Upon supersonic impaction, individual particles are found to sinter into a dense adherent film. Figure 3 shows an example of a high density film produced by impaction from a helium carrier gas at room temperature. The size of the film on the substrate varies with nozzle orifice size and nozzle-substrate distance, but is nominally 2-3 mm in diameter. Thickness is controlled by deposition time with growth rates on the order of 0.1 microns per second. The rebounding of particles from the surface appears to decrease the deposition rate. When collecting the nanoparticles onto a substrate coated with high vacuum grease and measuring the mass increase, we measured film growth rates greater than 1 micron per second. PZT and $YBa_2Cu_3O_7$ films have already been grown at these rates in this system. The use of higher particle impaction velocities and elevated substrate temperatures is expected to reduce particle bounce-off. Under current conditions void area was determined from SEM images similar to that shown in Fig. 3. Parameters such as gas type, nozzle orifice diameter and nozzle-substrate distance were varied to determine conditions for the fewest voids. From this analysis, the smaller orifice size (150 μm) with helium gas yielded the densest films.

Phase composition was determined using x-ray diffraction (XRD) from films deposited onto glass slides with a thin coating of high vacuum grease to minimize particle bounce-off. The results show that the films are pure WC in agreement with the starting feedstock. In addition, qualitative tests of the mechanical properties of the films deposited on stainless steel, single crystal silicon and aluminum were performed. Adhesion was determined by applying a piece of adhesive tape over the deposit, pressing firmly and then removing the tape to observe if any of the film was pulled off. In general, a halo of WC "dust" was removed from around the deposit with no lift off of the central deposit. The outer halo is believed to be due to particles that have settled on the surface after bouncing from the center region. Using a hardened steel scribe, scratch tests were performed. Films deposited at small nozzle-substrate distances showed good scratch resistance while films made at large distances were easily scratched. These results indicate that at room temperature the velocity of particle impaction is vital to dense, hard film growth. Future research will measure film hardness.

CONCLUSIONS

We have demonstrated that nanoparticles formed by laser ablation of microparticle aerosols and supersonically impacted onto a substrate is a viable method for producing nanostructured films. Tungsten carbide nanoparticles produced in the ablation were found to be primarily

spheroidal and non-agglomerated with a mean size of 7 nm as determined by TEM. Laser fluence was found to have little effect on the nanoparticles, however ablation in helium carrier gas appeared to make the smallest particles. Compositional purity of the impacted films was confirmed by x-ray diffraction. SEM images of the films indicate that they are dense with nanostructured grains. Qualitative tests of the mechanical properties of the films demonstrate that they are adhesive and scratch resistant.

ACKNOWLEDGMENTS

We gratefully acknowledge support from the NSF GOALI Program (grant no. CTS-9530347), the Texas Advanced Technology Program (grant no. 3658-348), the Robert A. Welch Foundation and the Materials Research Society (Undergraduate Materials Research Initiative). We would also like to thank M. Schmerling for assistance in obtaining the SEM data.

REFERENCES

1. H. Holleck, J. Vac. Sci. Technology **A 4**, p. 2661 (1986).
2. J. Fernandez de la Mora, S.V Hering, N. Rao and P.H. McMurry, J. Aerosol Sci. **21**, p. 169 (1990).
3. S. Kashu, E. Fuchita, T. Manabe and C. Hayashi, Japn. J. Appl. Phys. **23**, p. L910 (1984).
4. N.P. Rao, H.J. Lee, M. Kelkar, D.J. Hansen, J.V.R Heberlein, P.H. McMurry and S.L. Girshick, Nanostructured Materials **9**, p. 129 (1997).
5. N.P. Rao, N. Tymiak, J. Blum, A. Neuman, H.J. Lee, S.L. Girshick, P.H. McMurry and J Heberlein, J. Aerosol Sci. **29**, p. 707 (1998).
6. A. Neuman, J. Blum, N. Tymiak, Z. Wong, N.P. Rao, W. Gerberich, P.H. McMurry, J.V.R. Heberlein and S.L. Girshick, IEEE Trans. Plasma Sci. **27**, p. 46 (1999).
7. D.H. Lowndes, D.B Geohegan, A.A. Puretzky, D.P. Norton and C.M. Rouleau, Science **273**, p. 898 (1996).
8. W.D. Sproul, Science **273**, p. 889 (1996).
9. W.T. Nichols, D.E. Henneke, G. Malyavanatham, M.F. Becker, J.R. Brock, J.W. Keto, H.D. Glicksman, to be published.
10. H. Cai, N. Chaudhary, J. Lee, M.F. Becker, J.R. Brock and J.W. Keto, J. Aerosol Sci. **29**, p. 627 (1998).
11. M.F. Becker, J.R. Brock, H. Cai, D.E. Henneke, J.W. Keto, J. Lee, W.T. Nichols, H.D. Glicksman, Nanostructured Materials **10**, p. 853 (1998).
12. Jaemyoung Lee, Michael F. Becker, James R. Brock, John W. Keto, and Rodger M. Walser, IEEE. Trans. on Magnetics **32**, p. 4484 (1996).
13. W.T. Nichols, G. Malyavanatham, D.E. Henneke, M.F. Becker, J.R. Brock, J.W. Keto, H.D. Glicksman, submitted to J. Nanoparticle Research.

STRUCTURE OF POLYCRYSTALLINE SILICON FILMS BY GLOW-DISCHARGE DECOMPOSITION USING SiH_4/ H_2/ SiF_4 AT LOW TEMPERATURE

R. TSUCHIDA, M. SYED, T. INOKUMA, Y. KURATA, and S. HASEGAWA
Department of Electronics, Faculty of Technology, Kanazawa University, Kanazawa 920-8667, Japan

ABSTRACT

For poly-Si films prepared by a plasma-enhanced chemical vapor deposition, we examined the changes in the local structure caused by adding H_2 and/or SiF_4 in the SiH_4 feed gases and by changing supplied rf power values. The conditions of low rf power supply, low H_2 addition, and SiF_4 addition allow formation of films with microcrystalline or nanocrystalline structures. In addition, the H_2 or SiF_4 addition was found to be effective in promotive growth of <111> or <110> grains, respectively. In such low crystallized films, it was suggested that high-angle boundary would be formed, leading to a decrease in the density of SiH_2 and Si dangling bonds, and to an increase in g values.

INTRODUCTION

Polycrystalline silicon (poly-Si) films are widely used in a variety of electronic devices, such as a semiconductor in thin-film transistors (TFTs) and electrodes in Si integrated circuits. Furthermore, nanocrystalline Si (nc-Si) have attracted increased interest as a material in optical devices. Properties of poly-Si and nc-Si strongly depend on changes in the local bonding structure. In the present work, poly-Si and nc-Si films were prepared by a plasma-enhanced chemical vapor deposition (PECVD) method and we report the crystallization phenomena and the changes in the local structure caused by adding H_2 and/or SiF_4 in the SIH_4 feed gases and by changing supplied rf power values. These properties were investigated by x-ray diffraction (XRD), Raman scattering, Fourier transform-infrared (FT-IR) absorption, and electron spin resonance (ESR) of Si dangling bonds.

EXPERIMENTAL

The poly-Si films were prepared by PECVD of $SIH_4/SiF_4/H_2$ mixtures with different gas-flow-rate ratios. The SIH_4 flow rate, $[SIH_4]$, was fixed at 1.0 sccm and the conditions of $[H_2]$ = 0, 5, 10, and 20 sccm and $[SiF_4]$ = 0 and 0.5 sccm were used. The dynamic gas pressure and the deposition temperature were 0.8 Torr and 300 ° C, respectively. A rf power between 5 and 40 W was supplied and the film thickness was fixed at around 1 μm. The samples were deposited on glass (Corning 7059) substrates for XRD and Raman scattering measurements, and on crystal Si substrates for ESR and Fourier transform-infrared (FT-IR) absorption measurements.

RESULTS AND DISCUSSION

Figure 1 shows the Raman spectra for films with (A) $[H_2]$ = 0 and $[SiF_4]$ = 0 sccm, (B) $[H_2]$ = 0 and $[SiF_4]$ = 0.5 sccm, (C) $[H_2]$ = 20 and $[SiF_4]$ = 0 sccm, (D) $[H_2]$ = 20 and $[SiF_4]$ = 0.5 sccm, deposited at a rf power value of 5 W (solid curves) or 20 W (broken curves). In these spectra, the Raman spectra due to amorphous and crystalline phases in a film can be observed at around 480 and 520 cm^{-1}, respectively. The volume fraction of the crystalline phase, ρ, in the films can be estimated from the intensity ratio of the amorphous and crystalline components [1]. As seen in Fig. (A), for the film with $[H_2]$ = 0 and $[SiF_4]$ = 0 sccm the Raman spectrum is found around 500 cm^{-1} as the film is deposited at 5 W. This 500-cm^{-1} component may arise from microcrystalline (mc-) or nc- structures in the film. However, an increase in the rf power is found to assist the crystallization, and to shift the spectrum toward a higher wave number side, though the peak wave number does not reach that expected for crystalline phases (520 cm^{-1}). On the other hand, when the rf power condition of 5 W is used, the addition of SiF_4 under $[H_2]$ = 0 conditions allows the observation of a broad spectrum around 470 cm^{-1} [Fig. (B)], which will be also related to amorphous phases in the films. Thus, the SiF_4 addition is likely to suppress the

Mat. Res. Soc. Symp. Proc. Vol. 581 © 2000 Materials Research Society

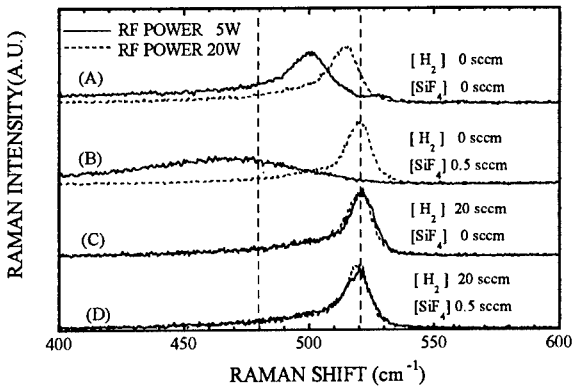


Fig. 1. Raman spectra for films with different $[H_2]$ and $[SiF_4]$ values and rf power values of 5 and 20 W.

crystallization as low rf power conditions are used, but the SiF_4 addition under high rf power supply appears to assist the crystallization as seen in Figs. (A) and (B). On the other hand, we find that an increase in $[H_2]$ acts to monotonically enhance the crystallization, independent of the rf power values, as seen in Figs. (C) and (D).

Enhanced crystallization with adding SiF_4 under high rf power supply, as seen in Fig. (B), has also been found in a previous work [2]. In that work, we examined the structural changes of poly-Si films which were deposited at rf power of 20 W and by changing $[SiF_4]$ under $[SiH_4]$ = 0.15 or 1 sccm conditions in SiH_4/SiF_4 feed gases without H_2 dilution. As a result, under $[SiH_4]$ =1 sccm, the crystallization was found to increase monotonically with increasing $[SiF_4]$. We suggested that the enhanced crystallization with adding SiF_4 would be caused by the effects of a change in the surface morphology of the substrates at an initial stage of film deposition [2]. These results will be discussed again at a later stage. As seen in Fig. 1, the effects of H_2 addition on the crystallinity are more sensitive for lower rf power. Furthermore, as seen in the results for two kinds of films with $[H_2]$ = 20 sccm, the H_2 addition is also found to weaken the effects of adding SiF_4 on the crystallinity. This may be due to the formation of more stable H-F bonds in the gas phase [3,4], since the binding energy of H-F bonds, E(H-F), is the highest among those of various bonds related to film growth: E(H-F) = 5.8 eV, E(Si-F) = 5.6 eV, E(Si-Si) = 1.8 eV, E(Si-H) = 3.1 eV, and E(H-H) = 4.5 eV (ref. 5). Thus, the increase in the density of H-related radicals may eliminate active F-related radicals in plasma. Based on the results shown in Fig. 1, the addition of SiF_4 or H_2 in SiH_4 feed gases not only causes a different contribution to the change in ρ (crystallinity) as a macro property of the films, but also strongly affects the local structure of Si network in the films.

Figure 2 shows (a) the relative intensities (integrated area) of <111> x-ray diffraction (XRD) spectra and (b) those of the <110> XRD spectra for films with $[H_2]$ = 0 and 20 sccm and $[SiF_4]$ = 0 and 0.5 sccm, as a function of rf power. The relative intensity with different textures, as shown in Fig. 2, was normalized using the intensity of the corresponding XRD from Si powder. The difference in film thickness among samples was corrected using the x-ray absorption coefficient for Si. As shown in this diagram, the <110> texture for films with $[H_2]$ = 0 and $[SiF_4]$ = 0.5 sccm under high rf power supply is found to be the strongest spectrum among those from different textures. The average grain size, δ (*nkl*), of grains with a *nkl* crystal plane was estimated from the half-width values of the XPD spectra, using the Scherrer's formula [6]. Figures 3(a) and 3(b) shows the average grain size, δ, estimated from (a) the <111> and (b) <110> XRD spectra for the films shown in Fig. 2, as a function of rf power. As seen in Figs. 2 and 3, it is found that the <111> grain growth is enhanced as $[H_2]$ increases, while the <110> grain growth is enhanced as $[SiF_4]$ increases under $[H_2]$ = 0 sccm conditions. In a previous work, we found that the increase in $[SiF_4]$ weakened the <111> texture and strengthened the <110> texture [2], along with the increase in ρ as stated above. These results are consistent with those in Figs. 2 and 3.

Based on Figs. 1 – 3, the results obtained would be summarized as follows:

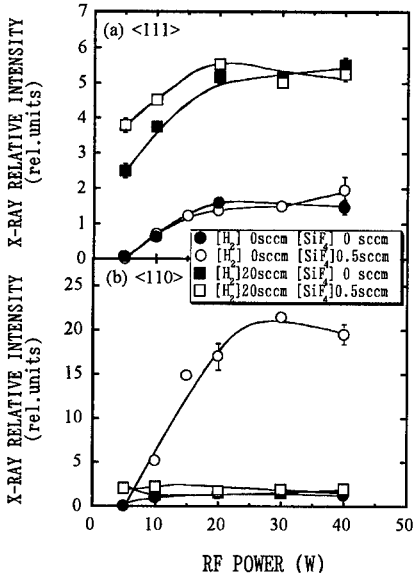


Fig. 2. (a) <111> and (b) <110> XRD relative intensities for films with different $[H_2]$ and $[SiF_4]$ values, as a function of rf power.

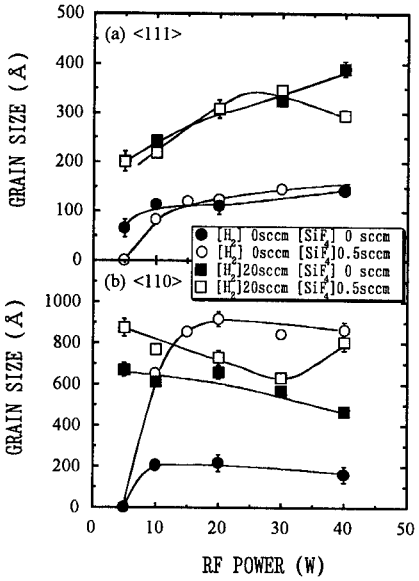


Fig. 3. (a) <111> and (b) <110> XRD grain size for films with different $[H_2]$ and $[SiF_4]$ values, as a function of rf power

(1) The SiF_4 addition under low rf power supply and low H_2 addition suppresses the crystallization, but the SiF_4 addition under high rf power supply enhances the crystallization.
(2) An increase in $[H_2]$ monotonically enhances the crystallization, independent of rf power.
(3) The H_2 or SiF_4 addition is effective in promotive <111> or <110> grain growth, respectively.
(4) The H_2 addition weakens the effects of adding SiF_4 on the crystallinity.
(5) Conditions of low rf power supply, low H_2 addition, and SiF_4 addition allow preparation of films with mc- or nc- structures.

For the result (4), a larger binding-energy value of H-F bonds would be considered as its origin as stated above. As revealed in the results (1) – (3), the addition of H_2 or SiF_4 in the feed gases is likely to play a different role in the grain growth mechanisms, though both H- and F-related radicals would act as an etchant for Si. Although origins causing the above results are unknown at present, the following mechanisms might be considered as their potential factors:
(*i*) A difference in the etching ability, depending on the crystal direction of Si networks during film growth. In addition, H radicals also act to form nucleation sits [2,7,8].
(*ii*) A change in surface coverage by H atoms on the growing surface, which may act to change the surface migration of adsorbates on the growing surface [9].
(*iii*) A change in the surface morphology of substrates, which may be caused by etching of the substrate surface at an initial stage of deposition. Smooth surface of the substrates would result in enhanced crystallization of the resultant Si films [2,3,10].
(*iv*) A change in the cleaning effect, which may act to remove impurities such as oxygen from the growing surface and/or from the substrate surface [7,11].

The addition of H_2 or SiF_4 in the feed gases was also found to cause different bonding network. Figure 4 shows the IR absorption spectra (transmittance) over the range 400-4000 cm^{-1} for films with (A) $[H_2] = 0$ and $[SiF_4] = 0$ sccm, (B) $[H_2] = 0$ and $[SiF_4] = 0.5$ sccm, (C) $[H_2] = 20$ and $[SiF_4] = 0$ sccm, (D) $[H_2] = 20$ and $[SiF_4] = 0.5$ sccm In these spectra, the solid and broken lines denote the results measured within 10 min (for "virgin" films) and those for the films exposed to air for two weeks after deposition, respectively. Furthermore, the results obtained for

the film deposited at 5 W and 20 W are shown in Figs. 4(a) and 4(b), respectively. For the spectra shown in Fig. 4, the difference in film thickness among films was corrected. The spectra at around 650 cm^{-1}, 800-900 cm^{-1}, and 2000-2100 cm^{-1} are assigned to the Si-H wagging, bending and stretching absorption bands, respectively. In the Si-H absorption bands, the spectrum around 2000 cm^{-1} is due to monohydride (SiH) and that around 2100 cm^{-1} is due to dihydride (SiH_2) [12]. In the case of ordinary poly-Si films and partially-crystallized Si films such as nc-Si including amorphous phases, it was suggested that the 2000 cm^{-1} band is due to isolated SiH bonds in amorphous regions in the latter films, and the 2100 cm^{-1} band is due to SiH_2 bonds in the above amorphous regions or the grain boundary regions in the case of poly-Si films. As seen in Fig. 4, the addition of H_2 or an increase in the rf power decreases the Si-H stretching absorption bands, in good correspondence with the changes in the degree of crystallization as shown in Fig. 1. This will be because numerous H radicals in plasma extract H atoms from SiH bonds on growing surface of the films, through a chemical reaction as H + SiH $\rightarrow$ Si + H_2. Also, this surface reaction may be closely related to enhanced crystallization.

As seen in Fig. 4(b), when the films were deposited at [H_2] = 0 sccm under rf 0power supply of 20 W, a large increment in O contamination, in which O atoms will be imported in the films after deposition, is observed after two-week air exposure [Figs. (A) and (B)], in which the Si-O stretching absorption band should be observed around 1100 cm^{-1}. On the other hand, when the films were deposited at 5 W, no O contamination was observed. Thus, we can not find a relationship between the O contamination and the crystallization degree. The concentration of Si, F, and O atoms incorporated into films deposited at 20 W was also measured using x-ray photoelectron spectroscopy (XPS), in which the film surface was cleaned by Ar etching just before the XPS measurements. The results are summarized in Table I. The XPS of sample NO. 3 was measured within 2 days after deposition and the XPS measurements for other samples were carried out after exposure to air for one month or more. In these measurements, the effects of C

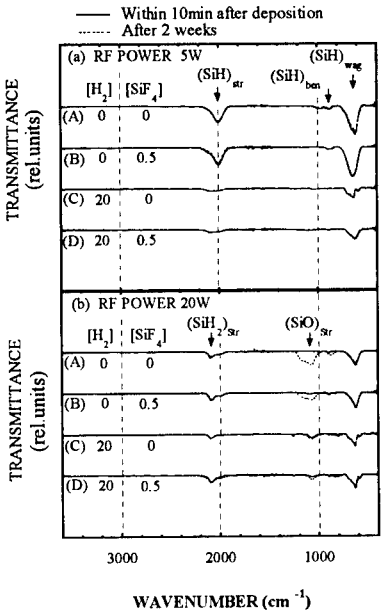


Fig. 4. IR absorption spectra over the range 400-4000 cm^{-1} for films with different [H_2] and [SiF_4] values. The spectra of (a) and (b) were measured within 10 min and after two-week air exposure, respectively.

Table I. Concentration of Si, O, F atoms obtained by XPS measurements for films deposited at 20 W. The samples of No. 2 and No. 3 were deposited under the same conditions. The XPS for the sample of No. 3 was measured within 2 days after deposition, and those for other samples were measured after 1 month or more.

	Samples	Si (%)	O (%)	F (%)
1	[SiF_4]=0, [H_2]=0 sccm	83	17	-
2	[SiF_4]=0.5, [H_2]=0 sccm	85	15	-
3	[SiF_4]=0.5, [H_2]=0 sccm	94	6	-
4	[SiF_4]=0, [H_2]=20 sccm	86	14	-
5	[SiF_4]=0.5, [H_2]=20 sccm	89	11	-

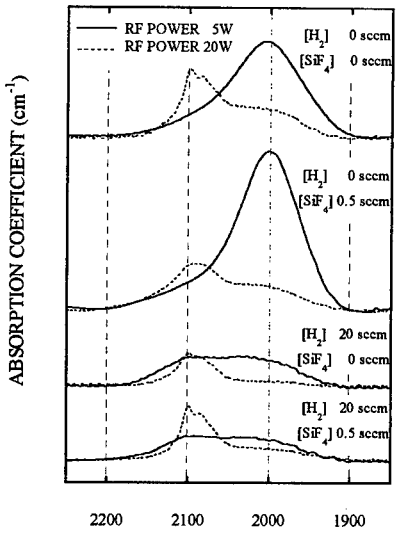


Fig. 5. IR absorption spectra over the range 1800-2300 cm^{-1} for films with different $[H_2]$ and $[SiF_4]$ values.

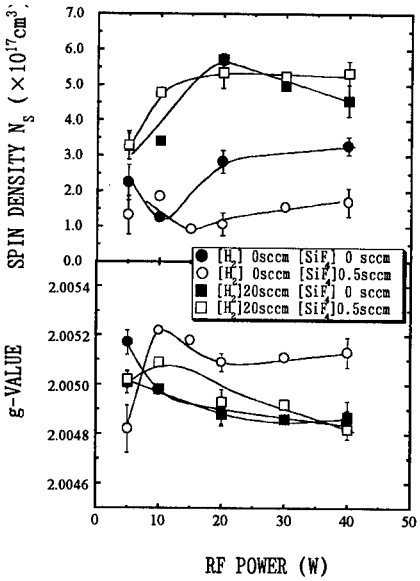


Fig. 6. (a) Spin density, *N*s, and (b) *g* factors for films with different $[H_2]$ and $[SiF_4]$ values, as a function of rf power.

contamination imported during XPS measurements have been corrected. As seen in this Table I, no incorporation of F atoms was detected for all films used, though their structural properties were strongly affected due to incorporation of F atoms (Figs. 1 – 3). As shown in Fig. 4 and Table I, the addition of H_2 is likely to prevent the O contamination. Furthermore, the SiF_4 addition appears to suppress also the O contamination, in contrast with the results found for a-SiO_2:F films. In a-SiO_2:F films, the O contamination after deposition has been reported to be enhanced with increasing the F density, through effects of water absorption due to the presence of Si-F bonds [13]. So, in the case of F-doped poly-Si films, the formation of Si-F bonds, which will exist in the grain boundary regions, may act to relax and densify the structure of the boundary regions, suppressing O incorporation. The SiF stretching absorption band should occur at around 930 cm^{-1} [13]. However, the occurrence of the Si-H bending absorption around 800-900 cm^{-1}, as shown above, would make the detection of the SiF band difficult. We found that the Si-H stretching absorption bands are also strongly affected by adding H_2 or SiF_4. Figure 5 shows the absorption spectra (absorption coefficient in a unit of cm^{-1}) over 1800-2300 cm^{-1} for virgin films deposited at 5 W (solid curves) or 20 W (broken curves), in which the main absorption is the Si-H stretching band. As seen in Fig. 5, the addition of SiF_4 under $[H_2]$ = 0 sccm and rf power = 5 W increases the 2000 cm^{-1} component. By contrast, the addition of H_2 and/or an increase in the rf power cause an increase in the 2100 cm^{-1} component along with a decrease in the 2000 cm^{-1} component. These results are well consistent with those in Fig. 1, as judged from the origins of the 2000 and 2100 cm^{-1} components, that is, the 2000 cm^{-1} component increases as amorphous regions increase, while the 2100 cm^{-1} component increases as the crystallization proceeds.

For Si films deposited on single-crystal Si substrates with thermally grown SiO_2 layer, the ESR spectra arising from Si dangling bonds (Si DB) were measured using X-band ESR spectrometer. Figure 6 shows (a) the spin density, N_s, and (b) the *g* factor for films with $[H_2]$ = 0 and 20 sccm and $[SiF_4]$ = 0 and 0.5 sccm, as a function of rf power. As seen in Fig. 6(a), it is found that the addition of SiF_4 under $[H_2]$ = 0 sccm decreases DB density, while the H_2 addition largely increases the DB density, independent of rf power. These results also correspond well with the change in the crystallization (Fig. 1), as well as the dependence of the incorporated SiH

and SiH_2 bond density shown in Fig. 5. Thus, it is found that the densities of both SiH_2 bonds and DB's increase as the degree of crystallization is enhanced. These results would be closely related to formation of grain boundary regions with high density of SiH_2 bonds and DB's in highly crystallized films.

As seen in Fig. 6(b), with the exception of the films deposited at 5 W, the g values appear to decrease with increasing rf power. Furthermore, it is found that the H_2 addition causes a decrease in g, while the SiF_4 addition increases the g values. Accordingly, based on the results shown in Figs. 1 and 6(b), the decrease in g, due to an increase in $[H_2]$ or rf power, is found to correspond well with an increase in the degree of crystallization. However, the SiF_4 addition appears to give the opposite effect on the g value and the degree of crystallization. As seen in the discussion located near Figs. 2 and 3, it is suggested that H- and F-related radicals play a different role in the grain growth mechanisms, and may be due to different factors as stated above. In such a change in g, the g values would reflect the local structure of Si networks around DB's. Ishii *et al.* demonstrated that g decreases from 2.0060 to 2.0048 as a trivalent Si atom with DB moves vertically toward the plane formed by three backbonded Si atoms by 0.033 nm [14]. In the case of poly-Si films, such a lattice deformation should exist in the grain boundary regions [15], because most of Si DB's exist in the boundaries. The structure of the grain boundaries in poly-Si can be classified into two types of boundary: Low-angle boundary with simple defects such as dislocations and high-angle boundary with amorphouslike structure that may be free from large strain [15]. Therefore, occurrence of high crystallization under high rf power supply or high H_2 addition may form low-angle boundary leading to a decrease in g, as expected. This is because formation of Si-Si bonds in the low-angle boundary will be rather tight.

CONCLUSIONS

For poly-Si films prepared by a plasma-enhanced chemical vapor deposition, we examined the changes in the local structure caused by adding H_2 and/or SiF_4 in the SiH_4 feed gases and by changing supplied rf power values. The addition of H_2 or SiF_4 in the feed gases is likely to play a different role in the grain growth mechanisms, though both H- and F-related radicals would act as an etchant for Si. The increase in the rf power and the H_2 addition give the same effect on the structural properties, independent of the effects of the SiF_4 addition. The conditions of low rf power supply, low H_2 addition, and SiF_4 addition allow preparation of films with mc- or nc- structures.

The authors wish to thank Professor T. Shimizu for the use of the Raman spectrometer.

REFERENCES

1. R. Tsu, G. Gonzales-Hernandez, S. S. Chao, S. C. Lee, and K. Tanaka, Appl. Phys. Lett., **40**, 534 (1982).
2. M. Syed, T. Inokuma, Y. Kurata, and S. Hasegawa, Jpn. J. Appl. Phys., **36**, 6625 (1997).
3. M. Syed, T. Inokuma, Y. Kurata, and S. Hasegawa, Jpn. J. Appl. Phys., **38**, 1303 (1999).
4. A. M. Ali, T. Inokuma, Y. Kurata, and S. Hasegawa, Jpn. J. Appl. Phys., **38**, 6047 (1999).
5. L. Pauling: *The Nature of the Chemical Bond*, 3rd ed., Cornell University Press, New York, 1960, p. 75.
6. B. D. Cully, *Element of x-ray Diffraction,* 2nd ed., Addison-Wesley, Massachusetts, 1978, p. 102.
7. H. Kakinuma, M. Mohri, and T. Tsuruoka, J. Appl. Phys., **77**, 646 (1995).
8. S. K. Kim, K. C. Park, and J. Jang, J. Appl. Phys., **77**, 5115 (1995).
9. A. Matsuda, J. Non-Cryst. Solids, **59&60**, 767 (1983).
10. S. Hasegawa, N. Uchida, S. Takenaka, T. Inokuma, and Y. Kurata, Jpn. J. Appl. Phys., **37**, 4711 (1998).
11. Y.-B Park and S.-W. Rhee, Appl. Phys. Lett., **68**, 2219 (1996).
12. A. A. Langford, A. H. Mahan, M. L. Fleet, and J. Bende, Phys. Rev. B, **41**, 8359 (1990).
13. H. Miyajima, R. Katsumata, Y. Nakasaki, and N. Hayasaka, Jpn. J. Appl. Phys., **35**, 6217 (1996).
14. N. Ishii, M. Kumeda, and T. Shimizu, Jpn. J. Appl. Phys., **20**, L673 (1981).
15. S. Hasegawa, E. Fujimoto, T. Inokuma, and Y. Kurata, J. Appl. Phys., **77**, 357 (1995).

Formation of Nanocrystalline SiC Powder from Chlorine-Containing Polycarbosilane Precursors

Brian S. Mitchell, Haoyue Zhang
Department of Chemical Engineering, Tulane University
New Orleans, LA 70118

Martin Ade, Dirk Kurtenbach, Eberhard Müller
TU Bergakademie Freiberg
Institut für Keramische Werkstoffe
Freiberg, GERMANY

ABSTRACT

Nanocrystalline β-SiC particulates with a grain size range of 5-20 nm were prepared by heating a pre-pyrolyzed, chlorine-containing polysilane/polycarbosilane (PS/PCS) to 1600°C. The transformation from the pre-pyrolyzed PS/PCS to nanocrystalline SiC was investigated by differential thermal analysis (DTA), thermogravimetric analysis (TGA), X-ray diffraction (XRD), mass-spectrometry and infrared spectroscopy. The results indicated that the nanocrystalline β-SiC was formed by the crystallization of the PS/PCS random network, and crosslinking of Si-Si, Si-Cl, and Si-CH_2-Si bonds. The TEM observation showed that SiC particulates consist of equiaxed, randomly oriented, ultrafine grains.

INTRODUCTION

Ultrafine SiC particulates are an important composite reinforcement [1-4] Submicrometer-sized SiC offer a significant improvement in ceramic nanocomposite mechanical properties compared to micrometer-sized particulates.[5-7] The morphology, microstructure, size distribution, surface chemistry, and dispersion uniformity of the SiC particulate all play significant roles in ultimate property determination.

Little work regarding SiC particulates with nanometer-sized grains formed from chlorine-containing polysilane/polycarbosilanes (PS/PCS) has been reported. In previous work,[8-10] the polysilane to polycarbosilane conversion, the conversion of organosilicon compounds into a random SiC network, and crosslinking of molecules has been investigated. SiC derived from polymeric precursors shows inhomogeneities in the nanometer range.[8,9] Stoichiometric silicon carbide can be obtained as a consequence of the chlorine content in poly-(methylchlorosilane) which allows an adjustment of the carbon content in the precursor molecules in contrast to silicon polymers with alkyl or aryl groups.[11,12] In this work, we elaborate upon the structural changes that take place during heat treatment and subsequent transformation from chlorine containing PS/PCS to cubic (β-) polycrystalline SiC with nanometer-sized grains.

EXPERIMENT

Chlorine-containing PS/PCS was synthesized by catalytic redistribution of bis(chloromethylsilane)s to yield monosilanes and poly(chloromethylsilane) oligomers.[9] The oligomers were converted to poly(chloromethylsilane) by thermally-induced crosslinking reactions, increasing the molecular weight, accompanied by simultaneous cleavage of trichloromethylsilane

Mat. Res. Soc. Symp. Proc. Vol. 581 © 2000 Materials Research Society

(monosilane). Styrene was added to the reaction mixture at the redistribution reaction, yielding a copolymer with improved spinning properties. Pre-pyrolysis was performed with ground, solid poly(chloromethylsilane-co-styrene) of about 2-10 g by heating at 2°C /min to 700°C and holding for 1 hour under argon. The pre-pyrolyzed sample was an inorganic amorphous network with Si-Si-, Si-C-, Si-Cl-, and Si-CH_2 bonds as identified by XRD, IR, and NMR. The resulting chlorine-containing PS/PCS sample was fractionated into 200–315 μm diameter batches which were used as the precursor of nanocrystalline SiC powder.

Pyrolysis and crystallization of the precursor were performed on a TA Instruments DTA 2920, at heating rates of 5, 15, 20, 30, and 40°C/min to 1600°C in argon. The transformation processing of nanocrystalline SiC from the precursor was analyzed on a TA Instruments SDT 2960; gas evolution from the SDT was monitored by a FISONS quadrupole mass spectrometer (QMS) and a Bruker FS55 Fourier Transform Infrared (FTIR) Spectrometer. XRD analyses were performed on an Scintag XDS 2000 X-ray diffractometer, with CuKα radiation. Mean grain sizes were determined using the Scherrer and Wilson[13] equations from the breadth of the β-SiC [220] and [311] diffraction lines, unless specified otherwise. The morphology and chemical characterization of the crystallized SiC sample were carried out on a conventional and analytical Philips CM-200 TEM equipped with EDS.

RESULTS

Differential Thermal Analysis (Figure 1) shows two exothermic peaks (except at 15°C/min where there are three peaks), indicating a multi-step reaction in the heating process. Activation energies of 667 kJ/mol for the first exothermic peak and 381 kJ/mol for the second exothermic peak were determined by the Kissinger equation.[15]

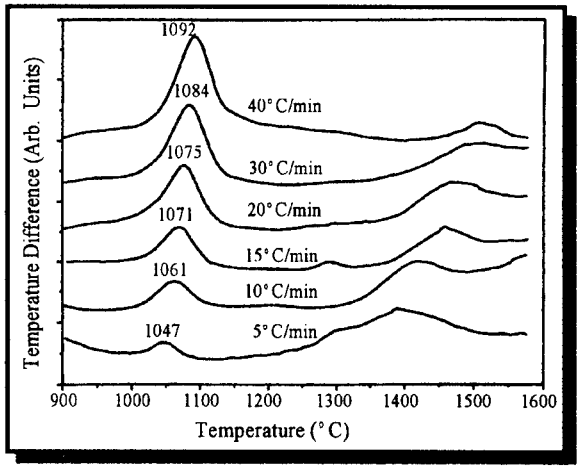


Figure 1 DTA curves of chlorine containing PS/PCS precursor heated to 1600 °C at heating rates of 5, 10, 15, 20, 30, 40 °C/min.

Sample heated to 1600°C at 15°C/min is polycrystalline β-SiC with mean grain size 10±1 nm (Figure 2). EDS of the nanocrystalline SiC powder shows Si and C, with small amounts of Cl and O. In previous work[10], IR analysis of pyrolyzed samples did not show Si-Cl and Si-O bands in PS/PCS sample heated to 900°C at a rate of 5°C/min. This is attributed to the higher heating rate in our samples compared to the IR samples, or the higher resolution of our EDS.

SDT of PS/PCS sample heated to 800°C, then from 800 to 1520°C at 5°C/min (Figure 3) with gas evolution simultaneously analyzed by QMS and FTIR shows three weight loss steps at 1204, 1314, and 1483°C. Before the completion of the first exothermic peak of the DTA curve, low weight loss is seen in the sample, and the intensities of the mass-spectra of the sample do not change with time (not shown).

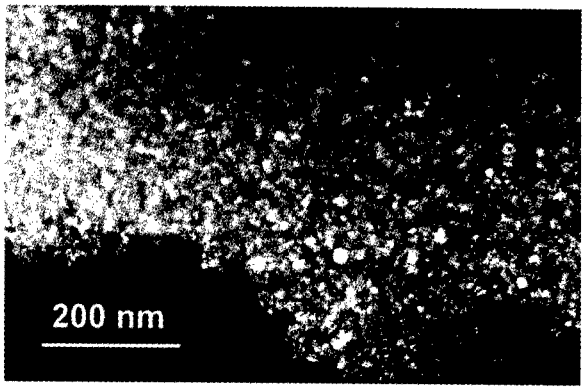


Figure 2. Darkfield TEM image of nanocrystalline SiC.

At 1204°C, the peak in the derivative weight curve corresponds to the evolution of HCl, which appears in the MS as chloride ions and HCl, as well as in the IR spectrum (not shown), indicating that the weight loss is due in part to the breaking of Si-Cl bonds. There is no corresponding endothermic peak in the DTA trace at 1204°C. At 1314°C, the second peak of the derivative TGA curve appears, and the intensity of mass 44 species increase. The increase in 44 atomic mass units could be due to SiO, CO_2 or other carbosilane fragments, although CO_2 does not show up in the IR spectrum until 1400°C. There is a corresponding second-order transition (change in heat capacity) in the DTA trace at the onset to the 1314°C TGA derivative peak. Finally, there is another second-order transition in the DTA curve that begins around 1350°C, and corresponds to the onset of the final weight loss event at 1483°C. In light of the DTA traces in Figure 1 that clearly show a broad, exothermic peak from 1300 to 1500°C in the sample heated at 5°C/min, the change in slope of the DTA trace at 1350°C in Figure 3 is attributed to the onset of a first-order transition (exothermic event). The peak in the TGA curve at 1483°C is attributed to formation of both CO and CO_2, as shown by IR spectroscopy. The total mass loss is then attributed

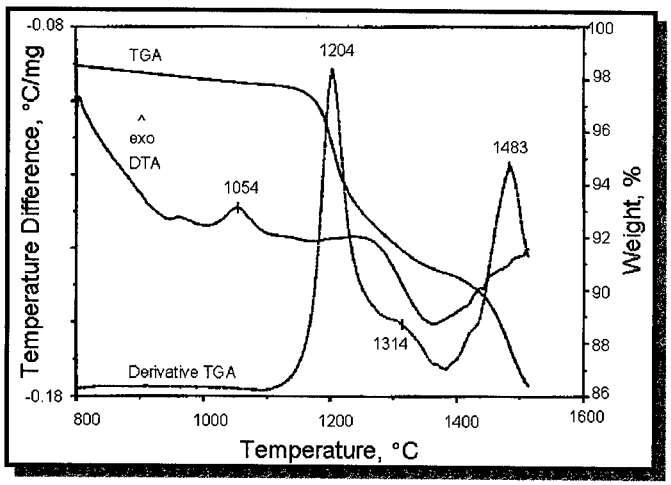


Figure 3. DTA/TGA of chlorine-containing PS/PCS precuror heated to 1520°C at a rate of 5°C/mon.

to the following events:

1. active oxidation of the reactive, nanocrystalline SiC due to low oxygen partial pressure from trace amounts of oxygen in the carrier gas
2. release of atoms that do not fit into the SiC structure as it forms during pyrolysis, i.e., chlorine and hydrogen;
3. degradation of an intergranular phase (SiCxOy) originated by oxygen impurites into SiO and CO gas; and
4. oxidation of free carbon from the amorphous network to form CO and CO_2.

XRD experiments on precursor samples that were heated with no dwell time to 1080 (A), 1200 (B), and 1512°C (C), at a heating rate of 5°C/min in the SDT, and then cooled show that these three temperatures correspond roughly to the first exothermic DTA peak, the first TGA derivative peak, and the third TGA derivative peak, respectively. In Fig. 4, it can be seen that the samples were polycrystalline β-SiC with some small amount of a quartz phase. The quartz may develop during heat treatment due to traces of oxygen in the carrier gas. The grain size was approximately 6 nm for sample B, and the mean grain size for sample C was 15 ± 1 nm. It is evident from the XRD line widths, however, that any crystallinity in sample A must have an average grain size smaller than that in samples B and C. These results further reinforce the conclusion that the first exothermic peak in the DTA traces corresponds to the highest crystallization rate of the amorphous, covalent ceramic. The XRD pattern at 1512°C is a clear indication of grain growth after 1200°C, which corresponds to the broad exotherms in the DTA traces of Figure 1.

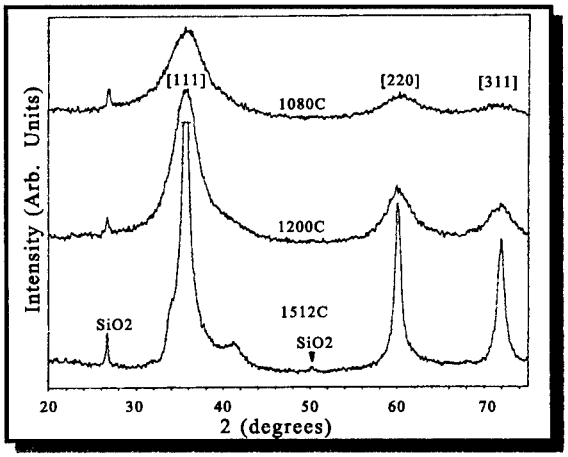


Figure 4. XRD of chlorine-containing PS/PCS heated to 1080, 1200 and 1512°C at a rate of 5°C/min.

CONCLUSIONS

Cubic nanocrystalline SiC powders with grain sizes from 5 to 20 nm were successfully synthesized by pyrolysis of a chlorine-containing polysilane/polycarbosilane (PS/PCS). Transformation from the PS/PCS precursor to cubic nanocrystalline SiC was accomplished in two steps the crystallization of the network, gas evolution and grain growth during the pyrolysis process. Activation energies of crystallization and crystal growth were 667 and 381 kJ/mol, respectively. Redistribution and crosslinking of Si-Si, Si-Cl, and Si-CH_2-Si bonds in the precursor were realized by evolution of Hcl. Some weight loss of the sample is due to CO and CO_2 evolution at temperatures > 1314°C, which comes from degradation/decomposition of the intergranular phase built from

oxygen impurities. Nanocrystalline SiC consists of equiaxed, randomly oriented grains ranging from 5 to 20 nm. The nanocrystalline morphology of the grains and the structure of the interfacial grain boundaries should improve the mechanical properties of SiC particulate-reinforced composites[16,17] Mechanical property determination of nanocrystalline β-SiC , as well as the refinement of the particulates is proceeding in future work..

REFERENCES

1. D. L. Mcdanels, "Analysis of Stress-Strain, Fracture and Ductility Behavior of Aluminum Matrix Composites Containing Discontinuous Silicon Carbide Reinforcement," 113th Annual Meeting of the Am. Inst. Min. Metal. Petr. Eng., Los Angeles, 1984; published as NASA Technical Memorandum 83610.
2. W. R. Mohn and D. Vukobratovich, "Engineered Metal Matrix Composites for Precision Optical System" Optomechanical Systems Engineering, Proceedings, Soc. Photo-Optical Instrum. Eng., Vol. 817, 1987.
3. K. Schmidt, C. Zweben, and R. Arsenault, Thermal and Mechanical Behavior of Metal Matrix and Ceramic Matrix Composites, ASTM STP 1080, J. M. Kennedy, H. H. Moeller, and W. S. Johnson, Eds., Am. Soc. Test. Mater., Philadelphia, 1990, pp. 155-164.
4. H. J. Hwang and K. Niihara, J. Mater. Res., 13 [10] 2866-70 (1998).
5. J. Zhao, L. C. Stearns, M. P. Harmer, H. M. Chan, G. A. Miller, and R. F. Cook, J. Am. Ceram. Soc., 76 [2] 503-10 (1993).
6. H. J. Hwang, T. Sekino, K. Ota, and K. Niihara, J. Mater. Sci. 31, 4617-24 (1996).
7. X. Pan, J. Mayer, and M. Rühle, J. Am. Ceram. Soc., 79 [3] 585-90 (1996).
8. H. -P. Martin, G. Irmer, and E. Müller, J. Europ. Ceram. Soc., 18, 193-9 (1998).
9. R. Richter, G. Roewer, U. Boehme, K. Busch, F. Babonneau, H. P. Martin, E. Mdller, Appl. Organomet. Chem., 11, 71-106 (1997).
10. H. –P. Martin, E. Müller, R. Richter, G. Roewer, and E. Brendler, J. Mater. Sci. 32, 1381-7 (1997).
11. R. West, in: Comprehensive Organometallic Chemistry, G. Wilkinson, F. G. A. Stone, and E. Abel, Eds., Pergamon, Oxford, 1982, pp 365-97.
12. E. BacquJ, J. -P. Pillot, M. Birot, J. Dunogus and P. Lapouyade, Chem. Mater. 3, 348 (1991).
13. H.P. Klug and L.E. Alexander, "X-ray Diffraction Procedures for Polycrystalline and Amorphous Materials," 2nd edition, Wiley, NY, 1974, p. 662.
14. H. Jagodzinski and H. Arnold, "Silicon Carbide, a High Temperature Semiconductor", Pergamon Press, Oxford, J.R. O'Connor and J. Smiltens, eds., 1960, pp. 136-146.
15. H. E. Kissinger, Annal. Chem. 29, 1702 (1957).
16. H. Karch, R. Birringer and H. Gleiter, Nature (London), 330, 556-8 (1987).
17. R. W. Siegel and H. Hahn, in: Current Trends in Physics of Materials, M. Yussouff, ed., World Scientific, Singapore, 1987, p. 403.

Nanowires

STRUCTURE AND COMPOSITION OF BISMUTH NANOWIRE ARRAYS

M. S. Sander,* Y-M. Lin,** M. S. Dresselhaus,*** R. Gronsky****
*Department of Chemistry, University of California, Berkeley
**Department of Computer Sciences & Electrical Engineering, M.I.T
***Departments of Physics and Computer Sciences & Electrical Engineering, M.I.T
****Department of Materials Science & Engineering, University of California, Berkeley

ABSTRACT
Arrays of nanowires have attracted considerable recent attention due to their unique electronic and optical properties. While much effort has been directed at fabricating arrays and measuring their properties, much less has been done to characterize these materials. Understanding the structure and composition of the constituents in these arrays is crucial in order to control their properties. In this work, arrays with wire diameters from 35-90nm were fabricated by pressure injecting liquid bismuth into porous alumina templates. Transmission electron microscopy (TEM) and analytical electron microscopy (AEM) were used to characterize the arrays.

INTRODUCTION
Metal and semiconductor nanowire arrays exhibit properties that differ from the corresponding bulk materials as a result of the two-dimensional quantum confinement of the charge carriers.[1] Quantum confinement effects become significant in bismuth at larger, more easily accessible sizes than in other materials because of bismuth's relatively small effective mass. These effects have been observed in magnetotransport[2] and optical[3] measurements of bismuth nanowire arrays. In addition, nanowire arrays have been predicted to demonstrate enhanced thermoelectric properties compared to bulk bismuth.[4]
Because of the small wire diameters and large interfacial areas associated with nanowire arrays, the array properties are strongly dependent upon the wire and interface structure and composition. The effects of structure variation have been studied in bismuth thin films, where carrier mobility is found to vary by approximately an order of magnitude depending on whether the films are single or polycrystalline.[5] This effect will be exaggerated in nanowires because transport is further confined to a single dimension. Compositional effects due to impurities or reaction products will also play a significant role in determining the properties of such wires. When nanowires are configured in arrays, the interface morphology enters as another determinant in carrier scattering.
To understand the effect of these parameters, it is necessary to determine the local structure and composition of the wires and at the interfaces in the arrays. In this work, TEM and AEM, including energy dispersive x-ray spectroscopy (EDX) and electron energy loss spectroscopy (EELS), have been applied to characterize bismuth nanowire arrays.

EXPERIMENTAL PROCEDURES
The arrays of bismuth nanowires were fabricated by a pressure injection process. A basic overview of the method is given here; the detailed procedure has been described elsewhere.[6] Templates of alumina with an ordered array of nanochannels were made by anodization of aluminum foils. Pieces of pure bismuth were placed on top of the alumina template in an iconel reactor chamber. The chamber was then evacuated to a pressure of 10^{-2}mTorr and heated to 325°C, above the bismuth melting temperature of 270°C. After the bismuth was melted, argon was pumped into the chamber to a pressure of 4500 psi in order to force the molten bismuth into the pores of the template. The arrays were allowed to cool to room temperature over a period of

Mat. Res. Soc. Symp. Proc. Vol. 581 © 2000 Materials Research Society

approximately twelve hours. Basic microstructural analysis was performed in a JEOL 200CX microscope; high resolution and analytical electron microscopy were performed in a Philips CM200 microscope equipped with a Gatan Imaging Filter for EELS analysis and an EmiSpec™ system for EDX. Cross-section samples were prepared by dimpling and ion milling the arrays to electron transparency. To obtain isolated nanowires, the wires were released from the matrix by etching away the alumina with a solution of 3.5 vol% H_3PO_4 and 45g/L CrO_3. After etching, the acid was replaced with ethanol through a series of dilutions, and the wires were dispersed onto a holey carbon grid.

RESULTS AND DISCUSSION

An image of a bismuth nanowire array is shown in Figure 1, revealing the wire packing to be uniform and dense. Previous x-ray diffraction studies indicate that there is a strong amount of texturing along the wire axis, as evidenced by a strong 202 peak.[6]

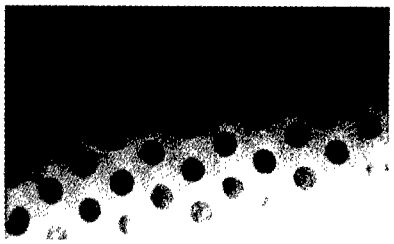


Figure 1. Cross-section TEM image of bismuth nanowire array. The average wire diameter is 50nm.

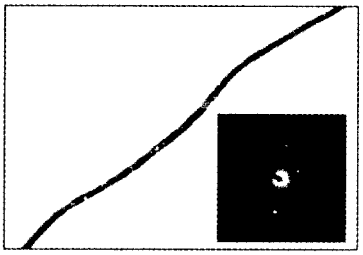


Figure 2. TEM image of a single 50nm diameter bismuth nanowire with inset selected area diffraction pattern.

Bismuth Nanowires

A TEM image of a single bismuth nanowire released from the alumina is shown in Figure 2. There are clearly visible contrast variations along the length of the wire. Because the wires are dense and have uniform diameter, the contrast variations are due to either compositional or structural changes. The composition of the wires was monitored using EDX. In spot analyses along the wires, only bismuth was observed to be present, with an impurity content of less than one percent. Although the presence of trace impurities cannot be ruled out, the observed variations in contrast in the wires are not due to variations in the wire composition.

In order to document more thoroughly the structure of the nanowires, electron diffraction and dark field imaging were employed. Diffraction patterns from selected regions of the wire, as shown in Figure 2, consist of several overlapping spot patterns, indicating that several grains are contributing to the pattern. In some regions along the wire, dark field images from pairs of +g/-g diffraction spots show reversal of contrast compared to the bright field image within the same areas, as revealed in Figure 3. This indicates the presence of distinct grains and not simply bend extinction contours within a single grain. This identification is supported by the magnified dark field image in Figure 3 showing a series of thickness fringes resulting from an inclined grain boundary. In the wires that were studied, with wire diameters from 35-90nm, most grains had high aspect ratios.

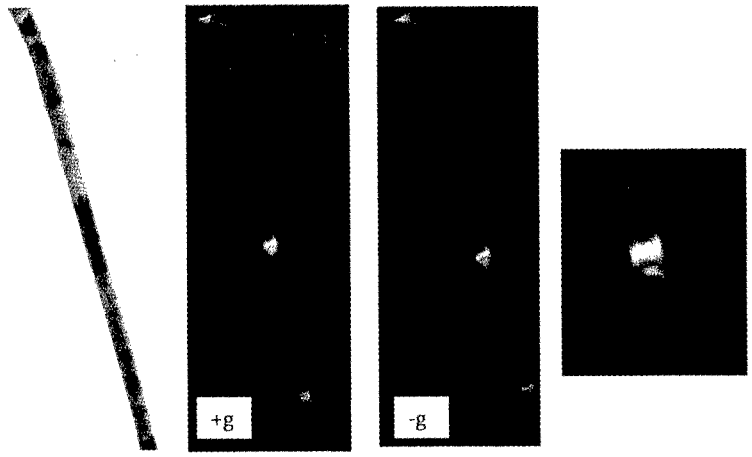


Figure 3. A bright field and +g/-g dark field images of a single 50nm diameter bismuth wire. Thickness fringes due to an inclined grain boundary are visible in the magnified image at the right.

A second type of contrast variation was also observed in the wires, as exhibited in Figure 4. In this case, the +g and -g dark field images have reversed contrast in different regions, originating from localized strain fields within the wire. Such strain fields can be caused by wire bending, residual stress from the solidification process, or other structural defects within the wire structure. The exact nature of the strain fields observed here has not yet been determined.

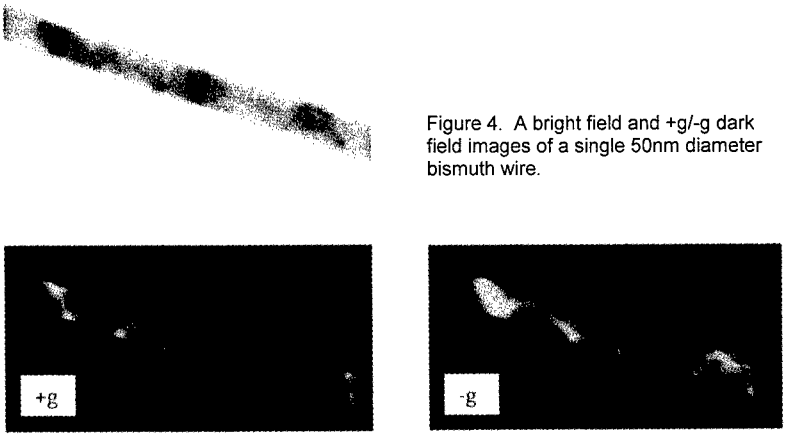


Figure 4. A bright field and +g/-g dark field images of a single 50nm diameter bismuth wire.

Bi-Al_2O_3 Interface

A high resolution TEM image of the bismuth-alumina interface is shown in Figure 5. Several series of oxygen K-edge spectra from one-nanometer areas were taken at the positions labeled in Figure 5, and these are shown in Figure 6. The wire has no perceptible oxygen signal. At the interface, the oxygen ionization edge (~540eV) is shifted approximately 2.7eV relative to the alumina. This shift in the ionization edge position is due to a change in the environment of the oxygen, which is attributed to Bi-O bonding. However, because of the size of the probe, it is not possible to obtain a spectrum that can be attributed solely to Bi-O bonding. No shift in the ionization edge was observed for spectra collected away from the one-nanometer area at the interface. This indicates that there is not a significant interphase region between the nanowire and the matrix. Spectra of the aluminum L-edge were also recorded, as shown in Figure 7. No shift in the ionization edge was observed, indicating that there is not a significant amount of Bi-Al bonding at the interface. The difference in intensity in the post edge structure in these spectra may be attributed to a change in sample thickness at the interface as compared to the alumina. These EELS results are consistent with theoretical predictions that Bi-O bonding dominates at Bi-Al_2O_3 interfaces.[7]

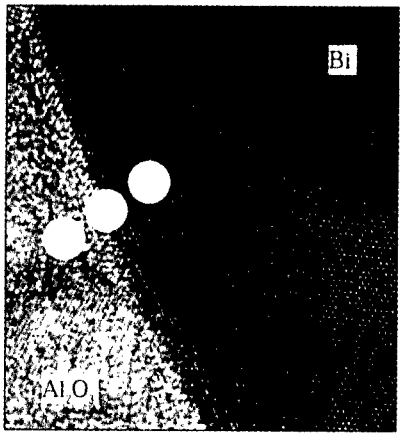


Figure 5. High resolution TEM image of the Bi-Al_2O_3 interface. The circles represent the nanometer probe as it samples the alumina, the interface, and the bismuth.

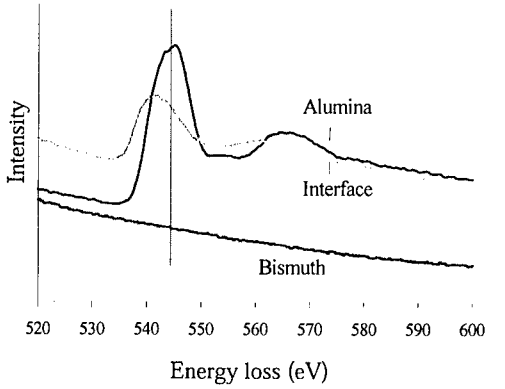


Figure 6. Oxygen K-edge spectra from one-nanometer areas in the bismuth nanowire, at the Bi-Al_2O_3 interface, and in the alumina matrix.

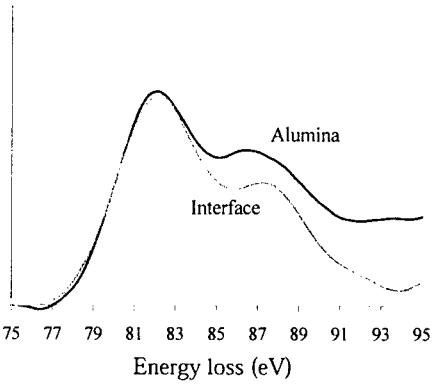


Figure 7. Aluminum L-edge spectra from the alumina and interfacial regions. The background has been subtracted to accentuate the edge features.

CONCLUSIONS

The structure and composition in bismuth nanowires and at the Bi-Al_2O_3 interface have been studied. The wires are determined to be of constant composition within the detection limit of EDX spectroscopy (approx. 1%). They are polycrystalline with high aspect-ratio grains, and there is evidence of internal localized strain fields. Both the grain structure and local strain fields in the wires are expected to have a significant impact on the nanowire transport properties due to restriction of transport along a single dimension. EELS studies of the interface reveal that there is no significant interdiffusion and interphase formation. A shift in the oxygen ionization edge is observed at the interface relative to the alumina, while no shift is observed for the aluminum ionization edge. This suggests that Bi-O bonding dominates at the interface and agrees with theoretical work. The composition and structure at the interface affect scattering of the charge carriers and therefore influence array properties.

Future work will focus on controlling the structure and composition in the arrays by varying the fabrication conditions. For instance, because there is a high degree of texturing of the grains, it may be possible to produce single crystalline wires by establishing the proper thermal gradient along the wires during solidification. Also, by annealing the arrays after deposition, it may be possible to induce interdiffusion and a wider interphase region, which would result in an effective decrease in the wire diameter. As structure and composition are further correlated with property measurements, arrays can be tailored to optimize their properties.

ACKNOWLEDGMENTS

This work is supported through a Multi-University Research Initiative, funded by the Office of Naval Research under contract number N00014-97-1-0516. Access to microscopes and technical assistance at the National Center for Electron Microscopy, Lawrence Berkeley National Laboratory, is also gratefully acknowledged.

REFERENCES

[1] J. Heremans, C. M. Thrush, Z. Zhang, X. Sun, M. S. Dresselhaus, J. Y. Ying, and D. T. Morelli, *Phys. Rev. B* **58**, R10091 (1998).
[2] Z. Zhang, J. Y. Ying, and M. S. Dresselhaus, *J. Mater. Res.* **13**, 1745 (1998).
[3] X. Sun, Z. Zhang, and M. S. Dresselhaus, *App. Phys. Lett.* **74**, 4005 (1999).
[4] D. L. Partin, J. Heremans, D. T. Morelli, C.M. Thrush, C. H. Olk, and T. A. Perry, *Phys. Rev. B* **38**, 3818 (1988).
[5] S. Nahm, L. Salamanca-Riba, D. L. Partin, J. Heremans, *J. Mat. Res.* **5**, 784 (1990).
[6] Z. B. Zhang, D. Gekhtman, M. S. Dresselhaus, J. Y. Ying, *Chem. Mat.* **11**,1659 (1999).
[7] D. Sotiropoulou, *J. Mater. Sci. Lett.* **16**, 693 (1997).

SYNTHESIS OF SINGLE CRYSTAL BISMUTH-TELLURIDE AND LEAD-TELLURIDE NANOWIRES FOR NEW THERMOELECTRIC MATERIALS

Q. WEI, C.M. LIEBER
Department of Chemistry and Chemical Biology, Harvard University, Cambridge, MA 02138

ABSTRACT

Dimensionality can play an important role in determining the properties of materials. In the case of thermoelectric materials, it has been proposed that one-dimensional quantum wires, or nanowires, and two-dimensional superlattices could exhibit substantially higher efficiencies compared to the corresponding bulk, three-dimensional solids. To explore such predictions we have initiated a program directed towards the controlled growth of nanowires, and herein, we report the synthesis of single crystal Bi_2Te_3 and PbTe nanowires by a pulsed laser ablation method. Scanning electron microscopy (SEM) and transmission electron microscopy (TEM) show that Bi_2Te_3 wires 80 nm to 200 nm in diameter and lengths exceeding 10 microns, and PbTe wires 25 nm to 60 nm in diameter and lengths to 2 microns can be readily produced by the laser ablation method. High-resolution TEM and electron diffraction show that Bi_2Te_3 nanowires are single crystals with wire axes along the <110> crystal direction. TEM and electron diffraction measurements also show that the PbTe nanowires are single crystals with a <100> growth axis. The transport properties of these new nanowire materials will be discussed.

INTRODUCTION

There has been considerable interest in the past few years in finding new thermoelectric materials for use in solid state refrigerators with no moving parts [1]. The efficiency of a thermoelectric solid is found to depend on material properties through the dimensionless figure of merit ZT [2]. It is defined by $ZT = \sigma S^2 T/\kappa$, where σ is the electrical conductivity, S the Seebeck coefficient, or thermoelectric power, T the temperature, and κ the thermal conductivity. For a material to be a good thermoelectric cooler it must have a high ZT at room temperature and below. In general, it is difficult to improve ZT, because increases in the electrical conductivity for simple materials also lead to a simultaneous decrease in the thermoelectric power and a comparable increase in the electronic contribution to the thermal conductivity. Currently, the materials with the highest ZT are alloys based on Bi_2Te_3 with ZT near 1 at 300 K [2]. Bi_2Te_3 is the most important thermoelectric material that works below T = 300 K. However, the efficiency is rather low compared to freon-based compressors, and it can not be used to cool below 160 K [1, 3]. Therefore, there is a pressing need for new materials with higher efficiencies.

Dimensionality can play an important role in determining the properties of materials. The reduction of dimensionality from 3D to 1D results in a dramatic increase in the electronic density of states (DOS) at near energy band edges. In thermoelectrics it is known [3] that the power factor, σS^2, increases with DOS. Therefore, the increased DOS of 1D structures is predicted to produce an enhanced power factor, and consequently, an enhanced ZT. In addition, there will be increased phonon scattering from the surfaces of 1D wires. This will lead to a reduction in the lattice thermal conductivity and hence an increase in ZT. There have been several theoretical calculations [4, 5] reported that support these ideas. To explore such predictions experimentally we have initiated a program directed towards the controlled growth of nanowires, and herein, we report the synthesis of single crystal Bi_2Te_3 and PbTe (another important thermoelectric material) nanowires by a laser ablation method [6-8].

Mat. Res. Soc. Symp. Proc. Vol. 581 © 2000 Materials Research Society

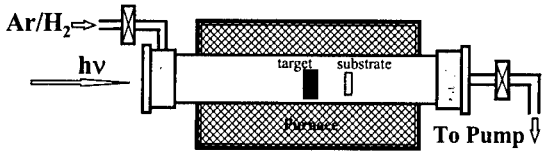


Figure 1. Schematic of the nanowire growth apparatus.

EXPERIMENTAL METHODS

Synthesis of Nanowires

Pulsed laser ablation (Spectra Physics GCR-16s, 355 nm or 532 nm) of targets composed of Bi_2Te_3 or PbTe was used to generate nanoclusters for 1D growth at thermodynamic non-equilibrium conditions. The growth apparatus is shown schematically in figure 1. The pressure in the growth chamber was kept at 100 – 250 torr. A mixture of Ar and H_2 (10% H_2) was used as a buffer gas with a flow rate of about 100 sccm. The growth temperature is 530 °C for Bi_2Te_3, and 815 °C for PbTe. The products were collected on a substrate located behind the target.

Structural Characterization of Nanowires

The morphology and structure of the products were examined by field-emission scanning electron microscopy (SEM) (LEO 982), high-resolution transmission electron microscopy (TEM) and electron diffraction (Philips EM420). Energy dispersive X-ray (EDX) spectra were recorded with the TEM to evaluate the elemental compositions.

Electrical Conductivity Measurement of Single Bi_2Te_3 Nanowires

After registering the position of single Bi_2Te_3 nanowires on oxidized Si substrates under SEM (JEOL JSM6400), electron beam resist was spun over the substrates and electron-beam lithography was used to define electrical leads to individual nanowires. After metalization of the leads I-V curves were obtained using Keithley 6517 electrometer and Keithley 220 programmable current source.

RESULTS

Bi_2Te_3 nanowires can be reproducibly prepared via vapor phase growth using our laser ablation method. Figure 2 shows SEM images of Bi_2Te_3 nanowires at different magnifications. They are faceted nanowires with diameters of 80 nm to 200 nm and lengths exceeding 10 μm. TEM and electron diffraction studies (figure 3) show that the nanowires are single crystals. The diffraction pattern can be indexed to the hexagonal lattice of Bi_2Te_3 (a = 4.385 Å, c = 30.48 Å) with the electron beam direction along [001] zone axis. A schematic illustration of Bi_2Te_3 structure viewed along the c axis superimposed on the TEM image of Bi_2Te_3 nanowire is shown in figure 3. These data show that the nanowires grow along the <110> crystal direction. The single crystal nature and growth direction are further confirmed by high-resolution TEM measurements (figure 4). The lattice fringes in figure 4 are (101) crystal planes with an inter-

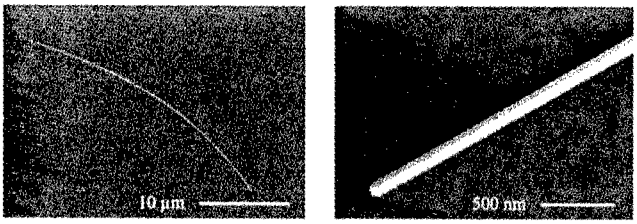


Figure 2. SEM images of Bi_2Te_3 nanowires.

plane distance of 3.80 Å. The angle between the fringes and the nanowire edge is 60°, which is expected from the <110> growth direction. EDX measurements show no other heavy elements except Bi and Te. Average atomic ratio of Te to Bi from 6 samples is 1.46. It gives a formula of $Bi_2Te_{2.92}$. The deviation from Bi_2Te_3 is within our experimental error.

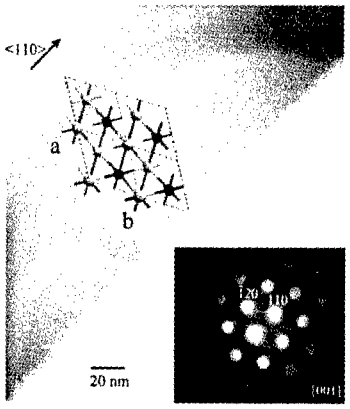


Figure 3. TEM image of a portion of Bi_2Te_3 nanowire with a schematic view of the Bi_2Te_3 structure in the ab plane superimposed on it. (inset) Electron diffraction pattern recorded along [001] zone axis.

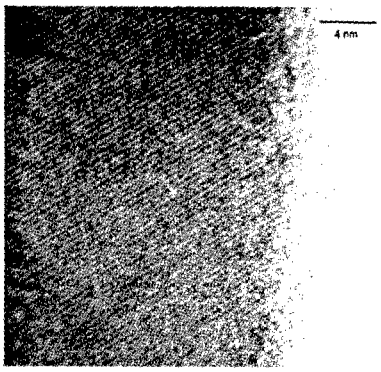


Figure 4. High-resolution TEM micrograph of the Bi_2Te_3 nanowire. The lattice fringes shown are (101) planes with an inter-plane distance of 3.80 Å. The angle between the fringes and the wire edge is 60°.

Similar results are obtained for PbTe nanowires. PbTe nanowires are 25 nm to 60 nm in diameter with lengths to 2 μm and can be readily produced. Figure 5 shows the TEM micrograph of one PbTe nanowire and its electron diffraction pattern. The diffraction pattern can be indexed to the face-center cubic structure of PbTe (a = 6.443 Å) with the electron beam along the [001] zone axis. These data show that the PbTe nanowires are single crystals and grow along the <100> crystal direction. EDX measurements from 5 samples give an average atomic ratio of Pb to Te as 1:1.01.

To evaluate the intrinsic thermoelectric figure of merit, the properties of individual nanowires must be measured. The electrical conductivity, σ, and thermoelectric power, S, can be

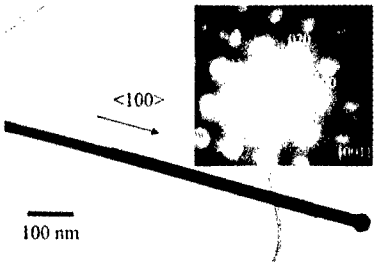


Figure 5. TEM image of a PbTe nanowire. (inset) Electron diffraction pattern recorded along [001] zone axis.

determined from transport measurements using micro/nanofabricated electrodes. Below are the preliminary results of electrical conductivity measurements of individual single crystal Bi_2Te_3 nanowires. Electrodes defined by electron-beam lithography can be routinely fabricated on the desired individual nanowires. Figure 6 shows a SEM image of lithographically defined Au leads on one Bi_2Te_3 nanowire. The electrodes are usually separated by 2 μm to 10 μm. An I-V curve obtained at room temperature on a portion of Bi_2Te_3 nanowire with diameter of 120 nm and length of 13 μm is shown in figure 7. The resistivity determined for this wire, 1400 μΩ·cm, is comparable to the literature value for Bi_2Te_3 single crystals, 1700 μΩ·cm [3]. The dependence of the electrical conductivity on temperature is currently being investigated.

CONCLUSIONS

Nanowires of Bi_2Te_3 and PbTe, two of the most important thermoelectric materials for thermoelectric refrigeration, have been successfully synthesized by a laser ablation method. Both nanowires have high aspect ratios and are single crystals. They grow along <110> direction and <100> direction, respectively. E-beam lithography has been used to make reproducible connections to these nanostructures, and preliminary transport measurements show promising behavior for these 1D structures. It is also expected that increased phonon scattering from the

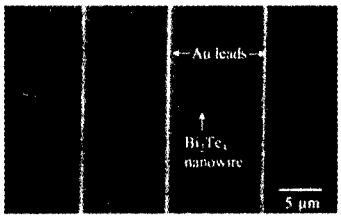


Figure 6. SEM image of lithographically defined electrodes on top of a single Bi_2Te_3 nanowire.

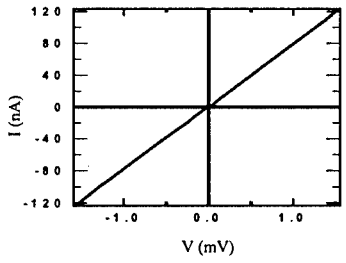


Figure 7. I-V curve from a portion of single Bi_2Te_3 nanowire with diameter of 120 nm and length of 13 μm at room temperature. The resistivity of this nanowire is 1400 μΩ·cm at room temperature.

surfaces of the nanowires will significantly lower the thermal conductivity, and hence enhance the thermoelectric figure of merit. An approach for measuring the thermal conductivity of individual nanowires is being developed in our laboratory. Studies of the transport properties of these individual nanowires will enable us to better understand the fundamental physics of 1D structures.

ACKNOWLEDGMENTS

We thank Y. Lu for help with TEM. C.M.L. acknowledges support of this work by the Office of Naval Research.

REFERENCES

1. G. Mahan, B. Sales and J. Sharp, Physics Today, **50**(3), p. 42 (1997).
2. H.J. Goldsmid, *Thermoelectric Refrigeration*, Plenum, New York, 1964.
3. G. Mahan, Solid State Physics, **51**, p. 82 (1998).
4. L.D. Hicks and M.S. Dresselhaus, Phys. Rev. B, **47**(24), p. 16,631 (1993).
5. D.A. Broido and T.L. Reinecke, Appl. Phys. Lett., **67**(1), p. 100 (1995).
6. A. Morales and C.M. Lieber, Science, **279**, p. 208 (1998).
7. C.M. Lieber, Solid State Commun., **107**, p. 607 (1998).
8. J. Hu, T.W. Odom and C.M. Lieber, Acc. Chem. Res., **32**, p. 435 (1999).

CONTROLLED GROWTH OF AMORPHOUS SILICON NANOWIRES VIA A SOLID-LIQUID-SOLID (SLS) MECHANISM

H. F. YAN, Y. J. XING[§], Q. L. HANG, D. P. YU*, J. XU, H. Z. ZHANG,Z. H. XI[§], S. Q. FENG
Department of Physics, State Key Laboratory of Mesoscopic Physics, and Electron Microscopy Laboratory, Peking University, Beijing, China, *yudp@pku.edu.cn
[§] Department of Electronics, Peking University, Beijing, China

ABSTRACT

Amorphous silicon nanowires (a-SiNW's) with average diameter around 20 nm were synthesized at about 950° C under an Ar/H_2 atmosphere on large area of a (111) Si substrate without supplying any gaseous or liquid Si sources. The Si substrate, deposited with a layer of Ni of about 40 nm thick, served itself as a silicon source for the growth of the a-SiNWs. Different from the well-known vapor-liquid-solid (VLS) for conventional whisker growth, it was found that growth of the a-SiNWs was controlled by a solid-liquid-solid mechanism, which is analogous to the VLS model.

INTRODUCTION

Nanostructured materials have been a focused research field either due to the novel physical properties related to mesoscopic system, or to the potential device application in nano and opto-electronics. The synthesis of Si whiskers via the vapor-liquid-solid (VLS) growth mechanism was first described in detail by Wagner and Co-workers [1-3]. Givargizov developed the growth model and discussed it within a kinetics framework [4]. Since then, a few papers on vapor phase whisker growth discussed the other possible growth mechanism, as VLS growth became more and more evident. Yazawa[5] and Westwater[6] produced Si nanowires with VLS growth induced by Au metal layer on a Si surface. Recently, Yu[7] reported oven-laser ablation method, or through simple physical evaporation approach[8], to produce very pure ultrafine freestanding silicon nanowires. These experimental results also can be explained well by VLS mechanism, which seemingly has became the main method to synthesize one-dimension nano materials [9-11]. In the previous work for silicon nanowire synthesis, however, vapor phase with considerable Si concentration was either supplied from laser ablation of a powder target, or directly from silane. In this letter, we report that a-SiNWs can be controllably grown on a silicon substrate via a solid-liquid-solid (SLS) growth mechanism.

EXPERIMENTALS

Heavily-doped ($1.5\times10^{-2}\Omega$/cm) *n-type* Si (111) chips were used as substrate. The silicon substrate was cleaned ultrasonically in pure petroleum ether and in ethanol in turns for 5 min, and leached in distilled water, then dried. A thin layer of 40 nm nickel was thermally deposited on the substrate. The substrate was placed in a quartz tube which was heated in a tube furnace at 950℃. H_2 (36 sccm) and H_2 (4 sccm) were introduced during growth at an ambient pressure of about 200 Torr. After cooling down to room temperature, a thin layer of gray-colored deposit was found on the surface of the substrate. An Amray FEG-1910 scanning electron microscope (SEM), and a Hitachi-9000NAR high resolution transmission electron microscope (HREM) equipped with

Mat. Res. Soc. Symp. Proc. Vol. 581 © 2000 Materials Research Society

energy dispersive spectrum (EDS) were employed for analysis of the morphology and microstructure of the product.

RESULTS AND DISCUSSION

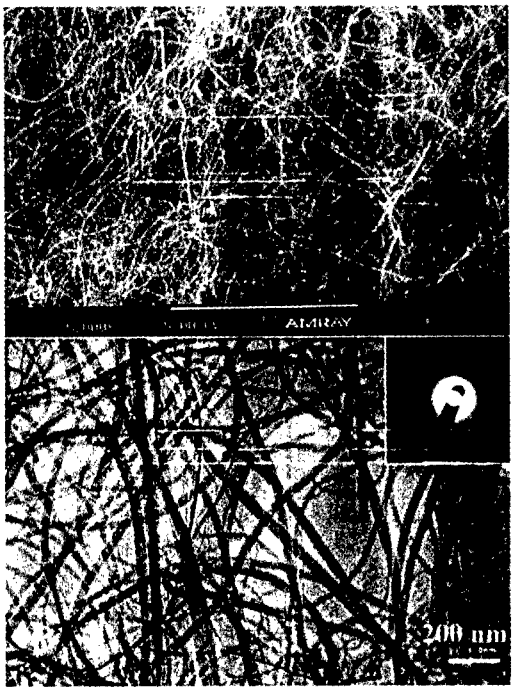


Fig.1 (a): SEM image showing the general morphology of the SiNWs grown via a SLS growth mechanism. (b): TEM image revealing that the SiNWs have smooth morphology and average diameter around 40 nm. The SAED pattern shown in inset reveals characteristic diffusive ring pattern, showing that the nanowires are completely amorphous

Fig. 1(a) shows in plan view an SEM image revealing the general morphology of the Si nanowires grown on a large area (10 mm x 10 mm) of 111 Si substrate after one hour's growth. The nanowires grew directly on the substrate without introduction of other Si source in the vapor phase. It is visible that the deposit consists of nearly pure SiNWs. The growth rate of the nanowires is estimated about 30 nm/second. The TEM image shown in fig. 1(b) reveals that the SiNWs have smooth morphology, and have a diameter of 10~50 nm and length up to a few tens of micrometers. The highly diffusive ring pattern (inset) of selected area electron diffraction (SAED) revealed that the Si nanowires are completely amorphous (a-SiNWs). EDS analysis proved that there exists a small amount of oxygen in the a-SiNWs, which was attributed to the surface oxidation when the freshly-made nanowires were exposed in air, because the growth

process was controlled under a reduction atmosphere with a mixture of argon and hydrogen. The growth environment is quite different from that of laser ablation, or physical evaporation, and it indeed reveals a different growth mechanism.

In the case of oven-laser ablation[7] approach, silicon source for SiNWs growth was supplied from the vapor phase in which atomic Si species were ablated off by the laser beam. While in the high temperature evaporation method[8], sufficient silicon atoms were evaporated at high temperature from the powder target due to the extremely high specific ratio of surface/volume compared to bulk silicon. Such a high specific surface/volume ratio guarantees a Si concentration high enough in the vapor phase. In these two cases, the growth of the SiNWs is controlled by the well-known vapor-liquid-solid (VLS) mechanism, in which the vapor phase plays an important role in the growth of the SiNWs. The central idea of the VLS growth of SiNWs is that, the catalysts (usually Ni, or Fe as impurity) act as a liquid-forming agent, which react with the vapor phase, and forms the $NiSi_2$ eutectic liquid droplets. The vapor phase is rich in Si atoms. With the further absorption of Si atoms into the droplets from the vapor phase, the droplets become supersaturated, resulting in the precipitation of SiNWs from the droplets.

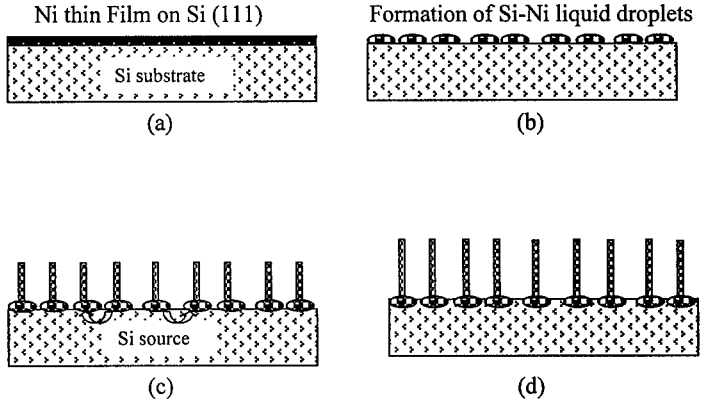


Fig. 2 Schematic depiction of the SiNW growth via the SLS mechanism: (a) Deposition of a thin layer of Ni on the Si (111) substrate; (b) Formation of the Si-Ni eutectic liquid droplets; (c) The continuous diffusion of Si atoms through the substrate-liquid (S-L) interface into the liquid droplets, and growth of SiNWs through the liquid-wire (L-S) interface; (d) Final state of the SiNW growth. The smooth surface of the original substrate becomes rough at the end of the SiNW growth.

In the present circumstance, however, the Si concentration in the vapor phase is negligible at the growth temperature, because the specific surface/volume ratio of bulk Si substrate is extremely low compared with that of the micro-sized Si powder target, or in the case by laser ablation. On the other hand, the Si substrate was covered by a thin layer of Ni. Therefore, the only possible silicon source comes from the bulk silicon substrate, because no extra Si source was introduced in the vapor phase. From the binary Ni-Si diagram, it is visible that the eutectic point of $NiSi_2$ is 993℃. However, due to the melting effect of small-size grains, the eutectic

compound $NiSi_2$ can begin to form at a temperature lower than 993℃. As we proved, the deposited Ni film can react with the Si substrate at temperature above 930℃, and forms Si_2Ni eutectic liquid alloy droplets. Because of the relatively high solubility of Si in Si_2Ni eutectic alloy, more Si atoms will diffuse through the solid (the substrate) – liquid interface into the liquid phase (the $NiSi_2$ droplets). A second liquid -solid (nanowire) interface will form when the liquid phase becomes supersaturated due to thermal or compositional fluctuations, resulting in the growth of SiNWs. Because this growth process involves solid-liquid-solid phases, it is named as a SLS growth, which is in fact an analogy of the VLS mechanism. The growth process of the a-SiNWs via an SLS model is depicted schematically in Fig. 2.

Cross-sectional SEM analysis of the sample provided direct evidence to support the a-SiNW growth via a SLS mechanism. In low magnified cross-sectional SEM image in Fig. 3, it is visible that a layer of a-SiNWs with a thickness of about 20 μm were grown on the substrate. EDS analysis between the Si substrate and the a-SiNW layer further confirmed that there is a thin layer of Si-Ni alloy. We also found that the a-SiNWs grow from the base, which manifests itself by the fact that the solidified Si-Ni nano particles were visible between the surface of the substrate and the a-SiNW film, instead of being attached at the free tip of the SiNWs.

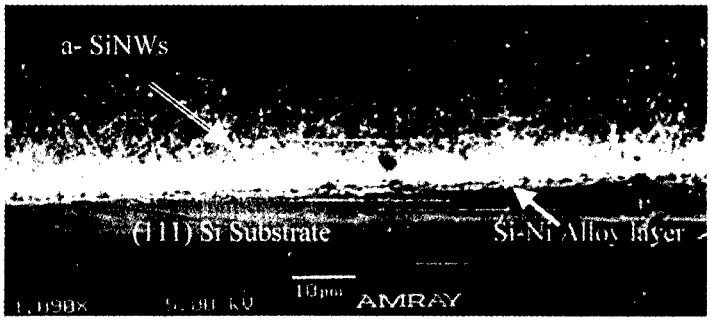


Fig. 3 Low magnification of cross-sectional SEM image of the SiNWs grown on Si (111) substrate, which is controlled by a SLS mechanism. The length of the SiNWs is about 20 μm. The Si-Ni particles are visible attached to the Si substrate surface.

One question about the SLS growth is what is the driving force for such a continuous diffusion of Si atoms from the substrate through the substrate-liquid interface into the liquid droplets, and then through the liquid droplets-nanowire to stack themselves into nanowires? From kinetic view point, the concentration gradient, and the supersaturation due to fluctuation in the Si-Ni liquid droplets are the driving force of the growth. On the other hand, the carrier gas Ar/H_2 will collide with the surface of the semisphere-shaped Si-Ni liquid droplets, and exchange energy and momentum with the atoms at the surface of the Si-Ni nanoparticles, causing overcooling at the surface of the droplets. Such an overcooling is critical to initiate the preferential unidirectional growth of the a-SiNWs. The second question is why the resultant nanowires are amorphous instead of being crystalline. The most possible reason is that the growth was performed under H_2/Ar atmosphere, and the Si-Si bonds were partially substituted by Si-H bondings, which destroys the diamond structure of the crystalline silicon.

The silicon nanowires are interesting to evaluate the quantum confinement effect related to low dimensionality[12]. The controlled growth of a-SiNWs on substrate is important, because the remarkable surface/volume ratio of the nanowires enables the materials show physical chemical properties completely different from the bulk, which makes it excellent candidate for possible applications such as rechargeable battery of high capacity with portable size, which is closely related to the surface effects. It was recently revealed that the lithium battery using silicon nanowires as electrode materials showed a capacity as high as 8 times that of the ordinary one[13,14]. By optimizing dopants, it is believed that the a-SiNW film thus prepared will find applications in other fields such as opto-electronics, and wave-absorbing media.

CONCLUSIONS

In conclusions, a-SiNWs were controllably grown directly on Si substrate without supplying any gaseous or liquid Si sources. It was shown that the growth of the a-SiNWs was different from the conventional VLS model. Instead, the a-SiNWs were grown via an SLS mechanism, in which the substrate served as a Si source. The present results also provide an alternative but simple approach for nanostructure preparation.

ACKNOWLEDGEMENT

This project was financially supported by national Natural Science Foundation of China (NSFC), and by the Research Fund for the Doctoral Program of higher Education (RFDP), China.

REFERENCES

1. R. S. Wager and W. C. Ellis, Appl. Phys. Letter. **4**. P.89 (1964).
2. R. S. Wager and W. C. Ellis, Trans. Met. Soc. AIME **233**, p.1053 (1965).
3. R. S. Wager and C. J. Doherty, J. Electrochem. Soc **115**, .93 (1968).
4. E. I. Givargizov, J. Cryst. Growth **31**, 20 (1975).
5. M. Yazawa, M. Koguchi, A. Muto, M. Ozawa, K.Hiruma, Appl. Phys. Lett. **61**, p.2051 (1992).
6. J. Westwater, D. P. Gosain, S. Tomiya, S. Usui, H. Ruda, J. Vac. Sci. Technol. *B* **15**, p.554 (1997).
7. D. P. Yu, C. S .Lee, I. Bello, X. S. Sun, Y. H. Tang, G. W. Zhou, Z .G. Bai, Z. Zhang and S. Q. Feng, Solid State Communications **105**, p.403(1998).
8. D. P. Yu, Z.G. Bai, Y. Ding, Q. L. Hang, H. Z. Zhang, J. J. Wang, Y. H. Zou, W. Qian, H. T. Zhou, G. C. Xiong and S. Q. Feng, Appl. Phys. Letters **72**, p.3458(1998)
9. N. Ozaki, Y. Ohno, and S. Takeda, Appl. Phys. Letters **73**, p.3700(1998).
10. Z. G. Bai, D. P. Yu, H. Z. Zhang, Y. Ding, Q. L. Hang, G. C. Xiong and S. Q. Feng, Chemical Physics Letters **303**, 311(1999).
11. H. Z. Zhang, Y. C. Kong, Y. Z. Wang, X. Du, Z. G. Bai, J. J. Wang, D. P. Yu, Y. Ding, Q. L. Hang, S. Q. Feng, Solid State Communications **109**, p.677(1999).
12. D. P. Yu, Z. G. Bai, J. J. Wang, Y. H. Zou, W. Qian, J. S. Fu, H. Z. Zhang, Y. Ding, G. C. Xiong and S. Q. Feng, Physical Review **B 59**, p.2498(1999).
13. H. Li, G. W. Zhou, D. P. Yu, X. J. Huang, L. Q. Chen, Z. Zhang, to be published, (1999).
14. G. W. Zhou, H. Li, H. P. Sun, D. P Yu, Y. Q. Wang, L. Q. Chen, and Ze Zhang, Applied Physics Letters **75**, p.2447 (1999).

Oriented Si nanowires grown via an SLS mechanism

Y. J. Xing[1,2], Z. H. Xi[1] , Q. L. Hang[2], H. F. Yan[2], S. Q. Feng[2] , J.Xu[2],H.Z.ZHANG[2] and D. P. Yu[2*]

[1] Department of Electronics, Peking University, Beijing, China

[2] Department of Physics, State Key Laboratory of Mesoscopic Physics, and Electron Microscopy Laboratory, Peking University, Beijing, China, *yudp@pku.edu.cn

ABSTRACT

Highly oriented silicon nanowires were grown on Si (111) substrate via a solid-liquid-solid (SLS) mechanism. Unlike the well known vapor-liquid-solid (VLS) mechanism of whisker growth, no gaseous or liquid Si source was supplied during growth. Ni was used as the liquid forming agent and mixture of H_2 and Ar was introduced in the experiment. Oriented silicon nanowires grew at 950℃ and the ambient pressure kept at about 200 Torr. The oriented silicon nanowires have a length around 1 μ m and uniform diameter about 25nm. Selected area electron diffraction showed that silicon nanowires are completely amorphous. The approach used here is simple and controllable, and may be useful in large-scale synthesis of various nanowires.

INTRODUCTION

The pioneering work of the discovery of multi-walled carbon nanotubes by Iijima[1] has stimulated intensive research interests on one dimension nanomaterials. Compared with the indirect gap nature of bulk Si, silicon nanowires (SiNWs) are a novel one-dimension nanostructures whose physical properties are modified through quantum confinement effect[2-4]. It has been reported that silicon nanowires can emit full visible band light[5]. Molecular level semiconductor/metal hetero junctions using silicon nanowire/carbon nanotube were synthesized, which show typical rectifying effect of a nano diode[6]. These results reveal that silicon nanowires are a promising material in the fundamental research and potential application. Several methods, such as laser ablation[2], physical evaporation[3], or thermal decomposition of silane[7], were employed to synthesize silicon nanowires, and controlled growth of the nanowires is yet to be achieved, which is important in device application. In this paper, we will report highly oriented amorphous silicon nanowires were controllable grown on Si substrate in a new large-scale and low-cost. Though the Si nanowires are of amorphous nature, the approach described here proved to be effective to realize the controlled growth of nanowires.

EXPERIMENTALS

Heavy-doped ($1.5\times10^{-2}\Omega$/cm) *n-type* Si (111) wafers were used as substrates. The silicon substrates were cleaned ultrasonically in pure petroleum ether and in ethanol in turns for 5 min, and leached in distilled water, then dried. A thin layer of 40

Mat. Res. Soc. Symp. Proc. Vol. 581 © 2000 Materials Research Society

nm nickel was thermal deposited on the substrate. The substrate was placed in a quartz tube which was heated in a tube furnace. A three-step heating procedure was involved in the growth. Firstly, the system was heated to 800℃, and a mixture of H_2 (36sccm)/Ar (4sccm) were introduced to the tube. The temperature was then raised from 800℃ to 950℃ and pure Ar (100sccm) was used as a carrier gas in this step. The ambient pressure of the tube was kept near 750 Torr by adjusting the exit valve, then evacuated the tube. This procedure was repeated three times. Finally, the temperature was held at 950℃ at the pressure of about 200 Torr for one hour. A mixture of H_2 (4sccm) and Ar (36sccm) was introduced to the tube. After cooling down to room temperature, a dark thin layer was found on the substrate. An Amray FEG-1910 scanning electron microscope (SEM), and a Hitachi-9000NAR high resolution transmission electron microscope (HREM) equipped with energy dispersive spectrum (EDS) were employed for analysis of the morphology and microstructure of the product.

RESULTS AND DISCUSSIONS

A low-magnified SEM image of the SiNWs is shown in Fig. 1 (a), representing a general planar view of the oriented SiNWs. It is visible that the nanowires were grown on centimeter-sized substrate. An interesting phenomenon is that the nanowire film was found chapped in a network of white-contrasted lines. The inclined view at a crossover point of the white in Fig. 1 (b) revealed the white lines are in fact V-shaped chaps. From this image it is visible that the film consists of pure silicon nanowires. Parts of SiNWs on the edge of chaps fall on the substrate.

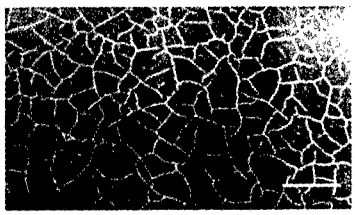


Fig. 1 (a)

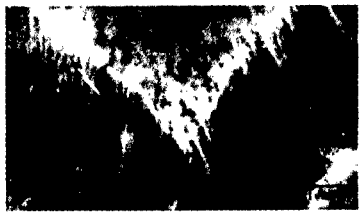


Fig.1 (b)

Fig. 1 SEM image of oriented SiNWs on the substrate, regions except white lines are composed of SiNWs perpendicular to the substrate. (a) Low magnified SEM image; (b) Magnified SEM image of the chaps of the white lines, revealing that the film consists of pure oriented SiNWs.

Fig. 2 shows the cross-sectional view of the silicon naonwire film. It is visible that SiNWs grew densely and were well oriented perpendicularly to the substrate. The length of SiNW is about 1 micrometer.

Fig. 3 is the TEM image of ultra fine SiNW, which were scratched from the substrate. It shows the diameter of SiNWs is about 25nm.The highly diffusive ring pattern (inset) in select area electron diffraction (SAED) revealed that SiNWs are completely amorphous.

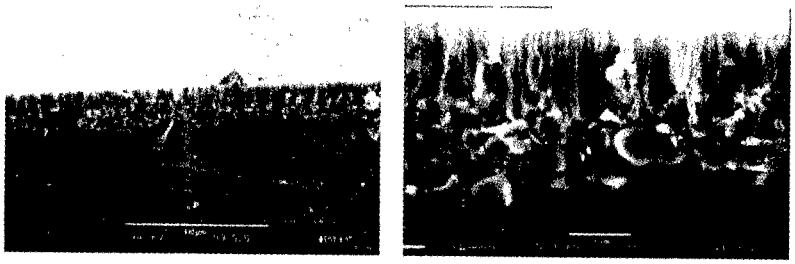


Fig. 2(a) Fig. 2(b)

Fig. 2 SEM image of oriented SiNWs grown on the substrate (cross-sectional view). SiNWs grew densely and are all perpendicular to the substrate. The length of SiNWs is about 1 μ m. (a) Low magnified SEM image; (b) Magnified SEM image. It is visible that between the SiNWs and the substrate there is a layer of nano-sized particles which proved to consist of Ni and Si.

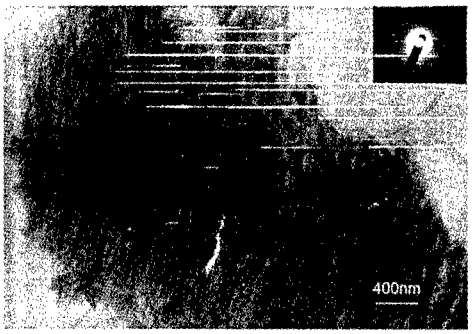


Fig. 3

Fig. 3 TEM image of SiNWs, which were scratched off from the substrate.The SiNWs have uniform diameter around 25nm. The SAED pattern shown in the inset reveals a characteristic diffusive ring pattern, showing that the nanowires are completely amorphous (a-SiNWs).

It was found that the growth of the SiNWs here is different from the VLS mechanism for conventional whiskers[8]. Instead, the growth mechanism of the a-SiNWs were controlled by a solid-liquid-solid mechanism (SLS), which is discussed in detail in another article[9]. A brief explanation of such a model is described here.In the present circumstance, the Si concentration in the vapor phase is negligible at the growth temperature, because the specific surface/volume ratio of bulk Si substrate is extremely low compared with that of the micro-sized Si powder target, or in the case by laser ablation. On the other hand, the Si substrate was covered by a thin layer of Ni. Therefore, the only possible silicon source comes from the bulk silicon substrate, because no extra Si source was introduced in the vapor phase. From the binary Ni-Si diagram, it is visible that the eutectic point of $NiSi_2$ is 993℃. However, due to the melting effect of small-size grains, the eutectic compound $NiSi_2$ can begin to form in

a temperature lower than 993℃. As we proved, the deposited Ni film can react with the Si substrate at temperature above 930℃, and forms Si_2Ni eutectic liquid alloy droplets. Because of the relatively high solubility of Si in Si_2Ni eutectic alloy, more Si atoms will diffuse through the solid (the substrate)-liquid interface into the liquid phase (the Si_2Ni droplets). A second liquid-solid (nanowire) interface will form when the liquid phase becomes supersaturated due to thermal or compositional fluctuations, resulting in the growth of SiNWs. Because this growth process involves solid-liquid-solid phases, it is nominated as a SLS growth, which is in fact an analogy of the VLS mechanism.

Because SiNWs grew very densely and closely to each other, Van der Waals interactions among SiNWs are so strong that they hold SiNWs oriented perpendicularly to the substrate. The chaps were caused during the second step because liquid drops tend to shrink when eutectic Si-Ni nanoparticles are formed. There is no nickel film left in chaps, so that no eutectic Si-Ni nanoparticle can formed and then no SiNW will grow on the crack aera.

CONCLUSSION

In summary, oriented silicon nanowires were synthesized via a solid-liquid-solid mechanism. The Si substrate serves itself as Si source by heating. The SiNWs have uniform diameter and length up to 1 μ m . Such a growth was explained by an SLS model. This synthesis method of oriented SiNWs is simple and controllable. It can also be used to synthesize other nanowires.

ACKNOWLEDGEMENT

This project was financially supported by national Natural Science Foundation of China (NSFC), and by the reaearch Fund for the Doctoral Program of higher Eduacation (RFDP), China.

REFERENCES

1. S.Iijima,Nature **354**.56(1991)
2. D. P. Yu, C. S .Lee, I. Bello, X. S. Sun, Y. H. Tang, G. W. Zhou, Z .G. Bai, Z. Zhang and S. Q. Feng, Solid State Communications **105**, 403(1998).
3. D.P.Yu, Z.G.Bai, Y.Ding, Q. L. Hang, H.Z.Zhang, J.J.Wang, Y.H.Zou, W.Qian, G.C.Xiong and S.Q.Feng, Applied Physics Letters **72**,3458(1998)
4. H.Z.Zhang, D.P.Yu, Y.Ding, Z.G.Bai, Q. L. Hang and S.Q.Feng, , Applied Physics Letters **73**,3396(1998)
5. D.P.Yu,Z.G.Bai, J.J.Wang, Y.H.Zou, W.Qian, J.S.Fu, H.Z.Zhang, Y.Ding, G.C.Xiong and S.Q.Feng Physical Review **B 59**, 2498(1999).
6. J.Hu,M.Ouyang, P.Yang, C.M.Lieber, Nature **399**,48(1999)
7. J. Westwater, D. P. Gosain, S. Tomiya, S. Usui, H. Ruda, J. Vac. Sci. Technol.. ***B* 15**, 554 (1997)
8. R.S.Wager and W.C.Ellis, Appl.Phys.Letter.**4**.P.89(1964).
9. H. F. Yan, Y. J. Xing, Q. L. Hang, D. P. Yu, P. Zhang, J. Xu, Z. H. Xi, S. Q. Feng. Controlled growth of amorphous silicon nanowires via a solid-liquid-solid (SLS), submitted to Applied Physics Letters (1999).

COMPOSITE NANOWIRES FROM ION BEAM MODIFICATION OF SI NANOWIRES

X. T. ZHOU, H. Y. PENG, N. G. SHANG, N. WANG, I. BELLO, C. S. LEE, S. T. LEE
Center of Super-Diamond and Advanced Films and Department of Physics and Materials Science, City University of Hong Kong, Kowloon, Hong Kong

ABSTRACT

Composite nanowires with typical diameters of 30-100nm, which consisted of Si, β-SiC, amorphous carbon were converted from Si nanowires by ion beam deposition. The Si nanorods were exposed to broad low energy ion beams. The low energy hydrocarbon, argon and hydrogen ions, generated in a Kaufman ion source, reacted with Si nanowires and formed the composite nanowires. It has been assumed that the reaction pathway to form the composite nanowires were driven by both thermal diffusion and kinetic energic of interacting particles.

INTRODUCTION

Since the discovery of carbon nanotubes[1], nanoscale one-dimensional structures have stimulated great interest in the research community because of their exotic electronic and mechanical properties. H. J. Dai et al.[2] first reported an alternative approach to the synthesis of solid carbide nanoscale rods of TiC, NbC, Fe_3C, SiC, and BC_X from carbon nanotubes. W. Q. Han et al.[3] reported a method to prepare GaN using carbon nanotubes. Recently, another very important nanoscale material, bulk-quantity Si nanowires, have been successfully synthesize from silicon oxide[4]. This makes it possible to prepare some other nanoscale materials by using Si nanowires as temp. So far, most work reported on nanoscale materials has focused on the single structure materials. In fact, composite nanoscale materials may have some different properties which every pure material does not have. For instance, J. T. Hu et al.[5] reported that the heterojunction of carbon nanotubes and Si nanowires have diode-like I-V characteristics.

From the technique point of view, direct deposition by ion beam technique is the most direct method to study the effect of ion bombardment. In fact, low energy species of tens of eV have been used in film deposition in either plasma form or the ion beam technique.[6-8] Recently, Chen et al.[9] reported the formation of bulk-buried stoichiomtric SiC layer in the silicon substrates via ion implantation and subsequent annealing treatment. In this letter, we report the synthesis of composite nanowires by the bombardment of a fixed ion beam of CH_4, H_2 and Ar on Si nanowires.

EXPERIMENT

A vacuum chamber equipped with a Kaufman ion source (3.0-1500-1000, ION. TECH, INC. USA) was used for the treatment of Si nanowires synthesized by thermal evaporation of a powder mixture of Si and SiO_2 were used as substrate. In order to eliminate contamination, the Si nanowires were put on a mirror-polished Si wafer. The deposition process was carried out in the vacuum chamber with a base pressure of 2×10^{-7} Torr. A mixture of methane (>99.9%), hydrogen (>99.999%) and argon (>99.995%) was introduced into the ion source as the working gas with the ratio of CH_4:H_2:Ar=1:50:173. The total flow rate was 2 sccm and the deposition pressure

Mat. Res. Soc. Symp. Proc. Vol. 581 © 2000 Materials Research Society

was kept at about 5×10^{-4} Torr. Ions generated from the ion source were accelerated to bombard the Si nanowires with an accelerating voltage of 200eV. The ion dose measured by a Faraday cup was $3\times10^{19}/cm^2$. The substrate temperature measured by an infrared thermometer was $700^{O}C$. A high- resolution transmission electron microscope (HRTEM, Philips CM200 FEG) was used to characterise the samples.

RESULTS AND DISCUSSION

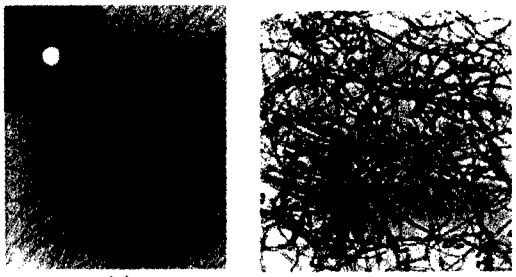


Fig. 1 TEM images (at lower magnification) of Si nanowires (a) and composite nanowires (b). Inset shows the corresponding electron diffraction pattern.

The transmission electron microscope (TEM) images in Fig. 1(a) shows the general morphology of Si nanowires synthesized by the thermal evaporation of the powder mixture of Si and SiO_2[4]. The nanowires are extremely long (>10μm) with uniform diameter and smooth surfaces. The average diameter of the Si nanowires is 20nm. The electron diffraction pattern showed that the wires are Si nanowires. The previous results[4] indicated that each nanowire consists of a single crystalline Si core and a very thin amorphous SiO_x. Fig. 1(b) shows the TEM morphology (at lower magnification) of the above Si nanowires after bombardment of ion beam. The diameter of the nanowires after treatment is about 30-100nm; it is much larger than that of Si nanowires before treatment. For some nanowires, a black core and grey shell can be seen. The diameter of the black core is close to that of the Si nanowires. We called the nanowires after treatment as composite nanowires.

Fig. 2 shows the bright field (Fig. 2(a)), dark field (Fig. 2(b)) TEM image at larger magnification and the corresponding electron diffraction pattern (in set) of the composite nanowires. From this figure, we can see the surface of the composite nanowires became very ruffle due to the existence of very small particle on its surface. The electron diffraction pattern shows that very small β-SiC particles formed on the Si nanowire surface. The dark field image proves that the electron diffraction pattern resulted from the very small crystallises on the surface of the composite nanowires.

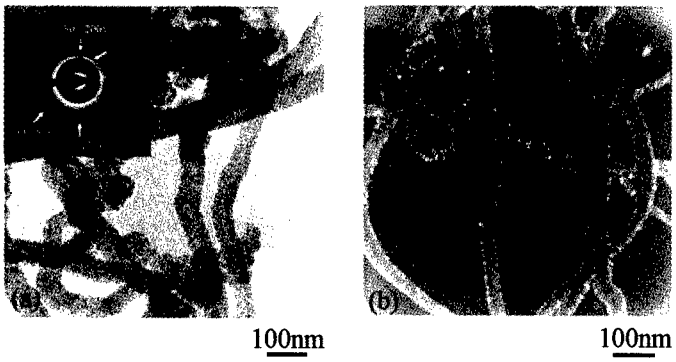


Fig. 2. Bright field (a) and dark field (b) TEM images (at larger magnification) of the composite nanowires and the corresponding electron diffraction pattern



Fig. 3. High resolution TEM images of the composite nanowires

Fig. 3 shows the high resolution TEM images of some different composite nanowires. There are only some β-SiC nanopaticles on the surface of the composite nanowires, and these β-SiC nanopaticles contact the core of the Si nanowire directly (Fig. 3(a)). For some nanowires, only the β-SiC nanopaticles can be observed by high resolution TEM image (Fig. 3 (b)). In this case, the thickness of the outer shell is too thick and makes it impossible to observe the core of the Si nanowire by high resolution TEM. For some nanowires, besides the β-SiC nanopaticles, an amorphous outlay on the β-SiC nanopaticles were observed (Fig. 3(c)), the EDX result indicates that the amorphous outlay should be amorphous carbon layer. The sizes of the β-SiC nanocrystallines showed in the above figures are almost the same (several nanometers). All these β-SiC nanoparticles are allied randomly.

Based on the present experimental data, the mechanism of ion bombardment induced the formation of the composite nanowires can be attributed to both thermal diffusion and kinetic energy of interacting particles. During the treatment of ion beam, atomic hydrogen, hydrogen ions and CH_x radicals formed in the ion source by means of Ar plasma assistance and were abstracted from the ion gun by the acceleration bias. The CH_x radicals with high energy bombarded the silicon wires surface and decomposed into carbon and hydrogen atoms. The carbon atoms diffused into the Si nanowires, furthermore reacted with the silicon nanowires and formed SiC nanocrystallines on the surface of the Si nanowires. On the other hand, the atomic hydrogen and hydrogen ions with high energy reacted with the silicon nanowires and formed S_xH_y radicals on the Si nanowires surface. The radicals S_xH_y decomposed into silicon and hydrogen atoms. The silicon atoms diffused through the outlay, reacted with CH_x radicals and also formed SiC nanocrystallines. During the early stage of the ion bombardment on Si nanowires, SiC

nanocrystallines formed directly on the surface of the Si nanowires. Fig. 3(a) provides the direct evidence of the existence of the SiC nanocrystallines on Si nanowire. With increasing of the thickness of the outlay, the quantity of the carbon and silicon atoms which transferred through the outlay decreased and amorphous carbon began to deposit due to the decomposition of the CH_x radicals. So, what we see in Fig. 3(b) may be a kind of a mixture of SiC nanoparticles and amorphous carbon matrix. When the film covered the Si nanowires core was enough thick, the silicon and carbon atoms could not diffuse so long distance and only amorphous carbon formed on the out surface of the composite nanowires (Fig. 3(c)). In conclusion, two type composite nanowires can be produced by ion beam deposition. One is the nanowire which consists of single crystalline silicon nanowire core and polycrystalline β-SiC shall (Fig. 3(a), (b)). The other is the nanowire which consists of single crystalline silicon nanowire core and two out shells: polycrystalline β-SiC and amorphous carbon (Fig. 3(c)).

CONCLUSIONS

In summary, we report and study the synthesis of two kinds of composite nanowires from Si nanowires by ion beam deposition. The composite nanowires consist of Si, β-SiC or amorphous carbon.

ACKNOWLEDGMENTS

Financial support by the Research Grant Council of Hong Kong under Grant No. 9040459 is gratefully acknowledged.

REFERENCES

1. Iijima, Nature (London) **354**, 56 (1991).

2. H. G. Dai, E. W. Wong, Y. Z. Lu, S. S. Fan, and M. Lieber, Nature (London) **375**, 769 (1995).

3. W. Q. Han, S. S. Fan, Q. Q. Li, and X. D. Hu, Science **277**, 1287 (1997).

4. N. Wang, Y. H. Tang, Y. F. Zhang, C. S. Lee, I. Bello, and S. T. Lee, Chem. Phys. Lett. **299**, 237 (1999).

5. J. T. Hu, M. Ouyang, P. D. Yang, and M. Lieber, Nature (London) **399**, 48 (1999).

6. C. Weissmantell, in Thin Films From Free Atoms and Particles, edited by K. J. Klabunde (Academic, Orlando, FL, 1985).

7. J. C. Angus, P. Kiodl, and Domitz, in Plasma Deposited in Thin Films, edited by J. Mort and F. Jansen (CRC, Boca Raton, FL, 1986).

8. T. Takai, Thin solid Films **92**, 1 (1982).

9. D. Chen, S. P. Wong, W. Y. Cheung, I. H. Wilson, and R. W. M. Kwok, Amorphous and Crystalline Insulating Thin Films, Oct. 12-14, Hong Kong.

ARC DISCHARGE FOR THE SYNTHESIS OF MONOCLINIC Ga_2O_3 NANOWIRES

YOUNG CHUL CHOI*, DONG JAE BAE*, SEUNG MI LEE*, YOUNG SOO PARK*, YOUNG HEE LEE*, GYEONG-SU PARK**, WON BONG CHOI***, NAE SUNG LEE***, JONG MIN KIM***

* Department of Semiconductor Science and Technology, Jeonbuk National University, Jeonju 561-756, R. O. Korea, leeyh@sprc2.chonbuk.ac.kr

** Analytical Engineering Laboratory, Samsung Advanced Institute of Technology, Suwon 440-600, R. O. Korea

*** Display Laboratory, Samsung Advanced Institute of Technology, Suwon 440-600, R. O. Korea

ABSTRACT

Monoclinic gallium oxide (β-Ga_2O_3) nanowires were catalytically synthesized by electric arc discharge of GaN powders mixed with a small amount (less than 5 %) of transition metals under a pressure of 500 Torr (80 %-Ar + 20 %-O_2). Scanning electron microscope (SEM) and high-resolution transmission electron microscope (HRTEM) images showed that the average diameter of the wires were about 30 nm and their lengths were as long as up to one hundred micrometer, resulting in extremely large aspect ratio. Fourier diffractogram was indicative of single crystalline nature of the β-Ga_2O_3 wire. HRTEM image also showed β-Ga_2O_3 with twin defects at the center of the wire which might play as nucleation seeds. Both X-ray diffraction (XRD) patterns and FT-Raman spectra of the wires identified the observed nanowires as monoclinic crystalline gallium oxides.

INTRODUCTION

Nanowires of various materials have recently attracted much attention due to their mesoscopic phases that provide new physical properties and strong application to devices. However, from energetical point of view, it is rather unusual to have the nanostructures compared with bulk phase. Nonetheless, various nanowires are experimentally observed [1-3], although the formation mechanism is still far from being clearly understood. The key issue here is how to compensate the energy penalty in forming β-Ga_2O_3 nanowires and further accelerate the formation of the nanowires. We focus in particular here the role of transition metals, which seems to an essential ingredient in forming nanowires. Unfortunately, the transition metals play different roles with different synthesis approaches. Therefore, a comprehensive understanding of a role of transition metals for a given synthesis approach is required to control the growth process.

In this study, we synthesized monoclinic gallium oxide (β-Ga_2O_3) nanowires by dc arc discharge method, and the structural and optical properties of the nanowires were investigated. It was found from structural analyses that the arc discharged products were β-Ga_2O_3 nanowires with [001] direction of axis. Optical characterization showed that the indirect band gap of the wires are about 3.6 eV.

EXPERIMENTS

Conventional dc arc discharge method was used to synthesize β-Ga_2O_3 nanowires. GaN powder (99.999 %, High Purity Chemicals) with 5 wt% of transition metal powders (Ni:Co=1:1

Mat. Res. Soc. Symp. Proc. Vol. 581 © 2000 Materials Research Society

and Ni:Co:Y=4.5:4.5:1) was pressed into a small hole (diameter:4 mm, depth:25 mm) of the graphite anode (diameter:6 mm). DC current of 55-65 A with a voltage of 13-15 V was applied between two electrodes under a total pressure of 500 torr of argon and oxygen gases (p_{Ar}:p_{O2}=400:100). Arching time was typically 5-6 sec. The chamber wall was kept cooled by circulated water.

Scanning electron microscope (SEM) and high-resolution transmission electron microscope (HRTEM) were used to investigate the morphology and the microstructure of nanowires. X-ray diffraction (XRD) and Fourier transformed (FT) Raman spectroscopy were employed to confirm β-Ga_2O_3 structure. UV adsorption measurement was done for determining optical band gap.

RESULTS AND DISCUSSION

Nanowires were deposited on the cathode, chamber wall, and in-between as a form of web-like network. Bluish grey powders were obtained from three regions, although original GaN powder was white in color. In addition, small amount of carbon nanotubes were detected sometimes as a black powder. Therefore, a careful control of arcing time was required to minimize the production of carbon nanotubes. The pressure is also a very important factor for forming nanowires. We could not obtain the nanowires at pressures under 450 torr. Bluish grey powders were extracted exclusively for characterizations.

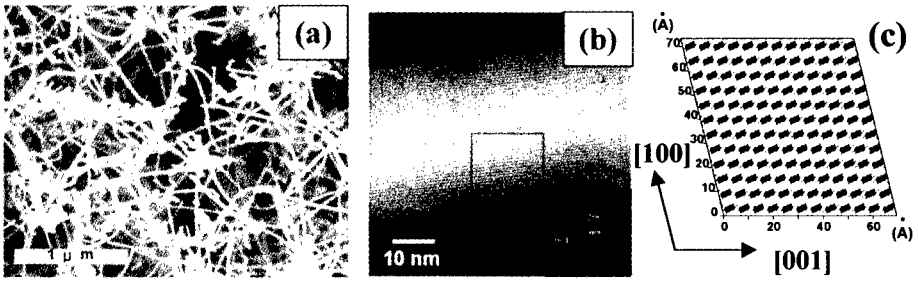


Fig. 1. (a) SEM image of β-Ga_2O_3 nanowires, (b) HRTEM image of β-Ga_2O_3 nanowire, (c) Simulated image of β-Ga_2O_3 nanowires with 6×6×12 supercell.

Figure 1(a) shows a typical SEM image from web-like network. A large quantity of nanowires are formed with relatively uniform diameters. The nanowires are straight and long, resulting in large aspect ratio. We observed from cathode deposits that nanowires are as long as one hundred micrometer, in some cases [4]. In this case, very pure nanowires were obtained, in contrast with carbon nanotubes generated by arc discharge where large amount of nanoparticles were produced in addition to carbon nanotubes [5]. We found that addition of small amount of yttrium was necessary for massive production of nanowires, suggesting that yttrium may play as an effective catalyst. Note that no nanowire was formed without transition metals.

Figure 1(b) shows a HRTEM image of the nanowire. The image clearly illustrates crystalline structure of nanowire with twin defects (twin angle of about 160°) at the center of the nanowire. The nanowire reveals a smooth surface without step edges. The typical diameter of the nanowires is about 33 nm. Note that no amorphous layer was formed on the surface. The inset shows the Fourier diffractogram obtained from the HRTEM image, indicating a crystalline

nature and the direction of the nanowire axis to be [001]. In order to confirm these, we constructed a monoclinic Ga_2O_3 nanowire and obtained simulated pattern for the HRTEM image, as shown in Fig. 1(c), again clearly demonstrating the similar properties. The crystallographic directions in the simulated pattern agree with the observed HRTEM image with lattice parameters of a = 12.23 Å, b = 3.04 Å, c = 5.8 Å (α = 90°, β = 103.7°, γ = 90°). The distance between bright lines along wire axis is 6.1 Å in simulated pattern, in good agreement with about 6 Å in the HRTEM image (Fig. 1(b)). The energy dispersive X-ray spectroscopy (EDS) carried out with high-spatial resolution of a field-emission (FE) TEM shows peaks of Ga and O only, again indicating the formation of gallium oxide [4].

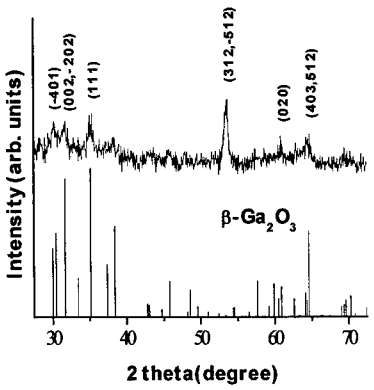


Fig. 2. XRD pattern of β-Ga_2O_3 nanowires and relative XRD intensities from JCPDS card.

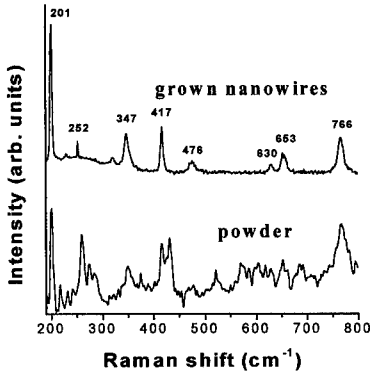


Fig. 3. FT-Raman spectra of β-Ga_2O_3 nanowires and powder.

Figure 2 shows XRD pattern of nanowires. The peak positions are in good agreement with those of monoclinic Ga_2O_3 powder obtained from JCPDS card [6]. However, the relative intensity is different, which may indicate the formation of quantum nanowires. Strong peaks at (312) and (-512) planes are shown in nanowires, whereas the peak at (111) plane shows the highest intensity in Ga_2O_3 powder.

Figure 3 shows FT-Raman spectra of obtained nanowires and monoclinic Ga_2O_3 powder (5N, Aldrich). Several sharp peaks at 252, 321, 347, 476, 630, 653, and 766 cm^{-1} were observed in addition to the previously reported peaks at 201 and 417 cm^{-1} [7]. The peak positions of nanowires are in excellent agreement with those of powders, although the peaks become narrower, indicating good crystallinity. We note that neither GaN nor carbon-related peaks are observed. It can be concluded from these structural analyses that the observed nanowires are monoclinic gallium oxide (β-Ga_2O_3) with [001] direction of nanowire axis.

Although β-Ga_2O_3 nanowires were clearly confirmed from the above analyses, it is still not clear how β-Ga_2O_3 nanowires are formed from GaN powders both energetically and kinetically. Here, we evaluate Gibbs free energy of the reaction. The reaction can be expressed as

$$2GaN + (3/2 + x)O_2(g) \xrightarrow{Ni+Co} Ga_2O_3 + 2\,NO_x(g) \qquad (1)$$

In order for the above reaction to occur, the standard Gibbs free energy ($\Delta G°$) of the reaction should be negative. To calculate the $\Delta G°$ of the reaction, we chose NO gas, i.e., x=1, as a

produced gas, and the estimated reaction temperature of 5000 K [8]. We observed through the window that bluish gases were formed during the reaction, suggesting the formation of NO_x gas. This excludes the possibility of forming N_2 gas. $\Delta G°$ was then estimated by the handbook [9]. The calculated value, $\Delta G° = -620$ KJ/mol, assures that this reaction is energetically favorable. The standard Gibbs free energy varies with temperature. This value becomes maximum (-570 KJ/mol) at 2300 K and decreases with increasing temperature [9]. The reaction temperature in arc discharge is usually greater than 5000 K, again ensuring more preferable reaction to occur. Since nanowires were not formed without transition metals, we believe that transition metals play a crucial role in forming nanowires. Furthermore, even Ga_2O_3 powders were not formed without transition metals, suggesting that transition metals promote catalytically the above reaction in transforming GaN powders into gallium oxides. One may believe that nickel oxide and cobalt oxide can be also formed during the reaction. However, standard Gibbs free energies of the reactions for forming these oxides are positive at arcing temperature [9], excluding the possibility of producing transition metal oxides.

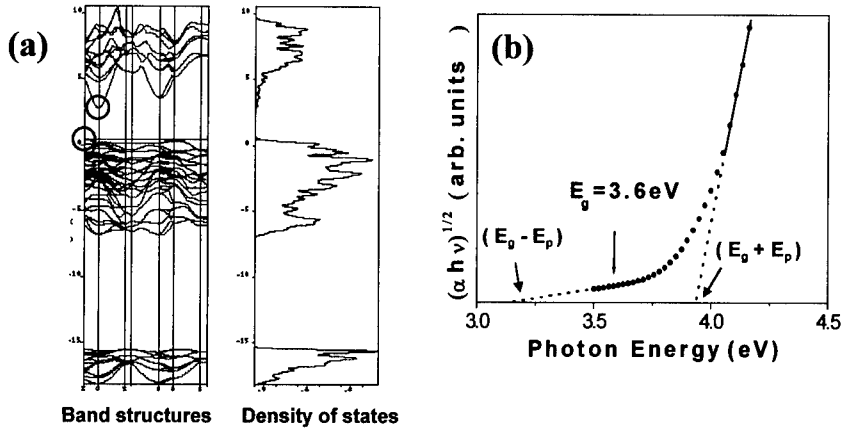


Fig. 4. (a) Calculated band structures and density of states of β-Ga_2O_3. (The circles in band structures indicate indirect band gap), (b) UV absorption spectrum of β-Ga_2O_3 nanowires.

Figure 4(a) shows theoretically calculated band structure and corresponding density of states of β-Ga_2O_3. We performed density-functional calculations based on the local density approximation (LDA) and generalized gradient approximation (GGA) [10]. The ionic potentials are described by a norm-conserving nonlocal pseudopotential generated by Troullier-Martins [11] in a separable form of Kleinman and Bylander [12]. Exchange-correlation functions parameterized by the Perdew-Zunger scheme [13] are used. The energy cutoff for the plane-wave expansion of wavefunctions is 70 Ry, and periodic boundary conditions are applied. Brillouin zone integrations are done using 54 special *k*-points sampling, as suggested by Monkhorst and Pack [14]. Our LDA calculations give indirect band gap Z to G, as shown in Fig. 4(a). The GGA calculations also give indirect band gap. The band gap was 2.35 eV and 2.04 eV, by LDA and GGA method, respectively. It is well-known that LDA and GGA underestimate the band gap.

Figure 4(b) shows UV absorption spectrum of β-Ga_2O_3 nanowires. It has been reported that band gap (E_g) of β-Ga_2O_3 was determined to be about 4 eV from absorption measurement

by assuming direct band gap [15]. If β-Ga_2O_3 has direct band gap, obtained β-Ga_2O_3 nanowires have the band gap of about 4.0 eV, as shown in Fig. 4(b). However, our LDA and GGA calculations demonstrated that β-Ga_2O_3 has an indirect band gap. Thus, E_g was determined by

$$E_g = [(E_g - E_p) + (E_g + E_p)]/2$$

, resulting in the band gap of about 3.6 eV.

CONCLUSION

Monoclinic gallium oxide (β-Ga_2O_3) nanowires were synthesized by dc arc discharge of GaN powders with a small amount of transition metals in a gas mixture of argon and oxygen. The structural analyses showed that the observed nanowires are monoclinic gallium oxide (β-Ga_2O_3) with [001] direction of nanowire axis. LDA and GGA calculations revealed that β-Ga_2O_3 has an indirect band gap. Using UV absorption measurements, the band gap of β-Ga_2O_3 was determined to be about 3.6 eV.

ACKNOWLEDGMENTS

We acknowledge the financial support by the Korea Science and Engineering Foundation through Semiconductor Physics Research Center at Jeonbuk National University.

REFERENCES

1. A. M. Morales and C. M. Lieber, Science **279**, 208 (1998).
2. J. Zhu and S. Fan, J. Mater. Res. **14**, 1175 (1999)
3. S. T. Lee, N. Wang, Y. F. Zhang, and Y. H. Tang, MRS Bulletin **24**, 36 (1999).
4. Y. C. Choi and Y. H. Lee, unpublished.
5. J. –M. Bonard, T. Stora, J. –P. Salvetat, F. Maier, T. Stockli, C. Daschl, L. Forro, W. A. de Heer, and A. Chatelain, Adv. Mater. **9**, 827 (1997).
6. JCPDS card no. 43-1012.
7. H. Z. Zhang, Y. C. Kong, Y. Z. Wang, X. Du, Z. G. Bai, J. J. Wang, D. P. Yu, Y. Ding, Q. L. Hang, S. Q. Feng, Solid State Commun. **109**, 677 (1999).
8. L. C. Qin, D. Zhou, A. R. Krauss, and D. M. Gruen, Appl. Phys. Lett. **72**, 3437 (1998).
9. HSC Chemistry ver. 3.0.
10. We used CASTEP code, a registered software product of Molecular Simulations Inc.
11. N. Troullier and J. L. Martins, Phys. Rev. B **43**, 1993 (1991).
12. L. Kleinman and D. M. Bylander, Phys. Rev. Lett. **48**, 1425 (1982).
13. J. P. Perdew and A. Zunger, Phys. Rev. B **23**, 5048 (1981).
14. H. J. Monkhorst and J. D. Pack, Phys. Rev. B **13**, 5188 (1976).
15. H. –G. Kim and W. –T. Kim, J. Appl. Phys. **62**, 2000 (1987).

STRUCTURAL, MAGNETIC PROPERTIES OF THE ELECTROCHEMICALLY DEPOSITED ARRAYS OF NICKEL NANOWIRES

H.R. KHAN AND K. PETRIKOWSKI
FEM, Materials Physics Department, 73525 Schwaebisch Gmuend, Germany

ABSTRACT

The room temperature structural, magnetization and magnetoresistive properties of Ni-nanowires of diameters 18, 30 and 78 nm and various lengths, fabricated by electrochemical deposition of Ni in the nanopores of anodic alumina, are investigated. The crystallographic orientation depends on the diameter of nanowires. Nanowires show perpendicular magnetic anisotropy and enhanced coercivity (H_c) and remanent magnetization (M_r) values of up to 500 Oe and 50% respectively. An electrodeposited Ni-layer (5 μm) on copper substrate shows in plane magnetic anisotropy and the H_c and M_r values are 97 Oe and 37%. Ni-nanowires and Ni–layer show an anisotropic magnetoresistive behaviour.

INTRODUCTION

Arrays of small magnetic particles show different magnetic interactions and anisotropies compared to the bulk state. The magnetic properties depend on the size and shape of these nanostructured arrays [1 - 5]. Arrays of discs and nanowires that are few tens of nanometers in diameter may be fabricated by several methods. In the template method, metallic nanowires are produced inside the voids of nanoporous nonconducting host materials [6 - 9]. The other method uses the lithographic techniques [10 – 12]. Fabrication of nickel and cobalt nanowires by electrochemical deposition of metals into templates with nanometer sized pores prepared by nuclear track etching of polycarbonates was reported [9]. These nanowires show perpendicular magnetic anisotropy (magnetization perpendicular to the substrate and parallel to the axis of nanowires) and enhanced coercivity (H_c) and remanent magnetization (M_r). The shape anisotropy compels the magnetization to be along the axial direction of the nanowires and is a consequence of the geometry of the nanowire arrays. A porous aluminum oxide (anodic alumina) layer is formed when the aluminum metal is electrochemically oxidized in the acid electrolytes e.g. sulphuric, chromic and phosphoric acids. The pores in the anodic alumina are quite uniform, parallel and open only at the oxide-electrolyte interface. Metal can be electrochemically deposited into the pores by transferring the preanodized aluminum to an appropriate electrolyte followed by a.c. electrolysis. As the electrodeposition continues, metal fills the pores from the bottom upwards. Metal nanowires can be fabricated in this manner with different lengths and diameters. Arrays of ferromagnetic nanowires fabricated in this way also show perpendicular magnetic anisotropy and enhanced H_c and M_r values depending on the diameter, length and packing density of the ferromagnetic nanostuctures [7]. Earlier we reported the fabrication of cobalt and permalloy nanowires by electrodeposition into the pores of anodic alumina and their structural, magnetic and magnetoresistive properties [13, 14]. These nanowires are of potential applications in the high density perpendicular recording media [15 - 17] and microsensors such as reading head or high sensitivity magnetic field sensors based on the magnetoresistive properties.

In this paper we report the fabrication of Ni-nanowires of diameters 18, 30 and 78 nm and different lengths by anodic oxidation of (Al-1%Mg) substrate and then electrodepositing the nickel into the pores by a.c. electrolysis. The morphological, structural, magnetic and

Mat. Res. Soc. Symp. Proc. Vol. 581 © 2000 Materials Research Society

magnetoresistive properties as a function of the diameter and length of the nanowires are investigated and compared with an electroplated continuous nickel layer of 5 μm thickness on copper substrate and 25 nm crystallite size.

EXPERIMENTAL DETAILS

The fabrication of the Ni-nanowires consists of two step process: First anodic alumina of different pore diameters is obtained by electrochemically oxidizing an (Al-1% Mg) substrate in electrolytes at different temperatures and potentials e.g. A: Pores of 18 nm diameter: 7 wt.% H_2SO_4 electrolyte, 25 V and 0°C; B: Pores of 30 nm diameter: 10 wt.% H_3PO_4, 30 V and 30°C; C: Pores of 78 nm diameter: 3wt.% CrO_3, 40 V and 40°C. The pore morphology was checked by scanning electron microscopy.

Table I: Anodic oxidation of (Al-1% Mg) in various electrolytes and the pore characteristics

	Electrolyte	Pore diameter (nm)	Inter-pore distance (nm)	Wall thickness (nm)	Pore density/cm^2
1.	7 wt.% H_2SO_4; 25 V; 0°C	18	42	30	7.5×10^{10}
2.	10 wt.% H_3PO_4; 30 V; 30°C	30	46	19	6.5×10^{10}
3.	3 wt.% CrO_3; 40 V; 40°C	78	89	15	2×10^{10}

The nickel nanowires of different diameters and lengths were deposited into the pores of anodic alumina using a sulphate bath (112 g/l $NiSO_4 \cdot 6H_2O$ + 40 g/l H_3BO_3) with a pH value of 3.9 at 50°C temperature using an a.c. voltage (20 – 40 V; 50 Hz). A Ni layer of 5 μm was also deposited on a copper substrate using the same electrolyte and a current density of 10 mA/cm^2. The crystallographic structure and texture of the Ni-nanowires and layer were checked by X-ray diffraction technique using CuK_α-radiation. The crystallite size of the Ni layer was determined using the Scherrer formula: $0.9*\lambda / \beta * \cos\theta$ [18] (β is the full width at half maximum of a (θ – 2θ) diffraction line of Bragg angle θ and λ is the wave length of the CuK_α-radiation). The magnetization measurements were made at room temperature using a vibration magnetometer. The magnetoresistive measurements were made by two point technique by applying magnetic field parallel and perpendicular to the substrate plane.

RESULTS AND DISCUSSION

Fig. 1 shows the SEM-images of anodized (Al-1% Mg) substrate using different electrolytes. The pore characteristics are listed in table I. The wall thickness decreases with increasing pore diameter. Fig. 2 shows the (θ – 2θ) X-ray diffractograms of Ni-layer (5μm) on a copper substrate and the Ni-nanowires of diameters 18, 30 and 78 nm in the pores of anodic alumina. A crystallographic preferred orientation of <200> and <220> is observed in the Ni-layer of f.c.c. structure. The Ni crystallite size estimated from the Scherrer formula is ~ 25 nm. The Ni-nanowires of 18 nm diameter show only <220> crystallographic orientation, where as the 30 nm and 78 nm diameter nanowires show both <200> and <220> crystallographic preferred orientations similar to the Ni-layer but with different intensities. This shows that the

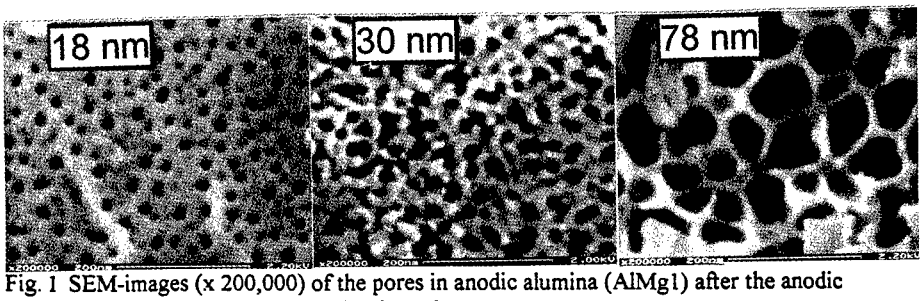


Fig. 1 SEM-images (x 200,000) of the pores in anodic alumina (AlMg1) after the anodic oxidation by H_2SO_4, CrO_3 and H_3PO_4 electrolytes

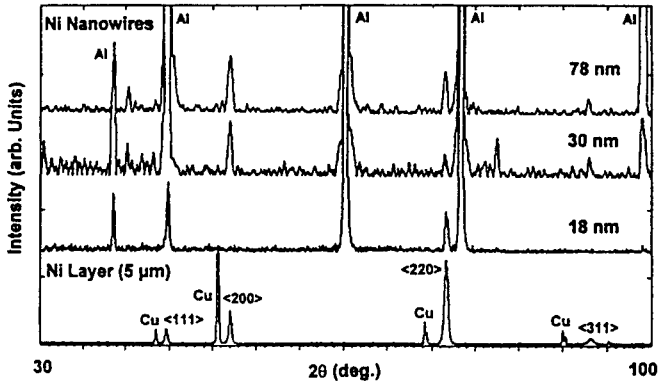


Fig. 2 (θ - 2θ) Bragg-Brentano X-ray diffraction patterns of Ni layer of 5 μm thickness on Cu substrate and Ni nanowires of diameters: 18, 30 and 78 nm

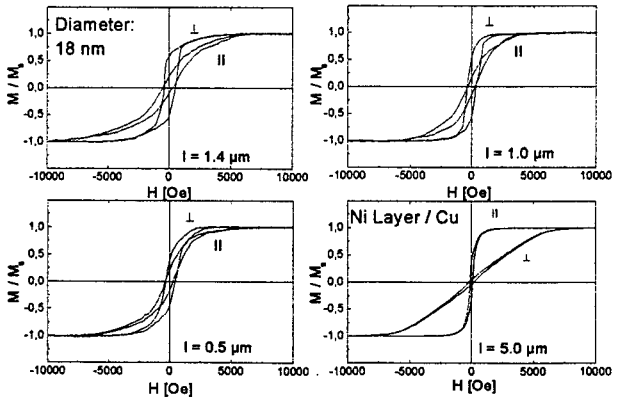


Fig. 3 Hysteresis loops of Ni layer (5 μm) and Ni nanowires of diameter 18 nm and length: 0.5, 1.0 and 1.4 μm with H parallel and perpendicular to substrate plane

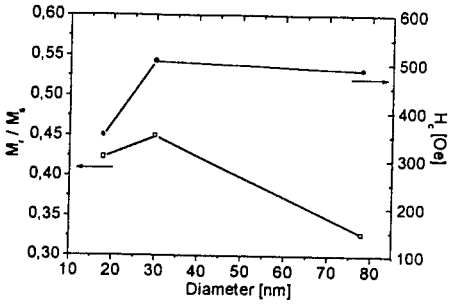


Fig. 4 Variation of the (M_r/M_s) ratio and coercivity H_c with the diameter of Ni nanowires

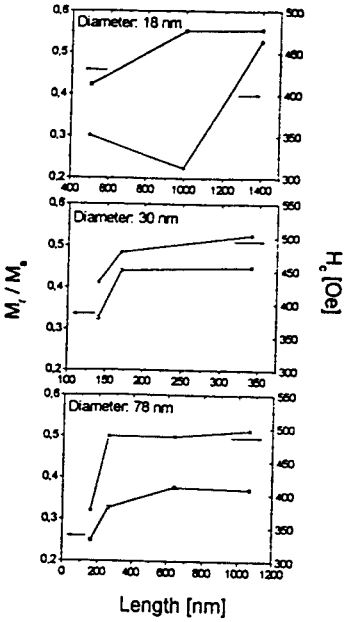


Fig. 5 (M_r/M_s) as a function of the length of the Ni nanowires of 18, 30 and 78 nm diameters

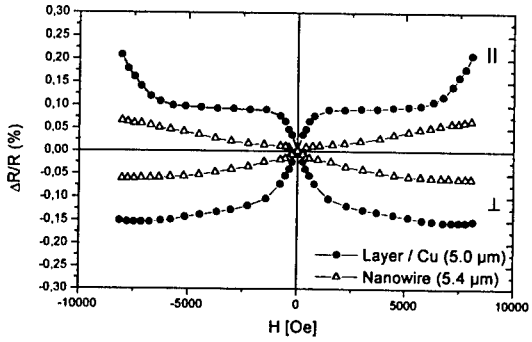


Fig. 6 Room temperature magnetoresistance curves of Ni layer (5 μm) and Ni nanowires with magnetic field parallel and perpendicular to the current flow

nanowires of diameter larger than 18 nm do not have a single orientation perpendicular to the substrate.

The magnetization hysteresis loops of the Ni-layer and nanowires of 18 nm diameter and different lengths with magnetic field parallel and perpendicular to the substrate plane taken at room temperature are shown in Fig. 3. The easy axis of magnetization of Ni-layer is parallel to the surface (parallel to the substrate) and the H_c and M_r/M_s (squareness) values are 97 Oe and 0.37 respectively. The easy axis of magnetization of Ni-nanowires is parallel to the axis of the nanowires. The values of H_c and M_r/M_s are enhanced compared to the Ni-layer and vary with the length e.g. between 0.5 and 1.4 μm.

Magnetization hysteresis loops of Ni-nanowires of 30 and 78 nm diameters and different lengths were also taken at room temperature. Fig. 4 shows the plot of H_c and M_r/M_s as a function of diameter of a nanowire of length 0.3 μm. Maximum H_c and M_r/M_s values of 500 Oe and 0.45 are observed for the nanowires of 30 nm diameter. The lower values of H_c of the 18 nm diameter nanowires may be due to the imperfections in the nanostructure formation [9]. An enhancement of coercivity with decreasing wire diameter is expected. Because larger diameter facilitates the formation of multidomain structure and degradation of coercivity. The dependence of H_c and M_r/M_s on the length of the nanowires of diameters 18, 30 and 78 nm is shown in Fig. 5. In general the H_c and M_r/M_s values increase with increasing length of the nanowires except an anomaly is observed in the case of nanowires of 18 nm diameter.

Fig. 6 shows the magnetoresistance (MR%), $\Delta R/R(0)\% = [R(H) - R(0)] / R(0) * 100$ where R(H) and R(0) are the resistances of the nanowires in magnetic field H and without field as a function of magnetic field applied parallel and perpendicular to the axis of the wires and current flow. These nanowires show an anisotropic magnetoresistance behaviour similar to the Ni-layer.

CONCLUSIONS

In summary we have fabricated the Ni-nanowires of different diameters and lengths. The effect of the diameter and length on the H_c and M_r/M_S is investigated. And an enhancement of H_c and M_r/M_s in the nanowires of Ni compared to the Ni-layer is observed. Ni-nanowires show an anisotropic magnetoresistance behaviour similar to the Ni-layer. The value of H_c and M_r/M_s depend on the diameter and length of the nanowires.

ACKNOWLEDGEMENTS

This work was supported by the „Bundesministerium for Wirtschaft through Arbeitsgemeinschaft industrieller Forschungsvereinigungen Otto von Guericke e.V.""and grant no (AIF 11429 N). We are thankful to H. Labitzke (Abt.: Prof.Dr. F. Aldinger, MPI for Metallforschung, Stuttgart) for SEM images. The technical assistance of A. Weiler is gratefully acknowledged.

REFERENCES

1. G.A. Gibson, J.F. Smyth and S. Schultz, IEEE Trans. Magn. 27 (1991) 5787

2. M.S. Wei and S.Y. Chou, J. Appl. Phys. 76 (1994) 6679

3. R.M.H. New, R.F.W. Pease and R.L. White, J. Vac. Sci. Technol. 12 (1994) 3196

4. A.D. Kent, S. von Molnar, S. Gider and D.D. Awschalom, J. Appl. Phys. 76 (1994) 6656

5. J.F. Smyth, S. Schultz, D. Kern, H. Schmid and D. Yee, J. Appl. Phys. 63 (1988) 4237

6. J.C. Lodder and L. Cheng-Zhang, IEEE Trans. Magn. 25 (1989) 4171

7. K.I. Arai, K. Ishiyama, Y. Ohoka and H.W. Kang, J. Magn. Soc. Jpn. 13 (1989) 789

8. D. Al Mawlawi, N. Coombs and M. Moskovits, J. Appl. Phys. 70 (1991) 4421

9. T.M. Whitney, J.S. Jiang, P.C. Searson and C.L. Chien, Science 261 (1993) 1316

10. K. Hong and N. Giordano, Phys. Rev. B 51 (1995) 9855

11. S.J. Blundell, C. Shearwood, M. Gester, M.J. Baird, J.A.C. Bland and H. Ahmed, J. Magn. Magn. Mater. 135 (1994) L17

12. A. Maeda, M. Kume, T. Ogura, K. Kuroki, T. Yamada, M. Nishikawa and Y. Harada, J. Appl. Phys. 76 (1994) 6667

13. H.R. Khan, O. Loebich and G. Rauscher, Thin Solid Films 275 (1996) 207-209

14. H.R. Khan and K. Petrikowski, J. Magn. Magn. Mater. (In Press)

15. S. Iwasaki and K. Ouchi, IEEE Trans. Magn. MAG-13 (1977) 1272

16. M. Shiraki, Y. Wakui, T. Tokashima, N. Tsuya, Trans. Magn. MAG-21 (1985) 1465

17. N. Tsuya, T. Tokashima, M. Shiraki, Y. Wakui, Y. Saito, H. Nakamura and Y. Harada, IEEE Trans. Magn. MAG-24 (1988) 2661

18. P. Scherrer, Nachr. Göttinger Gesell., vol. 98, Zwigmondys, Kolloidchemie, 3rd edn., 1918, 394

Mechanical Milling and Other Techniques for Alloys

NANOCOMPOSITES IN THE SYSTEMS $Fe_{1-x}O$-Fe_3O_4 and MgO-$MgFe_2O_4$ PRODUCED BY MECHANICAL ALLOYING

A. HUERTA[1], H. A. CALDERON[1], H. YEE-MADEIRA[1], M. UMEMOTO[2], K. TSUCHIYA[2]
[1]Instituto Politécnico Nacional, UPALM Ed. 9, Zacatenco, 07300 MEXICO. hcalder@esfm.ipn.mx
[2]Toyohashi University of Technology, Tenpaku-cho, Toyohashi, Aichi, JAPAN

ABSTRACT

Wüstite-magnetite and magnesia-magnesioferrite nanocrystalline ceramics have been prepared by mechanical milling and spark plasma sintering. As-milled powders have a nanocrystalline structure in both systems. Low energy milling gives rise to an increasingly higher volume fraction of wüstite as a function of milling time in the $Fe_{1-x}O$-Fe_3O_4 system. Similar results are obtained in the MgO-$MgFe_2O_4$ system with increasingly larger amounts of $MgFe_2O_4$ produced by milling. Composites of magnetic particles (Fe_3O_4 or $MgFe_2O_4$) in a nonconductive matrix (FeO or MgO, respectively) are found in the sintered samples. Measurement of magnetic properties can be used to determine conclusively the nature of the developed phases and the effect of grain size.

INTRODUCTION

Oxide ceramics are under intense investigation for their technological advantages in magnetization, dielectric response and chemical stability in such diverse applications as magnetic recording media, induction cores and microwave resonant circuits [1]. Several researchers have mixed iron oxides with other ceramics as MgO, NiO, and ZnO to improve mechanical and magnetic properties [2-5]. In such systems, the matrix (NaCl-type structure) is paramagnetic and the magnetism is provided by precipitation of a second phase with spinel structure. Groves and Fine [4] have shown that precipitation of coherent particles in a NaCl-structure matrix can occur merely by rearrangement of the concentration of cations and the interstitial–site occupancy. This transformation produces octahedral precipitates. However, clear evidence regarding the phase transformation mechanism in oxide ceramics is rather scarce. Groves and Fine produced their specimens by diffusing Fe into a solid MgO matrix. The present investigation is carried out in order to produce and characterize nanocomposites in the systems $Fe_{1-x}O$-Fe_3O_4 and MgO-$MgFe_2O_4$. The combination of a nonconductive matrix and magnetic particles is interesting due to the expected magnetic and physical properties. The spatial and size distribution of precipitates is expected to affect the nanocomposite properties. In addition, the expected effect of the nanosize grains needs to be documented in order to study the relationship between nanostructure and magnetic and physical properties in oxide ceramics.

EXPERIMENTAL PROCEDURE

Powders of $Fe_{1-x}O$-Fe_3O_4 were produced by the mechanochemical reaction of Fe_3O_4+C, Fe_3O_4+Fe, pure Fe_3O_4, Fe_2O_3+Fe and pure Fe_2O_3 powders. The materials in the system MgO-$MgFe_2O_4$ were obtained by milling MgO and Fe_2O_3. Low and high energy ball mills were used (horizontal and planetary mills, respectively). All powder handling was performed in an Ar-filled glove box with an oxygen content below 0.01 ppm. Table 1 gives the nominal composition of the prepared samples. The consolidation was performed by spark plasma sintering. Cylindrical sintered samples of approximately 18 mm and 13 mm in diameter were produced by sintering at high temperature (873-1273 K) and low pressure (50 MPa) with a carbon die and, at low temperature (673-773 K) and high-pressure (100 MPa) with an inconel die. Characterization is made

Mat. Res. Soc. Symp. Proc. Vol. 581 © 2000 Materials Research Society

by X-Ray diffraction (XRD), Mössbauer spectroscopy (MöS, Co_{60} source), transmission electron microscopy (TEM) and measurement of magnetic properties by means of a vibrating sample magnetometer (VSM).

TABLE 1. CHEMICAL COMPOSITION OF MILLED POWDERS

Wüstite-Magnetite System		Magnesia-Magnesioferrite System	
Identification	Added Powders	Identification	Added Powders
Fe_3O_4 + C	Fe_3O_4-3 wt.% C	MgO-0.5 cat.% Fe	MgO-1 wt.% Fe_2O_3
Fe_3O_4 + Fe	Fe_3O_4-12 wt.% Fe	MgO-1 cat.% Fe	MgO-2 wt.% Fe_2O_3
Fe_3O_4	Fe_3O_4	MgO-4 cat.% Fe	MgO-7.6wt.% Fe_2O_3
Fe_2O_3 + Fe	Fe_2O_3-15 wt.% Fe	MgO-10 cat.% Fe	MgO-18 wt.% Fe_2O_3
Fe_2O_3	Fe_2O_3	MgO-20 cat.% Fe	MgO-33 wt.% Fe_2O_3

RESULTS AND DISCUSSION

Figure 1 shows examples of XRD patterns of as-milled powders in the wüstite-magnetite system. The microstructural evolution of the powders after different milling times (horizontal mill) is shown in this figure for two samples i. e., Fe_3O_4+Fe (Fig. 1a) and pure Fe_3O_4 (Fig. 1b). The angular positions corresponding to the pure phases are also indicated. In both cases, development of broad peaks in the neighborhood of the angular positions for $Fe_{1-x}O$ is observed. Some of the diffraction maxima coincide also with positions expected for Fe_3O_4. However, the longer the milling time, the better is the match to the Fe_xO peaks. The peak positions of the as-milled powders are slightly different to those of pure wüstite. Such difference can be interpreted as the formation of a wüstite phase poor in iron.

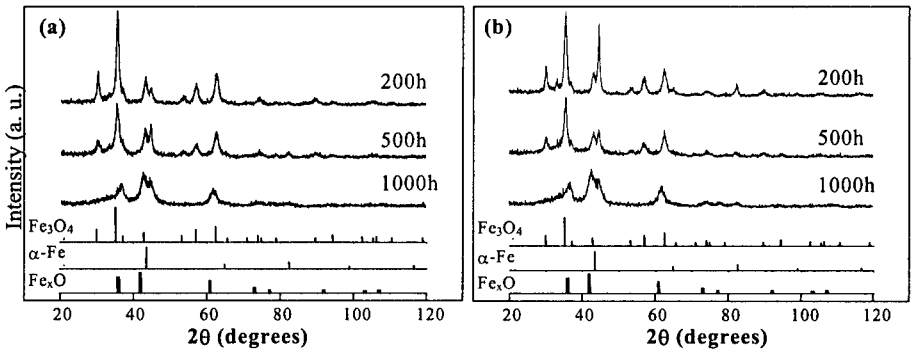


Fig. 1. XRD patterns after mechanical milling. (a) Fe_3O_4+Fe sample. (b) Fe_3O_4 sample.

Mössbauer spectroscopy is a technique that allows identification of the nature of iron phases. Fig. 2 shows an example of MöS spectra of a pure Fe_3O_4 sample milled for 500 h and 1000 h. They consist of two separate sextets (magnetic effect) and one doublet (paramagnetic effect). Magnetite has a spinel (AB_2O_4) structure and it can also be written as $Fe^{3+}[Fe^{2+}Fe^{3+}]O_4$. The A ions have a regular tetrahedral coordination in the oxygen lattice and the B ions are coordinated octahedrically. The internal sextet (*ii*) is due to Fe ions at tetrahedral sites (A-type) and the external one (*i*) is due to Fe ions at octahedral sites (B-type). Wüstite has a NaCl structure with cation vacancies and the appropriate proportion of Fe^{3+} to balance the charge. The doublet (*iii*) is due to the Fe^{2+} on tetrahedral sites which exchange with Fe^{3+} on octahedral sites. The asymmetry of the doublet (see arrows) is related to the Fe^{3+} content. The spectra exhibit a magnetic relaxation as a

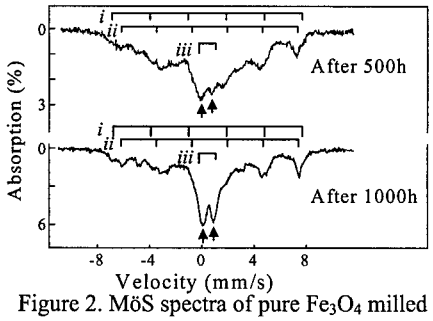


Figure 2. MöS spectra of pure Fe_3O_4 milled 500 and 1000 h.

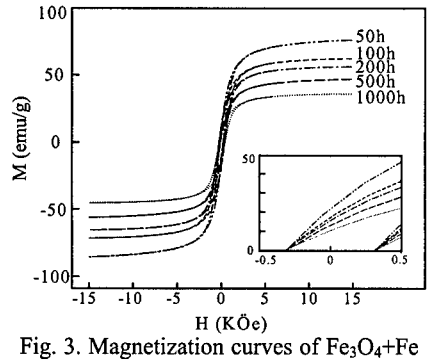


Fig. 3. Magnetization curves of Fe_3O_4+Fe after mechanical milling.

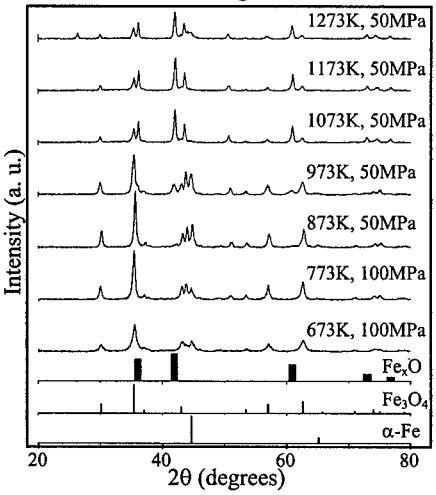


Fig. 4. XRD results of pure Fe_3O_4 milled 500 h after sintering.

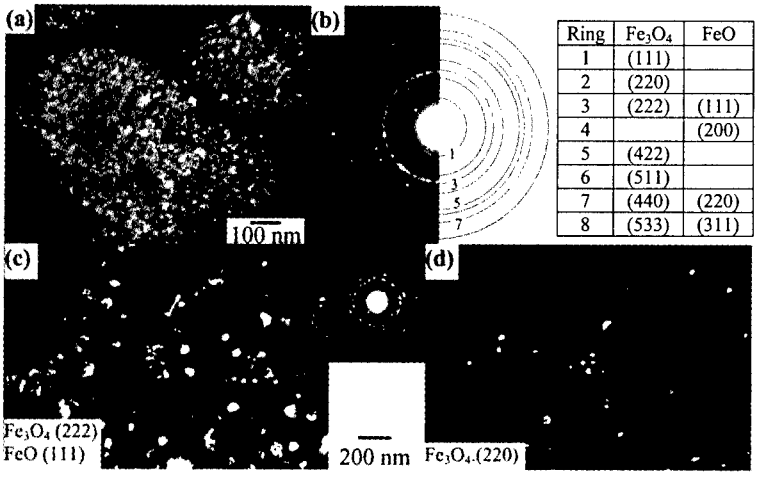
function of the milling time i. e., the intensity of the doublet (wüstite phase) is higher for the sample milled for 1000 h. Thus only two phases can be identified: magnetite and wüstite. The amount of $Fe_{1-x}O$ increases with longer milling times. In addition, the spectra show a strong absorption asymmetry which can be related to disordered phases or nanosized grains.

Figure 3 shows magnetization curves of Fe_3O_4 + Fe powders after 50, 100, 200, 500 and 1000 h of milling. The saturation magnetization (M_s) at 15 KÖe decreases as a function of milling time. This behavior can be explained by the transformation of magnetic phases into non-magnetic phases i.e., magnetite and/or Fe to wüstite. The formation of this paramagnetic phase produces a reduction of M_s. However it is important to notice that 1000 h of low energy milling are insufficient to promote a full transformation to wüstite.

Figure 4 shows representative XRD results of the sintered samples. The pattern corresponds to pure Fe_3O_4 milled for 500 h and sintered under different conditions. The angular positions for the pure phases are also indicated. The diffractograms show the formation of wüstite with low amounts of magnetite in all cases. Higher sintering temperatures promote higher amounts of magnetite as shown by the stronger intensities of the corresponding diffraction peaks. Lower sintering temperatures essentially preserve the powder microstructure with larger volume fractions of non-equilibrium wüstite (angular positions of the peaks). The recorded broad peaks indicate that the nanosized grains of the powders are retained.

Figure 5 shows the microstructure of both as-milled powders and sintered samples in TEM. Fig. 5a shows nanosized grains in a sample of Fe_3O_4 +Fe milled 500 h. The average grain size is smaller than 20 nm. The corresponding electron diffraction pattern (Fig. 5b) shows reflections probably belonging to wüstite and magnetite. However, this technique does not allow to register small displacements of the intensity maxima with precision and it is used only for viewing the grain size dimensions. Figs. 5 c-d are dark field images (same area) of pure Fe_3O_4 milled 1000 h and sintered at 1073 K. Sintering at this temperature (as discussed above) produces mostly equilibrium phases. Fig. 5c corresponds to the overlapping

reflections (222) magnetite and (111) of wüstite while Fig. 5d is obtained with the (220) reflection of magnetite. Thus nanocrystalline grains can be seen in the specimen, some of them corresponding to magnetite (Fig. 5d) with a random spatial distribution. An average grain size of 150±70 nm has been evaluated from this and similar TEM images. The grain size obtained after sintering depends on the processing temperature. For example powders milled for 1000 h produce an average size of 230±120 nm for a sample sintered at 1173 K while a value of 150±70 nm is found after sintering at 1073 K. In general sintering below 1073 K allows retention of the nanocrystalline grain structure.



Ring	Fe_3O_4	FeO
1	(111)	
2	(220)	
3	(222)	(111)
4		(200)
5	(422)	
6	(511)	
7	(440)	(220)
8	(533)	(311)

Fig. 5. (a) Fe_3O_4+Fe milled 500 h; (b) Diffraction pattern of (a); (c) Fe_3O_4 milled 1000 h and sintered at 1073 K, DF-TEM image using the overlapping reflections (222) Fe_3O_4 and (111) FeO; mostly FeO grains are seen; (d) Same as (c) but using the reflection (220) Fe_3O_4. Only Fe_3O_4 grains are seen.

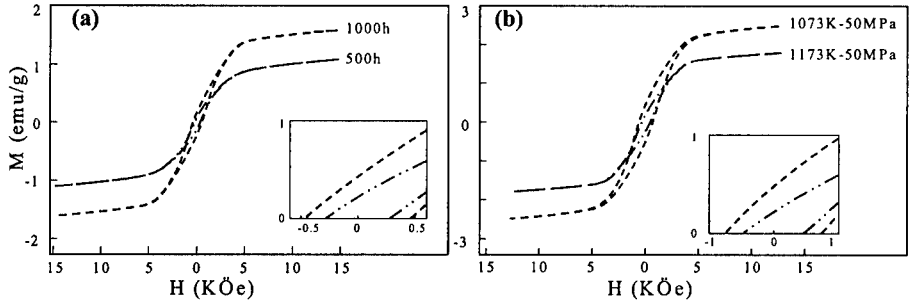


Fig. 6. Magnetization curves of sintered samples. (a) Pure Fe_3O_4 milled 500 h and 1000 h and sintered at 1173 K. (b) Pure Fe_3O_4 milled 1000 h and sintered at 1073 and 1173 K.

Figure 6 shows representative measurements of magnetic properties in sintered samples. Fig. 6a shows results corresponding to pure Fe_3O_4 milled for different periods of time (500 and 1000 h) and sintered at 1173 K. The higher M_s value of the sample milled for 1000 h can be due to two effects i. e., smaller magnetic domain size and higher volume fraction of magnetite. As shown above longer milling times promote the formation of larger amounts of wüstite. On the other hand a larger coercivity can be expected for smaller magnetic particle sizes. Thus Fig. 6a strongly

suggests that a finer distribution of magnetic particles has been achieved in the sample milled for 1000 h and sintered at 1173 K. Fig. 6b shows results of two samples sintered at two different temperatures, 1073 and 1173 K. Both samples were produced from pure Fe_3O_4 milled for 1000 h. A higher magnetization is found for the sample sintered at lower temperature with an important increment of the coercitivity. This can again be explained as a consequence of the nanostructure obtained i. e., smaller grain size. Therefore it is possible to control the magnetic behavior by controlling the milling time and the sintering temperature.

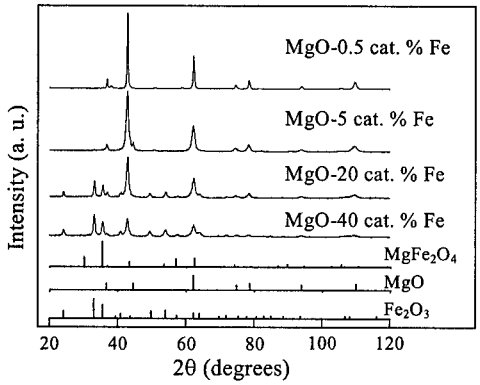


Fig. 7. XRD patterns after mechanical milling (500 h) of $MgO+Fe_2O_3$ in a planetary mill.

Some representative results are given for the $MgO-MgFe_2O_4$ system. Fig. 7 shows XRD patterns of powders milled 500 h with different nominal compositions in a planetary mill. Low amounts of Fe_2O_3 can be apparently dissolved into the MgO lattice. Such a reaction produces a distortion of the MgO lattice which accounts for the small displacement of the diffraction maxima. Samples with higher Fe_2O_3 contents show still some reflections corresponding to this compound but also displaced MgO and $MgFe_2O_4$ peaks. It is likely that the MgO lattice saturates with Fe and the microstructure is formed by $Mg_{1-x}Fe_xO$ (magnesiowüstite), $MgFe_2O_4$ and retained Fe_2O_3 in these cases.

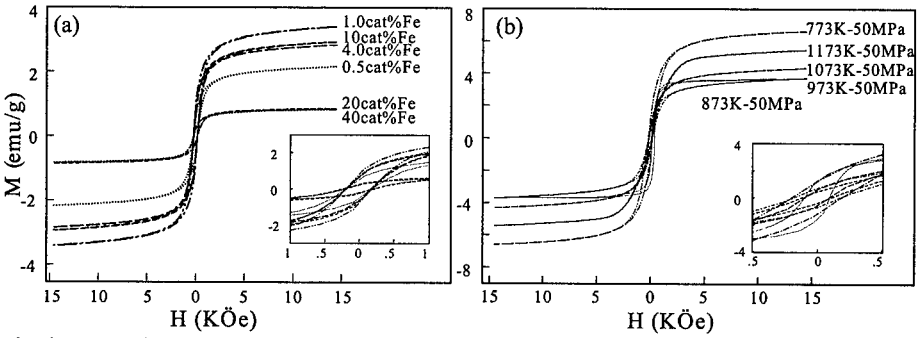
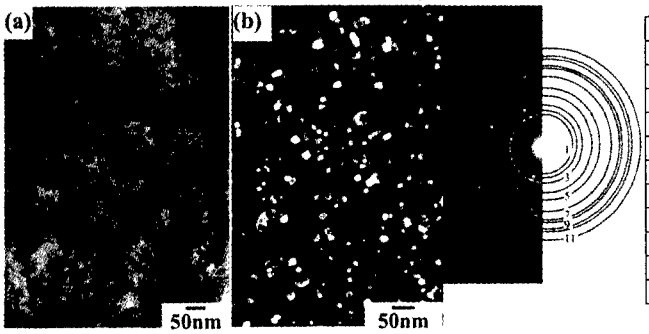


Fig. 8. Magnetization curves of $MgO-MgFe_2O_4$ system. (a) $MgO-Fe_2O_3$ milled 500 h in a planetary mill. (b) MgO-40 cat.% Fe sintered at different temperatures.

Figure 8 shows the measurement of magnetic properties of as-milled powders (Fig. 8a) and sintered samples (Fig. 8b) of the $MgO-MgFe_2O_4$ system. There is a magnetic response in the as-milled powders which indicates the formation of a new magnetic phase during milling (Fig. 8a). The most likely in this case is $MgFe_2O_4$ as suggested by XRD too. Nevertheless the magnetic response of the as-milled powders cannot be directly related to the nominal Fe or Fe_2O_3 content. Fig. 8a shows higher values of M_s for mixtures with intermediate Fe or Fe_2O_3 contents e.g. 1, 4 and 10 cat.% Fe. This can be related to the efficiency of mixing during mechanical milling. Large amounts of Fe_2O_3 require higher milling energies to combine with MgO, thus relatively larger amounts of paramagnetic MgO and Fe_2O_3 are retained. In the case of the sample containing 0.5 cat.% Fe, the milling produces most likely a total combination of the original oxides but the total

amount of magnetic phase is low and the magnetic response becomes correspondingly modest. The insert in Fig. 8a shows an enlargement of the central section of the hysteresis loops. It can be seen that the coercitivity changes only for the samples with larger Fe_2O_3 contents and thus a smaller grain size can be expected. On the other hand, Fig. 8b shows that higher values of M_s are recorded in sintered samples and also that the sintering temperature has a definite influence on the magnetic response. Apparently there is a temperature range (around 773 K) that favors the formation of magnetic phases (most likely $MgFe_2O_4$). Higher temperatures promote the formation of paramagnetic phases such as $Mg_{1-x}Fe_xO$. The formation of $Mg_{1-x}Fe_xO$ cannot be considered deleterious since exsolution of $MgFe_2O_4$ from this phase, is thermodynamically possible.

Figure 9 shows TEM images of MgO-40 cat.% Fe milled 500 h and sintered at 873 K. The diffraction pattern shows reflections belonging to $MgFe_2O_4$ and $Mg_{1-x}Fe_xO$ as given in the inserted table. The bright field image (Fig. 9a) shows particles with a cuboidal shape, that correspond to the magnetic phase $MgFe_2O_4$. The dark field image (Fig. 9b) shows more clearly the cuboidal particle morphology. This image is obtained with a (311) reflection which in principle overlaps with a (111) reflection of magnesiowüstite. The contrast is larger for the particles but some $Mg_{1-x}Fe_xO$ grains (irregular shapes) can also be seen. Additionally, Fig. 9 also shows that the sintered material has a nanocrystalline grain size.



Ring	$MgFe_2O_4$	$Mg_{1-x}Fe_xO$
1	220	
2	331, 222	111
3	400	200
4	422	
5	511,440	220
6	620	311
7	533	222
8	642	
9	731	
10	800	
11	822	

Fig. 9. TEM images of MgO-40 cat.% Fe milled 500 h and sintered at 1073 K. (a) Bright field image. (b) Dark field image from $MgFe_2O_4$ (331) reflection adn $Mg_{1-x}Fe_xO$ (111).

Concluding Remarks

Nanocrystalline materials of FeO-Fe_3O_4 and MgO-$MgFe_2O_4$ can be produced by mechanical milling and powder sintering techniques. The microstructure consists of nanocrystalline grains with a homogeneous spatial distribution of magnetic particles in an insulating matrix. The microstructure is very sensitive to the processing variables. Magnetic properties are very sensitive to the nature of phases and to the grain size.

Acknowledgments

AHR wishes to acknowledge financial support from CONACYT and TUT. HAC and HYM acknowledges support from CONACYT (Project 28925 U) and COFFA-IPN.

REFERENCES

1. I. Yamaguchi, T. Manabe, T. Kumagai, W. Kondo and S. Mizuta, J. Mater. Res. **13**, 935 (1998).
2. F. C. Voogt, T. T. Palstra, L. Niesen, O. C. Rogojanu, M. A. James and T. Hibma, Phys. Rev. B **57**, R8107 (1998).
3. M. E. Fine. *Advances in Materials Research 4*, (John Wiley & Sons, Inc., 1970), p. 1.
4. G. W. Groves and M. E. Fine. J. Appl. Phys. **35**, 3587 (1964).
5. A. Recnik, D. L. Carroll K. A. Rühle J. Mater. Res. **12**, 2143 (1997).

MAGNETIC HARDENING OF MECHANICHALLY ALLOYED $SmFe_{11-x}Co_xTi$

L. BESSAIS and C. DJEGA-MARIADASSOU
CNRS, LCMTR UPR 209, 94320 Thiais, France. bessais@glvt-cnrs.fr

ABSTRACT

Mechanical alloying of ternary $SmFe_{11-x}Co_xTi$ (x = 0, 0.5, 1, 1.5, 2) alloys was carried out under an Ar atmosphere. Milled samples were annealed for 30 min in a vacuum at different temperatures T_a from 650 °C to 1150 °C. The effects of heat treatment, on structure and magnetic property changes, have been investigated by means of x-ray diffraction using the Rietveld method, Mössbauer spectroscopy and differential sample magnetometer. Tetragonal $ThMn_{12}$-type structure is observed for samples annealed at T_a> 900 °C. For 650<T_a<800 °C the $TbCu_7$ type phase was identified as the major phase. Between these two regions a mixture of $TbCu_7$ and $ThMn_{12}$-type nanocrystalline phases is obtained with a maximum of the coercive field H_C (H_C > 5kOe). The Mössbauer spectra relative to the hexagonal phase show sextuplets broadened by the statistical occupancies of the iron sites. An enhancement of the magnetic properties results from the Co substitution.

INTRODUCTION

Magnetic nanoparticles receive significant attention due to their novel magnetic properties and potential technological applications. Rare earth transition metal intermetallic compounds with magnetocrystalline anisotropy are suitable systems for the study of the finite size effects. Mechanical processing have been successfully used in the synthesis of numerous nanosized material. Due to the induced plastic deformation high energy ball milling may result in solid state alloying producing in situ metastable structure but, depending on the thermodynamic of the system, the inter-diffusion reaction to form alloy needs, often, a further heat treatment.

In this paper we will investigate the effect of thermal treatment and Co substitution for Fe, on the coercivity of tetragonal $SmFe_{11}Ti$ semi-hard nanocrystalline alloy, obtained after mechanical milling and subsequent annealing of elemental powders. After the structural study which gives information about the phase transformations, diffraction domain size, lattice stress and nature of minor phases, the recurrent coercivity will be presented. Curie temperature and mean hyperfine field evolution will attest for the pertinence of the Fe substitution. The study of the $SmFe_{11-x}Co_xTi$ series has been limited up to x = 2 where the easy direction of magnetization of the tetragonal phase remains axial [1].

EXPERIMENT

Five alloys of nominal composition $SmFe_{11-x}Co_xTi$ (x = 0, 0.5, 1, 1.5, 2) were prepared. Elemental 40 mesh powders of Sm, Ti, Fe and Co 99.9% were milled in steel vials hermetically sealed in an argon filled glove box with O_2 and H_2O rate of 1ppm. The high energy ball milling process was performed in a Fritsch planetary ball mill (Pulverisette P7) with five steel balls of 15mm during 5h. The speed rotation of the vial was 1500tr/min and the disk rotation speed was 750tr/min. Powder were subsequently heat treated for 30min at temperature between 650 °C and 1150 °C. Atomic emission spectroscopy (AES) was used to check the overall alloy composition of all samples. Energy dispersed x-ray spectrometry (EDX) with equipment LINK AN10000 and a beam size of 25nm, mounted on a JEM 100 CX

Mat. Res. Soc. Symp. Proc. Vol. 581 © 2000 Materials Research Society

II microscope, was employed to analyze specifically the $ThMn_{12}$-type structure of all alloys annealed at 1150 °C. The structure were studied by means of a Brucker x-ray diffractometer (XRD) with automatic divergence slit (CuKα radiation λ = 1.54178Å). The Rietveld method was used to analyze the crystal structures and calculate the lattice parameters, the diffraction domain size and strain rate. The "goodness of fit" indicator R_B has been calculated as in [2].

The magnetization has been measured using a Manics differential sample magnetometer (DSM) in magnetic fields up to 18kOe. Thermomagnetic data were measured under an applied field of 1000 Oe with heating rate of 10 °C/min. Curie temperatures T_C were determined from the *M-T* curves by extrapolating the linear part of the *M-T* curve and finding the temperature values of the intersection with the extended baseline. When necessary, the samples were sealed in silica tubes to avoid oxidation upon heating. ^{57}Fe Mössbauer spectra were taken at room temperature with a conventional constant acceleration spectrometer. The γ-ray source was ^{57}Co in a Rh matrix. The calibration was performed with α-Fe at room temperature with line width at half eight equal to 0.25 mm/s.

RESULTS

Structural Properties

The XRD diagrams of the annealed material at temperature up to 800 °C show a main phase contribution of about 85 volume per cent for $0 < x < 2$, indexed by the disordered $TbCu_7$ type hexagonal *P6/mmm* cell, in agreement with [3] for rapidly quenched $SmFe_{11}Ti$. The additional weak lines are assigned to b.c.ç. αFe-T, around 5%, Fe_2Ti 5%, and small amounts of SmO-N and Sm_2O_3. For $x = 2$, extra lines are assigned to $Sm_3(FeCoTi)_{29}$.

Annealing at higher temperature, $800 < T_a < 900$ °C, leads to a more ordered state indicated by the emergence of extra reflections (310), (002), (202), relevant of the $ThMn_{12}$ type structure *I4/mmm*. Moreover, with increasing annealing temperature, the broadening of the diffraction peaks reduces (Fig. 1).

For samples annealed at 1150 °C, the agreement between theoretical and experimental XRD diagrams related to the $ThMn_{12}$ phase has been calculated with the Fe/Ti and Fe/Co ratio given by the XDS analysis. In the $RFe_{11-x}M_x$ compounds, the Fe atoms occupy three crystallographic non-equivalent sites, denoted Fe(8i), Fe(8j) and Fe(8f). First, the refinement was performed with Ti and Co statistically distributed among all sites. Such hypothesis could be assumed owing to the out of equilibrium elaboration process of the material, possibly responsible for high defect rate. However, the agreement was improved with Ti atoms distributed on i sites as observed for bulk material, the Co atoms were assumed to occupy the f site [4]. Figure 2 shows such a Rietveld refinement for sample x=0.5. The results concerning the fit of the various samples are given in table I.

It appears that the *a* parameter remains constant with increasing *x*, a noticeable decrease is observed for *c*. The small trend to a reduction of the diffraction domain size as the Co content increases is consistent with the disorder brought by the fourth element slowing down the diffusion process.

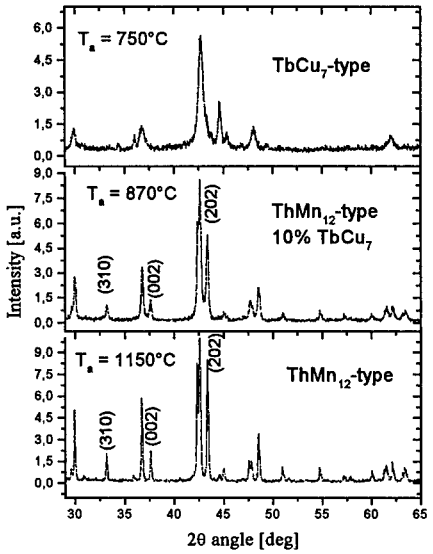


Fig. 1. X-ray diffraction diagram of $SmFe_{9.5}TiCo_{1.5}$ annealed at 750 °C, 870 °C and

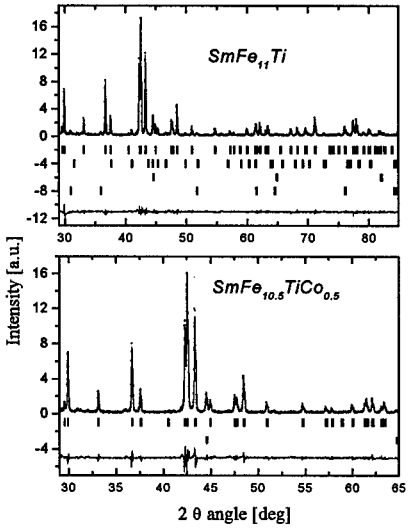


Fig. 2. Rietveld analysis for $SmFe_{11}Ti$ and $SmFe_{10.5}TiCo_{0.5}$ annealed respectively at 1150 °C and 750 °C.

Table I T composition of the *I4/mmm* phase as given by EDX analysis for the various nominal composition *x* , *a*, *c* cell parameters, D mean diffraction domain size, strain rate and R_B factors from the Rietveld fit for Ta = 1150 °C.

	x=0	*x*=0.5	*x*=1	*x*=1.5	*x*=2
T atoms	Fe 10.97	Fe 10.46	Fe 9.76	Fe 9.31	Fe 8.74
EDX analysis	Ti 1.02	Ti 1.03	Ti 1.04	Ti 1.08	Ti 1.04
±5%	Co 0.	Co 0.50	Co 1.19	Co 1.60	Co 2.21
a nm	0.8555(3)	0.8552(3)	0.8555(3)	0.8552(3)	0.8555(3)
c nm	0.4794(3)	0.4791(3)	0.4788(3)	0.4787(3)	0.4785(3)
D nm	95	107	89	80	87
Strain rate (%)	0.18	0.26	0.33	0.30	0.36
R_B	3.79	5.21	4.94	7.31	6.47

The Rietveld refinement of the hexagonal phase is more complex than the tetragonal one, for which the crystallographic atom occupancy parameter *s* is always equal to 1. The existence of the hexagonal $TbCu_7$ phase is governed by the *s* parameter [5]. In the fitting procedure, we have taken into account all the following parameters: *a, c,* the strain rate, diffraction domain size D, Debye-Waller factors, atom space-group position, and *s.*

Moreover, the relative distribution of the Fe, Ti, Co atoms was assumed according to the distribution in the $ThMn_{12}$ structure and the evolution of the crystallographic families from the hexagonal parent to the tetragonal structure. The results of the Rietveld analysis of the hexagonal $TbCu_7$ type phase are given in table II for sample $x = 0$, 0.5, 1.5, and an example of a Rietveld fit for sample $SmFe_{10.5}TiCo_{0.5}$ annealed at 750 °C is reported on figure 2. The

stoichiometry of the hexagonal phase is 1:10 and the diffraction domain size are drastically reduced.

Table II : *P6/mmm* characteristics deduced from the Rietveld fit, *s* is atom occupancy parameter.

	x=0	X=0.5	x=1.5
S	0.406	0.392	0.380
Sm content in P6/mmm phase	8.7	9.0	9.3
a (nm)	0.4899(3)	0.4899(3)	0.4906(3)
c (nm)	0.4225(3)	0.4232(3)	0.4232(3)
D (nm)	17	16	16
Strain rate (%)	0.45	1.00	1.00
R_B	3.99	6.38	5.57

Magnetic Properties

From figure 3 it can be seen that the Curie temperatures and the mean hyperfine fields increase monotonously with increasing Co content for both structures ($ThMn_{12}$ and $TbCu_7$). There are three types of exchange interaction existing in $RFe_{11-x}M_x$ compounds, namely the R-R interaction between the magnetic moments on the R-sublattice, the T-T interaction between the magnetic moments on the T- sublattice, and the R-T intersublattice interaction. Among them, the T-T interaction is the strongest and determines the ordering temperature. It is well known that the T-T interaction is very sensitive to the distance between the transition metal moments. Hu *et al.* [6] have reported that Fe at the 8i site has the largest magnetic moment while Fe at the 8f site has the smallest moment. The inter-atomic distances between the near neighbors of Fe atoms at the different sites are different. According to Givord and Lemaire [7], there are two T-T exchange interactions in R_2Fe_{17} compounds, positive and negative. When the distance of the Fe-Fe pairs is smaller than 2.45Å, the exchange interaction is negative; whereas at larger Fe-Fe distances the interaction is positive. It may be assumed that this is also the case in 1:12 systems. So, when the substitution of Co for Fe occurs at sites where the distance between Fe-Fe pairs is smaller than a certain critical distance, the negative interaction will be reduced and the total interaction will be enhanced, so that the Curie temperature and the

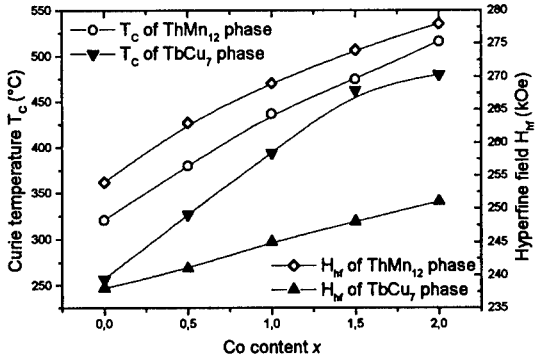


Fig.3. Curie temperature and Hyperfine field of $ThMn_{12}$ phase and $TbCu_7$ phase as a function of the Co content, *x*.

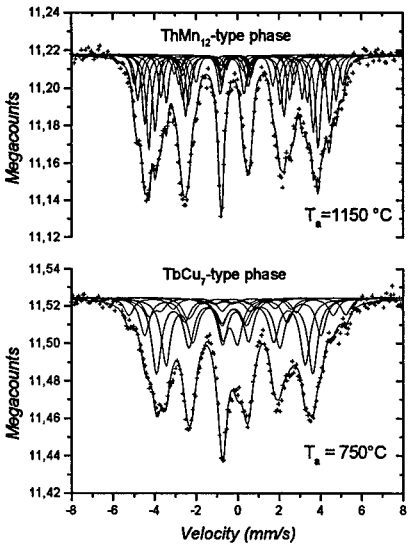


Fig. 4. Mössbauer spectra of $SmFe_{10}CoTi$ for two annealing temperatures.

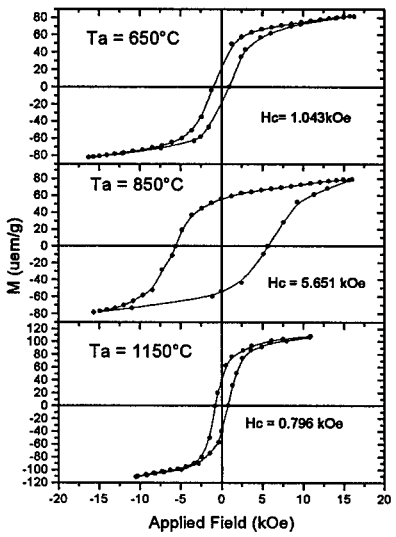


Fig. 5. Hysteresis loops of $SmFe_{9.5}Co_{1.5}Ti$, annealed at 650°C, 850°C and 1150°C from top to bottom.

hyperfine field will increase due to the substitution of Co for Fe.

The Mössbauer spectra (Fig. 4.) relative to the hexagonal phase are broadened comparatively to those of the tetragonal one. Ti is located on one crystallographic position while in the hexagonal structure it is statistically distributed over two sites.

The hysteresis loops of $SmFe_{9.5}TiCo_{1.5}$ measured at room temperature are illustrated in figure 5, the effect of annealing temperature on magnetic properties is demonstrated (Table III). The coercive field increases with increasing annealing temperature up to 5.67 kOe (D = 35nm). The small coercivity for an annealing temperature of 650 °C must be due to an unfavorable microstructure, probably resulting from a small grain size containing many defaults. Furthermore, it is well established that the coercive field H_C decreases with increasing grain size i.e. with increasing annealing temperature, this is the reason for the small H_C value for samples annealed at T_a = 1150 °C.

Table III. The coercive field H_C for $SmFe_{11-x}Co_xTi$ annealed at 650 °C, 850 °C and 1150 °C.

	H_C (kOe)		
Co content x	650 °C	850 °C	1150 °C
0	0.69	4.08	2.00
0.5	0.80	5.45	2.02
1	0.72	5.57	1.70
1.5	0.68	5.65	1.90
.2	0.70	5.67	1.35

CONCLUSIONS

(i) High energy ball milling and subsequent annealing at $T_a > 900$ °C lead to a continuous and homogeneous substitution of Co for Fe in the *I4/mmm* $SmFe_{11}Ti$ compound. The unit cell parameter *a* remains constant, *c* shows a small decrease. The increase of Curie temperature T_C and hyperfine field H_{hf} attest for the Co continuous substitution, corroborated by EDX analysis.

(ii) For $T_a < 800$ °C an hexagonal *P6/mmm* $TbCu_7$-type phase, precursor of the tetragonal *I4/mmm* $SmFe_{11-x}Co_xTi$ phase, is detected as the main phase. The Rietveld analysis gives a phase stoichiometry described as 1:10.

(iii) For $820 < T_a < 900$ °C the hexagonal phase is transformed into the tetragonal phase. We suggest that this evolution is favored by a recovery of stacking fault between the hexagonal phase and the coexisting b.c.c. phase.

(iv) Coercivity exhibits two antagonist behaviors as a function of annealing temperature T_a. When increasing T_a, on the one hand, the number of surface defects are reduced, it results an increase of H_C, on the other hand, the diffraction domain size increases which reduces H_C. The intersection of both behaviors occurs around 850 °C where H_C shows a maximum. The high H_C value up to 5.67kOe suggests that such samples are potential candidates for magnetic recording media and eventually permanent magnets.

ACKOWLEDGEMENTS

The authors are grateful to Patricia Beaunier from Université Pierre et Marie Curie - Paris 6- (SIAR) for the EDX analysis.

REFERENCES

1. S. F. Cheng, V. K. Sinha, Y. Xu, J. M. Elbicki, E. B. Boltich ,W. E. Wallace , S. G. Sankar, and D. E. Laughlin, J. Magn. Magn. Mater. **75**, 330 (1988).

2. J. Rodriguez-Carvajal, Physica **B192**, 55 (1993).

3. Q.F. Xiao, Z.D. Zhang, T. Zhao, W. Liu, C. Sui, X.G. Zhao, and D.Y. Geng, J. Appl. Phys. **82**, 6170 (1997).

4. Z.W. Li, X.Z. Zhou, and A.H. Morrish, J. Appl. Phys **69**, 5602 (1991).

5. D. Givrod, J. Laforest, J. Schweizer and F. Tasset, J. Appl. Phys. **50**, 2008 (1979).

6. B. Hu, K. Wang, Y. Wang, Z. Wang, Q. Yan, and X. Sun, Phys. Rev. B **51,** 2905 (1995).

7. D. Givord and R. Lemaire, IEEE Trans. Magn. Mag. **10,** 109 (1974).

THE ROLE OF BORON IN THE MECHANICAL MILLING OF TITANIUM-6%ALUMINIUM-4%VANADIUM POWDERS

A.P. Brown*, R. Brydson*, C. Hammond*, T.M.T. Godfrey**, and A. Wisbey**.

*Department of Materials, School of Process, Environmental and Materials Engineering, University of Leeds, Leeds, LS2 9JT, UK.
**Structural Materials Centre, Defence Evaluation Research Agency (DERA), Farnborough, Hants, GU14 OLX, UK.

ABSTRACT

The reduction in grain size of a metal can lead to significant improvement in mechanical properties. Mechanical alloying (MA) with a second phase is a possible route to producing fine-grained, particulate reinforced material. This study describes the microstructural development of Ti-6%Al-4%V milled with increasing concentrations of boron. Mechanical milling of Ti-6%Al-4%V powder produces a nanocrystalline material. MA of Ti-6%Al-4%V with boron results in the alloying of the two to form either a boride or an amorphous phase when the local concentration of boron is ~ 50 at.%. During milling, the boron tends to remain near to its original particle form and in these boron-rich regions TiB is formed. Beyond these regions small amounts of boron (a few at.%) mix with the titanium matrix and reduce further the grain size of the titanium. An increase in the global concentration of boron increases the volume fraction of boride produced.

INTRODUCTION

To investigate the enhancement of the mechanical properties of titanium alloys it is of interest to reduce grain size and provide a grain-refining phase that will prevent grain growth during high temperature processing. Such a reduction in grain size may be achieved using high-energy ball-milling, which can produce nanocrystalline material and fine dispersions of a grain refining second phase [e.g., 1, 2].

Prior to this study, the clean mechanical alloying of gas-atomised Ti–6%Al-4%V (Ti-6-4) with 0, and 2 at.% boron powder under a purified argon atmosphere has been carried out [3]. These powders were consolidated by hot isostatic pressing (HIPing) at temperatures between 600 and 900 °C. For the 0 % boron alloy, it has been shown that milling results in nanocrystalline α-Ti-6-4 (an hcp phase), which on consolidation grows rapidly (highlighting the low contamination levels in the milling process). The addition of 2 at.% boron to the alloy produces highly faulted/twinned boride plates and needles on consolidation (e.g., Fig. 1). These precipitates do provide good localized grain refinement, however unfortunately they are distributed inhomogeneously throughout the alloy.

Therefore, it is clearly of interest to understand how the boron mixes in the milling process and so powder mixtures of gas-atomised Ti-6-4 with 25 and 50 at.% boron powders have been milled. Boron is known to add intensity to the ball-mill by decreasing the sticking of material to the vial [e.g., 4], but it has low solid solubility in titanium (< 0.2 at.%) [5]. Preliminary thermodynamic modelling of the titanium-boron system can be used to investigate any potential phase formation during milling (Fig. 2). Energetically it may be possible for boron to atomically mix with titanium to form an amorphous alloy. However, a mixture of α-titanium and TiB with the same overall composition as an equivalent amorphous alloy may have a lower energy than the amorphous alloy. So, given that the MA

Mat. Res. Soc. Symp. Proc. Vol. 581 © 2000 Materials Research Society

process can provide nanoscale mixing of the boron, there is potential for either of these phases to be formed.

The present study will describe the microstructural development of the milled Ti – B powders and investigate the mixing of the boron.

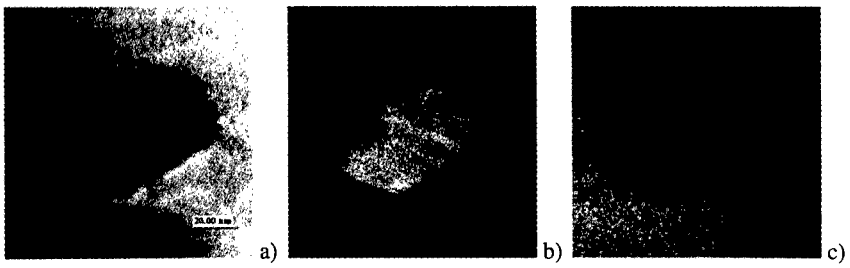
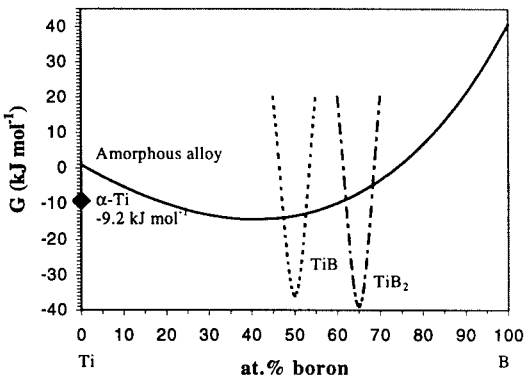


Figure 1, Energy filtered TEM images of a faulted/twinned boride precipitate in the titanium matrix of the consolidated 2% boron alloy. a) Bright field image of the precipitate, b) boron map (EELS jump ratio) and c) titanium map (EELS jump ratio). The precipitate shows boron enrichment and titanium deficiency relative to the matrix.

Selected area electron diffraction patterns of needle and plate shaped precipitates in the 2 % boron alloy can be indexed to TiB in either the B27 or the B_f orthorhombic structures. TiB is expected to form in the B27 structure, however twinning of this can produce intergrowths of the B_f structure [6]. Furthermore vanadium boride forms in the B_f structure and so vanadium may stabilize the B_f precipitates. It is interesting to note that both these structures are similar and are based on a modified fcc titanium framework (a_{fcc} ~ 4.5 Å).

Figure 2, Gibbs free energy curves, at 300 K, of the Ti-B phases that may be formed during milling. The energies of α-titanium [7], an amorphous Ti-B mixture [7, 8], TiB and TiB_2 are plotted [6]. Mixtures with < 50 % B will have lower energy when a mixture of α-Ti and TiB are formed rather than when an amorphous alloy is formed. It is interesting to see if MA can produce any of these phases.



EXPERIMENTAL

The initial powders used for milling were a Ti-6-4, produced by gas atomization, with a particle size < 250 μm and an amorphous boron powder with a particle size of ~ 1 μm. The 0 and 2 at.% boron powder mixtures were mechanically milled using a proprietary milling process under a purified argon atmosphere, where the O_2 and N_2 pickup is minimal [9]. The 25 and 50 at.% boron powder mixtures were ground (for 24 hours) in a Spex mill under a

purified argon atmosphere. The milled powders were prepared for TEM examination by crushing in a pestle and mortar under acetone and then pipetting onto holey carbon films. The consolidated material was prepared for TEM by producing 3 mm diameter discs, 100 μm thick and electropolishing these at 20 V and 120 mA in a solution of 5 % perchloric acid held at –20 °C. The foils were examined in a Philips CM20 TEM operating at 200 kV and fitted with a LaB_6 filament, an Oxford Instruments UTW EDX detector and a Gatan 666 PEELS system. The energy-filtered images were obtained using a JEOL 2010 FEG TEM and Gatan Imaging filter. X-ray diffraction data was obtained using a Philips diffractometer with Cu $K\alpha_1$ radiation.

RESULTS

X-Ray Diffraction

X-ray diffraction of the gas-atomized Ti-6-4 reveals only the α phase and it is expected that the powder would consist of martensitic α [10]. X-ray diffraction patterns for all the milled powders are presented in Fig. 3. The 0 and 2 % boron powders show only α-Ti-6-4 reflections and size-broadening analysis suggests crystallite sizes of 10 – 50 nm (dependent on strain). The 25 % boron powder has a significant decrease in signal intensity but still shows only α-Ti-6-4 reflections. Qualitatively an increase in line broadening can be seen. The 50 % boron powder also has low signal intensity and yields a complex set of reflections that can be best approximated by a mixture of α-Ti-6-4, $TiB_{(B27)}$ and TiB_2 reflections. However, there is little or no amorphous phase present in any of the samples as there is no broad diffraction peak at ~ 25° in the diffraction patterns.

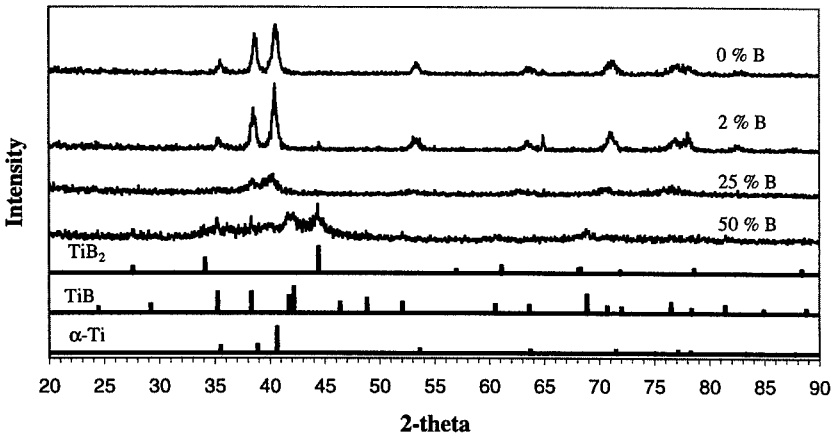


Figure 3, X-Ray diffraction patterns of the milled powders and the standard spacings for α-Ti-6%Al-4%V, $TiB_{(B27)}$ and TiB_2. The 0, 2 and 25 % B samples consist of α-Ti-6-4 reflections while the 50 % B sample is composed of a mixture of α-Ti-6-4, TiB and TiB_2 reflections.

Transmission Electron Microscopy

The 0 and 2 % boron powders have a metallic appearance and are agglomerated into particles ~ 1 mm in size. The crystallites are 10 – 50 nm in size, which is consistent with XRD (Fig. 4). Contamination analysis shows minimal oxygen (1100 ppm), nitrogen (110 ppm), and iron (0.13 %) content, which is comparable to the as received material. The only phase observed by electron diffraction was α–Ti-6-4.

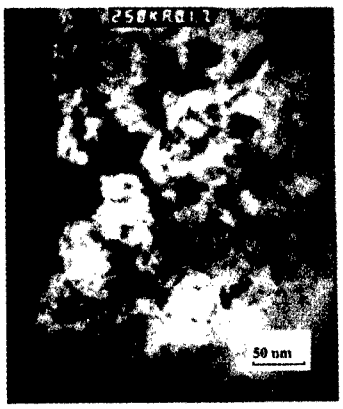


Figure 4, Bright field TEM image of the mechanically milled Ti-6-4 powder. The polycrystalline nature of the powders is evident with crystallite sizes of 10 – 50 nm. Electron diffraction yields a ring pattern that indexes to the α phase.

The 25 % boron powder also has a metallic appearance but a slightly more agglomerated particle size of ~ 3 mm. In this powder two phases are evident; α–Ti-6-4 crystallites with size < 10 nm in an amorphous matrix (Fig. 5) and small 'pores' some of which contain TiB (Fig. 6). Quantitative elemental analysis using EELS shows that the α–Ti-6-4 regions have Ti:B atomic ratios of 95:5, while the 'pores' containing TiB to have Ti:B atomic ratios of 1. Furthermore, the pores *containing* TiB exhibit moiré fringes from the TiB crystals (Fig. 6). However there are also 'pores' showing similar image contrast but low Ti:B ratios, no TiB diffraction spots and no moiré fringes within the pore.

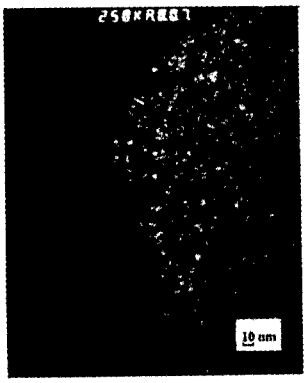


Figure 5, Dark field image of Ti-6-4 matrix within the 25 % B sample. The crystallites are < 10 nm in size, and quantitative EELS reveals a 95:5 atomic ratio of Ti:B within the matrix. Electron diffraction produces a ring pattern that indexes to the α phase.

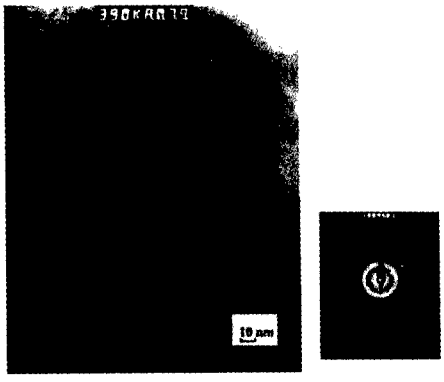


Figure 6, Bright field image of the 25 % B sample showing a 'pore' surrounded by Ti-6-4 matrix. Quantitative EELS reveals a 1:1 atomic ratio of Ti:B within the pore. The corresponding diffraction pattern shows rings from the α-Ti-6-4 matrix and spots from $TiB_{(B27)}$ within the pore (confirmed by dark field imaging). Moiré fringes from the TiB crystals can be seen within the pore.

The 50 % boron powder has a ceramic appearance and a much finer particle size of ~ 100 μm. Three phases are evident in this powder; an amorphous phase, α–Ti-6-4 crystallites and titanium boride phases of varying crystallinity (Fig. 7). The amorphous phase, is not yet well characterized but EDX analysis reveals silicon contamination of 10 – 80 at % as well as the expected Ti-6-4 phase; the source of the silicon is unknown. In the α-Ti-6-4 phase, as for the 25% boron case, there are crystallites < 10 nm in size in an amorphous matrix. Finally in the boride phases, which are of varying crystallinity but are all highly faulted/twinned, the only structure to be identified by electron diffraction is $TiB_{(B27)}$ (Fig. 8).

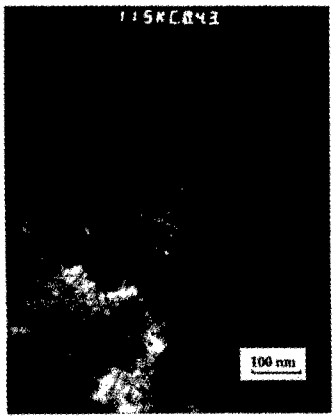


Figure 7, Dark field image of the 50 % B sample showing amorphous regions, fine α-Ti-6-4 crystallites and faulted boride phases.

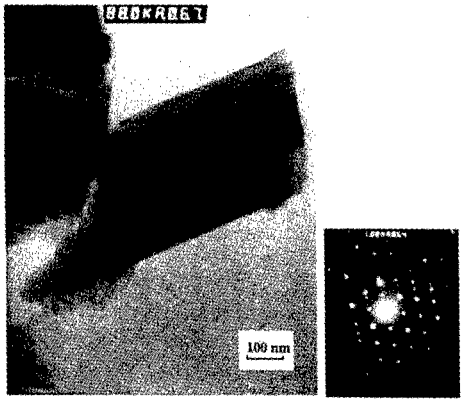


Figure 8, Bright field image of 50 % B sample showing a faulted TiB particle. The corresponding selected area diffraction pattern from the precipitate can be indexed to $TiB_{(B27)}$. Twinning and the similarity to fcc-packing of this orthorhombic structure are evident in the diffraction pattern.

DISCUSSION

Mechanical milling of Ti-6%Al-4%V produces α phase powders, which have 10 – 50 nm grain sizes. Mechanical alloying (MA) the Ti-6%Al-4%V with amorphous boron (1 μm particle size) can result in alloying of the two to form either a boride or an amorphous phase (Fig. 7).

It is suggested that during MA the boron remains localized to its near-original particle form (Fig 6) providing limited sites for mixing. However, it appears that fine (possibly disordered) hcp titanium (c ~ 4.67 Å) produced during milling is pushed into these boron rich regions resulting in the production of highly faulted orthorhombic TiB (that essentially has a modified fcc titanium framework, a ~ 4.57 Å). Certainly, within these regions of high boron concentration it is more energetically favourable for a boride phase to form (Fig. 2). In the region surrounding the original boron particle, some of the boron (a few at.%) mixes into the Ti-6%Al-4%V matrix, apparently adding intensity to the ball-mill and reducing the α-Ti-6-4

grain size to < 10 nm. It would seem likely that this boron is not in solid solution with the titanium but is located at the disordered α-grain boundaries.

This description of the boron behaviour during milling is consistent with the thermodynamic idea that an atomic mixture of titanium and boron, with less than 50 % boron, would energetically tend to form as a combination of α-titanium and TiB (Fig. 2). However, the high surface area of a nucleating TiB phase may raise its Gibbs energy and any significant rise could make it (energetically) possible to form *either* an amorphous phase or a boride phase. The production of amorphous material is evident in the 50 at.% powder. The above description of the boron behaviour suggests that boride and possibly amorphous phase formation occurs in all the milled boron powder mixtures and that the boride and amorphous phase fractions simply increase as the boron concentration increases.

The localization of the boron powder during milling probably contributes to the inhomogeneous distribution of the boride precipitates in the consolidated 2 at.% boron alloy [3]. Therefore it is suggested that mechanically alloying Ti-6%Al-4%V with ~ 2 at.% boron that is already fine-grained (nanocrystalline) may result in a more even dispersion of boron and may significantly reduce further the grain size of the consolidated Ti-6%Al-4%V – boron material.

CONCLUSION

Mechanical alloying of Ti-6%Al-4%V with amorphous boron results in the production of nanocrystalline powders with α- Ti-6%Al-4%V, titanium boride and amorphous phases. During the milling the boron remains localized to its near-original particle form.

ACKNOWLEDGEMENT

This work is supported by an EPSRC research grant (Grant No. GR/M28927).

REFERENCES

[1] H. Inagaki, Zeitschrift fur Metallkunde, **86**, 643, (1995).
[2] B.S. Murty and S. Ranganathan, Int. Mat. Rev., **43** (3), 101, (1998).
[3] A.P. Brown, R. Brydson, C. Hammond, T.M.T. Godfrey and A.Wisbey, Proceedings of EMAG 99, IOP, (1999).
[4] K. Brand, C. Suryanarayana, B.F. Kieback and F.H. Froes, Mat. Sci. Forum, **225-227**, 471, (1996).
[5] J.L. Murray (ed.), Phase Diagrams of Binary Titanium Alloys, Metals Park, OH, ASM International, p.33, (1987).
[6] M. de Graef, J.P.A. Löfvander, C. McCullough and C.G. Levi, Acta Metall. Mater., **40** (12), 3395, (1992).
[7] A.T. Dinsdale, CALPHAD, **15** (4), 317, (1991).
[8] A.R. Miedema, P.F. de Châtel and F.R. de Boer, Physica **100B**, 1-28, (1980).
[9] T.M.T. Godfrey, A.Wisbey, P.S. Goodwin, C.M. Ward-Close, A. Brown, R. Brydson, and C. Hammond, Proceedings of 9th World Conference on Titanium, (1999).
[10] G. Itoh, T.T. Cheng, and M.H., Loretto, Mat Trans., JIM, **35** (8), 501, (1994).

STEADY STATE PHASE DIAGRAM OF Cu-Ag UNDER BALL MILLING: AN XRD AND APFIM STUDY

F. Wu[+], P. Bellon[+], A.J. Melmed*, T.A. Lusby*
[+]Department of Materials Science and Engineering, University of Illinois at Urbana-Champaign, Urbana, IL61801, USA
*Department of Materials Science and Engineering, Johns Hopkins University, Baltimore, MD 21218, USA

ABSTRACT

The nature of the steady state reached during ball milling of Cu_xAg_{1-x} powders (x=35 to 75) is studied as a function of the milling temperature ($85K \leq T \leq 503K$). The characterization of the powders is performed by using x-ray diffraction, differential calorimetry and atom probe field ion microscopy. A steady-state phase diagram is built. Three-phase coexistence is shown to generally take place at intermediate milling temperatures. Atom probe data reveals that the solid solution stabilized by low milling temperature is nearly random, where as milling at elevated temperatures results in the decomposition of the elements at a lengthscale of 20~30 nm.

INTRODUCTION

High energy ball milling is a process that has gained wide interest in the last decade since it offers opportunities for synthesizing a wide range of alloys and microstructures that are ordinarily very difficult or even impossible to obtain by more conventional processing routes [1,2]. Amorphous phases, nanomaterials, metastable extended solid solutions, e.g., in Ni-Ag alloys [3], and, even more surprisingly, unstable phases can be stabilized, e.g., Fe-Cu [4] or Cu-Co [5] solid solutions that are located deep within equilibrium miscibility gaps.

Recently a detailed study has been reported by Klassen *et al* [6] on the effect of the milling temperature on $Cu_{50}Ag_{50}$ powders. They show that if the powders are milled long enough, a steady state is reached, and that the nature of this steady-sate is independent of the initial state of the powders. At low milling temperatures (~85K), the steady state is found to be a single solid solution with a lattice parameter compatible with a $Cu_{50}Ag_{50}$ fcc solid solution. At high milling temperatures (above 443K), the steady state consists of two terminal solid solutions, one very copper-rich, one very silver-rich. Surprisingly, they found that at intermediate milling temperatures (373K to 423K) the central solid solution and the two terminal solid solutions coexist at steady state.

These results cannot be explained adequately by thermodynamic approaches, in particular since the central solid solution is thermodynamically unstable. A theoretical framework based on a kinetic approach has been developed in the last decades to explain phase modifications in alloys submitted to an external dynamical forcing, as observed for instance in alloys under irradiation or under sustained plastic deformation [7]. In these kinetic models, atoms are assumed to move because of two dynamic processes acting in parallel, a first one thermally-activated and assisted by the migration of point defects, and a second one that results from the external forcing, and which produces forced motion of atoms. This approach provides a simple and direct explanation for the stabilization of solid solutions at low milling temperatures [6,7].

Recently experimental observations on Cu-Fe [8], Cu-Co [9] and atomistic computer simulations [10] indicate additionally that phase separation under ball milling may saturate at a mesoscopic scale, and that the characteristic length of this decomposition can be tuned by

Mat. Res. Soc. Symp. Proc. Vol. 581 © 2000 Materials Research Society

adjusting the experimental control parameters. This offers the possibility of synthesizing new microstructures with specially tailored properties.

In this paper we investigate how two milling parameters, the composition of the powders and the milling temperature, affect the steady state that is reached during ball milling of Cu-Ag powders. Particular emphasis is put on the analysis of the composition field at the atomic scale, by using the atom probe technique.

EXPERIMENTS

Ball milling of Cu and Ag powders was performed following the procedure described in detail by Klassen *et al* [6]. Powders of copper and silver were mixed according to the desired nominal (atomic) composition, Cu_xAg_{100-x}, with x ranging from 35 to 75. Ball milling was performed with a Spex 8000 mill at temperatures ranging from 85K to 503K. A purified argon atmosphere was used for all temperatures except for liquid nitrogen temperature (LN2) milling, which was performed in air. The milling temperature was estimated to be ~85K for LN2 milling. All millings performed at a temperature different from 315K were preceded by a 24 hour milling treatment at 315K so as to alloy the initial powders. Ball milled powders were systematically characterized using x-ray diffraction (XRD) and differential scanning calorimetry (DSC).

Atom probe field ion microscopy (APFIM) was used to analyze the composition of the ball milled powders at the atomic scale. A new method has been devised to prepare APFIM samples from ball milled powders, without altering significantly their microstructure. The $Cu_{50}Ag_{50}$ as-milled powders were compacted into a copper tube with an inside diameter of 500 microns and then cold-swaged down to a diameter of 200-300 microns. Optical and scanning electron microscopy indicate that the deformation during swaging takes place mostly in the soft copper tubing, the copper becoming a binding agent of the ball milled aggregates. The swaged wires were then electrochemically polished to make sharp tips using the micro-zone electropolishing technique with a phosphoric acid-glycerin solution.

RESULTS

X-ray analysis:

Because of the large lattice parameter difference between pure copper and pure silver, $\Delta a/a \sim 13\%$, identification of the phases in presence after milling is in principle possible by x-ray diffraction. In practice, the broadening of the peaks resulting from the formation of nanograins and the presence of several fcc solid solutions can make the analysis challenging [6]. We discuss here first the results obtained for equiatomic or near-equiatomic compositions, and then address the case of silver-rich and copper-rich mixtures.

For the $Cu_{50}Ag_{50}$ powder, results very similar to that reported by Klassen *et al* [6] are obtained (see fig. 1a). Milling at 80K results in the stabilization of a solid solution with a lattice parameter of 3.89Å, very close to that expected for a $Cu_{50}Ag_{50}$ fcc solid solution [11]. Intermediate temperature milling ($373K \leq T \leq 423K$) produces the coexistence of three fcc solid solutions: in addition to the $Cu_{50}Ag_{50}$ phase identified at low temperature, two terminal solid solutions are also present. Milling at elevated temperatures ($T \geq 453K$) results in the decomposition of the alloy, as shown by the presence of only two terminal solid solutions. Similar results are observed for other near-equiatomic compositions, $Cu_{55}Ag_{45}$ and $Cu_{65}Ag_{35}$, clearly revealing the coexistence of three solid solutions at intermediate milling temperatures. One noticeable feature is however that the composition of the central solid solution is not fixed: for a given nominal composition, this central solid solution has in fact the same lattice parameter

as the solid solution obtained for that composition by milling at 315K. The composition of the central solid solution is therefore identical to the nominal composition of the powder.

The analysis for the $Cu_{35}Ag_{65}$ powder (see fig. 1b) is more difficult because of the strong overlapping of the (111) peaks for the nominal solid solution and for the silver-rich terminal solid solution. Only one (111) peak seems to be present at intermediate milling temperatures (393K and 423K). However one notices that this peak is strongly asymmetric and that this asymmetry is reversed between these two temperatures. This behavior can be simply explained by assuming the presence of two fcc solid solutions, the volume fractions of which are changing when the temperature is varied. This is in fact exactly what is observed for the equiatomic or near-equiatomic compositions discussed in the previous paragraph. A copper-rich phase is also visible at high temperatures (423K and 453K), but it is difficult to determine accurately its lattice parameter.

In the case of copper-rich powders, $Cu_{75}Ag_{25}$ (not shown here), the analysis is also difficult because of peak overlapping problems. Similarly to the silver-rich case the complex behavior can be simply interpreted by the presence of three solid solutions at intermediate milling temperatures, the central solid solution now having a x= .75 composition.

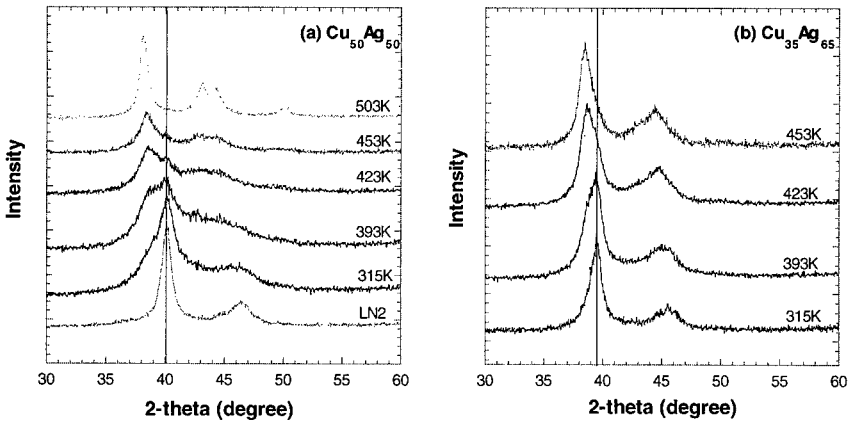


Fig. 1: x-ray diffraction spectra of (a) $Cu_{50}Ag_{50}$ and (b) $Cu_{35}Ag_{65}$ powders obtained at steady state for various milling temperatures. The vertical line is a marker for the central solid solution.

The above x-ray diffraction analysis can be summarized by building a steady-state phase diagram for the Cu-Ag system, as shown in fig. 2. Two-theta values were used to calculate the lattice parameters. When there is a strong overlapping, the (111) peak positions were determined by using a least-square x-ray fitting program [6]. For the lattice parameter, a positive deviation from the Vegard's law is expected due to the positive heat of mixing [11]. So experimental data from rapid-quenched samples [12] were used as references to determine phase compositions. The analysis of the XRD spectra obtained for silver-rich and copper-rich powders is clearly not unique. However since all spectra can be rationalized using the same analysis established for near-equiatomic compositions, it appears legitimate to propose that qualitatively the same sequence is obtained for all compositions: upon increasing the milling temperature the steady-state changes from one central solid solution to three phase coexistence and then to the

coexistence of two terminal solid solutions. The compositions of the terminal solid solutions are essentially independent of the nominal composition. In sharp contrast to this result, the composition of the central solid solution is found to follow the nominal composition of the alloy.

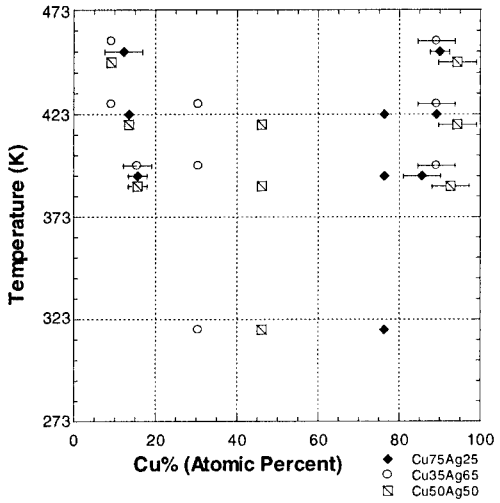


Fig. 2: Steady-state phase diagram obtained from XRD analysis of ball milled Cu_xAg_{1-x} powders under ball milling. For clarity, the temperature values of $Cu_{35}Ag_{65}$ and $Cu_{50}Ag_{50}$ are shifted up and down by 5 degrees, respectively. An error bar is shown when there is an uncertainty in the determination of the peak position.

Atom Probe analysis:

Three milling temperatures were studied for $Cu_{50}Ag_{50}$: LN2, 315K and 453K. A composition depth profile at each temperature is shown in fig. 3. A block size of 100 ions has been chosen, and for this study, one such block corresponds roughly to an analyzed depth of 1 nm. The amplitude of the composition fluctuations is quite small for the 80K sample (fig. 3a). Statistical analysis [13] indicates that the amplitude of these fluctuations is in fact just above that expected from a random alloy (binomial distribution). A medium range (~50 nm) composition fluctuation, with a small amplitude, about 5at. %, is also present and clearly revealed by a Fourier analysis. In contrast, well-defined and large fluctuations are observed for the 315K sample (fig. 3b). One would argue that in fact decomposition has already taken place at a short scale in this alloy. Further analysis is under progress to establish this point. At higher milling temperature (fig. 3c), phase decomposition has clearly taken place, with a characteristic length scale of 20-30 nm.

We note that along with Cu and Ag, a small amount of both Cu and Ag oxides were found (<3 at%), and that in addition to the depth-probe data shown, the LN2 sample showed regions with very high (90%) concentration of Cu and Ag. The exact origin of these heterogeneities remains unclear. TEM observations under progress indeed confirm that LN2 milled powders contain a small amount of Cu-rich and Ag-rich regions. Only random mixed region is showed in depth profile and is used for statistical analysis.

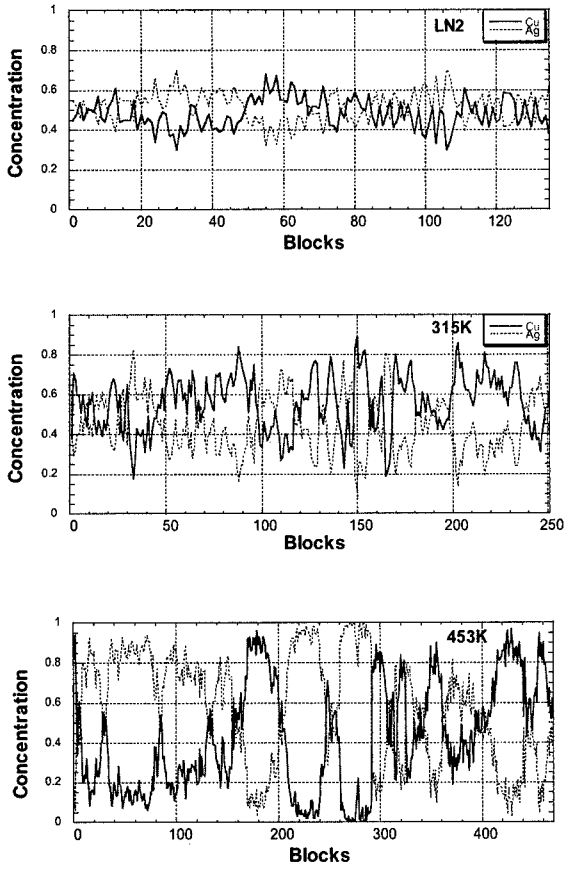


Fig. 3: Atom probe depth profiles obtained for $Cu_{50}Ag_{50}$ powders ball-milled at (a) LN2, (b) 315K, and (c) 453K. One block contains 100 detected ions and corresponds roughly to a depth of 1 nm.

DISCUSSION AND CONCLUSION

Klassen *et al* [*6*] have shown that the formation of a solid solution at low milling temperatures can be simply rationalized by appealing to the theory of driven alloys [7]. This stabilization would result from a forced dynamics, which competes with thermally activated and defect-promoted atomic diffusion. At low milling temperatures, the latter dynamics is very slow and the forced dynamics drives the alloy into a solid solution. It has been proposed that this forced dynamics originates from the shearing of atomic planes resulting from dislocation glide [10]. The origin of the three-phase coexistence at intermediate milling temperature was however not fully elucidated. The systematic study undertaken here and summarized in the steady-state phase diagram (fig. 2) sheds light on this question. Since the central solid solution has a

composition equal to the nominal composition of the powders, this coexistence is likely to originate from the existence of local variations in the shearing intensity. It has been proposed (Klassen [6], Xu [14]) that the variations originate from a composition dependence of the mechanical or diffusional properties of the ball milled powders. Our present results, however, indicate that these variations may simply result from the intrinsically heterogeneous nature of deformation during ball milling. Local regions may experience different milling intensities at different times. In an XRD spectrum, an average of all these regions would be made, giving rise to a superposition of the spectra obtained for a range of milling intensities. Rather low milling intensity would produce phase-separated regions, where as higher milling intensities would produce solid solutions with the nominal composition. To test this explanation, it would be important to determine the scale at which the three phases co-exist. Transmission electron microscopy is under progress to address this point.

The APFIM analysis used in this work shows directly that low temperature ball milling of moderately immiscible elements can produce a random solid solution. This conclusion has been previously reached by using macroscopic measurements (e.g., DSC [6]), diffraction techniques (e.g., EXAFS for Cu-Fe alloys [15]) or local probes, such Mössbauer spectroscopy. The present technique provides however a direct and unique evidence of the mixing at the atomic scale. It also reveals the scale of decomposition at higher milling temperatures, and the existence of medium range composition variations for most temperatures. Work is under progress to use quantitatively the information available in APFIM spectra, and to compare it with the microstructures obtained by computer simulations [10].

Acknowledgements

Stimulating discussions with Profs. R. S. Averback, D. N. Seidman and with Dr. D. Isheim, M. Arnett, T. Klassen and U. Herr are gratefully acknowledged. This work is supported by the National Science Foundation under the grant DMR 97-33582 and also partly supported by ONR grant N00014-97-1-0559.

References

[1] C.C. Koch, *Mechanical Milling and Alloying*, Materials Science and Technology Vol.**15**, ed. R.W. Cahn, P. Haasen, E.J. Kramer (VCH, Weinheim, 1991) p.193.
[2] E. Ma and M. Atzmon, Mater. Chem. Phys. **39**, p.249 (1995).
[3] J. Xu, U. Herr, T. Klassen, R. S. Averback, J. Appl. Phys. **79**, p.3935 (1996).
[4] A. R. Yavari and P. J. Desre, Phys. Rev. Lett. **68**, p.2235 (1992).
[5] C. Gente, M. Oehring and R. Bormann, Phys. Rev. B **48**, p.13244 (1993).
[6] T. Klassen, U. Herr and R.S. Averback, Acta Mater. **45**, p.2921 (1997).
[7] G. Martin and P. Bellon, Solid State Phys. **50**, p.189 (1997).
[8] J. Y. Huang, Y. D. Yu, Y. K. Wu, D. X. Li, and H. Q. Ye, Acta Mater. **45**, p.113 (1997).
[9] J. Y. Huang, Y. D. Yu, Y. K. Wu, D. X. Li, and H. Q. Ye, J. Mater. Res. **12**, p.936 (1997).
[10] P. Bellon, R.S. Averback, Phys.Rev.Lett. **74**, p.1819 (1995).
[11] R. Najafabadi, D.J. Srolovitz, E. Ma and M. Atzmon, J.Apply.Phys. **74**, p.3144 (1993).
[12] R.K. Linde, J.Apply.Phys. **37**, p.934 (1996).
[13] F. Wu, P. Bellon, A.J. Melmed, T.A. Lusby, to be published.
[14] J. Xu, G.S. Collins, L.S.J. Peng and M. Atzmon, Acta Mater. **47**, p.1241(1999).
[15] E. Ma, J.H. He, P. J. Schilling, Phys. Rev. B. **55**, 5542 (1997).

Formation of bulk magnetic nanostructured $Fe_{40}Ni_{40}P_{14}B_6$ alloys by metastable liquid state phase separation

Q. Li and H.W. Kui
Department of Physics, The Chinese University of Hong Kong
Shatin, N.T., Hong Kong, China

ABSTRACT

METGLAS alloy #2826 ($Fe_{40}Ni_{40}P_{14}B_6$) is a eutectic alloy. Its melt can undergo metastable liquid state spinodal decomposition deep in the undercooling regime ΔT defined as $\Delta T = T_l - T$ where T_l is the liquidus of the alloy and T is the temperature at which the decomposition reaction takes place. Micrographs of undercooled $Fe_{40}Ni_{40}P_{14}B_6$ of ΔT = 209, 260 and 307 K were displayed. All of them exhibit refined microstructures, esp. the one with the largest ΔT.

INTRODUCTION

Bulk nanostructured materials are systems that comprise of grains of diameter d that falls in the range of $1 \leq d \leq 100$ nm. They are mostly synthesized through two techniques. In the first method [1, 2] nanometer powders are compacted together, sometimes also under an elevated temperature, to produce a bulk nanostructured specimen. The main drawback is that an as-prepared specimen is filled with flaws, mostly microvoids, serving to reduce the mechanical strength of the nanostructured material [3]. Thermal annealing is very often undesirable for it causes grain growth giving rise to wide grain-size distribution [3].

In the second method [4], a bulk amorphous specimen is annealed at an elevated temperature. Nanocrystals then emerge. However, it turned out the size distribution of these nanocrystals can be quite wide that would smear out the unique properties of the nanostructured alloys.

Fe based nanostructured alloy also possesses interesting magnetic properties [2, 5]. At very small grain size, $d < 30$ nm, Fe based nanostructured materials start to exhibit soft magnetic properties. At $d \approx 15$ nm, the soft magnetic properties become very interesting and they are comparable to those of the amorphous alloys [5]. It is however important to keep the size of the constituent grains uniform if the attractive magnetic properties are to be kept.

Recently it [6, 7, 8] was found that when a eutectic alloy melt is undercooled to a temperature way below its thermodynamic melting temperature, it undergoes metastable liquid state spinodal decomposition. Right after the decomposition reaction, the system consists of intertwining undercooled liquid networks of characteristic wavelength λ. The magnitude of λ depends on how far the temperature T of the decomposition reaction is taken place below T_l where T_l is the liquidus of the eutectic alloy. The extent below T_l is called undercooling ΔT ($\Delta T = T_l - T$.). More precisely, according to Cahn [9], $\lambda \propto \{(T_s - T)/T_c\}^{-1/2}$ where T_s is the temperature of the chemical spinodal and T_c is the critical temperature of the metastable liquid miscibility gap.

It turned out that when the undercooling is sufficiently large, λ can enter the nanometer scale regime[10,11]. The physical dimension of an as-prepared nanostructured specimen in the shape of droplet can have a diameter > 1 cm. Furthermore, it is microvoid free and the size distribution of the constituent grains is narrow. So far the systems under investigation are non-magnetic. In this article, we report the formation of nanostructured

Mat. Res. Soc. Symp. Proc. Vol. 581 © 2000 Materials Research Society

$Fe_{40}Ni_{40}P_{14}B_6$ alloys, also by means of metastable liquid state spinodal decomposition. $Fe_{40}Ni_{40}P_{14}B_6$ or METGLAS alloy #2826 was chosen for it is a glass former.

EXPERIMENT

$Fe_{40}Ni_{40}P_{14}B_6$ ingots were prepared from elemental Fe (99.98% pure), Ni (99.95% pure) and B (99% pure) granules, and Ni_2P (98% pure) powders. To prepare an $Fe_{40}Ni_{40}P_{14}B_6$ ingot, Ni_2P powders were first melted by a torch in a clean fused silica tube to form a Ni_2P ingot. Then the right proportions of Fe, Ni, B, and the Ni_2P ingot were put in a clean fused silica tube. Alloying were carried out in a rf induction furnace under Ar atmosphere. All the as-prepared ingots had a diameter of ~3 mm.

It was necessary to conduct isothermal annealing experiments at elevated temperatures. They were done in a Transtemp furnace, which consists of a heating coil enclosed in a fused silica tube that was coated with Au. The thin Au layer serves to trapped heat from radiating away from the chamber of the furnace.

It was demonstrated that by a fluxing technique, molten metals could be undercooled substantially below its thermodynamic melting temperature, for example, a $Pd_{40}Ni_{40}P_{20}$ melt [12] can be undercooled to its glass state bypassing crystallization with a cooling rate of ~0.75 K min^{-1}. Ge melt [13] can be undercooled as much as 342 K below its T_l also in a molten flux of B_2O_3. In this work, the fluxing technique was again employed with B_2O_3 as the fluxing agent.

In the experiment, B_2O_3 was put into a fused silica tube that was connected to a mechanical pump (vacuum ~10^{-3} Torr). Then it was heated up by a torch to ~1350 K for 3 hr. The high temperature heat treatment serves to drive out water in the oxide. Afterward, a $Fe_{40}Ni_{40}P_{14}B_6$ ingot was dropped into the tube and would completely immersed into the B_2O_3 flux. The high temperature heat treatment was applied for a further period of 4 hr. to facilitate the removal of impurities from the molten ingot. Next the fused silica tube was transferred into the Trantemp furnace of temperature T that was below the T_l of $Fe_{40}Ni_{40}P_{14}B_6$. It sat on a thermocouple that was connected to a personal computer (PC) (Fig. 1). The PC first recorded a sharp increase in temperature followed by a rapid drop in a short period. Then it fell steadily to T.

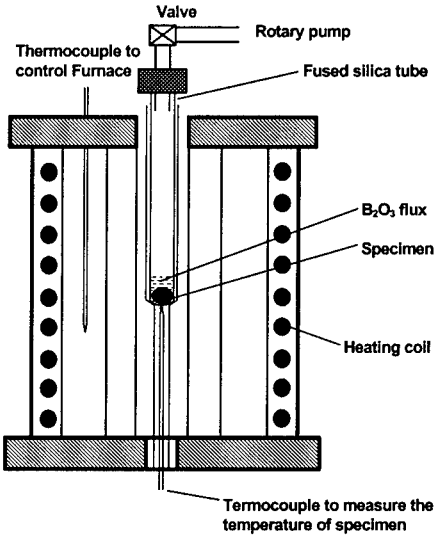


Fig. 1 Schematic diagram of the experimental setup.

Usually, it took hours for a molten specimen to crystallize if the undercooling $\Delta T = T_l - T$ is small. On the other hand, at very large undercoolings, a molten specimen could hardly be sustained in the molten state. In any case, only those undercooled or crystallized specimens that had stayed in the isothermal condition for at least 10 min were chosen for microstructural analysis. When crystallization occurred, the PC recorded a spike in the thermal profile. After crystallization, the undercooled specimen was immediately removed from the furnace and quenched in water to minimize grain growth.

Microstructures of the undercooled Fe-Ni-P-B were mainly studied by x-ray analysis, scanning electron microscopy (SEM) and electron transmission microscopy (TEM). Both SEM and TEM were equipped with EDX to conduct composition analysis.

RESULTS

The underlying mechanism of the formation of nanostructured alloys by means of metastable liquid state spinodal decomposition have been discussed in Ref. [6, 7, 8]. We therefore do not attempt to displace all microstructures of undercooled $Fe_{40}Ni_{40}P_{14}B_6$ so as demonstrated that liquid state spinodal decomposition indeed taking place, but rather only those microstructures with nanometer scale are shown. The detailed microstructural evolution would be published elsewhere.

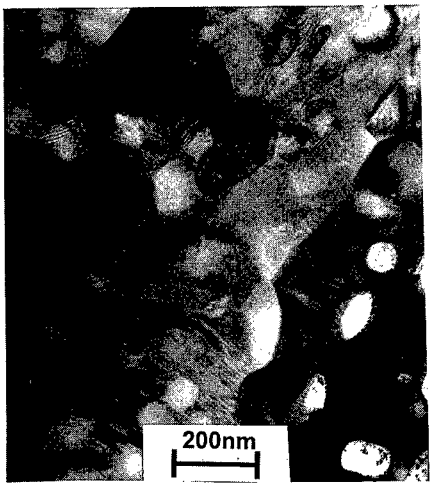
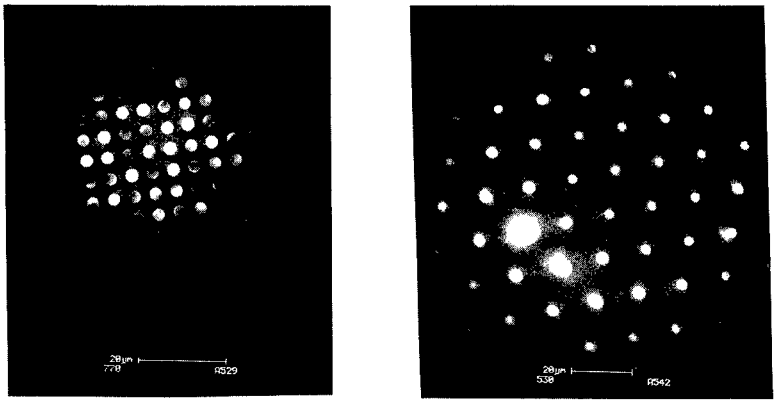


Fig. 2a Microstructures of an undercooled specimen with $\Delta T = 209$ K.

The microstructures of an undercooled specimen with $\Delta T = 209$ K is shown in the TEM micrograph in Fig. 2a. There are roughly two types of grains classified according to their sizes. The larger grains are fairly large, but still of submicron scale. The smaller ones have an average size just less than 100 nm. Furthermore, the size distribution of these smaller grains is quite narrow. It is noted that most of the smaller grains are embedded inside the larger grains. Electron diffraction patterns of a grain and a precipitate are shown in Fig. 2b. It



(i) (ii)

Fig. 2b Electron diffraction patterns of the undercooled specimen with $\Delta T = 209$ K, (i) taken from a large grain; (ii) taken from a small grain.

is difficult to determine the concentration of B by means of an EDX. X-ray analysis was also employed. The diffraction pattern is shown in Fig. 2c. Combining the EDX and x-ray results, it can be concluded that composition of the grains and the precipitates shown in Fig. 2a are $(Fe,Ni)_3(P,B)$ and (Fe,Ni), respectively. These phases are the same as those appeared during crystallization of glassy $Fe_{40}Ni_{40}P_{14}B_6$ ribbons [14]. We had examined many parts of this undercooled specimen. Not a single microvoid was found.

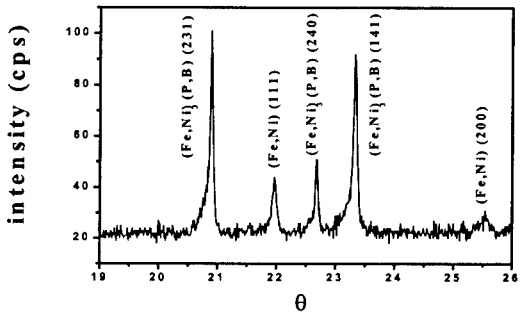


Fig. 2c X-ray diffraction pattern of undercooled specimens with $\Delta T = 209$ K.

An undercooled specimen with $\Delta T = 260$ K is shown in the TEM micrograph shown in Fig. 3. The microstructures can again be described as consisting of two types of grains classified according to their sizes. The smaller grains with an average size of 40 nm are again of narrow size distribution. The large grains exhibit some interesting features. They are somewhat interconnected and the grain boundaries are wavy. The large and small grains now positioned themselves differently when compared with those shown in Fig. 2a. Besides residing inside the large grains, a lot of them are found at the boundaries of the large grains. The composition of the large grains is $(Fe,Ni)_3(P,B)$ while that of the smaller ones is (Fe,Ni). Again, after examining many parts of this undercooled specimen, not a single microvoid could be identified. For comparison, there are two differences between the microstructures shown in Fig. 2a and Fig. 3. First, the microstructures become finer with increasing ΔT, which is expected. Second, more grains of smaller size find their way to the boundaries of the larger grains.

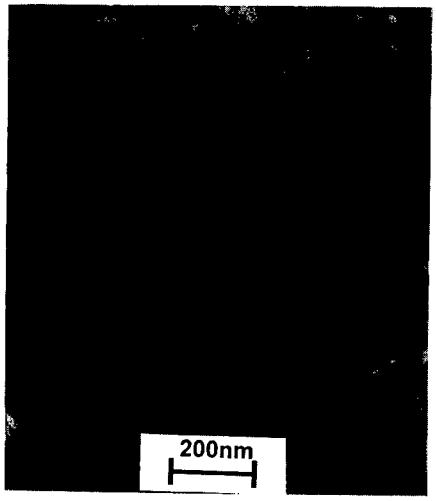


Fig. 3 Microstructures of an undercooled specimen with $\Delta T = 260$ K.

The microstructures of an undercooled specimen with $\Delta T = 307$ K is shown in Fig. 4a. It can best be described as granular. The grains can be roughly divided into two classes classified according to their sizes. The larger ones have an average size somewhat smaller than 100 nm while that of the smaller ones is ~30 nm. The smaller grains are seldom found inside the larger ones. A micrograph of the same undercooled specimen shown in Fig. 4a but of larger magnification is shown in Fig. 4b to illustrate this point. Again there are only two different phases. The

smaller grains have a composition of (Fe,Ni) while that of the larger ones is $(Fe,Ni)_3(P,B)$. Connectivity of the large grains is less obvious. After examining many different parts of the undercooled specimen, microvoid was not found at all.

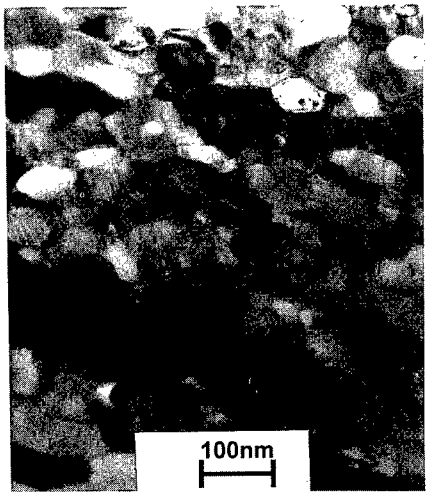


Fig. 4a Microstructures of an undercooled specimen with $\Delta T = 307$ K.

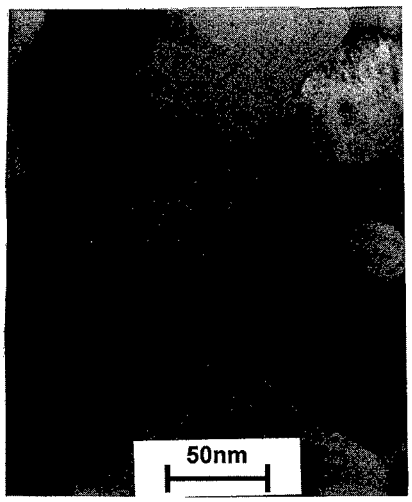


Fig. 4b Enlarged picture of the undercooled specimen shown in Fig. 4a.

DISCUSSIONS

It follows from the microstructures of the three undercooled specimens that the larger the undercooling, the finer is the microstructure. This is consistent with traditional metallurgical results. The undercooled specimen with $\Delta T = 307$ K can be called a nanostructured alloy for its average grain size is < 100 nm, which is the conventional definition of nanostructured materials.

It is interesting to observe how the two different kinds of grains distributed themselves differently at different ΔT. The smaller ones tend to move to the boundaries of the large ones as ΔT increases. This behavior can be explained in the framework of metastable liquid state spinodal decomposition and has been discussed in detail in Ref. [7]. At small ΔT, such as $\Delta T = 209$ K, the liquid spinodals of wavelength λ formed after the occurrence of metastable liquid state spinodal decomposition intertwined with each other. Since the composition of the liquid spinodal is different from $(Fe,Ni)_3(P,B)$ and (Fe,Ni), the later austin (Fe,Ni) would precipitate out during the crystallization of the liquid spinodal. The best locations for austin (Fe,Ni) are grain boundaries of the large grains so as to reduce grain boundary areas. However, at $\Delta T = 209$ K, atomic diffusion across a liquid spinodal of large λ to the boundary is difficult. This explains why smaller austin (Fe,Ni) grains precipitate out inside $(Fe,Ni)_3(P,B)$.

As undercooling increases, λ becomes shorter. As a result, some atoms can diffuse to the boundaries of the crystallized spinodals such as the undercooled specimen with $\Delta T = 260$ K. Finally for the undercooled specimen with $\Delta T = 307$ K, $\lambda \approx 100$ nm. Since diffusion distance is only ~100 nm, (Fe,Ni) prefer to diffuse to and nucleate at the boundaries of

$(Fe,Ni)_3(P,B)$ to reduce grain boundary areas. For estimation purpose, assume liquid diffusion $D \approx 10^{-7}$ m^2 s^{-1} (The value is relatively large for $Fe_{40}Ni_{40}P_{14}B_6$ is a glass former and $\Delta T = 307$ K is large.) and growth velocity $U \approx 1$ m s^{-1} (The liquid/crystal interface can still barely be seen during crystallization). Then an undercooled liquid spinodal (of $\lambda \sim 100$ nm) would turn into a crystal in $5x10^{-8}$ s. During this time, diffusion distance is: $x \sim 6 (D t)^{-1/2} \sim$ 400nm. This is about the right value to explain the observed microstructures shown in Fig. 2a, 3 and 4a.

Consider a system that consists of liquid spinodals of $\lambda \sim$ a few hundreds nm. It is likely that they would break up into droplets driven by surface tension. It is also expected that the shorter the wavelength, the faster the spinodals break up. In Fig. 3, there is still some degree of connectivity left. This is attributed to the somewhat longer wavelength of the spinodals. On the other hand, λ of the undercooled specimen with $\Delta T = 307$ K is short, leading to early spinodal break up that results in granular microstructures.

CONCLUSIONS

Nanostructured $Fe_{40}Ni_{40}P_{14}B_6$ alloys were synthesized by metastable liquid state spinodal decomposition. An as-prepared specimen consists of two types of grains classified according to their sizes. The composition of the smaller ones is austin (Fe,Ni) and that of the larger ones is $(Fe,Ni)_3(P,B)$.

ACKNOWLEDGMENTS

We thank Hong Kong Research Grants Council for financial support.

REFERENCES

1. H. Gleiter, in *Deformation of Ploycrystals: Mechanisms and Microstructures*, edited by N. Hansen et al., (Riso National Laboratory, Roskilde, Denmark, 1981), p. 15.

2. A. Kojima, A. Makino, and A. Inoue, IEEE Trans. Maga., **33**, 3817 (1997).

3. J.R. Weertman, D. Farkas, K. Hemker, H. Kung, M. Mayo, R. Mitra, and H. Van Swygenhoven, MRS Bulletin, p. 44, Feb., 1999.

4. S. Schneider, P. Thiyagarajan, and W.L. Johnson, Appl. Phys. Lett. **68**, 493 (1996).

5. G. Herzer, in *Nanomagnetism*, edited by A. Hernando (Kluwer Academic Publishers, Netherlands, 1993), p. 111.

6. C.W. Yuen and H.W. Kui, J. Mater. Res. **13**, 3034 (1998); **13**, 3043 (1998).

7. K.L. Lee and H.W. Kui, J. Mater. Res. **14**, 3653 (1999); **14**, 3663 (1999).

8. S.Y. Hong, W.H. Guo, and H.W. Kui, J. Mater. Res. **14**, 3668 (1999).

9. J.W. Cahn, Trans. Met. Soc. AIME **242**, 166 (1968).

10. W.H. Guo and H.W. Kui, J. Mater. Res., (submitted).

11. W.H. Guo and H.W. Kui, Acta Mater., (accepted).

12. H.W. Kui, A.L. Greer, and D. Turnbull, Appl. Phys. Lett. **45**, 615 (1984).

13. C.F. Lau and H.W. Kui, J. Appl. Phys. **73**, 2599 (1993).

14. D.G. Morris, Acta Metall. **29**, 1213, (1981).

SUPERSONIC CLUSTER BEAM SYNTHESIS OF NANOPHASE MATERIALS

P. Milani[1], S. Iannotta[2], F. Biasioli[2], P. Piseri[1], E. Barborini[1]
[1]INFM-Dipartimento di Fisica, Universita' di Milano, Via Celoria 16, 20133 Milano, Italy
[2]CEFSA-CNR, 38050 Povo di Trento, Italy

ABSTRACT

We present the characterization of supersonic cluster beam deposition as a viable technique for the synthesis of nanostructured materials. Stable and intense cluster beams can be obtained with a pulsed microplasma cluster source. This technique has been applied to produce TiNi nanostructured thin films on various substrates at room temperature. The morphology and the structure of the film are strongly influenced by the precursor clusters. Films characterized by crystallite sizes of a few tens of nanometers can be grown without recrystallization by thermal annealing. The stoichiometry of the original TiNi alloy is maintained.

INTRODUCTION

Recently low energy supersonic cluster beam deposition (LESCBD) has gained a considerable attention as a viable technique for the synthesis of nanostructured thin films [1]. The properties of clusters as building blocks can be adjusted by changing their size prior to deposition; if the clusters retain their individuality once deposited, it is possible to synthesize a material with tunable physico-chemical properties. An essential requisite for the use of LESCBD, in alternative to more traditional synthesis routes, is the capability of producing beams with high intensity, stability and tunability in terms of cluster mass distribution.

Here we present a source of pulsed supersonic cluster beams able to provide long-time stability, high deposition rates and control on cluster mass distribution suitable for an efficient production of refractory material nanostructured films.

We have used LESCBD to deposit TiNi nanostructured thin films. The synthesis of thin films of shape memory alloys, with well-controlled and reproducible properties, is a key factor for the development and fabrication of micromechanical devices [2-4]. TiNi alloys are known to exhibit shape memory properties and are considered promising candidates for a variety of applications such as microactuators and micromachines [5-7]. The understanding and control of martensitic transformations in thin films is more difficult than in bulk samples mainly because of the role played by the film-substrate interaction. Together with film-interface effects other parameters as degree of crystallinity, the stoichiometry and the presence of contaminants affect the martensitic transformation [2, 7-9]. The most widely adopted technique for the deposition of TiNi thin films is sputtering under controlled atmosphere [2-4, 10]. This method allows a good control of stoichiometry but produces amorphous films which must be annealed (temperature range 700-900 K) during or after deposition to induce the crystallization necessary to obtain the shape memory effect [2, 3].

Compared to sputtering, LESCBD allows the deposition on films characterized by a nanocrystalline structure with a substrate at room temperature. Cluster mass distribution and kinetic energies influence nanocrystalline film growth. The refinement of grain size can strongly modify the structural and thermodynamic properties of shape memory alloys [11].

Mat. Res. Soc. Symp. Proc. Vol. 581 © 2000 Materials Research Society

EXPERIMENT

The cluster beam deposition apparatus is schematically sketched in Fig. 1. It consists of three differentially pumped high vacuum chambers separated by two skimmers. The cluster source is located in the first chamber; the second one contains the substrate manipulator to intercept the beam for the deposition. The third chamber hosts a linear Time of Flight (TOF) mass spectrometer for cluster mass distribution characterization [12].

The pulsed microplasma cluster source (PMCS) is based on the following principle: a He pulse is directed against a target and it is ionized by a pulsed discharge fired between the target (cathode) and an electrode (anode). The target ablation is obtained by He plasma sputtering. The PMCS is shown in Fig. 1, it consists of a ceramic body with a channel drilled to intersect perpendicularly a larger cylindrical cavity. The channel hosts two rods of the material to be vaporized. A solenoid pulsed valve faces one side of the cavity. A removable nozzle closes the other side of the cavity. For the production of TiNi films we used two 6 mm TiNi rods, the starting material was manufactured in a graphite crucible by inductive heating of electrolytic Ni and grade 1-ASTM Ti. After hot forging, the rods were obtained by electroerosion.

The principle of operation can be resumed as follows:

- The rods face each other in a cavity of 1.8 cm^3 of volume, hence the discharge is not constrained to fire into the gap between the electrodes nor the carrier gas is constrained to flush in the gap;
- the pulsed valve nozzle does not face the gap but the cathode surface (see fig. 1a);
- the front plate of the pulsed valve, modified to be insulating, is few millimeters far from the cathode.

The solenoid valve backed with a pressure of 8 bar, delivers He pulses with an opening time of few hundreds of microseconds. An intense helium jet is formed towards the cathode surface facing the valve. In this region the gas density is substantially higher than in the rest of the cavity. During standard operation the mean He pressure in the source cavity is of roughly 4000 Pa. Just before the valve closing, a voltage ranging from 500 V up to 1500 V is applied to the electrodes, causing the firing of the discharge and the production of the plasma. The ablation occurs when He plasma strikes the cathode surface removing atoms via sputtering. The electrode surface where ablation occurs is very small and comparable to what could be obtained in the case of laser vaporization. Well-defined paths can be burned on the cathode, which is constantly rotated along its axis by a stepping motor external to vacuum to allow constant ablation conditions over days.

A very important feature of PMCS is the highly localized and efficient target sputtering process in the source cavity. The ablated material does not preferentially accumulate on the counter electrode (the anode), since we can select the position of ablation by controlling where, the helium jet, exiting the valve, strikes the cathode. This position can be chosen in order to avoid the formation of an anode deposit which would lead to a short circuit of the electrodes during source operation. This feature together with the possibility of decoupling the cluster residence time, before the expansion, from the target ablation, improve the beam intensity, stability and control on mass distribution.

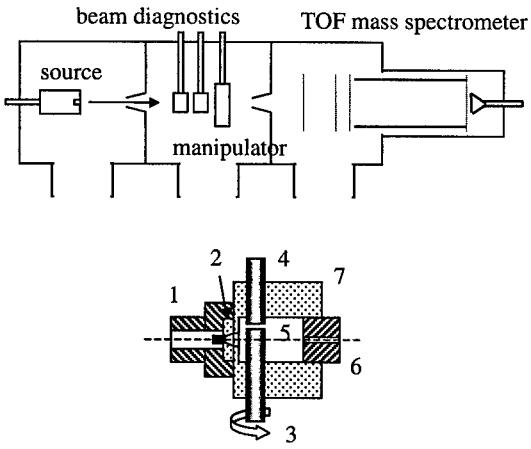


Fig.1 Schematic diagram of the apparatus. The expanded view of the PMCS shows: 1) pulsed valve; 2) insulating valve nozzle; 3) cathode; 4) anode; 5) thermalization cavity; 6) cylindrical nozzle; 7) ceramic main body.

RESULTS

Cluster beams

The main source parameters affecting the cluster intensity and mass distribution have been studied with a time-of-flight mass spectrometer [13]. Neutral clusters have been ionized using the fourth harmonic of a Nd:Yag laser (266 nm). A typical mass spectrum is shown in Fig. 2. Small clusters are not detected due to their high ionization potential; the atomic species in the spectrum are probably due to fragmentation of larger clusters. The shape of the distribution can be fitted with several lognormal functions, as it is common for gas phase grown particles [14]. The cluster mass distribution is affected by several parameters such as source and nozzle geometry and by the nature of the ablation process. In Fig. 3 we show mass spectra of TiNi clusters produced by varying the pulsed valve opening time and hence the He pressure in the source during the ablation.

The cluster distribution depends on the gas pressure in the source during the discharge and in particular the center of the mass distribution moves towards larger masses by increasing the gas pressure.

Thin film deposition

Fig. 4 shows two atomic force microscope micrographs a film deposited with TiNi cluster beams on Si substrates at room temperature. The deposition rate was 6nm/min and the film thickness 300 nm. A portion of the substrate has been masked in order to produce a step in the film. Fig. 4A shows, at low magnification, the film region near the step.

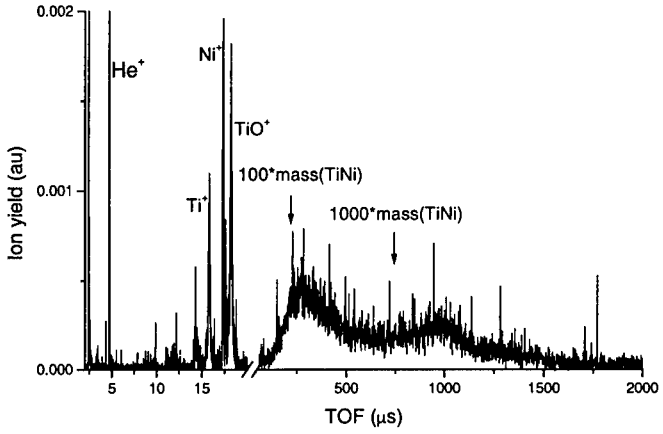


Fig.2 Typical time-of-flight mass spectrum of neutral TiNi clusters as exiting from the source. The atomic species are the product of fragmentation due to multiphoton ionization of small clusters, which are depleted from the beam.

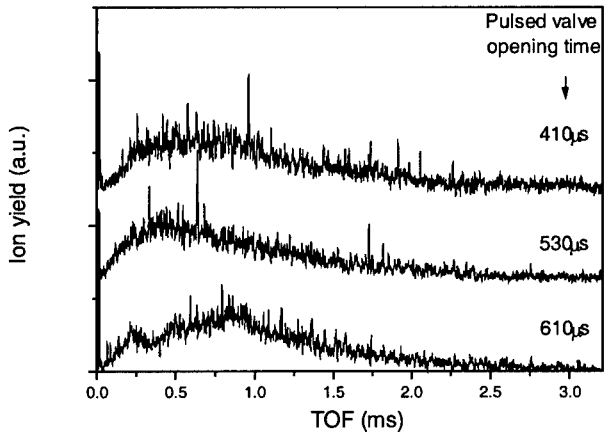


Fig.3 Time-of-flight mass spectra of TiNi clusters produced with different gas pressure in the source during ablation. Note the evolution towards a multimodal distribution. The mass of the clusters ranges roughly from 100 TiNi units up to several thousands TiNi units.

We can observe a region where the growth of island is visible indicating that the deposited particles have a high mobility on the substrate and that they can coalesce. These island-like structures have been observed also in other systems produced by LESCBD of metallic clusters

[15]. Fig 4B shows, at higher magnification, the central region of the film characterized by grains with a diameter of several tens of nanometers.

Transmission electron microscopy characterization [16] of nanostructured TiNi films shows a different structure depending on the mass distribution of the precursor clusters. Films deposited with small clusters are basically amorphous with a diffuse electron diffraction pattern, while film deposited with large clusters have a nanocrystalline structure with a diffraction pattern typical of TiNi (B2-ordered cubic) and TiO_2 (rutile) crystalline phases.

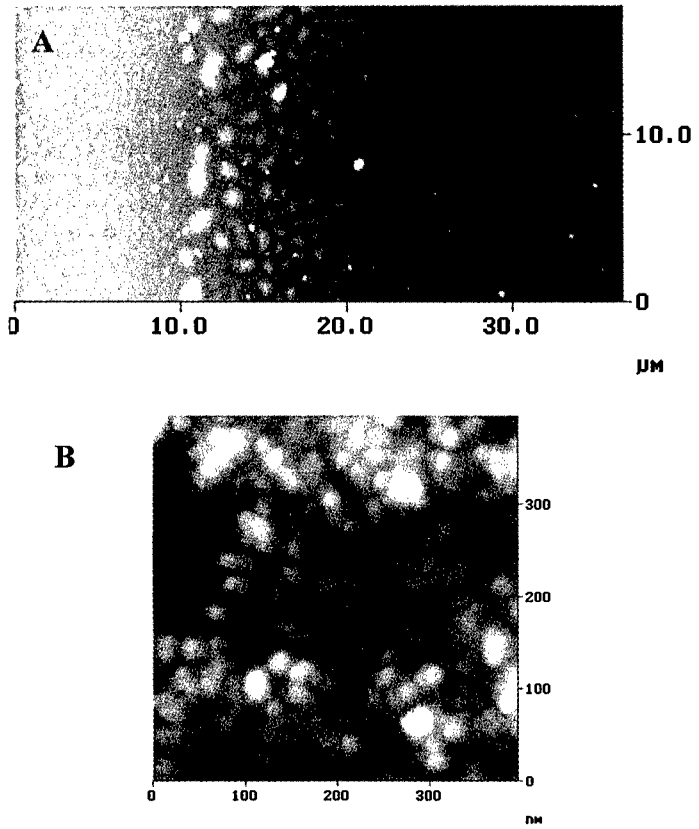


Fig. 4 A) AFM picture of the step edge of a nanostructured TiNi. film taken from a micrograph obtained with a scan size of 60 μm x 60 μm. B) AFM picture of the central part of the film taken with a scan size of 500 nm x 500 nm.

The stoichiometry of TiNi films was checked by energy dispersive X-ray measurements [16]. In the limit of sensitivity of the methods used, results are consistent with the composition of rods used in the source. An ex-situ characterization of the oxygen contamination of the sample was carried out by Auger and X-ray Photoelectron Spectroscopy. A strong presence of Titanium and partial Ni oxidation is present on the surface in all samples. The analysis of depth profiles

shows that in several samples the presence of oxides decreases from the surface towards the inner parts of the films. The combined effect of the mentioned presence of oxides in the beam and of the oxidation processes induced by air exposure, after the growth of films, is very likely the cause of oxygen contamination.

CONCLUSIONS

We have shown that it is possible to deposit nanostructured TiNi thin films with LESCBD. Deposition rates of 6 nm/sec can be achieved with very high stability. The control of cluster beam distribution can be obtained by varying the source parameters. Cluster size plays a major role in determining the film structure: large aggregates can induce the formation of nanocrystalline films on substrate kept at room temperature. Further work is in progress to investigate the influence of different nanostructures, film stoichiometry and oxygen contamination on the mechanical properties and on the martensitic transformation of the films.

ACKNOWLEDGEMENTS

Financial support from CNR (Progetto Finalizzato MSTAII) and INFM is gratefully acknowledged. We thank Prof. S. Ceresara and A. Tuissi for providing the TiNi rods, S. Gialanella for TEM characterization, A. Podesta' for AFM measurements.

REFERENCES

1. P. Milani, S. Iannotta, Cluster Beam Synthesis of Nanostructured Materials, Springer Verlag, Berlin, (1999)
2. D.S. Grumon, J.A. Litton, Z. Zhoo, T.J. Pence, J. Phys. IV, Colloque **C-8**, 665 (1995)
3. K.R.C. Gisser, J.D. Busch, A.D. Johnson, A.B. Ellis, Appl. Phys. Lett. **61**, 1632 (1992)
4. J.D. Busch, A.D. Johnson, C.H. Lee, D.A. Stevenson, J. Appl. Phys. **68**, 6224 (1990)
5. see, for example: J. Phys IV. (Paris), Colloque **C-8** (1995)
6. see, for example: J. Phys IV. (Paris), Colloque **C-4** (1991)
7. Q. Su, S.Z. Hua, M. Wuttig, Trans. Mat. Res. Soc. Jpn. **18B**, 1057 (1994)
8. K. Ikuta, H. Fujishiro, M. Hayashi, T. Matsuura, Proc. 1st Int. Conf. on Shape Memory and Superelastic Technologies, Pacific Grove, Ca, (1994)
9. A. Ishida, A. Takei, M. Sato, S. Miyazaki, Mat. Res. Soc. Symp. Proc. Vol. 360, 381 (1995)
10. M. Bendaham, P. Canet, J.-L. Seguin, H. Carchano, Mater. Sci. Eng. B **34**, 112 (1995)
11. J.D. Shi, et al., Mat. Res. Symp. Proc. vol. 400, 221 (1996)
12. E. Barborini, P. Piseri, P. Milani, J. Phys. D: Appl. Phys. **10**, L105 (1999)
13. P. Piseri, P. Milani S. Iannotta, Int. J. Mass Spectrom. Ion Proc. **135**, 23 (1996)
14. J. Soederlund, et al. Phys. Rev. Lett. **80**, 2386 (1998)
15. G. Fuchs, et al., Phys. Rev. B **44**, 3926 (1991)
16. E. Barborini et al., Nanostruct. Mater. **10**, 1023 (1998)

Nanocomposites

SYNTHESIS AND CHARACTERIZATION OF CdSe/CdS CORE–SHELL and CdSe/CdS COMPOSITES

M. Azad Malik,[a] Paul O'Brien,[b*] and N. Revaprasadu[ac]

a. Department of Chemistry, Imperial College of Science, Technology and Medicine, Exhibition Road, London, SW7 2AZ, UK.
b. Manchester Materials Science Centre and Department of Chemistry, Manchester University, Oxford Rd, Manchester M13 9PL.
c. Department of Chemistry, University of Zululand, Private Bag X1001, Kwadlangezwa, 3886. South Africa.
E-mail: p.obrien@ic.ac.uk

ABSTRACT

Highly mono-dispersed CdSe/CdS core-shell and CdSe/CdS composites have been prepared by a novel route involving thermolysis in TOPO using $Cd(Se_2CNMe(^nHex))_2$ and $Cd(S_2CNMe(^nHex))_2$. The absorption band edge (652 nm, 1.90 eV) of the CdSe-CdS core-shell structure is red shifted (22 nm, 0.017 eV) as compared to the CdSe nanoparticles (630 nm, 1.96 eV) whereas the absorption spectrum of the CdSe-CdS composites shows the absorption band edge at (584 nm, 2.12 eV), blue shifted (46 nm, 0.037 eV) as expected. Photoluminescence (PL, $\lambda_{ex.}$ = 400 nm) of both the core-shell (622 nm) and the composites (588 nm) show values close to band edge emission. A sharper emission maximum with a considerable increase of intensity is observed for core-shell structure as compared to that of CdSe whereas the composite showed a broader emission maximum. The TEM images of the CdSe/CdS core-shell nanoparticles show crystalline, spherical particles with the average size of 53 Å (±7 %), a increase of 8 Å than the average size of CdSe (45 Å) nanoparticles, with a narrow size distribution. The High Resolution Transmission Electron Microscopy (HRTEM) showed lattice spacing intermediate between those for CdSe and CdS as is observed by Selected Area Electron Diffraction (SAED) and X-ray patterns (hexagonal phase). As expected no interface can be observed by HRTEM between CdSe core and CdS shell. The TEM image of the CdSe-CdS composites show particles with an average size of 48.7 Å (±10%).

INTRODUCTION

Unique physical and chemical properties due to quantum confinement effects have been reported for a wide range of nano-dimensional semiconductor materials.[1-6] The high surface to volume ratio of these materials means that their surfaces play an important role in determining their electronic and optical properties. Surface modification of these particles has been the subject of intensive investigation. The synthesis of core-shell structures, the epitaxial growth of a second material on a core of another material forming a heterostructure has generated a lot of interest. Composite structures involving nanoparticle passivation by organic ligands such as thiopyridine,[4] thiolates,[5] and 2,2' bypyrimidine,[6] and core/shell structures such as CdSe/ZnS,[7] CdSe/ZnSe,[8,9] and CdSe/CdS[10-12] have been reported. Such systems show an increase in photoluminescence efficiency and reduced fluorescence lifetimes.

In this paper we report the synthesis of a CdSe/CdS core-shell structure and a CdSe/CdS composites using the air stable precursors, $[Cd(Se_2CNMe(Hex))_2]$ and $[Cd(S_2CNMe(Hex))_2]$.

Mat. Res. Soc. Symp. Proc. Vol. 581 © 2000 Materials Research Society

EXPERIMENTAL

Chemicals

Tri-*n*-octylphosphine oxide (TOPO), tri-*n*-octylphosphine (TOP), *n*-methylhexylamine, and carbon disulfide were purchased from Aldrich Chemical Company Ltd and methanol and toluene from BDH.

TOPO was purified by vacuum distillation at ca. 250 °C (0.1 torr). The solvents used for air sensitive chemistry were distilled , deoxygenated under a nitrogen flow and stored over molecular sieves (type 4 Å, BDH) before use.

Instrumentation

Ultra violet/Visible (UV/Vis) Absorption Spectroscopy: A Philips PU 8710 spectrophotometer was used to carry out the optical measurements of the semiconductor nanoparticles. The samples were placed in silica cuvettes (1 cm path length).

Photoluminescence Spectroscopy: A Spex FluoroMax instrument with a xenon lamp (150W) and a 152 P photomultiplier tube as a detector was used to measure the photoluminescence of the particles. Good spectral data was recorded with the slits set at 2mm and an integration time of 1 second. The samples were quantitatively prepared by dissolving 25 mg in 10 ml toluene.

The samples were placed in quartz cuvettes (1 cm path length) used as blank for all measurements. The wavelength of excitation was set at a lower value than onset of absorption of a typical sample.

X-Ray Diffraction (XRD): X- Ray diffraction patterns were measured using a Philips PW 1700 series automated powder diffractometer using Cu- K(radiation at 40kV/40mA with a secondary graphite crystal monochromator. Samples were prepared on glass slides (5 cm). A concentrated toluene solution was slowly evaporated at room temperature on a glass slide to obtain a sample for analysis.

Electron microscopy: A Joel 2000 FX MK 1 operated at 200KV electron microscope with an Oxford Instrument AN 10000 EDS Analyser was used for the conventional TEM (transmission electron microscopy) images. Selected area electron diffraction (SAED) patterns were obtained using a JEOL 2000FX MK 2 electron microscope operated at 200kV. The samples for TEM and SAED were prepared by placing a drop of a dilute solution of sample in toluene on a copper grid (400 mesh, agar). The excess solvent was wicked away with a paper tip and completely dried at room temperature.

Synthesis

All experiments were carried out by using dry solvents and standard Schlenck techniques. Glassware was dried in the oven before use.

(i) Preparation of CdSe/CdS core-shell nanoparticles

In a typical synthesis, $[Cd(Se_2CNMe(Hex))_2]$ (0.8 g) was dissolved in tri-*n*-octylphosphine (TOP) (15 ml). This solution was then injected into hot (250° C) tri-*n*-octylphosphine oxide (TOPO) (20 g) and kept at this temperature for 30 minutes. After this time a small amount of sample was syringed out of the reaction mixture for characterization as the CdSe nanoparticles. Then a solution of $[Cd(S_2CNMe(Hex))_2]$ (0.5 g) in TOP (10 ml) was injected into the deep red reaction mixture. The reaction was allowed to proceeded for a further 30 minutes and the resulting solution was cooled to *ca.* 70° C. Methanol was then added and a

flocculant precipitate formed which was separated by centrifugation. CdS and CdSe nanocrystals were also synthesized as described previously.[13]

(ii) Preparation of CdS/CdS composites

$[Cd(Se_2CNMe(Hex))_2]$ (0.5g) and $[Cd(S_2CNMe(Hex))_2]$ (0.5 g) were dissolved in tri-*n*-octylphosphine (15 ml). This solution was injected into hot (250° C) tri-*n*-octylphosphine oxide (TOPO) (20 g) and kept at this temperature for 45 minutes. The resulting solution was then cooled to *ca.* 70° C, and excess methanol was added, forming a flocculant precipitate. The precipitate was seperated by centrifugation and dissolved in toluene.

RESULTS AND DISCUSSION

We observe differences in the optical spectra of the core-shell type composites and the simple composites (Figures 1 and 2). The absorption band edge (652 nm, 1.90 eV), due to the first electronic transition (1s-1s) of the CdSe-CdS core-shell structure is red shifted (22 nm, 0.02 eV) as compared to the CdSe nanoparticles (630 nm, 1.96 eV) (Figure 1). This red shift, consistent with relaxation of quantum confinement, is due to the growth of the CdS shell. The overall shape of the spectrum is similar to that of CdSe, however a slight sharpening of the features at 535 and 613 nm is observed which may suggest a narrower size distribution. The absorption spectrum of the simple composites shows a sharp excitonic feature at (417 nm) with the absorption band edge at (584 nm, 2.12 eV) (Figure 2). The blue shift of (46 nm, 0.037 eV) in relation to CdSe is indicative of alloying.[9,10]

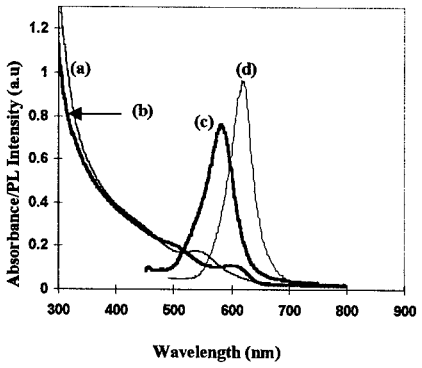


Figure 1. Optical spectra of CdSe/CdS core-shell and CdSe showing absorption spectra of (a)CdSe (b) CdSe/CdS and PL spectra of (c) CdSe (d) CdSe/CdS

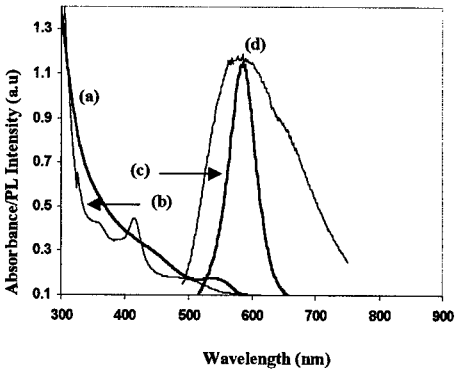


Figure 2. Optical spectra of the composite CdSe-CdS and CdSe showing absorption spectra of (a) CdSe (b) CdSe-CdS and PL spectra of (c) CdSe (d) CdSe-CdS

Photoluminescence (PL, $\lambda_{ex.}$ = 400 nm) of both the core-shell (622 nm) and composites (588 nm) show values close to band edge emission. The intensity of the emission maximum is considerably increased in the core-shell structure as compared to that of CdSe. The emission spectrum of the composite is broader than that of CdSe, which could be due to a broad size distribution. However the sharp band edge and the observed size distribution from the TEM

micrographs suggest a narrow size distribution. The optical data provides evidence that a CdSe/CdS core-shell type structure and a CdSe-CdS composite have been synthesized.

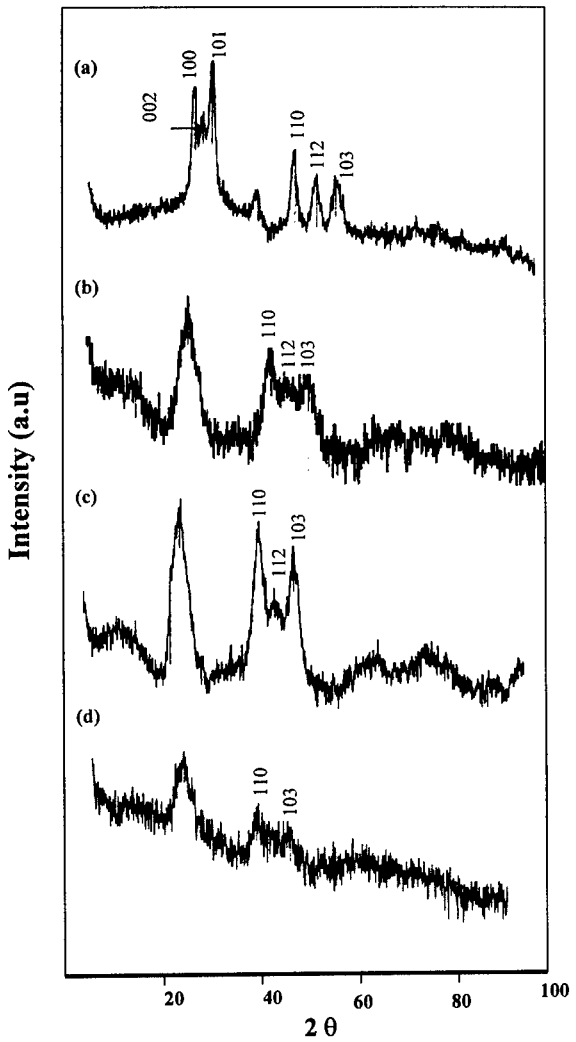


Figure 3. X-ray diffraction patterns of (a) CdS (b) CdSe (c) CdSe/CdS core/shell and (d) CdSe-CdS composites

The X-ray diffraction pattern of CdSe/CdS core/shell shows broad peaks along the (110), (103) and (112) planes that are assigned to the hexagonal phase of CdSe suggesting that the diffraction is predominantly due to the CdSe core (Figure 3c). The diffraction pattern show an increased coherence length, hence the sharper lines, an indication of the epitaxial growth of the shell. Similarly, in the comparison of the SAED patterns, the CdSe/CdS pattern is intermediate between that for CdS and that for CdSe as expected. The X-ray diffraction of the CdSe-CdS composite shows broad poorly, defined peaks along the (110) and (103) planes (Figure 3d). The shift in the peaks to lower 2θ values and the blue shift in the absorption spectrum are evidence for composite formation. The peaks along (002), (100) and (101) planes shown in the hexagonal CdS diffraction pattern are not visible in the CdSe and CdSe/CdS patterns due to broadening of the peak in the region $d\theta \cong 20\text{-}25°$.

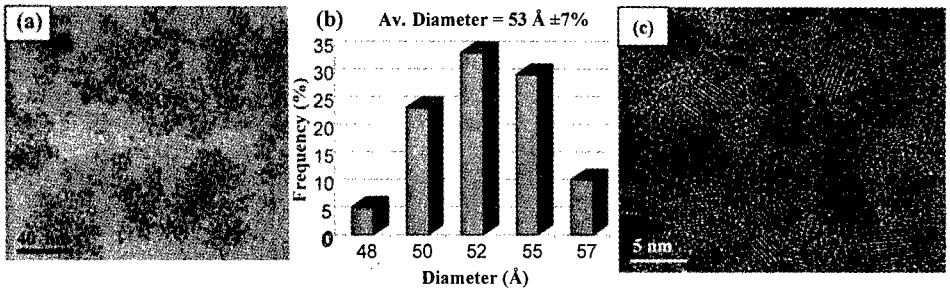


Figure 4. CdSe/CdS core shell nanoparticles (a) TEM image (b) particle size distribution and (c) HRTEM image.

The TEM images of the CdSe/CdS core-shell nanoparticles show well-defined, spherical particles (Figure 4a) with the average size of 53 Å (±7 %) with a narrow size distribution. The average size of CdSe nanoparticles is 45 Å, which indicates an increase of 8 Å due to CdS shell in core/shell nanoparticles. The crystallinity of the core/shell structure is confirmed in an HRTEM image (Figure 4c) which shows clear lattice fringes for the CdSe core (hexagonal phase). The HRTEM showed lattice spacing intermediate between those for CdSe and CdS as is observed by SAED and X-ray patterns. As expected no interface can be observed by HRTEM between CdSe core and CdS shell. The TEM image of the CdSe-CdS composites show particles with an average size of 48.7 Å (±10%) (Figure 5a). The 'darker' particles appearing in the micrograph are indicative of a dense agglomeration of particles. The standard deviation (±10%) is higher than that of the core/shell sample (±7%), however this cannot alone account for the broad emission spectrum.

The EDAX pattern and the ICP analysis confirmed the presence of Cd, Se, and S in the core-shell and the composite nanoparticles. The peak for phosphorus in each case was due to the capping of the particles by TOPO which was further confirmed by shift in IR band (from ν1146 to 1120 cm^{-1}, P=O) for TOPO. The shift of the ν(P=O) frequency to lower values is due to the binding of TOPO to Cd^{2+} sites on the CdS shell.

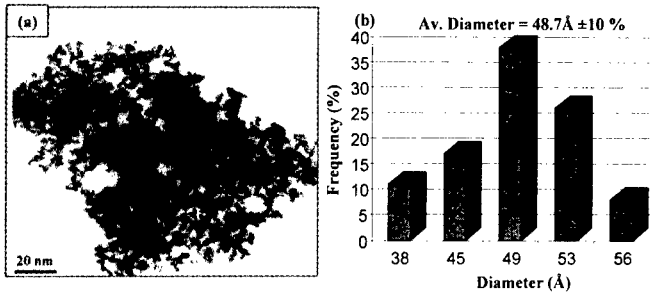


Figure 5. CdSe/CdS composite nanoparticles (a) TEM image and (b) particle size distribution.

CONCLUSIONS

Highly mono-dispersed CdSe/CdS core-shell and CdSe/CdS composites have been prepared by a novel route involving thermolysis in TOPO using $Cd(Se_2CNMe(^nHex))_2$ and $Cd(S_2CNMe(^nHex))_2$ as single molecule precursors in a one pot synthesis. Clear differences have been observed in the optical spectra of CdSe/CdS core-shell and CdSe/CdS composites indicating the difference in structures. The absorption spectra showed a red shift (22 nm, 0.017 eV) for core-shell and a blue shift (46 nm, 0.037 eV) for composite structure in relation to CdSe nanoparticles as expected. Photoluminescence (PL, $\lambda_{ex.}$ = 400 nm) showed a sharper emission maximum with a considerable increase in intensity for core-shell structure as compared to that of CdSe whereas the composite showed a broader emission maximum. TEM and HRTEM showed crystalline nanoparticles with a narrow size distribution for both structures.

ACKNOWLEDGEMENTS

We thank the Royal Society and the National Research Foundation (SA) for support to NR and a program of collaboration between UZULU and ICSTM. P.O.B thanks the EPSRC for grant. P.O.B is the Sumitomo/STS visiting Professor of Materials Chemistry at IC and Professor of Inorganic Materials at The Manchester Materials Science Centre and The Chemistry Department. We also thank Richard Sweeney (IC) for X- ray diffraction and G. Wakefield (Oxford) and K. Pell (QMW) for the electron microscopy.

REFERENCES

1. A. Henglein, Chem. Rev., **89,** 1861(1989).
2. H. Weller, Adv. Mater., **5**, 88 (1993).
3. M. L. Steigerwald and L. E. Brus, Acc. Chem. Rev., **23**, 183 (1990).
4. H. Noglik and W.J. Pietro, Chem. Mater.,**6**, 1593(1994).
5. J. E. Katari, V. L. Colvin and A. P. Alivisatos, J. Phys. Chem., **98**, 4109 (1994).
6. T.Trindade, X. Zhang, P.O' Brien, Chem. Mater., **9**, 523 (1997).
7. M. Danek, K. F. Jensen, C. B. Murray, and M. G. Bawendi, Chem. Mater., **8**, 173 (1996).
8. M. A Hines and P. Guyot-Sionnest, J. Phys. Chem., **100**, 468 (1996).
9. A. R. Kortan, R. Hull, R. L. Opila, M. G. Bawendi, M. L. Steigerwald, P. J. Carrol and L. E. Brus, J. Am. Chem. Soc., **112**, 1327 (1990).
10. X. Peng, M. C. Schlamp, A. V. Kadavanich and A. P. Alivisatos, J. Am. Chem. Soc., **119**, 7019 (1997).
11. Y. Tian, T. Newton, N. A. Kotov, D. M. Guldi, and J. H. Fendler, J. Phys. Chem. **100**, 8927 (1996).
12. U. Banin, M. Bruchez, A. P. Alivisatos, T. Ha, S. Weiss and D. S. Chemla, *J. Chem. Phys.*, **110**, 1195 (1999).
13. B. Ludolph, M. A. Malik, N. Revaprasadu and P. O'Brien, J. Chem. Soc. Chem,. Commun., 1849 (1998).

MAGNETIC ENTROPY CHANGE OF NANOCOMPOSITES COMPOSED OF A SILVER MATRIX AND GRAINS OF IRON-OXIDE OR -NITRIDE

T. A. YAMAMOTO, M. TANAKA, K. SHIOMI, *T. NAKAYAMA, K. NISHIMAKI, T. NAKAGAWA, **T. NUMAZAWA, M. KATSURA and *K. NIIHARA

Department of Nuclear Engineering, Osaka University, 2-1 Yamadaoka, Suita, Osaka 565-0871, Japan. takao@nucl.eng.osaka-u.ac.jp

*Institute of Scientific and Industrial Research, Osaka University, 8-1 Mihogaoka, Ibaraki, Osaka 567-0047, Japan

**Magnet Laboratories, National Research Institute for Metals, 1-2-1, Sengen, Tsukuba 305-0003, Japan

ABSTRACT

Magnetocaloric effect of nanocomposites composed of iron-oxide or iron-nitride grains dispersed in a silver matrix was studied by calculating magnetic entropy change ΔS induced by a change in applied magnetic field H. These nanocomposites were synthesized by the inert gas condensation technique and nitridation by heat treatment in an ammonia gas stream. Average sizes of the iron-containing grains were 10-35 nm. Magnetic phases in the materials were Fe_3O_4 or γ-Fe_2O_3 for the oxide-composites and γ'-Fe_4N or ε-Fe_3N for the nitride-composites. Values of the ΔS were obtained by applying a thermodynamic Maxwell's relation, $(\partial S/\partial H)_T = (\partial M/\partial T)_H$, to data set of magnetization M measured at various temperatures T. They clearly indicated significant enhancement due to the nanostructure as predicted.

INTRODUCTION

The magnetocaloric effect is a process converting magnetic energy into thermal energy, which is described by a relation of $Q = T\Delta S$ where ΔS is entropy change of magnetic spins contained in a substance and Q is heat absorbed by it [1]. This ΔS is accompanied by an order-disorder transition of the magnetic spin system induced by applying and removing external magnetic field. Most substance gives only a trivial ΔS with an ordinary field strength at ambient temperatures, while some paramagnets and ferromagnets can give significant ΔS and work as magnetic refrigerants. However, they still require a large field of several Tesla even at cryogenic temperatures, lower than 20K. In early 90's, it was predicted that some kind of nanostructured material would show highly enhanced magnetocaloric effect and make the magnetic refrigeration system work even with lower fields and at higher temperatures [2]. The required material is such that consists of ferromagnetic nanograins behaving as the unit magnetic moment in the material. When the nanograins are single-domained and magnetically isolated each other, and their magnetocrystalline anisotropy energies are smaller than the thermal energy, the superparamagnetism occurs. This magnetism may be the simplest of those expected to occur in the magnetic nanocomposites, and is reasonably described by the classical Langevin paramagnetism model. Its magnetocaloric effect was also described on the basis of this model and thermodynamics, indicating a considerable enhancement of ΔS [3].

We have synthesized nanocomposites composed of a silver matrices and $10-30$ nm nanograins of iron-oxide [4] or iron-nitride [5] by the inert gas condensation method, and confirmed superparamagnetism to occur in some of them. The magnetic species in them was mainly of γ-Fe_2O_3, γ'-Fe_4N or ε-Fe_3N. These two nitrides are both of ferromagnetism and

Mat. Res. Soc. Symp. Proc. Vol. 581 © 2000 Materials Research Society

regarded as attractive magnetic components in the nanocomposite because of some advantages over the iron oxides and metal: their magnetic moments are larger than those of the oxides and comparable to that of metallic iron, and these nitrides are chemically stabler than metallic iron especially in the nanophase. The γ'-Fe_4N phase is practically stoichiometric and in fcc structure, while the ε-Fe_3N phase has a wide nonstoichiometry designated by the formula of $Fe_{2\text{-}4}N$ and in hcp structure. This variety would also provide versatility in magnetism of the resultant composites. We have evaluated ΔS of our superparamagnetic nanocomposites of iron-oxide and made sure of the enhancement of their magnetocaloric effect caused by the nanostructure [6]. The purpose of this work is to evaluate ΔS of the nitride nanocomposites and compare them with those of the oxide nanocomposites.

NANOCOMPOSITE MATERIALS

The nanocomposites composed of iron-oxide grains and a silver matrix were obtained by the inert gas condensation involving coevaporation of metallic iron and silver from resistance heated boats in an ultrahigh vacuum chamber filled with a static helium gas. The helium gas quenched the vapors just above the boats to form nanoparticles, which were collected on the surface of a rotating cylinder cooled by liquid nitrogen. Only iron particles were oxidized by O_2 gas introduced slowly to form grains mainly of ferrimagnetic γ-Fe_2O_3. These iron-oxide grains were converted into nitride grains by a heat treatment at 450°C in a gas stream containing NH_3 after reduction in H_2 gas at 350°C. Metallic silver does not react with NH_3. During nitridation reaction, the nitrogen potential was controlled by adjusting the flow rate and adding H_2 gas into the stream in order to form selectively γ'-Fe_4N or ε-Fe_3N. These composites are abbreviated as ONC (oxide containing nanocomposite), γ'-NNC (γ'-Fe_4N containing --) and ε-NNC (ε-Fe_3N containing --) in the below.

The magnetization of the materials was measured with a SQUID magnetometer at various temperatures from room temperature down to the lowest temperature (7.5 K) by sweeping the applied field between ± 5 Tesla. Grain sizes in the composites obtained were determined by a transmission electron microscope. Grain sizes in the ONC were about 15 nm and those of NNC were about 35 nm. Their iron contents were evaluated by the energy dispersive x-ray fluorescence spectroscopy (EDX). The present ONC contained 9 at% iron and the NNCs 6 at% iron. Phases of oxides and nitrides existing in the composites were determined by x-ray absorption spectroscopy technique [7].

EVALUATION OF ENTROPY CHANGE

In this work, magnetic entropy changes, ΔS, of the samples were evaluated from their data sets of $M-H$ relations measured at various temperatures, T, where M is magnetization, H applied magnetic field. By using thermodynamic Maxwell's relation,

$$(\partial S/\partial H)_T = (\partial M/\partial T)_H, \qquad (1)$$

these data sets were converted into ΔS accompanied by a demagnetization, $H \rightarrow 0$, at T.

$$\Delta S = \int_H^0 (\partial S/\partial H)_T dH = \int_H^0 (\partial M/\partial T)_H dH. \qquad (2)$$

This ΔS was numerically calculated by substituting the magnetization data, in which

differentials and integrals were replaced with finite differences and trapezoid areas, respectively. Equation (1) is valid only when M is regarded as a state property determined by independent variables of T and H. The ideal superparamagnet has magnetization described as vector sum of magnetic moment vectors which are independent of each other, which is expressed by using Langevin function $L(x)$ as,

$$M = N\mu L(x), \tag{4}$$

$$L(x) = \coth x - 1/x, \tag{5}$$

where $x = \mu H / k_B T$, k_B is the Boltzmann's constant, μ is size of the elemental moment, N is number of moments existing in the substance. By inserting eqs.(4) and (5) into eq.(2), formulation for ΔS of the ideal superparamagnet is obtained as

$$\Delta S / N k_B = -1 + x\coth x - \ln\{(\sinh x)/x\}. \tag{6}$$

RESULTS AND DISCUSSION

Figure 1 shows M vs. H/T plots of the present ONC and γ'-NNC measured at temperatures higher than each threshold temperature, which indicates that each plot sets fall onto a single curve, and therefore, that the nanocomposites may be regarded as superparamagnets in these temperature regions. At lower temperatures, the remainder plots considerably deviated from the curves. On the contrary the ε-NNC shows widely scattered plots even at higher temperatures as shown in **Fig. 2**. These remarkable differences in magnetization behavior among the three materials of similar iron concentrations are considered to reflect differences mainly in properties of the magnetic species existing in them. The saturation magnetization, σ_S, possessed by an iron atom in the relevant species are

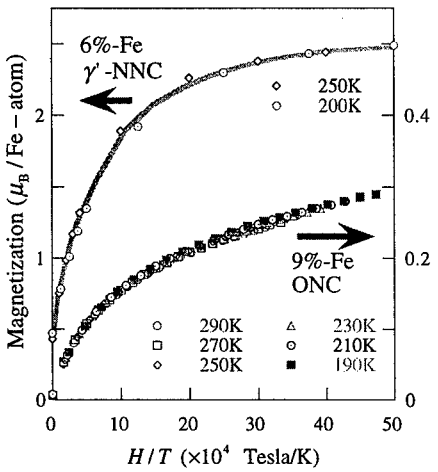


Fig.1 M vs. H/T plots of ONC and γ'-NNC measured at various temperatures. Note each has individual ordinate scale.

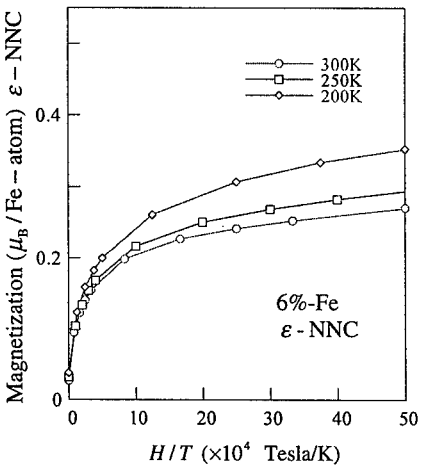


Fig.2 M vs. H/T plots of ε-NNC measured at various temperatures. Note each has individual ordinate scale.

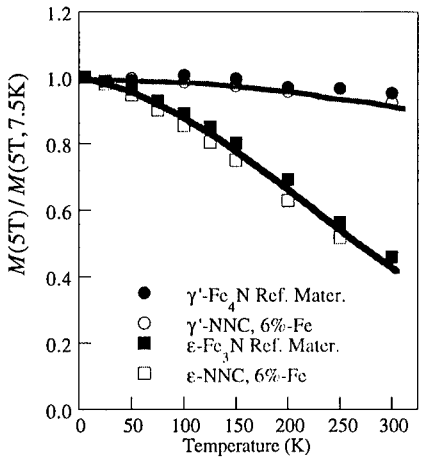


Fig.3 Temperature dependencies of magnetzation under 5 Tesla of γ' - and ε - NNC, normalized to values at 7.5 K.

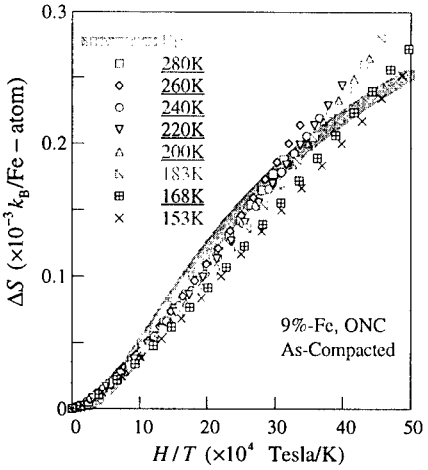


Fig.4 ΔS vs. H/T plots of ONC . The curve is of an ideal superparamagnet with optimized parameters.

$$\sigma_S(\gamma'\text{-}Fe_4N) = 2.0\mu_B > \sigma_S(\varepsilon\text{-}Fe_3N) = 1.5\mu_B > \sigma_S(\gamma\text{-}Fe_2O_3) = 1.2\mu_B,$$

where μ_B is size of the Bohr magneton. The nanograin in the present γ'-NNC is of the magnetically strongest phase and its geometric size is also larger than that in ONC because of the grain growth, so that its magnetic moment size is largest among the three. These facts account for the largest M values and the steepest increasing with increasing H/T near the origin in **Fig. 1**. Since the ordinates in **Fig.1** are expressed as M for each iron atom assuming it exists as Fe_2O_3 or Fe_4N, $M(\gamma'\text{-}Fe_4N)$ should never have exceeded $\sigma_S(\gamma'\text{-}Fe_4N) = 2.0\mu_B$. This too large moment size could be due to an uncertainty in determining iron concentration with EDX.

The widely scattered plots found in **Fig.2** for ε - NNC is ascribed to the intrinsic temperature dependence of $\sigma_S(\varepsilon\text{-}Fe_3N)$. Generally, σ_S decreases with increasing temperature and disappears at the transition temperature, T_C. The Curie's temperatures of these nitrides are reported as

$$T_C(\gamma'\text{-}Fe_4N) = 761 \text{ K} \quad \text{and} \quad T_C(\varepsilon\text{-}Fe_3N) = 398 \text{ K}.$$

This relatively lower T_C of ε - Fe_3N has possibly caused the significant temperature dependence even at the high temperatures as shown in **Fig. 2**. Recall the reason why exhibition of an single curve by M vs. H/T plots is an evidence of the superparamagnetism is based on the temperature independency of μ in eqs.(4-5). In fact, this temperature dependence was clearly observed on the ε - NNC as shown in **Fig.3**, in which M at 5 Tesla, M(5T), measured at various T was plotted as values normalized with those at 7.5 K. M(5T) may be regarded as σ_S as the first approximation, because their $M-H$ curves have exhibited considerable saturation under 5 T. The ε - NNC showed a steep descent as temperature increases, while the γ' -NNC showed an insignificant change. In this figure, values of reference materials examined with

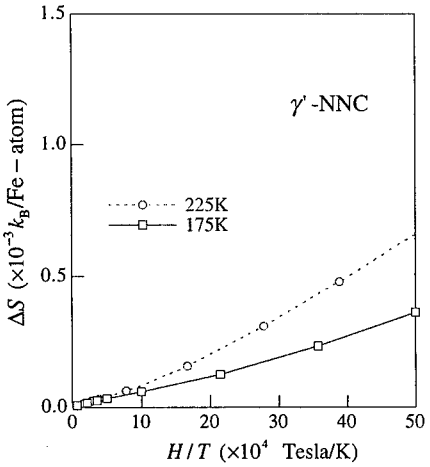


Fig.5 Magnetic entropy changes of γ'-NNC plotted against H/T.

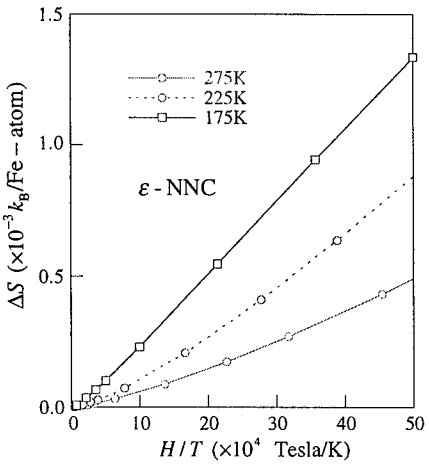


Fig.6 Magnetic entropy changes of ε-NNC plotted against H/T.

XRD are plotted together and they exhibited behavior same with the present samples. Thus, the present γ'- and ε-NNCs really contains mono-phased γ'- and ε-nitrides.

Magnetic entropy changes were evaluated by substituting these data into eqs. (1) -(2) and are plotted in **Figs. 4-6** against H/T for the ONC, γ'- and ε-NNC, respectively. The reliability of the present calculations was examined by checking the reproducibility of results of analytical formula when simulated sparse data were loaded. Since M of the ONC were measured at small intervals both in H- and T-domains so that errors accompanied with the numerical calculation were insignificant. However, those of nitrides nanocomposites were measured with larger intervals, that resultant ΔS were estimated to be relatively smaller than true ones about by 20% at most.

It is noted that ΔS(ONC) vs. H/T plots show a clear tendency of falling on a single curve especially at higher temperatures while not those of γ'- nor ε-NNC. Equation (6) predicted such behavior for the ideal superparamagnet. The shaded curve in the figure was obtained by optimizing μ and N for the plots, which corresponds to that the ONC is composed of nanograins containing 6.7×10^3 iron atoms and possessing a magnetic size of $2200\mu_B$. Inconsistency between thus determined two values were explained by taking account of existence of iron atoms magnetically dead. These ΔS(ONC) values were compared with those of the paramagnet, iron aluminum alum with Fe^{3+}, to find that an iron atom in the ONC gives entropy change ca. 10 times as large as that in the alum in spite of employing magnetically reduced species, γ-Fe_2O_3.

Figures 5-6 show advantages of employing the iron nitrides as magnetic species of nanocomposites for magnetic refrigerants. $\Delta S(\gamma'$-NNC) and $\Delta S(\varepsilon$-NNC) were found to be further enhanced; they are larger than ΔS(ONC). ΔS vs. H/T plots of the NNCs shows considerable temperature dependencies in both the figures, indicating invalidity of the Langevin

superparamagnetism model to them. It is noticed that $\Delta S(\gamma'\text{-NNC})$ are a few times of $\Delta S(\text{ONC})$ in spite that its M is almost one-order larger. The magnetic moments in the γ'-NNC could have been too large to be magnetically independent and agglomerated. In fact significant remanences were observed.

Another remarkable point is that ΔS of the ε-NNC is enhanced so as to be several times of the ONC in spite of that its magnetization values are merely comparable to the ONC. It is possibly caused by the temperature dependence of ε-Fe_3N as shown in **Fig.** 3. According to eq.(1) this dependence of magnetization, $(\partial M/\partial T)_H$, of the grains would have contributed to entropy change, $(\partial S/\partial H)_T$ of the composite as well. In other words, ΔS of the ε-NNC consists of two components; one is that due to the orientation of the nanograin's magnetic moments and the other is that due to temperature dependence of ferromagnetic coupling strength between electrons in ε-Fe_3N phase. The latter is significant exclusively in ε-NNC.

SUMMARY

We have synthesized nanocomposites composed of nanograins of γ-Fe_2O_3, γ'-Fe_4N or ε-Fe_3N dispersed in a silver matrix, and evaluated their magnetocaloric effects by calculating the magnetic entropy changes from their magnetization data sets measured at various temperatures. The nitride nanocomposite showed entropy changes higher than that of the oxide, almost by one order. Enhancement of magnetocaloric effect observed with ε-Fe_3N gains was inferred as that due to temperature dependence of the saturation magnetization of the grain-constituting phase.

ACKNOWLEDGEMENTS

The author would like to thank Drs. I. Matsubara and R. Funahashi (Osaka National Res. Inst.) for their support in the SQUID measurements. A part of this work was supported by the Grant of Education Ministry of Japan.

REFERENCES

[1] M. W. Zemansky, *Heat and Thermodynamics, 5th.-ed.*, p.461, McGraw-Hill, (1972).

[2] R.D.Shull, L.J.Swartzendruber and L.H.Bennet: *Proc. 6-th Int'l. Cryocoolers Conf., ed. G.Green & M.Knox, David Tayler Res. Center Publ. #DTRC-91/002, Annapolis, MD* (1991) 231.

[3] R. D. McMichael, R. D. Shull, L. J. Swartzendruber, L. H. Bennett and R. E. Watson, J. Mag. Mag. Mater. **111,** 29 (1992).

[4] T.Yamamoto, R. D. Shull, P. R. Bandaru, F. Cosandey and H. W. Hahn, Jpn. J. Appl. Phys. **33,** L1301 (1994).

[5] T. A. Yamamoto, K. Nishimaki, T. Harabe, K. Shiomi, T. Nakagawa and M. Katsura, NanoStructured Materials, **12** 523 (1999)

[6] T. A. Yamamoto, M. Tanaka, T. Nakayama, K. Nishimaki, T. Nakagawa, M. Katsura and K. Niihara, J. Appl. Phys., *(to be accepted).*

[7] T.Yamamoto, M.C.Croft, R.D.Shull and H.W.Hahn, NanoStructured Mater., **6**, 965 (1995). and K. Nishimaki, T. A. Yamamoto, T. Nakagawa and M. Katsura, Jpn. J. Appl. Phys., *(to be accepted).*

RESIDUAL STRESS DETERMINATION AND SUBSURFACE MICROSTRUCTURE IN GROUND AND POLISHED ALUMINA/SILICON CARBIDE NANOCOMPOSITES AND MONOLITHIC ALUMINA CERAMICS

H.Z. WU*, S.G. ROBERTS*, A.J. WINN**, B. DERBY**
*Department of Materials, University of Oxford, Parks Road, Oxford OX1 3PH, UK
**Manchester Materials Science Centre, Grosvenor Street, Manchester M1 7HS, UK

ABSTRACT

The surface residual stress state induced by grinding and polishing an alumina/silicon carbide nanocomposite and monolithic alumina has been investigated using Hertzian indentation and fluorescence spectroscopy. Specimens were ground and then polished with diamond slurry with grit sizes ranging between 8 μm and 1 μm. The results show that the surface residual stress state in the nanocomposites is more sensitive to surface treatment than that in the monolithic alumina. Surfaces of both ceramics were examined in cross-section by TEM and direct observations were made of the plastic deformation induced by different surface treatments. There is a change in the predominant deformation micromechanism from twinning in the alumina to dislocation generation in the nanocomposites.

INTRODUCTION

In an earlier study we used a Hertzian indentation method to show that coarse surface grinding introduced a much greater residual stress level in an Al_2O_3/SiC nanocomposite than in an equivalent grain size Al_2O_3 polycrystal [1]. However, by using a thin plate bending method, Chou etc. [2] measured a similar residual stress level on both nanocomposite and monolithic Al_2O_3 ground surfaces machined under identical conditions, and found that the stress level varies from batch to batch. Here we investigate further the machining-induced surface residual stress, using Hertzian indentation and fluorescence spectroscopy to determine the different behaviour of Al_2O_3/SiC nanocomposites and monolithic polycrystalline Al_2O_3 after grinding and polishing. We also use cross-sectional TEM to study the micromechanisms of deformation in the sub-surface region and so help us interpret our results.

EXPERIMENTS

A sub-micron α-Al_2O_3 powder (AKP53 Sumitomo, Japan) was mixed with SiC particles (UF 45, Lonza, Germany) of about 90 nm mean particle size by attrition milling in water with a dispersant (Dispex, Allied Colloids, UK). All the material in this study had 5% by volume SiC. The powder suspension was freeze dried and the powder packed into a graphite die. Powders were consolidated by hot-pressing at 1650 °C for 1 hr under 20-25 MPa pressure in flowing argon, as was the monolithic alumina but with a hot-pressing temperature of 1500 °C. These conditions were chosen to ensure a final grain size of about 3 μm in both materials. Further details of the processing are presented elsewhere [1].

All of the hot pressed discs were first ground with a 150 μm resin-bonded diamond wheel to remove the top surface on both sides to achieve a sample thickness of about 2.5 to 3.0 mm. The grinding conditions were: wheel rotation of 1250 rpm, table speed of 0.8 m/s and grinding depth of 12.5 μm per pass of the table. Specimens for Hertzian indentation and fluorescence spectroscopy were cut from the disc. Surfaces were further finished as required using the following procedure. At least 150 μm of material was removed from the ground surface using a

Mat. Res. Soc. Symp. Proc. Vol. 581 © 2000 Materials Research Society

25 μm grit size diamond slurry. This was followed by the removal of at least 100 μm using an 8 μm slurry, and 50 μm by a 3 μm and a 1 μm slurry in turn if required. All polishing was carried out on a Kemet polishing machine (Engis Ltd., UK) with a rotating rate of about 60 rpm and an external load of 1.5 kg. The 3 and 8 μm polishing operations were done on hard plates and 1 μm finishing was done on a soft cloth.

Hertzian indentation tests were carried out using a CK10 testing machine (Engineering Systems, Nottingham, U.K.). The indenter is a 5 mm diameter polycrystalline alumina ball. For every specimen, at least 40 tests were made. After chemical etching and light lapping, optical microscopy was used to check for the presence of a Hertzian "ring" crack around each site; data from tests with no visible crack were not used.

Fluorescence spectroscopy was carried out on the same surfaces as used for Hertzian indentation. Fluorescence spectra were obtained using an unmodified Raman microprobe system [3]. The fluorescence spectra were obtained using the 632.8 nm red line of a 15 mW He-Ne laser with an intensity of about 1.0 mW. This beam intensity was found to cause minimum shift in the wavenumber of the fluorescence lines due to heating effects. Measurements were made using a ×40 microscope objective lens with a numerical aperture of 0.65, giving an approximate beam diameter on the specimen of 2 μm. 30 probing sites were randomly selected for measurement on each specimen.

The details of TEM cross-section specimen preparation are described in a companion paper in these proceedings [4]. The TEM observations were carried out using JEM 200CX and CM20 microscopes operated at 200 kV.

RESULTS

Surface Residual Stress

Contact mechanics analysis shows that a given test material/indenter ball combination, there is a minimum indentation load required to produce Hertzian fracture [5,6]. If indenter and test material are of elastically identical materials, and the test surface is stress free, this minimum fracture load depends only on the K_{IC}, Young's modulus and Poisson's ratio of the material [6]. Thus measuring the minimum fracture load can be used to determine K_{IC}. If there is a residual stress in the test surface, the minimum load to fracture will change [5]. The stress can be calculated by using the "apparent fracture toughness" (K_{IC}^{σ}) derived from the minimum load for Hertzian fracture on the stressed surface, and the real fracture toughness (K_{IC}^{0}) as follows:

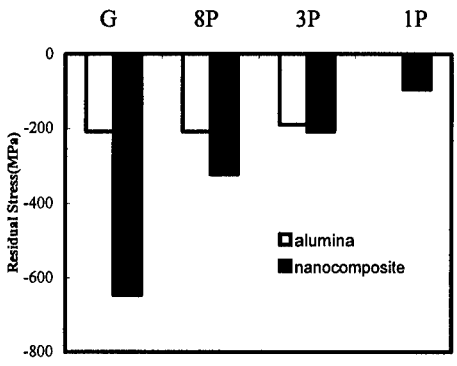


Figure 1 Surface residual stress detected by Hertzian indentation. Surface finish conditions include: machine grinding (G), 8 μm polishing (8P), 3 μm polishing (3P) and 1 μm polishing (1P).

$$\sigma_r = \frac{(K_{IC}^{\sigma} - K_{IC}^{0})}{1.12\sqrt{\pi c^*}} \qquad (1)$$

where c^* is the surface crack depth

giving rise to fracture at the minimum load; for a 5 mm diameter ball indenter on alumina c^* is 7 μm [5]. The calculated surface residual stress values are shown in figure 1 for both ceramics under a range of surface finish conditions. Here, we assume that the 1 μm polished alumina surface is stress free; this is then used to give K_{IC}^0 (=3.08 MPa.m$^{1/2}$). For the nanocomposite, the surface residual stress reaches the highest level after machine grinding and decreases from the 8 μm finish to the 1 μm finish. With the alumina specimens, the level of residual stress was constant for the 3 μm, 8 μm and ground surface finishes.

It is possible to use fluorescence spectroscopy to characterise surface residual stress in appropriate systems. In Al_2O_3, a particular fluorescence can be excited from electronic transitions of Cr^{3+} dopants. The frequency shift ($\Delta\nu$) of the characteristic fluorescence can be correlated with the stress tensor (σ_{ij}) as follows [7]:

$$\Delta\nu=\Pi_{ij}\sigma_{ij} \qquad (2)$$

where Π_{ij} are the piezospectroscopic coefficients. In this paper, only shifts in R_2 fluorescence line are considered. The corresponding piezospectroscopic coefficient used here is 3.3 cm^{-1}.GPa. The details of calibrating this value are given in reference [8]. The definition of an absolute stress free reference for the fluorescence is difficult. Here we have chosen the signal obtained from a fresh fracture surface as a reference for alumina and nanocomposite. Thus our computed stress values are relative to this surface.

The measured surface residual stress values are summarised in figure 2(a) and (b) for the nanocomposite and Al_2O_3 respectively. On each surface 30 random positions were used for measurement to determine the average residual stress and standard deviation, minimum residual stress and maximum residual stress. The scatter observed is not from any inherent error in the measuring method, as repeated measurements at the same location show a typical error of 2.5 - 10 MPa. The fluorescence spectroscopy results for the nanocomposite are in general agreement with our Hertzian indentation data as they show the surface residual stress to be a maximum after the machine grinding and to decease with progressive polishing. However, the magnitude of stress measured is about half the value obtained by indentation. For alumina, the fluorescence spectroscopy results are confusing because of the large experimental scatter. As with the

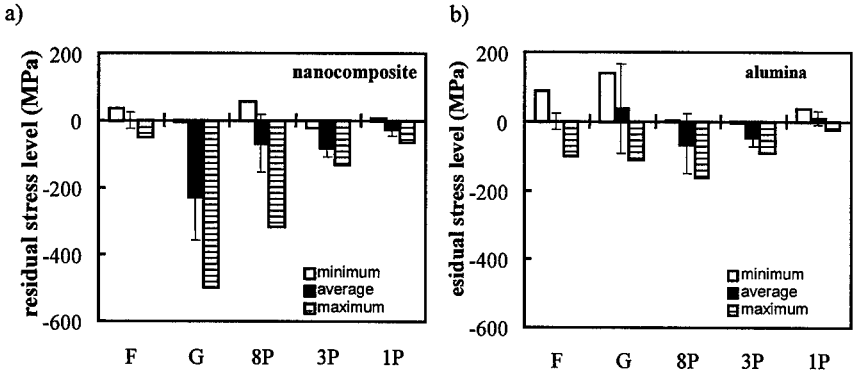


Figure 2 Surface residual stress detected by fluorescence spectroscopy for (a) nanocomposite and (b) alumina under surface condition: fracture surface (F), ground (G), polished with diamond of 8 μm grits (8P), 3 μm grits (3P) and 1 μm (1P).

nanocomposites, they show a much lower residual stress levels than found by indentation. Grinding appears to introduce a zero (or even a slightly tensile) mean stress but this result is with considerable scatter.

Subsurface Microstructure

We have studied the subsurface deformation microstructure of these materials using cross-section transmission microscopy. Results are summarised in table 1.

Table 1 The general subsurface microstructure features for machined surfaces.

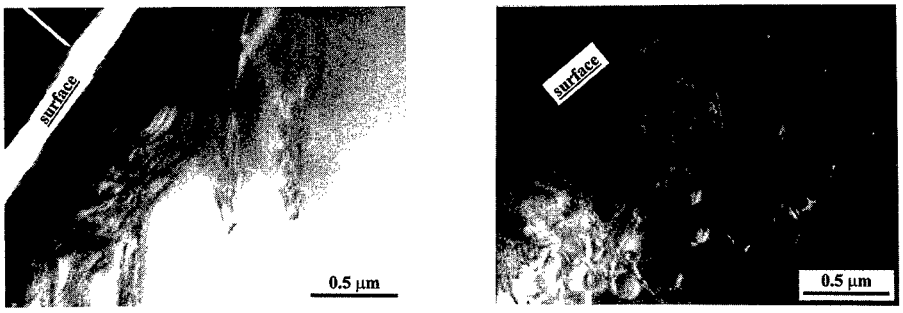
Grit size	Materials	Subsurface deformation characteristics	Cracking
ground	Alumina	a. twinning to depth of whole grain; b. slip near the top surface less < ~ 1 μm; c. no defects between twins	Yes
	Nanocomposite	a. dislocations dominate throughout the grains b. a few twins d. highly strained between the twins	Yes
8 μm	Alumina	Deformation by dislocation: depth >1.5 μm Non deformed area existed	Visible near top
	Nanocomposite	Deformation by dislocation: depth >1.5 μm to whole grain	N/A
3 μm	Alumina	Deformation by dislocation: depth 0.5 - > 1 μm	None visible
	Nanocomposite	Deformation by dislocation: depth > 1 μm	None visible
1 μm	Alumina	Deformation by dislocation: depth < 0.3 μm	None visible
	Nanocomposite	Deformation by dislocation: depth 0.5-1.5 μm	None visible

During machine grinding, the ceramic surfaces undergo severe damage from the large, rapidly moving diamond grits. In monolithic alumina, subsurface deformation occurs mainly by twinning, as shown in figure 3(a), which is generally in agreement with previous investigators' results, e.g. like Heuer [9] and Inkson [10] on either single crystal or polycrystalline Al_2O_3. Some dislocation activity is also visible near the top surface close to the twins. For the nanocomposites, there are very few twins observed; instead, there is a high dislocation density (see figure 3b). This dislocation structure exists in the top two layers of grains.



a) b)

Figure 3 Subsurface deformation after machine grinding in alumina (a) and nanocomposite (b)



a) b)

Figure 4 Subsurface deformation after polishing with 3 μm diamond in (a) alumina and (b) nanocomposite

Figure 4 shows the deformed subsurface microstructure for alumina and the nanocomposite finished with a 3 μm diamond grit. The polished surfaces of both Al_2O_3 and the nanocomposite show similar deformation substructures, especially at fine diamond grit sizes, consisting of dense tangles of near-surface dislocations. Generally the nanocomposite was found to have a more homogenous dislocation structure than the Al_2O_3. This suggests that dislocation slip in the nanocomposite may be easier and less orientation dependent than in α-Al_2O_3.

DISCUSSION

The two techniques we have used to probe the subsurface residual stress level, Hertzian indentation and fluorescence piezospectroscopy, produce broadly similar trends in the effect of grinding on stress level. However, the spectroscopy method shows greater scatter and also indicates a mean stress level about a factor of two lower than obtained from indentation. If a single fluorescence experiment was repeated at the same spot, we found little variation in the measured stress. We thus believe that the greater scatter seen with the fluorescence spectroscopy method reflects a real variation in residual stress across the microstructure. The fluorescence technique probes the stress by exciting Cr^{3+} fluorescence using a 2 μm diameter illuminated spot. The depth of penetration of the fluorescence technique is not so clearly defined, but the beam is likely to penetrate a few grain diameters into the material, i.e. ~10 μm. The scatter may represent the influence of local grain orientation on residual stress level or alternatively, as only a small quantity of material is sampled, may reflect the local damage state (e.g. local presence of cracks). The Hertzian indentation method measures a residual stress by determining the minimum load for crack extension. Warren [6] has shown that this minimum load is identified with a characteristic crack length for the indented system; for Al_2O_3 and with the ball radius used this defect is about 7 μm in length. Thus the Hertzian indentation method measures the residual stress state associated with a crack of this depth; this crack is the first one activated by the indenter as it samples a large test area (~300 μm diameter) with increasing load. The difference in stress measured by the two techniques may be a function of the depth sampled or may be a more fundamental difference caused by different components of the stress tensor being sampled.

Both methods of stress measurement found a significant change in residual stress in the nanocomposite with decreasing diamond grit size and no real effect of grit size on residual stress in the Al_2O_3. The TEM results show that in the nanocomposite there is a deformed zone, containing a high dislocation density, which decreases in depth with decreasing grit size. This explains the decreasing stress levels. This is in contrast with the twinning deformation found in

Al_2O_3. However, why the presence of relatively small quantities of SiC should so dramatically change the deformation behaviour of α-Al_2O_3 is not clear.

It has been noticed that the interactions of twins or twin components with grain boundaries can initiate crack nucleation and development in the deformed region [9,10]. This may explain why the dislocated nanocomposite surfaces appear to be less sensitive to polishing and wear damage than the twinned Al_2O_3 surfaces [1].

CONCLUSIONS

1. The residual stress measured in a nanocomposite after surface machining is greater than that measured from an Al_2O_3 surface for grinding grits greater in size than 3 μm. The residual stress found on a ground Al_2O_3 surface is relatively independent of grinding grit size while that from the nanocomposite decreases with decreasing grit size.
2. The subsurface deformation in the nanocomposite occurs by dislocation generation at all grinding grit sizes. In the Al_2O_3 surfaces deformation occurred by twinning at large grit sizes but underwent a transition to dislocation mechanisms at the smallest grinding grit sizes (< 8 μm).

ACKNOWLEDGEMENTS

This work is funded by EPSRC under grant GR/L95908.

REFERNCES

1. H.Z. Wu, C.W. Lawrence, S.G. Roberts and B. Derby, Acta Mater., **46**, 839 (1998).
2. I.A. Chou, H.M. Chan and M.P. Harmer, J. Amer. Ceram. Soc., **78**, 567 (1995).
3. R.B. Yallee, M.C. Andrew and R.J. Young, J. Mater. Sci., **31**, 3349 (1996).
4. H.Z. Wu, J. Titchmarsh, S.G. Roberts and B. Derby, in this proceedings.
5. S.G. Roberts, C.W. Lawrence, Y. Bisrat, P.D. Warren and D.A. Hill, J. Amer. Ceram. Soc., **82**, 1809 (1999).
6. P.D. Warren, J. Europ. Ceram. Soc. **15**, 201 (1995).
7. L. Grabneer, J. Appl. Phys., **49**, 580 (1978).
8. R.B. Yalee, PhD Thesis, UMIST, 1997.
9. A.H. Heuer, Phil. Mag., **13**, 379 (1966).
10. B.J. Inkson, Acta Mater. in press (1999).

NANOCOMPOSITE MATERIAL,LIQUID CRYSTAL-AEROSIL PARTICLES: DIELECTRIC AND PHOTON CORRELATION SPECTROSCOPY INVESTIGATIONS

F.M. ALIEV and G.P. SINHA,
Dept. of Physics, University of Puerto Rico, San Juan, PR 00931-3343, USA

ABSTRACT

Nematic liquid crystal filled with Aerosil particles – prospective inorganic-organic nanocomposite material for optoelectronic application – has been investigated by broadband dielectric spectroscopy (BDS) and photon correlation spectroscopy (PCS). The aerosil particles of diameter $\simeq$ 10 nm in filled nematic liquid crystals form a network structure with linear size of LC domains about 250 nm and with random distribution of the director orientation of each domain. This material has a very developed liquid crystal-solid particle interface that makes the role of the surface layers of LC important in the determination of the properties of the material. BDS provides information on reorientational motion of polar molecules of liquid crystal while PCS probes dynamics of collective modes associated with director fluctuations. We found that the properties of 5CB are considerably affected by the network. Two bulk-like dielectric modes due to the rotation of molecules around short axes and the tumbling motion were observed in filled 5CB. Additionally, a low frequency relaxation process and dispersion of dielectric permittivity due to conductivity were observed. The treatment of the surface of filling particles has strongest influence on the properties of the slow process and it is less important for molecular modes. PCS experiment shows that two new relaxation processes appear in filled 5CB in addition to the director fluctuations process in bulk.

INTRODUCTION

The heterogeneous nanoscale systems based on liquid crystals (LC), such as liquid crystals dispersed in polymer matrices (PDLC) [1] and in inorganic porous matrices [2] as well as filled liquid crystals are materials extremely important for both applications and fundamental physics.

Filled nematics (FN) have attracted a great deal of attention as materials for display applications [3,4]. These materials are suspensions of highly dispersed silica in the nematic phase of a liquid crystal (LC). Investigations have shown that the agglomeration of 2-3 volume percent of Aerosil particles in a nematic phase forms a three-dimensional network dividing the liquid crystal into LC domains with a linear size of approximately 250 nm [2] and with a random distribution of director orientation of each domain.

Filled liquid crystals have some similarities with other types of liquid crystal based heterogeneous materials: liquid crystals dispersed in polymer matrices (PDLC) [1] and in inorganic porous matrices [2]. These systems are anisotropic (at least at short spatial scales) and heterogeneous materials characterized by a very developed interface. The particles in FN are capable of changing their mutual arrangement which results in changes of the network structure at nanoscale level [4].

The investigations of filled nematics are in the initial [5-10] stage and have been mainly concerned with static properties such as the influence of filling on the phase transitions [5-7] and optical properties [4,6]. The first attempts to investigate the dynamics of director fluctuations were made in Ref. [8] and the dielectric properties of filled LC in Ref. [9,10].

In this paper we present the results of investigations of 5CB – filled with Aerosil particles with hydrophilic and hydrophobic surfaces by broad band dielectric and photon correlation spectroscopies in the nematic phase and the supercooled state. These two methods provide complementary information on dynamical properties of material. Broad band dielectric spectroscopy is a powerful technique for investigations of condensed matter. Relaxation of different physical origin such as molecular reorientation, dynamics of collective or surface

Mat. Res. Soc. Symp. Proc. Vol. 581 © 2000 Materials Research Society

polarization modes, and conductivity can be investigated in different systems. Photon correlation spectroscopy applied to nematic liquid crystal provides information on the dynamics of director fluctuations determined by elastic and viscous properties of LC.

EXPERIMENT

We used liquid crystalline 5CB filled with Aerosil particles, both hydrophilic (A200) as well as hydrophobic (R974), as materials. The volume concentration of the filling particles was 2.3 % for both samples. The hydrophilic particles are made of silica with OH-groups (1.4 - 2 groups per nm^2) on the surface. In the hydrophobic Aerosil particles, about 70 % of the surface hydrophilic groups are replaced by hydrophobic groups reducing the interaction with the liquid crystal molecules and between particles. Investigations have shown that the agglomeration of 2-3 volume percent of Aerosil particles in a nematic phase forms a three-dimensional network dividing the liquid crystal into LC domains with a linear size of approximately 250 nm [2] with random distribution of director orientation of each domain.

The bulk 5CB has a nematic phase in the temperature range of 22.5-35°C. Measurements of the real (ϵ') and the imaginary (ϵ'') parts of the complex dielectric permittivity in the frequency range 10^{-3} Hz to 1.5 GHz were performed using two sets of devices. In the range from 10^{-3} Hz to 3 MHz we used the Schlumberger Technologies 1260 Impedance/Gain-Phase Analyzer in combination with Novocontrol Broad Band Dielectric Converter and an active sample cell (BDC-S). For measurements in the frequency range from 1 MHz to 1.5 GHz we used Hewlett-Packard 4291A rf Impedance Analyzer.

Photon correlation measurements were performed using a $\lambda = 0.6328\mu m$ He-Ne laser and the ALV-5000/Fast Digital Multiple Tau Correlator (real time) operating over delay times from 12.5 ns up to 10^3 s with the Thorn EMI 9130/100B03 photomultiplier and the ALV preamplifier. The temperature stabilization in both experiments was better than 0.01°C.

DIELECTRIC RELAXATION

In the nematic phase of bulk 5CB there are two dielectrically active relaxation processes of molecular origin [11-15]. For a geometry in which the electric field **E** is parallel to the director **n** i.e. $\mathbf{E}\|\mathbf{n}$, the Debye type process due to the restricted rotation of the molecules about their short axis exists. The characteristic frequency of this process is ~ 5 MHz and the temperature dependencies of the corresponding relaxation times obey empirical Arrhenius equation. For the geometry in which the electric field **E** is perpendicular to the director **n**, i.e. $\mathbf{E}\perp\mathbf{n}$, the most prominent relaxation process with a characteristic frequency about 70 MHz has been attributed to the tumbling of the molecules [16,17]. No dielectrically active collective modes are present in 5CB.

For the quantitative analysis of the dielectric spectra the Havriliak-Negami function [18] has been used. For the case of more than one relaxation process, taking into account the contribution of the dc conductivity to the imaginary part of dielectric permittivity, the Havriliak-Negami function is given by

$$\epsilon^* = \epsilon_\infty + \sum_j \frac{\Delta\epsilon_j}{[1 + (i2\pi f\tau_j)^{1-\alpha_j}]^{\beta_j}} - i\frac{\sigma}{2\pi\epsilon_0 f^n}, \qquad (1)$$

where ϵ^* is the complex dielectric permittivity, ϵ_∞ the high-frequency limit of the permittivity, $\Delta\epsilon_j$ the dielectric strength, τ_j the mean relaxation time, f frequency, and j the number of the relaxation process. The exponents α_j and β_j describe the symmetric and asymmetric distribution of relaxation times. The term $i\,\sigma/2\pi\epsilon_0 f^n$ accounts for the contribution of conductivity σ, with n as fitting parameter.

The broadband spectra of filled 5CB are different from spectra typical for bulk 5CB. Figure 1 represents the spectra in frequency range from 10 mHz to 1 GHz for both filled samples at T = 303 K. Two more relaxation processes in addition to two bulk-like processes

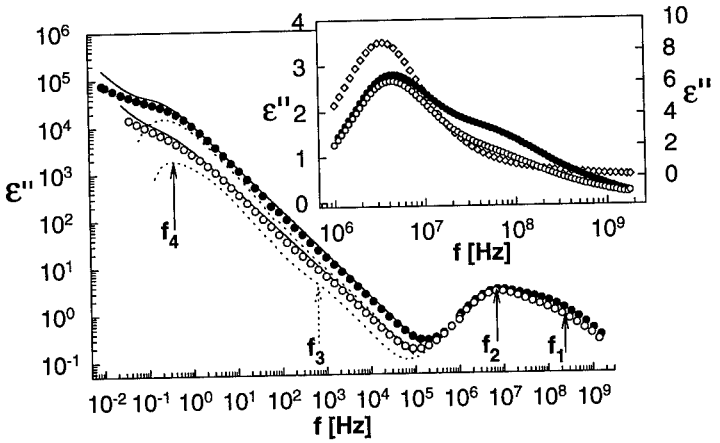


Figure 1: Broad band dielectric spectra of filled nematics at T = 303 K. Open circles: hydrophobic; closed circles: hydrophilic Aerosil. Solid lines: fitting curves for low frequency part of the spectra using Havriliak-Negami function. Dotted lines have been plotted after subtraction of the contribution due to d.c. conductivity. The arrows identify characteristic frequencies of relaxation processes. Inset: high frequency dielectric spectra of bulk and filled 5CB at T = 297 K. Bulk 5CB - opened diamonds (right axis), filled with hydrophilic and hydrophobic particles (left axis).

as well as dispersion due to contribution from conductivity, were observed for both systems in the low frequency range ($f \leq 100$ kHz). The frequency dependencies of ϵ'' after the subtraction of the contribution from conductivity are represented by the dotted lines in Fig. 1. These dependencies have relaxation origin and are quantitatively described by the Havriliak-Negami formula. The contributions from conductivity is perfectly described by the second term in formula (1) and their values at T = 303 K are: $2.48 \cdot 10^{-9}$ S·cm^{-1} (hydrophilic) and $1.13 \cdot 10^{-9}$ S·cm^{-1} (hydrophobic). After subtraction of the contribution from conductivity we observe a clear maximum (f_4) at $f \approx 0.5$ Hz. We suggest that this low frequency process is the relaxation of the interfacial polarization arising at the Aerosil particle-liquid crystal interface. The relatively faster process is just a shoulder at $f \approx 1$ kHz (f_3) and is hard to analyze.

The difference between the molecular relaxation processes of bulk nematic 5CB and filled 5CB can be seen by comparing curves in the inset of Fig. 1 that represents the imaginary part of dielectric permittivity as a function of frequency measured at 297 K. In bulk 5CB the observed process is the relaxation due to the restricted rotation of the molecules about their short axis. This process is described by the Debye relaxation function ($\alpha = 0$ and $\beta = 1$ in formula (1)) with a single relaxation time. In filled nematics the characteristic frequencies of the main process are slightly changed from the bulk value and the contribution from the tumbling process in filled 5CB is clearly observed. This is due to the fact that filling of nematic liquid crystals with Aerosil particles introduces disorder with random orientation of the director of domains. Therefore in filled 5CB there are molecules oriented both parallel as well as perpendicular to the direction of probing electric field and both molecular modes are detected in the same experiment. The amplitude of the tumbling mode in hydrophilic sample is greater than in hydrophobic one.

Figure 2 shows the temperature dependencies of the relaxation times of the bulk-like processes due to the flip-flop reorientation around the short axis and tumbling motion of molecules. The temperature dependence of the relaxation time of flip-flop reorientation

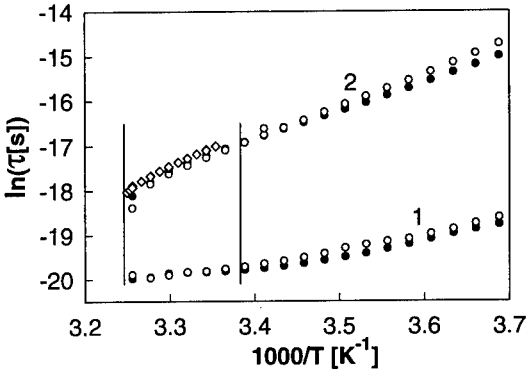


Figure 2: Temperature dependence of relaxation times for bulk-like and bulk processes. Open circles - hydrophobic; closed circles - hydrophilic Aerosil, open diamonds - bulk 5CB. 1 - tumbling mode; 2 - flip-flop reorientation around short axis. Vertical solid lines indicate the bulk nematic temperature range.

process of bulk 5CB is also presented in Fig. 2 for comparison. It should be mentioned that all relaxation processes in filled 5CB are not frozen even 25 K below the crystallization point of bulk 5CB.

In the temperature range corresponding to bulk nematic phase the relaxation times of reorientation motion around the short axis in filled 5CB are very close to bulk values with the same temperature dependence. In the supercooled state the temperature dependence deviates from the bulk behavior. The relaxation times of both bulk-like modes depend on temperature stronger in the supercooled state than in the nematic phase.

The filling of 5CB with Aerosil particles as well as the modification of the surface of filling particles has weak influence on the dynamics of bulk-like modes and it is much stronger for the low frequency relaxation process.

PHOTON CORRELATION SPECTROSCOPY

In the dynamic light scattering experiment, one measures the intensity-intensity autocorrelation function

$$g_2(t) = \langle I(t)I(0)\rangle / \langle I(0)\rangle^2$$

which is related to the dynamic structure factor $f(q,t)$ of the sample by

$$g_2(t) = 1 + kf^2(q,t),$$

where I is the intensity of scattered light, k a contrast factor and $q = 4\pi n \sin(\Theta/2)/\lambda$, ($n$ is the refractive index, Θ the scattering angle and λ is the wavelength of laser radiation).

In bulk nematic liquid crystals the main contribution to the intensity of scattered light is due to the director fluctuations. In the single elastic constant (K) approximation, if we assume that the six Leslie coefficients have the same order of magnitude and are $\sim \eta$ (η is an average viscosity), then the relaxation time of director fluctuations is [19]: $\tau = \eta/Kq^2$ with order of magnitude $\sim 10^{-4}$ s. The corresponding decay function is exponential.

The autocorrelation functions of filled nematic samples are strongly modified by the network (see Fig.3): (i) the bulk-like director fluctuation process in filled 5CB is considerably slower than in the bulk and (ii) the autocorrelation functions of filled 5CB show two slow decays. These low frequency decays are more pronounced in 5CB filled with hydrophilic particles than in the hydrophobic sample.

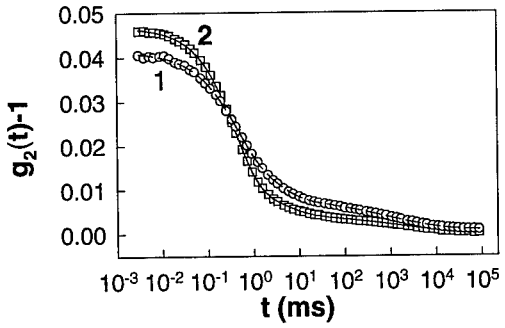


Figure 3: The intensity/ intensity autocorrelation functions of 5CB filled with hydrophilic (1) and hydrophobic (2) particles at 293.6 K. Symbols - experiment, solid lines - fitting.

The mode corresponding to motions of individual Aerosil nanoparticles was not detected. This confirms that the Aerosil particles form a network in the LC.

The intensity-intensity autocorrelation functions of filled 5CB measured in the dynamic light scattering experiment, have been fitted by the superposition of three stretched exponential decays:

$$f(q,t) = \left[\sum_{i=1}^{m} a_i \cdot \exp(-(t/\tau_i)^{\beta_i})\right]^2, \qquad (2)$$

where a_i, τ_i and β_i are the amplitude, relaxation time, and stretching exponent of ith relaxation process, and m is the number of processes.

We assign the first decay to the bulk-like director fluctuations. This relaxation process is broader and slower ($\beta = 0.84$, $\tau = 0.51$ ms at 293.6 K) than in bulk 5CB at the same temperature ($\beta = 1$, $\tau = 0.14$ ms).

The second ($1< t <100$ms) relaxation process is most probably due to the director fluctuations in a thin LC layer in the vicinity of Aerosil particles. The relative contribution of this process to autocorrelation function in hydrophilic sample is considerably ($a_2/a_1 \simeq 0.9$) higher than in the hydrophobic one ($a_2/a_1 \simeq 0.4$) because of higher number of hydrophilic OH groups, which has resulted in stronger modification of the surface LC layer. This relaxation process is notably slower than the bulk-like director fluctuations due to higher viscosity in the vicinity of Aerosil particle-liquid crystal interface (so-called surface viscosity) and coupling of molecules to the surface.

The third (slowest) process could be due to a motion of LC domains as a whole. However this third process is masked by the first two processes with much greater aptitude and the quantitative analysis of this process is very difficult.

CONCLUSION

The dielectric and photon correlation experiments show that the filling of LC with Aerosil particles significantly changes the physical properties of nematic liquid crystals. Filling of nematic LC has resulted in the appearance of a low frequency relaxation process dependent on the surface condition of the filling particles. The low frequency relaxation is Aerosil particle-liquid crystal interface related phenomena. It is more pronounced in hydrophilic samples since the modification of the surface LC layer in these samples is stronger than in hydrophobic one.

Two bulk-like modes due to the rotation of molecules around the short axes and the tumbling motion are less affected by filling or modification of the surface of the filling parti-

cles. All relaxation processes in filled 5CB are not frozen even 25 K below the crystallization temperature of bulk 5CB.

ACKNOWLEDGEMENTS

This work was supported by Naval Research Office grant N00014-99-1-0558.

REFERENCES

1. P.S. Drzaic, *Liquid Crystal Dispersions*, (World Scientific, Singapore, 1995).

2. *Liquid Crystals in Complex Geometries*, edited by G.P. Crawford and S. Zumer (Taylor and Francis, London, 1996).

3. M. Kreuzer, T. Tschudi, W.H. de Jeu, and R. Eidenschink, Appl. Phys. Lett. **62**, 1712 (1993).

4. M. Kreuzer and R. Eidenschink in *Liquid Crystals in Complex Geometries*, edited by G.P. Crawford and S. Zumer (Taylor & Francis, London, 1996), pp. 307-324.

5. B. Zhou, G.S. Iannacchione, C.W. Garland, and T. Bellini, Phys. Rev. E **55**, 2962 (1997).

6. T. Bellini, N.A. Clark, V. Degiorgio, F. Mantegazza, and G. Natale, Phys. Rev. E. **57**, 2996 (1998).

7. G.S. Iannacchione, C.W. Garland, J.T. Mang, and T.P. Rieker, Phys. Rev. E **58**, 5966 (1998).

8. F. Aliev, M. Kreuzer, N. Tabiryan, and B. Zel'dovich, Mol. Cryst. Liq. Cryst. **320**, 173 (1998).

9. S. Tschierske, O.V. Yaroshchuk, and H. Kresse, Cryst. Res. Technol. **30**, 571 (1995).

10. S.L. Abd-El-Messiah, J. Werner, H. Schmalfuss, W. Weissflog and H. Kresse, Liq. Cryst. **26**, 535 (1999).

11. P.G. Cummins, D.A. Danmur, and D.A. Laidler, Mol. Cryst. Liq. Cryst. **30**, 109 (1975).

12. D. Lippens, J.P. Parneix, and A. Chapoton, J. de Phys. **38**, 1465 (1977).

13. J.M. Wacrenier, C. Druon, and D. Lippens, Mol. Phys. **43**, 97 (1981).

14. T.K. Bose, R. Chahine, M. Merabet, and J. Thoen, J. de Phys. **45**, 11329 (1984).

15. T. K. Bose, B. Campbell, S. Yagihara, and J. Thoen, Phys. Rev. A **36**, 5767 (1987).

16. S.R. Rozanski, R. Stanarius, H. Groothues, and F. Kremer, Liquid Crystals **20**, 59 (1996).

17. G.P. Sinha and F.M. Aliev, Phys. Rev. E **58**, 2001 (1998).

18. S. Havriliak and S. Negami, Polymer **8**, 101 (1967).

19. P.G. de Gennes and J. Prost, *The Physics of Liquid Crystals*, second ed., (Clarendon Press, Oxford 1993).

THE MICROSTRUCTURE AND PROPERTIES OF FRAMEWORK ZIRCONIUM PHOSPHATES BASED NANOCOMPOSITES -CATALYSTS OF ALKANE ISOMERIZATION

Vladislav A. Sadykov*, S. N. Pavlova*, G. V. Zabolotnaya*, R. I. Maximovskaya*, D. I. Kochubei*, V. V. Kriventsov*, G. V. Odegova*, N. M. Ostrovskii*, O. B. Bel'skaya*, V. K. Duplyakin*, V. I. Zaikovskii*, E. A. Paukshtis*, E. B. Burgina*, S. V. Tsybulya, M. V. Chaikina**, N. N. Kuznetsova***, V. V. Lunin***, R. Roy****, D. K. Agrawal****.
*Boreskov Institute of Catalysis, Siberian Branch of the Russian Academy of Sciences, Lavrentieva, 5; Novosibirsk State University, Pirogova, 1; Novosibirsk, RUSSIA 630090; sadykov@catalysis.nsk.su
**Chemical Department, Lomonosov Moscow State University, Vorobyovy gory, Moscow, Russia 119899
***Institute of Solid State Chemistry, Siberian Branch of the Russian Academy of Sciences, Kutateladze, 18, Novosibirsk, RUSSIA 630090
****Materials Research Laboratory, The Pennsylvania State University, University Park, PA 16802

ABSTRACT

The structure and surface properties of composites based upon high-surface-area framework zirconium phosphates with supported WO_3, MoO_3 and Pt nanoparticles were studied by using combination of structural and spectral methods. The effect of these promoters on performance of zirconium phosphates in the reaction of pentane and hexane isomerization is considered.

INTRODUCTION

Recently [1-3], the procedures for synthesis of highly dispersed mesoporous framework zirconium phosphates via hydrothermal treatment (HTT) in the presence of polyethylene oxide of amorphous sols or products of mechanical activation of the mixture of solid salts were elaborated. Genesis of samples real structure as a function of the preparation procedure and nature of modifying cations (La, Si) as well as its impact on the surface acidic properties and catalytic performance in the reactions of hexane isomerization and dehydroaromatization have been studied. This work aims at synthesis of composite systems based upon those zirconium phosphates with supported WO_3, MoO_3 and Pt nanoparticles known as promoters in the reactions of paraffins isomerization, elucidation their microstructural features and surface properties as related to catalysis of the reactions of interest.

EXPERIMENTAL

Table 1 lists starting materials and some details of preparation procedures similar to those described earlier [1-3]. When organometallic precursors were used, 1 M $(NH_4)_2HPO_4$ water solution was added under stirring to 80% solution of zirconium butoxide in n-butanol or to its mixture with tetraethylorthosilicate (Si/Zr~ 0.3). PEO was then added, and this mixture was stirred at room temperature for 18 hours. Suspensions of sols or activated mechanical mixtures in distilled water with addition of polyethylene oxide were kept in bombs at 175-200

Mat. Res. Soc. Symp. Proc. Vol. 581 © 2000 Materials Research Society

°C for 5-7 days. After HTT, the solids were separated by centrifugation, washed with ethanol and distilled water, dried at 120 °C and calcined at 400 °C. Platinum, WO_3, and MoO_3 were usually supported by the incipient wetness impregnation methods from solutions of H_2PtCl_6, ammonium tungstate and molybdate, respectively, followed by drying and air calcination. For comparison, in one sample (K-8), W was added through the mechanical co-activation of crystalline cubic zirconium phosphate with solid ammonium tungstate followed by air calcination.

Table 1. Parameters of synthesis and some properties of samples calcined at 400 °C.

Sample[1]	Starting compounds[2]	Specific surface m^2/g	I Zr-0H, arb. un.	$[Zr^{4+}]$ μmolCO/m^2	Pt-CO μmolCO/m^2	Phase composition (XRD)[3]
MA -2	LN + ZrCl+N3P	60	0	0.27		C+O
K-3*	2%Pt/MA-2	50			0.44	C+O
K-4	11.2%W/MA-2	30	0			C+O
K-4*	2%Pt/K-4	30		0	0.23	C+O
K-5	3.6%W+9.6%Mo/ MA-2	40	0	0.17		C+O
K-5*	2%Pt/K-5	40		0	0.15	C+O
K-6	0.3%Pt/K-4					C+O
K-7	0.3%Pt/K-5	35		0	0.63	C+O
K-8[4)]	10%W/MA-2	20				C+O
SiSG-32	ZrPr+TES+N2P	187	160	0.37		A
K-19	0.3%Pt/SiSG-32	180	66	0.27		A
K-32	10%W/SiSG-32	140				A
K-33	0.3%Pt/K-32	110				A
K-33*	2%Pt/K-32	100			0.1	A

[1] SG and MA-- samples prepared via sol-gel and mechanochemical methods, resp.
[2] $La(NO_3)_3\ 6H_2O$ =LN; $ZrOCl_2\ 8H_2O$ =ZrCl; $(NH_4)_3PO_4\ 3H_2O$ = N3P; $(NH_4)_2HPO_4$ =N2P; ZrPr—zirconium butoxide; TES-tertaetoxysilane;
[3]C-cubic; O-orthorhombic; A- amorphous phases of ammonium zirconium phosphates.
[4] W was added via mechanochemical activation of MA-2

The bulk structure of samples was characterized by EXAFS (spectra were acquired at the EXAFS Station of the Siberian Center of Synchrotron Radiation, Novosibirsk) combined with the X-ray diffraction (XRD, CuK_α, an URD-63 diffractometer) and Infra-red spectroscopy (FTIRS, (FTIRS, a Fourier-transform IFS113V Bruker) and UV-VIS DRS spectra were measured by Carl Zeis spectrometer Specord-M-40). The microstructure of samples was studied using transmission electron microscopy (TEM, JEM 2010, 200 kv).

Surface properties were probed by the IR spectroscopy of surface hydroxyls (Broensted acid centers) and CO test molecule. CO was adsorbed at 150-160 K at 5 Torr on samples pressed in wafers with densities 4.4-22.7 mg/cm^2 vacuum pretreated in the IR cell at 400 °C for 1 h.

Catalytic transformation of n-pentane and n-hexane in the pulse regime was studied using a plug-flow reactor loaded with a 0.1 g of catalysts pretreated in H_2 at 350 °C for 2 h. A

1 mkL of liquid hexane or 0.15 ml of pentane + H_2 (1:1) gas mixture was fed into H_2 flowing through the reactor at velocity of 14 cm^3/min.

RESULTS

Microstructural features

According to TEM and XRD, in Mo-containing samples, MoO_3 is present as a separate bulk-like phase. For W -supported samples thin WoO_3 particles epitaxially bound with support (Fig. 1a) dominate, though relatively big (200-300 Å) particles of cubic or hexagonal trioxide phase are observed as well.

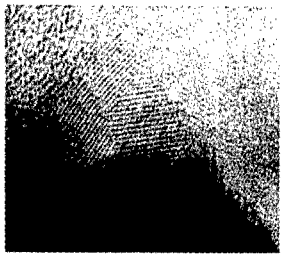


Fig. 1a. High resolution (x4*10^6) TEM image of hexagonal WO_3 particles (d_{200} = 3.17 Å, d_{001}= 3.91 Å) on the surface of amorphous NZP-Si sample

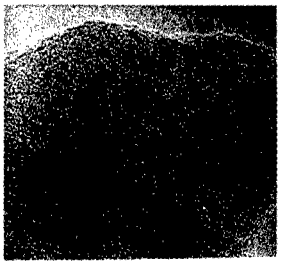


Fig. 1b. High resolution (x4*10^6) TEM image of small platinum clusters embedded into the surface of MA sample

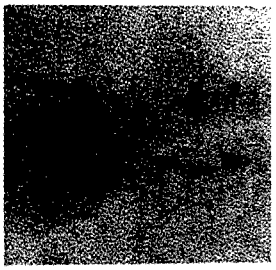


Fig. 1c. High resolution (x4*10^6) TEM image of bigger platinum clusters embedded into the surface of MA sample. d_{111} spacings of Pt (2.27 Å) are resolved

For Pt-supported samples without oxide additives, Pt particles with a rather broad size distribution were revealed (Fig. 1b, c), bigger particles displaying the typical Pt (111) lattice spacing. When Pt was supported after W, Pt particles sizes appear to be bigger.

The local structure of Zr, W, Mo and Pt was characterized by EXAFS. Pt local coordination was studied only for W-free samples since superposition of WL_2 and PtL_3 edges makes those measurements impossible.

Initial MA and silica –modified SG samples possess the same type of local zirconium environment typical for cubic NZP samples [2,3]. For crystalline MA sample Zr-O (R 2.06 Å, CN 6.6) и Zr-P (R 3.61 Å, CN 4.8) peaks are more intense as compared with those for the amorphous sample (Zr-O (R 2.07 Å, CN 5.6) and Zr-P (R 3.63 Å, CN 2.6), respectively). It implies a more disordered and/or less rigid structure for the amorphous sample. No changes in Zr environment were observed after addition of promoters.

The coordination environment of Pt supported onto NZP- type systems (K-5 sample) is the best approximated by three spheres with distances Pt-O (R 2.00 Å, CN 3.4), Pt-Pt (R 2.96 Å, CN 1.1) и Pt-Zr(La) (R 3.68 Å, CN 1.3). A decreased CN for the Pt-O distance implies the existence of two Pt species with slightly differing distances. The first one corresponds to PtO_2 , while the second can be assigned to Pt cations located in the surface vacant positions of the NZP structure.

The typical EXAFS spectra of WL_2 edge are shown in Fig. 2. For W supported on amorphous samples (K-32, K-33), the oxygen environment is close to an ideal octahedron

with the W-O distance ca 2.0 Å. The W—W distance is not observed, while two new peaks corresponding to W-P and W-Zr distances emerge. Hence, a predominant part of W is atomically dispersed at the surface being located in the same positions as Pt (vide supra)..

Mechanochemical addition of W (sample K-8) has resulted in formation of bulk WO_3 phase (Fig. 2). In agreement with TEM data, in sample K-4 prepared by wet impregnation, tungsta is present both as bulk WO_3 phase and small clusters or nearly atomically dispersed species. In sample K-5 containing both Mo and W, the former is present as bulk MoO_3 phase, while the latter is more dispersed than in sample K-4 probably due to location of tungsten cations both on the surface of zirconium phosphate as well as MoO_3 particles. These conclusions agree with the results obtained by UV-VIS (Fig. 3). For sample K-8, the spectrum is similar to that of bulk WO_3 phase, while in K-5 sample, absorption at ~14000 cm^{-1} typical to MoO_3 phase is observed. For samples K-32 and K-4, the spectra differ considerably from those typical for the unpromoted zirconium phosphate and bulk WO_3, thus evidencing a pronounced interaction between the promoters and support.

Addition of Pt to samples promoted by oxides does not change the tungsten environment in K-4 sample. For K-5 sample containing both Mo and W, W-Zr (La) distances were not changed as well, while for W-O distances the ratio between the peaks corresponding to long and short bonds changes approaching that for bulk WO_3 . Simultaneously, the intensity of peak corresponding to the Mo-Mo- distance declines. It implies a redispersion of molybdena due to Pt action, so that new MoO_3 clusters are anchored to W cations incorporated into the surface, thus distorting their oxygen environment.

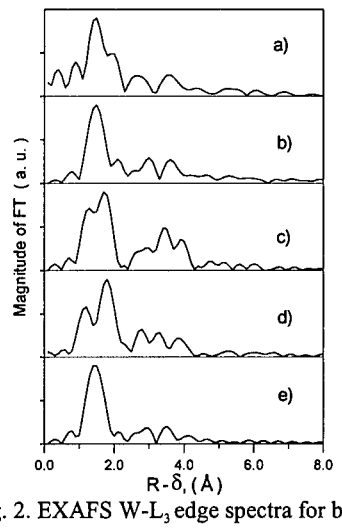


Fig. 2. EXAFS W-L_3 edge spectra for bulk WO_3 (a) and WO_3 -supported NZP samples: K-8 (b), K-4 (c), K-5 (d) and K-33(e).

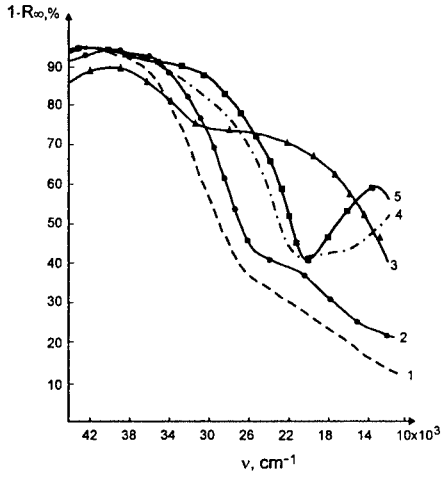


Fig. 3. UV-VIS DRS spectra for samples: 1 – K-32; 2 – K-4; 3 - MA-2; 4 – K-8; 5 – K-5

Surface properties

IR spectra of Pt-containing samples are shown in Fig. 4. A broad absorption in the 3000-3600 cm^{-1} range corresponds to stretching vibrations of ammonia and ammonium

cation strongly bound with the surface acid centers. A narrow band at ca 1430 cm^{-1} and a broader one at ~ 1608 cm^{-1} can be assigned to the asymmetric deformation of NH_4^+ and NH_3, respectively [4,5]. Hence, due to strong acidity of the surface sites created by supported tungsta and molybdena, residual ammonia species remain strongly bound with the surface of samples calcined at 400 °C, thus masking strong Broensted centers. Weakly acidic P-OH groups are not blocked by supported promoters (band at ~3670 cm^{-1} typical for those groups is observed). CO complexes with these groups are revealed by band at 2166 cm^{-1}. For all promoted samples, the density of Lewis acid sites–coordinatively unsaturated Zr^{4+} cations sharply declines being detectable only for K-33* sample (carbonyl band at 2188 cm^{-1}.).

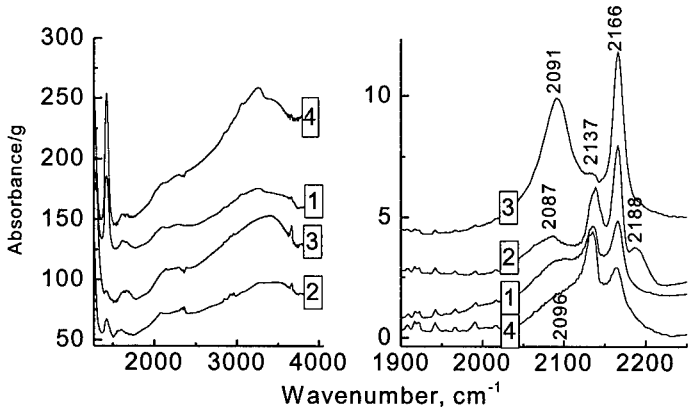


Fig. 4. IR spectra of Pt-containing samples with adsorbed CO (enlarged carbonyls stretching region shown on the right). 1-K-4*, 2-K-33*, 3-K-3*, 4-K-5*.

Hence, both Broensted and Lewis acid centers appear to take part in anchoring clusters of oxidic promoters [4].

In the carbonyl stretching region, bands at ca 2090 cm^{-1} and ca 2137 cm^{-1} correspond to linear carbonyl complexes with Pt^0 and Pt^+ species, respectively. This result agrees with EXAFS data implying the presence of oxidic Pt species (vide supra). The absence of bridging carbonyls (bands at $\nu CO < 1900$ cm^{-1}.) is explained by a small size of Pt clusters and their strong interaction with support, that correlates with low coordination numbers for the Pt-Pt distance revealed by EXAFS.

Catalytic properties

Promoted zirconium phosphates demonstrated a reasonably good and stable low- temperature performance in the reactions of pentane and hexane isomerization (Fig. 5). Earlier, in these low-temperature conditions, unpromoted zirconium phosphates were shown either being inactive at low temperatures or revealed rather high yield of aromatics and/or cracking products [1-3]. A high isomerization selectivity of promoted samples and their stability can be assigned to such factors as Pt enhanced dehydrogenation/hydrogenation ability, generation of strong Broensted acidity due to surface WOx species and suppression of coking via blocking of Lewis acid sites [4-6].

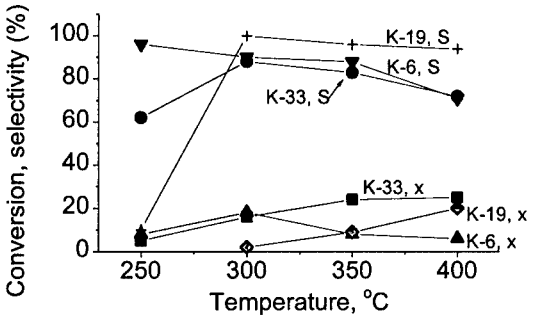


Fig. 5. The temperature dependence of conversion (x) and isomerization selectivity (S) for promoted zirconium phosphate catalysts in the reaction of pentane (K-6, K-19) and hexane (K-33) transformation.

CONCLUSIONS

The microstructure and surface properties of nanocomposites based upon crystalline or amorphous framework zirconium phosphates loaded with nanoparticles of Pt, W and Mo oxides were shown to differ considerably from the properties of bulk analogs due to effects of mutual interaction. Improved catalytic performance of such systems in the reactions of pentane and hexane isomerization can be explained by such an interaction.

ACKNOWLEDGMENTS

In Russia, this research has been supported by the University of Russia Program under Grant No 3414.

REFERENCES

1. V. A. Sadykov, S. N. Pavlova, G. V. Zabolotnaya, R. I. Maximovskaya, S. V. Tsybulya, E. B. Burgina, V. I. Zaikovskii, G. S. Litvak, M. V. Chaikina, N. N. Kuznetsova, V. V. Lunin, R. Roy, and D. K. Agrawal,. Mat. Res. Innov., **2**, 328 (1999)
2. V. A. Sadykov, S. N. Pavlova,. G. V. Zabolotnaya, D. I. Kochubei, R. I. Maximovskaya, V. I. Zaikovskii, V. V. Kriventsov, S. V. Tsybulya, E. B. Burgina, E. A. Paukshtis, A. M. Volodin, V. B. Fenelonov, N. N. Kuznetsova, V. V. Lunin, M. V. Chaikina, R. Roy, and D. K. Agrawal in *Advanced Catalytic Materials,* edited by P. W. Lednor, D. A. Nagaki and L. T. Thompson (Mater. Res. Soc. Proc. **549**, Warendale, PA 1999), p. 255-260.
3. S. N. Pavlova,. V. A. Sadykov, G. V. Zabolotnaya, D. I. Kochubei, R. I. Maximovskaya, V. I. Zaikovskii, V. V. Kriventsov, E. B. Burgina, S. V. Tsybulya, A. M. Volodin, E. A. Paukshtis, V. N. Kolomiichuk, M. V. Chaikina, N. N. Kuznetsova, V. V. Lunin, D. K. Agrawal and R. Roy, Phosph. Res. Bull., **10**, 400 (1999)
4. N. Naito, N. Katoda, and M. Niwa, J. Phys. Chem.B., **103**, 7206 (1999)
5. E. Zhao, Yu. Isaev, A. Sklyarov, and J. J. Fripiat, Catal. Lett., **60**, 173 (1999).
6. E. Iglesia, D. G. Barton, S. L. Soled, S. Miseo, J. E. Baumgartner, W. E. Gates, G. A. Fuentes, and G. D. Mertzner, Stud. Surf. Sci. Catal., **101,** 533 (1996).

NANOCOMPOSITES nc-TiN/a-Si_3N_4/a- and nc-$TiSi_2$ WITH HARDNESS EXCEEDING 100 GPa AND HIGH FRACTURE TOUGHNESS

S. VEPŘEK, A. NIEDERHOFER, K. MOTO, P. NESLÁDEK, H. MÄNNLING AND T. BOLOM
Institute for Chemistry of Inorganic Materials, Technical University Munich
Lichtenbergstr. 4, D-85747 Garching b. Munich, Germany. E-mail: stan.veprek@ch.tum.de

ABSTRACT

In course of further development of our generic concept for the design of novel superhard nanocomposites [1,2] we have recently developed new multi-phase ultrahard nanocomposite coatings with Vickers mirohardness of 80 to 105 GPa which is in the range of natural diamond. The coatings show a high elastic recovery of up to 90% upon a relatively large indentation deformation. The hardness measured by the depth sensing technique agree with those calculated from the area of the remaining pseudoplastic deformation. The very high apparent fracture toughness is illustrated by the absence of any radial cracks upon indentation with a large load of 1 N into 10.3 μm thick film [3]. The unusual combination of high hardness, elastic recovery and apparent fracture toughness was attributed to the ample possibility of cracks deflection, meandering and termination during loading and cracks closure upon unloading [1,2,4]. The suggested nanostructure of the coatings has been elucidated on a basis of a complex analysis by means XRD, EDX, ERD, XPS and HR TEM.

INTRODUCTION

The practically achievable strength and hardness of materials is orders of magnitude smaller than the theoretical one. It is controlled by their microstructure which hinders the usual mechanisms of plastic deformation and fracture, such as multiplication and movement of dislocations and growth of microcracks [5,6]. Grain boundary hardening is one of the possibilities to control the microstructure in order to increase the hardness (and strength): With decreasing crystallite size d the hardness of materials increases according to the 'Hall-Petch' relationship $H(d) = H_0 + k \cdot d^{-0.5}$ [5-8] which should be regarded as a semiempirical formula because different mechanisms yield a similar dependence [9] and also the growth of microcracks in ceramics results in a similar proportionality (see [2] and references therein). However, when the crystallite size decreases to about 10 nm, softening is observed ('reverse Hall-Petch') due to increasing grain boundary sliding [10] (for review see [2,11-13]). Recent computer simulations showed that the plastic deformation and finally a failure of nanocrystalline metals is due predominantly to a large number of small 'sliding' events of atomic planes at the grain boundaries which can occur without thermal activation at room temperature and thus "impose a limit on how strong nanocrystalline materials may become" [14].

Therefore we suggested to design new superhard materials by the formation of a nanocomposite consisting of hard nanocrystalline material imbedded in a thin amorphous (or coherent) interface, when both phases form a strong and structurally flexible interface due to a strong thermodynamically driven segregation [1]. The superhardness of 40-50 GPa has been achieved in various nanocomposites, such as nc-M_nN/a-Si_3N_4 (M=Ti, W, V) [1,2,15], nc-TiN/BN [16,17], nc-TiN/TiB_x [18,19], in quaternary nc-$(Ti_{1-x}Al_x)N/Si_3N_4$ [17] and various carbides and other materials combinations (for a review see [2]) thus underlining the universality of the design principle [1,2]. In this paper we report on nc-TiN/a-Si_3N_4/a- and nc$TiSi_2$ nanocomposites with hardness of 80 to more than 100 GPa which corresponds to that of diamond. The hardness of diamond ranges between about 70 and 90 GPa, depending on its quality and impurity content [2,20,21]. For example, with nitrogen bounded as atomic

Mat. Res. Soc. Symp. Proc. Vol. 581 © 2000 Materials Research Society

paramagnetic centers the strength of synthetic diamond crystals increases to a maximum at a concentration of about $(2 - 3)\cdot10^{19}$ N-Atoms/cm^3 [22].

EXPERIMENTAL

Because reliable measurement of the hardness in the range of ≥ 60 GPa is a difficult task [2], we have carefully compared the measurements on our nc-TiN/a- and nc-$TiSi_2$ coatings with the measurements on various diamond films. In this paper we shall present a comparison with the hardest diamond coatings which we have received from various laboratories, namely with pure, single phase nanocrystalline diamond films [23]. In order to avoid possible artifacts which may be associated with the nanoindentation we deposited 3 to 11 μm thick films, used relatively large loads and performed at least six to ten indentation measurements at each applied load. The measurements (indentometer Fischerscope 100) were done repetitively on many deposited coatings with the standard calibration (Si, Sapphire and 3C-SiC) and measurements on the nc-diamond in-between the measurements on our coatings. Finally, the size of the remaining "pseudoplastic" indentation was measured in scanning electron microscope (SEM) and the hardness was calculated according to the Vickers formula [24]. Measurements of the Vickers hardness in the range of ≥ 80 GPa are possible because the diamond indentor is loaded mainly in compression whereas the "plastic" deformation of the measured sample is to a large extent in shear. Under compression, diamond is about 8 to 10 times stronger than under shear [6].

The coatings were prepared by plasma chemical vapor deposition (CVD) in abnormal direct current glow discharge with the substrate connected as cathode from $TiCl_4$, SiH_4 in a large excess of H_2 and N_2 at a temperature of 550 °C [16]. In our earlier work [1,15] we used discharge operating at a high frequency, power density and pressure in order to minimize the energy of ions bombarding the surface of the growing film. These films had the composition of nc-TiN/a-Si_3N_4 [1] and their hardness showed a pronounced increase with decreasing crystallite size (which was controlled by the silicon content [1,25]) in the range of 3-10 nm. The minimum crystallite size and maximum hardness of ≥ 50 GPa was achieved at a silicon content of 7-9 at.% which corresponds to a content of Si_3N_4 of 16-21 mol.%, close to the percolation threshold [26]. This behavior indicates that the segregated non-polar Si_3N_4 is wetting the surfaces of the TiN nanocrystals which decreases the total Gibbs free energy of the system [4]. In our more recent work we used the abnormal DC discharge [16] in order to increase the ion bombardment of the film during the deposition. The recent studies have shown, that the hardness correlates with the Si_3N_4 content in the same way as found in the HF discharge, but not with the crystallite size when this is decreased by the energetic ion bombardment at a relatively large discharge current density of 2.5-3 mA/cm^2 [27]. At such a high current density stoichiometric nc-TiN/a-Si_3N_4 with hardness in the range of 40 to 60 GPa is formed in agreement with our earlier reports [1].

Our next hypothesis was if the formation of a multiphase nc-TiN/a-Si_3N_4/a- and nc-$TiSi_2$ nanocomposite with a strong TiN/Si_3N_4 interface may be decisive for a further increase of the hardness. For these reasons we decreased the discharge current density which generally results in a decrease of chemical activity of nitrogen and resultant formation of TiN and $TiSi_2$ [1,2]. The coatings reported here were deposited under the following conditions: T=550 °C, substrate stainless steel, current density 1 mA/cm^2, flow rate of H_2 100 sccm, gas flow rate ratios H_2:N_2:$TiCl_4$:SiH_4 = 100:10:1:0.1 to 0.9, total pressure 5 mbar and deposition rate of about 0.5 nm/sec.

RESULTS

The results of extended investigations by means of XRD, EDX (energy dispersive analysis of X-rays), ERD (energy recoil detection spectroscopy), XPS, SEM, HR TEM and

measurements of the mechanical properties ('plastic' Vickers microhardness, 'universal hardness', elastic modulus and elastic recovery) can be summarized as follows: At a high discharge current density of ≥ 2.5 mA/cm^2 the amorphous matrix consists of stoichiometric Si_3N_4 as reported earlier [1,2,15] whereas at ≤ 1 mA/cm^2 a multiphase nanocomposite consisting of nc-TiN, a-Si_3N_4 and a- and nc-$TiSi_2$ is formed The nc-TiN/a-Si_3N_4 films are superhard (H $\approx$ 40-60 GPa) whereas the nc-TiN/a-Si_3N_4/a- and nc-$TiSi_2$ are ultrahard (H $\geq$ 80 GPa). Depending on the total silicon content [Si] which was varied between 1-2 at.% and 25 at.% two kinds of the ultrahard nanocomposites are found. At [Si] of about 5 at.% nc-TiN/a-Si_3N_4/a-$TiSi_2$ nanocomposites with hardness of 80 GPa are formed. The crystallite size of TiN is about 10 to 11 nm). Above about [Si] = 10 at.% the precipitation of nanocrystalline nc-$TiSi_2$ commences. At [Si] of about 17 at.%, approximately 3 nm small nanocrystallites of $TiSi_2$ precipitate in the nc-TiN/a-$TiSi_2$ (crystallite size of TiN 4 to 6 nm) and the hardness reaches $\geq$ 90 GPa. Hereafter we present an example of such coatings.

Figure 1 shows indentation curves into the hardest, single phase nc-diamond (Fig. 1a) and into our nc-TiN/a- and nc-$TiSi_2$ (Fig. 1b). A comparison of elastic moduli E, of the "universal hardness" HU and of the whole indentation curves clearly underlines the reliability of the resultant values of the Vickers "plastic" hardness H_V (details of the measurements [2]). Of a particular importance is the similarity of the areas between the unloading (upper) and loading (lower) curves which is proportional to the energy of the plastic deformation. Because it is small as compared to the total area under the unloading curve in both cases, both the "plastic" hardness and the elastic recovery are indeed high [28]. The elastic recovery of about 80 % reported earlier for superhard (H $\approx$ 50 GPa) nc-TiN/a-Si_3N_4 and nc-W_2N/a-Si_3N_4 coatings [1] increases to about 90 % for the present ones. The Vickers hardness calculated from the size of indentation at 100 mN (Fig. 2a) of 91 GPa agrees with that from the indentometer (Fig. 3).

Figure 3 shows the average value of "plastic" hardness of this coating and of the nc-diamond vs. the maximum applied load. One notices that at a load of 50-70 mN the average value of the hardness of our nanocomposites exceeds 105 GPa. The apparent decrease at 30 mN is due to the a surface roughness which is comparable to the small indentation depth. At a load of 100 mN the indentation depth is about 17 % of the film thickness and the effect of the soft steel substrate becomes apparent [2]. Nevertheless, the depth sensing indentation measurements as well as the determination of the hardness from the area of the remaining 'pseudoplastic' indentation (Fig. 2a) yield the same hardness of about 90 GPa.

The measured hardness of coatings may be increased by a biaxial compressive stress of $\geq$ 5 GPa caused by energetic ion bombardment during the deposition [29,30]. Upon annealing to 600-700 °C this stress relaxes [30] and the hardness of the coatings decreases to the usual value of a given material [31]. Such an enhancement can be certainly ruled out in our coatings because the biaxial stress measured from the bending of the substrate is less that 0.5 GPa even for 10 μm thick films. Furthermore, the hardness remains constant after 0.5 hr annealing at $\geq$ 600 °C [27].

The fracture toughness of coatings is determined form the measured dependence of the length of "radial cracks" on the applied load [3,32,33]. Figure 2b shows typical example of the indentation 'inverse pyramids' obtained under a high load of 1000 mN into a somewhat softer coating of a thickness of 10.7 μm. The observed absence of any cracks at such a high load is typical for both, superhard nc-TiN/a-Si_3N_4 (H = 40–60 GPa) and ultrahard nc-TiN/a-Si_3N_4/a- and nc-$TiSi_2$ (H $\geq$ 80 GPa) if the film thickness exceeds about 10 μm. In the case of the 3-4 μm thin coating and load of 1000 mN the film is pressed $\geq$ 5 μm into the soft substrate: only circular but no radial cracks are found within the crater. Our present study concentrates on the question if the absence of radial cracks reported here is due to either high fracture toughness or to a high threshold for crack initiation [3,33].

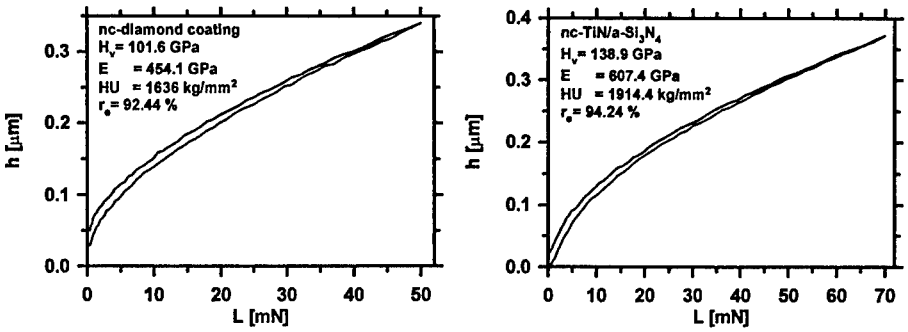
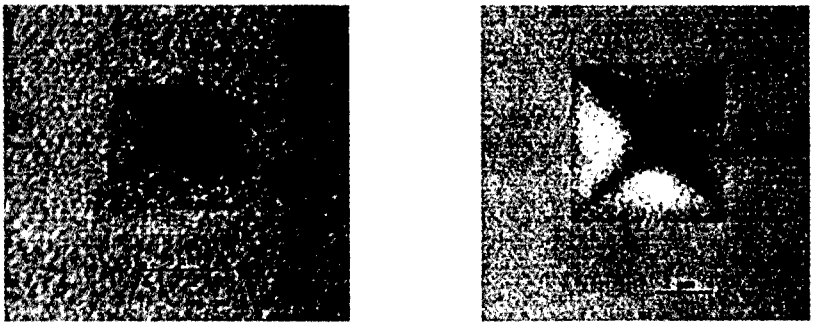


Fig. 1: Example of indentation curves into **a:** 1.5 µm thick single phase nc-diamond [23] and **b:** 3.5 µm thick nc-TiN/a-Si_3N_4/a- and nc-$TiSi_2$ coatings. The inserts show the corresponding Vickers "plastic" hardness H_V, elastic modulus corrected for the elastic deformation of the indentor E and the "universal hardness" HU (the elastic plus plastic deformation under the maximal load). Notice that a higher load was used in Fig. b than in a.



3.5 µm, 100 mN **10.3 µm, 1000 mN**

Fig. 2: Scanning electron micrographs of remaining "plastic" indentation: **a:** 3.5 µm thick ultrahard coating from Fig. 1 after applied load of 100 mN, **b:** a somewhat softer 10.7 µm thick coating after indentation with a load of 1000 mN. The absence of radial cracks in the diagonal direction shows the high toughness of the material.

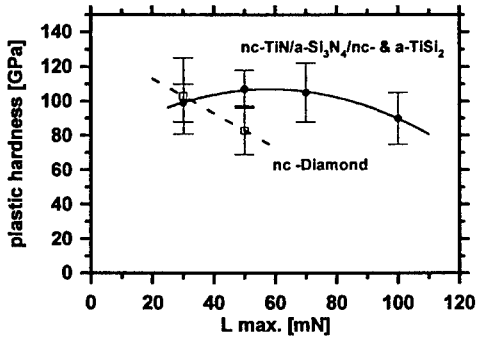


Fig. 3: Hardness of 3.5 µm thick nc-TiN/a-Si_3N_4/a- and nc-$TiSi_2$ nanocomposite and of 1.5 µm thick single phase nanocrystalline diamond [23] vs. the maximum applied load.

CONCLUSIONS

The hardness of about 105 GPa reported here for the nc-TiN/a- and nc-$TiSi_2$ is about a factor of 4 to 5 higher than that of TiN and about a factor of 5.5 higher than that of Si_3N_4. This is within the usual range of strengthening of engineering materials by an appropriate tailoring of their microstructure (see e.g. [34]). Therefore the ultrahardness of our nanocomposites in the range of diamond is a simple consequence of the appropriate design of their nanostructure and of the TiN/Si_3N_4 interface which avoids the grain boundary sliding.

The high elasticity and toughness is also a logical consequence of the nanostructure: The high elasticity follows from the absence of dislocation activity in $\leq$ 10 nm small nanocrystals. The "pseudoplastic" deformation observed under the indentation is due to a brittle fracture, such as observed in glasses and ceramics. The high hardness and toughness can be understood in terms of ample possibilities for deflection, meandering and termination of nanocracks, all of which can absorb a high energy, in the randomly oriented nanocomposite, and in their reversible closure upon unloading. These superior mechanical properties are a simple consequence of the appropriate design of the nanostructure. These results lend further support to our generic concept for the design of superhard nanocomposites and underline its fairly broad validity.

ACKNOWLEDGMENT

We should like to thank Drs. D. M. Gruen and A. R. Krauss for providing us with the single phase nanocrystalline diamond films. This work has been supported in part by the German Science Foundation (DFG) and by the NATO Programme Science for Peace SfP 972379.

REFERENCES

[1] S. Veprek, S. Reiprich and Li Shizhi, Appl. Phys. Lett. **66**, 2640 (1995); S. Veprek and S. Reiprich, Thin Solid Films **268**, 64 (1996); S. Veprek, M. Haussmann and S. Reiprich, J. Vac. Sci. Technol. **A 14**, 46 (1996).
[2] S. Veprek, Critical Review in J. Vac. Sci. Technol. **A 17** (1999) (Sept. /Oct.) in press
[3] Our current work concentrates on the question if the absence of radial cracks is due to a high specific energy of crack propagation ('toughness' [4]) $K_C \propto (E/H)(P/a^{3/2}$ (E-elastic modulus, H-hardness, P-applied load, a-length of the radial crack) or to a high threshold of the cracks initiation (see below).
[4] A. Niederhofer, P. Nesladek, H. Männling, K. Moto, S. Veprek and M. Jilek, ICMCTF 1999 (San Diego April 1999), Surf. Coatings Technol. in press.
[5] R. W. Hertzberg, *Deformation and Fracture Mechanics of Engineering Materials*, 3rd ed. (Wiley, New York, 1989).
[6] A. Kelly and N. H. MacMillan, *Strong Solids*, 3rd. ed. (Clarendon Press, Oxford, 1986).
[7] E. O. Hall, Proc. Phys. Soc. **B 64**, 747 (1951).
[8] N. J. Petch, J. Iron Steel Inst. **174**, 25 (1953).
[9] A. Lasalmonie and J.L. Strudel, J. Mater. Sci. **21**, 1837 (1986).
[10] A. H. Chokshi, A. Rosen, J. Karch and H. Gleiter, Scripta Metal. **23**, 1679 (1989).
[11] R. W. Siegel and G. E. Fougere, NanoStructured Mater. **6**, 205 (1995).
[12] H. Hahn and K. A. Padmanabhan, Phil. Mag. B **76**, 559 (1997).
[13] S. Yip, Nature **391**, 532 (1998).
[14] J. Schiotz, E. D. Di Tolla and K. W. Jacobsen, Nature **391**, 561 (1998)
[15] S. Veprek, M. Haussmann, S. Reiprich, Li Shizhi and J. Dian, Surf. Coatings Technol. **86/87**, 394 (1996).
[16] S. Veprek, P. Nesladek, A. Niederhofer, F. Glatz, M. Jilek and M. Sima, Surf. Coatings Technol. **108/109**, 138 (1998).

[17] P. Holubar, M. Jilek and M. Sima, Int. Conf. Metallurgical Coatings and Thin Films, San Diego, April 1999, Surf. Coatings Technol. (1999) in press.
[18] W. Gissler, M. A. Baker, J. Haupt, P. N. Gibson, R. Gilmore and T. P. Mollart, Diamond Films and Technology, **7**, 165 (1997).
[19] C. Mitterer, P. Losbichler, F. Hofer, P. Warbichler, P. N. Gibson and W. Gissler, Vacuum **50**, 313 (1998).
[20] Ch.-M. Sung and M. Sung, Materials Chemistry and Physics, **43**, 1 (1996).
[21] J. Wilks and E. Wilks, *Properties and Applications of Diamond* (Butterworth-Heineman, Oxford 1991)
[22] G.B. Bokii, N. F. Kirova and V. I. Nepsha, Sov. Phys. Dokladi, **24**, 83 (1979).
[23] D. M. Gruen, MRS Bulletin **23**, 32 (1998) No. 9, September.
[24] G. Tabor, *The Hardness of Metals* (Clarendon Press, Oxford, 1951).
[25] S. Christiansen, M. Albrecht, H.P. Strunk and S. Veprek, J. Vac. Sci. Technol. **B 16**, 19 (1998).
[26] R. Zallen, *The Physics of Amorphous Solids* (John Willey, New York 1983).
[27] A. Niederhofer, P. Nesladek, H.-D. Männling, S. Veprek and M. Jilek, Int. Conf. Metallurgical Coatings and Thin Films, San Diego, April 1999, Surf. Coatings Technol., (1999) in press.
[28] T. F. Page and S. V. Hainsworth, Surf. Coatings Technol. **61**, 201 (1993).
[29] S. Veprek, F.-A. Sarott and Z. Iqbal, Phys. Rev. **36**, 3344 (1987).
[30] H. Ottel, R. Wiedemann and S. Preissler, Surf. Coatings Technol. **74/75**, 273 (1995).
[31] W. Herr and E. Broszeit, Surf. Coatings Technol. **97**, 335 (1997).
[32] C. B. Ponton and R. D. Rawlings, Mater. Sci. Technol. **5**, 865 (1989)
[33] G. M. Pharr, Mater. Sci. Eng. **A 253**, 151 (1998).
[34] A. Inoue, H. M. Kimura, K. Sasamori and T. Matsumoto **35**, 85 (1994).

CRACK HEALING IN AN ALUMINA/SILICON CARBIDE NANOCOMPOSITE AFTER GRINDING AND ANNEALING

H.Z. WU*, J.M. TITCHMARSH*, S.G. ROBERTS*, B. DERBY**
*Department of Materials, University of Oxford, Parks Road, Oxford OX1 3PH, UK
**Manchester Materials Science Centre, Grosvenor Street, Manchester M1 7HS, UK

ABSTRACT

Alumina/silicon carbide nanocomposites are known to show their highest strength levels after surface grinding followed by annealing. After annealing in flowing argon, nanocomposites with very coarsely ground surfaces have strengths exceeding those with a finely polished surface. Specimens with lapped surfaces also show a small improvement in strength on annealing. TEM investigations of annealed cross-sections show that the annealing process leads to surface crack healing. The chemical composition of the subsurface region has been studied, and reactive products on and close to the nanocomposite surface after annealing have been investigated by energy dispersive X-ray analysis in the STEM.

INTRODUCTON

Strengthening of Al_2O_3/SiC nanocomposites after annealing was reported by Niihara *et al.* [1]. They found that after annealing at 1300°C for 2 hrs in argon or air, the Al_2O_3/SiC nanocomposite increased in bending strength from 1000 MPa to 1500 MPa. They attributed this strengthening effect to the following possible mechanisms: healing of subsurface cracks, relaxation of local residual stress originating from different thermal expansion coefficients, and the formation of sub-grain boundaries. Later Zhao *et al.* [2] also reported a strengthening effect after annealing but with a smaller strength increase. They argued that annealing had the double effect of diminishing the compressive surface residual stress after surface machining while also healing the surface flaws. Thompson *et al.* [3] investigated whether machining flaws could be healed in Al_2O_3/SiC nanocomposites during annealing by comparing the healing behaviour of indentation cracks in Al_2O_3/SiC and Al_2O_3. Wu *et al.* [4] found that a machine ground nanocomposite, with a severely damaged surface, could be strengthened to a level greater than that of a finely lapped nanocomposite. By measuring the surface Rayleigh wave velocity with line-focus acoustic microscopy, the results showed that annealing increases the surface elastic modulus of the ground nanocomposite. This surface stiffness improvement is thought to be an indication of subsurface crack healing during annealing. Further study indicated that chemical reactions occured on the surfaces during annealing although the precise mechanisms leading to strengthening were unclear.

In this paper we investigate further the mechanisms of strengthening of Al_2O_3/SiC nanocomposites after grinding and annealing, using TEM of surface cross-sections.

EXPERIMENT

The Al_2O_3/SiC nanocomposites used in this investigation were prepared by hot-pressing with a standard freezing-drying powder preparation method explained in detail elsewhere [5]. α-Al_2O_3 powder (AKP53 Sumitoma, Japan) is mixed with 5% by volume SiC particles (UF45 Lonza, Germany) of diameter $\approx$ 90 nm by attrition milling and then hot pressed at 1650°C for 1 hour under flowing Ar. Two surface finishing conditions are investigated here: ground with a resin

Mat. Res. Soc. Symp. Proc. Vol. 581 © 2000 Materials Research Society

bonded diamond wheel containing 150 μm grit, and fine lapped with 1 μm diamond grit. All anneals were carried out at 1250 °C in flowing Ar for 10 hours. Small test bars were cut from the hot pressed plates for 4-point bending characterisation. Surface residual stresses in the samples before and after annealing were measured using a Hertzian indentation technique described in detail elsewhere and in a companion paper [6, 7].

All of the TEM foils were prepared from the bend strength test bars. The cross section TEM specimens were prepared in the conventional manner by gluing two surfaces together. The region of interest was dimpled on both sides to a thickness about 20-50 μm before ion milling the dimpled specimen for TEM observation. To prevent charging during TEM observation, some of the specimens were coated with carbon.

TEM observations were carried out using JEM 200CX and Philips CM20 microscopes at 200 kV. Energy dispersive X-ray analysis (EDX) was performed using a Vacuum Generator HB 501 dedicated scanning transmission electron microscope (STEM) with a cold field emission electron source (FEG) configured to provide a probe at the specimen with a diameter of approximately 2.5 nm. EDX spectra were recorded using an Oxford Instrument LZ5 windowless detector and AN10 system. Concentration profiles were derived by conventional spectral processing using the Oxford Instrument RTS2 software package.

RESULTS

Bend Strength and Surface Residual Stress

The 4-point bend strengths of ground and fine lapped nanocomposites before and after annealing are shown in figure 1. For comparison the data for ground alumina are also included. Annealing clearly increases the strength of the ground Al_2O_3/SiC nanocomposite but has no detectable effect on the ground Al_2O_3 specimen. Figure 2 shows the residual stress levels measured by Hertzian indentation. These residual stress values are relative to a finely polished Al_2O_3 surface which is assumed to be a reference stress-free surface. Grinding introduces large compressive surface residual stresses which are mostly removed by the polishing process. After annealing, both ground and fine lapped surfaces have a residual stress level of about 150 to 200 MPa. Thus annealing reduces the residual stress found on the nanocomposite surface but

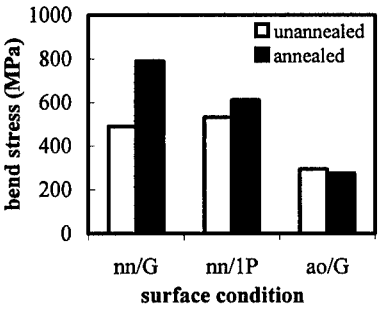


Fig. 1 4-point bending strength before and after annealing for nanocomposite finshed with machine grinding (nn/G), 1 μm diamond lapping (nn/1P) and alumina with grinding (ao/G).

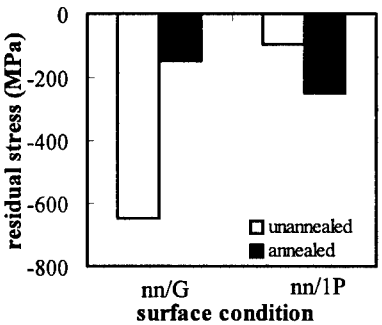
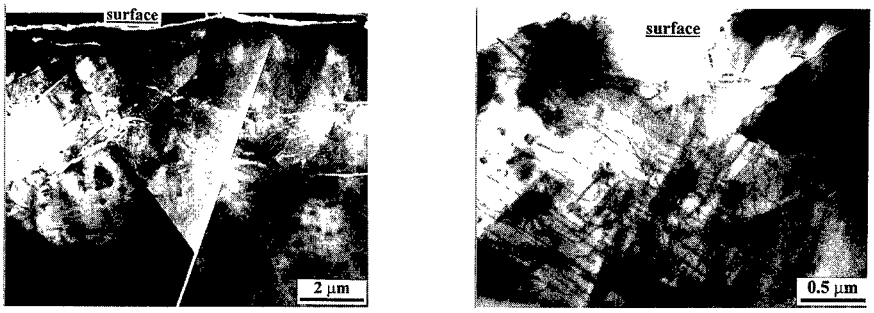


Fig. 2 Residual stress before and after annealing for nanocomposite finished with machine grinding (nn/G) and 1 μm diamond lapping (nn/1P).



A) B)

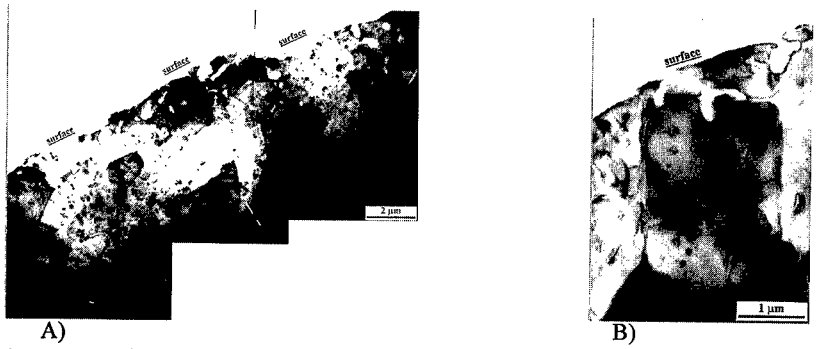
Fig. 3 TEM subsurface microstructure of ground nanocomposite

increases that of the polished surface. This is unexpected since the slow cooling rate (10 °C/min) should have little quenching effect.

Subsurface Microstructure

Figure 3 shows a cross-section beneath the surface of a ground Al_2O_3/SiC nanocomposite. In figure 3A extensive cracking can be seen extending about 10 μm beneath the surface. At higher magnifications, in figure 3B, we can see that the deformation substructure is dominated by dislocations. It is these which are believed to explain the high residual stress levels observed in the nanocomposite. Similarly treated Al_2O_3 surfaces show twinning rather than such extensive dislocation structures [7]. Figure 4A is a TEM cross-section of the ground nanocomposite surface after annealing: no cracks can be seen. This is true of many other locations studied and is consistent with other observations of crack healing elsewhere [3, 4]. Figure 4B shows a higher magnification of the subsurface microstructure; the dislocation networks introduced by grinding have been substantially removed by annealing. Grain boundaries near to the surface in the annealed specimens were observed to contain a thicker interfacial layer. This is analysed in more detail in the following section.

EDX Analysis



A) B)

Fig. 4 TEM microstructure of annealed ground nanocomposite subsurface

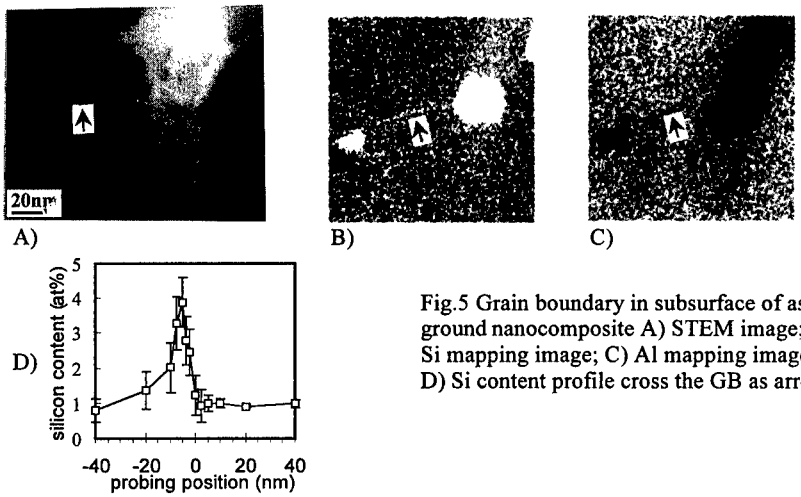


Fig.5 Grain boundary in subsurface of as-ground nanocomposite A) STEM image; B) Si mapping image; C) Al mapping image; D) Si content profile cross the GB as arrowed

EDX elemental maps contain random statistical noise, the level of which depends upon the count rate at each pixel. In addition, it is sometimes difficult to understand how the intensities of all the elements at a given pixel are inter-related. These problems can be addressed by applying a multivariate statistical analysis method to identify the correlation between elements and to separate them from the noise [8]. A program has been adapted from software originally written to analyse EDX spectra [9, 10]. The program outputs maps where the statistically significant correlations and anti-correlations between the elements are explicitly revealed. Figure 5a shows a grain boundary in an un-annealed nanocomposite; figures 5b, c show mapped images for Si and

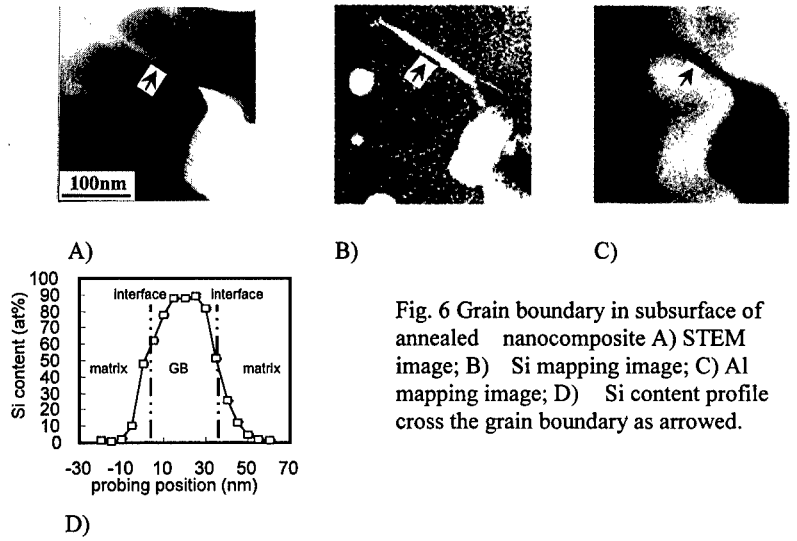


Fig. 6 Grain boundary in subsurface of annealed nanocomposite A) STEM image; B) Si mapping image; C) Al mapping image; D) Si content profile cross the grain boundary as arrowed.

Al elements respectively; figure 5d is the Si content profile cross the grain boundary shown in figure 5a. Figure 6a shows a grain boundary in an annealed nanocomposite; figures 6b and c mapped images for Si and Al element respectively; figure 6d is the Si content profile cross the reacted grain boundary. The method greatly enhances the visibility of elements present in low concentration that might otherwise be overlooked.

Figure 5 shows that Si segregates to the grain boundary during processing even though this grain boundary is very narrow, < 1nm. The Si content across this grain boundary shows a small peak on the boundary. Note that this does not represent the real element content as the probe size is bigger than the grain boundary width. After annealing, grain boundaries becomes wider as shown in figure 6. The Si profile cross the grain boundary now shows a massive local segregation and the almost total exclusion of Al from the bonding region.

Table 1 summarises our findings concerning the Si content of grain boundaries beneath the ground and annealed nanocomposite surfaces. The region of extreme Si segregation at boundaries in annealed material extends to a distance less than 20 μm below the surface. At depths greater than this the grain boundary composition was similar to that found with unannealed specimens. The trace Y and Zr detected in the nanocomposites is probably contamination introduced by attrition milling.

Table I Si and Al content on the subsurface grain boundaries before and after annealing

Sample condition	Annealed		Unannealed	
Detected GB position	Si (at%)	Al (at%)	Si (at%)	Al (at%)
Top surface	89.49	10.51	3.89	96.11
20 μm below top	4.88 (+Y, Zr)	95.12	N/A	N/A
100 μm below top	4.82 (+Y, Zr)	95.18	N/A	N/A

DISCUSSION

When the nanocomposites are annealed at 1250 °C in the flowing Ar, the damaged surfaces recover. This subsurface integrity recovery is thought to be a result of chemical reaction bonding between crack surfaces [3]. It is difficult to identify the locations of any healed cracks on an annealed surface because they are likely to be indistinguishable from grain boundaries. However, features of grain boundaries which intersect the surface of the annealed specimens may give some clues to the mechanisms of crack healing and/or surface strengthening. We note that near-surface grain boundaries in the annealed specimens show an increase in thickness and a high Si content when compared to unannealed boundaries or boundaries deep within annealed specimens. We propose that this thickening occurs by oxidation within the nanocomposite driven by diffusion of Si outwards and O from the atmosphere into the material along the grain boundaries, with the SiC particles located on grain boundaries within the nanocomposite acting as the Si source.

An internal oxidation mechanism, with its accompanying volume expansion, can also explain the residual compressive stress found in both the ground and polished nanocomposite specimens after annealing. It is well known that SiC particles undergo a volume expansion on oxidation to SiO_2 and that a further expansion occurs if the SiO_2 reacts with Al_2O_3 to form mullite. All these products (even when amorphous) have coefficients of thermal expansion lower than α-Al_2O_3. Thus in addition to any volume expansion on oxidation, a surface compressive stress could also be generated on cooling by thermal expansion mismatch between the surface and interior.

We conclude that our results are consistent with earlier findings [3, 4] that annealing results in crack healing of Al_2O_3/SiC nanocomposite surfaces. The most likely mechanism is driven by oxidation of the SiC particles and that it is this oxidation which results in the relatively high levels of retained surface compressive stress even after extensive annealing.

ACKNOWLEDGEMENTS

This work is funded by the EPSRC under grant GR/L95908.

REFERENCE

1. Niihara K., and Nakahira A., J. Ceram. Soc. Jpn., **99**, 974 (1991).
2. Zhao J., Stearns L.C., Harmer M.P., Chan H.M., Miller G.A., and Cook R.E., J. Amer. Ceram. Soc., **76**, 503 (1993).
3. A.M. Thompson, H.M. Chan and M.P. Harmer, J. Amer. Ceram. Soc., **78**, 567 (1995).
4. H.Z. Wu, C.W. Lawrence, S.G. Roberts and B. Derby, Acta Mater., **46**, 3839 (1998).
5. M. Sternitzke, B. Derby and R.J. Brook, J. Amer. Ceram.Soc. **81**, 41 (1998).
6. Roberts S.G., Lawrence C.W., Bisrat Y., Warren P.D., and Hill D.A., J. Amer. Ceram. Soc., **82**, 1809 (1999).
7. H.Z Wu, S.G. Roberts, A. Winn and B. Derby, this proceedings (1999)
8. P. Trebbia and N. Bonnet, Ultramicroscopy, **34**, 165 (1990).
9. J.M. Titchmarsh and S.Dumbill, J. Microscopy, **184**, 195 (1996).
10. J.M. Titchmarsh, Micron, **30**, 159 (1999)
11. H.Z. Wu, S.G. Roberts and B. Derby, unpublished

Fe-Al_2O_3 NANOCOMPOSITE: SYNTHESIS AND MAGNETIC PROPERTIES

A. SANTOS,[1] W. A. A. MACEDO,[1] J. D. ARDISSON,[1] A. D. C. VIEGAS,[2] J. E. SCHMIDT[2]
[1] Laboratório de Física Aplicada, Centro de Desenvolvimento da Tecnologia Nuclear – CDTN, CNEN / MCT, 30123-970 Belo Horizonte, Brazil.
[2] Instituto de Física, Universidade Federal do Rio Grande do Sul, 91501 Porto Alegre, Brazil.

ABSTRACT

We have investigated the synthesis and the structural and magnetic properties of Fe nanoparticles embedded in Al_2O_3 matrix, a granular nanocomposite prepared by sol-gel processing. Samples with volumetric Fe content ranging from 20 to 62% were obtained starting from Al nitrate and Fe sulfate as precursors and the preparation method results initially in a mixture of Fe- and Al oxides. The conversion of Fe oxides into metallic Fe was done by calcination at 800° C followed of reduction at 600° C for 2 hours, in H_2 atmosphere. Our results indicated the following phases in the amorphous alumina matrix, after reduction: α-Fe, the main phase, α- and γ-Fe_2O_3, Fe_3O_4 and some interstitial Fe^{2+} and substitutional Fe^{3+} atoms in the Al_2O_3 lattice. For the investigated system, Fe reduction rate was very sensitive to the sample porosity and, with the applied method, we have obtained reductions of the Fe atoms into metallic Fe ranging from 45 to 68%, preserving the mean diameter of the α-Fe nanoparticles between 55 and 80 nm. VSM measurements at room temperature resulted in coercivity between 450 and 630 Oe and saturation magnetization between 40 and 110 emu/g. Magneto-transport measurements in samples with 25% metallic Fe (and 51% total Fe) reveal ΔR/R close to 2% at room temperature.

INTRODUCTION

The study of granular magnetic materials, composites of magnetic nanoparticles embedded in a nonmagnetic matrix, has attracted much attention in the last years since granular solids have been found to present interesting properties like giant magnetoresistance [1-3]. Several methods have been used to prepare magnetic granular Fe - ceramic systems. Sputtering [4], evaporation [5], ball milling [6] and different chemical routes are applied. Sol-gel method is one chemical route that present the advantages of high reproducibility and easy scale up from bench scale to the processing of high quantities. Sol-gel processing was applied, for example, to obtain Fe-SiO_2 [7], Ni-SiO_2 [8] and Fe-Al_2O_3 [9] nanocomposites. In ref. [7], the applied reduction at 350° C resulted in low reduction rate for Fe atoms. For Ni-SiO_2, reduction in H_2 at a temperature range of 600 - 900° C [8] allowed the complete reduction of Ni oxides to metallic Ni. In a previous work [9], we have investigated the sol-gel synthesis and the structural and magnetic properties of Fe nanoparticles homogeneously dispersed in alumina, within a range of low concentration of Fe (1 – 2.5 vol.%). For these samples, by applying H_2-reduction at temperatures ranging from 600 to 1000° C, we have obtained conversion rates as high as 74% and a maximal coercivity of 819 Oe. Granular Fe–Al_2O_3 powder prepared by ball milling within a broad Fe concentration range have shown maximal coercivity ranging from 230 to 550 Oe [6, 10, 11].

In this paper, we extend our investigation of the Fe-Al_2O_3 nanocomposite by increasing

Mat. Res. Soc. Symp. Proc. Vol. 581 © 2000 Materials Research Society

the Fe content to the range of 20 to 62% in volume. Moreover, in order to inhibit the particle growth and maximize the Fe reduction rate, by preserving the porosity of the matrix after calcination, we have changed the procedures for washing and drying the initial inorganic network obtained by sol-gel method. We present the obtained structural and magnetic properties.

EXPERIMENT

Samples with nominal volumetric Fe content ranging from 20 to 62% were prepared starting from solutions with adequate concentrations of $Al(NO_3)_3.9H_2O$ and $FeSO_4.7H_2O$ as precursors, dropped slowly in a NH_3 solution (the precipitating agent) under vigorous stirring and allowed to gel for 12 h. This procedure leads to the formation of complex Fe and Al salts and oxides particles via sol-gel transformation. After precipitation, the ferruginous gel was submitted to distillation in an azeotropic solution of 95.6% ethanol – 4.4% H_2O for remotion of water from the porous structure and than dried at 80°C for 12 hours. Next, the samples were calcinated at 300, 600 and 800° C in air and heat treated at 600° C in H_2 atmosphere during 2 hours for the reduction of Fe oxides into metallic Fe. After calcination, the total Fe content was determined by atomic absorption spectroscopy and the loss of mass was determined by thermogravimetry differential thermoanalysis (TG/DTA) measurements. The obtained powder samples with final composition Fe_X - $(Al_2O_3)_{1-X}$, $20 < X < 62$ vol.%, were characterized by atomic absorption, x-ray diffraction (XRD), employing Cu-k radiation, by Mössbauer spectroscopy (MS) and by vibrating sample magnetometry (VSM). XRD was used to identify the phases and also to estimate the average particle size by using the Scherrer's equation. Transmission ^{57}Fe Mössbauer spectra (20 K to room temperature) have been obtained on a constant acceleration transducer with a $^{57}Co/Rh$ source. The Normos least-squares fit program was used for data processing. After H_2-reduction, few powder samples were compacted at 4 ton/cm^2 and the resulting pellets (10 mm diameter) were submitted to magneto-transport measurements at room temperature.

RESULTS AND DISCUSSION

Fig.1 shows typical x-rays diffraction patterns for Fe-Al_2O_3 samples in the different stages of the synthesis process. The insulating medium is amorphous and largely featureless in XRD during all the process, as normally observed in similar systems. As-prepared samples (dried gels) are characterized by the absence of diffraction patterns of crystalline Fe-oxides (Fig. 1.a). Calcination at 800° C results in loss of mass of 45%, due to the decomposition of complex salts containing NH_4^+, SO_4^{2-} and Fe or Al ions and only diffraction patterns of α-Fe_2O_3, the predominant phase, and some Fe_3O_4 are observed in the different samples (Fig. 1.b). The elimination of NH_4^+ and SO_4^{2-} compounds induces a mesoporous structure with average diameter equal to 9 nm, as determined by the BET method. After H_2-reduction at 600° C for 2 h, only reflections due to metallic Fe and Fe_3O_4 are detected, as shown in Fig. 1.c. The average diameter of the α-Fe nanoparticles was calculated to be in the range 55 - 80 nm, very close to the diameter of the precursor α-Fe_2O_3 particles, demonstrating that a sintering process did not take place during the reduction heat treatment.

Typical room temperature Mössbauer spectra are shown in Figure 2, with the results for a samples with 51% Fe. Although not clearly observed in our XDR measurements (Fig.

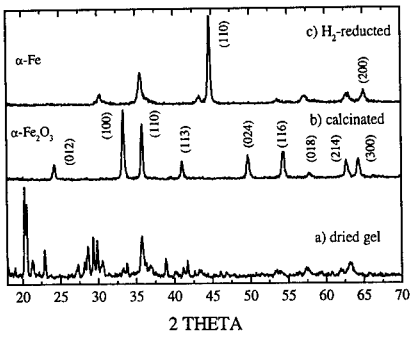


Fig. 1 – Typical x-ray diffraction patterns corresponding to the different phases of the synthesis process of granular Fe – Al_2O_3 nanocomposite, illustrated for a sample with 51% Fe after drying at 80° C (a), calcinated at 800° C (b) and after H_2 – reduction at 600° C (c). Fe_2O_3 peaks are labeled in (b) and α-Fe peaks are labeled in (c).

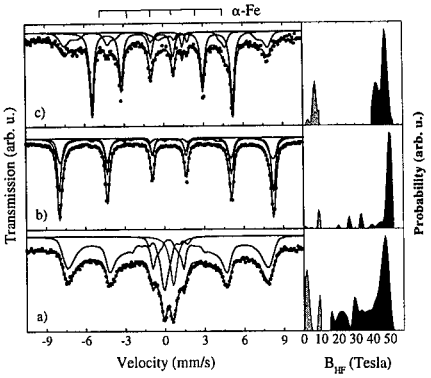


Fig. 2 – Typical room temperature Mössbauer spectra corresponding to the different phases of the synthesis process of granular Fe – Al_2O_3 nanocomposite, illustrated for a sample with 51% Fe after drying at 80° C (a), calcinated at 800° C (b) and after H_2 – reduction at 600° C (c).

1.a), the as-prepared samples have the Fe atoms distributed in Fe_3O_4, γ- and α-Fe_2O_3 and some Fe in the matrix (Fig. 2.a). Fe oxides are fitted as broad hyperfine field distribution at high fields (grey area) and Fe atoms in the matrix, whose Fe^{3+} and Fe^{2+} doublets are here taken in account by the distribution at low fields (light grey area), aspect better resolved at low temperature (see bellow). Fe_3O_4 and γ-Fe_2O_3 represent between 70 and 85% of the total Fe-phases and these samples present superparamagnetic behavior, characterized by the reduction and/or collapse of the magnetic hyperfine fields of the nanoparticles. After calcination, Mössbauer spectra are characterized by a broad six line pattern due to the superposition of sextets of α-Fe_2O_3, the predominant phase, and some Fe_3O_4 (Fig. 2.b). Due to the growth of the particles size, the superparamagnetic behavior is almost removed. The effectiveness of the applied H_2-reduction heat treatment is illustrated in Fig. 2.c, where α-Fe represents 52% of the spectral area.

Low temperature (20 K) Mössbauer spectra are shown in Figure 3 for samples with different Fe content, measurements that allow a better fit by resolving superparamagnetic behavior of the nanometric particles. The conversion rate of iron oxides into metallic iron is nearly constant for the different samples, as illustrated in Figure 4, where the spectral area of the Fe-phases is plotted against the total Fe volumetric fraction in Al_2O_3 assuming equal Debye-Waller factors at 20 K. The Fe oxides curve includes Fe_3O_4, α- and γ-Fe_2O_3. The Mössbauer results indicate that ~10% of the spectral areas can be attributed to Fe^{3+} ions occupying substitutional (Al^{3+}) and Fe^{2+} ions occupying interstitial positions in the Al_2O_3 lattice [12, 13], characterized by quadrupole splittings close to 0.85 mm/s and 1.75 mm/s, respectively, and represented by the distribution at low fields. Since the particles diameter does not change very much for different Fe fractions, as determined by XRD, we could speculate that the reduction of the oxide particles conduct to metallic particles with oxide

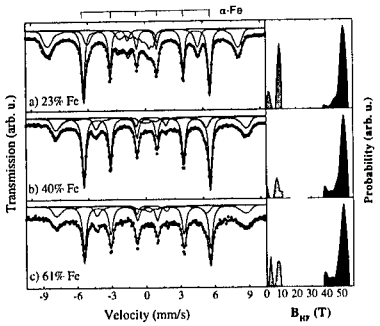


Fig. 3 – Mössbauer spectra at 20 K of granu lar F0e – Al_2O_3 nanocomposites with different Fe concentrations: 23% (a), 40% (b) and 61% (c) total Fe.

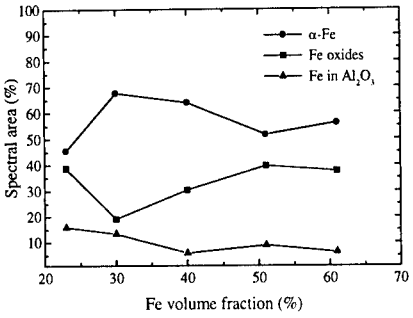


Fig. 4 – Spectral area of the different Fe-phases as a function of the Fe volumetric fraction, as obtained by Mössbauer spectroscopy

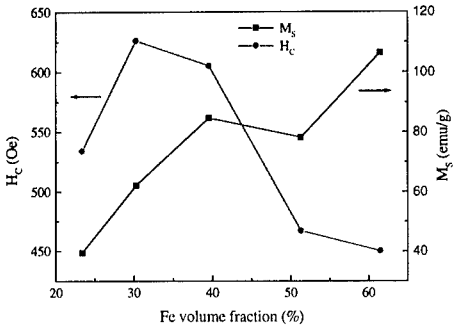


Fig. 5 – Room temperature saturation magnetization (M_S) and coercivity (H_C) of the Fe-Al_2O_3 granular samples, as obtained by VSM measurements.

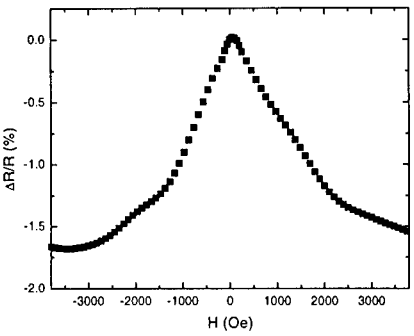


Fig. 6 – Room temperature Magneto-resistance of a 51% Fe – Al_2O_3 pellet sample, measured at 10 mA.

cores (~40%), instead of a mixture of reduced and non-reduced Fe particles.

The saturation magnetization at 1 T and coercivity presented by the samples were determined by VSM measurements at room temperature and are shown in Fig. 5 as a function of the Fe content. The observed saturation magnetization, ranging from 40 to 110 emu/g is in accordance with the expected value due to a mixture of α-Fe (218 emu/g), Fe_2O_3 (92 emu/g) and Fe_3O_4 (76 emu/g) diluted in a non-magnetic matrix. The coercivity presents a maximum (~ 630 Oe) near 30 – 40 vol.% Fe, fraction that represents the magnetic percolation of the particles and above which the coercivity decreases due to formation of magnetic closure domains and, than, multidomain behavior. The value of 630 Oe is higher than the coercivity

obtained by other authors for Fe – Al_2O_3 prepared by ball milling and after long milling time [6, 10, 11]. Giri [11], for example, has obtained a maximum coercivity of 550 Oe for 40 % Fe after 42 h. milling time.

Magneto-transport measurements were performed for few samples as pointed above. Fig. 6 shows the better result for the room temperature magnetoresistance, 1.8% measured at 10 mA, obtained for a 51% Fe – Al_2O_3 sample (25% metallic Fe). In the plot, the observed anomalies near ± 1500 – 2000 Oe are indication that the MR of the sample can be driven by two different processes. The low GMR value could be explained by the relatively big particles (60-70 nm) since tunneling assisted GMR requires smaller particles and defined dimensions of the non-magnetic spacers. Equivalent codeposited Fe-Al_2O_3 thin films reveal higher GMR effects (MR = 3% for 33% Fe-Al_2O_3) [14]. The influence of the sample structure with α-Fe, α- and γ-Fe_2O_3 and Fe_3O_4 dispersed in the Al_2O_3 matrix on the observed MR behavior is not clear. New experiments are in progress and the results will be presented elsewhere.

CONCLUSIONS

Concluding, we have investigated the synthesis and the structural and magnetic properties of granular nanocomposite Fe - Al_2O_3 prepared by sol-gel processing. Samples with volumetric Fe content ranging from 20 to 62% were prepared by calcination at 800° C followed of H_2-reduction at 600° C. For the investigated system, Fe reduction rate was very sensitive to the sample porosity and, with the applied method, we have obtained reductions of the Fe atoms into metallic Fe ranging from 45 to 68%, preserving the mean diameter of the α-Fe nanoparticles between 55 and 80 nm. Significant amount (~35%) of α- and γ-Fe_2O_3, Fe_3O_4 remains embedded in the alumina matrix, which present some diluted interstitial Fe^{2+} and substitutional Fe^{3+} ions in his lattice. VSM measurements at room temperature resulted in saturation magnetization between 40 and 110 emu/g and maximal coercivity of 630 Oe for 30 vol.% Fe, a high coercivity due to single domain nanoparticles dispersed in the alumina. Samples with 25% metallic Fe (and 51% total Fe) show giant magnetoresistance ΔR/R close to 2% at room temperature.

AKNOWLEDGEMENTS

The authors gratefully acknowledge the financial support of the CNEN, CNPq, FAPEMIG and FAPERGS (Brazilian agencies).

REFERENCES

1. J. Q. Xiao, J. S. Jiang and C. L. Chien, Phys. Rev. Lett. **68**, p. 3749 (1992).

2. A. Berkowitz, J. R. Mitchell, M. J. Carrey, A. P. Young, S. Zhang, F. E. Spada, F. T. Parker, A. Hutten and G. Thomas, Phys. Rev. Lett. **68**, p. 3745 (1992).

3. F. Schelp, G. Tosin, M. Carara, M. N. Baibich, A. A. Gomes and J. E. Schmidt, Appl. Phys. Lett. **61**, p. 1858 (1992).

4. G. Xiao and C. L. Chen, Appl. Phys. Lett. **51**, p. 1280 (1987).

5. B. Abeles, P. Sheng, M.D. Couts and Y. Arie, Adv. Phys. **24**, p. 407 (1975).

6. T. Ambrose, A. Gravin and C. L. Chien, J. Magn. Magn. Mater. **116**, L311 (1992).

7. R. D. Shull, J. J. Ritter, A. J. Shapiro, L. J.Schwartzendruber and L. H. Bennett, J. Appl. Phys. **67**, p. 4490 (1990).

8. C. Estournès, T. Lutz, J. Happich, T. Quaranta, P. Wissler and J. L. Guille, J. Magn. Magn. Mater. **173**, p. 83 (1997).

9. A. Santos, J. D. Ardisson, E. Tambourgi and W. A. A. Macedo, J. Magn. Magn. Mater. **177-181**, pp. 247-248 (1998).

10. S. Linderoth and M. S. Pedersen, J. Appl. Phys. **75**, p. 5867 (1994).

11. A. K. Giri, Mat. Res. Bull. **32**, p. 523 (1997).

12. S. K. Date, J. Phys. Soc. Japan **30**, p. 1203 (1971).

13. P. Gütlich, R. Link and A. Trautwein, *Mössbauer Spectroscopy and Metal Chemistry,* Springer, Berlin, 1978, pp. 95-99.

14. S. R. Teixeira, private communication.

CVD OF CARBIDE MULTI-PHASED COATINGS

K.E. Versprille*, Hua Xia Ji*, C.C.Amato-Wierda*, P.J. Ramsey** , D.A. Wierda***
*Materials Science Program, University of New Hampshire, Durham, NH 03824
** Mathematics Department, University of New Hampshire, Durham, NH 03824
***Chemistry Department, Saint Anselm College, Manchester, NH 03102

ABSTRACT

TiC and Ti-W-C films have been produced by chemical vapor deposition (CVD). A fractional factorial design was used to study the effects of deposition temperature, C:Ti input, H:Ti input, reactor pressure, and total mass flow on TiC film composition. Statistical models were developed for both titanium at.% and C:Ti in the film. It was found that the most significant affect on titanium at.% was the interaction of temperature, pressure and total mass flow. The most important affect on the C:Ti in the deposited film was the interaction C:Ti input, H:Ti, and total mass flow. Ti-W-C films have been deposited at 1050°C at various $(TiCl_4+W(CO)_6)/CH_4$ inlet ratios ranging from 0.53 to 1.01. The characterization of the films revealed that the changes in deposition rate, crystallinity, film orientation, and morphology of various Ti-W-C compositions were affected by $(TiCl_4+W(CO)_6)/CH_4$ inlet ratios.

INTRODUCTION

Titanium carbide, TiC, belongs to the class of materials known as transition metal carbides known for their refractory properties and high hardness [1,2]. Further improvement in the mechanical properties of carbide coatings exists by creating multiphase coatings consisting of two or more carbides. In particular, WC exhibits one of the highest Young's moduli among the transition metal carbides; it also has a different crystal structure than the other carbides [1]. Therefore, a multiphase coating consisting of TiC/WC is expected to demonstrate modulus hardening, especially if a nano-structured morphology consisting of nanometer-sized WC grains embedded within a TiC matrix is achieved.

In the study below, CVD is used to deposit Ti-W-C films of varying compositions. The study consists of two parts. First, the effect of CVD processing parameters are modeled against TiC film composition using a statistically significant factorial design. Then, film properties, including atomic composition, deposition rate, crystallinity, film orientation, and morphology of various Ti-W-C compositions are reported.

EXPERIMENT

TiC and Ti-W-C films were deposited on 440C steel by CVD using a gas mixture of $TiCl_4$, CH_4, H_2, Ar, and $W(CO)_6$ for W films. The reactor chamber was a quartz tube with inner diameter of 135mm, heated by a resistance furnace.

For the TiC deposition studies, total furnace pressure, reaction temperature, total mass flow, C:Ti input ratio and H:Ti ratios were adjusted for each experiment according to the fractional 2^{5-1} factorial design. The C:Ti and H:Ti variables were the ratio of mass flow rates of the individual reactants. A total of 22 experiments were completed, 16 different experiments varying the low or high value of each variable were completed and 6 replications of the mid-point experiment were completed. The software program "JMP" was used to analyze the composition fractional factorial design [3]. Table I lists the deposition variables and their low, mid-point, and high values.

Mat. Res. Soc. Symp. Proc. Vol. 581 © 2000 Materials Research Society

Table I. Deposition Variables and Values

Factor	Low value	Mid-point	High value
Reaction Temperature (°C)	950	1000	1050
C:Ti input	1	2	3
H:Ti input	0	9	18
Reaction Pressure (Torr)	50	175	300
Total Mass Flow (sccm)	130	265	400

For the Ti-W-C deposition studies, the reactor temperature and pressure were 1050°C and 150 Torr respectively. The total flow rates were varied in the range of 235-275 sccm. The theoretical inlet ratio of metal to carbide or $(TiCl_4+W(CO)_6)/CH_4$ was determined by the mass flow rates of $TiCl_4$, $W(CO)_6$ and CH_4. The films of varying atomic composition were deposited by varying mass flow rate of $TiCl_4$ while maintaining the mass flow rate of $W(CO)_6$ at constant.

The thickness of the deposits was determined by abrasion through the film, obtained by dimpling together with an abrasive agent (diamond 3μm). The thickness values were calculated from the diameters of the ring prints measured by optical microscopy. The deposition rate was then obtained by the thickness divided by the deposition time. X-ray diffraction was used to characterize phase formation in the films. The composition of the films was determined by auger electron spectroscopy (AES) and by X-ray photoelectron spectroscopy (XPS). The morphologies of the film surface were observed with scanning electron microscopy (SEM). The roughness of the films was obtained by atomic force microscopy (AFM).

RESULTS AND DISCUSSION

PART 1- The Deposition of TiC: How Deposition Variables Affect TiC Film Composition through Fractional Factorial Design

Titanium At.%

The reactor pressure, total mass flow, and H:Ti input exhibit significant main effects on the amount of titanium in the films. Figure 1 shows the prediction profiles of the main affects of these deposition variables. The presence of a slope in the relationship determines whether that variable, by itself, is significant to the titanium at.%, while the direction of the slope determines how the variable will affect titanium at.%. Despite the observation in Fig. 1 that C:Ti input has no main effect, its effect cannot yet be determined due to a highly non-linear relationship to the titanium at.%.

There are several two-way interactions that are important in determining the titanium at.%. They include interactions between C:Ti and total mass flow, reaction temperature and

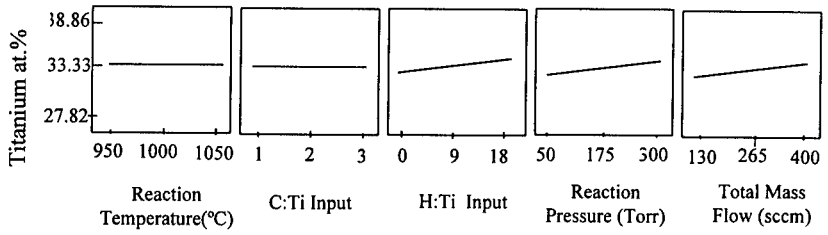


Fig. 1. Titanium at.% prediction profiles vs. main affects of the deposition variables.

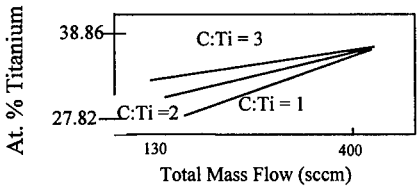


Fig. 2. Interaction between C:Ti input and total mass flow on at.% titanium in films

pressure, reaction temperature and total mass flow, and pressure and total mass flow. Figure 2 is an example of one of these two-way interactions, specifically that between C:Ti input and total mass flow.

The most significant affect on titanium at.% is a three-way interaction between temperature, total mass flow, and reactor pressure. This can be seen from a comparison of the plots in Fig. 3. In Fig. 3a, temperature is at its low value, in Fig. 3b temperature is at its mid value, and in Fig. 3c temperature is at its high value. Note how the interaction of pressure and total flow is a function of temperature as well; namely the relationship between total flow and pressure changes according to the temperature of the reaction.

The preliminary theoretical equation that relates titanium at.% to the most important deposition variables and their interactions is:

Titanium at. % = 33.3322 +(0.26*temperature)+(0.32875*C:Ti input)+ (0.965*H:Ti input) +(1.3337*Pressure)-(0.3475*Temperature*Pressure)+ (1.3562*Total Flow)+ (0.5175*Temperature*Total Flow)- (0.5863*C:Ti input*Total Flow) + (0.3513*Pressure*Total Flow) +(2.2117*Temperature*Total Flow*Pressure) (1)

C:Ti in the Deposited Films

The C:Ti in the deposited films was also studied. This modeling was more complicated since the value of C:Ti in the films will be affected by the deposition of titanium and of carbon. Only mass flow and C:Ti input exhibit main effects on the C:Ti in the film, as seen in Fig. 4.

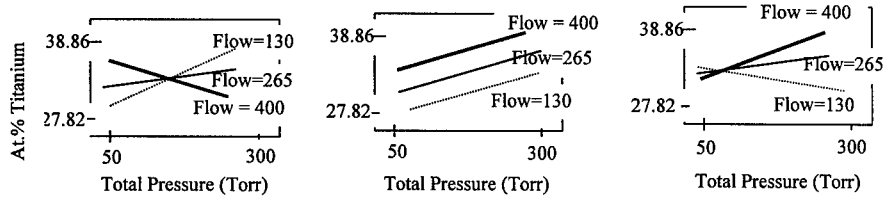


Figure 3a. Temperature 950°C

Figure 3b. Temperature=1000°C

Figure 3c. Temperature = 1050°C

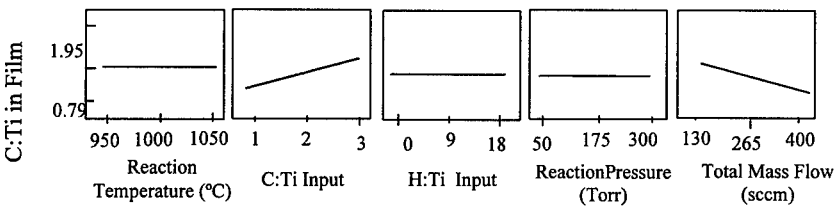


Fig. 4. C:Ti in film prediction profiles vs. main affects of the deposition variables.

There were also several two-way interactions as well as a three-way interaction for modelling the C:Ti in the film. There were two-way interactions between C:Ti input and total mass flow, C:Ti input and H:Ti input, and H:Ti input and total mass flow. The significance of these two way interactions was highlighted by the three-way interaction between total mass flow, C:Ti input, and H:Ti input as seen in Fig. 5.

The preliminary theoretical equation that relates C:Ti in the film to the most important deposition variables and their interactions is:

C:Ti in the film = 1.6500 +(0.08546* C:Ti input) + (0.02210*H:Ti input)
-(0.09672*C:Ti input*H:Ti input) - (0.16031* Total Mass Flow) +
(0.06854*C:Ti input*Total Mass Flow) +(0.043374*Hi:Ti input*Total Mass Flow) –
(0.28099*C:Ti input*H:Ti input*Total Mass Flow) (2)

PART 2- Deposition of Ti-W-C: Ti-W-C films formed at various $(TiCl_4+W(CO)_6)/CH_4$ inlet ratios

Figure 6 shows the results of the compositions determined by AES for the six films with different $(TiCl_4+W(CO)_6)/CH_4$ inlet ratios. The actual ratios of Ti/C and (Ti+W)/C are shown in Fig. 7.

The XRD spectra of samples S1, S3 and S6 are shown in Fig.8. The films consist mainly of TiC phase (PDF: 32-1383). The main reflections associated with TiC are the (111), (200) and (220) at 2θ=35.998, 41.886 and 60.601°, respectively. The intensity ratio of (200) to (111) changes with $(TiCl_4+W(CO)_6)/CH_4$ inlet ratio. It has been reported that the (111) orientation is most common in CVD f.c.c type films [4].

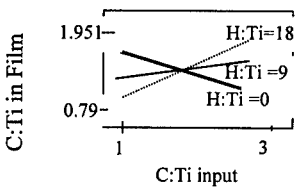


Fig. 5a. Total Flow 130 sccm

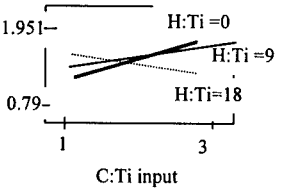


Fig. 5b. Total Flow 265 sccm

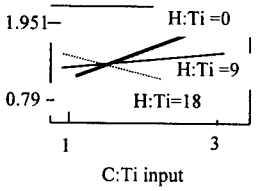


Fig. 5c. Total Flow 400 sccm

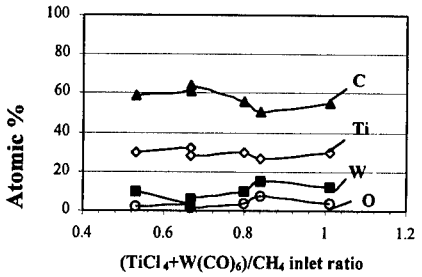


Fig. 6 Composition of Ti-W-C films determined by AES as a function of $(TiCl_4+W(CO)_6)/CH_4$ inlet ratios

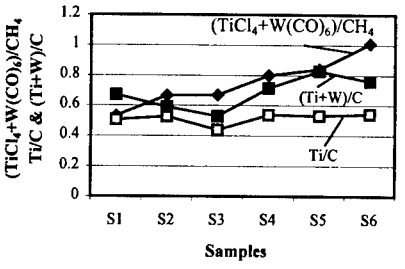


Fig. 7 $(TiCl_4+W(CO)_6)/CH_4$, actual Ti/C and (Ti+W)/C ratios of six samples from S1 to S6

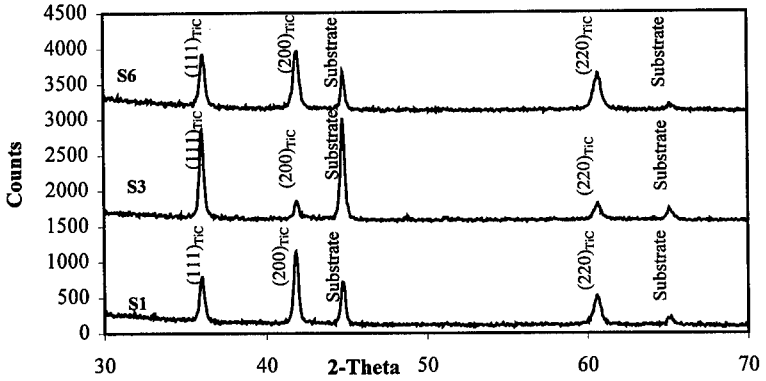


Fig. 8 XRD spectra of Ti-W-C films on stainless steel substrate showing variation intensities of (111)TiC and (200)TiC with $(TiCl_4+W(CO)_6)/CH_4$ inlet ratios; S1=0.53, S3=0.668, S6=1.01

The deposition rate and roughness as a function of $(TiCl_4+W(CO)_6)/CH_4$ inlet ratio are presented in Fig.9. The change in the deposition rate and roughness are associated with the $(TiCl_4+W(CO)_6)/CH_4$ inlet ratios. The low rates and smooth films are only obtained in the range between 0.5 and 0.8.

SEM micrographs of Ti-W-C films are shown in Fig.10. The surface morphologies are also dependent on the $(TiCl_4+W(CO)_6)/CH_4$ inlet ratio. At low and high $(TiCl_4+W(CO)_6)/CH_4$ inlet ratios, large rounded and equiaxed particles with clear crystal edge are formed and embedded into the films, as shown in Fig.10a and b. The number of the large equiaxed particles is increased slightly with the $(TiCl_4+W(CO)_6)/CH_4$ inlet ratio. In contrast, the large equiaxed particles no longer appear when the $(TiCl_4+W(CO)_6)/CH_4$ inlet ratio is in range of 0.668 – 0.8 (see Fig.10c and d). These smooth and dense films exhibit nanometer scale features. These films also exhibit preferred orientation in (111) direction and lower deposition rates. Furthermore, it can be seen that there are two types of faceted particles formed at high $(TiCl_4+W(CO)_6)/CH_4$ inlet ratio, as shown in Fig.10e and f.

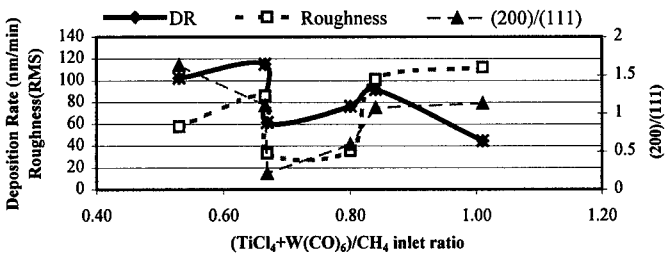


Fig.9 Deposition rate, roughness and intensity ratio of $(200)_{TiC}/(111)_{TiC}$ for Ti-W-C films as a function of $(TiCl_4+W(CO)_6)/CH_4$ inlet ratio

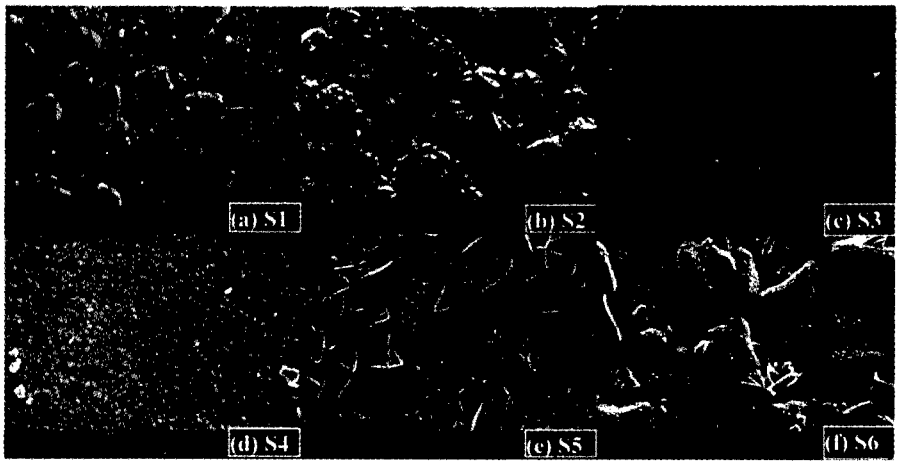


Fig. 10 SEM images of Ti-W-C films showing surface features at $(TiCl_4+W(CO)_6)/CH_4$ inlet ratios; (a) S1=0.53, (b) S2=0.665, (c) S3=0.668, (d) S4=0.8, (e) S5=0.84 and (f) S6=1.01

CONCLUSIONS

The variables that most affect the deposition of TiC have been theoretically modeled. Titanium at.% in films is affected by a three way interaction between reaction temperature, pressure, and total mass flow. Total mass flow has a significant main effect on C:Ti in the deposited films, whereas all other variables and interactions are highly non-linear relationships.

Ti-W-C films have been deposited at 1050°C by the variation of $(TiCl_4+W(CO)_6)/CH_4$ inlet ratio from 0.53 to 1.01. Fine and uniform crystal size is obtained in the middle range of the explored ration range $(TiCl_4+W(CO)_6)/CH_4$ inlet ratio. The films in this range have preferred orientation in (111) direction.

ACKNOWLEDGEMENTS

The financial support of the Air Force Office of Scientific Research, under grant #F49620-98-1-0499, is gratefully acknowledged.

REFERENCES

1. Louis E. Toth, *Transition Metal Carbides and Nitrides* (Academic Press. New York, 1971), pp. 4-7.

2. S.T. Oyama in *The Chemistry of Transition Metal Carbides and Nitrides*, edited by S. Ted Oyama (Chapman and Hall, London, 1996), pp. 1-14.

3. JMP Statistical Discovery Software, SAS Institute, INC. 1995.

4. V. Stambouli, O. Burat, D. Bouchier, F. Meyer, J. Gilles and G. Guatherin, Thin Solid Films, **193/194**, p181 (1990)

XPS STUDY OF $Pt/Ce_xZr_{1-x}O_2/Si$ COMPOSITE SYSTEMS

A. Norman[1], R. Sporken[1*], A. Galtayries[1], F. Mirabella[1], K. Keveney[2], M.Pijolat[2], R. Baker[3] and S. Bernal[3].
1 Univ. of Namur, Laboratoire LISE, Namur, Belgium. * Robert.sporken@fundp.ac.be
2 Ecole des Mines, Saint-Etienne, France.
3 Universidad de Cadiz, Cadiz, Spain.

Abstract:

This work describes the study of the surface reduction of ceria zirconia mixed oxides (CeZrO) as either thin films or powders, both with and without Pt present. XPS was used to measure the composition of the surface and the oxidation states of all metals contained within the material. The thin films of CeZrO showed little reactivity towards the reducing conditions used. Grazing incidence angle XRD showed the presence of $Ce_{0.75}Zr_{0.25}O_2$. The thin films prepared with Pt showed that surface reduction of Ce^{4+} occurred under reducing conditions. The size of the Pt clusters was also determined from the data. The Pt was found to always exist in the metallic state. The Zr^{4+} was not seen to change during all treatments. For the powder samples the Ce^{4+} was readily reduced to approximately 60%. Pt was found to be initially oxidised with the % of metallic Pt increasing with reduction temperature. Again no change in the Zr was observed.

Introduction:

The latest generation of automotive exhaust three-way catalysts demonstrate better catalytic performances due to the supports containing ceria-zirconia solid solutions instead of pure cerium oxide [1,2]. These oxides have oxygen storage properties which are due to the ability of Ce^{4+} cations to be easily reduced to the Ce^{3+} form. The effect of the zirconia is to facilitate the bulk reduction of the materials giving greater Oxygen Storage Capacity (OSC) [2]. This study examines the surface reduction of both thin films and powders. The thin films have been prepared with and without Pt deposited on the surface. The powders have been wet impregnated with Pt. The work was focused on the surface reduction of ceria under reducing treatments at different temperatures. The highest reducing temperature used was 550°C. Low pressures and low temperatures were used for the reduction of the thin films to reduce the support-CeZrO (ceria-zirconia mixed oxides) interactions. Structural studies of the thin films have been analysed using grazing incidence angle XRD. The size of the Pt particles deposited by evaporation onto the thin films and the oxidation state of the Pt on the powders have also been calculated.

Experimental:

Mixed CeZrO samples as bare supports and NM impregnated supports, formulated as $\{xCeO_2, (1-x)ZrO_2\}$, where x is the cerium atomic, were prepared from nitrate precursors by Rhodia in order to obtain solid solutions [3]. NMs were impregnated onto the oxides using $NM(NH_3)_4(OH)_2$. Samples are denoted as x/(100-x), where x is the metal ratio of Ce. The BET specific surface areas of the powder was calculated to be 100 m^2g^{-1}. A standard cleaning pre-treatment for the elimination of the impurities was carried out for the powder samples prior to analysis [5]. This pre-treatment consisted of heating under $5\%O_2/Ar$ for 1h followed by evacuation. Reduction consisted of passing 5% H_2/Ar over the sample and heating. Preparation of the oxide thin films on silicon substrates is described by Galtayries [4]. Pt was evaporated

Mat. Res. Soc. Symp. Proc. Vol. 581 © 2000 Materials Research Society

onto some of these oxide films from a Pt wire wrapped around a hot W filament. The substrate was not heated during Pt deposition. Evaporation rate was about 10^{11} atoms $cm^{-2}s^{-1}$.
XPS measurements were performed on an SSX-100 spectrometer using a focused monochromatic Al Kα anode (hν = 1486.6 eV) and a spot size of 1000μm. Sample preparation details are also contained in ref. 3
All X-Ray Diffraction measurements were carried out on a Siemens D501 instrument fitted with a copper anode X-ray tube operating at 40KV and 30mA. Cu $K\alpha_1$ radiation, wavelength 1.54Å, was used. Data was recorded over the 2-theta angular range 22-50° using a step size of 0.005° and data acquisition time of 15.0 seconds per step. Incident angles of 0.5°, 0.6°, 0.8°, 1.0° and 3.0° were used.

Results:

Prior to all analysis, CeZrO thin film samples were transferred in air resulting in the formation of a layer of contaminants. Quantitative analysis gives a surface ratio of Ce/Zr = 48/52, close to that of the target (50/50). Interfacial reaction between the Si substrate and the mixed metal oxide occurred forming SiCeZrO type materials. This was seen by shifts in energy of the Si 2p core level. Results for the characterisation of the films and the interface can be found in greater detail elsewhere [4,5]. XRD diffraction experiments have been conducted to determine the structure of the CeZrO thin films. Diffraction patterns show the presence of peaks that are attributed to the mixed oxide phases of stoichiometric compositions $Ce_{0.75}Zr_{0.25}O_2$, CeO_2 and ZrO_2.
Figure 1 shows the XPS core level intensities of Zr 3d, Ce 3d, Ce 4d and Pt 4f core levels as a function of Pt deposition time for one of the samples. The intensities have been divided by appropriate sensitivity factors. The Ce 3d level decreases faster than the two other substrate core levels because of its shorter effective attenuation length. The ratio between Ce 4d and Zr 3d core levels can be used to determine the film composition. It does not change significantly with increasing Pt coverage, indicating that the Pt does not interact strongly with the oxide. Based on similar studies, it is reasonable to assume that Pt grows in the Volmer-Weber mode [6] (cluster growth). We shall see later that this is indeed consistent with the change of the Pt 4f binding energy with Pt coverage. As long as the Pt cluster size is small compared to the effective attenuation length of the photoelectrons, the Pt 4f XPS signal increases linearly with the total

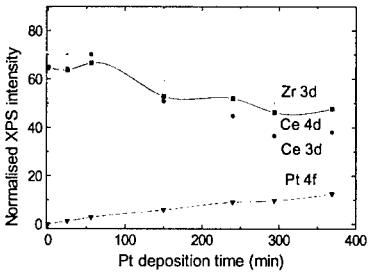


Figure 1: Intensity of Zr 3d, Ce 3d, Ce 4d and Pt 4f core levels as a function of Pt coverage on a CZO film on Si(111). All intensities have been divided by appropriate sensitivity factors.

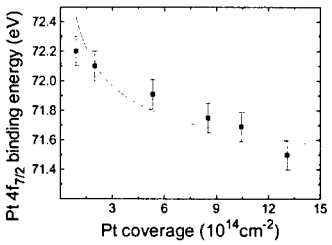


Figure 2: Binding energy of Pt 4f7/2 core level as a function of Pt coverage. The binding energy was measured using O 1s at 529.5 eV as a reference. The solid line is the calculation according to equation 2, with $N_{clusters}$ = 3.6 10^{12} cm^{-2}.

number of Pt atoms. In the limit of small coverage, one can then determine the Pt coverage according to the equation,

$$N_{Pt}(cm^{-2}) = N_{sub}(cm^{-3})\lambda_{sub}\frac{I_{Pt}}{I_{sub}}\frac{\sigma_{sub}}{\sigma_{Pt}} \qquad (1)$$

N_{sub} is the number of cations in the substrate (calculated from the composition and density), and σ_{sub} is the corresponding photoionisation cross-section. This gives values of the Pt coverage in the range of 5 10^{13} - 5 10^{15} cm^{-2}. The problem is then to determine the distribution of these Pt atoms. This can be done approximately because the size of Pt clusters affects the apparent Pt 4f binding energy. The shape of the Pt 4f lines is independent of Pt coverage hence we can conclude that the oxidation state of Pt does not change with Pt coverage and corresponds to Pt^0 (metallic Pt). The Pt 4f binding energy changes with Pt coverage (Figure 2). This variation is explained as a cluster size effect. Positive charge appears on the Pt cluster during the photoemission process. This charge is neutralised between photoemission events, but does not neutralise fast enough compared to the lifetime of the core hole. This leads to a size-dependent electrostatic potential on the cluster, which changes the apparent binding energy. For hemispherical clusters, as long as they conserve their metallic properties, the binding energy shift is given by equation,

$$E_B - E_B^{bulk} \cong \frac{1}{4\pi\varepsilon_0}\frac{e}{2r} \quad [7] \qquad (2)$$

where r is the radius of the cluster. For very small cluster sizes, the binding energy changes because the cluster loses its metallic properties. This occurs when the separation between energy levels in the valence band becomes of the order of kT. For Pt, the width of the valence band is of the order of 6 eV. Hence metallic behaviour is expected for clusters with more than ~24 atoms, corresponding to r = 5.6Å for a hemispherical cluster. Using the substrate as a reference we obtain the shift of Pt core level with coverage (determined from equation 1) as shown in Figure 2. If we assume that the transition from metallic to non-metallic behaviour occurs somewhere between the first two data points, the radius would be at most about 5 Å for the first data point. This corresponds to a number of Pt clusters of 3.6 x 10^{12} cm^{-2}. Assuming furthermore that the number of clusters is constant in the range of coverages studied here, we can calculate their radius as a function of coverage, and then calculate the binding energy shift according to equation 2. The result is shown by the solid line in Figure 2. For the largest clusters, we obtain

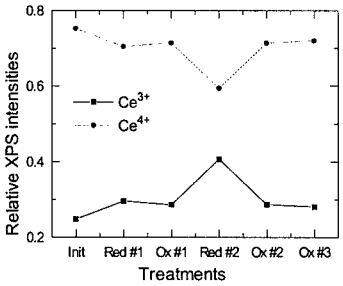


Figure 3: Relative Ce^{3+} and Ce^{4+} concentration determined from Ce 3d core level spectra, after various mild oxidising and reducing treatments described in table 1.

Table 1: Conditions of redox treatments used to study reactivity of Pt/CZO thin films. All treatment lasted 30 minutes. Pt coverage was calculated to be in the range 5 10^{13} cm^{-2} to 5 10^{15} cm^{-2} for this film.

Reduction #1	H_2, 10^{-5} Torr, ~350 °C
Oxidation #1	O_2, 10^{-5} Torr, ~350 °C
Reduction #1	H_2, 10^{-4} Torr, ~350 °C
Oxidation #2	O_2, 10^{-4} Torr, ~350 °C
Oxidation #3	O_2, 7.10^{-3} Torr, ~550 °C

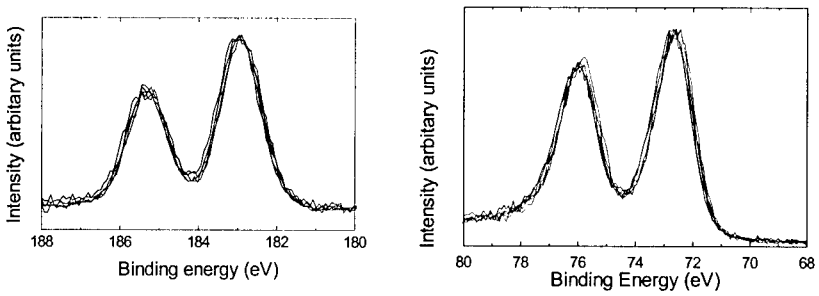


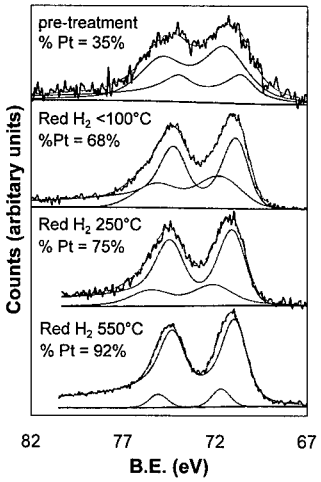
Figure 4: Pt 4f and Zr 3d core level spectra recorded after various oxidising and reducing treatments described in table 1. The spectra have been shifted and scaled to allow easy comparison of the line shape. Virtually no change in lineshape is detected, indicating that the oxidation state of Pt and Zr does not change during the treatments. This is confirmed by the XPS binding energies.

r = 14 Å, which is still less than the effective attenuation length of the Pt 4f photoelectrons. Given the many simplifying underlying assumptions, we do not expect perfect agreement between the calculated curve and the experimental data. However, the total variation agrees quite well. This suggests that we can at least determine the order of magnitude of the cluster radius. With this approach, we find the Pt particle size to be in the range of 5 - 25 Å for different samples and different deposition times. Again, these values should be considered estimates of the order of magnitude only.

For reactivity experiments all treatments for the Pt CeZrO thin films were mild, compared to those of the powders, in order to limit the interaction between the substrate and the film. The variation of the Ce^{3+} and Ce^{4+} components of the materials after the treatments, extracted from the Ce 3d spectra, is shown in Figure 3. Table 1 shows the conditions used for oxidation and reduction. There is no change in the spectra until reduction is carried out under H_2 at 10^{-4} Torr, the higher of the two pressures used in this study. These conditions caused some reduction of the surface. The lowest Ce^{3+} concentration is about 25 %. This is attributed to residual surface reduction due to exposure to x-rays in UHV.

The Zr 3d and Pt 4f core level spectra of the thin films, recorded after oxidising and reducing treatments, are shown in figure 4. From these results it can be seen that there is no change in the state of the Pt and the Zr for the duration of the experiment. The Pt is all in the metallic state evidenced by the lack of change in the peak shape and position after reducing conditions (figure 5). There is no evidence of an oxidised Pt 4f component. The Zr 3d peaks also show no peak shape or position changes indicating that Zr is not involved in the reduction process.

The XPS spectra of Ce 3d core levels after the oxidative and reductive treatments of the powder catalysts are shown in figure 5. The initial state of the material, the fresh catalyst, contains approximately 16-20% Ce^{3+} which appears to increase to 24% after the pre-treatment. These spectra were very broad and this has been attributed to charging effects. The application of a flood gun opposed the charging, but did not completely annul it. However, when placed in a reducing atmosphere, flowing H_2, at a temperature <100°C the spectrum recorded has greater resolution and the degree of the surface reduction has increased to 38%. Further heating under reducing conditions causes the reduction to increase to 45% for 250°C and to 62% for temperatures of 550°C. However, complete reduction of the surface was never observed. This could be due to the regeneration of the oxidised surface by the migration of oxygen from the bulk to the surface causing the bulk to become reduced. Using the data obtained from the peak



Fgure 5: Fitted Pt 4f core levels for HL Pt CZ 50/50 LS. Reduction temperature and calculated metallic Pt are shown above. All peaks are fitted with a Pt° and a PtO_X component.

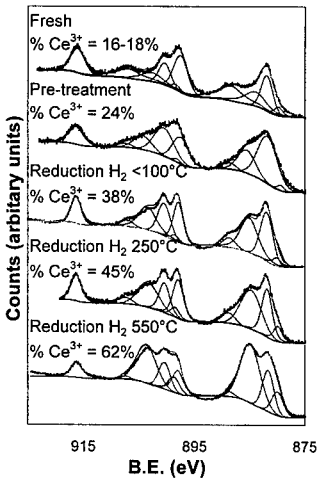


Figure 6: Fitted Ce 3d core levels levels for HL Pt CZ 50/50 LS. All peaks are fitted using 5 sets of doublets corresponding to Ce^{3+} and Ce^{4+} states. Quantification results are shown in table 2.

fitting it is possible to calculate other data also. This data is summarised in table 2. It can be seen that there is little variation of the surface composition during the experiment. The percentage of ceria is close to the expected value of 50/50 for ceria:zirconia. Also, it can be seen that there is little variation in the composition as a function of depth. This is gained from using the data from the Ce 3d and 4d core levels due to the shorter effective attenuation length of Ce 3d core level.

The XPS spectra of the Pt 4f core levels are shown in figure 6. Peaks were fitted with two doublets, corresponding to Pt° and PtO_x. The Pt° was fitted using a Duniach-Sunjić doublet and the platinum oxide with a gaussian-lorentzian mixed doublet. Approximate concentrations of each phase was calculated from these fits, table 2. The resolution of the fresh and pre-treated spectra is poor with resolution increasing for reduction at higher temperatures. The initial state of the NM is one where there is a large proportion of oxide present. Even reduction at low temperatures of less than 100°C causes a decrease in platinum oxide to 32%. The presence of the metallic form of the metal dominates at temperatures above 250°C and at 550°C 92% of metallic platinum was calculated to be present.

The spectra of the Zr 3d core levels show no change with treatments. The Zr^{4+} oxidation state is stable and is not expected to change with the reducing atmosphere used. Figure 7 shows selected spectra showing that there is no gross changes in the peak shape or position with reduction.

Conclusions:

It was seen for the formation of the ceria zirconia thin films that the thin films had a composition close to that of the starting powder material. Depth profiling was used to find the variation of composition with depth and to determine any substrate film interactions. XRD showed that there existed crystalline ceria zirconia phases present. Qualitative analysis indicated that probable compositions were $Ce_{0.75}Zr_{0.25}0_2$, CeO_2 and ZrO_2.

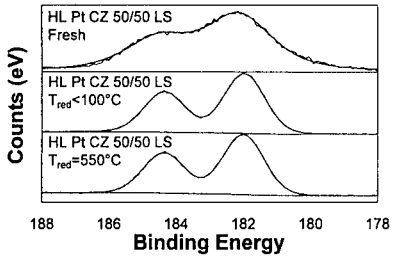


Figure 7: Fitted XPS spectra of Zr 3d core levels. No change, apart from broadening, is detected after reducing treatments indicating no change in the state of Zr.

Table 2: Table summarising the analysis of the peak fitting of the Ce 3d spectra for the Pt CeZrO materials.

	% Ce	% Ce3+	% Pt°	Uniformity
HL Pt CZ 50/50 LS fresh	50%	29%	44%	0.8
HL Pt CZ 50/50 LS pre treatment (Oxid)	50%	37%	35%	1.0
HL Pt CZ 50/50 LS H_2 <100°C 1 hr	46%	41%	68%	1.1
HL Pt CZ 50/50 LS H_2 250°C 1hr	50%	55%	75%	0.9
HL Pt CZ 50/50 LS H_2 550°C 1hr	48%	45%	92%	1.2
HL Pt CZ 50/50 LS reoxidation			12%	

XPS spectra were recorded after Pt deposition on the thin films. All Pt was in metallic form. Analysis allowed the calculation of the size and number of Pt particles deposited. The size was determined to be approximately 5-25Å for the particles formed.
Reactivity measurements of the thin films, under mild conditions of temperature and pressure, indicated that reduction of the thin films did occur. Mild conditions were used to reduce interactions occurring between the substrate and the oxide layer.
Powder samples were submitted to more severe conditions. At low temperatures, <100°C, there quantities of PtO_X were observed. This was reduced as the reaction temperature was increased. After temperatures of approximately 550°C there was only 8% oxide detected. Maximum ceria reduction of 62% occurred after reduction temperatures of 550°C. Zirconia was not observed to change during all treatments.

Acknowledgements:

This work has been supported by the TMR Programme of the EU under contract ERB FMRX-CT96-0060 (CEZIRENCAT Project). Robert Sporken acknowledges support from the Belgian Fund for Scientific Research.

References:

1) A. Galtayries, M. Crucifix, G. Blanchard, G. Terwagne, R. Sporken, Applied Surface Science, **142**, p 159-163 (1999)
2) A. Galtayries, R. Sporken, J. Riga, G. Blanchard, R. Caudano, Journal of Electron Specroscopy and Related Phenomena, **88-91**, p 951-956 (1998).
3) M. Daturi, C. Binet, J.C. Lavalley, H. Vidal, J. Kaspar, M. Graziani and G. Blanchard, J. Chim. Phys., Phys.-Chim. Biol., **95**, p 2048 (**1998**).
4) A. Galtayries, M. Crucifix, G. Blanchard, G. Terwagne, R. Sporken, Applied Surface Science, **142**, p 159-163 (1999).
5) G. Colón, M. Pijolat, F. Valdivieso, H. Vidal, J. Kašpar, E. Finocchio, M. Daturi, C. Binet, J.C. Lavalley, R.T. Baker and S. Bernal, J. Chem. Soc. Faraday Trans., **94**, p 3717. (1998).
6) E. Baner, Zeitschift Kristellographier, **110**, p372 (1958).
7) R. Sporken, Phys. Rev. B, **38** vol 2, P 1351-1356 (1988).

Sol-Gel and Organic-Inorganic Nanocomposites

TRANSPARENT MONOLITHIC METAL ION CONTAINING NANOPHASE AEROGELS

William M. Risen, Jr.*, Xiangjun Hu*, Shuang Ji*,and Kenneth Littrell**
*Department of Chemistry, Brown University, Providence, RI 02912, WRISEN@BROWN.EDU
**Argonne National Laboratory, Argonne, IL

ABSTRACT

The formation of monolithic and transparent transition metal containing aerogels has been achieved through cooperative interactions of high molecular weight functionalized carbohydrates and silica precursors, which strongly influence the kinetics of gelation. After initial gelation, subsequent modification of the ligating character of the system, coordination of the group VIII metal ions, and supercritical extraction afford the aerogels. The structures at the nanophase level have been probed by photon and electron transmission and neutron scattering techniques to help elucidate the basis for structural integrity together with the small entity sizes that permit transparency in the visible range. They also help with understanding the chemical reactivities of the metal-containing sites in these very high surface area materials. These results are discussed in connection with new reaction studies.

INTRODUCTION

There is considerable interest in the formation and properties of gels and aerogels based on silica. Some of this arises from the possibility of incorporating metal-containing species in the materials so that they can be used as precursors of catalysts. The catalyts then would be formed as composites containing metal particles [1] or metal oxide [2] or other metal complex compounds. That has led to a range of studies of transition metal species in silica areogels[3,4].

In this work, a general synthetic approach has been taken that is designed to provide for both the incorporation of metal ions and the preservation of other advantageous features of aerogels. These advantages can include more than just low density and high porosity. Indeed, some silica-based aerogels are monolithic structures with useful optical, thermal and electronic applications. Formation of transparent, monolithic metal ion containing aerogels potentially provides a way to attain a class of materials with these attributes as well as those imparted by metal ions.

The primary reported methods for incorporation reported to date include adsorption of metals from solution by functionalized aerogels. This is a method for the clean up of metal-ion contaminated sites [5]. It also includes the incorporation of transition metal complexes, such as copper amine complexes [3]. And, it includes the formation of complexes in aerogels through the reactive attachment of a complexing ligand into the sol-gel structure [4].

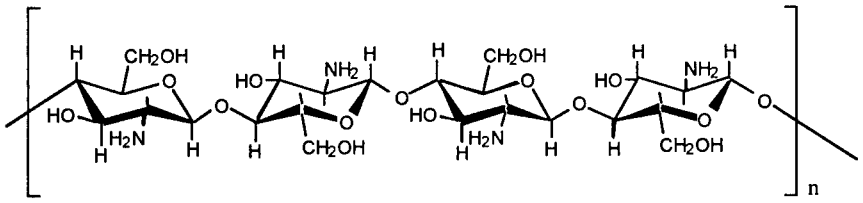
The approach reported here is to form a silica-and polymer-based aerogel in which the polymer can provide metal ion coordination sites for a range of metal ions. In order to be transparent, the gel must be formed at low enough pH to obtain nanometer scale fundamental particle sizes. The polymer must have the ability to strengthen the gel sufficiently to allow for the formation of an aerogel monolith. The polymer also must have the ability to provide useful metal ion coordinating sites in pH ranges at which the silica structure and particles size distribution are stable.

It is difficult to find materials and approaches to achieve this. The silica related structures are very small when they are formed at relatively high levels of acid, which correspond to pH values of less than 5 in the aqueous solution equivalent acidities. However, at

Mat. Res. Soc. Symp. Proc. Vol. 581 © 2000 Materials Research Society

these levels of acidity, the coordinating sites of polymers tend not to be in the forms that are favorable for complexation. For example, amine-sites usually have effective pKa values such that they are overwhelmingly in the $-NH_3^+$ form at pH less than 7, with typical pKa values of 9 – 10. Acid sites are somewhat more available for ionic association, but their form also is strongly pH dependent. Relatively few polymers are water soluble or soluble in the presence of reacting TEOS and its hydrolysis products. Those that are water soluble tend to have pH dependent shapes and functionalities. Finally, the polymeric materials that one can consider for this approach tend to be extractable from the wet gels when supercritical fluid extraction is employed, so it is necessary to prevent that from happening.

The types of polymers chosen for this study are polysaccharides of the type known as chitosans. These are partially or fully deacylated forms of chitin. At the sites of deacylation, typically 85% of the acyl amine groups of chitin, the functional group is an amine. A representation of a fully deacylated form of chitosan is shown below. Chitosan polymers with



this level of deacylation are soluble in aqueous acetic acid solution, and can form clear sols with gelling silica sources such as tetraethoxysilane (TEOS). Chitosan's hydroxyl groups as well as its other oxygen atoms provide ways for it to be solvated and for it to interact with moieties of the silicon-containing species condensing to form the gel. They and the amine groups can interact both with the silica-containing portion of a gel, and they can interact with metal ions. The amine groups, in particular, act as coordinating ligands when the pH is high enough.

As mentioned above, the typical amine has a pKa that is well above 7, but it is a special characteristic of chitosan that its pKa is effectively about 6.5 [6]. Despite numerous studies of the compound, it is not clear why that is its effective pKa. It presumably results from a combination of factors involving the site properties, polyelectrolyte effects, and intermolecular hydrogen bonding effects. Because of this, value, it is able to have a reasonable fraction of its amine sites in the form of NH_2 at pH 6.6 or less. This makes it possible for it to complex transition metal ions at pH values below those at which a silica network is depolymerized [7].

The combination of aqueous solubility, functional groups that could interact with a silica network, and amine groups that could provide general complexation sites for a wide range of transition metal ions made chitosan an interesting polymer with which to explore the possibility of forming transparent monolithic transition metal-containing aerogels [8-10].

EXPERIMENTS

The synthesis of the aerogels described here involves first the formation of a solution of chitosan (Fluka Biochemika, M_r of about 2, 000, 000, degree of deacylation 84.5%) in aqueous acetic acid. Typically 0.4 g chitosan and 0.4 mL glacial acetic acid were combined with 40 mL water [8,9]. The solution was mixed with 12.5 mL TEOS (Tetraethoxysilane, Fluka Chemika), an additional 0.9 mL glacial acetic acid was added and the mixture was stirred vigorously . After 8 hrs, the initially heterogeneous mixture was a clear sol. Some of the sol was placed in a

container to a depth of 1-3 mm, covered and allowed to gel and age for another 8 hours. Then it was treated with dilute ammonium hydroxide in absolute ethanol (ca. 2-3 drops of 29% (w/w) ammonium hydroxide in 50 mL ethanol). This solution was decanted after 24 hours and the gel was treated with absolute ethanol twice over 48 hours to replace the remaining water with ethanol. These gels were dried with supercritical CO_2 using a CCS 3100-1000 supercritical drier. Series of chitosan-silica areogels were prepared in this manner with chitosan concentrations ranging from 5 to 20 % (w/w).

In the case of the transition metal ion-containing gels, the gels were reacted with a metal salt dissolved in absolute ethanol. For example, a 0.01 M solution of $RuCl_3$ (Strem Chemicals) was added to the ethanol exchanged gel from the initial procedure. In the case of a 2% (w/w) Ru chitosan silica aerogel, mentioned below, the initial gel contained 10% (w/w on solids) chitosan and 90% (w/w on solids) silica and it was exposed to this 0.01M solution for 48 hours. The metal ion solution was replaced by an absolute ethanol solution. Then the gel was dried in supercritical CO_2. Other metal-containing aerogels of this type have been made with Rh(III), Co(II), Ni(II), Cu(II), Pt(II), and Pd(II) [8-10].

Physical properties were measured as follows. The surface areas were measured by standard multipoint BET methods using N_2 and H_2 on a Quantasorb surface area analyzer. Refractive indices were measured at 632.8 nm with a Metricon Model 2010 Prism Coupler with a He/Ne laser and a 200-P-4 prism. Infrared transmission measurements were made using an IBM/Bruker FV 130 FTIR spectrometer.

Structural studies [9,10] were carried out by high resolution transmission electron microscopy (TEM) in collaboration with David Pickles of Corning, Inc. The image presented here was measured on the edge of a fractured piece of aerogel. Small angle neutron scattering (SANS) studies were carried out at the Argonne National Laboratory (ANL). The SANS of the monolithic aerogels (placed between quartz windows) were measured with a time-of-flight instrument, SAD, at the Intense Pulsed Neutron Source at ANL. SAD uses neutrons from a solid CH_4 moderator at 24 K with a wavelength from 5 to 14 Angstroms (Ang). This instrument provides data in a Q (wavevector) range of 0.005 - 0.35 Ang^{-1} in a single measurement.

Chemical reaction studies have been carried out to explore the reactions of these metal ion-containing aerogels with small molecules, such as CO(g), H_2(g), and NO(g), which are of interest in catalysis and gas detection[10]. Thin monolithic aerogels were placed in a stainless steel reactor fitted with KBr windows. The temperature of the sample and the composition and pressure of the gases were controlled and measured. The reactions shown here are those of Ru(III) chitosan aerogels with the composition given in the preparation described above. They were treated with according to the procedures designated in the following section and the captions to the figures in which spectral results are shown.

RESULTS AND INTERPRETATION

The monolithic aerogels produced by this method have been made in pieces of about 5 cm x 5 cm x 0.2 cm, although they typically are prepared in a thinner form to facilitate spectroscopic study. They are clear and have the low densities and refractive indices illustrated in Table I. Their colors and, more fully, their visible spectra depend on the properties of the metal ions they contain[8].

Structural studies were carried out to discover two aspects of the structures formed in these materials. The most obvious aspect involves the question of whether the chitosan remains in the areogel after the various washing and solvent exchange processes and the supercritical drying procedure. A related question has to do with the functioning of such chitosan as a metal ion-coordinating ligand. The second main aspect of the structural studies has to do with the

Table I
Physical Properties of Typical Silica-chitosan-metal ion Aerogels

Sample Name	Density (g/cm^2)	Refractive Index at 632.8nm	BET Surface Area (m^2/g)*	Metal Content (mass %)
Silica-chitosan aerogel (10%(w/w) chitosan)	0.25	1.14	600	-
Co(II) silica-chitosan aerogel*	0.26	1.14	800	0.7%
Rh(III) silica-chitosan aerogel*	0.27	1.17	950	0.5%
Ru(III) silica-chitosan aerogel*	0.27	1.17	800	2.0%
*(all based on initial 90% silica/10% chitosan dry mass ratio compositions)			*observed from 500 to given value on range of measurements	

morphology. Specifically, the questions here concern the sizes of the ultimate nanoscale objects and how they are joined or collected together.

The first aspect can be addressed spectroscopically. The infrared spectra of three chitosan-silica aerogels without metal ions are shown in the *ca.* 1325 –2200 cm^{-1} range in Figure 1. The growth of the amine related band marked on the spectrum shows that the chitosan content in the aerogel grows with its content in the initial sol-gel. The FTIR spectrum of a chitosan-silica aerogel and an analogous aerogel with Ru(III) but otherwise the same composition is shown in Figure 2. Clearly, the band associated with the free amine in the aerogel without metal ions is reduced when the metal ions are present. Moreover, the band assigned to the metal ion-coordinated amine is present in the case of the Ru(III)-containing aerogel. The first issue seems to be resolved with these and analogous FTIR and ultraviolet-visible-near infrared spectral studies [8–10]. The chitosan is present and does participate in the coordination of the Ru(III) ions in this case. The details of the coordination vary with metal ion, since each has a unique set of thermodynamic and kinetic properties.

The second aspect has been addressed by a combination of TEM and SANS studies. They are informed initially by the fact that the aerogels are clear, so there are not ultimate particles larger than about 0.2 microns. The TEM images show that the ultimate particle sizes are much smaller than that [10]. The TEM image for the chitosan-silica with 10% chitosan is shown in Figure 3. As shown there, the fundamental particles are quite small. The scale makes it clear that they are much less than 10 nanometers in breadth. It is clear on close examination that this breadth is on the order of 1 to 2 nm. However, it also seems that there might be a somewhat larger scale order in which the fundamental particles are connected. The images are of high enough resolution only to permit speculation that such connected structures could have a coherence that extends over a few of the fundamental objects. This would correspond to about 3 to 8 nm.

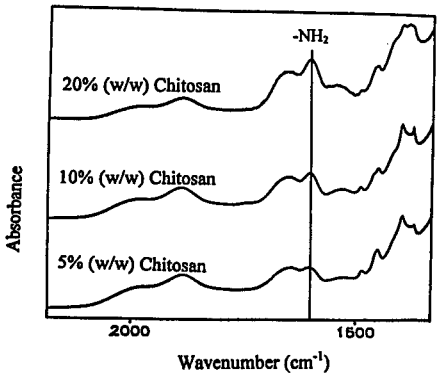


Figure 1. Infrared spectra in the 1325 to 2200 cm^{-1} range of chitosan-silica aerogels with varied chitosan contents. Spectra offset arbitrarily for display.

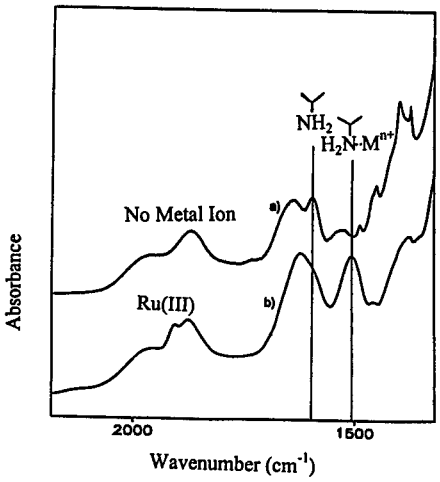


Figure 2. Infrared spectra in the 1325 to 2200 cm^{-1} range of a chitosan-silica aerogel and no metal ion and one with Ru(III) present, as indicated. Spectra offset arbitrarily for display.

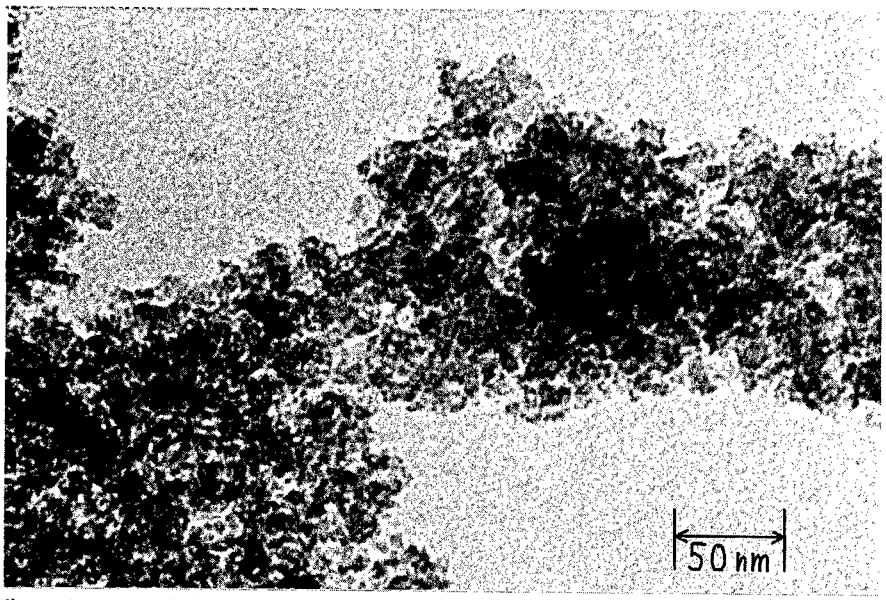


Figure 3. Transmission Electron Micrograph of a chitosan-silica aerogel containing 10% by weight of chitosan; the distance scale is indicated on the micrograph. TEM measured by D. Pickles [8].

The SANS experiments are a powerful complement to the TEM images, since they also probe on the nanometer scale. The SANS scattering data measured on a series of the transparent monolithic chitosan-silica aerogels with varied chitosan content but without metal ions are shown in Figure 4. The aerogels containing transition metal ions also have been studied by SANS [10]. The analysis of SANS data proceeds through a model fitting approach, as has been widely discussed [11-13]. In this work, the data have been fitted with a small particle mass fractal model equation derived from the Teixeira model for mass-factal aggregates of spheres [11]. The scattering function used here is given by the following equation, where I_{0A} is the

$$I(Q;\xi,D_F) = I_{0A}\frac{\sin[(D_F-1)\arctan(Q\xi)]}{(D_F-1)Q\xi\left(Q^2\xi^2+1\right)^{\frac{D_F-1}{2}}} + I_{Background}$$

overall intensity scattered by the aggregate extrapolated to Q = 0, D_F is the mass-fractal dimension, ξ is the exponential cutoff for the aggregate, and $I_{Background}$ is the background intensity. The detailed differences between this and the Teixeira model are discussed elsewhere[10]. Briefly, the model is a valid approximation when the scattering from the form factor for the fundamental sphere is not visible or, alternatively, whenever $\xi >> R$ (the radius of the spheres in the Teixeira model) and $Q_{max}R<<1$, where Q_{max} is the value of Q at which the power law scattering fades into the background scattering.

The analysis in terms of this model in the case of the chitosan-silica aerogels without metal ions results in fractal dimensions of 2.60 for 5% chitosan to 2.52 for the 10% chitosan aerogel. This compares to the dimensionality of 2.85 for the aerogel prepared without chitosan but with all other synthetic conditions held constant. The 20% and additional weight percentage

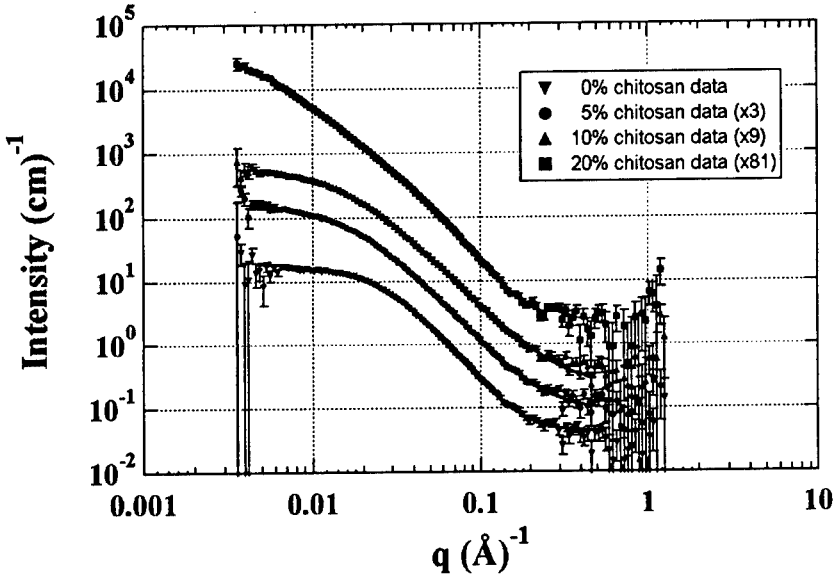


Figure 4. Small Angle Neutron Scattering data for chitosan-silica aerogels with 0, 5, 10 and 20% by weight of chitosan; as indicated by the symbols, the curves are in order of concentration from bottom to top.

chitosan aerogels remain under study. The fractal dimensionality decreases on going from the silica to the silica-chitosan aerogels, however the exponential cutoff length increases quite significantly from 3.25 nm to 5.74 nm in the 10% chitosan aerogel. The metal ion-containing materials based on 10% chitosan content initial gels, including Ru-, Rh- and Co- containing aerogels, typically have fractal dimensions in the 2.45 to 2.60 range. The corresponding exponential cutoff lengths are in the 5.8 to 7.9 nm range. These lengths are exponential cutoff lengths and are not directly object dimensions, but it is interesting to note that they are on the order of 3 to 6 times the diameter of the smallest fundamental objects seen by TEM.

Chemical reaction studies have been carried out to ascertain the extent to which these aerogels in the form of group VIII metal ions would be suitable for catalytic and gas absorption applications. The primary attention has been devoted to those containing either Rh(III) or Ru(III) ions coordinated to the chitosan and, to some extent, to the available sites on silica-rich moieties of the aerogels[9]. They display an extensive chemistry. Not only do the metal ions and added gases react, but the water associated with the aerogel can play an important role. This is shown by the following reactions of Ru(III) aerogels, which have extensive precedent in the reactions of other supported Ru(III) systems [14-17].

The availability of large thin monolithic aerogels makes it possible to measure the infrared spectra of the aerogels and their reaction products directly by transmission spectroscopy. Because of the compositions, the region of about 1500 to about 2600 cm^{-1} has low enough absorbance to act as a window to observe reactions involving CO(g), H_2(g), and NO(g) as well as some of the effects of water and oxygen.

When a hydrated Ru(III) aerogel is formed in the reactor by exposing the aerogel to water vapor at 20°C for 10 minutes, it reacts with CO to form metal carbonyls with bands at 2081 and 2018 cm^{-1}, as well as a band at 1972 cm^{-1}. This is shown in curves A and B of Figure 6. On the

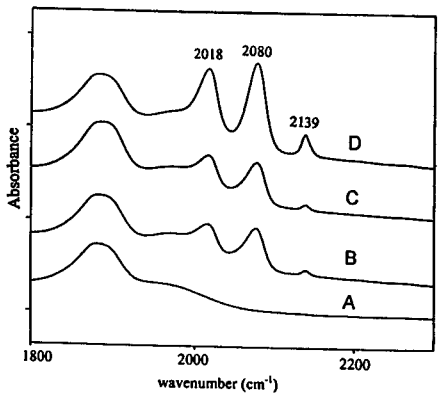


Figure 5. Infrared spectra of Ru(III) chitosan -silica aerogel with 2% Ru(III) and its reaction products where:

A. initial sample, dehydrated at 95°C for 7 hr *in vacuo*

B. A exposed to 0.4 atm. CO; 11 hr at 20°C

C. B exposed to 1.0 atm. H_2 ; 24 hr at 95°C

D. C exposed to 0.1 atm CO; 4 hr at 95°C

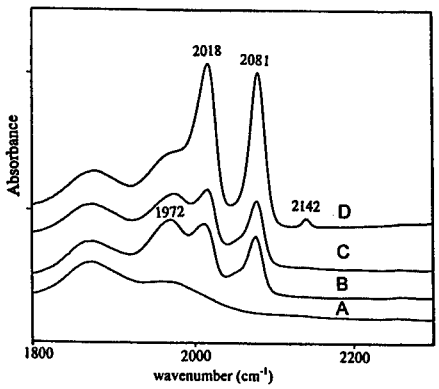


Figure 6. Infrared spectra of Ru(III) chitosan -silica aerogel with 2% Ru(III) and its reaction products where:

A. initial sample, hydrated at 20°C for 10 min. in saturated H_2O vapor.

B. A exposed to 0.1 atm. CO; 12 hr at 20°C

C. B dehydrated for 2 hr at 95°C

D. C exposed to 0.1 atm CO; 3 hr at 95°C

other hand, the reaction of a dehydrated Ru(III) aerogel with CO under essentially the same conditions but with a much higher CO pressure does not yield the 1972 cm^{-1} band. Thus, curves A and B of Figure 5 do not show such a band. The fact that it is formed when water is present and not when it is absent is quite interesting.

One reasonable hypothesis to explore is that water reacts with CO at these metal sites to form hydrogen through a form of the water gas shift reaction. The hydrogen would then reduce the metal and the reduced metal would form the new carbonyl associated with the 1972 cm^{-1} vibration. The CO-reacted dehydrated Ru(III) aerogel sample was next reacted with hydrogen for 24 hours at 95°C in order to achieve the reduction without water. However, no significant change occurred in the carbonyl region of the spectrum (see Figure 5 C). Thus, the sample was again reacted with CO, and the spectrum shown in Figure 5 D was observed. It does not provide strong evidence for a 1972 cm^{-1} band. Meanwhile, the species giving rise to the 1972 cm^{-1} band is quite stable, as shown by its presence throughout heating and CO reaction processes in Figure 6 C and D.

These two sets of reactions show that the Ru ions are reactive. There appear to be at least two types of metal carbonyls formed. The 2082 and 2018 cm^{-1} bands appear together at constant relative intensity. They are assigned to the same species, which probably is a dicarbonyl. The 1972 cm^{-1} band is assigned to a carbonyl vibration on a reduced Ru. The spectra both show bands near 2140 cm^{-1} due to adsorbed CO.

These assignments are consistent with known carbonyl chemistry and extensive catalysis literature [14-17]. However, they do not answer the question posed by these results: why does hydrogen from the water gas shift reaction reduce Ru(III) while hydrogen, added in the reaction sequence followed here does not? This appears to be quite unusual, and it may be due to another feature of the hydrated aerogel structure. That structure has a mechanism for forming and possibly transporting hydrated protons, a reduction reaction product. This could favor the reduction reaction in the hydrated aerogel case. That hypothesis and others related to water in the coordination sphere of the Ru(III) ion are under study.

It is clear from a number of the studies on these aerogels that the Ru can assume a range of environments and oxidation states. The spectra of Ru(III) aerogels reacted with NO and CO, in sequence, show the significance of such changes. The reaction of a dehydrated Ru(III) aerogel with NO leads to the product whose spectrum is given as Figure 7 B, with a metal nitrosyl vibration at 1894 cm^{-1}. The subsequent addition of CO leads to metal carbonyl bands at frequencies near their positions in Figure 5. Thus, they are at 2026, 2085 and 2140 cm^{-1} *vs.* 2018, 2080 and 2140 cm^{-1}, respectively. The subsequent addition of NO leads to a significant change, however, since the bands shift to 2036, 2092 and 2154 cm^{-1}. These shifts together with

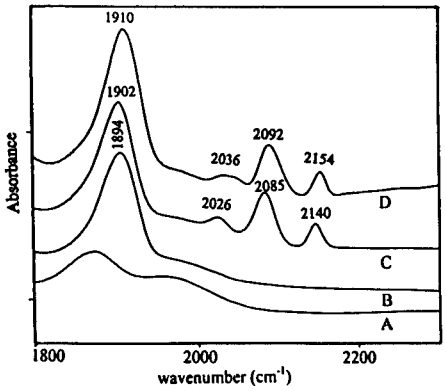


Figure 7. Infrared spectra of Ru(III) chitosan -silica aerogel with 2% Ru(III) and its reaction products where:

A. initial sample, dehydrated at 95°C for 6 hr *in vacuo*
B. A exposed to 0.1 atm. NO; 0.5 hr at 20°C
C. B exposed to 0.2 atm. CO ; 18 hr at 95°C
D. C exposed to 0.05 atm NO; 3.5 hr at 95°C

the symmetrical shapes of the bands indicates that the NO addition had the effect of increasing the effective oxidation state of the Ru(III) in at least the case of the dicarbonyl, to which the 2036 and 2092 cm^{-1} bands are assigned. The interpretation is more tentative in the case of the 2154 cm^{-1} band. It may not be due to physically adsorbed CO, as was suggested for the *ca.* 2140 cm^{-1} band in Figures 5 and 6. In Figure 7, the 2154 cm^{-1} band is stronger relatively, and it is at a quite high frequency relative to the vibration of free CO. The tentative assignment of this band is to a Ru(III) monocarbonyl whose bonding mode is primarily through dative interaction of Ru(III) with the sigma antibonding orbital of CO. This type of interaction can serve to strengthen the CO bond relative to that in CO itself.

CONCLUSIONS

The incorporation of chitosan, a functional polymer that is able to form a clear sol with hydrolyzing TEOS and to interact with both the silica and added metal ions, has been shown to lead to the formation of monolithic, transparent silica-based aerogels of low density and refractive index, and high surface area. They have ultimate particle sizes of less than about 2 nm, as judged from TEM observations. The study of their structure by SANS indicates that they are more generally described by a fractal model with dimensionality between 2.45 and 2.60 and exponential cutoff lengths of 5 to 8 nm. These may be compared to the values of 2.85 and 3.25 nm for silica aerogels made under the same conditions. The metal ion containing aerogels exhibit an extensive reaction chemistry, as illustrated by the reactions of Ru(III) aerogels with CO, H_2, NO and H_2O.

ACKNOWLEDGMENTS

The authors are grateful to Dr. Arthur Yang of Industrial Science and Technology Network, Inc. and Dr. Ruiyun Zhang for collaboration in aerogel research, Mr. David Pickles, of Corning, Inc. for TEM studies of these materials, and Dr. Pappannan Thiyagarajan and Mr. Dennis Wozniak of Argonne National Laboratory for collaboration on the SANS studies. The grant of the use of the SANS instrument at ANL is gratefully acknowledged.

REFERENCES

1. Y. Wang, H. Liu and Y Jiang, J. Chem. Soc. Chem. Commun. 1878 (1989)

2. J. M. Tour, S. L. Pendalwar and J. P. Cooper, Chem. Mater, **2,** 47 (1990).

3. A. M. Buckley and M. Greenblatt, J. Noncryst. Solids, **146,** 97 (1992).

4. A. Baiker, J-D. Grunwaldt, C. A. Muller and L. Schmid, Chimia **52,** 517 (1998).

5. A. Yang, Industrial Science and Technology Network, Inc., private communication.

6. H. P. Brack, Ph. D. Thesis, Brown University, 1994.

7. H. P. Brack, S. A. Tirmizi and W. M. Risen, Jr., Polymer **38**,151 (1996).

8. X. Hu, S. Ji, R. Zhang, D. Pickles, and W. M. Risen, Jr., to be published.

9. S. Ji, X. Hu, and W. M. Risen, Jr, to be published.

10. X. Hu, S. Ji, K. Littrell, D. Pickles, and W. M. Risen, Jr., to be published.

11. J. Teixeira, J. Appl. Cryst., **21**, 781 (1988).

12. J. S. Pedersen, Adv. in Colloid and Interface Sci., **70**, 171 (1997).

13. T. Freltoft, J. K. Kjems, and S. K. Sinha, Phys. Rev. B, **33**, 269 (1986).

14. I. W. Shim, V. D. Mattera, Jr. and W. M. Risen, Jr., Catalysis, **94**, 531 (1985).

15. V. D. Mattera, Jr., D. M. Barnes, S. N. Chaudhuri, R. D. Gonzalez, and W. M. Risen, Jr., J. Phys. Chem., **90**, 4819 (1986).

16. J. T. Yates, Jr., T. M. Duncan, S. D. Worley, and R. W. Vaughn, J. Chem. Phys. **70**, 1219 (1979).

17. C. S. Kellner and A. T. Bell, J. Catalysis, **75**, 251 (1982).

PREPARATION OF AEROGEL AND XEROGEL NANOCOMPOSITE MATERIALS

M.F. CASULA, A. CORRIAS, G. PASCHINA,
University of Cagliari, Department of Chemical Science, 09042 Cagliari, ITALY.

ABSTRACT

Sol-gel method was used to prepare nickel oxide-silica and iron oxide-silica nanocomposites materials in form of aerogels and xerogels. The samples were characterized by thermal analysis, X-ray diffraction, N_2 physisorption and transmission electron microscopy techniques. The variation of the supercritical solvent extraction conditions gives rise to differences in the morphological characteristics of the aerogels. These differences influence the size of the nickel oxide nanoparticles in nickel containing aerogels. On the other hand they do not affect the structure and size of the iron oxide nanoparticles in iron containing aerogels. The differences between the xerogel and aerogel nanocomposites are discussed.

INTRODUCTION

The sol-gel process has shown to be a valid method for the preparation of nanocomposite materials constituted of nanometric metal or metal oxide particles embedded in amorphous silica.[1-3] These materials present a variety of interesting magnetic, electric and catalytic properties which depend on the dimensions, distribution and concentration of the nanoparticles.[4-6]

It is well known that the sol-gel process allows a good control of composition, texture and structural characteristics of the final products.[7] In particular, the drying step plays an important role in determining the final properties of the materials. In fact, if the drying step is performed under supercritical conditions, aerogels with a high surface areas and pore volumes can be obtained, while xerogels, in which the original pore structure of the alcogels is lost, are obtained by slowly removing the solvent.

$NiO\text{-}SiO_2$ nanocomposites in form of aerogel seems to be particularly attractive since they can be easily converted into the corresponding $Ni\text{-}SiO_2$ nanocomposites, useful materials for catalytic applications.[8] $Fe_2O_3\text{-}SiO_2$ nanocomposites have shown to be able to stabilize the γ-Fe_2O_3 phase (maghemite), which has attractive magnetic properties.[3] In this case it is of interest to study the influence of the porous structure on maghemite formation and stabilization.

In this paper the effects of different drying procedures on the structural and morphological properties of $NiO\text{-}SiO_2$ and $Fe_2O_3\text{-}SiO_2$ nanocomposites in form of aerogels and xerogels are studied using TGA/DTA, XRD, N_2 physisorption and TEM techniques.

EXPERIMENT

Nickel oxide-silica (17% wt of nickel oxide) and iron oxide-silica (23% and 33% wt of iron oxide) nanocomposite materials were prepared by sol-gel method using TEOS and either nickel nitrate or iron nitrate as precursors.[3,8] The obtained alcogels were submitted to two different procedures of solvent drying. Xerogels were obtained by slow heat treatments in static air while aerogels were obtained by high temperature supercritical drying performed in an autoclave.

Four different conditions of supercritical drying were used to obtain the $NiO\text{-}SiO_2$ aerogels (A1, A2, A3, A4) by varying the heating ramp, the solvent used to fill the autoclave and the

Mat. Res. Soc. Symp. Proc. Vol. 581 © 2000 Materials Research Society

initial pressure in the autoclave, as reported in Table I. After supercritical drying, aerogel samples were calcined at 500 °C for 4 h. In order to obtain the xerogel sample, the fresh gel was powdered and directly calcined at 500 °C for 4 h.

Three different conditions (A1, A4, A5) of the supercritical drying were used to obtain the Fe_2O_3-SiO_2 aerogels, as reported in Table I. After supercritical drying, aerogel samples were heat treated with steps of 50 °C from 300 °C up to 500 °C and of 100 °C up to 900 °C, being kept for 30 min at each temperature. In order to obtain the xerogels, the fresh gels were powdered and kept for 24 h at 150 °C. The samples were then brought to higher temperatures with steps of 50 °C up to 500 °C and of 100 °C up to 900 °C, being kept for 30 min at each temperature.

Table I. Supercritical drying conditions

	Heating ramp	P_i	Solvent
A1	RT → 250°C 5°C/min, 250°C → T_f 1°C/min	1	EtOH 95%
A2	RT → 250°C 1°C/min, 250°C → T_f 0.5°C/min	1	EtOH 95%
A3	RT → 250°C 1°C/min, 250°C → T_f 0.5°C/min	1	EtOH 99%
A4	RT → 250°C 1°C/min, 250°C → T_f 0.5°C/min	7	EtOH 99%
A5	RT → 250°C 1°C/min, 250°C → T_f 0.5°C/min	45	EtOH 99%

RESULTS

In Fig. 1 the TGA curves and the corresponding DTA curves are reported for the fresh alcogel and for the four aerogels obtained using different supercritical drying conditions.

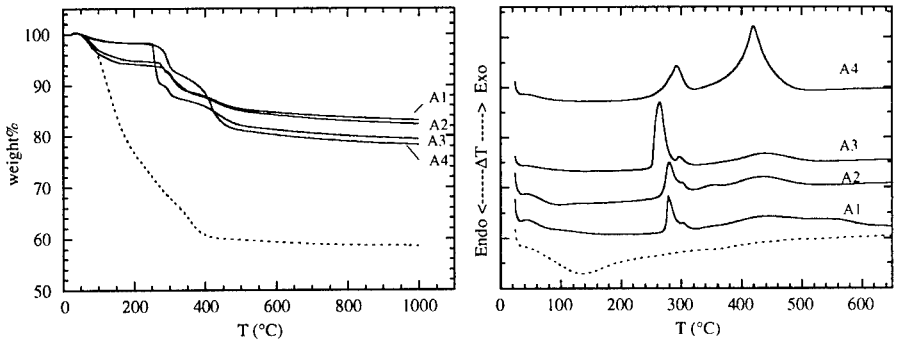


Figure 1. TGA and DTA curves for the fresh alcogel (----) and for the four NiO-SiO_2 aerogels

The fresh gel shows a remarkable weight loss up to 400 °C which corresponds to a broad endothermic peak in the DTA curve. The weight loss is due to solvent removal, decomposition of organics and of nickel nitrate. For higher temperatures the weight loss is very limited. The four aerogels show a much smaller weight loss, as expected. A1 and A2 samples show a larger weight loss in the low temperature range compared to A3 and A4 samples showing that the use of EtOH 99% to fill the autoclave is more effective in removing the solvent during supercritical extraction. The weight loss in the 250-500 °C range which corresponds to exothermic peaks in the DTA curves is due to the combustion of organics. The exothermic peak at lower temperature can be ascribed to the combustion of the most superficial organics while the one at higher

temperature to the organics in the inner pores. The different intensity of the exothermic peaks suggests the presence of a different porous structure in the four aerogel samples.

The XRD spectra for the four aerogel are reported in Fig. 2(a) and those of the same samples after calcination at 500 °C are reported in Fig. 2(b) together with that of the xerogel sample.

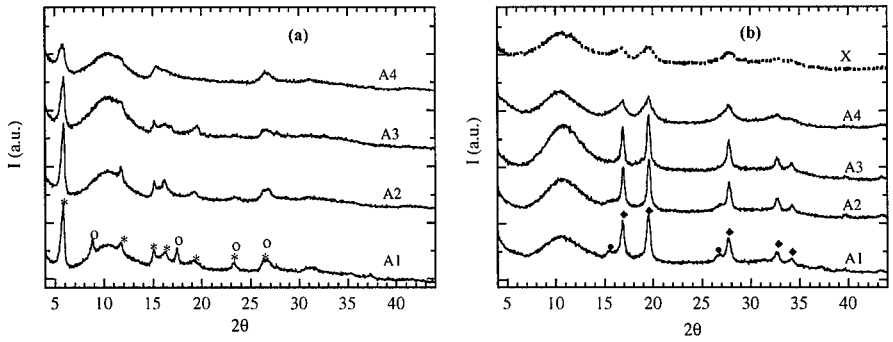


Figure 2. XRD spectra (MoKα) for (a) the four NiO-SiO_2 aerogels and (b) the aerogel and xerogel samples after calcination at 500 °C. (*) $Ni(NO_3)_2{\cdot}2Ni(OH)_2$, (o) $Ni(OH)_2$, (◆) NiO, (●)$Ni_3Si_2O_5(OH)_4$.

All the spectra show a broad halo due to amorphous silica. In the spectra of A1 sample peaks due to both $Ni(NO_3)_2{\cdot}2Ni(OH)_2$ and $Ni(OH)_2$ are also detectable while in the other spectra only the peaks due to $Ni(NO_3)_2{\cdot}2Ni(OH)_2$ are present and they become broader going from A2 to A4 sample. After calcination at 500 °C all the spectra show the peaks due to NiO which become broader going from A1 to A4 sample showing that the crystallite size becomes smaller. Peaks are slightly broader in the xerogel sample compared to A4. In A1 and A2 spectra some faint peaks due to $Ni_3SiO_5(OH)_4$ are also discernible.

In Tab. II the specific surface area and pore size distribution obtained from N_2 Adsorption-Desorption measurements at 77K are reported.

Table II. Surface area and pore size distribution for the 4 aerogels and the aerogel and xerogel samples after calcination at 500 °C.

SAMPLE	SURFACE AREA m^2/g (♦=BET; ✣=Dubinin)	PORE SIZE DISTRIBUTION			
		% (Vol) micropores	% (Vol) mesopores	% (Vol) macropores	method
A1	700 (♦)	11	86	2	BJH
A2	610 (✣)	84	16		HK
A3	780 (✣)	45	54		HK
A4	540 (✣)	94	6		HK
A1 500°C	940 (♦)	11	84	5	BJH
A2 500°C	600 (✣)	78	22		HK
A3 500°C	750 (✣)	62	37	1	HK
A4 500°C	470 (✣)	85	15		HK
X 500°C	250 (✣)	100			HK

As expected, all the aerogel samples show a very large surface area even after calcination at 500 °C. The xerogel sample after calcination exhibits a surface area smaller than the aerogel samples and a wholly microporous structure. The isotherms for the aerogel samples range from type IV isotherm[9] with a type H1 hysteresis[10] for A1 sample to a type I isotherm for sample A4,

and the same trend is observed in the calcined aerogels. These data show that variations of the supercritical extractions conditions leads to $NiO\text{-}SiO_2$ aerogels with different porous structure, from A1 sample, typically mesoporous, to A4 sample which is microporous.

The influence of the supercritical drying conditions on the porous structure of the aerogel samples is confirmed from TEM observations. In Fig. 3 the TEM micrographs for samples A1 and A4 are reported as an example.

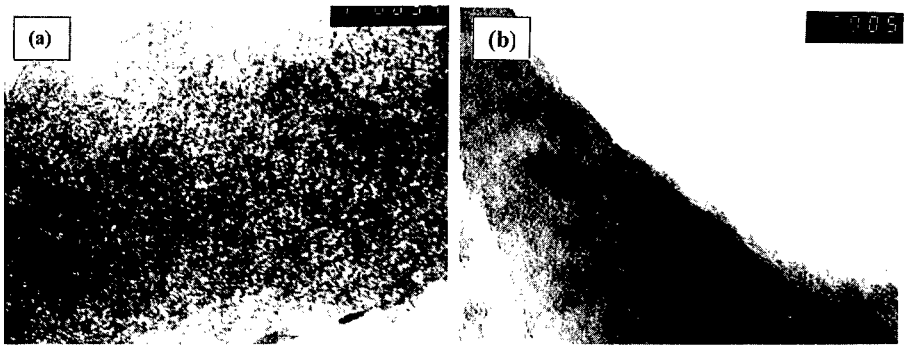


Figure 3. TEM micrographs (x 100000) for (a) A1 and (b) A4 $NiO{\cdot}SiO_2$ samples.

A similar influence of the supercritical drying conditions on the porous structure was observed on the $Fe_2O_3\text{-}SiO_2$ aerogel samples on the basis of their TGA/DTA, N_2 physisorption and TEM results. However, the evolution of the $Fe_2O_3{\cdot}SiO_2$ aerogel samples with thermal treatment is exactly the same regardless of the different conditions of the supercritical extraction and also the iron oxide content does not seem to have any influence.

In Fig. 4 the XRD spectra for A5 sample containing 33% Fe_2O_3 at different temperatures are reported as an example; exactly the same evolution was observed for all the other aerogel samples.

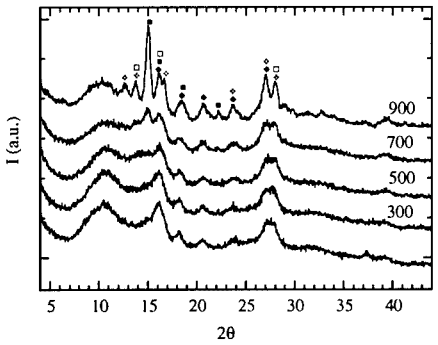


Figure 4. XRD spectra for A5 $Fe_2O_3{\cdot}SiO_2$ aerogel sample containing 33% Fe_2O_3 after extraction and after thermal treatment at increasing temperature. (♦)ferrihydrite, (■) $\alpha\text{-}Fe_2O_3$, (□) $\gamma\text{-}Fe_2O_3$, (⋄)$\varepsilon\text{-}Fe_2O_3$

The spectrum after supercritical extraction shows an amorphous halo and some broad peaks which can be attributed to 6-line ferrihydrite, a poorly crystalline ferric oxyhydroxide. After thermal treatment at 500 °C some new peaks begin to appear and they grow with increasing

temperature up to 900 °C when a mixture of different iron (III) oxides (α-Fe_2O_3, γ-Fe_2O_3, ε-Fe_2O_3.) are present together with ferrihydrite which shows to be stable up to high temperature.

On the other hand, a different evolution with thermal treatment was observed for the xerogel samples depending on the iron oxide content, as it can be inferred from the XRD spectra which are reported in Fig. 5.

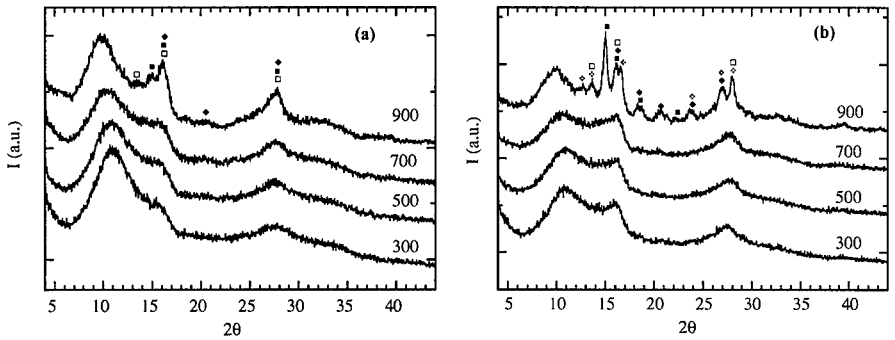


Figure 5. XRD spectra for Fe_2O_3-SiO_2 xerogels heat treated at increasing temperatures. (a) 23% and (b) 33% wt of iron oxide. (◆)ferrihydrite, (■) α-Fe_2O_3, (□) γ-Fe_2O_3, (❖)ε-Fe_2O_3

Xerogel samples heat treated at 300 °C show an halo due to amorphous silica and two very broad peaks due to 2-lines ferrihydrite. No significant changes appear in the XRD spectra up to 700 °C while the thermal treatment at 900 °C induces the formation of new crystalline phases. The xerogel sample containing 23% wt iron oxides at 900 °C mainly shows peaks due to maghemite while the sample containing 33% wt iron oxide show a very similar pattern to the aerogel samples treated at the same temperature, indicating the presence of a mixture of different iron (III) oxides. However, TEM observations show that the iron oxide nanoparticles are homogeneously distributed within the amorphous silica matrix in the xerogel sample while arrays of nanoparticles arranges in filars randomly oriented are often observed in the aerogel samples (see Fig. 6).

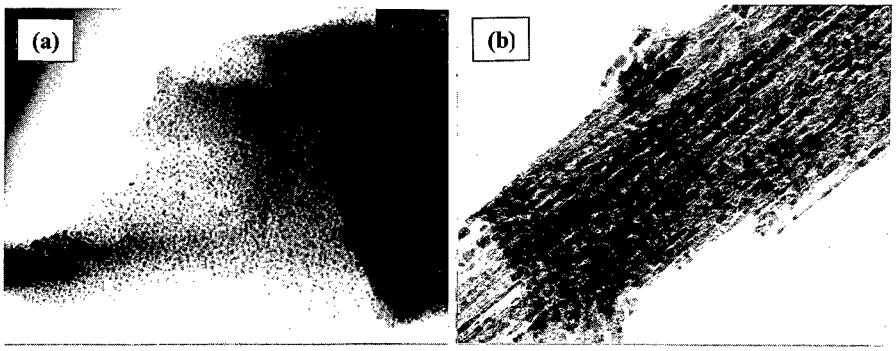


Figure 6. TEM micrographs (x 100000) for (a) xerogel and (b) aerogel Fe_2O_3-SiO_2 nanocomposites containing 23% wt iron oxide heat treated at 900 °C.

CONCLUSIONS

$NiO-SiO_2$ e $Fe_2O_3-SiO_2$ nanocomposites were obtained in form of aerogels and xerogels starting from the same alcogel. As expected, the surface area of the nanocomposite aerogel is much higher than that of the corresponding xerogel.

Moreover, the porous structure of the aerogel samples can be tailored by properly choosing the experimental conditions of the supercritical drying. This is particularly beneficial in the $NiO-SiO_2$ aerogels whose properties are very interesting for catalytic applications. In fact, specific surface area, pore size distribution, and crystallite dimensions strongly vary depending on the supercritical drying conditions. In particular, one aerogel sample calcined at 500°C presents very small NiO crystallites, similarly to the corresponding xerogel sample and, at the same time, the aerogel sample retains a much higher surface area than the corresponding xerogel.

The supercritical extraction conditions also influence the porous structure of iron containing aerogels but the structural evolution with thermal treatment is exactly the same in all the samples and the final aerogel samples always present a mixtures of different iron oxides. The iron content does not give rise to any difference in the evolution of the iron containing aerogel samples but it has an influence on the xerogel samples. In particular, the final xerogel sample with the highest iron content shows very similar results to the final aerogel samples, while the final xerogel sample with the lowest iron content mainly presents γ-Fe_2O_3. However, very recent results indicate that the preparation condition of the alcogel is the most important parameter in determining the amount of maghemite formation in the final nanocomposites both in form of xerogels and aerogels.

ACKNOWLEDGMENTS

This work was carried out within the project "Materiali Speciali per Tecnologie Avanzate II" of the Italian Consiglio Nazionale delle Ricerche.

REFERENCES

1. S. Roy, A. Chatterjee, D. Chakravorty, J. Mat. Res. **8**, 689(1993).
2. J.P. Wang, H.-L. Luo, J. Appl. Phys., **75**, 7425 (1994).
3. C. Cannas, D. Gatteschi, A. Musinu, G. Piccaluga, C. Sangregorio, J. Phys. Chem. B, **102**, 7721 (1998).
4. S. Komarneni, J. Mater. Chem. **2**, 1219(1992).
5. R.E. Newnham, S.E. McKinstry, H. Ikaua, Mater. Res. Soc. Symp. Proc. **175**, 161 (1990).
6. X. Gang, C.L. Chien, Appl. Phys. Lett. **51**, 1280(1987).
7. C.J. Brinker, G.W. Scherer, *Sol-gel Science*, Academic Press, San Diego, 1990.
8. G. Ennas, A. Mei, A. Musinu, G. Piccaluga, G. Pinna, S. Solinas, J. Non-Cryst. Solids **232-234**, 587 (1998).
9. S. Brunauer, L.S. Deming, W.S. Deming and E. Teller, J. Amer. Chem. Soc., **62**, 1723 (1940).
10. IUPAC Manual of Symbols and Terminology, Appendix 2, Pt. 1, Colloid and Surface Chemistry, Pure Appl. Chem. **31**, 578 (1972).

FIBER REINFORCED EPOXY RESIN COMPOSITE MATERIALS USING CARBOXYLATE-ALUMOXANES AS CROSS-LINKING AGENTS

CULLEN T. VOGELSON,[a] YOSHIHIRO KOIDE[a], AND ANDREW R. BARRON[a,b]*
[a] Department of Chemistry, Rice University, Houston, Texas 77005
[b] Department of Mechanical Engineering and Materials Science, Rice University, Houston, Texas, 77005

ABSTRACT

Chemically functionalized alumina nanoparticles (carboxylate-alumoxanes) are used as the inorganic component of a new class of inorganic-organic hybrid materials. Lysine- or *para*-hydroxybenzoic acid-derivatized alumoxanes are readily prepared from the reaction of boehmite, $[Al(O)(OH)]_n$, with the appropriate carboxylic acid. The peripheral organic hydroxides and amines of these carboxylate-alumoxanes either react directly with epoxide resins, such as the diglycidyl ether of bisphenol-A (DER 332), to form a hybrid material, or in the presence of an organic resin and hardener system to form a composite material. SEM and AFM show a uniform distribution of alumina nanoparticles within the resin matrix. The properties and cure times of the alumoxane hybrid and composite materials are distinct from both the pure resins and from a physical blend of the resins with traditional ceramic fillers. A significant increase in thermal stability and tensile strength is observed for both the hybrid and composite resin systems. In addition, both carbon fiber and carbon/Kevlar® matting have been successfully incorporated into the hybrid resin systems resulting in further property improvements.

INTRODUCTION

Traditional organic epoxy resin materials have great industrial use for numerous applications due to their easy processability and synthetically controllable physical properties.[1] A limitation to the use of purely organic resins, however, involves their inherent brittleness. Traditional methods of increasing the strength of organic polymers and resins have involved the addition of glass fibers, and more recently carbon and/or Kevlar® fibers and mattings. These fiber reinforced resins are used in a wealth of applications in the automotive, nautical, and aeronautical industries due to their advantageous combination of both high tensile and torsional strengths.[2]

In addition to the use of fibers as epoxide reinforcements, ceramic particles are commonly added as fillers to many polymer-based products. Ceramics, in general, have excellent mechanical properties such as heat-resistance, wear-resistance and strength, however, they are typically brittle and difficult to form into complex shapes. In addition, phase segregation often occurs in ceramic included resins which can be deleterious to the physical strength of the organic phase.[3] For example, the presence of ceramic fillers provides a point for crack initiation to occur. Further, the rational chemical design of new ceramics (and inorganic materials in general) is poorly understood.[4,5]

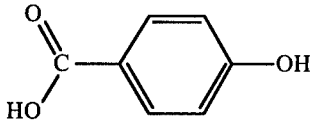
The performance of polymer-filler composites is strongly dependent on the particle size of the filler, and the interaction between the polymer and filler. The ideal filler then, is stable, hydrophobic, nano-sized, and covalently bound to the matrix. It has long been the goal of materials synthesis to prepare inorganic-organic hybrid composite materials that combine the properties of an organic polymer with that of a ceramic. For example, it would be desirable to rationally design a hybrid material that is easily processable and that has a high torsional strength. It is towards this end that the present research is aimed.

* Author to whom correspondence should be addressed.
(http://python.rice.edu/~arb/Barron.html)

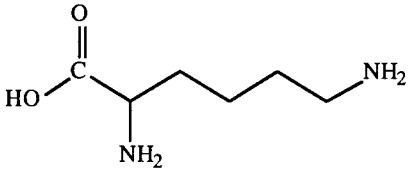
Mat. Res. Soc. Symp. Proc. Vol. 581 © 2000 Materials Research Society

We have previously reported that aluminum-oxide nanoparticles (5 to 80 nm) may be prepared by the reaction of the mineral boehmite with carboxylic acids.[6] The identity of the carboxylic acid appears to control the size of the nanoparticles.[7] These materials are termed carboxylate-alumoxanes and may be prepared with an almost limitless variety of functional groups.

One of the more common classes of organic resins is the epoxide-based materials. Epoxy resins are easily extruded and/or molded, have moderate strength, and low hardness.[8] Common resin systems usually consist of two parts, a resin and a hardener, which are mixed and cured at elevated temperatures (50 - 100 °C).[9] The resin component is often a bi-functional epoxide while the hardener contains a cross-linking agent along with a catalyst. Using such commercial resin systems, two classes of alumoxane-based materials are possible. First, a chemically functionalized carboxylate-alumoxane may be incorporated as an additional cross-linking agent into an existing resin/hardener system. Second, the chemically functionalized carboxylate-alumoxane may be used in place of the hardener (cross-linking agent). We have investigated both classes of material. In the present case two carboxylate-substituted alumoxanes were investigated: those derived from *para*-hydroxybenzoic acid (**I**) and lysine (**II**).

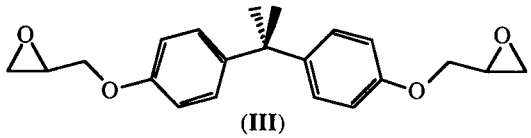


(**I**)



(**II**)

We have investigated two classes of epoxy-alumoxane materials. First, a chemically functionalized carboxylate-alumoxane was directly cross-linked with a common epoxy resin, the diglycidyl ether of bisphenol-A (Dow Chemical DER 332, **III**). This material has been termed a "hybrid alumoxane resin." The second class of material, referred to as a "composite alumoxane resin," is formed by the incorporation of the functionalized carboxylate-alumoxane into a commercially available resin/hardener system. Our results in these areas are reported herein.



(**III**)

RESULTS AND DISCUSSION

Hybrid Epoxy-Alumoxane Resins

The diglycidyl ether of bisphenol-A (DER 332, **III**) may be cross-linked directly with either *para*-hydroxybenzoate-alumoxane (*p*-HB-alumoxane) or lysine-alumoxane in the presence of a suitable base catalyst (e.g., 1-methylimidazole). By comparison with known epoxide reactivity[10] and model compound studies[11] it is proposed that the hydroxy group in *p*-HB-alumoxane and the amine groups in lysine-alumoxane undergo a ring opening reaction with the epoxide groups.

By reacting varying quantities of *p*-HB- and lysine-substituted alumoxanes with DER 332 an optimal weight ratio, based on a qualitative assessment of the physical properties of the cured materials, was found to be 1 part alumoxane to 2 parts resin. Variations of this ratio were found to yield cured materials with different properties ranging from extremely solid to almost "rubbery" in form. Neither *p*-HB-alumoxane or lysine-alumoxane are soluble in DER 332,

however, uniform mixtures may be readily prepared by stirring with a mechanical blender. Although reaction occurs over extended times at room temperature, some segregation occurs prior to complete reaction. Thus, it was found that more uniform materials are obtained by heating the samples, due to the reduced cure times. SEM, and AFM (Figure 1 and 2, respectively) analyses of the hybrid resins are consistent with a uniform distribution of the carboxylate-alumoxane particles throughout the material.

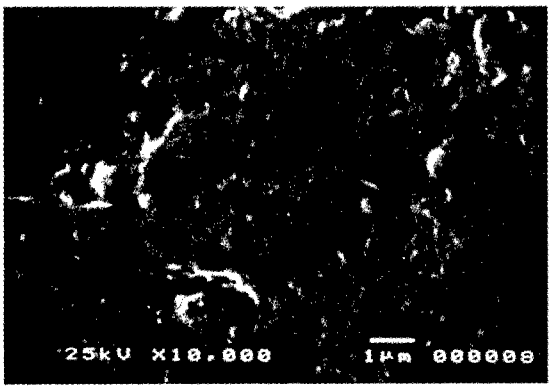


Figure 1. An SEI micrograph of the surface of the lysine-alumoxane hybrid resin.

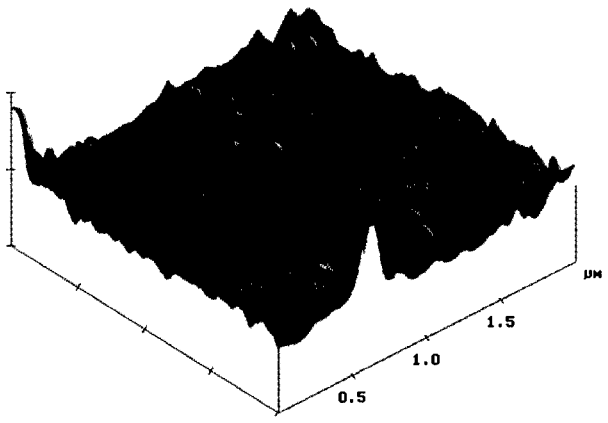


Figure 2. An AFM image of the surface of the lysine-alumoxane hybrid resin.

The cure time for the hybrid alumoxane resin (with an alumoxane:DER 332 ratio of 1:2) was found to be 10 hours at 50 °C, or 2 hours at 150 °C.[12] The set times were determined by differential thermal analysis (DTA) and found to be 6 minutes for the lysine hybrid material at 50 °C versus almost 20 minutes for the same resin cross-linked with ethylenediamine ($H_2NCH_2CH_2NH_2$, used for comparison). Thus, both set times and temperatures are significantly lower for the alumoxane hybrid resins than traditional, "purely organic," resins.

Post curing, both lysine- and *p*-HB-alumoxane hybrid resins have superior physical properties than were found for a purely organic resin system using ethylenediamine. While the

hardness of the hybrid resins is found to be similar to one another, the lysine-alumoxane resin was found to be qualitatively stronger than the *p*-HB-alumoxane resin. Tensile strength data, as seen in Table 1, show a seven fold increase in the peak load and peak stress observed with the use of the alumoxane cross-linking agents. This should be compared to a slight decrease observed with the addition of an "inert" filler such as boehmite. It should also be noted that the tensile strength of the alumoxane-based resins are between that of concrete (2 MPa) and aluminum (90 MPa), but with a lower modulus than either. In fact, while the modulus (1000 - 1700 MPa) is significantly higher than the purely "organic" resins (36 - 90 MPa), it is still lower than that of concrete (23 GPa) or bone (16 GPa).

Table 1. Summary of tensile strength measurements for various epoxy resin systems.

formulation	peak load (kN)	peak stress (MPa)	modulus (MPa)
"blank" DER 332[a]	0.111	2.083	36.2
"blank" DER 332 + boehmite	0.108	1.811	42.1
p-HB-alumoxane + DER 332	0.750	15.378	1058
"blank" Resin Services (RS) system[b]	0.451	8.937	905
p-HB-alumoxane + RS	2.251	68.022	1762

[a] The "blank" DER 332 system is composed of the Dow resin cross-linked with ethylenediamine.
[b] The Resin Services system is a composite composed of a commercial resin and hardener.

The thermal stability of the hybrid resins is also significantly enhanced. Thermogravimetric and differential thermal analysis (TG/DTA) indicates that the *p*-HB-alumoxane/DER 332 hybrid resin decomposes at 400 °C, without any prior mass loss. In contrast, the "blank" resin decomposes at 345 °C, but also shows mass loss above 180 °C. The lower temperature mass loss is possibly due to the volatilization of either unreacted or short chain species which are clearly not present in the alumoxane-based resin.

Composite Epoxy-Alumoxane Resins

In practical applications, it is unlikely that an epoxy resin system will utilize a functionalized carboxylate-alumoxane as its sole cross-linking agent. As a result, it is important to investigate the effect of the as synthesized alumoxanes on traditional two-part resin systems. To that end, lysine- and *p*-HB-alumoxanes were incorporated into a self-curing, commercially available epoxy resin system: Resin Services Resin HTR-212 with hardener #874. The epoxide base of the Resin Services Resin HTR-212 is the Dow DER 332 resin making for a ready comparison with the hybrid materials.

The sequential addition of different ratios of the carboxylate-alumoxanes into the resin system (similar to the procedure performed for the hybrid system), yielded an optimal weight ratio of incorporation found to be 2:5:1 for the alumoxane:resin:hardener. For comparative purposes, unreacted boehmite was added in the same ratio to the resin system, and a "blank" sample of the resin was also prepared without any additives (i.e., neat).

The neat resin and the resin/boehmite combination required full cure times of 4 hours at 50 °C. The presence of either carboxylate-alumoxane significantly lowered both the cure time (30 mins. at 50 °C) and the required temperature (2 hours at 35 °C). The set times, however, were unaffected by the addition of either alumoxane (8 min. at 25 °C). The hardness (scratch resistance) and strength of the resin composites are significantly increased by the presence of the carboxylate-alumoxanes, and these trends follow the order lysine-alumoxane resin > *para*-hydroxybenzoate-alumoxane resin >> neat resin > boehmite-impregnated resin. In addition, as may be seen from Table 1, the tensile strength of the alumoxane composite materials is significantly greater than the "blank" commercial resin. The peak load and peak stress are both

increased by a factor of five and seven, respectively. As with the hybrid system, the SEI micrograph of the lysine-alumoxane resin shows that the alumoxane particles are uniformly distributed throughout the composite. These results indicate that the carboxylate-alumoxanes are not simply acting as traditional ceramic fillers in the epoxy resin but are chemically bound to the organic backbone.

Fiber Incorporation into a Hybrid Epoxy-Alumoxane Resin

Fibers and mattings are commonly incorporated into epoxy materials due to their low mass and high tensile strength.[10,13] The advantages of fiber incorporation are most prominently seen in the automotive, nautical, and aeronautical industries where strong, lightweight epoxy-based materials serve numerous functions.[14] Both carbon fibers and carbon/Kevlar® mattings were incorporated into a *p*-HB-alumoxane hybrid resin prior to curing.

SEI micrographs of a cleaved sample show that the fibers reside within the epoxy matrix, see Figure 2. Thus the resin wets the fiber tow or mat allowing for full infiltration of the resin (i.e., no void spaces are observed) showing that the presence of the alumoxanes does not alter the processability of the commercial resin systems. Unlike previously reported studies,[15] the morphology of the alumoxane-based resins is unaffected by the presence/absence and identity of the fibers. No large particles or agglomerates were observed. As may also be seen from Figure 2, some fibers have pulled out of the matrix, leaving holes, whereas other fibers are clearly visible protruding from the epoxide. The opposing face of this purposely failed material shows fiber pull-out holes where the exposed fibers exist on the original face. This demonstrates that the alumoxane cross-linking agents do not effect fiber pull-out in an appreciable manner while increasing the strength of the matrix. This is near an ideal situation, since it shows that the fibers are not bound to the epoxy resin. Normally, it would take a great deal of force to pull a fiber from the matrix, however, upon impact, energy is transferred from the resin to the fiber, allowing it to "slip" from the matrix. The result of this energy transfer upon collision is that the epoxide is left relatively intact while the fibers are fully exposed thus creating a less disastrous material failure. Hence, the functionalized carboxylate-alumoxane hybrid resins are able to benefit from the incorporation of fibers and mats while at the same time allowing for a reasonable degree of fiber pull-out.



Figure 2. SEI micrographs of the surface of a purposely failed *para*-hydroxybenzoate-alumoxane composite resin containing fibers.

EXPERIMENTAL

The functionalized carboxylate-alumoxanes, and both the hybrid and composite resins were prepared using the methods published previously.[10] The various alumoxanes and resins have been characterized by IR, TGA, and solid state NMR. For fiber incorporation, an aluminum molded plate was placed flat on a countertop and coated with a mold-release agent. The pre-cured hybrid resin was then poured onto the surface of the plate, and fibers or matting were then layered across the surface of the resin. Additional fiber and resin layers were then added as

desired. A top mold plate, identical to the bottom plate, was placed on top of the "sandwich" of materials and held in place with C-Clamps. The entire mold was wrapped in aluminum foil to prevent spillage of the resin during cure. The mold was then placed in an oven at 150 °C for 2 hours to allow the resin to completely cure.

CONCLUSIONS

We have demonstrated that functionalized carboxylate-alumoxanes can readily be incorporated into both hybrid and composite epoxide resin systems in which the presence of the alumoxanes improves the overall cure times, temperatures, and physical properties of the organic resins. Unlike neat organic resins, the carboxylate-alumoxane composite resins do not undergo significant mold shrinkage, and the density of the resultant composites is uniform and comparable to, or higher than, that of the neat organic resin.

ACKNOWLEDGMENTS

Financial support for this work is provided by the Defense Advanced Research Project Agency (DARPA) and the Office of Naval Research (ONR). Resins and other materials were provided courtesy of Air Products, Axel Products, Inc., Dow Chemical Co., Resin Services Inc., Shell Chemical Co., and Union Carbide. The Bruker Avance 200 NMR spectrometer was purchased with funds from ONR Grant N00014-96-1-1146.

REFERENCES

1. J. M. G. Cowie, *Polymers: Chemistry and Physics of Modern Material* (Intertext, Aylesbury, 1973), p. 1.
2. A. Knop, W. Scheib, *Chemistry and Application of Phenolic Resins* (Springer-Verlag, New York, 1979), p. 155.
3. H. S. Katz, *Handbook of Fillers and Reinforcements for Plastics* (Van Nostrand Reinhold, New York, 1978), p. 562.
4. A. N. MacInnes, M. B. Power, A. F. Hepp, and A. R. Barron. *J. Organomet. Chem.*, **449** (1993) 95.
5. A. N. MacInnes, M. B. Power, and A. R. Barron, *Chem. Mater.*, **5** (1993) 1344.
6. C. C. Landry, N. Pappè, M. R. Mason, A. W. Apblett, A. N. Tyler, A. N. MacInnes, and A. R. Barron, *J. Mater. Chem.*, **5**, 331 (1995).
7. R. L. Callender, C. J. Harlan, N. M. Shapiro, C. D. Jones, D. L. Callahan, M. R. Wiesner, R. Cook, and A. R. Barron, *Chem. Mater.*, **9**, 2418 (1997).
8. M. P. Stevens, *Polymer Chemistry* (Oxford University Press, Oxford, 1990), p.374.
9. P. F. Bruins, *Epoxy Resins: Chemistry and Technology* (Marcel Dekker, Inc., New York, 1968), p. 4.
10. C. A. May, *Epoxy Resins: Chemistry and Technology* (Marcel Dekker, Inc., New York, 1988), p. 156.
11. (a) C. T. Vogelson, Y. Koide, L. B. Alemany, and A. R. Barron, submitted for publication; (b) C. T. Vogelson, Y. Koide, S. G. Bott, and A. R. Barron, *Advances in Science and Technology*, **15**, 499 (1999); (c) Y. Koide, S. G. Bott, and A. R. Barron, *J. Chem. Cryst.*, **29**, 247 (1999).
12. S. Han, W. G. Kim, H. G. Yoon, T. J. Moon, *J. Polym. Sci., Part A: Polym. Chem.* **36**, 773 (1998).
13. F. F. Lange, K. C. Radford, *J. Maters. Sci.* **6**, 1197 (1971).
14. R. W. Tess, *Epoxy Resins Chemistry and Technology*; 2 ed. (Marcel Dekker, Inc., New York, 1998), p. 45.
15. R. J. Varley, J. H. Hodgkin, *Polymer.* **38**, 1005 (1997).

THIN POLYTETRAFLUOROETHYLENE ORGANOSILANE NANOCOMPOSITE FILMS USED AS ULTRA LOW DIELECTRIC CONSTANT MATERIALS IN MICROELECTRONICS

Shichun Qu[1], Tom Rosenmayer[1], Ping Xu[2], Perry Spevack[2]
1. W. L. Gore and Associates, Inc., Eau Claire, WI
2. W. L. Gore & Associates, Inc., Elkton, MD.

ABSTRACT

Replacing the current on-chip dielectric materials such as silicon dioxide, which has a dielectric constant of approximately 4.0, with low dielectric constant materials can greatly improve the performance of high density VLSI device by reducing crosstalk and capacitive delay. Polytetrafluoroethylene (PTFE) has the lowest dielectric constant ($k < 2.0$) of any full density material, which makes it a promising candidate for this IC application. Pure PTFE thin films cast from PTFE nanoemulsion containing sub-20nm PTFE particles, though thermally stable, have some inherent sub-optimal properties. These include adhesion to other inorganic materials and mechanical strength at high processing temperatures. In order to improve these properties, we have developed a PTFE / silicon compound nanocomposite material. Initial tests have shown that this nanocomposite material has significantly improved high temperature mechanical properties and interfacial properties between the composite and inorganic materials such as silicon, silicon oxide, silicon nitride and some metals. The surface roughness of the thin film coatings is also reduced compared to pure PTFE thin film coatings. The coatings require no separate adhesion promoter to be applied to the substrate prior to deposition. Characterization work has been carried out with different techniques such as DMA, ToF-SIMS, XPS and AFM with hydrofluoric acid (HF) selective etching, in order to understand this novel nanocomposite and its surface and interfacial properties.

INTRODUCTION

As the microelectronics industry continues its trend towards progressively more demanding applications, the need for low dielectric constant materials has become more important than ever. Since as the size of the semiconductor device features shrinks without an accompanying reduction in die size, the RC delay associated with materials and processes used in interconnects contributes an increasingly large delay to signal propagation speed. To allow the industry to realize continued device performance improvements, two basic approaches to RC time constant reduction have been: reduction of "R" by the transition from aluminum-based to lower resistivity copper-based interconnect metallization; and reduction of "C" by introduction of low dielectric constant materials to replace SiO_2. In many cases, both paths are being taken simultaneously to afford the largest possible benefit.

PTFE is well known for its ultra low dielectric constant at full density, which makes it a promising candidate low-k material. Since 1995, W. L. Gore & Associates, Inc. has been developing a proprietary PTFE nanoemulsion (SPEEDFILM™) for ultra thin film coating applications. Previous work has proved that PTFE thin films cast from the Gore PTFE nanoemulsion have very good thermal stability up to 400°C, excellent electrical properties, as well as good chemical compatibility with all known chemicals currently used in the semiconductor industry[1-2]. However, there were also some noticeable problems with the first generation pure PTFE material. For example, in some occasions the instability of SiO_2 caps layered on top of pure PTFE thin film coatings, such as blistering and wrinkling during high temperature annealing, has been observed. In addition, an adhesion promoter is required prior to

Mat. Res. Soc. Symp. Proc. Vol. 581 © 2000 Materials Research Society

coating pure PTFE onto Si substrates. This extra coating step not only complicates the coating process but also increases the chances of contaminating wafers.

In order to improve the high temperature mechanical property and interfacial integrity and simplify the coating process, a PTFE/siloxane nanocomposite material was developed. Unlike previous composite materials, however, there are some constraints that limit the possible types of composites that could potentially be produced. First, the dielectric constant must remain low, preferably below 2.2. Second, phase separation must be avoided, because the materials are intended for integration into very fine metal structures, where line to line pitches could be less than 0.5 microns. Any inhomogeneity could degrade the performance of the IC devices and thus is unacceptable. Therefore, a composite that is homogeneous at molecular level must be developed.

A new PTFE/siloxane composite material has been developed by adding a small amount (< 3wt%) of a siloxane into the Gore PTFE nanoemulsion during formulation. Once added, the siloxane undergoes a series of reactions in the nanoemulsion. The color change from clear to yellow is one of the most noticeable effects. However, the emulsion remains stable at either low (8°C) or high temperature (50°C) for weeks. These accelerated aging processes indicate that the shelf life of the emulsion could be months at room temperature. A series of tests have proved that an adhesion promoter is no longer needed for coating this new PTFE/siloxane nanoemulsion. Tests have also shown that coated films have higher per pass crack resistance (> 5μm, without adhesion promoter) compared to the first generation pure PTFE coatings (~ 1.5μm, with adhesion promoter). Improved high temperature mechanical properties and better interfacial integrity between the PTFE and SiO_2 hard masks have also been demonstrated.

EXPERIMENTAL

Several nanoemulsion samples with different PTFE/siloxane concentrations were prepared together with control samples of pure PTFE. Then sub-micron thickness PTFE and PTFE/siloxane films were spin coated onto Si wafers. Coatings were done on a SVG 8868 coater track. Coated Si wafers were then scanned with a **di**-3100™ AFM after 250°C soft bake and 390°C sintering. Both soft bake and sintering were performed on the same SVG coater's hot plate in air. A thin layer of SiO_2 was deposited in a PlasmaTherm's plasma enhanced chemical vapor deposition (PECVD) tool. The stacked SiO_2/PTFE or PTFE composite samples were later annealed on a 400°C hot plate for up to 120 minutes or when failure occured. Typical failures for these type of stacks include blistering and haze caused by Euler buckling. AFM scans combined with HF selective etching and XPS depth profiling were performed to investigate the surface and interfacial properties.

ToF-SIMS and HF selective etching were combined to reveal possible microphase separation inside the PTFE/siloxane thin film coatings.

Dynamic mechanical analysis (DMA) is a typical small strain experiment for measuring linear viscoelasticity of polymer melts. As depicted in the drawings in Figure 1, a polymer sample is sandwiched between two parallel plates. At the set temperature a sinusoidal strain is introduced onto one plate, while the response stress is recorded from the other plate. Usually within a few cycles of start-up, the stress will also oscillate sinusoidally at the same frequency but in general will be shifted by a phase angle, δ, with respect to the strain wave. The stress and strain relationship is shown graphically in Figure 2 and described by the following mathematical expressions:

$$\gamma = \gamma_0 \sin \omega t \text{ and } \tau = \tau_0 \sin(\omega t + \delta) \qquad (1)$$

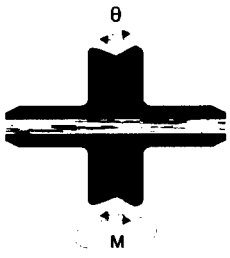


Figure 1. Parallel plates and polymer melt.

The stress wave may be decomposed into two waves of the same frequency, thus:

$$\tau = \tau' + \tau'' = \tau'_0 \sin\omega t + \tau''_0 \cos\omega t \quad (2)$$

$$\tan\delta = \tau''_0 / \tau'_0 \quad (3)$$

Here we get two dynamic moduli,

$G' = \tau'_0 / \gamma_0$, the in-phase elastic modulus. (4)

$G'' = \tau''_0 / \gamma_0$, the out-of-phase viscous modulus. (5)

Also the tan of phase angle can be re-written as,

$$\tan\delta = G''/G' \quad (6)$$

Normally a DMA experiment is performed in a certain temperature range to obtain the temperature dependent mechanical responses of the test materials. For linear crystalline polymers a typical elastic modulus response curve is illustrated in Figure 3. Characteristic transitions that can be observed are: the glass transition (T_g), the crystalline phase melting transition (T_m) and the melt flow transition (T_f). DMA is also sensitive to picking up crosslink effects.

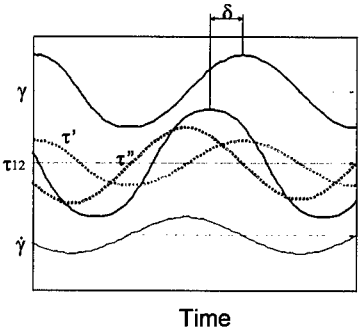


Figure 2. Strain (γ) and stress wave curve (τ), component stress wave curves (τ' and τ") and strain rate curve (γ̇).

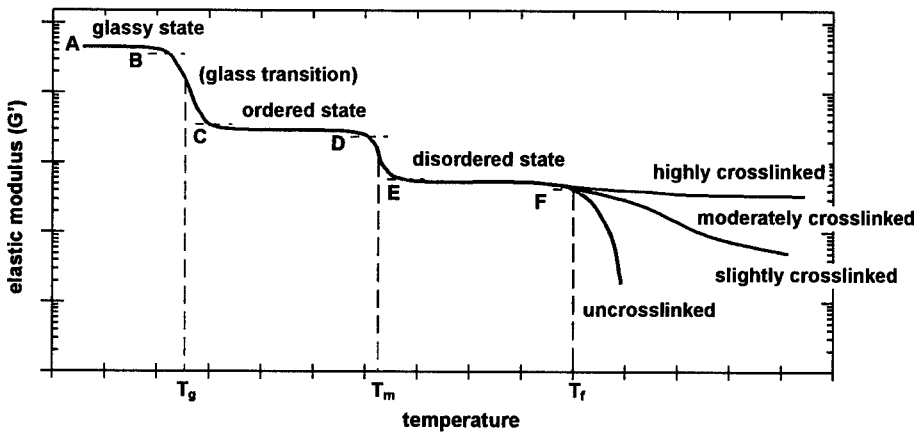


Figure 3. Schematic showing typical elastic modulus vs. temperature curve of a linear crystalline polymer with characteristic transitions and the effects of crosslinking. The shaded area is the actual test region.

For DMA measurements on pure PTFE and PTFE/siloxane composite materials, nanoemulsion samples were baked sequentially at 105 °C, 250 °C and 390 °C to simulate a standard coating process. Final powder samples were then pressed into thin disks for DMA experiments. A Rheometric Scientific ARES-LS-M rheometer with 25 mm parallel plates at about 0.8 mm gap was used to measure the viscoelastic properties of the PTFE and PTFE/siloxane melts in the temperature range from 270 °C to 400 °C.

RESULTS AND DISCUSSION

AFM scans in Figure 4 show dramatic surface morphology changes due to the siloxane addition. After a soft bake at 250 °C, pure PTFE shows rod-like PTFE aggregations, while the

PTFE/siloxane composite samples show no such phenomenon. The surface difference becomes more obvious after high temperature sintering. The roughness of the composite sample is greatly reduced, which was also observed and confirmed using optical microscopy.

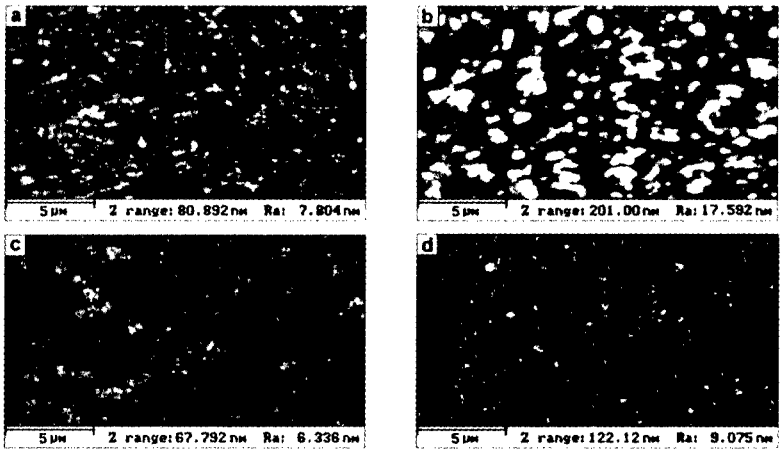


Figure 4. AFM scans of PTFE, PTFE/siloxane coatings. a). Pure PTFE after 250°C soft bake; b) pure PTFE after 390°C sintering; c) PTFE/siloxane after 250°C soft bake; d) PTFE/siloxane after 390°C sintering.

Optical micrographs taken after the SiO_2 capping and annealing procedures of both PTFE and the PTFE/siloxane composite coatings are shown in Figure 5 below. In both cases, CVD oxide caps about 300nm thick were layered on the top of pure PTFE or PTFE composite thin films. The PTFE and PTFE composite films are about 500nm thick. The SiO_2/pure PTFE stack actually failed (became hazy) after 20 minutes of annealing at 400°C, while the SiO_2/PTFE composite stack survived even after 120 minutes. A 6:1 buffered HF solution was used to partly remove the SiO_2 cap from the stack samples to expose the underlying PTFE or PTFE composite surface. A Tencor profilometer was used to profile both the SiO_2 and PTFE or PTFE composite surfaces yielding arithmetic roughness values of 33nm for the pure PTFE sample and 5nm for the PTFE composite material.

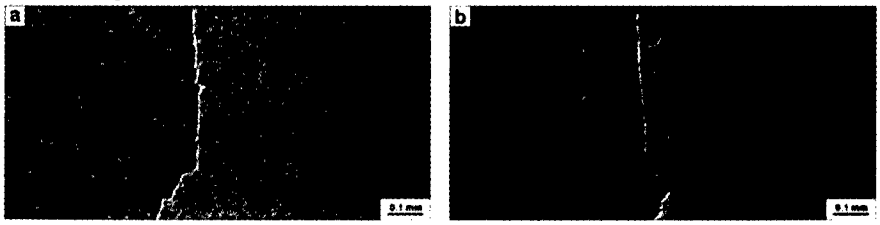


Figure 5. a) Optical micrographs of a SiO_2/pure PTFE stack taken after annealing for 20 minutes at 400°C. b) SiO_2/PTFE composite stack after annealing for 120 minutes at 400°C. Oxide cap of both samples (shown on the left side of each figure) was removed using HF.

DMA measurements on both pure PTFE powder and PTFE composite powder samples quantified the differences observed in the oxide cap annealing test. As plotted in Figure 6, DMA data of both samples' elastic moduli indicates that both samples have a melting transition at

320°C, which is normal for the specific PTFE material. The pure PTFE sample starts viscous flow at 360°C (elastic modulus drops several orders of magnitude), while the PTFE composite material can still maintain some elasticity at even 400°C, which is the upper temperature limit of the instrument. Based on the sketch in Figure 3, it may be observed that the PTFE composite material has a moderately crosslinked structure. Interestingly, the PTFE composite and an ultra high molecular weight (UHMW) PTFE sample have comparable modulus values at 400°C. It should be pointed out that the UHMW PTFE has M_n of 60×10^6 [g/mol], while our nanoemulsion PTFE has M_n of 0.4×10^6 [g/mol]. The improvement of high temperature mechanical properties of the nanoemulsion PTFE given the relatively low level of siloxane additions is remarkable.

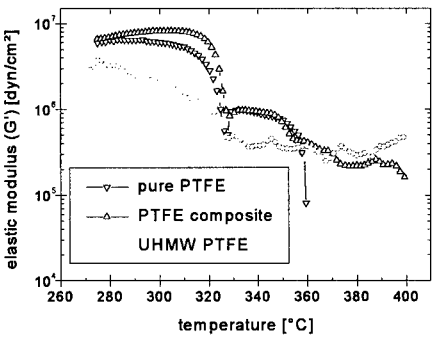


Figure 6. Elastic modulus measurements of pure PTFE, PTFE composite and Ultra high molecular weight (UHMW) PTFE.

With the above DMA results, it is possible to explain what was observed in the SiO_2 capping test. PECVD SiO_2 typically has a residual compressive stress. When the film stack is annealed above the melt flow temperature of the PTFE, the PTFE can flow viscously. Over time, in this case about 20 minutes, this viscous flow permits Euler buckling of the compressed SiO_2 film. In the case of the PTFE/siloxane composite film, the melt flow temperature has been raised above 400°C and no flow occurs.

Optical micrographs taken after a HF selective etch results on pure PTFE and PTFE composite thin films are shown in Figure 7. The pure PTFE sample shows no changes following the treatment. The slight edge lift is due to HF attack at the adhesion promoter present at the Si/PTFE interface. The PTFE composite material surface shows micron-sized craters. This indicates the presence of silica-like material in the thin films. AFM was attempted to reveal possible mechanisms for the appearance of craters, such as microphase separations caused by silica clusters embedded in the PTFE matrix, but no such microphase separation was observed. The craters are about 60nm deep on 500nm PTFE composite thin films.

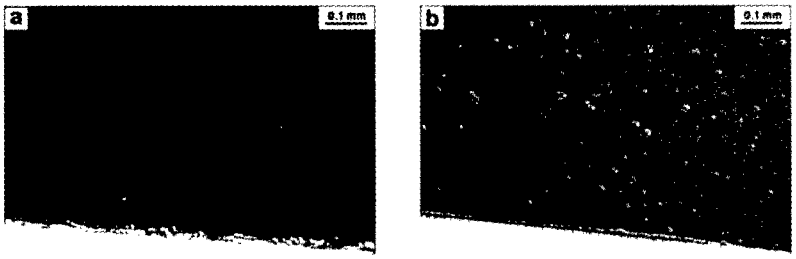


Figure 7. Optical micrographs taken after HF selective etching on both pure PTFE (a) and PTFE composite (b) thin films.

To investigate the possible microphase separation inside the PTFE composite films, ToF-SIMS surface elemental analysis was carried out. Results are summarized in Figure 8. For as-received sample surface mapping, hydrocarbons, fluorocarbon, and silicon were monitored (Figure 8a). The PTFE composite surface is almost 100% fluorocarbon. The trace amounts of

hydrocarbon are likely caused by surface contamination during shipping and handling. A shallow crater of about 50nm is then sputtered into the composite thin film. ToF-SIMS elemental mapping of fluorocarbon, carbon and silicon is then performed on the bottom of the etched crater (Figure 8b). Uniformly distributed silicon signal is detected inside the PTFE composite. The scan is 100 microns by 100 microns. No microphase separation is observed. Quantitative XPS analysis on the bottom gives surface concentration of silicon of 2%, which further confirmed the ToF-SIMS observation.

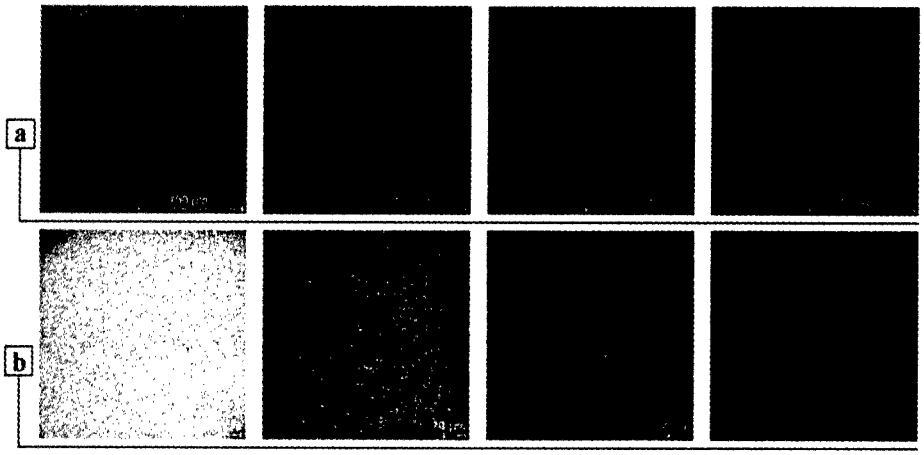


Figure 8. ToF-SIMS surface elemental mapping on as received PTFE composite thin film surface (a) and 50nm deep inside the thin film (b).

CONCLUSIONS

A novel PTFE/siloxane nanocomposite material has been successfully developed with very low inorganic material concentration. The new composite material shows much improved high temperature mechanical properties demonstrated by SiO_2 capping and annealing tests and DMA. Unlike other composite materials, this PTFE/siloxane composite is a true molecular level composite material. No microphase separation is detected. A complete set of thin film characterization relative to the IC dielectric applications is underway. More detailed results will be published in several forthcoming papers.

ACKNOLEDGEMENTS

The authors acknowledge special contributions by fellow Gore associates Jami Riggs, John Bartz, Huey Wu, Mike Zumbrum, Jack Hegenbarth. Thanks also go to Dr. Ken Batzar (consultant), Scott Krahn (intern), Dr. Paul Vlasak, John Newman and Jim Gibson at Physical Electronics, Inc.

REFERENCES

1. S. C. Sun in *Low-Dielectric Constant Materials II*, edited by André Lagendijk, et al, (Mater. Res. Soc. Proc. 443, Pittsburgh, PA, 1997), p. 85-90.
2. C. T. Rosenmayer, in *Low-Dielectric Constant Materials III*, edited by Carlye Case, et al, (Mater. Res. Soc. Proc. 476, Pittsburgh, PA, 1997), p. 231-236.
3. C. W. Macosko, *Rheology Principles, Measurements, and Applications*, (Wiley-VCH, 1994).

Proton Conducting Organic/Inorganic Nanocomposite Polymer Electrolytic Membrane Synthesized by Sol-Gel Process

I. Honma, *S. Nomura and H. Nakajima
Energy Fundamental Division, Electrotechnical Laboratory, AIST, Umezono, Tsukuba, Ibaraki, 305-8568, Japan, ihonma@etl.go.jp
* Minase Research Institute, Sekisui Chemical Co.,Ltd., Osaka 618-8589, Japan

ABSTRACT

In this paper, new synthetic routes have been investigated for the preparation of Organic/inorganic nanocomposite polymer membranes consisting of SiO_2 /PTMO(polytetramethylene oxide) hybrids and novel proton conducting materials. These materials have been synthesized through sol-gel processes in flexible, ductile, free-standing thin membrane form. The hybrid membrane has been found to be thermally stable up to 160 C and possesses proton conductivities of approximately 10^{-4} S/cm from a room temperature to 160 C.

INTRODUCTION

Recently, new synthetic routes have been developed for the preparation of organic/inorganic hybrid materials as realistic ionic conducting membranes for electrochemical devices such as fuel cells and batteries[1-13]. In those materials, the structure of the hybrid has been designed at a molecular scale to possess fast proton as well as Lithium ion conduction through mostly manipulating organic ligand to inorganic surfaces[1-13].

In this paper, a new class of organic/inorganic nanocomposite membranes consisting of SiO_2 / Polymer (PEO: Polyethylene Oxides; PPO: polypropylene oxide; PTMO: polytetrapropylene oxide) hybrids have been synthesized through sol-gel processes. Membranes doped with an acidic moiety such as 12-phosphotungstic acid (PWA) show high proton conductivities at temperatures up to 160 ^{o}C and were found to be flexible, as well as, thermally stable due to the closs-linking with temperature tolerant polymer frameworks in the hybrids. The effect of molecular structure and molecular weight of the polymers have been studied on the thermal stability and proton conducting properties of the membranes.

EXPERIMENT

Molecular Design of the Hybrid Membrane

Molecular precursors designed for organic/inorganic hybrid membranes have been developed in our previous papers[9-12]. Organic polymers of polyethylene oxide (PEO), polypropylene oxide (PPO), and polytetramethylene oxide (PTMO) have been closs-linked with alkoxysilanes through isocyanato coupling. These precursors then hydrolyze and condense to form macromolecules of flexible, glassy hybrid materials as shown in fig.1. In the present work, the molecular weight of PEO, PPO, and PTMO have been systematically changed to control the thermal stability and proton

Mat. Res. Soc. Symp. Proc. Vol. 581 © 2000 Materials Research Society

conductivity of the hybrid electrolyte membranes. In particular, PEO600 (molecular weight of PEO is 600), PPO700, PTMO250, PTMO650 and PTMO2000 (Wako Pure Chemical) have been used for studying the effects of molecular structure and molecular weight on the thermal and conductive properties of the membrane.

Membrane Synthetic procedure

Figure 2 inset shows a synthetic route of the production of a silica/PTMO hybrid membrane. Endcapped precursor, i.e., triethoxysilane derivatized PTMO 250, 650, 2000, was made by reacting icocyanatopropyltriethoxysilane with polytetramethyleneglycol (PTMG), separately. Then it is dissolved in isopropanol solution and stirred for 1 hour. Propylene carbonate (PC) and PWA were then added to the above solution and further stirred for 20 minutes. The doping amount of PC and PWA was changed from 0 % (non-doped) to 100 % by weight. The solutions were cast in a flat vessel and annealed in a dry atmosphere overnight. The first step annealing was conducted at 60 C, for 12 hours to allow condensation of the membrane, while the second step annealing was conducted at 140 C for 3 hours. This second step was also performed to further strengthen the organic/inorganic hybrid network. Propylene carbonate (PC) molecules are also incorporated to dissolve protons from PWA clusters.

Conductivity measurements

Electrical conductivity of hybrid electrolyte membrane was measured by two terminal impedance spectroscopic method using a computer-aided frequency response analyzer (Solartron 1260) at frequency range 1Hz ~2MHz at various temperatures, pressures and humidities. When the conductivity of the membrane was measured above 100C, the total pressure was elevated. Humidity against membrane was controlled by the temperature of the humidifier units, where the humidifier cell temperature was kept 10 degree higher than the measuring cell, and saturated water vapor was supplied to the measuring cell even at temperatures above 100C. For example, the cell was pressurized to 6 atm at 160C measurement. The protonic conductivities were measured in the typical frequency region (~ 10^4Hz) of relaxations for usual proton-conducting polymer electrolytes. The measuring system was same as our previous papers[9-12,16].

RESULTS AND DISCUSSIONS

The membranes were synthesized as transparent, flexible, homogeneous materials in a large concentration range of PWA and PC concentration with doping rate up to 100 wt%. Thermal stability of the hybrid membranes were studied in two annealing steps of 60C for 12 hours and 140C for 3 hours.

In spite of the heavy doping, PWA have never leaked out from the hybrid membrane, suggesting that all the doped PWA was chemically incorporated into the organic/inorganic hybrid network (fig.3). While the PWA doping into silica has been studied through sol-gel processes, PWA-silica interface interactions were studied elsewhere and it is suggested that PWA is stabilized within the silica skeleton and the two forms of entrapped PWA in nanophases of silica can be existing; one is in contact with silanol groups of the silica and the other is silica matrix[15].

Figure 4 shows the effects of PC doping concentration on the membrane (synthesized by PTMO650 and PWA of 50% annealed at 140 C) proton conductivities for (a) 0%, non-doped, (b) 25 wt% and (c) 50 wt%, respectively. Although the conductivity increases with temperature for these samples, The conductivity with higher PC doped membrane has larger proton conductivity. This is probably due to the enhanced proton dissociation and mobility by PC incorporations. Water molecules

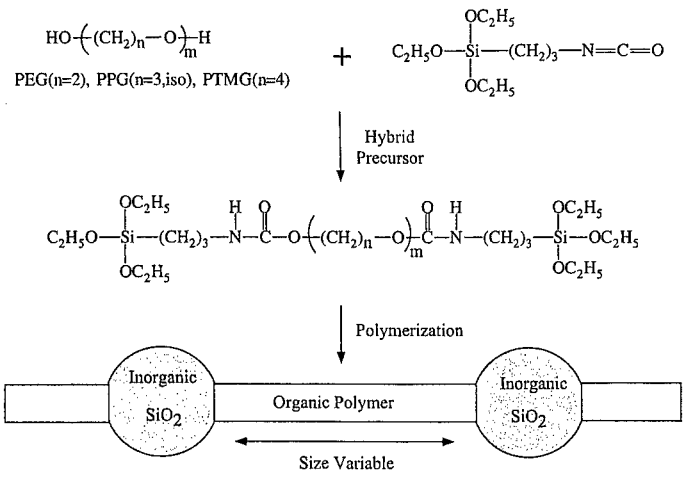


Figure 1. A molecular design of silica (SiO_2)/polymer nanocomposites, where the PEG, PPG, PTMG were end-capped by triethoxysilane or trimethoxysilane through isocyanato coupling. The chain length of the polymer part can be controlled by molecular weight.

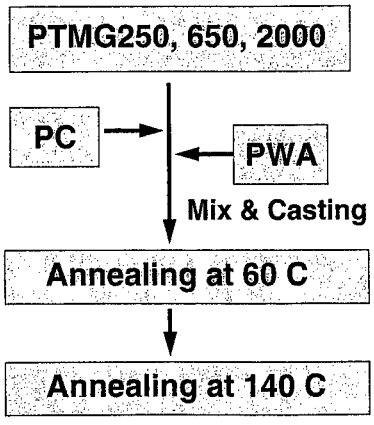


Figure 2. A synthetic route to the production of a silica/PTMO hybrid membrane.

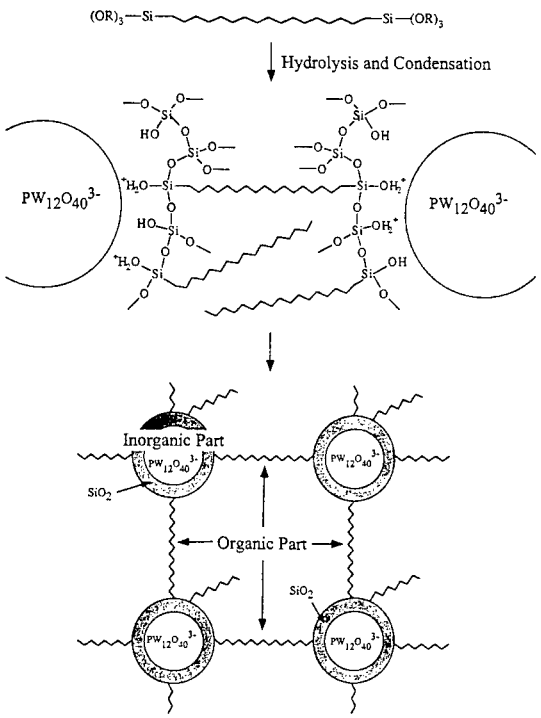


Figure 3. Organic/inorganic hybrid precursors hydrolyze and condense at PWA surfaces with structural water to form a proton conducting membrane.

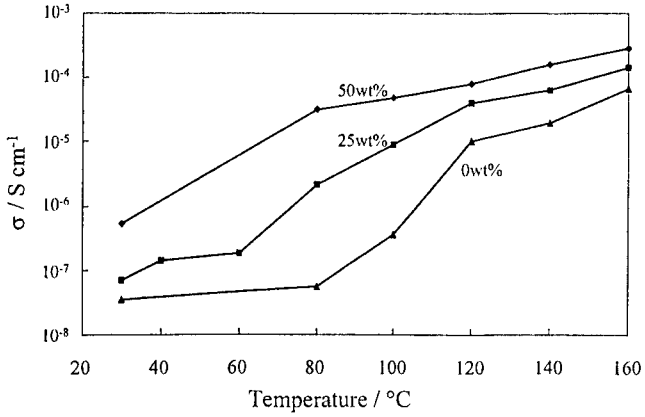


Figure 4. Effects of PC doping concentration on the membrane (synthesized by PTMO650 and PWA of 50% annealed at 140 C) conductivities for (a) 0%, non-doped, (b) 25 wt% and (c) 50 wt%, respectively.

are incorporated in the membrane by humidity conditions, however, PC might be used as proton carriers for possessing large dielectric constant for dissociation, similar to that of water. The conductivity of approximately 10^{-4} S/cm was achieved at 160 C in these doped membranes.

These results show that the general feature of the conductivity's change is not the same as that of other proton conducting polymer membranes such as Nafion. Nafion has almost identical proton conductivity in a wide temperature range from R.T. to 100 C when it is fully humidified, while our hybrid membrane has thermally activated proton conductivity from R.T. to 160 C. As temperature is increased, the conductivity increases at logarithmic scale even with saturated humudities. This is probably due to the fact that the protons on the PWA surfaces need thermally activated processes for dissociation to hydrated forms such as $H_3O^+$and $H_5O_2^+$. The conduction mechanism is quite similar to the novel fast proton conduction in inorganic ion-exchange compounds[14-20]. The thermal stability is enhanced for hybrids with PTMO 250 and PTMO 650, as no discernible chemical change or mechanical degradation was observed after several hours. The hybrid membrane was much stable than Nafion at elevated temperature range higher than 100 C.

CONCLUSION

High temperature proton conducting polymer membranes have been synthesized through the sol-gel processing of organic/inorganic nanocomposites consisting of SiO_2 /polymer hybrid materials. The hybrid membrane doped with 12-phosphotungstic acid (PWA) shows good proton conductivities at temperatures above 100 ^oC. The proton conductivities of 10^{-4} - 10^{-3} S/cm at 160 ^oC has been achieved under humid conditions. These organic/inorganic hybrid membrane can be identified as a remarkable family of proton conducting solid polymer electrolytes which, potentially, provides new technological applications for high temperature electrochemical devices including polymer electrolyte fuel cells, water hydrolysis, chemical sensors and other electrochemical devices.

References

1. L.Depre, J.Kappel and M.Popall, Electrochimica Acta, 43, 1301 (1998)
2. M.Popall and H.Durand, Electrochimica Acta, 37, 1593 (1992)
3. F.Croce, G.B.Appetecchi, L.Persi and B.Scrosati, Nature, 394, 456 (1998)
4. G.R.Goward, F.Leroux and L.F.Nazar, Electrochimica Acta, 43, 1307 (1998)
5. J-Y.Sanchez, A.Denoyelle and C.Poinsignon,
   Polymers for Advanced Technologies, 4, 99 (1993)
6. I.Gautier-Luneau, A.Denoyelle, J.Y.Sanchez and C.Poinsignon,
   Electrochimica Acta, 37, 1615 (1992)
7. Y.Charbouillot, D.Ravaine, M.Armand and C.Poinsignon,
   J. Non-Crystalline Solids, 103, 325 (1988)
8. G.Vaivars, J.Kleperis, A.Azens, C.G.Granqvist and A.Lusis,
   Solid State Ionics, 97, 365 (1997)

9. I. Honma, S. Hirakawa, K. Yamada and J.M. Bae,
Solid State Ionics, 118, 29 (1998)
10. I. Honma, S. Hirakawa and J.M. Bae
Proceeding MRS Fall meeting, Nov.30, 1998 Boston MA, USA
11. I. Honma, S. Hirakawa and J.M. Bae,
Proc. Electrochemical Society 194th meeting, Nov. 4. 1998 Boston MA, USA
12. J.M. Bae, S.Hirakawa and I. Honma
Proc. IUMRS-ICEM, August 25, 1998 Cheju Island, Korea
13. O. Nakamura, T. Kodama, I. Ogino and Y. Miyake,
Chem. Lett. 1979, 17
14. M.Tatsumisago, H.Honjo, Y. Sakai and T. Minami,
Solid State Ionics, 74, 105 (1994)
15. U.B.Moic, S.K.Milonjic, D.Malovic, V.Stamenkovic, Ph. Colomban,
M.M.Mitrovic, R.Dimitrijevic, Solid State Ionics 97, 239 (1997)
16. I. Honma, Y. Takeda and J.M. Bae,
Solid State Ionics, 120, 255 (1999)
17. W.A. England, M.G.Cross, A.Hamnett, P.J.Wiseman and J.B. Goodenough,
Solid State Ionics, 1, 231 (1980)
18. K.D. Kreuer, Solid State Ionics, 94, 55 (1997)
19. K.D.Kreuer, A.Fuchs, M.Ise, M.Spaeth and J.Maier,
Electrochimica Acta, 43, 1281 (1998)
20. Y.Sone, A.Kishimoto and T. Kudo,
Solid State Ionics, 66, 53 (1993)

MODIFIED SOL-GEL SYNTHESIS OF VANADIUM OXIDE NANOCOMPOSITES CONTAINING SURFACTANT IONS

ARTHUR DOBLEY, PETER Y. ZAVALIJ, AND M. STANLEY WHITTINGHAM.
Chemistry Department and Materials Research Center, State University of New York at Binghamton, Binghamton, New York 13902-6016, U.S.A.

ABSTRACT

Recently, there has been much interest in creating new layered transition metal oxides. Vanadium oxides may be used as sorbents, catalysts, and cathodes in lithium batteries. The modified sol-gel technique allows for some control towards the final structure of the compound. Using this technique, a new layered vanadium oxide compound - I, containing the surfactant dodecylphosphate, has been synthesized. After the removal of the organic ligand a new compound - II is formed which might be hexagonal. The compounds were analyzed using XRD, TGA, SEM, and NMR. $VO_2PO_3(OH)C_{12}H_{25}(H_2O)_n$ is the general formula of the layered product I with a layer spacing of about 40 angstroms. II appears to be hexagonal with a = 43Å. The synthesis, composition, and structure of these compounds are discussed.

INTRODUCTION

Since the discovery at Mobil [1, 2] of MCM-41, a mesoporous structured aluminum silicate, there has been a great interest in extending the research to include transition metals [3, 4]. However, very little of this work has targeted vanadium oxides. This is surprising as many vanadium oxide compounds are of particular interest as they have many potential commercial applications such as: molecular sieves, sorbents, catalysts, and energy storage devices. Vanadium oxides have a particularly rich structural chemistry [5] and have also been found to form a wide range of inorganic/organic materials [6]. Along with the quest of discovering new materials analogous to MCM-41, new techniques are being used to synthesize these compounds. One of the techniques is the modified sol-gel method. Sol-gel synthesis involves a sol (a fluid colloidal system) turning into a gel (jelly-like mass with 3D system). This occurs by a metal alkoxide undergoing hydrolysis and polymerization. Further drying yields a xerogel. Organics present in product make it a 'modified' sol-gel. Templating, done by surfactants, forms micelles (shapes) in solution. Metal oxides can be fashioned to a particular shape (*i.e.* tunneled, layered structures) around these micelles. Then the surfactants can be removed to leave behind the metal oxide in the desired shape. Earlier work in our laboratory showed that vanadium oxide surfactant materials were not mesoporous, despite TEM indications of a 40Å lattice, but rather Keggin-like vanadium oxide clusters [7, 8]. Single crystal X-ray diffraction confirmed the presence of clusters and of organic/inorganic system swellable by a wide range of solvents [9].

Mat. Res. Soc. Symp. Proc. Vol. 581 © 2000 Materials Research Society

EXPERIMENTAL

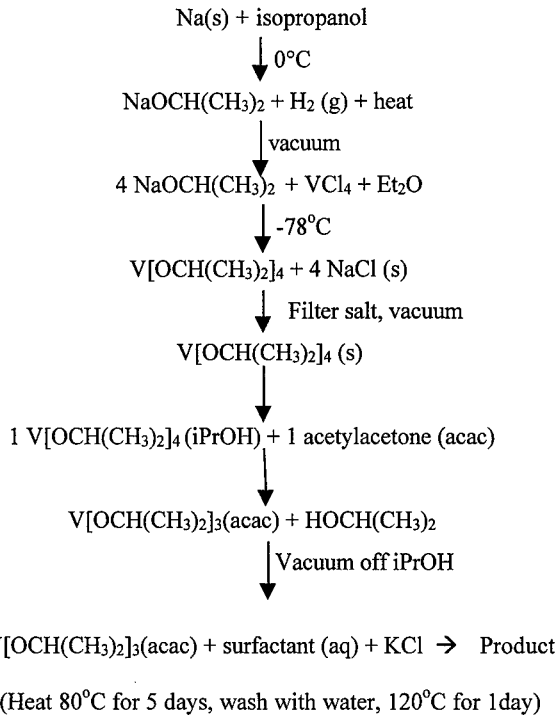
A modified sol-gel method [10] was used to react a vanadium alkoxide with the surfactant dodecylphosphate. The air sensitive reagents required the use of a double manifold system with vacuum and argon gas lines, together with ground joint glassware. Also a means of cooling the violent or exothermic reactions is needed, and water or slush baths were used for this purpose. A reflux set up was used with a cooling bath of ice water to react 5 grams of sodium metal (Aldrich) with 300 ml of isopropanol (Aldrich) in 300 ml of diethyl ether (Aldrich). After completion of the reaction the alcohol and ether were removed by vacuum to leave the white needle like crystals of $NaOCH(CH_3)_2$. The following synthesis, of the vanadium alkoxide, was modified from that of Turevskaya [11]. About 250 ml of dry diethyl ether was added, and a dry ice acetone bath was applied. 3.4 ml of VCl_4 (Aldrich) was added slowly via a syringe to the reaction vessel. The resulting NaCl was removed along with the ether to leave $V[OCH(CH_3)_2]_4$. Vanadium (IV) isopropoxide was then reacted with acetylacetone (also known as 2,4-pentanedione from Aldrich) with a 1:1 molar ratio in isopropanol. Acetylacetone acts as a chelating agent to slow down the hydrolysis reactions of the metal alkoxide. If hydrolysis occurs too fast then amorphous phases will be obtained. The isopropanol (iPrOH) was removed by vacuum. A 3.4 wt% aqueous solution of the surfactant was prepared by dissolving dodecylphosphate, from Lancaster, into pH5 adjusted water (with concentrated HCl). The reactants, in the molar ratio 1 $V[OCH(CH_3)_2]_4$: 1 acetylacetone (acac) : 1 surfactant :1 KCl were mixed and then heated at 80°C for 5 days, washed with water, then dried at 120°C for 1day. The product obtained will be called Material I. After drying the product was black in color suggesting partial reduction of the vanadium. This synthesis scheme is shown on the next page.

Samples were characterized via X-ray powder diffraction on a Phillips PW3040-MPD powder diffractometer using CuK_α radiation, fitted with an Anton Paar heating stage model HTK-10 calibrated to the m.p. of lead. Thermal gravimetric analysis, to determine water and organic content as well as overall stability, was done on a Perkin Elmer TGA 7. Magic angle spinning NMR analysis was performed on a Bruker AC-300 MHz instrument set up for solids; concentrated phosphoric acid (aq) used as a reference for ^{31}P NMR. Electron Microprobe analyses and SEM photographs were obtained on a JEOL 2000 Electron Microprobe.

RESULTS AND DISCUSSION

Material I upon drying was a black hardened gel with small variations in color, after grinding it became gray. Initial results from XRD indicated the presence of NaCl and KCl salts, byproducts of the synthesis. These were removed by washing the sample with reverse osmosis water. Thermal gravimetric analysis was performed in both oxygen and nitrogen gas (fig 1) which revealed a weight loss of 9.25% for H_2O, and 42.6% for the hydrocarbon chain of the surfactant.

Table 1. Synthesis Scheme



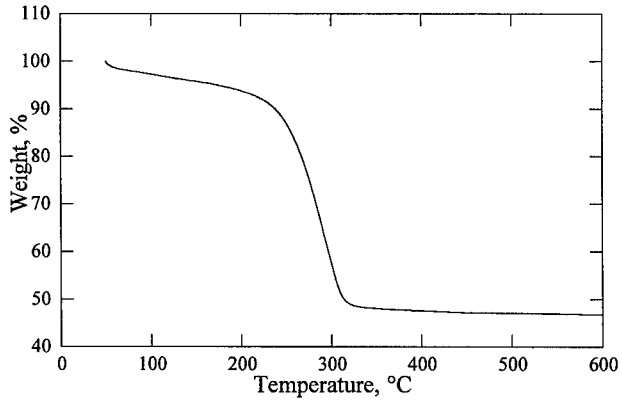


Figure 1. TGA curve of material I in an oxygen/nitrogen atmosphere.

The TGA of the surfactant itself showed a steep weight loss around 200°C, which is also seen in the TGA of the sample. The surfactant was removed by calcination in air to 400°C giving a new compound - Material II. This then absorbs water from the atmosphere and upon heating shows about 5% wt. loss. This supports a molecular formula of $VO_2PO_3(OH)C_{12}H_{25}$ $2H_2O$ for I.

The electron microprobe images showed a layered morphology for Material I. The image for Material II showed that the layering no longer existed and that a new organization was seen. Elemental analysis by EDS (energy-dispersive spectroscopy) exhibited the strong presence of V and P, with small traces of Na and K in both materials.

The XRD pattern of Material I, shown in figure 2a is consistent with a layered structure with d values at 40Å, 20Å, 12.3 Å. and 9.7Å. This lattice spacing of 40Å is consistent with a bilayer of surfactant molecules sandwiched between two sheets of vanadium oxide. No evidence for residual NaCl or KCl was observed. After the removal of organic this simple layered structure was changed. Material II showed just two peaks, shown in figure 2b, with d spacing values of 37Å and 22Å. These are consistent with a hexagonal lattice with a=43Å, but do not prove the hexagonal symmetry.

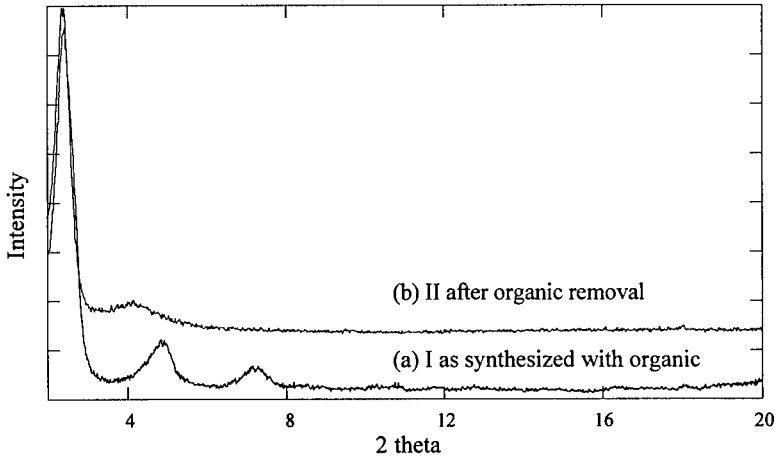


Figure 2. X-ray diffraction patterns (a) for I the as-prepared sample, and (b) for II the calcined sample.

The ^{31}P MAS NMR spectrum of material I is shown in figure 3. Concentrated aqueous phosphoric acid was used as the phosphorus reference. The phosphorus in the surfactant dodecylphosphate showed no shift relative to phosphoric acid. Figure 3 shows two peaks for Material I at about 0 and –10 ppm; the latter suggests one OH on the phosphorus. While Material II showed no peaks even after running over night. Additional data is being obtained on material II as well as on the vanadium nuclei.

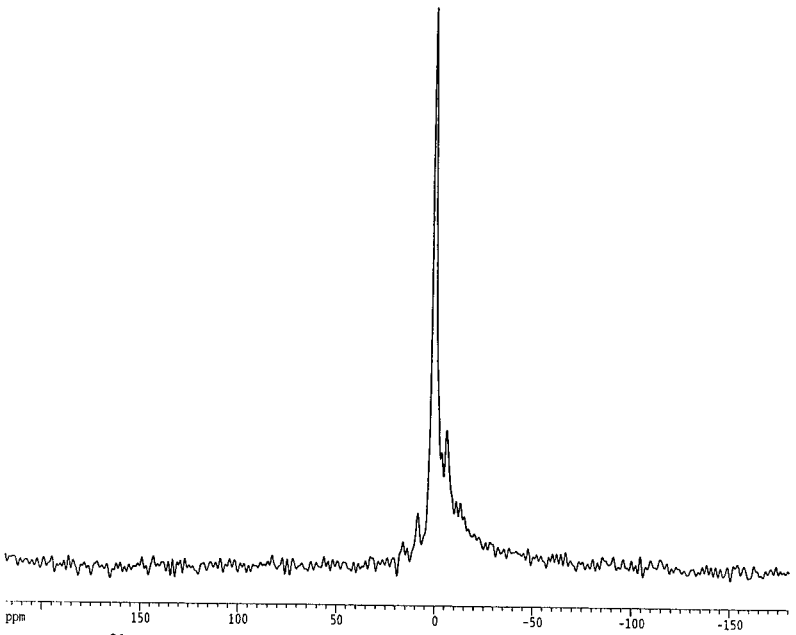


Figure 3. The ^{31}P MAS NMR spectrum of Material I, suggesting two phosphorus sites.

CONCLUSIONS

From the data Material I is a bilayer of surfactant molecules aligned with their hydrophobic hydrocarbon 'tails' together, and their phosphate 'heads' sticking out and bonded to or in a layer of vanadium oxide giving a 40Å interlayer distance. The TGA is consistent with the empirical formula of $VO_2PO_3(OH)C_{12}H_{25}$ $2H_2O$. Interestingly when Material I is heated in air to 400°C the compound undergoes a phase change. At this temperature the hydrocarbon portion of the surfactant has combusted with only the phosphate remaining with the vanadium oxide. Phosphates are tetrahedra which may have an oxygen bonded to a proton. The ^{31}P MAS NMR of Material I is not very clear but the signal at –10ppm can be interpreted as one proton being on the phosphate. As for Material II the V to P ratio should still be 1 to 1 from the molar ratio of reagents, the chemistry and TGA. But now the structure has changed to what looks like a hexagonal phase with a=43 Å; 37Å (100) and 22Å (110). More evidence is needed for the elucidation of the unit cell for both materials. Further NMR experiments and additional elemental analysis will help determine the structure.

ACKNOWLEDGEMENTS

We gratefully acknowledge the National Science Foundation for support of this work through grant DMR-9810198.

REFERENCES

1. J. S. Beck, J. C. Vartuli, W. J. Roth, M. E. Leonowicz, C. T. Kresge, K. D. Schmitt, C. T.-W. Chu, D. H. Olson, E. W. Sheppard, S. B. McCullen, J. B. Higgins, and J. L. Schlenker, J. Amer. Chem. Soc., **114,** 10834 (1992).
2. J. S. Beck, J. C. Vartuli, G. J. Kennedy, C. T. Kresge, W. J. Roth, and S. E. Schramm, Chem. Mater., **6,** 1816 (1994).
3. Q. S. Huo, D. I. Margolese, U. Ciesla, P. Feng, T. E. Gier, P. Sieger, R. Leon, P. M. Petroff, F. Schuff, and G. D. Stucky, Nature, **368,** 317 (1994).
4. Q. Huo, D. I. Margolese, U. Ciesla, D. G. Demuth, G. D. Stucky, and etal, Chem. Mater., **6,** 1176 (1994).
5. P. Y. Zavalij and M. S. Whittingham, Acta Cryst., **B55,** 627 (1999).
6. T. A. Chirayil, P. Y. Zavalij, and M. S. Whittingham, Chem. Mater., **10,** 2629 (1998).
7. G. G. Janauer, A. Dobley, J. Guo, P. Zavalij, and M. S. Whittingham, Chem Mater, **8,** 2096 (1996).
8. G. G. Janauer, R. Chen, A. D. Dobley, P. Y. Zavalij, and M. S. Whittingham, Mater. Res. Soc. Proc., **457,** 533 (1997).
9. G. G. Janauer, P. Y. Zavalij, and M. S. Whittingham, Chem. Mater., **9,** 647 (1997).
10. D. M. Antonelli and J. Y. Ying, Angew. Chem. Int. Ed. Engl., **34,** 2014 (1995).
11. E. P. Turevskaya and N. Y. Turova, Koord. Khim., **15,** 373 (1989).

VANADIUM OXIDE NANOTUBES WITH DIAMINE TEMPLATES

F. KRUMEICH, H.-J. MUHR, M. NIEDERBERGER, F. BIERI, M. REINOSO, R. NESPER
Laboratory of Inorganic Chemistry, ETH Zürich, CH-8092 Zürich, Switzerland

ABSTRACT

Diamine vanadium oxide nanotubes (DA-VO_x-NTs) have been prepared in high yields applying two different synthesis routes, namely either a sol-gel reaction followed by a hydrothermal treatment or an exchange reaction. The first route is analogous to the well-known preparation of VO_x-NTs containing monoamines: a vanadium(V) alkoxide is mixed with an α,ω-diamine ($H_2N[CH_2]_nNH_2$ with $12 \leq n \leq 20$), the resulting adduct is hydrolyzed, and, after aging, a hydrothermal treatment leads to the nanotubes in pure form. The exchange of the monoamine template in VO_x-NTs against diamines represents an alternative access to DA-VO_x-NTs. This reaction occurs readily and is also applicable for diamines with short CH_2 chains like, e.g., in ethylene diamine. The TEM characterization of the DA-VO_x-NTs confirms the tubular morphology which is widely preserved in the products of the exchange reactions. The characteristic feature of as-synthesized DA-VO_x-NTs is a thick tube wall with many VO_x layers while the exchange products are tubes comprising thin walls or bent packs of layers.

INTRODUCTION

The recently discovered vanadium oxide nanotubes (VO_x-NTs) [1-4] represent a further example for nano phases crystallizing with a tubular morphology [5] and, moreover, contribute to the multitude of vanadium oxide derivatives [6,7]. This novel vanadate with mixed valency (V^{4+}/V^{5+}) has been obtained as the main product of a sol-gel reaction followed by hydrothermal treatment from vanadium(V) precursors and primary monoamines ($C_nH_{2n+1}NH_2$ with $4 \leq n \leq 22$). In the course of the synthesis, which provides an easy access to large quantities of this material, the amines act as structure-directing templates. Furthermore, α,ω-diamines ($H_2N[CH_2]_nNH_2$ with $12 \leq n \leq 20$) are also applicable as templates [4]. In this contribution, we present an alternative synthesis route for diamine-containing nanotubes and discuss the structural properties in comparison.

EXPERIMENT

Synthesis

A solution of vanadium(V) triisopropoxide and a template (molar ratio of 2:1) in absolute ethanol was stirred under inert atmosphere for 1 hour. Primary monoamines ($C_nH_{2n+1}NH_2$ with $4 \leq n \leq 22$) or α,ω–diamines ($H_2N[CH_2]_nNH_2$ with $12 \leq n \leq 20$) can be used. The resulting yellow solution of the alkoxide-amine adduct was hydrolized with water under vigorous stirring, and, after aging (12-96 h), a vanadium oxide-surfactant composite was obtained. The hydrothermal reaction of this composite in an autoclave (180°C; 7 d) yielded a black product. After washing with ethanol and hexane, the product is phase-pure, consisting of tubes only.

The exchange reactions were performed by stirring a suspension of monoamine tubes (about 100 mg) in 25 ml ethanol with an excess of the exchanging diamine $H_2N[CH_2]_nNH_2$ with n = 2,

Mat. Res. Soc. Symp. Proc. Vol. 581 © 2000 Materials Research Society

Table I: Exchange Reactions. The inter-layer distances (XRD data) of as-synthesized monoamine VO_x-NTs before exchange and of diamine VO_x-NTs after exchange with α,ω-diamines are listed. The composition of some exchange products, as determined by elemental analysis, are also given and compared to that of the monoamine C_{12}-VO_x-NTs (see text).

As-synthesized monoamine C_n-VO_x-NTs		Diamine exchanged VO_x-NTs: C_n-DA-VO_x-NTs		
$C_nH_{2n+1}NH_2$ n	Distance [nm]	$H_2NC_nH_{2n}NH_2$ n	Composition	Distance [nm]
4	1.66	2	-	1.58
6	2.00	2	-	1.3
11	2.62	2	-	1.62
16	3.35	2	-	1.5
16	3.35	6	-	1.52
6	2.00	12	-	1.84
11	2.62	12	-	1.83
16	3.35	12	-	1.86
8	2.24	20	-	3.1
12	2.60	2	$VO_{2.40}[C_2H_{10}N_2]_{0.27}$	1.55
12	2.60	6	$VO_{2.40}[C_6H_{18}N_2]_{0.17}$	1.4
12	2.60	12	$VO_{2.40}[C_{12}H_{30}N_2]_{0.18}$	1.9
12	2.60	14	$VO_{2.40}[C_{14}H_{34}N_2]_{0.21}$	2.6
12	2.60		$VO_{2.40}[C_{12}H_{28}N]_{0.27}$	

6, 12, 14, or 20 (about 2/3 mol equivalent with respect to the amount of monoamine in the tubes) for 12-24 hours at room temperature (Table I).

Structural Characterization

X-ray powder diffraction (XRD) diagrams were measured in the transmission mode on a STOE STADI-P2 diffractometer ($CuK\alpha_1$ radiation). Transmission Electron Microscopy (TEM) investigations were performed on a CM30ST microscope (Philips; LaB_6 cathode, operated at 300 kV). For the investigation of the longitudinal shape and structure, the nanotube material was deposited onto a perforated carbon foil supported on a copper grid. In order to observe the structure perpendicular to the tube axis, a cross-sectional preparation technique was applied as described elsewhere [4].

RESULTS

As-synthesized DA-VO_x-NTs

The product of the final hydrothermal treatment consists almost exclusively of nanotubes as revealed in TEM images. The tube length is up to 10 μm. The tube ends are usually open (Figure 1a). Like in the case of monoamine-containing VO_x-NTs [4], the tube walls are built up of crystalline vanadium oxide layers with the template embedded in between. These VO_x layers appear as dark lines in the TEM images (Figure 1). The intercalation of the template molecules

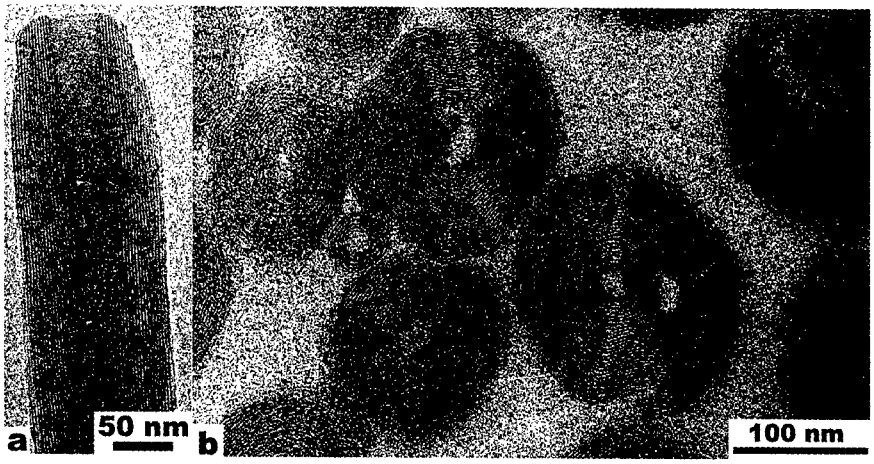


Figure 1. TEM images of as-synthesized C_{20}-DA-VO_x-NTs. (a) A nanotube with an open end in longitudinal projection. (b) Cross-sectional view. A small tube consisting of four concentric layers is present besides multi-layered scrolls with large diameters.

between the VO_x layers is evident from the increase of the inter-layer distance with increasing CH_2 chain length: e.g., C_{12}-DA-VO_x-NTs: 1.91 nm and C_{20}-DA-VO_x-NTs: 2.9 nm (XRD results).

The outer diameters of the DA-VO_x-NTs, typically ranging from 100 to 150 nm (Figure 1), are larger than those of monoamine VO_x-NTs. Their comparatively thick walls generally comprise 10-30 VO_x layers. Cross-sectional TEM investigations of C_{20}-DA-VO_x-NTs clearly reveal that by far most of the tubes are formed by serpentine-like scrolls of VO_x layers (Figure 1b). Interestingly, there are packs of about five scrolled VO_x layers while in the case of monoamine tubes mostly single- or double-layered scrolls have been observed [4]. Concentric tubular arrangement of layers like in carbon nanotubes are rarely present. An example of such an ideal tube comprising four closed concentric VO_x layers can be seen in Figure 1b.

Exchange Reactions

The treatment of VO_x-NTs with an excess of alkyl diamines leads to an easy and fast exchange of the intercalated monoamine templates against diamine molecules. TEM images (Figure 2) demonstrate that the tubular morphology has been widely preserved during this reaction. The obtained tubes have a well-ordered layer structure, and the inter-layer distances are uniform throughout the tube length (Figure 2a). In average, the inner diameters of these tubes are larger and the numbers of layers inside the walls are lower than in the case of as-synthesized DA-VO_x-NTs. On the other hand, it becomes evident from cross-sectional TEM images (Figure 2b), that only a part of the tubes appears as intact scrolls. Frequently, there are bent packs of ~3-7 VO_x layers which sometimes occur as half open circles. However, all arrays exhibit a well-ordered arrangement of parallel VO_x layers, and the tube walls are without those distortions that are frequently observed in VO_x-NTs with monoamines as templates [4]. This characteristic indicates a stiffening of the layer structure in the tube walls by the diamine.

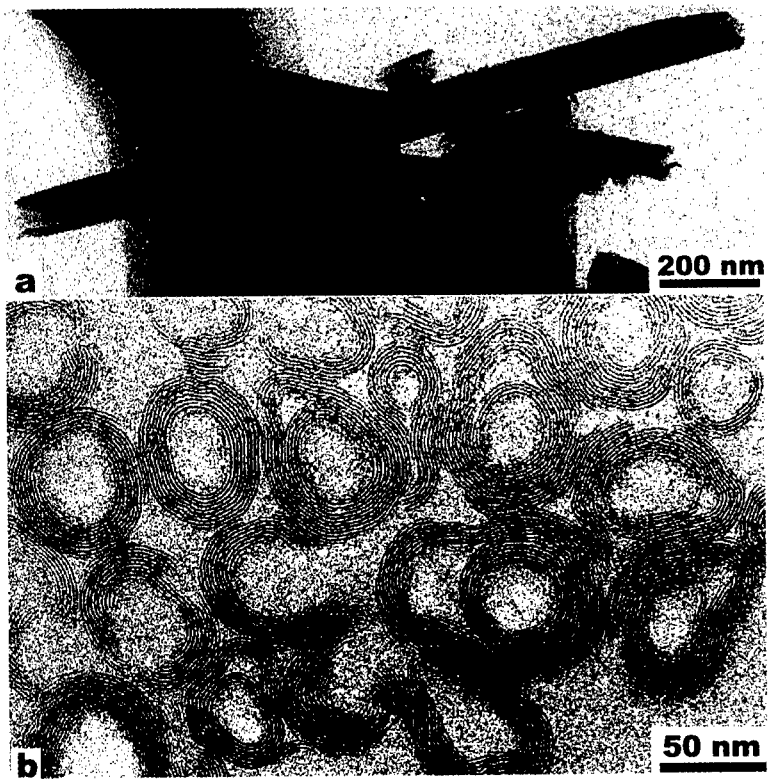


Figure 2. TEM images of exchange products. (a) C_2-DA-VO_x-NTs, obtained from C_{11}-VO_x-NTs. A ~1.5 mm long tube is present which has an outer diameter of ~100 nm and a relatively large inner core of ~50 nm. (b) C_{12}-DA-VO_x-NTs, obtained from C_{11}-VO_x-NTs. Two almost perfect scrolls can be seen on the upper left side. Bent packs of layers occur frequently.

Figure 3 shows the XRD patterns of as-synthesized C_{12}-VO_x-NTs and of C_2-DA-VO_x-NTs obtained by a template exchange reaction. Two independent sets of reflections appear in both diffractograms: the reflections indexed with 00l are caused by the regular distance between the nearly parallel VO_x layers while the reflections hk0 are generated by the structure of the crystalline VO_x layers. This indicates the presence of a two-dimensional square lattice with $a \approx 0.61$ nm. The positions of the reflections hk0 are the same for both tube types, the starting monoamine C_{12}-VO_x-NTs as well as the resulting C_2-DA-VO_x-NTs. In fact, the positions of these reflections are independent of the template size and the actually applied preparation procedure [4]. This gives unambiguous evidence that the VO_x layers always have the same structure. In contrast to that, the reflections 00l change with the length of the alkyl chain of the template, and they accordingly shift during the exchange reaction. In the course of the exchange reaction of C_{12}-VO_x-NTs with ethylene diamine, the inter-layer distance shrinks from 2.6 nm to 1.6 nm (Figure 3). On the other hand, substituting octylamine in C_8-VO_x-NTs by 1,20-eicosandiamine leads to a widening of the layers, i.e., the distance increases from 2.24 nm to 3.1

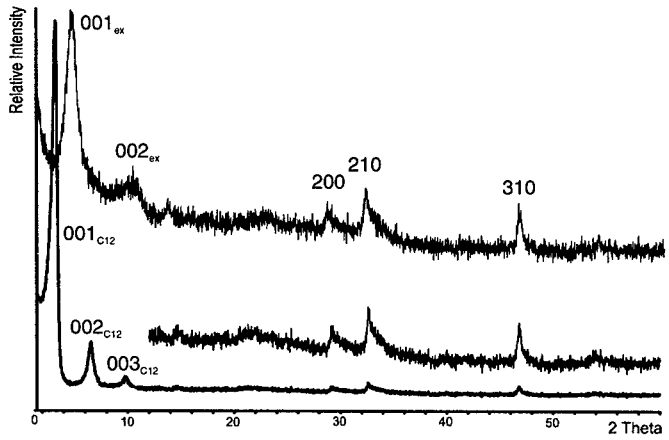


Figure 3. XRD patterns of C_{12}-VO_x-NTs (below) and of C_2-DA-VO_x-NTs (above). The C_2-DA-VO_x-NTs have been obtained from C_{12}-VO_x-NTs by a substitution of the monoamine by ethylene diamine. An enlargement of the region in the diffractogram of C_{12}-VO_x-NTs which contains the characteristic reflections hk0 is shown as well. In contrast to the stationary reflections hk0, the reflections 00l of the C_{12}-VO_x-NTs ($00l_{C12}$) are shifted in respect to those of C_2-DA-VO_x-NTs ($00l_{ex}$).

nm. Generally, a shrinkage as well as a widening of the inter-layer distance can be achieved by an appropriate selection of the size of the monoamine and of the exchanging diamine (cf. Table I).

The exchange of the intercalated monoamines by diamines occurs readily and fast even at room temperature. This indicates that the DA-VO_x-NTs are thermodynamically favored and represent a more stable arrangement compared to monoamine tubes. This assumption is further supported by the irreversibility of these exchange reactions. In a simple model (Figure 4), the monoamine molecule is embedded in a paraffin-like arrangement between the VO_x layers. According to XPS results [4], the NH_2 group is protonated. This positive charge counterbalances the negative one of the VO_x layers. Most likely, this proton is transferred in the first reaction step from the intercalated monoamine to the diamine which subsequently substitutes the monoamine. The importance of this proton exchange is demonstrated by the fact that less basic diamines (e.g., benzidine) cannot substitute the monoamine. Since bulky diamines (e.g., α,α'-diamino-p-xylene) do neither, steric effects seem to be important, too.

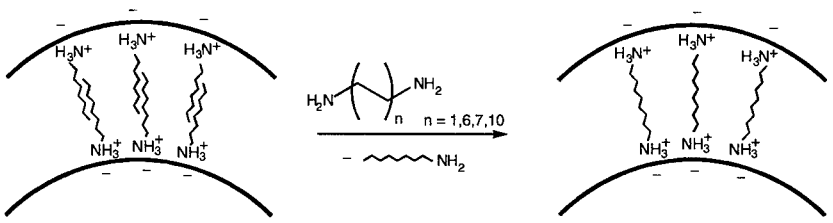


Figure 4. Schematic representation of the exchange of two amine molecules by a diamine molecule.

The determination of the compositions of the exchange products (Table I) exemplifies that approximately one diamine molecule substitutes two monoamine molecules. This creates an increase of entropy which contributes to the driving force of the exchange reaction. The molar ratio amine/V decreases considerably from amine/V = 0.27 for the starting monoamine C_{12}-VO_x-NTs to 0.17-0.21 for C_n-DA-VO_x-NTs (n=6,12,14). The exchange by ethylene diamine is exceptional since this ratio stays almost constant (Table I). Furthermore, the inter-layer distance is much too large if a monolayer of ethylene diamine molecule is present between the layers. Therefore, a double layer has to be considered.

CONCLUSIONS

The two independent routes to DA-VO_x-NTs allow us to control the tube properties to some extend: DA-VO_x-NTs synthesized on the conventional route by a reaction of vanadium(V) precursors with diamines are characterized by thick walls with many VO_x layers and by narrow cores. On the other hand, the exchange products resemble more or less the as-synthesized monoamine VO_x-NTs, and they typically have thin walls and wide tube cores. Remarkably, the exchange reactions with ethylene diamine or other small diamines lead to DA-VO_x-NTs that could not been obtained by the alternative route until now and consequently extends the area of existence for diamine-containing tubes. The scroll-like structure of the VO_x-NTs appears to be highly flexible, and it promotes the feasibility of exchange reactions without a destruction of the tubular morphology.

ACKNOWLEDGMENTS

This work is being generously supported by the ETH Zürich (TEMA-grant). We thank the group of Prof. Günther (ETH Zürich) for elemental analyses and Dr. Schnyder and Dr. Kötz (PSI Villingen) for XPS measurements.

REFERENCES

1. R. Nesper, M.E. Spahr, M. Niederberger, and P. Bitterli, Int. Patent Appl. PCT/CH97/00470, Bundesamt für Geistiges Eigentum, Bern 1997.

2. M.E. Spahr, P. Bitterli, R. Nesper, M. Müller, F. Krumeich, and H.-U. Nissen, Angew. Chem. Int. Ed. **37**, 1263-1265 (1998).

3. R. Nesper, H.-J. Muhr, Chimia **52,** 571-578 (1998).

4. F. Krumeich, H.-J. Muhr, M. Niederberger, F. Bieri, B. Schnyder, and R. Nesper, J. Am. Chem. Soc. **121,** 8324-8331 (1999).

5. W. Tremel, Angew. Chem. Int. Ed. **38,** 2175-2179 (1999).

6. T. Chirayil, P.Y. Zavalij, and M.S. Wittingham, Chem Mater. **10,** 2629-2640 (1998).

7. P.Y. Zavalij and M.S. Wittingham, Acta Crystallogr. B**55,** 627-663 (1999).

A NANO-COMPOSITE POLY(METHYL-METHACRYLATE) BONE CEMENT

Andreas H. Gomoll[‡], Anuj Bellare[‡], Wolfgang Fitz[‡], Thomas S. Thornhill[‡], Richard D. Scott[‡]
Peter R. Jemian[#], Gabrielle G. Long[*]

[‡] Orthopaedic Research Laboratory, Department of Orthopaedic Surgery, Brigham and Women's Hospital, Harvard Medical School, Boston, agomoll@rics.bwh.harvard.edu
[#] University of Illinois, Urbana-Champaign, IL
[*] National Institute of Standards and Technology, Gaithersburg, MD

ABSTRACT

Poly(methyl methacrylate) (PMMA) based orthopaedic bone cements contain 1-3 μm size radiopacifier particles. Incomplete dispersion of these particles leads to the presence of 50-200 μm size agglomerates. These large defects are sites of high-stress concentration that reduce the fracture toughness of PMMA. In this study, the micrometer-sized radiopacifying particles of a commercial bone cement were replaced by nanosized fillers. Both, commercial and nanocomposite PMMA bone cements were characterized using ultra-small angle x-ray scattering and low voltage scanning electron microscopy; mechanical properties were evaluated using ASTM standard tensile testing. The results showed a substantial reduction of particle agglomerate size and a significant increase in tensile properties of the nanocomposite over that of the standard microcomposite bone cement.

INTRODUCTION

Poly (methyl methacrylate) (PMMA) based bone cement is widely used for the fixation of orthopaedic implants. These cements contain 1-3 μm size filler particles of either barium sulfate or ceramic particles such as zirconium oxide. The purpose of adding fillers is to radiopacify the cement, thereby enabling the orthopaedic surgeon to monitor the cement using radiographs. A problem associated with the use of 1-3 μm diameter radiopacifier particles is that incomplete dispersion of the particles during mixing of the monomer and powder components results in the formation of particle agglomerates of 50-200 μm diameter. These large defects are sites of high stress concentration that reduce the fracture toughness of PMMA cements, leading to early fracture of the cement [1, 2] and loosening of the implant, ultimately necessitating early revision surgery to replace the implant. Previous studies have investigated this mechanism of failure by demonstrating a two-fold decrease in impact strength of bone cement with the addition of micro-meter size radiopacifying particles [3].

In this study, the micrometer size radiopacifying particles in PMMA bone cements were replaced by commercially available nanophase aluminum oxide particles. These nanocomposite PMMA bone cements were thereafter characterized using ultra-small angle x-ray scattering (USAXS) at the UNICAT beamline of the Advanced Photon Source, Argonne National Laboratory. Low-voltage scanning electron microscopy (LVSEM) was performed on the fracture surfaces of tensile specimens and on both micro- and nano-sized filler particles. These experiments provided the average inter-particle or inter-agglomerate distance between adjacent radiopacifier particles present in the cured cements. The nanocomposite and control PMMA bone cements were also subjected to ASTM standard tensile tests to determine their mechanical properties.

Mat. Res. Soc. Symp. Proc. Vol. 581 © 2000 Materials Research Society

EXPERIMENT

Specimen composition and preparation

Commercially available PMMA bone cement used in orthopaedic surgery is commonly provided as a two component system; a powder component consisting of pre-polymerized PMMA, radiopacifying particles (Barium Sulfate or Zirconium Oxide, 10 wt.%) and Benzoyl Peroxide (BPO, 2 wt.%) as initiator; and a liquid component consisting of Methyl-Methacrylate (MMA) monomer, Hydroquinone (25 ppm) as stabilizer and N,N-Dimethyl-p-toluidine (DMPT, 2 wt.%) as reaction promoter. Both components are mixed, commonly in a vacuum mixing device to reduce air introduction, initiating a polymerization process with an average setting time of 10-15 min.

For the experiment, Osteobond™ [‡] (Zimmer Inc, Warsaw, IN) bone cement containing $BaSO_4$ radiopacifying particles of 1-3 μm diameter was purchased as control. A separate PMMA powder component without radiopacifiers (Zimmer Inc, Warsaw, IN) was used for the nano-composites. Acrylic-coated aluminum oxide particles of 60 nm average diameter dispersed in ethanol were purchased (Nanophase Technologies Inc, Burr Ridge, IL). The particles were dried, re-dispersed in MMA, and mixed with PMMA for a final volume fraction of filler particles identical to that of radiopaque cements.

Specimens for USAXS were molded as thin sheets of 0.5 mm thickness, while tensile testing utilized Type V dumbbell shaped samples as specified in ASTM D638-97 [4].

Mechanical Testing

An Instron 4201 tensile tester was used to perform ASTM D638-97 standard tensile tests on all cement samples to determine their ultimate stress, ultimate strain and work-of-fracture (defined by the area under the stress-strain curve). Testing was performed at a crosshead-speed of 1 mm/s using a 5 kN load-cell. A minimum of 4 specimens were tested for each cement composition as required by ASTM standards. Means and standard errors were calculated for all parameters; a Fisher test was performed for analysis of variance and the unpaired Student's t-test for equal or unequal variances was chosen accordingly to test for statistical significance.

Morphological Investigations

A JEOL 6320FV low voltage scanning electron microscope (LVHRSEM) operating at 1 kV and a working distance of 3 mm was used to examine each type of radiopacifier particles and freeze-fractured samples of the cured cements. Cements were also subjected to ultra-small angle x-ray scattering (USAXS) at the UNICAT beamline of the Advanced Photon Source, Argonne National Laboratory. The available range of the scattering vector, $q = (4\pi/\lambda)\sin\theta$, was 0.00016 - 0.1 $Å^{-1}$, where $\lambda = 1.299$ Å was the synchrotron x-ray wavelength used and θ is one-half the scattering angle. The x-ray source was collimated using slits to produce a square beam size of 2 mm x 2 mm. The detector (scintillation counter with 5 mm x 5 mm window) also contributed to smearing effects.

RESULTS

Mechanical Testing

Statistical analysis revealed significant increases in work-of-fracture (WOF), elongation-to-break (ETB) and ultimate-tensile-stress (UTS) ($p<0.05$ each) when nano-composite samples were compared to the control (Figure 1). The reduction in particle size increased the means of work-of-fracture by 74 %, elongation-to-break by 35 % and ultimate-tensile-stress by 25%.

‡ The use of commercial designations or company names is for identification only and does not indicate endorsement by the National Institute of Standards and Technology.

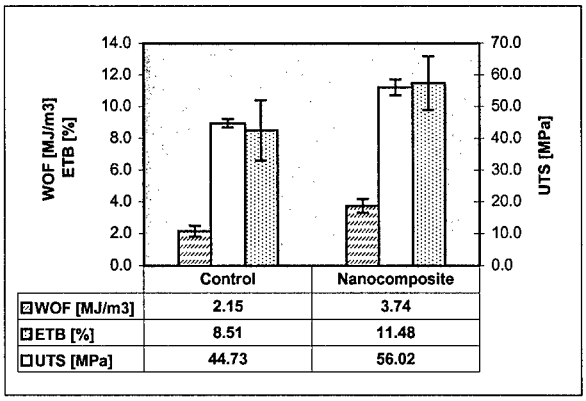


Figure 1: Comparison of Work-of-Fracture (WOF), Elongation-to-Break (ETB) and Ultimate-Tensile-Stress (UTS) for control and nano-composite bone cement. (mean±standard error)

Morphological Investigations

USAXS experiments performed on cements filled with barium sulfate showed substantially higher scattering intensity at ultra-low angles compared to that of the alumina filled cements (Figure 2). In both cases, the scattering curves were broad and sharp peaks were absent. This indicates that there was a large polydispersity in size and spacing of the scatterers, i.e. that there was a large variation in particle agglomerate size and inter-agglomerate spacing. This was in agreement with the LVHRSEM observations. In the case of the nanocomposite, the USAXS curve showed an increase in intensity in the ultra-low angular region, suggesting that there was an additional source of scattering at higher length scales, beyond the resolution of USAXS. The source of scattering at such high length scales is probably the PMMA powder particles against the regions to which the alumina filler is confined (see Figure 5a). Since the powder particles are on the order of 20-40 μm, the scattering peak is beyond the resolution of USAXS. The inter-agglomerate distance estimated using Bragg's law (see Eq. 1) was larger than 5 μm for barium sulfate agglomerates while the inter-agglomerate distance was approximately 0.2-0.1 μm for precoated alumina agglomerates.

$$n\lambda = 2d \sin\theta \qquad (1)$$

for: d=inter-agglomerate distance, λ = wavelength, θ = scattering angle.

Morphological analyses of barium sulfate particles using LVHRSEM showed that barium sulfate particles were of 0.5-3 μm size and were of various shapes (Fig. 3). A majority of the alumina nanoparticles were less than 0.2 μm in size, and were predominantly spherical in shape (Fig. 4). Investigation of freeze-fractured samples containing micro-sized fillers revealed agglomerates of 30-70 μm (Figure 5a and 5b), while nano-composites showed no agglomerates larger than 1 μm in size (Figure 6a and 6b).

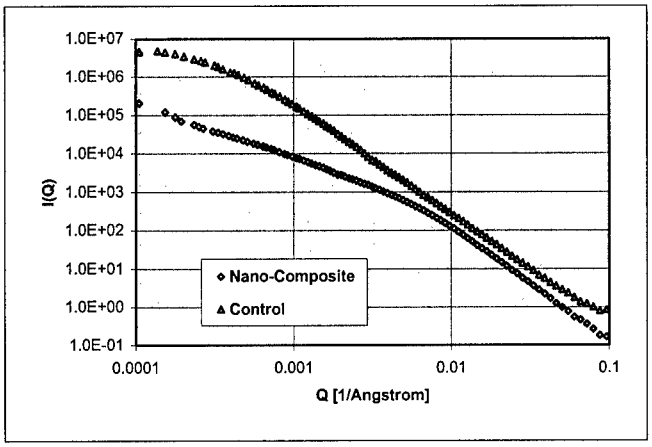


Figure 2: USAXS scattering intensities for nano-composite and control samples.

DISCUSSION

The results of this study demonstrate that a reduction in size of particle agglomerates by reduction in particle size and by precoating of particles increases the ultimate tensile properties of PMMA bone cement. LVHRSEM and USAXS confirmed that particle agglomerates were drastically reduced in size when precoated 200 nm size (60 nm alumina particles with 70 nm acrylic coating) alumina particles were used as a filler. While LVHRSEM provided images to confirm particle size, USAXS was particularly useful in providing more quantitative measurement of morphological parameters such as inter-agglomerate distance. USAXS has distinct advantages over conventional SAXS in that the angular range of scattered synchrotron x-rays enables the morphology to be quantitatively characterized over a large range of length scales, from approximately 4 micrometer down to 2 nanometer. Since the source of scattering was agglomerated particles against the PMMA matrix, higher scattering intensity at ultra-low angles indicated that the inter-agglomerate distance was larger for barium sulfate cements. A larger inter-agglomerate distance implies a larger agglomerate size since all cements contained the same volume fraction of fillers. Therefore, the precoated nanophase fillers mixed into PMMA cements resulted in agglomerates of smaller size than barium sulfate agglomerates. Mechanical tests revealed that tensile properties were strongly affected by a reduction in particle size.

In conclusion, surface treated nanophase filler particles showed significant increases in tensile properties of PMMA cement due to prevention of the formation of large size particle agglomerates. These results are in agreement with a previous study [5], suggesting that uniform dispersion of micrometer-size radiopacifier particles in current acrylic bone cements can improve the mechanical performance of PMMA cements.

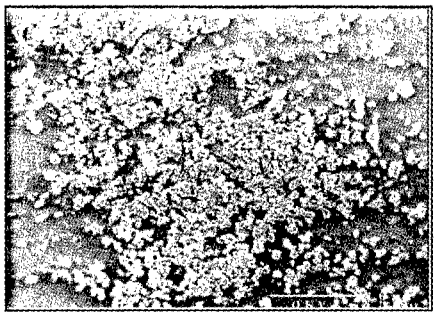


Figure 3: $BaSO_4$ radiopacifying particles as used in commercial bone cements (SEM, bar denotes 10 µm)

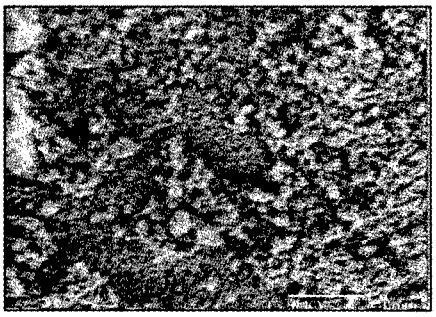


Figure 4: Aluminum oxide nanoparticles used in the nanocomposite cement (SEM, bar denotes 1 µm)

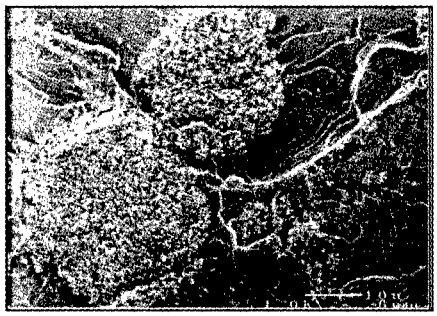


Figure 5a: Agglomerated $BaSO_4$ particles in control cement (SEM, bar denotes 10 µm)

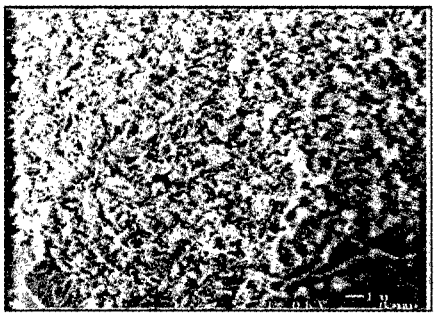


Figure 5b: Detail of agglomerated $BaSO_4$ particles (SEM, bar denotes 1 µm)

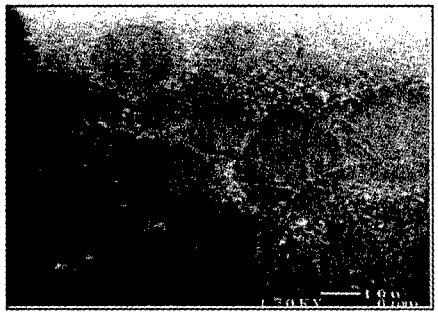


Figure 6a: Nanocomposite cement. Dark round shapes are pre-polymerized PMMA particles. (SEM, bar denotes 10 µm)

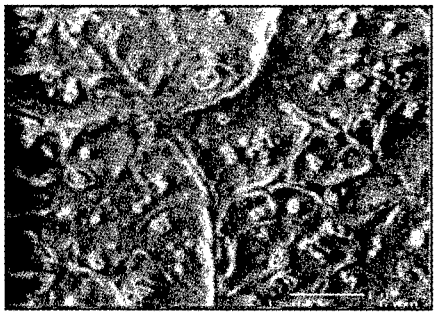


Figure 6b: Nanocomposite cement in detail. Dispersed filler particles between fracture lines (SEM, bar denotes 1 µm)

ACKNOWLEDGMENTS

This study was supported by the Brigham Orthopaedic Foundation.
The UNICAT facility at the Advanced Photon Source (APS) is supported by the University of Illinois at Urbana-Champaign, Materials Research Laboratory (U.S. Department of Energy (DoE), the State of Illinois-IBHE-HECA, and the National Science Foundation), the Oak Ridge National Laboratory (U.S. DoE), the National Institute of Standards and Technology (U.S. Department of Commerce) and UOP LLC. The APS is supported by the U.S. DoE, BES, Office of Energy Research under Contract No. W-31-109-ENG-38.

REFERENCES

1. H.W. Demian, K. McDermott, Biomaterials **19**, pp. 1607-1618 (1998)
2. G. Lewis, J., Biomed. Mater. Res. **38**, pp. 155-182 (1997)
3. J.R. de Wijn et al., Acta. Orthop. Scand. **46**, p. 38 (1975)
4. ASTM. Specification D638-97 (1997)
5. H.W. Demian, A.C. Wey, S.W. Shalaby, Trans Soc Biomat, p. 368 (1995)

ELECTROLUMINESCENCE DEVICES WITH CdS AND CdS:Mn NANOPARTICLES AND POLYMER BLENDS

Ch. Brugger[1], S. Tasch[1], M. Lal[2], P.N. Prasad[2], G. Leising[1]
[1] Institut fuer Festkoerperphysik, Technische Universitaet Graz, Austria
[2] Photonics Research Laboratory, State University of New York at Buffalo, Buffalo, NY

ABSTRACT

We have investigated the photophysical properties of surface capped CdS and CdS:Mn nanoparticles in the form of spin coated thin films of the pure nanoparticles and nanoparticle – polymer blends. The organic capping reagent was p-thiocresol.
Electroluminescence (EL) devices were fabricated and characterized by their current/voltage characteristics and EL emission performance. This is to our knowledge the first report on Mn doped CdS nanoparticles applied in EL devices with a single layer device structure (ITO/CdS:Mn/Al). Photoluminescence (PL) and PL excitation measurements were performed on CdS:Mn nanoparticles in pyridine dispersion and on thin films. The PL excitation spectrum shows a narrow peak at 390nm. Excitation at this wavelength yields a broad PL spectrum spanning from about 450 to 700nm, which is dominated by a strong emission band at 585nm. This emission is attributed to transitions involving Mn levels in previous works.
The EL emission peak is shifted to the red compared to the PL emission spectra. The characteristics and performance of these new types of EL devices will be presented and discussed.

INTRODUCTION

The photophysical properties of semiconductor nanocrystals have been in the focus of scientific interest during the past decade. Typically, the size of these crystallites is in the range from 1 to 100nm. In this size regime, quantum effects determine the physical properties and semiconducting nanocrystals have been the first real examples for quantum dots [1,2]. The possibility of tuning the bandgap of nanostructured materials makes them extremely attractive for applications in optoelectronic devices like light emitting diodes (LED) or solar cells [3-6]. Another approach to influence the optical properties of semiconducting materials is doping, which has been utilized in optoelectronics for many years. However, by now there is relatively little work on doped nanocrystals [7-10]. One of the most intensively studied aspects is the influence of the surface on the absorption and emission of nanosize particles, since a considerable fraction of atoms forming the crystallites is located at the surface. Consequently, the passivation of surface lone pairs by chemical encapsulation in an organic or inorganic shell is a major task in this field. Up to now, a variety of methods has been reported. Additionally, organic surface ligands offer the possibility of effectively dispersing nanocrystalline powders in appropriate solvents. As a consequence, organic/inorganic composite devices can be fabricated relatively easily and there already exists a large number of publications on such hybrid materials [11-15].

EXPERIMENTS

The synthesis of the CdS and CdS:Mn nanocrystals used in this work is based on the method reported by Wang et al. [15,16]. In the initiation phase of the synthesis, a solution containing cadmium ions generated from cadmium acetate is introduced into a solution containing S^{2-} and RS^- in the form of sodium sulfide and p-thiocresol. Crystal growth competes with the growth-

Mat. Res. Soc. Symp. Proc. Vol. 581 © 2000 Materials Research Society

terminating reaction of the thiolate with the particle surface. As a consequence, size control is possible by choosing an appropriate ratio of sulfur-ions S^{2-} and RS^-, or, in the present case, the molar ratio of sulfide and p-thiocresol (S:SH). In case of CdS:Mn nanocrystals, manganese is introduced as manganese acetate, which is mixed with cadmium acetate.
Photoluminescence and electroluminescence spectra were taken with a Shimadzu RF 5301 spectrofluorophotometer or with a glass fiber waveguide connected to an Oriel Instaspec CCD spectrometer. PL spectra were recorded from dispersions of nanocrystals in pyridine, from thin nanogranular films and from powders. In the latter case, the powder was scattered on a black non-luminescent double stick tape.
Absorption spectra were taken with a Shimadzu UV-3101PC spectrophotometer from dispersions in pyridine using a 1cm quartz cuvette.
Electroluminescence devices were fabricated by spin casting a film of nanoparticles on a glass/ITO substrate from dispersion. Composite devices were made by separately preparing a solution of m-LPPP and a dispersion of nanocrystals and blending prior to spin coating. The back electrode (aluminum) was deposited at high vacuum (~10^{-6} mbar) from a tungsten boat. I/V characteristics were measured with a Keithley 236 Source/measure unit. The light output was detected simultaneously with an integrating sphere and a photodiode. The complete setup is controlled by a PC.
Short circuit photocurrent as a function of the wavelength of the incident light was measured with a setup comprising a xenon lamp, a monochromator, a light beam chopper, a lock-in amplifier and a controlling PC.

RESULTS

The result of photoluminescence studies on CdS nanocrystals is depicted in Fig. 1. These spectra were recorded from a powder. Here, the excitation wavelength was 386nm and the emission wavelength for the excitation spectrum was 534nm. The absorption spectrum of the same sample (S:SH=1:2) is also shown.

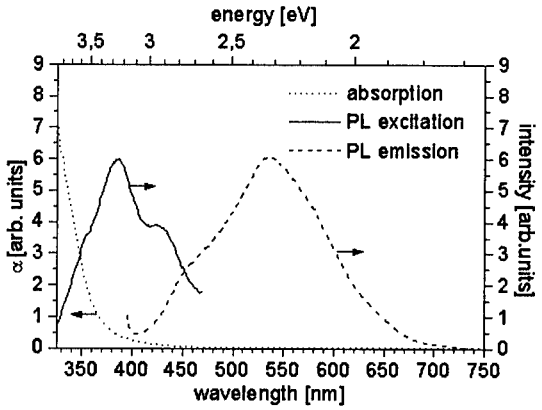


Fig. 1. Absorption-, PL excitation- and emission spectra of CdS nanoparticles (S:SH=1:2). The excitation wavelength was 386nm, the emission wavelength for the excitation spectrum was 534nm. Photoluminescence spectra were recorded from a powder, the absorption spectrum was measured on a dispersion of the same CdS nanoparticles in pyridine.

The emission spectrum is relatively broad and ranges from about 450nm to 650nm peaking at 534nm. Apart from the main peak, there is also a shoulder at about 480nm, indicating the presence of a second emission band. The excitation spectrum confirms this assumption, since a distinct second peak can be seen at 428nm. Excitation at this wavelength yields an emission spectrum, which is dominated by a peak at 480nm (not shown). So the emission spectrum mainly consists of two emission bands. Compared to the absorption and excitation spectra, there is a

considerable red-shift of the emission spectrum. No band to band luminescence is observed, but the emission is governed by deep trap states. We attribute these traps to surface states.

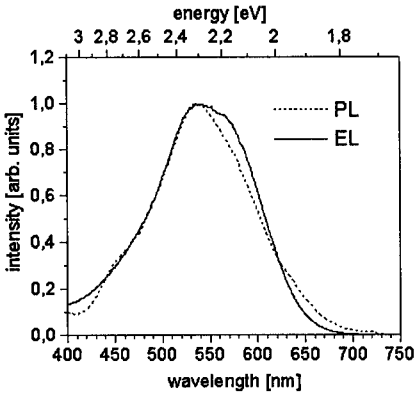


Fig. 2. Electroluminescence (EL) spectrum of a nano-CdS device. The bias voltage was 10V. For comparison, a photoluminescence (PL) spectrum recorded from the same CdS powder is also shown.

Electroluminescence devices have been fabricated with the same CdS powder, which had previously been used for photoluminescence measurements. DC bias in the range from 5–15V was applied. The electroluminescence spectrum along with a photoluminescence spectrum can be seen in Fig. 2. It should be noted that a considerable influence of the S:SH-ratio on the performance of electroluminescence devices was observed. The best results were achieved, if samples, which had been synthesized at a S:SH-ratio of 1:1 or 1:2, were used. More capping (e.g. 1:5) resulted in totally insulating layers. On the other hand, it is hardly possible to fabricate smooth nanocrystalline layers with less capped particles, since the S:SH-ratio significantly influences the solubility of the powder. In the present case, the ratio was 1:1. The electroluminescence spectrum ranges from about 450nm to 650nm and there is a peak at 535nm (Fig. 2). It perfectly matches with the photoluminescence spectrum. Apparently, the emission processes are the same for both, photo- and electroluminescence. These data are in good agreement with the results reported by Narayan et al. [6], who was working with significantly larger CdS nano-particles (~44Å) capped with 1-thioglycerol, which implies that the influence of the particle size on the emission properties of this kind of materials is relatively low.
Similar experiments were performed on manganese doped CdS nanocrystals. Fig. 3 shows PL spectra of CdS:Mn nanoparticles, recorded from a powder and a dispersion of the same powder in pyridine. The excitation wavelength for the emission spectra was 390nm, emission wavelength

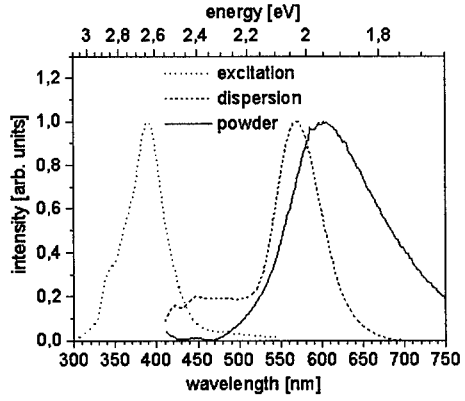


Fig. 3. Photoluminescence spectra of CdS:Mn nanocrystals recorded from a powder and a dispersion in pyridine, respectively. The excitation wavelength was 390nm. An excitation spectrum measured on the dispersion is also shown. The emission wavelength was 568nm.

for the excitation spectrum was 568nm. It can be seen that the PL excitation spectrum is essentially the same as for undoped CdS particles. Compared to undoped CdS nanocrystals, the spectrum is shifted to the red by about 50nm. The spectrum, which was recorded from a dispersion, has a maximum at 568nm. An emission band at this spectral position has previously been reported in CdS:Mn and ZnS:Mn nanocrystals and it was attributed to the internal Mn^{2+} transition $^4T_1 \rightarrow {}^6A_1$ [7]. But there is also a small contribution to the overall spectrum at 470nm. As mentioned above, this emission band was also observed for undoped samples.

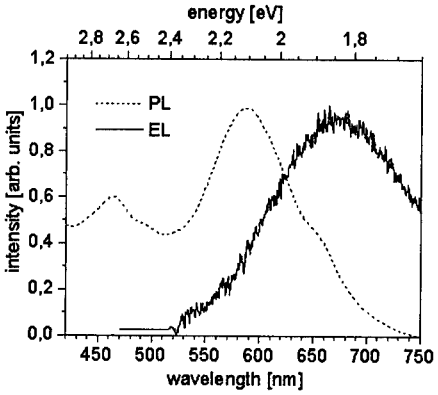


Fig. 4. EL spectrum of a CdS:Mn device. For comparison, a PL spectrum, measured on the same device, is also shown.

The powder spectrum, however, has a peak at 590nm, which indicates the presence of a second emission band at a higher wavelength, which is more pronounced for the powder spectrum. Electroluminescence experiments clearly confirm the presence of this second emission band. Moreover, the EL spectrum has a maximum at 665nm, as seen in Fig. 4. A photoluminescence spectrum recorded from the same EL device is also depicted. Again the excitation wavelength was 390nm. Note the small shoulder in the PL spectrum at about 660nm. Moreover, there is a considerable second peak at 470nm, similar to the dispersion-spectrum. Obviously, the red emission band at 665nm is more pronounced a) for closely packed particles than for particles dispersed in a solvent and b) for EL than for PL. Since no emission at this spectral position was found for undoped particles, it is evident that it is dopant-related. Furthermore, it is clear that the luminescence processes are totally different for PL and EL in CdS:Mn nanoparticles, as opposed to pure CdS crystallites, where the respective spectra are identical.

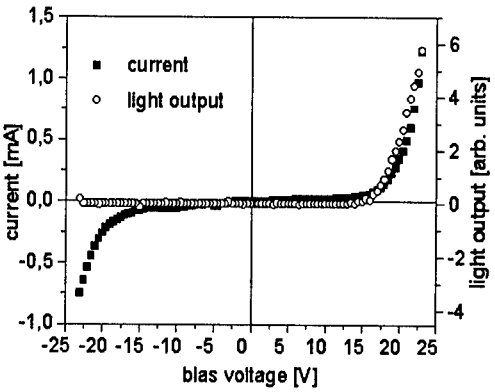


Fig. 5. I/V characteristic of a typical ITO/CdS:Mn/Al electroluminescence device.

The I/V characteristic of a ITO/CdS:Mn/Al device is depicted in Fig. 5. Light emission starts at about 15V. The shape of the I/V curve is almost symmetric, although a slightly rectifying behavior is observed. All the transitions contributing to the emission spectra of CdS:Mn nanoparticles are illustrated in an energy graph (Fig. 6). To determine the energetic positions of the band edges, the theoretical model of Lippens and Lannoo was applied [18]. Assuming an average particle size of 16Å, the electron affinity is 3.2eV and the ionization potential is 7eV, so the resulting band gap is 3.8eV. Since no band to band luminescence was observed in any spectrum, all the transitions are involving gap states. The transition at the right hand side in Fig. 6 represents the internal Mn^{2+} transition mentioned above.

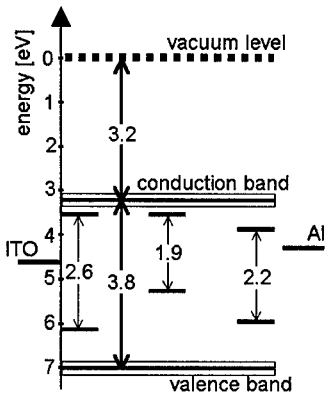


Fig. 6. Schematic diagram to illustrate the energetic levels and transitions which are relevant for the luminescence properties of CdS:Mn nanocrystals. All energy values are given in eV. The workfunctions of the electrode materials used in EL devices are also shown (Φ_{ITO}=4.7eV; Φ_{Al}=4.2eV).

The others are based on transitions between shallow electron traps and deep hole traps, as previously reported [19]. The energetic positions of electron- and hole traps in case of the low-energy transition (1.9eV) explain the symmetric shape of the I/V curve, assuming that charge carrier injection directly into the gap states is possible. Since the energetic barrier between the Al electrode and the electron-traps is about the same as between the ITO electrode and the deep hole-traps, injection of electrons and holes requires about the same electric energy for both, forward and reverse bias.

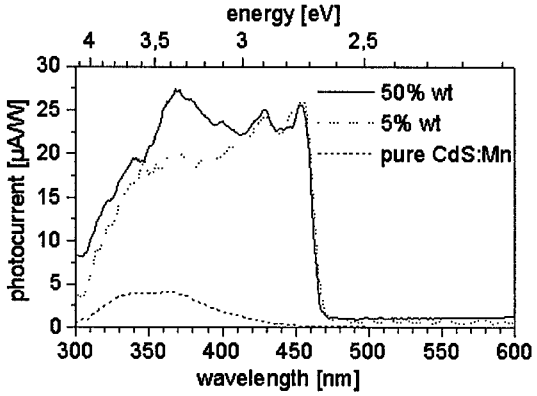


Fig. 7. Short circuit photocurrent as a function of the wavelength of the incident light, measured on two CdS:Mn/polymer blend devices with different nanoparticle content. For comparison, the photocurrent spectrum of a pure CdS:Mn device is also shown.

Photocurrent measurements have been performed on CdS:Mn nanocrystalline samples and on CdS:Mn/polymer blends. The polymer matrix was m-LPPP, a conjugated polymer which has been studied intensively in the last years [20]. The devices were illuminated through the ITO

contact. In Fig. 7 the results are depicted for two blend devices with different particle-content and for one entirely nanocrystalline device.

CONCLUSIONS

The photophysical properties of CdS and CdS:Mn nanoparticles capped with p-thiocresol were studied. Pure CdS particles show a broad PL emission spectrum, which is dominated by defect states introduced by the surface. For CdS:Mn, the PL spectrum consists of mainly two emission bands and both of them are dopant-related. By spin coating, EL devices could be fabricated and the EL spectrum perfectly matches the PL for undoped nano-CdS. PL spectra of manganese doped CdS particles are determined by an internal Mn^{2+} transition, whereas the EL spectrum is dominated by dopant-related defect states. Current/voltage characteristics of ITO/CdS:Mn/Al devices show only slight rectifying behavior and the I/V curves are almost symmetric. This was explained by a direct injection of charge carriers into shallow and deep trap states. Finally, results of photocurrent measurements on pure nanocrystalline and nanocrystal/polymer blend devices were presented. The photocurrent of blend devices was found to be significantly higher than for pure nanocrystalline samples and the efficiency of blend devices is enhanced by a higher particle content.

ACKNOWLEDGMENTS

One of us (Ch. Brugger) gratefully acknowledges the financial support provided by a Stipendium fuer kurzfristige wissenschaftliche Arbeiten im Ausland and the Research Foundation of the State University of New York (USA).

REFERENCES

1. A.I. Ekimov, A.L. Efros and A.A. Onushchenko, Solid State Comm. **56**, 921 (1985)
2. L.E. Brus, J. Chem. Phys. **80**, 4403 (1984)
3. V. Colvin, M. Schlamp and A. Alivisatos, Nature **370**, 354 (1994)
4. A. Alivisatos, Science **271**, 933 (1996)
5. B. Dabbousi, E. Thomas, M. Bawendi and M. Rubner, J. Appl. Phys. **83**(12), 7965 (1998)
6. K. Narayan, A. Manoj, J. Nanda and D. Sarma, Appl. Phys. Lett. **74**(6), 871 (1999)
7. G. Counio, S. Esnouf, T. Gacoin and J.-P. Boilot, J. Phys. Chem. **100**, 20021 (1996)
8. M. Chamarro, T. Gacoin, G. Counio, J.P. Boilot, J. Cryst. Growth **159**, 853 (1996)
9. N. Murase, R. Jagannathan, T. Yazawa and T. Kushida, J. Phys. Chem. B, **103**, 754 (1999)
10. L. Levy, D. Ingert, N. Feltin and M.P. Pileni, J. Cryst. Growth **184/185**, 377 (1998)
11. M. Gao, B. Richter, S. Kirstein and H. Möhwald, J. Phys. Chem. B **102**, 4096 (1998)
12. Y. Yang, J. Huang, B. Yang, S. Liu and J. Shen, Synt. Met. **91**, 347 (1997)
13. N. Greenham, X. Peng and A. Alivisatos, Phys. Rev. B **54** (24), 17628 (1996)
14. Y. Wang and N. Herron, J. Lumin. **70**, 48 (1996)
15. J. Winiarz, L. Zhang, M. Lal, C. Friend and P. Prasad, J. Am. Chem. Soc. **121** (22), 5287
16. N. Herron, Y. Wang and H. Eckert, J. Am. Chem. Soc. **112**, 1322 (1990)
17. S. Koch, Phys. Bl. **46** (6), 167 (1990)
18. P. Lippens and M. Lannoo, Phys. Rev. B **39** (15), 10935 (1989)
19. A. Hässelbarth, A. Eychmüller and H. Weller, Chem. Phys. Lett. **203**, 271 (1993)
20. G. Leising, S. Tasch and W. Graupner, "Fundamentals of Electroluminescence in Paraphenylene – Type Conjugated Polymers and Oligomers", published in Handbook of Conducting Polymers (Second Edition); Marcel Dekker 1998

PREPARATION OF SUBMICRON AND MICRON SIZE Cr (IV) OPTICAL COMPOSITES

L.L. Isaacs*, V. Petricevic**, BaoPing Wang***, Jinpin Ying**** R.R. Alfano**
*Chem. Eng. Department, CCNY/CUNY Grad. Ctr., New York, NY 10031,
chelli@che-mail.engr.ccny.cuny.edu
**Physics Department, CCNY/CUNY Grad. Ctr. and New York State Center for Advanced Technology for Ultra Fast Photonic Materials and Applications, New York, NY 10031
***Chem. Eng. Department, CCNY/CUNY Grad. Ctr. and New York State Center for Advanced Technology for Ultra Fast Photonic Materials and Applications, New York, NY 10031
****CCNY Institute for Ultra Fast Spectroscopy and Lasers, New York, NY 10031

ABSTRACT

Sol – gel technology is used to prepare sub-micron to micron size particles of Chromium (IV) doped materials. These materials show strong luminescence, as single crystals, in the 1-2 μm range. Such materials include; Cr (IV): (Ca_2GeO_4, Mg_2SiO_4, $LiScGeO_4$). The optically active particles are dispersed into glassy matrixes to form optical composites. Ongoing research is aimed at, a) reducing the size and the size distribution of the optically active particles, and b) finding suitable matrix materials.

INTRODUCTION

There is a need to develop new classes of improved, ultra-small, optoelectronic devices, displays and emitters, based on the use of nano/micro-scale materials and structures. Nano-crystals of Cr (IV) doped silicates and germanates, of the olivine type structure, dispersed in a glassy matrix could be employed in laser fiber amplifier applications [1]. The same materials could also be used as near infrared sources and displays.

We were successful in growing large, 1cm diameter, single crystals of Cr (IV) doped ceramics [2] and we also mastered the technique of preparing "sandwiches" of un-doped and doped single crystal materials by liquid phase epitaxy [3].

Large single crystals are rather expensive to produce. Furthermore they are difficult to "shape" into forms usable as device components. Therefore a large fraction of our research effort has shifted toward developing processes to obtain these materials in the form of optical composites.

An optical composite is a dispersion of an optically active material in a transparent matrix. The matrix material may be either inorganic or organic. The crucial issue is the matching of the properties of the optical and matrix components to minimize scattering losses [4].

Mat. Res. Soc. Symp. Proc. Vol. 581 © 2000 Materials Research Society

WORK IN PROGRESS

Synthesis of the Optical Nano-Particles

We have chosen the sol – gel technique for the preparation of the nano and micro-sized particles. A sol is a colloidal suspension of particles in a liquid. A gel is an interconnected, rigid network with pores of sub-micron dimensions and polymeric chains whose average length is greater then a micrometer. The sol – gel process involves a number of steps.

1) The mixing of the colloidal particles or the liquid alkoxide precursors to form a sol. In case of the metal alkoxides, the reactions are, hydrolysis, condensation, and poly-condensation to form the sol.
2) Gelling. With time, the colloid particles and condensed metal species link together to become a three dimensional network. At the gellation point the viscosity increases sharply and a solid or semi-solid "gel" is formed.
3) Aging, drying and densification. Aging (synersis) means keeping the system in the gel state for a period of time to allow the poly-condensation to continue. This increases the strength of the gel. During the drying stage water s removed from the interconnected pore network. Heating the porous, dehydrated, gel at high temperature causes densification to occur. This third step is crucial, because, here is where particle size ad particle size distribution can be controlled.

We used the method to prepare "nano and micro particles" of Cr (IV): Ca_2GeO_4, Cr (IV): Li_2CaGeO_4 and Cr (IV): Mg_2SiO_4. Using a simultaneously recording differential scanning calorimeter and thermo gravimetric analyzer (TA Instruments SDT 2960), we observed the sequence of events occurring during the process. This information is extremely useful for the planning of the third step of the sol – gel process. For instance, we see that formation of the Cr (IV) does not take place below 650 °C. Such thermal scans also allow the quantitative study of the chemistry of the particular process.

Comparing the emission spectra of Cr (IV): Ca_2GeO_4 prepared as single crystal and by the sol – gel method indicates that there is no difference between the optical properties of the two materials.

Optical microscopy indicated that the size of the powder produced ranged from sub-micron to microns. Control of particle and its distribution during the synthesis stage must take into account two factors: 1) Germanium alkoxide [Ge $(OCH_3)_4$] hydrolyses extremely fast. 2) The gels must be heat treated at 640 – 700 °C to obtain Cr (IV) luminescence.

Due to the extremely fast hydrolysis rate, control of particle size by controlling the pH of the reaction medium is not feasible. We can obtain transparent gels, indicating very small particle size, at low temperatures but the high temperature heat treatment leads to particle size coarsening. There are at least two approaches available to overcome the particle size problem.

One method is to add a salt (NaCl) solution to the reaction mixture, wash the product from the 700 °C heat treatment with water to remove the salt. Using a mortar and pestle crush the remaining solid and add more water and filter out the particles. The particles have the proper color and are smaller in size. Two drawbacks to this approach: The remaining solids tend to agglomerate. The filter liquid is turbid and green in color, signifying that we must have a significant portion of the fines in a colloidal suspension. This will need to be recovered (ultra-centrifuge and/or dehydration under vacuum). A more worrisome concern is that the salt may not be fully removed by the several washings.

The second alternative for particle size control is to change the heat treatment procedure. Rather than heat up and keep the aged and dried gel at high temperature, the heat treatment could be done in a spray drier or using a high temperature fluidizing gas in a fluid bed dryer.

Preparation of the Matrix Materials

The optically active nano - particles must be dispersed into a supporting matrix for the preparation of device components. The matrix material must be optically transparent to the nano – particles. Thus the refractive index, at the appropriate wavelength and its temperature coefficient, of the matrix must be matched to the optical material to minimize scattering losses.

The sol – gel route for the preparation of the matrix material is one avenue of approach. The sol – gel method of making glasses was intensely investigated during the 1970's. The main difficulty lay in the lengthy gellation time required to make glass "blocks" free of flaws (inclusions and micro-cracks). But controlling the composition and the heat treatment could easily control the refractive index and porosity of the glass.

$Ti_x Si_{1-x} O_2$, glass is readily be made by the sol – gel technique. Ti (IV) – isopropo – oxide reacts faster with water than with Si – alkoxide (TEOS). Acid conditions are required to avoid hydrolysis and to slow the condensation reaction. The gellation time is inversely proportional to the TiO_2 content. We need a refractive index of $\approx$1.64. This implies a TiO_2 content of about 30%, hence a gellation time of approximately 500 hours. However it must be pointed out that in obtaining the gellation time versus composition data we used a great excess of water to complete the hydrolysis reaction. The densification heat treatment can be used to fine - tune the value of the refractive index.

Preparation of the Optical Composites

We have two avenues of composite formation under investigation.

We start with the sol – gel process to make the matrix material and drive it to incipient gelling. Than we add the sol for the optical component, and bring the whole system to the gelling temperature of the optical component. The idea being that the optical nano – particles will form in the void spaces of the matrix gel. The problem we ran into was that when the composite gel was heat treated at 700 °C and cooled, the resulting product did not luminescence at the expected wavelength. Modification of the technique is being pursued.

In preliminary experiments the nano – particles were dispersed into a $Na_2O - SiO_2$ glass forming mixture. The mixture was melted at 1000 °C and the melt was poured into a form to obtain a glass block. The glass block was from the optical point of view of high quality. However the glass luminosity was not at the Cr (IV) wavelength but at the Cr (III) wavelength. This indicates [5] that the Cr (IV) via a redox reaction converts to Cr (III) and Cr (VI). We need temperatures in the range of 640 to 700 °C to convert the initial Cr (III) dopant to stable Cr (IV) in the olivine structure, hence finding a "glass" with a melting point below some critical temperature, will alleviate the problem.

ACKNOWLEDGMENTS

This work, which is the basis of BaoPing Wang's ongoing Doctoral Dissertation work, is supported in part by NASA and ARO. BaoPing Wang is also supported by Graduate Fellowships from the Graduate Center of CUNY.

REFERENCES

1. V. Petricevic, A.B. Bykov, J.M. Evans and R.R. Alfano, "Room temperature near infrared tunable laser operations of Cr^{4+}: Ca2GeO4", Optics Letters **21**, pp 1-4 (1996)

2. Di Yao, "Development of Cr^{4+} Doped Tunable Solid State Laser Materials", a dissertation submitted to the Graduate Faculty in Engineering, The City University of New York (May 1999)

3. A.B. Bykov, private communication

4. Duane B. Barber et al., "Amplification by Optical Composites", Optics Letters **22**, pp 1247-1249 (1997)

5. P.S. Devi, H.D. Gaffney, V. Petricevic, R.R. Alfano, "Synthesis and spectroscopic properties of (Cr^{4+}) doped sol-gels", J. Non-Crystalline Solids **203**, pp 78-83 (1996)

Nanocomposites Using Mesoporous and Layered Hosts

QUANTUM CONFINED GALLIUM NITRIDE IN A MESOPOROUS MATRIX OF MCM-41

H. Winkler, R. A. Fischer *
and
R. Schmechel, H. von Seggern **

* Institute of Inorganic Chemistry II, University of Bochum, D-44780 Bochum, GERMANY
** Dept. of Materials Science, University of Darmstadt, D-64872 Darmstadt, GERMANY

ABSTRACT

We report the synthesis of a nanocomposite materials consisting of gallium nitride (GaN) confined in the well ordered mesoporous transparent matrix MCM-41 with the help of the metalorganic single source precursor triazido(trimethylamine)gallium using solution impregnation technique. The loading of the pores of MCM-41 with GaN was confirmed by chemical analysis, XRD, TEM, BET, NMR and optical spectroscopy (PL and PL-excitation spectroscopy). The composites exhibit a blue shift of the bandgap of GaN due to quantum confinement.

INTRODUCTION

In the beginning of the nineties, gallium nitride has been changed from a laboratory obscurity into a rapidly increasing field of research. This has been due to some interesting properties:
For example the direct bandgap of about 3.4 eV which makes this semiconducting III-V compound suitable for optoelectronic devices operating in the blue region of light with high quantum efficiencies. Blue light emitting diodes and laser diodes based on thin films of GaN are commercial available products. The technology for producing these devices is well established using chemical vapour deposition methods [1].
In the case of nanoparticles of GaN, no such well established chemical practicability is available. Reliable chemical approaches for nanoparticles of II-VI semiconductors cannot be transferred to GaN because of different properties. Most of the chemical pathways leading to nano confined GaN are transformations of solid precursors, like the thermal decomposition of polymeric gallium imide, gallium amide or the detonation of derivates of triazido gallium [2 a, b]. With all these conversions, one is fighting against problems like particle-agglomeration leading to a broad size distribution, and it is difficult to get access to particle size control. In addition, a uniform arrangement of the particles is almost impossible.
To overcome these problems, we decided to grow GaN nanoparticles in a well-ordered porous matrix. We chose the silica mesoporous molecular sieve MCM-41 which can be characterisized by its porous system consisting of hexagonally arranged hollow cylinders [3].
The molecular sieve will act as a template according to the GaN particles which will be grown in the pores: the pore diameter of MCM-41 will limit the particle size leading to a small size distribution. The hexagonal pore arrangement will be transferred to the arrangement of the GaN particles.
The application of triazido(trimethylamine)gallium **1** as precursor, whose successful transformation into GaN was recently described by our group, combines several advantages [2

Mat. Res. Soc. Symp. Proc. Vol. 581 © 2000 Materials Research Society

b]: the donator stabilization with trimethylamine leads to a nonexplosive decomposition of triazido gallium into GaN and volatile compounds under low heating rates in ammonia atmosphere in a temperature region below 500 ° C where the host matrix MCM-41 is still intact. The precursor **1** is transferred into gallium amide **2** and polymeric gallium imide **3** (fig. 1). The conversion of these two compounds into GaN is well understood and described in several papers [2 a]. In addition, the donator causes solubility of the monomeric precursor. This leads to high mobility of the precursor which therefore gets access to the hosts porous system via impregnation taking advantage of capillary diffusion. Besides, the desired gallium-nitrogen-bonding is a structural feature of the precursor, and the volatile leaving compounds lead to high purity GaN.

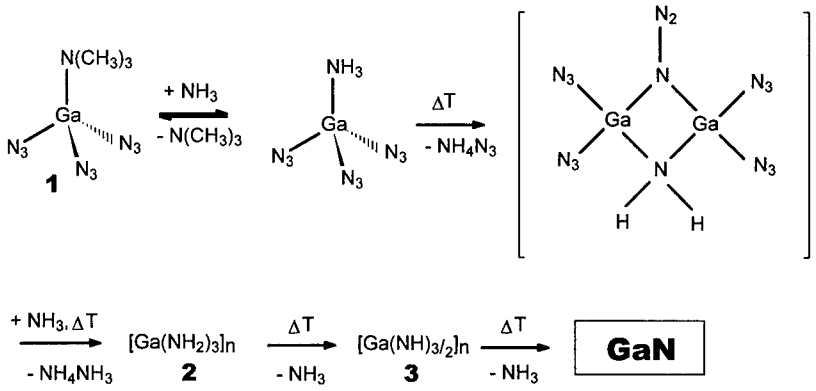


Fig. 1: hypothetical mechanism of the transformation of the precursor triazido-(trimethylamine)gallium **1** into gallium amide **2**, gallium imide **3** and gallium nitride (GaN).

EXPERIMENT

We prepared two different composites of GaN containing MCM-41. In contrast to other groups, which synthesized nano confined indium phosphide and gallium arsenide with the help of MCM-41 using vapor infiltration techniques, we used the solution impregnation method for synthesizing GaN in MCM-41 [4]. The problem of the vapour infiltration technique is that the desired material could also randomly be deposited on the outer surface of MCM-41 besides filling the pores.

0.5 g of vacuum-dried MCM-41 molecular sieve with a pore diameter of 2.7 nm (synthesized according to [5]) were combined with a solution of 0.5 g of triazido(trimethylamine)gallium **1** in 30 mL of toluene. This mixture was then stirred overnight to allow for loading the pores of MCM-41 with the precursor **1** by capillary diffusion. After filtration two different procedures led to two different composites:

One sample was washed twice with toluene before further treatment. This sample is called *washed composite*. The other sample, called *unwashed composite*, was directly heated in an atmosphere of flowing ammonia up to 300 °C, and after turning off the gas heated again up to 500 °C and kept at that temperature for 10 hours.

Both, the washed and the unwashed composite, were obtained as pale grey powders.

RESULTS AND CONCLUSIONS

The loading of the composite material with gallium and nitrogen was confirmed by chemical analysis (CHN and ICP) revealing 10.3 wt-% of Ga and 2.8 wt-% of N for the unwashed composite and 11.2 wt-% of Ga and 11.2 wt-% of Ga and 1.9 wt-% of N for the washed composite. This leads to a molar ratio of Ga : N of 0.7 : 1 for the unwashed composite and 1.1 : 1 for the washed composite [6].

Gas sorption measurements were carried out to calculate the surface area of the empty MCM-41 and the composites according to the BET-theory. The surface area of the empty molecular sieve was about 983 m^2/g and the surface area of the composites were about 290 m^2/g (unwashed composite) and about 226 m^2/g (washed composite) [7]. The decrease of the surface area in the case of the composites is consistent with filling of the pores of the molecular sieve.

The powder XRD-pattern of the empty MCM-41 consists of seven reflections in the small angle region (2 Theta = 1–10°) which can be indexed on the basis of a hexagonal symmetry (fig. 2a) [8]. This symmetry results from the regular periodic variation of the electron density between the empty pores and the silicate wall leading to a scattering contrast. If the pores are filled with material, the scattering contrast will decrease, i. e. the intensity of the reflections will decrease, too (fig. 2a) [5]. Having a look on the high-angle region (2 Theta = 10–80°, fig. 2b), the XRD pattern of the unwashed composite exhibits the reflections of hexagonal GaN broadened due to small particle size (of about 10 nm evaluated by Rietveld analysis). The high-angle pattern of the washed composite does not show any feature of GaN. This indicates very small (2–3 nm) or amorphous particles of GaN.

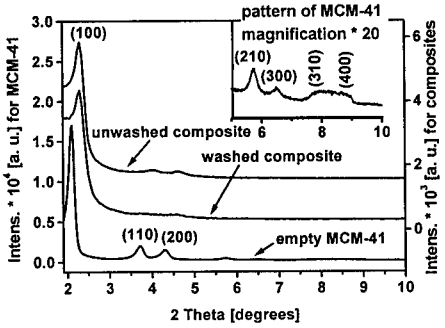


Fig. 2 a: the low-angle region XRD pattern of empty MCM-41 and the composites.

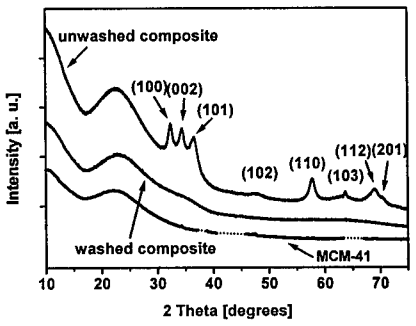


Fig. 2 b: the high-angle region XRD-pattern of empty MCM-41 and the composites.

The transmission electron microscope (TEM) investigations on the materials confirm 1. the uniform and hexagonal arrangement of the pores of the empty MCM-41 and 2. the porous system still being intact after the filling procedure [9]. In addition, the washing cycles led to a clean surface of the washed composite without particle-deposits whereas the surface of the unwashed composite contains particle-deposits of about 10 nm that cause the reflections of GaN in the XRD-pattern.

Solid state ^{71}Ga-NMR spectra were measured on the composites and a commercial bulk powder sample of GaN (FLUKA) [10]. The bulk GaN powder sample shows a typical

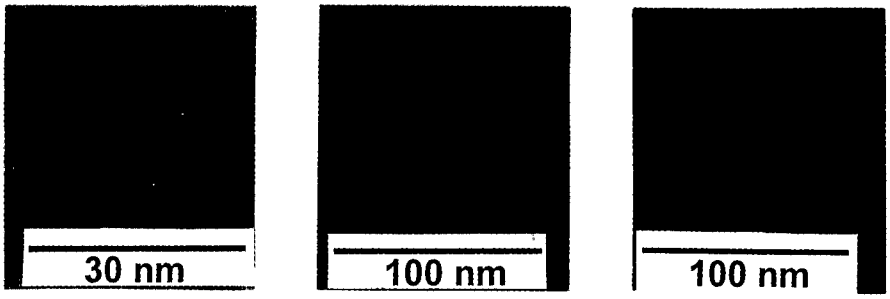


Fig. 3: Transmission electron micrographs. Left: empty MCM-41, middle: unwashed composite, right: washed composite.

quadrupole resonance at 350 ppm (FWHM = 550 ppm). The washed composite exhibits only a broader gaussian-type signal at 145 ppm (FWHM = 450 ppm). In contrast, the spectrum of the unwashed sample consists of two signals: an intense (95 %) Gaussian-type signal at 170 ppm (FWHM = 400 ppm) and a weak (5 %) quadrupole signal at 290 ppm (FWHM = 135 ppm). The broad Gaussian-type resonances of the composites are likely to be attributed to very small particles without an extended crystalline order being inside the pores of MCM-41. The quadrupole signal belongs to bulk GaN which is deposited on the outer surface of the unwashed composite.

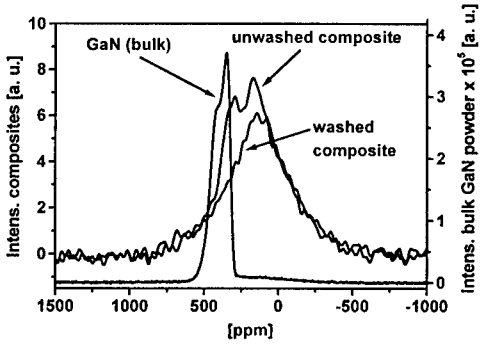


Fig. 4: solid state ^{71}Ga-NMR spectrum of bulk GaN powder and the composites (performed in static mode with 122 MHz resonance frequency and Hahn-echo- technique.

With the washing cycles, precursor molecules deposited on the outer surface of MCM-41 will be removed leading to a composite with gallium nitride being only inside the pores (washed composite). In the case of the unwashed composite we expected gallium nitride being inside the pores and deposited on the outer surface of MCM-41.

Photoluminescence (PL) spectra were taken at room temperature from the commercial bulk GaN powder, the empty MCM-41 matrix, and the washed and unwashed composites (fig. 5) [11]. The spectrum of the bulk GaN powder consists of the expected features: the typical yellow luminescence at about 2.1 eV caused by defects and impurities, and a weak blue emission at about 3.4 ev that corresponds to the band edge luminescence [12]. The empty

matrix shows no luminescence at all. The transparency of the empty MCM-41 is confirmed by the absence of any absorption down to 200 nm (results not shown). In contrast, the composites show broad and featureless bands peaking at about 2.5 eV.
In addition, room temperature excitation spectra of the bulk GaN powder and the composites were performed (fig. 6) [13]. Again, the bulk GaN shows the expected spectrum: a sharp peak at about 3.4 eV belonging to the C-exciton and the band-band-transition (indicated by dotted line) of about 3.4 eV agreeing with literature data. The excitation onset of the composites is shifted to higher energies (3.7 eV). This blue-shift can be attributed to quantum confinement of the GaN-particles being inside the pores of MCM-41: by applying the simple model of a semiconductor sphere (equation 1) and assuming the pore diameter of 2.7 nm as GaN particle size a, a blue shift of about 0.255 eV results [14].

$$\Delta E = \frac{h^2}{8a^2}\left(\frac{1}{m_e} + \frac{1}{m_h}\right) \qquad \text{equation (1)}$$

Despite the simple model, the agreement with the experimental data obtained from the two composites is surprisingly good. A detailed clarification of the involved effects leading to this perfect agreement needs further studies on the materials and is beyond the scope of this paper. In the spectrum of the unwashed composite a small peak remains at about 3.4 eV. This can be attributed to the GaN deposits on the outer surface of this material.
In summary, we have shown the synthesis of quantum confined GaN particles in MCM-41 with the help of a metalorganic single source precursor using solution impregnation technique. This pathway can include washing cycles that remove precursor material deposited on the outer surface of the matrix leading to composites with nanoparticles of GaN being only inside the pores of MCM-41. Latter acts as a template according to the size and arrangement of the nanoparticles.

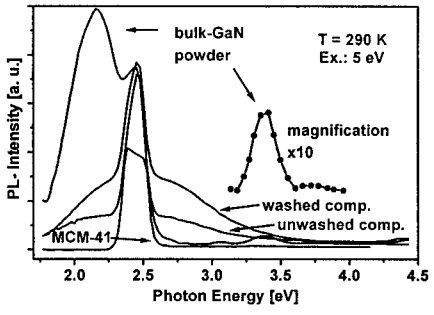


Fig. 5: Photoluminescence spectrum of bulk GaN powder and the composites. The peak at about 2.5 eV is second order light due to grid monochromator (Excitation 5 eV).

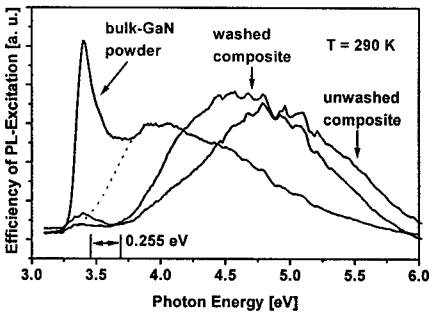


Fig. 6: Excitation spectrum of bulk GaN powder and the composites. The onset of the composites is blue-shifted due to quantum-confinement of GaN in the pores of MCM-41.

REFERENCES

[1] S. Nakamura and G. Fasol, *The Blue Laser Diode*, Springer, Berlin, Heidelberg, New York, 1997.

[2] a) J. F. Janik and R. L. Wells, Chem. Mater. **8**, p. 2,708 (1996) –b) A. C. Frank, F. Stowasser, H. Sussek, H. Pritzkow, C. R. Miskys, O. Ambacher, M. Giersig and R. A. Fischer, J. Am. Chem. Soc. **120**, p. 3,512 (1998).

[3] J. Y. Ying, C. P. Mehnert and M. S. Wong, Angew. Chem. Int. Ed. **38**, p. 56 (1999).

[4] V. I. Srdanov, I. Alxneit, G. D. Stucky, C. M. Renves and S. P. DenBaars, J. Phys. Chem. B, **102**, p. 3,341 (1998). J. R. Agger, M. W. Anderson, M. E. Pemble, O. Terasaki and Y. Nozoe, J. Phys. Chem. B. **102**, p. 3,345 (1998).

[5] B. Marler, U. Oberhagemann, S. Vortmann and H. Gies, Microporous Mater. **6**, p. 375 (1996).

[6] ICP data were obtained with a PU 7000 of Philips-Unicom. The samples were dissolved by sodium peroxide melt-cooking. Elemental analysis data were obtained with a Elementar VarioEL.

[7] S. Brunauer, P. H. Emmett and E. Teller, J. Am. Chem. Soc. **60**, p. 309 (1938). E. P. Barrett, L. G. Joyner and P. P. Halenda, J. Am. Chem. Soc. **73**, p. 373 (1951). Nitrogen sorption measurements were carried out using a Quantachrome Autosorb 1 at 77 K. The samples were degassed for 12 h at 300 °C in vacuum before measurement.

[8] Powder X-ray diffraction pattern were obtained using a D 8 advance of Bruker axs with Cu Kα radiation.

[9] Transmission electron micrographs were obtained using a Hitachi H 8100 operating at 200 kV. The samples were dissolved in ethanol with ultrasonics and dispersed on a carbon-copper-grid.

[10] The solid state ^{71}Ga-NMR spectra were obtained with a Bruker ASX 400 spectrometer in static mode with 122 MHz resonance frequency and hahn-echo-technique.

[11] Photoluminescence (PL) experimental setup: the sample was excited with 5 eV by a modulated (lock-in-technique) 30 W deuterium lamp combined with a band pass filter at room temperature. The resulting photoluminescence was collected by a quartz lens dispersed through a monochromator (Jobin-Yvon HR-640, spectral resolution 1 nm) and registered by means of a photomultiplier (Hamamatsu R 375 P). The spectra are not corrected for the spectral sensitivity of the equipment. The spectral components were weighted by he spectral slitwidth.

[12] O. Madelung, *Semiconductor-Basic Data*, Springer, Berlin, Heidelberg, New York, 1996.

[13] Photoluminescence excitation spectroscopy setup: Photoluminescence excitation spectroscopy setup: a modulated (lock-in technique) 150 W Xenon lamp combined with a double monochromator (Jobin Yvon DH 10, spectral resolution 8 nm) was used as excitation source. The luminescence was collected at room temperature by a quartz lens, filtered by a long pass filter (edge at 450 nm) and detected by means of a photomultiplier (Hamamatsu R 4220). The spectra were corrected by the spectral distribution of the excited light.

[14] A. L. Éfros and A. L. Éfros, Sov. Phys. Semicond. **16**, p. 772 (1982).
Parameters of equation (1) a: particle size and m_e and m_h effective electron and hole mass, respectively. $m_e = 0.27\ m_0$, $m_h = 0.8\ m_0$ (data from bulk GaN) and $m_0 = 9.1095 \cdot 10^{-31}$ kg being the electron rest mass.

Preparation of highly ordered Mesoporous thin film with Alkyltrimethylammonium(CnTMA$^+$)

Y. GOTO [A], N. SUGIMOTO[B], Y. FUKUSHIMA[B], Y. IMADA[C], Y. KUBOTA[C], Y. SUGI[C]
A) Japan Chemical Innovation Institute, 1-1 Yanagido, Gifu 501-1193 Japan
B) Toyota Central R&D Labs. Inc., 41-1 Yokomichi, Nagakute, Aichi 480-1192, Japan
C) Department of Applied Chemistry, Faculty of Engineering, Gifu University, 1-1 Yanagido, Gifu 501-1193 Japan

ABSTRACT

We synthesized the highly ordered mesoporous thin films with alkyltrimethyl-ammonium (CnTMA+). The arrangement of mesopores was depend on the Si/surfactant ratio. The hexagonal(P6mm) arrangement was observed, when Surfactant/Si ratio was 1/10. Increasing the Surfactant/Si ratio to 1.6/10, the cubic (Pm3n) arrangements were observed. A steel vessel for the measurement of the nitrogen adsorption isotherms of thin film on the substrate was designed. It was found that mesopore arrangements in the film is more regular than that in the powder samples prepared by the same acidic synthesis conditions.

INTRODUCTION

Recently developed mesoporous materials such as FSM-16[1], MCM-41[2,3] are expected to realize new field of nano-material science. The mesopore structure is controllable in nanometer range and accessible for outer guest molecules. We can use mesopore space as a Host to make nano-sized materials. Same efforts have done in the field of crystalline aluminosilicate, zeolites. Zeolites can be a host material to make sub-nanometer clusters such as CdS[4], K[5], and so on. But, zeolites are difficult to form thin film configuration with no crack or defect. That is coming from the nature of zeolite crystal. On the contrary, mesoporous materials has amorphous wall structure and periodic pore structures and continuous film formation is expected. Former work in this area by Ogawa with sol-gel method could make optically transparent mesoporous silicate thin films, but in micron-range it has many defects and low stability[6]. In this work, we try to make mesoporous silica thin film structure without defects and cracks. Another important point of Host material, orientation control must be required. Many efforts have been done with various technique[7-10]. We developed relatively simple one based on the nature of template micell.

EXPERIMENT

All thin films have been made with surfactants alkyltrimethylammonium chloride C_x-TMA-Cl (e.g. Cethyl-Trimethyl-ammonium-chloride) with chain length x of 12-18. As a silica source, tetramethylorthosilicate(TMOS) was used. At first, organic/silica complex solution as precursor for thin films has prepared in the molar ratio of 0.1 TMOS, 0.25 H_2O and 0.0002 HCl. The mixture has stirred for 1 hour. Then surfactants (0.01-0.02 mol) were added with stirring under control of pH in the range 1-3 for 10 minutes. Finally water (30-50ml) added to decrease viscosity. The thickness could be changed in the range of 100-500nm by

Mat. Res. Soc. Symp. Proc. Vol. 581 © 2000 Materials Research Society

viscosity and dipping speed. This organic/silica complex solution was transparent and stable for about 3 days.

This organic/silica complex solution could be coated on various substrates by dip-coating or spin-coating method. For example, mesoporous silica film has prepared on glass plate (coaning 7059) with dip-coating at room temperature. To remove surfactants, samples were dried at 373K for 1 hour and calcined at 773K in air for 6 hours.

The pore orientation on a substrate could be controlled with use of semiconductor micro fabrication technique (Si-semiconductor photolithography: Fig 1.). A Si substrate and photo-resist tapered pattern with stripe shape was prepared using standard UV exposure processes. The resist thickness were 1.5 μm and width of stripe pattern were 1 μm. The dip-coating method was applied for pore orientation control in the arrangement of matching the dipping direction and resist stripes. Following the drying process at 373K for 1 hour, lift-off process has been carried out in acetone or methylethylketone with use of supersonic mixer. Finally, Calcinations at 773K in air has done for removal of surfactants.

RESULTS AND DISCUSSION

The structure of mesoporous silica thin films was studied with SEM, TEM and XRD. The orientation controlled silica mesoporous thin film in stripe shape was shown in Fig. 2. Two different type of pore morphology were observed (Fig. 3). The pore type could be changed by

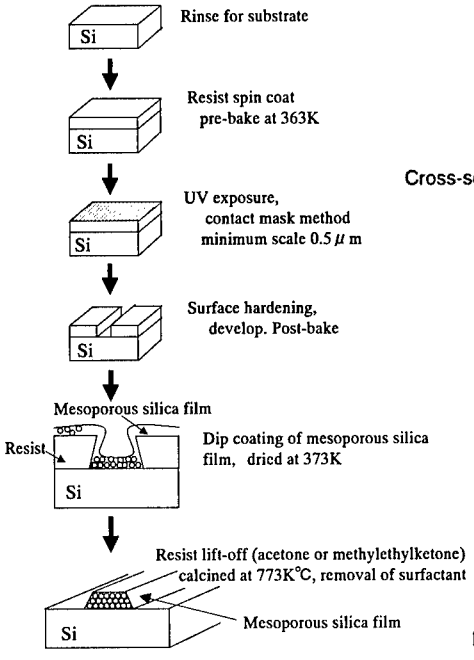


Fig. 1 Preparation of orientation controlled mesoporous silica films.

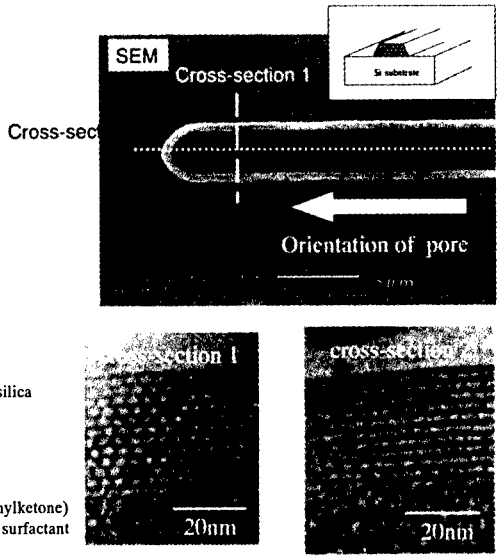


Fig 2. TEM and SEM images of the mesoporous silica thin film on Si substrate.

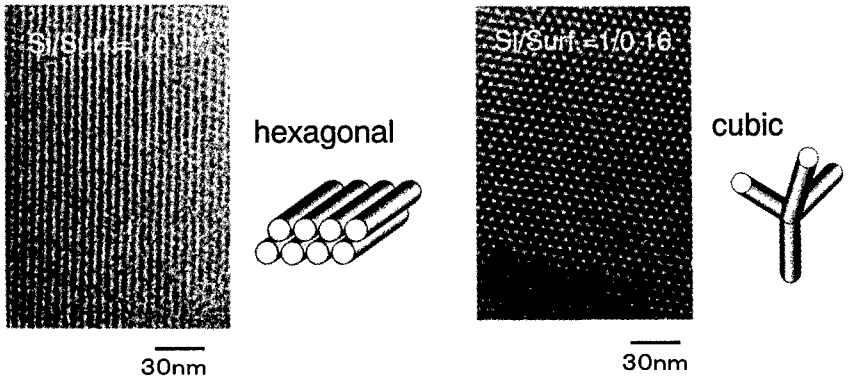


Fig 3 TEM images of the mesoporous silica thin films on glass plate

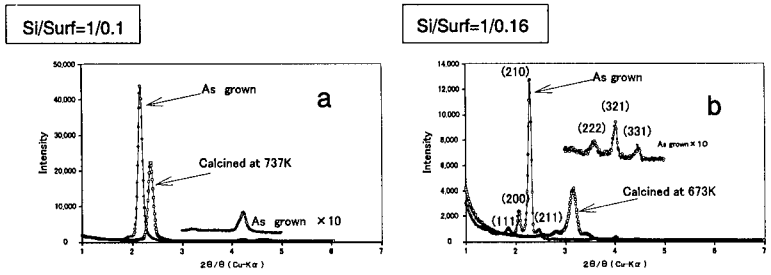


Fig 4. XRD patterns of mesoporous silica thin films on glass plate.
(a) Si/surf.=1/0.1 (b) Si/Surf.=1/0.16

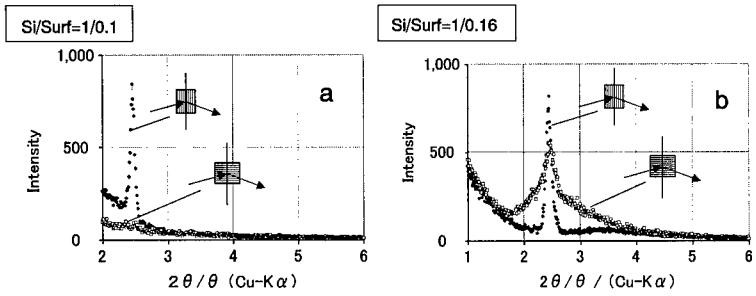


Fig 5. XRD patterns of mesoporous silica thin films on Si substrate.
(a) Si/surf.=1/0.1 (b) Si/Surf.=1/0.16

Si/surfactant ratio. Hexagonal(P6mm) type were obtained at Si/surfactant =1/0.1 and Cubic(Pm3n) type at 1/0.16. The results of X-ray diffraction measurement with 2 θ/ θ scan for continuous thin films on glass plate were shown in Fig. 4. It was good agreement with former results at hydro thermally grown Hexagonal and Cubic type mesoporous powders. In the hexagonal samples on glass plates, (110) peak did not observed. XRD patterns for the patterned films on Si substrate were measured in two geometries, in which X-ray scattering vector was parallel to the stripe direction in one geometry and perpendicular in another one. (Fig 5). The results of XRD suggested that the mesopore channels are running parallel to the stripe direction. That was also confirmed by TEM cross-sectional observation (Fig. 2). These orientation control must be come from the self-assembly nature of micells formed in precursor solutions on the substrate.

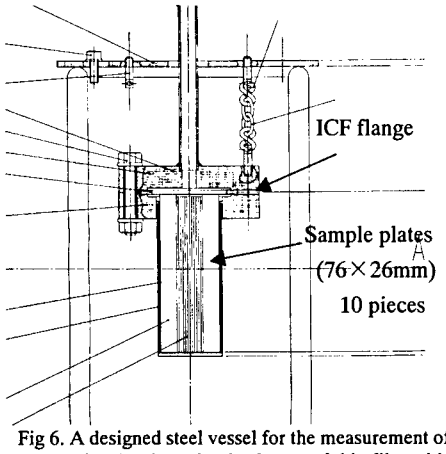


Fig 6. A designed steel vessel for the measurement of the N_2 adsorption isotherms of thin film with the substrates. The vessel is set in the liquid nitrogen.

The adsorption isotherms of N_2 were measured with specially designed steel vessel for thin film samples by means of volumetric method (Fig 6) . Measurements have carried out on ten pieces of glass plate (76×26×1mm) inserted to the vessel. Both surfaces of the glass substrates were coated by the silica thin films with about 500nm of thickness by dip-coating. Fig 7a, 7b shows N_2 adsorption isotherm and BJH pore distribution analysis of Hexagonal film, Cubic film and bulk samples. The bulk samples were prepared with same process that has not coated on substrate and dried to make optically transparent bulk sample. The bulk sample had mesopores near 2nm, but did not have periodic arrangement of pores like Hexagonal films. The diameter of pores derived was about 2.7nm at C18-TMA-Cl that is relatively smaller than FSM-16 or MCM-41 with use of same surfactant. The pore size control of thin films by variation of alkyl-chain length has evaluated (Fig 8a, 8b). The pore size could be control from 1.5-3.0nm.

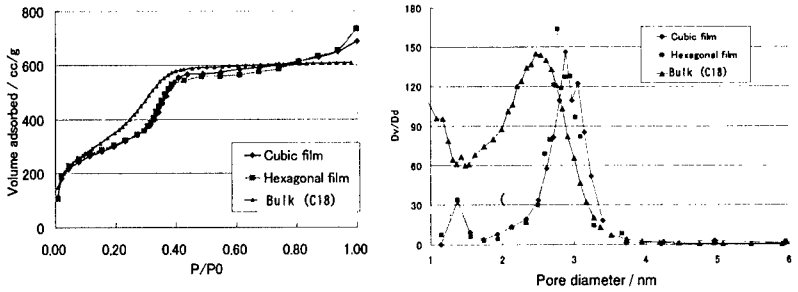


Fig 7. N_2 adsorption isotherms and pore distributions of the mesoporous silica thin films on glass plate. (C_{18}-TMA^+)

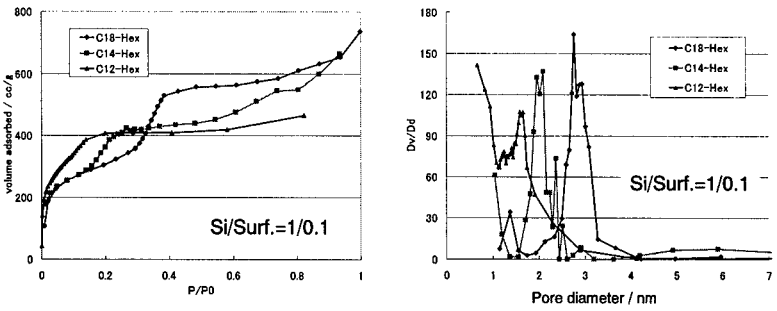


Fig 8. N_2 adsorption isotherms and pore distributions of the mesoporous silica thin films on glass plate. (C_{18}-TMA^+ ,C_{14}-TMA^+,C_{12}-TMA^+)

In this work, highly ordered silica mesoporous thin films were derived with simple method using stabilized organic/silica complex solutions. The important points in this method are the control of viscosity and pH during the preparation of the precursor. Organic/Silicate composite is stabilized with acidic condition (pH=1～2) and secondary addition of solvent (H_2O or organic solvent) lowered the viscosity ,which cause quick rearrangement of micells during drying process. And the high ordering makes thermal stability of mesoporous silica films up to 973K(Hexagonal), 773K(Cubic). Previous work by Lu et al.[10] reported the sol-gel dip-coating thin films, which had a few different phases in cross-sectional direction of the film. They proposed cooperative assembly mechanism concerning with drying process of organic/silica solutions. The same mechanism may influence on our thin films, but good reproducibility and uniform formation of large area (up to 10cm diameter Si wafer) is possible with this procedure.

CONCLUSIONS

The mesoporous silica thin film process with low viscosity and low pH can make highly ordered mesopore structure with good reproducibility. Uniform structure of hexagonal (P6mm) and cubic(Pm3n) pore arrangement was observed at Surfactant/Si ratio 1/10, 1.6/10 respectively. The photolithographic technique can control the orientation of pore direction inside the stripe shape film. N_2 adsorption measurements suggested that the mesopores in the films did not closed. We are going to use this procedure to catalytic, optical and electrical future applications.

ACKNOWLEDGMENTS

The New Energy and Industrial Technology Development Organization (NEDO) of Japan supported this work.

REFERENCES

1. S. Inagaki, Y. Fukushima and K. Kuroda, J. Chem. Soc., Chem. Commun. 680 (1993)
2. C.T. Kresge, M.E. Leonowicz, W.J. Roth, J.C. Vartuli and J.S. Beck, Nature, **359,** 710 (1992)
3. J.S. Beck, J.C. Vartuli, W.J. Roth, M.E. Leonowicz, C.T. Kresge, K.D. Schmitt, C.T-W. Chu, D.H. Olson, E.W. Sheppard, S.B. Higgins and J.L. Schlenker, J. Am. Chem. Soc., **114,** 10834, (1992)
4. Y. Wang and N. Herron, J. Phys. Chem., **95,** 525 (1991)
5. Y. Nozue, T. Kodaira, S. Ohwashi, T. Goto and O. Terasaki, Phys. Rev. B, **48,** 12253 (1993)
6. M. Ogawa, Chem.Commun. 1149 (1996)
7. H. Yang, N. Coombs, I. Sokolov and G.A. Ozin, Nature, **381,** 589 (1996)
8. M. Trau, N. Yao, E. Kim, Y. Xia, G.M. Whitesides and I.A. Aksay, Nature, **390,** 674 (1997)
9. S.H. Tolbert, A. Firouzi, G.D. Stucky and B.F. Chmelka, SCIENCE, **278,** 264 (1997)
10. Y.Lu, R. Ganguli, C.A. Drewien, M.T. Anderson, C.J. Brinker, W. Gong, Y. Guo, H. Soyez, B. Dunn, M.H. Huang and J.I. Zink Nature, **389** 364 (1997)

PHASE TRANSITION AND CONTROL OF SELF-ASSEMBLED MESOSTRUCTURED VANADIA/SURFACTANT COMPOSITES

I.HONMA,**Y.YAGI,H.S.ZHOU,*A.ENDO,**M.MIYAYAMA and **T.KUDO

Energy Fundamental Division, Electrotechnical Laboratory, AIST, Umezono, Tsukuba, Ibaraki, 305-8568, Japan, ihonma@etl.go.jp

* NIMC, AIST, Umezono, Tsukuba, Ibaraki, 305-8568, Japan

**Dept.of Applied Chemistry, University of Tokyo, Bunkyo-ku, Tokyo, 113, Japan

ABSTRACT

The mesostructured vanadia/surfactant composites are synthesized by self assembled processes and phase transition has been investigated. The lamellar mesostructure of the vanadia/surfactant has been shifted to monoclinic and hexagonal mesophase by low temperature annealing, possibly due to the change of the inorganic/surfactant ratio.

INTRODUCTION

The discovery of the mesoporous silicate and aluminnosilicate by Beck *et al.*[1] have opened up new synthetic route of self-assembled materials and numerous papers have been reported to examine the advantages of micelle templated approach and mechanism of the self-organization processing.[2] Processing methods of mesoporous materials have been studied mainly for the silica-surfactant system. The self-assembling surfactant micelle plays on roll for structure-directing agents of mesoporous silicates and other inorganic frameworks. The mesostructure of the product has been controlled by molecular structure of surfactant and other synthetic conditions such as surfactant/silicate ratio, concentrations and temperatures. The materials are calcined to open the mesopores at a dimension of few nanometers.

Vanadium oxide has been studied for a long term because of its potential application to the electrode materials. Zhou and Honma recently reported that spin-cast vanadate-surfactant composite film can change its mesostructure by low temperature annealing[3]. The mesophase of the film prepared from propyl vanadate(V) and C_{16}TMABr on glass substrate showed lamellar structure initially and transformed to hexagonal (p6m) after the heat treatment at 160 ℃ for 12.5 h, while, between lamellar and hexagonal phase, cubic phase, appears as an intermediate phase for transition. In this paper, we have investigated a mesophase transformation of vanadate/surfactant composite that can be controlled by low temperature annealing and the structural change behavior of the composite is discussed.

Mat. Res. Soc. Symp. Proc. Vol. 581 © 2000 Materials Research Society

EXPERIMENT

The surfactant-templated approach has been used for synthesizing mesostructured vanadate, reported elsewhere[4]. In our method, a surfactant solution was prepared by dissolving 3.84 g of C_{16}TMACl in 50 mL of water. An inorganic solution was prepared in another bottle by dissolving 1.17 g of ammonium vanadate(V) (NH_4VO_3) in 50 mL of sodium hydroxide aqueous solution (1.0 *N*). After stirring the inorganic solution for 2 h, hydrochloric acid (1.2 *N*) was added drop wise until its pH was decreased to 6.5. The surfactant solution was added to the inorganic solution, yielding soon a yellow precipitate of vanadate-surfactant composite. The composite was filtered, washed with ethanol and water, and then dried at 65 ℃ for 10 h. The purified composite powder (0.33 g in a sample bottle) was annealed in a furnace with the following heating program: increasing temperature up to objective temperature with the heating rate of 1 ℃/min., holding temperature for 1-64 h, and then furnace cooling for 2 h. The annealing experiments were carried out in two ways: one is heating for 2 hours at different temperatures, the other is at 160 ℃ for various hours. The samples before or after heat treatment was characterized by low angle X-ray diffraction (XRD) peaks. XRD measurements were performed by a Rigaku RINT 2400 diffractometer using CuK_a line. Thermal analysis (TG-DTA measurement) was performed to study phase transformations at elevated temperatures and associated structural change.

RESULTS

The mesophase of the as-prepared composite was lamellar structure as in the XRD pattern shown in Fig. 1. There are three peaks of lamellar phase observed at scattering angle (2q) of 3.6, 7.3, 11°, which is assigned a d-space of 2.4 nm. Although the synthetic condition of the solution pH and C_{16}TMACl/NH_4VO_3 molar ratio (0.1-1.2) has been widely changed, the products have been made only for lamellar phase with the same d-spacing value. Figure 2 shows a change of low-angle XRD pattern of the composite annealed at temperatures from 150 ° to 400 ℃ by the interval of 50 ℃. Below 200 ℃, low-angle XRD pattern preserved to show mesostructure of the product, however, the materials start destroying at annealing temperatures above 250 ℃ and completely deformed at 400 ℃. This is due to the removal of the surfactants in the lamellar structure; the mesophase can not survive without lamellar surfactant, otherwise, hexagonal or cubic phase should be stabilized by calcination.

The mesostructure's phase transformation has been also examined at low temperature annealing at 160 ℃ for various hours, which is shown in fig. 3 (a). From this experiment, it was found that this vanadate-surfactant composite system displayed the following sequence of the phase transformation: lamellar (as-prepared sample) Æ two-dimensional monoclinic, *p*2 (samples annealed for 1, 2 and 4 h) Æ hexagonal, *p6m* (annealed for over 8 h). We indexed XRD peaks as shown in Figs. 3 (b) and (c). Two-dimensional monoclinic phase (usually referred to as a "oblique"[5]) was identified in the meso-structured materials. This phase is not the three-dimensional monoclinic one

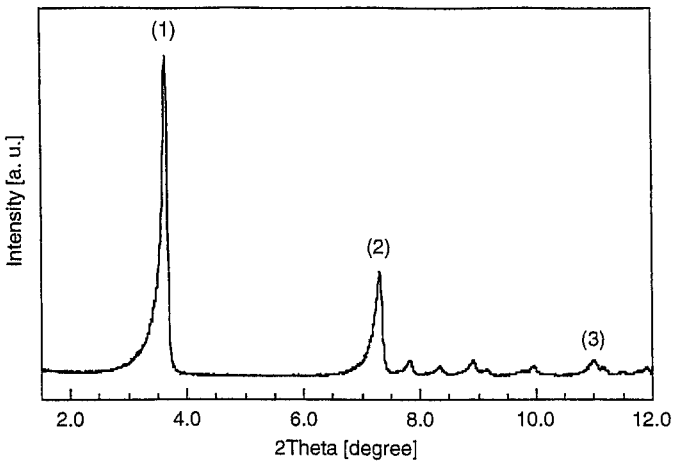


Fig. 1

Fig. 1

Low-angle XRD pattern of the as-prepared vanadia/surfactant composites.

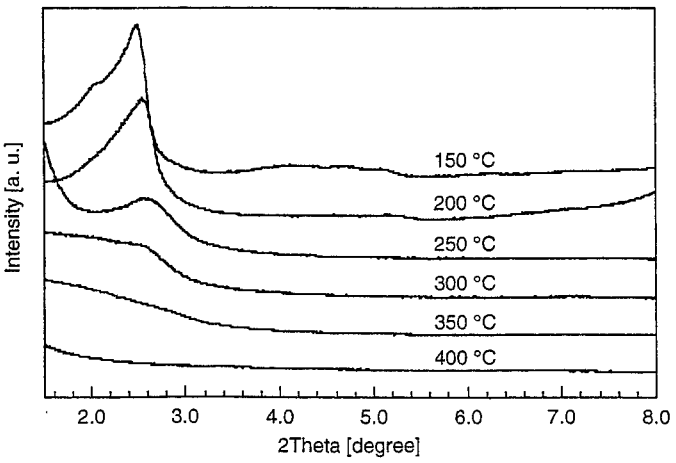


Fig. 2

Fig. 2

Low-angle XRD patterns of the samples annealed at various temperatures for 2 h.

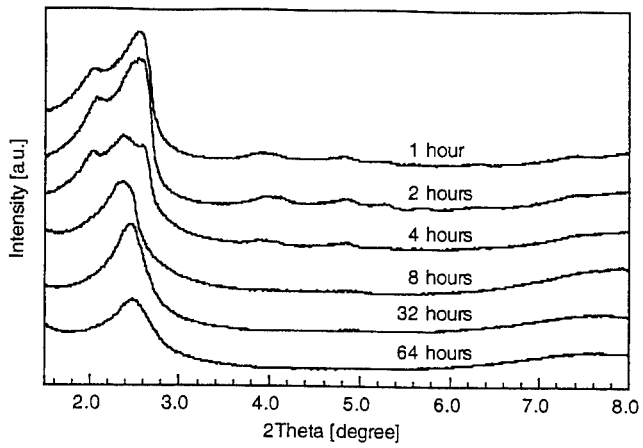


Fig. 3 (a)

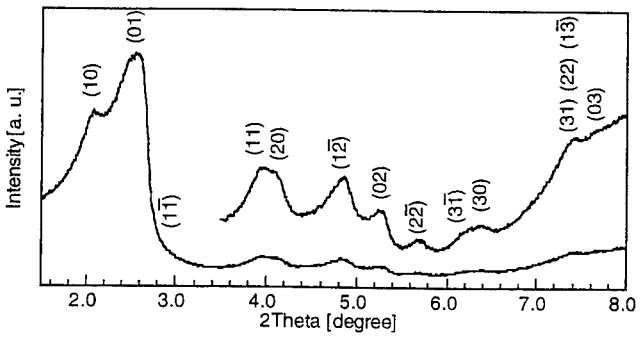


Fig. 3 (b)

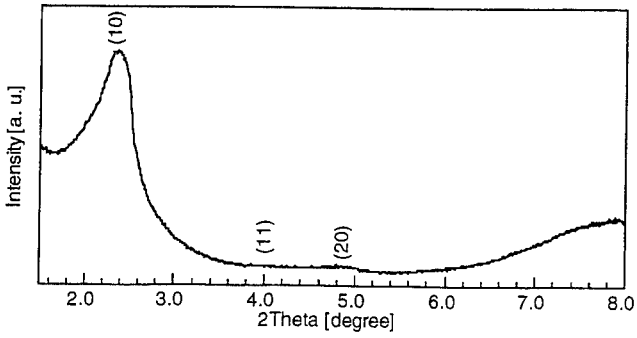


Fig. 3 (c)

Fig. 3

(a) Low-angle XRD patterns of the samples annealed at 160 °C for various hours, (b) the sample (annealed for 2 h.) of two-dimensional monoclinic ($p2$) mesostructure and (c) the sample (annealed for 8 h.) of hexagonal($p6m$) mesostructure are shown.

which was discovered in the tungstate-C_{16}TMA system by Stein *et al.*[6]. Auvray *et al.* investigated mesophase diagrams of C_{16}TMABr and polar solvents such as water, formamide and glycerol, and found *p*2 phase exists in the region between hexagonal and bicontinuous cubic.[7] The transformation sequence of our vanadate-C_{16}TMA system seems to be a reasonable result, although we could not find a cubic mesophase.

As the driving force of the phase transformation and deformation can be enumerated by two possibilities: one is atomic diffusion at the crystallization of vanadium oxide, and the other is interfacial tension applied when the surfactant is baked out. The former possibility is easily denied from a consideration of the crystallization temperature. We measured high angle XRD patterns of all the annealed samples (no data), and confirmed that only the 400 ℃-calcined one consisted of vanadium(V) oxide (V_2O_5) crystals. As shown in Fig. 2, the mesostructure was deformed by annealing at lower temperature than the crystallization temperature. The latter possibility is explained as follows: at the heating treatment, the surfactant is baked out with interfacial tension, which drives all components of the vanadate-surfactant composite to transfer, until the mesostructure stands in a certain region of liquid crystal phase diagram, corresponding to the vanadate/surfactant ratio. This discussion includes doubt because the melting point of C_{16}TMABr is 227-235 ℃[8]; so we may not comfortably accept that the surfactant is really baked out by the annealing at 160 ℃.

The chemical reaction of the vanadate-surfactant composite at the annealing process was studied by TG-DTA measurement. The heating treatment from room temperature to 600 ℃ has three sequential reactions: one endothermic reaction up to 160 ℃, followed by two exothermic reactions from 160 to 320 ℃, and above 320 ℃. All of the reactions involve weight loss, suggesting that those reactions correspond to desorption of adsorbed water, baking out of the surfactant, and crystallization accompanied with desorption of water in vanadate framework, respectively.

We found that the weight of residual surfactant decrease with both increasing annealing temperature and annealing time. The deformation of the composite mesophase was induced by the removal of the surfactant, i.e. the change of vanadia/surfactant ratio which is the mesophase determining parameter of the self-assembling systems. However, the transformation during the annealing at 160 ℃ cannot be discussed simply in the same way. Assuming the alkyl chain of the surfactant in the composite fractionally degrades and the head group keeps on binding with the vanadate framework at the heating treatment, it is realistic to consider that change of the packing parameter[9,10] of the average surfactant formula caused phase transformation, rather than the change of the concentration did. Namba *et al.* synthesized porous silica with single hexagonal mesostructure from silica and the mixture of C_{16}TMABr and C_{12}TMABr.[11] In addition, Huo *et al.* reported that self-organization silica products obtained from a mixture of two distinct surfactants vary from cubic (*Ia3d*) to three-dimensional hexagonal ($P6_3/mmc$) through hexagonal (*p6m*) as the fraction of one of the surfactant increases in the mixture.[9] The above discussion of the packing parameter cannot be

regarded as a reckless one. We could not decided from the present data whether a variation of the surfactant concentration or that of the average packing parameter is only the factor of the mesophase transformation during the annealing treatment at 160 ℃. The origin of the mesophase transformation might be a variation of the concentration of the surfactant, that of the packing parameter, or both of them.

CONCLUSIONS

The mesostructured vanadate/surfactant composites have been synthesized by the surfactant templated approach. The phase transition of the structure by low temperature was studied and the lamellar to hexagonal phase shift has been observed by the surfactant/vanadia composition ratio. Monoclinic phase was also founded in between lamellar and hexagonal. The product loses its mesostructure at high temperature annealing above 250 ℃.

REFERENCES

[1] J. S. Beck *et al.*, *J. Am. Chem. Soc.*, **114**, 10834 (1992).

[2] X. S. Zhao *et al.*, *Ind. Eng. Chem. Res*, **35**, 2075 (1996).

[3] H. Zhou *et al.*, *Mater. Res. Soc. Symp. Proc.* in printing.

[4] V. Luca *et al.*, *Chem. Mater.*, **7**, 2220 (1995).

[5] In International Tables for X-ray Crystallography Vol. I, p58.

[6] A. stein *et al.*, *Chem. Mater.*, **7**, 304 (1995).

[7] X. Auvray *et al.*, *J. Phys. Chem.*, **93**, 7458 (1989).

[8] E. F. J. Duynstee *et al.*, *J. Am. Chem. Soc.*, **81**, 4540 (1959).

[9] Q. Huo *et al.*, *Chem. Mater.*, **8**, 1147 (1996).

[10] J. N. Israelachivili, Intermolecular and Surface Foces 2 nd Ed. (Academic Press 1992).

[11] S. Namba *et al.*, *Chem. Lett.*, 569 (1998).

NANOCOMPOSITES BASED UPON ALUMINA AND ZIRCONIA PILLARED CLAYS LOADED WITH TRANSITION METAL CATIONS AND CLUSTERS OF PRECIOUS METALS: SYNTHESIS, PROPERTIES AND CATALYSIS OF NOx SELECTIVE REDUCTION BY HYDROCARBONS

Vladislav A. Sadykov*,**, R. V. Bunina*, G. M. Alikina*, V. P. Doronin*, T. P. Sorokina*, D. I. Kochubei*, B. N. Novgorodov*, E. A. Paukshtis*, V. B. Fenelonov*, A. Yu. Derevyankin*, A. S. Ivanova*, V. I. Zaikovskii*, T. G. Kuznetsova*, B. A. Beloshapkin**, V. N. Kolomiichuk*, L. M. Plasova*, V. A. Matyshak***, G. A. Konin***, A. Ya. Rozovskii****, V. F. Tretyakov****, T. N. Burdeynaya****, M. N. Davydova****, J. R. H. Ross*****, J. P. Breen*****, F. C. Meunier*****

**Boreskov Institute of Catalysis, Siberian Branch of the Russian Academy of Sciences, Lavrentieva, 5; Novosibirsk, RUSSIA 630090; sadykov@catalysis.nsk.su
** Novosibirsk State University, Pirogova, 1; Novosibirsk, RUSSIA 630090
***Semenov Institute of Chemical Physics RAS, Moscow, RUSSIA
****Topchiev Institute of Petrochemical Synthesis RAS, Moscow, RUSSIA
*****University of Limerick, Limerick, IRELAND

ABSTRACT

Thermally stable alumina and zirconia pillared clays loaded with copper and cobalt cations and silver nanoparticles were synthesized. The structural and surface features of these nanosystems were studied and compared with those of bulk analogs -partially stabilized zirconias and γ-alumina loaded with the same active components. Specificity of the catalytic properties of nanocomposites in the reactions of nitrogen oxides reduction by propane, propylene and decane in the excess of oxygen appears to be determined both by the degree of interaction between pillars and active components and the type of reducing agent.

INTRODUCTION

Alumina, zirconia and titania-pillared clays cation-exchanged with copper, iron, cobalt, cerium, silver and gallium were recently shown to be reasonably active and stable in the presence of water in the reaction of NO_x reduction by ethylene in the presence of oxygen [1]. However, factors determining catalytic activity of these nanostructured systems still remained unclear. In part it can be assigned to a lack of comparison between the properties of these systems and more extensively studied bulk prototypes such as transition metal oxides/precious metals supported onto alumina and/or partially stabilized zirconia. This work aims at covering this gap by using our early experience in dealing with catalysis of NO_x reduction by hydrocarbons (SCR-HC) on stabilized zirconia (PSZ) [2], alumina [3,4] and ZSM-5 [3] based systems.

EXPERIMENTAL

Alumina- and zirconia- (zirconia-ceria) pillared clays were synthesized using a Ca-montmorillonite clay (CaO content 2 wt.%) from the Kazakhstan Tagansk deposit with the cation-exchange capacity 90 meq/100g clay containing ~ 66 wt.% SiO_2 and 25% wt.% Al_2O_3. To synthesize pillaring macrocations, 0.1 M $ZrOCl_2$ 8 H_2O (0.05 M solution of cerium nitrate

Mat. Res. Soc. Symp. Proc. Vol. 581 © 2000 Materials Research Society

was added when required) and 0.1 M $AlCl_3$ starting solutions were used. The pillaring solutions obtained following earlier described procedures [5] as well as their suspensions with clay particles were aged at 60 °C for 16 h. By pillaring, up to 15 wt.% of alumina and ca 20 wt.% of zirconia (or CeO-ZrO_2 solid solution with ~ 1:1 ratio) were incorporated. Copper and cobalt cations were added using either cation exchange with corresponding nitrates solutions as in [1, 3] or impregnation. Silver was loaded either by wet impregnation or by the photoassisted deposition from nitrate solution using an ultraviolet radiation (a high pressure Hg lamp). Typically, up to 4 wt.% of Cu. 1% of Co and~1-2 wt.% of Ag were added to PILC.

Bulk samples of highly dispersed (specific surface area ~ 180m^2/g) mesoporous tetragonal ZrO_2 partially stabilized by Ca, Sr and Ba (Me^{2+} content ~ 3 at.%) were prepared by the ammonia coprecipitation from corresponding mixed nitrate solutions followed by the hydrothermal treatment at 100 °C in the presence of polyvinyl alcohol, drying and calcination at 600 °C. As bulk analog of alumina pillars, earlier studied [3] commercial γ-Al_2O_2 (A-1 type) with the specific surface area ~ 180 m^2/g was used. First copper (up to 1-4 wt.%) and cobalt (up to 1%) cations, then silver (up to 1-2%) were supported on the surface of these bulk systems from nitrate solutions by a standard wet impregnation procedure or photoassisted deposition from nitrate solution followed by drying and calcination at 600 °C.

Samples were characterized using TEM (Jeol 200 C, 200 kv), EXAFS (spectra were acquired at the EXAFS Station of the Siberian Center of Synchrotron Radiation, Novosibirsk) combined with the X-ray diffraction (XRD, CuK_α, an URD-63 diffractometer) and X-ray Small Angle Scattering (SAXS, a KMP-1 camera with CuK_α radiation, nickel filter and an amplitude analyzer). Adsorption characteristics were measured on a Micromeritics ASAP-2400 installation by N_2 adsorption at ~ 77 K. Surface properties were probed by the Infra-red spectroscopy of adsorbed CO test molecule (FTIRS, a Fourier-transform IFS 113V Bruker spectrometer). Temperature-programmed desorption of NO_x (TPD) was carried out following procedures earlier described in details [2, 3].

Catalytic properties in the NO_x SCR -HC and NO oxidation to NO_2 by O_2 were tested in the flow microreactors using earlier described procedures [2-4] at GHSV 12000/h (0.1% C_3H_8+0.1% NO +1%O_2 in He), 18000/h (0.2%C_3H_6 + 0.2% NO + 2.5% O_2 in N_2), 11200/h (0.05% C10H22 + 0.15% NO in air) and 30000/h (1% NO + 1% O_2 in He).

RESULTS

Pore structure of pillared clays

According to XRD, for all PILC the basal (001) spacing is in the range of 17-19 Å, which corresponds to the gallery height ~ 8-9 Å. The micropore volume estimated from the nitrogen adsorption isotherms (Fig. 1) was found to be ~ 0.1 cm^3/g, while the BET surface area was in the range of 200-320 m^2/g, both values decreasing due to incorporation of transition metal cations and silver. The hysteresis loop nearly identical for all samples is due to mesopores (mean diameter ~45 Å) created by defects in the clay sheets stacking.

Structural features

A typical spectra for Zr K edge are shown in Fig. 2. In all samples, Zr environment corresponds to that in the tetragonal zirconia phase. Here, a set of close Zr-O distances exists thus decreasing the average Zr-O coordination number (CN). For bulk samples, the nature of stabilizing alkaline-earth cation has a negligible effect on the Zr coordination sphere. As fol-

lows from Table 1, where the data are shown only for Ca-ZrO_2 as a typical support, Cu, Co and Ag loading has not changed the Zr environment as well. For pillars (Table 1), the structura differ considerably from that for the bulk zirconia: Zr-O distance and CN were

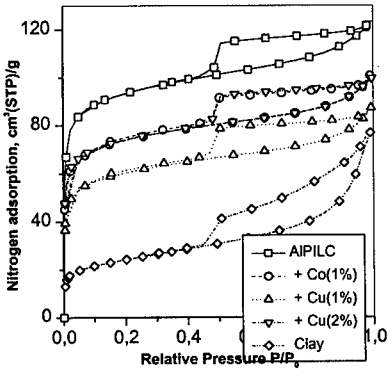


Fig. 1. Typical nitrogen adsorption isotherms for the initial clay, Al-PILC and Cu and Co-exchanged Al-PILC.

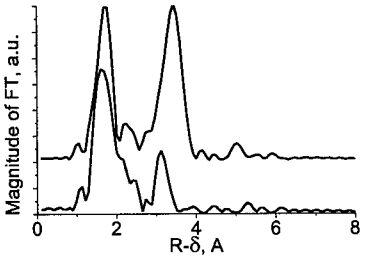


Fig.2 RDA function for Zr-K in 5%Cu/ SrO-ZrO_2-(upper curve) and Cu/Zr-Ce-PILC.

bigger, while for the Zr-Zr sphere, these parameters were smaller. It suggests a more symmetric oxygen environment around each Zr with a more disordered packing of Zr-O polyhedra in the nanosized pillars. These effects are less developed for pillars comprised of CeO-ZrO_2 species due to known Ce ability to stabilize a cubic zirconia phase. As the result, copper insertion has a negligible effect on their structure (Table 1), while changing appreciably the structural features of pure zirconia pillars. For both types of pillars, silver incorporation has a pronounced effect on their structure. These results imply location at least a part of promoters on the pillars. This conclusion agrees with the identical square-planar coordination of copper cations by the oxygen atoms situated at 1.99 Å distance for both bulk zirconia supported samples and Cu/Zr-PILC found in this work. These Cu cations are mainly isolated since no Cu-Cu distance was observed. The appearance of two Cu-Zr (Ce) distances at~3.0 and 4.0 Å implies the incorporation of copper into the surface layer of bulk samples or into the bulk of pillars. No bulk phases of copper or cobalt oxides were detected by TEM and XRD. EXAFS spectra of silver not shown here for brevity have a very high noise level suggesting that a considerable part of Ag exists as isolated cations with low Ag-O CN. Certainly, a considerable part of Ag in PILC is in the form of rather big particles located either in mesopores (diameters up to 30-35 Å; SAXS) or on the surface of PILC platelets (50-100 Å, Fig. 3) and bulk supports (SAXS mean diameter ~ 15 Å, ~200-300 Å particles revealed by TEM, Fig. 4).

The interaction between silver and oxidic promoters is visible as a "mushroom"-type Ag particles (Fig.3) or thin layers extended around them in zirconia supported samples promoted by Cu and Co (Fig. 4)

Surface properties

As follows from the data of adsorbed CO test molecule (Fig. 5,6), the state of transition metal cations supported onto the bulk supports or incorporated into the PILC greatly

depends upon the support nature and presence of silver. Usually, silver addition was found to

Table 1. EXAFS parameters for Zr-containing samples

Sample	Sphere	Coordination number	Distance, Å	Debye-Waller factor $2\sigma^2$, $Å^2$
ZrO_2-CaO	Zr-O	3.8	2.10	0.010
	Zr-Zr	6.4	3.66	0.016
5% Cu/ZrO_2-CaO	Zr-O	3.9	2.10	0.010
	Zr-Zr	5.4	3.65	0.015
CeZr-PILC	Zr-O	4.8	2.15	0.017
	Zr-Zr	0.9	3.52	0.016
Zr-PILC	Zr-O	5.1	2.15	0.019
	Zr-Zr	0.5	3.51	0.011
Cu/CeZr-PILC	Zr-O	5.1	2.14	0.017
	Zr-Zr	0.9	3.48	0.014
Cu/Zr-PILC	Zr-O	4.7	2.15	0.017
	Zr-Zr	0.6	3.52	0.013
Cu(5%)+Ag(2%)/	Zr-O	4.7	2.15	0.014
CeZr-PILC	Zr-Zr	0.6	3.49	0.011
Cu(5%)+Ag(2%)/	Zr-O	5.2	2.14	0.021
Zr-PILC	Zr-Zr	0.5	3.47	0.004



Fig. 3. Typical TEM image (x300000) of silver particles photodeposited into the Co/Al-PILC



Fig. 4. A typical TEM image of silver particles supported onto 5% Cu/Ca-ZrO_2 sample. Dark bulky particles-Ag, thin transparent platelets around them –mixed oxidic phase

increase the density of coordinatively unsaturated surface centers capable to retain CO, while the spectral features typical for the metallic silver (absorption band at ~ 2100 cm^{-1}) were not observed. Copper and cobalt cations appear to screen a part of support coordinatively unsaturated centers (Zr or alkaline earth cations for PSZ, Al cations for alumina) or surface hydroxyls (band at 2166 cm^{-1} for hydrogen-bonded CO) while creating new centers. As judged by the relatively high-frequency band position [3], copper and cobalt cations are mainly isolated and/or incorporated into the support. Appearance of the low-frequency band for CO adsorbed on Cu/zirconias as compared with Cu/PILC suggests a higher degree of copper clustering for the case of bulk zirconia supports. Due to high reactivity of surface oxygen in such clusters, Ag-promoted Cu/zirconia systems are capable to oxidize CO even at 77 K, which was manifested by emergence of a band at ~ 2340 cm^{-1} corresponding to adsorbed CO_2. Similarly, as

compared with Cu/Al-PILC, Cu/Zr-PILC have a higher degree of clustering and an order of magnitude higher density of CO adsorption centers.

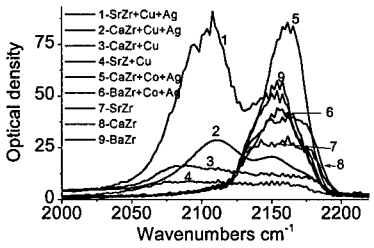


Fig. 5. Typical IR data for CO adsorbed at 77 K and 13 Torr for zirconia –based samples.

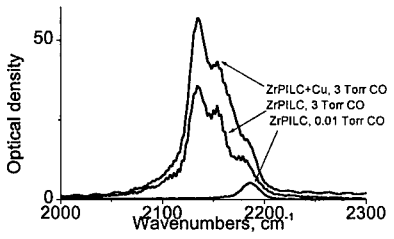


Fig. 6. Typical IR data for CO adsorbed at 77 K on the surface of Zr-PILC

Catalytic properties

In general, the systems studied here possess a rather good and stable performance in NO_x SCR-HC comparable with or exceeding that of the reference Cu-ZSM-5 system [3], and the best samples based upon PILC or bulk zirconia supports are certainly of a practical interest (Fig. 7,8; Table 2). For the same active component, the catalytic performance was found to depend strongly upon the type of support. Thus, zirconia and Zr-PILC based Cu catalysts have a higher level of the low-temperature activity as compared with systems based upon alumina or Al-PILC. In part, it can be assigned to a higher degree of Cu-Cu clustering for the former systems.Similarly, too strong interaction of cobalt cations with alumina pillars makes Co/Al-PILC catalysts inactive, though Co supported on γ-alumina has a very good activity. Interaction between silver and transition metal cations helps to increase NO conversion

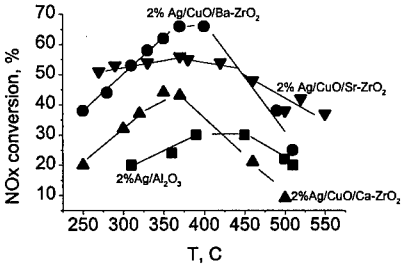


Fig. 7. Temperature dependence of NO_x reduction into N_2 by decane at 11000h^{-1} for catalysts based upon bulk supports.

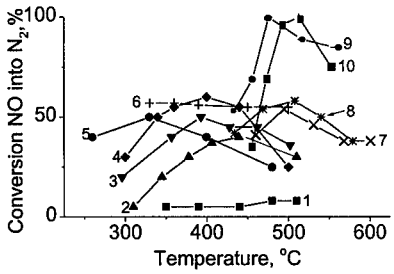


Fig. 8. Performance of basic types of catalysts in the NO reduction by C_3H_8 (2, 3, 7-10), C_3H_6 (4,5) and decane (1, 6). 1,2,5-- Cu/Ce-Zr-PILC, 3,4-Ag+Cu/Ce-Zr-PILC, 6-Ag+Cu/Al-PILC, 7,8-1% Cu/Al_2O_3 and 1%Ag+1%Cu/Al_2O_3, 9,10-0.7% Co/Al_2O_3 and 1% Ag+0.7% Co/Al_2O_3, resp.

into N_2, though operating temperature range can be shifted either to higher or lower temperatures. In general, there is no simple relation between the rate of NO reduction and the amount of adsorbed CO, NO_x or the rate of NO oxidation into NO_2 (Table 2).

Table 2. Comparison between NO_x TPD data and performance of Cu+ Ag active component supported onto bulk Me-ZrO_2

Support	TPD NO_x		X_{max}/T_{max}*			NO
	Coverage, 10^{19} mol/g	Tmax, °C	Propane -SCR	Propylene-SCR	Decane-SCR	into NO_2 at 225 °C, %
Ca-ZrO_2	6.3	180, 350	40/200	30/250	44/350	22.4
Sr-ZrO_2	7.1	180, 380	30/350	40/120-280	56/370	17.1
Ba-ZrO_2	4.8	220, 320	50/250	40/120-400	66/370	10.7

*The temperature (T_{max}) at which maximum conversion of NO into N_2 (X_{max}) is achieved

which is important for generation of reactive ad-NO_x species [3,4]. In part, it can be explained by a variety of ad-NO_x species (nitrates, nitrites, nitrosyls) with different reactivity existing on the surface, hence, integral data are not sufficient. Probably, such factors as specific activation of hydrocarbons by silver and stabilization of certain C,N-containing intermediates can be of importance as well.

CONCLUSIONS

Structural features and surface properties of zirconia and alumina pillars located between the clay layers and loaded with transition metal cations and silver were shown to differ appreciably from those of bulk analogs due to a stronger oxide-oxide and/or oxide-metal interaction. It is reflected in the catalytic performance of these systems in the NO_x selective reduction by hydrocarbons helping to obtain some active systems interesting for the practical application

ACKNOWLEDGMENTS

This work is in part supported by INTAS grant 97-1730

REFERENCES

1. R. T. Yang, N. Tharappiwattananon, and R. Q. Long, Appl. Catal. B **19**, 289 (1998).
2. V. A. Sadykov, A. S. Ivanova, V. P. Ivanov, G. M. Alikina, A. N. Kharlanov, E. V. Lunina, V. V. Lunin, V. A. Matyshak, N. A. Zubareva, A. Ya. Rozovskii in *Advanced Catalytic Materials*, edited by P. W. Lednor, D. A. Nagaki and L. T. Thompson (Mater. Res. Soc. Proc. **454**, Pittsburgh, PA 1997), p. 199-204.
3. V. A. Sadykov, S. L. Baron, V. A. Matyshak, G. M. Alikina, R. V. Bunina, A. Ya. Rozovskii, V. V. Lunin, E. V. Lunina, A. N. Kharlanov, A. S. Ivanova, S. A. Veniaminov, Catal. Lett., **37**, 157 (1996).
4. F. C. Meunier, J. P. Breen, V. Zuzaniuk, M. Olsson, and J. R. H. Ross, J. Catal., **187**, 493 (1999).
5. J. T. Kloprogge, J. Porous Mat., **5**, 5 (1998)

SOFT CHEMICAL DESIGN OF TRANSITION-METAL-OXIDE / CLAY LAYERED NANOCOMPOSITES.

Kiyoshi Fuda, Shuji Narita, Shuji Kudo, Kenji Murakami and Toshiaki Matsunaga,
Deptment of Materials-process Engineering and Applied Chemistry for environments,
Faculty of Engineering and Resource Science, Akita University,
Akita 010-8502, JAPAN, fudak@ipc.akita-u.ac.jp

ABSTRACT

Room-temperature synthesis of transition metal (TM = Co, Ni and Mn) oxide intercalated clays has been developed, which extends the potentiality of clay based materials for the design of electroactive nanophase. The structure was examined by using powder XRD - one-dimensional Fourier analysis, magnetic susceptibility measurement as well as conventional analytical methods. From the results, it was revealed that the oxidation by using NaClO as the oxidative reagent affords a new expanded layer structure with a basal spacing of about 1.96 nm wherein a conductive TM oxide sheet adjacent to two hydrated sodium ion layers resides in the gallery of the clay. The resultant sodium cobaltate interlayered smectite bears multi-functionality; an apparent bulk conductivity in the order of 10^{-5} Scm^{-1} and a cation exchange ability.

INTRODUCTION

Metal / insulator layered nanocomposite has attracted great interest from not only scientific but also industrial aspects [1]. For constructing such composites, layered transition metal dioxide and clay minerals are expected to be the conductor and insulator parts of the structure. In this concern, however, we focussed our attention to the fact that divalent transition metal hydroxides can be intercalated into the gallery of smectite clays to form a silicate / hydroxide intercalation compounds [2]. If the hydroxide sheets intercalated inside the gallery would be successfully oxidized, one can obtain a new nano-composite wherein conductive oxide layers and silicate layers are alternately stacking.

The authors have developed a new oxidation method with using NaClO as the oxidative reagent. Here, the structure of the product will be examined by XRD associated with one-dimensional Fourier analysis as well as magnetic susceptibility measurement. The structure determined was found to be essentially the same for Co, Ni and Mn species. Thus we will mainly describe on the case of Co, then the other cases will be mentioned as well.

PROCESSING

The cobalt hydroxide intercalated smectite compounds were prepared by the titration method [2,3,4]. Sodium fluoride tetrasilicic mica of 2.0 g (Somacif provided by Coop Chemical Co. Ltd.; ideal chemical formula: $Na_2Si_8Mg_5F_4O_{20}nH_2O$; Chemcal analysis data: SiO_2 58.73%; MgO 27.58%; Na_2O 4.96%; F 8.02%; CaO 0.16%; Fe_2O_3 0.07%; Al_2O_3 0.48%; CEC: 115meq/100g-clay) was dispersed into 150 ml of 0.1 M $CoCl_2$ aqueous solution. 300 ml of 0.1 M NaOH aqueous solution was added slowly with a drop rate of 1 ml/hour. The titration was carried out under nitrogen flow to avoid formation of cobalt carbonate throughout the procedure. The obtained powder was rinsed with 0.01 N HCl aqueous solution to remove the excess $Co(OH)_2$ precipitated on the outer surface of the clay and further washed with deionized water.

The oxidation was performed in aqueous suspension system at room temperature. About 1.0 g of the cobalt hydroxide intercalation compound prepared above was dispersed in 50 ml of 1.5 M NaClO aqueous solution and was vigorously stirred. The color of the

Mat. Res. Soc. Symp. Proc. Vol. 581 © 2000 Materials Research Society

sample immediately turned from original light pink to black, indicating the oxidation of cobalt hydroxide into electronically conductive phase. For equilibrium, the suspension was further stirred for 24 hours. The powder sample was washed with deionized water and separated centrifugally, then dried in vacuo at 313 K.

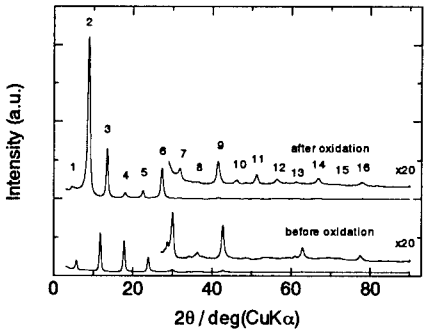


Figure 1. Powder x-ray diffraction patterns for Co hydroxide / fluoride teterasilicic mica intercalation compounds before and after oxidation. The numbers presented on the lines stand for the index *l* of (00*l*) reflections.

STRUCTURAL STUDY

The first change via the oxidation was observed in the basal spacing of the sample. The XRD patterns were recorded on a rotating-anode type high power X-ray diffractometer, Rigaku RINT-2000 with monochlomated Cu Kα radiation in step scan measuring mode of a 0.02° step in 2θ. The intensities of 00*l* reflections were determined by film technique. The powder XRD patterns as well as possible indices for the samples before and after oxidation are compared in Fig. 1. From the results, it is clear that the basal spacing expands from 1.48 to 1.96 nm via oxidation. The pattern of the before oxidation sample was quite similar to that reported by Ohtsuka et.al [2]. For the after oxidation sample, in the figure, at least 16 basal reflections can be distinguished from the noise level. The observed periodic appearance of the higher harmonics from basal plane indicates a considerably high regularity in the stacking of the silicate and transition metal oxide sheets in the structure.

From EDX observation revealed that Co and Na atoms were contained in the oxidized sample in addition to the original composition of the silicate host. The composition of Co and Na determined from AAS analysis was presented in Table I. The average valence of the Co ions was determined by iodometric titration to be 3.2±0.1. The TG profiles for the samples before and after oxidation were compared in Figure 2. The before-oxidation sample showed two steps of decomposition at 200 °C and 350 °C corresponding to dehydration and dehydroxylation from the cobalt hydroxide layer. On the other hand, the after oxidation sample showed three steps: (i) dehydration of loosely bonded water (T < 150 °C); (ii) release of oxygen and dehydroxylation (150 < T < 700 °C); (iii) release of oxygen associated with decomposition of silicate layer (T > 700 °C). It is apparent that the temperature of the major weight loss for the sample lowered via oxidation, suggesting conversion from hydroxide sheet to oxide or oxyhydroxide of cobalt as well as intercalation of water molecules through oxidation process. Taking account these results, the expansion in the basal spacing can be attributed to the intercalation of sodium ions and water molecules between silicate and CoO_2 slab.

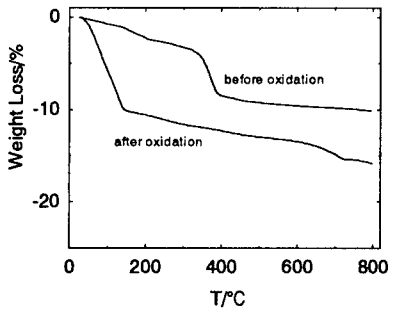


Figure 2. Thermogravimetry (TG) profiles for for Co hydroxide / fluoride teterasilicic mica intercalation compounds before and after oxidation.

Table I. Comparison of the interlayer compositions of the after oxidation sample between the experimental and the estimated values

	Amount [mmol/g-sample]		
	Co	Na	Interlayer H_2O
Experimental	3.33[a)]	1.69[a)]	5.78[b)]
Estimated[c)]	3.43	1.74	6.00

[a)]determined by atomic absorption analysis
[b)]determined by the weight loss below 150 °C
[c)]estimated by the contents of the model structure presented in Table II.

In order to check this argument further, we tried to compute and compare one-dimensional Fourier maps based on the observed 00*l* intensities and the model structure for the oxidized sample (Figure 2). In computation [5], we included the first 16th lines and the observed structure factors were phased with those calculated based on the model structure. The distribution of the atoms along z-axis in the unit cell of the model structure is presented in Table II. The observed and calculated values of the line intensities and structure factors for the basal reflections are compared in Table III. From good agreements (R_F=2.3%), we can realize the structure wherein CoO_2 slab is sandwiched by two monolayers of hydrated sodium ions in the interlayer space.

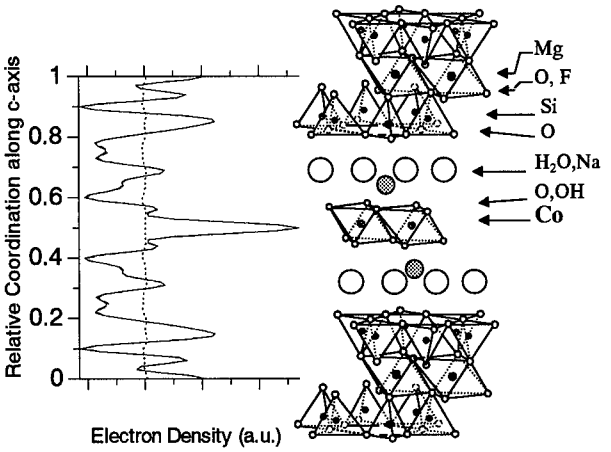


Figure 3. One-dimensional Fourier diagram and corresponding structure scheme for the after oxidation sample. In the diagram, three lines are presented; solid line: calculated based on the observed structure factors, Fobs; broken line: calculated based on the structure model (This line substantially overlaps with the former solid line.) ; dotted line: the difference Fourier map.

Table II Structural model and parameters used for the calculation of the XRD intensity and the structure factors of (00*l*)s for the after oxidation sample

	composition	z	d_z/Å
Silicate layer	6 O		
	4 Si		
	4 O, 2 F		
	5 Mg	0.00	0.00
	2 F	0.06	1.08
	4 O	0.06	1.11
	4 Si	0.14	2.77
	6 O	0.17	3.34
Interlayer	3.4 H_2O	0.31	6.09
	1.2 Na	0.34	6.72
	5.2 (O,OH)	0.45	8.84
	4.8 Co	0.50	9.80
	5.2 (O,OH)		
	1.2 Na,		
	3.4 H_2O		

Table III Comparison between the observed and the calculated XRD line intensities and structure factors for the after oxidation sample.

	d/Å(obs.)	I/I_0(obs.)	I/I_0(calc.)	*F*(obs.)	*F*(calc.)
(001)	19.62	3.09	2.96	7.76	7.61
(002)	9.86	100.00	100.00	88.75	88.75
(003)	6.56	27.04	27.23	69.90	-69.88
(004)	4.93	3.18	3.56	32.56	33.96
(005)	3.94	4.64	4.82	49.71	-49.92
(006)	3.26	21.63	21.51	132.23	128.09
(007)	2.81	0.83	0.33	18.67	18.68
(008)	2.46	0.07	0.09	12.70	-11.23
(009)	2.18	0.98	1.20	46.73	-47.73
(00,10)	1.97	0.21	0.25	24.10	-24.61
(00,11)	1.78	0.39	0.66	43.60	-44.76
(00,12)	1.63	0.28	0.40	38.40	38.89
(00,13)	1.52	0.07	0.10	25.05	21.04
(00,14)	1.40	0.40	0.57	56.03	55.97
(00,15)	-	0.00	0.00	0.00	-0.37
(00,16)	1.22	0.26	0.48	59.74	59.69

$$R_F = \frac{\sum \| F_{o(00l)} | - | F_{c(00l)} \|}{\sum | F_{o(00l)} |} = 2.1\%$$

MAGNETIC AND ELECTRIC PROPERTIES

The electronic configuration of Co ions was examined from magnetic aspect. The magnetic susceptibility of the samples were measured with Quantum Design MPMS XL-5 SQUID magnetometer in the temperature range, 2<T/K<300, in the field of 1 kOe. The temperature dependence of susceptibility phenomenologically seemed to be simple summation of a Curie paramagnetism and a temperature-independent term. By fitting an equation $\chi = C/T + \chi_0$ to the experimental data, we obtained the Curie constant C = 6.3x10^{-5} emu·Oe^{-1}g^{-1}K^{-1}, and χ_0 =1.4x10^{-6} emu·Oe^{-1}g^{-1}. The effective moment of cobalt was calculated from the C value to be 0.39 μ_B. This low value indicates that the Co ions adopt a

low spin configuration (t_{2g}^6 for Co^{3+} and t_{2g}^5 for Co^{4+}) in the octahedral center. It should be noted that a practically temperature-independent para-magnetism has been reported for $NaCoO_2$, adopting the $\alpha NaFeO_2$ structure wherein MO_2 slab is constructed of edge shared octahedron [6]. The constant term was considered to be due to non-diagonal term of the orbital moment. The qualitative similarity between $NaCoO_2$ and our sample suggests a structural similarity between the oxide sheets in these materials.

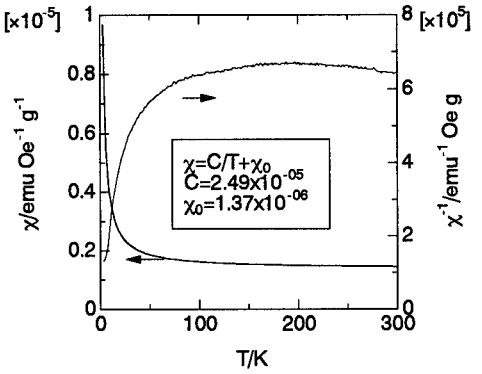


Figure 4. Magnetic susceptibility, χ, and reciprocal magnetic susceptibility, χ^{-1}, for the after oxidation sample as a function of temperature. The inset represents the Currie constant, C, and temperature independent term χ_0, determined by fitting an equation, $\chi=C/T+\chi_0$.

One can expect electrical conductivity for the mixed valence state of the Co ions in the layered structure. The conductivity measurement was made on pressed disk specimens with dimension of 1.0 cm diameter and about 0.7 mm thickness. To ensure ohmic contact, we coated gold on both sides of the disk by sputtering method. The conductivity was measured along the direction perpendicular to the plane of the disk. The V-I plot showed a fairly good linear behavior in the region observed (0 – 1.0 V). The apparent conductivity determined from the profile for the sample before oxidation was $5x10^{-10}$ Scm^{-1}, on the contrary, that for the oxidized sample jumped up to $6x10^{-5}$ Scm^{-1}. The temperature dependence of conductivity of the oxidized sample showed a thermally activated one; the activation energy was estimated to be 0.43 eV in the temperature range, $303 < T/K < 343$. As the characterization method, the conductivity measurement is not suitable enough for these heterogeneous systems, though the jump in conductivity via oxidation would suggest the potentiality for use in electric device for this material.

Finally, we focus our attention to the nature of the hydrated sodium ions. It was found that Na^+ ion can be easily exchanged by alkaline and alkaline earth cations at room temperature. The amount of the cation exchange was determined by the AAS analysis for both the solid phase and the supernatant after ion exchange. It was ca. 160 meq. per 100 g sample, which slightly varied depending on the pH of the suspension. Although in the case of mono-valent cations and Ba^{2+} the basal spacing was retained around 1.96 nm, in cases of alkaline earth ions, an expansion of the interlayer space by about 0.3 nm, resulting in a basal spacing of 2.2-2.3 nm, was observed. This difference may have come from difference in the number of water molecules solvated around the cations [7].

COMPARISON WITH OTHER METALS

For the other transition metal species, Ni and Mn, we also examined that basically the same processing procedure gives isomorphous materials. The properties for the obtained layered nano-composites containing different transition metal oxides are summarized in Table IV. The main difference was found in the magnetic properties. The results were also compared with corresponding oxides containing alkaline ions, A_xMO_2 with edge-sharing octahedral layered structure: $NaCoO_2$ [6], $LiNiO_2$ [8] and Na_xMnO_2 (birnessite) [9]. The observed good correlation in magnetic parameters suggested that the spin states of the

intercalated transition metal oxides are similar to those of the corresponding layered oxides. The fact that although the inter-layer spacing between TM oxide layers are different, the magnetic parameters are quite similar suggests that the magnetic properties of these oxide layer are mainly determined not by inter-layer interaction but by intra-layer interaction.

Table IV. Comparison of structure and properties among transition metal oxide / clay nano-composites as well as corresponding layered oxides

TM	Basal spacing	Valence	Magnetic properties[a]		Magnetic properties of A_xMO_2	
	/ nm	of TM ions	$\mu_{eff}(TM)/\mu_B$	θ_p/K	$\mu_{eff}(TM)/\mu_B$	θ_p/K
Co	1.96	3.2	0.38	-	Temp.-independent[b]	
Ni	1.96	3.1	2.07	14	2.1[c]	26[c]
Mn	1.98	3.8	3.89	-40	4.1[d]	-50[d]

[a]The parameters were determined by fitting the data with a Curie-Weiss low: $\chi = C/(T-\theta_p)$ for Ni and Mn (50 < T/K < 300), and an equation $\chi = \chi_0 + C/T$ for Co (2 < T/K < 300).

[b]$NaCoO_2$ from ref.[6], [c]$LiNiO_2$ from ref. [8]

[d]$Na_xMnO_2nH_2O$ (birnessite) from ref. [9]; the θ_p was estimated the figure in the reference.

CONCLUSION

The room temperature processing using NaClO as the oxidizing reagent has succeeded the oxidation of transition metal hydroxide sheet inside the clay gallery. A new expanded structure with 1.96 nm periodicity along c-axis was evidenced by XRD associated with one-dimesional Fourier analysis. Magnetic properties were found to be similar to those of layered metal oxides, suggesting quite similar structure of the oxide sheets accommodated in the gallery of the clay. Furthermore, the observed electric conduction and ion exchange ability would give new potentialities of these materials.

ACKNOWLEDGEMENTS

We thank Dr. Jun-ichi Shimoyama of Tokyo University for the help of the magnetic susceptibility measurement. We also thank Mr. Sekimoto of Coop Chemical Co. Ltd. for kind offer of the smectite clay sample.

REFERENCES AND NOTE

[1] S.-J. Hwu, Chem. Mater. **10**, 2846 (1998)
[2] K. Ohtsuka, M. Suda, M. Tsunoda, M. Ono, M. Chem. Mater. **2**, 511 (1990)
[3] S. Yamanaka, G. W.Brindley, Clays Clay Miner. **26**, 21 (1978)
[4] G. W. Brindley, C. Kao, Clays Clay Miner. **28**, 435 (1980)
[5] The analysis was carried out by using the following equations, $I_{00l} = A \bullet Lp(\theta) \bullet |F_{00l}|^2$, where $Lp(\theta) = (1+\cos^2(2\theta))/(\sin^2(\theta)\cos(\theta))$, and A stands for a instrumental constant. The electorn density $\rho(z)$ was calculated by using a equation, $\rho(z) = \Sigma F_{00l}\cos(2\pi zl)$. The signs of *F*obs were phased with the calculated ones on the basis of the structure model.
[6] Von M. Jansen and R. Hoppe, Z. anorg. Allg. Chem. **408**, 104 (1974)
[7] R. Schollhorn, Ang. Chemie **19**, 983 (1980)
[8] J. N. Reimers, J. R. Dahn, J. E. Greendan, C. V. Stager, G. Liu, I. Davison, and U. Von Sacken, J. Sol. St. Chem. **102**, 542 (1993)
[9] F. Leroux, D. Guyomard, and Y. Piffard, Sol. St. Ionics **80**, 299 (1995)

Characterization, Properties and Applications of Nanophases and Nanocomposites

CATALYTIC ACTIVITY AND SURFACE CHARACTERIZATION STUDY OF Pd SUPPORTED ON NANOCRYSTALLINE AND POLYCRYSTALLINE CeO_2

GAR B. HOFLUND*, ZHENHUA LI**, TIMOTHY J. CAMPBELL***, WILLIAM S. EPLING****, HORST W. HAHN*****
*Department of Chemical Engineering, University of Florida, Gainesville, Florida 32611, USA
**Department of Chemical Engineering, Tianjin University, Tianjin 300072, PRC
***AFRL/MLQ, 139 Barnes Drive, Tyndall AFB, FL 32403-5323, USA
****Department of Chemical Engineering, Box 870203, The University of Alabama, Tuscaloosa, AL 35487, USA
*****Darmstadt University of Technology, FB 21-Materials Science Department, Thin Films Division, Petersenstrasse 23, 64287 Darmstadt, GERMANY

ABSTRACT

The catalytic activity of polycrystalline and nanocrystalline CeO_2-supported Pd ($Pd/pCeO_2$ and $Pd/nCeO_2$) has been determined as a function of temperature and Pd loading. While the untreated $nCeO_2$ support gives 50% methane conversion at 420°C, the untreated $pCeO_2$ support exhibits little activity under the conditions examined due to its low surface area. A Pd loading of 5 wt% increases the activity of $pCeO_2$ to 50% conversion at 260°C, while a 40 wt% Pd loading on $nCeO_2$ exhibits a relatively smaller activity increase, yielding 50% conversion at 240°C. On a mass basis the 40 wt% $Pd/nCeO_2$ catalyst is the most active tested in this study, but it is less active than the 5 wt% $Pd/pCeO_2$ catalyst on a surface-area basis. Furthermore, the activity of the 40 wt% $Pd/nCeO_2$ catalyst does not decrease during 100 hrs of exposure to CH_4 and O_2 at 250°C.

X-ray photoelectron spectroscopy (XPS) and ion scattering spectroscopy (ISS) have been used to characterize the surfaces of both bare supports and Pd-containing catalysts before and after exposure to reactor conditions. The XPS results reveal that the Pd surface concentration is more than an order of magnitude higher for 5 wt% $Pd/pCeO_2$ than for 5 wt% $Pd/nCeO_2$ due to the larger surface area of $nCeO_2$ and that the 40 wt% $Pd/nCeO_2$ catalyst has a lower Pd loading on a surface-area basis than the 5 wt% $Pd/pCeO_2$ catalyst. Most of the supported Pd is in the form of PdO, but higher PdO_2/PdO ratios are observed for both CeO_2 supports compared to Pd supported on ZrO_2 or Co_3O_4. Furthermore, a significant amount of metallic Pd forms on $Pd/nCeO_2$ but not on $Pd/pCeO_2$ during reaction. The nanocrystalline and polycrystalline CeO_2 behave differently chemically which is consistent with the fact that the nanocrystalline catalysts are less active on a surface-area basis. Accumulation of H_2O on the $Pd/pCeO_2$ surface during reaction is significant but not on the $Pd/nCeO_2$ surface. This suggests that the rate limiting step may be H_2O desorption on $Pd/pCeO_2$ while for Pd on $nCeO_2$ adsorption of methane appears to be the slow step. The ISS data indicate that the outermost atomic layer of $Pd/nCeO_2$ consists mostly of O and C, which is not the case for $Pd/pCeO_2$. Site blockage by these species may also contribute to the lower activity on a surface-area basis of $Pd/nCeO_2$ compared to $Pd/pCeO_2$.

INTRODUCTION

The use of natural gas as an alternative automotive fuel could potentially lead to reduced levels of CO_2, NO_x, and SO_x emissions and decreased reliance on imported oil (1). However, an obstacle to widespread use of natural gas as an automotive fuel is the need to eliminate unburned methane from engine exhaust streams because methane is a much more potent greenhouse gas than CO_2 (2). A catalytic converter could be used to reduce methane emissions to acceptable levels, provided that a catalyst can be developed with sufficient methane-oxidation activity and stability at engine exhaust stream temperatures. The three-way catalyst commonly used in automobiles is not very effective in this application (3).

Cerium dioxide has been studied as a support for automotive exhaust gas conversion catalysts (4-6) because it has a unique capacity for storage and release of oxygen during oxidation/reduction processes (4). Since polycrystalline cerium dioxide ($pCeO_2$) and

Mat. Res. Soc. Symp. Proc. Vol. 581 © 2000 Materials Research Society

nanocrystalline cerium dioxide ($nCeO_2$) differ significantly in specific surface area, they may perform differently as supports for methane oxidation catalysts. The methane oxidation activities of Al_2O_3-, ZrO_2-, Mn_3O_4-, Co_3O_4-, and $pCeO_2$-supported Pd catalysts have been studied, and all show significant activities at temperatures above 300°C (6,7) although long-term stabilities vary. Activities of 5 wt% Pd supported on $pCeO_2$ and $nCeO_2$ (prepared by e-beam evaporation, gas-phase condensation and post oxidation) were compared by Hahn et al. (6) and were found to be similar, although the surface Pd concentration on the $pCeO_2$ support is significantly larger than that for the $nCeO_2$ support. The methane oxidation activities of $nCeO_2$-supported Pd at loadings higher than 5 wt% were not studied.

In this present study the catalytic activity of polycrystalline and nanocrystalline ceria has been determined for methane oxidation as a function of temperature and Pd loading. X-ray photoelectron spectroscopy (XPS) and ion scattering spectroscopy (ISS) have been used to characterize the surface compositions of $pCeO_2$- and $nCeO_2$-supported Pd and to determine the effects of exposure to reactor conditions on these surfaces. The observed differences are correlated with the activities of $nCeO_2$- and $pCeO_2$-supported Pd catalysts in an effort to gain information about how these catalysts function.

EXPERIMENTAL

The polycrystalline ceria ($pCeO_2$, 99.9%) used in these studies was obtained from Aldrich, and nanocrystalline ceria ($nCeO_2$) was obtained from Nanophase, Inc. The Pd/CeO_2 catalysts were prepared by stirring the CeO_2 powders and $Pd(NO_3)_2$ together in distilled water, then heating to boil off excess water and followed by calcining the slurry in air at 500°C for 4 hrs. The bare supports were calcined in air at 280°C for 2 hrs prior to analysis by XPS and ISS. The specific surface areas of the supports and the as-prepared catalysts were determined by N_2 adsorption (BET).

Catalyst activity studies were performed using 100 mg of catalyst in a horizontal quartz tubular reactor with a feed gas consisting of 1.2% CH_4 and 12% O_2 in N_2 flowing at a total rate of 33 standard cubic centimeters per min (sccm) and a pressure of 16 psia. Activity versus temperature curves were obtained by maintaining constant catalyst bed temperature at each temperature to within ±3°C until a maximum activity was observed. An activity decay study was performed using 40 wt% $Pd/nCeO_2$ by maintaining a constant bed temperature of 250°C for 100 hrs with intermittent activity determination.

Bare support and catalyst powder samples were pressed into Al cups and inserted into the ultrahigh vacuum (UHV) chamber (base pressure of 10^{-11} Torr) for analysis by XPS and ISS. For XPS the double-pass cylindrical mirror analyzer (DPCMA, Perkin-Elmer PHI Model 25-255AR) was operated in the retarding mode. XPS survey spectra were collected at a pass energy of 50 eV and high-resolution spectra at a pass energy of 25 eV using Mg Kα excitation. ISS data were collected using 1-keV He^+ and by operating the DPCMA in the nonretarding mode with a scattering angle of 137 ± 6°. Both XPS and ISS data were collected using a digital pulse-counting circuit (8) combined with digital filtering and smoothing (9). XPS spectra were collected prior to ISS analysis for all samples because XPS is less destructive than ISS. The ISS data collection times were kept as short as possible to minimize ion-sputter damage.

RESULTS AND DISCUSSION

Methane conversion activities for $pCeO_2$ and $nCeO_2$ with various Pd weight loadings are shown in figure 1. Untreated $nCeO_2$ exhibits significant activity, which is at least partially due to its high surface area (table 1), with an initial onset of activity at about 300°C and a 50% conversion at 420°C. Untreated $pCeO_2$ exhibits little activity even above 400°C. A 5 wt% loading of Pd significantly increases the activity of $pCeO_2$, decreasing the initial activity temperature to 180°C and yielding 50% conversion at 260°C. The 5 wt% $Pd/nCeO_2$ is somewhat less active with a 50% conversion at 290°C. Increasing the Pd loading on $nCeO_2$ from 5 wt% to 20 wt% decreases the 50% conversion temperature to 260°C, nearly identical to the 5% $Pd/pCeO_2$. A further increase to 40 wt% $Pd/nCeO_2$ decreases the 50% conversion temperature to 240°C, and gives 100% conversion at 300°C. This is the highest activity on a catalyst mass basis observed in this study.

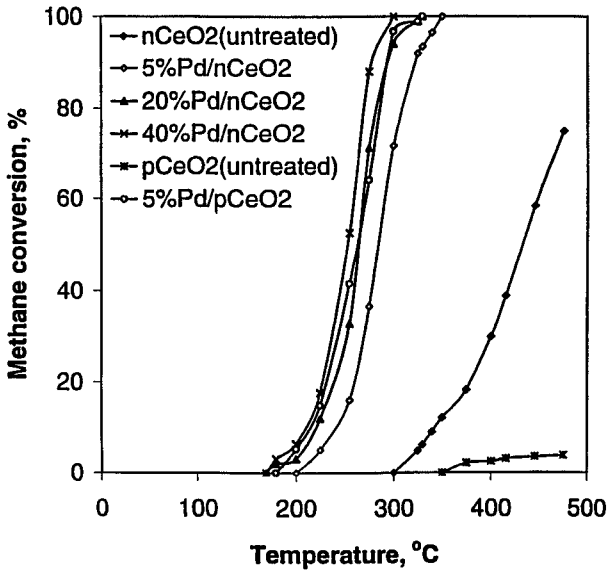


Figure 1. Methane conversion activities of untreated $pCeO_2$ and $nCeO_2$, 5 wt% Pd on $pCeO_2$ and 5, 20 and 40 wt% Pd on $nCeO_2$ as a function of temperature.

The results of an activity decay study using 40 wt% Pd/$nCeO_2$ at 250°C are shown in figure 2. The initial activity is about 60% conversion, and this increases to almost 70% over a period of 6000 min. A 5 wt% Pd/$pZrO_2$ catalyst exhibits a similar stability at 250°C, and both the Pd/$nCeO_2$ and Pd/$pZrO_2$ catalysts exhibit superior stability to Pd/Al_2O_3 catalysts at 250°C (7).

XPS survey spectra obtained from the as-prepared catalysts with various Pd loadings on $pCeO_2$ and $nCeO_2$ are shown in figures 3 and 4 respectively. The primary features include the O 1s, Pd 3d, C 1s, and Ce 3d and 4d, along with O, Pd, and Ce Auger peaks. The C 1s peak is barely discernable for the bare supports but increases with Pd loading indicating that hydrocarbons adsorb more readily on PdO than CeO_2 as discussed below. The fact that Pd-containing catalysts adsorb hydrocarbons more readily than ceria is consistent with their enhanced catalytic behavior since methane adsorption is a critical step in methane oxidation. The Pd 3d peak height increases faster with increasing Pd loading for $pCeO_2$ than for $nCeO_2$ which is consistent with the specific surface areas of the 5 wt% Pd-loaded catalysts and bare supports in table 1. A loading of 5 wt%

TABLE 1
BET Surface Areas

catalyst	treatment	surface area (m^2/g)
$pCeO_2$	none	1.5
5 wt% Pd/$pCeO_2$	calcined 280°C	7.5
$nCeO_2$	none	89
5 wt% Pd/$nCeO_2$	calcined 280°C	179

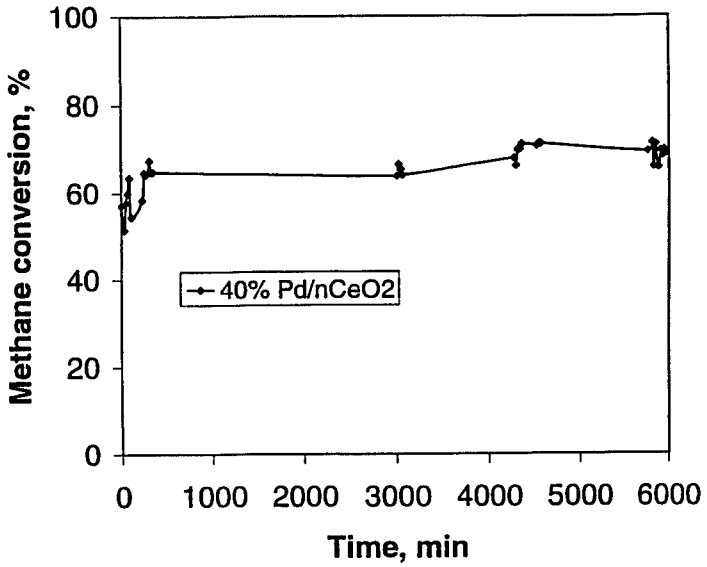


Figure 2. Methane conversion activity of the 40 wt% Pd/$nCeO_2$ catalyst as a function of time at 250°C.

Pd on $pCeO_2$ increases the specific surface area by a factor of five over that of the bare support. An increase has also been observed previously for Pd/Co_3O_4 catalysts (10). This increase could be due to an increase in surface roughness or the splitting up of larger particles by the impregnation process. Addition of 5 wt% Pd to $pCeO_2$ significantly diminishes the intensity of the Ce 3d, 4d, and Auger features relative to the bare support as shown in figure 3. This is the result of a matrix effect caused by coverage of the ceria support by Pd species. In contrast, a loading of 5 wt% Pd on $nCeO_2$ only doubles the specific surface area, and the intensity of the Ce XPS features for 5 wt% Pd/$nCeO_2$ shown in figure 4 are not significantly diminished relative to the bare support. The near-surface concentration of Pd is greater for 5 wt% Pd/$pCeO_2$ than for 5 wt% Pd/$nCeO_2$, as would be expected based on the surface areas of the bare supports. This concentration effect could at least partially explain the higher activity of 5 wt% Pd/$pCeO_2$ over 5 wt% Pd/$nCeO_2$ observed in figure 1. As the Pd loading is increased on $nCeO_2$, the Pd 3d features increase as expected. At a loading of 40 wt%, the survey spectrum becomes more similar to that obtained from the 5 wt% $pCeO_2$ catalyst but the areal Pd loading still is not as high.

High-resolution O 1s, Pd 3d, and C 1s XPS spectra obtained from untreated $pCeO_2$ and 5 wt% Pd/$pCeO_2$ before and after exposure to reactor conditions are shown in figure 5A, B and C respectively. The primary chemical state of oxygen for all three samples is CeO_2 as indicated by the peak at 529.3 eV in figure 5A. However, the presence of Pd results in the appearance of at least two more oxygen chemical states with features at 531.6 and 533.7 eV. The feature at 531.6 eV is due to O in PdO, and the shoulder at 533.7 eV is assigned as due to the presence of surface H_2O. Its intensity increases during reaction indicating that H_2O, which is one of the reaction products, accumulates on this surface. The Pd 3d spectra shown in figure 5B indicates that the primary form of Pd on the catalyst is PdO with a binding energy (BE) of 336.2 eV, but a small amount of PdO_2 is also apparent at a BE of 337.7 eV. The PdO_2/PdO ratio is greater than that for Pd catalysts supported on ZrO_2 (7) or Co_3O_4 (11). This ratio decreases during reaction but remains higher than for ZrO_2- or Co_3O_4-supported Pd catalysts. No structure due to metallic Pd is apparent in these spectra. The intensity of the C 1s peak increases during reaction, and the

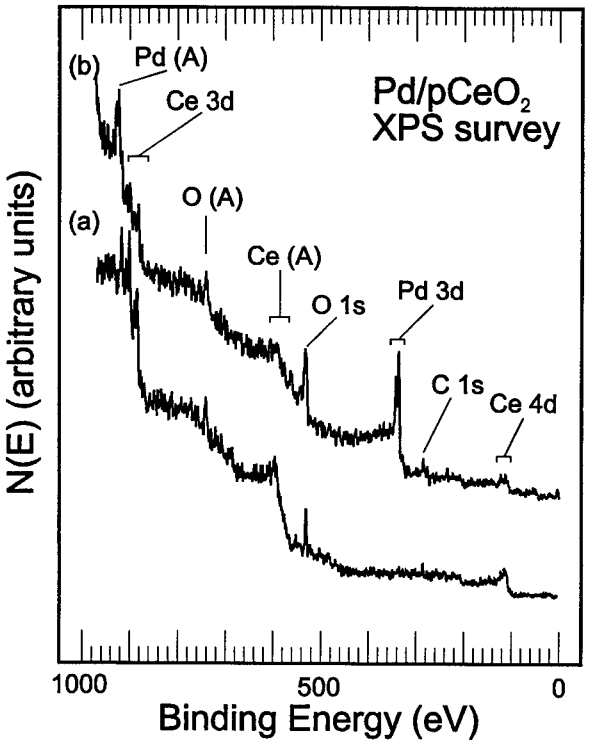


Figure 3. XPS survey spectra obtained from (a) untreated $pCeO_2$, and (b) 5 wt% $Pd/pCeO_2$ (fresh catalysts).

chemical state distribution changes. The spectrum shown in figure 5Cb consists of two contributions. The feature with a BE of 284.6 eV is due to C_xH_y species most likely adsorbed from the air. A shoulder has a BE of about 282.5 eV, which is in the range of carbides. This shoulder is most likely due to reactive C species which originally were hydrocarbon species but stripped of the hydrogen atoms. It is still present after reaction but smaller relative to the C_xH_y feature.

ISS data provide information about the outermost atomic layer of the sample surface in contrast to XPS which samples approximately 30 atomic layers beneath the sample surface. Therefore, ISS is a very important technique for characterization of catalysts because it probes the region of the solid where catalysis occurs (12). ISS spectra obtained from the bare $pCeO_2$ support, as-prepared 5 wt% $Pd/pCeO_2$, and the 5 wt% $Pd/pCeO_2$ catalyst after reaction are shown in figure 6a, b, and c respectively. The spectrum obtained from $pCeO_2$ consists of a large broad feature below an E/E_0 of 0.4 due to C and O. Although higher mass elements have higher ISS sensitivities, the Ce feature is very small indicating that the Ce is covered by C and O. The outermost atomic layer of the fresh 5 wt% Pd/CeO_2 catalyst consists of Pd, O and C with a small amount of Ce. The O concentration is larger for this surface relative to C compared to the bare surface as expected since the Pd is present as PdO. After reaction the Pd peak is larger relative to the C and O features indicating that most of the contamination species are cleaned off the surface during reaction. Also, a Ce shoulder is no longer apparent indicating that the Ce is covered by reactants and products, and the C peak is fairly well defined.

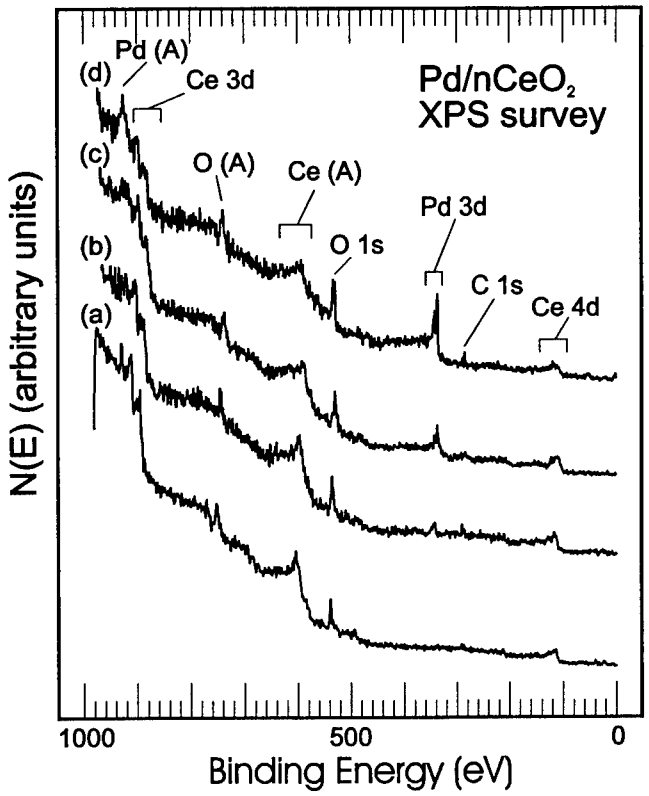


Figure 4. XPS survey spectra obtained from (a) untreated $nCeO_2$, (b) 5 wt% $Pd/nCeO_2$, (c) 20 wt% $Pd/nCeO_2$, and (d) 40 wt% $Pd/nCeO_2$ (fresh catalysts).

High-resolution O 1s, Pd 3d, and C 1s XPS spectra obtained from untreated $nCeO_2$ and 40 wt% $Pd/nCeO_2$ before and after reaction are shown in figure 7A, B and C respectively. Accumulation of H_2O with Pd loading is observed in figure 7Ab, similar to $pCeO_2$, but the intensity of the H_2O feature at 533.5 eV relative to the O 1s feature due to CeO_2 at 529.3 eV decreases during reaction for 40 wt% $Pd/nCeO_2$. The spectrum in figure 7Bb also exhibits an unusually large amount of PdO_2 relative to PdO, and the spectrum in figure 7Bc indicates that a large amount of metallic Pd forms in the near-surface region during reaction. The PdO_2 feature also becomes more well defined and less prominent with respect to the PdO and Pd features. A large metallic Pd feature has not been observed in previous studies of similar catalysts (7,11). According to XPS, a very small amount of C is present on the 40 wt% $Pd/nCeO_2$ catalyst after reaction, and the low BE feature, assigned above as due to a reactive form of adsorbed C, is not apparent in these spectra.

ISS spectra obtained from untreated $nCeO_2$ and 40 wt% $Pd/nCeO_2$ before and after reaction are shown in figure 8a, b and c respectively. No Ce signal is observed for the untreated $nCeO_2$ due to blocking primarily by O atoms. Unlike the bare $pCeO_2$, a large, well-resolved O peak is observed in the bare $nCeO_2$ ISS spectrum. This indicates that less C is present in the outermost atomic layer of $nCeO_2$. For the Pd-loaded surface, a feature due to C is apparent and the signal-to-

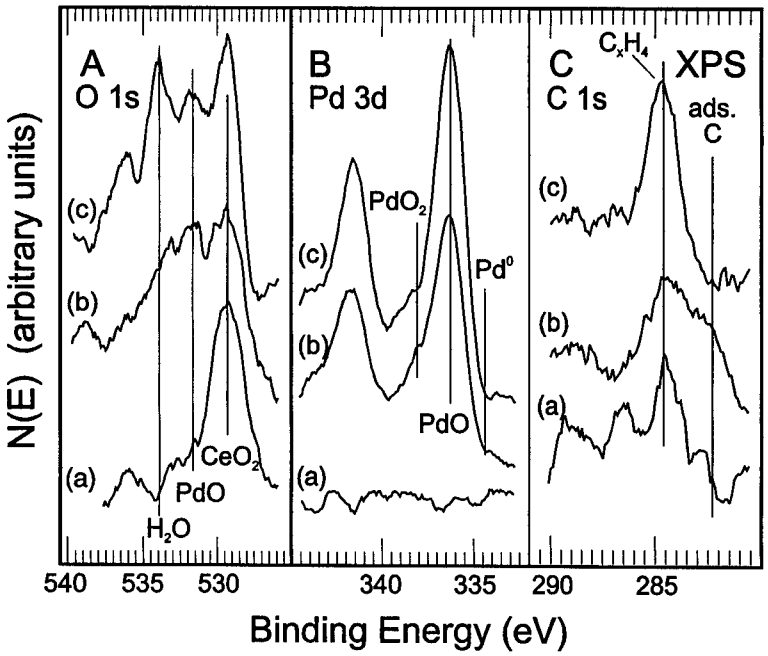


Figure 5. High-resolution XPS (A) O 1s, (B) Pd 3d, and (C) C 1s spectra obtained from (a) untreated $pCeO_2$, (b) fresh 5 wt% $Pd/pCeO_2$ and (c) 5 wt% $Pd/pCeO_2$ after exposure to reaction conditions.

noise ratio is lower. As expected, the Pd feature predominates and a very small Ce feature is apparent. After reaction most of the surface is covered by C and O. The signal-to-noise ratio is smaller, the Pd feature is smaller relative to the C and O features and an even smaller Ce feature is barely apparent. These ISS spectra are quite different than the ISS spectra obtained from 5 wt% $Pd/pCeO_2$ shown in figure 6. The large amounts of C and O on the 40 wt% $Pd/nCeO_2$ surface may result in catalytic site blockage and thereby explain why this surface is less active catalytically on an areal basis.

Previous studies (13,14) have shown that the XPS Ce 3d satellite peaks can be used to determine the relative amounts of Ce(III) and Ce(IV) oxidation states at a ceria surface. Specifically, using peak assignments and notation from Burroughs et al. (13), reduction of Ce(IV) to Ce(III) is accompanied by a decrease in the Ce 3d structures v''' and u''' and a corresponding increase in the v' and u' structures. The XPS Ce 3d spectra obtained from untreated $pCeO_2$ and 5 wt% $Pd/pCeO_2$ are shown in figure 9a and b respectively. The intensities of the v''' and u''' peaks are decreased relative to the u' peak with Pd loading indicating an increase in the Ce(III)/Ce(IV) ratio or reduction of CeO_2 to Ce_2O_3. The v' peak is broad and not well defined. This chemical-state change in the Ce may be due to a chemical interaction with the Pd. The Ce 3d spectra obtained from untreated $nCeO_2$ and 40 wt% $Pd/nCeO_2$ are shown in figure 9c and d respectively. Significant changes are not apparent in this case suggesting that a chemical alteration of the Ce due to an interaction with Pd does not occur for 40 wt% $Pd/nCeO_2$. A chemical interaction between Ce and Pd would also influence the chemical and catalytic behavior of the Pd. This interaction may be the reason that the ISS spectra obtained from the 5 wt% $Pd/pCeO_2$ and 40 wt% $Pd/nCeO_2$ are so different: i.e., the Ce-Pd interaction results in the Pd not being covered by C and O thus retaining a high catalytic activity. This stronger Ce-Pd interaction also may prevent

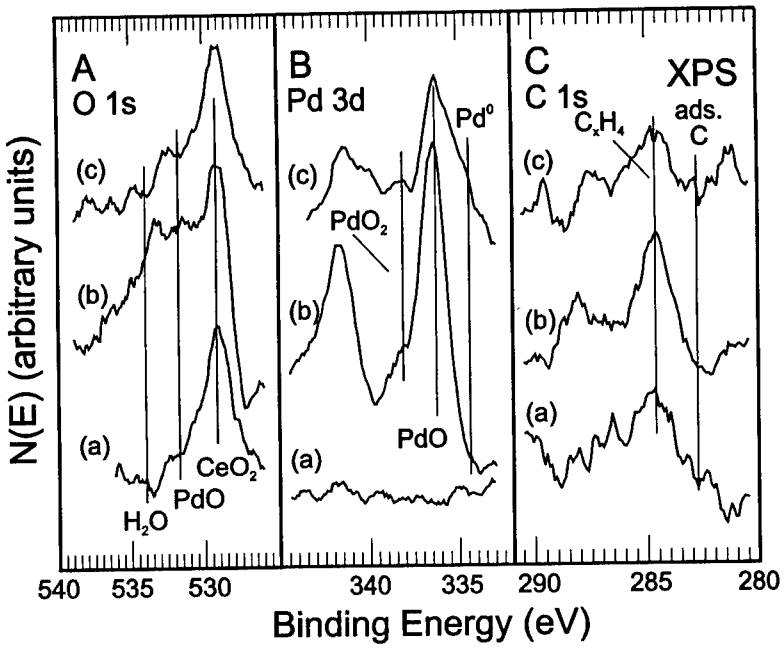


Figure 6. High-resolution XPS (A) O 1s, (B) Pd 3d, and (C) C 1s spectra obtained from (a) untreated $nCeO_2$, (b) fresh 40 wt% $Pd/nCeO_2$ and (c) 40 wt% $Pd/nCeO_2$ after exposure to reaction conditions.

the formation of Pd metal on $pCeO_2$. Another possibility is that the PdO is present on $nCeO_2$ as larger agglomerates so that not all of the Pd can interact with the ceria.

A mechanism has been proposed for methane oxidation on Pd/ZrO_2 and Pd/Co_3O_4 in which methane adsorbs dissociatively yielding surface methoxy and hydroxyl groups (7,11). Sequential loss of H atoms from the methoxy groups form more hydroxyl groups and water along with a reactive C species, which combines with surface O and desorbs as CO_2 product. Formation of surface CO and $CO_3^=$ groups during reaction on Pd/ZrO_2 has been reported (7), and accumulation of surface hydroxyl and oxyhydroxide species during methane oxidation on Pd/Co_3O_4 has been observed (11). The data described above for Pd/CeO_2 suggest that a similar mechanism may be operative but that the rates of the various steps of the process are different for $pCeO_2$ and $nCeO_2$. Accumulation of H_2O during reaction on the surface of $Pd/pCeO_2$ indicates that H_2O desorption may be the rate limiting step for this catalyst. Significant H_2O accumulation is not observed for methane oxidation over $Pd/nCeO_2$. The increase in the PdO_2/PdO ratio and the ISS data indicate accumulation of O on the surface during exposure to reaction conditions suggesting that methane adsorption may be the rate limiting step for the $Pd/nCeO_2$-catalyzed process. The lower activity on a surface-area basis of $Pd/nCeO_2$ may be due to site blockage caused by a minimal interaction between Ce and Pd on this surface.

SUMMARY

The catalytic activity of Pd supported on $pCeO_2$ and $nCeO_2$ for methane oxidation has been determined as a function of temperature and Pd loading. The activities of the untreated supports are quite different: $nCeO_2$ yields 50% conversion at 420°C for the conditions examined while

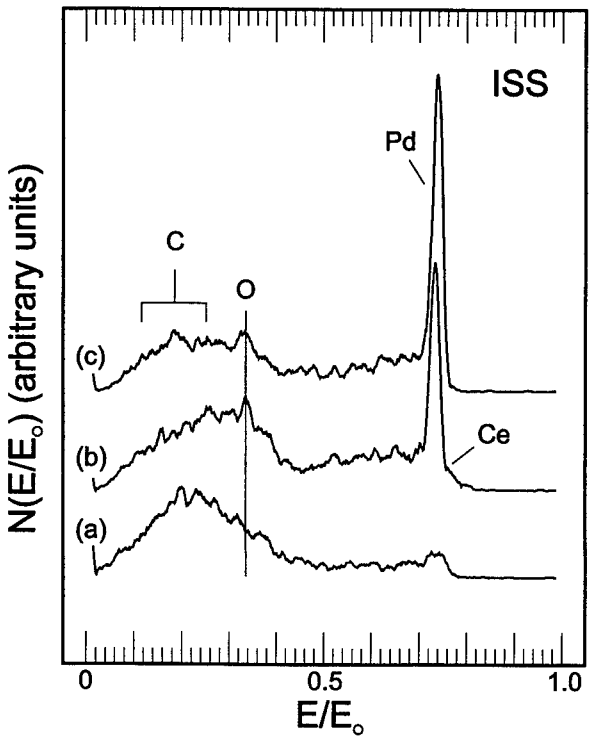


Figure 7. ISS spectra obtained from (a) untreated $pCeO_2$, (b) fresh 5 wt% $Pd/pCeO_2$ and (c) 5 wt% $Pd/pCeO_2$ after exposure to reactor conditions.

$pCeO_2$ exhibits little activity up to 500°C, but the surface area of $nCeO_2$ is 60 times greater than that of $pCeO_2$. A Pd loading of 5 wt% increases the activity of $pCeO_2$ to 50% conversion at 260°C. Supporting Pd on $nCeO_2$ has less of an effect yielding 50% conversion at 240°C for 40 wt% $Pd/nCeO_2$. The activity increases monotonically from 0 to 40 wt% Pd loading. On an areal basis the catalytic activity of 5 wt% $Pd/pCeO_2$ is much higher than that of 40 wt% $Pd/nCeO_2$ although the latter is more active on a mass basis due to its larger surface area.

XPS survey spectra indicate that the surface Pd concentration of 5 wt% $Pd/pCeO_2$ is more than an order of magnitude greater than that of 5 wt% $Pd/nCeO_2$ on an areal basis as expected based on the surface area differences. High resolution XPS data reveal significant accumulation of H_2O on the 5 wt% $Pd/pCeO_2$ surface during reaction, but not to such an extent on the 40 wt% $Pd/nCeO_2$ surface. High PdO_2/PdO ratios are observed for both $Pd/nCeO_2$ and $Pd/pCeO_2$ surfaces before and after exposure to reaction conditions. Evidence that the Ce(III)/Ce(IV) ratio of the $pCeO_2$ support increases with Pd loading is observed, suggesting that the increase in activity with Pd loading may be related to a change in Ce oxidation state caused by an interaction with the Pd. The $nCeO_2$ does not exhibit a similar change in oxidation state with Pd loading. For $Pd/pCeO_2$ the desorption of H_2O appears to be the rate limiting step while accumulation of O on the surface during reaction suggests that adsorption of methane may be rate limiting on $Pd/nCeO_2$. ISS data indicate that much more C- and O-containing species accumulate on the $Pd/nCeO_2$ surface compared to the $Pd/pCeO_2$ surface. Although the $Pd/nCeO_2$ catalysts are more active on a mass

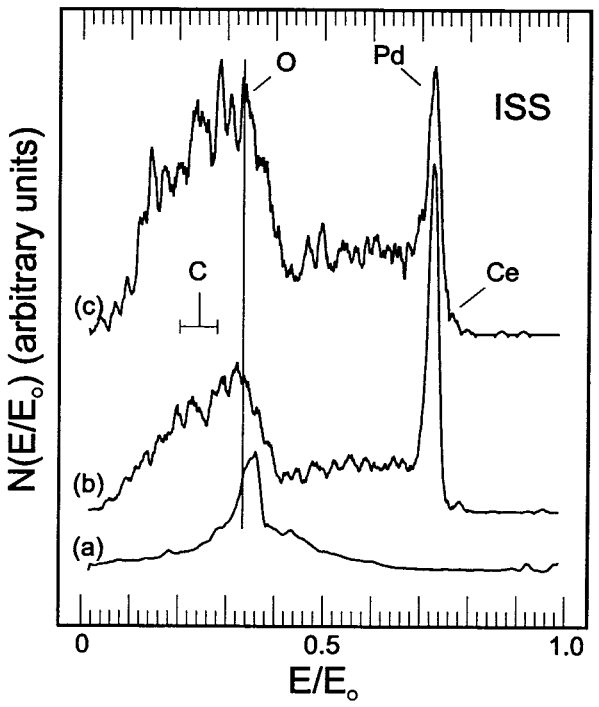


Figure 8. ISS spectra obtained from (a) untreated $nCeO_2$, (b) fresh 40 wt% $Pd/nCeO_2$, and (c) 40 wt% $Pd/nCeO_2$ after exposure to reactor conditions.

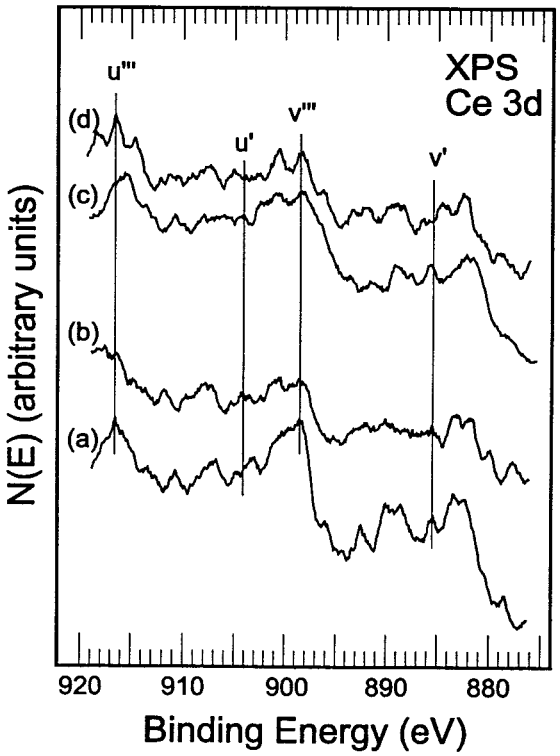


Figure 9. High-resolution Ce 3d spectra obtained from (a) untreated $pCeO_2$, (b) fresh 5 wt% $Pd/pCeO_2$, (c) untreated $nCeO_2$, and (d) fresh 40 wt% $Pd/nCeO_2$.

basis than the $Pd/pCeO_2$ catalysts, they are less active on a surface area basis, which may be due to site blockage by the C- and O-containing species on the 40 wt% $Pd/nCeO_2$. Significant differences are observed using XPS and ISS between the chemistry at the $nCeO_2$ and $pCeO_2$ surfaces which are related to differences in catalytic behavior.

REFERENCES

1. L.D. Pfefferle and W.C. Pfefferle, Catal. Rev. Sci. Eng. **29**, 219 (1987).
2. E.S. Rubin, R.N. Cooper, R.A. Frosch, T.H. Lee, G. Marland, A.H. Rosenfield, and D.D. Stine, Science **257**, 148 (1992).
3. S.H. Cadle, P.A. Mulawa, D.L. Hilden and R. Halsall, "Exhaust Emissions from Dual-Fuel Vehicles using Compressed Natural Gas and Gasoline," presented to the Air and Water Management Association, Pittsburgh, PA, 1990.
4. J.C. Summers and A. Ausen, J. Catal. **58**, 131 (1979).
5. K.C. Taylor, *Catalysis, Science and Technology*, edited by J.R. Anderson and M. Boudart (Springer Verlag **5**, Berlin, 1984) pp.119.
6. H.W. Hahn, H. Hesemann, W.S. Epling and G.B. Hoflund, in *Proc. Fall 1997 MRS Meeting: Rec. Adv. Catal. Mater.*, edited by N.M. Rodriguez, S.L. Soled and J. Hubek **497**, 35 (1998).
7. W.S. Epling and G.B. Hoflund, J. Catal. **182**, 5 (1999).
8. R.E. Gilbert, D.F. Cox, and G.B. Hoflund, Rev. Sci. Instrum. **52**, 1281 (1982).
9. A. Savitsky and M.K.E. Golay, Anal. Chem. **36**, 1627 (1964).
10. Z.-H. Li and G.B. Hoflund, Reac. Kin. Catal. Lett. **66**, 367 (1999).
11. T.J. Campbell, Z.-H. Li, J.T. Wolan, and G.B. Hoflund, to be published.
12. G.B. Hoflund, in *Handbook of Surface and Interface Analysis: Methods in Problem Solving*, edited by J.C. Rivière and S. Myhra (Marcel Dekker, Inc., New York, NY, 1998) pp. 57.
13. P. Burroughs, A. Hamnett, A.F. Orchard, and G. Thornton, J.C.S. Dalton, 1686 (1976).
14. M. Romeo, K. Bak, J. El Fallah, F. Le Normand, and L. Hillaire, Surf. Inter. Anal. **20**, 508 (1993).

ELECTRICAL RESISTIVITY AS A CHARACTERIZATION TOOL FOR NANOCRYSTALLINE METALS

J.L. McCrea*, K.T. Aust*, G. Palumbo** and U. Erb*
*Department of Metallurgy and Materials Science, University of Toronto, Toronto, ON, Canada M5S 3E4
**Integran Technologies Inc, 1 Meridian Rd., Toronto, ON, Canada M9W 4Z6

ABSTRACT

The electrical resistivity as a function of temperature (4K to 673K) of several electrodeposited nanocrystalline materials (Ni, Ni-Fe, Co) has been examined. The contribution of the grain boundaries to the electrical resistivity was quantified in terms of a specific grain boundary resistivity, which was found to be similar to previously reported values of specific grain boundary resistivity for copper and aluminum obtained from studies involving polycrystalline materials. In the high temperature range, the resistivity of the nanocrystalline samples was monitored as a function of time. The observed time dependence of the resistivity at elevated temperatures was correlated to microstructural changes in the material. The study has shown that electrical resistivity is an excellent characterization tool for nanocrystalline materials giving useful information regarding grain size and degree of thermal stability, as well as some insight into the grain growth kinetics at various temperatures.

INTRODUCTION

Grain boundaries have long been known to affect the electrical properties of metals [1]. Conventional polycrystalline metals (grain size > 1μm) contain a relatively low volume fraction of grain boundaries and therefore their effects on the electrical resistivity is only significant at low temperatures [2,3,4,5]. In the case of nanocrystalline materials (grain size < 100 nm), however, the grain boundary volume fraction can increase to levels that are comparable to that of the crystalline component and thus the effects of the grain boundaries quickly become a significant factor. As such, an increase in the electrical resistivity of various nanocrystalline materials has been reported even at room temperature [6,7,8,9,10].

In early studies using polycrystalline copper and aluminum a contribution to the overall electrical resistivity that was proportional to the grain boundary area per unit volume was found [2,3,4]. The incremental increase in the electrical resistivity caused by the grain boundary area per unit volume was referred to as the specific grain boundary resistivity (SGBR). In a later study by Nakamichi et al. [5] bicrystals of aluminum were used to determine the SGBR of general and special grain boundaries. Table I presents the results from several previous studies.

Earlier studies on nanocrystalline materials have indicated an increase in electrical resistivity as a result of the increased volume fraction of grain boundaries. The relationship between grain boundary area and the electrical resistivity, however, has yet to be investigated to determine the SGBR of a material in the nanocrystalline state. In this light, the focus of the present work has been to examine the effects of grain boundaries on the electrical resistivity of various electrodeposited nanocrystalline metals with the objective of developing a relationship between the grain size and the resistivity. The overall objective of this work is to quantify the effects of the boundaries so that electrical resistivity can be used as a rapid and inexpensive structural characterization tool for nanocrystalline materials.

Mat. Res. Soc. Symp. Proc. Vol. 581 © 2000 Materials Research Society

Table I. Specific grain boundary resistivities (SGBR) for various polycrystalline materials.

Material	SGBR	Reference
General Boundaries		
Copper	$3.12 \times 10^{-12}\ \Omega cm^2$	[2]
Aluminum	$2.45 \times 10^{-12}\ \Omega cm^2$	[2]
Aluminum	$2.40 \times 10^{-12}\ \Omega cm^2$	[3]
Aluminum	$3.26 \times 10^{-12}\ \Omega cm^2$	[5]
Special Boundaries		
Copper (Twin Boundary, Σ3)	$1.5 \times 10^{-12}\ \Omega cm^2$	[4]
Aluminum (Twin Boundary, Σ3)	$1.48 \times 10^{-12}\ \Omega cm^2$	[5]

EXPERIMENTAL

The bulk nanocrystalline nickel (fcc), cobalt (hcp) and nickel-iron (disordered fcc) materials tested in the present study were produced by an electrodeposition process described elsewhere [11,12]. Specimens were electrodeposited onto a titanium substrate to a uniform thickness (between 30 and 150μm) and subsequently stripped for structural characterization and electrical measurements on free-standing, deformation-free samples. For the nickel and cobalt materials the electroplating parameters were varied to produce specimens with mean grain sizes between 10 and 55nm. For the Ni-Fe samples a range of grain sizes was obtained through various annealing treatments. The average grain size for the nickel and nickel iron alloys was determined using X-ray line broadening and Scherrer's method [13]. TEM micrographs were used to determine the average grain size for the cobalt samples. Electrical resistivity measurements were made using a four-point probe between 4 and 300K. Isothermal high temperature electrical resistivities as a function of annealing time for Ni-Fe were measured in a salt bath.

RESULTS

Determining Specific Grain Boundary Resistivity

An example for the temperature dependence of the electrical resistivity of various nanocrystalline materials for the case of nickel ranging in grain size from 22 nm to 300 μm is shown in figure 1. As expected, the curves show an increase in the electrical resistivity with decreasing grain size. Figure 2 plots the electrical resistivity of the various nickel samples against the grain boundary area per unit volume at 4 K and 295 K. The grain boundary surface area per unit volume (S/V) was calculated using a tetrakaidecahedron as the grain shape which gives a S/V of 2.37/d, where d is the average grain diameter [14]. The SGBRs determined for nickel, cobalt and various nickel-iron alloys at 4 K are given in table II.

Table II. Specific grain boundary resistivities determined from nanocrystalline samples at 4K.

Material	Grain Size Range	SGBR
Nickel	17nm – 55 nm	$2.82 \times 10^{-12}\ \Omega cm$
Cobalt	10nm – 30 nm	$3.26 \times 10^{-12}\ \Omega cm$
Ni- 16% Fe	15nm – 300μm	$3.01 \times 10^{-12}\ \Omega cm$
Ni- 31% Fe	14nm – 300μm	$3.09 \times 10^{-12}\ \Omega cm$
Ni- 34% Fe	13nm – 300μm	$2.99 \times 10^{-12}\ \Omega cm$

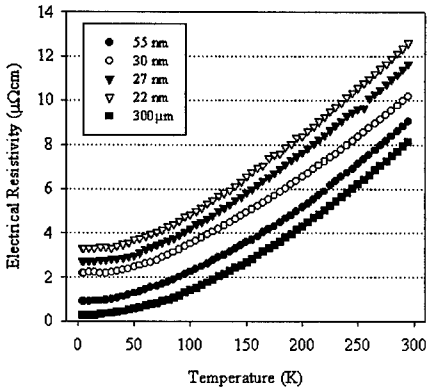


Figure 1. Temperature dependence of the electrical resistivity of nickel down to 4 K.

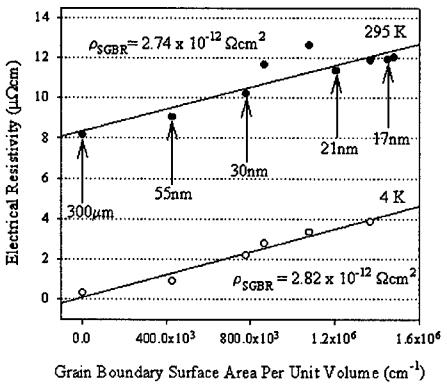


Figure 2. Observed variation of the electrical resistivity of nickel as a function of grain boundary surface area per unit volume.

The similarity between the specific grain boundary resistivities determined from nanocrystalline materials in the present study and those previously determined using conventional polycrystalline materials and bicrystals, bring out two important points. First, the specific grain boundary resistivity gives a relative value for the electron scattering power of a grain boundary, averaged over all the grain boundaries in the material. As this value is similar for SGBR's determined from polycrystalline and nanocrystalline materials, it indicates that in terms of electron scattering, the grain boundaries in electrodeposited nanocrystalline materials are virtually identical to grain boundaries in polycrystalline materials. This supports previous studies on the structure of grain boundaries in nanocrystalline materials using high resolution electron microscopy (HREM), which found the structure of grain boundaries in a nanocrystalline Ni-P alloy, also produced by electrodeposition, to be similar to the structure of grain boundaries in conventional polycrystalline materials [15]. Second, the similarity of the SGBR between the various materials also indicates that regardless of the composition of the material, the SGBR is very similar, suggesting that the scattering power of a grain boundary is similar in various materials, regardless of chemistry and crystal structure (fcc versus hcp in this case).

The total electrical resistivity of a material can be expressed as follows [16]:

$$\rho_{Total} = \rho_o + \rho_{SGBR}(S/V) \qquad (1)$$

where ρ_{Total} is the total electrical resistivity, ρ_o is the resistivity of the single crystal of the material (including effects due to temperature, solute, dislocations, etc.), ρ_{SGBR}(is the specific grain boundary resistivity, and S/V is the grain boundary surface area per unit volume. Figure 3 plots the electrical resistivity as a function of grain size according to equation 1. The main conclusion that can be made from this graph is that the effect of the grain boundaries on the electrical resistivity only becomes significant at grain sizes below ~100nm. Above 100nm grain size the resistivity is not significantly changed.

Estimating Grain Size from the Electrical Resistivity

If an estimate can be made for the electrical resistivity of the single crystalline material (ρ_o), then the measured electrical resistivity of a nanocrystalline material can be used to

estimate the average grain size through the use of equation 1. Figure 4 graphs the average grain size determined from line broadening in X-ray diffraction against the average grain size determined using the measured electrical resistivity at 295 K and equation 1 for an electrodeposited nanocrystalline Ni~30%Fe alloy that has undergone various annealing treatments producing a range of grain sizes. The remarkable correlation between the estimated grain sizes from the two methods shows that below 100nm the electrical resistivity is very sensitive to grain size and thus can be effectively used to determine the average grain size.

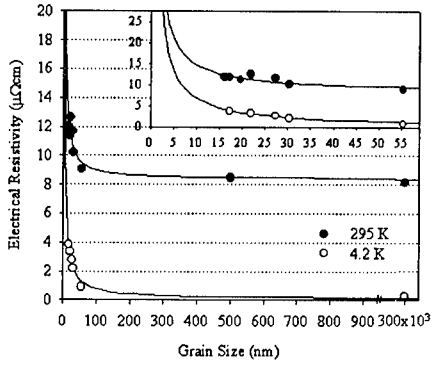


Figure 3. The measured electrical resistivity of Ni as a function of grain size at 4.2 and 295 K. The solid line represents the predicted grain size using equation 1.

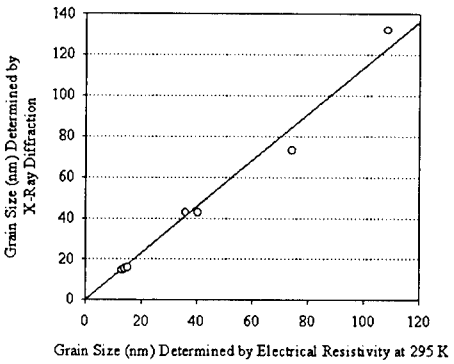


Figure 4. Grain size as determined by X-ray diffraction compared with the grain size as determined by the electrical resistivity for various Ni-Fe samples

Assessing the Thermal Stability of Nanocrystals

As the electrical resistivity is very sensitive to grain size for grain sizes under 100nm, any changes in grain size would thus result in a change in the measured electrical resistivity. As such, the electrical resistivity has been shown to be an in-situ indirect method for monitoring changes in grain size at elevated temperatures. Figure 5 shows the results of preliminary measurements of electrical resistivity as a function of annealing time at various temperatures for nanocrystalline Ni~30% Fe with a starting grain size of 10 nm. The curves show that the electrical resistivity decreases with time at temperatures above 200°C. The rate of the change increases with increasing temperature. Through equation 1, the change in electrical resistivity can be related to a change in the average grain size. Assuming normal grain growth, growth kinetics can be described by equation 2 [17]:

$$D_{avg}^2 - D_o^2 = Kt \qquad (2)$$

where D_{avg} is the average grain size after time t, D_o is the starting grain size. K is a proportionality constant which varies with temperature often described by the Arrhenius equation:

$$K(T) = A\exp(-E/k_BT) \qquad (3)$$

where A is the preexponential factor, E is the activation energy and k_B is Boltzman's constant.

Figure 6 graphs $\ln(D_{avg}^2 - D_o^2/t)$ against $1/k_BT$, in accordance with equations 2 and 3 in an attempt to estimate the activation energy for grain growth for the nanocrystalline Ni-30% Fe with a starting grain size of 10nm. The activation energy, using this method, was determined

to be 1.77eV. A previous study on the thermal stability of a nanocrystalline Ni-20%Fe alloy with a starting grain size of 15nm, gave an activation energy of 2.53eV determined using conventional differential scanning calorimetery (DSC) measurements [18]. While the value in the present study is lower, a direct comparison is difficult to make as both the composition of the alloy and the starting grain size are different. Other factors such as ordering of this alloy during grain growth and type of grain growth (normal vs. abnormal) must also be considered in future studies.

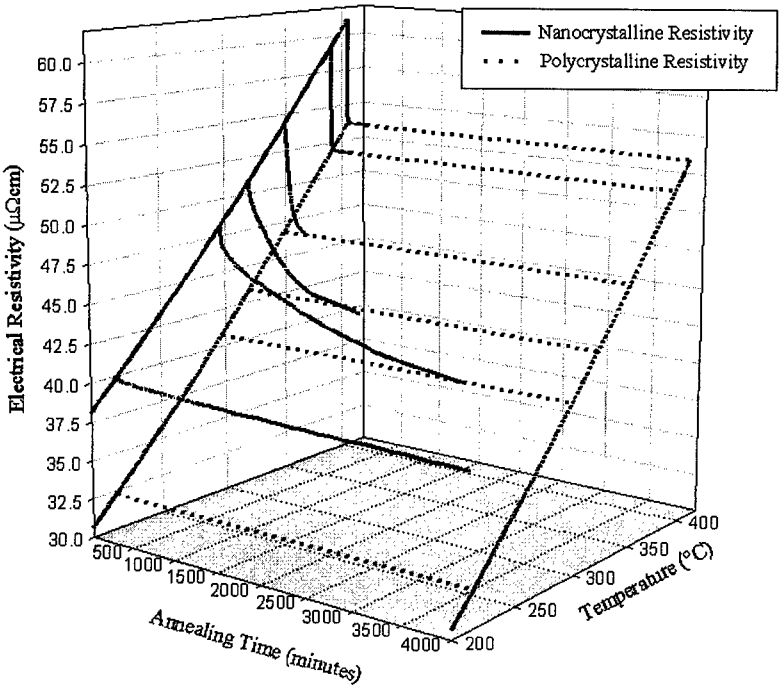


Figure 5. The electrical resistivity of nanocrystalline Ni-30%Fe as a function of annealing time and temperature.

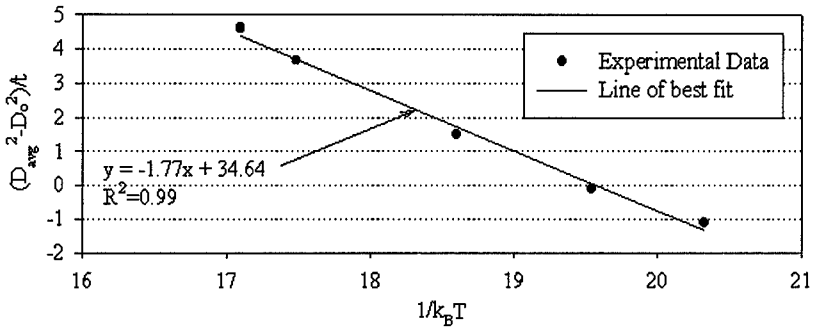


Figure 6. Determination of grain growth activation energy, E, for 10nm Ni-30%Fe, using D_{avg}=20nm and D_o=10nm based on equations 2 and 3.

CONCLUSIONS

The electrical resistivity has proved to be a very useful tool for the indirect structural characterization of nanocrystalline materials. The specific grain boundary resistivity determined using nanocrystalline materials was found to be similar to those previously determined using conventional polycrystalline materials, indicating that there is little difference between the grain boundaries in polycrystalline and nanocrystalline materials as far as electron scattering is concerned. Estimating the average grain size using the specific grain boundary resistivity was shown to be a comparable method to the line broadening method in X-ray diffraction. Preliminary results have shown that electrical resistivity measurements at elevated temperatures can be used to obtain useful information regarding thermal stability as well as the activation energy for grain growth in nanocrystalline materials.

ACKNOWLEDGMENTS

Financial support by the Natural Sciences and Engineering Research Council of Canada, Ontario Hydro and Ontario Graduate Scholarships Program is gratefully acknowledged.

REFERENCES

1. Seeger, A. and Schottky, G., Acta Met. **7,** p. 495 (1959).
2. Andrews, P.V., West, M.B. and Robenson, C.R., Phil. Mag. **19**, p. 887 (1969).
3. Kasen, M.B., Phil. Mag. **21**, p. 599 (1970).
4. Gangulee, A., J. Appl. Phys. **43** pp. 867-873 (1972).
5. Nakamichi, I., J. Sci. Hiroshima Univ. **54A**, p. 49 (1990).
6. Aus, M.J., Szpunar, B., Erb, U., El-Sherik, A.M., Palumbo, G. and Aust, K.T., J. Appl. Phys. **75**, p. 3632 (1994).
7. Aus, M.J., Szpunar, B., Erb, U., Palumbo, G. and Aust, K.T., Mat. Res. Soc. Symp. Proc. **318**, pp. 39-44 (1994).
8. Gleiter, H., Prog. Mater. Sci. **33**, pp. 223-315 (1989).
9. Bakonyi, I., Toth-Kadar, E., Tarnoczi, T., Varga, L.K., Cziraki, A., Gerocs, I. and Fogarassy, B., NanoStr. Mat. **3**, pp. 155-161 (1993).
10. Bakonyi, I., Toth-Kadar, E., Toth, J., Tarnoczi, T. and Cziraki, A. in *Processing and Properties of Nanocrystalline Materials*, C. Suryanarayana, J. Singh and F.H. Froes (eds.) (TMS) pp. 465-476 (1996).
11. Erb, U. and El-Sherik, A.M., US Patent No. 5 353 266 (October 1994).
12. Erb, U., El-Sherik, A.M., Cheung, C. and Aus, M.J., US Patent No. 5 433 797 (July 1995).
13. Cullity, B. D., *The Elements of X-Ray Diffraction*, 2nd ed. (Addison-Wesley Publishing Co., Don Mills, Ontario, 1978), p. 102.
14. DeHoff, R.T. and Rhines, F., *Quantitative Microscopy*, (McGraw-Hill, New York, 1968).
15. Mehta, S.C., Smith, D.A. and Erb, U., Mater. Sci. Eng. **A204**, pp. 227-232 (1995).
16. McCrea, J.L., Ph.D. Thesis, In Progress (1999).
17. Porter, D.A. and Easterling, K.E., *Phase Transformations in Metals and Alloys*, 2nd ed. (Chapman & Hall, New York, 1992), p. 139.
18. Turi, T., Ph.D. Thesis, Queen's University, Kingston, Canada (1997).

CHARACTERIZATION OF VOIDS IN RUTILE NANOPARTICLES BY TRANSMISSION ELECTRON MICROSCOPY

S. TURNER
Surface and Microanalysis Science Division, Chemical Science and Technology Laboratory, National Institute of Standards and Technology, Gaithersburg, MD 20899, shirley.turner@nist.gov

ABSTRACT

Rutile nanoparticles containing voids or cavities have been characterized using transmission electron microscopy. The general morphology of the voids has been determined from images of nanoparticles in different orientations. In general, the longest dimension is along the c axis of rutile. Many of the voids show a prismatic morphology with dipyramid terminations. The prism consists of primarily four {110} faces with rounded or faceted corners between the primary faces. The pyramidal terminations can appear ovoid or faceted. A major facet plane of the pyramids is (101). A model consistent with the morphology of many voids in rutile nanoparticles is proposed.

INTRODUCTION

Characterization of the morphology and microstructures of nanoparticles is important in understanding the properties of these materials and for the development of potential new applications of the materials. In this study, TiO_2 nanoparticles containing voids are characterized. TiO_2 nanoparticles have been the subject of considerable interest in part because TiO_2 can be used as a photocatalyst for dissociation of water, organic compounds and other compounds [1-3]. It can also be used to form ceramic, microporous membranes [4], to decrease the sintering temperature of titania ceramics [5], and, potentially, as coatings on surgical implants [6].

In previous work [7], it was shown that some rutile nanoparticles contain central inclusions. These inclusions were characterized as voids using electron holography. Similar cavities have been noted in palladium nanoparticles [8-10]. Faceted cavities have also been found in larger-grained material and have been termed negative crystals. Negative crystals form in β-V_4As_3 upon exposure to the electron beam of a transmission electron microscope (TEM) [11] and have been found in TiO_2 (B) crystals formed from $K_2Ti_4O_9$ precursor material [12]. Faceted cavities in sapphire form at the tips of indentation cracks during annealing [13].

The morphology of cavities in materials is of interest in determining volume changes if the host material is a transformation product from an unknown precursor. The morphology is also of interest in studies of the surface energies of crystals [13]. The morphology of faceted cavities in bulk materials has been studied by preparing the sample perpendicular to crystallographic directions of interest so that expected facets are viewed edge on [13]. Determination of morphology of cavities in nanoparticles is less straightforward as the nanoparticles are typically randomly oriented on a transmission

Mat. Res. Soc. Symp. Proc. Vol. 581 © 2000 Materials Research Society

electron microscope (TEM) grid. TEM imaging and electron holography has been used to show the presence of facets in palladium nanoparticles [8-10], however, the morphology of the faceted cavities in the palladium nanoparticles has not been fully described. In this work, the morphology of the rutile material defining the voids is characterized using selected area electron diffraction (SAED) and imaging. A three-dimensional model consistent with the observed morphology for the cavities is proposed.

EXPERIMENT

TiO_2 nanoparticles were generated in a flame burner system [7]. Titanium isopropoxide was aerosolized from solution and then oxidized in a flame fueled by oxygen and hydrogen. The temperature of the flame ranged from approximately 2000-2500 K and was varied by changing the flow rate of the hydrogen gas. Particles were collected at three different temperatures of the flame. Particles for characterization by transmission electron microscopy were collected by insertion of carbon-coated grids at 5 and 10 centimeters above the base of the flame.

The transmission electron microscopy was performed on a Philips CM30[1] TEM equipped with an energy dispersive analyzer. Bright-field imaging, dark field imaging and SAED were used to characterize particles. The microscope was operated at either 100 kV or 300 kV. A Gatan slow-scan CCD camera was used to collect images. Images were recorded using DigitalMicrograph software. Magnifications were calibrated using National Institute of Standards and Technology (NIST) Standard Reference Material (SRM) 1963.

Determination of the morphology of the cavities requires tilting experiments in the electron microscope. Double tilt holders were used with an x tilt angle of $\pm 45^{\circ}$ and a y tilt of $\pm 30^{\circ}$. The starting orientation of the particle on the carbon grid is critical to the orientations that can be obtained by tilting. A most useful starting orientation is when the c axis of rutile is aligned parallel to the x tilt axis of the TEM sample holder to allow for tilting around rutile [001]. To better reveal the structure of internal cavities, the particles were imaged in off-axis (1-3°) orientations.

RESULTS

Characterization of particles

Characterization of particles by x-ray diffraction (XRD) and transmission electron microscopy showed the presence of both rutile and anatase particles. The ratio of the amount of rutile to anatase and the morphology varied with the temperature of the flame [7]. The morphology of the particles generated ranged from polyhedral to rounded.

Unusual particles were noted for two of the sample sets (low and medium temperatures, lower height in flame). The particles were generally larger than the rest of the particles produced in the sample sets, with largest dimension ranging from approximately 80 nm to 180 nm. These particles contain central features that range in largest dimension from

[1] Certain commercial equipment, instruments, or materials are identified in this paper to specify adequately the experimental procedure. Such identification does not imply recommendation or endorsement by the National Institute of Standards and Technology, nor does it imply that the materials or equipment are necessarily the best available to the purpose.

approximately 30 nm to 100 nm. Characterization by energy dispersive spectroscopy (EDS) has shown that the particles contain Ti and O. SAED patterns are consistent with an identification of rutile. Electron holography work has shown the inclusions to be consistent with voids [7].

Characterization of void morphology

There are several challenges in determining the morphology of the internal surfaces of nanoparticles. By TEM imaging, only a projection of the three-dimensional shape is observed. Ideally, one would like to view a single nanoparticle in several orientations for which the crystallographic orientation is known. Further, one would like to obtain images by rotating around symmetry axes such as [001] (rutile is in space group $P4_2/mnm$, and has unit cell dimensions of $\underline{a}$ = 0.459 nm and $\underline{c}$ = 0.296 nm). Two-dimensional information from several orientations could then be combined to derive a model of the three-dimensional shape of the voids. In this work, the size of the rutile nanoparticles made their manipulation and tracking in the TEM challenging. Additionally, the crystallographic orientation of the nanoparticles relative to the x and y axes of the double-tilt sample holder commonly limited the amount of morphological information that could be collected from a single particle. With these constraints, limited information was usually obtained from any one particle.

Orientations that were obtained include [100], [110], [001], [101], [102], [111], [113], and [211]. In many cases, the projection of the cavities appears ovoid or circular; in other cases the projected outline of the cavity is at least partially linear or faceted. In general, the longest dimension of the projected voids is along the $\underline{c}$ axis of rutile.

Examples of some of the particles that were oriented close to major zone axes are shown in Figure 1. Figures 1a and 1c are images of the same particle that had its $\underline{c}$ axis nearly parallel to the x-axis of the microscope stage. The images are separated by approximately a 45° rotation to show both a [100] and [110] orientation. The shape of the cavity in the [100] orientation (Fig. 1a) appears to be roughly hexagonal. The angle between (100) and (101) faces in rutile is 123°. The hexagonal shape of Fig. 1a is therefore consistent with a projection of (100) and (101) facets of rutile. Small {001}facets may be present. The projection of the cavity oriented down [110] (Fig. 1c) is ovoid in morphology. The sides parallel to [001] are {110} faces. It is possible that the rounded appearance of the pyramidal terminations of Fig. 1a is due to a combination of at least two facets.

Particles viewed down [001] show a cavity with four primary sides corresponding to {110} (Fig. 1e). The "corners" of the squares appear rounded or to have small facets of [100]. The image from Fig. 1e is from a different particle than Figs. 1a and 1c. There is a consistency between the two particles represented in Fig. 1 in that the distance between the {100} faces is longer than the distance between {110} faces. It is likely that if the first particle could be viewed down [001], the void would have a projection similar to that in Figure 1c.

The three-dimensional morphology deduced from the images in Figure 1 is a four-sided prism with dipyramidal terminations. The exact nature of the pyramidal terminations is uncertain. The images are, however, consistent with morphology for some bulk rutile crystals such as shown in Fig. 2. The presence of {101} facets appears certain. The presence of {111} facets is possible. The relative sizes of the {101} and possible {111} faces are not known.

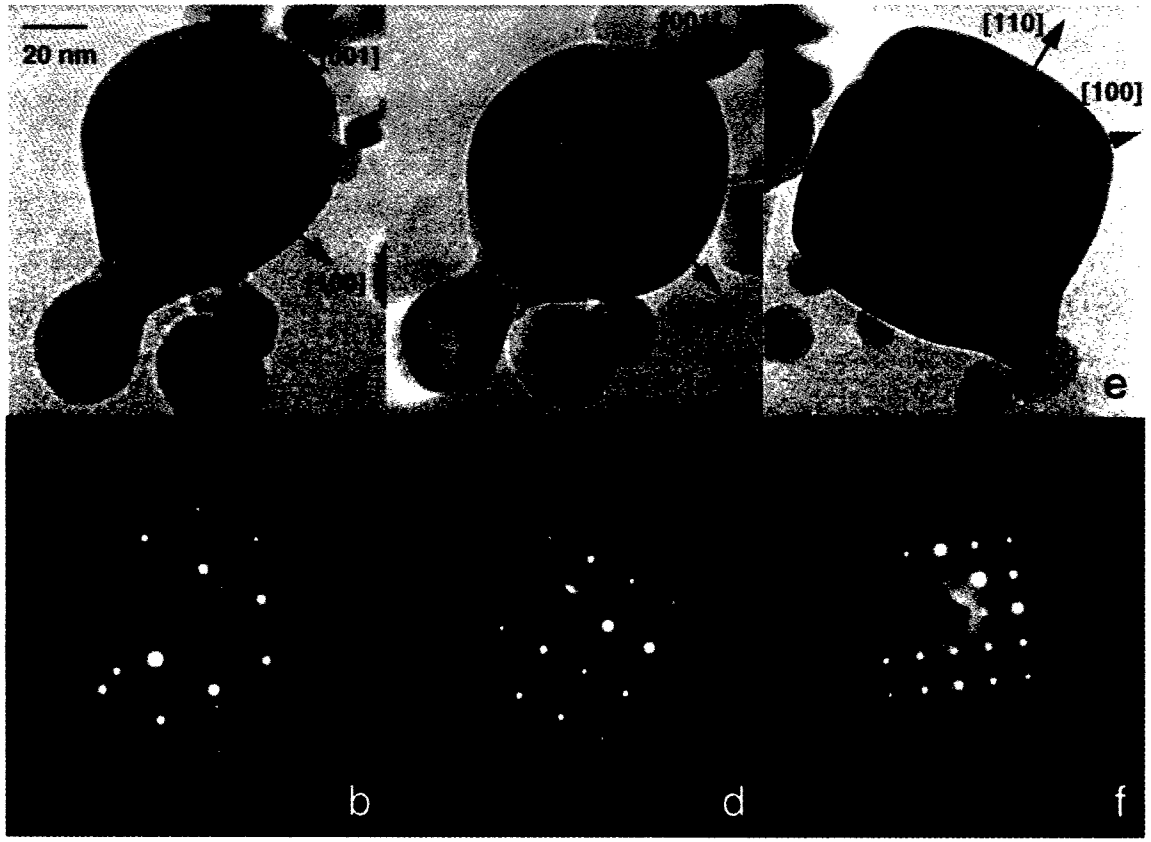


Fig. 1 Images and diffraction patterns from rutile nanoparticles viewed down (a,b) [100], (c,d) [110] and (e,f) [001]. Images (a-d) are from the same nanoparticle. The images are tilted a few degrees from the zone axis orientation.

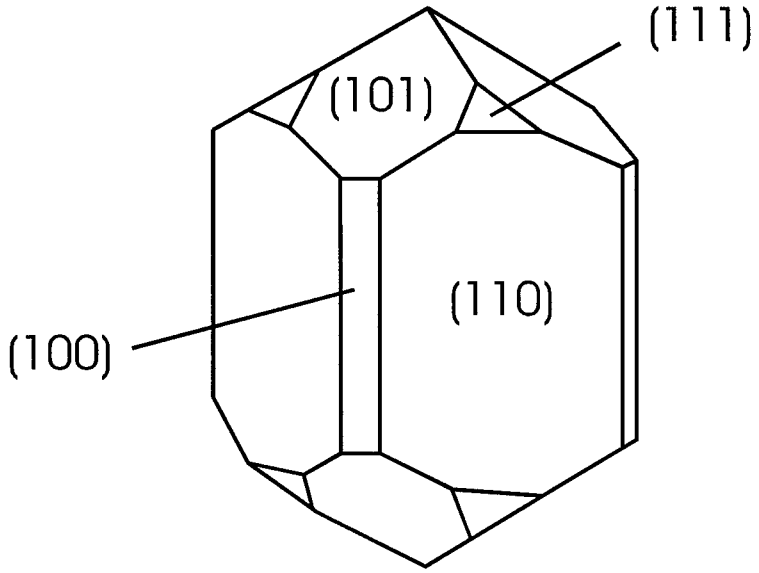


Fig. 2 Model consistent with some of the voids or negative crystals found in rutile nanoparticles. The rutile surfaces defining the void form a prism parallel to the c axis of rutile with {110} faces predominant. The prism is capped by two pyramids with {101} facets and likely {111} facets. This figure is a modification of a sketch of a bulk rutile crystal [14].

Simulation of cavity shapes and comparison to the projection of cavities observed in tilting experiments should provide a more definitive model for the morphology of the cavities [13].

SUMMARY

The general morphology of the some voids in rutile nanoparticles has been derived from imaging and SAED patterns obtained using transmission electron microsopy. The voids have a prismatic morphology with dipyramid terminations. Parallel to the c axis, {110} facets predominate. {101} facets are present at the dipyramid terminations. The morphology appears similar to that shown by some bulk rutile crystals. The derivation of the morphology of voids in nanoparticles by orientation experiments is possible with the larger nanoparticles found in this study. Development of improved sample holders and stage control for transmission electron microscopes will aid in such studies. Determination of equilibrium shapes for surface energy studies will likely require annealing of nanoparticles to ensure that equilibrium has been attained.

ACKNOWLEDGMENTS

Funding from the Advanced Technology Program is gratefully acknowledged. The samples were prepared in a project conducted by Maria Aquino, Jim Maslar and Michael Zachariah of the Chemical Science and Technology Laboratory at the National Institute of Standards and Technology.

REFERENCES

1. A. Fujishima, and K. Honda, Nature **238**, p. 37 (1972).

2. K. Sunada, Y. Kikuchi, K. Hashimoto and A. Fujishima, Envir. Sci. & Tech. **32**, p. 726 (1998).

3. D.D. Beck and R.W. Siegel, J. Mater. Res. **7**, p. 2840 (1992).

4. Q. Xu and M.A. Anderson, J. Am. Ceram. Soc. **77**, p. 1939 (1994).

5. E.A. Barringer and H.K. Bowen, J. Am. Ceram. Soc. **65** (12), p. C-199 (1982).

6. M. Shirkhanzadeh, NanoStructured Mater. **5**, p. 33 (1995).

7. S. Turner, J.E. Bonevich, J.E. Maslar, M.I Aquino, M.R. Zachariah, in *Nanophase and Nanocomposite Materials II*, edited by S. Komarneni, J.C. Parker, and H.J. Wollenberger (Mater. Res. Soc. Proc. **457**, Pittsburgh, PA 1997).

8. L.F. Allard, E. Voelkl, D.S. Kalakkad, A.K. Datye, J. of Mater. Sci. **29**, p. 5612 (1994).

9. L.F. Allard, E. Voelkl, A. Carim, A.K. Datye, and R. Ruoff, NanoStructured Mater. **7**, p. 137 (1996).

10. P.A. Crozier, R. Sharma, and A.K. Datye, Micros. and Microan. **4**, p. 278 (1998).

11. S. Andersson, H. Annehed, L. Stenberg, and R. Berger, J. Sol. St. Chem. **19**, p. 169 (1976).

12. L.R. Wallenberg, A. Andersson and M. Sanati, Ultramicros. **34**, p. 33 (1990).

13. J.H. Choi, D.Y. Kim, B.J. Hockey, S.M. Wiederhorn, C.A. Handwerker, J.E. Blendell, W.C. Carter, and A.R. Roosen, J. Am. Ceram. Soc. **80**, p. 62 (1997).

14. C. Klein and C.S. Hurlbut, *Manual of Mineralogy*, 21st ed. (John Wiley and Sons, New York, 1993), p. 381.

ULTRASONIC FORCE MICROSCOPIC CHARACTERIZATION OF NANOSIZED COPPER PARTICLES

E. J. SCHUMAKER *, L. SHEN *, M. J. RUDDELL *, S. SATHISH *, P. T. MURRAY **
* Center for Materials Diagnostics, University of Dayton Research Institute, 300 College Park, Dayton, Ohio 45469-0121
** Research Institute & Graduate Materials Engineering, University of Dayton, 300 College Park, Dayton, Ohio 45469-0160

ABSTRACT

An Ultrasonic Force Microscope capable of imaging elastic modulus variations with nanometer resolution has been developed by modifying a Scanning Probe Microscope. Images of ultrasonic properties have been simultaneously obtained with the topography images. The technique has been utilized to characterize nanoscale copper droplets and grains deposited on a quartz substrate by ionized cluster beam deposition. Images of the same region obtained with atomic force microscope, lateral force microscope, and ultrasonic force microscope are compared. The origin of image contrast in ultrasonic force microscopy and its utilization for quantitative elastic property measurement of nanometer particles are discussed.

INTRODUCTION

The Atomic Force Microscope (AFM) has been extensively used for surface topographic measurements with nanometer resolution [1]. Such high-resolution images are obtained by scanning a fine tip with a tip radius of 30-50 nm attached to a cantilever and detecting the height variations with a laser beam reflected off the cantilever's top surface. Several modifications to the AFM have led to various microscope systems capable of measuring different material properties. One such modification has been the Lateral Force Microscope (LFM) which operates in contact mode AFM [2]. The LFM detects the amount of torsion on the cantilever and thus measures the localized frictional forces.

The Ultrasonic Force Microscope (UFM) is another modification and has been developed to study the elastic properties at nanometer scales. In a UFM, a piezo-electric transducer is attached to one face of the sample, and an AFM tip is in contact with the other face. An acoustic wave propagates through the sample when the transducer is excited by an ultrasonic frequency signal. Surface displacements generated by the acoustic waves through the sample are detected by the AFM tip. Several displacement-detecting methodologies have been developed. Kolosov and Yamanaka detected the nonlinear response of the tip-sample interaction force by propagating an amplitude modulated longitudinal wave through the sample [3-4]. Rabe and Arnold utilized a beam splitter and a knife-edge detection system to investigate cantilever deflection by generating amplitude images using broadband needle impulse MHz frequencies [5-6]. Burnham, et.al. have investigated three different UFM modes of operation: contact, mechanical diode, and sub-harmonic [7-8]. In the contact mode, a small amplitude continuous longitudinal wave is propagated through the sample. The probing tip remains in constant contact with the sample due to the small amplitude of the excitation signal throughout the cycle. Larger amplitudes cause the

Mat. Res. Soc. Symp. Proc. Vol. 581 © 2000 Materials Research Society

tip to sporadically lose contact and bounce chaotically or under certain conditions, every nth transducer cycle (subharmonic mode). They have also developed a rheological model of the transducer-sample-cantilever system for contact mode UFM that shows the elastic modulus of the material is proportional to the amplitude of the tip displacement.

In this paper, we present a UFM designed to operate in contact mode, at frequencies in the range of a few kHz to a MHz. The microscope has been used to characterize nanometer sized copper grains and copper droplets. AFM, UFM and LFM images obtained on the same regions are compared and the origin of contrast in the images for each of the microscope is discussed.

EXPERIMENT

A Digital Instruments Multimode Nanoscope IIIa AFM was modified to operate as a UFM. The principle of operation and modifications to the AFM are shown schematically in Figure 1. An HP function generator is employed to drive a piezoelectric transducer in a continuous wave. The transducer is bonded to one face of the sample while an AFM tip is in contact with the other face. In contact mode, a continuous wave excites the transducer and the subsequent ultrasonic waves produce vertical surface displacements that are detected by the AFM tip. A Stanford Research Systems lock-in amplifier is then used to measure the magnitude and phase of the detected signal with respect to the signal from the function generator.

Specimen

A thin film of copper was deposited on a fused quartz substrate using ionized cluster beam deposition method [9]. The deposited region approximately had a bell shape with varying density of atoms. Figure 2 shows high and low density regions and the relative location of the 1μm × 1 μm areas chosen for imaging.

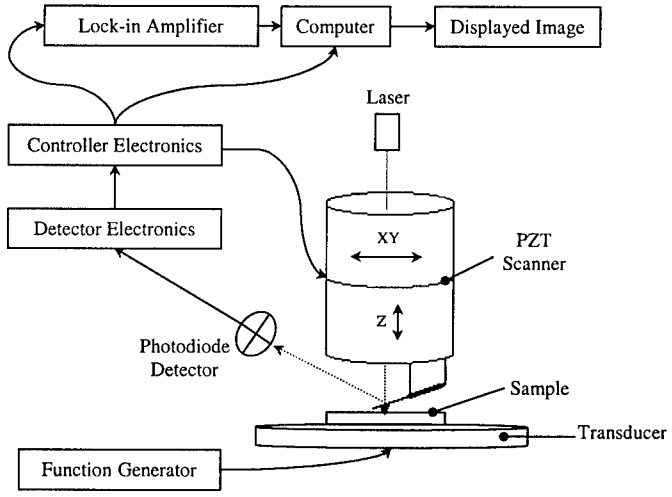


Figure 1 Schematic diagram of Ultrasonic Force Microscope.

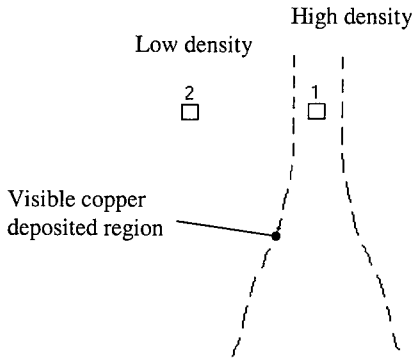


Figure 2 Enlarged view of copper deposited area with boxes (1-2) indicating location of scanned regions with different atom densities.

A PZT transducer operating in the range of a MHz frequency was bonded to the face of the quartz substrate that does not have the copper film. A low stiffness (k = 0.06 N/m) cantilever was used to obtain AFM, LFM, and UFM images.

RESULTS

AFM, LFM and UFM images were obtained on the same region of the sample over an area of 1 μm x 1 μm. Images acquired on the high-density region are shown in Figure 3. The surface topography AFM images show a height variation of 300 nm within the scan area and the contrast is hazy.

On the other hand, the contrast in the UFM image of the same region is very large and individual regions can be easily identified as grains. Each grain can be seen with different contrast. The average size of the grains is about 180 nm and the smallest grain observed is 20 nm. The contrast in UFM images is due to the variation in elastic modulus in the material. Based on the rheological model of UFM, the amplitude of the surface displacement measured by the AFM cantilever is proportional to the input amplitude to the piezo-electric transducer and the elastic modulus in the material [7]. The input amplitude to the transducer over the whole area is constant. Hence, the amplitude is directly proportional to the elastic modulus. Elastic anisotropy is defined as $2c_{44} / (c_{11}-c_{12})$; copper is elastically very anisotropic and has a value of 3.2. This indicates that the changes in the Young's modulus for different crystallographic orientation are quite large.

It is also known that the friction forces are dependent on the crystallographic orientation. Hence, we expected to observe a contrast in the LFM images of the same region due to anisotropy of the local friction forces. But the contrast in LFM images is not as good as it is in UFM images. It may be possible that the differences in the frictional forces are below the detection limit of our LFM. However, some contrast is observed in the LFM images and this is due to edge effects of the grains.

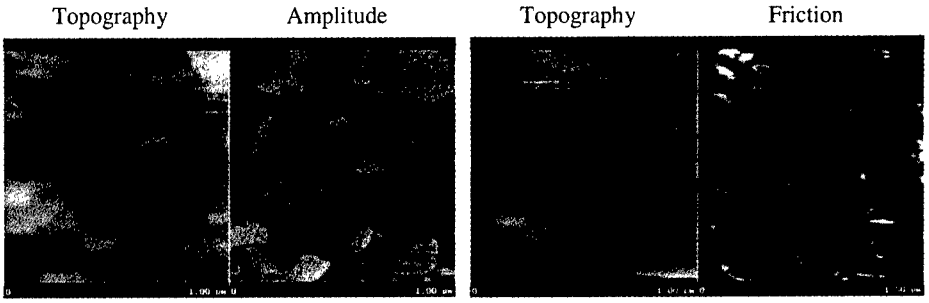


Figure 3 Images obtained from the high-density region. (a) AFM and UFM amplitude images. (b) AFM and LFM.

In comparison to the high-density region images, the low-density region images are very different. AFM, LFM, and UFM images of an area of 1μm × 1 μm of this region are shown in Figure 4. All the images indicate that the shape of the regions is almost spherical. In this region of the film, it appears that the copper atoms have collected together to form a droplet without having formed a definite crystallographic orientation. The droplet diameters range between 30 nm and 140 nm while the height variation is 100 nm within the scan area.

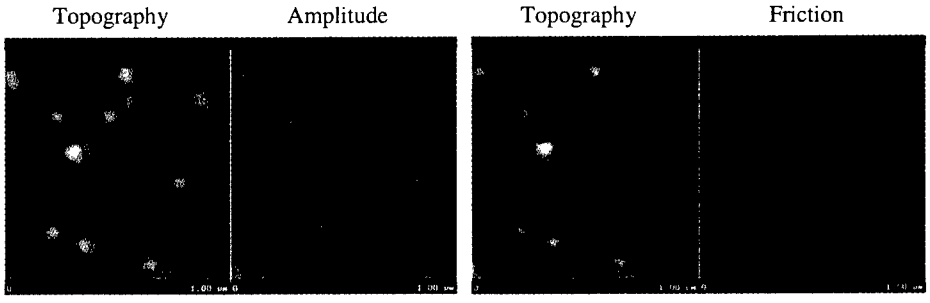


Figure 4 Images obtained from the low-density region. (a) AFM and UFM amplitude images. (b) AFM and LFM images.

CONCLUSIONS

The contrast in the images of copper thin films obtained using AFM, LFM and UFM has been compared. The contrast in AFM images is hazy and the contrast in LFM images is related to the edge effects. The UFM images reveal every grain of copper in the scanned region. This enhanced contrast is related to the anisotropic elastic modulus of the material. The contrast of

the low-density images of AFM, LFM and UFM are not very different and are dominated by the edge effect.

ACKNOWLEDGEMENTS

This research effort was supported by DARPA NDE-MURI under AFOSR Grant F49620-96-1-0442 and by National Science Foundation grant CMS-9905394. The authors would like to thank A. J. Kulik for helping with the development of our ultrasonic force microscope.

REFERENCES

1. S. Cohen, M. Bray, and M. Lightbody, eds., *Atomic Force Microscopy / Scanning Tunneling Microscopy* (Plenum Press, New York 1994), pp. 217-299.

2. G. Meyer and N. M. Amer, Appl. Phys. Lett. **57** (20), 2089-2091 (1990).

3. O. Kolosov and K. Yamanaka, Jpn. J. Appl. Phys. **32,** L1095-L1098 (1993).

4. K. Yamanaka, H. Ogiso, O. Kolosov, Appl. Phys. Lett. **64**, (2), 178-180 (1994); Jpn. J. Appl. Phys. **33**, 3197-3203 (1994).

5. U. Rabe and W. Arnold, Appl. Phys. Lett. **64** (12), 1493-1495 (1994); Ultrasonics Symposium, 367-370 (1994).

6. V. Scherer, B. Bhushan, U. Rabe, and W. Arnold, IEEE Transactions on Magnetics, **33** (5), 4077-4079 (1997).

7. N. A. Burnham, A. J. Kulik, G. Gremaud, P.-J. Gallo, and F. Oulevey, J. Vac. Sci. Technol. B **14** (2), 794-799 (1996).

8. F. Oulevey, G. Gremaud, A. Sémoroz, A. J. Kulik, N. A. Burnham, E. Dupas, and D. Gourdon, Rev. Sci. Instrum. **69** (5), 2085-2094 (1998).

9. P. T. Murray, K. D. Leedy, E. Schumaker, S. Sathish, L. Shen, and M. J. O'Keefe in Proceedings of ISCANI, edited by B. K. Rao (World Scientific, Singapore, 1999), (to be published).

POWER OF MASS SPECTROMETRY FOR ANALYZING ORGANOMETALLIC MOLECULES AS PRECURSOR OF NANOMATERIALS

G.F. STROUSE *, J.J. GAUMET **
* Department of Chemistry, UCSB, Santa Barbara, CA 93106-9510, strouse@chem.ucsb.edu
** LSMCL, Université de Metz, IPC, 1 bd Arago, 57078 Metz Cedex 03 France, gaumet@lsmcl.sciences.univ-metz.fr

ABSTRACT

A mass spectrometry method (Electrospray Mass Spectrometry [ESMS]) for analyzing organometallic precursors of nano-materials is described. We show that application of low-cone voltage ESMS is a useful technique for the rapid analysis of intact organometallic precursor molecules when both positive and negative ionic modes are analyzed. This method shows promise for extrapolation to analysis of the dynamics of growth in nano-scale materials.

INTRODUCTION

The development of nanoscale science has arisen from the observation of fascinating size dependent optical and electronic properties of these materials [1, 2]. Nanoparticles represent a boundary where a gradual transition from solid-state to molecular properties occurs as the particle size decreases [3, 4]. Such compounds are a class of materials whose properties are amenable to chemical tuning by manipulating particle size, cristallinity, dopant level, and surface tuning via ligand capping. Development of technology for analysis of such materials has centered on traditional solid state methods requiring efficient isolation of the samples after their syntheses. While TEM, X-ray diffraction, UV/Visible and IR spectroscopies, photoluminescence, Raman spectroscopy and TGA techniques are excellent tools for structure analysis, they do not specifically address the compositional integrity of the materials in an « on-line » fashion required for process control. Consequently, a significant disadvantage arises due to the inability to probe the real-time dynamics of nanomaterial growth.

An alternative pathway for real time analysis of particle size and composition is the application of mass spectrometry. More specially, we present herein the results from a soft mass spectrometry technique : the Electrospray Mass Spectrometry (ESMS). The main advantage of ESMS over other mass spectrometry techniques is the capabilities for direct analyses of mixtures and solvated molecules. ESMS ionization methods have been largely applied to molecules in biochemistry which due to their chemical composition and their bonding are susceptible to damage [5, 6]. We present in this paper the analysis of chalcogenide cadmium clusters of discrete size by positive and negative ion mode ESMS under low-cone voltage. Such ionic mode allows a small fragmentation and the observation of the parent ion [7-8]. The first study illustrates how ESMS allows differentiation of the physical properties of the precursor molecules arising from variability of the chalcogenide core and the surface capping of the cluster (S or Se). The second study illustrates the application of ESMS to the analysis of a binary metal chalcogenide nano-material precursor (Cd-Co). Analysis of the mass spectra for such materials provides insight into the applicability of ESMS methods to structure analysis, composition and stability of nano-semiconductor materials.

Mat. Res. Soc. Symp. Proc. Vol. 581 © 2000 Materials Research Society

EXPERIMENTAL

The clusters $[(CH_3)_4N]_4[E_4Cd_{10}(SPh)_{16}]$ (E = S or Se, Ph = C_6H_5) [9, 10] named in the paper as "Cd10" and the binary compound $[Li_2][S_4Cd_4Co_6(SPh)_{16}]$ [11] were prepared by literature methods. Figure 1 shows the general structure of the clusters. Note that each capped chalcogenide is bounded with a phenyl group not shown for clarity reason. X-ray powder diffraction, ICP and ^1H NMR measurements verify the composition of the clusters "Cd10". EPR and ICP-AE measurements made on the $[Li_2][S_4Cd_4Co_6(SPh)_{16}]$ compound confirms the mass ratios and suggests the ratio of 4 to 2 between Co^{II} and Co^{III}. Mass spectra were performed in positive and negative ion mode using a VG Platform II mass spectrometer (Fisons Instruments) coupled to a quadrupole mass filter with a m/z ion range from 0 to 3000 (See Figure 2). The quadrupole mass selector was calibrated using a solution of sodium iodide as a standard. Nitrogen was employed as both the drying and nebulizing gas. Freshly prepared samples [approximate concentration: 0.1 $mmol.L^{-1}$ in dry acetonitrile (4Å molecular sieve, HPLC Grade)] were injected into the spectrometer at a flow rate of 20 $mL.min^{-1}$ using a syringe infusion pump (Harvard Apparatus). The solutions are delivered to the mass spectrometer source at a temperature of 67°C.

The cone voltage used was +/- 5V for all samples to minimize fragmentation processes except for the selenium compounds which needed a negative voltage of –20 V for the observation of the parent ion. Cone voltage from –200 to +200 V were checked for reliability of the ion distribution. All assigned peaks in the presented mass spectra were identified by the most intense m/z value within the isotopic mass distribution. Confirmation of ionic species was made by comparison of the observed and predicted isotope distribution patterns using the software Mass Linx (Fisons Instruments).

RESULTS AND DISCUSSION

Differentiation between core and capping chalcogenide

Low cone voltage and direct infusion ESMS techniques allow rapid analysis of nano-scale metal chalcogenide clusters. Mass spectra for the positive and negative ion are displayed respectively in Figure 3a (+5V) and Figure 3b (-5V) for both core and capping sulfur and in Figure 4a (+5V) and Figure 4b (-20V) for selenium core and sulfur capping. We detect high mass peaks which arise from the respective parent clusters $[(CH_3)_4N]_4[S_4Cd_{10}(SPh)_{16}]$ and $[(CH_3)_4N]_4[Se_4Cd_{10}(SPh)_{16}]$.

$$[(CH_3)_4N]_4[S_4Cd_{10}(SPh)_{16}] \xrightarrow{+\,2\,(CH_3)_4N^+} [(CH_3)_4N]_6[S_4Cd_{10}(SPh)_{16}]^{2+} \quad (1)$$

$$[(CH_3)_4N]_4[S_4Cd_{10}(SPh)_{16}] \xrightarrow{-\,2\,(CH_3)_4N^+} [(CH_3)_4N]_2[S_4Cd_{10}(SPh)_{16}]^{2-} \quad (2)$$

$$[(CH_3)_4N]_4[Se_4Cd_{10}(SPh)_{16}] \xrightarrow{+\,2\,(CH_3)_4N^+} [(CH_3)_4N]_6[Se_4Cd_{10}(SPh)_{16}]^{2+} \quad (3)$$

$$[(CH_3)_4N]_4[Se_4Cd_{10}(SPh)_{16}] \xrightarrow{-\,2\,(CH_3)_4N^+ - SPh^- + H^+} [(CH_3)_4N]_2[Se_4Cd_{10}(SPh)_{15}H]^{2-} \quad (4)$$

These intense peaks in the 10-metal chalcogenide mass spectra are directly attributable to 'pseudo' parent ions by addition of two $(CH_3)_4N^+$ in the positive mode (Equations (1) and (3)). The singly charged parent-ion which arisises from loss of one ammonium cation is not observable due to mass range limitations of the quadrupole detector. Recently, we observed the singly charged ion at m/z = 3371 on an ES-TOF instrument, confirming our initial

assignements on the positive ion mode [12]. The positive ion parent peaks have a relative higher intensity and a better resolution compared to those in the negative ionic mode. In the negative ion mode, substantial fragmentation of the two clusters are observed, even at low cone voltage which is consistent with earlier studies on those materials [5, 7]. In the negative ion mode, there is an intriguing family with surprising stability, $[S_4Cd_8(SPh)_{10}]^{2-}$ at m/z = 1060. This species is generated by fragmentation of the Cd_{10} via the loss of 2 $[Cd(SPh)_3]^-$ at m/z = 441. The Cd_8 species has been suggested as a potentially stable cluster species and is potentially be involved in the growth of CdSe nanocrystals via a seeded lyothermal growth method [13].

ESMS Analysis a binary metal chalcogenide precursor cluster $[Li_2][S_4Cd_4Co_6(SPh)_{16}]$

The mass spectra displayed in Figure 3a (+5V) and Figure 3b (-5V) show high mass peaks connected to the parent cluster.

$$[Li_2][S_4Cd_4Co_6(SPh)_{16}] \xrightarrow{+\,2(Li^+\,SPh^-)+\,2\,Li^+} [Li_4][S_4Cd_4Co_6(SPh)_{16}][Li(SPh)]_2^{2+} \quad (5)$$

$$\xrightarrow{-\,2\,Li^+} [S_4Cd_4Co_6(SPh)_{16}]^{2-} \quad (6)$$

These observed m/z peaks can be described in terms of a mixed valence cluster having two oxidation states for cobalt, Co^{III} and Co^{II} in the Cd_4Co_6 cluster. The mixed valency on the cobalt cluster is confirmed by EPR masurements [14]. Negative ion spectra in Figure 4 is in agreement with the structural assignments of a Co6Cd4 cluster species. The flexibility of ESMS for the analysis of the structure of molecular recursors allows rapid identification of nanomaterial precursors available for nano-material growth. In the case of the mixed valence precursor, we are currently exploring the potential for growth of magnetically doped nanocrystalline CdSe using the Co precursor.

CONCLUDING REMARKS

The combination of positive and negative ion mode under low cone voltage on electrospray mass spectrometry is a potential tool for the characterization of organometallic molecules. Both mass spectra provide a specific fingerprint of the studied compounds. The ease of direct infusion ESMS technique can be used to follow on line synthesis of II-VI and III-V compounds leading to nano-materials characterization. Such materials are elaborated either on solution or in a solid state. Other mass spectrometry techniques using laser ionization processes should be used for getting some data for higher masses. An analytical device like MALDI-TOF (Matrix-Assisted by Laser Desorption/Ionization coupled to Time of Flight Mass Spectrometry) is also interesting. However it is fundamental to define the best conditions for laser/material interaction experiments. Our studies about nano-clusters are in progress for a better knowledge of the following parameters with MALDI analyses: i) the matrix/analyte ratio and ii) the laser wavelength and the power density.

ACKNOWLEDGEMENTS

We acknowledge financial support from the National Science Foundation under contract DMR 9875940 (NSF-CAREER).

REFERENCES

1. H. Weller, Angew. Chem., Int. Ed. Engl. **32**, p. 41-45 (1993).
2. L. E. Brus and J. K. Trautman, Phil. Trans. R. Soc. Lond. A, **353**, p. 313-321 (1995).
3. A. P. Alivisatos, Science, **271**, p. 933-937 (1996).
4. H. Herron, A. Suna and Y. Wang, J. Chem. Soc. Dalton Trans., p. 2329-2335 (1993).
5. S. J. Gaskell, J. Mass Spectrom., **32**, p 677-685 (1997).
6. D. L. Zechel, L. Konermann, S.G. Wilthers and D. J. Douglas, J. Biochemistry, **37**, p. 7664-7669 (1998).
7. J.J. Gaumet and G. Strouse, J.Am. Soc. Mass. Spectrom., accepted.
8. T. Løver, W. Henderson, G. A. Bowmaker, J. M. Seakins and R. P. Cooney, Inorg. Chem., **36**, p. 3711-3723 (1997).
9. I.G. Dance, A. Choy and M. L. Scudder, J. Am. Chem. Soc., **106**, p. 6285-6295 (1984).
10. G. S. H. Lee, D. C. Craig, I. Ma, M. L. Scudder, T. D. Bailey and I. G. Dance, J. Am. Chem. Soc., **110**, p. 4863-4864 (1988).
11. G. F. Strouse, R. Meulenburg and J. J. Gaumet, manuscript in preparation.
12. J. J. Gaumet and G. F. Strouse, unpublished results.
13. G. Khitrov and G. F. Strouse, manuscript in preparation.
14. R. Meulenburg and G. F. Strouse, unpublished results.

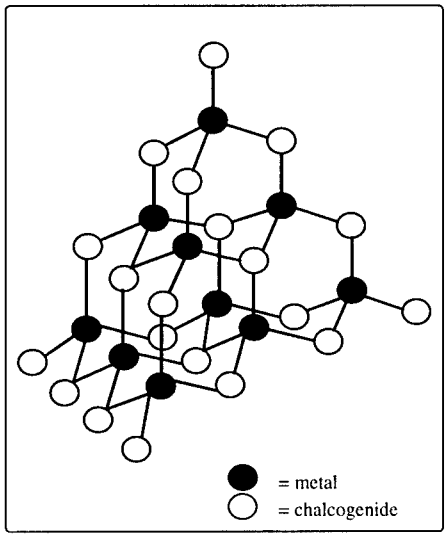


Figure 1 : Structure of a $[E_4Met_{10}(SPh)_{16}]^{4-}$ with E = S, Se, and Met = Cd and/or Co

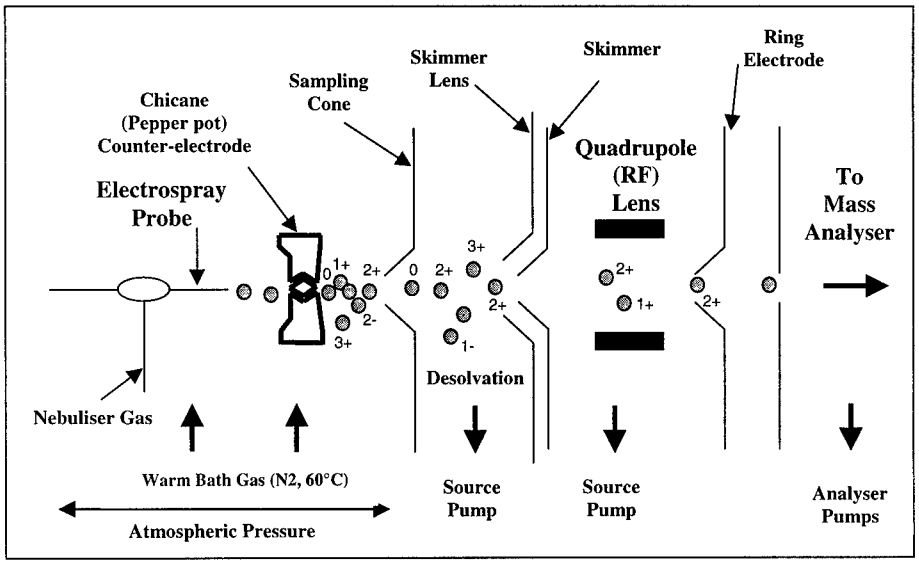


Figure 2: Schematic diagramme of an Electrospray Mass Spectrometer

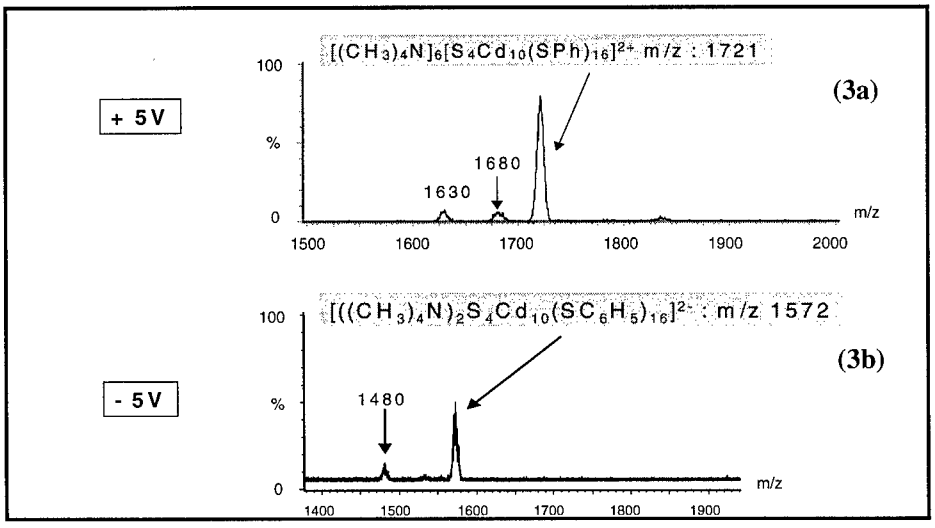


Figure 3 : Positive ion mass spectrum (3a) and negative ion mass spectrum (3b) of $[(CH_3)_4N]_4[S_4Cd_{10}(SPh)_{16}]$.

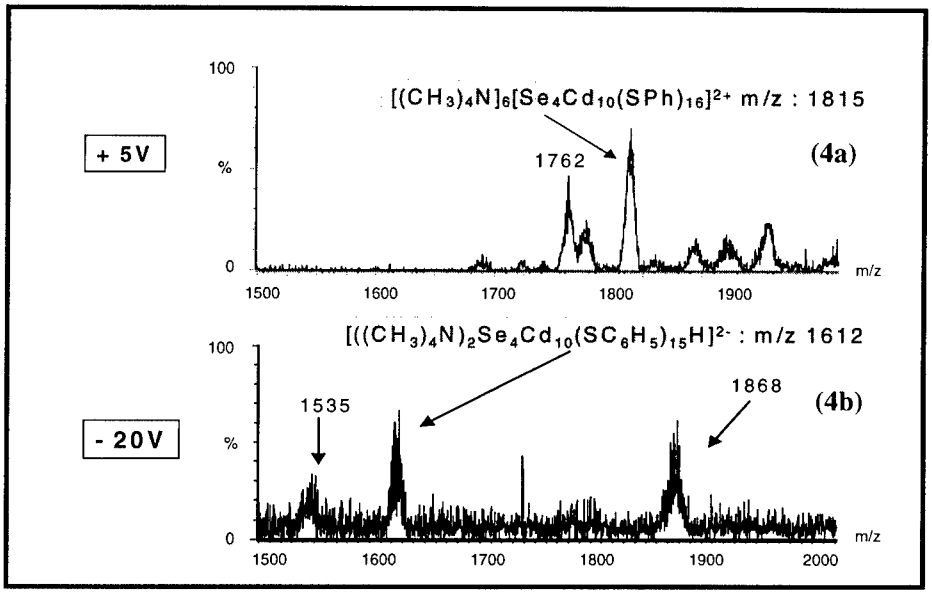


Figure 4 : Positive ion mass spectrum (4a) and negative ion mass spectrum (4b) of $[(CH_3)_4N]_4[Se_4Cd_{10}(SPh)_{16}]$.

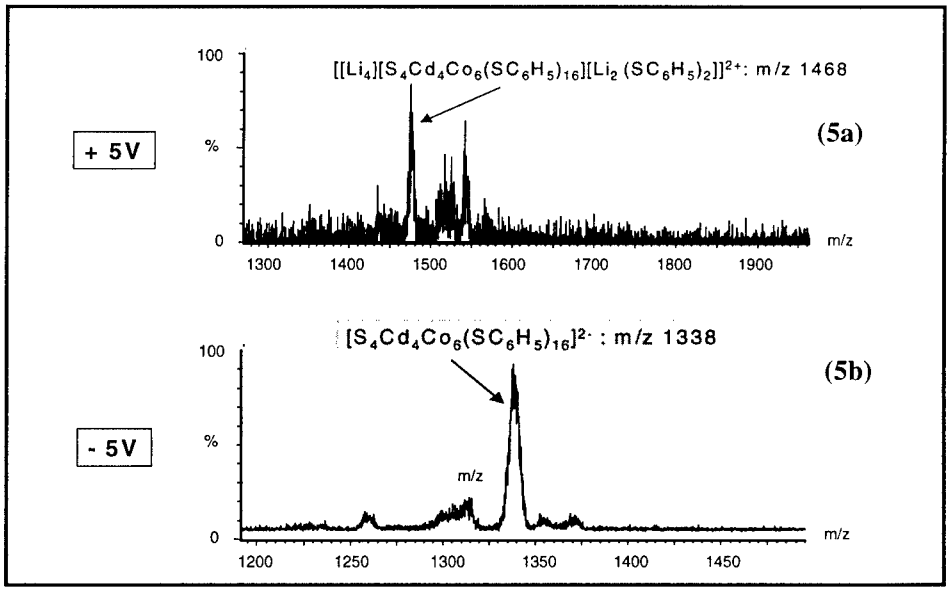


Figure 5 : Positive ion mass spectrum (5a) and negative ion mass spectrum (5b) of $[Li_2][S_4Cd_4Co_6(SPh)_{16}]$.

Optical Characterization of a Spheroidal Nanoparticle on a Substrate

Carlos E. Román-Velázquez, Cecilia Noguez and Rubén G. Barrera
Instituto de Física, Universidad Nacional Autónoma de México, Apartado Postal 20-364, México, D. F. 01000 MEXICO

ABSTRACT

With the help of a spectral formalism recently formulated, we study the effects in the optical response of the material properties of a nanoparticle lying over a substrate. A spectral representation was formulated to calculate the optical response of spheroidal nanoparticles including multipolar effects. We present our results in terms of Differential Reflectance spectra that can be compared directly with measurements. We have found that multipolar contributions depend in the shape of the particle and type of substrate.

INTRODUCTION

In recent times, the study of supported nanoparticle systems has attracted the attention of many reserchers due to some of their very interesting physical properties as well as the possibilities of promising tecnological applications [1]. In particular, the knowledge of the optical properties of a particle located above a substrate can be used as a tool to interpret optical spectra for the characterization of supported nanoparticle systems [2]. The fabrication of nanostructured systems and the growing process of thin films requires a precise characterization of the shape and size of the supported particles or islands. For this purpose the optical spectroscopies become an unvaluable tool due to their non destructive character and in-situ capabilities of measurement.

The optical spectra of metallic nanoparticles deposited on an insulating substrate is characterized by the presence of resonances. The location and broadening of these resonances depend on the morphological and physical properties of the system. For example, they depend on the properties of the substrate because the particle interacts with the charges induced on the substrate. The interaction between different supported particles is also important, specially in the case of a high concentration of particles. However, the study of an isolated supported particle can be also performed in the dilute regime [3].

The optical properties of a particle on a substrate are determined by its response to the local field. In the first attempts to describe the optical properties of these systems the interaction of the particle with the substrate was neglected [4]. Later, the presence of the substrate was included by taking a dipolar interaction between the particle and its image [5-8]. However, the calculation of the interaction between a particle of finite size and its image requires the inclusion of multipolar interactions. This is because the field produced by the image, rather than being homogeneous over the size of the particle, as required by the dipolar approximation, it is strongly inhomogeneous, specially when the particle is close to the substrate. Different authors have included these multipolar interactions considering particles of different shapes [9-11]. However, the numerical complexity of the problem restricts tremendously the number of multipolar interactions taken to describe the system. This situation restricts the study to only a few specific systems.

The inclusion of multipolar interactions between the particle and its image gives rise to resonances additional to the dipolar one, which is the one that characterizes an isolated particle. It has been also shown that the location and strength of the multipolar resonances depend strongly on the properties of the substrate and the geometry of the system [3,12]. For example, when a particle is in close contact with the substrate smooth spectra are obtained. On the contrary, when the particle is located at a certain distance above the substrate, a well defined structure of resonances is obtained. The structure of these resonances is more evident when the contrast in the dielectric response of the ambient and the substrate increases [3,12].

Recently a powerful theoretical procedure has been developed to calculate the optical response of a particle-substrate system using a spectral representation [12]. The main advantage of

Mat. Res. Soc. Symp. Proc. Vol. 581 © 2000 Materials Research Society

this representation is that the strength and localization of the resonances, when given in terms of the spectral variable, are independent of the dielectric properties of the particle, but depend only on its shape and the dielectric properties of the substrate. With this procedure one is also able to include a larger number of multipoles, allowing the treatment of substrates with a larger contrast in the dielectric constant and particles closer to the substrate. In this work we consider more asymmetric oblate particle than in previous treatments [12] and we also study the changes in differential-reflectance spectra for particles made of different materials.

FORMALISM

We consider an oblate particle located on a substrate. The particle is generated by the rotation around one of the axes of an ellipse with lengths $2a$ and $2b$, with $a > b$. The symmetry axis of the particle is perpendicular to the substrate, and its center is located at a distance d from the substrate which has a dielectric constant ε_s. The particle has a dielectric function ε_p and is embedded in an ambient of dielectric constant ε_a. We consider that the three media: particle, substrate and ambient are non-magnetic. The system is excited by light with frequency ω and a wavelength λ, such that $\lambda >> a, b$ and d. Under this condition, a quasistatic approximation is valid to calculate the electromagnetic fields.

In the linear approximation, the dipolar moment of the particle, in the presence of a substrate, linearly depends with the components of the applied external field, throughout the so called effective polarizability tensor α_{eff}. Due to the symmetry of the system, α_{eff} has only two independent components corresponding to the polarizabilities in the direction normal and perpendicular to the substrate. When the particle is far from the substrate the effective polarizability becomes the polarizability of the isolated particle. But, when the particle is close to the substrate the multipolar interactions induced by the substrate modifies the optical response of the system.

The analysis of α_{eff} for the system described above was done as follows. First, the electric potential induced in the system at any point in space was calculated to all multipolar orders. To find the solution for the induced potential a spectral representation (SR) of the Bergman-Fuchs-Milton type [13] was developed [12]. By identifying the dipole moment $\boldsymbol{p}$ induced in the particle, the components of α_{eff} were obtained. The behavior of the spectral function for different shapes and locations of the particles is analyzed. For a detailed description of the method see Ref. [12].

Within SR, we can write the components of α_{eff} in the following form:

$$\alpha_{eff}^{m} = -\frac{v}{4\pi}\sum_{s}\frac{G_s^m}{u(\omega)-n_s^m}, \qquad (1)$$

where v is the volume of the particle, m denotes the diagonal components of α_{eff}, and $u(\omega)=[1-\varepsilon_p(\omega)/\varepsilon_a]^{-1}$ is the spectral variable; $G_s^m=(U_{1s}^m)^2$ are the so-called spectral functions where U_{ls}^m is an orthogonal matrix that satisfies the relation,

$$\sum_{ll'} U_{ls}^m H_{ll'}^m U_{l's}^m = n_s^m \delta_{ss'}. \qquad (2)$$

The matrix $H_{ll'}^m$ depends only on the geometrical properties of the model and on the dielectric properties of substrate and ambient, through the contrast parameter $f_C = (\varepsilon_a - \varepsilon_s)/(\varepsilon_a + \varepsilon_s)$. $H_{ll'}^m$ is a symmetric matrix and can be written in the following form [12]

$$H^{m}_{ll'} = n^{0}_{lm}\delta_{ll'} + f_c D^{m}_{ll'}(d), \qquad (3)$$

here n^{0}_{lm} are the depolarization factors of an isolated spheroid, and $D^{m}_{ll'}$ is a matrix given by the multipolar coupling due to the presence of the substrate, this later vanishes when $d \to \infty$. Note that $H^{m}_{ll'}$ contains all the information on the geometry of the system and the dielectric constant of the substrate, and is independent of the material properties of the particle. From Eq. (1), α_{eff} is given as the sum of terms which show resonances at frequencies ω given by the poles of the equation, when $u(\omega) = n_s^{m}$. As a consequence, an explicit procedure to obtain the strengths G_s^{m} and the position of the resonances is obtained.

With this SR a systematic study of the spectral function in term of the parameters *a, b, d* and *fc*, has been reported in Ref. [12]. In this paper, we present a systematic study of the spectral function of oblate particles with different asymmetries and considering two different kinds of substrates. We present our results in terms of Differential Reflectance spectra, where different material properties of the particle are also considered.

RESULTS AND DISCUSSION

In order to determine the effective polarizability of spheroidal particles located at a distance *d* above a flat substrate, first we construct the interaction matrix $H^{m}_{ll'}$ choosing the value of *m* equal to 0 or 1, depending on whether the applied external field lies perpendicular or parallel to the substrate. A maximum value of multipolar excitations L_{max} is chosen in order to assure multipolar convergence in the spectral function G_s^{m}, which gives the strength of the coupling of the optical active modes labeled by $n_s{}^{m}$, to the applied field. Its actual value will depend on the values of *a/b*, f_c and *d*. A numerical procedure to calculate $D^{m}_{ll'}$ is given in [11]. However, that method has convergence problems in the case of oblate particles with a large asymmetry (*a/b*>1.7), where only a reduced number of multipolar interactions (L_{max} ~ 25) can be taken. Here we devised an alternative method starting from expressions given by Lam [14], which are valid for the case of particles with *c/d* < 1, where *c* is the semidistance between the foci of the ellipse. We then calculate the spectral function G_s^{m}, the effective polarizability and the spectrum of differential-reflectance (DR) for specific systems of supported spheroidal particles. Some recent DR measurements on metallic supported particles have shown the presence of multipolar effects [3, 12], and the shape of the particles has been determined through a detailed analysis of these spectra [12]. In DR spectroscopy one compares the reflectance of the substrate-film system with the reflectance of the clean substrate, that is,

$$\Delta R_p / R_p = \frac{R_p[film + substrate] - R_p[substrate]}{R_p[substrate]}. \qquad (4)$$

When one considers that the film is constituted by a dilute distribution of particles, all located at the same distance from the substrate, one obtains, for *p*-polarized light, the following expression

$$\Delta R_p / R_p = 16\frac{\omega}{c} b f_2 \cos\theta \,\mathrm{Im}\left[\frac{\alpha^{0}_{eff}\left(\varepsilon_s - \sin^2\theta\right) - \alpha^{1}_{eff}\varepsilon_s^2 \sin^2\theta}{\left(1-\varepsilon_s^2\right)\left(\sin^2\theta - \varepsilon_s\cos^2\theta\right)}\right], \qquad (5)$$

where θ (= 50^0) is the angle of incidence, f_2 is the two-dimensional filling fraction of particles and c is the speed of light. Note that the spectral representation of the effective polarizability α_{eff} leads to a spectral representation for the differential reflectance $\Delta R_p/R_p$. We consider here the case of particles of free-electrons metals whose dielectric function can be described by the Drude model $\varepsilon_p(\omega) = 1 - \omega_p^2/(\omega(\omega+i\tau))$, where ω_p is the frequency of the bulk plasma resonance and τ is a phenomenological factor associated with the dissipation process. For potassium these parameters are $\hbar\omega_p = 3.8$ eV and $\tau/\omega_p = 0.105$, while for aluminium they are $\hbar\omega_p = 15.8$ eV and $\tau/\omega_p = 0.04$. We also consider silver particles, and in this case we use, in our calculations, the experimentally-determined dielectric function (see Fig. 3).

In Fig. 1 we show differential reflectance spectra and its associated spectral weights for two oblate particles of aluminium with $a/b = 2.5$ and $a/b = 4.0$, each one in two different substrates. In all cases $d = 1.05$, $\theta = 50^0$ and $f_2 = 0.0046\text{nm}/b$. The spectral function is plotted as a series of s vertical lines whose location is given by the energy of the resonances and their length iproportional to the strength of the coupling with the applied external field. Although a reduced number of resonances is observed, to obtain these spectra 25 multipoles have to be included in order to attain multipolar convergence in the calculation of the spectral functions. In the spectra of a particle with $a/b = 2.5$ over a substrate with $fc = -0.773$ (titanium dioxide in air) one sees a structure of multipolar resonances. These resonances have different energies and the number of distinct resonances decreases with the magnitude of contrast factor; there are fewer for $fc = -0.516$, (sapphire in air). In the case of the more asymmetric particle $a/b = 4.0$, the strength of these resonances decreases further. When we compare the full multipolar calculation with the dipolar approximation one sees that the dipolar approximation gives better results for more symmetric particles, and it becomes even better in the case of a substrate with a smaller contrast factor fc.

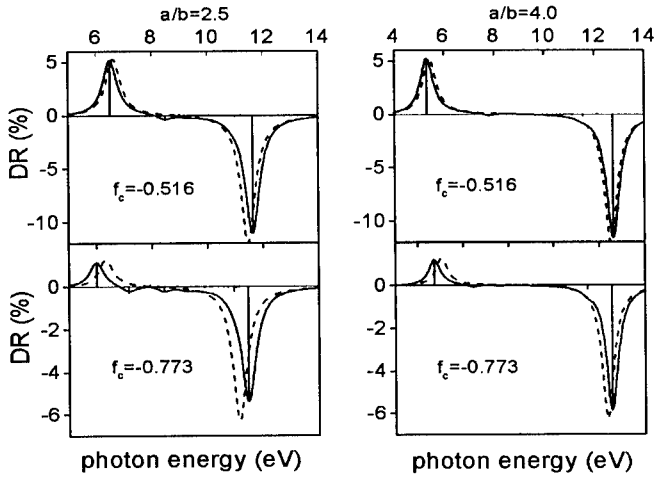


Figure 1. *DR for aluminium particles embedded in air and lying over a substrate at a distance d=1.05b. Left panels are OS particles with a/b=2.5, while right panels are particles with a/b=4.0. Upper panels correspont to substrates of sapphire and lower panels to substrates of TiO_2 . The solid lines are the calulation with L_{max}=25, meantime the dashed lines correspond to dipolar approximation. The spectral function is represented by the solid vertical lines*

In Fig. 2 we show the DR spectra corresponding to particles of potassium and silver. In two of the panels, $a/b = 1$ (spheres) while in the other two $a/b = 2.5$. In all cases the substrate has a contrast factor $fc = -0.516$. The spheres are located at $d/b = 1.0005$. Our procedure based in the spectral representation allows us to consider a number of multipolar contribution as large as $L_{max} = 2000$, which is the number required to obtain multipolar convergence in the calculation of the spectral function. In the left panels of Fig. 2 we observe how the final shape of the spectrum comes about by the superposition of resonances with strengths with different signs. In the rigth panels of Fig. 2 we also observe important differences in the shape of the spectra due to the difference in the dielectric response of the material the particles are made of, even when in both cases the resonance structure is the same. A more complex structure is observed in the case of particles of Ag. In potassium spheres the spectrum does not reflect such a rich resonance structure, and this is mainly because the particle lies too close to the substrate. From these differences in the spectra it is difficult imagine how an invariant feature could be obtained from them. The spectral representation is that invariant. We can give a more detailed explanation of the spectra of Fig.2 in the following way: In the Fig. 3 we show the imaginary part of $u(\omega)$ as function of frequency. We observe that in the region where the spheres have their resonances the imaginary part of $u(\omega)$ is smaller for silver than for potassium. This means that in the case of silver spheres the Lorentzian resonances associated to of each resonant term of Eq. (1) are taller and sharper than for potassium. As a consequence the resonance structure is richer than in potassium where the broadening effects wash out the details of this resonance structure. From Fig. 3 we can also explain the differences between the shape of the spectra for the oblate particle. The peak at low frequencies is thinner and higher than that observed at higher frequencies, the opposite of what happens in the case of potassium, which arises from the specific combination of parameters in Eq. (2). As we can see in Fig. 3, for silver, at low frequencies, the imaginary part of $u(\omega)$ is smaller than at higher frecuencies. Then, at low frequencies the Lorentizian resonances of each mode are taller and sharper than at high frequencies.

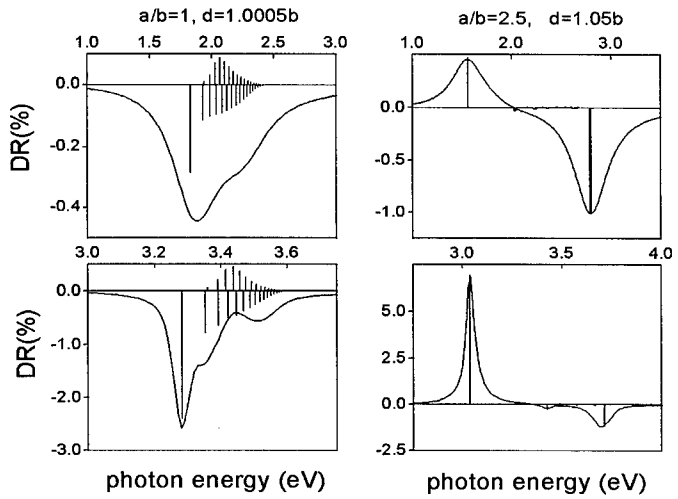


Figure 2. *DR for particles embedded in air lying over a substrate of sapphire. Left panels correspond to spherical particles at a distance d=1.0005b from the substrate, while right panels correspond to OS particles with a/b=2.5 at a distance d=1.05b. Upper panels correspond to particles of potassium and lower panels to particles of silver.*

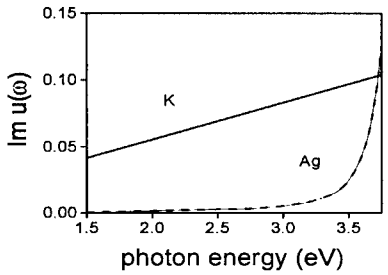


Figure 3. *Imaginary part of the spectral variable u(ω) for potassium and silver as function of the photon energy*

CONCLUSIONS

In conclusion, we have showed that the multipolar effects on the optical properties of a nanoparticle due to the presence of a substrate depend with the direction of the applied external field. We have found that for oblate particles with $a/b > 3$ the multipolar effects are reduced and the dipolar approximation gives a good description of the behavior of the system. Since multipolar effects become more important for systems where the substrate has a large dielectric constant, in this case the dipolar approximation is not good enough. We also have shown that very different spectra could be obtained considering particles of different material even if the geometry of the system is the same. Finally, we have demonstrated that the interpretation of the spectral representation could be helpful to elucidate the shape and size of the nanoparticles.

REFERENCES

1. H. Haberland, ed. *Cluster of Atoms and Molecules II*, Spinger Series in Chemical Physics **56**, Springer Verlag, Berlin (1994).
2. U. Kreibig and M. Vollmer, *Optical Properties of Metal Clusters*, Springer Series y Material Sciences, Vol. **65**, Springer Verlag, Berlin (1994).
3. C. Beitia, Y Borensztein, R. Lazzari, J. Nieto and R. G. Barrera, Phys. Rev. B **60**, 6018 (1999).
4. E. C. Chan and J. P. Marton, J. Appl. Phys. **45**, 5004 (1974).
5. H. G. Graighead and G. A. Niklasson Thin Solid Films. **125**, 165 (1985); J. Appl.. Phys. **55**, 3382 (1984).
6. T. Yamaguchi, S. Yoshida and A. Kinbara, Thin Solid. Films. **13**, 261 (1972); J. Opt. Soc. Am. **61**, 463 (1971); J. Opt. Soc. Am. **62**, 1415 (1972).
7. A. Bagchi, R.G. Barrera and A.K. Rajagopal., Phys. Rev. B, **20**, 4824-4833 (1979).
8. A. Bagchi, R.G. Barrera and B.B. Dasgupta, Phys. Rev. Letters, **44**, 1475-1478 (1980).
9. R. Ruppin, Surf. Sci. **127**, 108 (1983).
10. M. M. Wind, J Vlieger and D. Bedeaux, Physica **141A**, 33 (1987); M. M. Wind, P. A. Bobbert, J Vlieger and D. Bedeaux, Physica **143A**, 164 (1987).
11. P. A. Bobbert and J. Vlieger, Physica **137A**, 209, 243 (1986).
12. C. E. Román-Velázquez, C. Noguez and R. G. Barrera, phys. stat. sol. (a) **175**, 393 (1999); submitted to Phys. Rev. B.
13. D. J. Bergman, Phys. Rep. **43**, 377 (1978); D. Stroud, G. W. Milton and B. R. De, Phys. Rev B **34**, 5145 (1986); R. Fuchs, Phys. Rev. B **11**, 1732 (1975).
14. J. Lam, J. Appl. Phys. **68**, 392 (1990).

DIELECTRIC CHARACTERIZATION OF THIN FILMS CONSISTING OF TIN DOPED INDIUM OXIDE NANOPARTICLES

A. HULTÅKER and G. A. NIKLASSON
Department of Materials Science, Uppsala University, PO Box 534, SE-751 21 Uppsala, Sweden, Annette.Hultaker@Angstrom.uu.se

ABSTRACT

In recent years there has been a growing interest in cheap and easy production techniques for transparent conducting thin films. One way of making these uses a nanoparticle dispersion. We prepared thin films of tin doped indium oxide by spin-coating of a solution of nanoparticles. The sintering behavior of these ceramic particles was studied by dielectric spectroscopy and by grazing incidence X-ray diffraction. The grain growth was found to start at 1000°C and to be prominent at 1250°C. However, the electrical conductivity reached a maximum below these temperatures.

INTRODUCTION

There are a number of technological applications in which transparent conducting thin films of materials such as tin doped indium oxide (ITO), aluminium doped zinc oxide, or fluorine doped tin oxide are used, e.g. in light emitting diodes [1], heat mirrors [2], and other kinds of energy efficient window applications [3, 4]. Sometimes there is a need for a patterned structure, e.g. for solar cells and liquid crystal displays. Today's standard production methods - sputtering, chemical vapour deposition, or spray pyrolysis - followed by lithography and etching have drawbacks in long production times, high costs, and hazardous by-products. Much would be gained if instead the thin film could be printed in a one-step procedure [5-7]. A dispersion of nanoparticles can be used as an "ink" in such a process. In the present work we study the conduction mechanisms and sintering properties of spin coated thin films consisting of nanoparticles of ITO. We believe that these layers have the same properties as printed layers.

This paper presents data on grain growth as a function of sintering temperature, T_S, from grazing incidence X-ray diffraction (XRD). We also report impedance spectroscopy results taken under the application of an AC voltage of variable frequency to the film. The latter technique provides useful information on charge transfer and polarisation phenomena [8].

EXPERIMENTAL

Our samples were prepared from an ITO nanopowder doped with tin, with the Sn/(In+Sn) ratio being 0.05. The powder was dispersed in water and spin-coated onto glass, Al_2O_3, and fused silica substrates. These samples were then sintered in air at different temperatures, followed by reduction in N_2+H_2 gas by annealing at T_A = 480° C (Table I). The temperature in the oven was increased by 8 to 10°/min until the final temperature was attained. The sintering or annealing temperature was then kept constant for 30 minutes. The samples were cooled down with the furnace shut off. Film thicknesses between 41 and 87 nm were calculated from X-ray fluorescence measurements. These data correspond to the mass thickness and do not account for the porosity. Visual inspection revealed that the adhesion of the film to the substrate was good

Mat. Res. Soc. Symp. Proc. Vol. 581 © 2000 Materials Research Society

Table I: Heat treatment and resistivity values. T_S (T_A) denotes sintering (annealing) temperature.

	Sintering in air		Post heating for reduction in N_2 + 7 vol% H_2		Aged samples
Film thickness[a] (nm)	T_S (°C)	Resistivity (mΩcm)	T_A (°C)	Resistivity (mΩcm)	Resistivity (mΩcm)
80	480	690	480	70	1 800
74	750	48	480	57	430
74	1 000	500	480	27	11 000
41	1 250	-	480	-	-

[a] Thickness assuming fully dense layers.

only for samples sintered at 1250°C. The DC resistivity of the pristine samples was measured using a four-point probe.

Earlier experience has indicated an ageing effect, i.e., a decreasing conductivity, due to water up-take in the samples (Figure 1). According to Barlow et al. [5], ITO films consisting of fine particles also degrade when exposed to oxygen in air. The electrical properties were therefore measured at repeated occasions. The conductivity was not stable, and we were able to find a correlation to the atmospheric conditions. Table I gives resistivity values obtained from impedance measurements on samples that had been aged for six months in air. Figure 1 also shows the decrease in resistivity that occurs upon heating in a reducing atmosphere of N_2 + 7 vol% H_2 gas.

We investigated crystal structure and grain growth as a function of sintering temperature by use of grazing incidence XRD in a Siemens D5000 unit operating with CuK_α radiation. Samples on fused silica were used for these experiments. The Scherrer method was employed for evaluation of the crystal size [9].

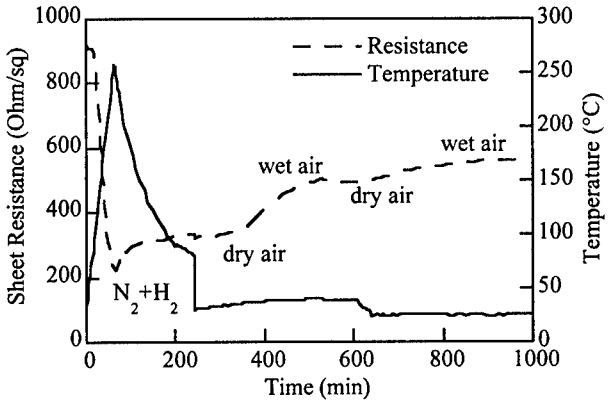


Figure 1: Effects on the resistance when a film consisting of ITO nanoparticles is exposed to heat, N_2 + 7 vol% H_2 gas, and humidity.

Impedance spectroscopy data were acquired on a Novocontrol broadband dielectric converter coupled to a Solartron SI1260 Impedance Analyzer. An AC voltage of 0.05 to 0.1 V was applied in the frequency interval of 10^{-3} to 10^{7} Hz parallel to the plane of the film in a two point configuration. Samples on Al_2O_3 substrates were used. Aluminium contacts, 18 to 38 mm long, were evaporated onto the samples with a spacing of 3 or 5 mm. The experiment included a manual calibration recommended for this type of conductive samples [10]. An equivalent circuit analysis was performed using the Zview program [11].

RESULTS AND DISCUSSION

The driving force in pressureless sintering of nanoparticles is reduction of the pore surface energy. Ceramic materials do not have the same plastic behaviour as metals and are therefore more difficult to densify, but claims have been made that the sintering behaviour of ceramic nanoparticles is similar to that of any ceramic material [12]. The route to a dense layer can be described by a three-step model [12, 13]: The first process step leads to necking between the particles at contact points. A spongelike structure with open pores then evolves during the second step. It is in this stage most of the densification takes place due to pore shrinkage. When the pores reach a critical size they become unstable and form small isolated units. In the third and final step, these residual pores are eliminated.

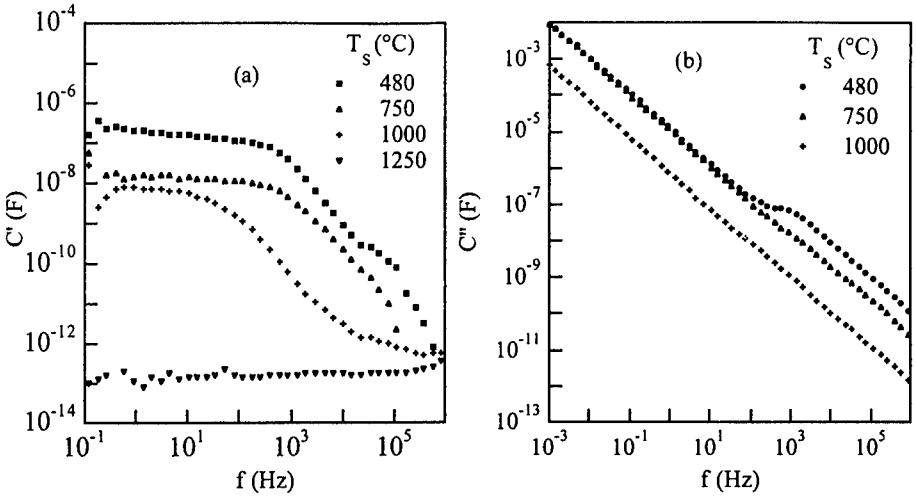
We only found crystalline In_2O_3 by XRD, which has a detection limit of 1%. An amorphous phase of Sn oxide or hydroxide cannot be excluded, however. We calculated the crystal size from the major XRD peak at the interplanar distance of 2.9 Å, which corresponds to cubic bixbyite In_2O_3 [14] with a preferred orientation normal to the (222) plane. The grains are approximately 35 nm for sintering temperatures up to 750°C. At 1000°C the grains start to grow, and at 1250°C they tripled their size (Table II). As mentioned earlier, only samples sintered at 1250°C adhered well to the substrate.

Table II: Crystal size as a function of sintering temperature

Sintering temperature (°C)	Crystal size (nm)
250 / 480[a]	36
480	35
750	34
1 000	42
1 250	100

[a] Sintered at 250° followed by annealing at 480°C

Table I presents the resistivity of the samples after sintering, annealing in N_2+H_2 gas and ageing. The high resistivity of the film sintered at 480°C can probably be ascribed to poor and few contacts between the particles. The sample sintered at 750°C remains almost unaffected by the annealing. The sample sintered at 1000°C appears to be oxidized during sintering and this oxidation is only temporarily reversed by the annealing. After sintering at 1250°C the grains have grown considerably. This fact and the high magnitude of the resistivity even after annealing, makes us believe that the third step of sintering has been reached in this case. Behr et al. [15] and Shigesato et al. [16] have found that oxidation might be connected to segregation of tin to the grain surfaces. Such a segregation has also been observed in antimony doped tin oxide which is similar to ITO [17].



Figures 2: Frequency dependencies for the real (a) and imaginary (b) parts of the capacitance, C' and C'', respectively, of the ITO samples sintered at different temperatures, T_S.

Figure 1 shows that the resistivity increases when a film of ITO nanoparticles is exposed to moist air. Since our samples were stored in air, we believe that the degradation of the samples, from the resistivity of the pristine film, is due to water absorption. This degradation takes place within a short period of time after film preparation. Results are presented in Table I. The sample treated at $T_S = 750°C$ does not show as much ageing as the other samples. The films sintered at 480°C and 1000°C, however, undergo a severe degradation of the conductivity with time.

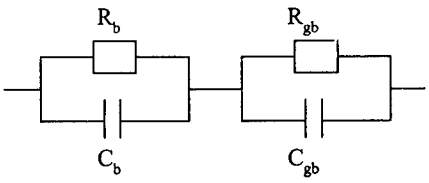


Figure 3: Equivalent circuit consisting of two elements in series, each comprising one capacitor and one resistor in parallel. One element probably describes the bulk (b) of the grains and the other element the grain boundaries (gb).

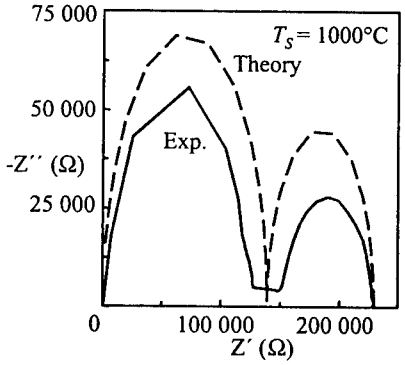


Figure 4: Complex impedance plot for the sample sintered at 1000°C. Z' (Z'') denotes the real (imaginary) part of the impedance The data correspond to measured results and to a fit to the equivalent circuit in Figure 3. The circuit parameters are presented in Table III.

Table III: Circuit parameters used to fit the impedance data to the model in Figure 3.

Sintering temperature (°C)	Grain boundary capacitance (F)	Grain boundary resistance (Ω)	Bulk capacitance (F)	Bulk resistance (Ω)
480	$1.7 \cdot 10^{-7}$	11 450	$\sim 10^{-10}$	1 700
750	$3.2 \cdot 10^{-8}$	8 300	$\sim 10^{-10}$	6 800
1 000	$3 \cdot 10^{-8}$	90 000	$1 \cdot 10^{-12}$	139 000

The impedance spectroscopy data are displayed as frequency dependent complex capacitance whose real and imaginary parts are denoted C' and C'', respectively, in Figure 2. The DC conductivity is proportional to the flat low frequency part of the curve for C'. We model the material as a series connection of two parallel *R-C* circuits assumed to represent the electrical properties of the interior of the grains and the grain boundaries, respectively [8] (Figure 3). For the sample sintered at 1000°C the complex impedance shown in Figure 4 is found to consist of two depressed semicircles. The same figure also shows a fit to the equivalent circuit in Figure 3. The circuit parameters for the three samples sintered at 480°C, 750°C, and 1000°C, are presented in Table III. No results could be obtained for the sample sintered at T_S = 1250°C due to detection limits of the instrument.

The bulk resistivity is found to increase with sintering temperature which is consistent with the assumption that the grains are depleted of the tin dopant so that fewer free conduction electrons are available. The bulk capacitance is of the order of 10^{-10} F or less. The grain boundary resistance reaches a minimum for the sample sintered at 750°C. This is in general agreement with the assumption that T_S = 480°C yields few grain contacts, while $T_S \geq$ 1000°C produces insulating layers on the particles. The grain boundary capacitance decreases at high sintering temperatures, which probably indicates a reduced porosity.

CONCLUSIONS

This paper has presented some initial results on transparent and conducting layers based on ultrafine ITO particles. Grain growth was found to occur by sintering, the effect being most prominent at temperatures above 1000°C. Impedance spectroscopy data could be given a consistent interpretation in terms of an equivalent circuit with elements signifying the bulk of the grains and their boundaries. Our work gives support to earlier claims by Behr et al. [15] and Shigesato et al. [16] that heat treatment of heavily doped oxide particles can lead to dopant segregation with ensuing decrease of the electrical conductivity.

ACKNOWLEDGEMENT

This work was financially supported by the European Union through contract BRPR-CT96-0346 ("Printracon"). Further support was obtained from Anna-Maria Lundin's Scholarship Foundation, Småland nation, Uppsala, Sweden. The authors would also like to thank the company H.C. Starck, Germany, for supplying the powder and A. W. M. de Laat and

C. van Haag at Philips CFT, The Netherlands, for sample preparation, and for the measurements of film thickness and initial resistivity.

REFERENCES

1. J. S. Kim, M. Granström, R. H. Friend, N. Johansson, W. R. Salaneck, R. Daik, W. J. Feast and F. Cacialli, J. Appl. Phys. **84**, pp. 6859-6870 (1998).

2. I. Hamberg and C. G. Granqvist, J. Appl. Phys. **60**, pp. R123-R159 (1986).

3. C. G. Granqvist, Appl. Phys. A **57**, pp. 19-24 (1993).

4. C. G. Granqvist, A. Azens, A. Hjelm, L. Kullman, G. A. Niklasson, D. Rönnow, M. Strømme Mattsson, M. Veszlei and G. Vaivars, Solar Energy **63**, pp. 199-216 (1998).

5. F. Barlow, M. A. Naby, A. Joshi and A. Elshabini-Riad, Solar Energy Mater. Solar Cells **33**, pp. 63-71 (1994).

6. K. Nakayama, S. Send and F. Uchida, Proc. 9th Int. Microelectronics Conf., Tokyo, Japan, 1996, pp. 54-57.

7. J. P. Coleman, A. T. Lynch and P. Madhukar, Proc. Third Symp. Electrochromic Materials, San Antonio, Texas, US, 1996, pp. 325-337.

8. A. K. Jonscher, *Dielectric Relaxation in Solids,* Chelsea Dielectrics Press, London, 1983, pp. 1-12 and pp. 75-78, 81.

9. M. F. Toney, in *Encyclopedia of Materials Characterization*, edited by C. R. Brundle, C. A. Evans, Jr. and S. Wilson, Butterworth-Heinemann and Manning Publications Co., Stoneham and Greenwich, 1992, pp. 207-208.

10. G. Schaumburg, , (private communication).

11. ZView for Windows 1.2 .

12. M. J. Mayo, D.-J. Chen and D. C. Hague, in *Nanomaterials; Synthesis, Properties and Applications*, edited by Edelstein and Cammarata, Institute of Physics Publishing, London, 1996, pp. 165-197.

13. W. E. Kuhn, in *Ultrafine Particles*, edited by W. E. Kuhn, Wiley, New York, 1963, pp. 41-103.

14. Powder diffraction file 06-0416.

15. G. Behr, J. Werner, S. Oswald, G. Krabbes, P. Dordor, D. Elefant and W. Pitschke, Solid State Ionics **101-103**, pp. 1183-1187 (1997).

16. Y. Shigesato, S. Takaki and T. Haranou, Appl. Surf. Sci. **48/49**, pp. 269-275 (1991).

17. M. J. v. Bommel, W. A. Groen, H. A. M. v. Hal, W. C. Keur and T. N. M. Bernards, J. Mater. Sci. **34**, pp. 4803-4809 (1999).

SYNTHESIS AND CHARACTERIZATION OF MANGANESE VANADIUM OXIDES AS CATHODES IN LITHIUM BATTERIES

Fan Zhang, Peter Zavalij, and M. Stanley Whittingham*
Materials Research Center and Chemistry Department
State University of New York at Binghamton, Binghamton, NY 13902-6000

ABSTRACT

Our research on new cathode nano-materials for advanced lithium batteries has focused on the hydrothermal method for synthesis. We have synthesized two novel manganese vanadium oxides using the hydrothermal reactions of vanadium (V) pentoxide, $[N(CH_3)_4]MnO_4$, and $MnSO_4$ with an organic templating cation at 165°C. The δ-type $[N(CH_3)_4]_zMn_yV_2O_5{\bullet}nH_2O$ has a monoclinic structure, a=11.66(2)Å, b=3.610(9)Å, c=13.91(4)Å, β=108.8(2)°. It has a disordered V_2O_5 double layer and the Mn and $N(CH_3)_4$ ions reside between the layers. The γ-type MnV_2O_5 is orthorhombic, belongs to the space group Pnma, a=9.7585(2) Å, b=3.5825(1)Å, c= 11.2653(2) Å. These compounds were also characterized by electron microprobe, FTIR and TGA. They reacted readily with lithium, and their electrochemical behavior in lithium cells was determined.

INTRODUCTION

Lithium is a very attractive material for high energy density batteries because of its low equivalent weight and high electrode potential. There has been much effort recently to find more cost-effective oxide cathodes for advanced lithium batteries, to replace the technically excellent but expensive lithium cobalt oxide. Soft chemistry was shown to be an effective method for the preparation of high surface area transition metal oxides that offer many advantages as cathodes in rechargeable lithium batteries. There has been much interest in the last two decades in layered vanadium oxides and their intercalates because of their potential use as secondary cathode materials for advanced lithium batteries. Therefore, the already rich crystal chemistry of the vanadates with open framework was expanded with many new structures. A significant part of them were done in our group. Earlier we reported the use of the tetramethyl ammonium ion (TMA) as a structure-directing cation [1] and showed that a number of new phases of tungsten, molybdenum, and vanadium could be formed. In the case of vanadium, two new structure types were reported in 1995 [2], the layered $N(CH_3)_4V_4O_{10}$ [3] and a hydrated vanadium dioxide [4, 5], also a new structure type formed by iron chloride and vanadium oxide in 1997, the layered $[N(CH_3)_4]_zFe_yV_2O_5{\bullet}nH_2O$, where z is 1/6, y≈ 0.1 and n is 1/6 [6]. Several other layer structure vanadium oxides were formed by various groups [7-9]. To date only the tetramethyl ammonium ion has shown the ability to form a range of different structure with differing organic to vanadium ratios [10]; the present count is six structures including two with a string-like morphology formed at pH values of 3 or less, $N(CH_3)_4V_3O_7$ and $[N(CH_3)_4]_5V_{18}O_{46}$.

A variety of new structures can also be formed when a second 'transition' metal is present, for example with zinc four new compounds, $Zn_{0.4}V_2O_5{\bullet}0.27H_2O$, $Zn_{0.39}V_2O_5{\bullet}0.5TMA$,

Mat. Res. Soc. Symp. Proc. Vol. 561 © 2000 Materials Research Society

$Zn_3(OH)_2(V_2O_7)\cdot H_2O$, and $Zn_2(OH)_3(VO_3)$, have been reported [11, 12]. Nickel forms $[NH_2(CH_2)_2NH_2]_2NiV_6O_{14}$ [13], whose structure is related to $N(CH_3)_4V_3O_7$. We also found that cobalt forms several compounds, including both the δ- and V_3O_7-type phases; however, they were contaminated with other phases such as $Co_2V_2O_7$ and CoV_2O_6 [14].

Manganese compounds are of particular interest for use as cathodes in reversible lithium batteries, because of their low cost. We have therefore made a study of the Mn-V-O system, using hydrothermal methods with organic "templates" as the synthesis approach. More than six different compounds have been formed, including the known MnV_2O_6 and $Mn_2V_2O_7$. The compound $Mn_{7-2/3x}(OH)_3(VO_4)_{4-2x}(V_2O_7)_x$(x=0.199) [15] has a pipe-like morphology with tunnels filled with manganese; it therefore shows little lithium redox behavior. In this paper, we report two novel manganese vanadium oxides, δ-type $[N(CH_3)_4]_zMn_yV_2O_5\cdot nH_2O$ and γ-type MnV_2O_5. They were prepared by reaction of V_2O_5, with $[N(CH_3)_4]MnO_4$, or with $MnSO_4$ and the organic diethanolamine, respectively.

EXPERIMENTAL

δ-$[N(CH_3)_4]_zMn_yV_2O_5\cdot nH_2O$ was prepared by the hydrothermal treatment of V_2O_5 powder from Johnson and $[N(CH_3)_4]MnO_4$ in a 1:2 molar ratio, respectively; the pH of this solution was 2.34. The reaction mixture was heated in a 125 ml Teflon-lined Parr Bomb reactor for 60 hrs. at 438K. The resulting dark green powder was filtered and dried in air. The pH of the solution after reaction was basic, pH=5.93. In the case of the γ-MnV_2O_5, a 1:1:2 aqueous solution of $MnSO_4$, V_2O_5 and diethanolamine were heated at 455 K for 72 hrs; the initial pH was 6.06 and the pH after reaction was 6.13.

X-ray powder diffraction was performed using Cu Kα radiation on a Scintag θ-θ diffractometer. The data was collected from 2θ = 4° to 2θ = 90° with 0.03° steps and 15 sec per step. The TGA data was obtained on a Perkin-Elmer model TGA 7 at 3°/min in oxygen on a platinum pan, the FTIR on a Perkin-Elmer 1500 series, and the Electron Microprobe on a JEOL8900. Initial electrochemical studies were conducted in lithium cells using 1.5 molar $LiPF_6$ in a 2:1 dimethyl carbonate/ethlycarbonate mixture as the electrolyte; the vanadium oxide was mixed with 10% carbon black and 10% Teflon powder, and hot pressed for 20 minutes at 227°C. A MacPile potentiostat was used to cycle the cells.

RESULTS AND DISCUSSION

δ-type $[N(CH_3)_4]_zMn_yV_2O_5\cdot nH_2O$

The crystals precipitated from the manganese reaction exhibited large greenish-black plates, and the SEM image is shown in Figure 1(a). The energy dispersive spectroscopy showed that they contained manganese and vanadium.

The x-ray diffraction data of the δ-$[N(CH_3)_4]_zMn_yV_2O_5\cdot nH_2O$ compound is shown in Figure 2(a). This pattern shows a repeat distance of 12.83 Å. Preliminary studies suggest a monoclinic unit cell with a=11.66(2), b=3.610(9), c=13.91(4), β=108.8(2)°. The structure contained δ-type double sheets of V_2O_5 layers, the V_2O_5 layers were built up with $V(1)O_6$ and $V(2)O_6$ octahedron. The octahedron has four vanadium oxygen single bonds in the square plane,

one short vanadium oxygen double bond above the plane and one long vanadium oxygen single bond below the plane or vice versa. TMA and manganese ions sit between the layers. TMA are the major pillars between the V_4O_{10} sheets (Figure 1(b)).

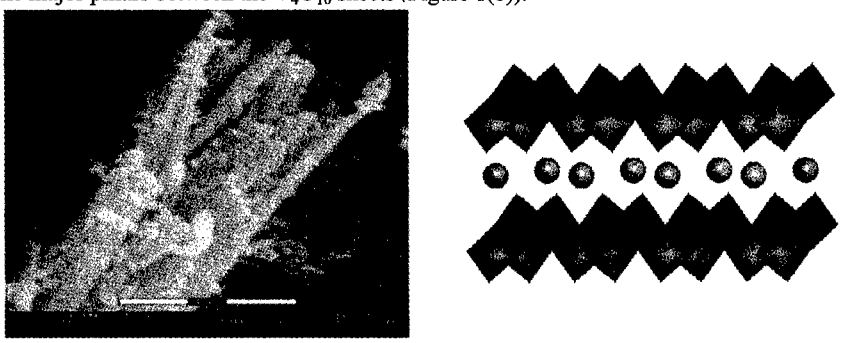


Fig. 1. (a) SEM image, black bar = 4 μm, and (b) the structure of δ-$[N(CH_3)_4]_zMn_yV_2O_5{\bullet}nH_2O$, showing the TMA ions between the double vanadium oxide sheets, from [16].

The X-ray of the product after heating to 150 °C showed a contraction of under 0.1Å, which returned to 12.8 Å on exposure to air, indicating that the water is not critical to the structure.

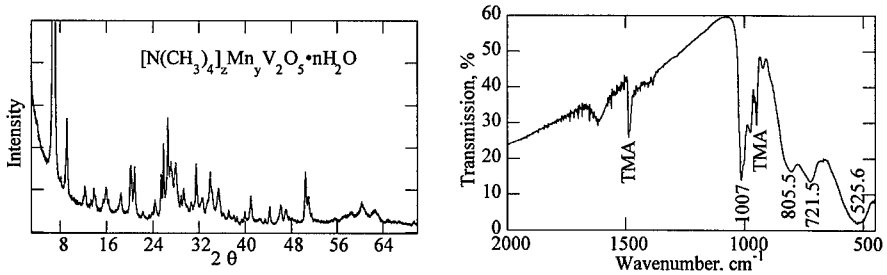


Fig. 2. (a) X-ray diffraction pattern [17] and (b) the FTIR of δ-$[N(CH_3)_4]_zMn_yV_2O_5{\bullet}nH_2O$

The FTIR spectrum of the δ-$[N(CH_3)_4]_zMn_yV_2O_5{\bullet}nH_2O$ is relatively simple, as can seen from Figure 2(b). The band at 1007 cm^{-1} is due to the V=O bond, those at 721.5 and 525 cm^{-1} are associated with the vanadium oxide network. This paucity of V-O bands speaks against the presence of a vanadium cluster. The bands at 1482.9 and 951.0 cm^{-1} are due to the organic species, $N(CH_3)_4$.

On thermal analysis, as shown in Fig. 3(a), this material lost 4 % of its weight at 60 °C, probably surface water. This compound lost a further 9.5% by 330°C. This suggests that the organic material is in the structure; z is probably around 1/6, with some associated water or oxygen. X-ray diffraction of the heated material showed the presence of both V_2O_5 and $Mn(VO_3)_2$, suggesting a greater than 2:1 ratio of V to Mn in the compound; y is also around 1/6.

The electrochemical data is shown in Fig. 3(b). The initial open circuit emf was around 3.62 volts, suggesting that the vanadium approaches the +5 oxidation state. Two lithiums could be

incorporated into the structure on discharge above 2 volts. The lithium insertion proceeded in a number of stages, reminiscent of that of V_2O_5. These steps were maintained during the subsequent charge and discharge cycles, showing that the material's structure did not change during the redox reactions.

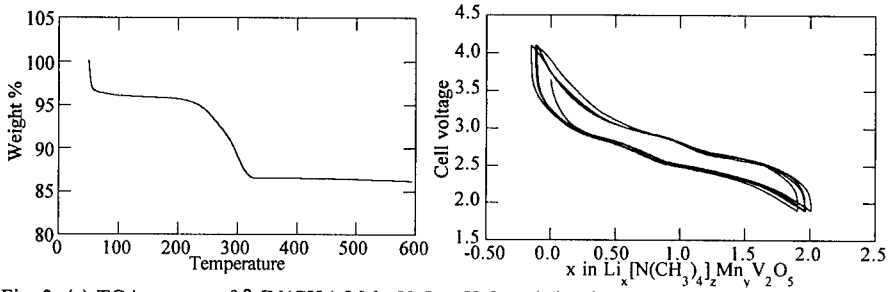


Fig. 3. (a) TGA pattern of δ-$[N(CH_3)_4]_zMn_yV_2O_5 \cdot nH_2O$ and (b) electrochemical cycling of dehydrated δ-$[N(CH_3)_4]_zMn_yV_2O_5$, after [17].

γ-MnV_2O_5.

The morphology of this manganese vanadium compound was well-formed dark brown large lathe-like sheets (Fig. 4a), around 1-2 μm thick, 10 μm across and a hundred μm on an edge. Electron microprobe showed that they contained manganese and vanadium but no sulfur and suggested around a 1:2 ratio of manganese to vanadium in the plates. The x-ray diffraction pattern of the manganese compound (Fig. 6a) was indexed with an orthorhombic lattice system and the space group Pnma. The cell parameters of this compound are a=9.7585(2) Å, b=3.5825(1)Å, c= 11.2653(2) Å. In this structure the vanadium oxide square pyramids form zig-zag sheets bwtween which sit the manganese in octahedral coordination, as show in Figure 4b.

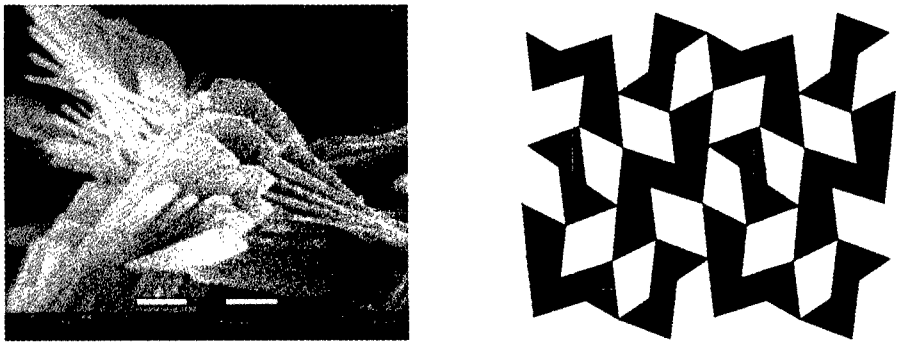


Fig. 4. (a) SEM image, black bar is 5μm long, and (b) structure of γ-MnV_2O_5, from [18]

The TGA analysis, figure 5(a), of this compound in oxygen shows a 6 % increase of its weight from 380 °C to 580 °C consistent with the addition of one oxygen and the formation of

$Mn(VO_3)_2$ as observed by x-ray analysis of the product after heating to 650°C.

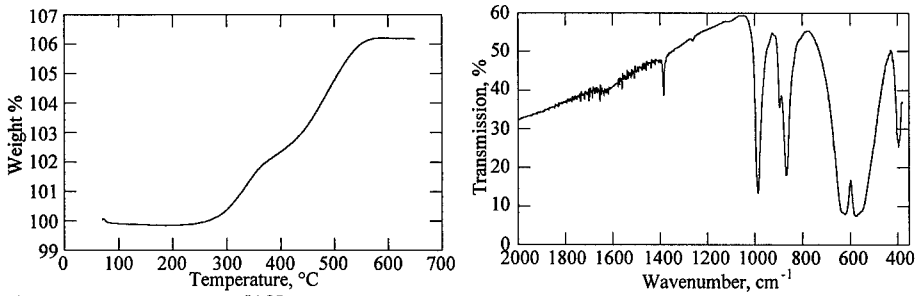


Figure 5. (a) TGA pattern [18], and (b) FTIR pattern of γ-MnV_2O_5

The FTIR pattern of γ-MnV_2O_5 is relatively simple as shown in Figure 5(b). The vanadyl group is at 984.2 cm^{-1}, and the other main vanadium-oxygen bands are at 865.3, 627.5, and 570.8 cm^{-1}.

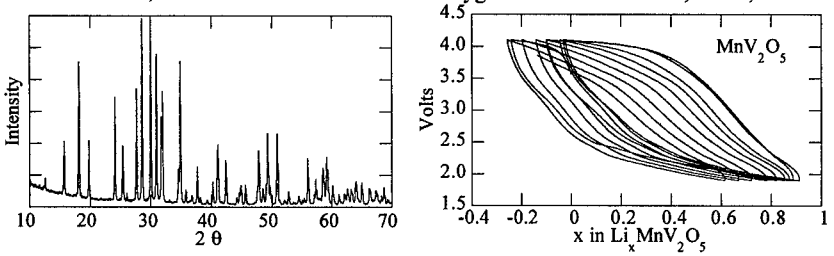


Fig. 6. (a) XRD pattern and (b) electrochemical cycling of γ-MnV_2O_5, after [18].

The electrochemical behavior of the γ-MnV_2O_5 phase is shown in Fig. 6(b). When there was no lithium present in the compound, it has an initial cell voltage of 3.6 V. Around 0.8 lithium could be incorporated into the structure on discharge down to 2 volts. On charge, a slight overcharge was observed and on subsequent discharge the lithium was reinserted reversibly. However, a successful cathode will need a higher capacity with the manganese and vanadium ions reversed in position and in their highest oxidation states, e.g. $VMn_2O_{6.5}$.

CONCLUSIONS

Two new manganese vanadium oxide structures have been synthesized hydrothermally, δ-type $[N(CH_3)_4]_2Mn_yV_2O_5 \cdot nH_2O$ and γ-type MnV_2O_5, and their structures determined. They intercalate lithium into their structures in a reversible manner. The structure of γ-type MnV_2O_5 is close to γ-LiV_2O_5 [19]. Mild hydrothermal reactions appear to be a general useful method for the synthesis of transition metal oxides. In many cases, new structures are formed as recently noted in the case of tungsten, molybdenum, and vanadium. Extensive research is now underway to explore the possibilities of this approach to new materials, and how structure effects properties [10, 16].

ACKNOWLEDGMENT

We thank the Department of Energy, Office of Transportation Technologies, through Lawrence Berkeley Laboratory and the National Science Foundation through grant DMR9810198 for partial support of this work. We also thank Bill Blackburn for the electron microprobe studies. This paper was also presented as paper CC5.4 at the Materials Research Society Spring Meeting in San Francisco, April 1999.

REFERENCES

1. M. S. Whittingham, J. Li, J. Guo, and P. Zavalij, Materials Science Forum, **152-153,** 99 (1994).
2. M. S. Whittingham, J. Guo, R. Chen, T. Chirayil, G. Janauer, and P. Zavalij, Solid State Ionics, **75,** 257 (1995).
3. P. Zavalij, M. S. Whittingham, E. A. Boylan, V. K. Pecharsky, and R. A. Jacobson, Z. Kryst., **211,** 464 (1996).
4. T. Chirayil, P. Zavalij, and M. S. Whittingham, Solid State Ionics, **84,** 163 (1996).
5. T. Chirayil, P. Zavalij, and M. S. Whittingham, J. Electrochem. Soc., **143,** L193 (1996).
6. F. Zhang, P. Y. Zavalij, and M. S. Whittingham, Mater. Res. Bull., **32,** 701 (1997).
7. D. Riou and G. r. Férey, J. Solid State Chem., **120,** 137 (1995).
8. D. Riou and G. r. Férey, J. Solid State Chem., **124,** 151 (1996).
9. Y. Zhang, J. R. D. DeBord, C. J. O'Connor, R. C. Haushalter, A. Clearfield, and J. Zubieta, Angew. Chem. Int. Ed. Engl., **35,** 989 (1996).
10. T. A. Chirayil, P. Y. Zavalij, and M. S. Whittingham, Chem. Mater., **10,** 2629 (1998).
11. F. Zhang, P. Y. Zavalij, and M. S. Whittingham, Mat. Res. Soc. Proc., **496,** 367 (1998).
12. P. Y. Zavalij, F. Zhang, and M. S. Whittingham, Acta Cryst, **C53,** 1738 (1997).
13. P. Y. Zavalij, F. Zhang, and M. S. Whittingham, Acta Cryst, **B55,** 953 (1999).
14. F. Zhang, PhD Thesis, SUNY at Binghamton, (1999).
15. F. Zhang, P. Y. Zavalij, and M. S. Whittingham, J. Mater. Chem., **9,** 3137 (1999).
16. P. Y. Zavalij and M. S. Whittingham, Acta Cryst., **B55,** 627 (1999).
17. F. Zhang and M. S. Whittingham, Electrochem. Commun., **2,** 69 (2000).
18. F. Zhang, P. Y. Zavalij, and M. S. Whittingham, Electrochem. Commun., **1,** 564 (1999).
19. J. Galy, J. Darriet, and P. Hagenmuller, Chim. Miner., **8,** 509 (1971).

Z-CONTRAST STEM IMAGING AND EELS OF CDSE NANOCRYSTALS: TOWARDS THE ANALYSIS OF INDIVIDUAL NANOCRYSTAL SURFACES

A.V. KADAVANICH†*, T. KIPPENY*, M. ERWIN*, S. J. ROSENTHAL*, S. J. PENNYCOOK†
†Oak Ridge National Laboratory, Solid State Division, Oak Ridge, TN 37831
*Vanderbilt University, Department of Chemistry, Nashville, TN 37235

ABSTRACT

We have applied Atomic Number Contrast Scanning Transmission Electron Microscopy (Z-Contrast STEM) and STEM/EELS (Electron Energy Loss Spectroscopy) towards the study of colloidal CdSe semiconductor nanocrystals embedded in MEH-PPV polymer films. Z-Contrast images are direct projections of the atomic structure. Hence they can be interpreted without the need for sophisticated image simulation and the image intensity is a direct measure of the thickness of a nanocrystal. Our thickness measurements are in agreement with the predicted faceted shape of these nanocrystals.

Our unique 1.3Å resolution STEM has successfully resolved the sublattice structure of these CdSe nanocrystals. In [010] projection (the polar axis in the image plane) we can distinguish Se atom columns from Cd columns.

EELS measurements on individual nanocrystals indicate a significant amount (equivalent to 0.5-1 surface monolayers) of oxygen on the nanocrystals, despite processing in an inert atmosphere. Spatially resolved measurements at 7Å resolution suggest a surface oxide layer.

INTRODUCTION

CdSe nanocrystals are under investigation for heterojunction optoelectronic devices, such as light-emitting devices (LED's) and photovoltaics (PV's). [1-3] The performance of such devices should be very sensitive to the nature of the junction interface which is the interface between the nanocrystal and the surrounding matrix, usually a conducting polymer. Despite many studies, nanocrystal surfaces are not very well understood in detail since bulk techniques average over all the different surfaces on a nanocrystal and scanning probes do not penetrate the organic ligands on the surface.

In this paper we present the use of a high resolution Scanning Transmission Electron Microscope (STEM) to obtain information about the individual surfaces on nanocrystal. In particular using a high-angle annular dark-field (HAADF) detector provides Z-Contrast which can resolve the sublattice in CdSe nanocrystals. Hence the polarity of the unit cell can be assigned directly from the Z-Contrast image without resorting to extensive image simulations. Furthermore, since the Z-Contrast image is a direct projection of the atomic positions, the technique is sensitive to aperiodic detail at the surface unlike phase-contrast HRTEM. [4, 5]

Using the sub-nanometer STEM probe for EELS analysis allows chemical analysis on the length scale of a few Å. In principle it should thus be possible to obtain both chemical and structural information from individual nanocrystal surfaces in the STEM. [6]

EXPERIMENT

Sample Preparation

CdSe nanocrystals were prepared by the method of Murray [7, 8] as modified by Peng [9] for size-focussing. The TOPO surface ligands were exchanged with pyridine by heating in anhydrous pyridine for several hours. The nanocrystals were subsequently precipitated with hexanes and dissolved in chloroform. Poly (2-methoxy,5-(2'-ethyl-hexyloxy)-p-phenylenevinylene) (MEH-PPV) was prepared by the method of Wudl [10] and dissolved in chloroform. CdSe samples were stored in a glovebox until use, MEH-PPV was stored under argon in brown glass vials. TEM samples were prepared by mixing the MEH-PPV and CdSe solutions and spin-coating onto single-crystal NaCl substrates (100 surfaces). Typical parameters were 20µl of 2 $mg \cdot ml^{-1}$ MEH-PPV/0.05 $mg \cdot ml^{-1}$ CdSe solution, spun at 2000 rpm. The films were removed by dipping into a water surface, whereupon the film floats onto the surface as the NaCl dissolves away. The floating films were picked up with lacey carbon coated copper TEM grids (Ted Pella Co.). Film thicknesses were typically in the range from 150-200 Å as judged

Mat. Res. Soc. Symp. Proc. Vol. 581 © 2000 Materials Research Society

from the optical absorption of identical films spun onto glass slides. Attempts to directly measure the film thickness using AFM have so far not yielded reliable results but indicate significant roughness on the order of 50Å consistent with ellipsometry measurements. Specimens for EELS analysis were prepared in a glovebag (Aldrich Atmosbag) purged with dry nitrogen and stored under nitrogen or argon. Specimens were loaded with a glovebag attached to the microscope under nitrogen flow directly from a standard gas cylinder. Specimens for Z-contrast imaging were prepared in air, stored under argon, and loaded in air.

STEM

EELS analysis was performed in a Vacuum Generators (VG) model HB501 STEM operating at 100kV with an ultimate resolution of 2.2Å. However, to optimize EELS data collection, the probe was run with low excitation of the condenser lens and the exact probe size was not measured. A parallel EELS system using a CCD detector with near single-electron sensitivity was employed. The system is described in more detail in [6]. Data were analyzed using Wavemetrics Igor Pro 3.13. Pre-edge backgrounds were fitted to a power law function and subtracted. Integration of stripped edges used Igor Pro's algorithm based on the trapezoidal method.

For scanning individual nanocrystals, the EELS signal was collected with the STEM in area imaging mode at a magnification such that only one nanocrystal was in the field of view. In this case it was possible to compensate for specimen drift by observing the image and adjusting the electronic image shifts so as to keep the nanocrystal centred on the screen. An area immediately adjacent to each nanocrystal was scanned at the same magnification for the same amount of time to obtain the MEH-PPV blank signal. Time series were acquired to gauge sample damage due to the beam. The oxygen K-edge signal at 532 eV was found to decay over time, but the rate of decay was similar for both nanocrystals and MEH-PPV.

For linescans it is not possible to observe the image while scanning. In this case an image was taken before and after scanning and scans with excessive image drift (more than ~10Å) were rejected. The actual linescan is obtained by scanning the probe at a constant rate across the specimen in the x-direction only. EELS spectra are acquired successively at fixed signal integration times resulting in a series of EELS measurements at different points along the line.

Z-Contrast imaging was performed in a VG HB603 STEM operating at 300kV with a nominal resolution of 1.3Å. Raw images were deconvoluted using a Maximum Entropy [11-13] algorithm running on a dedicated PC with a custom coprocessor card. The details are described elsewhere. [4] For presentation, image brightness/contrast was adjusted in NIH Image 1.61.

For a single atom, the image contrast is proportional to the square of the atomic number (Z^2). For a crystalline specimen in a channeling orientation, the intensity also depends on the thickness of an atomic column along the beam direction. The dependence is non-linear but monotonic and can be calculated from the known crystal structure for any given channeling direction. For typical nanocrystal sizes (<80Å) the dependence is nearly linear so that intensities can be used for comparing relative thicknesses between atomic columns. Intensities are measured in NIH Image by summing the values of all pixels in a chosen region and subtracting out the average value of the background intensity.

RESULTS/DISCUSSION

EELS

The expected nitrogen K-edge at 400eV arising from pyridine was not observed. This is consistent with other experiments suggesting that the pyridine is removed during the film-forming process. [1, 3]

The EELS spectrum in the vicinity of the oxygen K-edge for a single nanocrystal with a diameter of 65Å on the long axis is shown in the top of Figure 1. The nanocrystal lattice is not resolved under the imaging conditions used for the EELS measurement, so the size measurement is not very precise. The short axis diameter is approximately 60Å.

The corresponding spectrum for MEH-PPV is shown in the bottom of the figure. The stripped oxygen edges immediately indicate that the nanocrystal scan contains more oxygen, despite the fact that the amount of MEH-PPV is less due to the volume excluded by the nanocrystal.

To convert the integrated intensity of the MEH-PPV oxygen edge into amount of oxygen we take the volume of MEH-PPV in the scan (area • thickness) and multiply it by the density of MEH-PPV. The latter value is not well known. For our calculations we approximate it as 1 $g \cdot cm^{-3}$. Undissolved large pieces of MEH-PPV are buoyant in chloroform (density = 1.5 $g \cdot cm^{-3}$) so we believe our estimate to be valid to within a factor of two. However, this is our dominant source of error in the quantitation. This yields a conversion of edge intensity to number of oxygen atoms for a given scan.

To calculate the amount of oxygen on the nanocrystal surface [1] we first subtract out the contribution of the MEH-PPV matrix. To account for the volume excluded by the nanocrystal we approximate it as an ellipsoidal spheroid. We also use the spheroidal approximation to calculate the nanocrystal surface area. Using the density of surface sites of wurtzite CdSe (100) and (001) surfaces (the predominant surfaces in CdSe nanocrystals, both with about 0.064 sites•$Å^{-2}$) we calculate the total number of surface sites (both Cd and Se) on the nanocrystal. The coverage is defined as the ratio of oxygen atoms to available surface sites, 1 monolayer (ML) indicating all sites oxidized. This somewhat overestimates the coverage as edge atoms should have two surface dangling bonds capable of bonding to oxygen. However, given the other uncertainties we do not expect this to contribute significantly to our measurement error. For the nanocrystal shown in Figure 1, we obtain 1.3ML of oxygen on the nanocrystal surface. Another measurement in the same specimen gave a coverage of 0.5ML.

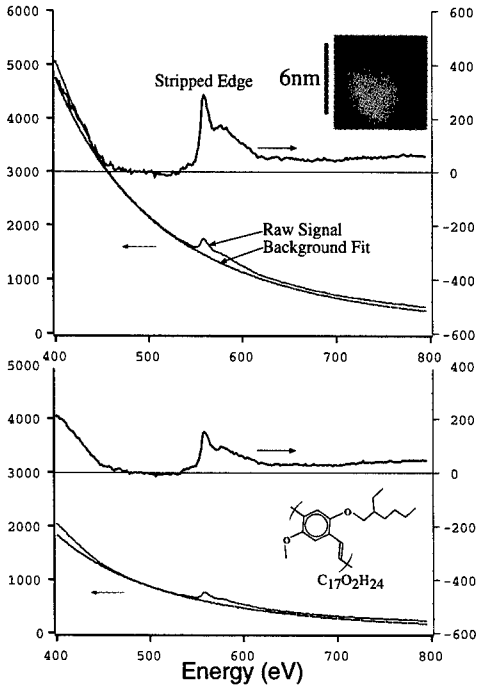


Fig. 1: EELS area scans (left axis) with pre-edge background fits (dotted gray line) and stripped oxygen K-edges (right) axis. The bottom axis shows the loss energy. Top: 10 second scan for the area indicated in the inset, with the single nanocrystal shown. Bottom, scan under identical conditions on the MEH-PPV film. The monomer unit of MEH-PPV is shown in the graph. Edges were integrated from 530ev to 600 eV to obtain the intensity of the oxgyen edge. The nanocrystal has a much larger pre-edge background due to the cadmium M-edge at 404eV.

At present these are our only quantifiable measurements. Given the many uncertainties in the quantitation and the poor statistics, the safest conclusion is that a large amount of oxygen occurs on the nanocrystal surface and the coverage is on the order of 1 ML. This is consistent with previous EELS measurements on ensembles of nanocrystals. The source of the oxygen is unknown at this time. Likely candidates are TOPO from the original synthesis, the MEH-PPV matrix, or the water bath used in the specimen preparation. We are currently pursuing control experiments to test these hypotheses.

The measurements shown so far still average over all the surfaces of a nanocrystal. To

[1]Since CdSe nanocrystals show good crystallinity in HRTEM, Z-STEM and diffraction measurements we assume the majority of the oxygen associated with nanocrystals to occur at the nanocrystal surface

test the feasibility of analyzing individual nanocrystal surfaces we have performed linescans across individual nanocrystals.

One such linescan is shown in Figure 2, with 17 scan increments in the line, acquiring for 4s in each step. Performing the pre-edge background fitting and subtraction in a similar fashion but without converting to absolute numbers of oxygen atoms, we obtain the position dependent oxygen concentration profile shown in the bottom part of Fig. 2. The total drift in the image for the entire linescan was about 10Å, predominantly to the right, so that the positional uncertainty in each step is less than 1 Å.

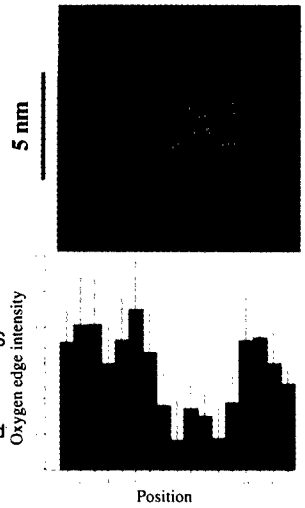


Fig. 2:
Top: DF image of a single nanocrystal with the linescan indicated by the horizontal line. The marker in the center indicates the length of each scan step and thus the area integrated for each EELS measurement.
Bottom:
The oxygen concentration profile calculated from the EELS oxygen K-edge intensity at each scan step. The depletion at the center is attributed to the excluded volume of MEH-PPV.

The depletion of oxygen at the center of the nanocrystal is due to the exclusion of MEH-PPV. The slight increase at the edges of the nanocrystal is suggestive of a thin oxide shell viewed in projection, but within the measurement uncertainty it is not significant. Hence no firm conclusion can be drawn although it does demonstrate the potential for surface specific chemical analysis. It should be noted that the acquisition parameters correspond to detecting less than 10 atoms of oxygen within a scan increment on the MEH-PPV. We expect to improve the measurement uncertainty by further fine-tuning the experimental parameters. In particular by reducing the specimen drift it will be possible to integrate longer in each individual scan and improve the signal-to-noise ratio. Furthermore acquiring a longer range of the pre-edge background should improve the extrapolation into the edge region, resulting in more reliable integration.

Z-STEM

The Z-STEM image of a nanocrystal near [010] zone axis orientation is shown in Figure 3. Panel (a) shows the raw image and panel (b) is the Maximum Entropy Reconstruction of the

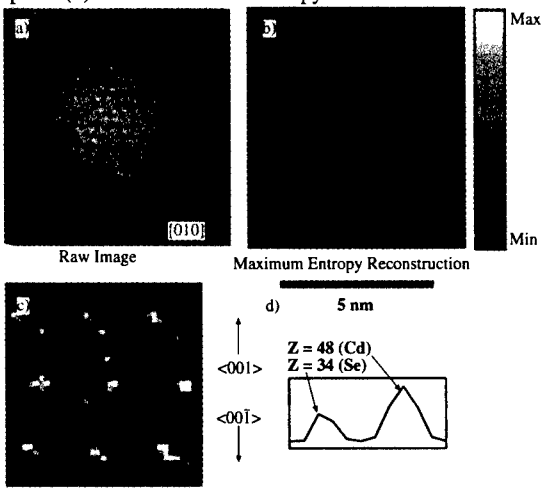


Fig. 3:
a) Z-STEM image of a CdSe nanocrystal near [010] zone axis orientation.
b) Maximum Entropy Reconstruction of the object function
c) enlarged view of the area delimited by the box in (b). The dumbbell pairs can be resolved into the atomic columns 1.5 Å apart.
d) line scan in the direction of the arrow in (c) showing the intensity in the two columns. The intensity distribution closely matches the expected contrast for Cd relative to Se (2:1). Hence the directions of the <001> and <00-1> lattice vectors can be assigned to the image as shown.

object function with the point spread function of the microscope removed. Panel (c) shows a magnified view of the area in (b) indicated by the square. The dumbbell pairs of Cd and Se columns spaced 1.5Å apart are just resolved. The different intensities indicate that the Cd comprises the top right column of the dumbbell pair. This is more evident from the integrated intensity profile in (d) of the area indicated. Not all columns are as well resolved within this image. This could indicate strain in the lattice, but it could also be due to image noise. Based on the contrast in the atomic column the <001> lattice vector direction is assigned as up in the image.

It is assumed that the Cd and Se columns are of equal thickness within each dumbbell column. One may reasonably expect them to differ by one atom at the entrance and exit surfaces each, depending on the exact nature of the surface termination. For the nanocrystal shown the thickness should be on the order of 15-18 atoms so the maximum error would be 13% which cannot account for the contrast difference observed. Hence the assignment of the elemental identities is clear-cut.

The overall noise level in the image is still too large to unambiguously determine atomic positions in the surface region. There is also some overlap with a second nanocrystal in the top

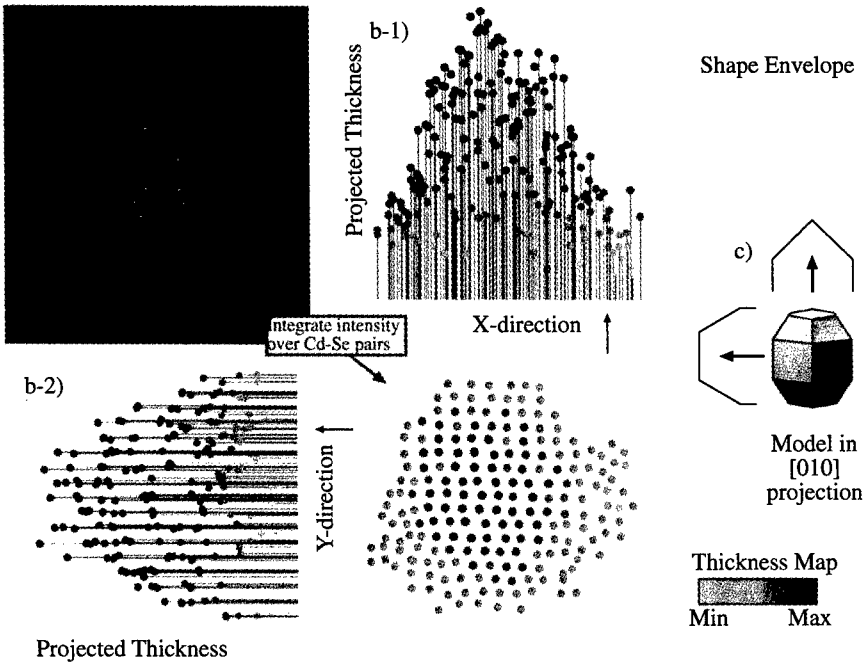


Fig. 4: 3-D Analysis of CdSe nanocrystal
a) the Z-STEM image after Maximum Entropy Reconstruction
b) Thickness map (raw intensity) on a grayscale after integrating the intensity in each dumbbell pair (or otherwise resolvable feature in the image). The indicated thickness is not corrected for the thickness dependence of the contrast, so values are not absolute.
b-1) Projection of the thickness map along the horizontal direction in the image. The envelope of the thicknesses should correspond to the shape envelope of the nanocrystal.
b-2) Same as b-1) in the vertical direction.
c) Schematic of the expected shape in [010] projection based on previous HRTEM studies and the expected shape envelopes in each projection.

left corner of the image. The right edge of the nanocrystal seems to exhibit some disorder, but such an assignment would be tentative at this time.

If we integrate the total intensity of each dumbbell pair we obtain a spatially resolved thickness map, since the intensities are then independent of composition. This analysis is shown in Figure 4. The thickness envelope corresponds to the expected shape based on previous HRTEM studies on such nanocrystals. [14] However, in this case the three-dimensional information is obtained in concert with the 2-dimensional projection, directly from the image.

CONCLUSIONS

Using sub-nanometer STEM probes it is possible to obtain chemical information on individual nanocrystals from spatially resolved EELS measurements. Applying this to CdSe nanocrystals embedded in MEH-PPV reveals oxygen equivalent to surface coverage on the order of 1 monolayer. Linescans suggest a surface oxide layer but the assignment is ambiguous at present.

Z-Contrast STEM is capable of resolving the lattice polarity in CdSe nanocrystals and can also provide thickness information directly from the image. Surface detail should be resolvable but the currently available data is not of sufficient quality yet.

ACKNOWLEDGEMENTS

The research presented here was funded by the Department of Energy, Basic Energy Sciences, Materials Sciences Division.

AVK gratefully acknowledges the assistance of P.D. Nellist, B.E. Rafferty, M. F. Chisholm, Y. Yan and G. Duscher in the operation of the STEM and EELS systems. We wish to thank C. Chen and G. Jellison for ellipsometry and J. Taylor for AFM measurements on films.

REFERENCES

Additional Figures are available at http://home.earthlink.net/~topchem/MRS_Spring99 until at least Dec. 1999.

1. Schlamp, M.C., Peng, X., and Alivisatos, A.P., *Improved efficiencies in light emitting diodes made with CdSe(CdS) core/shell type nanocrystals and a semiconducting polymer.* Journal of Applied Physics, 1997. **82** (11): p. 5837-42.
2. Colvin, V.L., Schlamp, M.C., and Alivisatos, A.P., *Light-emitting diodes made from cadmium selenide nanocrystals and a semiconducting polymer.* Nature, 1994. **370** (6488): p. 354-357.
3. Greenham, N.C., Xiaogang, P., and Alivisatos, A.P., *Charge separation and transport in conjugated-polymer/semiconductor-nanocrystal composites studied by photoluminescence quenching and photoconductivity.* Physical Review B (Condensed Matter), 1996. **54** (24): p. 17628-37.
4. Pennycook, S.J., Jesson, D.E., McGibbon, A.J., and Nellist, P.D., *High angle dark field STEM for advanced materials.* Journal of Electron Microscopy, 1996. **45** (1): p. 36-43.
5. Nellist, P.D. and Pennycook, S.J., *Accurate structure determination from image reconstruction in ADF STEM.* Journal of Microscopy-Oxford, 1998 : p. 159-170.
6. Duscher, G., Browning, N.D., and Pennycook, S.J., *Atomic column resolved electron energy-loss spectroscopy.* Physica Status Solidi A, 1998. **166** (1): p. 327-42.
7. Murray, C.B., Norris, D.J., and Bawendi, M.G., *Synthesis and characterization of nearly monodisperse CdE (E = S, Se, Te) semiconductor nanocrystallites.* Journal of the American Chemical Society, 1993. **115** (19): p. 8706-8715.
8. Bowen Katari, J.E., Colvin, V.L., and Alivisatos, A.P., *X-ray photoelectron spectroscopy of CdSe nanocrystals with applications to studies of the nanocrystal surface.* Journal of Physical Chemistry, 1994. **98** (15): p. 4109-17.
9. Peng, X.G., Wickham, J., and Alivisatos, A.P., *Kinetics of II-VI and III-V colloidal semiconductor nanocrystal growth: "focusing" of size distributions.* Journal Of the American Chemical Society, 1998. **120** (21): p. 5343-5344.
10. Wudl, F. and Srdanov, G., *Conducting polymer formed of poly(2-methoxy, 5-(2'-ethyl-*

hexyloxy)-p-phenylenevinylene), in *United States Patent*. 1993: United States of America.

11. Burch, S.F., Gull, S.F., and Skilling, J., *Image restoration by a powerful maximum entropy method.* Computer Vision, Graphics, and Image Processing, 1983. **23** (2): p. 113-28.
12. Skilling, J. and Bryan, R.K., *Maximum entropy image reconstruction: general algorithm.* Monthly Notices of the Royal Astronomical Society, 1984. **211** (1): p. 111-24.
13. Skilling, J. and Sibisi, S. *Fundamentals of MAXENT in data analysis.* in *Invited and Contributed Papers from the Conference.* 1990. Chilton, UK: IOP.
14. Shiang, J.J., Kadavanich, A.V., Grubbs, R.K., and Alivisatos, A.P., *Symmetry of annealed wurtzite CdSe nanocrystals: assignment to the C_{3v} point group.* Journal of Physical Chemistry, 1995. **99** (48): p. 17417-17422.

HYSTERESIS LOOP SHIFTS IN MAGNETIC FIELD COOLED FeOOH NANOPARTICLES

M.S. SEEHRA, PAROMITA ROY and A. MANIVANNAN
Physics Department, West Virginia University, Morgantown, WV 26506-6315

ABSTRACT

Measurements of the magnetization M as a function of temperature (5 K – 300 K) and applied magnetic field H (up to 50 kOe) in 30 Å particles of FeOOH are reported. M increases with decreasing T, peaking at $T_B \approx 65$ K below which the ZFC (zero-field-cooled) and the FC (field-cooled) data separate. Hysteresis loop measured at 10 K for ZFC shows an open loop up to 40 kOe with coercivity ≈ 2 kOe. For the FC case, the loop shifts and the loop-shift increases with the cooling field H_c, approaching saturation above $H_c \approx 20$ kOe. From the variation of M vs H above T_B, a magnetic moment/particle $\mu_p \approx 300\ \mu_B$ is determined. These results suggest that the FeOOH nanoparticles have an antiferromagnetically ordered core with uncompensated surface spins yielding μ_p and the surface spins order in a spin-glass-like state below T_B, possibly due to interparticle interactions.

INTRODUCTION

The study of the magnetic properties of nanoparticles is an exciting research area of current interest because these properties differ substantially from those of bulk materials and because of the technological importance of the finite size effects in magnetic recording media [1-9]. The large surface/volume ratio of the nanoparticles makes it reasonable to describe their magnetic properties in terms of a core-shell model, with the well-ordered spins in the core but with a significant amount of spin disorder in the surface spins [10,11]. The surface spin disorder arises from the lower coordination of the spins located in the shell and the resulting broken exchange bonds. The surface spins may also be affected by any adsorbed species from air such as water and hydrocarbons. In antiferromagnetic nanoparticles, the surface spin disorder may dominate the measured magnetization.

Recently, a number of reports on the structural, catalytic and magnetic properties of ferrihydrite ($FeOOH{\cdot}nH_2O$) nanoparticles have been published [12-15]. Ferrihydrite (FHYD) nanoparticles, usually characterized by the presence of two broad lines in their x-ray diffraction patterns, are easily synthesized, and are also available commercially [16]. Their particle size is typically 30 to 50 Å, with Fe being in the Fe^{3+} state [12]. Earlier magnetic studies showed that this material may be a superparamagnet with a blocking temperature $T_B \approx 65$ K [13]. However the nature of the magnetic state below T_B is not understood since T_B does not scale with the measuring time scale according to the predictions of superparamagnetism [13-15]. In this paper, we report investigations of the hysteresis loops observed below T_B in FHYD, under the zero-field-cooled (ZFC) and the field-cooled (FC) conditions, in magnetic fields up to 50 kOe. The hysteresis loops are open up to about 40 kOe and large loop shifts are observed under the FC conditions. The magnetization (M) versus magnetic field (H) data are used to determine μ_p, the magnetic moment/particle, resulting from the surface spin disorder. These results suggest spin-glass-like ordering of the surface spins, with an anisotropy of about 20 kOe. Details of these results and their discussion are presented below.

Mat. Res. Soc. Symp. Proc. Vol. 581 © 2000 Materials Research Society

EXPERIMENTAL DETAILS

The experimental studies reported here were carried out on the commercial FHYD sample known as the Nanocat [16]. The particle size distribution of this sample, as determined by transmission electron microscopy (TEM), gives a nearly symmetrical distribution centered around 35 Å with the range of 15 to 55 Å [12]. Air exposure of the Nanocat results in some adsorption of moisture and agglomeration, making it resemble the laboratory synthesized FHYD with particle size ≈ 40 Å. During preparation of the samples for our magnetic measurements, some air exposure was unavoidable. The magnetic measurements were carried out on a SQUID magnetometer, Quantum Design Model MPMS.

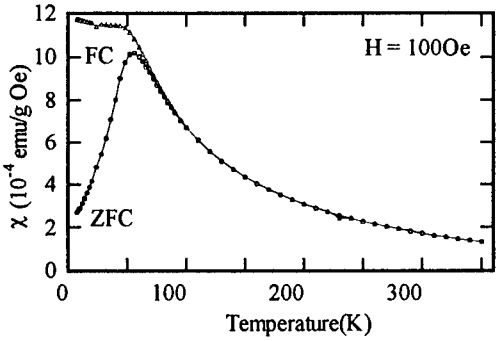


Fig.1. Temperature variation of the magnetic susceptibility.

RESULTS AND ANALYSIS

The temperature variations of the magnetic susceptibility $\chi = M/H$, in H = 100 Oe, for the FC and ZFC cases, are shown in Fig. 1. It is clear that below $T_B \approx 65$ K the data for the FC and ZFC cases separate indicating either superparamagnetism or spin-glass-like behavior. Recent neutron diffraction measurements in the $FeOOD \cdot nD_2O$ nanoparticles have shown that the Néel temperature T_N of the core spins equals 350 K and that spin-glass-like ordering of the surface spins at $T_B \approx 65$ K is not ruled out [17].

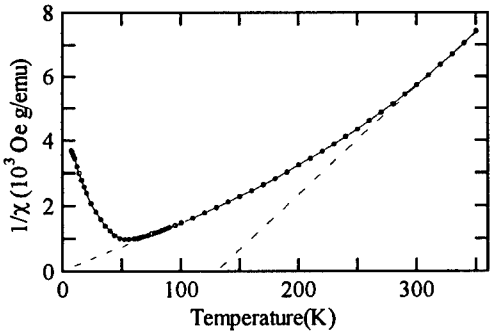


Fig.2. Plot of $1/\chi$ against temperature. The extrapolation for the high and low temperatures yield $T_i = 130$K and $T_O \approx 0$K.

The plot of $1/\chi$ against T is shown in Fig. 2. Following the procedures used in the analysis of the similar data in $FeOOD{\cdot}nD_2O$ nanoparticles, the data are fit to the Curie-Weiss law, $\chi = C/(T - T_0)$ predicted by the model of El-Hilo et al [18]. Here T_0 (= T_i + T_b) has contributions from both the interparticle interaction (T_i) and a log-normal particle-size distribution (T_b). At high enough temperatures, particles of all sizes are unblocked yielding $T_0 = T_i$, whereas at lower temperatures, both T_i and T_b contribute, with T_b expected to be negative [18]. From the data in Fig. 2, we determine T_i = 130 K for T > 270 K whereas $T_O \approx 0$K for lower T yielding $T_b \approx -T_i = -130$ K, similar to the values obtained for the FeOOD nanoparticles [17].

The hysteresis loops measured at 10 K, under the ZFC and the FC case for H = 30 kOe, are shown in Fig. 3. There is a clear shift of the hysteresis loop when the sample is cooled in a magnetic field. The loop shifts were measured in the cooling fields H_c = 10, 15, 20 and 30 kOe and the plot of the observed loop shift with the cooling fields is shown in Fig. 4. The results show that the loop shift becomes constant for $H_c \geq 20$ kOe. The details of the behavior of the hysteresis loop for the small field region are shown in Fig. 5. The rapid changes observed in the magnetization upon changing H from positive to negative values in the neighborhood of H = 0 are mostly likely due to the magnetic viscosity effects reported in this material [19].

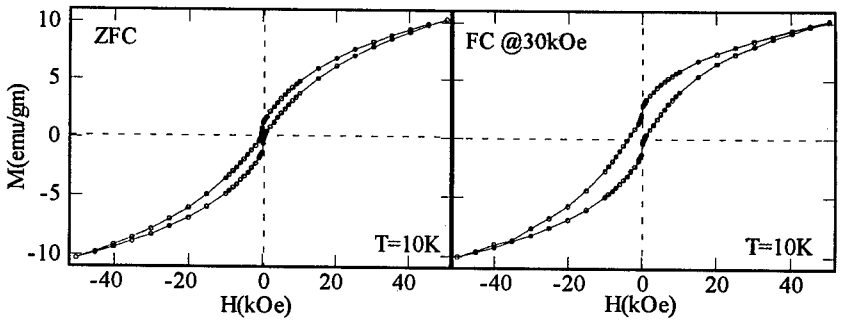


Fig.3. Hysteresis loops at 10K for ZFC and FC(H_C = 30kOe) cases.

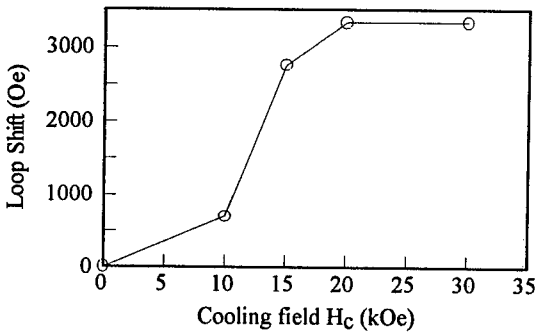


Fig.4. Variation of loop shift with the cooling field H_C . Line joining the points is for visual aid.

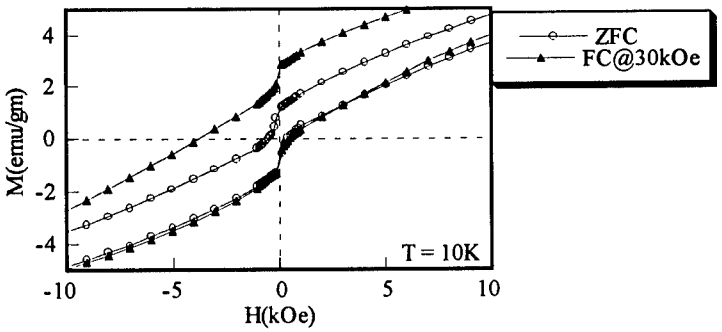


Fig.5. Details of the hysteresis loops for the lower field regions.

The variations of the magnetization M with applied field H (Fig. 6) at T = 150, 200, 250 and 300 K show that M does not saturate even at 50 kOe. This is similar to the observations in ferritin [7,8] and FeOOD nanoparticles [17]. These data are therefore fit to a modified Langevin function [7,8,17]:

$$M = M_0 L(\mu_p H/k_B T) + \chi_a H \qquad (1)$$

Here M_0 is the saturation magnetization, μ_p is the magnetic moment per particle, χ_a is the antiferromagnetic susceptibility of the core determined from the slope of the high H data and $L(x) = \coth x - 1/x$. M_0 is evaluated by plotting $(M - \chi_a H)$ against 1/H and taking the limit $1/H \rightarrow 0$. The plot of $(M - \chi_a H)/M_0$ against H/T is shown in Fig. 7. It is seen that the data fit Eq. (1) with $\mu_p \approx 320\ \mu_B$, at T = 150K. At higher temperatures, μ_p increases (inset of Fig.7), possibly due to the interparticle interactions, as also observed in the FeOOD.nD2 O nanoparticles[17]. The magnitude of $\chi_a \approx 7.5 \times 10^{-5}$/gm agrees with the expected antiferromagnetic susceptibility [20].

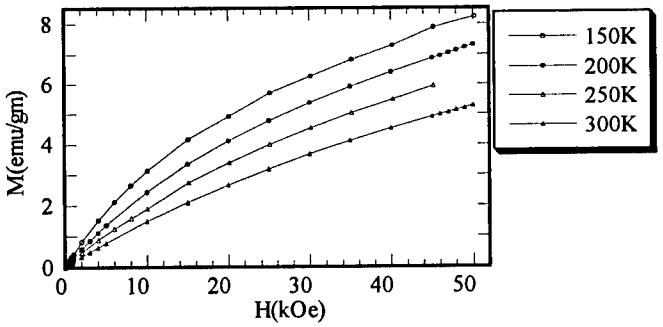


Fig.6. Measured magnetization against applied field H at several temperatures.

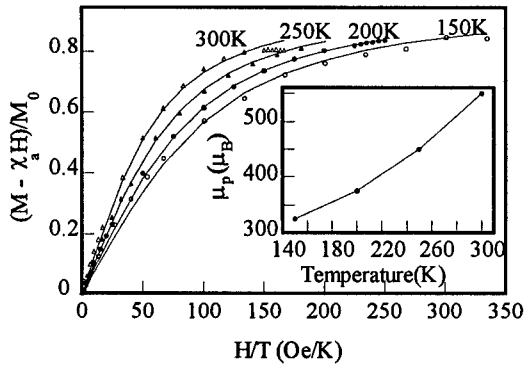


Fig.7. Plot of normalized $(M - \chi_a H)/M_O$ vs H/T. The solid lines are fits to the Langevin function, with μ_p against temperature shown in the inset.

DISCUSSION

The results presented above show that the FeOOH nanoparticles of size d ≈ 40 Å have a magnetic moment $\mu_p = 300\ \mu_B$. Assuming that there are $\sqrt{N}$ uncompensated surface spins in an antiferromagnetic particle with N spins [20], $\sqrt{N} \approx 49$ is obtained for a particle of volume $V = d^3$ and Fe^{3+} - Fe^{3+} separation of 3.0 Å [12]. Using $\mu = 5.9\ \mu_B$ per Fe^{3+} ion yields $\mu_p \approx 290\ \mu_B$ in agreement with the experimental value. These numbers give an effective shell thickness of less than 1 Å, suggesting that only a fraction of the surface spins are affected by spin disorder. The recent simulations of the magnetic structures of oxide nanoparticles in Ref.11 is consistent with this picture.

The presence of interparticle interaction is evident from the $1/\chi$ vs T plot. It has been suggested that such interaction can lead to spin-glass-like ordering of the surface spins [6,10,11]. The loop shifts observed here for the FC case are a clear evidence for the spin-glass transition since for a superparamagnet, an unshifted loop should be observed for the FC case [21]. The peak in χ observed at $T_B \approx 65$ K is then associated with spin-glass ordering of the surface spins, with an associated surface anisotropy of about 20 kOe.

ACKNOWLEDGMENT

This work was supported in part by the U.S. Department of Energy (Contract # DE-FC22-93PC3053 and DE-FC26-99FT40540).

REFERENCES

1. Nanophase Materials: Synthesis, Properties, Applications, edited by G. C. Hadjipanayis and R. W. Siegel (Kluwer, Dordrecht, 1994).

2. Magnetic Properties of Fine Particles edited by J. L. Dormann and D. Fiorani (Elsevier Science, Amsterdam, 1992).

3. J. L. Dormann, D. Fiorani, and E. Tronc, Adv. Chem. Phys. 98, 183 (1997).

4. F. C. Meldrum, B. R. Heywood and S. Mann, Science 257, 522 (1992).

5. S. Gider, D. D. Awschalom, T. Douglas, S. Mann and M. Chaparala, Science 268, 77 (1995).

6. S. Mørup, F. Bødker, P. V. Hendriksen and S. Linderoth, Phys. Rev. B 52, 287 (1995-I).

7. S. H. Kilcoyne and R. Cywinski, J. Magn. Magn. Mater. 140-144, 1466 (1995).

8. S. A. Makhlouf, F. T. Parker and A. E. Berkowitz, Phys. Rev. B 55, R14717 (1997-II).

9. M. F. Hansen, F. Bødker, S. Mørup, K. Lefmann, K. N. Clausen and P. –A. Lindgard, Phys. Rev. Lett. 79, 4910 (1997).

10. R. H. Kodama, A. E. Berkowitz, E. J. McNiff, Jr. and S. Foner, Phys. Rev. Lett. 77, 394 (1996).

11. R. H. Kodama and A. E. Berkowitz, Phys. Rev. B 59, 6321 (1999-I).

12. J. Zhao, F. E. Huggins, Z. Feng, F. Lu, N. Shah and G. P. Huffman, J. Catal. 143, 499 (1993).

13. M. M. Ibrahim, G. Edwards, M. S. Seehra, B. Ganguly and G. P. Huffman, J. Appl. Phys. 75, 873 (1994).

14. B. Ganguly, F. E. Huggins, Z. Feng and G. P. Huffman, Phys. Rev. B 49, 3036 (1994).

15. J. Zhao, F. E. Huggins, Z. Feng and G. P. Huffman, Phys. Rev. B 54, 3403 (1996-I).

16. Mach I, Inc., 340 East Church Road, King of Prussia, PA 19406.

17. M. S. Seehra, V. S. Babu, A. Manivannan and J. W. Lynn, Phys. Rev. B (in press).

18. M. El-Hilo, K. O'Grady and R. W. Chantrell, J. Magn. Magn. Mater. 114, 295 (1992); ibid 117, 21 (1992).

19. M. M. Ibrahim, S. Darwish and M. S. Seehra, Phys. Rev. B 51, 2955 (1995).

20. L. Néel, C. R. Acad. Sci. 252, 4075 (1961); 253, 9 (1961); 253, 203 (1961); 253, 1286 (1961).

21. J. K. Vassiliou, V. Mehrotra, M. W. Russell, E. P. Giannelis, R. D. McMichael, R. D. Shull and R. F. Ziolo, J. Appl. Phys. 73, 5109 (1993).

ATOMIC SCALE CHARACTERISATION OF ELECTRODEPOSITED NANOCRYSTALLINE Ni-P ALLOYS

Matthias Abraham, Mattias Thuvander†, Helen M. Lane, Alfred Cerezo, George D.W. Smith
Dept. of Materials, Oxford Univ., Oxford OX1 3PH, U.K., matthias.abraham@materials.ox.ac.uk
† present address: Volvo Technological Development Corporation, Dept 06420 Z1.1, SE-405 08 Göteborg, Sweden

ABSTRACT

Nanocrystalline Ni-P alloys produced by electrodeposition have been characterised by three-dimensional atom probe (3DAP) analysis. In the as-deposited materials, there are indications of some variation in P concentration between grains and segregation to grain boundaries. After heat treatment however, strong grain boundary segregation and the formation of Ni_3P precipitates have been observed.

INTRODUCTION

The thermal stability of nanocrystalline materials is a very important issue. Due to the large driving force for grain growth, provided by the considerable volume fraction of high energy grain boundaries, pure nanocrystalline materials can be unstable even at moderate temperatures. By introducing certain elements such as P into the materials, their thermal stability can be greatly improved. In order to understand the mechanism by which these elements affect the thermal stability of nanocrystals, and to predict the long-term behaviour of these materials, characterisation methods at the atomic scale are required.

In this paper, the three-dimensional atom probe (3DAP) analysis [1, 2] has been used to investigate the grain boundary chemistry within nanocrystalline Ni-P produced by electrodeposition [3].

EXPERIMENT

Electrodeposition is a well established method for the production of bulk nanocrystalline materials of low porosity and high purity [4, 5]. In this work nanocrystalline Ni-P alloys were produced from a nickel sulphate based bath with additions of phosphoric acid and phosphorous acid. The plating was performed at a constant current density of typically $6.6\,\mathrm{A\,dm^{-2}}$. The materials were deposited as discs of about 0.3 mm thickness and 22 mm diameter onto either copper or stainless steel sheets, from where they could be peeled off easily. The P concentration could be controlled over a wide range by changing the concentration of phosphorous acid in the plating solution. One surprising observation to be noted here is that saccharin which is often used as a grain refining additive in electrodeposition of pure Ni was found to inhibit the deposition of P and was therefore not used subsequently.

To perform 3DAP analysis, specimens in the form of a sharp needle with tip radius below 100 nm have to be produced. Conventional electropolishing methods can be applied for this purpose. The principle of the 3DAP is sketched schematically in Fig. 1. The specimen is brought into a UHV system and subjected to a positive voltage of a few kV. The voltage is high enough to cause field evaporation of individual atoms at the tip where the electric field is strongest. To control the time of evaporation, a short pulse is added to the voltage such that evaporation only occurs during the pulse. The ions, leaving the tip with nearly radial trajectories, will eventually hit a position sensitive detector. The position of impact corresponds to a position (x,y) on the specimen surface with

Mat. Res. Soc. Symp. Proc. Vol. 581 © 2000 Materials Research Society

a magnification of about one million times. Measuring the time of flight of detected ions allows to determine their mass-to-charge ratio. Continued field evaporation will remove atoms layer-by-layer. Hence the z coordinate of an atom can be deduced from the sequence of detection. In this way a three-dimensional reconstruction of typically $20\times20\times100\,\mathrm{nm}^3$ of the analysed material can be obtained.

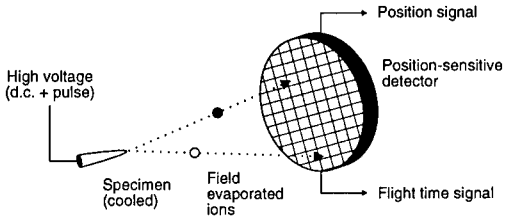


Figure 1: Schematic drawing of the 3DAP

Under certain circumstances, if the analysis direction is close to a low-index crystallographic pole, atomic planes can be identified in the 3D reconstruction, allowing grain boundaries to be located. However, in the case of Ni-P the presence of P atoms disturbs the ion trajectories so that it is impossible to identify planes in this material.

As the volume analysed by 3DAP is very small, complementary methods must be applied to get bulk information. We used X-ray diffraction (XRD) for phase identification and to determine the grain size with the Scherrer method. Transmission electron microscopy (TEM) was performed to obtain microstructural information over a wider area. Bulk composition and impurity concentration were measured by means of proton induced X-ray emission (PIXE) as well as energy dispersive X-ray analysis (EDX) in a scanning electron microscope (SEM).

RESULTS

Table 1 lists the grain size and Vickers hardness as functions of the P concentration for some of the electrodeposited materials produced in this work. Phosphorus has a strong influence on the size of the grains in the deposits and therefore on the resulting hardness. A maximum in Vickers hardness of more than $700\,\mathrm{kg/mm}^2$ was found for P concentrations of 10-12 at.%.

P conc. (at.%)	d (nm)	VHN ($\mathrm{kg/mm}^2$)
0.08 ± 0.01	81.1 ± 5.0	238 ± 11
6.92 ± 0.06	16.0 ± 1.0	507 ± 36
9.10 ± 0.08	13.3 ± 0.7	642 ± 38
11.20 ± 0.10	12.1 ± 0.6	711 ± 40
22.31 ± 0.20	7.3 ± 0.2	533 ± 22
$23.05 \pm 0.20^{\dagger}$	5.9 ± 0.1	552 ± 25
25.01 ± 0.22	$1.5 \pm 0.1^{\ddagger}$	548 ± 23

† As calibrated from EDX ‡ From TEM: amorphous

Table 1: Grain size and Vickers hardness of Ni-P deposits with different P concentration

The grain size values in Table 1 were determined from the broadening of the Ni [111] XRD peak. The lower curve in Fig. 2 is a typical XRD pattern of Ni-P. It was obtained from as-deposited Ni-6.0 at.% P with a grain size of (18.5 ± 0.2) nm. The upper curve in the figure shows an XRD pattern of the same material, heat treated at 425 °C for 15 min. Several new peaks showed up in the pattern, which were identified as Ni_3P peaks. The grains grew only very little during the annealing. By comparison, considerable grain growth was observed in pure nanocrystalline Ni even at temperatures below 250 °C [6]. It is likely that the enhanced thermal stability of Ni-P is caused by Ni_3P precipitation within the material.

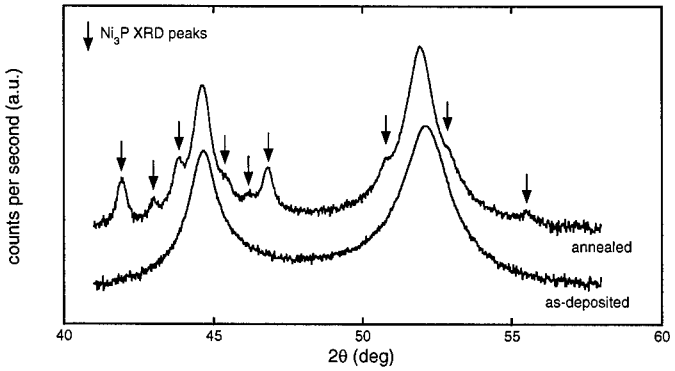


Figure 2: XRD patterns (log scale) of as-deposited and annealed (15 min at 425 °C) Ni-6.0 at.% P

Fig. 3a shows a 3D reconstruction of P atoms from an analysis of as-deposited Ni-4.3 at.% P. There are no enrichment effects immediately visible in the atom map. However, the frequency distribution in Fig. 3b, performed by partitioning the volume into blocks of 100 atoms, indicates a deviation from a random binomial distribution. There appears to be a small peak at ca. 6 at.% P. Isosurfaces (surfaces of constant concentration) rendered at this composition suggest a grained structure, see Fig. 3c. The size of the grains in this picture is comparable to the value obtained from XRD. These results suggest only weak P segregation at grain boundaries in as-deposited Ni-P. It has yet to be explained how the incorporation of P into the Ni can have such a large effect on the resulting grain size. Färber et al. reported a much stronger P segregation at grain boundaries in electroless plated Ni-3.6 at.% P [7].

3DAP analysis was also used to study the influence of heat treatment on the microstructure of Ni-P. Fig. 4a shows the distribution of P atoms in Ni-6.0 at.% P annealed at 425 °C for 15 min. There is a clear enrichment of P along what appears to be two grain boundaries, and a strong P concentration at the point where the two grain boundaries meet. From the concentration profile through this feature (Fig. 4b) it may be identified as a Ni_3P precipitate which, from the angle of the two boundaries, appears to be located at a triple junction. A concentration profile of the lower grain boundary is also shown. It illustrates that there is a significant area of P depletion around the grain boundary.

Given the concentration profiles in Fig. 4 the bulk diffusion coefficient of P in Ni was calculated to $\sim 1.2 \cdot 10^{-20}\,m^2/s$. The calculated value for the Gibbsian interfacial excess of P is $3 \cdot 10^{18}$ atoms/m^2.

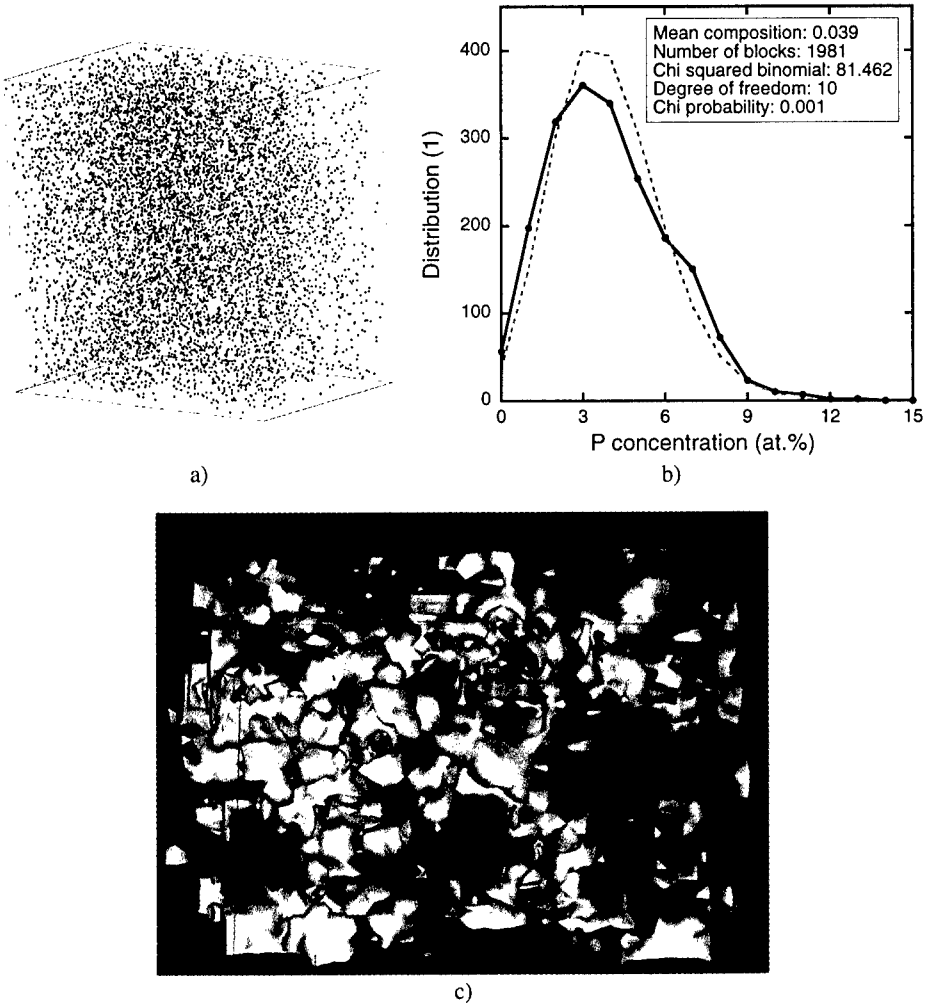
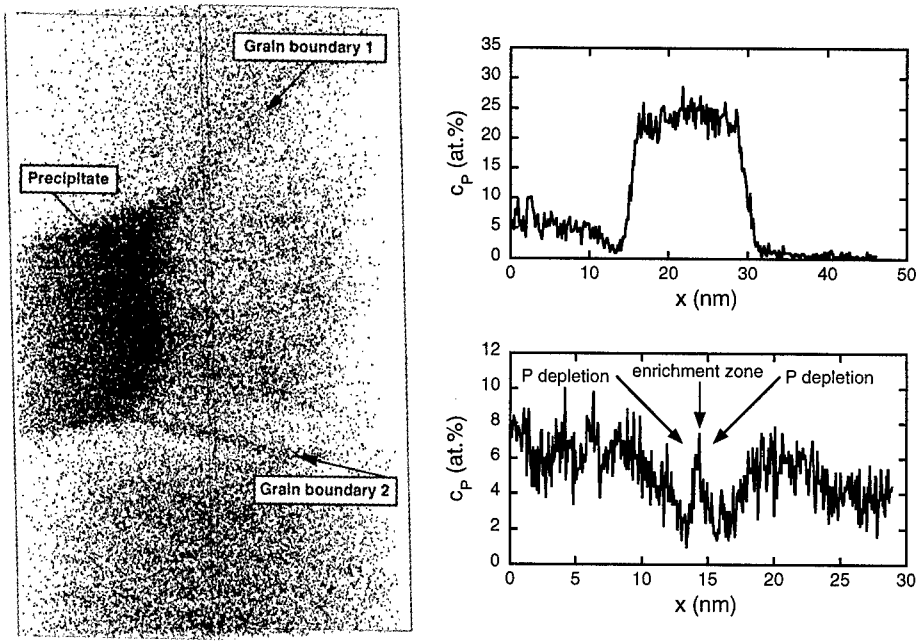


Figure 3: As-deposited Ni-4.3 at.% P: a) 3DAP analysis showing the distribution of P atoms ($27 \times 28 \times 19\ nm^3$), b) frequency distribution and c) iso-concentration (6 at.% P) surfaces



a) b)

Figure 4: a) 3D atom map showing the distribution of P atoms in Ni-6.0 at.% P heat treated at 425 °C for 15 min (24×24×46 nm^3), and b) composition profiles through the Ni_3P precipitate and the lower grain boundary shown in (a)

CONCLUSIONS

We have used 3DAP to study the distribution of P atoms in electrodeposited nanocrystalline Ni-P. In the as-deposited materials, we found some indications of variation in P concentration between grains. Our results suggest a weak P enrichment at grain boundaries which might explain how the addition of P causes the observed grain refinement in this system.

As one would expect from the Ni-P phase diagram, in annealed Ni-P we found Ni_3P particles from both XRD and 3DAP measurements. The 3DAP analysis also revealed a considerable amount of P segregated at grain boundaries. Both Ni_3P precipitation and P segregation are responsible for the greatly improved thermal stability of Ni-P compared to that of pure nanocrystalline Ni. Using high resolution 3DAP concentration profiles through P enrichments we were able to determine an approximate value for the bulk diffusion coefficient of P in Ni.

ACKNOWLEDGMENTS

The authors thank Prof. B. Cantor for provision of laboratory facilities. One of the authors (M. Thuvander) gratefully acknowledges The Swedish Foundation for International Cooperation in Research and Higher Education (STINT) for financial support. The authors acknowledge contributions of M. Rothfield, C. Weston, D. Franklin and T. Jing to the earlier stages of this work, especially to the development of several experimental techniques. This research was supported by the EPSRC under Grant No. GR/L66717.

REFERENCES

[1] M. K. Miller, A. Cerezo, G. D. W. Smith, M. G. Hetherington, *Atom Probe Field Ion Microscopy* (Oxford University Press, Oxford, U.K., 1996).

[2] A. Cerezo, T. J. Godfrey, S. J. Sijbrandij, G. D. W. Smith, P. J. Warren. Rev. Sci. Instrum. **69**, 49 (1998).

[3] H. Lane, M. Eng. Thesis, Oxford University, 1999.

[4] U. Erb, G. Palumbo, B. Szpunar, K. T. Aust, NanoStructured Mater. **9**, 261 (1997).

[5] U. Erb, G. Palumbo, R. Zugic, K. T. Aust in *Processing and Properties of Nanocrystalline Materials*, edited by C. Suryanarayana, J. Singh and F. H. Froes (TMS, Warrendale, PA, 1996) pp. 93-110.

[6] A. Cziraki, Zs. Tonkovics, I. Gerocs, B. Fogarassy, I. Groma, E. Toth-Kadar and I. Bakonyi, Mater. Sci. Eng. **A179/A180**, 531 (1994).

[7] B. Färber, E. Cadel, A. Menand, G. Schmitz and R. Kirchheim, Acta Mater. (in press).

Nanoporous Alumina Coatings for Medical Implants and Stents - Radiotherapy, Drug Delivery, Biological Compatibility

T. Sawitowski[*], W. Brandau[+], A. Fischer[#*], A. Heilmann[o], G. Schmid

*: Institut für Anorganische Chemie, University of Essen, Universitätsstr. 5-7, 45130 Essen, Germany
#: Institut für Werkstofftechnik, University of Essen, Universitätsstr. 5-7, 45130 Essen, Germany
+: Institut für Nuklearchemie und Radiopharmacie, University of Essen, 45122 Essen, Germany
o: Fraunhofer Institut für Werkstoffmechanik, Heideallee 19, D-06210 Halle, Germany

ABSTRACT

The body implant interaction is strongly affected by the implant surface structure and chemistry [1,2]. Thus by applying a nanoporous coating to metallic implants the implant surface can be adjusted to different needs. Compared to biological molecules the size of the pores is so small (between 5 nm and 250 nm) that the cellular response to this surface modification is not affected by the structure itself. Nevertheless by loading the pores with bioactive molecules it is possible to achieve a new kind of active implants surfaces for soft and hard tissue implants. With this coating it is possible to irreversibly bind radioactive isotopes like ^{99m}Tc, $^{186/188}Re$, ^{103}Pd, and many more for local radiotherapy onto soft tissue implants like stents or seeds.

INTRODUCTION

Surface chemistry and structure play a major role in body implant interaction [1,2]. In the range from traumatic reaction to full biocompatibility almost every type of cellular response depends on these two factors. By changing and adjusting the surface chemistry and structure the properties and the applicability of implants can be tailored to certain needs.

There are two major types of implants depending on the tissue involved. The one is applied to bones (hard tissue) like hip joints while the second group is in contact with the soft tissue of the body for example stents.

Stents are implanted after balloon dilatation of an artherosclerotic coronary vessel (percutaneous transluminal coronary angioplasty - PTCA) to prevent fast restenosis of the vessel. Due to the implantation of the stent the vessel wall is injured by the stent as well as by the balloon necessary to expand the stent inside the vessel. In addition heavy metal ions dissolved from the stent material irritate the tissue even more [3].

Due to this injury an excess of smooth muscle cells (SMCs) growth can occur which leads to the formation of thick layer of neointima and a restenosis of the vessel in 15 - 50 % of all surgeries which is a major draw back of the PTCA [4]. One way to overcome this draw back is to coat the surface of the stent either with a passive (barrier) layer or an active layer.

Barrier coatings have extensively been tested. On the one hand they can reduce the leakage of heavy metal ions like Ni^{2+} while on the other hand sometimes unfavorable reactions of the body can occur. For example electroplated noble metal coatings increase the restenosis rate significantly [5].
In addition to this barrier like coating applying a drug delivery or radioactive coating to a stent and by this preventing SMC growth should improve the restenosis rate. While the drug can be "wound healing" the radioactivity "destroys" the injured tissue and prevents further proliferation. For this reason functional coatings are a major challenge to improve the stent applicability.

Table 1 gives an overview of isotopes which are currently under investigation or already in clinical use for local radiotherapy (brachytherapy). [6].

Mat. Res. Soc. Symp. Proc. Vol. 581 © 2000 Materials Research Society

Table 1: Radioactive Isotopes for brachytherapy [6]

	Source	emission	Half-life	Maximum energy [keV]
Clinical	**^{188}Re**	**β**	**17 h**	**2120**
	^{192}Ir	γ	74 d	612
	^{90}Sr (Y)	β	28,6 y	2280
	^{90}Y	β	64 h	2280
	^{32}P	β	14,3 d	1710
Preclinical	**^{186}Re**	**β**	**90,6 h**	**1080**
	^{99m}Tc	**γ**	**6,02 h**	**140**
	^{131}I	***β,γ***	***8,04 d***	***810 (β) 723 (γ)***
	^{188}W (Re)	β	69,4 d	2120
	^{133}Xe	β	5,25 d	350
Theoretical	**^{103}Pd**	**X-Ray**	**17 d**	**23**
	^{125}I	***X-Ray***	***60 d***	***35***
	^{106}Ru (Rh)	***β***	***368 d***	***3450***
	^{68}Ge (Ga)	β+	288 d	1900
	^{144}Ce (Pr)	β	284 d	3000

(In brackets: Carrier elements)

While the ^{32}P activated Palmaz-Schatz stent has shown negative effects on the restenosis rate due to the "candy wrapper" effect, the brachytherapy via filled balloons or guided radioactive wire sources (catheter) reduced the restenosis rate to about 5 % [7]. The main difference between those two systems is the dose applied to the tissue. While the stent has an activity of a few 100 kBq with an irradiation time of 14 days, the balloon systems can apply up to several GBq within a few minutes [8]. In between those two limits no system exists with a medium activity of a few MBq within a few days after PTCA. This is the major challenge in stent modification. By using a variable surface coating like the multifunctional nanoporous coating it is possible to bind different types of isotopes with different types of emission and energy characteristics to the stent allowing optimization of the stent system without any major constructive variations. The isotopes printed in bold letters have been applied to the nanoporous coating, while the bold italics printed are currently under investigation (table 1). By simple variations γ– as well as β– emitters can be applied with half-life times between 6 hours and 368 days and maximum energies ranging from 23 keV up to 3450 keV. In the following the ^{99m}Tc as well as the ^{188}Re modified coating will be discussed in detail as a reference for the different isotope modifications.

EXPERIMENT

The expanded stent is plasma coated by aluminum metal in a special coating process leading to a very thin (100 nm), adhesive, and dense layer of metal (step 1 in Figure 1). This thin metallic film is then transformed into a nanoporous ceramic layer by anodic oxidation in polyprotic acids like sulfuric or oxalic acid which is a well known process [9] (step 2 in Figure 1). By simply changing the anodic potential, pores with diameters between 20 nm and 250 nm can be formed. The pore surface carries hydroxyl groups which reacts for example with silanes (step 3 in Figure 1) leading to different types of chemically modified nanoporous aluminum oxide surfaces (white symbols in Figure 1).

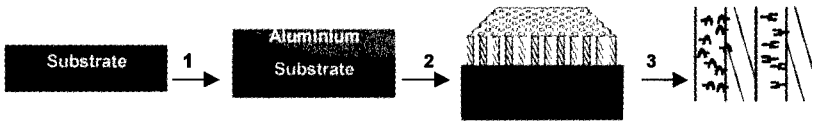


Figure 1:Sketch of the formation of an chemically modified, nanoporous alumina surface

The coating on the stent can best be imaged by atomic force microscopy (AFM). Figures 2 and, 3 show AFM images of an uncoated and a nanoporous coated stent surface.

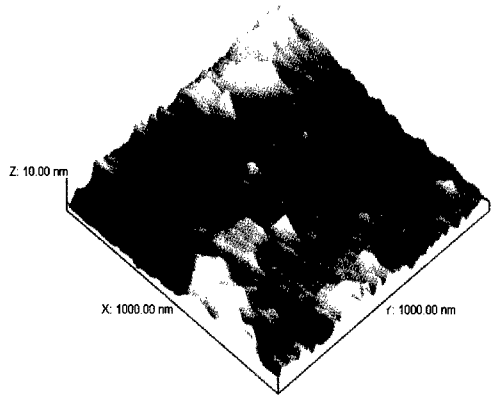


Figure 2: AFM image of the surface of the multifunctional coating

The surface of an electropolished stent shows a roughness of about 10 nm. Aluminum metal coating and anodisation in oxalic acid (40 V) leads to a porous surface layer with pore diameter in the range of 30 nm, as can be seen in Figure 3.

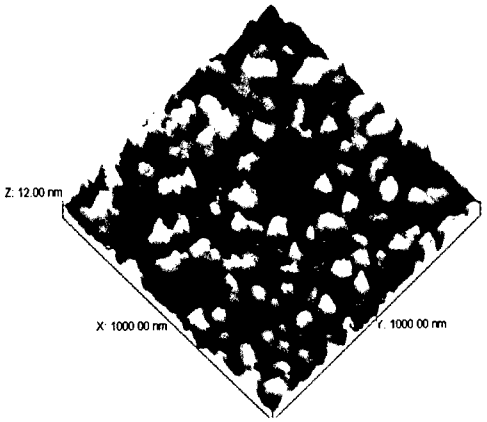


Figure 3: AFM image of an Aluminium coated and anodized stent surface

The (amorphous) alumina is still attached to the substrate and can chemically be modified to meet the desired properties of the implant. The nanoporous coating shown in Figure 3 with pore diameter of ~30 nm and a pore density of $2 \cdot 10^{10}$ cm^{-2} is treated with a boiling solution of the 3-Mercaptopropyltrimethoxysilane in cyclohexane for 5 hours. By this the methoxy moieties of the silane react with the hydroxyl moieties on the aluminum oxide surface to form stable Si-O-Al bonds (Figure 1). The sample is washed several times with cyclohexane to remove any excess of silane and is dried under normal condition.

The silanized sample is dipped into a ^{99m}Tc solution with an activity of 1,2 MBq/mg. To achieve complete wetting of the sample ultrasound is applied. The sample is removed from the solution and washed several times with water to remove unbound ^{99m}Tc. To prove the effect of the porosity and the chemical modification on the ^{99m}Tc loading, the different samples are shaken heavily in water (and with no difference in the results also in blood plasma) trying to wash off ^{99m}Tc. The determined activity is corrected for the radioactive decay occurring over time and is directly compared to the starting activity of the sample.

Using the Sulfur containing silane ^{99m}Tc forms a stable complex with the silane molecules. By this ^{99m}Tc can be bound irreversibly to the nanoporous coating as can be seen in Figure 4.

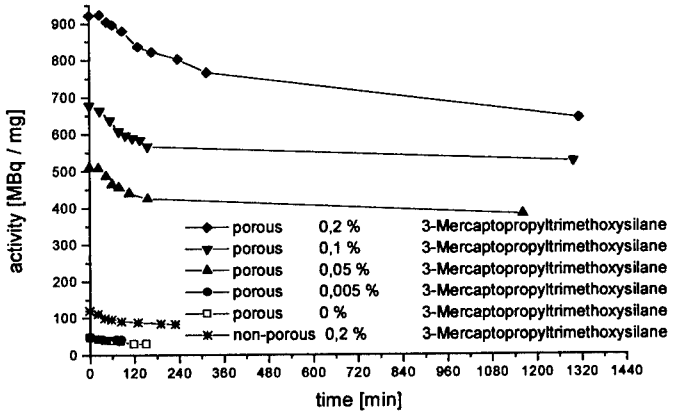


Figure 4 : Influence of silane concentration and porosity on ^{99m}Tc loading

Comparing the porous and non-porous surface treated equally with 3-Mercaptopropyltrimethoxysilane, it is clearly seen, that the amount of ^{99m}Tc bound to the surface can be increased by a factor of 10 due to the increased active surface. In addition only the modification with silane leads to substantial amount of ^{99m}Tc in the coating. With increasing silane concentration the ^{99m}Tc loading is increased as well (Figure 4) while the stability of the ^{99m}Tc loading is not affected. All trials to remove the radioactive isotope from the inner pore wall by washing either with water or blood plasma shows almost no decrease in the activity. The small decrease at the beginning is due to the ^{99m}Tc which is bound to the outer surface and can be washed away. Beside ^{99m}Tc, $^{186/188}$Rh can also be chemically fixed by sulfur silanes. Depending on the dipping time, the specific activity can be varied between 80 and 1000 kBq/mg (see Figure 5). This is an increase in the specific activity by a factor of 115 compared to the unmodified coating.

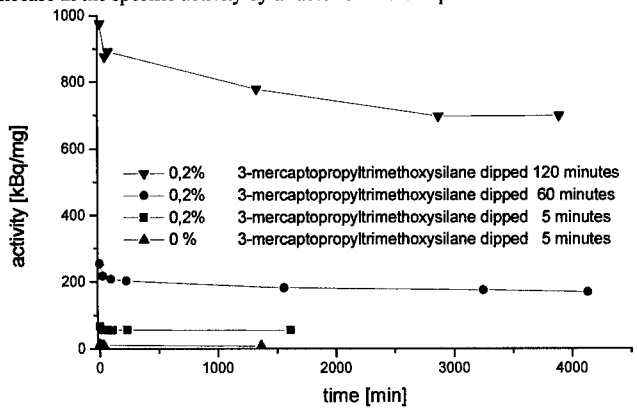


Figure 5: Influence of silane concentration and porosity on ^{188}Re loading

The ^{188}Re is again irreversibly bound to the pore surface. The activity lost in the beginning is due to the outer sample surface, while the later loss in activity might be ascribed to experimental errors (experimental accuracy in determining the activity is about 10 % which led to mistakes due to half life time corrections), aluminum oxide dissolution (the samples are heated up to 50°C due to shaking), and maybe also to the hydrolysis of weakly bound silane groups.

SUMMARY

Via a simple 4 step process implants surfaces are coated with a radioactive nanoporous alumina layer. By varying the pore structure, the thickness of the layer, the substrate and the chemical modification a great variety of different surfaces are accessible. Different types of radioactive isotopes like ^{99m}Tc, $^{188/186}$Re or ^{103}Pd can almost irreversibly be fixed to the inner surface. Isotope combinations as well as different isotope concentration on different implant positions seem to be possible and lead to a new generation of radioactive implants [10,11,12].

1. Adam Curtis, Chris Wilkinson, *Topographical control of cells*, Biomaterials, 1997, 18, pp. 1573-1583
2. D.M. Brunette, *The effect of Surface Topography on cell migration and Adhesion*, in "Surface Characterization of Biomaterials", edited by B.D. Ratner, 1988, pp. 203-21
3. J.J. Jacobs, L. Jermy, R.M. Urban, *Corrosion of metal Orthopedic Implants*. The Journal of Bone and Joint Surgery, 1998, Vol. 80-A, pp. 268-282

4. P.W. Serruys, S.G. Carlier, *The scope of the Problem of Vascular Restenosis*, in "Vascular brachytherapy – new perspectives", edited by P.C. Levendag, 1999, pp. 4 – 7
5. Hehrlein C, et al, *Influence of surface texture and charge on the biocompatibility of endovascular stents*, Coron Artery Dis. 1995, 6, pp. 581 - 586.
6. W.J.F. Dries, *Endovascular Brachytherapy: Physics and Equipment*, in "Vascular brachytherapy – new perspectives", edited by P.C. Levendag, 1999, pp.22 -25
7. R. Waksman, *Clinical Trials for coronary artery disease using beta sources*, in "Vascular brachytherapy – new perspectives", edited by P.C. Levendag, 1999, pp.31 -36
8. U. Quast, *Definition and determination of the relevant parameters of vascular brachytherapy*, in "Vascular brachytherapy – new perspectives", edited by P.C. Levendag, 1999, pp. 51 - 74
9. T. Sawitowski, *Neue Nanokomposite - Goldcluster, Goldkolloide und Silizium in Aluminiumoxidmembranen - Struktur und Eigenschaften*, Thesis, 1999
10. A. Fischer, W. Brandau, T. Sawitowski, G. Schmid, German Patent Application No. 198 55 421.4, *Radioactive Implants*, (November 1998)
11. A. Fischer, W. Brandau, T. Sawitowski, G. Schmid, German Patent Application No. 199 10 188.4, *Local Drug Delivery – 1*, (March 1999)
12. A. Fischer, W. Brandau, T. Sawitowski, G. Schmid, German Patent Application No. 199 48 783.9, *Local Drug Delivery – 2*, (August 1999)

MICRO-RAMAN STUDY OF SELF-ASSEMBLED NANOSTRUCTURES: (1-x)PZN:xPT SOLID SOLUTION

S. GUPTA, R. S. KATIYAR, R. GUO*, AND A. S. BHALLA*
Department of Physics, University of Puerto Rico, San Juan, PR00931-3343, USA.
*Materials Research Laboratory, Pennsylvania State University, University Park, Pennsylvania, PA16802, USA.

ABSTRACT

Relaxor ferroelectrics are one of the important classes of self-assembled nanostructure composite materials. Interesting features associated with the nanoregions give rise to the most interesting device related characteristics and unusual properties in these materials. Besides, they possess the largest property coefficients by themselves or when modified with lead titanate (PT). In this report, a detailed temperature dependent study has been carried out on (1-x)PZN-xPT relaxors with compositions x = 0.05 and 0.085 using polarized Raman scattering under optical and E-field variables and inferred the structure-property relations in order to obtain information to characterize the material for matching the application criteria. In addition, phase transitions associated with the relaxors have also been investigated to understand the polarization mechanism(s) for the unpoled and poled specimens.

INTRODUCTION

In the family of ferroelectrics a group of mixed and disordered "relaxors" have been identified including several perovskites, such as $PbMg_{1/3}Nb_{2/3}O_3$ (PMN), $PbSc_{1/2}Ta_{1/2}O_3$ (PST) etc. [1]. Due to the effect of configurational or orientational disorder the properties of relaxor ferroelectrics are very different from those in translationally invariant or regular ferroelectrics. Relaxors are functional and self-assembled nanostructures (analogous to semiconductor quantum dots) and are characterized by some unusual properties: (a) the simultaneous existence of slow kinetics typical for spin glasses with a very large dielectric constant indicating intermediate-range polar order on the nanometer length scale which can be transformed to true long-range order *(i.e.,* to macroscopic polarization) by a suitable change of composition and application of an external electric field; (b) the existence of a frequency-dependent slim hysteresis loop even above the transition temperature etc., [2,3]. All of these findings or characteristics indicate that the observed properties of relaxor ferroelectrics are non-equilibrium properties and thermodynamically the system is metastable [4]. In addition, these unique properties of relaxors are associated with the peculiar polarization mechanism and the understanding of which is still at a rudimentary level. Experiments show that there is symmetry breaking on a nanometer scale as observed from Raman scattering [5] and X-ray and neutron diffraction [6,7]. These observations imply that polar clusters exist even well above the so-called mean Curie temperature (T_m) and the observed properties are strongly affected by the reorientation of the clusters. In particular, cluster reorientation in the applied electric field induces strong polar-strain coupling which makes relaxors the potential candidate material for the next generation ultrasonic transducers and actuator devices [8]. Despite the existence of several models [9] they suffer from the difficulty to explain the cluster or nanoregions dynamics. However, it is widely accepted that the polarization is associated with the behavior of the polar self-assembled nanoregions or clusters in these materials.

Lead zinc niobate $Pb(Zn_{1/3}Nb_{2/3})O_3$ (PZN) is a relaxor material [10] having a complex

Mat. Res. Soc. Symp. Proc. Vol. 581 © 2000 Materials Research Society

perovskite structure in which the Zn^{2+} and Nb^{3+} are disordered on the B-site. The phase transition is broad because of either composition fluctuations or the existence of diffusion of an intermediate dipole-glass and mixed (partially ordered) phases in these crystals between O_h^1, cubic and C_{3v}^5, rhombohedral ferroelectric phases. Hence, this transition occurs over a range of temperature called the Curie region or the mean Curie temperature (T_m) and the transition is a diffuse phase transition (DPT). PZN has a maximum dielectric constant at about 410K [10,11]. From the crystallographic data the symmetry of PZN above the phase transition temperature is cubic *(Pm3m)* and below it is rhombohedral (3m) [12]. A complete solid solution (1-x)PZN-xPT is formed in the range $0<x<0.2$. The solid solution between PZN-PT has a morphotropic phase boundary (MPB) at around 9.5mol% of PT content at room temperature (25 °C) in T-x phase diagram [13]. Of all the solid solutions, the composition at x = 0.09 near the MPB has excellent piezoelectric and dielectric properties. Two structural phase transitions were reported around 440 K and 340 K on cooling from cubic (C) to tetragonal (T) and from the tetragonal to rhombohedral phases, respectively [14,15]. In our study, we have selected the representative compositions with x = 0.02 and 0.05 for the (1-x)PZN-xPT system. According to the previous studies [13], these compositions represent the fully rhombohedral (R) phase. In single crystal studies, the PZN composition contains only -9% PT, lower PT concentration facilitate more homogenous crystal growth. These ratios are chosen because they correspond to 5 mole% or higher to the R side of the MPB, where the composition dependence of the electrical properties is least dramatic. Also, it was observed that in addition to the composition, the crystallographic direction is equally significant to obtain a high performance o f the device and huge property coefficients in the material [16]. The rhombohedral crystals oriented along their pseudocubic <001> direction exhibited large property coefficients as compared to when oriented along the polar axis <111> and is superior to tetragonal composition along <111> [17]. In order to emphasize this issue, we have chosen (1-x)PZN-xPT samples with compositions x =0.02 and 0.05; entitled as unpoled and poled respectively because the latter is poled along the <001> direction with an application o f unipolar electric field o f 20 kV/cm from 200 °C to room temperature. The phase transitions in these apparent anisotropic crystals were investigated by inelastic light scattering.

Raman scattering has been shown to be an excellent probe for the proposed nanodomain structures that are important for the interpretation of the properties of relaxors. The studies on relaxors by Raman scattering have been reported by several authors [18,19], the spectra are typical for relaxors, no soft modes are observed, all of the bands are broad. Moreover, the spectra are inconsistent to the high temperature symmetry because of the presence of first-order Raman modes. PZN-PT should be easier to favor ordering compared to PMN-PT due to the larger atomic radii differences between B' and B" $R_{Nb}<R_{Mg}<R_{Zn}$, and the addition of PT contents will decrease the charge effect associated with the nanoregions. Therefore, we carried out Raman investigations on these crystals to elucidate the diffuseness of the phase transition away from the MPB. The present paper reports fragmentary findings of Raman study of (1-x)PZN-xPT system as function of temperature and electric field variables to explore the polarization mechanism in the course of thermal evolution and in conjunction with the crystallographic direction. To the best of our knowledge, such studies have not yet been reported.

EXPERIMENTAL PROCEDURE

Two single crystals of (1-x)PZN-xPT solid solutions with compositions x = 0.02 and 0.05 were investigated. The samples were prepared by the molten flux method with excess lead oxide (PbO) as described in ref.[20]. The sample of PZN-5%PT was poled in the (001) direction

with a dc bias of 20 kV/cm from 200 °C ($T>>T_m$) to room temperature. The phase purity was confirmed by X-ray diffraction measurements using D5000 Siemens diffractometer. The sample PZN-2%PT is of (001) and (111) orientation while PZN- 5 %PT is preferentially (001) oriented.

Raman spectra were measured using a triple Raman spectrometer [ISA Jobin- Yvon T64000] and the 514.5 nm line of an Ar^+-laser as an excitation source. The system was operated with an output power of 10 mW and the focal spot of the order of a few micrometers (1-3μm). The Raman spectra were recorded in the backscattered configuration. The illumination of the samples was adjusted before each measurements and at each temperature to maximize the throughput.

For measuring the temperature dependence of the Raman spectra, the samples were mounted on the cold stage of an MMR Joule-Thompson refrigerator equipped with a programmable temperature controller (Model # K-20) giving a temperature range of 70K-580.

The Raman spectra were deconvoluted wherever needed using the Peakfit software program from Jandel scientific Co, (Peakfit Ver 4.0). Also, these spectra have been corrected for the thermal population factor (Bose factor). All o f the bands were fitted using above-mentioned software that employs the Marquardt- Levenberg algorithm to the absolute minimum of χ^2 and maximizing the randomness of the residuals [3,19].

RESULTS AND DISCUSSION

Raman spectrum is analyzed to probe the structural phase transition in the course of thermal evolution and the influence of poling on the "order parameters deduced from Raman spectra for a particular Raman band and subsequent phase transition temperature. Fig. 1(a) and (b) show the raw Raman spectra for both of the samples at 70 K and 580 K respectively. Raman spectra were measured at intermediate temperature intervals of 20 K. The spectra beyond the transition temperature appear to be similar. The typical and obvious observation is that the bands are broad and their shapes indicate overlapping bands. In the spectra measured at low temperature of 70 K the bands are sharper and have higher intensities for both of the samples. In fact, the bands are significantly narrower in the case of poled sample than the unpoled one. It is to be noted that Raman spectra do not vary much with composition, but the weaker bands or shoulders in the unpoled sample (x=0.02) becomes more apparent or stronger in the case of poled sample (x=0.05). This occurrence may be attributed to the suppression of the interference of fluorescence and photoluminescence and consequently improving the signal to noise ratio or simply reduction of the background.

In general, the new modes arise due to several reasons such as impurities, vacancies, symmetry variation etc. We suggest that, upon poling it is more likely to have a symmetry transformation based on the proposition that nanodomains are oriented substantially as compared to that of the unpoled case. This point was more clarified by the polarization studies where Raman spectra were measured both in its parallel [Z(XX)Z] and perpendicular [Z(XY)Z] configurations in backscattered geometry. It was found that even in the poled samples one cannot ascertain a single domain state or uniquely defined polarization state. In one of the previous studies, it was claimed that it can be achieved only for E >30kV/cm [21]. The presence of Raman bands even after the phase transition in both the samples evidence that no long-range ferroelectric order is established. No soft mode behavior is observed, indicative of relaxors in contrast to conventional or regular ferroelectrics.

With the assumption of Gaussian line shape-a better approximation for the disordered materials-all of the band envelopes are deconvoluted into a series of bands of varying wavenumber (frequency) and full width at half maximum (FWHM). Fig. 2 shows a representative example for

the Raman band at 277 cm^{-1}; belonging to the O-B-O bending mode [22]. It has a poorly defined shoulder in the 70K spectra for both of the crystals, but more apparent in the poled one. The band envelope deconvolutes into two distinct components of higher and lower wavenumber of 277 cm^{-1} and 192 cm^{-1} respectively. The temperature variation of the frequency and FWHM for the band at 277 cm^{-1} was analyzed and is shown in Fig. 3(a) and (b) respectively. The temperature sensitivity of 192 cm^{-1} band, that disappears at ≈340 K, may account for the movement of Pb(1) and Zn from their centro- symmetric positions. From the careful analysis, it was found that there is a clear blue-shift in the wavenumber (frequency position) and significant narrowing in the width of the representative Raman band at 277 cm^{-1}. Quantitative changes at 70 K in the wavenumber and FWHM correspond to 5-7 cm^{-1} and 8-10 cm^{-1} respectively. These findings clearly suggest the enhanced local ordering and a change in the volume of the proposed polar nanoregions for the poled case. Our initial results indicate an apparent anomaly in the 277 cm^{-1} band in the vicinity of 440K-460K. Moreover, the analysis finds a slight shift in the phase transition temperature on poling the sample. This transition manifests itself undoubtedly by a considerable change in the intensity of Raman spectra. We may consider that the anomaly represents the T-C structural phase transition. The steep changes in the wavenumber (frequency) and FWHM (damping) near to 460 K is associated with a Landau-Khalatnikov like maximum [23]. Such an anomaly is usually associated to a rapid growth of long-range electric ordering. Thus we conclude that the PZN-PT crystals possess a sharp first-order ferroelectric-phase transition at ≈460K. This value is consistent with the transition temperature of cubic PE phase ↔ tetragonal FE phase, predicted from the MPB in Ref.13. Since the FE transitions are known to be associated with a soft mode lattice motion, if the transition is strongly first-order, mode softening may not be detectable [24]. Therefore, the non- zero minimum of phonon frequency at = 460 K implies either a first-order phase transition or that the structural instabilities (as $T \rightarrow T_c^+$) may be associated with some other complicated mode. These temperatures also signify the breaking of macro- to nano- dynamic polarization regions. It is widely accepted that the polarization is associated with the behavior of the polar nanoregions in these materials, and local B-site chemical disorder undergoes a first-order relaxor ferroelectric phase transition at T_c =460 K. However detailed investigation is needed in order to confirm this conclusion.

CONCLUSIONS

The measured Raman spectra are certainly different for both the unpoled (x=0.02) and poled (x=0.05) single crystalline (1-x)PZN-xPT samples. Despite the fact that both samples represent rhombohedral symmetry (*3m*), the difference in the Raman studies in the case of poled specimen is accounted for by the influence of the residual electric field, because the dc bias was removed while carrying out the temperature dependent measurements. On analysis of one of the representative band at 277cm^{-1} for its wavenumber (frequency) and half-width (FWHM), a distinct inflexion at ≈460 K was observed, which was associated to a sharp first-order ferroelectric-phase transition. Distinct quantitative changes in the wavenumber (frequency) and width (FWHM) of the bending mode at 277cm^{-1} on poling suggest an enhanced local ordering and the increase in the volume of the polar nanoregions or the self-assembled nanostructures.

ACKNOWLEDGMENTS

The authors wish to acknowledge the financial support from the US Grants NSF-DMR-9801759, DAAG55-98-1-0012 and DAAD19-99-1-0362.

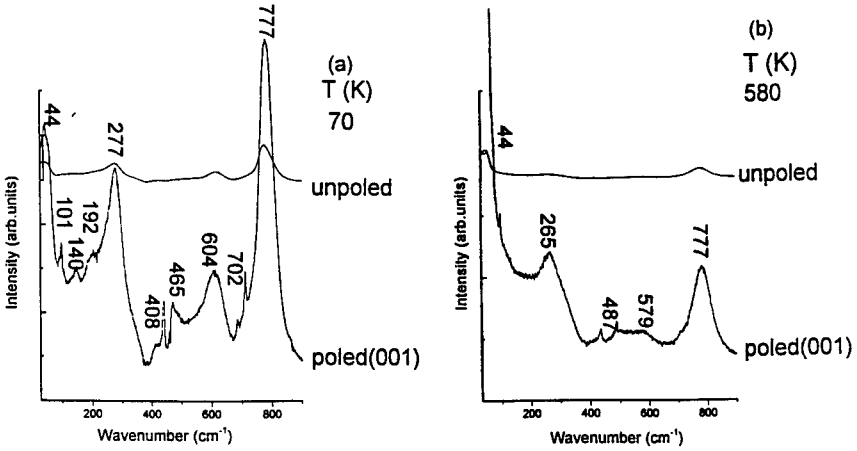


Fig.1 Raman spectra of PZN-PT crystals at (a) 70 K and (b) 580 K.

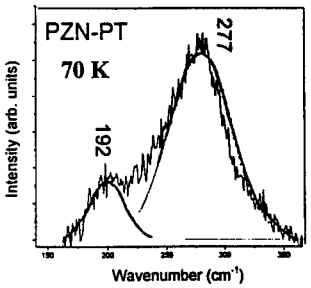


Fig.2 Raman spectrum of PZN-PT showing deconvolution of the 277 cm^{-1} band with superimposed Gaussian functions.

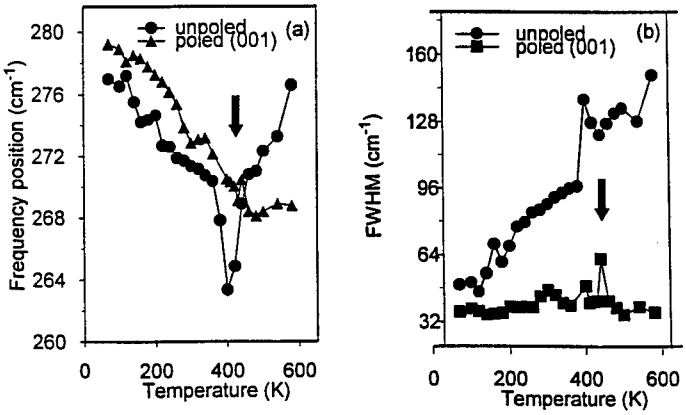


Fig.3 Temperature dependence of the (a) frequency position and (b) FWHM of intense 277 cm^{-1} band for both of the PZN-PT samples. The phase transition is indicated by an arrow.

REFERENCES

1. G. A. Smolensky et al., *Ferroelectrics and Related Materials* (Gordon and Breach, New York, 1984).
2. L. E. Cross, *Ferroelectrics* ***76,*** 241 (1987).
3. S. Gupta, R. S. Katiyar and A. S. Bhalla, *Mater. Res. Symp. Proc.* ***457,*** 145 (1999).
4. B. E. Vughmeister and H. Rabitz, *Physical Rev.* B ***57,*** **1** (1998).
5. G. Burns and F. H. Dacol, *Ferroelectrics* **104,** 25 (1990).
6. N. de Mathan, E. Husson, G. Galvarin, J. R. Gavarri, A. W. Hewat, and A. Morell, *J.Phys.: Condens. Matter* ***3,*** 8159 (1991).
7. V. Westphal, W. Kleemann, and M. D. Glinchuk, *Phys. Rev. Lett.* **68, 847** (1992).
8. R. Sommer, N. K. Yushin, and J. J. Van der Klink, *Phys. Rev.* **B 48,** 13 230 (1993).
9. For review pl. see Z.- Y. Cheng et al., *Phys. Rev.* **B** ***57,*** 8166 (1998).
10. N. P. Khuchua, V. A. Bokov, and I. E. Myl'nikova, *Sov. Phys.-Solid State* **10,** 192 (196S) and references therein.
11. Y. Yokomizo, T. Takahashi, and S. Nomura, *Ferroelectrics* ***22,*** S63 (1979).
12. Powder Diffraction File, Card No. 22-663. International Center for Diffraction Data, Newtowne Square, PA, 1991.
13. J. Kuwata, K. Uchino, and S. Nomura, *Ferroelectrics* ***37,*** 863 (1981).
14. S. Nomura, T. Takahashi, and Y. Yokomizo, *J. Phys. Soc. Japan* ***27,*** 262 (1969).
15. J. Kuwata, K. Uchino, and S. Nomura, *Jpn. J. Appl. Phys.* 21, 1298 (19S2).
16. S.- E. Park and T. R. Shrout, *J. Appl. Phys.* **82,** 1804 (1997).
17. S.- F. Lin, S.- E. Park, T. R. Shrout, and L. E. Cross, *J. Appl. Phys.* ***S5,*** 2810 (1999).
18. I. Siny, S. Lushnikov and R. S. Katiyar *Phys. Rev. B* ***56,*** 7962 (1997).
19. For review pl. see S. Gupta, R. S. Katiyar and A. S. Bhalla, *Integrated Ferroleectrics* (1999) (in Press).
20. S. Nomura, and H. Arima, *Jpn. J. Appl. Phys.* 11, 358 (1972).
21. D.- S. Paik, S.- E. Park, S. Wada, S.- F. Liu and T. R. Shrout, *J. Appl. Phys.* ***S5,*** 1080 (1999).
22. E. Husson, L. Abello and A. Morell, *Mater. Res. Bull.* ***25,*** 539 (1990).
23. C.- S. Tu, F.- C. Chao, C.- H. Yeh, C.- L. Tsai and V. H. Schmidt, *Phys. Rev.* **B 60,** 6348 (1999).
24. M. E. Lines and A. M. Glass, in *Principles and Applications of Ferroelectrics and Related Materials.* (Oxford University Press, London 1977).

MICROSTRUCTURAL AND MAGNETIC PROPERTIES ON GRAPHITIC ENCAPSULATED Ni NANOCRYSTALS AND PURE Ni NANOPARTICLES WITH NiO LAYER

Xiangcheng Sun[a,1] **and M. Jose Yacaman**[a]
[a]Instituto Nacional de Investigaciones Nuclears (*ININ*), Km.36.5, Carr. México-Toluca, C.P. 52045 Ocoyoacac, Edo. de México, MEXICO. [1]E-mail: sunxc@nuclear.inin.mx

F. Morales
Instituto de Investigaciones en Materiales, Universidad Nacional Autónoma de México, A.P.70-360, México 04510, D. F. México, MEXICO

ABSTRACT

Two kinds of different nickel nanoparticles with distinct morphological properties, Ni(C) and Ni(O), are studied. Magnetization measurements for the assembly of two kinds of Ni nanoparticles show, a larger coercivity and remanence as well as the deviation between the zero field cooling (ZFC) and the field cooling (FC) magnetization have been observed in the Ni(O) particles. This deviation may be explained as a typical cluster glass-like behavior due to ferromagnetic interaction among the assembly of Ni(O) particles. However, Ni(C) particles exhibit superparamagnetism at room temperature. The average blocking temperature (T_B) is determined to around 115K. We also observe gradual decrease in saturation magnetization, which is attributed to the nanocrystalline nature of the encapsulated particles.

INTRODUCTION

Nickel (Ni) nanoparticles have been attracted considerable attention over the last decade because the many interesting optical, magnetic, chemical properties and by it's potentially technological applications [1-3]. In this work, we use the modified arc-discharge (carbon-arc) method to fabricate two types of nickel nanoparticles at a methane and a mixture of H_2 and Ar atmospheres, respectively. Microstructural characteristics and magnetic properties at different temperatures and magnetic fields have been extensively studied and are reported here.

EXPERIMENT

The detailed experimental apparatus (modified arc-discharge) is illustrated in reference [4]. JEOL-2010EX high-resolution transmission electron microscope (HRTEM), equipped with energy dispersive X-ray spectroscopic (EDS) analysis, is used to determine the phase, and morphology of the particle, they also allow us to record selected area electron diffraction (SAED) patterns.

The magnetization measurements are performed by using SQUID magnetometer in the temperature range from 2 to 300K at different applied magnetic fields. Measurements are performed by the following useful method: zero-field-cooling (ZFC) and field-cooling (FC).

Mat. Res. Soc. Symp. Proc. Vol. 581 © 2000 Materials Research Society

In the first method, the sample is cooled down to the target temperature, then the applied magnetic field is put on; the measurement is performed as the temperature is raised; in this case to room temperature. FC measurements are performed with the magnetic field applied at high temperature; and the measurement performed as the sample is cooled down.

In measurements of M *vs* T, it is convenient to define the blocking temperature, T_B; as the temperature at which the two curves, ZFC and FC, merge in one. The average blocking temperature is defined as the maximum of ZFC curve. Above T_B, thermal fluctuations flips and scatters the direction of the magnetic moment; and no hysteresis is observed in the M(H) measurement. Magnetic properties of small ferromagnetic particles may present different features when the size is smaller than the exchange correlation length; i.e. in the superparamagnetic state. In this case for such an assembly of particles, the coercive field H_C, will be given by $H_C = H_C(0)[\ 1-(T/T_B)^{1/2}]$. And above T_B, the ensemble of nanoparticles (assuming those are single domain) behave as paramagnetic cluster with great magnetic moments [5].

RESULTS and DISCUSSION

HRTEM observations and SAED patterns for this two kinds Ni particles clearly indicate, those Ni nanoparticles size are typically 10-50nm, most of particles are spherical or ellipsoidal in shape. Besides, from Fig.1 (a) and Fig.1 (b), graphitic encapsulated fcc-Ni and Ni_3C nanoparticles; pure Ni nanocrystals coated with NiO layer are identified, respectively. It is more interesting to note, from HRTEM images (Fig.1 (a)), neither gaps nor intermediate phases are observed between the outer graphitic layers and the core Ni nanocrystal for Ni(C) graphitic cages materials. This typical characteristics reflect a growth history of this nanoencapsulted Ni particles, carbon atoms dissolve into a molten or solid carbon-metal alloy and then graphite precipitates to the surface under carbon-arc discharge plasma process [6]. The EDS spectra elemental analysis for this two types Ni nanoparticles is shown in Fig.2(a, b), for Ni(C) nanoparticles, this reveals the presence of only Ni and carbon, no signal corresponding to oxygen are detected. Whereas, only Ni and oxygen have been found in Ni(O) nanoparticles. These EDS spectra further reconfirm the SAED results.

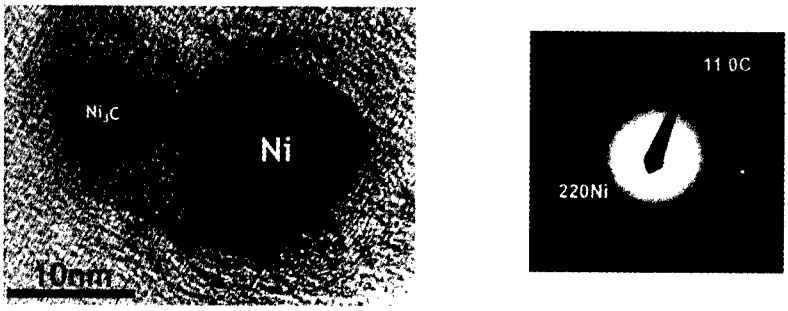


Fig.1 (a) HRTEM morphologies and corresponding SAED patterns for Ni(C) nanoparticles. Note, arrows indicate the graphitic layers; G symbol is graphite; C symbol is Ni_3C phase.

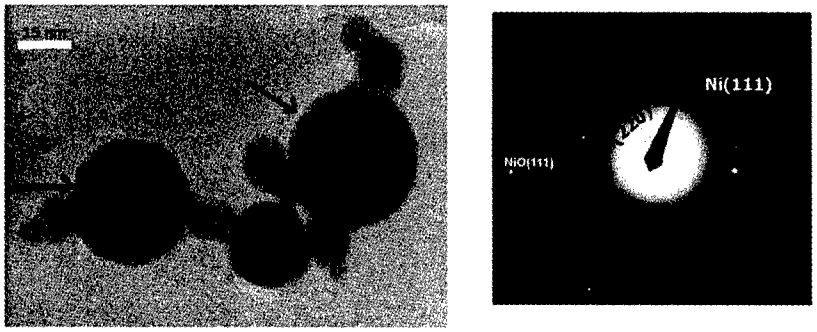
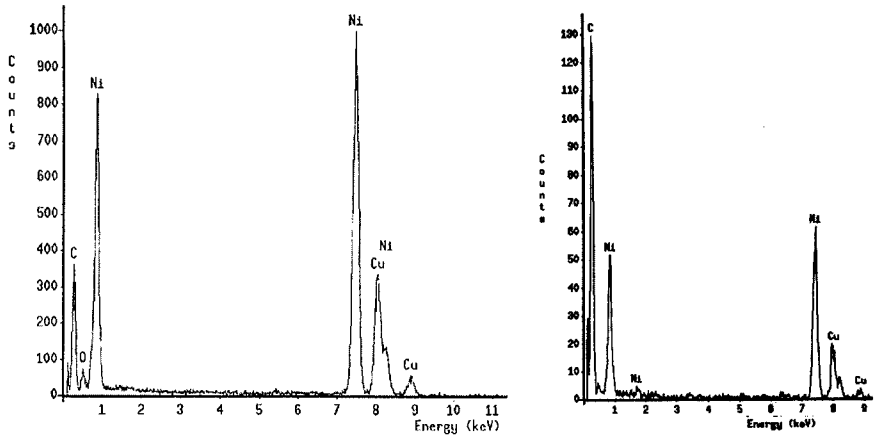


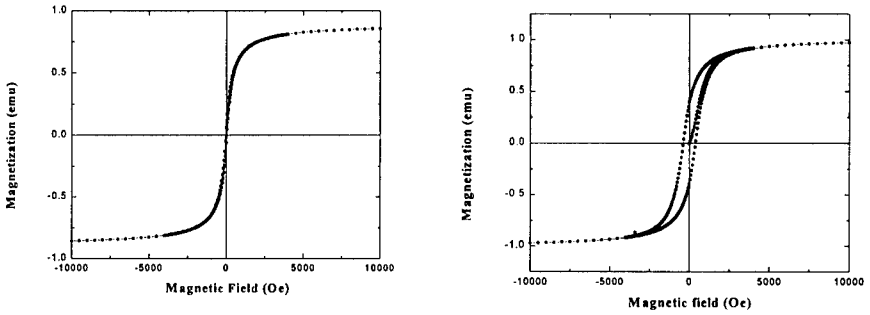
Fig. 1 (b) HRTEM morphologies and corresponding SEAD patterns for Ni(O) nanoparticles. Note, arrows indicate the NiO layers.



(a) **(b)**

Fig. 2 EDS spectra of; (a) Ni(O) and (b) Ni(C) nanoparticles. Note, the Cu symbols from TEM copper grid.

Magnetization *vs* field plots for Ni(C) nanoparticles at 300K and 2K are shown in Fig.3, respectively. It is evident from Fig. 3 (a) and Fig. 3 (b) that two different processes are occurring on those Ni(C) nanoparticles, and those are depending on the temperature. At high temperatures the process can be characterized as the particles are in a pure superparamgnetic sate; whereas at lower temperature the materials become in ferromagnetic state, as evidenced by the hysteretic behavior observed in Fig. 3 (b).



(a) (b)

Fig. 3 Field dependence of magnetization for Ni(C) nanoparticles at; (a) 300K and (b) 2K.

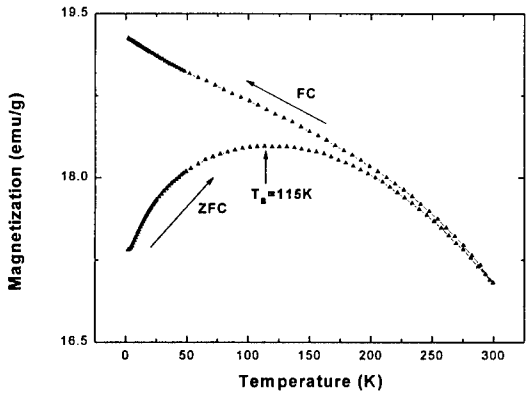


Fig. 4 Temperature dependence of magnetization for Ni(C) nanoparticles at applied field of 1000 Oe, the blocking temperature is about 115K.

In fact, this behavior also can be clearly observed in Fig.4, where the temperature dependence of the magnetization is plotted by following ZFC and FC sequences; indicating a transition to the above two different states. In this case, the T_B is about 115K, and the shape of the curve also indicates that there is wide distribution of sizes of Ni(C) nanoparticles.

It is well known that a small magnetic particle becomes single domain below some critical size. Which is due to the interplay between the total magnetic energy and domain wall creation [7, 8]. According to this Ni (C) nanoparticles, with an average size of about 10.5nm, may be considered to have a single magnetic domain. Thus the magnetic behavior is

therefore size-dependent and should be considered in conjunction with thermal energy and surface anisotropy aspects.

Magnetization *vs* temperatures for Ni(O) nanoparticles measurements at different magnetic filed (H = 100, 1000, and 10, 000 Oe) are shown in Fig.5 a, b, and c. It seems that this is a typical cluster glass behavior for the assembly of nanoparticles [9-12]. Note the deviation between the zero field cooling (ZFC) and field cooling (FC) magnetization below the certain blocking temperature, this strong irreversibility is well dependent on the applied magnetic fields. This behavior may be attributed to the random distribution of anisotropic interaction, and surface effects.

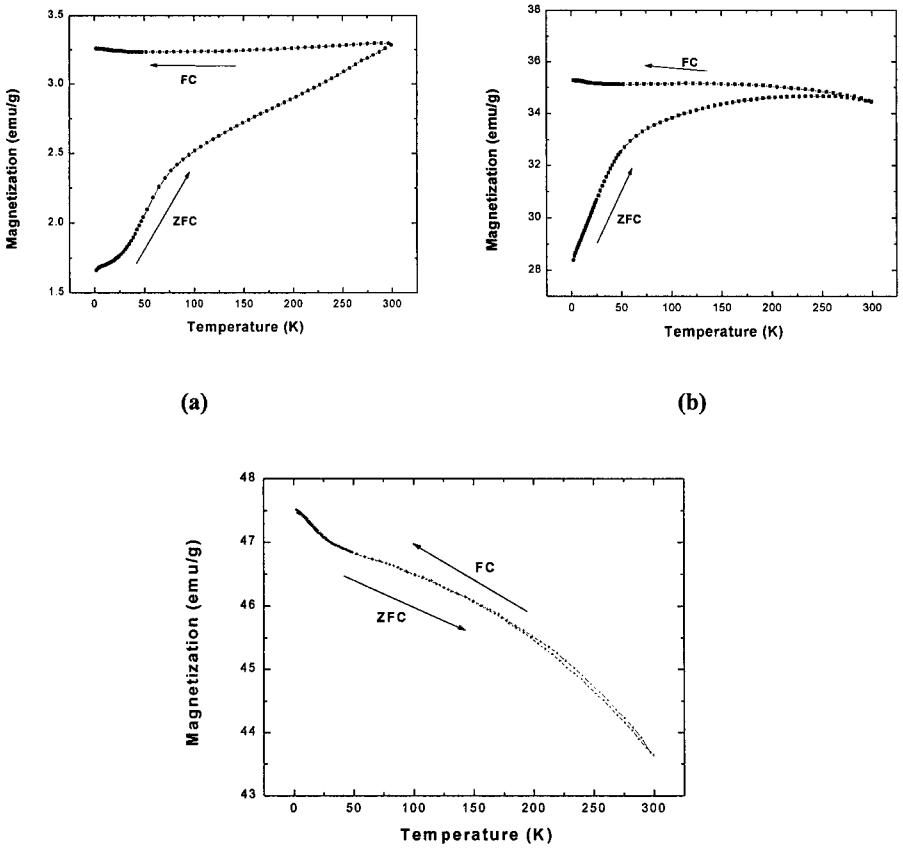


Fig. 5 Temperature dependence of magnetization for Ni(O) nanoparticles at different applied magnetic fields; (a) 100 Oe, (b) 1000 Oe, and (c) 1 T.

It is interesting to observe that the strong irreversibility present in curves of Fig. 5 (a) and 5 (b) and disappear for magnetic fields of about 1 T in Fig.5 (c). This is occurring as soon the anisotropy field of the Ni(O) nanoparticles is surpassed.

CONCLUSIONS

In the study, graphitic encapsulated Ni nanocrystals and pure Ni nanoparticles coated with NiO layers have been successfully synthesized by modified arc-discharge method in different atmospheres. High-resolution transmission electron spectroscopy, and nanoarea electron diffraction have been used to study the distinct morphological properties of two kinds of Ni nanoparticles. Graphitic encapsulated fcc-Ni and Ni_3C nanoparticles are determined in the Ni(C) particles. For Ni(O) particles, pure Ni nanocrystals coated with NiO layer is observed. Magnetization measurements under different fields and temperatures indicates, typical cluster glass-like behavior due to ferromagnetic interaction among the assembly of Ni(C) particles have been observed; however, Ni(C) particles exhibits superparamagnetic behavior at room temperature under a certain applied filed, the blocking temperature, T_B, is determined to be near 115K.

ACKNOWLEDMENTS

X.C. S and M.J.Y gratefully acknowledge support by CONACyT projects through grant "Quantum Colloids" in México. F. M. gratefully acknowledge support by CONACyT (Contract No. G0017E) and DGAPA-UNAM (Contract No. IN-105597).

REFERENCES

1. E. Anno, and T. Yamaguchi, Surface Sci., 286, 168(1993)
2. L.Y. Jiang, Y.D. Yao, Y.Y. Chen and Y. Hwu, Nanostruct. Mater., 9, 581(1997)
3. K.Z. Chen, Z.K. Zhang, Z.L. Cui, D.H. Zuo and D.Z. Yang, Nanostruct. Mater., 8, 205(1997)
4. X.L.Dong, Z.D. Zhang, Q.F. Xiao, X.G. Zhao, Y. C. Chuing, S.R. Jin, W.M. Sun, Z. J. Lin, Z.X. Zhang, H.Yang, J .Mater. Sci., 33, 1915(1998)
5. D. Mendoza, F. Morales, R. Escudero, and J. Walter, J. Phys.: Condens. Matter, 11, L317 (1999).
6. Y. Saito, T. Yoshikawa, M. Okuda, N. Fujimoto, K. Suzuki, A. Kasuya, and Y. Nishina, J. Phys. Chem. Solids, 54 (12), 1849(1993)
7. S. Morup, Europhys. Lett., 28, 671(1994)
8. Y.S. Kang, S.Risbud, J. F. Rabolt, P. Stroeve, Chem. Mater., 8, 2209(1996)
9. J.L. Dorman, R. Charkaoui, L. Spinu, M. Nogues, F. Lucari, D. Fiorani, A. Garcia, F. Tronc and J.P. Jolivct, J. Magn. Magn. Mater., 187, L139(1998)
10. S. Morup, F. Bodker, P. V. Hendriksen, and S.Linderoth, Phys. Rev. B 52, 287(1995)
11. A. Garcia del Muro, X. Battle and A. Labarta, Phys. Rev. B 59, 13584(1999)
12. A. Giguere, M. Foldeaki, R.A. Dunlap, and R. Chahine, Phys. Rev. B 59, 431(1999)

TEMPERATURE DEPENDENCE OF THE ELECTRICAL RESISTIVITY IN NANOCRYSTALLINE GOLD FILMS MADE BY ADVANCED GAS DEPOSITION

J. EDERTH, L. B. KISS, G. A. NIKLASSON, C. G. GRANQVIST, and E. OLSSON
Department of Materials Science, Uppsala University, BOX 534, S-751 21 Uppsala, SWEDEN

ABSTRACT

Nanocrystalline thin Au films with grain size 10 – 76 nm have been analyzed regarding the temperature dependence of the electrical resistivity. A sudden change in the power function, $\rho \propto T^n$, was found at ~10 K, where $n = 1.7$ in the range 5 – 10 K and $n = 3.3$ in the range 10 – 15 K. This effect disappears after annealing at 773 K for 0.5 h in air at atmospheric pressure. After the annealing the grain size was ~ 100 nm. This is an indication of interference between electron-phonon scattering and electron-grain boundary scattering in nanocrystalline materials at low temperatures.

The temperature coefficient of resistivity, *TCR*, increased with increasing grain size at any temperature and the position of the maximum *TCR* was shifted towards lower temperatures with increasing grain size.

INTRODUCTION

Nanocrystalline materials attract much interest because of their ability to attain special properties such as high thermal stability, extreme hardness,[1] and high elasticity.[2] The nanocrystalline metals are therefore of great interest as conductors employed in environments with high stresses. The present work is concentrated upon the electrical properties of nanocrystalline gold made by the advanced gas deposition method.

Many investigations[3-8] have been carried out on the temperature dependent electrical resistivity, denoted $\rho(T)$, in metals. The scattering mechanisms of electrons in the high temperature range, $T > \theta/2$ (where θ is the Debye temperature), have been thoroughly investigated and elucidated. The resistivity decreases linearly with the temperature due to the fact that the number of phonons is proportional to the temperature.

At low temperatures, $T << \theta$, there is still a somewhat unclear situation regarding the scattering mechanisms of electrons. There are some indications of electron-electron scattering at low temperatures. Work by Nishi et al.[5] on 10 to 40 nm thick Au films yielded, $\rho \propto T^2$ at $30 < T < 90$ K and $\rho \propto T^4$ at $15 < T < 30$ K. They also showed that the derivative $d(\log \rho(T))/d(\log T)$ decreased discontinuously indicating two different scattering mechanisms. However, Sambles and Elsom[4] reported that no evidence was found for a T^2-term in the electrical resistivity of thin Au films. There are also results reported by Echternach et al.[7] on thin Au films exhibiting a T^2-term in the resistivity due to interaction between electron-phonon scattering and electron-impurity scattering.

Given the unclear situation regarding $\rho(T)$ in Au at low temperatures we found it worthwhile to carry out a detailed investigation on the electrical resistivity of thin nanocrystalline gold films.

SAMPLE PREPARATION

The samples were fabricated using inert gas evaporation (Ultra Fine Particle Equipment, ULVAC Ltd). This technique was introduced several years ago[9] and has become the leading

Mat. Res. Soc. Symp. Proc. Vol. 581 © 2000 Materials Research Society

one for the production of high-quality nanoparticles.[10-13] The evaporation of a material takes place in the presence of a gas. The vapor is thereby cooled so that nucleation and growth of ultrafine particles takes place in the gas. Recent developments of this technique have shown that a high laminar gas flow can lead to particle growth under near-equilibrium conditions, with only a weak tendency towards coagulation. The growth can be determined by first-passage-time dynamics in the vapor zone, so that the size distribution is narrow.[14] The gas-evaporated particles can be single crystalline. The technique is applicable to many materials and can produce particles with a wide range of sizes.

Essentially, evaporation from an ingot takes place in an evaporation chamber containing the gas. The heating is provided by an induction coil of copper surrounding a carbon crucible. A stream of gas and particles runs through a transfer pipe into an evacuated upper chamber where the particles are collected. The upper end of the transfer pipe is connected to a jet nozzle, with a diameter of 0.5 mm, which accelerates the gas and the particles to a high speed. He gas is introduced below the crucible. The transfer pipe is positioned centrally in the zone where particles are formed. Particles in an outer zone are removed by an exhaust pipe connected to a pump. Strong precautions must be taken to avoid turbulence and eddy formation. Particle deposition took place onto a glass substrate mounted on a movable table so that it was possible to produce patterned thin nanocrystalline gold films.

Four samples, denoted I-IV, were fabricated with different temperatures of the melt in the crucible T_M, temperatures of the substrate holder T_S, and gas pressures in the evaporation chamber p. Data are given in Table 1. We determined T_M to an accuracy of ± 5 % by optical pyrometry.

Table I. Data for nanocrystalline gold samples prepared by inert gas evaporation for different temperatures of the melt T_M, substrate temperature T_S, and inert gas pressure p. The mean crystallite diameter was D, as determined by x-ray diffractometry.

Sample	$T_M(K)$	$T_S(K)$	*p(mbar)*	*D(nm)*
I	1513	323	480	10
II	1663	523	500	40
III	1713	523	500	59
IV	1753	523	500	76

SAMPLE CHARACTERIZATION

X-ray diffraction (Siemens Diffractometer D5000) was used to determine the grain size, D, of the four different specimens and the results are presented in Table I. The grain sizes were between 10 and 76 nm.

The Scherrer method, used to evaluate grain sizes, are sensitive to internal stress in the specimens so this method needs verification by an independent method. To do this, a TEM (transmission electron microscopy) sample was prepared by placing a copper grid, with a holey carbon film, on the glass substrate and exposing it to the particle beam while sample I was fabricated. The grains are spherical, see Fig. 1(a), and the mean grain size from this

investigation was 11 nm, which is in good agreement with the x-ray diffraction result. This shows that our technique for particle sizing is reliable. It should be noted that larger grains are seen under the spherical nanoparticles in Fig. 1(a). This can be explained by a poor heat transfer from the carbon film to the TEM copper grid, causing sintering of the gold nanoparticles. Figure 1(b) is taken from the same TEM copper grid, but after annealing for 0.5 h at 773 K in air at atmospheric pressure. The grains have grown to approximately 100 nm and are no longer spherically shaped and the number of twins has increased to a high concentration.

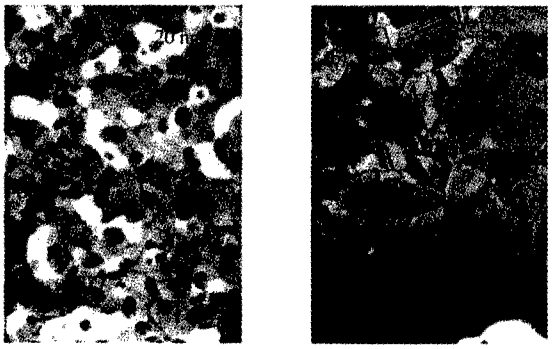


Fig. 1. TEM micrographs showing: (a) the nanocrystalline gold film before annealing and (b) the nanocrystalline gold film after annealing at 773 K for 0.5 h in air at atmospheric pressure.

RESULTS

Measurement technique

A four-probe method was employed to measure the resistance of the specimens. The current was set to 3 mA and the voltage was recorded in the temperature range $4 < T < 300$ K. Measuring data were taken twice, with the current running in either direction, at each temperature after temperature stabilization. The arithmetic means of these readings are presented below. The length of the sample was 10 mm, the width was 0.5 mm, and the thickness was ~ 1 μm.

Electrical data for as-deposited films

The $\rho(T)$ for the four nanocrystalline Au samples, as well as literature data[15] for polycrystalline gold, are presented in Fig. 2. The magnitude of the resistivity, at any temperature increases drastically as the grain size decreases. It is also observed that the residual resistivity is much higher for the specimens with small grains as compared to the specimens with larger grains. All the specimens exhibits a linear part in the $\rho(T)$ down to approximately $\theta/2$ ($\theta = 185$ K for gold).

Another way of presenting the temperature dependence is to analyze the temperature coefficient of resistivity, *TCR*, defined as

$$\alpha = (1/R)*dR/dT = (1/\rho)*d\rho/dT \qquad (1)$$

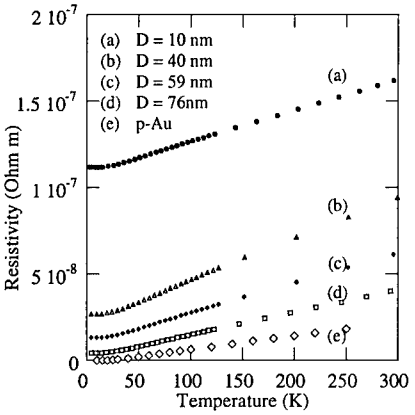


Fig. 2. Resistivity versus temperature for the nanocrystalline gold films (a,b,c,d) and the polycrystalline gold (e).

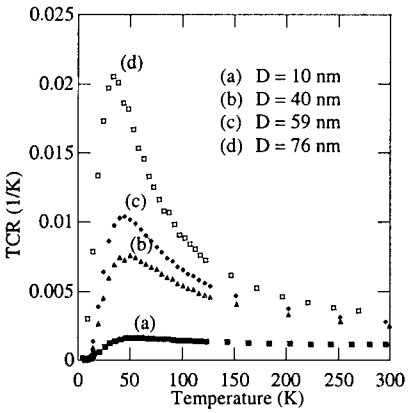


Fig. 3. Temperature coefficient of resistivity, α, versus temperature for the nanocrystalline gold films.

Thus, to analyze α we do not need to consider the geometry of the specimen. In Fig. 3 α, for all specimens, is plotted versus temperature in the range 4 – 300 K. It is observed that at any temperature α is decreasing with diminishing grain size. The position of the maximum is shifted towards lower temperatures with increasing grain size. This position indicates at what temperature the specimen deviates from its linear temperature dependence.

Effects of post annealing

Further information on the temperature dependent resistivity was obtained by plotting *log* ρ versus *log* T for sample I. Figure 4(a) gives clear evidence for a power law dependence, $\rho \propto T^n$ with $n \approx 1.7$ for $T < 10$ K and $\eta \approx 3.3$ for $T > 10$ K. This sudden change may be a sign of interference between electron-phonon scattering and electron-impurity scattering at low temperatures, as further elaborated below.

Effects of annealing were investigated for sample I being heated in air at 0.5 h for successively higher temperature T_A. Electrical measurements at $4 < T < 300$ K were conducted after each annealing step. Figure 4(b,c,d) report data for T_A being 473, 673, and 773 K. The discontinuity in the data becomes weak at $T_A = 673$ K and is not to be seen at $T_A = 773$. For the latter case we observe $n \approx 3.9$ at $5 < T < 15$ K.

DISCUSSION

The resistivity in nanocrystalline materials is more dependent on grain size than in polycrystalline materials (grain sizes larger than 1 μm). This is due to the fact that the fraction of grain boundaries is increasing with decreasing grain size, and can therefore not be neglected when analysing the resistivity of nanocrystalline materials, especially at low temperatures.

In Fig. 4(a), where *log* ρ is plotted as a function of *log* T for sample I, there is a change in the slope at 10 K from $n = 3.3$ in the range 10 – 15 K to approximately $n = 1.7$ in the range 5 – 10 K. Echternach et al.[11] observed similar effects in very thin (10 – 40 nm) evaporated polycrystalline Au films. The mean free paths in the films were estimated to be 10 – 25 nm.

This effect was explained as interference between the electron-phonon scattering and the electron-impurity scattering. In their experiments the mean free path was limited by

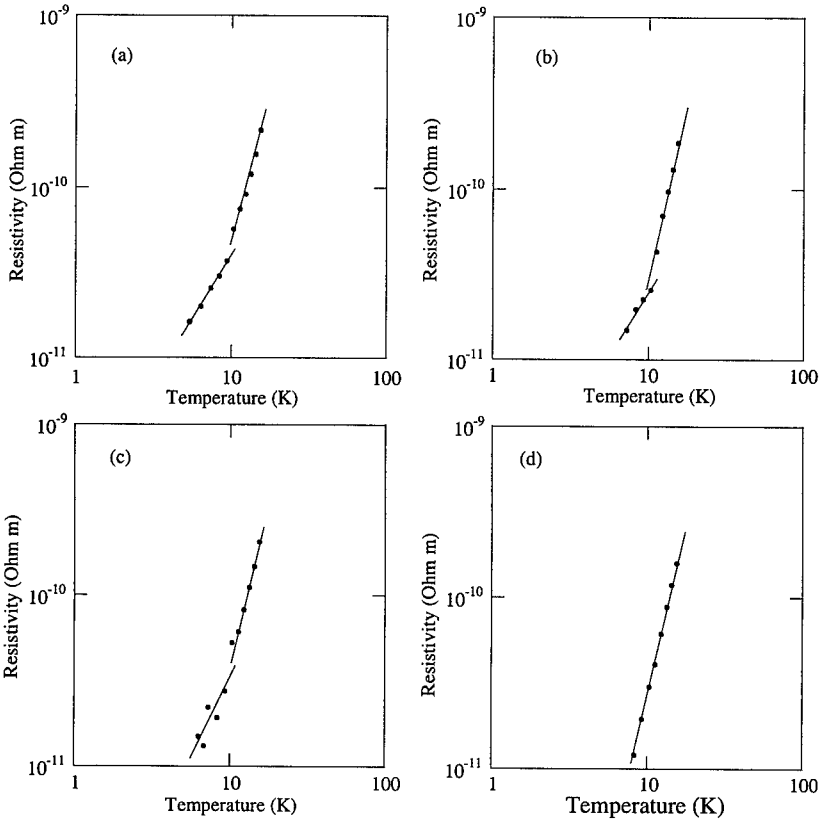


Fig. 4. Resistivity versus temperature for sample I (D = 10 nm)
(a) No annealing
(b) Annealing at 473 K for 0.5 h in air at atmospheric pressure.
(c) Annealing at 673 K for 0.5 h in air at atmospheric pressure.
(d) Annealing at 773 K for 0.5 h in air at atmospheric pressure

the thickness of the specimens. It is likely that electron-grain boundary scattering would give similar effects. Let us now assume that the mean free paths in our specimens are confined by the grain size. This means that the mean free path in specimen I should be approximately 10 nm. In order to analyse this effect by changing the mean free path the film was annealed at different temperatures for 0.5 h in air at atmospheric pressure. The resistivity was measured as a function of temperature after each annealing step. The $\log \rho$ was plotted as a function of $\log T$ for the different annealing temperatures, see Fig. 4(b,c,d). It was observed that practically no change happened by annealing at 473 K. At 673 K we observed a small change, the magnitude of the resistivity decreased. After annealing at 673 K the resistivity decreased further and the effect of interference between electron-phonon scattering and electron-grain boundary

scattering was no longer observable. The resistivity was then following the same power law, with $n = 3.9$, in the whole temperature range 5 – 15 K. According to a TEM analysis, the grain size had grown to approximately ~ 100 nm. From energy dispersive X-ray spectrometry analysis, using a Link AN 1000 system attached to the TEM instrument, we found no significant amount of oxygen in the specimens after annealing.

Thus, this is a strong indication of interference between electron-phonon scattering and electron-impurity scattering where the impurities are the grain boundaries and the mean free path is confined by the grain size of the specimen. The fact that the interference effect disappears when the grains have grown to approximately 100 nm upon annealing supports this conclusion.

CONCLUSIONS

The electrical resistivity was analyzed in nanocrystalline gold films with different grain sizes (10 – 76 nm). At 10 K there is a change in the power function, from $n = 1.7$ when $T < 10$ K to $n = 3.3$ when $T > 10$ K. This is explained in terms of interference between the electron-grain boundary scattering and the electron-phonon scattering, and this effect disappears when the specimen is annealed at 500 °C for 0.5 h in air at atmospheric pressure reaching a grain size of ~ 100 nm.

In the high temperature range all samples exhibited metallic behavior with a linear temperature dependence down to $T \sim \theta/2$. The resistivity increased with decreasing grain size indicating an additional resistivity component due to the grain boundary scattering.

The TCR as a function of temperature shows that the TCR at any constant temperature increases with increasing grain size. The position of the maximum TCR is shifted towards lower temperatures with increasing grain size.

ACKNOWLEDGMENTS

This work was supported by the Swedish Foundation for Strategic Research.

REFERENCES

[1] S. Okuda and F. Tang, NanoStruct. Mater. **6,** 585 (1995)
[2] H. Tanimoto, H. Mizubayashi, H. Fujita, and S. Okuda, J. Phys. IV (Paris) **6,** p. C8-199 (1996)
[3] B. R. Barnard, A. D. Caplin, and M. N. B. Dalimin, J. Phys. F **12,** 719 (1982)
[4] J. R. Sambles and K. C. Elsom, Solid State Commun. **52,** 367 (1984)
[5] Y. Nishi, A. Igarashi, and K. Mikagi, J. Mater. Sci. Lett. **6,** 87 (1987)
[6] J. F. Kos, J. Phys. Condens. Matter. **2,** 4859 (1990)
[7] P. M. Echternach, M. E. Gersehenson, and H. M. Bozler, Phys. Rev. B **47,** 13659 (1993)
[8] X. Y. Qin, W. Zhang, L. D. Zhang, L. D. Jiang, and D. Jin, Phys. Rev. B **56,** 10596 (1997)
[9] C. G. Granqvist and R. A. Buhrman, J. Appl. Phys. **47**, 2200 (1976)
[10] J. Ederth, A. Hoel, C. I. Johansson, L. B. Kiss, E. Olsson, C.G. Granqvist, and P. Nordblad, J. Appl. Phys. **86**, 6571 (1999)
[11] C. Hayashi, R. Uyeda and A. Tasaki, "Ultra-Fine Particles" (Noyes, Westwood, New Jersey, U.S.A, 1997)
[12] R.W. Siegel, Ann. Rev. Mater. Sci. **21**, 559 (1991)
[13] H. Gleiter, NanoStruct. Mater. **1**, 1 (1992)
[14] J. Söderlund, L.B. Kiss, G.A. Niklasson and C.G. Granqvist, Phys. Rev. Lett. **80**, 2386 (1997)
[15] American Institute of Physics Handbook, McGraw-Hill, Third Edition, ch. 9 p. 41 (1972)

SINTERING BEHAVIOR OF NANO-CERAMIC COATINGS

J.Th.M. De Hosson, R. Popma and J. Hooijmans, Department of Applied Physics, Materials science Centre and Netherlands Institute of Metals Research, University of Groningen, Nijenborgh 4, 9747 AG Groningen, The Netherlands, e-mail: hossonj@phys.rug.nl.

ABSTRACT

This paper concentrates on the densification of sol gel derived thin nano-ceramic coatings by laser radiation and by furnace treatment. Deposition of the film is done by means of spin coating of Zirconia. The sintering of the layer is observed using a number of different measuring techniques. Especially, attention is paid to the densification behavior and the grain growth in the layer, investigated by scanning electron microscopy and ellipsometry. Also the different crystal phases observed are addressed. During sintering at a constant temperature a change in the sintering behavior with time is observed. This change is observed for most temperatures. Both the initial fast sintering of the process (for all sintering temperatures), and the final slow sintering (only at the higher sintering temperatures) are explained.

INTRODUCTION

A decade ago the emergence of the field of coatings was greatly driven by the realization that the surface is often the most important part of any engineering component. Structural components fail by wear, corrosion, high cycle fatigue etc., that is to say affected by the surface conditions. Consequently, an appropriate approach would be to modify the surface layer of a base-material or to apply a coating, so as to provide enhanced performance [1, 2]. A number of techniques were developed for coating fabrication. But the fabrication of coatings is often a difficult and laborious process. The conventional method of slipcasting to produce ceramic foils suffers from thickness limitations. An industrially applicable method to obtain coatings is wet-chemical processing, also called sol-gel processing [3,4]. The sol-gel method allows films to be made with almost any composition and degree of porosity. The problem of homogeneity, often encountered in the processing of powders, is absent in the sol-gel preparation technique because no comminution is required. Moreover the processing temperatures can be significantly reduced, and combining different coating liquids (hybrid systems) is easy. This latter aspect offers a great deal of freedom to fabricate coatings with different properties. In our work the sol-gel concept is combined with inkjet technology and laser treatment of surfaces. The entire combination is called 'Stereostiction' [5]. A solution containing nano-sized ceramic particles is fed to an inkjet nozzle that generates a software-controlled pattern on a surface. Afterwards the drops are exposed to an intense laser beam that dries and densifies the drops, thereby forming a sintered ceramic layer. The heating damage to the product by the intense laser beam is minimized by using short laser pulses resulting in very small heat affected zones. It is possible to apply different coating compositions using multicolor techniques, which nowadays are in a mature stage of development. 3-D products up to several millimeters can be manufactured by repetitive passing of the inkjet nozzle, drying and sintering. However, sintering behavior of the sol-gel coating is a crucial aspect and very little microscopic information is available. This paper concentrates on the microscopic mechanism of sintering of nanosized sol-gel ceramic zirconia coatings on fused silica substrates. Here we report explicitly about the sintering by furnace treatments. The laser treated materials will be published elsewhere.

EXPERIMENTS

The zirconia sol-gel is prepared from precursors which react with each other to form monodisperse zirconia particles of about 3 nm (existing of zirconiumhydroxide) that are suspended in an aqueous fluid (sol-gels were obtained from Merck-Germany). The layers of zirconia sol-gel were deposited on fused silica substrates, and by means of spin coating the desired thickness was achieved. After coating the samples were dried in ambient air atmosphere. Experimentally it was found that a green layer with a

Mat. Res. Soc. Symp. Proc. Vol. 581 © 2000 Materials Research Society

maximum thickness of about 350 nm could be attained. At greater thickness the green layer exhibited severe cracking. Although this starting layer thickness is rather thin, the phenomenon is commonly found in green layer drying, that is to say above a thickness of 1 μm the layers are always cracked and only below 0.5 μm no cracking is observed, independently of drying conditions [6, 7].[h1] The fused silica samples covered with a dried sol-gel layer were put in an air furnace for different sintering times (ranging from 1 minute to 6 hours) at temperatures ranging from 150°C to 1200°C (this is the upper limit for the fused silica substrate to withstand the temperature). Subsequently the samples were cooled down to room temperature in ambient air. Because the green coating is very thin (350 nm) it will heat up fast, so that almost instantly the same temperature as the furnace atmosphere is reached (calculations predict within 2 microseconds). The samples were examined using ellipsometry, scanning electron microscopy, transmission electron microscopy and X-ray diffraction. With the use of an ellipsometer (VASE Ellipsometer, a rotating analyzer type measuring the spectral range between 185 and 1700 nm) layer thickness and density were studied. An SEM equipped with a special electromagnetic lens in order to obtain higher resolution (Philips XL30-S FEG SEM) was used to study the layers. Grain size (from top view images) and layer thickness (from cross section images obtained by breaking the samples) were determined. A TEM (JEOL 4000/II) able to obtain high resolution images was used to study the original sol-gel particles. X-ray equipment (Philips PW 1820 with a Cu anode) was used to determine the presence or absence of crystalline phases in the layer.

RESULTS

The green layer exists of particles too small to be visible in the SEM. In the TEM the particles can be made visible, but are obviously affected by the electron beam, and most particles crystallize almost immediately. The particles have a spherical shape with a radius of about 2 to 3 nm. In addition clusters of particles can be found. These clusters form larger conglomerates very easily, indicating that the material is very reactive.The property related to sintering that is most easily studied is the thickness of the ceramic surface layer. In figure 1 the layer thickness is plotted as a function of the sintering temperature, while the sintering time was 30 minutes for all samples. There is good agreement between the results obtained with the SEM and those obtained by ellipsometry. Only at very low sintering temperatures (less than 300°C) there appears to be a difference. At those temperatures the layer thickness values obtained with the ellipsometer were less than half of those obtained with the SEM. The values obtained with SEM can be assumed to be correct, and the differences with the ellipsometry results can be explained by the high degree of porosity of the layer and the fact that some hydroxyl groups are probably still present. It is obvious that the layer thickness will shrink when heat is applied, and in this case the layer shrinks from about 350 nm to 100 nm, i.e. approximately 70%. The change in thickness of the coating is related to the change in density. In figure 2 the density is plotted as a function of the sintering temperature. At a temperature of 1200°C a completely densified zirconia layer is achieved. This can be observed by SEM and was detected by ellipsometry. It is clear that the density increases continuously with increasing temperature. The green layer density is very low, about 30%. The density values at low temperatures are obtained from SEM-images, assuming that the 1200°C layer is completely dense and that all layers had the same green layer thickness (those obtained with ellipsometry are too high due to the high degree of porosity).

The grain size as a function of sintering time is displayed in figure 3 for different sintering temperatures. At the lowest temperatures (300°C or less) no, or almost no grain growth took place. XRD measurements showed that no crystal phases were present, even at longer sintering times. When the sintering temperature gets higher (between 500 and 1000°C) the curves show two distinct regions. Instead of a continuous growth of the grains, the grains seem to obtain a certain size very quickly (this grain size depending on temperature) and after that hardly any grain growth takes place. In these samples the XRD measurements show a mixed composition of tetragonal and monoclinic phases. This can be explained by the fact that part of the grains are still very small, which favors the tetragonal phase instead of the monoclinic phase, normally stable at room temperature [8]. When the sintering temperature is even higher (1100 and 1200°C) there is an additional slow grain growth after the initial rapid growth . In this case the XRD results show only the monoclinic phase for all samples.

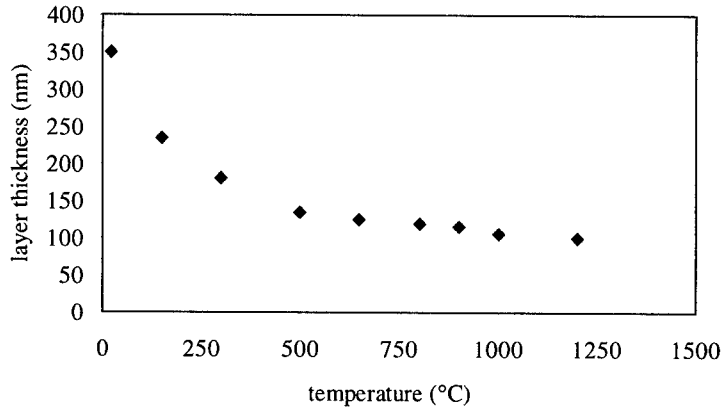


Figure 1: thickness of the zirconia layer as a function of sintering temperature. All samples were sintered for 30 minutes

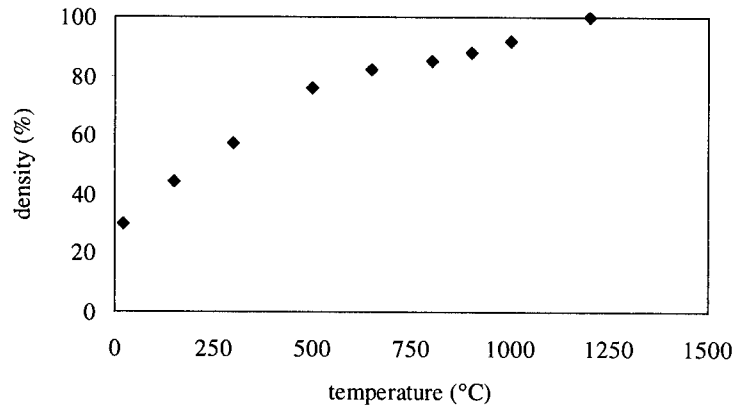


Figure 2: density of the zirconia layer as a function of sintering temperature. All samples were sintered for 30 minutes.

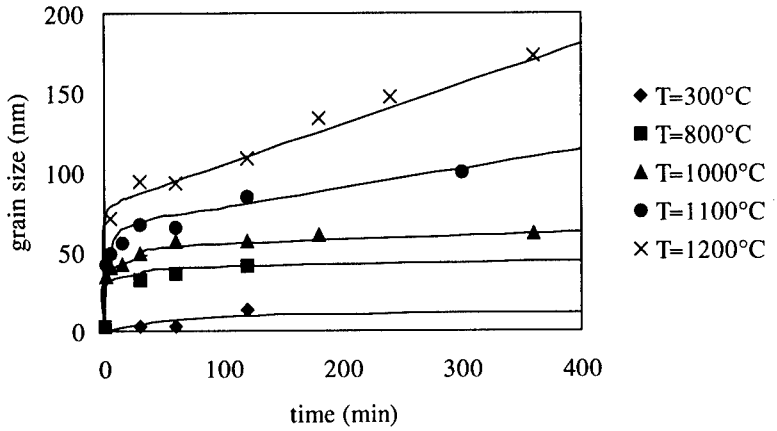


Figure 3: grain size for zirconia surface layer as a function of the sintering time at various sintering temperatures.

DISCUSSION AND CONCLUSIONS

Amorphous materials sinter by viscous flow and crystalline materials sinter by diffusion, so the paths along which material moves, and the relationship between the rate of transport and the driving force, are quite different [9]. But very little information is available on the kinetics of thin film sintering. It was shown previously that films densify faster than bulk material, even though the film has lower surface area [9]. This is contrary to the theory, which predicts that a film will sinter more slowly than an unconstrained gel, because a film can shrink only in the direction perpendicular to the substrate [10].

In the case of viscous sintering, analysis of the densification process of the layer can yield satisfactory results. As shown in figure 2 the density quickly reaches a constant value. This behavior can be described by viscous sintering, which is relatively simple in principle, but exact treatments are prevented by the complex geometry of the porous body. Fortunately, simple approximations, while not strictly realistic, yield satisfactory results. Given a microstructural model, it is possible to relate the change in surface area to the overall change in dimensions. Frenkel [11] suggested that the rate of densification could be found by equating the rate of change in surface energy to the rate of energy dissipation. This insight is the basis for all analysis of viscous sintering, which differ only in the models they adopt to represent the geometry of the body. Frenkel [11] started with the coalescence of a pair of spheres, which is representative of the sintering process. An equation for the growth in radius of the neck between spheres was derived for this case. When the neck is relatively small, there is a geometrical relationship between the neck and the distance between the centers of the spheres, which is used to obtain an expression for the change in linear dimension L of the sintering body [12].

$$\frac{L(t)}{L(0)} = 1 - \frac{3\gamma t}{8\eta a}$$

where L(t) is the linear dimension at time t, L(0) the initial linear dimension, γ the surface energy, a the original particle diameter and η the viscosity. In the original work of Frenkel [11] a numerical factor of ¾ was proposed which does not account for center-to-center approach. This factor is of little importance as long as precise values for γ and η are not available. Further, for slow creep deformation of two identical spheres of a linearly viscous material the neck radius grows proportionally to $t^{1/3}$. Consequently the

shrinkage, which is proportional to the neck radius squared, is proportional to $t^{2/3}$. Further it should be stressed that the commonly used sintering models are based on a two-sphere approximation. It is speculated that in reality the deviations from this two-particle description might be considerable. In particular, asymmetric neck growth, caused by the local packing and atmosphere, will cause rearrangement of particles in regions of smaller packing and opening of larger pores [12]. This is also observed by in-situ heating in a FEG –XL30- Philips environmental scanning electron microscope (ESEM) as displayed in figure 4. At any rate, the viscosity of a material decreases, and the coupled shrinkage rate of the layer increases upon increasing temperature. This results in a very high densification rate, much higher than densification of crystalline materials. Because the values after 1 minute of sintering already show some crystalline phases, the viscous flow must have taken place before that. At a temperature of 800°C this leads to a value for the viscosity (using γ is 0.3 J/m^2 [13]) between 10^{-7} and 10^{-10} Pa.s, depending on the initial shrinkage rate. These values are rough estimates because of the lack of measurements with shorter sintering times, but the values are of the right order of magnitude (e.g. 10^{-7} Pa.s for silica at 800°C [14]). Also from silica it is known that the viscosity decreases as the hydroxyl content increases [15], which could be of importance because the zirconia layer looses its hydroxyl groups during the process. It should be noted that the original viscous flow model assumes that the geometry of the neck formation is based on a simple tangent circle model and that the behavior of irregularly packed arrays of spheres can be directly derived from that of two single particles. In fact both of these assumptions are incorrect depending on the sintering atmosphere [12]. Fig.2 shows an almost linear increase in density as a function of temperature which cannot be explained by a single thermally activated process. Obviously more than one process takes place, like removal of physically adsorbed water, polymerization and structural relaxations. It implies that in these nanoceramic systems viscous sintering mechanisms may be questionable at these temperatures and times. It is anticipated that the removal of adsorbed water is the principal reason for densification at the beginning and that viscous sintering becomes important at much higher temperatures. During the first part the zirconium hydroxide is transformed to zirconium oxide and water, and after that, or concurrently, the particles may grow together forming larger grains. This second part of the process is the growth of the crystalline grains. That the grains in the layer have crystallized can be concluded through XRD measurements. The grain growth can be described by [16]:

$$G_t^n - G_t^0 = BD_0 te^{-\frac{Q_{GB}}{kT}}$$

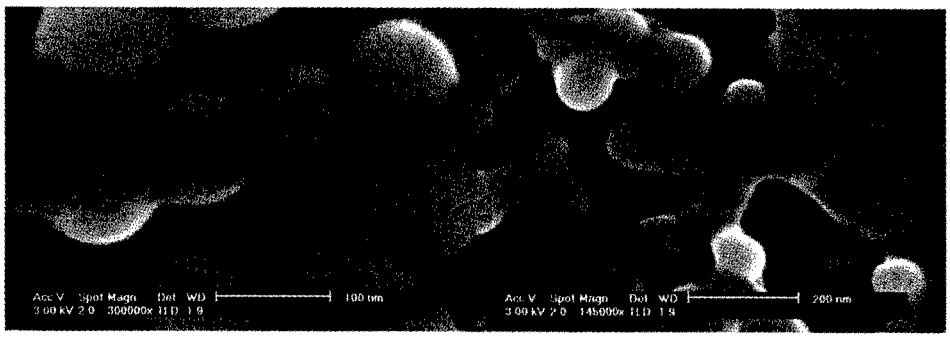


Figure 4: top view of in-situ heated nanoceramic particles inside a FEG-Philips- XL30 Environmental Scanning Electrn Microscope (ESEM) at 1200°C.

where G_t stands for the instantaneous grain size at time t, G_0 the initial grain size and n a constant dependent on the agglomerate size, B a constant close to unity, D_0 diffusivity and Q_{GB} activation energy for grain boundary diffusion.

The constant n must be determined experimentally (theoretical considerations yield a value of two [17]). Fitting the equation to the measured data can lead to the determination of n. Previous experiments [18] have shown that it usually lies between 2 and 4. A value of three is mostly used for n, but in very homogeneous materials a value of two is found. With the use of this relation (where Q_{GB} is 350 kJ, D_0 is 4.85 10^{-5} m^2/s [19]) the value for n can be calculated. This is done for the second part of the 1100°C and 1200°C curves (at lower temperatures the grain growth is too slow to be observed). The value of n is 2.3 and 2.1, respectively. These values agree with the theory, which predicts a value of two for very homogeneous materials.

ACKNOWLEDGEMENTS

Thanks are due to Philips -CFT-The Netherlands (Otto Märten, Ton de Laat) , Philips-Drachten -The Netherlands (Rinus Bliek) and other partners, like Fraunhofer Institut ISC-Germany (Frank Hutter), Merck (Lutz Buettgenbach), Pelikan-Zurich-Switserland (Markus Schudel), MIT-Jarfalla-Sweden (Werner Zapka), Sandvik-Sweden (Mats Sjöstrand, Jeanette Persson) for their collaboration and the stimulating discussions. The work described is supported by FOM-Fundamental Research on Matter,Utrecht-The Netherlands.

REFERENCES

1. R.A. Eppler in Glazes and Enamels, Advances in Ceramics, vol. 18, eds. J.F. MacDowell and D. Boyd, (American Ceramic Society, 1986).
2. J.Th.M. De Hosson, in: Intermetallic and ceramic caotings, eds. N. B. Dahotre and T.S. Sudarshan, Marcel Dekker, New York, chapter 8, p.307-439, 1999.
3. W. Geffcken and E. Berger, German Patent 736 411 (May 1939).
4. Sol-Gel Technology for Thin Films, Fibres, Preforms, Electronics, and Speciality Shapes, ed. L.C. Klein (Noyes, Park Ridge, N.J., 1988).
5. J.Th.M. De Hosson and D.H.J. Teeuw, in : Lasers in surface engineering, ed. N. B. Dahotre, ASM, USA, chapter 6, p.205-254, 1998.
6. H. Dislich in Sol-Gel Technology for Thin Films, Fibres, Preforms, Electronics, and Speciality Shapes, ed. L.C. Klein (Noyes, Park Ridge, N.J., 1988), 50-79.
7. I. Strawbridge and P. F. James, Journal of Non-Crystalline Solids, 86 (1986), 381-393.
8. R.C. Garvie, The Occurrence of Metastable Tetragonal Zirconia as a Crystallite Size Effect, Journal of Physical Chemistry, 69 (1965), 1238-1243.
9. C.J. Brinker and S.P. Mukherjee, Thin Solid Films, 77 (1981), 141-148.
10. G.W. Scherer and T.A. Garino, Journal of American Ceramic Society, 68 (1985), 216-220.
11. J. Frenkel, Journal of Physics (Moscow), 9 (1945), 385-391.
12. H.E Exner and G. Petzow in Sintering and Catalysis, Materials Science Research, vol. 10, ed. G.C. Kuczynski (Plenum, New York, 1975), 279-293.
13. W.D. Kingery, Journal of the American Ceramic Society, 42 (1959), 6-10.
14. A. Napolitano, J.H. Simmons, D.H. Blackburn and R.E.Chidester, Journal of Res. of National Bureau of Standards, 78A (1974), 323-329.
15. G. Hetherington, K.H. Jack and J.C. Kennedy, Physics and Chemistry of Glasses, 5 (1964), 130-136.
16. R.L. Coble, Journal of Applied Physics, 32 (1961), 787-799.
17. J.G. Byrne, Recovery, Recrystallization, and Grain Growth, (Macmillan, 1965).
18. A.S. Edelstein and R.C. Cammarata, Nanomaterials: Synthesis, Properties and Applications (Institute of Physics Publishing, 1996).

NANOPOROUS ALUMINA FILMS PREPARED FROM COLLOIDAL SOLUTION

VLADIMIR PETROVSKY, HARLAN U. ANDERSON, TATIANA PETROVSKY
EMARC, University Missouri-Rolla, MO 65401.

ABSTRACT

Alumina layers were deposited by spin coating and dip coating on different substrates (Pt, Si, Al_2O_3) from the water suspension of nanosize boehmite particles. It was shown, that addition of the butoxyethanol in the suspension improves wetting and the quality of the film. No separation from the substrate or cracking of the film took place up to 1000°C on all types of the substrates for the film thickness up to 10μm. Because of the minimal shrinkage, the coating can be used to smooth rough substrates as well as provide interfacial layers for either single layer or multilayer structures.

INTRODUCTION

Gamma-alumina coatings are of interest for a variety of applications including porous membrane preparation, planaryzing interlayers, diffusion barrier layers, etc. This is connected with the low reactivity of this material over a wide temperature range, which makes it possibile to use it with a number of different substrates and materials.

At the present time the basis of the γ-alumina layer preparation is sol-gel technology. The main limitation of this method is the high shrinkage which occurs during the transition of the gel to the solid phase, which limits the film thickness to the submicron region. Since the initial introduction of the sol-gel preparation technique by Yoldas in 1975 [1,2], a number of attempts have been made to overcame this thickness limitation. However, none of the attempts have been completely successful [3-6].

It appears that the presence of the gel in the precursor limits the amount of solid phase in the solution and the thickness of the resulting films that may be deposited. The purpose of this investigation is to investigate the possibility of using water based suspensions of nanosize boehmite particles to produce continious micron thick γ-alumina films.

EXPERIMENT

Precursors were prepared by the mixing of nanosize boehmite powder with water and nitric acid. Homogenous colloidal suspensions with pH of about 4 containing up to 30w% alumina were made by ultrasonic processing of the suspensions for two days followed by filtration through 0.45μm glass filter. The resulting suspensions had low viscosity (about the water), were semitransparent and stable for periods up to at least a year (at room temperature) for <100nm boehmite particles. This was the basic formulation used in the investigation, however modifications had to be made in order to improve wetting of the substrates (specially for polished Si substrates) by the pure water suspension. It was found that the addition of 2-butoxyethanol to the suspensions at a 2-butoxyethanol/water ratio in the range between 1:2 and 2:1 gave good wetting with no gelation.

Substrates used in the investigation were Al_2O_3 ceramic with grain size 10μm and the average surface roughness of 2μm, polished Si and Pt foil. All substrates were washed in an ultrasonic bath by alcohol and dried at 70°C in a clean room. Two deposition techniques were used: spin coating at the low speed (500-2000rpm), and dip coating (withdrawal speed 1-2 inch/min). Both methods provide ~2μm coating for one deposition and it was possible to dry it

Mat. Res. Soc. Symp. Proc. Vol. 581 © 2000 Materials Research Society

at 70-100°C immediately after deposition without cracking the layer. It was possible to deposit thicker layers (up to 10μm), but drying process should be accomplished slowly (1-2 days at room temperature).

TGA and DTA measurements were done to characterize the precursor (Fig.1). It can be seen that mass drops rapidly at 100°C, practically no changes in the mass taking place after 120°C. The final mass in the high temperature region corresponds to the alumina content in the suspension (23%). The DTA curve has sharp peak at 100°C connected with the evaporation of water. The second smaller peak at 420°C corresponds to the transition from the boehmite to the γ-alumina phase. After the transition to the γ-alumina phase at temperatures above 450°C, no further transitions occurred until the temperature reached 1300°C when α-alumina forms.

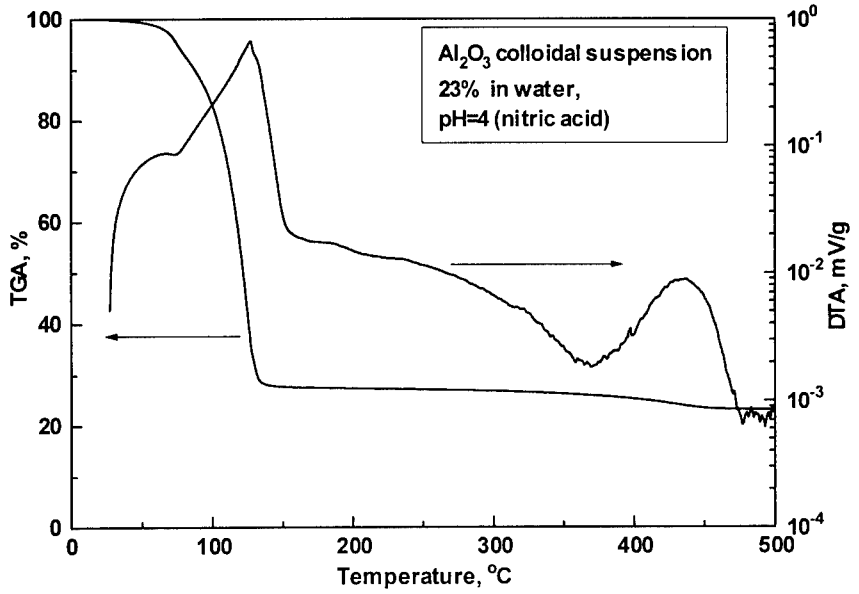


Fig.1. TGA and DTA analyses of the alumina colloidal suspension. Al_2O_3 content in the suspension is 23%.

The main problem encountered with film deposition was the wetting of the substrate by the suspension. For example, it was possible to deposit coatings on the alumina substrates by both dipping and spinning, but only spin coating was successful for coating Si substrates. Poor wetting resulted in the lack of adhesion of the coatings to the substrates which resulted in separation of the coating from the substrate and between the layers, particularly when the coated substrates were heat treated (Fig.2a). The addition of 2-butoxyethanol to the suspension improved the wetting characteristics and made it possible to dip or spin coat all of the substrates without separation from the substrate and cracking between the layers, even after high temperature treatment (Fig.2b). The maximum temperature used in these experiments was 1500°C for the coatings on alumina and platinum substrates, when the coatings contained only α-alumina phase. Oxidation of the silicon limits the maximum temperature to 1000°C for the coatings on silicon substrate.



Fig.2. SEM micrograph of the cross-section of the coatings on alumina substrate.
a) Water colloidal suspension (six depositions, T_a=1000°C);
b) Suspension improved by 2-butoxyethanol (six depositions, T_a=1000°C).

The quality of the coatings was estimated by AFM and optical measurements. In accordance with AFM the coating consisted of connected spherical particles with an average diameter of 50nm and porosity P_s~50%. Optical density of the films was measured by ellipsometer and spectrophotometer (Fig.3.). The value of the refractive index n_{eff}=1.3 which is smaller than that of the dense γ-alumina (n_s=1.7). The Lorentz-Lorenz equation [7,8,9]:

$$(n_{eff}^2-1)/(n_{eff}^2+2)=(1-P_s)(n_s^2-1)/(n_s^2+2) \quad (1)$$

was used to calculate a porosity of 52% from the refractive index measurements, which is in good agreement with the value estimated by AFM. This value of the porosity was used in the theoretical estimation of the shrinkage at the drying process and the efficiency of the planarization.

The efficiency as a planarizing agent can be estimated by assuming that the thickness of liquid precursor which coats the substrate from either spin or dip coating is greater than the amplitude of the surface roughness, d. As a result the liquid precursor overlaps all surface relief. Its surface is flat and remains flat as the solvent evaporates until the precursor will transform in a solid or a very viscous phase (critical concentration) at which time non uniform shrinkage will take place. This shrinkage should be one dimensional in the direction perpendicular to the surface because the coating is still relatively liquid at this stage of the process with the change in the thickness being proportional to the change in the volume of the film, i.e. the concentration of

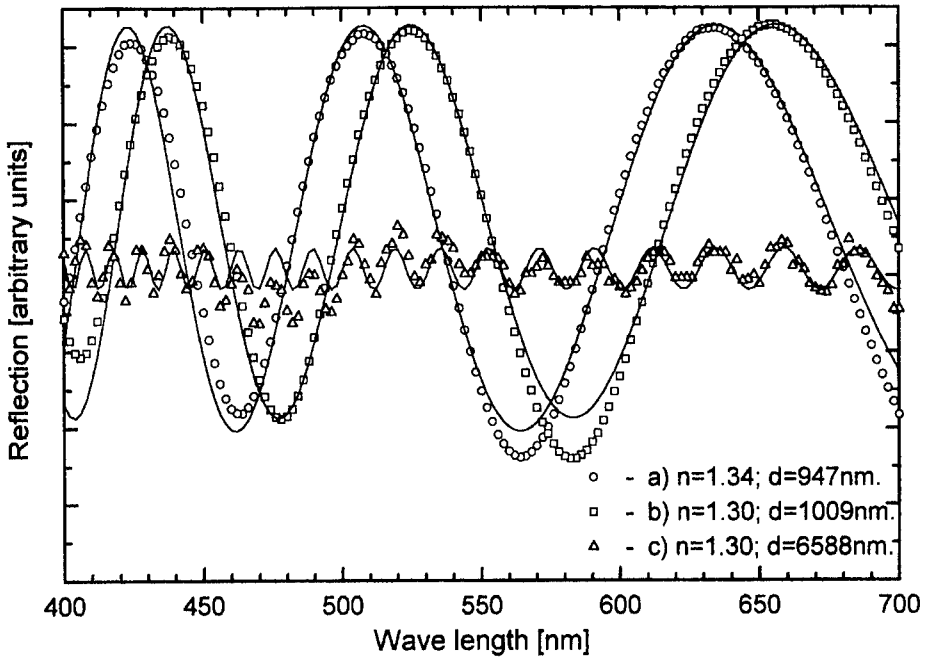


Fig.3. Reflection optical spectra for the alumina films on silicon substrate.
a) One-layer structure, suspension diluted by 2-butoxyethanol (1:1);
b) One-layer structure, suspension diluted by 2-butoxyethanol (2:1);
c) Five-layer structure, suspension diluted by 2-butoxyethanol (1:1);

Al_2O_3 in the suspension. The resulting roughness at the end of the drying process will be defined by the ratio of the precursor volumes after and before drying process and the number of depositions as follows:

$$d_1=d(1-x) \text{ for one coating and } d_n=d(1-x)^n \text{ for multi deposition process} \quad (2)$$

where x is shrinkage of the film from the point with the critical concentration to the final solid phase phase.

It can be seen that the efficiency of the planarization depends upon the number of the deposition and the volume fraction x, but not upon the thickness of the layer. So, in order to optimize planarization it is better to use several coatings with the minimal thickness which overlaps the relief than one thick coating. For this reason five depositions of the precursor were used which gave 1.5μm for each deposition rather than a single coating of 7.5μm.

Fig.4. presents the measurements of the roughness of the initial alumina substrate (Fig.4a) and for two coated samples. Both samples had the same amount of coatings at the same spinner speed and were treated at the same final temperature 1000°C. But the first sample (Fig.4b) was

dried at 150°C after each layer deposition and was treated at 1000°C only after deposition of all the layers. The second sample (Fig.4c) was treated at 1000°C after deposition of each layer. It can be seen that roughness decreases for both samples but in different degrees. This is because of shrinkage with the transition of boehmite to γ-alumina phase at 450°C. The first sample had this transition as one layer and the second as a five-layer structure. This shrinkage should be three dimensional, because it take place in the solid phase and will be proportional to the cube root of the change of the volume at the transition. The estimation of the changes in the volume of the coating by Eq.2 using this assumption gives the result, which is in good agreement with the calculated value for this phase transition.

It is possible to show that the shrinkage is connected with the critical concentration in the suspension by the equation:

$$(1-x) = \frac{1}{(1-P_s)\cdot\left(1+\left(\frac{1}{k}-1\right)\cdot\frac{\rho_{Al2O3}}{\rho_{H2O}}\right)} \qquad (3)$$

where k is the weight fracture of the solid phase at the transition point,
P_s is porosity of the coating,
ρ_{Al2O3} and ρ_{H2O} are the densities of boehmite and water correspondingly.

The value of k calculated from (3) is 51%, which is ten times higher, than the one for sol-gel precursors. That is the reason why colloidal suspension is so effective as a planarizing agent.

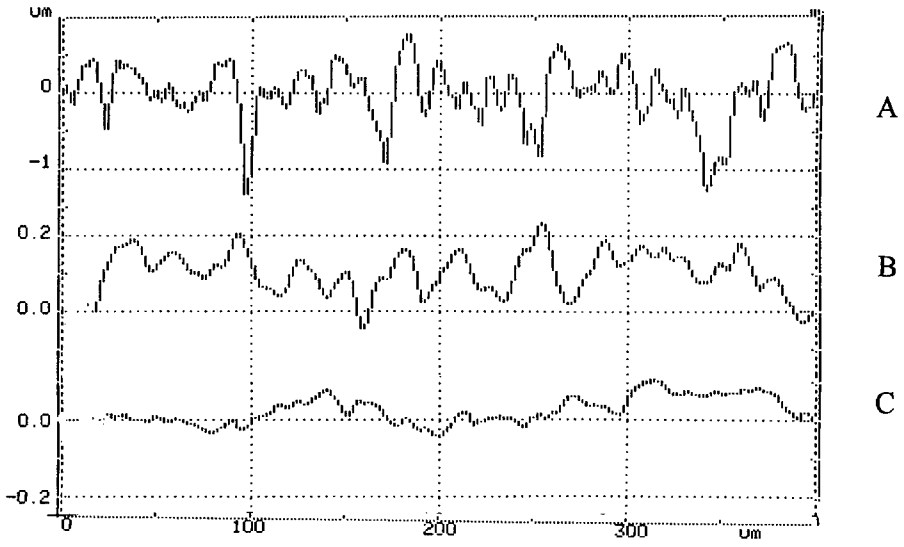


Fig.4. Planarizing properties of the alumina colloidal suspension.
a) Surface profile of the polished substrate;
b) Five layer coating treated at 1000°C after all layers were deposited;
c) Five layer coating treated at 1000°C after each layer deposition.

CONCLUSIONS

- Colloidal water suspensions of nanosize boehmite particles have two advantages in comparison with sol-gel solutions and different modified precursors, based on sol-gel technology: higher content of the solid phase and lower viscosity.

- The addition of the 2-butoxyethanol to the suspension improves wetting of the substrate by the precursor and adhesion of the coating. It is possible to deposit one-layer or multilayer coatings from this precursor on different substrates (Al_2O_3, Pt, Si) without cracking the film or separation from the substrate.

- The mechanical properties, optical transparency and porosity of the coatings from the suspension are analogous to those prepared from sol-gel solution, but the cracking limit is higher (2μm at the quick drying process and 10μm at the slow drying process).

- Colloidal suspensions provide good planarization of the rough surfaces. It is at least 10 times more effective than sol-gel solutions. A substrate with a roughness of 2μm can be planarized up to 50nm by 5 coatings and is limited only by the particle size in the suspension.

REFERENCES

1.B.E.Yoldas, *Am.Ceram.Soc.Bull.*, **54** [3], pp.289-90 (1975).

2. B.E.Yoldas, *J.Amer.Chem.Biotechnol.*, **23** [11], pp.803-9 (1975).

3. Yue-Sheng Lin, and Anthonie J.Burggraaf, *J.Am.Ceram.Soc.*, **74** [1], pp.219-24 (1991).

4. R.J.R.Uhlhorn, M.H.B.J.Huisintvelt, K.Keizer, and A.J.Burggraaf, *J.Mater.Sci*, **27**, pp.527-37 (1992).

5. E.Drabarek, K.S.Finnie, J.R.Bartlett, J.L.Woolfrey, D.Mitchell in *Sol-Gel Processing of Advanced Materials*, edited by Lisa C.Klein, Edward J.A.Pope, Simo Sakka, James L.Woolfrey (Am.Ceram.Soc., **81**, Westerville, Ohio 1998).

6. Leon Shaw, and Reza Abbaschian, *J.Am.Ceram.Soc.*, **78** [12], pp.3376-82 (1995).

7. C.J.Brinker, and G.W.Scherer, *Sol-Gel Science: The Physics and Chemestry of Sol-Gel Processing*, Academic Press, San Diego, CA, 1990.

8. C.J.Brinker, A.J.Hurd, G.C.Frye, K.J.Ward, and C.S.Ashly, *J.Non-Cryst.Solids*, 121, p.294 (1990).

9. K.Vorotilov, V.Petrovsky, and V.Vasiljev, *J. Sol-Gel Sci. & Technol.*, **5**, pp.173-83 (1995).

CHEMICAL REACTIONS ON THE SURFACE OF SnO_2 NANOSIZED POWDERS AT THE ORIGIN OF THE GAS SENSING PROPERTIES: FTIR INVESTIGATION

M.-I. BARATON *, L. MERHARI **
*SPCTS-UMR 6638 CNRS, University of Limoges, F-87060 Limoges (France), baraton@unilim.fr
**CERAMEC, F-87000 Limoges (France), ceramec@wanadoo.fr

ABSTRACT

The surface chemical reactions at the origin of the CO detection by SnO_2-based sensors are investigated by Fourier transform infrared spectrometry for two different SnO_2 particle sizes. Knowing that the variations of the infrared energy transmitted by the sample versus surrounding gases are related to the variations of the electrical conductivity, correlation of surface chemical reactions with the sensor response is established and discussed.

INTRODUCTION

The increasing demand for environment monitoring calls for gas sensors capable of detecting pollutants at sub-ppm levels. Such a high sensitivity can be reached by using nanosized particles in the fabrication of screen-printed chemical gas sensors. The benefit of using nanoparticles is double. Firstly, their high surface-to-bulk ratio leads to a larger area exposed to the gases to be detected. Secondly, the grain size of the nanoparticles becomes comparable to the depth of the depletion layer. It is therefore expected that the sensitivity will be influenced by the particle size.

Besides, it has been proved that nanosized SnO_2-based sensors exhibit a maximum sensitivity toward CO at two different temperatures, one of them being close to room temperature [1]. Although it is known that CO detection is based on redox mechanisms, the oxidation of CO into CO_2 is not expected to take place at room temperature. To clearly understand the CO detection mechanism, the chemical reactions occurring at the surface of SnO_2-based sensors have to be studied in close connection with the electrical conductivity variations. A convenient tool for this dual analysis is Fourier transform infrared (FTIR) spectrometry. Indeed, it allows the *in situ* investigation of the surface chemical species modifications under various environments [2], simultaneously with the measurement of the infrared energy transmitted by the semiconductor sample directly related to the variations of the electrical conductivity. According to the Drude-Zener theory, the infrared energy (E_{IR}) transmitted by the semiconductor sample is related to the concentration of the free carriers, that is the E_{IR} variations are directly related to the variations of the electrical conductivity due to modifications of the gaseous environment of the semiconductor sample, provided that the surface states are not strongly affected [3]. Practically speaking, when a n-type semiconductor is in contact with a reducing gas such as CO, its electrical conductivity increases due to the increase of the free carriers density. This results in a higher absorption of the infrared radiation by the semiconductor sample and, therefore, to a decrease of the infrared energy transmitted by the sample. Conversely, when the n-type semiconductor is subjected to an oxidizing gas such as oxygen, its electrical conductivity decreases and the sample becomes more transparent to the infrared radiation. In summary, when the electrical conductivity decreases, we should observe an increase of the infrared energy transmitted by the sample and *vice versa*. It is therefore easy to realize the unique contribution of FTIR spectrometry in the understanding of the gas detection mechanism. Although our FTIR experiments were performed on pressed nanosized powders, the surface chemical reactions inducing the sensor response have been demonstrated to be identical on the real sensor fabricated from these nanopowders [4].

Mat. Res. Soc. Symp. Proc. Vol. 581 © 2000 Materials Research Society

EXPERIMENTAL

The SnO_2 nanosized powders used in the present experiments were synthesized by evaporation of compressed micron-sized SnO_2 powder with the pulse radiation of a Nd:YAG-laser and subsequent condensation of the vapor in a controlled atmosphere [5]. Two batches corresponding to the average particle diameters of 15 nm (S15) and 8 nm (S8) have been studied. XRD analyses essentially showed the quadratic phase.

The FTIR measurements were performed by using a Perkin-Elmer Spectrum 2000 spectrometer, equipped with a MCT cryodetector. A specially designed vacuum cell allowed the *in situ* analyses at different temperatures (from room temperature up to 500°C) under vacuum or controlled atmospheres [2]. The nanopowders to be analyzed were gently pressed into thin pellets and placed inside the furnace of the vacuum cell. The spectra were recorded from 7800 to 450 cm^{-1} with a 4 cm^{-1} resolution. For the real sensors prepared from 15 and 8 nm SnO_2 particles, it has been determined that two sensitivity maxima for CO detection occurred around 120°C and 350°C [1]. Therefore, our FTIR experiments were performed on the two SnO_2 nanopowders at these two temperatures. To simulate the gas sensors, the experiments were conducted the following way [6]. The pellet of pressed SnO_2 nanopowder was placed inside the furnace of the vacuum cell and evacuated at room temperature (10^{-2} mbar). Fifty mbar of oxygen were then introduced in the cell and the SnO_2 pellet was heated at 400°C for one hour. This heat-treatment under O_2 actually corresponds to the pretreatment undergone by the real sensors before operation. To eliminate all the gaseous impurities which could have possibly desorbed from the SnO_2 sample during the heat-treatment (e.g. humidity and other surface contaminants), the cell was quickly evacuated at 400°C and a new dose (50 mbar) of fresh oxygen was introduced. The sample was cooled at room temperature under O_2 and heated again at the temperature chosen for the gas sensing experiments (120°C or 350°C). At the selected temperature, oxygen was quickly evacuated and replaced with a dose of CO (10 mbar). After a 10-minute contact, CO was evacuated before the addition of a new dose of CO, thus starting a new measurement cycle. These CO doses (10 mbar) can be also added in presence of O_2 (50 mbar) to simulate the working conditions of the real sensors in air. In this latter case, oxygen was introduced for 10 (or 20) minutes followed by the addition of CO for 10 minutes before quick evacuation of the cell. At each step of the experiments, both the infrared spectrum and the infrared energy transmitted by the sample were recorded.

RESULTS AND DISCUSSION

After a heat-treatment under oxygen as described above, the S15 nanopowder was subjected to three subsequent CO doses in absence of O_2, followed by four subsequent doses of CO in presence of O_2 at 120°C and 350°C. The E_{IR} variations versus gas exposures are reported in Figure 1. By analogy with the real sensor, these E_{IR} variations will be referred to as the nanopowder response. It can be easily seen that, whatever the temperature, the addition of the first CO dose causes a strong decrease of E_{IR} transmitted by the sample, thus indicating an increase of the electrical conductivity, which is in agreement with the response of the real sensor. However, the sample does not recover its original transparency after CO evacuation, meaning that the original oxidation state of the SnO_2 particles is not restored. The addition of the second and third CO doses at 350°C, still in absence of O_2, does not lead to further reduction, showing that the SnO_2 particles are already totally reduced by the first CO dose. At 120°C, a very weak decrease of the electrical conductivity can still be noted. The addition of 50 mbar of O_2 for 20 minutes completely restores the SnO_2 oxidation state at 350°C, while it leads to a very limited

oxidation state recovery at 120°C. This can be explained by a higher oxygen diffusion rate at 350°C than at 120°C inside the lattice. When CO is added in presence of O_2, a reproducible response is observed and the oxidation state of SnO_2 is restored after each oxygen addition.

In parallel, the infrared spectra recorded at the different stages of the experiments show strong modifications of their baseline corresponding to variations of the background infrared absorption due to changes in the free carriers density (that is, changes in the electrical conductivity). When these baseline modifications are not too strong, it is possible to perform the difference between two spectra recorded at two different stages of the experiment in order to highlight the surface chemical species which can be perturbed, created or eliminated during the considered experimental step. In the following, we have chosen to present the difference spectra corresponding to the evacuation steps (that is, the spectrum recorded just after evacuation minus the spectrum recorded just before evacuation). Indeed, because the SnO_2 oxidation state is not strongly affected by quick cell evacuation, the modification of the spectrum baseline during the evacuation steps is not as important as it is during the CO-addition steps. These difference spectra actually give information on the species which are eliminated (negative bands), created or restored (positive bands) during evacuation. Apart from the negative bands centered at 2143 cm^{-1} due to the elimination of gaseous CO, the only surface modification which can be observed at 120°C is the perturbation of the OH groups as indicated by the positive bands at 1250 and 965 cm^{-1} (Figure 2a,b). But at 350°C in absence of O_2, a small amount of CO_2 is detected (negative band centered at 2340 cm^{-1}) proving that oxygen species are available at the surface of the SnO_2 particles for the CO oxidation (Figure 3a). When CO is added at 350°C in presence of O_2, CO_2 is instantaneously formed (Figure 3b) in addition with carbonate groups totally reversible by evacuation (negative bands at 1426 and 1372 cm^{-1}). Moreover, the OH groups are perturbed. At 120°C neither CO_2 nor carbonate groups can be identified. However, a weak response of the SnO_2 nanopowder toward CO is noted. This has been confirmed by the electrical measurements performed on the real sensors [1].

The same series of experiments were performed on the S8 nanopowder. The E_{IR} variations are given in Figure 4 at 120°C and 350°C versus gas exposures. Like in the case of the S15 nanopowder and whatever the temperature, the response toward the first CO dose in absence of O_2 is very intense compared to that toward the second and third CO doses. Still in absence of O_2, the perturbation of the OH groups is noted at 120°C (Figure 5a), but it is not observed at 350°C (Figure 6a) whereas, in presence of O_2, it is observed whatever the temperature (Figures 5b and 6b). Unlike the case of the S15 nanopowder, a small amount of CO_2 is formed at 120°C in absence or in presence of O_2 (Figure 5). This means that the oxidation of CO can take place at a lower temperature on the surface of these small particles. Carbonates are formed only at 350°C and in presence of oxygen (Figure 6b). We also note that the recovery of the SnO_2 oxidation state at 120°C is faster on S8 than on S15.

Table I summarizes the surface modifications occurring on the SnO_2 particles under CO versus particle size and experimental conditions. The unexpected oxidation of CO at lower temperature on S8 means that the surface oxygen species are more reactive on S8 than on S15. This is however in agreement with the general observation made on surface reactivity of nanosized powders: the decrease of the particle size usually increases the density of defect sites on the particle surface, thus increasing the surface reactivity. This leads to a higher response of S8 toward CO at 120°C, which is in agreement with the electrical measurements performed on real sensors made of 8-nm and 15-nm SnO_2 nanopowders. In addition, the faster recovery of the S8 oxidation state at 120°C is obviously due to the smaller particle size allowing a deeper oxygen diffusion in the core of the particle even at this low temperature. The perturbation of the surface

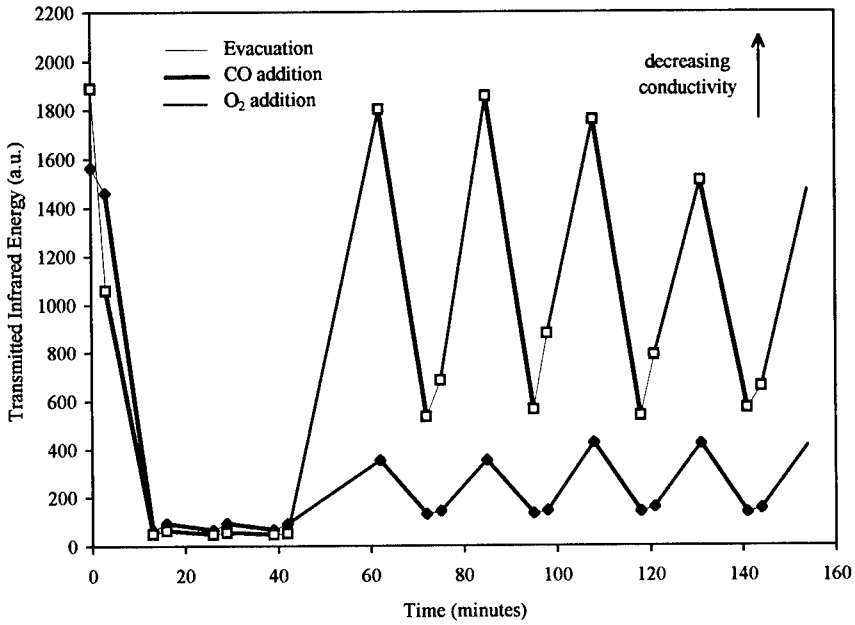


Figure 1: Variations of the infrared energy transmitted by the S15 nanopowder versus gas exposures: a) ◆ at 120°C; b) □ at 350°C.

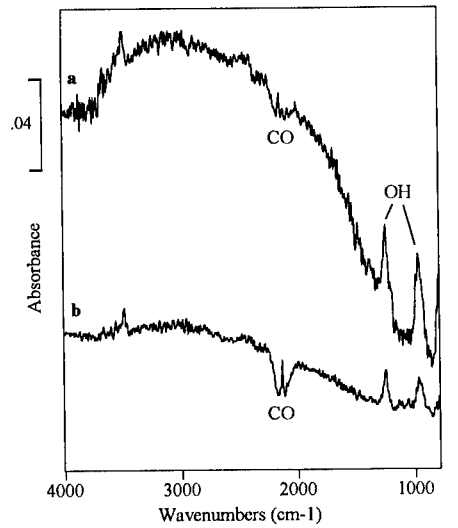


Figure 2: Difference IR spectra of the S15 powder corresponding to the evacuation step at 120°C: a) in absence of O_2; b) in presence of O_2.

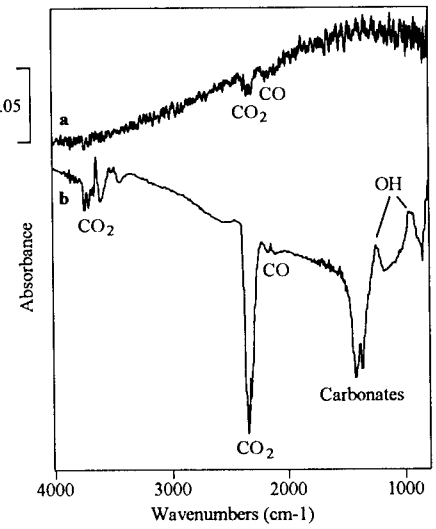


Figure 3: Difference IR spectra of the S15 powder corresponding to the evacuation step at 350°C: a) in absence of O_2; b) in presence of O_2.

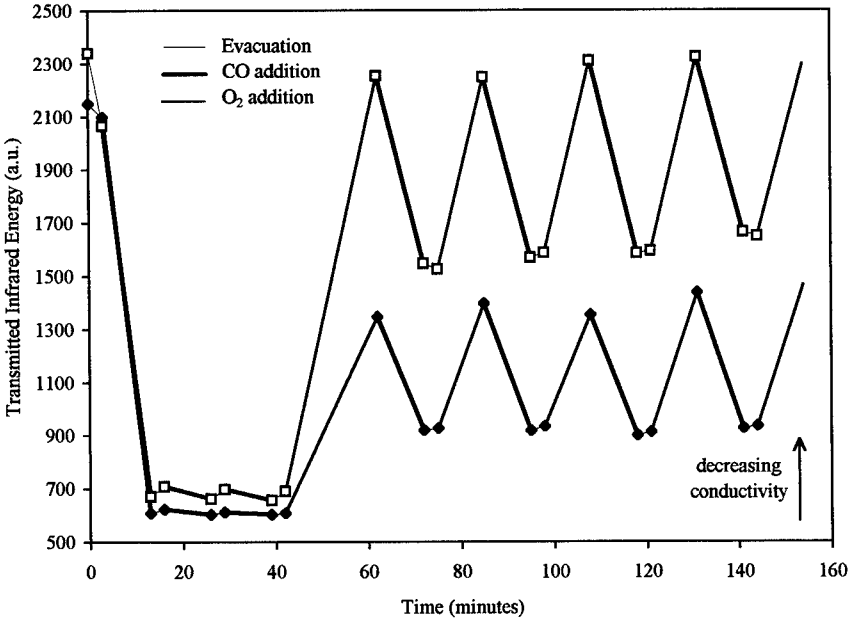


Figure 4: Variations of the infrared energy transmitted by the S8 nanopowder versus gas exposures: a) ◆ at 120°C; b) □ at 350°C.

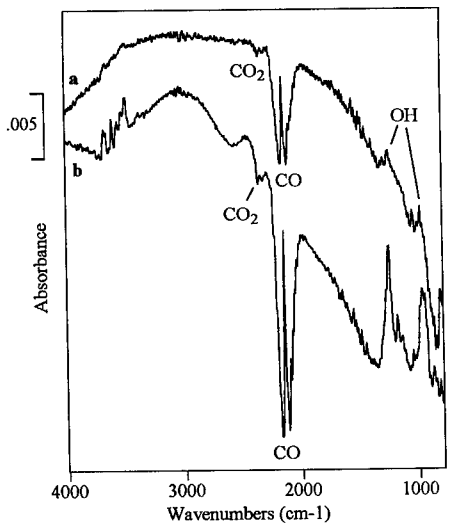


Figure 5: Difference IR spectra of the S8 powder corresponding to the evacuation step at 120°C: a) in absence of O_2;
b) in presence of O_2.

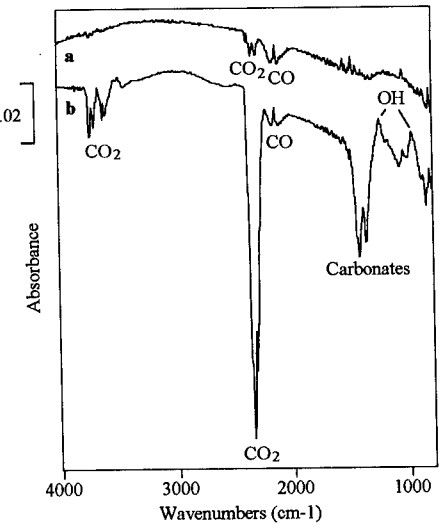


Figure 6: Difference IR spectra of the S8 powder corresponding to the evacuation step at 350°C: a) in absence of O_2;
b) in presence of O_2.

OH groups may play a role in the sensor response since it is the only effect observed on the S15 at 120°C. Obviously, the perturbation of the OH vibrational frequencies translates into a perturbation of the electronic distribution in the surface OH bonds, which may have consequences on the free carrier density at the surface and, thus, on the thickness of the depletion layer. We have mentioned that, whatever the powder size, the OH groups are not perturbed at 350°C in absence of O_2. However, it must be reminded that under these conditions, the addition of CO leads to a very strong increase of the electrical conductivity corresponding to a very strong modification of the spectra baseline. Moreover, after this first CO addition, the samples become almost opaque to the IR radiation. As a result, changes in the OH absorption bands may be masked.

Table I: Comparison of the surface species formed on the two SnO_2 nanopowders under CO.

	In Absence of Oxygen		In Presence of Oxygen	
Temperature	15-nm diameter (S15)	8-nm diameter (S8)	15-nm diameter (S15)	8-nm diameter (S8)
120°C	No CO_2 No Carbonates OH perturbed	CO_2 No Carbonates OH perturbed	No CO_2 No Carbonates OH perturbed	CO_2 No Carbonates OH perturbed
350°C	CO_2 No Carbonates OH not perturbed	CO_2 No Carbonates OH not perturbed	CO_2 Carbonates OH perturbed	CO_2 Carbonates OH perturbed

CONCLUSION

FTIR spectrometry is proved to be an extremely valuable tool to investigate the sensing properties of nanosized powders and to correlate the gas detection mechanism to the chemical reactions occurring on the very surface of the semiconductor particles. In agreement with the electrical measurements performed on the real sensors, the 8-nm diameter SnO_2 powder appears to be the most sensitive material at low temperature. It has thus been demonstrated that the decrease of the particle size leading to a higher surface reactivity is fundamentally beneficial to the sensitivity of gas sensors.

ACKNOWLEDGMENTS

This work has been performed under a BRITE-EURAM III project (contract number BRPR-CT95-0002) funded by the European Commission.

REFERENCES

1. G. Williams & G.S.V. Coles, MRS Bull. **24**, p. 25 (1999); J. Mater. Chem. **8**, p. 1657 (1998).
2. M.-I. Baraton in *Handbook of Nanostructured Materials and Nanotechnology*, edited by H.S. Nalwa, Academic Press, San Diego, 1999, pp. 89-153.
3. N.J. Harrick, *Internal Reflection Spectroscopy*, 2nd ed. (Harrick Scientific Corporation, Ossining N.Y., 1979).
4. M.-I. Baraton in *Nanostructured Films and Coatings*, edited by G.M. Chow *et al.*, Kluwer Academic Publishers, Dordrecht, 2000, in press.
5. W. Riehemann in *Surface-Controlled Nanoscale Materials for High-Added-Value Applications*, edited by K.E. Gonsalves, M.-I. Baraton *et al.* (Mater. Res. Soc. Proc. **501**, Warrendale, PA, 1998), pp. 3-14.
6. M.-I. Baraton & L. Merhari, Nanostruct. Mater. **10**, p. 699 (1998).

OPTICAL PROPERTIES OF NANOCRYSTALLINE SILICON FILMS WITH DIFFERENT DEPOSITION TEMPERATURES

A. M. Ali, T. Inokuma, Y. Kurata and S. Hasegawa
Department of Electronics, Faculty of Technology, Kanazawa University,
Kanazawa 920-8667, Japan

ABSTACT

Nanocrystalline silicon (nc-Si) films were deposited on fused quartz and single (100) crystal Si substrates by plasma-enhanced chemical vapor deposition from a SiH_4-H_2 mixture at various deposition temperatures, T_d. The effects of plasma-assisted hydrogenation at 300 °C on the optical and structural properties were examined for the nc-Si films. The film deposited at T_d = 730 °C exhibits photoluminescence (PL) in its as-deposited state, but the intensity of PL decreases after hydrogenation. We find that a correlation between the PL intensity and infrared absorption bands at around 850 and 1000 cm^{-1}.

INTRODUCTION

Nanocrystalline silicon (nc-Si) and polycrysilline silicon (poly-Si) are expected to be applied to optoelectronic devices, optical interconnections, electroluminescence devices, and thin film transistors (TFTs). Because such materials would be suitable with the existing industrial infrastructure for ultra-large scale integrated circuits, and its higher mobility than that of amorphous Si (a-Si). In addition, the intensive photoluminescence (PL) at room temperature has attracted much attention for nc-Si films. However, the mechanism of the observed visible PL is still unclear; Some researchers attribute the PL to quantum size effects in the Si nanostructures [1-4] while others attribute it to a-Si [5,6], siloxene [7,8], hydrides/polysilanes [9,10] and oxygen-related defect centers [11-13]. Plasma-enhanced chemical vapor deposition (PECVD) is one of methods to grow nc-Si and poly-Si films having some advantages such as low deposition temperature and large-area deposition. The PECVD nc-Si thin films usually contain randomly orientated nanocrystals (5-50 nm) embedded in a hydrogenated amorphous tissue (SiH_x), with a variable volume fraction of nanocrystals dependent on the growth conditions [14,15]. In our previous papers [16,17], we reported the properties of PECVD poly-Si films deposited by changing the deposition temperature (T_d) and film thickness. It was shown that the <110> preferential orientation occurred in the range of T_d higher than 500 °C, while the <111> preferential orientation occurred at T_d lower than 500 °C. In addition, we found no crystallization of the films at T_d around both 150 and 650 °C.

In this article, 0.2-μm-thick nc-Si films were deposited using SiH_4-H_2 mixtures by changing T_d. The effects of plasma-assisted hydrogenation at 300 °C on the optical and the structural properties were investigated for the nc-Si films.

EXPERIMENTAL

The samples were deposited by rf glow-discharge decomposition of SiH_4-H_2 mixtures in a hot-wall type fused quartz reactor, employing inductive coupling of rf power. The SiH_4 and H_2 flow rates were 1.0 and 3.0 sccm, respectively. The rf power (13.56 MHz) and gas pressure were

Mat. Res. Soc. Symp. Proc. Vol. 581 © 2000 Materials Research Society

maintained at 20 W and 0.15 Torr, respectively, and 0.2-μm-thick films were deposited. T_d was varied from 500 to 730 °C. For the plasma-assisted hydrogenation, the flow rate of H_2, gas pressure, rf power, the temperature, and duration were 3.0 sccm, 0.3 Torr, 5 W and 300 °C and 30 min, respectively. Fused quartz substrates were used for measurements of Raman scattering, x-ray diffraction (XRD) and stress measurements, and (100) Si substrates for measurement of Fourier transform infrared (FT-IR) spectroscopy. The crystal structure was investigated by XRD (SHIMADZU XD-D1). The average grain size, <δ>, in the depth direction of the film was estimated from the half-value width of the XRD spectrum using Scherrer's formula [18]. The Raman spectra are composed of signals from a crystalline phase at around 520 cm^{-1} and an amorphous phase at around 480 cm^{-1}. The crystalline volume fraction, ρ, was estimated from the Raman spectra using the procedure proposed by Tsu *et al.* [19]. The structural properties were also examined by vibrational absorption measurements using IR spectrometer (JASCO, FT/IR-610) at a normal light incident and under vacuum conditions, using a bare silicon wafer similar to the substrates used for the samples, as a reference in the range of 400-4000 cm^{-1}. PL spectra were measured using a Jobin Yvon RAMANOR HG 2S spectrometer coupled with a cold photo-multiplier tube (Hamamatsu R649S). The 488-nm Ar-ion laser with power ranging from 100 to 150 mW was used as a PL exitation source. The stress in the films was evaluated from the curvature of the film/substrate system, using Stoney's formula [20].

RESULTS AND DISCUSSION

Figure 1 shows the Raman spectra as deposited films with T_d = 500, 600, 640 and 730 °C. The peaks at ~520 cm^{-1} and ~480 cm^{-1} are due to the transverse optic (TO) mode of the crystalline phase and TO-like modes in an amorphous phase, respectively. In the films deposited at 500 °C and 730 °C, the signal from crystalline phase was clearly observed.

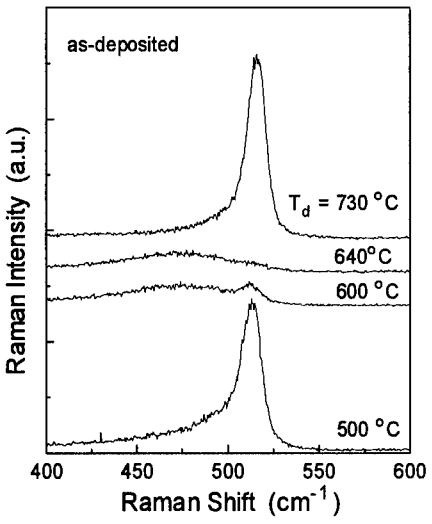


Fig. 1. Raman spectra for nc-Si films deposited at different temperatures.

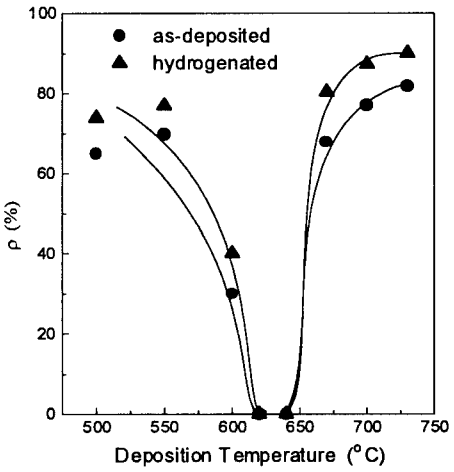


Fig. 2. The crystalline volume fraction, ρ, as a function of deposition temperature, T_d, for nc-Si films as-deposited (closed circles) and annealed in a hydrogen-plasma at 300 °C for 30 min (closed triangles).

Figure 2 shows the dependence of ρ in the as-deposited and hydrogenated films on T_d. As shown in this figure the values of ρ decrease up to T_d = 600 °C, and when T_d is over 650 °C, ρ increase with increasing T_d. No crystalline phase was found for the films deposited at T_d = 620 and 640 °C. In a previous paper [16], it is suggested that no crystallization at T_d = 620 and 640 °C may be interpreted as a result of competition among growth of crystal grains with different textures. The increase in ρ after hydrogenation may be caused by an etching effects due to hydrogen radicals, which while predominantly act to locations of amorphous phase.

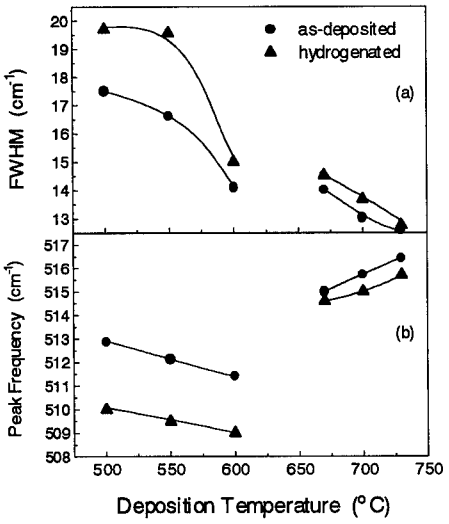


Fig. 3. (a) Full-width at half maximum (FWHM) and (b) peak frequency of the crystalline-phase regions for nc-Si films, as a function of deposition temperature, T_d. As-deposited (closed circles) and annealed in a hydrogen-plasma at 300 °C for 30 min (closed triangles).

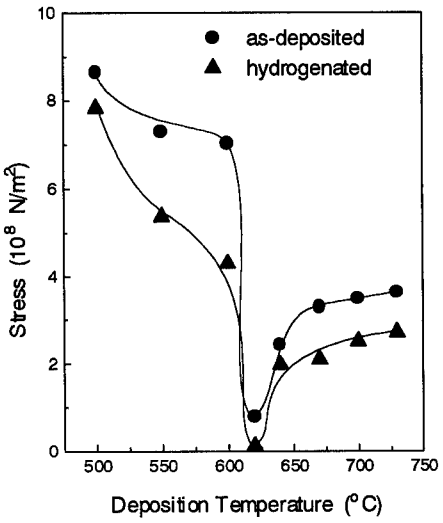


Fig. 4. Stress measured for nc-Si films as a function of deposition temperature, T_d. As-deposited (closed circles) and annealed in a hydrogen-plasma at 300 °C for 30 min (closed triangles).

Figure 3 shows the full width at half maximum (FWHM) and the peak frequency estimated for the crystalline components in Raman signals of the as-deposited and hydrogenated films, as a function of T_d. As shown in Fig. 3(a), the FWHM value decreases with increasing T_d, while it increases after hydrogenation. As shown in Fig. 3(b), the peak frequency decreases with an increase in T_d up to T_d = 600 °C but then increases for T_d > 670 °C. The peak shift toward lower frequency with increasing T_d up to 600 °C is considered to be caused by a deterioration in the crystallinity, as seen in Figs. 1 and 2. Such a deterioration in the crystallinity may be related to a change in the robustness in the Si network [21]. On the other hand, the peak shift toward higher frequency for T_d > 670 °C was found to correspond to a decrease in the tensile stress of the films, as seen in Fig. 4.

The dependence of stress in the film on T_d is shown in Fig. 4. The measured stress, σ, is composed of two different type of stress: One is the intrinsic stress, σ_i, depending on the growth

process of the film, and another stress, σ_t, due to the thermal expansion mismatch between the film and the substrate. The films used in the stress measurements were deposited on fused quartz substrates which has a small thermal expansion coefficient compared with the Si films. Therefore, the tensile stress observed for films with high T_d may be due to the thermal expansion mismatch.

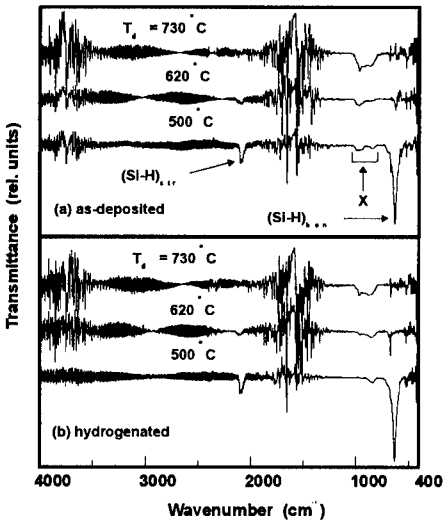


Fig. 5. IR transmittance spectra for Si films with different deposition temperature, T_d, values (a) as-deposited and (b) annealed in a hydrogen-plasma at 300 °C for 30 min.

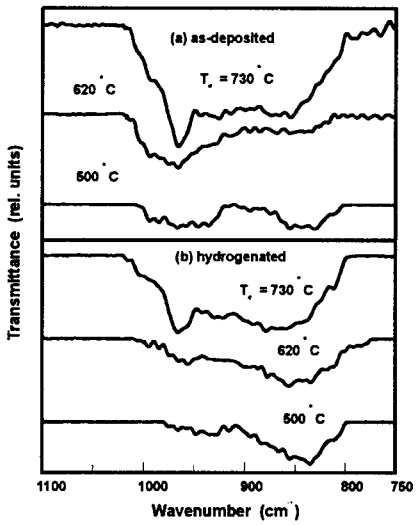


Fig. 6. Magnified transmittance spectra over the range 750-1100 cm^{-1} for the films shown in Fig. 5.

Figure 5 shows the IR transmission spectra over the wavenumber range, 400-4000 cm^{-1}, for (a) the as-deposited and (b) the hydrogenated films deposited at different T_d. As shown in Fig. 5, the absorption bands observed at around 650 $cm^{-1}$and 2100 cm^{-1} are assigned to the Si-H bending and stretching absorption, respectively. The intensities of both the bands decrease with increasing T_d and disappeared for T_d > 620 °C. After hydrogenation, the intensities of 650 cm^{-1} and 2100 cm^{-1} bands were almost same as as-deposited ones. On the other hand, there are two broad absorption bands around 850 and 1000 cm^{-1}. Figure 6 shows the magnified absorption spectra for these bands. As seen in Fig. 6, both the 850 and 1000 cm^{-1} bands are found to increase with increasing T_d and decrease after hydrogenation. We can not assign these bands at present but will discuss it in connection with the result of the PL spectra at the following stage.

The PL spectra for the (a) as-deposited and (b) hydrogenated films are shown in Fig. 7. Some of them exhibit two peaks at ~1.9 eV and ~2.2 eV. As seen in Figs. 6(a) and 7(a), the increase in PL intensity and peak energy for the films as deposited at 500 °C and 730 °C is found to correspond well with an increase in the intensities of the 850- and 1000-cm^{-1}-IR-absorption bands. In addition, no PL is observed for the film as-deposited at 620 °C, which was amorphous as seen in Fig. 2. Therefore, it is considered that an amorphous Si phase is not responsible for the

observed luminescence in the present case. In Fig. 7(b) we can also see a strong reduction of PL intensity as an effect of plasma-assisted hydrogenation. The reduction of PL after hydrogenation is consistent with the decrease in the intensity of 850- and 1000-cm^{-1} IR bands as shown in Fig. 6(b). From XRD measurements, we obtained values of $<\delta>$ = 20-50 nm. From this result along with those in Figs. 5 and 7, it is suggested that the PL does not correlate with the particle size (quantum size effects) and also hydrides/polysilanes because the SiH absorption around 2100 and 650 cm^{-1} is not observed for films with T_d > 620 °C. Thus, the PL is considered to be connected with the structures related to the unknown IR absorption bands around 850 cm^{-1} and 1000 cm^{-1}.

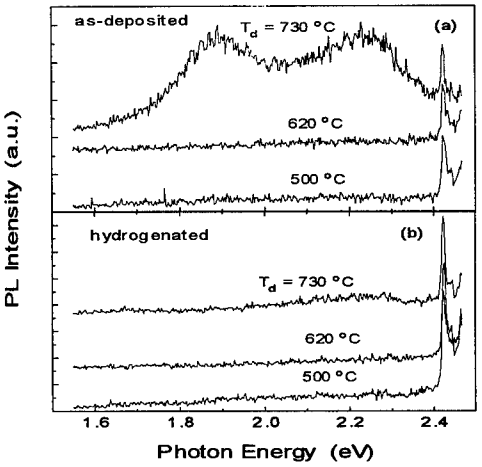


Fig. 7. Photoluminescence (PL) spectra for nc-Si films, (a) as-deposited and (b) annealed in a hydrogen-plasma at 300 °C for 30 min.

CONCLUSIONS

0.2-μm-thick nanocrystalline silicon (nc-Si) films were deposited using SiH_4-H_2 mixtures by changing deposition temperature, T_d. The effects of plasma-assisted hydrogenation on crystallinity and optical properties were examined. When T_d increases the crystalline volume fraction, ρ, decreased with T_d up to T_d = 600 °C and then increased. No crystalline phase was found at T_d = 620 and 640 °C. The peak frequency of Raman spectra decreased with increasing T_d up to T_d = 600 °C but then increased for T_d > 670 °C. Such Raman shifts corresponded well with a decrease and increase in the tensile stress of the films. The intensities of Si-H bending and stretching absorption at around 650 cm^{-1} and 2100 cm^{-1}, respectively, decrease with increasing T_d and disappeared for T_d > 620 °C. In addition, there were two broad absorption bands around 850 and 1000 cm^{-1}, and which increased with increasing T_d and decreased after hydrogenation. The photoluminescence spectra were also found to exhibit the highest intensity at T_d = 730 °C but it showed a strong reduction after hydrogenation. Our results supported the hypotheses that the luminescence is unlikely to originate from quantum size effects, amorphous Si and silicon hydrides but may be connected with the structures related to unknown absorption band around 850 and 1000 cm^{-1}.

ACKNOWLEDGMENTS

The authors wish to thank Professor T. Shimizu for the use of the Raman spectrometer.

REFERENCES

1. L. T. Canham, Appl. Phys. Lett. **57**, 1046 (1990).

2. S. Schuppler, S. L. Friedman, M. A. Marcus, D. L. Adler, Y. H. Xie, F. M. Ross, Y. J. Chabal, T. D. Harris, L. E. Brus, W. L. Brown, E. E. Chaban, P. F. Szajowski, S. B. Christman and P. H. Citrin, Phys. Rev. B **52**, 4910 (1995).
3. W. L. Wilson, P. F. Szajowski and L. E. Brus, Science **262**, 1242 (1993).
4. L. N. Dinh, L. L. Chase, M. Balooch, W. J. Siekhaus, and F. Wooten, Phys. Rev. B. **54**, 5029 (1996).
5. R. P. Vasquez, R. W. Fathauer, T. George, A. Ksendzow and T. L. Lin, Appl. Phys. Lett. **60**, 1004 (1992).
6. T. George, M.S. Anderson, W. T. Pike, T. L. Lin, R. W. Fathauer, K. H. Jung and D. L. Wong, Appl. Phys. Lett. **60**, 2359 (1992).
7. J. S. Tse, J. R. Dahn and F. Buda, J. Phys. Chem. **99**, 1896 (1995).
8. M. S. Brandt, H. D. Fuchs, M. Stuzmann, J. Weber and M. Cardona, Solid State Commun. **81**, 302 (1992).
9. S. M. Prokes, O. J. Glembocki, V. M. Bermudez, R. Kaplan, L. E. Friedersdorf and P. C. Searson, Phys. Rev. B **45**, 13788 (1992).
10. K. H. Li, C. Tsai, J. Sarathy and J. C. Campbell, Appl. Phys. Lett. **62**, 3192 (1993).
11. H. Morisaki, H. Hashimoto, F. W. Ping, H. Nozawa and H. Ono, Appl. Phys. Lett. **27**, 2977 (1933).
12. S. M. Prokes and W. E. Carlos, J. Appl. Phys. **78**, 2671 (1995).
13. S. M. Prokes and O. J. Glemocki, Phys. Rev. B **49**, 2238 (1994).
14. C. Godet, N. Layadi and P. Roca i Cabarrocas, Appl. Phys. Lett. **66**, 3146 (1995).
15. C. Goda, B. Marchon and M. Schhimdt, Thin Solid Films **155**, 227 (1987).
16. S. Hasegawa, M. Sakata, T. Inokuma and Y. Kurata, J. Appl. Phys. **84**, 584 (1998).
17. S. Hasegawa, M. Sakata, T. Inokuma and Y. Kurata, J. Appl. Phys. **85**, 3844 (1999).
18. B. D. Cullity: *Element of X-ray Diffraction* (Addison-Wesley, Reading, 1978) 2nd ed., p. 102.
19. R. Tsu, G. Gonzales-Hernandez, S. S. Chao, S. C. Lee and K. Tanaka, Appl. Phys. Lett. **40**, 534 (1982).
20. G. G. Stoney, Proc. R. Soc. London Ser. A **82**, 172 (1909).
21. M. Syed, T. Inokuma, Y. Kurata and S. Hasegawa, Jpn. J. Appl. Phys. **36**, 6625 (1997).

INSULATOR-METAL TRANSITION IN NANOSTRUCTURED Ni-Al THIN FILMS

H.P. NG, A.H.W. NGAN
Department of Mechanical Engineering, The University of Hong Kong, Pokfulam Road, Hong Kong, PR China.

ABSTRACT

The electrical resistance of Ni-Al alloy thin films prepared by dc magnetron sputtering process was found to be abnormally high at room temperature. However, when heated at elevated temperatures, the resistance dropped significantly, exhibiting a remarkable negative temperature coefficient of resistance (TCR). The phenomenon was found to be substrate-independent. Cross-sectional transmission electron microscopy revealed that the films were essentially nanocrystalline and porous in nature. Analysis of the current density-electric field characteristics yielded a satisfactory agreement with either the space charge limited or the Poole-Frenkel models for electrical conduction. The negative TCR effect diminishes and the usual metallic resistance is restored in thicker films, probably due to reduction in particle separation and further coalescence of neighbouring crystallites.

INTRODUCTION

Materials exhibiting insulator-conductor transition have been extensively investigated in the last few decades because of their scientific interest and potential engineering applications. Electrical resistivity of this range of materials will undergo drastic changes under the influence of stress or thermal agitation. It is, for instance, reviewed by Mott that certain metals such as barium undergo band-crossing transition and become insulators under sufficient compression [1]. Some ceramics and transitional metal oxide materials, on the other hand, have conduction mechanisms being sensitive to temperature changes with either positive or negative temperature coefficients of resistance (TCR). Apart from the intrinsic material properties, which give rise to the above striking conductivity transitions, the nano-sized crystalline structure has also been found to have substantial influence on the electrical properties of the materials [2]. Thin films have therefore received much for the effects of their miniaturised crystal size and the correlated short-range ordered (SRO) structure on the behaviour of electrical conduction. In this paper, we report an electrical anomaly observed on our Ni-Al binary alloy thin films. Ni-Al coatings with a 3:1 stoichiometry have been investigated in our previous work with respect to its mechanical strengthening and oxidation protection effects on Ni substrates [3]. Although the Ni-Al alloy films conform to a normal metallic conductivity when the thickness is well above 1 micron, an abnormally high electrical resistance is exhibited at room temperature when the film is thinner than a few hundred nanometers. The electrical resistance ramps down drastically, however, when the film is heated up to a moderate temperature. The aim of the present work is to characterise the negative temperature coefficient of resistance (T.C.R.) observed in the Ni-Al alloy films and to attempt to explain such a behaviour.

Mat. Res. Soc. Symp. Proc. Vol. 581 © 2000 Materials Research Society

EXPERIMENTAL PROCEDURE

Thin Film Preparation

The Ni-Al thin films were deposited by a water-cooled DC magnetron-sputtering device (Bal-Tec MED020) using a nickel-aluminide alloy target with the 3Ni:1Al stoichiometry. The sputtering vacuum chamber was evacuated to a base pressure of below 1×10^{-5} mbar and a continuous flux of ultra high purity Ar was introduced at a pressure of 2×10^{-2} mbar afterwards. In order to ensure a clean deposit, pre-sputtering of the target was performed for an adequate time period. Pure nickel approximately 15mm×20mm×1mm in size was used as substrates. Prior to depositions, the substrates were mechanically polished and then treated with acetone and methyl alcohol to remove any organic contamination. The Ni-Al films were deposited at a sputtering power of 70W. Although there was no additional thermal source applied to the nickel substrate during the deposition process, the substrates became warmed up to approximately 80°C by the plasma-discharge heating. The thickness of the Ni-Al films was limited to 200nm by means of sputtering time control.

Characterisation of Film Microstructure

Cross-sectional transmission electron microscope (XTEM) specimens were prepared by slicing a cylindrical assembly consisting of two deposited substrates glued together with their films facing against each other. The slices were mechanically polished to a thickness less than 80 microns, followed by twin-jet electropolishing with 90% methanol + 10% perchloric acid at 5V and -50°C. All the XTEM specimens were examined using a JOEL 2000FX TEM operating at 200kV.

Electrical Properties Measurement

The variation of electrical resistance with respect to temperature was measured for the Ni-Al thin films. The deposited specimens were rested, with the films facing downward, on two thin copper electrodes connected to a high accuracy digital ohmmeter (Tektronix DM257). A piece of ceramic block was inserted between the electrodes and the heater surface to facilitate electrical insulation. The temperature of the films was monitored by a surface contact type thermocouple mounted on the top of the specimens. The power of the heater was gradually controlled such that the samples were heated up at a sufficiently low speed to ensure a quasi-steady state.

The J-E characteristics were also measured for the thin films. The deposited specimen was placed in between two copper electrodes, each with an area of $0.78cm^2$, under a constant contact pressure of approximately 5×10^3 Pa. The potential difference across the film specimen was monitored by a voltmeter connected in parallel across both the specimen and a high accuracy ammeter.

RESULTS AND DISCUSSIONS

As revealed by the XTEM micrographs shown in Fig.1, the Ni-Al thin film exhibits a pronounced columnar structure, which is a common structure observed in thin films under low

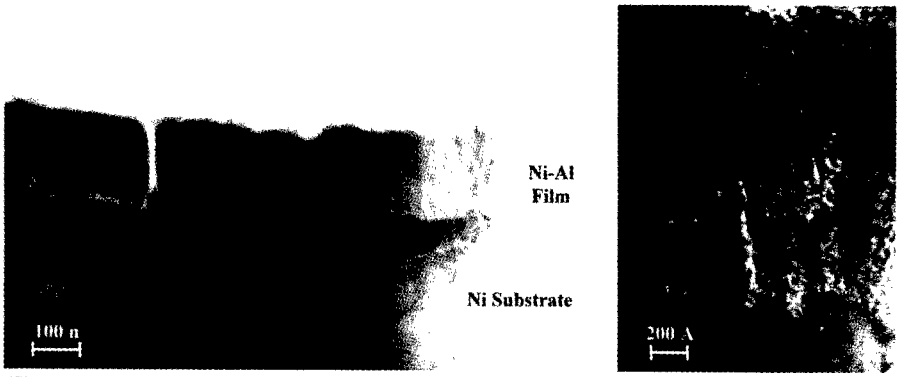


Fig.1 XTEM micrographs showing (a) the columnar structure associated with a Ni-Al thin film sputter-deposited on a Ni substrate at 80°C; (b) the constituent nano-crystals of about 50Å in size.

temperatures. However, the columns are found to consist of aggregation of nano-crystals with size around 50Å. Such a fine crystallite structure is accompanied by an exceptionally high density of inter-granular boundaries, which makes the film porous in nature.

Fig.2a shows the variation of the electrical resistance of the Ni-Al thin film grown on a nickel substrate during a number of sequential heating and cooling processes. It can be seen that the resistance of the film drops from an unmeasurable high level (over 20 MΩ) down to the kilo-ohm range at a decaying speed as the temperature rises to above 200°C. This clearly demonstrates that the conduction in the thin film is associated with a negative temperature coefficient of resistance (TCR), the magnitude of which is describable as an insulator-to-metal transition. Between every heating and cooling curve, a resistance gap is present, and this declines upon cyclic repetitions of heating and cooling until the two curves coincide with one another. This can be interpreted as a consequence of crystallinity enhancement of the amorphous-like structure in the film by thermal agitation, or equally likely, a progressive release of charge carries, which are originally confined to traps, to promote the conductivity. Similar Ni-Al films, which were deposited on silicate glass substrates, have been found to follow a similar electrical behaviour, suggesting that the negative TCR phenomenon of the Ni-Al films is substrate-independent. A supplementary resistance measurement has also been made on a pure nickel thin film prepared under similar experimental conditions. The result shows that the negative TCR effect is, however, negligible in the pure Ni film when compared with the Ni-Al counterpart (Fig.2a).

The extremely low conductivity of the Ni-Al thin film is once anticipated to be due to the formation oxides materials like NiO and Al_2O_3, both of which are essentially insulators at room temperature. Yet it has been well reported that NiO showed hardly any increase in conductivity even well above its Néel temperature (523K) [4]. On the other hand, it would be difficult to imagine that alumina would participate in conduction at elevated temperatures. So it is evident that such an electrical anomaly is largely attributed to the Ni-Al binary system itself. It is also found that the negative TCR effect of the Ni-Al thin films gradually diminishes as the thickness increases. This is anticipated to be a consequence of further crystallite coalescence and the associated reduction in the defect concentration and inter-particulate separations.

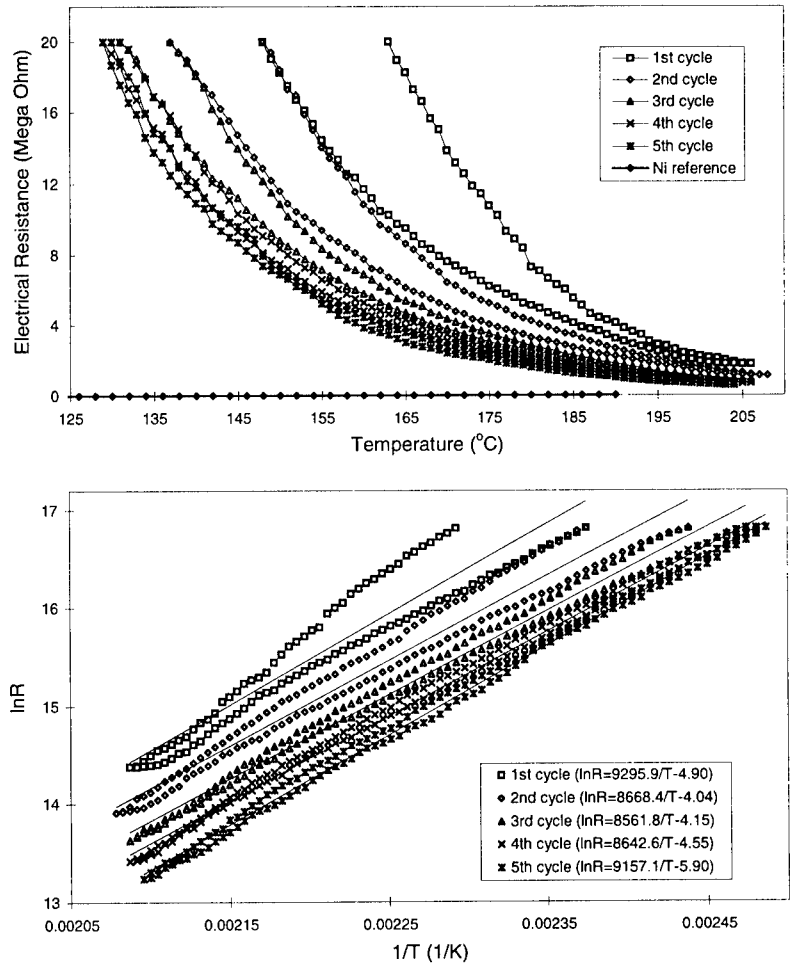


Fig.2 Temperature dependence of electrical resistance of nanostructured Ni-Al thin films: (a) resistance as a function of temperature; (b) lnR-1/T relationship.

The electron transport behaviour has long been investigated by different workers for thin metal films of structures ranged from being discontinuous to continuous [5]. Porous films, being the intermediate type, are believed to possess a complicated conduction mechanism influenced by a number of additional factors, such as intergranular boundary and diffuse scatterings [6]. There has been a tendency to explain the transport in porous film in terms of tunnelling for its lower activation energy involved when compared with thermionic emissions, especially when the porosity is high. It is therefore of interest to know more about the effective conduction mechanisms in our nanostructured Ni-Al films, which show an intrinsic porous nature.

The plot of the logarithm of electrical resistance against the reciprocal of temperature is shown in Fig.2b. The data are well described by linear relationships, especially when the negative TCR behaviour becomes stabilised. It can be noted that, for each of the heating-cooling cycles, the resistance change exhibits similar activation energies of 0.7-0.8eV. This rate-controlling phenomenon makes satisfactory agreement with a simplified thermionic emission model, which is described by:

$$R = C\frac{k}{eT}\exp(\frac{E}{kT}) \qquad (1)$$

where C is a film-dependent constant, k the Boltzmann constant and E the activation energy. Mechanical quantum tunnelling is a process known to be independent of temperature, unless it is otherwise thermally activated [6]. Fig.3 shows the current density (J)-electric field (E) characteristics of the Ni-Al thin films under room conditions, which resembles that of an ordinary semiconductor diode but with a much higher current density level. The J vs E curve can be represented by a polynomial of the forth order, which indicates that a space-charge-limited (SCL) emission mechanism actually takes effect in the electrical conduction. A fairly linear relationship obtained in the log J vs $E^{1/2}$ plot in Fig.4, on the other hand, suggests that the Poole-Frenkel (P-F) themionic emission can also be another effective transport mechanism in the thin films [6]. Summing up the above, it is apparent that the conduction in our Ni-Al thin films is largely facilitated by emission mechanisms, which are successively enhanced at elevated temperatures to facilitate the insulator-conductor transitions. Although adequate evidence to rule out tunnelling conduction is yet to be found, it is believed that, for the Ni-Al films, tunnelling should not be the predominating mechanism as expected in other porous thin film systems.

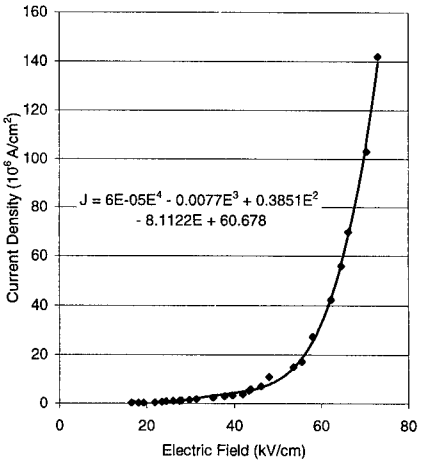


Fig.3. J–E characteristics of a Ni-Al thin film with a negative TCR.

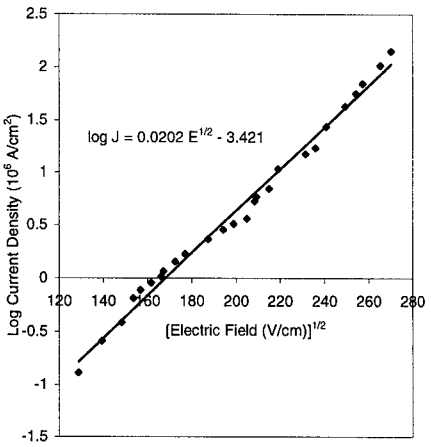


Fig.4. log J vs $E^{1/2}$ plot showing a good agreement with the P-F emission conduction model.

CONCLUSION

In the present study, a striking electrical conduction phenomenon has been detected in sputter-deposited Ni-Al thin films. The alloy Ni-Al films, which are essentially metallic-based, exhibit an inherent insulating property. A large negative TCR was recorded under moderate heating, after which the conductivity approaches metallic behaviour. The insulator-conductor transition is noted to be rate-controlling with an activation energy of 0.7-0.8eV. J-E characteristics of the film shows that conduction models including space–charge-limited (SCL) and Poole-Frenkel (P-F) emissions may be dominating in our thin film systems.

ACKNOWLEDGEMENT

The present work was supported by a CRGC grant from HKU (project no. 10202005/16180/14500/301/01).

REFERENCES

1. N. F. Mott, *Metal-Insulator Transitions*, Taylor & Francis, 1990.

2. U. Banin, C. J. Lee, A. A. Guzelian, A. V. Kadavanich, A. P. Alivisatos, W. Jaskolski, G. W. Bryant, A. L. Efros, and M. Rosen, J. Chem. Phys., Vol 109, **6**, (1998), 2306-2309.

3. H. P. Ng, X. K. Meng and A. H. W. Ngan, Scripta Meter., Vol. 39 No. 12 (1998), 1737.

4. C. N. R. Rao, B. Raveau, *Transitional Metal Oxides – Structure, Properties, and Synthesis of Ceramic Oxides*, WILEY-VCH, 1998.

5. T. J. Coutts, *Electrical Conduction in Thin Metal Films*, Elsevier Scientific Publishing Company, 1974.

6. K.L. Chopra, *Thin Film Phenomena*, McGraw-Hill Book Company, 1969.

7. K.C. Kao, W. Hwang, *Electrical Transportation in Solids*, Oxford, 1981.

MICROSTRUCTURE AND MECHANICAL PROPERTIES OF OXIDE EUTECTIC FIBERS

S. D. DURBIN*, A. YOSHIKAWA*, K. HASEGAWA*, J.-H. LEE*, B. M. EPELBAUM*, T. FUKUDA*, Y. WAKU**
*Institute for Materials Research, Tohoku University, Sendai 980-8577, Japan
**Japan Ultra-high Temperature Materials Research Center Ube 755-0001, Japan

ABSTRACT

Some oxide eutectic materials, such as sapphire/YAG, display an intricate "Chinese script" microstructure which strongly influences properties such as mechanical strength. We used the micro pulling-down technique to grow fibers of a series of such materials at rates over 20 mm/min, giving a uniform microstructure with a characteristic size as low as 150 nm. Bulk and surface characteristics of this microstructure were investigated by electron and atomic force microscopy. Smaller microstructure size gave higher tensile strength at 1500°C. Annealing of the fibers produced some coarsening of the microstructure, but increased the strength at lower temperatures.

INTRODUCTION

Directionally solidified oxide eutectics are promising as structural materials in high-temperature environments, because of their combination of high strength and high thermal stability and oxidation resistance. Although bulk oxide eutectic samples often exhibit areas with well-aligned structure, overall structures are generally non-homogeneous. Structures exist at different length scales, from grains to colonies to the inherent eutectic microstructure. In such non-uniform structures, the strength-controlling parameter appears to be the coarse size of the colony areas [1]. This makes the real strength much lower than expected from the characteristic microstructural or lamellar size. As structural applications require materials that are both strong and uniform, investigation of eutectic morphologies in oxide systems remains of primary importance.

Here we discuss results of systematic investigations of six members of the sapphire/garnet eutectic family, namely $Al_2O_3/R_3Al_5O_{12}$ with R = Y, Dy, Ho, Er, Yb, and Lu. Microstructures were investigated by scanning and transmission electron microscopy (SEM and TEM), as well as atomic force microscopy (AFM). In order to permit quantitative comparison of the "Chinese script" microstructure of these materials, we used image analysis techniques to characterize the microstructure in terms of objectively measureable and physically significant parameters. We also measured the thermal stability at 1500°C in oxidizing atmosphere and the tensile strength at temperatures up to 1700°C for some of the materials..

EXPERIMENT

The starting oxide materials, all of 99.99% purity, were mixed in eutectic molar ratios [2,3], all nearly equal to 81 mol% Al_2O_3/19 mol% R_2O_3 for the sapphire/garnets, and 77 mol% Al_2O_3/23 mol% Gd_2O_3 for the sapphire/perovskite. The μ-PD method involves pulling down of the fiber through a small hole in an iridium crucible which is heated inductively in an Ar atmosphere. These systems were non-wetting, so stable anchoring of the melt meniscus at the crucible edge took place in all experiments. The seed, usually <0001> oriented single crystal Al_2O_3, was positioned using an x-y manipulator, and was moved down during growth at constant rates in the range of 0 - 40 mm/min over a maximal distance of 500 mm. Details of the method have been reported elsewhere [4,5].

Mat. Res. Soc. Symp. Proc. Vol. 581 © 2000 Materials Research Society

The SEM images were analyzed by processing the digitized micrographs with the public domain NIH Image program (available at http://rsb.info.nih.gov/nih-image/), using custom procedures to calculate parameters characterizing the microstructure, as described in the next section. When we segmented the grayscale images into distinct sapphire and garnet domains by visual inspection, the calculated sapphire volume fraction f_s closely matched the value of 0.45 expected from the proportions of the initial powder mixture. To facilitate consistent, objective analysis, further processing was performed with images automatically segmented subject to the constraint that f_s equal the expected volume fraction. This procedure gave results agreeing with individual judgement, and was justified by the high homogeneity of the microstructure. The data obtained from such analysis represented averages over tens or hundreds of domains, and the variation from region to region or fiber to fiber was roughly 10%.

The atomic force microscope provides higher resolution than SEM, yet lacks a direct means of distinguishing the sapphire and garnet phases. Samples observed in their as-grown condition had a suggestive though indistinct appearance, but we found that samples etched for 30 minutes in Ar atmosphere at 1300 - 1500°C (far below the eutectic temperature of 1830 °C) exhibited clearly discernable domains, which had different morphologies and were separated by grooves where the etching was stronger. Samples prepared in this way from both the outer surface of fibers and from inside the fibers as exposed by fracture were imaged in air with a Digital Instruments Nanoscope III AFM. Analysis of these images also made use of the NIH Image software with custom extensions.

RESULTS AND DISCUSSION

The fibers obtained in our experiments were generally milky and opaque in appearance, sometimes with slight coloring due to the rare earth ion (e.g. pinkish for Er, yellowish for Dy, brownish for Ho). The fiber diameter could be controlled over the range 200 μm to 2 mm by adjustment of the heating power and pulling rate. Stable growth was observed from a pulling rate of 0.1 mm/min to 20 mm/min, the diameter varying less than 5%. The maximum length of 500 mm was limited by the apparatus.

Powder XRD patterns from crushed fibers showed the presence of only the Al_2O_3 α-alumina and $R_3Al_5O_{12}$ garnet crystal forms. The interface between these phases in the fiber was sharp and devoid of amorphous material, as evidenced by the TEM lattice images for $Al_2O_3/R_3Al_5O_{12}$ shown in [6].

Figure 1 shows backscattered electron images (BEI) of microstructures of various fibers grown at a range of pulling rates. The two phases form interpenetrating, three-dimensional networks, which in cross section display the "Chinese script" microstructure homogeneously over the whole fiber. The conventional concept of lamellar spacing is not clearly defined for this complex pattern, so we characterized the average domain size for a phase p by the mean boundary distance d_p, the average over all points (pixels) of that phase of the shortest distance to a phase boundary. The parameter d_p has the physical interpretation that the sum $d = d_s + d_g$, where s and g refer to sapphire and garnet phases, is the typical distance each species must diffuse through the melt to accomplish the eutectic phase segregation during solidification. In a conventional lamellar structure, d is equal to half the average lamellar width, i.e. one fourth the lamellar wavelength.

The calculated mean boundary distances for our samples were uniform over the fibers, and varied with pulling rate v as illustrated in Figure 2. The different materials showed similar dependences, with the exception that the Y and Er materials showed a noticeably larger size microstructure at low growth rates, especially at 1 mm/min or less. The theoretical relation for conventional lamellar structures, $d \sim v^{-1/2}$, also seems to obtain for these eutectics with Chinese script microstructure.

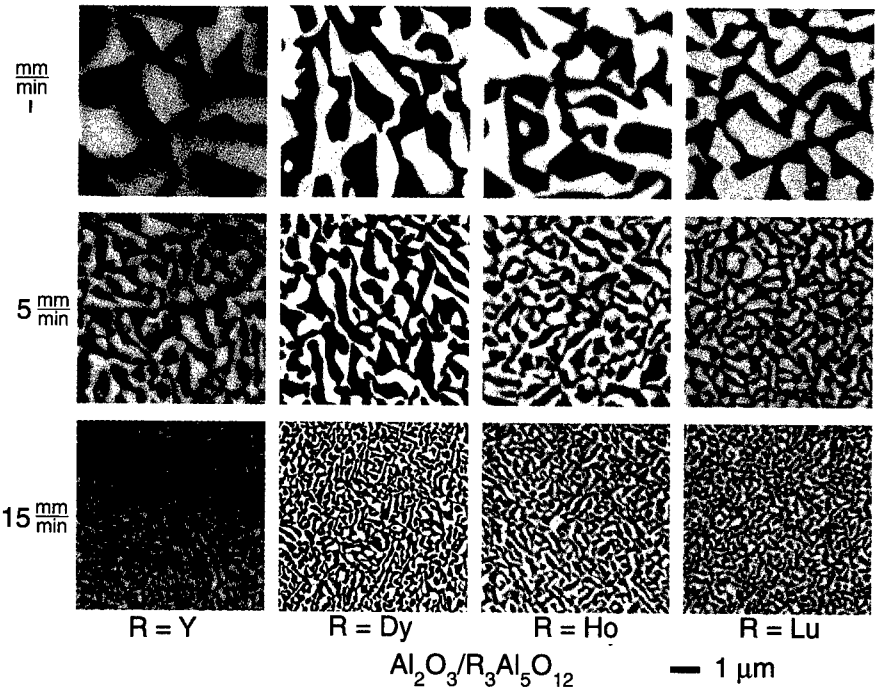


Figure 1. Electron micrographs showing the Chinese script microstructure of various fibers grown at a range of pulling rates. Bright regions are $R_3Al_5O_{12}$ and dark regions are Al_2O_3.

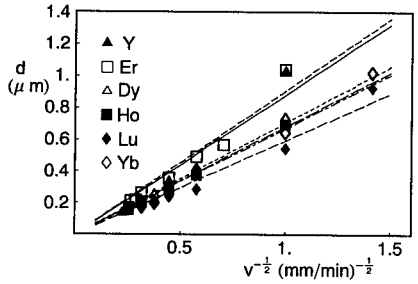


Figure 2. Variation of mean boundary distance d with pulling rate v. Lines represent best fits to the relation $d \sim v^{-1/2}$, which also holds for conventional lamellar structures.

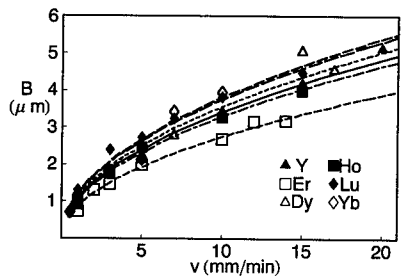


Figure 3. Total length per unit area of the boundaries between domains, B. Curves represent best fits to the relation $B \sim v^{1/2}$.

An additional characterization parameter is the interphase boundary length B, i.e. the total length per unit area of the boundaries between domains. Processes important for both crystal growth and mechanical properties occur along these boundaries, for example, impurity segregation during solidification, and grain growth and slip processes after solidification. Figure 3 shows the variation of B with pulling rate. The quantity B is also related to the shape of the domains: larger values correspond to longer and narrower domains, smaller values to more compact ones. However, since B is also larger for smaller scale microstructure, even with unchanged shape, the best parameter to use as a shape descriptor is the scale-invariant product $\alpha = B (d_s + d_g)$. We found that α does not depend on pulling rate or material.

The discussion of the microstructure has so far been based on electron micrographs of fiber cross sections. Recently, using AFM, we have shown that the script microstructure extends to the surface of the fibers. Figure 4 shows AFM micrographs of the surface layer and of the interior of a fiber grown at 1 mm/min. As can be seen, the slight etch treatment prior to imaging resulted in one component typically having a relatively smooth, rounded surface, while the other displayed a more faceted or stepped appearance. By comparison with similarly treated pure sapphire and YAG fibers, the rounded phase was identified as YAG and the faceted one as sapphire. Given this identification, domain characteristics and volume fractions could be obtained with image analysis techniques, as was done for the SEM images. For the bulk microstructure in the fiber interior, the two techniques yielded the same results. However, the surface was found to have a higher volume fraction of sapphire (over 0.60 at 1 mm/min vs. 0.45 in bulk) and smaller domain size by a factor of 1.5 - 2. The difference varies with growth rate, and the surface microstructure tends to resemble the bulk more closely as the growth rate increases.

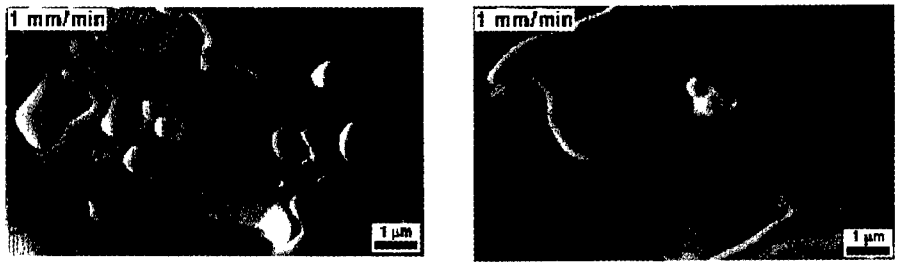


Figure 4. AFM images from the surface (left) and interior (right) of a sapphire/YAG fiber grown at a pulling rate of 1 mm/min. Rounded regions are YAG domains and more faceted ones are sapphire. The surface microstructure has smaller size and higher sapphire fraction.

For the systems with R = Y, Er, Dy, and Ho, the effect of annealing in air at 1500°C was investigated [7]. Some grain growth and was observed and the sapphire domains tended to become more compact and less continuous. Figures 5 and 6 show this change quantitatively in terms of the values of the parameters d and B. We observed an increase of d and decrease of B with treatment time, corresponding to a slight coarsening of the microstructure. The rate of change of d and of B with time is about the same for the materials studied, except for the more rapid change taking place within the first 25 hours for R = Dy, and Ho. However, this is probably due to the smaller initial microstructure size for these fibers. The shape parameter α is nearly the same for all materials, but drops by about 7% after 75 hours of treatment. This is a small change, but consistent for all samples, and corresponds to more compact domains.

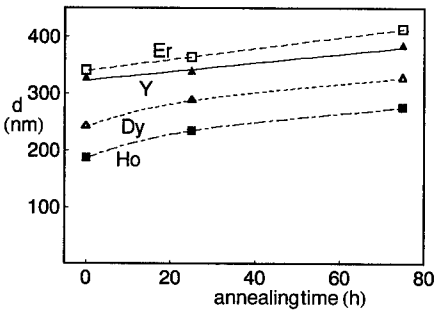


Figure 5. Microstructure size, as measured by the mean boundary distance d, as a function of annealing time in air at 1500°C. Different materials are affected in the same way, but the initial microstructure size is smaller for R = Dy and Ho, so they change more rapidly at first.

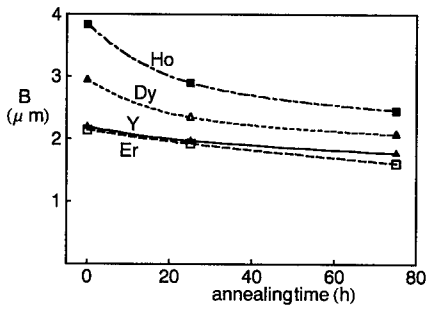


Figure 6. Phase boundary length per unit area, B, which increases with annealing time. The variation is not exactly inverse to that of mean boundary distance d, so the shape of the phase domains is changing slightly, becoming more compact.

We found that the maximum tensile stress of as-grown fibers depended on growth rate, as shown in Fig. 7 for fibers of $Al_2O_3/Y_3Al_5O_{12}$. The reason for the lower strength at room temperature is not clear, but may be due to some defects associated with the processing. Indeed, we have found that prior annealing of the fibers improved the room temperature strength by a factor of two.

Tensile strength measurements at temperatures up to 1700°C are being conducted for the materials with R = Y, Er, Dy, and Ho. Preliminary results indicate that they have comparable strength at lower temperatures, and that fibers with R = Y and Er retained significantly higher strength at temperatures above 800°C, despite their larger microstructure size.

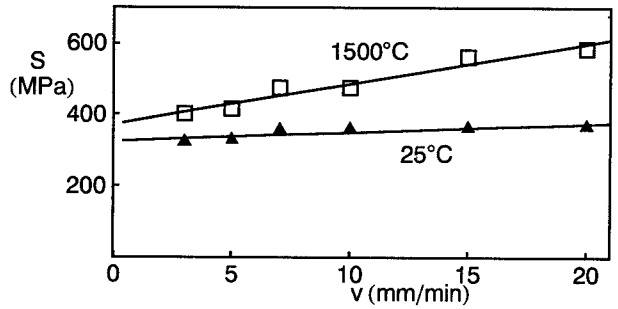


Figure 7. Growth rate dependence of the maximum tensile stress of as-grown fibers. Smaller microstructure size gives improved high temperature performance.

CONCLUSIONS

We have grown oxide eutectic fibers of composition $Al_2O_3/R_3Al_5O_{12}$ (R = Y, Er, Dy, Ho, Yb, and Lu) with uniform microstructure using the micro pulling-down method. With our

apparatus, the diameter was controllable from 200 μm to 2 mm, and the maximal length was about 500 mm. The Chinese script microstructure was characterized by the mean boundary distance and the interphase boundary length, as obtained by image analysis of SEM and AFM micrographs. The mean boundary distance varies with growth velocity in the same way as for conventional lamellar eutectics, except for some deviations at low growth velocity with the Y and Er materials. The interphase boundary length varies almost inversely to the mean boundary distance, and the shape of the phase domains is approximately constant for all materials and growth velocities. As surface flaws are often the limiting factor in fiber strength, the smaller microstructure scale at the surface observed by AFM may have a significant influence on the mechanical properties. The eutectic fibers have excellent high-temperature strength. These results can guide appropriate material selection for various applications. For example, the different behavior of Y and Er with regard to microstructure size at low growth rates suggests that these represent the best candidates for pursuing self-clad fibers, which should be obtainable as the domain size approaches the fiber radius [5, 8].

ACKNOWLEDGEMENTS

The authors thank Mr. Aoyagi of Tohoku University for his help with the SEM and TEM observation, and Mr. Murakami of the Laboratory for Developmental Research of Advanced Materials in the IMR for his assistance with the EPMA analysis. This research was partially supported by the Ministry of Education, Science, Sports and Culture, Grant-in-Aid for Scientific Research (A), 10304023, 1998 (SD) and Grant-in-Aid for Scientific Research (B), 10555254, 1998 (TF).

REFERENCES

[1] V.S. Stubican and R.C. Bradt, Ann. Rev. Mater. Sci. **11**, 267 (1981).
[2] P. Wu and A. D. Pelton, J. Alloys and Comp. **179**, 259 (1992).
[3] D. Viechniki and F. Schmid, J. Mater. Sci. **4**, 84 (1969).
[4] B.M. Epelbaum, A. Yoshikawa, K. Shimamura, T. Fukuda, K.Suzuki and Y.Waku, Journal of Crystal Growth, **198/199**, 471 (1999).
[5] A. Yoshikawa, B. M. Epelbaum, K. Hasegawa, S. D. Durbin, T. Fukuda, J. Cryst. Growth **205**, 305 (1999).
[6] A. Yoshikawa, B. M. Epelbaum, T. Fukuda, K. Suzuki, and Y. Waku, Jpn. J. Appl. Phys. **38**, L1623 (1999).
[7] K. Hasegawa, A. Yoshikawa, S. D. Durbin, B. M. Epelbaum, T. Fukuda and Y. Waku, J. Korean Assoc. Cryst. Growth **9**, 432 (1999).
[8] R. S. Feigelson, Mater. Sci. Eng. B **1**, 67 (1988).

FEATURES OF FRACTURE SURFACE AND GRAIN BOUNDARY STRUCTURE OF BORIDE/NITRIDE MATERIALS

R.A. ANDRIEVSKI*, G.V. KALINNIKOV* and D.V. SHTANSKY**
* Institute of Problems of Chemical Physics, Russian Academy of Sciences, Chernogolovka, Moscow Region, 142432, RUSSIA ara@icp.ac.ru
** State Scientific Center "TSNIIchermet named I.P.Bardin", Moscow, 107005, RUSSIA

ABSTRACT

Nanostructured bulks and films of TiB_2, TiN, AlN, Ti(B,N), and (Ti,Al)N prepared by high pressure sintering and nonreactive magnetron sputtering accordingly. Fracture surfaces and structure of grain boundaries have been investigated by high-resolution scanning and transmission electron microscopy as well as by atomic force microscopy. The revealing of transgranular fracture, homogeneous and inhomogeneous deformation, and the availability of dislocations and amorphous phases in structure are discussed.

INTRODUCTION

Unusual properties of nanostructured (nanocomposite, nanophase) materials (NM), which are normally characterized by a grain size in the range 3-100 nm, catalyzed the numerous investigations in this field. However, the mechanism of the fracture and deformation as well as grain boundary structure are still not clear understood and need further consideration (see, for example, reviews [1, 2]). In addition, only metals, alloys, intermetallics, and oxides are the subjects of the majority of these investigations. High-melting point compounds such as borides, carbides, and nitrides have been studied in limited scale. In elaboration of our previous works [3-5], the present report is devoted to high-resolution electron microscopy (HREM) and atomic force microscopy (AFM) study of boride/nitride NM.

EXPERIMENT

Bulks and films of Ti (B,N) and other compounds have been prepared both by high pressure sintering of ultrafine powders and by nonreactive magnetron sputtering respectively. The details and features of this experimental technique have been published elsewhere [6, 7].

Fracture surfaces of bulks and films have been studied by high-resolution scanning electron microscopy (SEM), using a Hitachi S-4000 field emission gun, and AFM [8, 9]. The structure of films was examined in a JEM-3010 transmission electron micriscope operating at 300 kV [10].

Deformation was realized by cleavage fracture and under a Vickers indentor.

RESULTS AND DISCUSSION

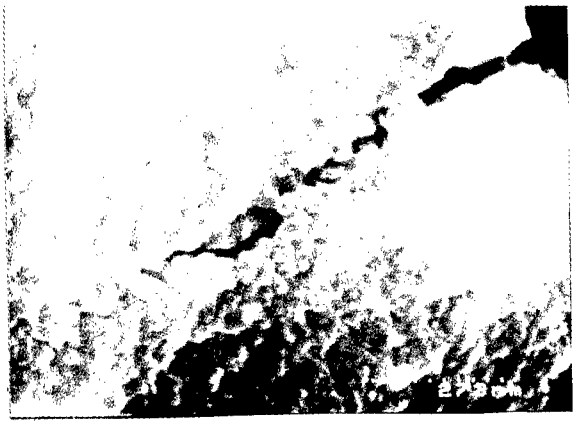
Fracture surface of consolidated bulks

In addition to previous our observations [3], Figs. 1 (a) and (b) show SEM micrographs of fracture surfaces of TiN bulks. As is easy to see, there are intergranular fracture and moreover the feature of crack propagation is also clearly visible. This observation of intergranular fracture seems to be important for understanding and explanation of fracture toughness data for one-phase and two-phase NM (see, for example, [11]).

Mat. Res. Soc. Symp. Proc. Vol. 581 © 2000 Materials Research Society



(a)



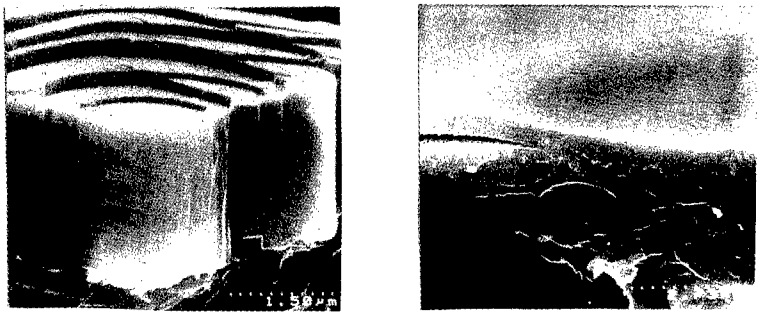
(b)

Figure 1: SEM images of fracture surface (a) of nanostructured TiN bulk including that with crack propagated through crystallite boundaries (b).

Fracture surface of films

Some preliminary results have been published elsewhere [5, 8]. These results were obtained by the cross-section SEM observation of the indentation impressions. Fig. 2 shows two types of deformation. The formation of shear bands and localization of deformation is observed in the case of boride film with the hexagonal structure (Fig. 2, a). On the other side, homogeneous deformation is typical for nitride film with cubic structure (Fig. 2, b). The same character of TiN film deformation was also fixed by Shiwa et al. [12].

The availability of shear bands on the indentation surface can also be observed by AFM [9]. Fig. 3 shows a step-like surface in the case of TiB_2 film; the nearly same situation has been observed in AlN film examination. However, for (Ti, Al)N film homogeneous deformation without step formation was fixed.



(a) (b)

Figure 2. Fracture SEM images through indentations on TiB_2 (a) and TiN (b) films deposited on Si substrates.

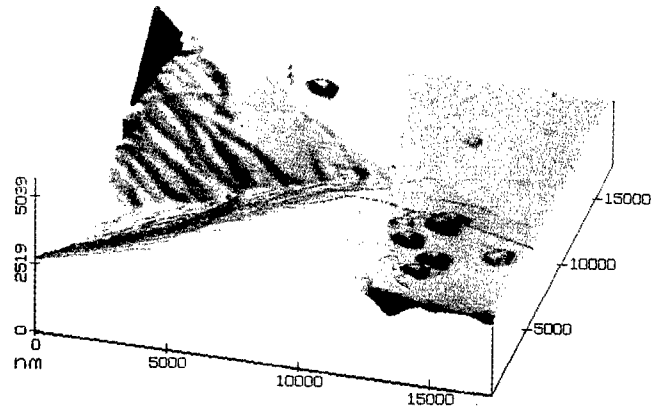
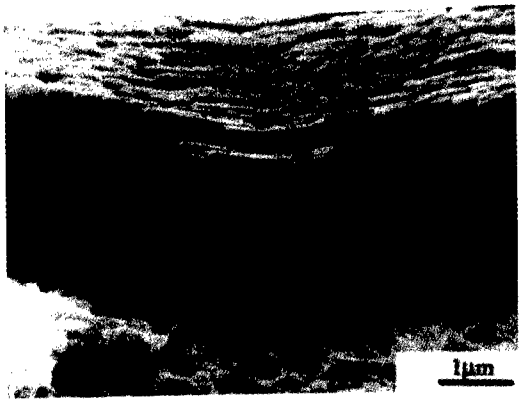
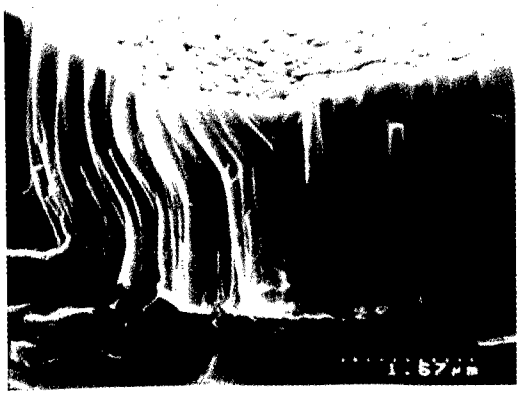


Figure 3. Three dimensional AFM image of TiB_2 film.

Analysis of deformation of boride and nitride films (TiB_2, TiN, AlN, Ti(N,B), (Ti,Al)N) has revealed that because of the feature of the film compression test, the difference in deformation for TiB_2 and AlN films, on the one hand, and TiN, Ti(N,B), and (Ti,Al)N films, on the other hand, seems to be connected with the presence of columnar structure. In the case of clearly defined columnar structure, homogeneous deformation by slip on the interfaces of columns, with the development of brittle (Fig. 4, a) or residual plastic deformation (Fig. 4, b), is dominant and evident. For the most part, films with partly columnar or stonelike structure, such as TiB_2 and AlN films, are characterized by inhomogeneous deformation. Intense shear banding observed in these subjects seems to be very similar to behavior exhibited in other NM (Fe, Fe-Cu, and 3Y-TZP) as well as in amorphous polymers and metallic glasses (see, for example, [14-16]). Some qualitative considerations of possible different dislocation behavior in nanostructured TiB_2 and TiN films have been formulated by Gutkin and Ovid'ko [17]. However, in general the mechanism of inhomogeneous deformation is still unclear and the understanding of the formation and evolution of the shear bands calls for further investigation.



(a)

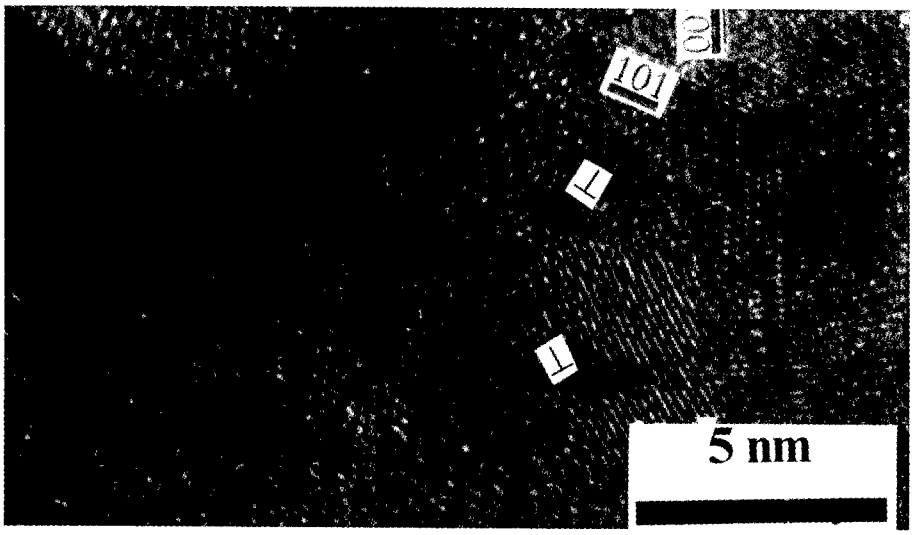


(b)

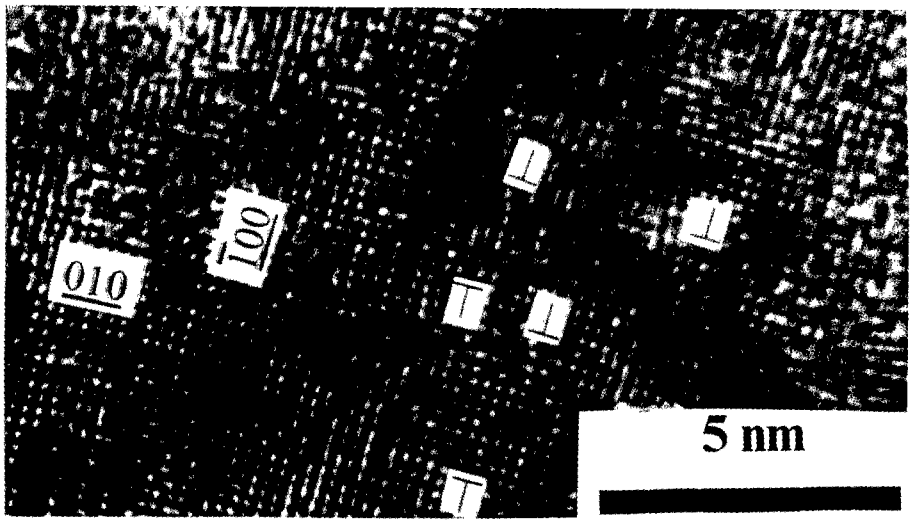
Figure 4. Fracture SEM images through indentation on columnar TiN films accompanied by slip of columns with brittle (a) and plastic (b) deformation (courtesy of Ma and Bloyce [8, 13]).

Dislocations and grain boundaries

Fig. 5 shows HREM images of boride and nitride films.



(a)



(b)

Figure 5. HREM micrographs of boride (a) and nitride (b) films

Edge dislocations are virtually visible inside the crystallites especially in the case of nitride film. In last case as is obvious from selected area electron diffraction (SAED) data, the investigated area was a single crystallite. Systematic studies of dislocations in NM are scarce (see, for example, [18-20]). To our knowledge, the dislocations in NM based on high-melting point compounds were first observed (see also [10, 21]). This fact seems to be very important in connection with a manifestation of plastic deformation in TiN film (Fig. 4, b). So dislocations inside crystallites in nanostructured nitrides can be not only in sedentary positions, but they can also move under compressive strengths at room temperature. It should be also noted that in a qualitative sense the availability of dislocations in nanostructured TiN and TiB_2 films agrees with calculations of Gryaznov et al.[18, 21].

The state of grain boundaries and availability of amorphous phases or layers is another interesting problem in analysis of NM structure. As can be seen from Fig. 5, the lattice fringes are typical for the most crystallites although there are also the lattice distortions and bending in some of grains. The structure of films is almost fully crystalline and there is negligible evidence of extensive areas of amorphous phases or layers. That is consistent with X-Ray diffraction and SAED data. In relation to nanograin SnO_2 films, Rickerby et al. [22] have suggested that in most cases grain boundaries seem to be in general relatively ordered, with eventual perturbation of the lattice fringe contrast restricted to within < 1 nm from interface. The same conclusion could be made as applied to Fig. 5. It should be also noted that some defocused images can be due to local microstresses and the change in contrast within a separate grain can be attributed to different chemical composition [10].

Fig. 6 shows a HREM photomicrographs of nitride film characterized by a very small crystallite size of 0.5 to 3 nm. As can be seen, Figure reveals an order-disorder structure.

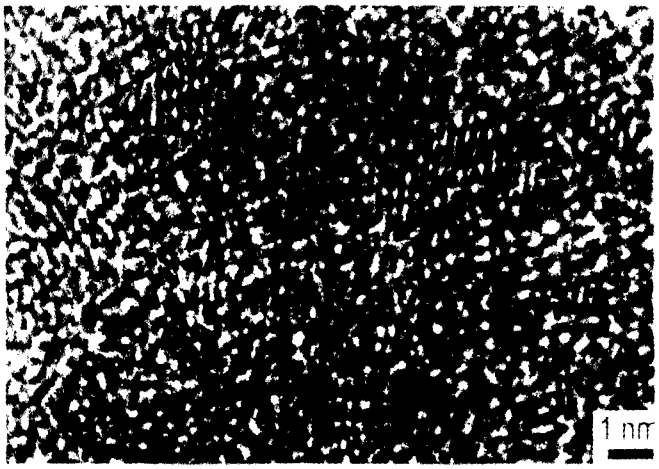


Figure 6. HREM micrograph of Ti-N-B film with a grain size of 0.5 to 3 nm

However, it is known that the availability of very small crystallites (lower than ~2-3 nm) makes possible mixing picture of diffraction in HREM images. So in this case it is very difficult to explain such images and nature of film structure with a very small grain size need further consideration.

CONCLUSIONS

This work shows that fracture surface and crack propagation in NM are intergranular. There are two types of deformation of nanostructured films such as homogeneous deformation and inhomogeneous that. In first approximation, such difference is connected with the availability of columnar structure.

In the case of films with a grain size of 3-15 nm, the majority of grains is to a great extent crystalline in nature and has typical clear fringe contrast. Essentially amorphous phases or layers do not reveal in the grain boundaries. Edge dislocations have been observed inside some crystallites. The availability of dislocations in structure agrees with possibility of plastic deformation of nanostructured nitride films. However, HREM images of films with a very small grain size of 0.5-3 nm are difficult to interpret and their nature is open to question.

ACKNOWLEDGMENTS

The authors are grateful to the INTAS Program (Project No 96-2232) and Russian Program "Integration"(Project No 855) for their support. Friendly assistance of Drs. J. Jaberteau (France), V.S. Urbanovich (Belarus), K. Ma (UK, Taiwan) and A. Bloyce (UK) is greatly acknowledged.

REFERENCES

1. J.R. Weertman, D. Farkas, K. Hemker, H. Kung, M. Mayo, R. Mitra, and H. Van Swygenhoven, MRS Bulletin **24** (2), 44-53 (1999).
2. C.C. Koch, D.G. Morris, K. Lu, and A. Inoe, MRS Bulletin **24** (2), 54-58 (1999).
3. R.A. Andrievski, Nanostruct. Mater. **9**, 607 (1997).
4. R.A. Andrievski, G.V. Kalinnikov, and C.S. Urbanovich, in *Nanophase and Nanocomposite Materials II,* edited by S. Komarneni, J.C. Parker, and H.J. Wollenberger (Mater. Res. Proc. **457**, Pittsburgh, PA, 1997), p. 413-418.
5. R.A. Andrievski, in *Surface-Controlled Nanoscale Materials for High-Added-Value Applications*, edited by K.E. Gonsalves, M.-I. Baraton, R. Singh, H. Hoffmann, J.X. Chen, and J.A. Akkara (Mater. Res. Proc. **501**, Warrendale, PA, 1998), p.149-160.
6. R.A. Andrievski, G.V. Kalinnikov, N.P. Kobelev, and V.M. Kuchinski, in *FOURTH EURO CERAMICS*, edited by A. Bellosi (Gruppo Edit. Faenza **4**, Printed in Italy, 1995), p. 307-312.
7. R.A. Andrievski, G.V. Kalinnikov, N.P. Kobelev, Y.M. Soifer, and D.V. Shtansky, Rus. Phys. Solid State **39**, 1661 (1997).
8. K.J. Ma, A. Bloyce, R.A. Andrievski, and G.V. Kalinnikov, Surf. Coat. Technol. **94-95**, 322 (1997).
9. R.A. Andrievski, G.V. Kalinnikov, J. Jaberteau, and J. Bates, J. Mater. Sci., accepted for publication.
10. D.V. Shtansky, E.A. Levashov, A.N. Sheveiko, and J.J. Moore, Metall. Mater. Trans. **A 30**, 2439 (1999).
11. R.A. Andrievski, in *Nanostructured Materials: Science & Technology*, edited by G.-M. Chow and N.I. Noskova (Kluwer Academic Publishers, Dordrecht, 1998), p. 263-282.

12. M. Shiwa, E. Wepelman, D. Munz, M.V. Swain, and T. Kishi, J. Mater. Sci. **31**, 5985 (1996).
13. K.J. Ma and A. Bloyce, Surf. Eng. **11**, 71 (1995).
14. D.S. Yan, Y.S Zheng, L. Gao, C.F. Zhu, X.W.Wang, C.L. Bai,, L. Xu, and M.Q. Li, J. Mater. Sci. **33**, 2719 (1998).
15. J.E. Carsley, A. Fisher, W.W. Milligan, and E.C.Aifantis, Metall. Mater. Trans. **A 29**, 2261 (1998).
16. T.R. Malow and C.C. Koch, Metall. Mater. Trans. **A 29**, 2285 (1998).
17. M.Yu. Gutkin and I.A. Ovid'ko, J. Mater. Proc. Manuf. Sci. **7**, 59 (1998).
18. V.G. Gryaznov, I. A. Polonsky, A.E. Romanov, and L.I. Trusov, Phys. Rev. **B44**, 42 (1991).
19. D.H. Ping, D.X. Li, H.G. Ye, J. Mater. Sci. Lett. **14**, 1536 (1995).
20. R.A. Andrievski and A.M. Glezer, Phys. Met. Metallography **88**, 45 (1999).
21. R.A. Andrievski, G.V. Kalinnikov, and D.V. Shtansky, Rus. Phys. Sol. State, accepted for publication.
22. D.G. Rickerby, M.C. Horrillo, J.P. Santos, and P. Serrini, Nanostruct. Mater. **9**, 43 (1997).

THERMOELECTRIC PROPERTIES OF Bi_2Te_3-Sb_2Te_3 COMPOUNDS PREPARED BY MA-PULSE DISCHARGE SINTERING PROCESS

R.E. Park, Y.H. Park, T. Abe
Materials Engineering Division, Tohoku National Industrial Research Institute, AIST, MITI, Sendai 983-8551, Japan, repark@tniri.go.jp

ABSTRACT

The Bi_2Te_3-Sb_2Te_3 compounds with the composition of useful thermoelectric cooling materials were prepared by mechanical alloying-pulse discharge sintering process. Effects of the process on the Seebeck coefficient, electrical resistivity and thermal conductivity were investigated. Temperature dependence of the Hall coefficient was also observed in the temperature range 80 - 325 K.

The figure of merit, Z, was found to be about 4.0 x $10^{-3}K^{-1}$ at room temperature in the 25%Bi_2Te_3-75%Sb_2Te_3 composition sintered at 618K using grain refined mechanically alloyed powders which had the size of under 32 μm. The value of Z was remarkably improved with a decrease of the thermal conductivity shown in the fine grain compacts fabricated by mechanical alloying-pulse discharge sintering process.

INTRODUCTION

Compounds of Bi_2Te_3, Sb_2Te_3 and their pseudo-binary system Bi_2Te_3- Sb_2Te_3 have been known as thermoelectric cooling and heating materials, since they had relatively large values of the figure of merit (3.2 - 3.4 X 10^{-3} K^{-1}) around room temperature. [1] The efficiency of the thermoelectric conversion is directly related to the temperature difference where the device is operated, its average temperature of the operation and the transport properties of thermocouple materials represented by ZT, the dimensionless figure of merit. The larger the ZT value, the larger the efficiency. The figure of merit, Z, is described by :

$$Z = \alpha^2 / \rho \cdot \kappa$$

where α is the Seebeck coefficient, ρ is electrical resistivity and κ is thermal conductivity. It is clear that in order to obtain the high Z value, the large Seebeck coefficient and the low electrical resistivity are required, as well as the low thermal conductivity.

Mechanical alloying (MA) method is expected to produce more uniform elemental dispersion and smaller grain sizes than the conventional melt and cast process. It was also reported that pulse discharge sintering (PDS) process could result in the higher thermoelectric efficiency in the case of the SiGe system. [2]

In the present study, MA-PDS process was used to improve the figure of merit of Bi_2Te_3-Sb_2Te_3 compounds which had three compositions of 25%Bi_2Te_3-75%Sb_2Te_3, 50%Bi_2Te_3-50%Sb_2Te_3 and 75%Bi_2Te_3-25%Sb_2Te_3. And then, the thermoelectric properties of the MA-PDS compacts were described.

Mat. Res. Soc. Symp. Proc. Vol. 581 © 2000 Materials Research Society

EXPERIMENT

High purity elemental powders of Bi, Sb and Te (> 99.999 %) were used as raw materials. Mechanical alloying was performed using a vibratory ball milling under high energy conditions. The vessel was approximately 780 ml in volume. Balls used were zirconia with a 15 mm diameter. Powder charge was 30 g, where the powder to ball weight ratio was 1:100. Typical milling duration was 200 hours.

After MA processing, green compacts were sintered by PDS (the type of spark plasma sintering) process using a graphite mold where the sintering temperature was 618 K and the pressure was 50 MPa. The phases in the sintered compacts were identified by X-ray diffraction with monochromatic Cu-K_{α} radiation. Measurements of electrical resistivity ($\Omega \cdot cm$) and thermal conductivity (w/mK) as well as the Seebeck coefficient ($\Delta V/\Delta K$) were carried out in the temperature range from 298 to 423 K. The Seebeck coefficient, as a function of temperature gradient (ΔK < 10, 20, 30 K), was measured by using two K-type thermocouples and nickel blocks. The measurement was carried out within twenty seconds to prevent a potential drop due to the Peltier effect. The electrical resistivity was measured by a direct current four-probe method while the thermal conductivity was measured with a laser flash method. Finally, measurements of the Hall coefficient were conducted with the magnetic field of 0.86 T perpendicular to cleavage planes and electrical current parallel to the same planes.

RESULTS

Figure 1 shows X-ray diffraction patterns for 25%Bi_2Te_3-75%Sb_2Te_3, 50%Bi_2Te_3-50%Sb_2Te_3

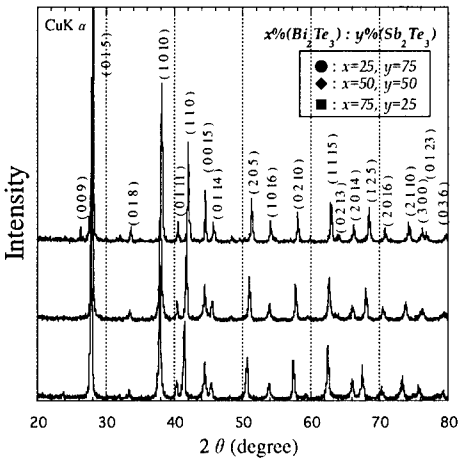


Figure 1 X-ray diffraction patterns for x%Bi_2Te_3-y%Sb_2Te_3 compacts after MA-PDS.

and 75%Bi_2Te_3-25%Sb_2Te_3 compacts after MA-PDS. The typical rhombohedral structure shown in V-VI compounds such as Bi_2Te_3 and Sb_2Te_3 was observed. The plane parallel to a rhombohedral c-axis, which corresponded to the pressure direction, had superior thermoelectric properties comparing to that of the plane perpendicular to the c-axis. Lattice constants were increased with the increase of Bi content. However, the small intensity of (0 0 9) plane, which was perpendicular to the c-axis, was observed only at the 25%Bi_2Te_3-75%Sb_2Te_3. It was recognized from Fig. 2 that the Seebeck coefficient and electrical resistivity were significantly

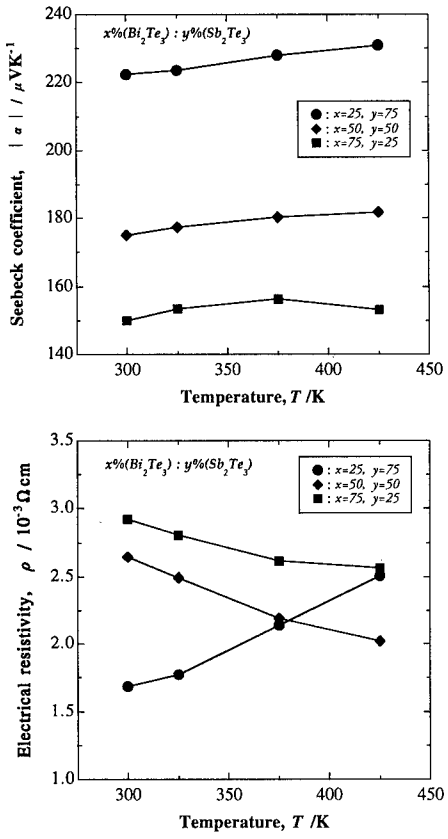


Figure 2 Temperature dependence of (a) Seebeck coefficient and (b) electrical resistivity of x%Bi_2Te_3-y%Sb_2Te_3 compacts by MA-pulse discharge sintering.

dependent on the composition of the compounds. The electrical resistivity induced by the conduction mechanism was increased with increasing the temperature in the 25%Bi_2Te_3-75%Sb_2Te_3 compact while those of 50%Bi_2Te_3-50%Sb_2Te_3 and 75%Bi_2Te_3-25%Sb_2Te_3 compacts were decreased. Figure 3 shows the temperature dependence of the thermal conductivity. In

the 25%Bi_2Te_3-75%Sb_2Te_3 compact, the thermal conductivity was slightly decreased with increasing the temperature, reached a minimum value at 375 K, and then, was increased up to 425 K.

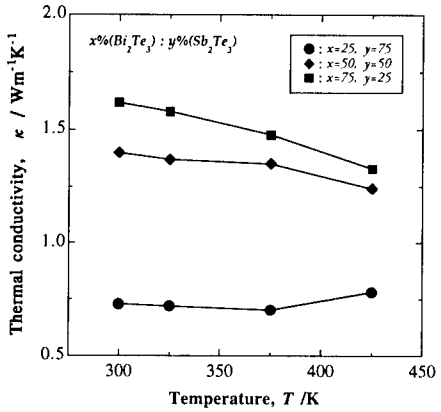


Figure 3 Temperature dependence of the thermal conductivity of x%Bi_2Te_3-y%Sb_2Te_3 compacts by MA-pulse discharge sintering.

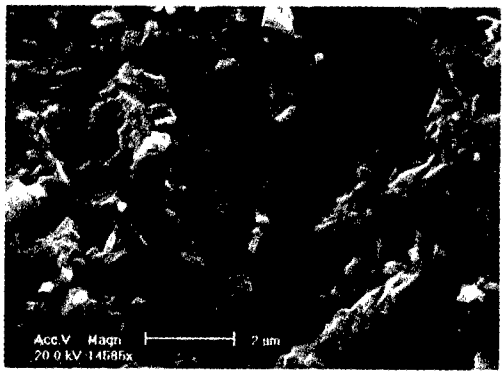


Figure 4 SEM fractograph of the 25%Bi_2Te_3-75%Sb_2Te_3 compact by MA-pulse discharge sintering. (618 K, 50 Mpa and milled for 200 hrs)

On the other hand, the thermal conductivity of the other two compositions was decreased in the temperature range investigated. This result clearly indicated that the MA-PDS process was very effective to decrease the thermal conductivity. It could be deduced from the following reasons. First, MA method significantly reduced the grain size of raw powders. Second, PDS process shortened the consolidation time and lower the sintering temperature in that the grain growth of

final product was suppressed. Figure 4 is a SEM fractograph of the 25%Bi_2Te_3-75%Sb_2Te_3 compact which showed a typical intergranular fracture mode. From this micrograph, the average grain size was estimated to be less than one micron. Moreover, ions and electrons generated by spark discharge purified surface layers and contact areas of particles and inhibited oxidation of particle surface. This phenomenon could have good influence on the electrical and thermal conductivity. Therefore, the decrease of the thermal conductivity could be considered to be due to the increased phonon scattering at grain boundaries with refined grains by MA-PDS process. Figure 5 shows the temperature dependence of the figure of merit, Z. Since the efficiency of thermoelectric conversion was represented by Z, the Z value was calculated from electrical resistivity, thermal conductivity and the Seebeck coefficient which were taken from Fig. 2 and 3. The largest Z value was 4.02 x $10^{-3}K^{-1}$ at room temperature in the 25%Bi_2Te_3-75%Sb_2Te_3 compact. The values for the other two compositions were lower than 1.20 x $10^{-3}K^{-1}$ in the whole temperature range.

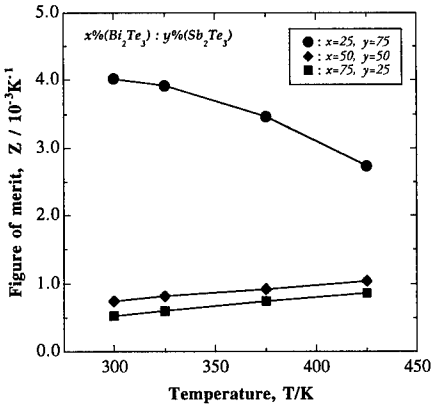


Figure 5 Temperature dependence of the figure of merit of x%Bi_2Te_3-y%Sb_2Te_3 compacts by MA-pulse discharge sintering.

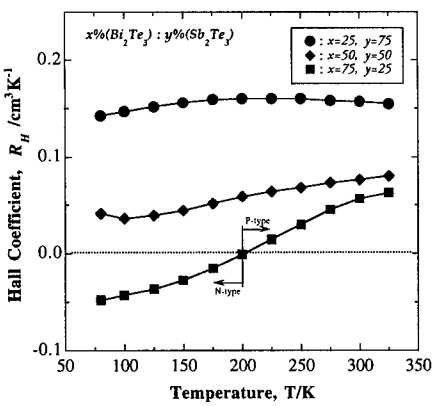


Figure 6 Temperature dependence of Hall coefficient of x%Bi_2Te_3-y%Sb_2Te_3 compacts by MA-pulse discharge sintering.

Figure 6 shows the result of Hall coefficient measurements between liquid nitrogen temperature and 325 K. The saturated 25%Bi_2Te_3-75%Sb_2Te_3 and 50%Bi_2Te_3-50%Sb_2Te_3 compacts were *p*-type in the temperature range tested and the slightly increase of the Hall coefficient was observed with increasing the temperature. On the other hand, 75%Bi_2Te_3-25%Sb_2Te_3 compact was changed from *n*-type to *p*-type as the temperature was increased above 200 K. The fact that the Hall coefficient of 25%Bi_2Te_3-75%Sb_2Te_3 compact was higher than those of the other two compositions indicated that the carrier concentration was lower in the 25%Bi_2Te_3-75%Sb_2Te_3 compact. Therefore, the decrease of thermal conductivity shown in Fig. 3 seems mainly due to the change of the carrier concentration. To explain the transport properties

of thermoelectric materials, many models were developed using a classical phonon scattering mechanism, an unusual behavior [3], [4] as well as a mixed-scattering mechanism. [5]

The high Z value in the 25%Bi_2Te_3-75%Sb_2Te_3 compact could be assumed that phonon scattering both at the grain boundaries and at nanometer scale inclusions such as zirconia introduced during MA contributed to the decrease of thermal conductivity.

CONCLUSIONS

25%Bi_2Te_3-75%Sb_2Te_3, 50%Bi_2Te_3-50%Sb_2Te_3 and 75%Bi_2Te_3-25%Sb_2Te_3 compacts were prepared by the MA-PDS process. The effects of MA-PDS process on the thermoelectric properties of these compacts as well as the material preparation process itself were described.

In the 25%Bi_2Te_3-75%Sb_2Te_3 composition, *p*-type compact was obtained and the largest Z value of 4.02 x $10^{-3}K^{-1}$ at room temperature was shown. This result could be related to the decrease of thermal conductivity, which was originated in the preparation of refined powders and the suppression of grain growth by MA method and PDS process with short consolidation time and low sintering temperature.

REFERENCES

1. W.M. Yim and F.D. Rosi, Solid State Electronics **15**, p. 1121-1140 (1972).
2. K. Suno, M. Sakai, H. Watanabe, and M. Shinmei, Proc. 12th Inter. Conf. Thermoelectrics, Inst. Elec. Eng. Jpn., p. 252-255 (1993).
3. C.H. Champness, P.T. Chiang and P. Parekh, Canadian J. Phys. **43**, p. 653-669 (1965).
4. R.L. Testardi, J.N. Bierly, Jr., and F.J. Donahoe, J. Phys. Chem. Solids **23**, p. 1209-1217 (1962).
5. J.P. Fleurial, L. Gailliard, R. Triboulet, H. Scherrer and S. Scherrer, J. Phys. Chem. Solids **49**, p. 1237-1247 (1988).

RAMAN SHIFT AND BROADENING IN STRESS-MINIMIZED GE NANOCRYSTALS IN SILICON OXIDE MATRIX

YX Jie, CHA Huan, ATS Wee and ZX Shen
Department of Physics, National University of Singapore,
Kent Ridge, Singapore 119260, SINGAPORE.

ABSTRACT:

Ge nanocrystals (nc-Ge) embedded in silicon oxide films were synthesized using RF magnetron sputtering and post-annealing procedure. To minimize the stress effect and inhomogeneity, we intentionally lower the cooling rates and reduce the temperature gradient during annealing. Significant Raman shifts ranging from 2.0 to 5.8 cm^{-1} have been observed from samples annealed at different temperatures. The size-dependent shift and broadening is found to be in good agreement with the phonon confinement mode together with the Gaussian weighting function, and the isotropic TO2 phonon dispersion relation introduced by Sasaki et al. The Raman spectra can also be well-fitted using peaks calculated from the phonon confinement model. The inhomogeneous Raman peak broadening from our samples annealed at lower temperatures are attributed to the non-Gaussian size distribution of Ge nanocrystals.

INTRODUCTION

The strong visible photoluminescence at room temperature from indirect band gap nanocrystals (especially group IV elements, such as Si, Ge etc) has attracted much attention recently due to their possible optoelectronic applications. Many studies on nc-Ge embedded in silicon oxide films have been carried out since strong light emission was observed from Ge nanocrystals embedded in silicon oxide films through quantum confinement effects. This material is of interest also because the sample preparation method is compatible with the conventional integrated circuit fabrication process [1-3].

As a fast, convenient and non-destructive method, Raman spectroscopy has been widely used in the characterization of the nc-Ge systems to determine nc-Ge size [5-11], crystallinity [12], etc. Due to phonon confinement effects, Raman spectra of nc-Ge show a downshift and broadening when the nanocrystal size is smaller than 30 nm [13, 14]. In order to interpret the Raman spectrum quantitatively, a phenomenological phonon confinement model has been developed by Richter et al to account for the peak position shift, broadening, and asymmetry of the bands observed in nanocrystals [15]. The essential parts of this model are the phonon confinement weighting function and the dispersion function. Campbell and Fauchet compared three kinds of weighting functions and suggested that the Gaussian weighting function $|C(0,q)|^2 \propto \exp(-q^2 \cdot L^2/16 \cdot \pi^2)$ could give the best agreement with Si and GaAs nanocrystal data. In the selection of dispersion function, the situation is controversial. A dispersion relation from the linear-chain model (LCM) was reported in 1987 [16]. A dispersion from the experimental neutron data of TO phonon scattering along the [100] direction (TO[100]) was also used [9]. Sasaki et al analyzed the Raman spectra from gas evaporated Ge small particles using a series of isotropic dispersion relations obtained through fitting neutron experimental data along [100], [110] and [111] directions, forcing a good fit near the Γ point [14]. Other dispersion functions were also reported in the literature [5, 6]. Since Raman spectra are easily influenced by homogeneous or inhomogeneous stress, inhomogeneity of nc-Ge shape and size distribution, Raman spectra are usually fitted to determine the nc-Ge size without considering the Raman shift or size distribution [7, 9].

Mat. Res. Soc. Symp. Proc. Vol. 581 © 2000 Materials Research Society

When the Ge nanocrystal size decreases to several nanometers, the large difference between the surface and internal energy of the diamond-like structure will drive a structure transition in nc-Ge systems [17]. In addition, surface Ge-Ge bonds may also introduce stress in the nc-Ge systems. When nc-Ge are embedded in an amorphous silicon oxide matrix, the matrix may saturate the surface dangling bonds and reduce the surface energy. The purpose of this study is to synthesize stress-minimized and well-dispersed nc-Ge systems by controlling the annealing process, as well as to examine Fauchet's phonon confinement model with different dispersion relations.

EXPERIMENTAL

The samples were prepared by co-sputtering in an argon ambient at room temperature using an Anelva (SPF-210H) sputtering system. The composite sputtering target was formed with several pieces of small polycrystalline Ge pieces (99.999% purity) attached to a 4-in quartz (99.99% purity) disc. Amorphous $Ge_xSi_yO_z$ alloy thin films were deposited on n-type silicon {100} substrates. Substrate temperatures were kept near room temperature during deposition. Subsequent thermal annealing at various temperatures from 600 to 900°C were performed in a quartz tube with an argon ambient to achieve crystallization at various grain sizes and crystallinity. The post-annealing processes consisted of a 30-minute temperature ramp, a 30-minute annealing at the predetermined temperature and a controlled cooling process to relax the stress. Two groups of samples have been synthesized, one cooled via natural cooling (initial cooling rate is about 10°C/min, the whole process lasting > 3 hrs.), and the other cooled to 600°C at the rate of –10°C/min to 600°C, stabilized for 10 minutes and then cooled to room temperature at the rate of –3°C/min. The internal temperature gradient on each sample was minimized by controlling the sample size and shape.

A Philips CM300 high-resolution transmission electron microscope (HRTEM) was used to determine the nc-Ge size. The EDX mounted in the HRTEM was used to determine the elemental composition in the imaging area. Room temperature Raman spectra from samples annealed at different temperatures were acquired using a Renishaw Ramanscope with the 514.5 line from an Ar^+ laser as excitation source.

RESULTS AND DISCUSSION

In Raman scattering processes in nanocrystals, the confinement of phonons results in the breakdown of the wave-vector selection rule. Therefore, phonons at $q \neq 0$ can also contribute to the Raman spectrum, resulting in the red shift of the spectrum peak from its bulk value with an asymmetrical broadening. The following phonon confinement model has been proposed by Richter et al to explain the phonon confinement effect on Raman spectrum [15]. The first-order Raman spectrum of a nanocrystal, $I(\omega)$, can be calculated using [4,7,9,15,18]:

$$I(\omega) \propto \oint \frac{|C(0,q)|^2}{[\omega - \omega(q)]^2 + (\frac{\Gamma_0}{2})^2} d^3q \qquad (1)$$

where $\omega(q)$ is the phonon dispersion curve of the infinite crystal and Γ_0 is the natural line width of the Raman peak from single crystal Ge. The integration should be applied through the entire Brillouin Zone. For simplification, the Brillouin zone is usually regarded as a sphere and its anisotropy is usually disregarded [4, 7, 9, 15, 18,]. In this work, we use a simplified analytical expression to obtain the isotopic dispersion curves given by [14]

$$\omega(q) = \omega_0 - \Delta \cdot \{[1 - \cos(\pi \cdot (\frac{ka}{\pi})^n)]/2\}^{\frac{1}{n}} \qquad (2)$$

where ω_0 is the frequency at $\vec{k} = 0$ and Δ and n are parameters adjusted to fit the dispersion relation obtained by neutron scattering at 80K [10]. The phonon frequency of the neutron data was shifted by –3.5 cm^{-1} on account of the difference in the temperature. A good fit has been achieved near the Γ point because the phonon state for $k > 0.4 \cdot \frac{\pi}{a}$ is not sensitive to RWL calculation. Three dispersion functions corresponding to two TO branches (TO1 and TO2) and one LO branches have been obtained as introduced by Sasaki et al. For comparison, the dispersion functions from the neutron experimental data from TO phonons along [100] direction $\Gamma \xrightarrow{\Delta} X$ from ref. 10 have also been calculated.

Since the Gaussian weighting function is the most widely used, we adopted this weighting function and computed Raman spectra using the various dispersion functions. The calculated relationship between Raman shift $\Delta\omega = \omega - \omega_0$ and Raman peak broadening $\Delta\Gamma = \Gamma - \Gamma_0$ for TO1, TO2 and LO are shown in Fig.1 as solid lines. The calculation for TO [100] dispersion function is shown as the dotted line. In order to be compatible with the literature [13,15], we use the absolute value of Raman shift in this figure. The circles and squares represent data from group (1) and group (2) samples respectively. It can be seen that the curves from TO1 and LO dispersion relations deviate significantly from experimental data. The data from Raman peaks with fewer shifts and lesser broadening correspond to the samples annealed at higher temperature. Most data are in good agreement with the theoretical calculations from TO2. It can also been seen that the calculation from TO2 makes a small modification from that from TO[100] dispersion. However, for those samples annealed at lower temperatures, the Raman peak deviate to the larger broadening side. This deviation indicates that the Raman spectra are broader than that predicted by the phonon confinement model for samples annealed at lower temperatures. From our XRD data, HRTEM image and temperature dependent Raman results (which will be published elsewhere), our samples are nearly stress-free. Therefore, we cannot attribute this deviation to the compressive stress effect. nc-Ge in our samples are well-dispersed and nearly spherical. The nc-Ge shape deformation is also unlikely to contribute to this deviation. In addition, the Raman spectra cannot be well fitted with a single calculated peak and amorphous Ge cluster peak. The Gaussian peak corresponding to the amorphous Ge-Ge mode TO band locats at 270 cm^{-1} with a FWHM of 46 cm^{-1}. The only explanation is that this deviation comes from nanocrystal size distribution, especially a non-Gaussian distribution as predicted by Fujii et al [9]. Since the phonon confinement mode with Gaussian weighting function has already partially taken into consideration the Gaussian size distribution [13], we use three peaks to fit the measured Raman spectra and to depict the size distribution deviation. The fitted Raman spectra from samples annealed at different temperatures using the peaks calculated with the TO2 dispersion function are shown in Fig 2. The computed Raman spectra from nc-Ge with large,

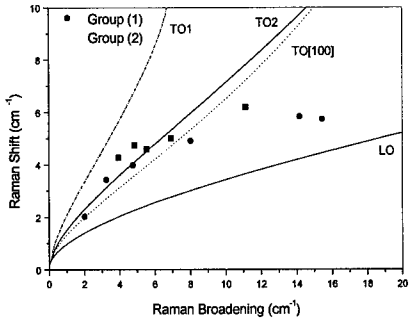


Fig.1 The computed relationship between Raman shift and broadening from different dispersion relations. The circles and diamonds represent experimental data from group (1) and group (2) samples annealed at different conditions respectively.

small, amorphous Ge clusters and their summation are shown in this figure as dot lines, dash lines, dash dot lines and solid lines respectively. The hollow circles represent the experimental Raman data. It can be seen that the measured Raman spectra can be well fitted using these three peaks.

The fitted Raman spectra from each sample are listed in Fig.2. The Raman peak from the sample annealed at 900°C can be well fitted with a single peak with a nanocrystal size d = 11.2 nm. For samples annealed at lower temperatures, one amorphous peak, one nanocrystal peak corresponding to d ~ 3 nm and a larger size peak are required to give a good fit, as has been done in reference [12]. However, unlike in reference [12], we fit the Raman spectra using the phonon confinement model instead of Gaussian peaks. Even after introducing the amorphous peak, we could not obtain a good fit to the Raman spectrum with one Raman peak. This suggests that the asymmetric broadening of Raman peaks may be due to inhomogeneous broadening from a non-Gaussian size distribution in our samples.

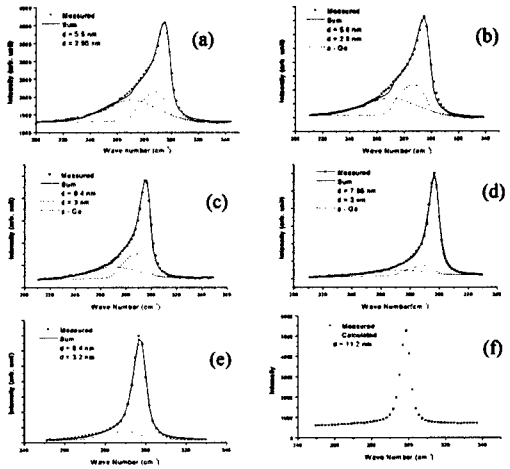


Fig. 2 The Raman spectra from different samples and fitted with calculated peaks with phonon confinement mode and TO2 dispersion function. (a) Sample annealed at 675°C for 30 min, (b) 700°C for 30 minutes (c) 700°C for 60 minutes (d) 750°C for 30 minutes (e) 800°C for 30 minutes and (f) 900°C for 30 minutes.

Fig. 2 indicates a gradual transition from amorphous to crystalline phase [12]. We observed that the amorphous Ge portion in the Raman peak decreases with increasing annealing temperature. The portion corresponding to the small nc-Ge component also decreases with increasing annealing temperature. The amorphous component becomes undetectable when the annealing temperature increases to 800°C. With the decrease of these two components, the Raman shift and broadening are determined mainly by the larger nc-Ge.

The results shown in Fig. 2 also confirm the phase transition discussed in reference [11]. Veprek, Iqbal, and Sarott [17] suggested that the Si lattice structure becomes unstable when the film thickness decreased significantly. They reported that a structural transition from the diamond structure to the amorphous phase takes place below a thickness of 3 nm. The large thermodynamic driving force for this structural transition comes from the large difference between surface energy and internal energy of the diamond structure when the size decreases. The critical size may depend on the energy of the dominant surface, in the case of Si and Ge, the {111} planes. From thermodynamic energy balance considerations, the critical size was estimated to be about 2 nm [11]. Ge nanocrystals around this critical value or smaller are unstable, especially during annealing. They can transit from the amorphous to crystalline phase, or vice versa. Before the film is fully crystallized, some proportion of Ge should be in the amorphous phase, and the smaller size (~ 3 nm) component peak should be larger than that predicted by the Gaussian distribution function.

If we assume the integrated Raman scattering cross section area to be the same for all nc-Ge sizes and σ to be the ratio of integrated scattering cross section area for the crystalline phase

to amorphous phase, the three-peak fitting can be used to calculate nc-Ge size and crystallinity using following weighed equations.

$$\overline{D} = \frac{D_s \cdot S_s + D_l \cdot S_l}{S_s + S_l} \tag{3}$$

and,

$$X_c = \frac{S_l + S_s}{(S_l + S_s) + S_a \cdot \sigma} \tag{4}$$

Here, S_l, S_s, S_a are the integrated Raman peak intensities or peak areas corresponding to the large nc-Ge, small nc-Ge and amorphous phase respectively. For nc-Ge systems, we may adopt $\sigma = 1.0$ which has been used for Si nanocrystals [12].

The computed relations between Raman shift and broadening with nc-Ge size are shown in Fig. 3. The measured Raman shift and broadening with nc-Ge size determined by the above method are shown as hollow circles. From Fig. 3 (a) and (b), we can see that both Raman shift and broadening can be used to calculate nc-Ge size for those samples with good crystallinity. For those partially crystallized samples, the nc-Ge size obtained from Raman shift and Raman broadening is usually larger and smaller than the actual case respectively.

Since the phonon confinement will lead to both Raman shift and broadening, we can use both the shift and broadening to determine nc-Ge size when the films are fully crystallized. The Raman shift and broadening are related to the nc-Ge size L that produces an uncertainty in the $\vec{q}$-vector $\approx 2\pi/L$ [19]. For several nanometer Ge nanocrystals, we have to integrate over all the Brillouin Zone. Therefore, we cannot convert the uncertainty into an ω uncertainty through phonon dispersion function as in ref 25. The square relationship between the Raman shift $\Delta\omega$ and $1/L$ may no longer be accurate. From Fig 3(b), we can see that the Raman broadening does not change linearly with the Raman shift. For convenience of applications, we use the following analytical relations to depict the Raman shift [4] and Raman broadening:

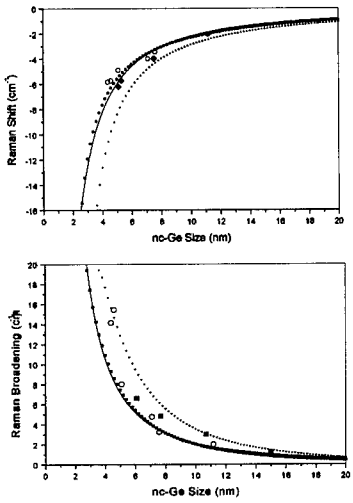


Fig. 3 (a) The calculated dependence between Raman Shift and nc-Ge size. (b) The calculated dependence between Raman broadening and nc-Ge size. The dot line in (a) represents the calculation from Zi's model. The solid circles and triangles represent calculation from TO2 and TO[100]. The solid lines are drawn from the analytical formulae (5) and (6). The diamonds represent our experimental results. The squares represent Fujii's experimental data. The hollow circles represent the results from the three-peak fitting.

$$\Delta\omega = -A \cdot \left(\frac{a}{L}\right)^{\alpha} \tag{5}$$

and

$$\Delta\Gamma = B \cdot \left(\frac{a}{L}\right)^{\beta} \tag{6}$$

where a is the lattice constant of Ge nanocrystals, A = 138 cm^{-1}, $\alpha = 1.44$ and B = 323 cm^{-1}, $\beta = 1.75$. These two functions are shown in Fig. 3 as solid lines. Here, we can see that these two relations conform with the phonon confinement mode well.

From Fig 1, we can see that the theoretical calculations from both TO2 and TO [100] dispersion functions are in good agreement with the experimental Raman shift and broadening data. The difference is that the TO2 dispersion function allows a slightly larger Raman shift for

the same Raman broadening than TO[100] dispersion function. Fig. 3 shows that the discrepancy in nc-Ge size from TO2 and TO[100] dispersion functions is about 2 nm. The solid squares are data from Fujii's experimental data [9]. From the Fig. 3 (a), our experimental data (diamond labels) are closer to the theoretical curve calculated from the TO2 dispersion function. From Fig. 3 (b), it can be seen that Fujii's data lies between the TO2 and TO [100] curves. During TEM measurements, nc-Ge near the critical size becomes unstable under high-energy electron irradiation and transits to the amorphous phase. The TEM image is not sensitive to the amorphous Ge clusters because the silicon oxide matrix is also amorphous. We deduce that the average nc-Ge size determined from the TEM images should be a little larger than the actual case, i.e., the isotropic TO2 dispersion can give a better description of the nc-Ge system.

CONCLUSION

We have synthesized stress-minimized Ge nanocrystals in a silicon oxide matrix. The phonon confinement model with various dispersion functions has been compared with Raman spectra taken from nearly stress-free nc-Ge samples. It was found that the phenomenological phonon confinement model using Fauchet's Gaussian weighting function and TO2 phonon dispersion gives the best description of the Raman shift, broadening and spectra shape. A three-peak fitting method based on the phonon confinement model is found to be useful in quantifying the nanocrystal size, crystallinity, size distribution and phase. The Raman shift and broadening in this stress-free nc-Ge system can be described by an $L^{-1.44}$ and $L^{-1.75}$ law respectively.

REFERENCES

1. S. Takeoka, M. Fujii, S. Hayashi, and K. Yamamoto, Phys. Rev. B, Vol. 58, No. 12, 7921(1998).
2. D. C. Paine, C. Caragianis, T. Y. Kim, and Y. Shigesato, Appl. Phys. Lett. 62(22), 1993.
3. M. Zacharias and P. M. Fauchet, Appl. Phys. Lett., 71 (3), 380 – 382, 1997.
4. J. Zi, K. Zhang and X. Xie, Phys. Rev. B, 55, 9263 (1997).
5. X. L. Wu, T. Gao, X. M. Bao, F. Yan, S. S. Jiang, and D. Feng, J. Appl. Phys. 82(5), 2704(1997).
6. S. Y. Ma, Z. C. Ma, W. H. Zong, H. X. Han, Z. P. Wang, G. H. Li, G. Qin, and G. G. Qin, J. Appl. Phys. 84(1), 559(1998).
7. S. Guha, M. Wall and L. L. Chase, Nuclear Instruments and Methods in Physics Research B, 147(1999), 367 – 372.
8. L. P. Yue, Y. Z. He, Acta Physica Sinica, 45(10), 1756(1996).
9. M. Fujii, S. Hayashi and K. Yamamoto, Jap. J. Appl. Phys. 30, 687(1991).
10. G. Nilsson and G. Nelin, Phys. Rev. B 15(1971) 364.
11. Y. Maeda, Phys. Rev. B 51(3), 1658(1995).
12. Per R. Poulsen, M. Wang, J. Xu, W. Li, K. Chen, G. Wang, and D. Feng, J. Appl. Phys. Vol. 84, No. 6, 3386(1998).
13. I. H. Campbell and P. M. Fauchet, Solid State Commun. 58, 739 (1986).
14. Y. Sasaki and C. Horie, Phys. Rev. B 47(7), 3811, 1993.
15. H. Richter, Z. P. Wang, and L. Ley, Solid State Commun. 39, 625(1981).
16. T. Kanata, H. Murai, and K. Kubota, J. Appl. Phys. 61(3), 969(1987).
17. S. Veprek, Z. Iqbal, and E. A. Sarott, Philos. Mag. B 45, 137(1982).
18. R. Tubino, L. Piseri, and G. Zerbi, The Journal of Chemical Physics, 56(3), 1022-1039(1972).
19. M. Cardona, *Lighting Scattering in Solids*, Edited by M. Cardona and G. Guntherodt (Springer, Berlin, 1982), Vol. 2, p. 80.

MORPHOLOGICAL STABILITY OF Ni(Al)/Ni_3Al NANOLAMINATE COMPOSITES

JASON P. FAIN*, RAJARSHI BANERJEE*, DANIEL JOSELL**, PETER M. ANDERSON*, HAMISH FRASER*, NATALIA TYMIAK***, AND WILLIAM GERBERICH***
*Dept. MSE, The Ohio State University, 2041 College Rd., Columbus, OH 43210-1179, anderson.1@osu.edu.
**Materials B164 NIST 100 Bureau Dr, Stop 8554 Gaithersburg, MD 20899-8554.
***Dept. of Chemical Eng. and Materials Science, University of Minnesota, Minneapolis, MN.

ABSTRACT

This manuscript discusses the morphological instability observed when multilayered samples with alternating layers of γ-Ni(Al)/γ'-Ni_3Al are exposed to 800C for approximately 100 hours. Samples with 20nm/20nm or 120nm/120nm layer thickness and <001> or <111> crystal orientation to the interface normal were tested. Pinching off of layers is strongly affected by crystal orientation and layer thickness. Corresponding modeling suggests that the stability of this system is sensitive to fluctuations in the volume fraction of the two phases, the aspect ratio of columnar grains in the layers, and whether coherent or semi-coherent interfaces are present.

INTRODUCTION

Nanolayered materials consisting of alternating A/B type layers of metals exhibit large values of hardness that increase monotonically as individual layer thickness is decreased [1]. The large resistance to plastic deformation has been explained by considering dislocation motion that is confined to small volumes of material by numerous interfaces [e.g., 2]. However, if such materials are to be used at elevated temperature, a better understanding of the morphological stability of the layered structure at high temperature is needed.

The system studied is a multilayered version of γ-Ni(Al)/γ'-Ni_3Al. These phases form the basis for Ni-base superalloys that are used for turbine blade applications and that derive their strength from a fine dispersion of cuboidal γ' precipitates in a γ matrix. A morphological transition from a particulate to a lamellar, or rafted, microstructure with 180 nm layer thickness has been observed when NASAIR 100 superalloy is stressed at 140MPa for 50hrs at 1000C [3] and interfacial misfit dislocations appear to form as part of the process [4]. However, the creep properties of rafted material compared to the particulate morphology appear to be mixed [5,3,6].

This manuscript discusses the morphological stability of γ-Ni(Al)/γ'-Ni_3Al multilayers that are deposited by sputtering as to control both layer thickness and crystallographic orientation of the layers. The experimental observations from heating the samples to 800C for 101 hours are discussed in light of two models, which suggest regimes of columnar grain aspect ratio, interfacial energy, and volume fraction for which the multilayers are predicted to be stable.

EXPERIMENTAL PROCEDURE

Sample fabrication

Multilayered γ-Ni(Al)/γ'-Ni_3Al thin films were produced using dc magnetron sputtering. Prior to sputtering, a vacuum base pressure of less than 5×10^{-8} torr was produced and during sputtering, Argon pressure was maintained at 2×10^{-3} torr. Prior to introduction into the chamber, the Argon gas was gettered through a titanium sponge at 800C to increase purity. Cleaved <001> NaCl wafers were used for substrates and Ni-10wt%Al solid solution and Ni-

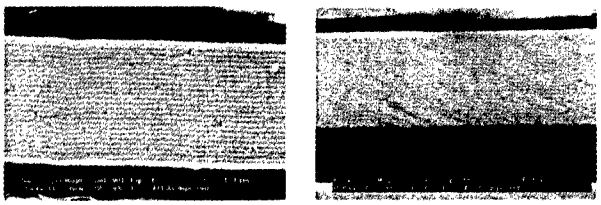
Mat. Res. Soc. Symp. Proc. Vol. 581 © 2000 Materials Research Society

25at%Al (Ni_3Al) targets were used. The target compositions were chosen based on reported equilibrium compositions for the γ-γ' system in the vicinity of 800C. Power to the targets was maintained at 200W DC during deposition.

Samples with both <001> and <111> crystal orientation to the interface normal were produced, with individual layer thickness ranging from 20nm to 120nm, and overall sample thickness from 5 to 7μm. The <001> oriented samples were produced by pre-baking cleaved <001> NaCl substrates to approximately 400C for approximately one hour and maintaining the substrate at a minimum of 400C during deposition. NaCl substrates were also used to deposit the <111> oriented samples, but no pre-baking or substrate heating was used. Following deposition, substrates were removed by dissolving them in water, so that free-standing γ-Ni(Al)/γ'-Ni_3Al thin films were produced.

Elevated Temperature Excursions

Four samples were chosen for exposure to elevated temperature: i. <001> 120nm γ // <001> 120nm γ'; ii. <111> 120nm γ // <111> 120nm γ'; iii. <001> 20nm γ // <001> 20nm γ'; iv. <111> 20nm γ // <111> 20nm γ'. Portions of the samples were enclosed in glass tubes under an Argon atmosphere to help maintain an oxidation-free environment. The samples were then heated continuously for 101 hours at 800C and then cooled to room temperature for characterization.



(a) –5μm— (b) –5μm–

Figure 1: As-deposited 120nm/120nm γ/γ' multilayer samples with (a) <001> and (b) <111> orientation.

Characterization

Prior to the elevated temperature excursion, all samples had a continuous layered morphology. Figure 1 shows representative backscattered scanning electron microscope (SEM) images of as-deposited <001> 120nm/120nm and <111> 120nm/120nm samples. The layers of γ-Ni(Al) appear lighter in contrast. The lamellar morphology is continuous in both cases, although the layers have some non-planarity, particularly for the <111> orientation. The 20nm/20nm multilayers are difficult to resolve well in a SEM, but display a layered morphology.

Additional characterization with X-ray diffraction and plan view and cross-sectional transmission electron microscopy (TEM) has been performed on layers produced in the same manner, but with a Ni rather than γ-Ni(Al) target. These studies reveal a strong <001> orientation for deposition at greater than 400C and a <111> orientation for deposition at lower temperatures. Faults are present in both <001> and <111> Ni/γ' samples. They lie along {111} planes of both Ni and Ni_3Al and appear to be more dense for the <111> oriented case. A parallel TEM study of the γ/γ' multilayers is in progress, with a goal to measure the in-plane dimension of the columnar grains in the multilayered samples, as an important parameter in the morphological stability theory to follow.

SEM images of the samples after heat treatment are shown in Fig. 2. There is evidence of breakdown of the layered structure in all cases, but especially so for samples with <111> orientation. The <111> 20nm/20nm sample has broken down the most to produce a polycrystalline sample with more or less equiaxed grains as large as 3μm. There is little evidence of any layered morphology after this heat treatment. The <111> 120nm/120nm sample also shows regions of severe breakdown, with grains as large as 2μm. However, there is

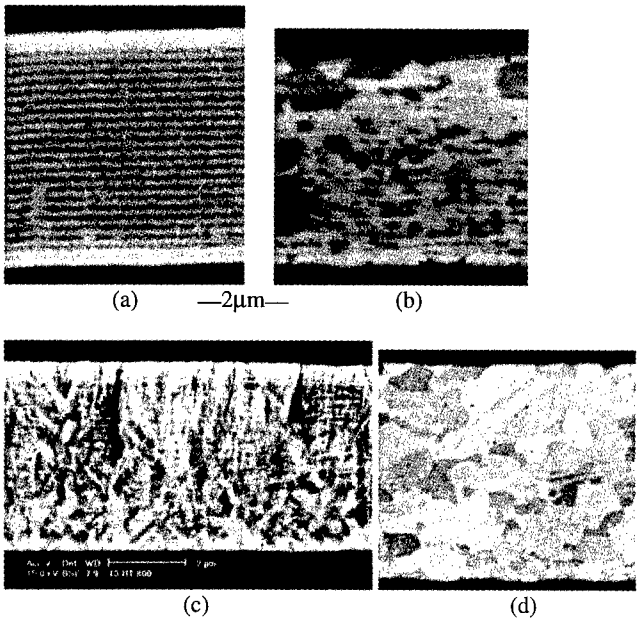


Figure 2: Backscattered scanning electron microscope images of γ/γ' multilayer samples after 101 hrs at 800C in an Argon environment, for (a) <001> 120nm/120nm, (b) <111> 120nm/120nm, (c) <001> 20nm/20nm, and (d) <111> 20nm/20nm

evidence of the original layered structure, in the form of horizontal bands of alternating grains of γ and γ'. The heights of the grains are comparable to the former layer thickness.

The samples with <001> orientation appear to have a broken-down layer morphology, but not to the extent displayed in the <111> cases. Further, the 120nm/120nm sample appears to be more stable than the finer 20nm/20nm case. The thicker layer sample has several locations at which layers of Ni_3Al have pinched off. Pinch off locations appear to be stacked vertically, so that the breakdown may have progressed vertically through the thickness of the sample. However, there are numerous locations along an individual Ni_3Al layer at which pinching off is in progress, and this produces a variation in layer thickness that is much more pronounced than in the as-deposited state.

The <001> 20nm/20nm sample shows a nonuniform breakdown of the layered morphology, ranging from grains as large as 0.5μm (bottom) to regions where layers are still in the process of pinching off (upper right). The overall image indicates that there are strong patterns of grain formation along diagonal directions through the multilayer.

In summary, all samples held at 800C for approximately 100hrs display a breakdown in multilayered morphology, but to different amounts. The <001> 120nm/120nm sample appears to have retained more of the multilayered morphology than the other samples, followed by the <001> 20nm/20nm case. The <111> 120nm/120nm sample retains little of the layer morphology and the <111> 20nm/20nm case retains none. The results suggest that samples with <001> orientation and larger layer thickness break down more slowly.

MODELING

Layer Breakdown based on Minimization of Interfacial and Grain Boundary Energies

It is well known that capillary forces affect the shape of a liquid vapor surface and wetting of a solid by a liquid and serve to minimize the excess free energy of the relevant liquid-vapor or liquid-solid interfaces. The same principles apply to a solid-solid interface and they have been used to determine conditions for the stability of multilayered materials [7, 8]. The concept is that

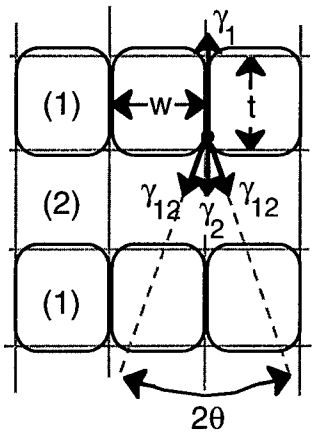


Figure 3: Geometry for pinching off of stacked columnar grains.

the morphology of a laminate will evolve toward a geometry that minimizes the sum of interfacial grain boundary free energies.

The layer geometry shown in Fig. 3 is considered relevant to modeling the multilayered samples. It assumes that columnar grains within a layer are stacked on top of one another. Prior to any elevated temperature excursion, each layer may be thought of as an array of square prisms with in-plane width w and height t. Thus, Fig. 3 is only a two-dimensional cross section of the structure. Upon heating, there will be a tendency to reduce area defect content and the layer with the larger grain boundary energy (layer type 1 in Fig. 3) will begin to pinch off. A basic equilibrium condition for the node shown in Fig. 3 is

$$2\gamma_{12}\cos\theta + \gamma_2 - \gamma_1 = 0 \qquad (1)$$

where γ_{12}, γ_2, and γ_1 are the energies per unit area of the interface, grain boundary in phase 2, and grain boundary in phase 1, respectively.

The stability issue amounts to determining the critical depth to which a groove will penetrate into layer type 1 before the equilibrium grooving angle θ is reached. To do so, the areas of interfaces and grain boundaries are varied to reach a minimum in area defect energy, subject to the constraint that the volume of a grain cannot change. The analysis predicts a critical initial aspect ratio, t/w, of columnar grains, below which the layer will pinch off. Clearly, stable multilayers are more likely when the magnitude of $(\gamma_1 - \gamma_2)/2\gamma_{12}$ is small. If this ratio exceeds 1, then there is no equilibrium θ possible and instability is predicted for all t/w. In the limit of $(\gamma_1 - \gamma_2)/2\gamma_{12} = 0$, multilayers with any t/w are predicted to be stable and for $(\gamma_1 - \gamma_2)/2\gamma_{12} \geq 1$, no multilayers are predicted to be stable.

Another geometry (not shown), with staggered placement of columnar grains in one layer relative to another, introduces a different mode of instability in which both layer types may pinch off. Although this geometry is not expected in as-deposited samples, grain boundaries may migrate to this staggered configuration at elevated temperature. The driving force to do so occurs since the area of the lower energy grain boundary (assumed to be γ_2 in Fig. 3) can be reduced significantly if the staggered geometry is adopted. The limiting scenarios for the staggered geometry are that all t/w are stable when $\gamma_1/2\gamma_{12}$ and $\gamma_2/2\gamma_{12}$ approach 0, and no values of t/w are stable when either $\gamma_1/2\gamma_{12}$ or $\gamma_2/2\gamma_{12}$ approach or exceed 1.

Layer Breakdown based on Minimization of Interfacial and Elastic Strain Energies

Sridhar et al. [9] consider instability of multilayers based on the computation of the elastic energy and interfacial energy of multilayered systems which are perturbed from a flat interfacial morphology. The analysis includes the change in elastic energy of layered structures with elastic misfit between layers but neglects the contribution from changes in energy of columnar grain boundaries. Stability for multilayered systems is described in terms of the misfit strain, mismatch $\alpha = (E_2 - E_1)/(E_2 + E_1)$ in Young's moduli of the two alternating layer types in the multilayer, and volume fraction f_2 of layer type 2. To summarize, stable morphologies occur when the layer type with the larger elastic modulus also has the larger volume fraction or equivalently, when the layer type with the smaller volume fraction also has the smaller elastic

modulus. Additional results are provided for externally stressed multilayers but since free-standing multilayers were tested, those results are not reviewed here.

RESULTS

Stability Plot for γ-Ni(Al)/γ'-Ni_3Al Multilayers based on Minimization of Grain Boundary and Interfacial Energies

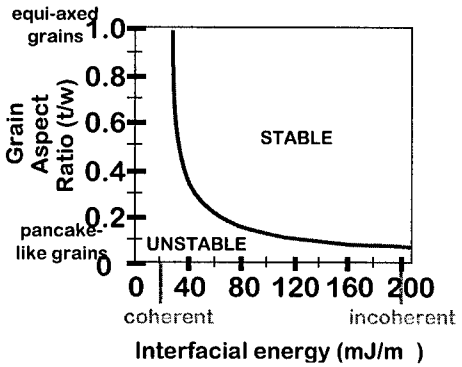


Figure 4. Stability plot for the γ-Ni(Al)/γ'-Ni_3Al multilayer system.

Figure 4 shows the predictions of the Josell theory to γ-Ni(Al)/γ'-Ni_3Al multilayers. Regions of stability and instability to pinching off of γ'(Ni_3Al) layers are shown as a function of columnar grain aspect ratio and energy of the γ/γ' interface. The plot is based on estimates of 866 mJ/m^2 for a γ-Ni(Al) grain boundary and 902 mJ/m^2 for a Ni_3Al grain boundary. They are obtained using both experimental measurements and theoretical predictions of grain boundary energies as summarized in Table I. There are no experimental or theoretical values for γ_{gb}(Ni(Al)). However, estimates for γ_{gb}(Ni) range from an experimental value of 866 mJ/m^2 to a theoretical value of 1210 mJ/m^2. We approximate $\gamma_{gb}(Ni(Al)) \approx \gamma_{gb}(Ni) = 866$ mJ/m^2, and use the experimental value since the theoretical estimate appears to be an overestimate [10]. A corresponding value $\gamma'_{gb}(Ni_3Al) = 902$ mJ/m^2 is adopted in Fig. 4, based on the observation that the theoretical value of $\gamma'_{gb}(Ni_3Al)$ in Table I is approximately 4% larger than the theoretical value of γ_{gb}(Ni).

Table I Grain Boundary and Interfacial Energies in mJ/m^2

Quantity	Exper.	Theor.	Value used in Fig. 4
γ_{gb}(Ni)	866 [11]	1210 [12]	
γ_{gb}(Al)	325 [11]		
γ_{gb}(Ni(Al))			866
$\gamma'_{gb}(Ni_3Al)$		1260 [12]	902
$\gamma_{\gamma/\gamma}$interface	10-20 [13] 200[14]		

Effect of Coherent and Incoherent Interface Structure

The stable versus unstable nature of γ-Ni(Al)/γ'-Ni_3Al multilayers in Fig. 4 depends on the value of interfacial energy. The most striking effect is that estimates of interfacial energy reported in Table I range from (10 to 20) mJ/m^2 for coherent <001> interfaces in γ-Ni(Al)/γ'-Ni_3Al superalloys with cuboidal particles to 200 mJ/m^2 for semicoherent interfaces in rafted γ-Ni(Al)/γ'-Ni_3Al structures. Thus, the stability diagram in Fig. 4 predicts that if interfaces are semicoherent, then γ/γ' multilayers with grain boundary aspect ratios t/w > 0.1 would be *stable*. Multilayers with coherent interfaces, with $\gamma_{\gamma/\gamma}$interface ~ 20mJ/m^2 are predicted to be *unstable* for all t/w shown.

Stability Plot for γ-Ni(Al)/γ'-Ni_3Al Multilayers based on Minimization of Interfacial and Elastic Energies

The theory by Sridhar et al. [9] can be applied to γ-Ni(Al)/γ'-Ni_3Al multilayers of equal volume fraction by selecting $f_{Ni(Al)} = 0.5$ and estimating $\alpha = (E_{Ni(Al)} - E_{Ni_3Al})/(E_{Ni(Al)} + E_{Ni_3Al})$. Based on work by Gada et al. [15], $E_{Ni(Al)} = 134$ GPa and $E_{Ni_3Al} = 113$GPa at 25C, but $E_{Ni(Al)} = 72$ GPa and $E_{Ni_3Al} = 81$ GPa at 1000C. Thus, α ranges from +0.08 at 25C to -0.06 at 1000C. At 500C, α is nearly zero. It is most appropriate to apply the stability condition at elevated temperatures at which diffusion can take place but regardless, the theory predicts that multilayers with equal volume fraction should be stable for all values of α. However, the theory does show that for negative values of α that are anticipated at elevated temperature, modest deviation in $f_{Ni(Al)}$ to greater than 0.5 may cause instability. Since the energetic contribution of grain boundaries is not considered, the theory is expected to predict stability when, in fact, multilayers with columnar grains are unstable.

CONCLUSIONS

Multilayers consisting of alternating layers of γ-Ni(Al) and γ'-Ni_3Al appear to be inherently unstable to pinching off of γ'-Ni_3Al layers when held at 800C for 100 hours. However, the rate at which pinching off occurs is larger for 20nm/20nm than for 120nm/120nm layer thickness, and much larger for samples with <111> compared to <001> crystal orientation to the interface normal. Models based on minimization of interfacial and grain boundary energies and elastic energy suggest that such multilayers are more stable to pinching off when they have semi-coherent or incoherent interfaces, columnar grains with a large needle-like aspect ratio, and uniform layer thickness so that the volume fraction of each layer type does not deviate from 0.5.

ACKNOWLEDGEMENTS

PMA and JPF acknowledge the support of the Air Force Office of Scientific Research Grant F49620-96-1-0238.

REFERENCES

1. B.M. Clemens, H. King, S.A. Barnett, MRS Bulletin **24(2)**, p. 20 (1999).
2. P.M. Anderson, T. Foecke, and P.M. Hazzledine, MRS Bulletin **24(2)**, p. 27 (1999).
3. M.V. Nathal, R.A. MacKay, and R.V. Miner, Metall. Trans. A **20A**, p. 133 (1989).
4. O. Paris, M. Fahrmann, E. Fahrmann, T.M. Pollock, and P. Fratzl, Acta Mater. **45(3)**, p. 1085 (1997).
5. R.A. MacKay and L.J. Ebert, Metall. Trans. A **16A**, p. 1969 (1985).
6. P. Caron, P.J. Henderson, T. Khan, and M. McLean, Scripta Metall. **20**, p. 875 (1996).
7. D. Josell, S.R. Coriell, and G.B. McFadden, Acta Metall. Mater. **43(5)**, p. 1987 (1995).
8. D. Josell and F. Spaepen, MRS Bulletin **24(2)**, p. 39 (1999).
9. N.J. Sridhar, J.M. Rickman, and D.J. Srolovitz, Acta Mater. **45(7)**, 2715 (1997).
10. A. Ardell, personal communication with JPF (1998).
11. L.E. Murr, *Interfacial Phenomena in Metals and Alloys*, Addison-Wesley, NY (1975).
12. S.P Chen, D.J. Srolovitz, and A.F. Voter, J. Mater. Res. **4(1)**, p. 62 (1989).
13. C. Marsh and H. Chen, Acta Metall. Mater. **38(11)**, p. 2287 (1990).
14. Y. Mishin, N. Orekhov, I. Razumovskii, G. Alyoshin, and P. Noat, Mater. Sci. Eng. **A171**, p. 163 (1993).
15. J. Gada and R.A. MacKay, Scripta Metall. **23**, p. 1835 (1989).

RELATIONSHIP BETWEEN THERMALLY ACTIVATED ATOMIC DIFFUSION PROCESSES IN Co–Cu NANOSCALE GRANULAR FILMS AND ELECTRIC/MAGNETIC PROPERTIES

F. Spizzo[a], F. Ronconi[a], P. Vavassori[a], G. Bordin[a], D. Bisero[a], L. Pareti[b] and G. Turilli[b]
[a] INFM and Department of Physics, University of Ferrara, Italy
[b] MASPEC-CNR, Parma, Italy

ABSTRACT

Co–Cu multilayer granular films deposited onto Si substrates have been submitted to thermal treatments in scanning mode. Their magnetisation and resistance have been studied after applying two different heating rates. The comparison between the experimental data measured before and after the treatment points out that the effect of the annealings depends strongly on the heating rate used. We also present XPS data collected as a function of depth to show how the different heating rate modify the composition and chemical environment produced by thermal treatments.

INTRODUCTION

The discovery of giant magnetoresistance (GMR) in magnetic granular materials has raised more and more interest on these systems thanks to the ease of their production, the possibility of gaining information regarding electronic conductivity in multilayers and the possibility of studying systems with arbitrary magnetic configuration [1]. Usually, thermal treatments have relevant effects when applied on this kind of systems; in particular, they may allow tailoring the magnetoresistive properties of the as–prepared materials and to change the dependence of their magnetisation on applied magnetic field. These modifications in magnetic and magnetoresistive behaviour of the samples are related to structural changes regarding, for example, the crystalline structure of the grains [2], their dimensions as well as their relative distances [3]. Experimental techniques such as transmission electron microscopy (TEM) or X–ray diffraction (XRD) are widely used to gain information about the structure of granular materials [4]; on the other side, when the grains are very small or the material is characterised by structural defects such techniques are not always effective in providing an estimation of the dimensions or the distribution of the grains [5]. In this case magnetisation curves, susceptibility and resistivity measurements can give insights about the nanometric structure of superparamagnetic–diamagnetic granular media. In this paper, we induce the diffusion of atomic species submitting Co–Cu granular systems to thermal annealings with different heating rate (HR). We then study the modifications the system undergoes to with magnetic and resistive measurements and perform XPS analysis to detect possible changes in samples composition.

EXPERIMENTAL

The granular materials have been obtained depositing alternately very thin cobalt and copper layers onto Si substrates by RF–sputtering in Ar atmosphere. The nominal thickness are 0.4 nm for Co and 1.4 nm for Cu; the whole film is 80 nm thick. Resistivity measurements at various temperatures have been performed with the Van der Pauw method. Magnetisation curves have been measured with an alternating gradient field magnetometer (AGFM) at room temperature and with a vibrating sample magnetometer (VSM) as a function of temperature. Thermal treatments have been performed by a differential scanning calorimeter (DSC) in

Mat. Res. Soc. Symp. Proc. Vol. 581 © 2000 Materials Research Society

scanning mode with Ar flowing inside the sample holder in laminar regime. We used two different HR, 10 K/min and 20 K/min, and during each annealing the temperature of the sample was varied starting from 373 K (initial temperature) up to 773 K (final temperature). Every sample has been submitted to more than one thermal treatment with the same HR. XPS measurements have been performed with a synchrotron light source at the SuperEsca beamline with photon energies equal to 183 eV and 650 eV. The XPS data have been collected at various depths inside the sample after etching procedure.

RESULTS

The in–plane magnetisation curve of the as–prepared sample is reported in fig. 1(a): it doesn't show a coercive field and displays superparamagnetic features. The loop can be well approximated by a weighted sum of Langevin functions [5], $\sum_{i=1}^{N} p_i L(\mu_i H/kT)$, where μ_i is proportional to the volume V_i of the non–interacting Co particles. The best fit is obtained when we use just two values of μ_i, μ_1 and μ_2; if we suppose to have disk–like particles and that $\mu_i = M_{sat}^{Co} \cdot V_i$ we find that their mean diameters are 8 and 2 nm, respectively. The superparamagnetic nature of the samples is confirmed by the presence of a broad maximum in the susceptibility curve as a function of temperature ascribable to the average blocking temperature of the cobalt particles [6].

Resistivity of the as–prepared samples, ρ_o, depends linearly on temperature between 40 K and 300 K and $\partial\rho_o/\partial T > 0$ (fig. 1(b)). Its value at room temperature (RT) is 31 $\mu\Omega$·cm and the value of ρ_o extrapolated at 0 K is 23 $\mu\Omega$·cm. The higher value of ρ_o(300 K) respect to those of Co and Cu (ρ_{Co} equals to 5.8 $\mu\Omega$·cm and ρ_{Cu} to 1.7 $\mu\Omega$·cm at RT) and the small value of the temperature–dependent contribution to ρ_o, $(\rho_o(300\text{ K})-\rho_o(0\text{ K}))/\rho_o(300\text{ K}) \approx 0.25$, evidence the presence of strong structural disorder [7]. Magnetoresistance of as–grown samples, $\Delta\rho_o(H)/\rho_o=(\rho_o(H)-\rho_o(H=0))/\rho_o(H=0)$, exhibits GMR features and its value is about – 5 % with an applied field of $1.2 \cdot 10^6$ A/m (see the inset of fig. 1(a)).

The heat treatment performed with the higher HR (20 K/min) produces the effects shown in fig. 2. The magnetisation curve M(H) at room–temperature (fig. 2(a)) shows an hysteresis loop with a coercive field of $16 \cdot 10^3$ A/m and a relative remanence equal to

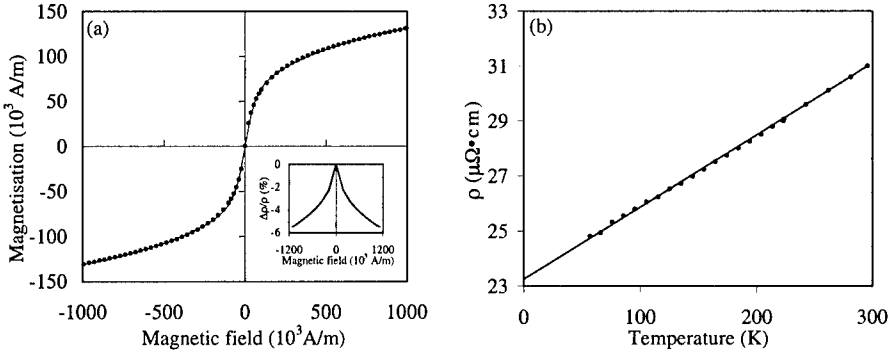


Figure 1: Measurements on the as–prepared sample: (a) magnetisation curve (dots) and fit performed with Langevin functions (line); the inset shows the magnetoresistance at RT. (b) Resistance as a function of temperature.

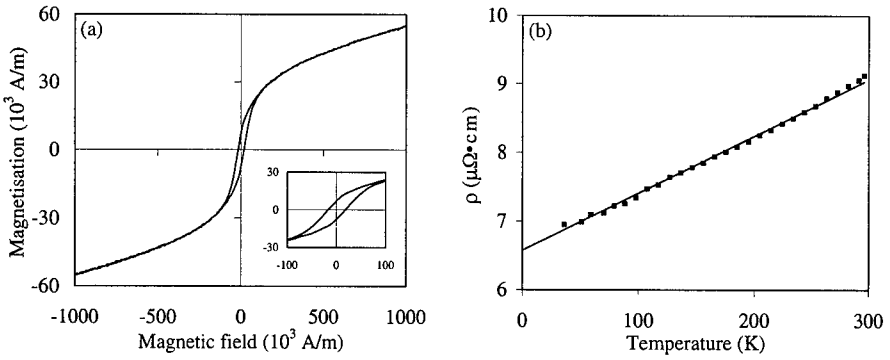


Figure 2: Measurements after thermal annealing at 20 K/min: (a) magnetisation at room temperature and (b) resistance as a function of temperature.

$7 \cdot 10^3$ A/m; furthermore the magnetisation measured with an applied field of $H_{max} = 1.5 \cdot 10^6$ A/m is about one half respect to the as–prepared sample. If we consider M(H) as the sum of two major contributions, one relative to the hysteretic part of the curve at low field and the other relative to the superparamagnetic part at high field we find that the latter is well approximated by a Langevin function corresponding to Co disks with a value of μ very similar to the value μ_2 found in the as prepared sample. This might mean that after the treatment the biggest particles have coalesced, determining the ferromagnetic contribution, while the smallest ones are still dispersed inside the Cu matrix. The decrease of $M(H_{max})$ (about one half respect to the as–grown sample) can be explained assuming that the thermally activated diffusion processes might have produced a partial oxidation of Co grains, giving origin to paramagnetic species, and thus reducing their contribution to magnetisation.

Room temperature resistivity of the samples treated with HR = 20 K/min, ρ_{20}(300 K), is lower than ρ_o(300 K) and its dependence on temperature is still metal–like, that is $\partial\rho_{20}/\partial$T is constant and positive (fig. 2(b)). Further annealings performed on the same sample do not alter significantly the effects observed after the first one. This possibly means that the leading effect of diffusion processes is to promote the growth of a ferromagnetic phase.

Differently, we observe that treatments performed with HR = 10 K/min produce a deeper modification on conductivity and magnetisation of the samples. Indeed, their room temperature resistivity, ρ_{10}(300 K), after the series of annealing has a value about two orders of magnitude higher than ρ_o(300 K). Its dependence on temperature, as well, is strongly modified and, after three thermal treatments, $\partial\rho_{10}/\partial T$ is negative, it changes with temperature and $\rho_{10}(40\text{ K})/\rho_{10}(300\text{ K}) \sim 10^3$ (fig. 3(b)). These results are not detected with HR = 20 K/min under the same total treatment time, suggesting that thermally activated processes could depend on solid state reaction kinetic due to the metastable nature of the as–prepared samples. With total treatment time we indicate the product $n \cdot \text{HR}^{-1} \cdot \Delta$T, where n is the number of treatments and ΔT is the temperature range.

In the same film, room–temperature magnetisation measured at H_{max} is one order of magnitude lower than that measured in the as–prepared sample and magnetisation curves do not show hysteresis (fig. 3(a)). In our opinion, these results may be interpreted as a sigmoidal feature at low fields that could be produced by a small ferromagnetic component superimposed to a paramagnetic signal. The properties showed by this sample clearly in-

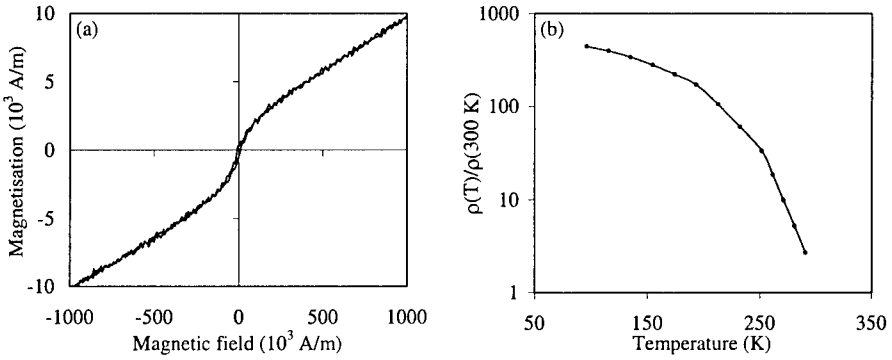


Figure 3: Magnetisation as a function of magnetic field (a) and reduced resistivity as a function of temperature (b) after thermal annealings at 10 K/min.

dicate that the original film structure and composition have been deeply changed by the thermal treatments performed with HR = 10 K/min. In order to detect possible modifications in composition or chemical environment inside the film we have performed XPS measurements at various depths inside the sample [8].

The analysis of experimental data (see fig. 4) points out that the binding energy of the Co3p peak is higher with respect to that measured in the as-prepared sample and its lineshape is different. Furthermore, the area of this peak increases with depth. Differently, $Cu3p_{1/2}$ and $Cu3p_{3/2}$ levels have not been modified by the treatments. Inside the treated film we also observe the presence of peaks of non-metallic species: silicon and oxygen. XPS data supports the hypothesis that Co has reacted with oxygen and that silicon has diffused into the film.

CONCLUSIONS

We have studied the influence of diffusion processes activated by annealings performed in scanning mode on magnetisation and resistivity in Co-Cu granular multilayers. The results indicate that the as-prepared samples are characterised by strong structural disorder and are constituted of Co disk-like non-interacting particles having a bimodal distribution of dimensions. The major effect of thermal treatments with HR = 20 K/min is the coalescence of the biggest particles producing an appreciable ferromagnetic contribution to the magnetisation. On the other hand, annealing with HR = 10 K/min is connected with a strong modification of magnetisation curves, a great increase of resistivity at room temperature and a modification of its dependence on temperature. XPS measurements point out the presence of diffusion processes involving cobalt as well as silicon and support the presence of Co oxide. Further analysis is planned in order to explain the influence that reaction kinetic has on thermal treatments.

ACKNOWLEDGEMENTS

The authors wish to thank Terry Wood of Oxford Instruments for the magnetic measurements by vibrating sample magnetometer. This work was supported by Ministero dell'Università e della Ricerca Scientifica e Tecnologica (MURST) Istituto Nazionale per

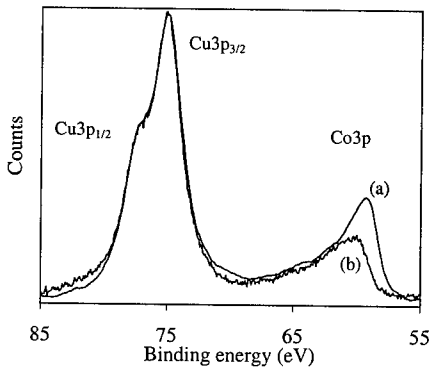


Figure 4: $Cu3p_{1/2}$, $Cu3p_{3/2}$ and Co3p peaks before (a) and after (b) the treatment at HR = 10 K/min.

la Fisica della Materia (INFM) and Consiglio Nazionale delle Ricerche (CNR).

REFERENCES

[1] H. E. Cablong, S. Zhang, and P. M. Levy, J. Appl. Phys. **75**, 6906 (1994).

[2] H. Sato, O. Kitakami, T. Sakurai, Y. Shimada, Y. Otani, and K. Fukamichi, J. Appl. Phys. **81**, 1858 (1997).

[3] P. Allia, M. Knobel, P. Tiberto, and F. Vinai, Phys. Rev. B **52**, 15398 (1995).

[4] J. Q. Wang and G. Xiao, Phys. Rev. B **49**, 3982 (1994).

[5] N. Peleg, S. Shtrikman, G. Gorodetsky, and I. Felner, J. Magn. Magn. Mat. **191**, 349 (1999).

[6] J. L. Dorman, D. Fiorani, and E. Tronc, Advances in Chemical Physics **98**, 283 (1997).

[7] George Terence Meaden, *Electrical resistance of metals* (Heywood books, London, 1965).

[8] D. Bisero, G. Bordin, M. Minelli, F. Ronconi, F. Spizzo, A. Baraldi, S. Lizzit, G. Paolucci, L. Pareti, and G. Turilli, to be published on Nanostructured Materials .

Understanding the Second Harmonic Generation of Light from Nanometal Composites

M. L. Sandrock, Colby A. Foss, Jr.*
*Dept. of Chemistry, Georgetown University, Washington, DC 90057,
fossc@gusun.georgetown.edu

ABSTRACT

We have synthesized two sets of nanometal composites of different metal concentrations via electrodeposition of gold into porous aluminum oxide membranes[1,2] Within each set, both centrosymmetric and non-centrosymmetric particles were produced whose linear and nonlinear optical effects were investigated.

Because our method of template synthesis allows for the close examination of our composite materials in terms of shape, size, and symmetry, we can interpret the SHG response in terms of differences in local field enhancements of magnetic dipole and quadrupole modes.[3]

INTRODUCTION

It is well-known that nanoscopic metal particles can exhibit strong absorption and/or scattering bands in the visible spectrum. This effect allows for a wide variety of practical applications of nanoscopic metal systems in the fine arts,[4] surface-enhanced spectroscopy,[5,6] and biochemistry.[7] Additionally, the size and shape of these particles can be tuned to produce the desired linear optical effects, such as a specific spectral band position (λ_{max}).

The wavelength of maximum optical extinction, as well as the wavelength of optimal local electric field enhancement, depends on such factors as the size, shape, and orientation of the particle, as well as spacing between particles.[8-10] Thus, we recently extended the template synthesis method to prepare nanoparticles that differ in symmetry and size. In doing so, we are able to probe the mechanisms for the second order nonlinear response of these materials.

In this paper, we describe the details of the synthesis of non-centrosymmetric gold particle pair structures. We also discuss the UV/vis/near-IR linear polarization spectra of non-centrosymmetric gold particle/porous aluminum oxide film composites and their symmetric gold particle analogues for two distinct sizes. Finally, we present the results of an SHG study from these composite materials and begin to discern the possible mechanisms for this nonlinear effect.

EXPERIMENT

Porous Aluminum Oxide Synthesis

Porous aluminum oxide films were prepared using the anodization/voltage reduction method of Furneaux, et al.[11] The details of our procedure have been given elsewhere.[12,13] In this study, we employed porous alumina films prepared via anodization of aluminum foil (Aldrich, 99.999 %) at 20 V in 6 % sulfuric acid at 0 °C. The mean pore diameters of these films were determined (via TEM analysis) to be 32 ± 1 nm. Typical film thicknesses were in the 40 - 60 μm range.

Gold Nanoparticle Preparation

The porous alumina membranes were used as a template to synthesize gold particles of different symmetries. The barrier side of the film was sputtered with ca. 45 nm of silver using an Anatech Hummer 10.2 plasma deposition device. The silver coated oxide film was then attached to a three-electrode cell equipped with an Ag/AgCl reference electrode and a platinum mesh counter electrode. The power source was an EG & G Princeton Applied Research Model 273A Potentiostat. Nitrogen was purged into the system for mixing.

Mat. Res. Soc. Symp. Proc. Vol. 581 © 2000 Materials Research Society

The details for this synthesis are reported elsewhere.[1] Symmetric gold particles were prepared by depositing 0.3 C Au and 0.6 C Au over the 3.14 cm^2 area for small and large particles, respectively. Additionally, for non-centrosymmetric particles, 0.1 C of Au was first deposited over the area, followed by another layer of Ag (0.1 C) and finally another layer of Au (0.2 C for small particles and 0.5 C for large particles).

All of the composites were immersed in nitric acid (69-71 % EM), to dissolve any silver, leaving only gold in the pores. The composite films were rinsed with deionized water, ethanol, and acetone and air-dried. The procedure for preparing both types of particle composites is summarized in **Figure 1**.

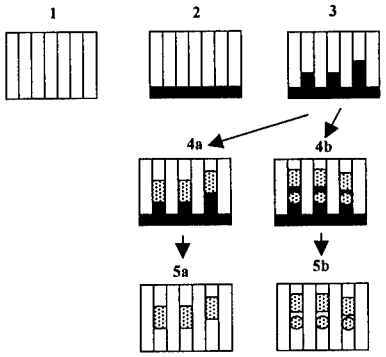


Figure 1. Schematic of nanoparticle synthesis: (1) porous anodic alumina film after detachment from Al substrate; (2) one face of alumina film coated with silver using plasma deposition; (3) electrodeposit silver foundation into pores; (4a) electrodeposit gold onto silver foundation to form centrosymmetric gold particles; (4b) electrodeposit layers of gold, silver, and then a second layer to form noncentrosymmetric gold particles; (5a and 5b) immerse film in nitric acid to remove silver foundation and silver spacing segments.

Nanoparticle Characterization

Transmission electron microscopy was used to characterize the dimensions of the template synthesized gold nanoparticles. Additional sample preparation was required in order to obtain TEM (transmission electron microscope) images. The gold particle composite films were embedded in a resin and heated at 70 °C for 12 hours. A 70 μm section was cut using a diamond knife (SPI Inc.) and placed on a Formvar-coated Cu grid (200 mesh, EM Sciences). The samples were then examined with a JEOL 1200 EX transmission electron microscope.

Linear Optical Analysis

The linear polarization analysis of the composite films was performed using a Hitachi U - 3501 spectrophotometer equipped with a 210-2130 polarizer accessory. Extinction spectra were obtained between λ = 350 nm and λ = 800 nm at normal incidence (defined as $\theta = 0^\circ$, and corresponding to the case where the incident electric field is perpendicular to the pore axes), and at incidence angles $\theta = 20^\circ$, 30°, and 45°, under p-polarization (the incident electric field polarized parallel to the plane of incidence). A schematic of the sample/polarizer configuration is shown in **Figure 2**.

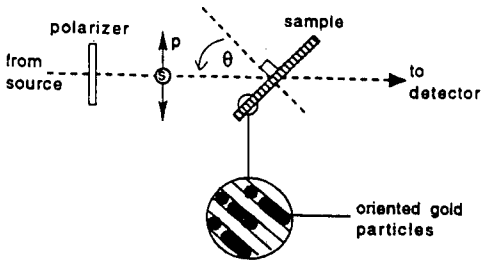


Figure 2. Schematic of polarzation spectroscopy setup. The sample film is rotated about an axis perpendicular to the page. The angle of incidence is indicated by θ. p-Polarization corresponds to an incident electric field in the plane of the page. s-Polarization corresponds to an electric field oscillating perpendicular to the page.

Second Harmonic Generation Studies

The SHG studies employed a high repetition rate femtosecond titanium-sapphire laser system, which was constructed following the design of Murnane[14] and pumped by an Argon-Ion laser (Spectra Physics 2060). The Ti:sapphire laser has a tunable output range of 710 to 900 nm. We restricted our initial studies to an output of 780 nm. The pulse widths employed were ca. 150 fs at an 80 MHz repetition rate. The average power was 100-300 mW, corresponding to an energy of ca. 3 nJ per pulse. The details of this experiment have been described in detail elsewhere.[1] **Figure 3** shows a schematic of the optical bench used in the SHG studies.

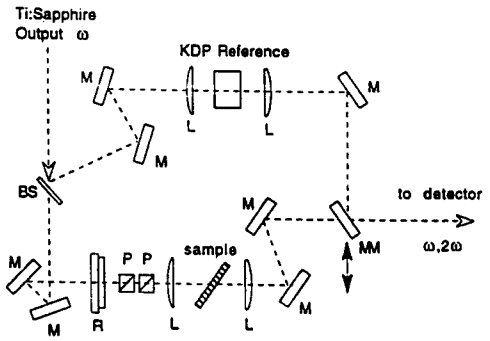


Figure 3. Schematic of second harmonic generation optics bench. Meaning of symbols: BS, beam splitter; M, stationary mirror; R, retarder; P, polarizer; L, lens; MM, moving mirror to select sample or reference beam for measurement.

Results and Discussion

Transmission Electron Microscopy

TEM images were obtained for all porous anodic alumina films containing centrosymmetric and non-centrosymmetric gold structures. The non-centrosymmetric structures consist of two segments of gold, one roughly spherical and the other rod-like in geometry. For the small particle systems, the longer segments of the non-centrosymmetric pair particles show an average length a = 37 ± 6 nm, and the smaller segments have an average length a = 27 ± 5 nm. The diameter of the particles is ca. 26 ± 3 nm. The surface-to-surface separation distance between the two segments is 22 ± 8 nm. The centrosymmetric particles have an axial length a = 54 ± 7 nm and a diameter b = 30 ± 4 nm.[1]

In the larger particle systems, the single rod centrosymmetric structures have an average length a = 133 ± 20 nm and diameter b = 31 ± 4 nm. The non-centrosymmetric pair structures are composed of the rod-like segment (a= 100 ± 10 nm, b = 33 ± 4 nm) and the sphere-like

segment (a = 34 ± 5 nm, b = 33 ± 4 nm). The surface-to-surface separation distance between the rod and sphere segments is 57 ± 13 nm.[2]

Linear Polarization Spectra

Figures 4 and **5** show the UV/Vis spectra of various Au/particle/alumina composites at four incidence angles under p-polarization. Figures **4A** and **4B** show the polarization spectra for both symmetries (centro- and non-centrosymmetric, respectively) of 0.3 C Au particles (small particles) and **Figures 5A** and **5B** depict the spectra for both symmetries of 0.6 C Au particles (large particles). An in-depth discussion on these results is given elsewhere.[1,2,13] However, it is important to notice that as the particles grow longer, the long axis plasmon absorption band red shifts.

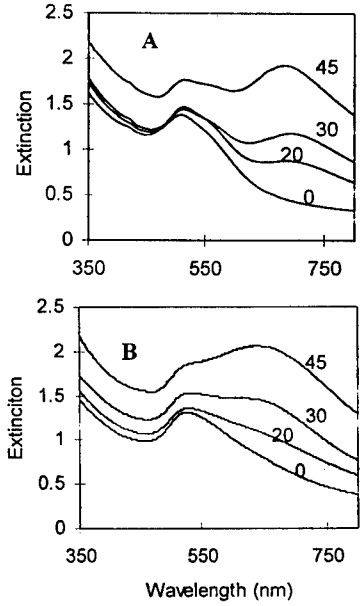


Figure 4. UV/visible p-polarization spectra: (A)centrosymmetric Au particle/alumina composite; (B) noncentrosymmetric Au pair/alumina composite. Incidence angles indicated next to curves. "Extinction" abscissa is unitless and corresponds to spectrometer "absorbance" output. However, the measured extinction includes losses due to absorption, scattering and reflectance. All measurements were made in double-beam mode, with no material in the reference beam.

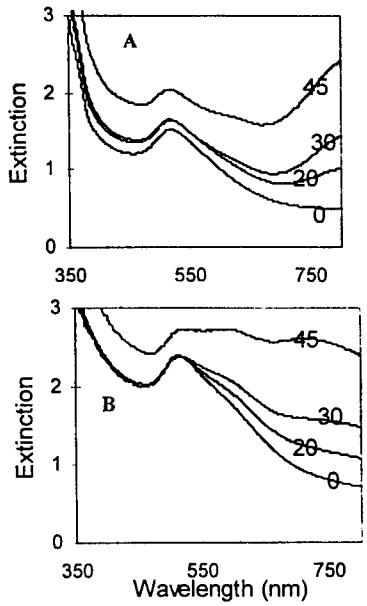


Figure 5. UV/visible p-polarization spectra: (A)centro-symmetric Au particle/alumina composite; (B) non-centrosymmetric Au pair/alumina composite. Incident angles are indicated next to curves.

SHG Analysis

In the SHG studies, we examined the same centro- and non-centrosymmetric Au particle alumina composite samples considered in the polarization spectroscopic measurements. For all

sample types, we measured SHG intensities at normal incidence and incidence angles of 20°, 30°, and 40°, under s and p-polarization. **Figure 6** summarizes the results of the studies in p-polarization. In all cases, the SHG counts from the Au particle/alumina samples are normalized against the counts from the KDP reference. The error bars are based on the results of measurements on three different locations of the composite films. We should also note that SHG studies on porous oxide films containing no gold were also performed, and showed negligible signals for all incidence angles and polarizations.

With our laser system, SHG yields are small (8 -30 counts) for the 0.3 C Au centro-symmetric particles. The signal shows a small increase with incidence angle θ. In contrast, SHG yields for the small particle systems lacking inversion symmetry range from 4 to 210 counts. The SHG counts under p-polarization increase dramatically with incidence angle (ca. 30-200 counts). At θ = 40°, the normalized SHG counts are about 6 times higher than the corresponding signal for the centrosymmetric particle composite (**Figure 6A**).

The observed dependence of the SHG signal on incidence angle for the non-centrosymmetric particles under p-polarization is reasonable in two respects. Firstly, as the incidence angle increases, the component of the incident electric field directed along the asymmetry axis (the axis perpendicular to the rotation axis of the rod) of the gold pair-particle structure increases. Secondly, enhancement effects associated with the long-axis dipolar plasmon resonance are increased with θ.

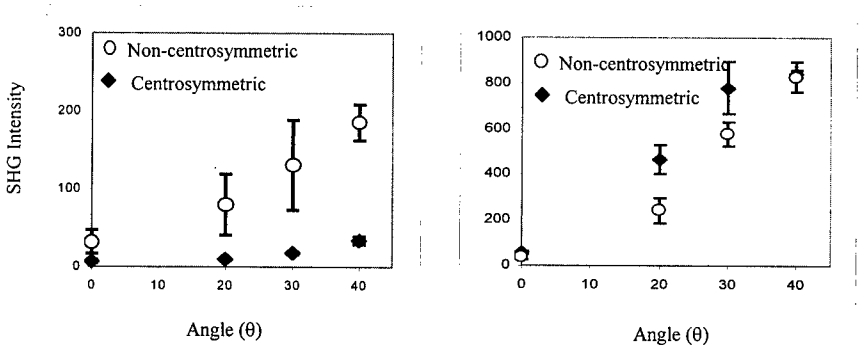


Figure 6. Second Harmonic generation (SHG) intensity as a function of the angle of incidence. (A) smaller ca. 60 nm particles (B) larger ca. 130 nm particles. Circles correspond to noncentrosymmetric particles and diamonds correspond to symmetric particles.

The connection between the linear spectra and the local field enhancement factor R for SHG can be seen in the approximate expression[15,16]

$$R = |L^2(\omega)L(2\omega)| \qquad (1a)$$

where the function L is given by:

$$L(\omega) = \left(\frac{\varepsilon_o(\omega)}{L_x(\varepsilon_m(\omega) + \kappa\varepsilon_o(\omega))} \right)^2 \qquad (1b)$$

Thus, the local field and R are large when either the fundamental frequency (ω) or the second harmonic (2ω) is close to a plasmon resonance.

We calculated the local field enhancement factors for gold rods of various aspect ratios in a non-absorbing host (refractive index n_o = 1.33 at both λ = 780 nm and λ = 390 nm). The optical constants of gold were taken from Johnson and Christy.[17] In the quasi-static limit, where the gold particle dimensions are assumed to be negligibly small compared to the incident wavelength, R becomes significant only for particles with aspect ratios greater than ca. 2.5, which is clearly greater than a/b for the smaller Au particles considered in our experiments. However, if particle size is incorporated into L_x and κ,[9,18] R becomes significant at lower aspect ratios, reaches a maximum at a/b $\approx$ 2.5, and then decreases as the particles become more needle-like (see **Figure 7**).

The enhancement factor curves shown in **Figure 7** pertain specifically to an incident electric field, which is parallel to the axis of rotation of the particles. When the electric field is perpendicular to the rotation axis, the calculated enhancements are negligibly small. Thus, at normal incidence (θ= 0), R is very small. In p-polarization as θ increases, a greater component of the electric field is parallel to the long axis, and R increases.

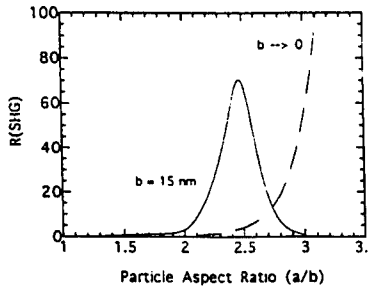


Figure 7. Calculated SHG local field enhancement factors as a function of particle aspect ratio for gold particles where incident wavelength is 780 nm, and second harmonic output wavelength is 390 nm. Dashed curve corresponds to quasistatic limit where particle dimensions are assumed to be negligibly small relative to λ. Solid curve: SHG local field enhancement calculation taking into account dynamic depolarization and radiation damping in rod-like particles of radius 15 nm.

The local field model also explains in part the observed SHG in the centrosymmetric particle composites. From the dipole approximation treatment of nonlinear optical processes, we would not expect to observe SHG from small centrosymmetric particles.[19,20] However, metal spheres a few nanometers in diameter or larger can support quadrupolar electric and magnetic induction modes, which in theory can give rise to SHG.[21-23] With the small particle experiment, the dimensions of the Au particles are such that quadrupole modes would necessarily be quite weak (we do not observe quadrupole bands in the linear spectra), local field enhancements must play an important role in the SHG from the centrosymmetric particles. The observation that SHG counts increase for p-polarized excitation (**Figure 6A**) is consistent with a local field enhanced process.

For the 0.6 C Au large particle systems, although we observe the expected increase of SHG intensity with incidence angle (centrosymmetric particles ca. 54 - 859 counts and non-centrosymmetric particles ca. 27 - 894 counts). We do not observe any significant difference in SHG intensity between centrosymmetric and non-centrosymmetric particle composites (**Figure 6B**). Upon inspection of the linear spectra, we can see that there is a large absorption corresponding to the fundamental frequency of the incident field in the SHG studies; however,

these particles are too large to support local field enhancements. When dynamic depolarization and radiation damping are taken into account, the large particles (aspect ratio ca. 4) should show negligible enhancements due to resonance of the plasmon absorption band with the fundamental frequency (**Figure 7**).

When particles become a significant in size as related to the incident field, we see that symmetry no longer plays an important role as it does for smaller particles. In fact, for ca. 130 nm particles, there is no significant difference in SHG intensity as a function of incidence angle for the particles differing in symmetry. Moreover, local field enhancements become negligible as well. Thus, there is a possibility that we are activating quadrupole and/or magnetic induction modes. The dipole approximation is no longer an appropriate framework when looking at these larger particles. In fact, SHG has been generated under the same experimental conditions for 150 nm gold spheres. In this case, we are activating the quadrupole modes of the particle.

CONCLUSIONS

We have prepared centro- and non-centrosymmetric Au particle composites of different sizes in porous anodic alumina hosts using an electrochemical template synthesis method. The linear polarization spectra of the materials reveal that all types of composites are dichroic under p-polarization for incidence angles > 0.

Second harmonic generation studies of both small and large centro- and non-centrosymmetric particle composites reveal that the SHG intensity under p-polarized extinction increases with incidence angle (i.e., as the component of the incident electric field parallel to the asymmetry axis increases). These observations are consistent with local field enhancements arising from long-axis dipolar resonances. As the particles get larger, symmetry no longer plays an important role in the generation of SHG and local field enhancements are less than optimal. Rather, electric quadrupole and magnetic dipole effects must be taken into account to understand the mechanism for the production of the second harmonic generation of light.

ACKNOWLEDGEMENT

The authors are grateful to the National Science Foundation for its support of this work (Grant DMR 9625151). M.L.S. also acknowledges the support of the ARCS Foundation.

REFERENCES

1. Sandrock, M.L.; Pibel, C.D.; Geiger, F.M.; Foss, C.A., Jr., J. Phys. Chem B.,**103**, 2668 (1999).
2. Sandrock, M.L.; Foss, C.A., Jr., J. Phys. Chem. B., **December 1999** (accepted).
3. Leitner, A. Molecular Physics, **2**, 197 (1990).
4. Lam, D.M.K.; Rossiter, B.W., Scientific American, **November 1991**, 80.
5. Chumanov, G.; Sokolov, K.; Gregory, B.W.; Cotton, T.M., J. Phys. Chem, **99**, 9466 (1995).
6. Moskovits, M., Rev. Mod. Phys., **57**, 783 (1985).
7. Storhoff, J.J.; Eighanian, R.; Mucic, R.C.; Mirkin, C.A.; Letsinger, R.L., J. Am. Chem. Soc., **120**, 1959 (1998).
8. Kerker, M. Ed. *Selected Papers on Surface-Enhanced Raman Scattering*; SPIE Optical Engineering Press: Bellingham, WA, 1990.
9. Zeman, E.; Schatz, G.C. J. Phys. Chem., **91**, 634 (1987).
10. Bergman, D.J.; Nitzan, A., Chem. Phys. Lett., **88**, 409 (1982).
11. Furneaux, R.C.; Rigby, W.R.; Davidson, A.P., Nature, **337**, 147 (1989).
12. Foss, C.A. Jr.; Hornyak, G.L.; Stockert, J.A.; Martin, C.R., J. Phys. Chem, **98**, 2963 (1994).
13. Al-Rawashdeh, N.R.; Sandrock, M.L.; Seugling, C.J.; Foss, C.A., Jr., J. Phys. Chem B, **102**,

361 (1998).
14. Murnane, M.; Kapteyn, H.C.; Huang, C.P.; Asaki, M.T.; Garvey, D. *Mode-locked Ti-Sapphire Laser*; Washington State University, 1992.
15. Guyot-Sionnest, P.; Shen, Y.R. Phys. Rev. B, **38**, 7985 (1988).
16. Berkovic, G.; Efrima, S. Langmuir, **9**, 355 (1993).
17. Johnson, P.B.; Christy, R.W., Phys. Rev. B, **6**, 4370 (1972).
18. Meier, M.; Wokaun, A., Opt. Lett., **8**, 851 (1983).
19. Boyd, R.W. *Nonlinear Optics*; Academic Press: Boston, 1992.
20. Within the dipole approximation, SHG from centrosymmetric particles is also possible provided that the particle dimensions are comparable to the coherence length of the SHG process (see for example: Yan, E.C.Y.; Liu, Y.; Eisenthal, K.B., J. Phys. Chem. B, **102**, 6331 (1998)). For the conditions employed in our experiments, the coherence length is much smaller than the gold particle dimensions.
21. Dewitz, J.P.; Hubner, W.; Bennemann, K.H., Z. Phys. D. **37**, 75 (1996).
22. Östling, D.; Stampfli, P.; Bennemann, K.H., Z. Phys. D, **28**, 169 (1993).
23. Hua, X.M.; Gersten, J.I. Phys. Rev. B, **33**, 3756 (1986).

Measuring the Dielectric Properties of Nanostructures using Optical Reflection and Transmission: Bismuth Nanowires in Porous Alumina

M. R. Black[1], Y. M. Lin[1], M. S. Dresselhaus[1,2], M. Tachibama[5], S. Fang[4], O. Rabin[3], F. Ragot[6], P. C. Eklund[5], Bruce Dunn[6]
[1]Department of EECS, Massachusetts Institute of Technology, Cambridge, MA
[2]Department of Physics, Massachusetts Institute of Technology, Cambridge, MA
[3]Department of Chemistry, Massachusetts Institute of Technology, Cambridge, MA
[4]Department of Physics and Astronomy, University of Kentucky, Lexington, KY
[5]Department of Physics, Pennsylvania State University, State College, PA
[6]Department of Materials Science, UCLA, Los Angeles, CA

ABSTRACT

This paper develops a method to deduce the dielectric function of nanostructures smaller than the chosen wavelength of light. It modifies the Maxwell - Garnett Effective Medium Theory equations to calculate the dielectric function of a metal embedded inside a dielectric. Specifically, reflection and transmission measurements of an array of bismuth nanowires in an anodized porous alumina template are used to calculate the frequency - dependent dielectric function of the nanowires. The spectra are taken using Fourier transform infrared spectroscopy covering the 500 to 4000 cm^{-1} frequency range. These data are used to determine the real and imaginary parts of the dielectric function of the composite materials. Next, the percentage of the total volume occupied by either Bi or air in the porous alumina (the "filling factor") was found by scanning electron microscopy. The modified Maxwell-Garnett (M-G) equations specify how to use the filling factor and the dielectric function of the composite material to calculate the dielectric function of the alumina. Finally, the modified M-G equations are used a second time to calculate the dielectric function of Bi nanowires using the dielectric function of alumina, the dielectric function of the filled template, and the filling factor. The resulting dielectric function of Bi nanowires is then compared to theoretical predictions.

INTRODUCTION AND METHODOLOGY

A material's dielectric function offers considerable insight into its electronic structure. It sheds light on the bandgap, the free carrier concentration, and the phonon frequencies. Many groups are interested in studying nanostructures using wavelengths of light larger than their sample's feature size. Unfortunately, obtaining the dielectric function at such large wavelengths requires extracting the relevant information from measurements on composite samples that include both the nanostructure of interest and the host material.

Many prior studies have developed an effective medium theory (EMT) for such a situation [1-4]. When a sample is composed of more than one constituent material with the size of the constituent smaller than the wavelength (λ) of the optical fields, EMT models this inhomogeneous material as a single material with a single dielectric function. In this study we utilize Maxwell-Garnett (M-G) EMT which is valid for metal nanoparticles smaller than λ inside a dielectric material. M-G EMT relates the dielectric function of the composite to that of the metal and host material by :

$$\frac{\epsilon_{\text{composite}} - \epsilon_{\text{host}}}{\epsilon_{\text{composite}} + K * \epsilon_{\text{host}}} = f \frac{\epsilon_{\text{metal}} - \epsilon_{\text{composite}}}{\epsilon_{\text{metal}} + K * \epsilon_{\text{host}}} \quad (1)$$

Mat. Res. Soc. Symp. Proc. Vol. 581 © 2000 Materials Research Society

where K is the screening parameter and f is the volume fraction of the metal in the composite. For infinitesimally small nanowires, K = 1.

EMT has been used by several groups to determine the dielectric function of a composite material when the dielectric functions of the separate materials were known [5-14]. In this study, we use M-G EMT to deduce the dielectric function of a metallic constituent when the dielectric functions of the composite and of the host material are found by experimental measurements.

In this study, anodic alumina was chosen as the host material, since it forms an ordered template for metallic nanowires in the form of self assembled cylindrical pores. In addition, the pore diameter and the distance between the pores can be controlled by varying the anodization voltage and the etch time. Alumina is also a good host material because it is a wide bandgap semiconductor and therefore electrically isolates each wire.

The alumina templates can be filled with different metals. We have chosen bismuth for this study for several reasons. First, bismuth has a small, anisotropic effective electron mass tensor with $m^* = 0.001$ - $0.26\ m_0$ depending on the crystalline direction. The small effective electron mass of Bi and the large mean free path allow for quantum confinement at manufacturable dimensions. Secondly, Bi is a semi-metal with a small (38meV at 0 K) band overlap. As the wire size becomes small enough to cause significant quantum confinement of the electrons, the band overlap decreases. Because of the small mass and small band overlap, Bi in the (202) direction (the growth direction of our nanowires) changes from a semi-metal to a semiconductor at a wire diameter less than 48nm. The change from a metal to a semi-conductor should have drastic effects on the dielectric function of Bi. Thirdly, Bi has a low melting point, which makes it compatible with our fabrication techniques.

In bulk bismuth, the direct band gap transition and free carrier plasmon frequencies are at $290cm^{-1}$ and $333cm^{-1}$ respectively. When Bi is placed into an alumina template, quantum confinement occurs. The direct (L-point) band transition increases in energy with decreasing nanowire diameter, while the plasmon frequency is expected to decrease. Our calculations show that a semi-metal to semi-conductor transition requires that the Bi nanowires be 48 nm or less in diameter. For the wires used in this study, (50nm (202) wires), the first intersubband transition is calculated to occur at $1450cm^{-1}$. Therefore we are interested in an energy region where the wavelength of light (λ) is much larger than the diameter of the nanowires (d): $\lambda >> d$. In this study, the direction of propagation of light is parallel to the nanowire axis so that one oscillation of the electric field in real space crosses over many alumina / Bi boundaries. Since a single wavelength of the electric field sees an array of Bi wires in an alumina host, we must consider the effect of both Bi and alumina in our interpretation of the reflection(ω) and transmission(ω) data.

EXPERIMENTAL DETAILS

Porous anodic aluminum oxide templates were fabricated by the anodization of aluminum sheets in an oxalic acid solution [15]. During this process, cylindrical holes 7-200nm in diameter are self assembled into a hexagonal array, as shown in Fig. 1. The pores in the alumina templates are then filled with Bi using a pressure injection technique. Scanning electron micrographs of unfilled and filled alumina templates are shown in Fig. 1. The nanowires in this study are 50nm in diameter. From the SEM pictures, the volume fraction of air and Bi in the sample was found to be 16%, with 84% being alumina.

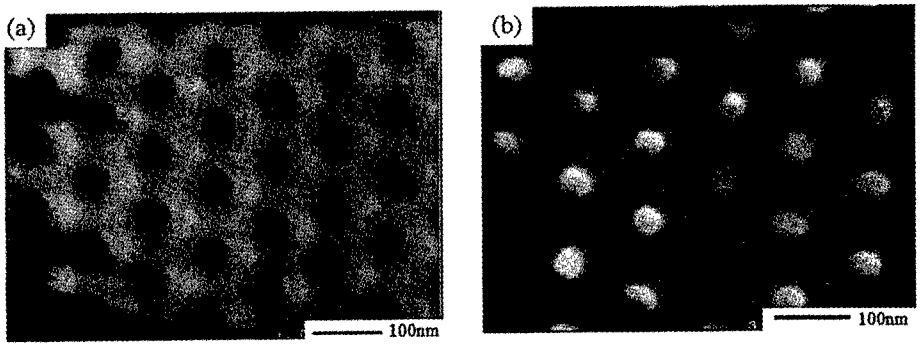


Figure 1: Scanning electron microscope picture of an unfilled (a) and filled (b) alumina template. The dark holes in the filled template are pores that remain unfilled after pressure injection.

Optical reflection (R(ω)) and transmission (T(ω)) as a function of frequency were measured using a Bomen FTIR spectrometer (model number DA3). Data were taken in the infrared region from $500 < 1/\lambda < 4000 cm^{-1}$ at 300K using a gold reference for reflection. A resolution of 2 cm^{-1} was used. The reflection and transmission data vs. photon energy for unfilled and Bi filled porous alumina templates (Fig. 2) were then analyzed to yield the frequency dependent dielectric function $\epsilon(\omega) = \epsilon_1(\omega) + i\epsilon_2(\omega)$ for the unfilled and filled porous templates, and from these results $\epsilon_1(\omega)$ and $\epsilon_2(\omega)$ for the nanowires themselves were deduced.

RESULTS AND DISCUSSION

The dielectric function ($\epsilon_1 + i\epsilon_2$) of the composite materials was calculated from the reflection and transmission data by solving Maxwell's equations with appropriate boundary conditions for each of the two sample - air interfaces. A matrix of possible ϵ_1 and ϵ_2 values with a step size of 0.05 for ϵ_1 and 0.01 for ϵ_2 was explored. For each measured frequency from 500 to 4000 cm^{-1}, the combination of ϵ_1 and ϵ_2 yielding the minimum error was found.

$$Error = |R_{\text{calculated}} - R_{\text{measured}}| + |T_{\text{calculated}} - T_{\text{measured}}| \quad (2)$$

For regions where $\epsilon_2 < 0.01$, the transmission is almost 100% and the reflection is small; hence the previously described method to obtain ϵ_1 is inaccurate. A different approach is required. Instead of solving Maxwell's equations in this regime the interference patterns were used to determine $\epsilon_1(\omega)$. Both the periodicity and magnitude of the interference patterns are used to simultaneously solve for the thickness and for $\epsilon_1(\omega)$. The transition from this method of obtaining ϵ_1 to the previously described method occurs at $1750 cm^{-1}$ and is fairly smooth. The resulting dielectric function results for the filled and unfilled alumina templates are shown in Fig. 3.

Fig. 2 shows that both the transmission and reflection data of the unfilled template have a large interference pattern for $2000 < 1/\lambda < 4000 cm^{-1}$ indicating a low absorption in the template material. The absence of interference patterns in the filled templates is a result of an increase in absorption with the addition of Bi. Also indicating an increase

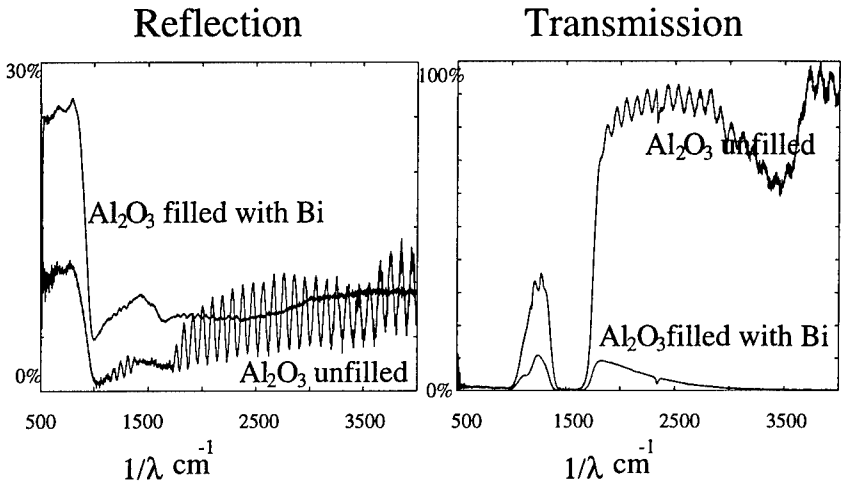


Figure 2: Photon energy dependence of the reflection and transmission of porous alumina and porous alumina filled with Bi nanowires: Both the transmission and reflection data show a large interference pattern in the range 2000 - 4000 cm^{-1} only for the unfilled sample. The absence of interference patterns in the Bi filled templates indicates an increase in absorption with the addition of Bi. Also, indicating an increase in absorption, the transmission through the sample is decreased with the addition of Bi. The larger reflection in the filled samples is a result of an increase in the index of refraction with the addition of Bi.

in absorption, the transmission through the sample decreases with the addition of Bi. In addition to the differences in interference, Fig. 2 shows an increase in reflection predominant for $1/\lambda < 1000cm^{-1}$. The larger reflection in the filled samples is a result of an increase in ϵ_1 with the addition of Bi.

An increase in both $\epsilon_2(\omega)$ and $\epsilon_1(\omega)$ with the addition of Bi is observed in Fig. 3. The increase in $\epsilon_2(\omega)$ is for the full frequency range. Above $2000cm^{-1}$, $\epsilon_2(\omega)$ of the filled sample is fairly constant at around 0.1 while $\epsilon_2(\omega)$ of the unfilled template is less than the 0.01. The increase in $\epsilon_1(\omega)$ is especially large for $1/\lambda < 1000cm^{-1}$, where $\epsilon_1(\omega)$ increases from 4 to 10 with the addition of Bi.

Once the dielectric function results for the composite are obtained, the dielectric function of the alumina is found by substituting the values of the dielectric function of the unfilled alumina, a filling factor of 0.16, and the dielectric constant of air (1) into Eq. 1. Likewise by substituting into Eq. 1 the previously deduced dielectric function of alumina, a filling factor of 0.16, and the dielectric function of the filled alumina template, the dielectric function $\epsilon_1 + i\epsilon_2$ for the Bi nanowires was obtained for the energy range $500-4000cm^{-1}$. The calculated $\epsilon_1(\omega)$ and $\epsilon_2(\omega)$ for Bi nanowires determined in this way is shown in Fig. 4. Characteristic features in both $\epsilon_1(\omega)$ and $\epsilon_2(\omega)$ are identified with oscillators at 1000 and 1650 cm^{-1}. These oscillators are a result of an increased optical absorption by the Bi nanowires at these values of ω. Since the measured absorption peak is in the same energy range as the predicted first intersubband transition, $1450cm^{-1}$ for our wires, we identify our oscillators with intersubband transitions. A detailed analysis of these data for bismuth nanowires will be published elsewhere.

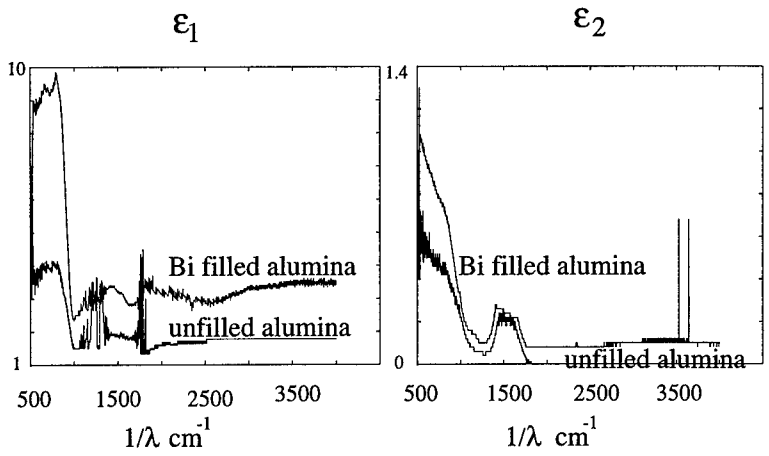


Figure 3: The real (ϵ_1) and imaginary (ϵ_2) parts of the dielectric function ($\epsilon(\omega) = \epsilon_1(\omega) + \epsilon_2(\omega)$) of empty and Bi-filled alumina templates for $500 < 1/\lambda < 4000cm^{-1}$. The addition of Bi into the alumina increases both ϵ_1 and ϵ_2 throughout the frequency range, predominantly for $1/\lambda$ less than $1000cm^{-1}$. The increase in ϵ_2 is a result of the increased absorption observed in R(ω) and T(ω).

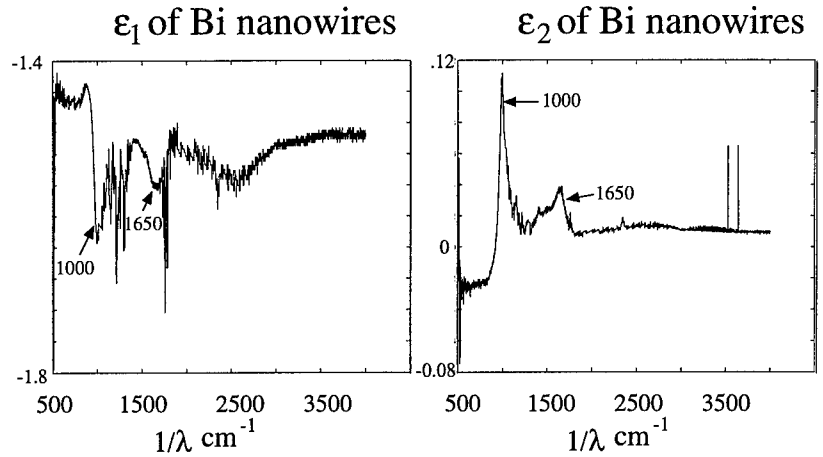


Figure 4: ϵ_1 and ϵ_2 of Bi nanowires: Peaks in $\epsilon_2(\omega)$ are observed at 1000 and $1650cm^{-1}$, and are a result of the increased optical absorption by the Bi nanowires at these values of ω. ϵ_1 also shows the characteristic shape of a resonator at these frequencies.

CONCLUSION

This study utilizes previous work on effective medium theory to demonstrate that the dielectric function of a nanostructural material can be obtained by optical measurements even if the feature size is smaller than the wavelength of the applied light. It illustrates this procedure for bismuth nanowires. Reflection and transmission data, $R(\omega)$ and $T(\omega)$ for Bi nanowires embedded in alumina were measured for wavelengths of light from $500 < 1/\lambda < 4000 cm^{-1}$. Using M-G effective medium theory, the dielectric function of the Bi quantum wires was deduced over this frequency range. Although these methods were developed for bismuth, they can easily be adapted to other nanostructure materials. Investigators could use this technique to examine a range of effects, including surface plasmons, semi-metal/ semi-conductor transitions, and one dimensional conduction.

Acknowledgments

The authors gratefully acknowledge Dr. Gene Dresselhaus and Steve Cronin for helpful discussions; MURI subcontract 0205-G-7A114-01, NSF grant CTS-9257223 and DMR-98-04734, and the US Navy contract N00167-92-K005 for support.

References

[1] D. E. Aspnes, Thin Solid Films **89**, 249–262 (1982).

[2] D. E. Aspnes, A. Heller, and J. D. Porter, J. Appl. Phys. **60**, 3028–3034 (1986).

[3] J. C. Maxwell Garnett, Phil. Trans. A. **203**, 385–420 (1904).

[4] J. C. Maxwell Garnett, Phil. Trans. A. **205**, 237–288 (1906).

[5] Colby A. Foss, Jr. Gabor L. Hornyak, Jon A. Stockert, and Charles R. Martin, J. Phys. Chem. **96**, 7497–7499 (1992).

[6] A. Anderson, O. Hunderi, and C. G. Granqvist, J. Appl. Phys. **51**, 754–764 (1980).

[7] V. V. Poborchii, Jpn. J. Appl. Phys. **34**, 271–274 (1995).

[8] P. N. Sen, C. Scala, and M. H. Cohen, Geophysics **46**, 781–795 (1981).

[9] U. Kreibig, A. Althoff, and H. Pressmann, Surface Science **106**, 308–317 (1991).

[10] U. Kreibig and L. Genzel, Surface Science **156**, 678–700 (1985).

[11] S. Link, M. B. Mohamed, and M.A. El-Sayed, J. Phys. Chem. B. **103**, 3073–3077 (1999).

[12] Gabor L. Hornyak, Charles J. Patrissi, and Charles R. Martin, J. Phys. Chem. B. **101**, 1548–1555 (1997).

[13] Colby A. Foss, Jr. Gabor L. Hornyak, Jon A. Stockert, and Charles R. Martin, J. Phys. Chem. B. **98**, 2963–2971 (1994).

[14] C. G. Granqvist and O. Hunderi, Phys. Rev. B. **18**, 2897–2906 (1978).

[15] Z. Zhang, J. Ying, and M. Dressehaus, J. Mater. Res. **13**, 1745–1748 (1998).

COLOSSAL HOPPING MAGNETORESISTANCE OF GaAs/ErAs NANOCOMPOSITES

A. G. PETUKHOV, M. FOYGEL, and A.CHANTIS
Department of Physics, South Dakota School of Mines and Technology, Rapid City, SD 57701-3995

ABSTRACT

A theory of bound magnetic polaron (BMP) hopping, driven by thermodynamic fluctuations of the local magnetization, has been developed. It is based on a two-site model of BMP's. The BMP hopping probability rate was calculated in the framework of the "Golden Rule" approach by using the Ginzburg-Landau effective Hamiltonian method. The theory explains the main features of hopping resistivity observed in a variety of experiments in dilute magnetic semiconductors and magnetic nanocomposites, namely: (a) negative giant magnetoresistance, the scale of which is governed by a magnetic polaron localization volume, and (b) low magnetic field positive magnetoresistance, which usually preceeds negative magnetoresistance.

INTRODUCTION

Spin-polarized electronic transport in solids has attracted much interest mainly due to the discovery of giant magnetoresistance (GMR) and the development of new device applications (high-speed magnetic sensors and memory elements) based on this phenomenon [1]. Several different mechanisms have been proposed for the spin-dependent GMR. Their common feature is the exchange interaction of charge carriers with the itinerant and/or localized magnetic moments of transition- or rare-earth-metal atoms. In this paper, we will restrict ourselves to hopping conductivity in magnetic semiconductors and nanostructures [2, 3]. In these systems, an electron or hole trapped by any kind of attractive potential of a defect, quantum dot, etc., can form a "cloud" of aligned spins of the surrounding magnetic atoms. Creation of such a complex (referred to as bound magnetic polaron (BMP) [4]) will further lower the free energy of the system by a quantity W_p called the polaron shift. The first consistent semiclassical analysis of BMP formation in dilute magnetic semiconductors was given by Dietl and Spałek [5], while its quantum-mechanical generalization was developed by Wolff et al (for references see [6]). This theory successfully described the spin-flip Raman scattering in magnetic semiconductors [7].

In order to describe BMP hopping conductivity, we need, first, to specify the mechanism of an elementary hopping event. Dietl et al [3, 7] considered a "static" picture in which the electron is transferred from an occupied site to an empty one with frozen equilibrium local magnetizations at both sites. For two identical sites this process is driven by absorption of an acoustic phonon and requires an activation energy $2W_p$ [3, 8]. Another mechanism, which was first suggested by Ioselevich [8], takes into account thermodynamic fluctuations of the local magnetizations that control the elementary hopping act. Indeed, since the electron energy levels at both sites follow the fluctuations of local magnetic order parameters, it is likely that the levels at the occupied and empty sites will move in opposite directions briefly establishing a resonance condition. For this to occur, the occupied site should spontaneously decrease its local magnetization while the empty one should increase it. The electron can then tunnel from one site to another resonantly. This process somewhat resembles the multiphonon mechanism of small-polaron hopping [9]. It requires an activation energy $W_p/2$ [8] which is four times smaller compared to that of the "static" mechanism.

The giant negative magnetoresistance observed in dilute magnetic semiconductors was properly attributed by many authors [4, 7] to the BMP phenomenon. The application of a large magnetic field will quench magnetic polarons by reducing the magnetic part of their binding energy and therefore the activation energy of the hopping conductivity. However, the presence of a significant (up to 300%) positive magnetoresistance, which is typical for situations when the carriers are localized [7], remains unclear. We will show that the latter is a signature of the fluctuation hopping mechanism and ultimately reflects the fact that, in contrast to conventional lattice polarons, the BMPs are described by a vector order parameter. We will develop a unified and consistent semiclassical description of BMP hopping based on the Ginzburg-Landau effective Hamiltonian formalism [5, 10] and Holstein's occurence probability approach [9]. It will be shown that the fluctuation driven BMP hopping may lead to non-monotonic behavior of the magnetoresistance. (Recently, a simple two-site model of this kind has been applied to the description of resistance, including the GMR of the ErAs islands in GaAs [11].) Our approach also allows us to take into account single-phonon assisted BMP hopping of the Miller-Abrahams type [12]. This process plays a dominant role only at high magnetic fields and will be considered elsewhere [13].

Mat. Res. Soc. Symp. Proc. Vol. 581 © 2000 Materials Research Society

BMP HOPPING CONDUCTIVITY

Let us consider two centers, 1 and 2, separated by a distance r_{12}. We assume that each site can localize an electron even when no magnetic forces are involved. In the vicinity of each center there is a finite concentration of localized magnetic moments that is described by the spatial distribution of the local magnetization vectors $\vec{M}_{1,2}(\vec{r})$ generated by a fluctuating field of atomic spins. The effective Hamiltonian of the problem is

$$H = H_1 + H_2 + H_{12} + H_{e-ph} \tag{1}$$

where

$$H_l = \epsilon_l n_l - \hat{\vec{s}}_l \vec{\Delta}_l + (1/2\chi) \int \delta \vec{M}_l^2(\vec{r}) d\vec{r} \tag{2}$$

is the Hamiltonian of a BMP localized at a site l ($l = 1, 2$). Here $n_l = \sum_{\sigma=\pm 1} a_{l\sigma}^{\dagger} a_{l\sigma}$ is an occupation number of site l (there is only one electron per two sites, i.e. $n_1 + n_2 = 1$); ϵ_l is the "bare" energy of a bound electron at the site l. The second term in (2) describes the exchange interaction between the trapped electron and localized atomic spins of the magnetic atoms within the region of electron localization together with the direct interaction with the magnetic field $\vec{B}$ taken into account, where

$$\vec{\Delta}_l = (\Gamma_{ex}/g\mu_B) \int |\Psi_l(\vec{r})|^2 \vec{M}_l(\vec{r}) d\vec{r} + g^* \mu_B \vec{B} \tag{3}$$

is a vector of the local exchange field. The magnitude, Δ_l, of this vector is equal to the Zeeman splitting of the localized electron state with the wave-function Ψ_l. The vector $\vec{\Delta}$, as a rule, is not directed along the local average magnetic field inside the localization region. Here Γ_{ex} is an exchange coupling constant, μ_B is the Bohr magneton, and g and g^* are the Lande factors of the atomic spin and that of free electron. Also, $2\hat{\vec{s}}_l = (\hat{\sigma}_l^x, \hat{\sigma}_l^y, \hat{\sigma}_l^z)$, with $\hat{\sigma}_l^{\alpha}$ being the conventional Pauli matrices. The last term in (2) represents the lowest term in the Ginzburg-Landau expansion [5, 10] of the free energy of atomic spins, $\vec{M}_0$ is the equilibrium magnetization vector, and $\delta \vec{M}_l^2(\vec{r}) \equiv \left[\vec{M}_l(\vec{r}) - \vec{M}_0\right]^2$ is a squared fluctuation of magnetization at the site l. We assume that our medium is described by means of a macroscopic, scalar, and isotropic magnetic susceptibility $\chi(B,T)$. In the effective Hamiltonian (1), the term

$$H_{12} = -t_0 \exp(-r_{12}/a) \sum_{\sigma=\pm 1} (a_{1\sigma}^{\dagger} a_{2\sigma} + c.c.) \tag{4}$$

is responsible for electronic hopping between sites 1 and 2. As a starting point, we assume that spin-flip processes are forbidden. Here a is a localization radius of the electron at any of two centers. Due to an exponentially small hopping integral in (4) we will treat H_{12} as a small perturbation. In (4) and (2), the operator $a_{l\sigma}^{\dagger}(a_{l\sigma})$ describes creation (annihilation) of an electron at the site l with spin parallel ($\sigma = 1$) or anti-parallel ($\sigma = -1$) to the external magnetic field $\vec{B}$. The term H_{e-ph} in (1) describes electron-phonon interaction.

We assume that initially the electron is localized at site $l = 1$ while site $l = 2$ is empty, i.e. $n_1 = 1, n_2 = 0$. In the final state, after the hop, $n_1 = 0$, and $n_2 = 1$. We treat the last two terms in the Hamiltonian (1) as a small perturbation. By applying the "Fermi Golden Rule" [10, 14] with subsequent statistical averaging over initial states, one can calculate the BMP hopping rate in the so called non-adiabatic regime [9], when the small hopping integral controls the probability of the hopping event:

$$w_{12} = (2\pi/\hbar Z_i) \sum_{\sigma_1,\sigma_2} \int\int \mathcal{D}\vec{M}_1 \mathcal{D}\vec{M}_2 \, |\tilde{t}_{\sigma_1\sigma_2}|^2 \exp\left(-E_{i\sigma_1}/T\right) \delta\left(E_{i,\sigma_1} - E_{f,\sigma_2}\right), \tag{5}$$

where quantum numbers σ_1 and σ_2 are defined with respect to the local excange fields $\vec{\Delta}_1$ and $\vec{\Delta}_2$. And,

$$|\tilde{t}_{\sigma_1,\sigma_2}|^2 = |t_0|^2 \exp\left(-2r_{12}/a\right) \left[\delta_{\sigma_1,\sigma_2} \cos^2(\theta_{12}/2) + (1 - \delta_{\sigma_1,\sigma_2}) \sin^2(\theta_{12}/2)\right] \tag{6}$$

with θ_{12} defined as the angle between $\vec{\Delta}_1$ and $\vec{\Delta}_2$. In (5), $\mathcal{D}\vec{M}_l$ represents functional integration over all possible configurations of the local magnetizations $\vec{M}_l(\vec{r})$. The energies of the initial ($n_1 = 1$, $n_2 = 0$) and final ($n_1 = 0$, $n_2 = 1$) states are functionals of magnetization (see Eq.(2)), and Z_i is the partition function of the initial state. Here and below we assume $k_B = 1$.

Expression (5) is derived under the assumptions: (1) the spin of the electron follows an instantaneous configuration of the local atomic spins at the site where it is localized; (2) the electron hopping integral $|t_0| \exp\left(-2r_{12}/a\right) \ll (W_p T)^{1/2}$. The last assumption is well known in the theory of small lattice polarons

[9]. It is usually believed that this condition justifies the applicability of the "Golden Rule" for the problem in question. Performing the functional integration in (5) finally yields:

$$w_{12} = \frac{2\pi}{\hbar Z_p Z_0} \sum_{\sigma_1,\sigma_2} \int\int |\bar{t}_{\sigma_1\sigma_2}|^2 \exp\left(\frac{\sigma_1\Delta/2 - \epsilon_1}{T}\right) P\left(\vec{\Delta}\right) P\left(\vec{\Delta}'\right) \delta\left(\epsilon_1 - \epsilon_2 - \frac{\sigma_1\Delta - \sigma_2\Delta'}{2}\right) d\vec{\Delta} d\vec{\Delta}' \quad (7)$$

where Z_p and Z_0 are the partion functions of the BMP and the empty site respectively [5] and

$$P\left(\vec{\Delta}\right) = \int \mathcal{D}\vec{M}\delta\left(\vec{\Delta} - \vec{\Delta}\left\{\vec{M}\left(\vec{r}\right)\right\}\right) \exp\left(-\frac{1}{2\chi T}\int \delta\vec{M}^2(\vec{r})d\vec{r}\right) = \frac{Z_0}{(16W_pT)^{1/2}} \exp\left[-\frac{\left(\vec{\Delta} - \vec{\Delta}_0\right)^2}{16W_pT}\right] \quad (8)$$

is a distribution function of the spin-splitting vectors in the absence of a localized electron, with $\vec{\Delta}_0 = (\Gamma_{ex}/g\mu_B)\vec{M}_0 + g^*\mu_B\vec{B}$ the equilibrium Zeeman splitting vector. In (8), the polaron shift W_p was introduced:

$$W_p = 2\left(\Gamma_{ex}/4g\mu_B\right)^2 \chi(B,T) \int |\Psi(\vec{r})|^4 \, d\vec{r} \quad (9)$$

The Gaussian functional integral (8) was calculated by Dietl and Spałek [5]. Its form allows us to evaluate the BMP hopping rate (7) analytically:

$$w_{12} = \frac{\sqrt{\pi}|t_0|^2}{2\hbar T} F(\mu,\nu) \exp\left[-\frac{(2W_p - \epsilon_{12})^2}{8W_pT} - \frac{2r_{12}}{a}\right] \quad (10)$$

where

$$F(\mu,\nu) = \left(\mu\sqrt{\nu}\right)^{-1}\left[\frac{\left(\mu^2+2\right)\cosh\mu - 2\exp(-\nu)}{2(\mu\sinh\mu + \nu\cosh\mu)} + 2\nu - 1\right] \quad (11)$$

and the following dimensionless parameters were introduced: $\mu = \Delta_0/2T$, $\nu = \Delta_0^2/8W_pT$. Exprsession (10) describes the rate of BMP hopping between two almost identical sites that belong to a percolation cluster and will be used below to calculate the hopping conductivity. The pre-exponential factor (11) corresponds to the hopping integral given by Eq. (6) which, in turn, is derived assuming that there are no spin-flip processes. If, however, the latter assumption is relaxed (e. g. the probabilities of spin-flip and non-spin-flip processes are equal) then the hopping integral $\bar{t}_{\sigma,\sigma'}$ does not depend on the angles. In this case, the prefactor F in Eq. (10) should be replaced with

$$\tilde{F}(\mu,\nu) = \left(\mu\sqrt{\nu}\right)^{-1}\left[\frac{\left(\mu^2+2\nu\right)\left(\cosh\mu - \exp(-\nu)\right)}{2(\mu\sinh\mu + \nu\cosh\mu)} + 2\nu\right] \quad (12)$$

In the case of sufficiently large magnetic fields ($B \to \infty$) the angular fluctuations of the magnetizations are effectively suppressed. That implies that $W_p \to 0$ ($\chi \to 0$ as $B \to \infty$) while Δ_0 and $F(\mu,\nu)$ approach their saturation values. Therefore the exponential factor in (10) describes the negative GMR caused by the quenching of BMPs [4].

Using the standard technique of the percolation theory [12, 15] and expression (10) for the hopping probability one can calculate the effective electrical hopping resistance between sites i and j:

$$R_{ij} = T/\left(e^2 w_{ij} f_i(1-f_j)\right) \propto F^{-1}(\mu,\nu)\exp\left(2r_{ij}/a + \tilde{\epsilon}_{ij}/T\right) \quad (13)$$

where $f_i \equiv f(\epsilon_i)$ is Fermi's distribution function,r_{ij} is the distance between the sites in question, and

$$\tilde{\epsilon}_{ij} = \frac{1}{2}\left(|\epsilon_i - E_F| + |\epsilon_j - E_F|\right) + \begin{cases} W_p/2 + \left(\epsilon_i - \epsilon_j\right)^2/(8W_p), & |\epsilon_i - \epsilon_j| \le 2W_p \\ |\epsilon_i - \epsilon_j|/2, & |\epsilon_i - \epsilon_j| > 2W_p \end{cases} \quad (14)$$

With the exception of a very important magnetic-field-dependent factor F^{-1} , expression (13) coincides with that of Ref. [8]. This factor, which is specific for BMP hopping, takes into account the vector nature of the magentic order parameter. It is responsible for the *positive* magneto-resistance observed at small and intermediate magnetic fields in different magnetic semiconductors and nano-structures [7, 11]. The positive component of the GMR is a signature of the fluctuation mechanism describing the BMP hopping rate as an ovelap integral between distribution functions of Zeeman splitting vectors at the BMP and empty sites (see Eq.(7)). It can be understood as a reduction of this overlap due to the instant rotation of the BMP magnetization in the direction of a relatively small magnetic field [11]. The interpolation formula (13) takes into account two limiting cases: (i) large polaron shifts $2W_p > \langle|\epsilon_{ij}|\rangle$, which is appropriate for

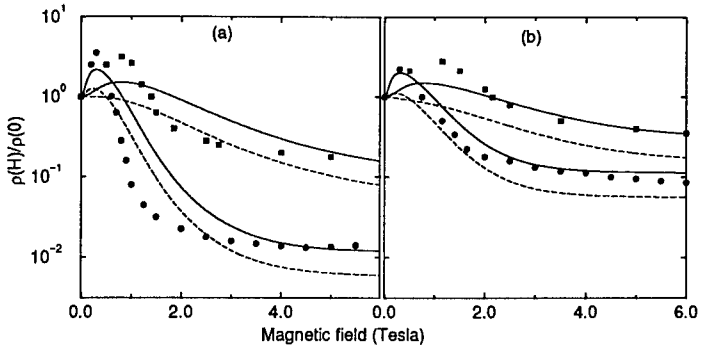


Figure 1: Magnetoresistance of $Cd_{0.95}Mn_{0.05}Se$ for various donor concentrations n: (a) $6 \cdot 10^{16}$ cm^{-3}, (b) $1.2 \cdot 10^{17}$ cm^{-3}. The circles and squares represent the experimental data [3] taken at T = 1.7 and 4.2 K, respectively. The solid and dashed lines represent the theoretical results obtained with and without spin-flip processes taken into account, respectively, with the following set of parameters: (a) $W_p(0)$=16.4 K, δ =3.6 K, E_F=3.4 K; (b) $W_p(0)$=9.0 K, δ=4.2 K, E_F=0.9 K.

BMP's with appreciable polaron shift when the magnetic field is not strong, and (ii) small polaron shifts $2W_p < \langle|\epsilon_{ij}|\rangle$ when the nagnetic field is strong. Here, $\langle|\epsilon_{ij}|\rangle = \langle|\epsilon_i - \epsilon_j|\rangle$ is the average scatter of the "bare" electron energies.

While evaluating the hopping resistivity ρ we will consider the case of ϵ_3-conductivity [15], when the typical dispersion of the activation energies $\tilde{\epsilon}_{ij}$ is small compared to that of the inter-site distances r_{ij}, namely, $\langle\tilde{\epsilon}_{ij}\rangle/T \ll 2\langle r_{ij}\rangle/a$. In this case the connectivity criterion can be written as: $2r_{ij}/a + \tilde{\epsilon}_{ij}/T \leq \xi_c = 2r_c/a + \langle\tilde{\epsilon}_{ij}\rangle/T$ where r_c is a percolation threshold for the random-site r-percolation problem [15] (usually r_c is of the order of the average distance between sites). It yields the following expression for the resistivity:

$$\rho(B) \propto F^{-1}(\mu,\nu) \exp\left[2r_c/a + \left(\epsilon_3^{MA} + \frac{W_p}{2} f(\alpha)\right)/T\right] \tag{15}$$

Here ϵ_3^{MA} is the activation energy for the Miller-Abrahams hopping conductivity in the absence of the BMP effect; $\alpha = 2W_p/\delta$, where δ is the typical scatter of electron energies, and $f(\alpha)$ is a dimensionless function such that $f(\alpha) \to 0$ when $\alpha \ll 1$, and $f(\alpha) \to 1$ when $\alpha \gg 1$. It should be noted that the activation energy for the magnetoresistance, (15), driven by fluctuations of the local magnetization is one-fourth the value obtained for the static BMP states [3, 7]. Therefore, the fluctuation-driven mechanism of hopping will always dominate the static one [8].

To analyze the field dependence of magnetoresistance (15), one should specify the magnetic susceptibility $\chi(B,T)$. Usually, for dilute magnetic semiconductors in the paramagnetic phase [5, 6, 7], $\chi(B,T)$ can be expressed in terms of a modified Brillouin function $B_J(z)$, where $z = g\mu_B B/(T + T_0)$ and the parameter $T_0 > 0$ is associated with the possible antiferromagnetic interaction of magnetic atoms with the total angular momentum J and Lande factor g. Then the average Zeeman splitting in the absence of the localized electron is: $\Delta_0(B) = n_0\Gamma_{ex}JB_J(z) = \Delta_s B_J(z)$, where $\Delta_s = \Delta(B \to \infty) = n_0\Gamma_{ex}J$ is the splitting at saturation fields.

COMPARISON WITH EXPERIMENT

Dilute magnetic semicondactors (DMS). Both positive and negative magneto-resistance has been experimentally observed in the insulating region in several II-VI semiconductors, such as CdSe, HgTe, CdHgTe, ZnSe, doped to high (up to several atomic percent) concentrations with transition metals, mainly, with Mn. For p-type materials, several, sometimes controversial, explanations of these phenomena were put forward (see [7] and references therein) that are based on the complex nature of the localized acceptor states involved [7]. To avoid unnecessary complications, we will restrict ourselves to a case of n-doped $Cd_{0.95}Mn_{0.05}Se$, where donors, on which the magnetic polarons reside, can be described by means of a simple hydrogen-like model. (A detailed and consistent theory of the BMPs in this material was developed by T. Dietl and J. Spałek [5] who successfully applied it to the description of the experiments on spin-flip Raman scattering (see also [6])). Subsequently, BMP hopping conduction has been studied experimentally

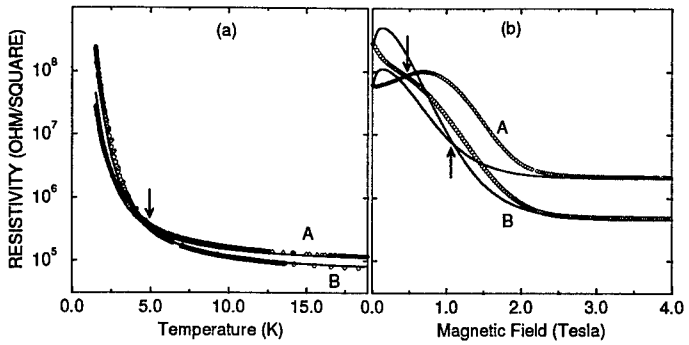


Figure 2: Resistivity of the ErAs/GaAs nanostructures as a function of: (a) temperature and (b) magnetic field perpendicular to the direction of growth [11]. Diamonds reperesent sample A, circles represent sample B. Solid lines are theoretical results.

in these materials [3]. However, the theoretical interpretation of these experiments given in[3] was based on the static model that grossly overestimates the magnetoresistance. We will analyze these experiments in terms of the above developed fluctuation-driven hopping model.

We start our analysis from the experimental data (Fig. 1 from [3]) on the temperature dependence of the resistivity (measured at zero magnetic field and at the $B = 6$ T i.e., close to saturation) of two $Cd_{0.95}Mn_{0.05}Se$ samples (a) and (b) with different donor concentration equal to $6 \cdot 10^{16}$ cm^{-3} and $1.2 \cdot 10^{17}$ cm^{-3}, respectively. Then, by means of our basic formula (15), taken at B=0 and $B \to \infty$ (when the polaron shift $W_p(B) \to 0$), we extracted the values of the zero-field polaron shift $W_p(0)$. The data yield zero-field polaron shift values of 16.4 and 9.0 K for samples (a) and (b), respectively. These shifts together with Δ_s=180 K and the parameters T_0=1.2 K, g=2, and J =5/2 [5] for the modified Brilluoin function were used to plot the calculated magneto-resistance (15) of DMS (Fig.1) for $T = 1.7$ and 4.2 K. These plots are then compared with experimental data from [3]. In calculating the magnetoresistance (15), we used expressions (11) (spin-flips are forbidden) and (12) (spin-flip processes are allowed). It can be seen that the latter leads to a better agreement with the experiment.

ErAs/GaAs magnetic nanocomposites. Recently, MBE techniques have been used to grow self-assembled nanometer-sized ErAs magnetic islands (quantum dots) embedded in a semi-insulating GaAs matrix. The amount of material deposited in the ErAs layers ranged from 0.5 to 2.5 molecular layers (ML)[11]. Precise control of the deposition conditions made it possible to control not only the concentration of these islands and inter-island distances, but also their size, which ranged from 4 to 80 nm. Analysis of the temperature dependence of the zero-field resistivity together with the data on the magnetoresistance for different samples clearly shows that the low-temperature conductivity in these materials can be explained in the framework of fluctuation-driven BMP hopping [2, 11].

In the analysis of the data on magnetoresistance [11] we used the modified Brillouin function to fit the experimental data for magnetization $M_0(B)$ and susceptibility $\chi(B,T)$. Here, the Er spin and g-factor are given by $J = 3/2$ [16], and $g = 7.4$, respectively. The effective temperature describing antiferromagnetic interaction T_0= 4 K. One can see that formula (15) describes the temperature dependence of the zero-field resistivity well (Fig.2(a)). For samples B and A, zero-field polaron shift values of 24.2 K and 17.4 K, respectively, were used along with electron energy scatters δ=15.0 K and δ=22.2 K. The data shown in this Fig. correspond to samples A and B grown with the same 2ML ErAs depositions and at different temperatures. Sample B (Fig.2), with islands of smaller lateral size d than that of sample A, has smaller average distance $\bar{r}$ between them. The observed crossover results from the competition between the activation energy term (that increases as the islands' size decreases) and the hopping integral term (that decreases as the separation between the islands decreases) in expression (15). At low temperatures the activation term prevails, while at high temperatures the conductivity is governed by activationless r-hopping. This crossover can be reversed at low temperatures by applying magnetic field that quenches the activation energy (Fig. 2(b). The theoretical curves in Fig. 2 were calculated for typical lateral island size $d \simeq 50$Å(W_p=17.4 K) and 40Å(W_p=24.2 K) for samples A and B respectively, which is consistent with TEM observations[11]. We used Zeeman splitting at saturation, of Δ_s=50 meV. Relatively small (< 20%) changes in d have a dramatic effect not only on the zero-field resistivity but also on the scale of the negative magnetoresistance. In accordance with our model, the latter definitely correlates with the islands' size d and

volume V and, therefore, with the magnitude of the zero-field polaron shift $W_p(0) = (\Gamma_{ex}/2g\mu_B)^2 \chi(0)/2V$ (Fig.2(b)). At intermediate fields, the resistivity as a function of magnetic field B may reveal a maximum the origin of which has been explained in the previous section. The experimental curves [2, 11] clearly display a dependence of the magnetoresistance on the orientation of the magnetic field that cannot be explained in the framework of our simple isotropic model. A few factors may contribute to this effect, such as the anisotropy of the magnetization and the anisotropy in the shape of the islands. These anisotropies, together with the complex nature of the confined electronic states, may cause an anisotropy of the exchange coupling.

CONCLUSIONS

A simple theory of bound magnetic polaron hopping driven by fluctuations of local magnetizations gives a reasonably good explanation, both qualitative and quantitative, of the experimental data for giant negative and positive magneto-resistance in dilute magnetic semiconductors and nano-structures. Future refinements of the theory of BMP hopping presented in this paper should incorporate magnetic-field orientation effects that are believed to be connected with the shape anisotropy of magnetic nanostructures.

ACKNOWLEDGEMENTS

This work was supported by the AFOSR grant No. F49620-96-1-0383. The authors are grateful to S. J. Allen and D. Schmidt for numerous fruitful discussions.

REFERENCES

1. G. A. Prinz, Science **250**, 1092 (1990).
2. D. R. Schmidt, J. P. Ibbetson, D. E. Brehmer, C. J. Palmstrøm, and S. J. Allen in *Materials Research Society Proceedings*, 1997, Vol. 475, p. 251.
3. T. Dietl, J. Antozsewski and L. Swierkowski, Physica **117B & 118B**, 491 (1983).
4. T. Kasuya and A. Yanase, Rev. Mod. Phys. **40**, 684 (1968).
5. T. Dietl and J. Spałek, Phys. Rev. B **28**, 1548 (1983).
6. P. A. Wolff, in *Semiconductors and Semimetals*, edited by R. K. Willardson and A. C. Beer, v. 25 (Academic Press, N.Y. 1988), p. 413.
7. T. Dietl in *Diluted Magnetic Semiconductors,* edited by M. Jain (World Scientific, Singapore, 1991) p. 141.
8. A. S. Ioselevich, JETP Lett. **43**, 188 (1986); Phys. Rev. Lett. **71**, 1067 (1993).
9. T. Holstein, Ann. Phys. (N. Y.) **8**, 343 (1959); D. Emin in: *Electronic and Structural Properties of Amorphous Semiconductors*, edited by J. Mort (Academic Press, N. Y., 1973), p. 261; D. Emin, Phys. Rev. B **43**, 11720 (1991).
10. L. D. Landau and E. M. Lifshitz, *Statistical Physics* (Pergamon Press, Cambridge, 1980).
11. D. Schmidt, A.G. Petukhov, M.Foygel, J. P Ibbetson, and S. J. Allen, Phys. Rev. Lett **82**, 823 (1999).
12. A. Miller and E. Abrahams, Phys. Rev. **120**, 745 (1960).
13. A. G. Petukhov and M. G. Foygel, to be published.
14. A. J. Leggett, S. Chakravarty, A. T. Dorsey, M. P. A. Fisher, A. Garg, and W. Zwerger, Rev. Mod. Phys. **59**, 1 (1987).
15. B. I. Shklovskii and A. L. Efros, *Electronic Properties of Doped Semiconductors*, Springer Series in Solid State Sciences, v. 45 (Springer- Verlag, Berlin, 1984).
16. S. J. Allen, Jr., F. DeRosa, C. J. Palmstrøm and A. Zrenner, Phys. Rev. B **43**, 9599 (1990).

THERMALLY DRIVEN SHAPE INSTABILITY OF MULTILAYER STRUCTURES

P. TROCHE *, J. HOFFMANN *, C. HERWEG *, CH. LANG *, H.C. FREYHARDT *
D. RUDOLPH **
* Institut für Materialphysik, Universität Göttingen, Hospitalstr. 3-7, D-37073 Göttingen, ptroche@gwdg.de
**Institut für Röntgenphysik, Universität Göttingen, Geiststraße 3, D-37073 Göttingen

ABSTRACT

The thermally induced shape instability of Fe/Au, Fe/Ag, and Nb/Cu multilayer systems during heat treatments was investigated. The disintegration temperature of these systems decreases with decreasing single-layer thickness. Up to a critical thickness, the disintegration temperature is proportional to the reciprocal layer thickness. The driving force of this process is related to the interfacial stress and the local variation of the interface curvature. After heat treatment, spherically shaped Fe and Nb nanoparticles, located in chains perpendicular to the substrate, were observed and depicted by means of transmission electron microscopy (TEM) and X-ray microscopy (XRM).

INTRODUCTION

The preparation of nanosized metallic particles in a metallic matrix by thermal disintegration was observed in Nb/Cu multilayers [1,2]. Such multilayers can be easily prepared by conventional thin-film deposition techniques. However, the mechanism of disintegration of multilayer structures is not well understood. Theoretical investigations are published only for cylindrically shaped Nb filaments in a Cu matrix [3]. From these calculations a strong dependence of the disintegration on the initial interface roughness, the interface tension, as well as on the filament dimensions are expected [4]. For a better understanding of this process in real planar systems, the disintegration was studied in non-miscible metallic systems like Fe/Au, Fe/Ag, and Nb/Cu.

In addition to the driving forces causing this process, the final distribution of the formed particles is of interest. A process of self-ordering might occur, resulting in a non-statistical distribution of the particles. Due to its rather large area of observation, XRM [5] was used in addition to TEM to investigate the particle distribution.

EXPERIMENT

Fe/Au, Fe/Ag, Cu/Co, and Nb/Cu multilayered thin films were grown on sapphire and silicon substrates in an UHV-triode-magnetron sputtering device. The pressure of residual gases like O_2, H_2O, or N_2 during the deposition was better than 10^{-8} mbar. Two single metal triode magnetron sputtering sources were directed onto a heatable substrate holder, so that the direction of the incoming metal atoms and the substrate normal enclosed an angle of about 30°. The deposition rates were adjusted to about 0.8 nm/s for the Au, Ag, Cu, and Nb and about 0,2 nm/s for Fe, respectively. In order to minimize the intermixing at the interfaces, the source was switched off and additionally closed by a shutter after the deposition of each single layer. Partial heat treatments of the samples were performed after the deposition without breaking the vacuum. To study the dependence of the disintegration temperature on the layer thickness, a series of Fe/Au and Nb/Cu samples were deposited with varying layer thickness of only one of the metals (Fe and Nb) and constant thicknesses of the second one. The thinner layers are called intercalated layers (thickness d) and the thicker ones are called matrix layers (thickness D). The samples

Mat. Res. Soc. Symp. Proc. Vol. 581 © 2000 Materials Research Society

were composed of 0.5 up to 5 nm thick intercalated compound (Fe or Nb) and a 10 nm thick matrix layer of Au, Ag, and Cu, respectively. The investigations of the microstructure were performed with samples composed of 2 nm Fe or Nb and 10 nm Au, Ag, and Cu respectively. The number of bilayers amounted to 100 for transmission electron microscopy (TEM) measurements and to 10 for X-ray microscopy. In the latter case the number of bilayers was reduced because films of this thickness can be transmitted by X-ray without any additional thinning of the film; only the substrate has to be removed by chemical etching.

Beside room temperature investigations of *in-situ* annealed samples, XRD measurements were performed in the hot stage of a X-ray diffractometer under a vacuum of better than 10^{-5} mbar. X-ray scans were recorded as a function of annealing time (in 5-minutes steps) at a fixed temperature or at a fixed heating rate of 0.2 K/min. The lattice constant of the compounds and the grain size were determined from these scans.

The microstructure of the samples was investigated by means of TEM and XRM. For the cross-sectional TEM investigations the samples were ground, dimple-thinned and finally ion-milled.

The experimental set up of the X-ray microscope is similar to an optical microscope. The samples are irradiated by synchrotron radiation, which is focused by a zone plate working as a fresnel lens. Due to the strong wavelength dependence of the focal length, the radiation becomes monochromatic by employing a monochromator pinhole. The camera in the picture field can detect either intensity contrasts or phase contrasts. The micrographs presented in this paper are taken by using an amplitude contrast.

RESULTS

The disintegration process of multilayered systems can be easily detected by X-ray diffraction during a heat treatment, observing the change of the superstructure diffraction pattern. In multilayered systems satellite reflexes due to the periodicity of the multilayer structure are also visible, modifying the common Bragg pattern. A model proposed by [6] was used to analyze the degree of periodicity, the roughness, and the intermixing from the diffraction pattern. Therefore, the change of this pattern reflects the change of the microstructure. In particular, the disappearing superstructure reflections indicate the disintegration of the layered structure. Fig. 1 depicts the development of the diffraction pattern of an Fe/Au multilayer (1.25 nm / 10 nm) during a heat treatment with increasing temperature up to 330°C. The diffraction pattern of the as-prepared samples results from both the atomic Au lattice and the multilayer superlattice. The Fe does not cause any diffraction pattern due to its small atomic form factor and its strongly disordered structure. The latter has been confirmed by TEM investigations, which reveal no lattice fringes in Fe (Fig. 4). During the heat treatment the sample lost its periodicity at about 320°C (red line, Fig. 1). At the same time, when the multilayer disintegrates, the Fe

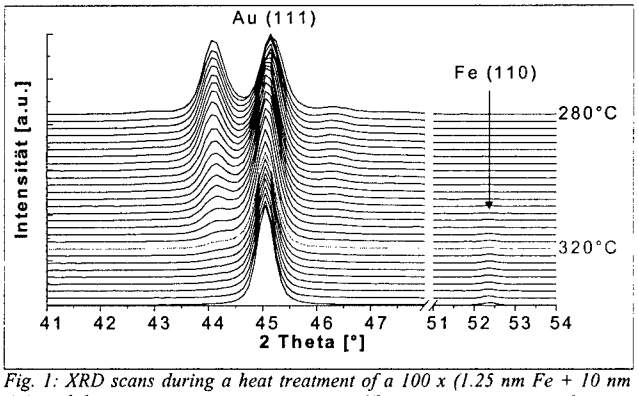


Fig. 1: XRD scans during a heat treatment of a 100 x (1.25 nm Fe + 10 nm Au) multilayer at increasing temperature. The superstructure vanishes at about 320°C.

(110) peak becomes visible, i.e. larger Fe particles were formed. Qualitatively, the same behavior was observed for the systems Fe/Ag and Nb/Cu, but at different temperatures of disintegration.

The disintegration temperature depends on the thickness of the intercalated layer. The results are summarized in Fig. 2, which depicts this dependence for Nb/Cu and Fe/Au multilayers.

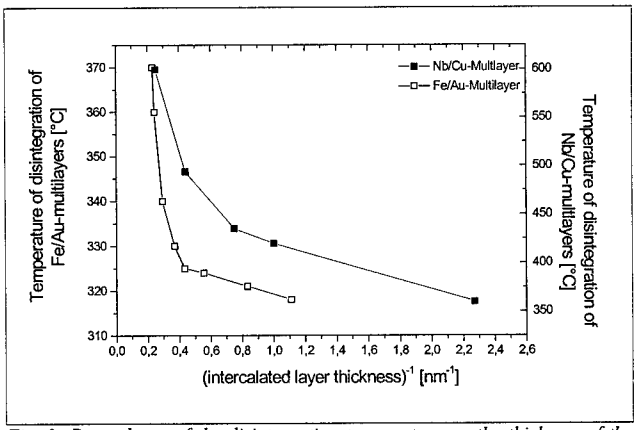


Fig. 2: Dependence of the disintegration temperature on the thickness of the intercalated layer.

The samples for the TEM investigations were heat treated *in-situ* for 60 min. at temperatures 20°C above the disintegration temperature deduced from XRD investigations. All the samples had the same composition, d = 2nm for the intercalated layer (Fe or Nb) and D = 10 nm for the matrix (Au, Ag, or Cu). In all these systems a pronounced columnar growth was observed. The columns show a width of between 40 nm for Fe/Au, 70 nm for Fe/Ag and about 100 nm for Nb/Cu. The interfaces of the different layers within the columns are convex, deep on the grain boundaries. The amplitude of this roughness increases with increasing film thickness as long as no additional grain boundaries are formed inside a column. The next layers above such a boundary reveal a lower interface roughness. The columns don't grow perpendicular to the substrate, but under an angle of about 12° normal to the substrate, which was also confirmed by X-ray texture measurements. This effect of a tilted columnar growth is not unknown in the literature. It is due to the angle between the substrate normal and the direction of the sputter sources (30°). The columns grew in the direction of the source of the matrix metal, i.e. Au, Ag, and Cu.

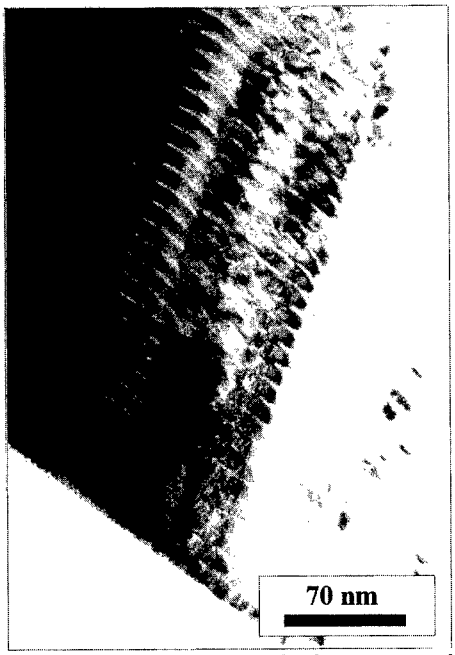


Fig. 3: Cross-section micrograph of an as-prepared Fe/Au multilayer. Macro-grains are clearly visible.

Within these columns the crystallographic orientation of the Au, Ag, and Cu layers is identical (Fig. 3). Fig. 4 depicts two Fe layers (the bright horizontal area) separated by an Au layer. On the right-hand side of this picture a grain boundary is visible. Dark field TEM investigations reveal the crystallographic orientation to be different between the grains but equal within them. Therefore, the columns might be considered to be macro-grains. Such a growth of the layered structure indicates an epitaxial relationship between intercalated layers and the spacer. Due to the large lattice mis-

match, the intercalated layers should be strongly strained. This is indeed observed for the Nb layers by XRD. Although TEM investigations clearly demonstrate the orientational relationship between Au or Ag layers, even HRTEM did not reveal any lattice fringes in Fe. Therefore, we conclude, that the Fe layers are strongly disordered but able to transfer the texture information from one noble metal layer to the next. During the heat treatment the microstructure changes dramatically. As expected from XRD measurements Fe or Nb particles were formed in the nobelmetal matrix. By Scherrer's formula [7] the particle size in the 2 nm / 10 nm samples could be estimated to about 25 nm in Nb/Cu, 10 nm in Fe/Ag, and 25 nm in Fe/Ag. To characterize the distribution of the different metals in the sample, the so called Z-contrast was used in TEM. Different than in the normal bright-field TEM micrographs, Z-contrast depicts a mass contrast. Therefore, the particles formed could be distinguished from the surrounding matrix very clearly. An example of a Z-contrast image of a disintegrated Fe/Au multilayer is shown in Fig. 5a. The Fe particles are visible as dark nearly spherically shaped areas. The grain boundaries are marked by white lines. For comparison a bright-field TEM picture of a disintegrated Fe/Ag sample is shown in Fig. 5b. Comparing Fig. 5a and b, several similarities but also some differences between Fe/Ag and Fe/Au can be obtained. In both systems the originally layered structure is partly preserved, but the interface between the Au or the Ag layers is strongly flattened. Most of the Fe is agglomerated in the boundaries of the macro-grains, forming a chain of pearls particles along these boundaries. Therefore, the lateral mean distance between the par-

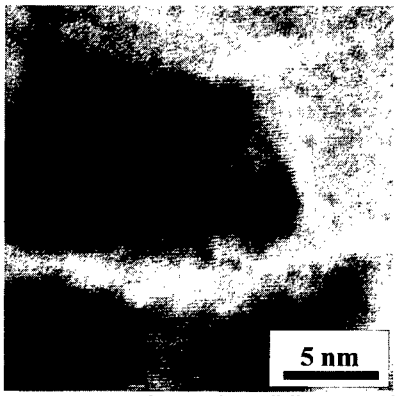


Fig. 4: 10 nm Au layer with parallelly orientated lattices fringes interrupted by a 2 nm Fe-layer (bright area). On the right side of the picture a macro-grain boundary is visible.

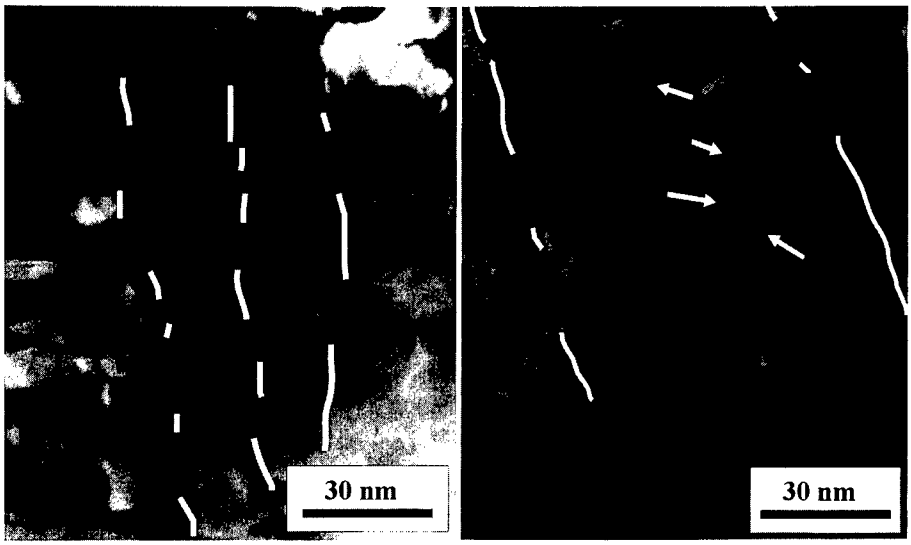


Fig. 5: Disintegrated Fe/Au multilayer (left) and disintegrated Fe/Ag multilayer (right). Nearly spherically- shaped Fe particles are found in the macro-grain boundaries and especially in the system Fe/Ag small flat particles within the macro-grains (white arrows). Macro-grain boundaries are marked with white lines.

ticles corresponds to the width of the columns. The distribution along the boundaries is not so regular, partly in each layer an Fe sphere is formed, but also large segments of the boundary are free of Fe particles. The mean size of the particles in Fe/Ag of about 20 nm is two times larger than in Fe/Au, which agrees with the higher disintegration temperature of Fe/Ag. However, in Fe/Ag also disc-like particles are visible, which are located in the macro-grains. The lateral size is about 10 nm, their thickness only a few nm.

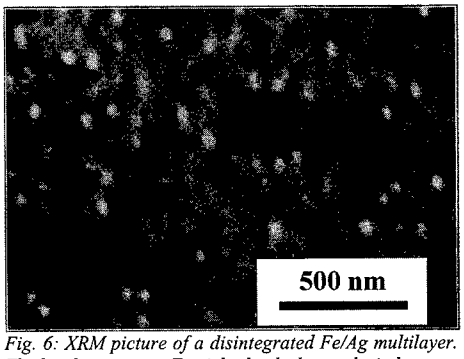


Fig. 6: XRM picture of a disintegrated Fe/Ag multilayer. The bright parts are Fe-rich, the darker paths in between contain more Ag.

The non-statistical distribution of the particles can also be visualized in XRM. Because of its lower lateral resolution in the transmission mode, an amplitude contrast only occurs, if there are several particles stacked over each other, separated by areas free of particles. A statistical distribution of particles in each layer would give no contrast, because in this case the average content of the metals is nearly constant over the whole sample. Fig. 6 depicts the transmission picture of a disintegrated Fe/Ag multilayer. The bright areas i.e. the weak absorbing areas, contain more Fe. In all disintegrated samples a contrast could be observed, indicating a non-statistical distribution on large parts of the sample. It could be also seen clearly that the particle size in Fe/Au multilayers is much smaller than in Fe/Ag multilayer. In both cases it seemed to be even larger than the ones measured in TEM. This could be explained by the slight tilt of the chains of Fe particles. Consequently, the projection of such a chain is larger than a particle diameter.

Discussion

It has been suggested that a spatial variation of the interface energy causes the driving force of the disintegration process [3]. Since the nanoparticles are primarily formed at the grain boundaries, the mass transport is directed from the center of the macro-grains to the grain boundaries.

The first contribution to the interface energy, which causes such a transport, is the variation of the curvature of the interface. The curvature is directly related to the chemical potential of the interface by Thomson's relation:

$$\mu \propto \frac{\gamma}{r} \qquad (1)$$

The radius of curvature, having its maximum at the center of the macro-grains is very small at the grain boundaries (Fig. 3). The flattening of the interface after the heat treatment (Fig. 5) also indicates that this mechanism is responsible for the disintegration. In addition, a numerical simulation of this process, taking into account the local variation of the layer thickness, reveals the essential features of the disintegration, i.e. the formation of particles at the grain boundaries and of pancake-like particles within the macro-grains. However, with a decreasing thickness of the intercalated layer, a second contribution to the driving force becomes important. Because of the epitaxial growth within the macro-grain, a high amount of lattice misfit strain is generated in the layered structure. This stress is partly released by mistfit dislocations as long as the layer thickness is large enough. Below a critical thickness, which is found to be around 3.6 nm for Fe, the misfit dislocations become unstable [8]. Streitz et al. [9] have calculated the strain-depending interfacial energy of a multilayered system in dependence on the length of periodicity λ_0. In this model the interfaces are assumed to be coherent and only elastic relaxation occurs. With the unstrained interfacial energy f_0, the biaxial modulus is Y_∞, and the area A_0 of the interfaces the

interfacial energy per area is calculated to

$$\frac{\Delta U}{2A_0} = -2\frac{f_0^2}{\lambda_0 Y_\infty} + O(\lambda_\infty) \qquad (2)$$

Since the strain is released at the grain boundaries, this contribution also results in a mass transport directed to the boundaries. Equation (2) might be considered as the difference of the interfacial energy within the macro-grain and at the boundary, and therefore as an estimation of the driving force. Indeed, two experimentally different regimes were found (Fig. 2). For thin intercalated layers, the temperature of disintegration is proportional to the reciprocal thickness of the intercalated layers. This regime ranges up to a Fe-layer thickness of d = 2.5 nm for Fe/Au multilayers and up to d = 1.4 nm for Nb/Cu multilayers. Upon further increasing of the layer thickness the disintegration temperature increases more rapidly. In view of the two contributions proposed, in thin intercalated layers the high amount of stored elastic energy causes a strong driving force, i.e. the disintegration occurs at a low temperature. With increasing layer thickness, the strain is released by dislocations and the less effective curvature-induced transport controls the disintegration.

In addition, it was observed that some of the grain boundaries are free of particles whereas other boundaries contain a high number of particles. Since at tripel grain boundaries the interface curvature and the strain relaxation is strongest, the tripel grain boundaries might be the preferred sites for the formation of the nano-particles.

CONCLUSIONS

Multilayers consisting of non miscible metals are unstable in view of the formation of small spherical particles of the intercalated compound. The disintegration of the layered structure occurs at moderate temperatures. In XRD, the superstructure of the multilayer vanishes and a pronounced sharpening of the single metal diffraction pattern, i.e. a growth of the particle size, becomes visible. The disintegration temperature deduced from this measurement depends on both, the combination of metals and the thickness of the intercalated layers.

Most of the particles are located within the grain boundaries of the macro-grains. Taking this into account, two different contributions to the driving force were proposed. In thick intercalated layers, the initial curvature of the interface causes a mass transport to the boundaries. In thin intercalated layers the misfit induced strain at the interface dominates the disintegration process. The required temperature is lower and follows an reciprocal dependence on the layer thickness.

REFERENCES

1. P. Troche, J. Hoffmann, K. Heinemann, F. Hartung, G. Schmitz, H.C. Freyhardt, D. Rudolph, J. Thieme, P. Guttmann, Thin Solid Films **353**, pp. 33-39 (1999)
2. P. Troche, J. Hoffmann, K. Heinemann, F. Hartung, G. Schmitz, H.C. Freyhardt, D. Rudolph, J. Thieme, P. Guttmann, *X-ray microscopy and spectroscopy*, Springer-Verlag, Heidelberg, 1998, pp. 123-129
3. H.E. Cline, Acta Met. **19**, p. 481-490 (1957)
4. J. van Suchtelen, J. Cryst. Growth **43**, pp. 28-46 (1978)
5. G. Schmahl, D. Rudolph, B. Niemann, P. Guttmann, J. Thieme, Naturwissenschaften **83**, pp. 61-70 (1996)
6. J.-P. Locquet, D. Neerinck, L. Stockman, and Y. Bruynseraede, Phys. Rev. B **39**, pp. 13338-13342 (1989)
7. B.D. Cullity, *Elements of X-Ray Diffraction*, Addison-Wesley Publishing Comp., 1967 p. 99
8. D. Ariosa, O. Fischer, M.G. Karkut, J.-M. Triscone, Phys. Rev. B **37**, pp. 2421-2425 (1988)
9. F.H. Streitz, R.C. Cammarata, K. Sieradzki, Phys. Rev. B **49**, pp. 10707-10716 (1994)

MAGNETIC HARDENING INDUCED BY EXCHANGE COUPLING IN MECHANICALLY MILLED ANTIFERROMAGNETIC – FERROMAGNETIC COMPOSITES

J. SORT, J. NOGUÉS, X. AMILS, S. SURIÑACH, J.S. MUÑOZ, M.D. BARÓ
Departament de Física, Universitat Autònoma de Barcelona, 08193 Bellaterra, Spain

ABSTRACT

Mechanical milling has been used to synthesize ferromagnetic (FM, Co) - antiferromagnetic (AFM, NiO) composites. The coercivity, H_C, and energy product, BH_{Max}, of these composites can be enhanced at room temperature after appropriate heat treatments above the Néel temperature of the AFM, T_N. Although the maximum H_C is achieved for the (NiO)1:1(Co) weight ratio, BH_{Max} is further enhanced for the (NiO)2:3(Co) ratio, where higher saturation magnetization is obtained due to the larger amount of FM. Exchange coupling, responsible for these effects, decreases as the temperature is increased and vanishes close to T_N. The thermal stability of the coercivity enhancement remains rather insensitive to the somewhat broad distribution of blocking temperatures of this system.

INTRODUCTION

Since mechanical alloying (MA) was developed in the late 1960s [1], this technique has been used as a processing route for the synthesis of a large variety of equilibrium and non-equilibrium phases and phase mixtures [2]. This technique has been shown to be successful in reducing crystallite sizes to the nanometric range. These small particles can exhibit rather different physical properties from those of their bulk counterpart [3].

Mechanical alloying has also been used to produce direct or indirect magnetic interactions, like in exchange spring magnets (milling soft-hard ferromagnets) [4,5] or giant magnetoresistance materials (milling magnetic-nonmagnetic phases) [6]. However, studies of exchange interaction between ferromagnetic and antiferromagnetic materials induced by ball milling are scarce. Nevertheless, recently the possibility of increasing the room temperature coercivity by mechanical alloying transition metals (Ni, Co, Fe) and their own antiferromagnetic oxides (NiO or CoO) or sulfides (FeS) has been proven [7]. Moreover, it is well known that oxidized ferromagnetic fine particles can also exhibit coercivity enhancements [8]. However, this enhancement is mainly observed far below room temperature, which makes this property not useful for applications. It is noteworthy that coercivity increases due to AFM-FM exchange coupling are also being studied in thin film systems [9,10].

In this paper we show the possibility of increasing the room temperature coercivity and energy product by ball milling FM and AFM composed of *different* transition metals, e.g. Co and NiO, after adequate magnetic field heat treatments. The hardening of the FM phase is optimized by varying the AFM:FM ratio.

EXPERIMENTAL

Different AFM:FM weight ratios (0:1, 3:7, 2:3, 1:1 and 3:2) of gas - atomized powders of NiO (99%, <100 μm, T_N = 590 K) and Co (99.5%, < 44 μm, T_C = 1404 K) were mixed and sealed under Ar atmosphere in an agate vial (V = 20 ml), together with 6 agate balls (10 mm diameter), with a ball to powder weight ratio of 2:1. The milling was carried out for different

Mat. Res. Soc. Symp. Proc. Vol. 581 © 2000 Materials Research Society

times (0.1-30 hours), at 500 rpm, using a planetary mill. To induce exchange coupling, the as milled powders were annealed at different temperatures, T_{ANN} = 300 - 850 K, for different times (0-5 hours) under vacuum, in the presence of different magnetic fields (0 - 10 kOe), and field cooled to room temperature.

The microstructure of the powders was studied using standard x-ray diffraction (XRD) (Cu-K_α radiation). The x-ray diffraction peaks were deconvoluted and fitted using a pseudo-Voigt function. The crystallite size, <D>, was evaluated using a single peak method from its integral breadth (Cauchy component), following Scherrer's approximation. Their morphological characterization was performed by using scanning electron microscopy (SEM), equipped with energy dispersive x-ray analysis (EDX). Magnetic hysteresis loops, up to 10 kOe, were measured in loosely packed powders, at temperatures between room temperature and 750 K, by means of vibrating sample magnetometry (VSM).

RESULTS AND DISCUSSION

Shown in fig. 1(a) is a SEM image (secondary electron) for the NiO-Co powders ball milled for 20 hours in a weight ratio of 1:1. Ball milling induces a broad range of particle sizes, from 1 μm to 30 μm [11]. The larger particles (an enlargement of one of these particles is shown in fig. 1) are composed of about 1 μm thick lamellae, surrounded by small particles. As can be seen in fig. 1(b) the Co x-ray mapping indicates that the lamellae (bright in fig. 1(a)) correspond to Co while the particles (gray in fig. 1(a)) correspond to NiO. This microstructure, typical of ball milled ceramic-metal mixtures, is due to the ductile and brittle character of Co and NiO respectively. Moreover, this microstructure allows the existence of a large interface area between the FM and the AFM phases.

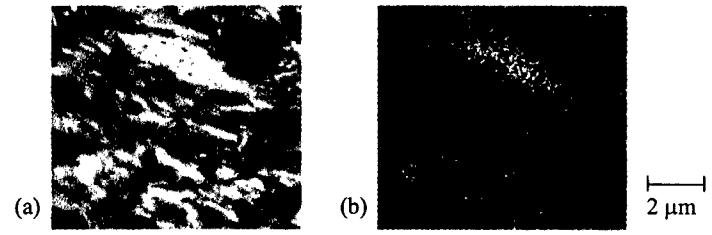


Fig. 1 (a) SEM secondary electron image and (b) Co EDX mapping for a (NiO)1:1(Co) ball milled for 20 h.

X-ray diffraction (XRD) patterns have been obtained for the unmilled Co and NiO and for the 20 h ball milled NiO-Co in a weight ratio of 1:1, before and after field annealing them in a 5 kOe magnetic field at T_{ANN} = 600 K. The XRD patterns of the unmilled Co reveal that it corresponds to a mixture of hcp and fcc Co, while the unmilled NiO powder diffraction peaks correspond to a fcc phase. The crystallite sizes, evaluated for the Co hexagonal (002) and the NiO (111) peaks, are $\langle D \rangle_{Co,Hex} = 42 \pm 4$ nm and $\langle D \rangle_{NiO} > 100$ nm, respectively [11].

When Co and NiO powders are ball milled together in a 1:1 weight ratio the intensity of the peaks corresponding to the fcc Co phase rapidly decreases. This allotropic transformation has been previously reported for ball milled Co powders [12]. The peak widths of the different phases after ball milling show an important increase. This is related to the crystallite size reduction, the introduction of planar defects and the microstrain increase. The crystallite sizes, after 20 hours of milling, estimated from the $(002)_{Co,Hex}$ and the $(111)_{NiO}$ reflections, are: $\langle D \rangle_{Co,Hex} = 10 \pm 2$ nm and $\langle D \rangle_{NiO} = 14 \pm 2$ nm, respectively. In addition, the positions of the

NiO peaks do not change after ball-milling, indicating no important variation in its lattice parameter. This suggests that the diffusion of Co into the NiO cell is very small [11].

When the ball milled NiO-Co powders are annealed at T_{ANN} = 600 K for 0.5 hours the x-ray diffraction pattern is very similar to that of the as milled powders, where the NiO peaks are not displaced and only a minor decrease in the peak width is obtained. The crystallite size calculated from the (11[illegible])$_{NiO}$ reflection is $\langle D \rangle_{NiO}$ = 18 ± 2 nm. The Co-hcp phase shows a similar behavior, with $\langle D \rangle_{Co,Hex}$ = 18 ± 2 nm, calculated from the $(002)_{Co,Hex}$ peak. Moreover, at this annealing temperature, a slight increase in the intensity of the $(200)_{Co,Cubic}$ peak can already be observed, indicating the starting point for an allotropic transformation from hcp to hcp+fcc [12]. However, after annealing at T_{ANN} = 740 K for 0.5 hours, the crystallite sizes, calculated from $(100)_{Co,Hex}$ and $(111)_{NiO}$ peaks, increase significantly to $\langle D \rangle_{Co,Hex}$ = 44 ± 4 nm and $\langle D \rangle_{NiO}$ = 40 ± 4 nm and the intensity of the peaks corresponding to the cubic phase increases. Thus, annealing at T_{ANN} = 740 K induces an important crystal growth and the allotropic phase transformation from hcp to fcc Co [11].

The room-temperature coercivity, H_C, has been measured as a function of the milling time for the different NiO:Co weight ratios for both as-milled and annealed (T_{ANN} = 600 K) powders. In pure Co, H_C increases after a short milling time (1 hour) from H_C = 170 Oe (as obtained) to 290 Oe (1 hour ball milled) [13]. This increase is attributed to the allotropic phase transformation from fcc+hcp Co to hcp Co, where hcp Co is known to have larger H_C than fcc Co [14]. Further milling decreases H_C (e.g. H_C = 125 Oe after milling 30 hours), which is probably linked with the disordering of the hexagonal structure, as has been reported for long-term milling [12]. A maximum in H_C is also observed for ball milled NiO:Co. However, for each AFM:FM ratio, the largest H_C is obtained for different milling times, which increase as the NiO content increases, indicating that NiO probably delays the Co structural changes.

Annealing the ball milled pure Co powders at T_{ANN} = 600 K (i.e. $T_N < T_{ANN} < T_C$) for 0.5 hours in H = 5 kOe results in a slight decrease in H_C. However, a significant enhancement of H_C is observed after annealing the ball milled NiO-Co powders at the same temperature, T_{ANN} = 600 K, and field cooling (H = 5 kOe) to room temperature [13]. Shown in fig. 2 is the dependence of the coercivity enhancement (defined as the difference of H_C after and before annealing at T_{ANN}, ΔH_C) on the annealing temperature for (NiO)1:1(Co) ball milled 20 h. As can be seen in the figure, the room-temperature H_C increases only when the annealing temperature is larger than the NiO Néel temperature (i.e. T_N = 590 K), as expected for an exchange coupled FM-AFM system [9]. The decrease of ΔH_C after annealing at exceedingly high temperatures (T_{ANN} > 700 K) is due to the allotropic phase transformation from fcc+hcp Co to fcc Co, as

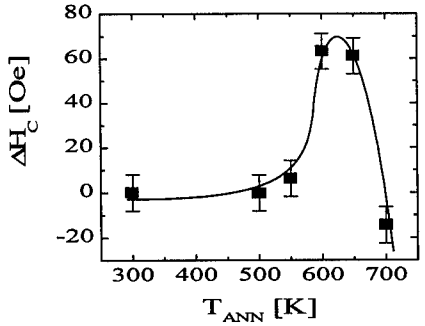


Fig. 2 Dependence of the coercivity enhancement, ΔH_C, on the annealing temperature for a (NiO)1:1(Co) ball milled for 20 h.

observed from XRD. Loop shifts in the field axis, H_E, towards the negative field axis are also present in the hysteresis loops of the ball milled NiO-Co samples for all AFM:FM ratios, except in pure Co. The loop shifts depend on the annealing temperature with a similar dependence as ΔH_C, confirming the assumption that the exchange coupling between the AFM and the FM is responsible for both effects, ΔH_C and H_E.

Exchange coupling produces not only an enhancement of H_C but also an enhancement of the squareness, M_R/M_S [13], and consequently an increase of the energy product, BH_{Max}. The dependence of H_E, ΔH_C and ΔBH_{Max} (defined as the difference of BH_{Max} after and before annealing at T_{ANN} = 600 K) on the Co content (NiO:Co ratio) is shown in fig. 3. The values shown in the figure correspond to the milling times which give the maximum values of H_C for each NiO:Co ratio. As can be seen in the figure, the largest exchange coupling effects, i.e. maximum enhancements of H_C and BH_{Max} and maximum loop shifts, are exhibited for the (NiO)1:1(Co) ratio. However, the maximum value of BH_{Max} after annealing at T_{ANN} = 600 K is not obtained for (NiO)1:1(Co) (BH_{Max} = 62000 G.Oe) but for (NiO)2:3(Co) (BH_{Max} = 83000 G.Oe). This is due to the interplay between H_C and M_S on BH_{Max}. The addition of an AFM and the subsequent heat treatments increase H_C, however the AFM also promotes a reduction in the overall M_S of the composite. Hence, the enhancement of BH_{Max} is a compromise between both effects.

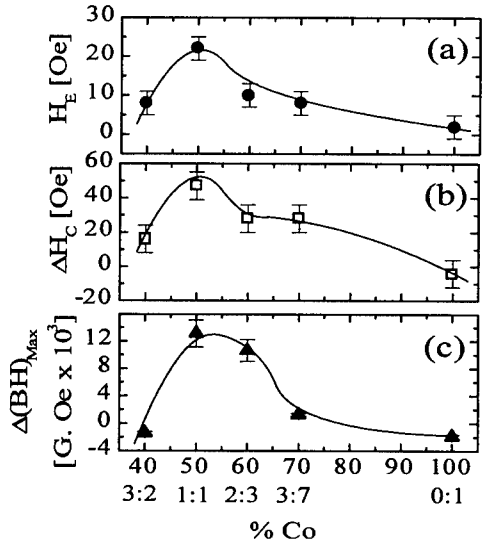


Fig. 3 Dependence of the (a) exchange bias, H_E, (b) coercivity enhancement, ΔH_C, and (c) enhancement of the energy product, $\Delta(BH)_{Max}$, on the Co percentage (NiO:Co ratio).

Shown in fig. 4 is the dependence of the loop shift on the measuring temperature. As expected from exchange coupled AFM-FM systems, H_E decreases as measuring temperature increases, becoming zero at $T \approx 600$ K, i.e. at the Néel temperature of the AFM (T_N (NiO) = 590 K). A similar behavior is observed for ΔH_C and $\Delta(BH)_{Max}$. The decrease of these properties with increasing measuring temperature is the result of a reduction of the AFM/FM interface coupling,

as a consequence of either the loss of the magnetic order in the AFM and/or the reduction of the AFM magnetocrystalline anisotropy. The critical temperature at which exchange coupling effects completely vanish is usually denoted as the blocking temperature, T_B [9].

To study the thermal stability of the ball milled NiO:Co systems due to the concomitant distribution of blocking temperatures [15] (brought about by the distribution of crystallite sizes and defects), the NiO:Co samples were warmed to a temperature T_D, 300 K < T_D < 700 K, and subsequently cooled to room temperature in a field H = - 5 kOe, i.e. opposite to the one used to induce the original coupling (H = 5 kOe).

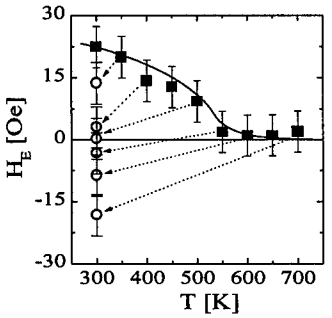


Fig. 4 Temperature dependence of the exchange bias, H_E (■), on the measuring temperature, and H_E (○) after field cooling in H = -5 kOe from different temperatures.

Following this procedure, if the local blocking temperature of a crystallite (T_{Bi}) is below T_D, the crystallite becomes paramagnetic, thus losing the information of the original coupling. Cooling such crystallite in H = - 5 kOe induces a coupling opposite to the original one, hence shifting the loop towards *positive* fields. However, crystallites with $T_{Bi} > T_D$ remain unchanged. Consequently, the H_E obtained after warming to each T_D gives a measure of the number of crystallites with $T_{Bi} < T_D$ [15]. As can be seen in fig. 4, already at T_D = 350 K a reduction in H_E can be observed. Moreover, for T_D = 500 K H_E is reduced to zero (i.e. 50 % of the crystallites have T_{Bi} < 500 K). These results indicate a broad distribution of blocking temperatures in this system. However, although the thermal stability of H_E is strongly influenced by the distribution of T_B, we observed that H_C is rather insensitive to it. This is probably because although the overall H_E depends on the *strength* and *sign* of the coupling for each crystallite, the enhancement of H_C depends only on the *strength* of the coupling.

CONCLUSIONS

In conclusion, we have shown that mechanically milled AFM(NiO) - FM(Co) composites display significant enhancements of the room temperature coercivity and energy product due to the exchange coupling induced after heat treating the samples at $T_{ANN} > T_N$ under magnetic fields. The as-milled powders exhibit a peculiar microstructure (Co lamellae surrounded by refined NiO particles), which allows the existence of a large interface area between the FM and the AFM. The maximum magnetic hardening is shown to be a trade off between the coercivity enhancement produced by exchange coupling and the overall reduction of saturation magnetization due to the antiferromagnet. All the effects (H_C, H_E and BH_{Max}) decrease with increasing temperature and the NiO-Co samples become uncoupled when the

measuring temperature is larger than the antiferromagnetic Néel temperature. Although H_E is strongly influenced by the distribution of T_B, H_C remains rather insensitive to it.

ACKNOWLEDGEMENTS

This work was supported in part by DGESEIC under contract MAT98-0730 and by CICYT under contract PETRI95-0311-OP. J.S. thanks the DGU for his fellowship. J.N. and X.A. acknowledge the Spanish Government for its financial support.

REFERENCES

1. J. S. Benjamin, Metall. Trans. **1**, 2943 (1970); Mater. Sci. Forum **88-90**, 1 (1992).

2. For a review, see B. S. Murty and S. Ranganathan, Inter. Mater. Rev. **43**, 101 (1998).

3. For a review, see R. W. Siegel, Nanostruct. Mater. **3**, 1 (1993).

4. P. G. McCormick, W. R. Miao, P. A. I. Smith, J. Ding, R. Street, J. Appl. Phys. **83**, 6256 (1998).

5. K. Raviprasad, M. Runakoshi and M. Umemoto, J. Appl. Phys. **83**, 921 (1998).

6. A. J. Fargan, M. Viret and J. M. D. Coey, J. Phys: Cond. Matter. **7**, 8953 (1998).

7. D. S. Geoghegan, P. G. McCormick and R. Street, Mat. Sci. Forum **179-181**, 629 (1995).

8.W. H. Meiklejohn and C. P. Bean, Phys. Rev. **102**, 1413 (1956); **105**, 904 (1957).

9. For a review, see J. Nogués and Ivan K. Schuller, J. Magn. Magn. Mater. **192**, 203 (1999).

10. A. S. Edelstein, R. H. Kodama, M. Miller, V. Browning, P. Lubitz, S. F. Cheng and H. Sieber, Appl. Phys. Lett. **74**, 3872 (1999); Y. J. Tsang, B. Roos, T. Mewes, S. O. Demokritov, B. Hillebrands and Y. J. Wang, Appl. Phys. Lett. **75**, 707 (1999).

11. J. Sort, J. Nogués, X. Amils, S. Suriñach, J. S. Muñoz and M. D. Baró, Mater. Sci. Forum (2000) in press.

12. J. Y. Huang, Y. K. Wu and H. Q. Ye, Appl. Phys. Lett. **66**, 308 (1995); F. Cardellini and G. Mazzone, Philos. Mag. A **67**, 1289 (1993).

13. J. Sort, J. Nogués, X. Amils, S. Suriñach, J. S. Muñoz and M. D. Baró, Appl. Phys. Lett. **75**, 3177 (1999).

14. H. Sato, O. Kitakami, T. Sakurai, Y. Shimada, Y. Otani and K. Fukamichi, J. Appl. Phys. **81**, 1858 (1997).

15. S. Soeya, T. Imagawa, K. Mitsuoka and S. Narishige, J. Appl. Phys. **76**, 5356 (1994); C. Tsang and Kenneth Lee, J. Appl. Phys. **53**, 2605 (1982).

STUDY OF THE LUMINESCENCE OF Eu-DOPED NANOCRYSTALLINE Si/SiO_2 SYSTEMS PREPARED BY RF CO-SPUTTERING

G.A. NERY*, A. MAHFOUD**, L.F. FONSECA, H. LIU**, O. RESTO, AND S.Z. WEISZ
Physics Department, University of Puerto Rico, San Juan, PR, USA.
*Physics and Chemistry Department, University of Puerto Rico, Arecibo, PR, USA.
**Physics Department, University of Puerto Rico, Mayaguez, PR, USA.

ABSTRACT

We prepared Eu-doped films of Si nanoparticles embedded in SiO_2 using pellets of Eu_2O_3 by sputtering. We studied their photoemission, transmission and fluorescence to obtain data about their composition and particle size and the Eu interaction characteristics. We were able to incorporate Eu(III) into the Si nanoparticle / SiO_2 host. We also found we obtained Eu(II) in the process. We found a lowering of photoluminescence intensity with lowering of temperature. An as yet unanswered question is the reason for the intense whitish luminescence found in some regions of the samples. Some involvement with Eu(II) is suspected. Eu(III) related peaks were only observed where the size distribution peak of the nanoparticles was lower than 1.3nm. Whitish luminescence was related to peak sizes ranging from 1.1nm to 1.4nm. Annealing the samples had clear effects upon their photoluminescence, but did not necessarily involve changes in particle sizes, nor were these size changes necessary to increase luminescence. The Eu doping has a tendency to halt the annealing effects on size and, when changes did occur, the particles generally became smaller.

INTRODUCTION

Europium is an interesting material when incorporated as a dopant into solid state materials. This is because trivalent Eu(III) ions can be used as a structure probe, and due to its large quadrupole splitting and spin-lattice relaxation times, Eu(III) is particularly attractive in high-resolution laser spectroscopy [1]. One proposed application is in a frequency domain optical data memory, based on the large ratio of inhomogeneous-to-homogeneous line widths present. In some solid state materials the Eu(III) dopant ions exhibit the longest ever dephasing time of 822μs and the narrowest homogeneous line width at low temperature [2]. This has stimulated interest in searching for appropriate materials to host Eu(III) ions, which could be optimized for operation at room temperature.

We have produced and studied Si/SiO_2 material in which visible light emitting Si nanoparticles are embedded in a SiO_2 matrix. We made subsequent studies incorporating another rare-earth metal, Er, into the Si nanoparticle embedded SiO2 matrix and verified that the luminescence of Er is enhanced due to energy transfer between the nanoparticles and the Er [3].

These considerations led us to attempt to ascertain the interactions between Eu and this new host material. Due to the amorphous nature of the SiO_2 material prepared by this particular technique, the dopant europium ions must experience large variations of their environment. Additionally, some Eu(III) ions may be placed at the Si nanoparticle / SiO_2 interface while the others are inside the SiO_2 host. This would produce fluorescence line broadening. Also, our use of Eu_2O_3 as the source of our dopant could lead to interactions between the oxygen thus incorporated into our samples and the Si, as had apparently happened in our previous Er incorporation experiments.

Mat. Res. Soc. Symp. Proc. Vol. 581 © 2000 Materials Research Society

EXPERIMENT

We combined Eu_2O_3, Si and SiO_2 producing a series of samples by sputtering deposition. We produced samples with Si and SiO_2; Eu_2O_3 and SiO_2; Eu_2O_3 and Si; and Eu_2O_3, Si and SiO_2. The samples were deposited on a quartz substrate which was previously cleaned by a 30 min. immersion in an acid (20%HF), rinsed in de-ionized water, and dried with N_2. It was placed above the sputtering targets. For the sputtering we first reached a vacuum of about $5*10^{-7}$torr. After 30 min. of pre-sputtering the samples were made by a 12hr deposition. Argon at 20 mtorr pressure was used for the sputtering. The plates holding the sample and the target materials reached temperatures in the vicinity of 110°C. The target voltage was 1100V with a 0.12A plate current.

The largest portion of the target was a 13.2cm diameter disk of SiO_2 (except for the Eu_2O_3 with Si sample, in which case it was a disk of Si). When including Si in the sample (for the nanoparticles) we placed a 3.00cm by 2.30cm Si rectangle on the border of the SiO_2 disk. The 14cm x 1cm x 0.1cm rectangular quartz substrate was placed with one end above the Si rectangle and oriented almost along the diameter of the SiO_2 disk. The target to substrate distance was about 5cm. This produced a gradient in the Si concentration along the sample. The Eu_2O_3 pellet was a half-circle placed with its 1cm diameter perpendicular to the length of the substrate. For different samples, the pellet's position was varied from being next to the Si rectangle, to beneath approximately halfway along the substrate, to a bit beyond the substrate on the side opposite to the Si rectangle. This way we could see the effects of a variety of Si-Eu combination proportions. The Eu_2O_3 / SiO_2 sample had the pellet near the center. The Eu_2O_3 / Si sample had it near one edge of the sample. The samples were marked lengthwise. Position 50 is closest to the Si .

We measured the luminescence and transmission of the samples, and then annealed them at 700°C, except in the case of pure Si with SiO_2, which was annealed at 1100°C. Annealing took place in a Lindberg Heavy Duty Oven in a N_2 or Ar rich atmosphere. Annealing the as-sputtered Si/SiO_2 at 1100°C results in Si nanoparticles with sizes ranging from about 1 to greater than 3nm, with the dominant sizes ranging from about 1.0 to 2.1 nm as we go from position 1 to position 50. We observed that higher annealing temperatures result in smaller particles and less variation in size at each position and overall. Annealing should help crystallization and other bond formation processes, and perhaps nanoparticle growth, but some oxidation could also take place with O_2 from the atmosphere (or, in the Eu-doped samples, from the Eu_2O_3). For Er doped Si/SiO_2 700°C was sufficient [4], and we tried it for Eu .

The photoluminescence was measured with an Argon laser 514.5nm beam. We used an ISA Triax 320 spectrometer. We measured the luminescence of the Eu_2O_3 pellet and a $EuCl_3$ pellet to characterize the Eu(III) luminescence peaks for comparison with our samples. The results were comparable to others found in the literature [4]. A CW Ar laser at 488nm and a high power pulsed YAG laser were used for further studies to again observe the general behavior and also identify the components of the luminescence via luminescence decay and time resolved spectroscopy measurements.

RESULTS

The Eu_2O_3 / SiO_2 samples were transparent and colorless. The Eu_2O_3 / Si sample looked like Si. The Si / SiO_2 sample was caramel like at the Si rich end, getting lighter in color until about three centimeters from the Si side it was almost transparent, and finally completely transparent at the Si poor end. The Eu_2O_3 / Si / SiO_2 samples were the same as the Si / SiO_2 samples except that in the vicinity of where the Eu pellet had been the Si caramel color (when

present) gave way to transparency. If this "bleaching effect was due to Eu_2O_3 donating some of its oxygen atoms to Si, the oxidizing of Si would have to be accompanied by a change in the Eu bonding. In Eu_2O_3 we have Eu(III) present. Upon donating the oxygen it could become Eu(II), which is also a relatively stable valence state for Eu.

The photoluminescence (PL) studies with the 514.5nm Ar laser showed two types of spectra. On the one hand we saw wide bands (from 550nm-800nm) with peaks in the vicinity of 600-680nm. On the other hand, we saw a well defined peak at 619nm. This peak only occurred in Eu doped samples and corresponded to the $^5D_0$-$^7F_2$ Eu(III) transition. Quite a few times we saw the Eu(III) peak piggybacked atop one of the larger bands. In those cases the bands tended to be triangular in shape (Fig. 1).

The as-sputtered samples were also viewed under the light of a 366nm u-v lamp. To the naked eye, a strong whitish luminescence was observed on either side of the Eu_2O_3 pellet position in the Eu_2O_3 / Si / SiO_2 samples, while the position corresponding to the pellet itself tended to be transparent and not luminescent. Farther off this luminescence ceased. The positions where the whitish luminescence occurred were somewhat affected by annealing later. It should be noted that the whitish luminescence occurred in non-caramel areas in the sample but not in the most Eu rich bleached areas centered where the Eu pellet was located. The lone exception may have occurred where the Si rich side was bleached when the Eu pellet was next to the Si rectangle. This luminescence had not been observed either in the Si, SiO_2 samples or a series of Er_2O_3, Si, SiO_2 samples. The source for this luminescence was not clear. We considered that the Eu could be serving as a nucleation center for the growth of Si nanoparticles and that they be present even before annealing, but we had never observed a whitish luminescence nor one as strong as we were seeing due to only Si nanoparticles. Another option was that the Eu itself was emitting.

The transmission measurements were used to obtain the size distributions of the Si nanoparticles through the derivative of the transmission curves. From each of these distributions, the peak position was used to obtain the size of the most numerous particles [5]. We assumed the absorption is from the nanoparticles and that they are of spherical shape for these calculations. Distribution peak particle sizes were found to range from 1.0nm to 2.1nm among the Eu_2O_3 / Si / SiO_2 samples while sizes go up to 2.2nm in the Si / SiO_2 sample. As we continue it is to these distribution peak particle sizes to which we will refer.

All the Si containing samples showed variation in size of the particles with position along the sample. However, it was present before annealing and, we did not detect significant changes in that particle size (Fig. 2a) upon annealing except in the sample where the Eu pellet was on the side opposite to the Si rectangle. In this latter case the changes occurred only after about the midpoint of the sample, on the Si rich side. In fact, in this case the particles did not grow but rather reduced in size. These changes may have been due to an oxidation process with oxygen from the Eu_2O_3 doping material. Interestingly enough, also, the changes in size began just at the location where the whitish

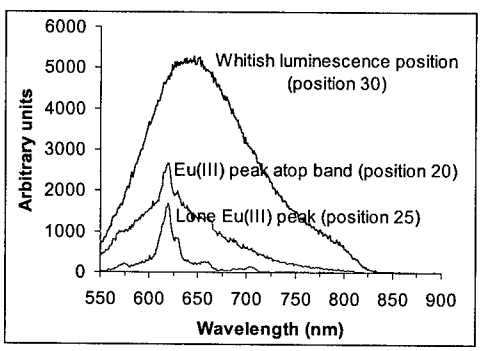


Figure 1 Photoluminescence with 514.5nm excitation. Sample with: Eu_2O_3 (middle) / Si / SiO_2, positions 20, 25, 30.

luminescence occurred. It would seem that the Eu_2O_3 was interfering because the particles sizes vary along the whole length of the Si / SiO_2 sample (Fig. 2b).

Upon annealing the luminescence peaks in the Eu opposite side to Si sample shifted to lower wavelengths values after annealing. This also occurred in the Eu and Si on the same side sample. The Eu opposite side to Si sample showed a large increase in absolute and relative luminescence in the Si rich Eu poor side, beginning at the whitish luminescence location and correlated with the increasing particle size region where the change in size also occurred. No changes in size occurred in the Eu in the middle sample. In all Eu containing samples, other luminescence changes also occurred (Fig. 2a).

The very bleached Eu rich locations tended to show the Eu(III) peak both before and after annealing. They did not occur at the high Si concentration areas. Particle sizes ranged from 1.1nm to 1.3nm in these regions. To the sides of these regions we noticed an intense band of luminescence similar in shape and peak position (640-650nm) to that of the Si / SiO_2 bands. These correspond to the positions at which we saw the whitish luminescence present before and after annealing. The particles ranged from 1.1nm to 1.4nm there. Farther from these areas, we reach the positions at which we could find Eu(III) peaks piggybacked atop bands. These were seen after annealing in locations where previously there was a band. The bands luminescence was reduced relative to the other locations after annealing. They occurred in the lower Si concentration areas. Particle sizes here were lower than 1.3nm. Only one piggyback case occurred between the Eu(III) peak and the whitish luminescence position. It occurred in a relatively large Si concentration (for these peaks) and also large Eu concentration area (right next to the Eu(III) peak) in the Eu at the middle sample. It almost disappeared completely both relative to the rest and in absolute terms. Particle size here and in the whitish luminescence position next to it was 1.3nm, and in the pure Eu(III) peak position particle size was 1.1nm.

With respect to the cause for the strong whitish luminescence, various sources indicate that Eu(II) can luminesce in the visible range, with a very wide band going from IR to UV with a maxima in the green region of the spectrum [6, 7, 8, 9]. Given that it was possibly due to Eu(II) but our deposition source had Eu(III) we had to check for a clear Eu(II) signal. The problem was that in the whitish luminescence regions of our samples we would observe a Si / SiO_2 like curve upon illuminating with our 514.5nm laser (albeit a very strong one relative to the rest). Finally, to excite Eu(II) we might need photons in the blue to u-v region [9]. Since we observe the whitish luminescence under u-v light, this might indicate that Eu(II) is the actual source, even if

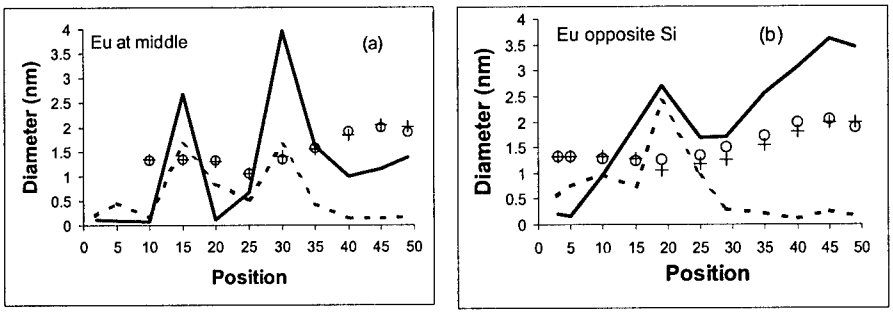


Figure 2 Sizes of particles (in nm) and maximum photoluminescence values (in arb. units) versus position. Solid line and crosses: photoluminescence and particle size, respectively, after annealing. Dotted line and circles: photoluminescence and particle size, respectively, before annealing

we only observe the nanoparticles with our 514.5nm or other blue source.

Time-resolved fluorescence measurement was employed to identify the origin of the observed photoluminescence. Using a CW Ar laser tuned at 488 nm the general behavior of the observed integrated fluorescence was characterized by a broad band feature with the peak varying in the region of 600 - 750 nm, recognizable as the luminescence from Si/SiO_2 host material [10-12]. The measured luminescence decay was very fast with a lifetime typically being < 10 ns [10]. For some samples the fine PL features from Eu(III) emission which is overlapped with host emission could be identified.

Using a high-power pulsed YAG laser with a pulse width of 30 ps as a light source the PL decay at ~ 600 - 620 nm was carefully examined. We identified 2 components. Right after excitation a fast decay component occurs with a lifetime of 800 ns followed by a buildup of a long-lived signal which has a lifetime of 2 ms. Time-resolved spectroscopy was thereafter used to separate the two PL components.

Setting a gate width of 400ns with the delay at 300ns (to eliminate the host emission) a broadband luminescence was obtained, it was PL from Eu(II) ions. In order to verify this, a sample without the Europium dopant was measured. With the same setup, in this other sample no fast PL component nor long-lived component could be observed. This pointed to the possible origin of the observed fast PL in Eu-doped sample as divalent europium ions.

Eu(II) has an f^7 electron configuration. The ground state, 3.8 eV below the conduction band, is the $^8S_{7/2}$ level and the first excited state is ^6P level of the $4f^65d$ electron configuration. The characteristic optical absorption band of ground state $^8S_{7/2}$ to excited state ^6P transition is at around 270 - 300 nm. Using the 3rd harmonics of an intense YAG laser operating at 355 nm, this PL was just observable, but overlapped by a strong Eu(III) emission. Using the laser operating at 532 nm with a high-power output of ~27 GW/cm^2, we increased the relative intensity of Eu(II) w/r Eu(III). The two-photon-absorption (TPA) induced Eu(II) emission is shown in Fig.3. This photoluminescence has a lifetime of ~800ns, the peak is at ~540 nm, and FWHM is ~4200 cm^{-1}. This emission profile looks similar to the PL from the Si nanoparticles and from defect centers in SiO_2 as well [13]. But the lifetime measurement as well as the experimental results with the non-doped sample convinced us in making the judgement.

The luminescence from Eu(III) ions showed a well resolved feature in the range of 575 nm to 705 nm. The PL intensity versus temperature showed an interesting behavior. It was

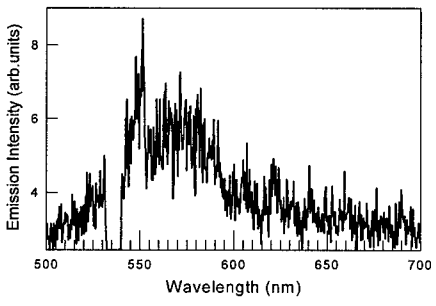


Figure 3. TPA-induced Eu(II) PL in Si/SiO_2. Data points are missing at laser wavelength.

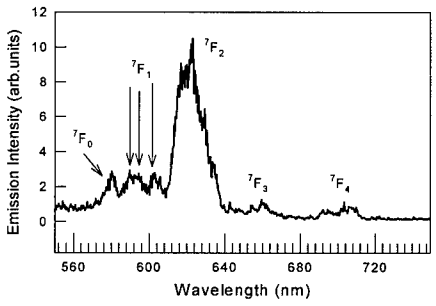


Figure 4. PL of Eu(III) dopant in Si/SiO_2 at 25°C. The transitions are labeled.

found to decrease with lower temperature. Presumably it is associated with the phonon-assisted photodynamical processes in the host conduction band. Its emission decay rate is 3 orders of magnitude greater than that of Eu(II). With a large delay of the sampling gate the fluorescence spectra of Eu(III) was obtained as in Fig.4. It shows a nature typical of Eu(III) in an amorphous host. Its PL profile consists of 5 emission groups. In the spectral range from 584 to 609 nm there is a triplet structure. At first glance it looks like the triple components of the transition from metastable $^5D_0$ to $^7F_1$ state with j = 0, ± 1. If the first peak at 580 nm of the triplet were assigned to $^5D_0$ - $^7F_1$ transition, the $^5D_0$ - $^7F_0$ transition would occur at an even shorter wavelength. This is inconsistent with most data obtained for Eu(III) in crystals. Actually, the component in the middle at ~590 nm is broadened, can be seen as a twin peak due to the superposition of two subcomponents. Therefore the spectral features within 584 - 609 nm can be assigned to the $^5D_0$ - $^7F_1$ transition while the first peak at 580 nm is assigned to $^5D_0$ - $^7F_0$. An intense emission peaked at 622 nm is due to the $^5D_0$ - $^7F_2$ transition. The other two weak groups of emission at longer wavelengths of 659 and 703 nm belong to the transitions of $^5D_0$ - $^7F_3$ and $^5D_0$ - $^7F_4$ respectively. All components were well resolved at room temperature.

CONCLUSIONS

We were able to incorporate Eu(III) into the Si nanoparticle / SiO_2 host. We also found we obtained Eu(II) in the process. We found a lowering of photoluminescence intensity with lowering of temperature. An as yet unaswered question is the reason for the intense whitish luminescence found in some regions of the samples. Some involvement with Eu(II) or Eu(III) is suspected. Eu(III) related peaks were only observed where the peak distribution size of the nanoparticles was lower than 1.3nm. Whitish luminescence was related to peak sizes ranging from 1.1nm to 1.4nm. Annealing the samples had clear effects upon their photoluminescence, but did not necessarily involve changes in particle sizes, nor were these size changes necessary to increase luminescence. The Eu doping has a tendency to halt the annealing effects on size and, when changes did occur, the particles generally became smaller.

REFERENCES

1. R.M.Macfarlane and R.M. Shelby, in *Spectroscopy of Solids Containing Rare-Earth ions*, ed., by A.A. Kaplyanskii and R.M. Macfarlane (North-Holland, Amsterdam, 1987) 51.
2. R. Yano, M.Mitsunaga and N. Uesugi, J.Opt.Soc.Am.B **9**, 992 (1992).
3. L. F. Fonseca, O. Resto, R. K. Soni, M. Buzaianu, S. Z. Weisz, and M. Gomez, to be published in Materials Science and Engineering B
4. R. Reisfeld, R. A. Velapoldi, L. Boehm and M. Ish-Shalom, The Journal of Physical Chemistry **75,** 3980 (1971).
5. L. F. Fonseca, O. Resto, S. Gupta, R. S. Katiyar, S. Z. Weisz, Y. Goldstein, A. Many, and J. Shapir, Proc. of the ICPS. CD-version (1998).
6. M. Nogami and Y. Abe, App. Phys. Lett. **69**, 3776 (1996).
7. E. Kaldis, P. Streit and P. Wachter, J. Phys. Chem. Solids **32**, 159 (1971).
8. J. Qi, T. Matsumoto, M. Tanaka, and Y. Masumoto, App. Phys. Lett. **74,** 3203 (1999).
9. M. Nogami, T. Yamazaki, and T. Abe, J. of Luminescence **78,** 63 (1998).
10. D.B. Geohegan, A.A. Puretzky, G. Duscher and S.J. Pennycook, Appl.Phys.Lett. **73**, 438 (1998).
11. P.Li, G.Wang, Y.Ma and R. Fang, Phys.Rev.B, 58 (1998) 4057.
12. V.M. Akulin, E. Borsella, G. Onida, O. Pulci and A Sarfati, Phys.Rev.B, 57 (1998) 6514.
13. N. Itoh, T. Shimizu-Iwayama, T. Fujita, J.Non-Cryst.Solids **179**, 194 (1994).

SCREEN-PRINTED DYE-SENSITIZED LARGE AREA NANOCRYSTALLINE SOLAR CELL

T.K.GUPTA*, L.J. CIRIGNANO*, K.S. SHAH*, L.P. MOY*, D.J. KELLY*,
M.R. SQUILLANTE*, G. ENTINE*, and G.P. SMESTAD**,
*Radiation Monitoring Devices (RMD), Watertown, Massachusetts 02472
**Sol Ideas Technology Development, Pacific Grove, CA

ABSTRACT
The fabrication and testing of screen printed dye-sensitized large solar cell (15 cm x 15 cm) based on nanocrystalline TiO_2 is described. It is the largest photo-electrochemical (PEC) cell that is based on the dye sensitization of thin (8-18 μm) films of TiO_2 nanoparticles in contact with a non-aqueous liquid electrolyte. The cell has the potential to be a low cost, commercial, environmentally friendly, photovoltaic option. Surface as well as electrical characterization, of the nanostructured PEC cells have been performed. The efficiency of these large commercial cells are compared to the laboratory-made small PEC cells.

Key words: Photoelectrochemical, solar cells, nanocrystalline, dye-sensitized

INTRODUCTION

Compared to the available commercial solar cells, dye sensitized PEC solar cells are cost effective, environmentally friendly, and with a prospect of meeting 12-15% photovoltaic electricity generation [1] at less than $ 1.5 per peak watt. The nanocrystalline dye-sensitized solar cell developed by Grätzel and his associates [2-3] is transferred into a commercially viable screen printed cell. We have fabricated large PEC cells of 15 cm x 15 cm area, which are promising as potential cost effective, environmentally friendly, commercial solar cells. The most difficult problem with these screen printed PEC solar cells is low efficiency (6-10%) compared to the other commercial solar cells (single crystal or amorphous silicon or other thin film solar cells available in the market with efficiencies ~ 15-17%) [4]. The main difficulties in achieving higher efficiencies with these screen printed PEC cells are the large dark currents arising mostly from the semiconductor-electrolyte junction [5].

The photoelectrode of a PEC cell consists of a 12-18 μm screen printed film of nanocrystalline TiO_2 particles (5-25 nm in diameter) with a monolayer of adsorbed dye molecules. An electrolyte is applied on the dye-soaked TiO_2 by screen printing. Platinum deposited conducting glass serves as a counter electrode. Upon photoexcitation, the dye molecules inject electrons efficiently into the TiO_2 conduction band, effecting charge separation. The injected electrons traverse the nanocrystalline film and are collected at the conducting surface of the glass substrate. These electrons then traverse through the external load and re-enter the cell at the counter electrode and reduce the electrolyte, which then diffuses into the pores of the dye-soaked TiO_2 film to reduce the photoexcited dye back to its original state. Figure 1 illustrates the operating principle of the dye sensitized cell.

In this paper we report the fabrication of a large 15 cm x 15 cm cell by a commercially viable screen printing method using nanocrystalline films of TiO_2 in aqueous solution. The efficiency of these large cells are compared to the laboratory made small cells.

Mat. Res. Soc. Symp. Proc. Vol. 581 © 2000 Materials Research Society

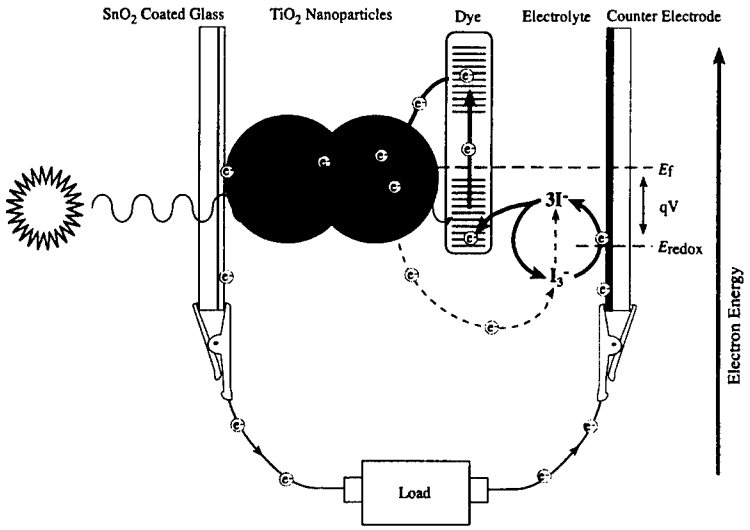


Figure 1. Dye-sensitized operation principle of TiO_2 solar cell. The photoexcited dye (S/S^*) transfers an electron to the semiconducting TiO_2 layer via electron injection. The electron is then transported through the rough, porous TiO_2 layer and collected by the conductive layer on the glass. Within the electrolyte, the mediator (I^-/I_3^-) undergoes oxidation (and regeneration). The electrons lost by the dye to the TiO_2 are replaced by the iodide, resulting in iodine or triiodide, which in turn obtains an electron at the catalyst-coated counter electrode as current flows through the load [8].

EXPERIMENTAL

(a) Preparation of the TiO_2 Slurry (ink) for screen printing:

Nanocrystalline TiO_2 powders were procured from MIT, Cambridge, Massachusetts and Degussa, Germany. 12 g TiO_2, procured either from Degussa or from MIT, was ground in a porcelain mortar with a small amount of water containing acetylacetone. The product was diluted with de-ionized water and ground again. The final ground material was thoroughly mixed with ethylene glycol and the viscosity of the material was adjusted by thoroughly mixing with a low-melting point glass. Finally, a detergent was added to make the final slurry ready for screen printing.

The slurry thus prepared was screen printed using a 230 mesh silk screen. The screen printed films were air dried for 30 minutes followed by sintering ~ 480° C. Film thickness was measured with a digital gauge and with a Dek Tak profilometer [Dek Tak 8000] after firing.

(b) Physical Characterization

Surface morphologies of the screen printed TiO_2 films were performed using scanning electron microscope (SEM, JEOL 6320FV EEG). X-ray diffraction (XRD) analysis was performed using a Rigaku Rotaflex RTP 500 diffractometer and the surface area and the grain size distribution of

TiO_2 in the screen printed films were measured following 5-point BET (Brunauer, Emmett and Teller) analysis. All these measurements were performed at MIT.

(c) Cell Assembly:

Transparent pyrex glass plates 15 cm x 15 cm coated with a conductive layer of Tin Oxide (SnO_2) on one side were used as substrate material. The screen printed TiO_2 on the conductive surface of the glass was soaked with the dye.

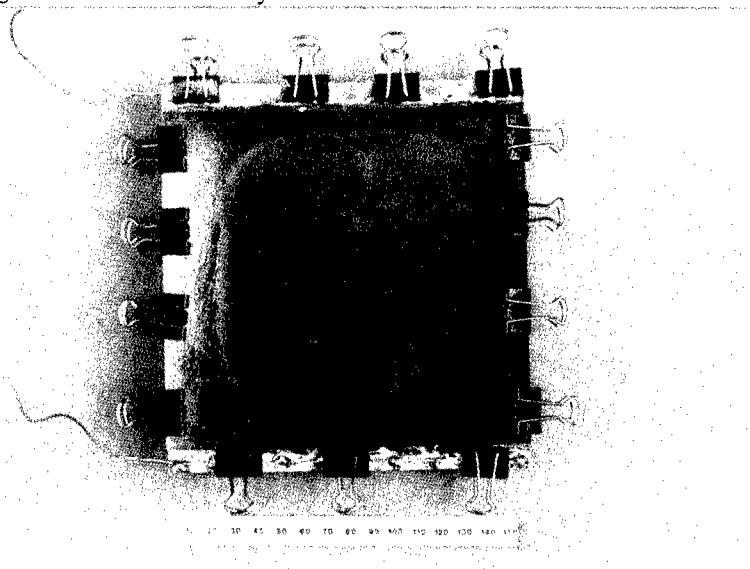


Figure 2. Photograph of the large area solar cell (15 cm x 15 cm).

Two types of dyes [anthocyanin and Ru-(II) (4,4'-dicarboxy-2,2'-bipyridine)$_2$(NCS)$_2$ complex)] were used. Fresh black berry juice served as a convenient and inexpensive source of anthocyanin dye for our cells. The Ru-complex dye was made by mixing the dry powder in the proper ratio in acetonitrile solution. The overall efficiency for the screen printed cells with the anthocyanin dye was 1-2% whereas with ruthenium dye it was ~ 6.1%. An iodide electrolytic solution was prepared by dissolving 0.5 M of potassium iodide and 0.05 M iodine in ethylene glycol. A 10 mM solution of chloroplatinic acid in isopropanol was deposited on the conductive side of another glass substrate to serve as the counter electrode.

(d) Optical Characterization:

Quantum efficiency measurements (QE): We measured QE versus wavelength with an ELH lamp (Philips, 120, 300W) grating monochrometer (Bausch and Lomb, Model # 33-86-40-01), and a calibrated silicon p-i-n photo diode. An optical mask was used to insure that the photon flux on the solar cell under test and calibration photodiode was equal.

(e) Electrical Characterization of the cells:

Electrical characterization of the cells were performed at RMD and at Sol Ideas Technology, CA, by Dr. Smestad. The short circuit current density, the open circuit voltage and the fill factor

(f were measured under simulated air mass (AM) 1.5 condition (AM 1.5, 1000W/ m^2 standard spectrum).

RESULTS AND DISCUSSION

Microstructural Analysis of the Films

Scanning electron micrograph (SEM) observations showed the screen printed TiO_2 films to have particle size in the range 20-30 nm and to consist of densely packed small crystallites. The thickness of a typical screen printed TiO_2 film was determined from SEM and was found to be ~ 12 μm.

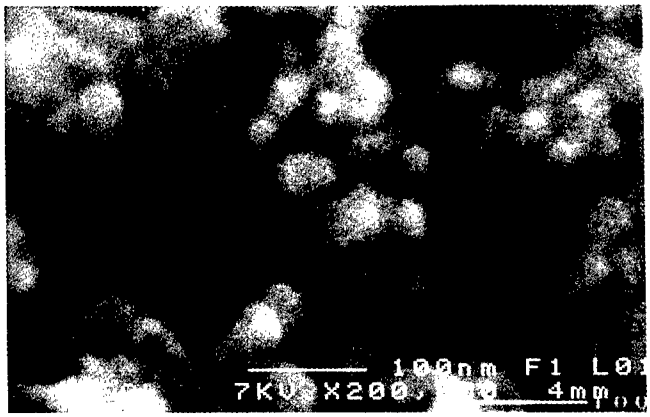


Figure. 3 Scanning electron micrograph of a nanocrystalline TiO_2 film deposited by screen printing onto conducting glass.

X-ray Diffraction (XRD)

Figure 4 shows the X-ray diffraction spectrum for the screen printed TiO_2 film. The XRD of the film shows that the film is polycrystalline with a large peak at $2\theta \sim 25.5^0$. The strongest reflection of the tetragonal anatase (101) phase is clearly observed while the rutile phase is absent [6]. The broadening of the peaks is due to the presence of small TiO_2 grain size [7].

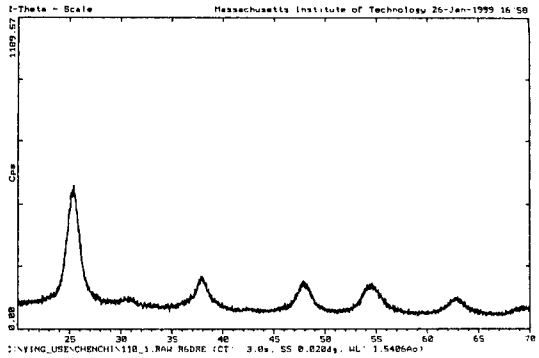


Figure. 4. X-ray diffraction spectrograph of a screen-printed TiO_2 film.

B.E.T. (Brunauer, Emmett, and Teller) Measurements

The surface area and grain size of the screen printed films were measured at MIT, following the B.E.T. method. The specific surface area obtained from 5-point B.E.T. analysis is 54.1128 m^2/g, which is typical for a commercial TiO_2 powder. Figure 5 shows the B.E.T. surface area plot. The nanostructured layer of TiO_2 possesses an internal surface of about 1000 times greater than the dense flat film [8].

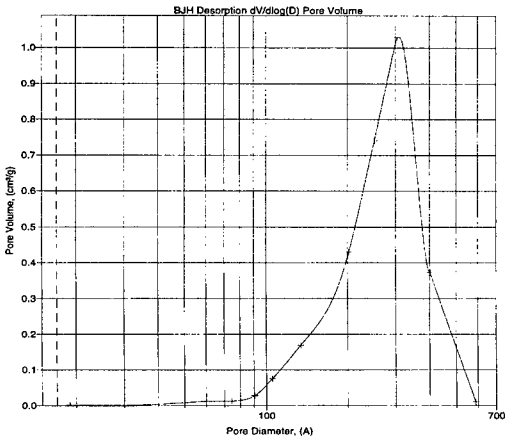


Figure 5. Pore volume distribution of the screen-printed TiO_2 film.

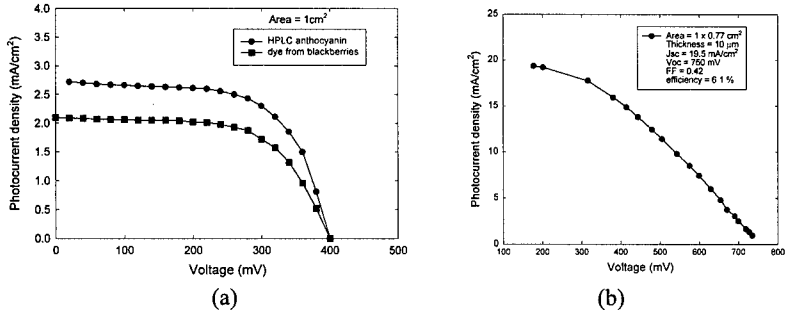


Figure 6. (a) I-V curves for pure anthocyanin dye and dye extracted from blackberries (b) I-V plot for a ruthenium dye-sensitized screen printed TiO_2 solar cell [9].

Current-Voltage Characteristics of the Solar Cells:

The current voltage (I-V) curve for an AM 1.5 illuminated cyanin-sensitized TiO_2 film, of active area 1 cm^2, is shown in figure 6(a). The measured open circuit voltage was 0.44-0.49 V and the short circuit photocurrent density was 2.5-1.5 mA/cm^2. The ff was 0.65 with an overall efficiency ~1%. The current voltage (I-V) curve for an AM 1.5 illuminated ruthenium dye

sensitized cell of active area 1 cm^2 is shown in figure 6(b). The open circuit voltage and the short circuit current density for this cell were found to be 750 mV and 19.5 mA/cm^2. The ff was ~0.42 and the efficiency calculated was ~6.1% .
The open circuit voltage and the short circuit current were measured for the 15 cm x 15 cm cells. Values of 0.48 V and 48 mA were obtained for measurements outside on a hazy day with the sun at 47° from zenith. The short circuit current density is significantly lower than for smaller area films while the open circuit voltage was similar. The lower short circuit current density can be attributed to nonuniformities in the cell and significant series resistance. Small (1 cm^2) areas of the cell were irradiated under simulated AM 1.5 conditions. The short circuit current density varied from 0.1 to 1.5 mA/cm^2 over the cell area.

SUMMARY AND CONCLUSIONS

Screen-printed titanium dioxide films and photoelectrochemical cells fabricated from these films were characterized by physical, optical, and electrical methods. Anthocyanin and ruthenium dyes were used to sensitize the films. Small (~ 1 cm^2) and large (15 cm x 15 cm) cells were fabricated from the anthocyanin-dyed films whereas only small cells were fabricated from the ruthenium-dyed films. As the ruthenium dye is very sensitive to air and moisture, it is difficult to do measurements without proper sealing. The efficiency of small cells with anthocyanin dye is ~ 1.0 to 1.5 % whereas with ruthenium dye it is ~ 6.1%. The current density measured for the large cell was less than for the small cells due to film nonuniformities and series resistance.

ACKNOWLEDGEMENTS

This work was supported by a grant from DOE grant # DE-FG02-98-ER82649. Experimental help from Professor Jackie Ying, of the Chemical Engineering Department of MIT, is thankfully acknowledged.

REFERENCES

1. M. Grätzel, MRS Bul. p.61, (October, 1993)

2. B. O' Regan, and.M. Grätzel, *Nature* 335, p.737 (1991)

3. M.K. Nazeeruddin et al., *J. Am. Chem. Soc.* 115, p.6382 (1993)

4. J. P. Benner and L. Kazmerski, *IEEE Spectrum,* 9, p.40 (1999)

5. S.K. Deb et al., *2nd World Conf. and Exhibition on PV solar Energy Conv.* Vienna, 6-10 July 1998

6. G.K. Boschloo, A. Gossens and J. Schonman, *J. Electrochem. Soc.* Vol 144, no. 4, p.1311 (1997)

7. S.B. Quadri et. al., *J. Vac. Sci. Technol.* A7 (3) p.1220 (1989)

8. G. Smestad, *The Spectrum,* p.7, Vol. 2 (1994)

9. T.K. Gupta et al., *SPIE Conf,* Denver CO, July 1999.

CARBOXYLATE-ALUMOXANES: PRECURSORS FOR HETEROGENEOUS CATALYSTS

CHRISTOPHER D. JONES,[a] DAVID S. BROWN,[b] LARRY L MARSHALL,[b] and ANDREW R. BARRON[a,c]*

[a] Department of Chemistry, Rice University, Houston, TX 77005
[b] Shell Chemical Company, Houston, TX, 77082
[c] Department of Mechanical Engineering and Materials Science, Rice University, Houston, TX 77005

ABSTRACT

Carboxylate-alumoxanes are organic substituted alumina nano-particles synthesized from boehmite in aqueous solution which are an inexpensive and environmentally benign precursor for the fabrication of nano-, meso-, and macro-scale aluminum based ceramics. The use of carboxylate-alumoxanes as a novel high surface area alumina support for heterogeneous catalysis will be discussed. The ability to perform further chemistry on the organic ligands of the carboxylate-alumoxanes allows for attachment of catalysts. During calcination, the organic ligands are burned out, leaving behind the catalyst in a well-dispersed manner. To demonstrate this concept, the metathesis of C_{16} olefins using a molybdenum oxide catalyst supported on alumina will be discussed using the carboxylate-alumoxane method.

INTRODUCTION

Since the introduction, in 1875, of the platinum catalyzed oxidation of SO_2 to SO_3, heterogeneous catalysis has become arguably the most important component of the modern chemical industry.[1] The anatomy of a generic heterogeneous catalyst involves an active component, such as a metal (e.g., Pt, Pd, Ni, etc.) or metal oxide (e.g., Fe_2O_3, V_2O_5, etc.), dispersed on the surface of a support, ordinarily an oxide (e.g., Al_2O_3, SiO_2, etc.).[1] Traditional routes to supported catalysts involve five different methods: (a) dry mixing of individual components, (b) co-precipitation of catalyst and support, (c) impregnation of the support with substances that decompose at high temperature to leave the catalyst deposited on the support, (d) sublimation of the catalyst onto the support, and (e) reaction with compounds to surface hydroxyl groups. In all cases, subsequent activation of the catalyst species may be required, e.g., reduction of a Pd compound to Pd metal. While a uniform distribution of the catalyst on the support is readily obtained by these methods, the final material is a physical mixture at the μm level rather than at the atomic level. Alumina is the most widely used support because it is inexpensive, structurally stable and can be prepared with a wide variety of pore sizes and distributions. Furthermore, alumina has several crystallographic phases with differing surface acidities, and hence catalytic applications.[2]

Since the interaction between the catalyst and the support are significant in determining the catalyst activity, it would be desirable to achieve controlled modifications of the surface chemistry of alumina *via* simple chemical modification. Similarly, it would be advantageous to prepare a uniformly atomically dispersed catalyst within the support structure. This may allow for more economic use of expensive catalysts, higher activity, or greater selectivity.

* To whom correspondence should be addressed.
(http://pchem1.rice.edu/~arb/Barron.html)

Mat. Res. Soc. Symp. Proc. Vol. 581 © 2000 Materials Research Society

We have previously reported the preparation of carboxylate-alumoxanes, $[Al(O)_x(OH)_y(O_2CR)_z]_n$, from the reaction of boehmite, $[Al(O)(OH)]_n$, with carboxylic acids.[3,4,5] These carboxylate-alumoxanes are readily converted to alumina bodies or films upon pyrolysis. Importantly, the physical properties of the resulting alumoxanes may be readily controlled by the organic substituent of the carboxylate group (i.e., R) making them adaptable to a wide range of processing techniques.

Reaction of the carboxylate-alumoxane with either a metal acetylacetonate complex, $M(acac)_n$, or a salt, results in transmetallation and the formation of a doped-alumoxane.[6] Upon thermolysis, these doped-alumoxanes result in homogeneously doped-alumina. Our results in the use of doped-alumoxanes as precursors to mixed metal and doped aluminum oxides as alumina based catalysts and catalyst supports led us to investigate the possibility of using carboxlyate-alumoxanes as precursors to heterogeneous catalysts.[6] We proposed that by reacting a catalytically active metal with chemically functionalized carboxlyate-alumoxanes, it should be possible to covalently bond these metals to an inorganic support with great dispersion. The initial studies of this method involve metathesis of higher olefins.

Olefin metathesis is an interchange of carbon atoms between a pair of double bonds. These reactions can be grouped into three categories: exchange, ring-opening metathesis polymerization (ROMP), and ring-closing metathesis.[7] We are currently interested in investigating the exchange reaction for higher olefins, i. e., Equation 1.

$$\begin{array}{l} R_1CH{=}CHR_2 \\ \quad + \\ R_3CH{=}CHR_4 \end{array} \longrightarrow \begin{array}{l} R_1CH \quad CHR_2 \\ \quad\| \quad + \quad\| \\ R_3CH \quad CHR_4 \end{array} \qquad (1)$$

There are many different transition metals that show activity for metathesis reaction, however only three show high activities: molybdenum, tungsten, and rhenium, (see Table 1).[8]

Table 1. Transition metals that are active for metathesis[7]

IV	V	VI	VII	VIII	X
Ti					
	Nb	**Mo**		Ru	
	Ta	**W**	**Re**	Os	Ir

* Metals having highest activity are in boldface

Traditional methods for the synthesis of MoO_3 supported catalysts for metathesis can be grouped into three categories: (a) Impregnation of the support,[9] (b) treatment of the support with $Mo(CO)_6$, [10] and (c) treatment of the support with organomolybdenum compounds [e. g. $(\pi\text{-}C_3H_5)_4Mo$].[11] Supports are generally metal oxides such as alumina, silica, or titania. After the catalyst is attached to the support, heat treatment and oxidation or reduction is often necessary to bring the catalyst into an active state.[12] Catalysis is initiated and then propagated by the formation of metal carbene complexes.[13] It is usually important to pay special attention to how the catalyst systems are prepared due to many factors that affect metathesis activity. These factors include the proportions of components, pre-treatment procedures, order in which the components of the system are mixed, the period of incubation, and the nature and concentration of the active species.[7]

Heterogeneous MoO_3 catalysts are widely used in industrial petrochemical processes. We are interested in metathesis of higher olefins for the Shell Higher Olefin Process (SHOP).[14,15] The SHOP process converts ethene to detergent-range alkenes.

Unfortunately, not all of the olefins made from oligomerization of ethene are within the valuable C_6-C_{18} range. The olefins above and below than this range have their double bonds fully isomerized, and metathesis is performed to enhance the yield of detergent-range olefins.

RESULTS AND DISCUSSION

Synthesis of the Molybdenum Catalyst

Boehmite was refluxed in a water solution containing an appropriate amount of gluconic acid, $HO_2C[CH(OH)]_5CH_2OH$, to form gluconate-alumoxane, see Experimental. Gluconate-alumoxane is reacted with either 8% or 20% wt MoO_3 in an aqueous solution for 24 hours. The reaction is then filtered to collect the molybdate

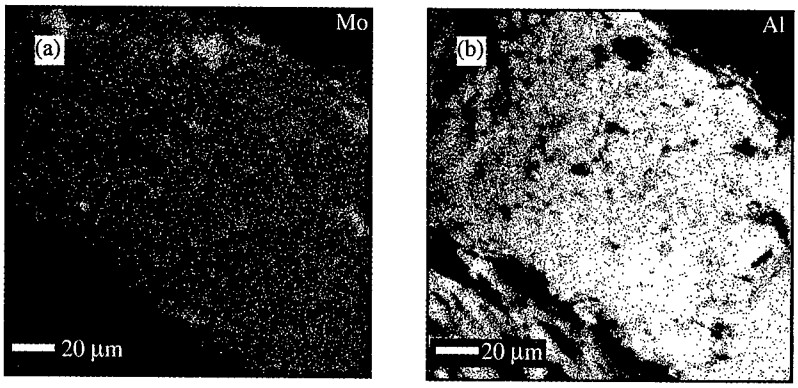


Figure 1. EDX map of (a) 8% wt Mo-alumina particle showing uniform MoO_3 dispersion and (b) corresponding aluminum map.

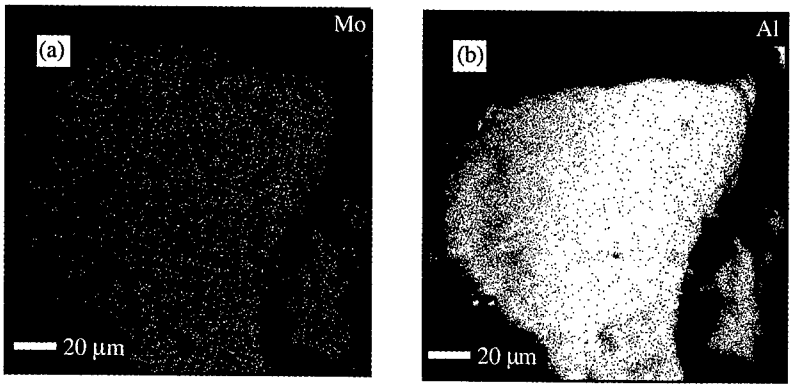


Figure 2. EDX map of (a) 20% wt Mo-alumina particle showing agglomeration of MoO_3 and (b) corresponding aluminum map.

substituted alumoxane nanoparticles. Because the gluconate-alumoxane has hydroxyl sites available on the organic ligand, the molybdenum is covalently bonded to the inorganic support. The catalyst precursor is then fired to 500 °C to form alumina with MoO_3 uniformly dispersed on the surface. As can be seen in Figure 1, the 8% wt Mo-Al_2O_3 catalyst shows molybdenum uniformly dispersed with no agglomeration of MoO_3. However, as the wt % of MoO_3 is increased to 20%, agglomeration of MoO_3 occurs, see Figure 2.

After the organics are fired out of the catalyst precursor, the heterogeneous catalyst is fired again to 500 °C in a reducing atmosphere. The catalyst is then added to fully isomerized C_{16} olefin under an argon atmosphere. The metathesis reaction is performed at 120 °C. The amount of C_{16} conversion is monitored by gas chromatography (GC). The conversion of fully isomerized C_{16} olefins by our 8% wt Mo-Al_2O_3 and our 20 % wt Mo-Al_2O_3 catalysts are compared to an Al_2O_3 impregnated with 8% wt MoO_3 and a commercial catalyst, see Figure 3. As may be expected, the highly optimized catalyst has the best activity of all the catalysts investigated. The 8% wt Mo-Al_2O_3 shows an activity about two-thirds that of the commercial catalyst. A traditional method of impregnation of alumina and our 20 % wt Mo-Al_2O_3 catalyst shows no activity for C_{16} olefin metathesis under these conditions. It has been shown that a high molybdenum concentration decreases the activity, probably due to inactive bulk MoO_3.[16] This is most likely why the 20% wt Mo-Al_2O_3 shows no activity as agglomeration of MoO_3 is observed by EDX analysis, Figure 2. It is unknown why the impregnated alumina shows no activity, however inactive bulk MoO_3 may also be an explanation because this traditional method does not ensure fully dispersed MoO_3.

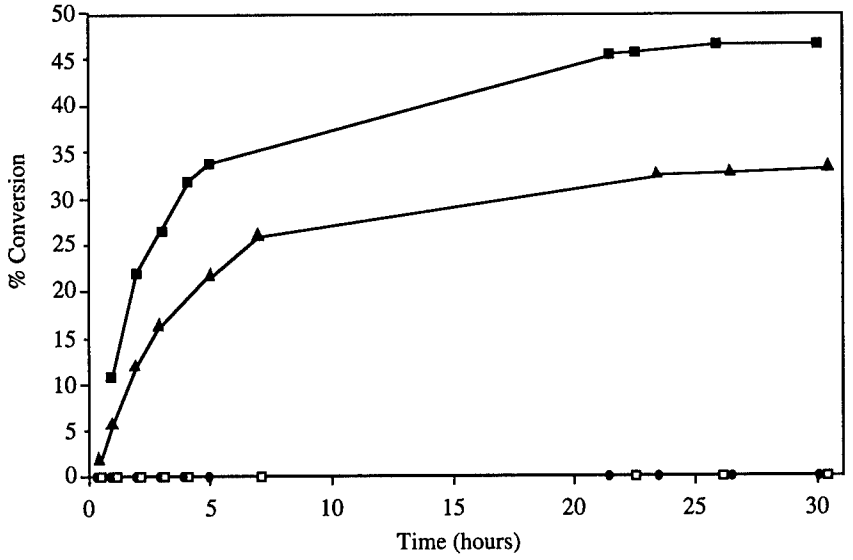


Figure 3. The % conversion of fully isomerized C_{16} olefin by the commercial catalyst (■), the 8% wt Mo-Al_2O_3 catalyst (▲), the 20% wt Mo-Al_2O_3 catalyst (●), and the Al_2O_3 impregnated with 8% wt MoO_3 (□).

CONCLUSIONS

The carboxylate-alumoxane derived catalyst (8% wt Mo-Al_2O_3) for the metathesis of C_{16} olefins showed high activity when compared to a catalyst made by the impregnation method, however at higher loadings (20% wt Mo-Al_2O_3) no activity is observed. When compared to the highly optimized commercial catalyst, these results appear promising. Studies including investigation into the active sites, varying concentrations of MoO_3, and different catalytic metals are currently being investigated.

EXPERIMENTAL

Capatal® B boehmite was kindly provided by the CONDEA Vista Company. All solvents, carboxylic acids, and MoO_3 were obtained commercially (Strem and Aldrich) and were used as received. Electron probe microanalysis (EPMA) was performed on a Cameca SX50 Electron Microprobe using techniques and imaging modes including: energy dispersive X-ray spectroscopy (EDS), secondary electron emission (topography, morphology), back scattered electron emission (atomic number contrast), X-ray emission (quantitative analysis and element distribution mapping), and cathodoluminescence (trace element distribution). In addition, wavelength dispersive X-ray distribution maps (i.e., elemental maps) were used to determine the compositional homogeneity of the catalysts. The following microprobe calibration standards were used: Mo metal (Mo), corundum Al_2O_3 (Al), and quartz SiO_2 (O). Gas Chromatography was performed on a HP 6890 using a DB-5 column. The samples were diluted with dichloromethane.

Synthesis of Gluconate-Alumoxane

A 50 % wt aqueous solution of gluconic acid (421 g) was added to 1200 mL of water and stirred. Capatal® B boehmite (64 g) was then slowly added and refluxed for 24 hrs. The brown solution was then cooled to room temperature and the solvent was removed under reduced pressure to form a brown gel. The tan-colored gluconate-alumoxane was then precipitated by the addition of ethanol and collected by filtration.

Synthesis of MoO_3 Supported on Gluconate-Alumoxane

Gluconate-alumoxane (30.0 g) was dissolved in 500 mL of water and refluxed. MoO_3 (3.21 g and 20.04 g for 8 % and 20 % respectively) was added and allowed to reflux for 24 hours. The solution was then cooled and the solvent was removed under reduced pressure to leave a dark brown solid. The solid was then refluxed for 1.5 hours in ethanol resulting in a light brown powder. The MoO_3 supported on gluconate-alumoxane was collected by filtration and activated as below.

Synthesis of Impregnated Alumina Catalyst

Ammonium molybdate (Aldrich) (8 % wt) was dissolved in water and added to an extruded alumina. The water was removed under reduced pressure. The catalyst was then dried at 100 °C and activated as below.

Activation of MoO_3-Al_2O_3 catalysts

All catalysts were activated by heating to 500 °C in air for four hours, then under nitrogen for 12 hours.

Methathesis of Fully Isomerized C_{16} olefins

The MoO_3-Al_2O_3 catalyst (1.0 g) was added to 20 mL of fully isomerized C_{16} olefins in a flask under argon atmosphere, along with 2500 ppm $SnBu_4$ as a promoter. The reaction was heated to 120 °C and aliquots were taken at numerous time intervals and analyzed by gas chromatography to determine the amount of C_{16} conversion.

ACKNOWLEDGMENTS

The authors gratefully acknowledge Milton Pierson for assistance with electron probe microanalysis. Financial support for this work was provided jointly by the Environmental Protection Agency and the National Science Foundation under the Technology for a Sustainable Environment Program.

REFERENCES

1 J. M. Thomas and K. Zamaraev, Eds. *Perspectives in Catalysis*, (Blackwell, Oxford, 1991).
2 K. Wefers and C. Misra, *Oxides and Hydroxides of Aluminum*, (Alcoa Laboratories, 1987).
3 A. W. Apblett, C. C. Landry, M. R. Mason, and A. R. Barron in *Synthesis and Processing of Ceramics: Scientific Issues*, edited by W. E. Rhine, T. M. Shaw, R. J. Gottschall, and Y. Chen (Mat. Res. Soc., Symp. Proc., **249**, 1992. pp. 75-86.
4 C. C. Landry, N. Pappè, M. R. Mason, A. W. Apblett, A. W. Tyler, A. N. MacInnes, and A. R. Barron, *J. Mater. Chem..*, **5**, 331(1995).
5 R. L. Callender, C. J. Harlan, N. M. Shapiro, C. D. Jones, D. L. Callahan, M. R. Wiesner, R. Cook, and A. R. Barron, *Chem. Mater.*, **9**, 2418 (1997).
6 R. L. Cook, C. Wong, C. J. Harlan, A. Kareiva, and A. R. Barron in *Advanced Catalytic Materials-1996*, edited by P. W. Lednor, M. J. Ledous, D. A. Nagake, and L. T. Thompson, (Mater. Res. Soc. Symp. Proc., **454**, 1997), pp. 169-176.
7 K. J. Ivin and J. C. Mol, *Olefin Metathesis and Metathesis Polymerization*, (Academic Press, San Diego, CA, 1997).
8 J. C. Mol in *Olefin Metathesis and Polymerization Catalysts*, edited by Y. Imamoglu (Kluwer Academic Publishers, Netherlands, 1990), p. 247.
9 E. Etienne, E. Ponthieu, E. Payen, and J. Grimblot, *J. Non-Crystal. Solids*, **147-148**, 764 (1992).
10 G. W. Wagner and B. E. Hanson, *Organometallics*, **6**, 2494 (1987).
11 Y. Iwasawa and S. Ogasawara, *J. Faraday Trans. 1*, **75**, 1465 (1979).
12 W. Grunert, A. Y. Stakheev, R. Feldhaus, K. Anders, E. S. Shpiro, and K. M. Minachev, *J. Catal.*, **135**, 287 (1992).
13 K. A. Vikulov, I. V. Elev, B. N. Shelimov, and V. B. Kazansky, *J. Mol. Catal.*, **55**, 126 (1989).
14 J. Skupinska, *Chem. Rev.*, **91**, 613 (1991).
15 E. R. Freitas and C. R. Gum, *Chem. Eng. Progress*, **75**, 73 (1979).
16 B. Zhang, N. Liu, Q. Lin, and D. Jin, *J. Mol. Catal.*, **65**, 12 (1990).

Molecular-Dynamics Simulations

INTERCLUSTER INTERACTION OF TiO_2 NANOCLUSTERS USING VARIABLE-CHARGE INTERATOMIC POTENTIALS

Shuji Ogata,[a] Hiroshi Iyetomi,[b] Kenji Tsuruta,[c] Fuyuki Shimojo,[d] Rajiv K. Kalia,[e] Aiichiro Nakano,[e] and Priya Vashishta[e]

[a]Department of Applied Sciences, Yamaguchi University, Ube 755-8611, JAPAN
ogata@po.cc.yamaguchi-u.ac.jp

[b]Department of Physics, Niigata University, Niigata 950-2181, JAPAN

[c]Department of Electrical and Electronic Engineering, Okayama University, Okayama 700-8530, JAPAN

[d]Faculty of Integrated Arts and Sciences, Hiroshima University, Higashi-Hiroshima 739-8521, JAPAN

[e]Concurrent Computing Laboratory for Materials Simulations, Louisiana State University, Baton Rouge, LA 70803-4001

ABSTRACT

A new interatomic potential has been developed for molecular-dynamics simulations of TiO_2 based on the formalism of Streitz and Mintmire [J. Adhesion Sci. Technol. **8**, 853 (1994)], in which atomic charges vary dynamically according to the generalized electronegativity-equalization principle. The present potential reproduces various quantities of rutile crystal including vibrational density of states, static dielectric constants, melting temperature, elastic moduli, and surface relaxation. Calculated cohesive-energy and dielectric constants for anatase crystal agree well with experimental data. The potential is applied to TiO_2 nanoclusters (size 60-80Å) for both anatase and rutile phases to analyze their equilibrium configuration and space-charge distribution. Stable double-charge layer is found in the surface region of a spherical nanocluster for both rutile and anatase, resulting in enhanced Coulomb-repulsion between the nanoclusters at close proximity.

INTRODUCTION

Nanophase materials synthesized by consolidating nanometer-sized clusters have attracted much attention in the last decade [1]. It is because nanophase materials often display novel or improved properties such as high strength, high toughness, and high catalytic-reactivity compared to conventional materials, due to the small size of individual phases [1]. TiO_2 is one of the fundamental ceramics with wide applications as photocatalysts, high dielectrics, and pigments [1,2]. Major phases of TiO_2 include rutile and anatase; rutile corresponds to the ground state, and anatase is a metastable state. Despite their importance, little is known about the properties of TiO_2 nanoclusters and nanophase TiO_2.

Recently Streitz and Mintmire [3] proposed a variable-charge interatomic potential for bulk rutile. This potential allows atomic charges to vary dynamically in response to changes in the local environment. The calculated cohesive energy and elastic moduli are in reasonable agreement with experimental results. In this paper we describe a new variable-charge interatomic potential [4] based on the formulation of Streitz and Mintmire [3], which reproduces the pressure-dependent static dielectric constants, vibrational density of states, melting temperature, and surface relaxation of the rutile crystal, as well as the cohesive energy and elastic moduli. The potential is applicable to anatase; its experimental cohesive energy, lattice constants, and dielectric constants are reproduced as well. We apply the present potential to TiO_2 nanoclusters to investigate their intercluster interactions.

Mat. Res. Soc. Symp. Proc. Vol. 581 © 2000 Materials Research Society

VARIBLE-CHARGE INTERATOMIC POTENTIAL FOR TiO_2

We consider a charge-neutral system composed of N_{Ti} titanium and N_O ($=2N_{Ti}$ for TiO_2) oxygen atoms with masses $\{m_i\}$ and charges $\{q_i e\}$ located at $\{\vec{r}_i\}$ ($i = 1,2,...,N_{Ti}+N_O$). The total potential-energy E_{pot} is modeled as composed of four terms:

$$E_{pot} = \sum_i E_i^{atom}(q_i) + \sum_{i<j} V_{ij}^{es}(r_{ij};q_i,q_j) + \sum_{i<j} V_{ij}^{c}(r_{ij}) + \sum_{i\in\{Ti\},j\in\{O\}} \Delta V_{ij}^{TiO}(r_{ij};q_i,q_j). \quad (1)$$

The first term in the right-hand side of Eq. (1) represents the atomic energy [3-5]

$$E_i^{atom}(q_i) = E_i^{atom}(0) + q_i\chi_i + \frac{1}{2}J_i q_i^2 \quad (2)$$

with electronegativity χ_i and hardness J_i. In the present formulation we regard them as free parameters in optimizing the potential formulas. The second term in Eq. (1) denotes the electrostatic interaction-energy:

$$V_{ij}^{es}(r_{ij};q_i,q_j) = \int d\vec{p}_1 \int d\vec{p}_2 \frac{\rho_i(\vec{p}_1,q_i)\rho_j(\vec{p}_2,q_j)}{p_{12}}, \quad (3)$$

where $\rho_i(\vec{p},q_i) = Z_i e\delta(\vec{p}-\vec{r}_i) + (q_i e - Z_i e)f_i(\vec{p}-\vec{r}_i)$ is the charge-density distribution around the i-th atom with a "core" charge $Z_i e$ and a normalized valence-electron density distribution f_i. As in the original parameterization [3] we take Z_{Ti}=4, Z_O=0, and f_i to be a 1s-like function: $f_i(r) = (\varsigma_i^3/\pi)\exp(-2\varsigma_i r)$. The third term in Eq. (1) represents the covalent bonding and the steric repulsion between the atomic cores. Following Streitz and Mintmire [3], we adopt a modified Rydberg form for V_{ij}^c:

$$V_{ij}^c(r_{ij}) = -C_{ij}[1 + (r_{ij} - r_{ij}^e)/l_{ij}]\exp[-\alpha_{ij}(r_{ij} - r_{ij}^e)/l_{ij}]. \quad (4)$$

We follow Streitz and Mintmire [3] and omit terms proportional to $Z_i Z_j$ in Eq. (3) since they are independent of both q_i and q_j and hence may be regarded as effectively included in V_{ij}^c. First-principles calculations have shown that atoms in the vicinity of surfaces move away substantially from the crystalline sites. The Rydberg-like form, Eq. (4), is too restrictive to take account of this behavior. The last term in Eq. (1), involving only neighboring Ti and O atoms, is introduced to include the surface relaxation effects when a low-index surface (e.g., (110)) is created. We adopt the form:

$$\Delta V_{ij}^{TiO}(r_{ij};q_i,q_j) = \tau[q_O + q_{Ti}g(r_{ij})]^2 h(r_{ij}), \quad (5)$$

with

$$h(r) = \frac{1+\exp[(\xi-r)/\sigma]}{1+\exp[(r-\gamma)/\eta]} \quad \text{and} \quad g(r) = 1.5 - \frac{1}{1+\exp[(\lambda-r)/w]}. \quad (6)$$

The neighboring Ti-O pairs with distances less than ~γ contribute in the denominator of $h(r)$. The numerator of $h(r)$, on the other hand, controls anharmonic vibrations between Ti-O pairs. We determine its functional parameters to adjust melting temperature of the rutile structure. The effect of $g(r)$ in ΔV_{ij}^{TiO} on charge transfer between Ti and O atoms has been discussed in Ref. 4.

The parameters $\{\chi_i, J_i, \varsigma_i, C_{ij}, r_{ij}^e, l_{ij}, \alpha_{ij}, \lambda, w, \gamma, \tau, \eta, \xi, \sigma\}$ in the potential are determined by fitting to experimental and first-principles electronic structure calculation data on the lattice constant, cohesive energy, elastic moduli, static dielectric constants, surface energies of low-index planes [(110) and (100)], melting temperature at ambient pressures, and surface relaxation properties for (110) of the rutile structure. Atomic charges, q_i, are determined

dynamically by minimizing E_{pot} with respect to a set $\{q_i\}$ under the constraint of charge conservation. Table I lists values of the parameters so determined. Table II compares calculated values for several physical quantities with corresponding experimental values.

TABLE I. Optimized values of the potential parameters in the present model.

	Atomic parameters			
	χ_i(eV)	J_i(eV)	ς_i (Å^{-1})	Z_i
Ti	0	10.3	0.530	4.0
O	5.44	8.25	0.720	0.0
	Interatomic parameters			
	r_{ij}^e (Å)	l_{ij} (Å)	C_{ij}(eV)	α_{ij}
Ti-Ti	2.85	0.130	0.281	1.0
Ti-O	2.53	0.504	0.104	1.0
O-O	3.47	0.490	0.0704	1.27

	λ (Å)	w (Å)	τ(eV)	γ (Å)	η (Å)	ξ (Å)	σ (Å)
Ti-O	1.76	0.018	16.33	2.50	0.30	0.60	0.20

We have also calculated the surface energies of (110) and (100) surfaces of the rutile structure. From the crystalline rutile system, we create a slab (width ~25.0Å) with (110) surfaces. The slab is placed in a supercell (19.8Å×19.8Å×33.1Å), as was done in Ref. 6. The slab contains five Ti-layers parallel to the surface. Subsequently the lowest total-energy configuration is obtained with the conjugate-gradient (CG) method. Displacements of each atom from the crystalline position agree well with the results in a first-principles calculation. Our results for the deviation of the atomic charge from the bulk value show reasonable agreement with those calculated using a tight-binding interatomic potential [7]. We find the surface energies to be 39meV/Å^2 and 41meV/Å^2 for (110) and (100) surfaces, which agree reasonably with first-principles calculation data [6] 55meV/Å^2 and 70meV/Å^2, respectively.

TABLE II. Comparison of the theoretical results based on the present potential model with experimental data for various quantities of bulk rutile.

	Present	Experiment
a (Å)	4.6781	4.5936 [8]
c (Å)	2.5818	2.5987 [8]
q_{Ti}	2.43	2.6 [9]
E_c/N_{Ti} (eV)	19.8	19.8 [10]
bulk modulus (GPa)	228	216 [11]
C_{11} (GPa)	412	271 [11]
C_{33} (GPa)	519	484 [11]
C_{44} (GPa)	136	124 [11]
C_{13} (GPa)	123	150 [11]
ε_{xx}	91.8	86 [12]
ε_{zz}	195.9	170 [12]
melting temperature (K)	2,000~2,400	2,100 [13]

To test the transferability of our interaction potential, we investigate the properties of the anatase phase of TiO_2. We have calculated the ground-state energy of anatase and find it to be larger than that of rutile. The resulting energy difference, 0.09eV per Ti atom, compares

favorably with the heat of formation [13], 0.068eV per Ti atom. The lattice constants at zero temperature are determined to be $a = b = 3.85$ (3.79) Å and $c = 8.78$ (9.51) Å where the numbers in the parentheses are the corresponding experimental values [2]; the density has an error of 4 %. We have also calculated the dielectric constants along the a- and c-axes and the values are ε_{xx}=38.1 and ε_{zz}=61.6, respectively. The experimental value [2] of ε for a powder sample of anatase is 48, which is much lower than $\varepsilon = 114$ for rutile. Averaging our values for anatase over the principal directions yields $\varepsilon = (2 \times 38.1 + 61.6) / 3 \approx 46$. This is in excellent agreement with the experimental value.

INTERACTION BETWEEN TiO_2-NANOCLUSTERS

TiO_2 nanoclusters may be synthesized by several methods [14-16]. In the sol-gel method [16], anatase nanoclusters of smaller sizes (3 – 10 nm) can be processed with various degrees of aggregation, by precisely controlling pH of the alkoxide/water solution and doping surfactants [1]. Those anatase-nanoclusters sinter at relatively low temperatures [17] ~ 900 K than that for the rutile nanoclusters (~ 1,300 K). During the sintering of anatase nanoclusters, anatase-to-rutile phase transformation has been found at grain boundaries [17]. Such low sintering-temperatures are desirable for technical applications since grain growth is significantly suppressed during the sintering. Dispersed nanoclusters are desirable for their use in high-quality nanophase TiO_2. Theoretical investigation of aggregation mechanisms of TiO_2 nanoclusters will offer valuable information for improved processing of nanoclusters.

Anatase nanoclusters processed in the sol-gel method [16] are spherical with diameter d = 30 – 100 Å. This observation indicates that the ground state of an anatase nanocluster in this range of diameter is spherical. For comparison we study the ground state of free rutile-nanoclusters in the same size-range by calculating the total potential-energies of spherical and faceted nanoclusters. We cut out rutile spheres with d = 60 Å and 80 Å from a rutile crystal; total number of atoms N = 10,446 for d = 60 Å and N = 24,870 for d = 80 Å. The total potential-energy $E_{p\alpha}$ of each nanosphere is minimized by moving atomic positions and changing atomic charges following the CG method. Faceted rutile-nanoclusters with nearly same numbers of atoms (N = 10,164 and 24,102) are also prepared following the Wulff construction using surface energies in Ref. 4. The CG minimization of $E_{p\alpha}$ with respect to the atomic positions and charges are thereon performed. We find $E_{p\alpha}/N = -6.609$ eV for the nanosphere with d = 60 Å (N = 10,446), $E_{p\alpha}/N = -6.601$ eV for the faceted nanocluster with N = 10,164. The $E_{p\alpha}/N = -6.615$ eV for the nanosphere with d = 80 Å (N = 24,870), $E_{p\alpha}/N = -6.608$ eV for the faceted nanocluster with N = 24,102. Comparing the energies, we predict that the ground state of a rutile nanocluster with size 60 – 80 Å is spherical. In the following paragraphs we consider TiO_2 nanospheres with d = 60 Å.

We analyze distribution of space charges in the nanospheres. Figure 1(a) shows the radial distribution of atomic charges in the rutile nanosphere at the ground state, in which deviations of the charges from the bulk values, $dq = \langle q \rangle - q_{bulk}$, with respect to Ti and O averaged in each radial shell (Δr = 2 Å) are plotted. Figure 1(b) shows the corresponding data for the anatase nanosphere at the ground state. Both for rutile and anatase nanospheres, net charge of the surface region (r = 28 – 30 Å) is positive while it is negative for the adjacent inner-region (r = 24 – 28 Å). This double-charge layer structure is maintained at elevated temperature T = 1,400 K for both rutile and anatase nanospheres.

Similar double-charge layer structure is found also for low-index surfaces of rutile in the calculations by Shelling *et al.* [7] for slab geometry using a tight-binding interaction potential. We calculate surface charges by taking two or three atomic layers in the slab, depending on the surface index, from the vacuum boundary so that the number ratio becomes Ti:O = 1:2. We find that the surface-charge per TiO_2 to be 0.005e for the (110) surface, 0.01e for the (100), and 0.01e

for the (001). Despite differences in geometry, both sphere and slab systems form similar double-charge layer structures.

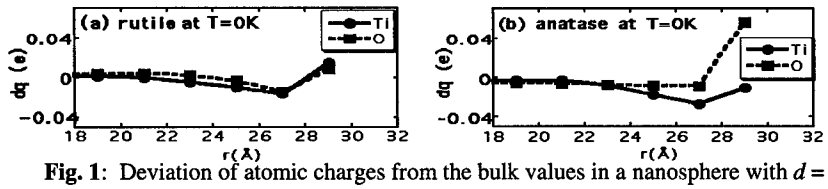


Fig. 1: Deviation of atomic charges from the bulk values in a nanosphere with $d = 60$ Å.

Interaction potential between two nanospheres is affected by the double-charge layer structure in each nanosphere. Let us denote the center-of-mass (COM) position of each nanosphere ($d = 60$ Å) as $\vec{r}_{\rm COM}$. We evaluate intercluster interaction-potential $\Delta E_{\rm pot}$ of two nanospheres ($T = 1{,}400$ K) as a function of the distance between two COM's $R = |\Delta\vec{r}_{\rm COM}|$. Figure 2 shows $\Delta E_{\rm pot}$ for three combinations of crystalline orientations. Both <100> direction of one nanosphere and <100> of the other are parallel to the line connecting two COM's in the case <100>-<100>; <100> and <001> in the case <100>-<001>, <001> and <001> in the case <001>-<001>. Solid curves in Fig. 2 represent calculations which include dynamic charge-transfer between atoms; while for dashed curves, atomic charges are fixed to the bulk crystalline-values at the ground state. Space charges are homogeneous in the cases of rigid-ions.

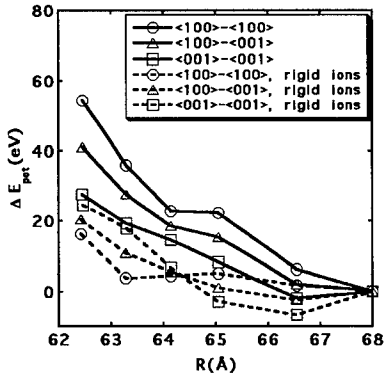


Fig. 2: Intercluster interaction-potential, $\Delta E_{\rm pot}$, as a function of intercluster separation, $R = |\Delta\vec{r}_{\rm COM}|$, for two rutile-nanospheres with $d = 60$ Å.

To obtain values plotted in Fig. 2 we first set two thermalized nanospheres at $R = R_0 = 69$Å along the x-axis. We then increase velocities of all the atoms in the smaller-x nanosphere by $\Delta v_x = 100$m/s, and similarly those in the larger-x nanosphere by $\Delta v_x = -100$m/s. We perform the microcanonical molecular-dynamics (MD) simulation staring from that configuration. Value of $\Delta E_{\rm pot}$ at R ($< R_0$) is obtained in the simulation as negative of the change with respect to the total kinetic energies of COM's. Qualitatively same results are obtained for two anatase-nanospheres. For $R < 62$ - 62.5 Å, Ti and O atoms on the contacting surfaces of the nanospheres slide to form a bridge between the two nanospheres in both rutile and anatase cases. Possible uncertainty of $\Delta E_{\rm pot}$ in Fig. 2 is 2 – 3 eV. We note that effects of dynamic charge-transfer lower the total potential-energy of the two-nanosphere system with $R = 69$ Å by ~ 8.0×10^2 eV for both

rutile and anatase. For all R values, the total potential-energy in the variable-charge case is substantially lower than that in the corresponding rigid-ions case.

We observe in Fig. 2 that effects of dynamic charge-transfer add repulsive intercluster interaction-potential at R = 62 - 65Å for both rutile and anatase nanospheres. Since the surface region (r > 28 Å) in each nanosphere has a net positive-charge, Coulomb repulsion between the two nanoclusters results at close proximity.

CONCLUSIONS

We have developed a new variable-charge interatomic potential for TiO_2 based on the formalism of Streitz and Mintmire. We have applied the potential to rutile and anatase nanoclusters (d = 60 – 80 Å) in vacuum, to investigate equilibrium configuration and space-charge distribution of the nanoclusters. We have found that the nanosphere self-organizes double-charge layer structure in the surface region. The double-charge layer structure enhances the barrier potential for contact of two nanospheres (d = 60 Å and T = 1,400 K). Such double-charge layer structure may have significant effects on aggregation and sintering mechanisms of TiO_2 nanoclusters. MD simulations of aggregation of two nanospheres (d = 60 Å) with various combinations of crystalline orientations are in progress.

REFERENCES

1. *Nanomaterials Synthesis, Properties, and Application*, edited by A.S. Edelstein and R.C. Cammarata (IOP Pub., London, 1996).
2. *Concise Encyclopedia of Advanced Ceramic Materials*, edited by R.J. Brook (Pergamon, Cambridge, 1991), pp. 486-488.
3. F.H. Streitz and J.W. Mintmire, J. Adhesion Sci. Technol. **8**, 853 (1994).
4. S. Ogata, H. Iyetomi, K. Tsuruta, F. Shimojo, R.K. Kalia, A. Nakano, and P. Vashishta, J. Appl. Phys. **86**, 3036 (1999).
5. A.K. Rappe and W.A. Goddard, J. Phys. Chem. **95**, 3355 (1991).
6. M. Ramamoorthy, D. Vanderbilt, and R.D. King-Smith, Phys. Rev. B **49**, 16721 (1994).
7. P.K. Schelling, N. Yu, and J.W. Halley, Phys. Rev. B **58**, 1279 (1998).
8. J.C. Abrahams and J.L. Bernstein, J. Chem. Phys. **55**, 3206 (1971).
9. J.G. Traylor, H.G. Smith, R.M. Nicklow, and M.K. Wilkson, Phys. Rev. B **3**, 3457 (1971).
10. *CRC Handbook of Chemistry and Physics, 79th edn.* (CRC Press, Florida, 1996).
11. M.H. Manghnani, J. Geophys. Res. **74**, 4317 (1969).
12. R.A. Parker, Phys. Rev. **124**, 1719 (1961).
13. *JANAF Thermodynamic Tables, 3rd edn*, edited by Chase *et al.* (AIP, New York, 1985).
14. R.W. Siegel, S. Ramasamy, H. Hahn, L. Zongquan, L. Ting, and R. Gronsky, J. Mater. Res. **3**, 1367 (1988).
15. H. Hahn, J. Logas, and R.S. Averback, J. Mater. Res. **5**, 609 (1990).
16. Q. Xu and M.A. Anderson, Mat. Res. Soc. Symp. Proc. **132**, 41 (1989).
17. K.-N.P. Kumar, K. Keizer, A.J. Burggraaf, T. Okubo, H. Nagamoto, and S. Morooka, Nature **358**, 48 (1992).

TIGHT-BINDING MOLECULAR DYNAMICS OF CERAMIC NANOCRYSTALS USING PC-BASED PARALLEL MACHINES

Kenji Tsuruta, Hiroo Totsuji, and Chieko Totsuji

Department of Electrical and Electronic Engineering, Okayama University,
3-1-1 Tsushima-naka, Okayama 700-8530, JAPAN
Email: tsuruta@elec.okayama-u.ac.jp, URL: http://www.mat.elec.okayama-u.ac.jp

ABSTRACT

Evolution of atomic and electronic structures of silicon-carbide (SiC) nanocrystals during sintering is investigated by a tight-binding molecular dynamics (TBMD) method. An $O(N)$ algorithm (the Fermi-operator expansion method) is employed for calculating electronic contributions in the energy and forces. Simulations are performed on our eight-node parallel PC cluster. In a sintering simulation of aligned (no tilt or twist) SiC nanocrystals at T=1000K, we find that a neck is formed promptly without formation of defects. Analyses of local electronic density-of-states (DOS) and effective charges reveal that unsaturated bonds exist only in grain surfaces accompanying the gap states. In the case of tilted (<122>) nanocrystals, surface structures formed before sintering affect significantly the grain-boundary formation.

INTRODUCTION

Silicon-carbide (SiC) ceramic has drawn great deal of interest as a promising material for new electronic applications including high-power, high-frequency, and high-temperature electronic systems, in which silicon or gallium-arsenic devices cannot effectively work. Applications of this material to gas sensors and irradiation detectors in harsh environment have also been investigated extensively [1]. Such wide variety of industrial applications is made possible by the excellent properties of this material such as high barrier for electric breakdown, chemical stability, and high thermal conductivity. However, the brittleness of this hard ceramic is a major drawback in reliability and in tailoring the materials for specific applications. Nanocrystalline SiC (nc-SiC) synthesized by consolidating nano-particles may improve mechanical stability of SiC-based devices: It has been known [2] that ceramics with ultrafine microstructure tend to have enhanced ductility against the coarse-grained counterpart. In order to optimize the material properties and fabrication processes for electronic applications, it is essential to understand the relationship between microstructures and electrical properties of the nanocrystalline ceramic. Semiempirical tight-binding molecular dynamics method [3] is powerful tool to investigate theoretically both atomistic and electronic processes in synthesizing nanocrystalline materials.

In this paper, we report on tight-binding molecular-dynamics simulations for sintering of SiC nanocrystals (diameter ~ 24 Å) at a temperature of 1000K. The Fermi-operator expansion method (FOEM) [3, 4] has been employed to calculate efficiently the electronic part of the energy and forces, and it has been run on our eight-node parallel PC cluster. Using the parallel TBMD, we investigate the processes of neck formation (a) between aligned nanocrystals, and (b) between tilted nanocrystals. In the case (a), we find that effect of surface relaxation prior to the neck formation is small, and the neck is formed quickly with no defect trapped in the grain boundary. In the case (b), on the other hand, the surface structures relaxed at T=1000K before sintering affect significantly processes in the grain-boundary formation. Disordered structures are formed transiently in the grain boundaries.

TIGHT-BINDING MODEL FOR SILICON CARBIDE

In the tight-binding (TB) model, the total energy of a system consisting of N atoms is defined as

$$E_{\mathrm{tot}} = E_{\mathrm{kin}} + E_{\mathrm{bs}} + E_{\mathrm{rep}} \qquad (1)$$

Mat. Res. Soc. Symp. Proc. Vol. 581 © 2000 Materials Research Society

where E_{kin} stands for the kinetic energy, E_{bs} is the band-structure energy, and E_{rep} represents the repulsive term that takes into account the core-core interactions and neglected contributions in E_{bs} to the true electronic energy such as a correction for double counting of electron-electron interactions. In many of the semiempirical TB method, the repulsive energy is modeled by the sum of short-range 2-body interaction. The band-structure energy is calculated by diagonalizing the effective one-electron Hamiltonian matrix, **H**. Each off-diagonal element of the Hamiltonian involves interactions between valence electrons within the two-center hopping approximation. The TB-Hamiltonian plays an essential role in the TBMD simulations of covalent systems.

Several parametrizations of the TB Hamiltonian matrix for covalent systems have been proposed [5]. Among them, we have chosen Mercer's parametrization of the TB Hamiltonian for SiC [6], which is based on the sp^3 orthogonal basis. In addition, it includes the effects of environment around each atom on its onsite energies by introducing intra-atomic terms. These terms give important contributions to variation of the charge transfer between Si and C atoms, especially for inhomogeneous systems. In the original work by Mercer, there are some discrepancies with experimental data such as the lattice constant and the interfacial energies. We have therefore made minor modifications of the parameters so that magnitudes of these discrepancies are reduced. Table I summarizes comparisons of the present model with other works.

Table I: Comparison of the physical quantities in the present TB model with other works

Physical quantities	Present	Other work
lattice constant [Å]	4.36	4.36 [1)]
cohesive energy [eV]	6.53	6.34 [1)]
bulk modulus [GPa]	234	224 [1)]
grain-boundary energy[2)] [J/m^2]	1.75	1.27 [2)]

1) Experimental values referred to in Ref. [7]

2) {122}Σ=9 non-polar grain boundary energy in Ref. [5]

O(*N*) PARALLEL TIGHT-BINDING ALGORITHM

In conventional TB method, the calculation of E_{bs} involves matrix diagonalization with which the computational cost increases as ~ N^3, where N is the number of atoms in the simulation cell. This has limited the system size of the TBMD simulations to a few hundred atoms, which is too small for realistic simulations of nanostructured materials. Recently, several efficient algorithms for TB calculations are proposed. We adopt the Fermi-operator expansion method, proposed originally by Goedecker and Colombo [4], for calculating E_{bs}. This algorithm is based on moment expansions of a pseudo-density matrix (the Fermi operator) of the TB Hamiltonian by Chebyshev polynomials. Combining an appropriate truncation at a finite order of the expansion and a truncation in the multiplication between each element of the matrix by introducing a physical cutoff distance, the number of floating-point operations in the expansion is reduced to that proportional to the number of atom, N.

Figure 1 shows a comparison of the cpu time for calculating E_{bs} of bulk Si crystal by the present algorithm with that by the conventional method based on the matrix diagonalization. Clearly, the calculation of E_{bs} by the conventional method [$O(N^3)$] becomes overwhelming for systems with more than 100 atoms, whereas the present method stays in reasonable time scale for the calculation.

This algorithm is suitable for parallel computing, since the truncation at the physical distance between atomic sites can make the data structures localized. We employ the domain-decomposition technique for distributing the matrix elements on each computing node. Data transmission between neighboring nodes is performed only for near-boundary atoms and matrix elements because of the localized nature of the density matrix.

In the present study, we have performed the parallel TBMD simulations on our eight-node parallel cluster: It consists of PentiumII-based personal computers. Data communications are done through network connected by Fast Ethernet switching hub. Figure 2 depicts the parallel PC cluster in our laboratory.

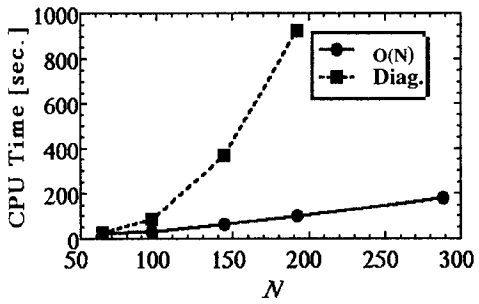


Fig 1: Comparison of cpu time for calculating band-structure energy of bulk silicon crystal by $O(N)$ algorithm with that by diagonalization, $O(N^3)$. The TB parameters for Si crystal were taken from Ref. [8].



Fig 2: Parallel PC cluster connected via Fast Ethernet switch.

NECK FORMATION BETWEEN SILICON-CARBIDE NANOCRYSTALS

Dynamics of neck formation at high temperatures is an important issue because it may determine not only mechanical stability of the grain boundaries but also carrier transport properties. We investigate effects of surface relaxation, or surface reconstruction, and of

grain-boundary orientation on the neck formation processes between β-SiC nanocrystals by the TBMD simulation.

Figure 3(a) shows xy projection of the initial configuration of 'aligned' (no tilt or twist) nanocrystals: The nanocrystals are prepared by removing a cylindrical system with radius 14Å from β-crystalline bulk SiC. The total number of atoms in the simulation box is 460 (230 Si atoms and 230 C atoms) and the initial size of the simulation box is 32.05Å x 30.82Å x 7.55Å. The periodic boundary condition is used to reduce the number of atoms in the simulation while keeping the particulate size reasonably large. The time step for molecular dynamics is 1fs and the Chebyshev order in the moment calculation is 30, which keeps energy conservation at 1000K to be about 10^{-3} eV/atom.

First, the system is heated gradually to 300K, and thermalized for 200fs. Temperature is then increased to 1000K gradually, and thermalized for 1ps. After this thermalization, the system is compressed gradually along y direction ([11-2] by reducing the box length in the direction. Again it is thermalized for 1ps. Figure 3(b) is snapshot of the final configuration. The figure shows that even after compression at T=1000K the structure at the neck is crystal-like while surface reconstruction occurs on cluster surfaces. Through analyses of effective charges (Mulliken charges) and local density of states we find that unsaturated bonds or effect of bond distortions exist only on the free surfaces. The grain boundary is therefore regular structure (defect free).

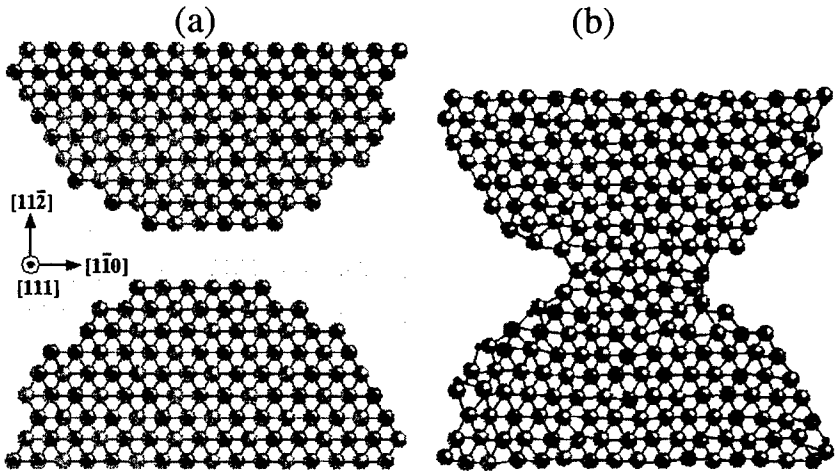


Fig 3: Neck formation of SiC nanocrystals: (a) initial configuration, (b) configuration after compression at T=1000K. Large and small spheres represent Si atom and C atom, respectively.

In addition to the regular grain boundary, we have performed TBMD simulation of nanocrystals with a tilt angle. Figure 4(a) shows the initial configuration of 816-atom system (408 atoms per grain). Initially, the grain at the center of the MD cell and the surrounding grains are tilted to each other, so that it corresponds to a coincidence grain boundary ({122}Σ=9) found typically in experiments [1, 5]. After the same thermal process as in the previous case, the system was compressed along x and y direction at T=1000K. Figure 4(b)

depicts the configuration after compression. Contrary to the previous case, the figure indicates that disordered structure is formed in the grain boundaries.

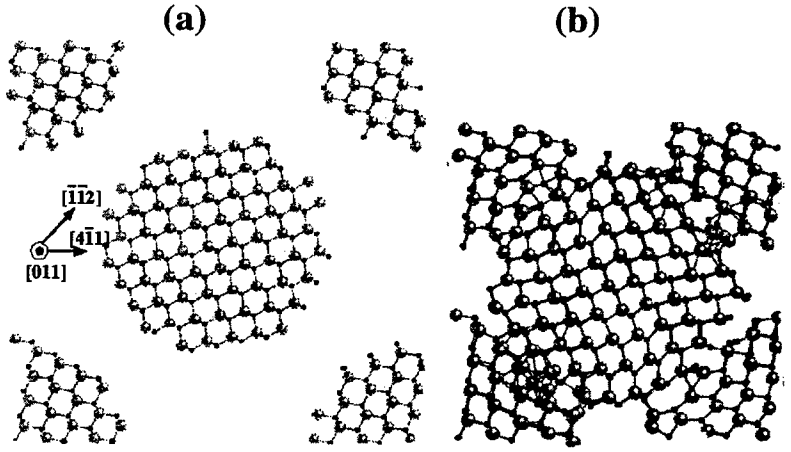


Fig 4: Neck formation of SiC nanocrystals: (a) initial configuration, (b) configuration after compression at T=1000K. Large and small spheres represent Si atom and C atom, respectively.

CONCLUSIONS

We have performed large-scale TBMD simulations for the neck formations between nanocrystals of diameters 24~28Å. The $O(N)$ algorithm has been implemented for efficient computation of the band-structure energy. The code has been fully parallelized on PC-based parallel machines. We have found that the neck formation at 1000K occurs very quickly in regular grain boundary, whereas the surface structure or reconstruction before compression affects significantly the tilt grain-boundary formation. The results indicate that a transient disordered phase in grain boundaries before the formation of ideal low-energy grain boundaries may exist in actual sintering processes.

ACKNOWLEDGMENTS

This work was supported partially by the Grants-in-Aid for Scientific Research (B) 08458109 and (B) 11480110 from the Ministry of Education, Science, Sports, and Culture of Japan, and by a scholarship from Hitachi Co. Ltd. One of us (KT) was also supported partially by Okayama Foundation for Science and Technology.

REFERENCES

1. E.g., IEEE Trans. Elec. Dev. (Special Issue) Vol. 46 (3) (1999); *Silicon Carbide Ceramics - 1: Fundamental and Solid Reaction*, edited by S. Somiya and Y. Inomata (Elsevier Applied Science, London and New York, 1991).
2. *Nanophase and Nanocomposite Materials II*, edited by S. Komarneni, J. C. Paker, and H. J. Wollenberger, Mater. Res. Soc. Symp. Proc. vol. 457 (MRS, 1997).
3. *Tight-Binding Approach to Computational Materials Science*, edited by P. Turchi, A. Gonis, L. Colombo, Mater. Res. Soc. Symp. Proc. vol. 491 (MRS, 1998).

4. S. Goedecker and L. Colombo, Phys. Rev. Lett. **73**, 122 (1994).

5. M. Kohyama *et al.*, J. Phys. Condens. Matter **2**, 7791 (1990); *ibid.* **2**, 7809 (1990); J. Robertoson, Phil. Mag. B **66**, 615 (1992); D. Sanchez-Portal *et al.*, Solid State Comm. **95**, 685 (1995)

6. J. L. Mercer, Phys. Rev. B **54**, 4650 (1996).

7. K. J. Chang and M. L. Cohen, Phys. Rev. B **35**, 8196 (1987).

8. L. Goodwin, A. J. Skinner, and D. G. Pettifor, Europhys. Lett. **9**, 701 (1989).

AUTHOR INDEX

Abe, T., 591
Abraham, Matthias, 517
Ade, Martin, 205
Agrawal, D.K., 315
Alfano, R.R., 411
Ali, A.M., 565
Aliev, F.M., 309
Alikina, G.M., 435
Amato-Wierda, C.C., 339
Amils, X., 641
Anderson, Harlan U., 553
Anderson, Peter M., 603
Andres, Ronald P., 59
Andrievski, R.A., 583
Ardisson, J.D., 333
Armistead, J. Paul, 53
Aust, K.T., 461

Bae, Dong Jae, 239
Baker, R., 345
Banerjee, Rajarshi, 603
Baraton, M-I., 559
Barborini, E., 283
Baró, M.D., 641
Barrera, Rubén, G., 485
Barron, Andrew R., 369, 659
Baum, M., 65
Bawendi, Moungi G., 139
Beam, M.P., 193
Becker, M.F., 193
Behrens, S., 65
Bellare, Anuj, 399
Bello, I., 235
Bellon, P., 271
Beloshapkin, B.A., 435
Bel'skaya, O.B., 315
Bernal, S., 345
Berry, Alan D., 53
Bessais, L., 95, 259
Beyer, W., 187
Bhalla, A.S., 529
Biasioli, F., 283
Bieri, F., 393
Bisero, D., 609
Black, M.R., 623
Boatner, L.A., 71
Bolom, T., 321
Bordin, G., 609
Börner, F., 187
Boukis, N., 65
Brandau, W., 523
Breen, J.P., 435
Brock, J.R., 193
Brown, A.P., 265
Brown, David S., 659
Brugger, Ch., 405
Brydson, R., 265
Budaik, J.D., 71
Bulthaup, Colin A., 115
Bunina, R.V., 435
Burdeynaya, T.N., 435
Burgina, E.B., 315
Butz, R., 187

Calderon, H.A., 253
Campbell, Timothy J., 449
Carotta, Maria Cristina, 121
Carpenter, E.E., 107
Casula, M.F., 363
Cerezo, Alfred, 517
Chaikina, M.V., 315
Chang, Se-Hong, 27
Chantis, A., 629
Choi, Won Bong, 239
Choi, Young Chul, 239
Cirignano, L.J., 653
Corrias, A., 363
Cristofolini, L., 151
Curtis, C.J., 157

Davydova, M.N., 435
De Hosson, J.Th.M., 547
Derby, B., 303, 327
Derevyankin, A.Yu., 435
Dinjus, E., 65
Djega-Mariadassou, C., 95, 259
Dobley, Arthur, 387
Doronin, V.P., 435
Dresselhaus, M.S., 213, 623
Dunn, Bruce, 623
Duplyakin, V.K., 315
Durbin, S.D., 577

Edelman, F., 9, 187
Ederth, J., 541
Eklund, P.C., 623
Endo, A., 429
Entine, G., 653
Epelbaum, B.M., 577
Epling, William S., 449
Erb, U., 461
Erwin, M., 503

Facci, P., 151
Fain, Jason P., 603
Fang, S., 623

Fenelonov, V.B., 435
Feng, S.Q., 225, 231
Fischer, A., 523
Fischer, R.A., 417
Fitz, Wolfgang, 399
Flowers, Jr., Billy H., 145
Fonseca, L.F., 647
Fontana, M.P., 151
Foos, Edward E., 53
Foss, Jr., Colby A., 615
Foygel, M., 629
Fraser, Hamish, 603
Freyhardt, H.C., 635
Fuda, Kiyoshi, 441
Fukuda, T., 577
Fukushima, Y., 423

Galtayries, A., 345
Gates, Byron, 83
Gaumet, J.J., 479
Gerberich, William, 603
Gessert, T., 157
Ginley, D.S., 157
Godfrey, T.M.T., 265
Godoi, R.H.M., 21
Gomoll, Andreas H., 399
Goto, Y., 423
Granqvist, C.G., 15, 541
Green, Mark, 47
Gritsyna, V.T., 181
Gronsky, R., 213
Guo, R., 529
Gupta, S., 529
Gupta, T.K., 653

Habicht, W., 65
Hahn, Horst W., 9, 449
Hammond, C., 265
Hang, Q.L., 225, 231
Happek, Uwe, 145
Hasegawa, K., 577
Hasegawa, S., 199, 565
Hassan, K.M., 163
Haynes, T.E., 71
Heilmann, A., 523
Henneke, D.E., 193
Herweg, C., 635
Hoche, H., 9
Hoel, A., 15
Hoffmann, J., 635
Hoflund, Gar B., 449
Honda, S., 71
Honma, I., 381, 429
Hooijmans, J., 547
Hu, Xiangjun, 353
Huan, C.H.A., 597
Hubert, Brian N., 115
Huerta, A., 253
Hultåker, A., 491

Iannotta, S., 283
Imada, Y., 423
Inokuma, T., 199, 565
Isaacs, L.L., 411
Ivanova, A.S., 435
Iyetomi, Hiroshi, 667

Jacobson, Joseph M., 115
Jafelicci, Jr., M., 21
Jardim, P.M., 89
Jemian, Peter R., 399
Ji, Hua Xia, 339
Ji, Shuang, 353
Jie, Y.X., 597
Jones, Christopher D., 659
Jones, K.M., 157
Josell, Daniel, 603

Kadavanich, A.V., 503
Kalia, Rajiv K., 667
Kalinnikov, G.V., 583
Katiyar, R.S., 529
Katsura, M., 297
Kelly, D.J., 653
Keto, J.W., 193
Keveney, K., 345
Khan, H.R., 245
Kim, Bong-Chull, 27
Kim, Jeong-Joo, 27
Kim, Jong Min, 239
Kim, S.J., 33
Kippeny, T., 503
Kish, L.B., 15
Kishimoto, N., 181
Kiss, L.B., 541
Kochubei, D.I., 315, 435
Koide, Yoshihiro, 369
Kolbas, R.M., 163
Kolomiichuk, V.N., 435
Konin, G.A., 435
Krause-Rehrberg, R., 187
Kriventsov, V.V., 315
Krumeich, F., 393
Kubota, Y., 423
Kudo, Shuji, 441
Kudo, T., 429
Kui, H.W., 277
Kumbhar, A., 107
Kurata, Y., 199, 565
Kurtenbach, Dirk, 205
Kuznetsova, N.N., 315
Kuznetsova, T.G., 435

Lal, M., 405

Lane, Helen M., 517
Lang, Ch., 635
Lazell, Michael, 169, 175
Lee, C.G., 181
Lee, C.S., 235
Lee, J-H., 577
Lee, K.R., 33
Lee, Nae Sung, 239
Lee, S.T., 235
Lee, Seung Mi, 239
Lee, Young Hee, 239
Leising, G., 405
Li, Q., 277
Li, Zhenhua, 449
Lieber, C.M., 3, 219
Lin, Y-M., 213, 623
Littrell, Kenneth, 353
Liu, H., 647
Long, Gabrielle G., 399
Lunin, V.V., 315
Lusby, T.A., 271

Macedo, W.A.A., 333
Maddox, Clinton B., 145
Mahfoud, A., 647
Malik, M. Azad, 133, 291
Malyavanatham, G., 193
Manivannan, A., 511
Männling, H., 321
Marshall, Larry L., 659
Martinelli, Giuliano, 121
Mathe, Kenneth, 145
Matson, R.J., 157
Matsunaga, Toshiaki, 441
Matyshak, V.A., 435
Maximovskaya, R.I., 315
McCrea, J.L., 461
Meldrum, A., 71
Melmed, A.J., 271
Merhari, L., 559
Meunier, F.C., 435
Mikulec, Frederic V., 139
Milani, P., 283
Mirabella, F., 345
Mitchell, Brian S., 205
Miyayama, M., 429
Modine, F.A., 71
Morales, F., 535
Moto, K., 321
Moy, L.P., 653
Muhr, H-J., 393
Müller, Eberhard, 205
Muñoz, J.S., 641
Murakami, Kenji, 441
Murray, P.T., 473
Muth, J.F., 163

Nagel, R., 9
Nakagawa, T., 297
Nakajima, H., 381
Nakano, Aiichiro, 667
Nakayama, T., 297
Narayan, J., 163
Narita, Shuji, 441
Nery, G.A., 647
Nesládek, P., 321
Nesper, R., 393
Ng, H.P., 571
Ngan, A.H.W., 571
Nichols, W.T., 193
Niederberger, M., 393
Niederhofer, A., 321
Niihara, K., 297
Niklasson, G.A., 15, 491, 541
Nishimaki, K., 297
Nivi, Babak, 115
Nogués, J., 641
Noguez, Cecilia, 485
Nomura, S., 381
Nørager, Sebastian J., 169
Norman, A., 345
Novgorodov, B.N., 435
Numazawa, T., 297

O'Brien, Paul, 47, 133, 169, 175, 291
O'Connor, C.J., 107
Odegova, G.V., 315
Ogata, Shuji, 667
Olsson, E., 15, 541
Ostrovskii, N.M., 315

Palumbo, G., 461
Pareti, L., 609
Park, Gyeong-Su, 239
Park, R.E., 591
Park, S., 33
Park, W.W., 89
Park, Y.H., 591
Park, Young Soo, 239
Paschina, G., 363
Paukshtis, E.A., 315, 435
Pavlova, S.N., 315
Pellegrin, E., 41
Peng, H.Y., 235
Pennycook, S.J., 503
Perepezko, J.H., 101
Petricevic, V., 411
Petrikowski, K., 245
Petrovsky, Tatiana, 553
Petrovsky, Vladimir, 553
Petukhov, A.G., 629
Pijolat, M., 345
Piseri, P., 283
Plasova, L.M., 435

Popma, R., 547
Portillo, Joaquim, 21
Prasad, P.N., 405
Pusztay, Stephen V., 59

Qu, Shichun, 375

Rabin, O., 623
Ragot, F., 623
Ramsey, P.J., 339
Reinoso, M., 393
Resto, O., 647
Revaprasadu, N., 133, 291
Ribelin, R., 157
Ridley, Brent A., 115
Risen, Jr., William M., 353
Roberts, S.G., 303, 327
Román-Velázquez, Carlos E., 485
Ronconi, F., 609
Rosenmayer, Tom, 375
Rosenthal, S.J., 503
Ross, J.R.H., 435
Roy, Paromita, 511
Roy, R., 315
Rozovskii, A.Ya., 435
Ruddell, M.J., 473
Rudolph, D., 635

Sadykov, Vladislav A., 315, 435
Sander, M.S., 213
Sandrock, M.L., 615
Santos, A., 333
Sathish, S., 473
Sawitowski, T., 523
Schmechel, R., 417
Schmid, G., 523
Schmidt, J.E., 333
Schulz, Doug, 157
Schumaker, E.J., 473
Scott, Richard D., 399
Seehra, M.S., 511
Shah, K.S., 653
Shang, N.G., 235
Sharma, A.K., 163
Shen, L., 473
Shen, Z.X., 597
Shimojo, Fuyuki, 667
Shiomi, K., 297
Shtansky, D.V., 583
Simon, U., 77
Sims, J., 107
Sinha, G.P., 309
Smestad, G.P., 653
Smith, George D.W., 517
Snow, Arthur W., 53
Solórzano, I.G., 89
Song, J.S., 33
Song, K.J., 71
Sorokina, T.P., 435
Sort, J., 641
Spevack, Perry, 375
Spizzo, F., 609
Sporken, R., 345
Squillante, M.R., 653
Stavens, Kevin B., 59
Stickney, John L., 145
Strouse, G.F., 479
Sugi, Y., 423
Sugimoto, N., 423
Sun, Xiangcheng, 535
Suriñach, S., 641
Syed, M., 199
Szabó, D.V., 41

Tachibama, M., 623
Takeda, Y., 181
Tanaka, M., 297
Tasch, S., 405
Teng, C.W., 163
Thompson, J.R., 71
Thornhill, Thomas S., 399
Thuvander, Mattias, 517
Titchmarsh, J.M., 327
Totsuji, Chieko, 673
Totsuji, Hiroo, 673
Traversa, Enrico, 121
Tretyakov, V.F., 435
Troche, P., 635
Tsuchida, R., 199
Tsuchiya, K., 253
Tsuruta, Kenji, 667, 673
Tsybulya, S.V., 315
Turilli, G., 609
Turner, S., 467
Tymiak, Natalia, 603

Umeda, N., 181
Umemoto, M., 253
Unger, E., 65

Vaidyanathan, Raman, 145
Vajtai, R., 15
Vander Sande, J.B., 89
Vashishta, Priya, 667
Vavassori, P., 609
Veprek, S., 321
Versprille, K.E., 339
Viegas, A.D.C., 333
Vogelson, Cullen T., 369
Vollath, D., 41
von Seggern, H., 417

Wade, Travis L., 145
Waku, Y., 577

Wang, BaoPing, 411
Wang, N., 235
Wee, A.T.S., 597
Wei, Alexander, 59
Wei, Q., 3, 219
Weil, R., 187
Weisz, S.Z., 647
Werner, P., 9, 187
Whittingham, M. Stanley, 387, 497
Wierda, D.A., 339
Wilde, G., 101
Wilhelm, Eric J., 115
Winkler, H., 417
Winn, A.J., 303
Wisbey, A., 265
Wu, F., 271
Wu, H.Z., 303, 327
Wu, R.I., 101
Wu, X., 157

Xi, Z.H., 225, 231
Xia, Younan, 83
Xing, Y.J., 225, 231
Xu, J., 225, 231
Xu, Ping, 375

Yacaman, M. Jose, 535
Yagi, Y., 429
Yamamoto, T.A., 297
Yan, H.F., 225, 231
Yee-Madeira, H., 253
Yin, Yadong, 83
Ying, Jinpin, 411
Yoshikawa, A., 577
You, B.S., 89
Yu, D.P., 225, 231

Zabolotnaya, G.V., 315
Zaikovskii, V.I., 315, 435
Zavalij, Peter Y., 387, 497
Zhang, Fan, 497
Zhang, H.Z., 225, 231
Zhang, Haoyue, 205
Zhong, Ziyi, 83
Zhou, H.S., 429
Zhou, W.L., 107
Zhou, X.T., 235

SUBJECT INDEX

acrylic/PMMA, 399
aerogel, 353
age hardening, 89
aging, 27
Al, 157
alloy, 291
alumina, 303, 435, 659
aluminum alloy, 101
amines, 393
amorphous state, 187
anatase, 33
annealing, 327
antiferromagnetic-ferromagnetic, 641
arc discharge, 239
a-SiO_2, 181
atom probe, 517
  field ion microscopy (APFIM), 271

ball milling, 95, 271
battery, 497
β-Ga_2O_3, 239
biotechnology, 523
bismuth, 53, 213, 623
  telluride, 219
blocking temperature, 535
boehmite particles, 553
bone cement, 399
boron, 265
bound-magnetic-polaron, 629

cadmium sulfide, 133
calixarene, 59
capping groups, 169
carboxylate-alumoxane, 369, 659
catalysis, 345
catalyst, 65, 353
  support, 659
catalytic methane oxidation, 449
CdS, 175, 405
CdSe, 169
CdTe, 139
ceramic, 369
ceria(-), 345
  supported palladium, 449
characterization, 461
chemical vapor deposition, 339
chitosan, 353
chromium, 47
clay, 441
cluster(s)(-), 77
  beams, 283
  glass like, 535
CO detection, 559
cobalt, 441
Co-Cu granular films, 609
coercive field, 257
coercivity, 345
colloidal suspension, 553
colossal hopping magnetoresistance, 629
columnar structure, 571
composites, 291
conductivity, 77
copper and cobalt cations, 435
coprecipitation, 21, 27
core shell, 107, 291
Cr(IV) laser, 411
crack healing, 327
crystalline Si, 565
crystallization, 187
Cu, 157
Cu-Ag, 271
Curie temperature, 95

dielectric, 375
  constant, 623
  response, 491
  spectroscopy, 309
differential thermal analysis, 205
diffusion processes, 609
disintegration, 635
dithiocarbamates, 175
drug delivery, 523
dye-sensitized, 653

effective medium theory, 623
elastic properties, 473
electrical
  properties, 15
  resistivity, 461, 541
electrochemical
  atomic-layer epitaxy, 145
  deposition, 245
electrodeposition, 145, 517
electroluminescence, 405
electron-positron annihilation, 187
encapsulation, 59
energy product, 641
environmental monitoring, 121
epoxide, 369
europium, 647
eutectic, 577
exchange
  coupling, 641
  reactions, 393

factorial design, 339

Fe-Al_2O_3, 333
$Fe_{40}Ni_{40}P_{14}B_6$ alloy, 277
fiber, 577
figure of merit, 591
filler, 369
fluorescent, 139
fracture toughness, 321
framework zirconium phosphates, 315
FTIR spectroscopy, 559, 623

GaAs, 169
GaAs/ErAs nanocomposites, 629
gallium nitride, 417
gas
  deposition, 541
  sensing properties, 559
  sensors, 9, 121
germanium, 163, 597
gold, 47, 53, 541
  particles, 605
grain
  boundary, 461
  growth, 547
granular nanocomposite, 333
grinding, 327
growth mechanism, 231, 393

H_2 addition, 199
hardness, 321
heterocoagulation, 21
hexane isomerization, 315
high(-)
  coercivity particles, 71
  melting point compounds, 583
  resolution electron microscopy, 583
  T_c superconductors, 3
homogeneous deformation, 583
hopping resistivity, 629
hybrid materials, 381
hydrogenation, 565
hydrothermal, 497
hyperfine field, 95
hysteresis loop, 511

indium tin oxide, 491
inhomogeneous deformation, 583
$In(OH)_3$ structure, 27
InOOH structure, 27
insulator-metal transition, 571
interaction potential, 667
interface, 503
intergranular fracture, 583
ion
  beam, 235
  implantation, 71

Langmuir-Blodgett, 145
large-scale synthesis, 231
laser
  ablation, 193
  sintering, 547
lead telluride, 219
liquid
  crystal, 309
  phase separation, 277
local
  field enhancements, 605
  structure, 199
luminescent, 163

machining, 303
magnesium oxide, 3
magnetic
  entropy change, 297
  hardening, 257
  precipitates, 71
  properties, 245, 333, 511, 641
magnetocaloric effect, 297
manganese, 497
mass spectrometry, 479
MCM-41, 417
mechanical
  alloying, 257, 265, 591, 641
  milling, 641
melt spinning, 89
melting point, 115
mesoporous, 387, 423
  matrix, 417
mesostructure, 429
metallic glass, 101
metals, 635
methasis, 659
Mg-Ca-Zn, 89
micro-Raman, 529
microstructure(s), 225, 577
microtubules, 65
microwave plasma process, 41
Mn-doped, 133
modification, 235
modulated-temperature differential scanning
  calorimetry, 101
molecular dynamic simulation, 667, 673
molybdenum oxide, 659
monodisperse, 83
morphological, 603
Mössbauer
  effect, 41
  spectroscopy, 257
multilayer, 635
multi-phased nanostructures coatings, 339

nanoceramics, 547
nanocluster, 667
nanocomposite(s), 253, 297, 303, 327, 353, 363, 375, 399, 405, 441, 641
  film, 597
  material, 417
  of molybdenum, 315
  of tungsten, 315
nanocrystal(s), 115, 139, 151, 405, 503, 597
nanocrystalline, 53, 101, 205, 461, 541, 647, 653
  ceramics, 253
  ceria, 447
  ITO, 27
  phase, 95
  silicon, 199
nanolaminate, 603
nanomaterials, 497
nanometal composites, 605
nanoparticles, 15, 41, 47, 59, 65, 77, 107, 167, 175, 291, 467, 472, 479, 491, 511, 635
  of platinum, 315
nanophase materials, 283
nanoporous alumina, 553
nanorods, 3
nano-sized powders, 121
nanostructure, 297, 353, 571
nanostructured, 277
  films, 193, 283
nanotechnology, 523
nanotubes, 393
nanowires, 213, 219, 235, 239, 245, 623
negative
  capacitance, 15
  ion implantation, 181
Ni-Al thin films, 571
Ni(C) and Ni(O) nanoparticles, 535
nickel, 47, 517
nonlinear optics, 605
non-lithographic patterning, 115

olivine structure, 411
optical
  characterization, 485
  composites, 411
organic/inorganic composite, 381
organometallic precursor, 479
orientated co-precipitates, 71
oxide ceramics, 641

parallel computer, 673
pentane isomerization, 315
phase
  transformation, 89
  transition, 429
phosphate, 387
phosphorous, 517
photoelectrochemical, 653
photolithographic technique, 423
photoluminescence, 565, 647
photon correlation spectroscopy, 309
pillared clays, 435
planarization, 553
plasma(-)
  CVD, 565
  enhanced chemical vapor deposition, 199
polycarbosilane, 205
polycrystalline, 461
  ceria, 449
  silicon, 199
polymer, 405, 503
  electrolyte, 381
positron spectroscopy, 187
powders, 53
protein assemblies, 65
proton conductor, 381
pulse discharge sintering, 591
pulsed laser deposition, 163

quantum
  dot, 139
  size effects, 163

radioactive implants, 523
Raman spectroscopy, 145, 597
rapid solidification processing, 101
reduction, 53, 345
relaxation, 309
relaxors, 529
residual stress, 303
resin, 369
resorcinarene, 59
reverse micelles, 107
Rietveld analysis, 257
rutile, 33, 467

sapphire, 577
second harmonic generation, 605
segregation, 517
selective reduction of nitrogen oxides by hydrocarbons, 435
self-assembly, 47, 181
self-assembled nanostructures, 529
self-assembling, 429
self-capped, 175
semiconducting oxides, 121
SiC, 205
SiGe, 187
silica on yttrium iron garnet, 21
silicon, 235, 647
  carbide, 235, 673
  dioxide, 647
  nanowires, 225, 231
siloxane, 375

silver, 435
  colloid, 83
  nanoparticles, 83
single crystalline nanoparticles, 83
sintering, 491, 673
SnO_2-based sensors, 559
soft chemistry, 441
sol gel, 547
solar, 157
  cells, 653
sol-gel, 363, 411
  process, 381
  processing, 333
solid solution, 529
spheroid, 485
spin-glass ordering, 511
stability, 603
steady state, 271
stents, 523
strength, 577
structural and optical properties, 565
structure, 213, 245
subsurface
  microstructure, 303
  reaction, 327
superhard nanocomposites, 321
superhardness, 321
superparamagnetism, 41, 535
supersonic impaction, 193
surface
  characterization, 449
  functionalization, 169
  nanocomposites, 71
  reactions, 559
surfactant(/), 387
  Si ratio, 423
susceptibility, 41
synthesis, 3, 219

Te, 157
TEM, 107, 213
templates, 393
thermal
  analysis, 363
  conductivity, 591
  treatments, 609
thermoelectric materials, 219, 591
thermolysis, 133, 291
thick films, 121, 193
thin film, 423
  transistor, 115
thiocarbamate, 133
III-V compound semiconductors, 145
Ti-6%Al-4%V, 133
TiC, 33
tight binding method, 673
tin, 283
  oxide, 9
$TiN-Si_3N_4-TiS_2$, 321
TiO_2, 33, 667
titanium
  boride, 265
  oxide, 9
Ti-W-C, 339
Tollen's process, 83
TOPO (tri-n-octylphosphine oxide), 133
transition metal, 239, 353
  oxide, 441
transmission electron microscopy, 89, 363, 467
tungsten
  carbide, 193
  trioxide, 15
twin defect, 239
II-VI
  compound semiconductors, 145
  semiconductors, 151

ultrafine powder, 33
ultra-small angle x-ray scattering, 399
ultrasonic force microscopy, 473
undercooled, 277

vanadia(/), 429
  surfactant composites, 429
vanadium, 497
  oxide, 387, 393
voids, 467

WC, 339

XPS, 345, 609
x-ray diffraction, 363

yttrium iron garnet, 21

Z-contrast, 503
zirconia, 345, 435, 547